

Advances in Material Research and Technology

Shadia Jamil Ikhmayies *Editor*

Advanced Composites

 Springer

Advances in Material Research and Technology

Series Editor

Shadia Jamil Ikhmayies, Physics Department, Isra University, Amman, Jordan


This Series covers the advances and developments in a wide range of materials such as energy materials, optoelectronic materials, minerals, composites, alloys and compounds, polymers, green materials, semiconductors, polymers, glasses, nanomaterials, magnetic materials, superconducting materials, high temperature materials, environmental materials, Piezoelectric Materials, ceramics, and fibers.

Shadia Jamil Ikhmayies
Editor

Advanced Composites

 Springer

Editor

Shadia Jamil Ikhmayies 
Department of Physics, School of Science
University of Jordan
Amman, Jordan

ISSN 2662-4761

ISSN 2662-477X (electronic)

Advances in Material Research and Technology

ISBN 978-3-031-42730-5

ISBN 978-3-031-42731-2 (eBook)

<https://doi.org/10.1007/978-3-031-42731-2>

© The Editor(s) (if applicable) and The Author(s), under exclusive license to Springer Nature Switzerland AG 2024

This work is subject to copyright. All rights are solely and exclusively licensed by the Publisher, whether the whole or part of the material is concerned, specifically the rights of translation, reprinting, reuse of illustrations, recitation, broadcasting, reproduction on microfilms or in any other physical way, and transmission or information storage and retrieval, electronic adaptation, computer software, or by similar or dissimilar methodology now known or hereafter developed.

The use of general descriptive names, registered names, trademarks, service marks, etc. in this publication does not imply, even in the absence of a specific statement, that such names are exempt from the relevant protective laws and regulations and therefore free for general use.

The publisher, the authors, and the editors are safe to assume that the advice and information in this book are believed to be true and accurate at the date of publication. Neither the publisher nor the authors or the editors give a warranty, expressed or implied, with respect to the material contained herein or for any errors or omissions that may have been made. The publisher remains neutral with regard to jurisdictional claims in published maps and institutional affiliations.

This Springer imprint is published by the registered company Springer Nature Switzerland AG
The registered company address is: Gewerbestrasse 11, 6330 Cham, Switzerland

Paper in this product is recyclable.

Preface

It is well known that composites have two phases, the matrix phase and the dispersed phase, where the matrix phase known as the “binder” is a continuous phase, and may be metallic, non-metallic, or polymeric materials. Whereas the dispersed phase, known as “reinforcement” or “filler” is a phase that enters the matrix, and can be a fibrous material such as glass or organic fibers, among others. The matrix phase presents specific physical and mechanical properties such as ductility, formability, and thermal conductivity. The reinforcement phase is generally stronger and more rigid than the matrix phase, and has low coefficient of thermal expansion, high strength, and high rigidity, because it bears the load applied to the material. Properties of a composite material are different from those of the original constituents, but they are a synergistic combination of them. Composite materials are recognized as the most advanced substances, and are very important for a wide range of applications.

Advanced composites are recognized by light weight, high strength, high hardness, excellent fatigue resistance, and corrosion resistance. Advanced composites can be divided into three categories: Metal Matrix Composite (MMC), Ceramic Matrix Composite (CMC), and Polymer Matrix Composite (PMC). Advanced composites generally feature fibers that have a higher stiffness or elasticity modulus than other materials, while being bound together by weaker matrices. Due to their favorable properties, advanced composites are used in various industrial applications. These properties include but are not limited to stiffness, strength, light weight, and chemical resistance.

This book presents recent research results and reviews written by scientists and experts in the field of advanced composite materials from several countries in the globe. The chapters of this book are useful to a wide range of audience including but not restricted to undergraduate and graduate students, industrial professionals, composite manufacturers, materials scientists, and researchers. The book consists of eighteen chapters, dealing with manufacturing, structural, mechanical, thermodynamic, and electrical properties of advanced composites, as well as applications. The following paragraphs provide brief ideas about the contents of this book.

Chapter one, “[Classification and Application of Advanced Composite Materials](#)” by Manish Srivastava et al. is an introductory chapter dealing with the classification and applications of advanced composite materials. Chapter two, “[Advanced Composites of Nanomaterials and Their Applications](#)” by Priyanka Ghanghas et al., provides an introduction to advanced nanocomposites with brief ideas on fabrication techniques, engineering aspects, and applications. While chapter three, “[Advances in Composites for Solid-Phase \(Micro\) Extraction](#)” by Yanjuan Liu et al., discusses commonly used composites prepared based on Metalorganic Frameworks (MOFs), covalent organic frameworks (COFs), and carbon materials, where two important sample preparation techniques: Solid-phase Extraction (SPE) and Solid-phase Microextraction (SPME) are overviewed. Furthermore, the extraction mechanisms, current challenges, and potential directions for the applications of the composites in SPE and SPME are presented and discussed.

Chapter four, “[Composite Materials for Ballistic Applications](#)” by Ali Imran Ayten and Mehmet Atilla Tasdelen introduces the reader to ballistic threats, fibers and fabric types used in personnel ballistics, and ballistic impact mechanisms in armor structures. The chapter focuses on the synthesis, analysis, and modeling of composite materials used in ballistic applications. Possible future trends in ballistic materials and structures are summarized too. In chapter five “[Additive Manufacturing for Complex Geometries in Polymer Composites](#)” by López-Barroso Juventino et al., the authors present a review of additive manufacturing for the generation of complex geometries of polymer composites and their applications. The chapter gives investigations related to geometries in cores for sandwich structures in polymer composites. It also discusses cellular, auxetic, and complex geometrical properties, along with advances in polymer composites, and their applications. Chapter six, “[Eco/Friendly Polymer-Based Composites for Nuclear Shielding Applications](#)” by F. Akman et al. presents an experimental work in which the authors focus on gamma- and neutron-radiation shielding performance of polymer composites incorporated with Bismuth (III) Nitrate Pentahydrate (BiNO) as a filler. The gamma attenuation behavior of the prepared composites was measured and compared with the results calculated by (GEANT4) simulation code and WinXCOM software. Besides, fast neutron removal cross-section values of the investigated composites were calculated through the simulation code. It is expected that the researchers and scientists in the fields of nuclear and medical physics will benefit from this chapter.

Chapter seven, “[Mechanical and Tribological Behavior of Hybrid Polymer and Hybrid Sandwich Composites](#)” by Vasavi Boggarapu et al., deals with the mechanical, and tribological behavior of advanced particulate, hybrid polymer, and hybrid sandwich composites. Different fillers such as egg shell, arhar, $g-C_3N_4$, and TiO_2 were added to epoxy resin to prepare a variety of composites. The influence of parameters such as fiber orientation, filler size and content, and fiber volume fraction were discussed. Chapter eight, “[Nanocomposites Based on Conducting Polymers and Nanomaterials Derived from Natural Polymers](#)” by Alessandra Alves Correa et al., presents an overview of conducting polymers and nanocomposites based

on them and associated with nanostructures derived from natural polymers. It also discusses the fabrication techniques of these nanocomposites and their technological applications.

In chapter nine entitled “[Mechanical and Sliding Wear Performance of ZA27-Gr Alloy Composites for Bearing Applications: Analysis Using Preference Selection Index Method](#)” the authors Ashiwani Kumar and Mukesh Kumar present experimental work on mechanical and sliding wear performance of graphite (0–6 wt. %) reinforced ZA-27 alloy composites following ASTM standards. The authors found that the design of sliding wear experiments follows the Taguchi methodology. In chapter ten entitled “[Mechanical and Tribological Aspects of Aluminium Alloy Composites for Gear Application—A Review](#)” by the same authors, the mechanical and tribological aspects of aluminum alloy composites as a better alternative as a gear material are presented. They found that selection of particulate reinforcement type, proportion, size, and geometry lead to improved mechanical properties of aluminum alloy matrix that further enhances their sliding wear tribological performance.

In chapter eleven entitled “[Microcavity Mediated Light Emissions from Plasmonic and Dielectric Composites](#)” by Xianguang Yang et al. the authors reported an overview of plasmonic and dielectric composites. They have discussed the light emissions from quantum dots coupled to surface plasmons, and Mie resonances from gold spheres and silicon particles, respectively. The authors found that for gold microcavity, plasmon-mediated whispering-gallery-mode emission of quantum dots was realized, and for silicon microcavity, Mie resonance suppressed emission blinking of quantum dots was realized. These two types of plasmonic and dielectric composites would achieve the long-term goal of light confinement beyond the diffraction limit and provide various applications in nanophotonics. Chapter twelve, “[Fabrication and Application of Graphene-Composite Materials](#)” by Manish Srivastava et al., highlights some key findings regarding graphene polymers that can be used in electrochemical devices and have applications in the fields of coatings, solar cells, Light Emitting Diodes (LEDs), and others. The development of graphene in the form of nanofiller has been demonstrated as a novel source for the production of low-cost and high-performance composites for a wide range of applications. The authors briefly discussed the importance of graphene composites, their fabrication methods, properties, and applications, as well as some of the main challenges and their overcoming. Chapter thirteen, “[Sustainable Grinding Performances of Nano SiC Reinforced Al Matrix Composites Under Minimum Quantity Lubrication \(MQL\)](#)” by A. Nandakumar et al., presents experimental work on various Minimum Quantity Lubrication (MQL) as environmental cognisant machining with vegetable-based cutting fluids, and nano filled cutting fluids. A horizontal spindle cylindrical grinding machine is used for conducting the experiments while considering the process parameters such as wheel speed, workpiece speed, Depth of cut, and wt. % of nano SiC. The authors discussed the performance of eco-friendly machining with surface finish and cutting force. In addition, surface roughness and cutting forces were predicted by developing second-order mathematical models based on D-optimal design.

Chapter fourteen entitled “[Waste-Based Zeolites and their Advanced Composites for Wastewater and Environmental Remediation Applications](#)” by Niladri Shekhar Samanta et al. discusses techniques for preparing zeolite by conventional and advanced methods. The chapter mainly focuses on the use of various industrial waste sources for the preparation of zeolite. Furthermore, the synthesis of several advanced zeolite-based composites is described in this chapter along with their specific use in environmental remediation applications. This chapter also outlines recent developments and future scope of advanced zeolite composite materials which can prove to be more efficient in process-based applications. Chapter fifteen entitled “[Advanced Composites for Drug Adsorption](#)” by Thaís Strieder Machado et al. highlights developments in the use of composites for drug delivery. The chapter presents the state of the art in advanced composite materials that have been developed for drug removal through the adsorption technique. The authors described the classification of composites, addressed the principles of adsorption technique, and performed a bibliometric analysis to satisfy recent advances of composite materials.

Chapter sixteen entitled “[Advances in Manufacturing and Processing of Discontinuous Particle-Reinforced Titanium Matrix Composites \(TMCs\)](#)” by Yaya Wu et al. introduces key preparation technologies of discontinuous particle reinforced Titanium Matrix Composites (TMCs). TMCs are processed by heat treatment or Electro-Pulsing Treatment (EPT) to modify and improve their microstructure. By modifying the structure and the phase content of TMCs, the performance of TMCs can be improved. TMCs are used in the manufacturing of automobile industry, aerospace industry, and used to eliminate many potential safety hazards. Moreover, they play an important role in the field of medicine. Chapter seventeen which is entitled “[Metal-Based Electrical Contact Materials](#)” by Temel Varol and Onur Güler this outlines the synthesis, production methods, application fields, environmental effects, economic value, and performance requirements of Electrical Contact Materials (ECMs). The authors reported that the most effective method to be used for future fabrication of ECMs is Additive manufacturing techniques, although it is still early days for commercial manufacturers. Finally, chapter eighteen, “[Organosulfur Polymer Composites by Free Radical Polymerization of Sulfur with Vegetable Oils](#)” by Amin Abbasi et al. briefly reviews the progress taking place in the application of the inverse vulcanization process for the preparation of organosulfur polymeric composites made using vegetable oils as green monomers. The authors discussed properties of the reported organosulfur polymeric composites made based on a variety of vegetable oils. They also identified the challenges and the future perspectives for this type of environmentally friendly and low-cost polymeric composites.

Contents

| | |
|---|-----|
| Classification and Application of Advanced Composite Materials | 1 |
| Manish Srivastava, Anamika Srivastava, Nirmala Kumari Jangid, Anjali Yadav, and Sunidhi | |
| Advanced Composites of Nanomaterials and Their Applications | 37 |
| Priyanka Ghanghas, Nirmala Kumari Jangid, and Kavita Poonia | |
| Advances in Composites for Solid-Phase (Micro) Extraction | 59 |
| Yanjuan Liu, Zhen Wang, and Min Sun | |
| Composite Materials for Ballistic Applications | 93 |
| Ali Imran Ayten and Mehmet Atilla Tasdelen | |
| Additive Manufacturing for Complex Geometries in Polymer Composites | 121 |
| Juventino López-Barroso, Cynthia Graciela Flores-Hernández, Ana Laura Martínez-Hernández, Gonzalo Martínez-Barrera, and Carlos Velasco-Santos | |
| Eco/Friendly Polymer-Based Composites for Nuclear Shielding Applications | 187 |
| F. Akman, H. Ogul, M. R. Kaçal, H. Polat, K. Dilsiz, and O. Agar | |
| Mechanical and Tribological Behavior of Hybrid Polymer and Hybrid Sandwich Composites | 233 |
| Vasavi Boggarapu, Raghavendra Gujjala, Syam Prasad, Shakuntala Ojha, and Om Prakash Mingu | |
| Nanocomposites Based on Conducting Polymers and Nanomaterials Derived from Natural Polymers | 269 |
| Alessandra Alves Correa, Ana Carolina Correa, Kelcilene Bruna Ricardo Teodoro, José Manoel Marconcini, and Lucia Helena Mascaro | |

| | |
|---|-----|
| Mechanical and Sliding Wear Performance of ZA27-Gr Alloy Composites for Bearing Applications: Analysis Using Preference Selection Index Method | 317 |
| Ashiwani Kumar and Mukesh Kumar | |
| Mechanical and Tribological Aspects of Aluminium Alloy Composites for Gear Application—A Review | 343 |
| Ashiwani Kumar and Mukesh Kumar | |
| Microcavity Mediated Light Emissions from Plasmonic and Dielectric Composites | 369 |
| Xiangang Yang, Jiahao Yan, and Baojun Li | |
| Fabrication and Application of Graphene-Composite Materials | 391 |
| Manish Srivastava, Bharti Mehlawt, Anamika Srivastava, and Nirmala Kumari Jangid | |
| Sustainable Grinding Performances of Nano SiC Reinforced Al Matrix Composites Under Minimum Quantity Lubrication (MQL) | 423 |
| A. Nandakumar, T. Rajmohan, and S. Vijayabhaskar | |
| Waste-Based Zeolites and their Advanced Composites for Wastewater and Environmental Remediation Applications | 451 |
| Niladri Shekhar Samanta, Piyal Mondal, and Mihir K. Purkait | |
| Advanced Composites for Drug Adsorption | 491 |
| Thaís Strieder Machado, Brenda Isadora Soares Damin, Giovana Marchezi, Larissa Crestani, and Jeferson Steffanello Piccin | |
| Advances in Manufacturing and Processing of Discontinuous Particle-Reinforced Titanium Matrix Composites (TMCs) | 537 |
| Yaya Wu, Bingliang Liu, Siyu Ren, Run Miao, Liqiang Wang, Weijie Lu, and Lechun Xie | |
| Metal-Based Electrical Contact Materials | 565 |
| Temel Varol and Onur Güler | |
| Organosulfur Polymer Composites by Free Radical Polymerization of Sulfur with Vegetable Oils | 601 |
| Amin Abbasi, Ali Shaan Manzoor Ghumman, Mohamed Mahmoud Nasef, Wan Zaireen Nisa Yahya, Muhammad Rashid Shamsuddin, and Muhammad Moniruzzaman | |
| Index | 621 |

Classification and Application of Advanced Composite Materials



Manish Srivastava, Anamika Srivastava, Nirmala Kumari Jangid, Anjali Yadav, and Sunidhi

Abstract Composite materials are materials that consist of strong carry-load materials which are embedded in a somewhat weaker material. The stronger material is commonly referred to as reinforcement and the weaker material is commonly referred to as the matrix. The composite materials are based on the different types such as polymer matrix composites, nanocomposites, metal matrix composites, ceramic matrix composites, and carbon/carbon composites. Advanced composite materials have broad, proven applications, in the aircraft, aerospace, and sports equipment sectors. Metal matrix and ceramic matrix composites are widely used in engineering applications at different operating temperatures. Carbon/carbon composites meet applications ranging from rockets to aerospace because of their ability to maintain and even increase their structural properties at extreme temperatures. Similarly, nanocomposites are also applied in many areas, and in novel applications such as solid polymer electrolytes for batteries, automotive engine parts, thin-film capacitors for computer chips, and fuel tanks, impellers and blades, oxygen and gas barriers and food packaging source, etc. This chapter deals with the classification and application of advanced composite materials.

Keywords Polymer matrix composites · Metal matrix composites · Ceramic matrix composites · Carbon/carbon composites · Applications

M. Srivastava (✉)

Department of Chemistry, University of Allahabad, Prayagraj, Uttar Pradesh, India
e-mail: sagermanish1@gmail.com

A. Srivastava · N. K. Jangid · A. Yadav · Sunidhi
Department of Chemistry, Banasthali Vidyapith, Banasthali, Rajasthan, India

1 Introduction

Composites are materials with two or more constituents with considerably different chemical and physical properties (Fig. 1) [1]. They cover a wide range of dimensions of mixing components [2]. The breakthrough of new methods in composites has produced great effect in our daily life [3].

Nanocomposites are the materials with a size smaller than 100 nm. Unique physicochemical properties and large specific area is exhibited by the nanocomposites. In the last few decades, extensive research was going on this field and there are still a lot of challenges [4–8]. Mixed property is not produced simply by the combination of different constituents into one unit, but new physicochemical properties that were not present in the individual components are generated. For example, negative permittivity is not present in the traditional materials but exists in carbon nanocomposites and engineered polymer [9–11]. The hybrid and the composite materials, in which thermo sensitivity and mechanical strength are increased, magnetic, optical, thermal, anticorrosive, and electrical properties are regulated, chemical and thermal stability are improved by the synergistic combination of multi-scale components [12–15]. An example includes that about 85% development in the tensile strength was observed by introducing multi-wall carbon nanotubes functionalized polyaniline into the epoxy matrix [16]. Incorporation of 0.3 wt.% carbon nanotubes results in the increase of electrical conductivity of polypropylene by ~ 7 [17]. The thermal conductivity of polyphenylene sulfide increases 20 times on adding 40 wt.% functionalized graphite nanoplatelets as compared to pure polypropylene sulfide [18].

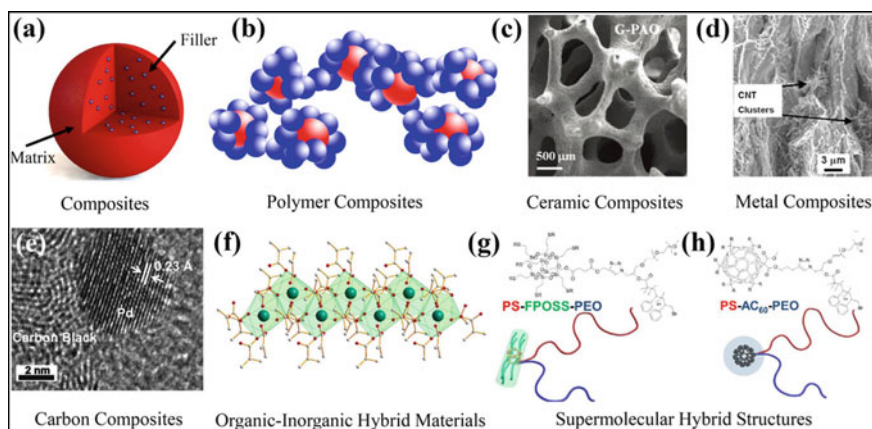


Fig. 1 **a** Composites, **b** polymer composites, **c** ceramic composites, **d** metal composites, **e** carbon composites, **f** organic-inorganic hybrid materials, **g**, **h** super molecular hybrid structure. Reprinted with permission from Gu et al. [1]. Copyright (2017). Springer Nature

1.1 Merits of Composite Materials

Composite materials are stiff, lightweight, and strong. The strength-to-weight ratios are several times higher than aluminum and steel. Moreover, composite materials are distinguished by

- Low density
- Low thermal conductivity
- Low coefficient of thermal expansion
- Better temperature-dependent behavior
- Better wear resistance
- Improved corrosion resistance
- High specific strength
- High specific stiffness
- High creep resistance
- Long fatigue life.

1.2 Disadvantages and Limitations of Composite Materials

- Anisotropic property is an important property of composite materials. The properties differ depending on the direction in which they are measured
- Composite materials are usually extremely expensive
- Expansion technique of determining the composite materials is normally very expensive and very slow
- Numerous polymer-based composites are subject to attack by chemicals or solvents.

2 Classification of Advanced Composite Materials

Composites are the materials consisting of two or more different phases bonded with each other. Polymers, carbon, metals, and ceramics are the four different classes of solid materials used for the matrix. Both matrix materials and reinforcements are found in each class. This results in the development of new materials with distinctive properties. Figure 2 [19] represents the types of material combinations that are now in use. Composites are generally classified by the materials utilized for the matrix and are divided into four categories: metal matrix composites (MMCs), carbon matrix composites (CAMCs), polymer matrix composites (PMCs), and ceramic matrix composites (CMCs). Nowadays, polymer matrix composites are the most extensively used composites.

Major types of reinforcements utilized in composite materials are whiskers, discontinuous fibers, aligned continuous fibers, and several forms of fibrous architectures which are formed by textile technology such as braids and fabrics. Carbon

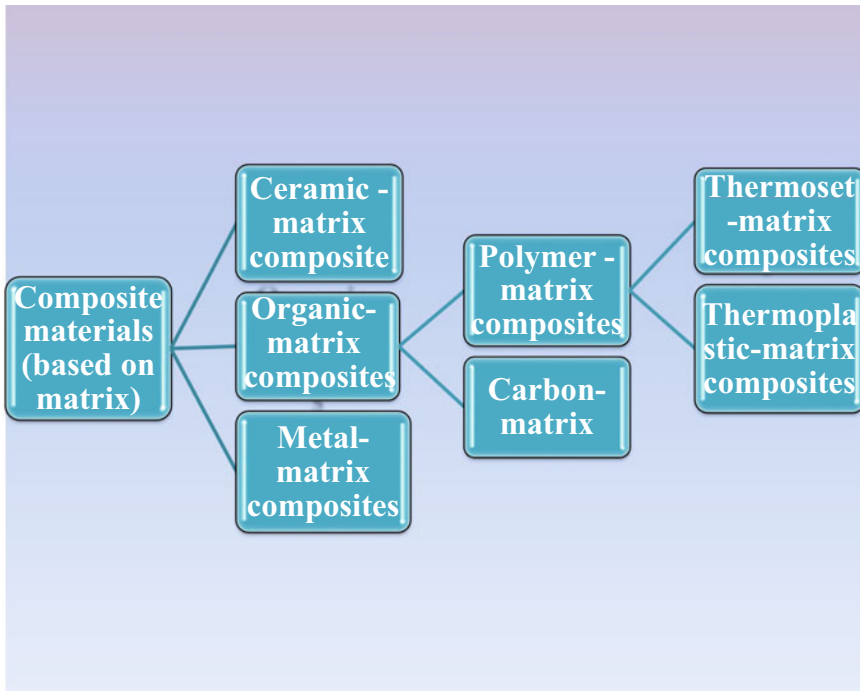


Fig. 2 Composite materials based on matrix material [19]

nanotubes (CNTs) are comparable to discontinuous fibers. Composites reinforced with fibers exhibit anisotropic properties, i.e., these properties change with direction. PMCs, MMCs, and CAMCs are various fiber-reinforced composites shown in Fig. 2 [19]. Materials reinforced with fibers produce strong, and reliable structural components in limitless applications. Based on the geometry of reinforcement, composites are classified as particulate reinforced composites, fiber-reinforced composites, and whisker/flakes reinforced composites.

Composites are considered as heterogeneous materials and their properties depend on the material phases. Toughness imparted due to the failure of the machine results in the heterogeneous nature of the composites. Special design methods are utilized by the unique individuality of composite materials.

2.1 Classification Based on Matrix

2.1.1 Polymer Matrix Composites

These composites are generally weak, viscoelastic, and low-stiffness materials. The reinforcing fibers result in the stiffness and strength of polymer matrix composites. Thermosets and thermoplastics are the two classifications of the polymer which are utilized as matrix materials. Nowadays, there is extensive usage of thermosets for structural applications. Thermosets exhibit more resistance to corrosive environments and solvents as compared to thermoplastics. The selection of resin is based on cost, design necessities, and manufacturing considerations. The representative properties of common matrix polymers are presented in Table 1 [20]. The maximum service temperature is the main concern for the selection of matrix. An increase in the temperature results in a decrease of the strength and elastic properties of the polymers. T_g is the glass transition temperature which indicates a transition of polymer from a comparatively stiff material to a rubbery one. However, a reasonable loss of stiffness and strength of polymers above the glass transition temperatures is expected. On the other hand, there is the development of polymers with enhanced high-temperature properties that can compete with a wide variety of metals. For example, titanium is replaced by carbon fiber reinforced polyimide in some engine parts of aircraft gas turbines. Moisture sensitivity is the major consideration in the polymer matrices selection. There is a decrease in the stiffness, glass transition temperature, and strength, which causes dimensional changes due to the adsorption of water by resins.

Thermoplastics exhibit superior biological and mechanical properties. Epoxy resin is the most significant matrix polymer. Moisture is desorbed by resins on placing in a dry place. The desorption and adsorption rates depend upon the temperature. Resins are moisture sensitive and some of them are very resistant. The organic and inorganic chemicals which are outgassed by resins in the vacuum are condensed on the surface. Emissivity and absorptivity are the surface properties which are affected by them. Outgassing can be restricted by baking out the components, and by choice of resin.

Thermosetting Resins: Thermosetting polyimides, epoxies, vinyl esters, phenolic, bismaleimides, thermosetting polyesters, cyanate esters, and benzoxazines are the main thermosetting resins which are utilized in composites. Epoxies have applications in aerospace and can generate composites with outstanding structural properties. Epoxies result in the high-temperature capabilities of Bismaleimide resins and this was utilized for aerospace applications up to 200 °C. The temperature employed for thermosetting polyimides is in the range 250–290 °C. Hence, resins are developed nowadays with higher temperature limits. Epoxies are more moisture sensitive as compared to cyanate ester resins. Thermosetting polyesters are cheaper, corrosion resistant, and easy to process. Vinyl esters also exhibit commercial applications but more expensive and exhibit better corrosion resistance as compared to polyesters. Less smoke is produced on burning, and high-temperature resistance is

Table 1 Properties of some thermosetting and thermoplastics composites [20]

| | Density (g/cm ³) | Modulus (GPa) | Tensile strength (MPa) | Elongation to break (%) | Thermal conductivity (W m ⁻¹ K ⁻¹) | Coefficient of thermal expansion (ppm/K) |
|-----------------------------|------------------------------|---------------|------------------------|-------------------------|---|--|
| Polypropylene (2) | 1.05 | 1-4.5 | 25-38 | >300 | 0.3 | 61 |
| Thermosetting polyester (1) | 1.2-1.5 | 3-4.5 | 40-92 | 3 | 0.4 | 100-250 |
| Nylon 6-6 (2) | 1.14(0.041) | 1.4-2.8 | 60-75 | 40-80 | 0.3 | 110 |
| Polyetherimide (2) | 1.27(0.046) | 3.3 | 110 | 60 | - | 90 |
| Polysulfone (2) | 1.25(0.045) | 2.2 | 76 | 50-100 | - | 70 |
| Epoxy (1) | 1.2-1.5 | 3.1-6.2 | 35.5-99 | 1.5-6.5 | 0.2 | 56 |
| Polycarbonate (2) | 1.06-1.20(0.038-0.043) | 2.2-2.5 | 45-70 | 50-100 | 0.3 | 62 |
| Polyphenylene sulfide (2) | 1.36(0.049) | 3.95 | (65) | 4 | - | 63 |
| Polyether Etherketone (2) | 1.26-1.32(0.046-0.048) | 3.55 | 94 | 51 | - | 54 |
| Polyamideimide (2) | 1.4(0.050) | 4.90 | 190 | 17 | - | 47 |

(1) = Thermoset, (2) = Thermoplastic

exhibited by phenolic resins. Offshore oil platform structures and aircraft interiors are applications, where fire resistance is a major design condition.

Thermoplastic Resins: Crystalline, amorphous, and liquid crystal are the three major classes of thermoplastics. Amorphous materials include polystyrene, polycarbonate, polyetherimide, acrylonitrile–butadiene–styrene (ABS), polysulfone. Polyphenylene sulfide, nylon, polyether sulfone, polyethylene, polypropylene, polyether ether ketone (PEEK), and acetal are the crystalline thermoplastics. Poor solvent resistance is exhibited by amorphous thermoplastics. Table 1 lists some properties of thermosetting and thermoplastics polymer matrix composites.

2.1.2 Metal Matrix Composites (MMCs)

Alloys are originally utilized for metal matrix composites. Special matrix materials have been developed for their utilization in composites in the last few decades. Alloys of Fe, Si, and Al are the major metallic matrix materials that are utilized for structural metal matrix composites. Numerous research have been made on composites formed by the intermetallic compound matrix materials. Various metals such as Pb, Mg, Cu, Ag, and Co are utilized as matrix materials. The process of manufacture is responsible for the in situ properties of metals in a composite. These composite materials reutilized in engineering, where the temperature ranges between 250 and 750 °C.

2.1.3 Ceramic Matrix Composites (CMCs)

Mullite, silicon carbide, silicon nitride, alumina, and various types of cement are materials that are utilized as ceramic matrix composites. Ceramic properties such as strength are more process sensitive. It is found that the ceramic matrix in situ properties are difficult to be determined in the composite. Ceramics exhibit size effect which results in an increase in the volume of the material with a decrease in the strength. Hence, the tensile strength of ceramics has no single value. The flexural and tensile strength of ceramics is difficult to measure due to their very brittle nature. It is observed that the flexural strength is dependent on the size of the specimen. 3–6 MPa m^{1/2} is the range of the fracture toughness of the ceramics. It was observed that the fracture toughness of structural metals is usually larger than 20 MPa m^{1/2}. Ceramic matrix composites are structural materials with ceramic matrix incorporated by metallic/non-metallic reinforcements. They are extensively utilized in engineering applications, where the temperature of operation ranges from 800 to 1650 °C.

2.1.4 Carbon Matrix Composites

The major subclass of carbon matrix composites is carbon-carbon composites, where the matrix is carbon (graphite) and reinforcement is carbon (graphite) fiber. Carbon exhibits outstanding properties and includes various materials such as diamonds, structural fibers, and lubricants. Carbon-carbon manufacturing processes result in the formation of carbon matrices which are brittle and weak materials. The precursor process and materials result in ranging of thermal conductivities from very low to high.

Applications

Carbon/carbon composites have wide applications ranging from rockets to aerospace.

Advantages

1. Stability at extreme temperatures.
2. Strength increases at higher temperatures.
3. High stiffness and strength.
4. Good stability to thermal shock.

2.2 Classification Based on Reinforcement

The mechanism of strengthening depends on the geometry and the shape of the reinforcements shown in Fig. 3 [19].

2.2.1 Particulate Reinforced Composites

These composites are used extensively due to their cost and availability. These composites are of two types:

1. Dispersion-strengthened
2. Particulate-reinforced composites.

These two types of sub-classes depend upon strengthening mechanism, i.e., dispersion-strengthened composites and particulate composites. The particles are in the range of 0.01–0.1 μm in the case of dispersion-strengthened composites. At this point, the strengthening occurs at an atomic/molecular level. Some of the examples are sintered aluminum powder, and thoria dispersed strengthened-alloy. Particulate composites are the second type of particle-reinforced composites. These composites consist of large amounts of moderately coarse particles. These composites are not designed to improve the strength but to produce unusual combinations of properties.

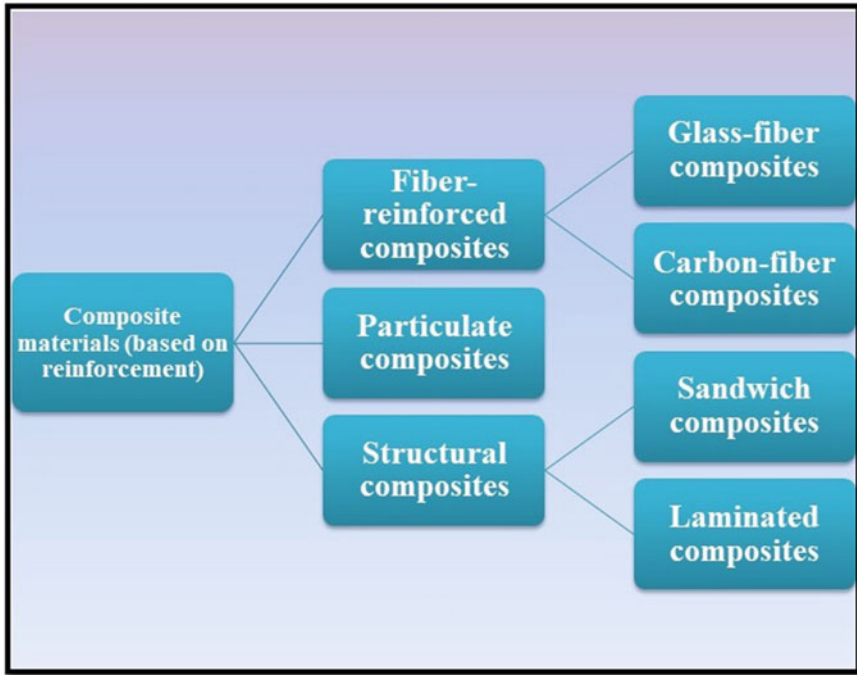


Fig. 3 Composite materials based on geometry and the shape of reinforcement [19]

2.2.2 Structural Composites

Structural composites are formed by glass, plastic, carbon fiber, and wood materials. This type of composite consists of both homogeneous and composite materials. Properties of structural composites depend on both the geometrical design of various structural elements, and on the properties of the constituents. Laminar composites and sandwich structures are the two types of composites that are extensively used [21].

(a) Laminar composites

These composites are formed by two-dimensional sheets/layers which have favored strength direction. Favored directions are possessed by these panels to attain high strength. Layers are stacked jointly in such a way that the direction of the high strength varies with each consecutive layer. Plywood is formed by gluing the alternative thin layers of wood together.

(b) Sandwich structures

These sandwich structures are formed by a combination of two or more individual components with different properties, thus resulting in materials with high performance. The skin material usually has high stiffness, while shear strength is exhibited by the core. High flexural modulus is exhibited by sandwich structure on their combination.

2.2.3 Fiber-Reinforced Composites (FRCs)

Fiber-reinforced composites are formed by cross-linking of cellulosic fiber molecules with resins, and they are considered as high-performance fiber composites. They are either continuous or discontinuous and they consist of three materials. Namely:

- The matrix as the continuous phase
- The fine inter-phase region
- The fibers as the discontinuous or dispersed phase.

Continuous reinforcement results in high stiffness and strength. Discontinuous fibers are utilized only when manufacturing economics dictate the use of a method where the fibers must be in this form. FRCs are further classified into glass fiber composites, and carbon fiber composites.

(a) Glass Fiber Composites

These composites are the most widely used reinforcement in end-market applications. These composites exhibit greater elongation-to-break, are more impact-resistant and weigh more than carbon fiber composites. The ratios of strength/weight for glass fiber composites are higher. They possess good electrical properties, resistance to chemicals and heat, and resistance to moisture and outdoor weathering [22].

(b) Carbon fiber composites

Matrix precursor by impregnation results in the formation of composites of carbon fiber in the liquid state. Pitch, polyacrylonitrile (PAN), and rayon are the various precursors that are used to prepare the high-performance carbon fibers. High-strength fibers are produced by chemically treating, heating, and stretching, then carbonizing the precursor fibers.

Fiber materials include

Glass: It has low density, high tensile strength, and is inexpensive. Glass fibers are generally utilized for the strengthening of polymer matrices.

Carbon-graphite: Carbon exhibits higher stiffness as compared to glass and has a density of 2.3 g cm^{-3} . The strength of carbon fibers is 15 times as compared to that of construction steel and 3 times as compared to the stiffness of steel. The graphitic structure due to its densely packed hexagonal layers is preferred over diamond-like crystalline forms to produce carbon fibers. It was observed that the thermal and mechanical properties are anisotropic.

Polymers: The impressive properties of polymers result from the strong covalent bonds. They have poor compressive properties, high stiffness, high tension, and toughness enhanced by Kevlar fibers.

Ceramics: Fibers prepared from ceramic materials such as silicon carbide and alumina are beneficial in high-temperature applications. They have poor shear properties and tension.

Metals: Metallic fibers exhibit high strength and density. The high density of metallic fibers results in their small use in weight critical applications. Drawing thin metallic fibers is very costly (Table 2).

2.3 Carbon Nanotubes (CNTs)-Based Nanocomposites

CNTs are considered as the strongest and stiffest man-made materials [23]. CNTs exhibit lower mass density, high tensile modulus, high flexibility, strength, and large aspect ratio. Single-walled carbon nanotubes are more conductive than copper due to transport of current without the considerable loss of strength [24–26]. Polymer nanocomposites formed by the CNTs were first reported in 1994 by Ajayan and coworkers [27]. After this much research in this area has been published. Production of carbon nanotube, chirality, length, and diameter are the various factors on which the properties of nanotubes/polymer depend. There is major difficulty due to carbon tube dispersion in the polymeric matrices. The poor electrical and mechanical properties result in the dispersion of carbon tubes failure. Also, the final products do not exhibit the excellent properties of carbon nanotubes such as high stiffness and strength [28]. A study has been made on the functionalization of CNTs to enhance their dispersion. Covalent or non-covalent modifications are the two important approaches on which functionalization is divided [29–31]. Chemical reaction of CNTs surface and the new species incorporation are involved in covalent modifications. Charge-transfer interactions, physical interactions, and van der Waals forces are covered by non-covalent interactions that can be utilized to wrap polymers around the CNTs.

3 Fabrication and Characterization of Advanced Composite Materials

3.1 Fabrication Technique

Several methods are used for the preparation of composite materials. Some techniques were developed to meet production challenges faced with fiber-reinforced polymers [32]. The choice of a technique for a meticulous part, consequently, will

Table 2 Properties of reinforcing fibers [20]

| S.N | Fiber | Density (g/cm ³) | Axial modulus (GPa) | Tensile strength (MPa) | Axial coefficient of thermal expansion (ppm/F) | Axial thermal conductivity (W m ⁻¹ k ⁻¹) |
|-----|-----------------------------------|------------------------------|---------------------|------------------------|--|---|
| | UHS ⁽¹⁾ carbon (PAN) | 1.79 | 290 | 7000 | -1.5 | 160 |
| | HS ⁽²⁾ glass | 2.5 | 83 | 4200 | 4.1 | 0.9 |
| | UHM ⁽³⁾ carbon (PAN) | 1.89 | 590 | 3800 | -1 | 18 |
| | SiC monofilament | 3 | 400 | 3600 | 4.9 | - |
| | Boron | 2.59 | 400 | 3600 | 4.5 | - |
| | Si-Ti-C-O | 2.4 | 190 | 3300 | 3.1 | - |
| | SM ⁽⁴⁾ carbon (PAN) | 1.7 | 235 | 3200 | -0.5 | 9 |
| | Aramid | 1.4 | 124 | 3200 | -5.2 | 0.04 |
| | SiC multifilament | 3 | 400 | 3100 | - | - |
| | High-density polyethylene | 0.97 | 172 | 3000 | - | - |
| | Basalt | 2.7 | 100 | 2900 | 5.5 | 1.7 |
| | Si-C-O | 2.6 | 190 | 2900 | 4.0 | 1.4 |
| | UHM ⁽⁵⁾ carbon (pitch) | 2.2 | 895 | 2200 | -1.59 | 640 |
| | E-glass ⁽⁶⁾ | 2.6 | 70 | 2000 | 4.9 | 0.9 |
| | Aluminum oxide | 3.9 | 370 | 1900 | 7.9 | - |
| | UHK ⁽⁷⁾ carbon (pitch) | 2.2 | 830 | 2200 | -1.6 | 1100 |

(1) UHS: Ultrahigh strength, (2) HS: Heat-strengthened, (3) UHM: Ultra high modulus
(4) SM: Standard modulus, (5) UHM: Ultra high modulus, (6) E-glass: Electrical glass, (7) UHK: Ultrahigh—thermal conductivity

depend on the end-use, materials, application, and design. Variety of preparation techniques are as follows.

3.1.1 Hand Layup

It is the most important method for the preparation of thermoset composites. This method involves the formation of a laminate stack by placing layers of fibers by hand on the tool. After the completion of layup, resin is applied to the dry plies. There is a coating of resin and debulked on each ply in wet layup.

3.1.2 Curing Methods

Various curing methods exist. The most important is at room temperature by applying heat, pressure, and other curing techniques.

Pressure: High consolidation pressure or heat is required by various high-performance thermosets to cure the conditions which want the usage of an autoclave.

Heat: The temperature is “ramped up” in small increments when the heat is necessary for heal, then the temperature is retained for a specified period. Then part distortion is avoided by “ramped down” of temperature to room temperature.

3.1.3 Alternative Curing Methods

Electron-beam curing has been considered as an efficient method for curing the thin laminates. This method involves exposure of composite layup to electron streams which offers ionizing radiation and hence results in cross-linking and polymerization in radiation-sensitive resins. Similar procedures are employed for microwave and X-ray curing methods. Ultraviolet curing is the other technique that involves the usage of ultra-violet radiation.

3.1.4 Cure Monitoring

It involves the monitoring of the cure itself. The extent of healing by gauging the conductivity of ions is used to measure the dielectric cure. There is a migration of ions to the opposite polarity of the electrode. But the speed of migration depends upon the viscosity of the resin. The increase in viscosity results in the lowering of the speed.

3.1.5 Out-of-Autoclave (OOA)

This technique is gaining interest in the industry for high-performance composite components. Autoclave systems due to the limited size and high cost lead to their use in aerospace. Out-of-autoclave rein is first prepared by Cytac Aerospace Materials HQ for aerospace applications.

3.1.6 Resin Film Infusion (RFI)

It is the hybrid process in which a dry preform is placed in a mold on top of a layer. Uniform resin distribution occurs due to the liquefaction of resins under applied pressure, heat, and vacuum.

3.1.7 Injection Molding

It is a low-pressure, fast, closed pressure, and high-volume process. This process involves the injection of material through a heated barrel into a heated and closed mold. There is an easy flow of liquefied bulk molding compound (BMC) into the closed mold. Minimum finishing is required by the parts after cure and ejection. About 2,000 small parts are formed every hour in some multiple-cavity molds with an injection speed of 1–5 s.

3.2 Fabrication Methods of Nanocomposites Materials

3.2.1 Ceramic Matrix Nanocomposites (CMNC)

Numerous techniques can be used for the fabrication of nanocomposites of ceramic matrix [33–38]. Vapor techniques, conventional powder method, template synthesis, polymer precursor route, chemical methods such as spray pyrolysis, sol–gel process, precipitation, and colloidal approaches are some of the many techniques for the fabrication of micro composites. Control of chemical and structural properties of the final oxide materials is controlled by various parameters that affect the sol-gel process such as timing, water/metal ratio, type of solvent, precursor, and pH [39]. Various approaches have been described for the processing of CNT-reinforced ceramic nanocomposites [40–48].

3.2.2 Metal Matrix Nanocomposites (MMNC)

Spray pyrolysis, chemical methods such as sol-gel and colloidal processes, liquid metal infiltration, electrode position, rapid solidification, and vapor method are the

various techniques used for the processing of nanocomposites of metal matrix [49–53]. Only two reports are established, for example, the solidification technique used for the synthesis of nanocomposites of iron. “Devitrified nanocomposites steel” is the first one given by Branagan et al. [54]. First, the metallic glass obtained by quenching from an iron-based alloy, and then the glass precursor is devitrifying by heat action. Material with crystalline multi-phase microstructure is formed. Novel nanostructures are studied by Branagan and Tang [55] to explain the hardness of iron-based composites. Non-homogenous distribution and agglomeration results in the difficulties for the preparation of composites with very fine particles. The wettability between the particles and the matrix is enhanced by the help of ultrasound. Various techniques are employed for the preparation of MMCs reinforced with carbon nanotubes [56–63].

3.2.3 Polymer Matrix Nanocomposites (PMNC)

Several techniques are employed for the synthesis of polymer matrix nanocomposites [64–78]. The most important ones are

- Direct mixture of particulates and polymer
- in situ polymerization
- Intercalation of the polymer from solution
- Melt intercalation
- Template synthesis
- in situ intercalative polymerization
- Sol-gel process.

A variety of methods are available for amalgamation to incorporate nano dispersions into conducting polymer [79–81]. Nanocomposites based on polymers can be prepared using the intercalative process. It may be noted that, in this technique, a variety of nanocomposites are formed by this process depending on the extent of penetration of polymer chains into the silicate galleries. Combinations of polymer-layered silicate are prepared by this procedure. Melt-mixing, direct mixing, in situ polymerization, and solution mixing techniques are employed for the synthesis of polymer nanocomposites reinforced with carbon nanotubes. These are applicable to various systems [82, 83].

3.3 *Fabrication of Polyaniline Nanocomposites Containing ZnO Nanorods*

Wu et al. proposed a method for the preparation of nanorods of ZnO [84]. For structural and phase characterization of ZnO nanorods, Fig. 4 shows the x-ray diffraction (XRD) pattern [83, 84]. The transmission electron microscope (TEM) image shown in Fig. 5 revealed that the range of length of ZnO nanorods is 50–200 nm, and the

diameter values are in the range 20–50 nm. Aniline was distilled under reduced pressure, and tetraethylene pentamine was used without any purification. Camphor sulfonic acid and ammonium peroxydisulfate were used for doping and as oxidant, respectively. 0.05 mol of aniline monomer is mixed with nanorods in 200 mL of water. Uniform suspension of nanocomposites of polyaniline-ZnO was mixed using magnetic stirrer for 240 min in an ice-water bath [85, 86].

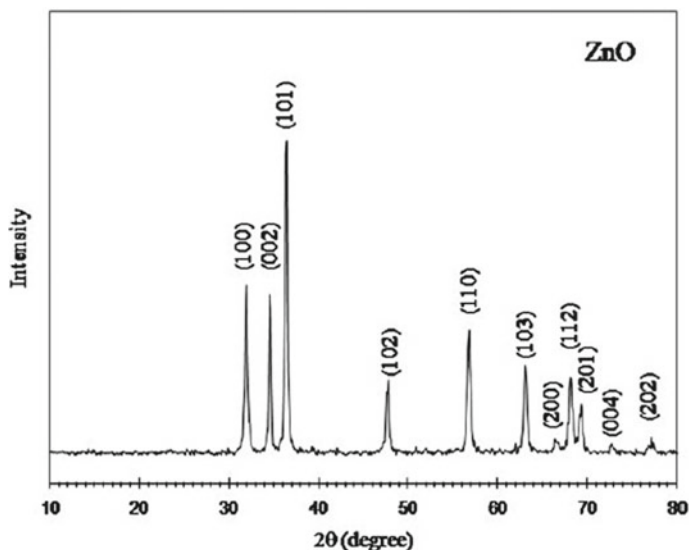
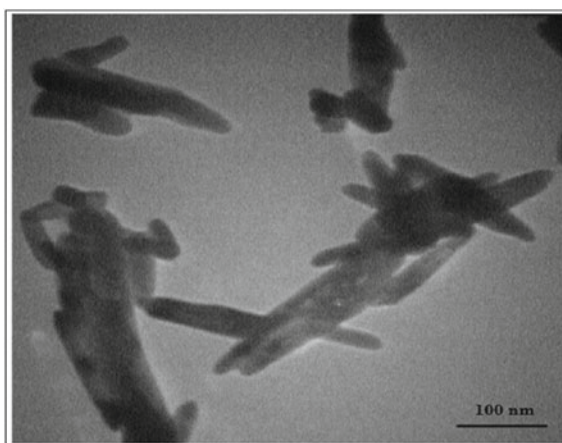


Fig. 4 XRD pattern of ZnO nanorods. Reprinted with permission from Mostafaeiand and Zolriasatein [87]. Copyright (2012), Elsevier

Fig. 5 TEM image of ZnO nanorods. Reprinted with permission from Mostafaeiand and Zolriasatein [87]. Copyright (2012), Elsevier



3.3.1 Characterization of Polyaniline Nanocomposites Containing ZnO Nanorods

IR analysis

Mostafaei and Zolriasatein [87] used Fourier transform infrared (FTIR) technique for the characterization of polyaniline and nanocomposites of polyaniline-ZnO. Figure 6 [87] shows the FTIR spectra of ZnO nanorods, polyaniline (PANI), and PANI-ZnO nanocomposites. 1572.51–1587.94 cm^{-1} matrix and elimination of agglomeration. The characteristic absorption bands of PANI are 515.71 cm^{-1} (C–N–C bonding mode of aromatic ring), 592.85 and 700.84 cm^{-1} (C–C, C–H bonding mode of aromatic ring), 831.98 cm^{-1} (C–H out of plane bonding in benzenoid ring), 1040.26 and 1155.97, 1302.53 and 1503.09 cm^{-1} (C–N stretching of benzenoid ring), and 1572.52 cm^{-1} (C=N stretching of quinoid ring). The PANI-ZnO nanocomposites show the same characteristic peaks. However, there is evidence of peak displacement when ZnO nanorods are added to the PANI. These shifts include 1572.51–1587.94, 1503.09–1510.81, 1155.97–1148.25, 1040.26–1047.97, 831.98–862.84, and 592.85–600.23 cm^{-1} . Furthermore, in PANI-ZnO nanocomposites, a broad peak appeared in 3470 cm^{-1} which can be associated with the interaction between ZnO nanorods and PANI by formation of hydrogen bonding between H–N and oxygen of ZnO, so the peak displacement which was observed in FTIR spectra may be ascribed to the formation of hydrogen bonding between ZnO and the N–H group of PANI on the surface of the ZnO nanorods [87].

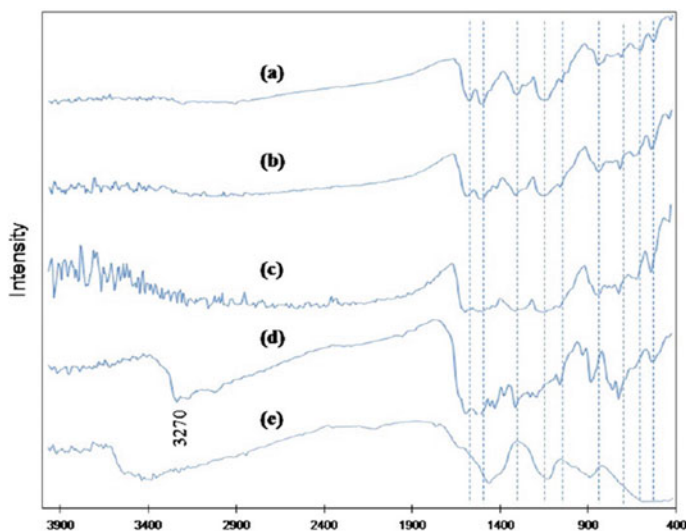


Fig. 6 FTIR spectra of **a** PANI, **b–d** PANI-ZnO (1 wt.%, 2 wt.%, and 4 wt.%) nanocomposites and **e** ZnO nanorods. Reprinted with permission from Mostafaei and Zolriasatein [87]. Copyright (2012), Elsevier

3.3.2 XRD Analysis

The structures of polyaniline and composite of polyaniline-ZnO were investigated by the XRD patterns. The perpendicular and parallel periodicity of the polymer chain results in the occurrence of broad diffraction peaks between 10° and 30° . PANI crystal size (D) is 4.4 nm, which was calculated by Scherrer's equation [87]. It was observed that polyaniline and nanocomposites exhibit similar XRD patterns (Fig. 7).

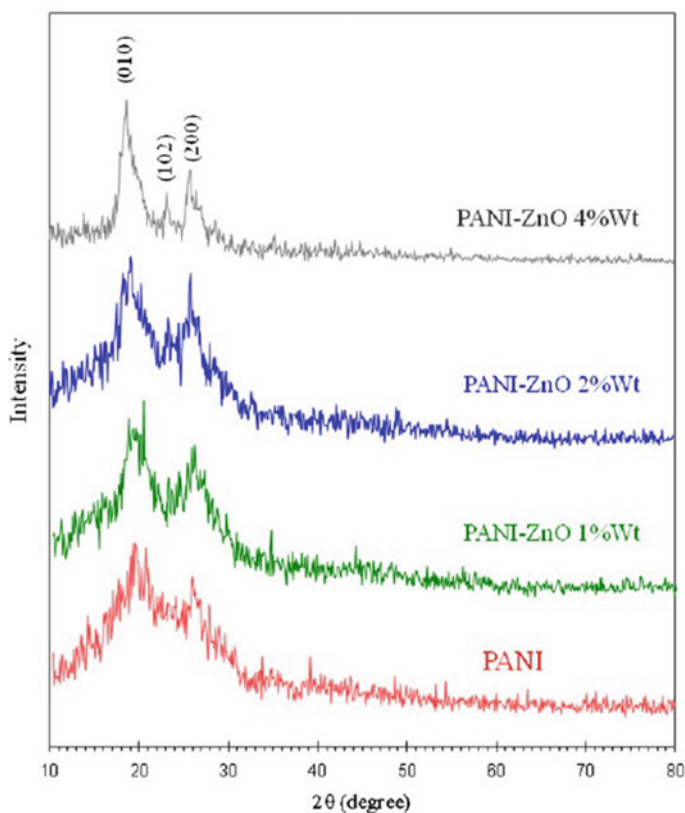


Fig. 7 X-Ray pattern of PANI and PANI-ZnO nanocomposites. Reprinted with permission from Mostafaei and Zolriasatein [87]. Copyright (2012), Elsevier

3.3.3 SEM Analysis

Figure 8 [87] presents the morphologies of the polyaniline and nanocomposites of polyaniline–ZnO with different ZnO nanorod contents. All the nanocomposites reveal the flaky shaped structure of nanocomposites, and its size decreases as ZnO nanorods percentage in polyaniline increases. The increase in the content of ZnO nanorods results in a decrease in the size of polyaniline/ZnO nanocomposite particles.

3.4 Fabrication of Chitosan–Polyaniline–Copper (II) Oxide Hybrid Composite

Rathore et al. [88] prepared chitosan–polyaniline–copper (II) oxide hybrid composite as follows. The solution of acetic acid and 1.0 g of chitosan was stirred for a day at room temperature. A homogenous solution of 1 M acetic acid and 0.01 M of aniline was obtained on stirring for half an hour. Solution of 15 g ammonium peroxydisulfate dissolved in acetic acid was added into the above solution and was stirred for 8 h. Greenish black precipitate obtained was converted into colorless by washing it with water and then with ethanol. The product obtained was dried for a day at 60 °C. Solution obtained by dissolving 1 g copper oxide and 5 g CuCl_2 in water is added into the composite of aniline–chitosan and this reaction mixture was heated for 120 min at 70 °C. The Greenish blue precipitate was obtained on cooling the reaction mixture for about 180 min and then washed with distilled water and methanol to obtain the colorless precipitate.

3.4.1 Characterization of Chitosan–Polyaniline–Copper (II) Oxide Hybrid Composite FTIR Spectra

Figure 9 [88] presents the FTIR spectra of (a) chitosan, (b) PANI, and (c) Ch–PANI–CuO nanocomposites. It shows the bands centered at 1645 and 1386 cm^{-1} are obtained for chitosan corresponding to the presence of residual –OH groups, which is due to the O–H vibrating mode of adsorbed water [89]. The range of bands for C–O–C linkage is 1154–1032 cm^{-1} . And the position of C–N peak is 898 cm^{-1} (Fig. 10a) [90]. The peak centered at 1460 cm^{-1} corresponds to C=C stretching of the benzenoid ring, peak centered at 1550 cm^{-1} corresponds to C=C stretching of the quinoid ring, peak located at 790 cm^{-1} corresponds to C–H stretching, while the peaks at 1230 and 1286 cm^{-1} correspond to C–N stretching and are the characteristic bands for polyaniline [91]. Peaks at 480, 530, and 580 cm^{-1} are the peaks corresponding to the vibrations of copper oxide in highly pure NPs of copper (II) oxide [92]. The combined peak of hydroxyl and N–H stretching vibrations leads to the appearance of a band at 3001 cm^{-1} . The amide group substituted with alkyl represents a peak at

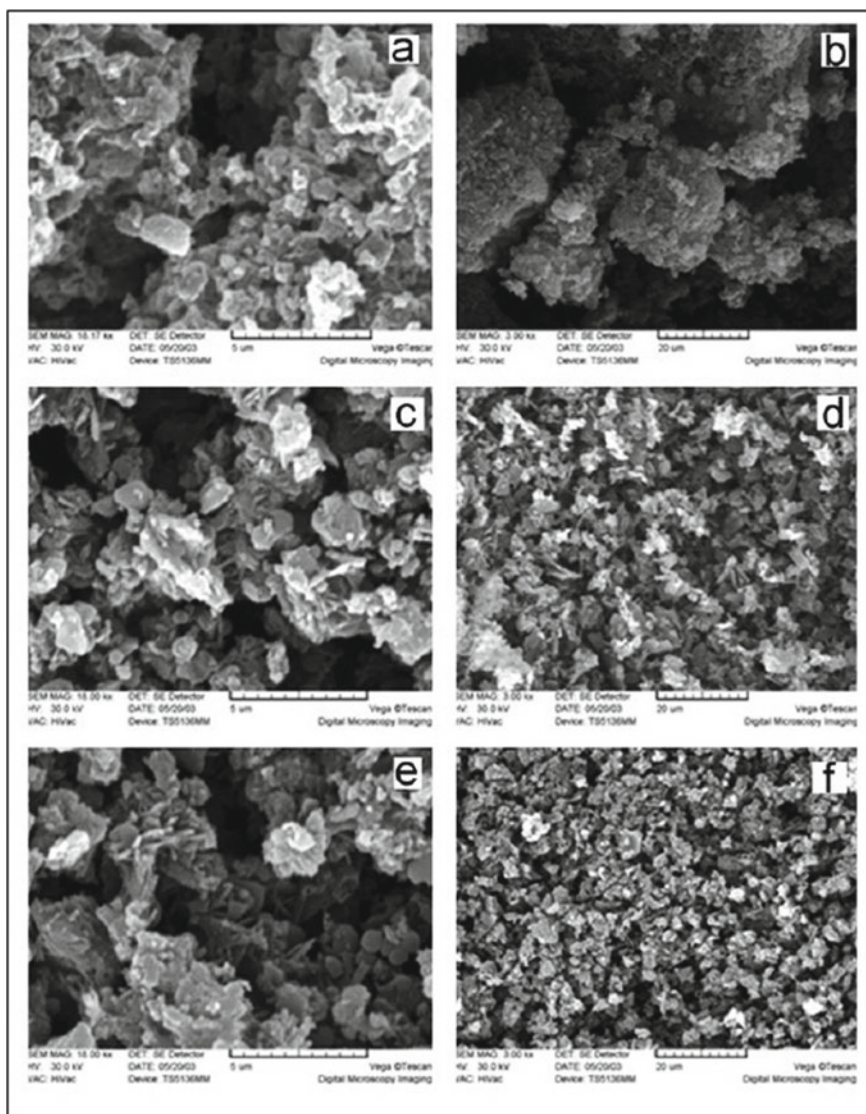


Fig. 8 SEM image of a, b PANI-ZnO 1 wt%, c, d PANI-ZnO₂ 1 wt% and e, f PANI-ZnO₄ 4 wt% nanocomposites. Reprinted with permission from Mostafaei and Zolriasatein [87]. Copyright (2012), Elsevier

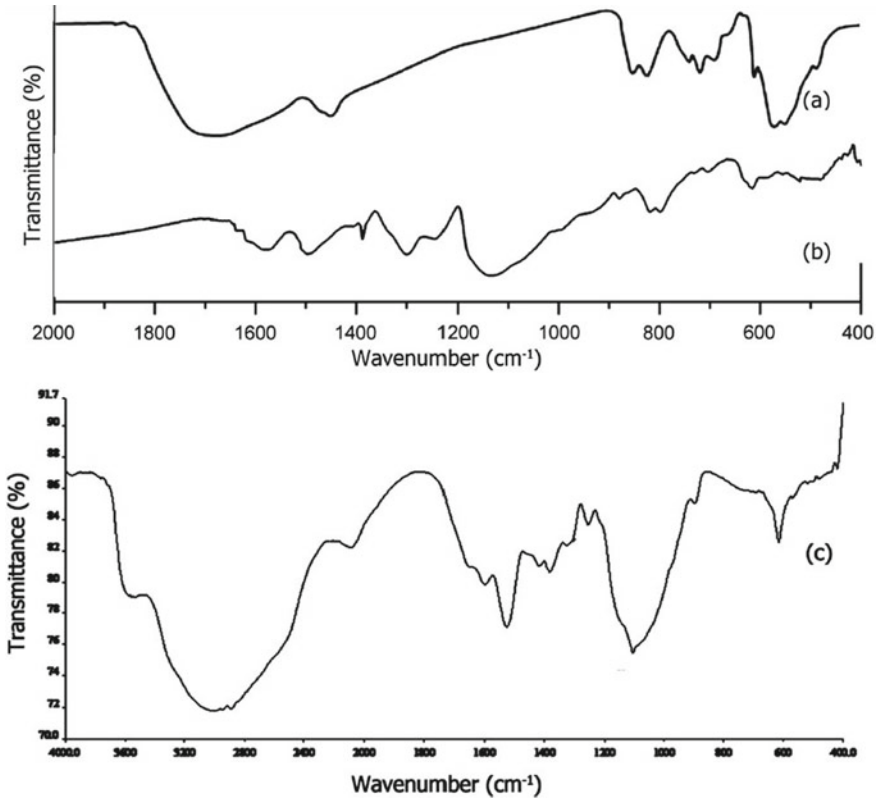


Fig. 9 FTIR spectra of **a** chitosan, **b** PANI, and **c** Ch-PANI-CuO nanocomposites. Reprinted with permission from Rathore et al. [88]. Copyright (2019), Springer Nature

1640 cm^{-1} [93]. The band at wavenumber 3001 cm^{-1} corresponds to the H-bonding of active hydroxyl groups between polyaniline and chitosan [94, 95]. The peak at 1527 cm^{-1} corresponds to N-H stretching, and peak at 1105 cm^{-1} was observed for C-O stretching vibration in chitosan. The band at 617 cm^{-1} corresponds to Cu-O vibrations in nanocomposites of chitosan-polyaniline-copper oxide.

3.4.2 XRD Analysis

The XRD patterns of chitosan in Fig. 10 [88] show diffraction peaks at 2θ values of 11.5° and 21° . The chitosan structure consists of inter- and intermolecular hydrogen between plenty of hydroxyl and amine groups, which results in higher extent of crystallinity (Fig. 10a). The semi-crystalline characteristic of polyaniline is indicated by the peaks at $2\theta = 9.8^\circ, 14.4^\circ, 19.6^\circ,$ and 24.8° (Fig. 10). The three peaks having

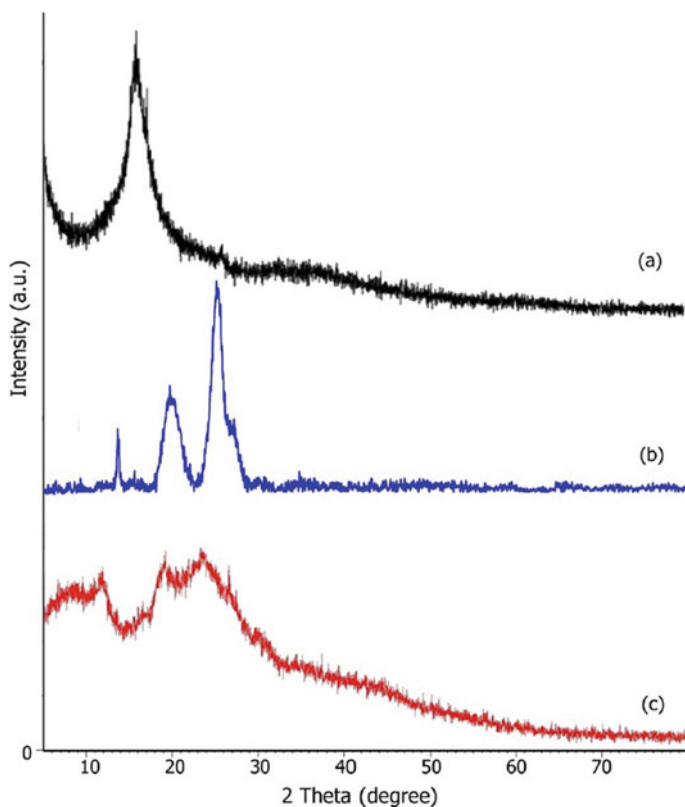


Fig. 10 XRD of **a** chitosan, **b** PANI, and **c** Ch-PANI-CuO nanocomposites. Reprinted with permission from Rathore et al. [88]. Copyright (2019), Springer Nature

2θ values of 35.6° , 38.8° , and 48.8° and have d-spacing values of 0.25, 0.23, and 0.18 nm, respectively, are related to monoclinic **structure** [88, 96, 97].

3.4.3 SEM Analysis

Figure 11 [88] shows the SEM and TEM images of nanocomposites of chitosan-polyaniline-copper oxide which have SEM image presented in Fig. 11. Spherical agglomerated particles are formed at few places. The substance homogeneity and uniform morphology can be observed in the images.

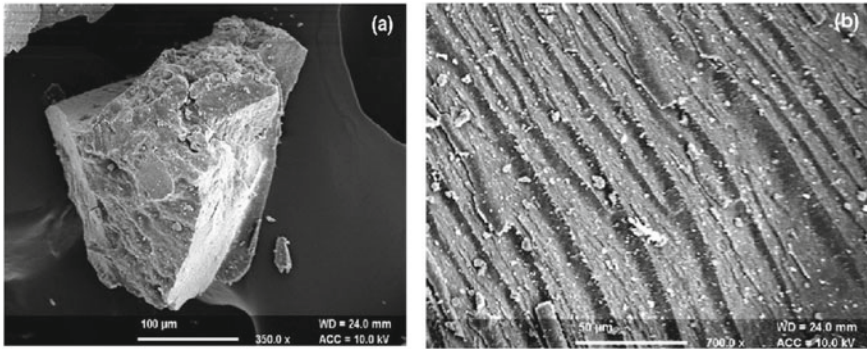


Fig. 11 SEM and TEM image of Ch-PANI-CuO nanocomposites. Reprinted with permission from Rathore et al. [88]. Copyright (2019), Springer Nature

4 Applications of Matrix Composite Materials

The four classes of composites have various applications. But the composites of polymer matrix are the main class of these materials. Applications of these composites and other types of composites are given below.

4.1 Polymer Matrix Composites Applications

Electrical glass (E-glass), carbon, aramid, and boron are the most significant fibers reinforced with polymer matrix. Thermosets exhibit structural applications. There is an increase in the usage of continuous fibers but the thermoplastic matrices are most frequently reinforced with discontinuous fibers. The most often used polymer matrix composites are glass-fiber-reinforced polymers (GFRPs). Glass fibers in thermosetting polyester and vinyl ester resins are exhibited by 90% of composites. The major reason behind this is their low cost. It was observed that high-performance applications are exhibited by carbon fiber-reinforced polymers (CFRPs) as compared to GFRPs. Rocket launchers, helicopter rotor blades, aircraft fairings flooring, patrol boats, interiors, ballistic armor, cargo containers, solid-fuel rocket motor cases, and mine hunter ships are the defense applications. Wind turbine blades, trains, truck cabs, trailers, building components, ships, water treatment equipment, compressed natural gas tanks, bridges, boats, electrical insulation products, chemical industry equipment such as pipes and tanks, transmission line poles, concrete rebar's, concrete forms, firefighter compressed air tank, oil and gas production, and endoscopic surgery equipment have the several industrial applications of glass fiber reinforced polymers. Gliders, boats, recreational vehicles, shower enclosures and bathtubs, sports equipment, and automobile machinery such as interior components, bodies, and engine parts are the various applications of consumer glass fiber reinforced polymer.

The high structural efficiency of continuous unidirectional fabrics in comparison to discontinuous reinforcement is the major form of the reinforcement in the above application. For example, consumer products consist of limitless injection-molded glass-fiber-reinforced parts. Sports equipment and military aircraft are the primary advantages of carbon fiber reinforced polymer composites. But their industrial advantages are the fastest growing market sector. Unmanned aerial vehicle (UAV) structures, military, and commercial aircraft structures, optomechanical systems, aircraft gas turbine fan blades, satellite antennas, ships, and spacecraft structures are the various carbon fiber reinforced polymer defense applications. X-ray equipment, hydrogen tanks, and compressed natural gas, energy storage flywheels, wind turbine blades, fuel cells, robots, and other machine components, transmission cable cores, optomechanical equipment, civil engineering structure repair and reinforcement, antennas, ships, uranium centrifuges, train structures, and interiors, firefighter compressed air tanks, natural gas and oil exploration and production, prosthetics and orthotics are the several industrial applications of carbon fiber reinforced polymers. Automobile machinery, such as drive shafts and structural components; musical instruments; sports equipment, such as fishing rods, golf clubs, bows and arrows, snowboards, tennis rackets, skis, hockey sticks, bicycles, and softball bats; boats; headphones; notebook computer cases; furniture; are the various consumer advantages of carbon fiber reinforced polymers. There is an extensive application of boron fiber-reinforced polymer in aerospace/defense. Boron fiber-reinforced epoxy F-14 horizontal stabilizer was the first advanced composite flight application. Polymer reinforced boron was also utilized in UAVs and other fighter aircraft. Brakes and other friction parts; ballistic armor, such as helmets; NASCAR race car bodies; commercial aircraft pressure bottles and freight containers; service and patrol; aircraft engine containment rings; kayaks, leisure boats, luxury yachts, and canoes; repair and reinforcement of civil engineering structures are the various applications of Aramid.

4.1.1 Metal Matrix Composites Applications

Cobalt reinforced with tungsten carbide particles, ferrous alloys reinforced with titanium carbide particles, and cobalt reinforced with diamond particles are the various metal matrix composites which are utilized commercially for years. Continuous fibers reinforced metal matrix composites are comparatively expensive and have prominent applications. Aluminum tubes reinforced with boron fiber are utilized by space shuttle orbiter mid-fuselage section which is composed of rib trusses. Aluminum reinforced with carbon fiber is utilized by the Hubble Space 34 Composite Materials Telescope. The antenna pointing accuracy is maintained due to its low axial coefficient of thermal expansion (CTE) and high axial stiffness. Titanium reinforced with silicon carbide fiber due to its high strength and axial modulus is utilized in aircraft actuators. Aluminum reinforced with alumina fiber is the major notable metal matrix composite which is utilized in transmission lines. It is possible to place support towers farther apart in new construction due to high specific strength and stiffness. High-temperature strength, cylinder bore, and piston wear resistance is improved

by using discontinuous ceramic fibers in trucks and automobiles. Titanium reinforced with titanium boride particle is utilized in engine valves. Aluminum reinforced with silicon carbide particle has been utilized in a limited number of optical structural, aerospace, and commercial applications. It has turned into a staple material in photonic and electronic applications. Race car mechanical components, optical systems, and high-performance automobiles are the other applications. Aluminum reinforced with silicon particles is utilized in automobile engine cylinder liners for wear resistance. Aluminum reinforced with boron carbide particles has been utilized for spent nuclear fuel containers. Aluminum reinforced with silicon carbide particles has the main advantage in packing applications and photonic and electronic thermal management, and these are usually known as AlSiC. Low density and CTE density are the major applications of AlSiC over traditional materials. Composites of silicon–aluminum are also utilized in electronic packaging. The lower conductivity of AlSiC composites as compared to copper is its main limitation.

4.1.2 Carbon-Carbon Composites

Carbon-carbon is the most significant form of carbon matrix composites. It has applications in commercial and defense areas. This composite has applications in aerospace, where ablation is the major requirement. Exit cones, reentry vehicle nose tips, and rocket nozzles are its various applications. Nose cap and edges are the various carbon-carbon components that are utilized by the Space Shuttle Orbiter. Significant weight savings over steel are provided by carbon-carbon aircrafts brakes that are extensively utilized. A wide range of thermal conductivities is used to form carbon-carbon composites. Wafer-heating elements, glass-making equipment, and heat treatment racks are the major applications of industrial carbon-carbon composites. The composites of carbon-carbon are utilized in brakes and clutches of motorcycles and racing cars.

4.1.3 Ceramic Matrix Composites Applications

Ceramics reinforced continuous fibers are useful structural materials. Fracture toughness is increased to a smaller extent by whiskers and discontinuous fibers. Significant weight reduction over incumbent nickel-based super alloys was achieved by using carbon reinforced silicon carbide in military aircraft engine flaps. 15% of fuel savings and 60% component weight savings were projected. The composites of C/SiC were utilized in an increasing number of spacecraft optical systems. The applications of commercial ceramic matrix composites are limited. Tools are cut by using alumina reinforced with silicon carbide whisker. Other advantages comprise high-temperature environments and heat exchangers for corrosive. The parts for abrasive slurry pumps are made by using alumina reinforced with silicon carbide particles. High-end automobiles utilize carbon-reinforced silicon carbide brakes. Glass-ceramics reinforced

with carbon and with SiC fibers and carbon-reinforced glass-ceramics are under study for various commercial and aerospace applications.

4.2 Applications of Advanced Composite Materials (ACMs)

Humans are facing numerous challenges to develop advanced engineering materials. Materials with better resistance against fatigue damage and corrosion are produced by an effort to originate Organic-Matrix Composites (OMC) by Aerospace Industry. Fiber tows consist of thousands of fine filaments, which is the most extensively utilized fiber in organic matrix composites. (ACMs) have found extensive applications including fiber-glass boats, pressure vessels, and airplane panels are the applications of glass-fiber-reinforced polymer composites.

It was observed that glass fibers are the first known fibers in comparison to epoxy matrices and polyester in advanced composites. Composites reinforced with boron were utilized as structural components. Boron fibers in the form of monofilaments were first developed in the 1960s. Boron-epoxy hybrids are utilized in tennis rackets and golf clubs. Polymer composites reinforced with carbon fiber (CFRPs) exhibit durability, lightweight, and strength. The components in the aerospace industry and sports goods utilize CFRP. Composites reinforced with aramid fiber are filament-wound for fixed-wing commercial aircraft, motor cases, helicopters, and gas pressure vessels. Carbon composites exhibit higher strength as compared to aramid fiber and aramid fiber decomposes on heating. Metal Matrix Composites (MMCs) were first produced in the 1950s. The major inspiration is to retain its high shear strength, high resistance, and high chemical inertness at elevated temperatures, while the structural efficiency of metallic materials was extended. The various applications of ACMs can be summarized by the following:

- Aerospace
- Civil/Structural Engineering
- Bio-Engineering
- Automotive Engineering
- Electrical Engineering
- Domestic
- Chemical Engineering
- Marine Engineering.

4.2.1 Aerospace

Epoxy composite reinforced with boron was the first composite that was utilized for the skins of the empennages of the U.S. F15 and F14 fighters [98]. Polymer composites reinforced with fiber are gaining interest in the manufacture of spacecraft and aircraft [99]. With the advancement of technology, there is an increase in the utilization of composite materials for fuselage and wing [100]. Considerable quantities of

high-strength carbon, lightweight, and composite honeycomb structures with resin-impregnated paper or metallic honeycomb core materials, glass-fiber, and Kevlar composites, as laminated moldings and panels, are contained in various civil and military aircraft. They are utilized in bulkheads, airframes, helicopter rotor blades, pressured gas containers, wing spars, seat components, spoilers, propellers, tail-plane structures, access panels, fuel tanks, air distribution ducts, drop tanks, nose and landing gear doors, flooring, fairings, randoms, structural components, and engine nacelles. Carbon-fiber-reinforced carbon is utilized for elevated temperature [101]. Reinforced plastics are utilized for rocket launchers and rocket motor casings.

4.2.2 Automotive Engineering

The increase in motoring economy and energy conservation is permitted by weight reduction. Primary weight-saving is achieved by the reduction in the weight of the automobiles, and substantial secondary improvements in fuel economy are achieved if they are carried to adequately large lengths, which enable the designer to use smaller power plants. It was observed that the reduction in the vehicle weight results in its contribution to increase fuel consumption [102]. Consumers are demanding superior electronic systems for entertainment, safety, navigation, and improved interior comforts which are responsible for adding needless weight and hence affect the fuel economy. General Motors EVI, Lotus Elise, Toyota RAVA-EV, Chrysler Prowler, and Volkswagen Lupo 3L are the various vehicles in which SiC reinforced aluminum brake rotors are incorporated.

4.2.3 Bioengineering

Composite materials have extensive application [103] in bone cement, bone fixation plates, bone grafts, and hip joint replacement. Ti-6Al-4V titanium alloy, 316L stainless steel, and CoCr alloys are the materials which are used in the total hip replacement and have very high stiffness in comparison to the bone they replace. Prosthetic purposes such as in femoral stems for hip replacements, orthopedic fracture fixation plates, external orthotic supports in cases of limb deformity, mandibular and maxillary prostheses, etc., uses the carbon and plastic components reinforced with carbon fiber. Heart valve components are manufactured by pyrolytic carbon. The development is going in the usage of particulate hydroxyapatite as filler in foregone remodeling or replacement [104]. Composites have superior dental applications in comparison to homogenous materials such as metal alloys and ceramics. The product should be aesthetically matched in translucence and color with the other teeth when there is replacement of tooth, repairs of cavities, and preparation of crowns [105].

4.2.4 Civil/Structural Engineering

Corrosion resistance, high stiffness-to-weight ratios, high strength-to-weight ratios, high durability, and light weight makes the polymer composites reinforced with fiber attractive for utilization in civil engineering [106]. Pipelines, buildings, bridges, etc., are the constructed facilities infrastructure [107]. There is a combination of fiber-reinforced polymer with suitable fillers in the polymeric resin matrix. There is an increase in the application of fiber-reinforced polymers in civil infrastructure such as externally bonded reinforcement for strengthening of slabs, walls, and beams, reinforcing rods and tendons, hybrid and all-composite structural systems, wraps for seismic retrofit of columns, and composite bridge decks. The considerable interest has been attracted by the usage of fiber-reinforced polymer sheets for rehabilitation and strengthening of concrete structures [108–110]. Fiber-reinforced polymer laminates are also utilized for retrofitting of concrete columns and for strengthening of concrete bridge girders by bonding them to the tension face of girder [111, 112]. Various researches have been made on the application of fiber-reinforced polymer in the construction industry. Building frames, pedestrian bridges, walkways, vehicular bridges, platforms, building bridges, and cooling towers, etc., are the various structures in which the fiber-reinforced polymer pultruded structures are used.

Fiberglass-reinforced polymer (FRP) materials are used over the past three decades for the manufacture of load-bearing civil engineering structures. Modular rooftop cooling towers [113], curved roofs, electricity transmission towers, pedestrian and vehicle bridges decks [114], chemical and offshore [115], energy-absorbing roadside guardrails [116], marine structures such as seawalls and fenders [117], building systems, power pole cross-arms, and light poles, access platforms for industrial, and power poles are the structures which are included in the civil engineering structures.

4.2.5 Domestic

Polyester molding compounds and injection-molded reinforced thermoplastics are the most usual composites that are utilized in consumer items for the domestic market. It is also utilized in professional electrical equipment, furniture, motor-cycle crash helmets, kitchen equipment, computer casings, and televisions. The heat-dissipating and corrosion resistance properties result in the increased use of these composites over the years.

4.2.6 Electrical Engineering

The arc resistance properties and high dielectric strength result in the electronic and electrical applications of advanced composite materials. Advanced composite materials exhibit electrically insulation applications. Highly engineered composites are the most appropriate approach. Structural components for switchgear, printed circuit

boards, large-diameter butterfly valves, radomes, casings for electronic equipment, and high-strength insulators are the various applications. E-glass/epoxy prepregs are used for the formation of various printed circuit boards. Hybrid blading or ACMs are incorporated by various prototypes. Low dielectric constant, high thermal conductivity, high/low electrical conductivity, and low thermal expansion are exhibited by electronic composites in comparison to structural composites [118].

4.2.7 Marine Engineering

For years, composite materials have been utilized in the marine industry. Piping, gratings, hull shells, ducts, shafts, etc., are the traditional applications for composites. Underwater applications, surface vessels, and offshore structures are included in marine applications. Low flexibility and maintenance, ability to adjust fiber strength, and ability to mold complex shapes are offered by the utilization of plastic reinforced with fiber in marine applications. E-glass fiber is the most commonly used reinforced material in the marine applications [119]. Nowadays, there is an increase in the usage of composites in the marine industry. Advanced polymer composites are utilized exclusively by racing yachts to enhance the durability and save the weight. There is an increase in the use of racing powerboats, which are formed by hybrid composites for high-performance craft and safety. Resistance to degradation in water, flexible fabrication to produce special shapes, and high specific properties are the various applications of composite materials for marine structures.

5 Conclusion

Composites are being widely researched due to several advantages in the field of aerospace, electrical engineering, domestic, civil engineering, bioengineering, marine engineering, etc. On varying the combinations of matrix and reinforcement, the properties of composites can be tailored. High strength, high service temperature, etc., are the environmental applications which are challenged by the synthetic fibers such as carbon, aramids, glass, etc. Natural fibers are utilized for the advancement of application- based bio composites. Both synthetic and natural fibers are utilized in the composite materials depending on the end-use application.

References

1. H. Gu, C. Liu, J. Zhu, J. Gu, E.K. Wujcik, L. Shao, N. Wang, H. Wei, R. Scaffaro, J. Zhang, Z. Guo, Introducing advanced composites and hybrid materials. *Adv. Compos. Hybrid Mater.* **1**, 1–5 (2018). <https://doi.org/10.1007/s42114-017-0017-y>
2. J. Zhu, S. Wei, M. Jr Alexander, T.D. Dang, T.C. Ho, Z. Guo, Enhanced electrical switching and electrochromic properties of poly (p-phenylenebenzobisthiazole) thin films embedded with Nano-WO₃. *Adv. Funct. Mater.* **20**, 3076–3084 (2010). <https://doi.org/10.1002/adfm.201000261>
3. Q. He, T. Yuan, S. Wei, N. Haldolaarachchige, Z. Luo, D.P. Young, A. Khasanov, Z. Guo, Morphology-and phase-controlled iron oxide nanoparticles stabilized with maleic anhydride grafted polypropylene. *Angew. Chem. Int. Ed.* **51**, 8842–8845 (2012). <https://doi.org/10.1002/anie.201203347>
4. X.Q. Cheng, Z.X. Wang, X. Jiang, T. Li, C.H. Lau, Z. Guo, J. Ma, L. Shao, Towards sustainable ultrafast molecular-separation membranes: From conventional polymers to emerging materials. *Prog. Mater. Sci.* **92**, 258–283 (2018). <https://doi.org/10.1016/j.pmatsci.2017.10.006>
5. Q. Luo, H. Ma, F. Hao, Q. Hou, J. Ren, L. Wu, Z. Yao, Y. Zhou, N. Wang, K. Jiang, H. Lin, Z. Guo, Carbon nanotube-based inverted flexible perovskite solar cells with all-inorganic charge contacts. *Adv. Funct. Mater.* **27**(1–8), 1703068 (2017). <https://doi.org/10.1002/adfm.201703068>
6. R. Zhang, K. Moon, W. Lin, C.P. Wong, Preparation of highly conductive polymer nanocomposites by low-temperature sintering of silver nanoparticles. *J. Mater. Chem.* **20**, 2018–2023 (2010). <https://doi.org/10.1039/B921072E>
7. Y. Ye, H. Chen, J. Wu, L. Ye, High impact strength epoxy nanocomposites with natural nanotubes. *Polymer* **48**, 6426–6433 (2007). <https://doi.org/10.1016/j.polymer.2007.08.035>
8. S. Deng, J. Zhang, L. Ye, J. Wu, Toughening epoxies with halloysite nanotubes. *Polymer* **49**, 5119–5127 (2008). <https://doi.org/10.1016/j.polymer.2008.09.027>
9. C. Cheng, R. Fan, Z. Wang, Q. Shao, X. Guo, P. Xie, Y. Yin, Y. Zhang, L. An, Y. Lei, J.E. Ryu, A. Shankar, Z. Guo, Tunable and weakly negative permittivity in carbon/silicon nitride composites with different carbonizing temperatures. *Carbon* **125**, 103–112 (2017). <https://doi.org/10.1016/j.carbon.2017.09.037>
10. J. Zhu, H. Gu, Z. Luo, N. Haldolaarachchige, D.P. Young, S. Wei, Z. Guo, Carbon nanostructure-derived polyaniline metal composites: electrical, dielectric, and giant magneto resistive properties. *Langmuir* **28**, 10246–10255 (2012). <https://doi.org/10.1021/la302031f>
11. J. Zhu, S. Wei, L. Zhang, Y. Mao, J. Ryu, P. Mavinakuli, A.B. Karki, D.P. Young, Z. Guo, Conductive polypyrrole/tungsten oxide meta composites with negative permittivity. *J. Phys. Chem. C* **114**, 16335–16342 (2010). <https://doi.org/10.1021/jp1062463>
12. S.R. Bakshi, A. Agarwal, An analysis of the factors affecting strengthening in carbon nanotube reinforced aluminum composites. *Carbon* **49**, 533–544 (2011). <https://doi.org/10.1016/j.carbon.2010.09.054>
13. Y. Lei, J. Lu, X. Luo, T. Wu, P. Du, X. Zhang, Y. Ren, J. Wen, D.J. Miller, J.T. Miller, Y. K. Sun, J.W. Elam, K. Amine, Synthesis of porous carbon supported palladium nanoparticle catalysts by atomic layer deposition: application for rechargeable lithium-O₂battery. *Nano Lett.* **13**, 4182–4189 (2013). <https://doi.org/10.1021/nl401833p>
14. A. Albinati, F. Faccini, S. Gross, G. Kickelbick, S. Rizzato, A. Venzo, New methacrylate-functionalized Ba and Ba–Tioxo clusters as potential nanosized building blocks for inorganic–organic hybrid materials: synthesis and characterization. *Inorg. Chem.* **46**, 3459–3466 (2007). <https://doi.org/10.1021/ic0615630>
15. A.P. Esser-Kahn, P.R. Thakre, H. Dong, J.F. Patrick, V.K. Vlasko-Vlasov, N.R. Sottos, J.S. Moore, S.R. White, Three-dimensional microvascular fiber-reinforced composites. *Adv. Mater.* **23**, 3654–3658 (2011). <https://doi.org/10.1002/adma.201100933>

16. H. Gu, S. Tadakamalla, X. Zhang, Y. Huang, Y. Jiang, H.A. Colorado, Z. Luo, S. Wei, Z. Guo, Epoxy resin nanosuspensions and reinforced nanocomposites from polyaniline stabilized multiwalled carbon nanotubes. *J. Mater. Chem. C*, **1**, 729–743 (2013). <https://doi.org/10.1039/C2TC00379A>
17. X. Zhang, X. Yan, Q. He, H. Wei, J. Long, J. Guo, H. Gu, J. Yu, J. Liu, D. Ding, L. Sun, S. Wei, Z. Guo, Electrically conductive polypropylene nanocomposites with negative permittivity at low carbon nanotube loading levels. *ACS Appl. Mater. Interfaces* **7**, 6125–6138 (2015). <https://doi.org/10.1021/am5082183>
18. N.M.Z. Abidin, M.T.H. Sultan, L.S. Hua, A.A. Basri, A.U.M. Shah, S.N.A. Safri, A brief review of computational analysis and experimental models of composite materials for aerospace applications. *J. Reinf. Plastics Compos.* **38**(23–24), 1031–1039 (2019). <https://doi.org/10.1177/0731684419862869>
19. J. Gu, J. Du, J. Dang, W. Geng, S. Hu, Q. Zhang, Thermal conductivities, mechanical and thermal properties of graphite nanoplatelets/polyphenylene sulfide composites. *RSC Adv.* **4**, 22101–22210 (2014). <https://doi.org/10.1039/C4RA01761G>
20. C. Zweben, in *Mechanical Engineer's Handbook: Materials and Engineering Mechanics*, ed. by M. Kutz (John Wiley & Sons, Hoboken, NJ, 2015), pp. 401–435
21. F.C. Campbell, *Structural Composite Materials* (ASM International, 2010), pp. 1–29
22. S.C. Das, Nizam, M.E.H. Nizam, Applications of fiber reinforced polymer composites in civil engineering. *Int. J. Adv. Struct. Geotech. Eng.* **3**, 299–309 (2014)
23. Z. Spitalsky, D. Tasis, K. Papagelis, C. Galiotis, Carbon nanotube–polymer composites: chemistry, processing, mechanical and electrical properties. *Prog. Polym. Sci.* **35**, 357–401 (2010). <https://doi.org/10.1016/j.progpolymsci.2009.09.003>
24. P.M. Ajayan, L.S. Schadler, C. Giannaris, A. Rubio, Single-walled carbon nanotube–polymer composites: strength and weakness. *Adv. Mater.* **12**, 750–753 (2000). [https://doi.org/10.1002/\(SICI\)1521-4095\(200005\)12:10%3c750::AID-ADMA750%3e3.0.CO;2-6](https://doi.org/10.1002/(SICI)1521-4095(200005)12:10%3c750::AID-ADMA750%3e3.0.CO;2-6)
25. T. Dürkop, B.M. Kim, M.S. Fuhrer, Properties and applications of high mobility semiconducting nanotubes. *J. Phys.:Condens. Matter.* **16**, R553 (2004)
26. B.Q. Wei, R. Vajtai, P.M. Ajayan, Reliability and current carrying capacity of carbon nanotubes. *Appl. Phys. Lett.* **79**, 1172–1174 (2001). <https://doi.org/10.1063/1.1396632>
27. P.M. Ajayan, O. Stephan, C. Colliex, D. Trauth, Aligned carbon nanotube arrays formed by cutting a polymer resin—Nanotube composite. *Science* **265**, 1212–1214 (1994). <https://doi.org/10.1126/science.265.5176.1212>
28. R. Andrews, M.C. Wiesenberger, Carbon nanotube polymer composites. *Curr. Opin. Solid-State Mater. Sci.* **8**, 31–37 (2004). <https://doi.org/10.1016/j.cossms.2003.10.006>
29. S. Bredeau, S. Peeterbroeck, D. Bonduel, M. Alexandre, P. Dubois, From carbon nanotube coatings to high-performance polymer nanocomposites. *Polym. Int.* **57**, 547–553 (2008). <https://doi.org/10.1002/pi.2375>
30. P. Liu, Modifications of carbon nanotubes with polymers. *Eur. Polym. J.* **41**, 2693–2703 (2005). <https://doi.org/10.1016/j.eurpolymj.2005.05.017>
31. P. Singh, S. Campidelli, S. Giordani, D. Bonifazi, A. Bianco, M. Prato, Organic functionalisation and characterization of single-walled carbon nanotubes. *Chem. Soc. Rev.* **38**, 2214–2230 (2009). <https://doi.org/10.1039/B518111A>
32. G. Yang, M. Park, S.J. Park, Recent progresses of fabrication and characterization of fibers-reinforced composites: a review. *Compos. Commun.* **14**, 34–42 (2019). <https://doi.org/10.1016/j.coco.2019.05.004>
33. Y.H. Choa, J.K. Yang, B.H. Kim, Y.K. Jeong, J.S. Lee, T. Nakayama, T. Sekino, K. Niihara, Preparation and characterization of metal: ceramic nanoporous nanocomposite powders. *J. Magn. Magn. Mater.* **266**, 12–19 (2003)
34. F. Wypych, N. Seefeld, I. Denicolo, Preparation of nanocomposites based on the encapsulation of conducting polymers into 2H-MoS₂ and 1T-TiS₂. *Quim. Nova.* **20**, 356–360 (1997)
35. S.T. Aruna, K.S. Rajam, Synthesis, characterization and properties of Ni/PSZ and Ni/YSZ nanocomposites. *Scr. Mater.* **48**, 507–512 (2003). [https://doi.org/10.1016/S1359-6462\(02\)00498-0](https://doi.org/10.1016/S1359-6462(02)00498-0)

36. E.P. Giannelis, Polymer layered silicate nanocomposites. *Adv. Mater.* **8**, 29–35 (1996). <https://doi.org/10.1002/adma.19960080104>
37. F. Wypych, L.B. Adad, M.C. Grothe, Synthesis and characterization of the nanocomposites K-0, K0,1(PEO) x MoS₂ (X = 0,5; 1,2). *Quim. Nova.* **21**, 687–692 (1998). <https://doi.org/10.1590/S0100-40421998000600002>
38. M. Sternitzke, Review: structural ceramic nanocomposites. *J. Eur. Ceram. Soc.* **17**, 1061–1082 (1997). [https://doi.org/10.1016/S0955-2219\(96\)00222-1](https://doi.org/10.1016/S0955-2219(96)00222-1)
39. G. Ennas, A. Mei, A. Musinu, G. Piccaluga, G. Pinna, S. Solinas, Sol-gel preparation and characterization of Ni–SiO₂ nanocomposites. *J. Non-Cryst. Solids.* **232–234**, 587–593 (1998). [https://doi.org/10.1016/S0022-3093\(98\)00430-X](https://doi.org/10.1016/S0022-3093(98)00430-X)
40. J. Ning, J. Zhang, Y. Pan, J. Guo, Fabrication and mechanical properties of SiO₂ matrix composites reinforced by carbon nanotube. *Mater. Sci. Eng. A.* **357**, 392–396 (2003). [https://doi.org/10.1016/S0921-5093\(03\)00256-9](https://doi.org/10.1016/S0921-5093(03)00256-9)
41. Z. Xia, L. Riester, W.A. Curtin, H. Li, B.W. Sheldon, J. Liang, B. Chang, J.M. Xu, Direct observation of toughening mechanisms in carbon nanotube ceramic matrix composites. *Acta Mater.* **52**, 931–944 (2004). <https://doi.org/10.1016/j.actamat.2003.10.050>
42. J.W. An, D.H. You, D.S. Lima, Tribological properties of hot-pressed alumina–CNT composites. *Wear* **255**, 677–681 (2003). [https://doi.org/10.1016/S0043-1648\(03\)00216-3](https://doi.org/10.1016/S0043-1648(03)00216-3)
43. R. Kamalakaran, F. Lupo, N. Grobert, D. Lozano-Castello, N.Y. Jin-Phillipp, M. Ruhle, In-situ formation of carbon nanotubes in an alumina-nanotube composite by spray pyrolysis. *Carbon* **41**, 2737–2741 (2003). [https://doi.org/10.1016/S0008-6223\(03\)00380-4](https://doi.org/10.1016/S0008-6223(03)00380-4)
44. L. Jiang, L. Gao, Carbon nanotubes magnetite nanocomposites from solvothermal processes: formation, characterization, and enhanced electrical properties. *Chem. Mater.* **15**, 2848–2853 (2003). <https://doi.org/10.1021/cm030007q>
45. W. Chaisan, R. Yimnirun, S. Ananta, Preparation and characterization of ceramic: nanocomposites in the PZT–BT system. *Ceram. Int.* **35**, 121–124 (2009). <https://doi.org/10.1016/j.ceramint.2007.10.032>
46. S.I. Cha, K. T. Kim, K.H. Lee, C.B. Mo, S.H. Hong, Strengthening and toughening of carbon nanotube reinforced alumina nanocomposites fabricated by molecular level mixing process. *Scr. Mater.* **53**, 793–797 (2005). <https://doi.org/10.1016/j.scriptamat.2005.06.011>
47. C. Balazsi, Z. Konya, F. Weber, L.P. Biro, P. Arato, Preparation and characterization of carbon nanotube reinforced silicon nitride composites. *Mater. Sci. Eng. C* **23**, 1133–1137 (2003). <https://doi.org/10.1016/j.msec.2003.09.085>
48. D.D.L. Chung, Cement-matrix structural nanocomposites. *Met. Mater. Int.* **10**, 55–67 (2004). <https://doi.org/10.1007/BF03027364>
49. C. Baker, S.I. Shah, S.K. Hasanain. Magnetic behavior of iron and iron-oxide nanoparticle/polymer composites. *J. Magn. Magn. Mater.* **280**, 412–418 (2004). <https://doi.org/10.1016/j.jmmm.2004.03.037>
50. E.S. Yoon, J.S. Lee, S.T. Oh, B.K. Kim, Microstructure and sintering behavior of W–Cu nanocomposites powder produced by thermo-chemical process. *Int. J. Refract. Met. H.* **20**, 201–206 (2002). [https://doi.org/10.1016/S0263-4368\(02\)00003-3](https://doi.org/10.1016/S0263-4368(02)00003-3)
51. V. Provenzano, N.P. Louat, M.A. Imam, K. Sadananda, Ultrafine superstrength materials. *Nanostruct. Mater.* **1**, 89–94 (1992). [https://doi.org/10.1016/0965-9773\(92\)90058-6](https://doi.org/10.1016/0965-9773(92)90058-6)
52. A. Contreras, V.H. Lopez, E. Bedolla, Mg/TiC composites manufactured by pressureless melt infiltration. *Scr. Mater.* **51**, 249–253 (2004). <https://doi.org/10.1016/j.scriptamat.2004.04.007>
53. F.A. Khalid, O. Beffort, U.E. Klotz, B.A., Keller, P. Gasser, S. Vaucher, Study of microstructure and interfaces in an aluminium–C60 composite material. *Acta Mater.* **51**, 4575–4582 (2003). [https://doi.org/10.1016/S1359-6454\(03\)00294-5](https://doi.org/10.1016/S1359-6454(03)00294-5)
54. D.J. Branagan, in *Powder Metallurgy, Particulate Materials for Industrial Applications Proceedings of a Symposia Sponsored by the MPMD Powder Materials Committee Held at the TMS Fall Meeting in St. Louis, Missouri October 8–12, 2000*, ed. by D.E. Alman, J.W. Newkirk (TMS Publication, St. Louis, 2000), pp. 111–122
55. D.J. Branagan, Y. Tang, Developing extreme hardness (>15 GPa) in iron-based nanocomposites. *Compos. Part A-Appl. Sci. Manuf.* **33**, 855–859 (2002). [https://doi.org/10.1016/S1359-835X\(02\)00028-3](https://doi.org/10.1016/S1359-835X(02)00028-3)

56. X. Chen, J. Xia, J. Peng, W. Li, S. Xie, Carbon-nanotube metal-matrix composites prepared by electroless plating. *Compos. Sci. Technol.* **60**, 301–306 (2002). [https://doi.org/10.1016/S0266-3538\(99\)00127-X](https://doi.org/10.1016/S0266-3538(99)00127-X)
57. W.X. Chen, J.Y. Lee, Z. Liu, The nanocomposites of carbon nanotube with Sb and SnSb_{0.5} as Li-ion battery anodes. *Carbon* **41**, 959–966 (2003). [https://doi.org/10.1016/S0008-6223\(02\)00425-6](https://doi.org/10.1016/S0008-6223(02)00425-6)
58. W.X. Chen, J.Y. Lee, Z. Liu, Electrochemical lithiation and de-lithiation of carbon nanotube-Sn₂Sb nanocomposites. *Electrochem. Commun.* **4**, 260–265 (2002). [https://doi.org/10.1016/S1388-2481\(02\)00268-0](https://doi.org/10.1016/S1388-2481(02)00268-0)
59. C.L. Xu, B.Q. Wei, R.Z. Ma, J. Liang, X.K. Ma, D.H. Wu, Fabrication of aluminium-carbon nanotube composites and their electrical properties. *Carbon* **37**, 855–858 (1999). [https://doi.org/10.1016/S0008-6223\(98\)00285-1](https://doi.org/10.1016/S0008-6223(98)00285-1)
60. T. Noguchi, A. Magario, S. Fuzukawa, S. Shimizu, J. Beppu, M. Seki, Carbon nanotube/aluminium composites with uniform dispersion. *Mater. Trans.* **45**, 602–604 (2004). <https://doi.org/10.2320/matertrans.45.602>
61. T. Kuzumaki, K. Miyazawa, H. Ichinose, K. Ito, Processing of carbon nanotube reinforced aluminum composite. *J. Mater. Sci.* **13**, 2445–2449 (1998). <https://doi.org/10.1557/JMR.1998.0340>
62. J. Yang, R. Schaller, Mechanical spectroscopy of mg reinforced with Al₂O₃ short fibers and carbon nanotubes. *Mater. Sci. Eng.* **370**, 512–515 (2004). <https://doi.org/10.1016/j.msea.2003.08.124>
63. D. Srinivasan, K. Chattopadhyay, Hardness of high strength nanocomposites Al–X–Zr (X = Si, Cu, Ni) alloys. *Mater. Sci. Eng. C* **375–377** (2004). <https://doi.org/10.1016/j.msea.2003.10.189>
64. G. Jimenez, N. Ogata, H. Kawai, T. Ogihara, Structure and thermal/mechanical properties of poly (ϵ -caprolactone)-clay blend. *J. Appl. Polym. Sci.* **64**, 2211–2220 (1997). [https://doi.org/10.1002/\(SICI\)1097-4628\(19970613\)64:11<2211::AID-APP17>3.0.CO;2-6](https://doi.org/10.1002/(SICI)1097-4628(19970613)64:11<2211::AID-APP17>3.0.CO;2-6)
65. N. Ogata, G. Jimenez, H. Kawai, T. Ogihara, Structure and thermal/mechanical properties of poly (l-lactide)-clay blend. *J. Polym. Sci. Pol. Phys.* **35**, 389–396 (1997). [https://doi.org/10.1002/\(SICI\)1099-0488\(19970130\)35:2<389::AID-POLB14>3.0.CO;2-E](https://doi.org/10.1002/(SICI)1099-0488(19970130)35:2<389::AID-POLB14>3.0.CO;2-E)
66. H.G. Jeon, H.T. Jung, S.W. Lee, S.D. Hudson, Morphology of polymer silicate nanocomposites. *Polym. Bull.* **41**, 107–113 (1998). <https://doi.org/10.1007/s002890050339>
67. P. Aranda, E. Ruiz-Hitzky, Poly (ethylene oxide)—Silicate intercalation materials. *Chem. Mater.* **4**, 1395–1403 (1992). <https://doi.org/10.1021/cm00024a048>
68. D.J. Greenland, Adsorption of polyvinyl alcohols by montmorillonite. *J. Colloid Sci.* **18**, 647–664 (1963). [https://doi.org/10.1016/0095-8522\(63\)90058-8](https://doi.org/10.1016/0095-8522(63)90058-8)
69. C.W. Francis, Adsorption of polyvinylpyrrolidone on reference clay minerals. *Soil Sci.* **115**, 40–54 (1973)
70. X. Zhao, K. Urano, S. Ogasawara, Adsorption of polyethylene glycol from aqueous solutions on monmorillonite clays. *Colloid Polym. Sci.* **267**, 899–906 (1989). <https://doi.org/10.1007/BF01410338>
71. A. Usuki, Y. Kojima, M. Kawasumi, A. Okada, Y. Fukushima, T. Kurauchi, O. Kamigaito, Synthesis of Nylon-6-clay hybrid. *J. Mater. Res.* **8**, 1179–1184 (1993). <https://doi.org/10.1557/JMR.1993.1179>
72. A. Usuki, M. Kawasumi, Y. Kojima, A. Okada, T. Kurauchi, O. Kamigaito, Swelling behaviour of montmorillonite cation exchanged for Ω -amino acid by ϵ -caprolactum. *J. Mater. Res.* **8**, 1174–1178 (1993). <https://doi.org/10.1557/JMR.1993.1174>
73. P.B. Messersmith, E.P. Giannelis, Polymer-layered silicate nanocomposites: in situ intercalative polymerization of ϵ -caprolactone in layered silicates. *Chem. Mater.* **5**, 1064–1066 (1993). <https://doi.org/10.1021/cm00032a005>
74. M. Okamoto, S. Morita, H. Taguchi, Y.H. Kim, T. Kotaka, H. Tateyama. Synthesis and structure of smectic clay/poly (methyl methacrylate) and clay/polystyrene nanocomposites via in situ intercalative polymerization. *Polymer* **41**, 3887–3890 (2000). [https://doi.org/10.1016/S0032-3861\(99\)00655-2](https://doi.org/10.1016/S0032-3861(99)00655-2)

75. M. Okamoto, S. Morita, T. Kotaka, Dispersed structure and ionic conductivity of smectic clay/polymer nanocomposites. *Polymer* **42**, 2685–2688 (2001). [https://doi.org/10.1016/S0032-3861\(00\)00642-X](https://doi.org/10.1016/S0032-3861(00)00642-X)
76. K.J. Yao, M. Song, D.J. Hourston, D.Z. Luo, Polymer/layered clay nanocomposites: 2-polyurethane nanocomposites. *Polymer* **43**, 1017–1020 (2002). [https://doi.org/10.1016/S0032-3861\(01\)00650-4](https://doi.org/10.1016/S0032-3861(01)00650-4)
77. P.B. Messersmith, E.P. Giannelis, Synthesis and characterization of layered silicate-epoxy nanocomposites. *Chem. Mater.* **6**, 1719–1725 (1994). <https://doi.org/10.1021/cm00046a026>
78. R.A. Vaia, E.P. Giannelis, Lattice of polymer melt intercalation in organically modified layered silicates. *Macromolecules.* **30**, 7990–7999 (1997). <https://doi.org/10.1021/ma9514333>
79. R. Gangopadhyay, A. De, Conducting polymer nanocomposites: a brief overview. *Chem. Mater.* **12**, 608–622 (2000). <https://doi.org/10.1021/cm990537f>
80. A. Azioune, K. Peck, B. Soudi, M.M. Chehimi, G.P. Mccarthy, S.P. Armes, Adsorption of human serum albumin onto polypyrrole powder and polypyrrole-silica nanocomposites. *Synth. Met.* **102**, 1419–1420 (1999)
81. H. Xia, Q. Wang, K. Li, G.H. Hu, Preparation of polypropylene/carbon nanotube composite powder with a solid-state mechanochemical pulverization process. *J. Appl. Polym. Sci.* **93**, 378–386 (2004). <https://doi.org/10.1002/app.20435>
82. J. Sandler, M.S.P. Shaffer, T. Prasse, W. Bauhofer, K. Schulte, A.H. Windle, Development of a dispersion process for carbon nanotubes in an epoxy matrix and the resulting electrical properties. *Polymer* **40**, 5967–5971 (1999). [https://doi.org/10.1016/S0032-3861\(99\)00166-4](https://doi.org/10.1016/S0032-3861(99)00166-4)
83. Z. Roslaniec, G. Broza, K. Schulte, Nanocomposites based on multiblock polyester elastomers (PEE) and carbon nanotubes (CNT). *Compos. Interface.* **10**, 95–102 (2003). <https://doi.org/10.1163/156855403763586819>
84. C. Wu, X. Qiao, J. Chen, H. Wang, F. Tan, S. Li, A novel chemical route to prepare ZnO nanoparticles. *Mater. Lett.* **60**, 1828–1832 (2006). <https://doi.org/10.1016/j.matlet.2005.12.046>
85. X.Y. Ma, W.D. Zhang, Effects of flower-like ZnO nano whiskers on the mechanical, thermal and antibacterial properties of waterborne polyurethane. *Polym. Degrad. Stabil.* **94**, 1103–1109 (2009). <https://doi.org/10.1016/j.polymdegradstab.2009.03.024>
86. B. Kulyk, V. Kapustianyk, V. Tsybul'sky, O. Krupka, B. Sahraoui, Optical properties of ZnO/PMMA nanocomposite films. *J. Alloys Compd.* **502**, 24–27 (2010). <https://doi.org/10.1016/j.jallcom.2010.04.162>
87. A. Mostafaei, A. Zolriasate, Synthesis and characterization of conducting polyaniline nanocomposites containing ZnO rods. *Progr. Nat. Sci.: Mater. Int.* **22**, 273–280 (2012). <https://doi.org/10.1016/j.pnsc.2012.07.002>
88. B.S. Rathore, N.P.S. Chauhan, M.K. Rawal, S.C. Ameta, R. Ameta, Chitosan–polyaniline–copper (II) oxide hybrid composite for the removal of methyl orange dye. *Polym. Bull.* **77**, 4833–4850 (2020). <https://doi.org/10.1007/s00289-019-02994-7>
89. A. Pawlak, M. Mucha, Thermogravimetric and FTIR studies of chitosan blends. *Thermochim. Acta.* **396**, 153–166 (2003). [https://doi.org/10.1016/S0040-6031\(02\)00523-3](https://doi.org/10.1016/S0040-6031(02)00523-3)
90. M. Ibrahim, A.A. Mahmoud, O. Osman, A. Refaat, E.S.M. El-Sayed, Molecular spectroscopic analysis of nano-chitosan blend as biosensor. *Spectrochim. Acta. A.* **77**, 802–806 (2010). <https://doi.org/10.1016/j.saa.2010.08.007>
91. N.P.S. Chauhan, R. Ameta, R. Ameta, S.C. Ameta, Thermal and conducting behavior of emeraldine base (EB) form of polyaniline (PANI). *Ind. J. Chem. Technol.* **18**, 118–122 (2011). <http://nopr.niscair.res.in/handle/123456789/11620>
92. Z.N. Kayani, M. Umer, S. Riaz, S. Naseem, Characterization of copper oxide nanoparticles fabricated by the sol-gel method. *J. Electron. Mater.* **44**, 3704–3709 (2015). <https://doi.org/10.1007/s11664-015-3867-5>
93. H. Zheng, Y. Du, J. Yu, R. Huang, L. Zhang, Preparation and characterization of chitosan/poly (vinyl alcohol) blend fibers. *J. Appl. Polym. Sci.* **80**, 2558–2565 (2001). <https://doi.org/10.1002/app.1365>

94. A.G. Yavuz, A. Uygun, V.R. Bhethanabotla, Preparation of substituted polyaniline/chitosan composites by in situ electropolymerization and their application to glucose sensing. *Carbohydr. Polym.* **81**, 712–719 (2010). <https://doi.org/10.1016/j.carbpol.2010.03.045>
95. R. Khan, M. Dhayal, Chitosan/polyaniline hybrid conducting biopolymer base impedimetric immunosensor to detect ochratoxin-A. *Biosens. Bioelectron.* **24**, 1700–1705 (2009). <https://doi.org/10.1016/j.bios.2008.08.046>
96. R.C. Silva, M.V. Sarmento, F.A.R. Nogueira, J. Tonholo, R.J. Mortimer, R. Faezc, A.S. Ribeiro, Enhancing the electrochromic response of polyaniline films by the preparation of hybrid materials based on polyaniline, chitosan and organically modified clay. *RSC Adv.* **4**, 14948–14955 (2014). <https://doi.org/10.1039/C3RA47474G>
97. R. Karthik, S. Meenakshi, Facile synthesis of cross linked-chitosan-grafted-polyaniline composite and its Cr (VI) uptake studies. *Int. J. Biol. Macromol.* **67**, 210–219 (2014). <https://doi.org/10.1016/j.ijbiomac.2014.03.035>
98. A. Quilter, Composites in aerospace applications. *IHS White Pap.* **444**, 1 (2001)
99. P.D. Mangalgi, Composite materials for aerospace applications. *Bull. Mater. Sci.* **22**, 657–664 (1999). <https://doi.org/10.1007/BF02749982>
100. F. Elaldi, In *Proceedings of 2nd International Conference on Recent Advances in Space Technologies. An Overview for Structural Health Monitoring of Composites in Aerospace Applications*, pp. 309–314 (2005)
101. C. Niu, Airframe structural design: practical design information and data on air. *Adv. Metals for Aerosp. Autom. Mater. Sci. Eng. A* **184**(2), 119 (1988)
102. F.H. Froes, Advanced metals for aerospace and automotive use. *Mater. Sci. Eng. A.* **184**, 119–133 (1994). [https://doi.org/10.1016/0921-5093\(94\)91026-X](https://doi.org/10.1016/0921-5093(94)91026-X)
103. S.L. Evans, P.J. Gregson, Composite technology in load-bearing orthopedic implants. *Biomaterials* **19**, 1329–1342 (1998). [https://doi.org/10.1016/S0142-9612\(97\)00217-2](https://doi.org/10.1016/S0142-9612(97)00217-2)
104. S. Ramakrishna, J. Mayer, E. Wintermantel, K.W. Leong, Biomedical applications of polymer-composite materials: a review. *Compos. Sci. Technol.* **61**, 1189–1224 (2001). [https://doi.org/10.1016/S0266-3538\(00\)00241-4](https://doi.org/10.1016/S0266-3538(00)00241-4)
105. J.W. Nicholson, Adhesive dental materials—A review. *Int. J. Adhes. Adhes.* **18**, 229–236 (1998). [https://doi.org/10.1016/S0143-7496\(98\)00027-X](https://doi.org/10.1016/S0143-7496(98)00027-X)
106. L.V.D. Einde, L. Zhao, F. Seible, Use of FRP composites in civil structural applications. *Constr. Build Mater.* **17**, 389–403 (2003). [https://doi.org/10.1016/S0950-0618\(03\)00040-0](https://doi.org/10.1016/S0950-0618(03)00040-0)
107. V.M. Karbhari, in *Durability of composites for civil structural applications*, in *A Volume in Woodhead Publishing Series in Civil and Structural Engineering*, ed. by V.M. Karbhari (Wood head Publishing, 2007), pp. 1–10
108. A. Nanni, Flexural behavior and design of RC members using FRP reinforcement. *J. Struct. Eng.* **119**, 3344–3359 (1993). [https://ascelibrary.org/doi/abs/https://doi.org/10.1061/\(ASCE\)0733-9445\(1993\)119:11\(3344\)](https://ascelibrary.org/doi/abs/https://doi.org/10.1061/(ASCE)0733-9445(1993)119:11(3344))
109. A.A. Mufti, FRPs and FOSs lead to innovation in Canadian civil engineering structures. *Constr. Build Mater.* **17**, 379–387 (2003). [https://doi.org/10.1016/S0950-0618\(03\)00039-4](https://doi.org/10.1016/S0950-0618(03)00039-4)
110. C.J. Ramu, K. Kumar, Palanikumar, mechanical characteristics and terminological behavior study on natural fiber nano reinforced polymer composite—A review. *Mater. Today Proc.* **16**, 1287–1296 (2019). <https://doi.org/10.1016/j.matpr.2019.05.226>
111. U. Meier, Carbon fiber-reinforced polymers: modern materials in bridge engineering. *Struct. Eng. Int.* **2**(1), 7 (1992)
112. H. Saadatmanesh, Fiber composites for new and existing structures. *Struct. J.* **91**, 346 (1994)
113. E. Barbero, Structural applications of composites in infrastructure. *SAMPE J.* **28**(1), 9 (1992)
114. C.E. Bakis, L.C. Bank, V.L. Brown, E. Cosenza, J.F. Davalos, J.J. Lesko, A. Machida, S.H. Rizkalla, T.C. Triantafillou, Fiber-reinforced polymer composites for construction—State-of-the-art review. *J. Compos. Constr.* **6**, 73 (2002)
115. J.M. Hale, G.A. Gibson, in *Proceedings of ICCM11 International Conference on Composite Materials, Australian Composites Structures Society* (Australia, 1997), pp. 411–420

116. R.P. Bligh, D.C. Alberson, A.O. Atahan, A.R. Bowen, Laboratory testing of recycled materials in roadside safety devices. Res. Rep. 1458–2 (2001). <https://doi.org/10.1016/j.matpr.2019.05.226>
117. A. Venci, A. Rac, I. Bobic, Tribological behavior of Al-based MMCs and their application in automotive industry. Tribol. Ind. **26**, 31–38(2004). <http://www.tribology.fink.rs/journals/2004/3-4/5>
118. D.D.L. Chung, Composite materials for electrical applications. Compos. Mater. 73–89 (2003). <https://doi.org/10.1007/978-1-4471-3732-04>
119. B. Ertuğ, Advanced fiber-reinforced composite materials for marine applications. Adv. Mater. Res. **772**, 173–177 (2013). <https://doi.org/10.4028/www.scientific.net/AMR.772.173>

Advanced Composites of Nanomaterials and Their Applications



Priyanka Ghanghas, Nirmala Kumari Jangid, and Kavita Poonia

Abstract Materials serve as the fundamental components of both natural and man-made structures. The pursuit of enhanced structural efficiency and performance has driven the emergence of new materials. The advancement of manufacturing platforms and innovative interface engineering technologies has become instrumental in propelling the field of composite science into a new era. Composites are formed by combining contrary materials to create a new material with a varied range of required properties and have the potential to achieve multifunctionality. Among these, nanocomposites have garnered significant interest because of their improved dimensional stability, mechanical properties, electrical conductivity, and thermal/chemical resistance. Moreover, the eco-friendly nature of nanocomposites opens up new technological and business opportunities across various sectors, including aerospace, automotive, electronics, and biotechnology. The ultimate goal of advanced composites is to seamlessly integrate materials, manufacturing techniques, and engineering aspects to unlock their full potential. This chapter summarizes the types and applications of advanced composites of nanomaterials, along with a discussion on recent advances and their future aspects.

Keywords Composites · Nanocomposites · Aerospace · Automotive · Biotechnology

1 Introduction

Nanoscience and Nanotechnology encompass the study of materials within the dimension of 1–100 nm (nm). This field has opened up new dimensions for basic science and has paved the way for a range of innovative technologies. On December 29, 1959 Nobel Laureate Richard Feynman delivered a seminal lecture at Caltech, the California Institute of Technology, titled “There’s Plenty of Room at the Bottom,” which became a catalyst for the future of nanotechnology. Feynman’s lecture brought

P. Ghanghas · N. K. Jangid · K. Poonia (✉)
Department of Chemistry, Banasthali Vidyapith, Banasthali, Rajasthan 304022, India
e-mail: kavita_poonia8318@yahoo.co.in

© The Author(s), under exclusive license to Springer Nature Switzerland AG 2024
S. J. Ikhmayies (ed.), *Advanced Composites*, Advances in Material Research and Technology, https://doi.org/10.1007/978-3-031-42731-2_2

the concept of manipulating matter at atomic level, laying the foundation for the field of Nanoscience and Technology.

In 1990, Eric Drexler defined nanotechnology as the manipulation of matter, atom by atom, to control its structure at the molecular level. Nanotechnology is widely recognized for its ability to manipulate matter with dimensions ranging from approximately 1–100 nm, where unique phenomena give rise to novel applications. It involves constructing molecular systems with precise control at the atomic and molecular scales, leading to the evolution of a wide range of nanomachines [1].

Nanoscience involves manipulating materials at the molecular, macromolecular, and atomic levels, where their properties differ significantly from larger scales. Nanotechnology focuses on designing, characterizing, applying, and producing devices, systems, and structures by controlling their size and shape at the nanometer scale. Metallic nanoparticles exhibit unique physical, chemical, and biological properties compared to their macro-scale counterparts due to their high surface-to-volume ratio. Consequently, nanoparticles (NPs) have played a significant role in recent research endeavors [2]. Nanomaterials are classified into four divisions:

1. Inorganic macromolecules, Quantum dots, Nanodots,
2. Nanophases, Nanocrystals, Nanostructures (nanocomposites, nanoparticles, nano intermediates)
3. Nanoplatelets, Nanorods, Nanotubes, Nanofibrils, Quantum wires
4. Composite, Nanoholes.

The word “nanomaterials” encompasses materials within various dimensions, including thin films (one-dimensional), nanofibers, nanowires, nanotubes (two-dimensional), and nano-capsules, nano-powders, dendrimers, fullerenes, precipitates, quantum dots, colloids, nanostructured materials, and nanoporous materials (three-dimensional) [3, 4]. Nanomaterials exhibit unique properties compared to other materials, primarily due to the quantum effect and the increased relative surface area. They possess diverse characteristics, such as mechanical, thermal, biological, optical, and chemical properties.

Nanoparticle synthesis can be accomplished using various methods, primarily categorized into two approaches: the top-down method and the bottom-up method. The top-down method utilizes techniques such as mechanical milling/ball milling, sputtering, laser ablation, and chemical etching. On the other hand, the bottom-up method encompasses chemical/electrochemical methods (electrochemical, chemical precipitation), vapor deposition methods (physical vapor deposition, chemical vapor deposition), sol-gel processes, atomic/molecular condensation, laser pyrolysis, aerosol processes, spray pyrolysis, bioreduction methods, and more [5–16].

Chemical synthesis has been a popular approach for nanoparticle production, but it often involves the usage of toxic chemicals as capping and reducing agents [17, 18]. In contrast, green synthesis methods of nanoparticles utilize non-toxic chemicals, making them more environmentally friendly. Green synthesis offers greater control over crystal growth and involves reduced capital investment compared to chemical methods [19]. Various sources such as microorganisms, fungi, plants, and

plant extracts have been explored for their potential in eco-friendly nanoparticle synthesis [20–30].

Nanoparticles find applications in diverse fields, including drug delivery, biomedical devices, medical imaging, flat-panel displays, sensors, automobile components, high-energy batteries, pigments, paints, ceramics, smart structures, higher-power magnets, kinetic energy penetrators/warheads, chemical mechanical planarization (CMP) slurries, catalysts, dielectrics, phosphors, fuel cells, cutting tools, optical devices, aerospace components, cosmetics, and more [31–33].

Nanometallic particles are utilized for antimicrobial purposes, conductive layers of screens, energetic materials, sensors, and catalysts. Nanoporous materials such as aerogels find applications in thermal insulation, biomedicine, optics, catalysis, and electronics. Nanotubes serve as structural materials and electrical conductive nanocomposites, with single-walled nanotubes finding use in conductive adhesives, ceramics, connectors, tires, and the optical industry. Large number of nanomaterials are employed in hard layers, structural components for automotive and aerospace industries, pipes for gas and oil, sports equipment, and anti-corrosion sectors. Dendrimers are being used in cosmetic preparations and medical applications such as rapid detection and drug administration. Quantum dots have applications in optoelectronics, photovoltaics, paints, inks, and anti-counterfeiting measures. Fullerenes are utilized in photovoltaic solar cells, sport materials, lightweight materials, healthcare applications, antioxidants, drug and gene delivery systems, and optical limiting properties. Nanowires find use in conductive sheets, electronic devices, and solar cells [34–36].

A nanocomposite material refers to a solid material consisting of multiple phases, where at least one phase possesses one or more dimensions at the nanoscale. Nanocomposites provide numerous advantages compared to other composite materials, including a significant surface-to-volume ratio, enhanced mechanical properties (retaining high ductility and scratch resistance), and improved optical properties (particle size-dependent light transmission). Nonetheless, certain challenges persist, such as addressing toughness, impact performance, establishing formulation-property-structure relationships, achieving particle exfoliation and dispersion, and ensuring cost-effectiveness [37].

2 Synthesis of Nanocomposites

2.1 Hydrothermal Synthesis

The hydrothermal synthesis method mainly includes the use of an aqueous solution inside a closed reaction vessel called the reaction system. By heating the reaction system high-temperature and high-pressure reaction environment will be created [38]. The hydrothermal synthesis is one of the most utilized strategies to produce nanomaterials from their homogeneous/heterogeneous solutions.

Hydrothermal union may be a preferred single-step handle for planning few mono/polyphase oxides and phosphates [39–42]. This method is simple, flexible, and cost effective, and is utilized to produce nanomaterial for applications extending from dye-sensitized solar cells to catalysis [43, 44].

2.2 *Sol-Gel synthesis*

The sol-gel process involves dispersing solid nanoparticles in a liquid colloidal solution (sol), which then undergo agglomeration, forming a three-dimensional network that permeates the liquid (gel). These nanoparticles can exist in either amorphous or crystalline form. The sol-gel process is a cost-effective method used for producing various fundamental nanocrystalline materials and nanocomposites. Additionally, the low reaction temperature enables precise control over the chemical composition of the synthesized products. This method offers significant control over process parameters and allows for the creation of mixtures containing a variety of metal/semiconductor metal oxides [43].

2.3 *Pechini Method*

The Pechini process, also known as the liquid-mix process, is a sol-gel route that offers several advantages. One of its key benefits is the ability to form a polymeric precursor that allows for the homogeneous dispersion of two or more metals throughout the network. This process relies on the formation of stable chelates between certain α -hydroxycarboxylic organic acids and multiple cations.

Compared to the traditional sol-gel method, the Pechini method differs in that the metal cations are trapped within the polymer gel, rather than forming particles as part of the gel structure. While this approach limits the ability to achieve controlled shapes and can lead to the formation of hard crystallite agglomerates, it also overcomes many of the disadvantages associated with alkoxide-based sol-gel processes. The Pechini method enables superior homogeneity, stoichiometric control, reproducibility, and uniform mixing of multiple ingredients at an atomic scale [45].

The Pechini method has found applications in the preparation of various ceramic oxides, ceramic powders, ceramic superconductors, dielectric films, fluorescent materials, high-temperature superconductors, and catalysts. It is also utilized in the synthesis of nanostructured materials for dye-sensitized solar cells and lithium-ion batteries [44–47]

2.4 Chemical Vapor Deposition

Chemical vapor deposition (CVD) is a process in which materials in the gaseous phase (volatile precursors) pass over a heated substrate inside a vacuum chamber, where these gases pass through a dynamic flow system and react chemically or decompose to produce a condensed coating (thin film) on the hot substrate in addition to gaseous products. These product gases plus any remaining reactant gases exit the hot reaction zone [48]. This method can be used to produce inorganic and polymeric thin films, powders, metal oxides, graphene, and 2D materials consisting of two or more elements, such as Mo_2C , $\text{Bi}_2\text{O}_2\text{Se}$, as well as carbon nanotubes and silicon carbide [49–51]. The main advantage of CVD is that it relies on the chemical reactions, which enables tunable deposition rates [52], as well as manufacture of single/multiphase nanomaterials. Moreover, it is recognized by high quality products with excellent conformality.

2.5 Microwave Irradiation

Microwave irradiation method is achieved through the interaction of electromagnetic radiation at the molecular level with the dielectric material, which absorbs microwave radiation and converts it into heat by dipolar polarization and ionic conduction mechanisms. Thus, the required energy to complete the reaction is produced [53]. Advantages of microwave irradiation can be summarized as short reaction times, non-solvent reactions, and higher yields. In addition, it lowers energy consumption, and it is ideal for optimization processes. These crucial properties made this method included in green chemistry procedures. Microwave irradiation can be utilized to produce ceramics, metal oxides, and carbon fibers [54].

3 Types of Nanocomposites

According to the matrix materials, nanocomposites are classified as.

3.1 Ceramic Matrix Nanocomposites (CMNC)

Ceramic matrix nanocomposites (CMNCs) are composite materials that consist of a ceramic matrix reinforced with ceramic or metal fibers. The incorporation of metal fibers enhances toughness, while ceramic fibers improve resistance to crack propagation. CMNCs have been developed to overcome the limitations of conventional

ceramics like Al_2O_3 , SiC, AlN, SiN, and Zr_2O_3 , which are prone to fracture under mechanical or thermomechanical loads due to cracks initiated by small defects.

To enhance crack resistance and fracture toughness, nanoparticles or nanofibers are embedded within the CMNC matrix. This reinforcement strategy improves the composite's fracture toughness while still benefiting from the high Young's modulus and strength of the ceramic matrix. Numerous studies have shown significant strengthening of the Al_2O_3 matrix by incorporating a small volume fraction (around 10%) of suitably sized SiC particles, followed by hot pressing of the mixture [55].

Several synthesis methods can be utilized for CMNCs, including powder methods, polymer precursor routes, spray pyrolysis, and vapor techniques such as chemical vapor deposition (CVD) and physical vapor deposition (PVD). Chemical methods like sol-gel, colloidal methods, precipitation methods, and template synthesis are also employed [55]. Additionally, there are various approaches for filling the ceramic matrix between the fibers, such as chemical vapor infiltration, chemical reaction techniques, preceramic polymers pyrolysis, electrophoresis processes, and matrix formation through high-temperature sintering.

CMNCs, especially carbon fiber-reinforced nanocomposites, find applications in diverse fields, including high-load automotive components [56]. They are also utilized in automobile paints, metal paints, corrosion-preventing coatings, aircraft components, and space shuttle sheets.

3.2 *Metal Matrix Nanocomposites (MMNC)*

Metal matrix nanocomposites (MMNCs) are materials that consist of an alloy matrix or a ductile metal with nanosized reinforcement materials. These materials combine the characteristics of ceramics and metals, such as toughness, ductility, high modulus, and strength [55]. MMNCs are known for their lightweight nature and high strength, making them suitable for applications in the aerospace and automotive industries, as well as in the development of structural materials and the biomedical sector. Typically, the matrix in MMNCs is composed of a lightweight metal like aluminum or magnesium, while the reinforcement includes various high-strength nanoparticles such as nanoceramics, nano-oxides/non-oxides, carbon-based nano-allotropes, and elements.

Various approaches are employed in the manufacturing and handling of Metal Matrix Nanocomposites (MMNCs). These methods include stir casting, disintegrated melt deposition (DMD), semi-solid casting (SSC), powder metallurgy (PM), friction stir processing, and accumulative roll bonding [57]. Furthermore, additional techniques used in the production of MMNCs include spray pyrolysis, liquid metal infiltration, rapid solidification, vapor-based methods such as physical vapor deposition (PVD) and chemical vapor deposition (CVD), electrodeposition, as well as chemical approaches like colloidal and sol-gel methods [55].

3.3 *Polymer Matrix Nanocomposites (PMNCs)*

Polymer matrix nanocomposites (PMNCs) are a type of nanocomposite where a polymer or copolymer matrix is dispersed with nanofillers or nanoparticles. PMNCs are particularly interesting due to their ability to tune properties by adjusting the shape, size, and volume fractions of the included nanoparticles [58]. These materials find applications in industries such as automobiles, aeronautics, and electronics [55, 59].

Various techniques have been utilized in the production of polymer nanocomposites, which involve the integration of layered materials and carbon nanotubes (CNTs). Key methods used in the synthesis of polymer nanocomposites include polymer or pre-polymer intercalation from a solution, in situ intercalative polymerization, melt intercalation, direct blending of polymer and particles, sol-gel method, template synthesis, and in situ polymerization [55, 59].

4 Applications

4.1 *Fuel Cells*

Fuel cell applications (Fig. 1) often utilize polymers in various components such as the proton exchange membrane, matrix for bipolar plates, and binder for the electrodes. Adzic et al. [60] highlighted that the electrodes are typically composed of carbon black particles, platinum (Pt) catalyst particles, and a polymeric binder. The Pt catalyst introduces a significant overpotential at the cathode, necessitating a larger amount of Pt aggregation on the cathode compared to the anode to meet the kinetic requirements. Furthermore, due to the limited availability and high cost of platinum-based catalysts, there is a need to reduce the amount of platinum used. Therefore, it is essential to explore new cathode catalysts that can enhance the oxygen electroreduction energy.

Nanoparticles play a crucial role in fuel cells. For instance, Pt nanoparticles embedded within single-walled carbon nanotubes, along with a binder like Nafion, have shown improved performance compared to conventional carbon black-based electrodes. Incorporating nanoparticles into proton exchange membranes has been widely studied to enhance proton conductivity and mechanical properties [61, 62]. Heteropolyacids have been introduced to enhance proton conductivity at higher temperatures. The incorporation of silica nanoparticles into proton exchange membranes has been found to reduce methanol intercalation. Studies have demonstrated that montmorillonite-modified nanoclay membranes offer improvements compared to unmodified membranes. Additionally, materials like TiO₂, zirconium hydrogen phosphate, and zirconium phosphate have shown promising potential for proton exchange membranes in direct methanol fuel cells.



Fig. 1 Applications of nano composites

4.2 *Electronics*

Nanotechnology plays a crucial role in the design and development of modern devices for optoelectronic and electronic applications, particularly as electronic devices have entered the nanoscale dimension. Polymer-based nanocomposites are widely utilized in these fields, offering unique properties and functionalities. One notable type of nanocomposite is the combination of conjugated polymers and carbon nanotubes, which holds great potential for applications such as photodiodes, superconductors, sensors, light-emitting diodes, field-effect transistors, and photovoltaic cells.

Silicon-based photovoltaic devices have already demonstrated commercial utility, exceptional stability, and high efficiency. However, organic/polymer-based photovoltaic devices offer the advantage of lower cost and more flexible manufacturing processes, with some promising results in terms of long-term stability and efficiency.

These devices show potential for providing cost-effective alternatives in the field of photovoltaics.

Graphene, a two-dimensional carbon allotrope, has garnered significant interest in electronics applications, much like the discovery of carbon nanotubes. Graphene exhibits exceptional electrical and mechanical properties, making it attractive for various electronic applications.

Conjugated polymers with nanoscale filler inclusions have been extensively studied for sensor applications, including biosensors, chemical sensors, and gas sensors. The incorporation of nanofillers, such as carbon nanotubes, can enhance the sensing capabilities of conjugated polymers. For example, a nanocomposite comprising single-wall carbon nanotubes showed gas sensor sensitivity comparable to that of the nanotubes alone. The sensing abilities of these nanocomposites often rely on the conductivity changes resulting from gas or chemical interactions with either the conjugated polymer or the nanofiller.

4.3 Aerospace Applications

In aerospace applications, nanocomposites are important due to their light weight and high performance. Nanocomposites have great significance in aerospace structures, e.g. crew gear, cockpit, aircraft interiors, equipment enclosures, nozzles, solar array substrates, coatings, and space durable mirrors. Nanocomposite materials provide fire resistance and chemical stability in addition to the advantage of the low operating cost, because of their light weight. Aerospace structures are vulnerable to be affected by widely varying environment that includes distinct temperature and moisture. They are also likely to be affected by contact with hydraulic fluid, deicing fluid, and jet fuel. The coatings shall remain unaffected by erosion, lightning strikes, and ultraviolet exposure [63].

4.4 Medical Applications

4.4.1 Wound Dressings

Robert Burrell is credited with developing the world's first nanosilver product for the treatment of various injuries in clinical settings, including chronic ulcers, burns, toxic epidermal necrolysis, and pemphigus. This development has led to the production of new antibacterial dressings that promote wound healing and enhance antibacterial effectiveness.

In a review by Konop et al. [64], the unique features of silver nanoparticles and their use in wound care treatment were discussed. They provided a historical overview of silver, explained the mechanism of silver's action, highlighted properties of the silver nanoparticles (antibacterial properties), discussed ways for conjugating silver

nanoparticles with antibiotics, and explored wound dressing materials involving silver. They also highlighted the applications and toxicity of silver nanoparticle dressings [65].

In another research by Burd et al. [66], the cytotoxicity of various commercially available silver-based dressings was compared using monolayer cell cultures, animal models, and tissue explants. The researchers evaluated dressings such as Urgotul[®]SSD, PolyMem[®]Silver, Ag, Contreet[®] Foam, Aquacel[®], and Acticoat[™]. The silver density in the culture medium was quantified, and the results revealed that the use of silver dressings caused a noticeable delay in epithelialization. When tested on a mouse excisional wound model, Contreet[®] Foam and Acticoat[™] exhibited significant inhibition of wound re-epithelialization by the seventh day after the initial injury.

In a study by Singh and Singh [67], chitin membranes having silver nanoparticles were examined for their potential use in wound dressing applications. The silver nanoparticles were synthesized in the presence of sodium alginate as a stabilizer, utilizing gamma irradiation at doses of 50 kGy. To assess their antimicrobial properties, chitin membranes with varying concentrations of nanosilver (30, 50, 70, and 100 ppm) were tested against *Staphylococcus aureus* and *Pseudomonas aeruginosa*. Remarkably, chitin membranes containing nanosilver with 100 ppm exhibited significant antimicrobial activity, effective against a variety of commonly encountered wound pathogens.

In a recent review by Hu and Yang [68], the importance of utilizing antimicrobial silver absorbent wound dressings for open wounds was highlighted. The study specifically examined dressings that were treated with silver particles or silver ions, known for their antimicrobial properties. Various techniques were explored to incorporate silver into the dressings, such as spraying or coating solutions containing silver onto the surface, embedding silver nanoparticles in non-woven fibers, and padding wetted dressings with pressure, were evaluated. The review highlighted that silver dressings, when absorbing exudate from wounds, activate the antimicrobial silver, which then acts by disrupting the bacterial cell wall and killing the bacteria. Silver alginate dressings and silver foam dressings, produced by many healthcare companies, are popular examples of antimicrobial absorbent dressings.

4.4.2 Catheters Silver

Silver has long been recognized for its antimicrobial properties and has been extensively studied for its use as an antimicrobial material in coating medical catheters. Medical catheters are inclined to bacterial infection, that can spread very fast to the surrounding wound and which may cause serious issues. The superior antimicrobial properties of nanoparticles make them a promising solution for reducing complications and bacterial infections associated with medical catheters [64, 67–69].

In a study by Wu et al. [70], a green and facile method was developed for depositing silver nanoparticles (AgNPs) onto the surface of central venous catheters (CVCs).

Inspired by mussel adhesive proteins, dopamine was utilized to create a thin poly-dopamine layer that facilitated the formation of AgNPs without the need for additional stabilizers or reductants. The antibacterial properties of the coated catheters were evaluated using *Staphylococcus aureus* culture experiments. The cytocompatibility of the coated catheters was assessed through scanning electron microscopy (SEM), WST-1: water-soluble tetrazolium salts assay, and fluorescence staining. The researchers found that the antibacterial activity of the catheters depended on the dose of AgNPs. Higher doses of AgNPs exhibited excellent antibacterial activity but also higher cytotoxicity. Optimal density of AgNPs on the catheter surface demonstrated sustained sterilization effects and improved biocompatibility. The study demonstrated the potential of developing mussel-inspired silver-releasing catheters with desirable biological properties and significant antimicrobial effectiveness.

Divya et al. [71] investigated the consequences of silver nanoparticles, particularly those synthesized through biogenic means. The researchers highlighted the efficacy of eco-friendly silver nanoparticles (AgNPs) derived from coral-associated bacteria in combating catheter-related urinary tract infections (UTIs). They conducted a screening of 57 coral bacterial isolates and identified the isolate MGL-D10 for AgNP preparation. The AgNPs synthesized from MGL-D10 were successfully coated onto catheters, demonstrating their ability to prevent biofilm formation and inhibit the growth of pathogens which were causing urinary tract infection.

These studies highlight the potential of silver nanoparticles for mitigating bacterial infections associated with medical catheters. The antimicrobial properties of silver nanoparticles, whether deposited through mussel-inspired methods or synthesized biogenically, offer promising solutions for reducing complications and improving patient outcomes.

4.4.3 Bone Cement

In a study conducted by Alt et al. [72], the antibacterial effectiveness of poly(methyl methacrylate) (PMMA) bone cement loaded with varying concentrations of nonstarch polysaccharides (NSP) was evaluated *in vitro*. The researchers discovered that the addition of 1% nanosilver to the bone cement completely inhibited the growth of methicillin-resistant *Staphylococcus aureus* (MRSA) and *Staphylococcus epidermidis*.

In the domain of joint replacements, nanoparticles have been incorporated into ultra-high molecular weight polyethylene to produce components. It has been observed that the inclusion of nanoparticles significantly decreases the deterioration of the polymer [73].

Russo et al. [74] investigated the antibacterial and mechanical properties of poly-methyl methacrylate-based bone cement laden with gold nanoparticles. Authors showed that nanocomposite cements with particular concentrations of gold nanoparticles exhibited increased antibacterial activity and improved punching performance. However, during the optimization of the nanocomposite bone cement, some adverse characteristics were observed [75].

Furthermore, the researchers synthesized lithium carbonate nanoparticles with the assistance of organic capping agents. In vitro experiments demonstrated that the nanoparticle composition, at concentrations of up to 600 $\mu\text{g/mL}$, did not impact cell viability. Moreover, the nanoparticles exhibited a positive effect on the differentiation of stem cells into bone-forming cells by releasing Li^+ ions at a concentration of 9.7 mM [75].

These studies highlight the potential of incorporating nanoparticles into bone cement to enhance its antibacterial activity, mechanical properties, and biocompatibility. Nanoparticles, such as nanosilver, gold, and lithium carbonate, offer promising avenues for improving the performance and functionality of bone cement in various orthopedic applications.

4.4.4 Dental Materials

Incorporating nanoparticles into resin composites has shown long-term inhibitory effects against *Streptococcus mutans*, a bacterium associated with dental caries [76]. The use of nanoparticles in endodontic filling materials and dental adhesives has demonstrated high antibacterial effects against oral *Streptococci*, *Staphylococcus aureus*, *Enterococcus faecalis*, and *Streptococcus milleri*, making them suitable for orthodontic treatments [77, 78].

Leontev et al. [79] developed antibacterial mouth rinse and other medications using liquid solution of metals and metal oxide-based semiconducting nanomaterials. They conducted microbiological research using dental plaque microflora and aqueous solutions containing Ag, Fe_3O_4 , ZnO, Cu, and SnO nanoparticles in the size range of 10–100 nm, with concentrations ranging from 1.53 to 10.12 mg/L. Study revealed that the antibacterial properties were primarily influenced with the help of chemical composition of the dispersed nanoparticles.

According to Zunita et al. [80], incorporating metal oxide nanoparticles into membrane materials enhanced their antifouling properties, as well as other significant characteristics such as rejection tendency, mechanical strength, porosity, hydrophilicity, water flux, and permeability.

Acosta Torres et al. [81] suggested the utilization of nanomedicine in prostheses to improve aesthetic features and mechanical properties. Nano-pigments can serve as antimicrobial agents and reinforcing fibers, preventing microbial infections.

In their research, Padovani et al. [82] investigated the integration of ceramic and silica rich glass nanoparticles into the commercially accessible resin composites. This approach aimed to gain the aesthetic characteristics of natural tooth structure and to achieve durable mechanical and physical properties, including wear resistance, toughness, high strength, and hardness.

However, when selecting the best suitable restorative material, the clinicians shall take into consideration following important factors like the ability to seal margins, long-term retention of indirect prosthodontic restorations, low risk for post-operative sensitivity, and evidence from long-term clinical studies. It is crucial to evaluate the

overall performance and clinical outcomes of these nanocomposite materials before their widespread application in dental treatments.

4.4.5 Bio-diagnosis

Nanocomposites and nanoparticles have significant applications in bio-diagnosis, particularly in the following areas:

1. Nano-shells: These are utilized to detect and destroy the cancer cells through photothermal therapy. Nano-shells can selectively target cancer cells and, when exposed to specific wavelengths of light, generate heat to destroy the targeted cells.
2. Nanoparticle array biosensors: These biosensors are employed for clinical identification of serum. They consist of an array of nanoparticles that can interact with specific biomarkers in the serum, enabling the detection and diagnosis of various diseases.
3. Detection of Alzheimer's disease: Nanoparticles are employed to determine the influence of amyloid β -derived diffusible ligands (ADDL) and the anti-ADDL antibody, which are associated with Alzheimer's disease. This allows for the identification and study of disease-related biomarkers [83–86].

Hariharan et al. [87] conducted electrochemical experiments using pure and PEG-supported tungsten oxide (WO_3) nanoparticles synthesized through a microwave irradiation process for L-dopa sensing applications. The results indicated that the PEG-supported samples exhibited improved selectivity and sensitivity compared to surfactant-free samples.

Jubete et al. [88] prepared electrodes which were screen-printed along with mushroom tyrosinase immobilized in a photo-crosslinkable polymeric gel on the working electrode. These electrodes were capable of detecting concentrations of L-Dopa and other catechols in a specific range.

Navarrete et al. [89] developed a methodology to enhance the selectivity and sensitivity of WO_3 nanowire gas sensors to different gases, such as H_2 , NH_3 , and NO_2 . By incorporating separate dopant agents, the sensing properties of the nanowire gas sensors were optimized for detecting specific gases.

Naveen Kumar et al. [90] presented various synthesis methods, preparation details of reduced graphene and metal oxide-based nanocomposites, and discussed the fabrication and gas sensing response of these nanocomposites. These materials have shown potential for gas sensing applications.

4.5 *Cosmetics Applications*

Nanoparticles are generally being used in the cosmetic preparations, including sunscreen lotions, make up creams, hair care products, moisturizers, and nail polish.

In sunblock creams, nanocomposites are used as UV filters. Titanium oxide and Zinc oxide nanocomposites have been used for their ability to scatter or absorb ultraviolet radiation, protecting the skin from sunburn. The reduction in particle size from micro-scale to nano-scale has enabled the development of sunscreens that can effectively penetrate the skin. 40 nm is the common size of nanoparticles which are being used in UV filters. The European Commission regularly updates the lists of nanomaterials which are used for preparation of cosmetics to ensure their safety [91, 92].

Lau et al. [93] reported the integration of nanoparticles produced by lasers into transparent nail polishes. This integration process allows for the direct incorporation of metal nanoparticles (such as alloy, silver, gold, and platinum) into varnishes, resulting in nanodoped polishes with unique optical properties. These nanoparticles do not have residual chemicals or capping agents surrounding them.

However, there have been concerns about the safety of nanoparticles, particularly nanosilver, incorporated into cosmetic products. It has been suggested that nanoparticles can easily penetrate the skin and reach different organs, potentially causing cellular damage and organ death [94]. While human skin is semi-permeable, making it difficult for nanomaterials to pass through [95], some researchers have found that nanoparticles incorporated into creams do not penetrate the skin [96, 97].

According to Kokura et al. [98], the penetration of silver nanoparticles through human skin is not easy, except when the skin's barrier function is disrupted. Typically, less than 2% is the penetration ratio of nanoparticles with concentrations reaching 0.02–0.002 ppm. They confirmed that no toxicity was observed when the bulk metals were turned to trace elements. [99]. Studies indicate that nanoparticles with size in a range of 20–200 nm are unable to penetrate the intact skin barrier. However, when the barrier is partially damaged, nanoparticles with a diameter of less than 10 nm can reach deeper layers of the stratum corneum, while those around 40 nm can penetrate only 5–8 μm into the stratum corneum. Specific nanoparticles such as silver, chromium, ZnO, and TiO₂ doesn't penetrate beyond the stratum corneum [97].

Sonia et al. [100] investigated the antioxidant and antimicrobial properties of biosynthesized colloidal zinc oxide nanoparticles which were used in a formulation of fortified cold creams. The zinc oxide nanoparticles were produced and characterized with the help of Akhmatova vesical leaf extract. The formulated cold cream infused with biosynthesized zinc oxide nanoparticles demonstrated antioxidant and antimicrobial properties against clinical skin pathogens, particularly *Candida* sp.

It is important to note that the safety and penetration of nanoparticles in cosmetic formulations are topics of ongoing research, and regulatory bodies continue to monitor and update guidelines to ensure consumer safety.

4.6 *Paint Formulation*

Nanomaterials have significant effects on the properties of paints because of their higher surface-to-volume ratio and unique structural characteristics. Different types of nanomaterials offer various functional benefits in paints. Here are some examples:

1. Titanium dioxide (anatase): works as a bactericidal agent, provides easy-to-clean surfaces, acts as a fire retardant, exhibits self-cleaning properties, and offers thermal insulation. The hydrophilic nature of titanium dioxide enables self-cleaning by preventing dirt, and water from binding to the surface. Additionally, its photocatalytic property can lead to the degradation of binders under UV irradiation.
2. Titanium dioxide (rutile): Similar to anatase, rutile titanium dioxide acts as a bactericidal agent, provides self cleaning properties, offers thermal insulation, and acts as a fire retardant.
3. Silicon dioxide: Provides anti-graffiti properties, acts as a fire retardant, enhances scratch resistance, exhibits water repellency, offers easy-to-clean surfaces, and provides thermal insulation. When mixed with polymeric resins, silicon dioxide nanomaterials improve the abrasion properties of paints, enhancing their micro and macro hardness, weather resistance, and scratch resistance. Silicon dioxide's excellent abrasion properties also help resist shrinking and swelling caused by moisture and temperature changes [101, 102].
4. Silver: Functions as a bactericidal agent, providing excellent antimicrobial properties against human pathogens and bacteria. Silver coatings are particularly effective in imparting antimicrobial properties to paints.

Among these nanomaterials silicon dioxide and titanium dioxide are particularly significant in the paint industry due to their functional properties [103, 104].

Bellotti et al. [105] incorporated zinc oxide, silver, and copper nanoparticles into water-based paints used for indoor applications. They evaluated the antifungal activities of the paints against *Chaetomiumglobose* and *Alternaria alternate* fungi on solid medium. The study concluded that the paint which was formulated with silver nanoparticles (10 nm) exhibited superior results compared to copper and zinc oxides in terms of antifungal properties.

Yedra et al. [106] carried out a study in which they enhanced the electrical properties of paints by adding multiwall carbon nanotubes (MWCNTs) to a commercially available polymeric base paint at a low concentration (less than 3 wt.%). The researchers applied the formulated paint to metallic and glass substrates and examined various parameters, including adhesion, thickness, electrical conductivity, hardness, and resistance to the environmental degradation. The results showed that the paint with MWCNTs exhibited a significant improvement in electrical conductivity, reaching up to 8 orders of magnitude that is higher than the pristine paint. Additionally, the modified paint demonstrated enhanced resistance to environmental degradation.

These studies demonstrate the potential of nanomaterials in improving the functional properties of paints, ranging from antimicrobial effects to electrical conductivity and resistance to environmental degradation.

4.7 Ceramics

Certainly! Here are some of the functions and properties exhibited by nanoceramics:

1. Dielectric: Nanoceramics can exhibit high dielectric constants, making them suitable for use in capacitors, insulators, and electronic components.
2. Piezoelectric: Nanoceramics can generate an electric charge when they are under mechanical stress, and vice versa. This property makes them valuable for applications such as sensors, actuators, and energy harvesting devices.
3. Ferroelectric: Ferroelectric nanoceramics can have a spontaneous electric polarization that can be reversed by an external electric field. They find applications in memory devices, sensors, and actuators.
4. Pyroelectric: Nanoceramics with pyroelectric properties can generate an electric charge in response to temperature changes. They are used in thermal sensors, infrared detectors, and energy harvesting devices.
5. Magneto-resistive: Certain nanoceramics exhibit changes in electrical resistance in the presence of a magnetic field. This property is utilized in magnetic sensors, data storage devices, and spintronic applications.
6. Ferromagnetic: Some nanoceramics possess ferromagnetic properties, meaning they can be magnetized and retain their magnetization even after the external magnetic field is removed. These materials find applications in magnetic storage, sensing, and magnetic devices.
7. Electro-optical: Nanoceramics can exhibit changes in their optical properties in response to an electric field. They are utilized in devices such as electro-optical modulators and displays.
8. Superconductive: Certain nanoceramics can exhibit zero electrical resistance when cooled below a specific temperature, enabling applications in high-performance electronics and energy transmission [107].

It's important to note that the specific properties and functions of nanoceramics can vary depending on their composition, structure, and size. Different ceramics are chosen for different applications based on their desired properties which are as follows:

- SiC + BeO, Al₂O₃ function as insulator for integrated circuit substrate applications.
- BaTiO₃ works as dielectric for the capacitor application.
- SiC, ZnO + Bi₂O₃, SnO₂, LaCrO₃, function as semiconductors for thermistor, gas defector and varistor application.

- SiO_2 , ZnO function as piezoelectric for piezo filter, piezo lighter, and surface wave transducer application.
- Lead zirconate titanate (PZT) acts as pyroelectric for infrared detectors applications.
- Lead lanthanum zirconium titanium oxide (PLZT) acts as ferroelectric for optical memory, and optical shutter applications. Also PLZT acts as polarizer for optical shutter applications
- ZrO_2 , Al_2O_3 function as ionic conductors for O_2 sensor and Na-S battery applications.
- $\text{Al}_2\text{O}_3:\text{Cr}$, $\text{ThO}_2:\text{Nd}$, $\text{Y}_2\text{O}_3:\text{Eu}$ function as luminescent for IR laser and cathode luminescence applications.
- SiO_2 acts as light guide for optical communication fiber applications.
- $\text{g-Fe}_2\text{O}_3$, $\text{Zn}_{1-x}\text{Mn}_x\text{Fe}_2\text{O}_4$ nanoparticles function as soft magnetic for magnetic tape applications ($x = 0, 0.2, 0.4, 0.6, 0.8, \text{ and } 1$).
- $\text{SrO}_6\text{Fe}_2\text{O}_3$ acts as hard magnetic for magnet seal applications.

Indeed, ceramics have significant applications in the biomedical field, particularly in the production of implants and tissue engineering. Here are some relevant points:

1. **Biocompatibility:** Ceramics such as zirconia, titania, and alumina possess excellent biocompatibility, means they are well-tolerated by living tissues without causing any adverse reactions. This property is crucial for their use in implants and prosthetics.
2. **Porous Ceramic Materials:** Porous ceramics, including zirconia, titania, and alumina, have the ability to integrate with natural tissues and promote bone ingrowth. They are commonly utilized in hip joints, dental caps, and bridges, where their porous structure encourages bone formation and osseointegration.
3. **Hydroxyapatite (HAp) Sponges:** Hydroxyapatite, a ceramic material resembling the mineral component of bones, can be formed into sponges [108]. Gonzalez-McQuire et al. [109] developed a method involving amino-acid-coated HAp nanoparticles immersed in a dextran sulfate matrix to create hydroxyapatite sponges. These sponges were evaluated for their feasibility and ability to support the growth of human bone marrow stromal cells. This research suggests significant applications in soft tissue and cartilage engineering.

Overall, ceramics offer favorable properties for biomedical applications, including biocompatibility, strength, and the ability to integrate with natural tissues. They play a crucial role in the development of implants and tissue engineering strategies aimed at restoring or replacing damaged or missing tissues in the human body.

4.8 Textiles

The textile industry is a major global sector involved in the production of textiles for various purposes, including household goods, furnishings, clothing, and technical

applications. Nanomaterials play a crucial role in enhancing and introducing unique functionalities to textiles, although their use raises concerns about their impact on the environment and human health [110]. These nanomaterials offer a range of functionalities to textiles, including antistatic properties, conductivity, UV protection, breathability, wrinkle resistance, stain and microbial resistance, as well as dirt and water repellence. They may be applied directly onto the surface of fibers or may be incorporated along with fiber coatings, such as polymers. To minimize potential impacts, it is important to carefully select suitable nanomaterials and integrate them responsibly into fabric. Different nanomaterials exhibit various functions based on their specific properties [111].

For example, silver nanoparticles exhibit antimicrobial, self-cleaning, antistatic, and electrical conductivity properties. They reduce microbial growth on textiles, such as household items, furnishings, and clothing, by emitting silver ions that react with the fiber's surface. Zinc oxide nanoparticles provide dirt repellence, antimicrobial activity, abrasion resistance, photocatalysis, UV absorption, self-cleaning, and water repellence. Zinc oxide nano-rods are particularly effective for coating cotton fabric because of their super hydrophobic properties, making the fabric water repellent. Silicon dioxide nanoparticles contribute to abrasion resistance, act as carriers for active substances, exhibit dirt and water repellence, chemical resistance, flame retardancy, self-cleaning properties. The hydrophobic nature of silicon dioxide nanoparticles imparts water-repellent properties to cotton surfaces. Titanium dioxide nanoparticles offer antimicrobial properties, dirt repellence, flame retardancy, photocatalysis, self-cleaning, UV absorption, and water repellence.

Additionally, aluminum oxide nanoparticles enhance textiles with abrasion resistance, chemical resistance, and flame retardancy. Nano clays provide abrasion resistance, act as carriers for active substances, and contribute to flame retardancy. Carbon nanotubes (CNTs) exhibit properties such as electrical conductivity, abrasion resistance, antistatic behavior, flame retardancy, and higher tensile strength. They can improve textiles and fibers by enhancing flame-retardant abilities and increasing electrical conductivity [112]. Carbon black nanoparticles function as antistatic agents and electrical conductors.

It is essential for manufacturers to exercise caution when selecting nanomaterials and ensure their responsible integration into fabrics to minimize potential harmful effects on both the human health and environment.

5 Conclusion

In summary, the advancements in nanotechnology and nanoscience have revolutionized various scientific disciplines such as physics, chemistry, biology, and biotechnology. Nanomaterials, characterized by their small size and large surface area, offer immense potential in medical diagnostics and have the capability to impart the understanding of quantum mechanics and fundamental scientific research. The synthesis methods of metal oxide-based semiconducting nanomaterials have been explored,

highlighting their diverse applications across different fields. Although nanocomposites hold significant importance in industrial applications, there are still many challenges to overcome in terms of cost-effectiveness and technical feasibility for their widespread commercialization.

References

1. J. Jeevanandam, A. Barhoum, Y.S. Chan, A. Dufresne, M.K. Danquah, Beilstein. J. Nanotechnol. **9**(3), 1050 (2018)
2. L. Li, J. Hu, W. Yang, A.P. Alivisatos, Nano Lett. **1**(7), 349 (2001)
3. K. Byrappa, S. Ohara, T. Adschiri, Adv. Drug Deliv. Rev. **60**(3), 299 (2008)
4. C.A. Charitidis, P. Georgiou, M.A. Koklioti, A.-F. Trompeta, V. Markakis, Manuf. Rev. **1**, 11 (2014)
5. A. Konrad, U. Herr, R. Tidecks, F. Samwer, K. Samwer, J. Appl. Phys. **90**(7), 3516 (2001)
6. R.A. Andrievskii, Russ. Chem. Rev. **63**(5), 411 (1994)
7. A.B. Sharma, M. Sharma, R.K. Pandey, Asian J. Chem. **21**(10), S033 (2009)
8. S. Gohil, R. Chandra, B. Chalke, S. Bose, P. Ayyub, J. Nanosci. Nanotechnol. **7**(2), 641 (2007)
9. W. Chang, G. Skandan, H. Hahn, S.C. Danforth, B.H. Kear, Nanostruct. Mater. **4**(3), 345 (1994)
10. M. Winterer, H. Hahn, Zeitschrift für Metallkunde (Materials research and advanced techniques) **94**(10), 1084 (2003)
11. A. Konrad, U. Herr, R. Tidecks, F. Kummer, K. Samwer, J. Appl. Phys. **90**(7), 3516 (2001)
12. N. Rajput, Int. J. Adv. Eng. Technol. **7**(4), 1806 (2015)
13. R.N. Bhargava, D. Gallagher, X. Hong, A. Nurmikko, Phys. Rev. Lett. **72**, 416 (1994)
14. M. Geetha, K. Suguna, P.M. Anbarasan, V. Aroulmoji, Int. J. Adv. Sci. Eng. **1**(1), 1 (2014)
15. C.-H. Lu, R. Jagannathan, Appl. Phys. Lett. **80**(19), 3608 (2002)
16. M. Morita, D. Rau, S. Kajiyama, T. Sakurai, M. Baba, M. Iwamura, Mater. Sci.-Poland **22**(1), 5 (2004)
17. A. Gole, C.J. Murphy, Chem. Mater. **16**, 3633 (2004)
18. J.Y. Song, B.S. Kim, Bioproc Biosyst. Eng. **32**, 79 (2009)
19. P.U. Rani, P. Rajasekharreddy, Colloids. Surf. A Physicochem. Eng. Asp. **389**, 188 (2011)
20. K. Vijayaraghavan, S.P.K. Nalini, Biotechnol. J. **5**(10), 1098 (2010)
21. T. Klaus, R. Joerger, E. Olsson, C.G. Granqvist, J. Proc. Natl. Acad. Sci. **96**(24), 13611 (1999)
22. B. Nair, T. Pradeep, Cryst. Growth. Des. **2**(4), 293 (2002)
23. Y. Konishi, K. Ohno, N. Saitoh, T. Nomura, S. Nagamine, H. Hishida, Y. Takahashi, T. Uruga, J. Biotechnol. **128**(3), 648 (2007)
24. I. Willner, R. Baron, B. Willner, Adv. Mater. **18**, 1109 (2006)
25. N. Vigneshwaran, N.M. Ashtaputre, P.V. Varadarajan, R.P. Nachane, K.M. Paralikar, R.H. Balasubramanya, Mater. Lett. **61**, 1413 (2007)
26. S.S. Shankar, A. Rai, B. Ankamwar, A. Singh, A. Ahmad, M. Sastry, Nat. Mater. **3**(7), 482 (2004)
27. R.S. Priya, D. Geetha, P.S. Ramesh, Int. J. Adv. Sci. Eng. **2**(1), 22 (2015)
28. N. Ahmad, S. Sharma, V.N. Singh, S.F. Shamsi, A. Fatma, B.R. Mehta, Biotechnol. Res. Int. **2011**, 454090 (2011)
29. S. Renganathan, V. Aroulmoji, G. Shanmugam, G. Devarajan, K.V. Rao, V. Rajendar, S.-H. Park, Mate. Res. Express **6**(3), 035028 (2018)
30. Y.S. Jae, S.K. Beom, Bioprocess Biosyst. Eng. **32**, 79 (2009)
31. J. Huang, Q. Li, D. Sun, Y. Lu, Y. Su, X. Yang, H. Wang, Y. Wang, W. Shao, N. He, N.J. Hong, C. Chen, Nanotechnology **18**(10), 105104 (2007)
32. S. Lanone, J. Boczkowski, Curr. Mol. Med. **6**(6), 651 (2006)

33. E. Gaffet, *Cond-mat.mtrl.Sci.* (2011). arXiv:1106.2206
34. M. Prato, *J. Mater. Chem.* **7**(7), 1097 (1997)
35. T. Albes, L. Xu, J. Wang, J. Hsu, A. Gagliardi, *J. Phys. Chem. C* **122**(27), 15140 (2018)
36. T. Abraham, Inc. P.O. Box 16760, Stamford, CT 06905, USA (2017)
37. E. Omanović-Miklićanin, A. Badnjević, A. Kazlagic, M. Hajlovac, *Health Technol.* **10**, 51 (2020)
38. G. Yang, S.-J. Park, *Materials (Basel)* **12**(7), 1177 (2019)
39. Y. Dai, C.M. Cobley, J. Zeng, Y. Sun, Y. Xia, *Nano Lett.* **9**(6), 2455 (2009)
40. Y.P. Fang, Q. Pang, X.G. Wen, B.N. Wang, S.H. Yang, *Small* **2**(5), 612 (2006)
41. J. Ye, H. Zhang, R. Yang, X. Li, L. Qi, *Small* **6**(2), 296 (2010)
42. S. Ji, S. Murakami, M. Kamitakahara, K. Ioku, *Mater. Res. Bull.* **44**(4), 768 (2009)
43. Y.F. Hsu, Y.Y. Xi, A.B. Djurišić, W.K. Chan, *Appl. Phys. Lett.* **92**(13), 133507 (2008)
44. M. Zhou, Y. Gao, B. Wang, Z. Rozynek, J.O. Fossum, *Eur. J. Inorg. Chem.* **5**, 729 (2010)
45. L. Dimesso, in *Handbook of Sol-Gel Science and Technology*, eds. by L. Klein, M. Aparicio, A. Jitianu (Springer International Publishing, Switzerland, 2016), pp. 1–22
46. N. Leventis, N. Chandrasekaran, A.G. Sadekar, C. Sotiriou-Leventis, H. Lu, *J. Am. Chem. Soc.* **131**(13), 4576 (2009)
47. R. Sahay, J. Sundaramurthy, P. Suresh Kumar, V. Thavasi, S.G. Mhaisalkar, S. Ramakrishna, *J. Solid. State. Chem.* **186**, 261 (2012)
48. K.E. Spear, *Pure Appl. Chem.* **54**(7), 1297 (1982)
49. R. Sahay, P. Suresh Kumar, V. Aravindan, J. Sundaramurthy, W.C. Ling, S.G. Mhaisalkar, S. Ramakrishna, S. Madhavi, *J. Phys. Chem. C* **116**(34), 18087 (2012)
50. P. Suresh Kumar, R. Sahay, V. Aravindan, J. Sundaramurthy, W.C. Ling, V. Thavasi, S.G. Mhaisalkar, S. Madhavi, S. Ramakrishna, *Phys. D: Appl. Phys.* **45**(26), 265302 (2012)
51. M.L. Hitchman, F. Tian, *J. Electroanal. Chem.* **538–539**, 165 (2002)
52. L. Sun, G. Yuan, L. Gao, J. Yang, M. Chhowalla, M.H. Gharahcheshmeh, K.K. Gleason, Y.S. Choi, B.H. Hong, Z. Liu, *Nat. Rev. Methods. Primers* **1**, 5 (2021)
53. H.M.T. Albuquerque, D.C.G.A. Pinto, A.M.S. Silva, *Molecules* **26**, 6293 (2021)
54. D. Nunes, A. Pimentel, P. Barquinha, P.A. Carvalho, E. Fortunato, R. Martins, *J. Mater. Chem. C* **2**, 6097 (2014)
55. P. Henrique C. Camargo, K. Gundappa Satyanarayana, F. Wypych, *Mat. Res.* **12**(1), 1 (2009)
56. A. Behera, S. Biswajit, D.K. Sahoo, in *Fiber-Reinforced Nanocomposites: Fundamentals and Applications*, ed. by B. Han, S. Sharma, T.A. Nguyen, L. Longbiao, K. Subrahmanya Bhat (Elsevier, 2020), pp. 359–368
57. M. Malaki, W. Xu, A.K. Kasar, P.L. Menezes, H. Dieringa, R.S. Varma, M. Gupta, *Metals* **9**, 330 (2019)
58. A.F.M. Alsayed, M. A. Ashraf, in *Handbook of Polymer and Ceramic Nanotechnology*, ed. by C.M. Hussain, S. Thomas (Springer Nature, Switzerland AG, 2021), pp.157–176
59. L.M. Manocha, J. Valand, N. Patel, A. Warriar, S. Manocha, *Indian J. Pure Appl. Phys.* **44**, 135 (2006)
60. R.R. Adzic, K. Sasaki, H. Naohara, Y. Cai, Y.M. Choi, P. Liu, B. Vukmirovic, J.X. Wang, *Angew. Chem. Int. Ed.* **49**, 8602 (2010)
61. P.H.C. Camargo, C. Kestur, K.G. Satyanarayana, F. Wypych, *Mat. Res.* **12**(1), 1 (2009)
62. M. Tyagi, D. Tyagi, *Int. J. Electro. Electr. Eng.* **7**(6), 603 (2014)
63. V.T. Rathod, J.S. Kumar, A. Jain, *Appl. Nanosci.* **7**(8), 519 (2017)
64. M. Konop, T. Damps, A. Misicka, L. Rudnicka, *J. Nanomater.* **2016**, 7614753 (2016)
65. L. Ge, Q. Li, M. Wang, J. Ouyang, X. Li, M.M. Xing, *Int. J. Nanomed.* **9**(1), 2399 (2014)
66. A. Burd, C.H. Kwok, S.C. Hung, H.S. Chan, H. Gu, W.K. Lam, L. Huang, *Wound. Repair. Regen.* **15**(1), 94 (2007)
67. R. Singh, D. Singh, *Int. Wound. J.* **11**(3), 264 (2014)
68. Y. Yang, H. Hu, *J. Microb. Biochem. Technol.* **7**(4), 228 (2015)
69. K. Chaloupka, Y. Malam, A.M. Seifalian, *Trends Biotechnol.* **28**(11), 580 (2010)
70. K. Wu, Y. Yang, Y. Zhang, J. Deng, C. Lin, *Int. J. Nanomedicine.* **10**, 7241 (2015)
71. M. Divya, G.S. Kiran, S. Hassan, J. Selvin, *ISBAB* **18**, 101037 (2019)

72. V. Alt, T. Bechert, P. Steinrücke, *Biomaterials* **25**(18), 4383 (2004)
73. K.S. Morley, P.B. Webb, N.V. Tokareva, *Eur. Polym. J.* **43**(2), 307 (2007)
74. T. Russo, A. Gloria, R.D. Santis, U. D'Amora, G. Balato, A. Vollaro, O. Oliviero, G. Improta, M. Triassi, L. Ambrosio, *Bioact. Mater.* **2**(3), 156 (2017)
75. C. Covarrubias, J.P. Durán, M. Maureira, *Mater. Lett.* **219**, 205 (2018)
76. K. Yamamoto, S. Ohashi, M. Aono, T. Kokubo, I. Yamada, J. Yamauchi, *Dent. Mater.* **12**(4), 227 (1996)
77. A.P.R. Magalhães, L.B. Santos, L.G. Lopes, *ISRN Nanotechnol.* **1** (2012); C.R.A. de Estrela, C. Estrela, É.M. Torres, A.F. Bakuzis, P.C. Cardoso, M.S. Carrião, *ISRN Nanotechnol.* **2012**, 365438 (2012)
78. S.J. Ahn, S.J. Lee, J.K. Kook, B.S. Lim, *Dent. Mater.* **25**(2), 206 (2009)
79. V.K. Leont'ev, I.P. Pogorel'skii, G.A. Frolov, Y.N. Karasenkov, A.A. Gusev, N.V. Latuta, L.L. Borozdkin, D.S. Stefantsova, *Nanotechnol. Russ.* **13**(34), 195 (2018)
80. M. Zunita, I.G.B.N. Makertihartha, F.A. Saputra, Y.S. Syaifi, I.G. Wenten, *IOP Conf. Ser.: Mater. Sci. Eng.* **395**, 012021 (2018)
81. L.S. Acosta Torres, V. Moreno Maldonado, F.H. Barceló Santana, R.D. Vanegas Lancón, M.E. Plata Rodríguez, V.M. Castano, *J. Appl. Polym. Sci.* **126**(1), 289 (2012)
82. G.C. Padovani, V.P. Feitosa, S. Sauro, F.R. Tay, G. Durán, A.J. Paula, N. Durán, *Trends. Biotechnol.* **33**(11), 621 (2015)
83. A.J. Haes, R.P. Van Duyne, *J. Am. Chem. Soc.* **124**(35), 10596 (2002)
84. W. Zhou, Y. Ma, H. Yang, Y. Ding, X. Luo, *Int. J. Nanomed.* **6**, 381 (2011)
85. C. Loo, A. Lowery, N. Halas, J. West, R. Drezek, *Nano. Lett.* **5**(4), 709 (2005)
86. A.J. Haes, W.P. Hall, L. Chang, W.L. Klein, R.P. Van Duyne, *Nano Lett.* **4**(6), 1029 (2004)
87. V. Hariharan, S. Radhakrishnan, M. Parthibavarman, R. Dhilipkumar, C. Sekar, *Talanta* **85**(4), 2166 (2011)
88. E. Jubete, E. Ochoteco, I. Loinaz, J. A. Pomposo, H. Grande, *IEEE Sens. Conf.* 239 (2008)
89. È. Navarrete, C. Bittencourt, E. Llobet, *Proceedings* **2**(13), 964 (2018)
90. J.R. Naveen Kumar, D. Mayya Shrinivasa, M.B. Savitha, P. Prasad, *Int. J. Appl. Eng. Manag. Lett. (IJAEML)* **2**(2), 98 (2018)
91. A. Lohani, A. Verma, H. Joshi, N. Yadav, N. Karki, *ISRN Dermatol.* **2014**, 843687 (2014)
92. An official website of the European Union, European Commission. https://commission.europa.eu/index_en. Accessed 28 Apr. 2023
93. M. Lau, F. Waag, S. Barcikowski, *Ind. Eng. Chem. Res.* **56**(12), 3291 (2017)
94. E. Bulut, M. Özacar, *Nanoscience and Nanotechnology Conference, ITU, Istanbul, Turkey*, **178**, 9 (2007)
95. R. Sathiyapriya, V. Hariharan, K. Prabakaran, M. Durairaj, V. Aroulmoji, *Int. J. Adv. Sci. Eng.* **5**(3), 1077 (2019)
96. S. Raj, S. Jose, U.S. Sumod, M. Sabitha, *J. Pharm. Bioallied Sci.* **4**(3), 186 (2012)
97. S. Gajbhiye, S. Sakharwade, *J. Cosmet. Dermatol. Sci. Appl. JCDSA* **6**, 48 (2016)
98. S. Kokura, O. Handa, T. Takagi, T. Ishikawa, Y. Naito, T. Yoshikawa, *Nanomed.: Nanotechnol. Biol. Med.* **6**(4), 570 (2010)
99. C.S.J. Campbell, L.R. Contreras-Rojas, M.B. Delgado-Charro, R.H. Guy, *J. Control. Release* **162**(1), 201 (2012)
100. S. Sonia, H.L.J. Kumari, K. Ruckmani, M. Sivakumar, *Mat. Sci. Eng. C. Mater. Biol. Appl.* **79**(1), 581 (2017)
101. T. Marolt, A.S. Škapin, J. Bernard, P. Živec, M. Gaberšček, *Surf. Coat. Technol.* **206**(6), 1355 (2011)
102. T. Künniger, A.C. Gerecke, A. Ulrich, A. Huch, R. Vonbank, M. Heeb, A. Wichser, R. Haag, P. Kunz, M. Faller, *Environ. Pollut.* **184**, 464 (2014)
103. S.X. Zhou, L.M. Wu, J. Sun, W.D. Shen, *Prog. Org. Coat.* **45**(1), 33 (2002)
104. S. Kumar, N.K. Verma, M.L. Singla, *J. Coat. Technol. Res.* **8**(2), 223 (2011)
105. N. Bellotti, R. Romagnoli, C. Quintero, C. Domínguez-Wong, F. Ruiz, C. Deyá, *Prog. Org. Coat.* **86**, 33 (2015)

106. Á. Yedra, G. Gutiérrez-Somavilla, C. Manteca-Martínez, M. González-Barriuso, L. Soriano, *Prog. Org. Coat.* **95**, 85 (2016)
107. A. Kumari, *Int. J. Comput. Bus. Res. (IJCBR)* **7**(1), 22296166V7I1201701 (2017)
108. P. Kumar, B.S. Dehiya, A. Sindhu, *Int. J. Appl. Eng. Res.* **13**(5), 2744 (2018)
109. R. Gonzalez-McQuire, D. Green, D. Walsh, S. Hall, J.-Y. Chane-Ching, R.O.C. Oreffo, S. Mann, *Biomaterials* **26**(33), 6652 (2005)
110. M. Byko, *JOM* **57**(7), 14 (2005)
111. C. Som, P. Wick, H. Krug, B. Nowack, *Environ. Int.* **37**(6), 1131 (2011)
112. L. Windler, M. Height, B. Nowack, *Environ. Int.* **53**, 62 (2013)

Advances in Composites for Solid-Phase (Micro) Extraction



Yanjuan Liu, Zhen Wang, and Min Sun

Abstract Composite materials prepared by combining various functional materials contain the useful properties of those functional materials. These promising properties together with the facile designability and functionalization make composite materials to be ideal adsorbents in sample preparation. In this chapter, we discuss two important sample preparation techniques: solid-phase extraction and solid-phase microextraction based on various composites as the adsorbents; also, their applications in preconcentrating biological molecules, organic compounds, and metal ions are discussed. Future research directions and challenges of the composite materials are identified.

Keywords Composite · Solid-phase extraction · Solid-phase microextraction · Metal organic frameworks · Covalent organic frameworks · Carbon materials

1 Introduction

The determination of target analytes at trace levels is challenging in analytical chemistry, and more effective and environmental-friendly methods are required. Although several kinds of advanced analytical instruments have emerged, a prior step before chromatographic analysis, consisting of the processing of raw complex matrices, is still essential in most cases [1]. The sample pretreatment step is applied mainly to remove coexisting interferences, purify the sample, and preconcentrate target analytes to reduce the sample complexity before determination. In general, this procedure is

Y. Liu · Z. Wang

College of Medicine, Linyi University, Shuangling Road, Linyi 276000, Shandong, China
e-mail: liuyanjuan@lyu.edu.cn; liuyanjuan09@163.com

Z. Wang

e-mail: wangzhen@lyu.edu.cn

M. Sun (✉)

Key Laboratory of Interfacial Reaction & Sensing Analysis in Universities of Shandong, School of Chemistry and Chemical Engineering, University of Jinan, Jinan 250022, PR China
e-mail: chm_sunm@ujn.edu.cn; sunmin-123456@163.com

the most time-consuming and laborious task in a typical analytical workflow. Solid-phase extraction (SPE) and solid-phase microextraction (SPME) are two of the most widely used sample preparation methods. SPE plays a key role in sample pretreatment, replacing the traditional liquid–liquid extraction (LLE) in food analysis and biological and environmental analysis [2–4]. The technique overcomes many drawbacks of LLE and is characterized by low solvent consumption, low intrinsic costs, and reduced processing time [5]. The SPME technique improves the main drawbacks of SPE such as higher amounts of solvent, several extraction steps, and non-reusable extraction cartridges [6, 7].

Considering that the adsorbent is primarily responsible for the separation of target analytes, several types of advanced materials used as adsorbents have emerged, such as metalorganic frameworks (MOFs) [8, 9]; covalent organic frameworks (COFs) [10, 11]; carbon materials [12], including graphene (G) [13], carbon fibers (CFs) [14], carbon nanotubes (CNTs) [15], and graphitic carbon nitride (g-C₃N₄) [16]; molecularly imprinted polymers (MIPs) [17, 18]; ionic liquids (ILs) [19, 20]; dendrimers [21, 22]; and polymers [23, 24]. However, the extraction capability and selectivity of the above-mentioned materials are limited, which restricts their further development and application in SPE and SPME. To realize the sensitive, selective, and high-throughput analysis of the targets in complex samples, it is vital to prepare novel materials as adsorbents for dispersive solid-phase extraction (DSPE), column SPE, magnetic SPE, and SPME. Composite materials have facile designability; they can be prepared using two or more kinds of materials with different chemical and physical properties, proportions, and distributions according to different requirements. The composite materials not only keep the excellent properties of each component but also can obtain comprehensive advantages that cannot be achieved by a single component. Based on the above reasons, composites have been used in various fields.

In this chapter, commonly used composites prepared based on MOFs, COFs, and carbon materials are discussed, and an overview of recently developed applications of these composites as SPE and SPME adsorbents is presented. Moreover, the synthesis of the composites, extraction mechanisms, current challenges, and possible trends for the applications of the composites in SPE and SPME are demonstrated and discussed.

2 Solid-Phase Extraction

2.1 Dispersive Solid-Phase Extraction

DSPE and dispersive micro-solid-phase extraction (D- μ -SPE) are rapid, simple, cheap, rugged, safe, and efficient clean-up techniques. They involve dispersing an adsorbent into the sample solution via vortexing or ultrasonication to adsorb either the targets or the interferents; then, the adsorbent is separated from the solution via centrifugation [25]. Therefore, the adsorbent plays a key role in the selectivity, sensitivity, anti-interference ability, and extraction/desorption dynamics of DSPE

and D- μ -SPE methods. Various composites prepared based on MOFs, COFs, CNTs, CFs, and porous silica have been used in DSPE and D- μ -SPE.

2.1.1 MOFs-Based Composites

MOFs have been used in DSPE and D- μ -SPE for the extraction of various targets due to their highly porous structures and superior adsorption affinity and capacity toward organic compounds. A Cu-based MOF composite (Cu-BDC) through a solvothermal method was synthesized and it was used as a DSPE adsorbent for the extraction of gallic acid from orange juice samples. The established dispersive solid-phase extraction–high-performance liquid chromatography–ultraviolet detection method (DSPE-HPLC-UV) showed a wide linear range of 0.5–15.0 mg L⁻¹, a low limit of detection (LOD) of 0.145 mg L⁻¹, and an acceptable relative standard deviation (RSD) of <6.0%, which indicates the suitability of the established method for the accurate detection of gallic acid from complex orange juice samples [26]. Moreover, the fabrication of new composites between MOFs and other materials is an alternative approach to improve the extraction ability. For example, ILs@Zr-MOFs composites have been synthesized and evaluated as a DSPE adsorbent for the extraction of sulfonamide antibiotics (SAs) (Fig. 1). The result showed that [H₂Nmim][NTf₂]@UiO-66-Br had good extraction performance with high efficiency. Through high-performance liquid chromatography–diode-array detection, SAs could be effectively extracted and sensitively detected, with enrichment factors higher than 270, extraction recoveries between 90.5 and 101.9% in 10 min, and limit of detections (LODs) lower than 0.03 mg L⁻¹ [27]. The satisfactory performance was attributed to the large surface area of the adsorbent and multiple extraction mechanisms, including electrostatic, hydrogen bonding, and π – π interactions.

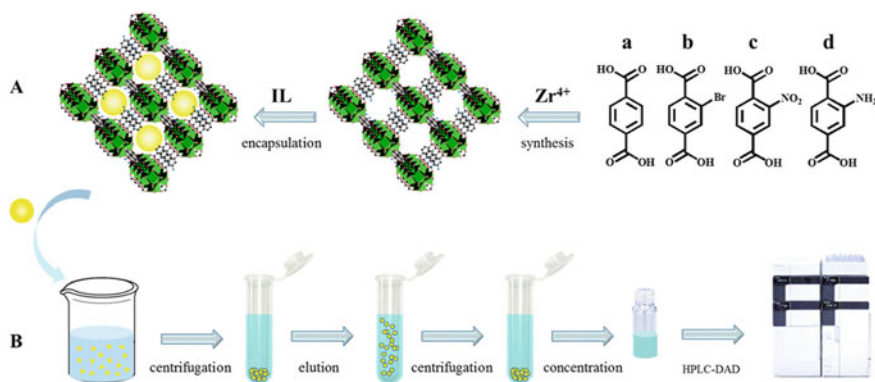


Fig. 1 Schematic of **a** the preparation of Zr-MOFs modified by ILs, and **b** ILs@Zr-MOFs-based DSPE procedure. Reprinted with permission from Lu et al. [27]. Copyright (2020), Elsevier

2.1.2 COFs-Based Composites

COFs are not often applied in the DSPE/D- μ -SPE technique compared with other techniques. These materials possess interesting characteristics such as porosity, low density, high thermal stability, large specific surface area, and tunable pore size; therefore, they have application potential for DSPE/D- μ -SPE. For example, in one study, ATP@COFs were prepared by grafting COFs onto salinized attapulgite (ATP), and the composite was used in the DSPE of pyrethroids from environmental water samples. The linear ranges of four pyrethroids were 2.5–500 $\mu\text{g L}^{-1}$, the enrichment factors ranged from 65.0 to 68.2, and the LODs were between 0.83 and 1.79 $\mu\text{g L}^{-1}$. Moreover, the intra-day and inter-day precisions were 1.4%–4.8% and 2.7%–3.6%, respectively. Finally, the approach was successfully used to determine pyrethroids from real environmental water with relative recoveries ranging from 71.2 to 88.7% [28]. However, the hydrophobicity of most COFs is high, which restricts their application in the adsorption of hydrophilic compounds. Therefore, the modification of COFs to improve their hydrophilicity is necessary. In one study, to extract N-nitrosamines from drinking water through DSPE, nano-titania containing a certain amount of hydroxy groups was introduced into COFs to prepare a clover-shaped nano-titania-functionalized COF (CSTF-COF) composite. The CSTF-COF had a high hydrophilicity and provided a hydrogen bonding interaction with polar analytes. Eight N-nitrosamines in drinking water were extracted via DSPE with this composite as the adsorbent. Due to the presence of hydroxy groups, CSTF-COFs exhibited high extraction efficiency for targets with a wide range of polarities through hydrophobic interaction, hydrogen bonding, and hydrophilic interaction. The established method provided relatively low LODs (0.13–2.45 ng L^{-1}) and satisfactory recoveries (88.6–105.5%), with percent relative standard deviations (RSDs) less than 8.3%. Therefore, with the assistance of the CSTF-COF composite, a sensitive and convenient approach could be established to quantitatively and sensitively determine N-nitrosamines in 31 out of 460 bottled drinking-water samples [29].

2.1.3 Carbon-Based Composites

Carbon-based composites have become one class of important adsorbent in sample preparation, and there are various studies about DSPE based on amine-functionalized reduced graphene oxide (amine-rGO), nanofibers doped with graphene oxide (GO), graphene-coated/polystyrene-divinylbenzene (PS-DVB), graphitized carbon black, multiwalled carbon nanotubes (MWCNTs), and graphenated-CNTs [30]. Amine-rGO with several different carbonic chains was synthesized [31]. The as-prepared composites were used as DSPE adsorbents to extract catechins, pesticides, and caffeine from tea samples. The result showed that the insertion of amino-carbonic chains onto the GO is an alternative strategy to achieve useful adsorbents to eliminate matrix interferences and preconcentrate analytes. Moreover, Lou et al. [32] studied another interesting method in which G sheets are coated onto polystyrene-divinylbenzene (PS-DVB) polymers to prepare G@PS-DVB composite, which was

used as a DSPE adsorbent to purify/preconcentrate allergenic-disperse dyes in industrial wastewater. The combination of G and PS-DVB can overcome the difficult separation of minuscule G sheets well-dispersed into the sample solution during the DSPE procedure. Therefore, G sheets were coated onto PS-DVB microspheres to improve particle size, thus facilitating their separation while maintaining the adsorption properties of G. The G@PS-DVB adsorbent showed satisfactory extraction efficiency, with LODs ranging from 1.1 to 15.6 ng/mL, and the recoveries in the range of 89.1–99.7% with an RSD lower than 10.5%. Therefore, the established method was repeatable, precise, green, and time-saving for the extraction and determination of target dyes. In addition, the G@PS-DVB composite as a DSPE adsorbent can be potentially applied to concentrate other aromatic compounds in various matrices [32]. Another study on the modification of CNTs was performed [33]. In this work, CNTs/TiO₂ composites were synthesized by coating titania nanoparticles (NPs) onto CNTs. The composite had a CNT core and a rough outer layer formed by titania NPs, which possessed a large specific surface area. The CNTs/TiO₂ composites were used as DSPE adsorbents to enrich phosphopeptides from digests of phosphoprotein, protein mixtures of β -casein and bovine serum albumin, human serum, and rat brain samples. An interesting and unique form of a carbon-based composite called electrospun nanofiber was investigated, which could function as a D- μ -SPE adsorbent [34]. This composite GO-PET was prepared by doping polyethylene terephthalate (PET) nanofiber with GO to detect tetracycline and cefotaxime in honey samples via HPLC-UV. This composite showed satisfactory robustness, being used over eight times with no loss in analytical signal, demonstrating its application as a green alternative material.

2.2 Column Solid-Phase Extraction

Column SPE can be considered one of the most frequently applied and well-established pretreatment techniques, and it includes the packing of extraction adsorbents, sample loading, and elution of analytes. Besides the common commercially available adsorbents utilized in packing column SPE cartridges (such as C₈, C₁₈, and –NH₂), many novel materials have been developed for the trace analysis of various targets (pharmaceutical drugs, preservatives, organic pollutants, pesticides, metal ions, and mycotoxins). Among these, various composites have attracted much attention due to their excellent properties in selective and effective adsorption. Composites based on MOFs, COFs, G, and other carbon materials have been widely researched, and they are described in this section.

2.2.1 MOFs-Based Composites

Although MOFs have many advantages, there are still some limitations in their use as column SPE adsorbents. To improve their adsorption properties, the development

of MOFs-based composites containing other functional materials is necessary. For example, in one study, an amino-functionalized zirconium MOF was combined with a 3D urea-based porous organic polymer (POP) to produce a composite termed UiO-66-NH₂/urea-POP. The oxygen- and nitrogen-containing functional groups, including amine (–NH₂), urea (–NHCONH–), Zr-oxo, and free carboxylates, could serve as coordinating ligands for the complexation of metal. Moreover, the introduction of abundant functional groups resulted in a strong hydrogen bond between the two components at the interface. Moreover, π – π stacking, hydrogen bonding, and electrostatic interactions between the two phases could enhance the interface compatibility. In addition, the organic aromatic components served as hydrophobic cavities/species to improve the interaction between targets and hybrid solid, leading to high penetration and adsorption of substrates inside the framework. The composite was successfully applied in column SPE for uranium in water samples, with the maximum sorption capacity obtained as 278 mg g^{–1}, and the sorption capacity was higher than that in the literature [35]. In another interesting work [36], GO-COOH/UiO-66 composites were prepared through the coordination of carboxyl groups of GO with zirconium ion of UiO-66 to obtain more void spaces of MOFs as active points and thus improve the adsorption capacity. The composites as SPE adsorbents were investigated for the adsorption of U(VI) from an aqueous solution and artificial seawater. The results indicated that the GO-COOH/UiO-66 composites had a high adsorption capacity for U(VI) from an aqueous solution. These results indicated that the composites have potential as an economical and effective adsorbent for removing U(VI) from simulated seawater.

2.2.2 COFs-Based Composites

Some COFs-based composites have been synthesized as novel adsorbents of SPE for various analytes. For example, a novel COF-functionalized poly (styrene-divinylbenzene-glycidyl methacrylate) composite (COF@PS-GMA) was synthesized via hydrothermal reaction. COF@PS-GMA possessed a porous structure, large surface area, and favorable chemical stability, and it was used to extract non-steroidal anti-inflammatory drugs (NSAIDs). The π -electron of COF layer could eliminate the large-scale interferences from the complicated matrix. Therefore, good linearity in a range of 0.005–5.0 $\mu\text{g mL}^{-1}$ was observed, and the limits of quantification (LOQs) were between 0.54 and 2.74 $\mu\text{g mL}^{-1}$. The recoveries of seven NSAIDs at the levels of 0.5, 5.0, and 20.0 $\mu\text{g L}^{-1}$ ranged from 84.3% to 99.6% [37]. In another study, a new imine-linked molecularly imprinted covalent organic framework (MICOF), another interesting COFs-based composite, was successfully prepared. The obtained MICOF showed large adsorption capacity, excellent selectivity, and good chemical and mechanical stabilities. As the SPE adsorbent, MICOF was successfully used for the selective extraction of four different cyano pyrethroids, including flucythrinate, fenvalerate, b-cyfluthrin, and l-cyhalothrin, from vegetable, fruit, and traditional Chinese medicine samples. The established MICOF-SPE-HPLC approach was

simple, sensitive, and selective. The linearity ranged from 0.1 to 200 ng g⁻¹, with a correlation coefficient (R) of 0.9981–0.9993, and the LODs and LOQs were in the ranges of 0.011–0.018 ng g⁻¹ and 0.036–0.060 ng g⁻¹, respectively. The recoveries of analytes at three spiked levels ranged from 94.3–102.7% [38]. The combination of COFs with other functional materials may further improve their adsorption capacity, reduce cost, and improve their chemical and mechanical stabilities. More efforts are still needed to develop novel COFs-based composites as SPE adsorbents to effectively separate and enrich targets from various complex samples.

2.2.3 Graphene and Other Carbon Materials-Based Composites

Graphene, CNTs, and other carbon materials have been applied as extractive phases in SPE. However, there are still some defects in using the single form of these materials as adsorbents. Therefore, a variety of composites with better performance based on these carbon materials have been prepared. For example, to overcome the bottlenecks of G (such as non-specificity, poor reliability, and repeatability), the composite rGO/Au has been prepared to establish a reliable and efficient SPE procedure for the simultaneous purification and enrichment of nine mycotoxins in milk. The composite proved to be an effective adsorbent for sample preparation, with satisfactory linearity ($R^2 \geq 0.992$), high sensitivity (LOQ of 0.02–0.18 ng mL⁻¹), acceptable precision (RSD, 2.0–14.9%), and adequate recovery (70.2–111.2%) [39]. The improvement in the extraction efficiency by the rGO/Au composite was due to the enhancement of the interlayer distances owing to the addition of other NPs in the rGO, thus minimizing the chances of G nanosheet agglomeration and increasing the analyte flow through the SPE cartridge. In another interesting work, Klongklaew et al. synthesized a composite composed of polypyrrole-coated GO and octadecyl silica incorporated in chitosan cryogel (PY/GOx/C18/chitosan) [40]. The main goal was to produce a highly porous composite and improve the analyte diffusion, related to the great adsorption capabilities supplied by the GO in the composite structure. This adsorbent exhibited high porosity and low back-pressure, which enabled its application at high sampling flow rates. The PY/GOx/C18/chitosan composite was used to preconcentrate carbamate pesticides from fruit juices. Moreover, the SPE adsorbent showed high recoveries ranging from 84.1 to 99.5%. The preconcentration and clean-up procedures were performed in one single step. Moreover, the composite monolith PPY/GOx/C18/chitosan cryogel adsorbent possessed good physical and chemical stabilities and could be reused as many as 13 times; its stability and reusability help to reduce analysis cost and save time. Based on the above reviews, the emergence of compounds with different properties to produce high-performance/selective composites as adsorbents is the current trend. Moreover, SPE features in the cartridge format will still be widely used in various fields in the coming years, due to the instrumentation simplicity of the technique, easy operation, and well-established procedure. Several recent applications combining novel materials (as carbon-based composites) and classical SPE indicate that this combination is a potential sample preparation method to be better explored in the coming years.

2.3 Magnetic Solid-Phase Extraction

Magnetic solid-phase extraction (MSPE) is performed by dispersing a magnetic adsorbent in the sample solution to adsorb the target through specific interactions. After the adsorption procedure, the magnetic adsorbent containing the analyte is separated from the sample matrix using an external magnet. The analyte is desorbed from the magnetic adsorbent through an elution procedure and dissolved in a desorption solvent. The desorption solution enriched with the target analyte is collected for further analysis and detection [41]. For MSPE, the magnetic adsorbent plays a key role in the extraction efficiency, enrichment factor, selectivity, and anti-interference ability and is thus an important factor for achieving good extraction performance.

Magnetic composites composed of versatile nanomaterials and magnetic nanoparticles (MNPs) can be used as MSPE adsorbents. These magnetic composites incorporate the distinct advantages of versatile nanomaterials and magnetic cores, which can well improve the extraction performance of MSPE. In recent years, diverse types of magnetic composites have emerged in SPE, such as MOFs-based magnetic composites, COFs-based magnetic composites, MIP-based magnetic composites, carbon material-based magnetic composites, and magnetic composites based on other materials. In the past few years, several reviews of MSPE have been published [41–44]. However, these reviews mostly discuss the application of one or two of the magnetic composites. In this review, we systematically summarize the recent advances in magnetic composites as MSPE adsorbents in separation and analysis science.

2.3.1 MOFs-Based Magnetic Composites

It is not convenient to pack MOFs into SPE cartridges owing to their non-spherical morphologies [45]. Moreover, MOFs with targets are difficult to separate from the aqueous solution. Therefore, the hybridization of MOFs and MNPs can overcome the above shortcomings and enable the direct separation of MOFs using an external magnet. In this case, tedious centrifugation and filtration procedures can be avoided. Until now, thousands of MOFs comprising different metals and organic linkers have been discussed in the scientific literature. The typical metals for the MOF construction include Zn(II), Cu(II), Fe(III), and Zr(IV), while the commonly used organic linkers, including terephthalic acid, trimesic acid, and 2-methylimidazole, are commercially available and low-cost [46].

The methods of synthesizing MOFs-based magnetic composites include embedding, layer-by-layer method, encapsulating, direct mixing, and the in-situ growth of MNPs. Among them, the embedding method (Fig. 2), which is mostly used, is performed by adding MNPs to MOFs precursors [47]. However, the MOF pores may be occupied, resulting in a reduction in the MOF porosity. In the layer-by-layer method, functional groups (such as carboxyl groups) on the MNP surface are necessary to control the growth of MOFs crystals and obtain a core-shell structure. The encapsulation method takes advantage of a polymer or carbonaceous layer as a

buffering interface between the MNPs and MOFs to promote the growth of MOFs around the interface and improve the compatibility between MOFs and MNPs [48]. The synthesis of the MOF-based magnetic composites and the MSPE procedure can be simultaneously realized by the direct mixing method, but it is difficult to maintain structural stability in the complex sample matrix. The structure of the pre-prepared MOFs must be robust under the conditions used for the in-situ growth of MNPs, which limits the application of this composite synthesis method.

Although there are numerous MOFs, only a small selection is applied as magnetic adsorbents for MSPE. The commonly used MOFs applied for MSPE include $\text{Cu}_3(\text{btc})_2$ (also called HKUST-1 or MOF-199), UiO-66, MIL-101, and MIL-100; these MOFs have high resistance to water and common solvents, which facilitate their application in the separation of hydrophobic target compounds [49]. In addition, other MOFs, such as MOF-5, MOF-177, MOF-235, ZIF-7, ZIF-8, and IRMOF-3, are also utilized for dye removal and the extraction of herbicides, pesticides, phthalate esters (PAEs), polycyclic aromatic hydrocarbons (PAHs), and heavy metals from environmental water, biological samples, and food matrices.

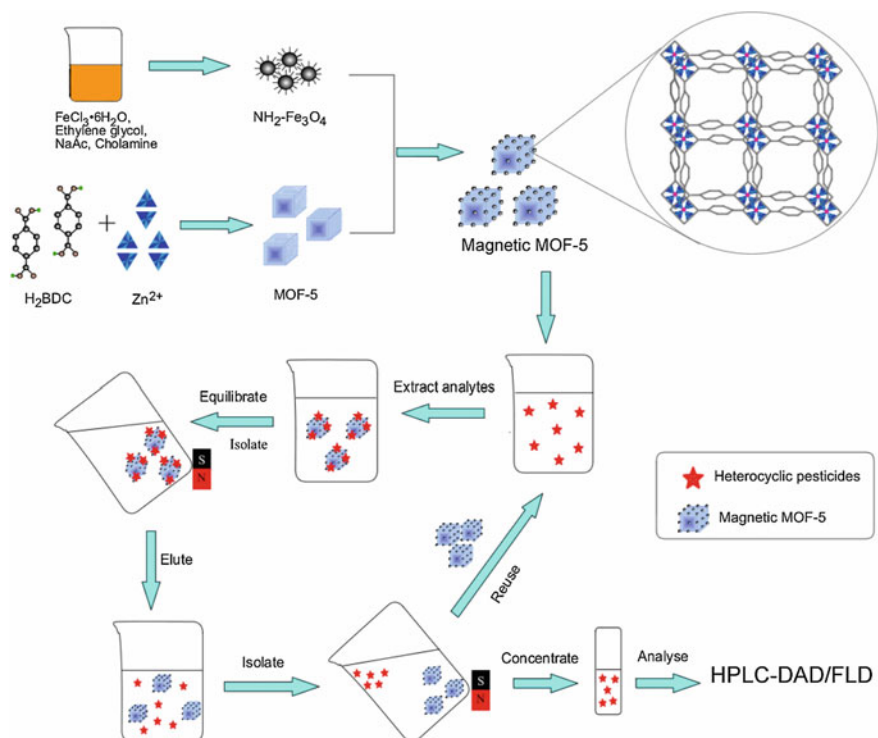


Fig. 2 Schematic illustration of the embedding process for the magnetic MOF-5 and the MSPE procedure. Reprinted with permission from Ma et al. [47]. Copyright (2018), Elsevier

Huo and Yan first reported the use of MOFs-based magnetic composites for MSPE [50]. In their research, magnetic MOF was obtained through the direct mixing of MIL-101(Cr) and $\text{Fe}_3\text{O}_4@\text{SiO}_2$ NPs. The resulting magnetic MOF was applied in the extraction of PAHs before high-performance liquid chromatography (HPLC) analysis. In this case, the magnetic MOF adsorbent could not be reused; only 0.6 mg of $\text{Fe}_3\text{O}_4@\text{SiO}_2$ NPs and 1 mg MIL-101(Cr) were needed in each extraction using 20 mL of the sample solution. The magnetization of MIL-101(Cr) and the extraction of PAHs were performed simultaneously by ultrasonating the mixture for 20 min, achieving enrichment factors of PAHs in the range of 101–180, and recoveries in the range of 81.3–105.0%. Other MIL-101(Cr)-based magnetic composites prepared via in-situ MOF growth or direct mixing have been used in the MSPE of estrogens [51] and pyrazole/pyrrole pesticides [52]. The water solubility of the MNPs of unmodified $\text{Fe}_3\text{O}_4@\text{MIL-101(Cr)}$ is low, and its selectivity for the adsorption of acid targets is limited. To solve these problems, $\text{Fe}_3\text{O}_4\text{-NH}_2@\text{MIL-101(Cr)}$ was synthesized via an embedding method [53]. Under the optimum conditions, only 10 mg of the resulting composite was needed to separate pyrethroids from 50 mL of environmental water, and the recovery remained stable for eight cycles in a reusability test. Furthermore, the main adsorption mechanisms of $\text{Fe}_3\text{O}_4\text{-NH}_2@\text{MIL-101(Cr)}$ were conjugation and hydrophobic effects, as well as molecular docking. In another study, MIL-101(Fe)-based magnetic composite prepared via the in-situ growth of MIL-101(Fe) on Fe_3O_4 NPs was applied to the extraction of organophosphorus pesticides [54]. Here, 20 mg of the magnetic MOF was added to 3 mL of the sample. The separation was performed by shaking the sample solution containing the magnetic MOF in an oscillator for 40 min. In addition, the result of repeated experiments shows that the extraction efficiency of this adsorbent remained stable after 10 runs. Thus, the as-prepared MIL-101-based magnetic composite was mechanically stable and easy to regenerate. The magnetic MOF was successfully used to extract metallic species by encapsulating magnetic NPs functionalized with ethylenediamine into the MOF structure [55]. The as-prepared magnetic MIL-101 could selectively extract Cd(II), Pb(II), Zn(II), and Cr(III) from agricultural samples. The effects of 14 potentially interfering ions were tested, and the obtained recoveries were between 94.5 and 101%, and the tolerance ratios were between 500-fold and 10,000-fold for all tested metal ions except Cu(II) (100-fold), Co(II) (50-fold), and Hg(II) (250-fold). The good selectivity of this magnetic MIL-101 is attributed to the coexistence of ethylenediamine and the MOF in the adsorbent. Moreover, MIL-100(Fe) from the MIL family has been used in MSPE. A dense MIL-100(Fe) coating was formed on the surface of methacrylic acid-functionalized Fe_3O_4 NPs (Fig. 3) [56]. This composite was used for the separation of polychlorinated biphenyl (PCBs) in real environmental water samples. This magnetic MOF has also been applied for the selective extraction of PAHs [57] and neurotransmitters [58].

Furthermore, zeolitic imidazolate frameworks (ZIF MOFs) belong to a water-stable MOF family. Among the ZIF materials, ZIF-8 is the most studied, and it has been applied for the extraction of herbicides, fungicides, PAHs, and inorganic arsenic in aqueous samples, due to its excellent water stability. In one study, $\text{Fe}_3\text{O}_4@\text{ZIF-8}$ core-shell composite was successfully fabricated via an encapsulation method using

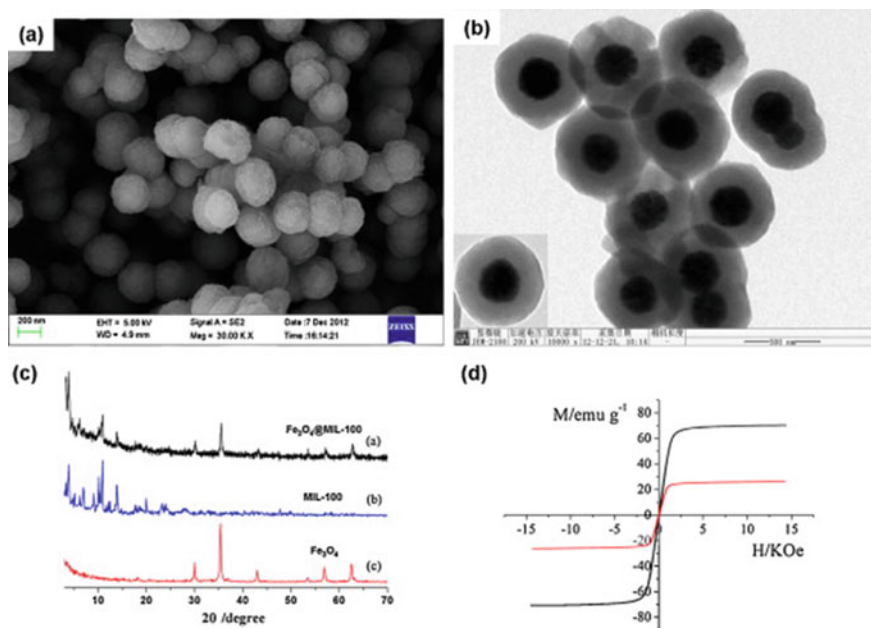


Fig. 3 **a** Scanning electron microscope (SEM) images. **b** Transmission electron microscope (TEM) images of the Fe₃O₄@MIL-100 core-shell magnetic microspheres. **c** Powder x-ray diffraction (PXRD) spectra of Fe₃O₄, MIL-100 and Fe₃O₄@MIL-100. **d** Magnetic curves of Fe₃O₄ and Fe₃O₄@MIL-100. Reprinted with permission from Chen et al. [56]. Copyright (2013), Elsevier

mercaptopropionic acid as a buffering interface [59]. The separation of PAEs from water samples using the Fe₃O₄@ZIF-8 composite in the presence of an external magnetic field was performed in 16 min with 20 mg of adsorbent per 20 mL sample. Moreover, LODs in the range of 0.08–0.24 mg L⁻¹ and accuracy of 85.6–103.6% were obtained in the HPLC (high-performance liquid chromatography)-UV (Ultraviolet) detection test. Fe₃O₄@SiO₂@ZIF-8 composite was fabricated using a layer-by-layer method and was post-modified with TiO₂ to extract fungicides from water samples. The introduced TiO₂ not only enhanced the weak interactions between the targets and ZIF-8 but also improved the mass transfer rate of the fungicides [60]. Another interesting member of the ZIF family is ZIF-7. In one study, magnetic ZIF-7 composite was successfully prepared and used to extract trace PAHs in rainwater and PM_{2.5} samples [61]. The extraction effect of Fe₃O₄@PDA/ZIF-7 was compared with those of Fe₃O₄@PDA and pure Fe₃O₄ NPs. The magnetic MOF (Fe₃O₄@PDA/ZIF-7) composite showed the highest extraction capacity for all the targets, which indicates that the MOF played an important role in the PAH extraction. Under optimized conditions, in the gas chromatography-mass spectrometry (GC-MS) detection analysis, LODs of 0.71–5.79 ng L⁻¹ and recoveries of 92.8–99.4% (water samples) and 82.1–96.7% (PM_{2.5} samples) were obtained.

In addition to the above-mentioned MOFs, MSPE applications have been described for other MOFs such as MOF-5, MOF-177, IRMOF-3, MOF-235, and HKUST-1. Magnetic composites based on these MOFs have been explored as MSPE adsorbents for the extraction of PAHs and gibberellic acids from organic extracts of solid samples [62]; phenols from water samples [63]; Cu(II) and Cd(II) from water samples [64, 65]; and Cd(II), Pb(II), and Zn(II) from baby food samples [66].

The introduction of MOFs to magnetic particles increases the surface area of the MSPE adsorbent and adds new functionalities according to the selected organic linkers and inorganic units used to build the MOFs. Moreover, MOF-based magnetic composites, combining MOFs and magnetic particles, show different advantages, including large surface area, good selectivity, and high extraction capability. Besides the MOFs already explored for MSPE, several other MOFs are yet to be studied for MSPE applications. The development of novel MSPE applications of unexplored MOFs after they are combined with magnetic particles is of interest. In addition, the application of post-synthetic modification strategies will be beneficial to increasing the selectivity of MOFs-based magnetic composites.

2.3.2 COFs-Based Magnetic Composites

COFs are crystalline porous polymers composed of building units with powerful covalent bonds. They show excellent properties that make them suitable as adsorbents, such as a high surface area, easy control of the structure, tunable pore sizes, functional properties, high thermostability, good chemical stability, and selectivity [67]. Therefore, COFs-based magnetic composites as MSPE adsorbents have attracted great attention. Table 1 presents the recent applications of COFs in MSPE.

Furthermore, Fe_3O_4 @COF-(TpBD) for the MSPE of trace PAHs in food samples (Fig. 4) has been reported [68]. This composite exhibited good adsorption ability and high enrichment efficiency for PAHs, due to the hydrophobic interaction and π - π -interaction between PAHs and Fe_3O_4 @COF-(TpBD). The combination of COFs and MNPs was attractive for the effective and quick enrichment of diverse trace analytes from food samples. In addition, the Fe_3O_4 @COF-(TpBD) has also been used to determine six steroidal and phenolic endocrine-disrupting chemicals in meat samples [69]. Moreover, a new COFs-based magnetic composite (denoted as COF-LZU1@PEI@ Fe_3O_4) for the MSPE of PAHs in environmental samples has been reported [70]. The COF-LZU1@PEI@ Fe_3O_4 adsorbent displayed great stability and high enrichment efficiency. Besides, the high sensitivity, great linearity, and good accuracy of the proposed method indicated that it was sensitive and efficient for the separation of PAHs from complex matrixes. Moreover, Chen et al. synthesized Fe_3O_4 @TbBd composites to separate estrogens from human urine samples [71]. This composite is an ideal MSPE adsorbent for the selective isolation and enrichment of estrogens owing to its fascinating features, including a high specific surface area ($202.18 \text{ m}^2 \text{ g}^{-1}$), uniform pore-size distribution (2.8 nm), high magnetic responsiveness (41.4 emu g^{-1}), and chemical stability. Moreover, in one study, the core-shell

Table 1 Applications of COFs for MSPE

| COFs | Analytes | Samples | Analytical techniques | LOD | Recovery | References |
|-------|--------------------------|------------------|-----------------------|------------------------------|----------------------------|------------|
| TpBD | PAHs | Food samples | HPLC-DAD | 0.83–11.7 ng L ⁻¹ | 84.3–107.1% | [68] |
| COF | Bisphenols | Human serum | HPLC-MS | 1.0–78.1 ng L ⁻¹ | 93.0–107.8% | [73] |
| LZU1 | PAHs | Water, soil | HPLC-UV | 0.2–20 pg mL ⁻¹ | 90.9–107.8% 85.1–105.0% | [70] |
| CTF-1 | Perfluorinated compounds | Water | LC-MS/MS | 0.62–1.39 ng L ⁻¹ | 81.8–114.0% | [74] |
| TbBd | Estrogens | Human urine | HPLC-MS | 0.2–7.7 ng L ⁻¹ | 80.6–111.6% | [71] |
| COF | Peptides | Human serum | HPLC-Q-TOF/MS | – | – | [75] |
| TbBd | Peptides | Human serum | HPLC-Q-TOF/MS | – | – | [76] |
| TpBD | Bisphenols | Aqueous solution | – | – | – | [72] |

magnetic nanocomposite Fe₃O₄@TpBD was prepared via a monomer-mediated in-situ growth technique [72]. This composite exhibited excellent properties, including a good magnetic response, a large specific surface area, porous structures, and great chemical stability. Also, bisphenols from complex matrix could be rapidly enriched for the π - π interaction and hydrogen bonding interaction between COF (TpBD) and bisphenols. In another study, bisphenols from human serum samples were separated using different core-shell structured COFs-based composites (with TAPB and TPA as the ligands). This Fe₃O₄@COF composite also featured fascinating properties (particularly porous size, large surface area, and excellent chemical stability); thus, it is an ideal MSPE adsorbent with excellent extraction capability [73]. Magnetic CTF/Fe₂O₃ composite as an MSPE adsorbent was prepared to separate and analyze perfluorinated compounds at trace levels from environmental water samples [74]. The applied MSPE–liquid chromatography–tandem mass spectrometry (MSPE-LC-MS/MS) method showed low LODs, good reproducibility, and a wide linear range. Thus, this MSPE with CTF/Fe₂O₃ composite as the adsorbent displays promising potential for the sensitive detection of perfluorinated compounds in real water samples.

All the above COFs were synthesized at high temperatures for a long time. In another study [75], COFs (TAPB and TPA as building blocks) constructed under room temperature were used to prepare magnetic composites (Fe₃O₄@COFs) for the MSPE of peptides and the simultaneous exclusion of proteins from complex biological samples. This Fe₃O₄@COFs had great adsorption capacity and selectivity for peptides, as well as great magnetic response, which made the enrichment of peptides from the complex matrix easy, fast, and efficient. Meanwhile, in one study, different COFs-based magnetic composites (Tb and BD as the organic ligands) were

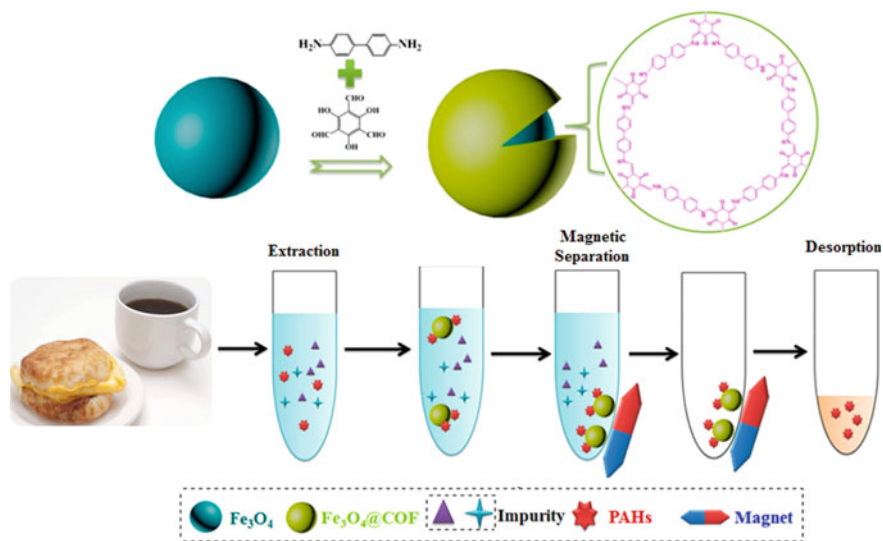


Fig. 4 The fabrication process of $\text{Fe}_3\text{O}_4@TpBD$ and the application to MSPE. Reprinted with permission from Li et al. [68]. Copyright (2018), American Chemical Society

used as an MSPE adsorbent for the extraction of peptides and a size-exclusion effect removal of proteins from human serum samples [76]. These COFs-based magnetic composites offered highly efficient enrichment factors for peptides and had a great ability to remove proteins. The well-ordered porous structures and abundant chemical compositions of the COFs endowed them with great potential for the extraction of peptides from complex samples. The above research expanded the use of COFs and showed promising potential for proteomics analysis [10].

2.3.3 MIPs-Based Magnetic Composites

MIPs are simple and well-established materials that can be employed for the selective extraction of target molecules. They are considered synthetic polymers of predetermined selectivity toward a given analyte or a group of structurally related species [77]. Until now, MIPs-based magnetic composites of various structures have been reported, including core-shell magnetic MIPs, magnetic-nanotube-supported MIPs, magnetic-nanosheet-supported MIPs, and porous-material-supported magnetic MIPs. MIPs present high mechanical, chemical, and thermal stabilities, in addition to their unique selectivity. Therefore, if MNPs are encapsulated into MIPs, the resulting magnetic MIPs will feature not only characteristic magnetic susceptibility but also selectivity for the guest molecule. The introduction of magnetic properties into MIPs can combine the selective sorption capacity of MIPs and the convenient separation of MNPs. Magnetic MIPs used as MSPE adsorbents have fascinating advantages in sample pretreatment, due to their high selectivity for targets and the fast and

easy isolation from complicated samples. Many studies have been conducted in which MIPs-based composites were used as adsorbents in MSPE for the extraction of complicated samples, including environmental, food, and biofluid samples [78].

Magnetic MIP composites as MSPE adsorbents have been used to extract different pollutants in environmental samples, including pesticides, herbicides, antibiotics, and metal ions (Table 2). A novel magnetic MIP was prepared through a surface imprinting technique using a sol-gel process, with di-(2-ethylhexyl) phthalate (DEHP) as the template. This MSPE adsorbent showed great extraction efficiency for DEHP. It was used for the detection of DEHP in different real water samples, with spiked recoveries of 93.3%–103.2% and RSDs of 1.2%–3.2%, and the LOD and LOQ were 0.02 and 0.075 $\mu\text{g L}^{-1}$, respectively [79]. The extraction of PAHs using MIP-based composites has also been reported [80–82]. At the same time, a selective MSPE adsorbent was prepared through surface polymerization onto magnetic $\text{Fe}_3\text{O}_4@ \text{SiO}_2$ NPs. The as-prepared magnetic MIPs ($\text{Fe}_3\text{O}_4@ \text{SiO}_2$ -MIPs) were used for the MSPE extraction of 16 PAHs as priority pollutants in aqueous matrices. The experimental results showed that the magnetic MIPs provided higher extraction efficiencies compared with Fe_3O_4 , $\text{Fe}_3\text{O}_4@ \text{SiO}_2$, and non-imprinted polymer, indicating the creation of selective recognition binding sites at the MNP surface. The LODs and LOQs ranged from 1 to 100 pg mL^{-1} and 2–200 pg mL^{-1} , respectively. Therefore, the $\text{Fe}_3\text{O}_4@ \text{SiO}_2$ -MIPs can be successfully used for the preconcentration and trace quantification of PAHs in real samples such as produced water and river water samples [80]. In other research, a novel magnetic MIP was prepared through a simple method to recognize phosalone, diazinon, and chlorpyrifos in water samples. The magnetic MIPs exhibited much higher adsorption capacity for the tested pesticides than the magnetic non-imprinted polymer. This work provides a simple and new method to realize the combination of magnetic separation and molecular imprinting. The prepared magnetic MIP has the potential for practical applications in the separation of various hazardous pesticides [83]. In addition, magnetic MIPs have been successfully applied in the separation of metal ions [78], sulfonylureas [84], diazinon [85], triazines [86], and auramine O [87] from environmental water or soil.

Furthermore, there has been significant research on the application of magnetic MIPs in food samples [88]. A multi-recognition magnetic MIP with sufficient thermal stability and magnetic properties was synthesized. The MIP exhibited multi-recognition ability and excellent binding capability for cyromazine, melamine, diaveridine, triamterene, and trimethoprim in milk samples, and the apparent maximum numbers of binding sites were 75.2, 77.5, 69.9, 72.5, and 70.4 $\mu\text{mol g}^{-1}$, respectively. The MIP-based composite was suitable for use as an MSPE adsorbent because it not only possessed adequate magnetic responsiveness for fast separation, but also avoided the risk of template leakage on trace component analysis [88]. In another study on milk samples, biocompatible magnetic MIPs were prepared to selectively enrich tetracycline compounds (oxytetracycline, chlortetracycline, doxycycline). The results showed that MIPs-based composites had good recognition ability for the targets, and the selective factors of oxytetracycline, chlortetracycline, and doxycycline were 4.78, 4.23, and 3.39, respectively. The linearity ranged from 0.025 to 500 $\mu\text{g mL}^{-1}$, with an LOD and LOQ of 0.025 and 0.083 $\mu\text{g mL}^{-1}$, respectively

Table 2 Application of magnetic MIPs-based composites as MSPE adsorbents in environmental samples

| Magnetic MIPs | Analytes | Samples | Analytical techniques | LOD | Recovery (%) | References |
|--|---------------------------------------|--|-----------------------|---------------------------|--------------|------------|
| Fe ₃ O ₄ @MIPs | PAHs | Tap water, mineral water, lake water and river water | HPLC-DAD | 33–790 ng L ⁻¹ | 99.8–101 | [81] |
| Fe ₃ O ₄ @MIPs | PAHs | Sea water | GC-MS | 30–375 ng L ⁻¹ | 76–104 | [82] |
| Fe ₃ O ₄ @SiO ₂ @MIPs | PAHs | River water and produced water | GC-MS/MS | 1–100 pg mL ⁻¹ | 4.5–97 | [80] |
| Fe ₃ O ₄ @MIPs | Phosalone, chlorpyrifos, and diazinon | Water samples | UV-Vis spectra | – | 98.8 | [83] |
| Fe ₃ O ₄ @SiO ₂ @MIPs | Sulfonylureas | Environmental water samples | LC-DAD | 6.4–9.5 nM | 73.21–102.00 | [84] |
| Fe ₃ O ₄ @SiO ₂ @MIPs | Diazinon | Water samples | HPLC-UV | 0.02 µg L ⁻¹ | 96.0–104.0 | [85] |
| Fe ₃ O ₄ @MIPs | Di-(2-ethylhexyl) phthalate | Water samples | GC-MS | 0.02 µg L ⁻¹ | 93.3–103.2 | [79] |
| Fe ₃ O ₄ @SiO ₂ @MIPs | Triazines | Soils | HPLC-DAD | 0.1–3 ng g ⁻¹ | 5.4–40.6 | [86] |
| Fe ₃ O ₄ @SiO ₂ @MIPs | Auramine O | Lake water | UV-Vis spectra | – | 99.66–108.75 | [87] |

[89]. Furthermore, MIPs-based composites as MSPE adsorbents have also been used in the extraction of residual triazoles, cinnamic acid, patulin, food additives (vanillin, ethyl vanillin, maltol, and ethyl maltol), and ofloxacin enantiomer food samples. The reasons for the good extraction efficiency of the MIPs-based composites toward the targets are mainly the interactions between the imprinting sites of MIPs and the targets, including noncovalent interactions (e.g., electrostatic interaction, hydrogen bonding, coordination bonding), semicovalent interactions (the template is bound covalently to the functional monomer, but the extraction is based on noncovalent interactions), and covalent interactions (reversible bonding).

2.3.4 Carbon Materials-Based Magnetic Composites

Various carbon materials have been used in the preparation of magnetic composites including G, GO, rGO, CNTs, carbon nanofibers (CNFs), carbon-based quantum dots (CQDs), and g-C₃N₄ [44, 90, 91]. Carbon-based composites as MSPE adsorbents have fascinating characteristics including good thermal, mechanical, and chemical stabilities; large specific surface area; and numerous active sites. The applications of the carbon-based composites as MSPE adsorbents to enrich target analytes in complex sample matrices have been widely reported. In this section, different carbon-based composites are discussed, and an overview of recently developed applications of these composites as MSPE adsorbents is discussed.

Graphene-Based Magnetic Composites

Graphene (G) is composed of sp² carbon atoms arranged in a two-dimensional hexagonal honeycomb lattice. G possesses many fascinating characteristics, such as ultrahigh theoretical surface area, delocalized π -electron system, high intrinsic mobility, nanosheet morphology, easy modification, and cost-effectiveness, which support its application as a material for preparing MSPE adsorbents. However, the lightweight and hydrophobicity of pristine G limit the recovery of pure G and lead to the aggregation of G in sample solutions. Moreover, some polar targets containing hydrophilic groups cannot be enriched by pristine G. Therefore, to broaden the application fields of G, the modification of this material is crucial. GO, with various active sites (hydroxyl, epoxy, carboxyl, and carbonyl), is obtained by modifying G, and the selective affinity of GO for targets is improved. Reduced GO is prepared by removing some of the oxygenated functional groups of GO, thus restoring the conjugated structure [92].

Several G-based magnetic composites, composed of MNPs and G-based materials, have been reported in the scientific literature. Moreover, several methods for the preparation of magnetic graphene composites (MGCs), functionalized MGC, and three-dimensional MGC have emerged (Fig. 5) [93]. The approaches for the fabrication of bare MGC mainly include direct G magnetization, in-situ growth

of magnetic materials method, and covalent functionalization. Direct G magnetization is performed by mixing the G and the MNPs in solution under oscillation or ultrasonication. The MNPs are attached to the G surface via physical adsorption; as a result, the magnetic composite obtained through this method is not stable enough. Chemical co-precipitation and hydrothermal synthesis are two in-situ growth methods that can be used to prepare MGCs. Chemical co-precipitation involves the co-precipitation of $\text{Fe}^{3+}/\text{Fe}^{2+}$ ions through the addition of ammonia solution into an aqueous dispersion of $\text{Fe}^{3+}/\text{Fe}^{2+}$ salts and G at elevated temperature. However, the morphology of the prepared composites is difficult to control, and numerous adsorption sites could be occupied by Fe_3O_4 particles distributed unevenly on the G surface. Hydrothermal synthesis is based on the reduction of GO and Fe^{3+} in the presence of sodium acetate and polyethyleneglycol in an autoclave at elevated temperature. The morphology of the composites can be more easily controlled using this method. Moreover, more adsorption sites of G can be exposed. In the covalent functionalization method, bare MGC is obtained by joining magnetic materials and G via chemical bonding (Fig. 6) [93]. The magnetic composites obtained by covalent functionalization are stable enough for reuse. Moreover, it is difficult to separate targets from a complex matrix with bare MGC as MSPE adsorbents. This phenomenon is due to the strong competitive adsorption between targets and interfering components [94]. Consequently, different kinds of organic groups, including MOFs, ionic surfactants, organic polymers (such as polydopamine, polythiophene, and polypyrrole), supramolecules, and ILs, are commonly introduced into the G-based magnetic composites to improve their adsorption selectivity via the change of interactions between adsorbents and targets [93]. For example, alkaline-modified GO/ Mn_3O_4 composite, $\text{Fe}_3\text{O}_4@/\text{SiO}_2$ -chitosan/GO, $\text{Fe}_3\text{O}_4/\text{RGO}@/\beta$ -CD (CD: carbon dot), polyethyleneimine-functionalized magnetic RGO-based composite ($\text{Fe}_3\text{O}_4@/\text{PEI-RGO}$), magnetic GO-functionalized with pyrrolothiophene copolymer ($\text{MGO}/\text{SiO}_2@/\text{coPPy-Th}$), ionic surfactant-modified GO ($\text{Fe}_3\text{O}_4@/\text{G}@/\text{CTAB/SDS}$) (CTAB: cetyltrimethylammonium bromide, SDS: sodium dodecyl sulfate), MOF-modified MGC, and IL-modified magnetic nanocomposite ($\text{MAG-MOS}_2\text{-RGO-IL}$) incorporated with RGO and molybdenum disulfide (MoS_2), have been prepared [92, 93].

G-based magnetic composites have been widely used in the separation and enrichment of pesticides [95–104], drug residues [105–112], endocrine disruptors [113–117], and heavy metals [118–121]. As seen in Table 3, G-based magnetic composites have been widely applied in the separation and analysis of drug residues. Moreover, various functionalities have been introduced into the magnetic G/GO composites to obtain higher extraction efficiencies and decreased LODs. In recent years, G-based MSPE has been widely used in the extraction of endocrine disruptors from a complex matrix (Table 3). Li et al. [122] prepared $\text{RGO}/\text{ZnFe}_2\text{O}_4$ as an MSPE adsorbent for the extraction of estrogens, including 17α -estradiol, 17β -estradiol, hexestrol, and estrone from water and soil samples. Satisfactory linearity was achieved, $0.05\text{--}500\text{ ng mL}^{-1}$; the LODs were between 0.01 and 0.02 ng mL^{-1} , and the enrichment factors were as high as 241–288. This method has potential use in the extraction and preconcentration of trace compounds in complex environmental matrices [122].

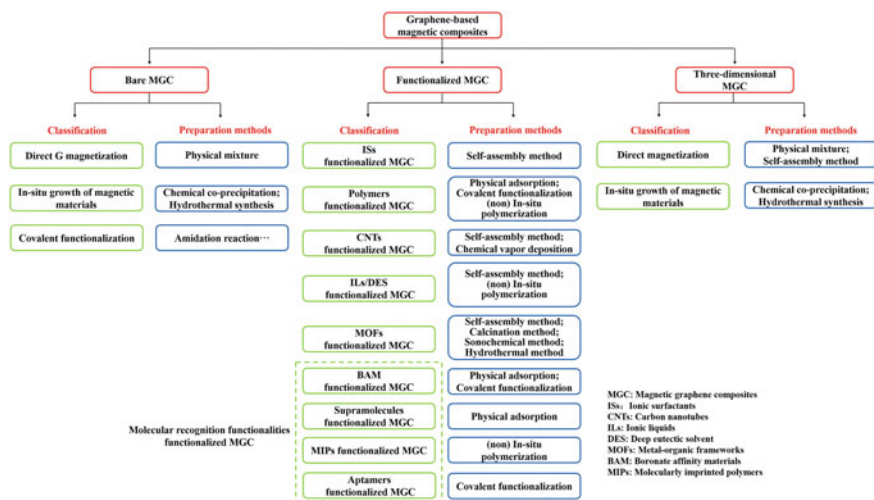


Fig. 5 Overview of graphene-based magnetic composites. Reprinted with permission from Li et al. [93]. Copyright (2018), Elsevier

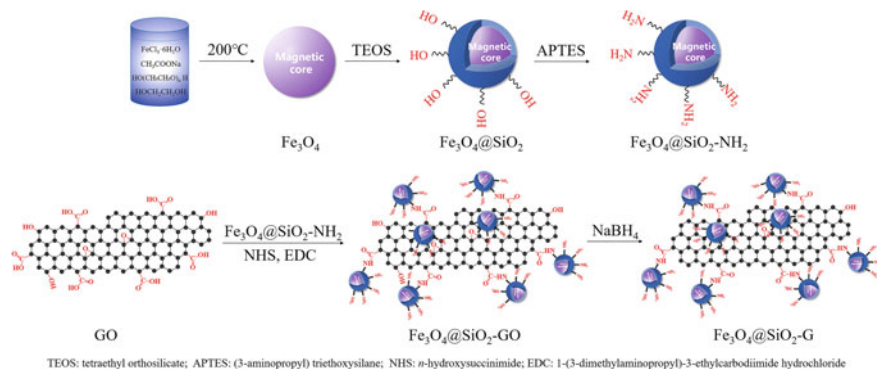


Fig. 6 Procedures for the preparation of Fe₃O₄@SiO₂-G. Reprinted with permission from Li et al. [93]. Copyright (2018), Elsevier

Heavy-metal contamination is a critical environmental problem. As deduced from Table 3 and other works, the application of G/GO-based MSPE in the separation and enrichment of heavy metals has become increasingly popular. G-based magnetic composites adsorb metal ions through cation π interactions, electrostatic interactions, hydrogen bonds, and dative bonds. A GO-based magnetic composite (MGO/SiO₂@coPPy-Th) rich in active reaction sites was synthesized [121]. The composite could be used to effectively extract Cu(II), Pb(II), Cr(III), Zn(II), and Cd(II), and as a potential MSPE adsorbent, it presented high hydrophilic performance, interaction activity, and magnetic susceptibility. This novel MSPE adsorbent showed higher

preconcentration factors (36–44) and adsorption capacities (80–230 mg g⁻¹) than other common MSPE adsorbents. The LODs and recoveries achieved by this method were 0.15–0.65 ng mL⁻¹ and 90%–106%, respectively.

CNT-Based Magnetic Composites

CNTs are formed by rolling up G sheets into cylinders. They are classified as single-walled carbon nanotubes (SWCNTs) and multi-walled carbon nanotubes (MWCNTs) based on the number of G layers. Both SWCNTs and MWCNTs have been widely used in separation and analysis due to their fascinating advantages, such as high aspect ratio (length to diameter ratio), small pore size, availability of well-developed mesopores, hollow/layered structures, high specific surface area (150–1500 m² g⁻¹), good chemical/mechanical stability, and easy modification. CNTs can interact with aromatic compounds through π - π coupling stacking because they possess sp²-hybridized carbon atoms. They exhibit strong affinities for nonpolar organic compounds, such as naphthalene, phenanthrene, and pyrene (Pyr) [123]. Moreover, CNTs have been widely used in the adsorption of gas molecules (CO₂, H₂, NO_x, CH₄, NH₃, and volatile organic carbon) [92]. However, bare CNTs usually have limited adsorption capacity for polar compounds, due to the agglomeration in aqueous solution and the shortage of polar functional groups; therefore, the modification of CNTs is necessary.

Generally, the introduction of MNPs to prepare magnetic carbon nanotubes (MCNTs) is a commonly used approach to enhance the separation efficiency during the separation and analysis procedure. The MCNT composites can provide large surface areas with rapid mass transfer for the enrichment of target analytes in a variety of environmental matrices. In one study, CNT-based magnetic composites were synthesized via one-pot oxidation with K₂FeO₄ as an oxidant [124]. The CNT-Fe₃O₄ as an adsorbent could extract typical environmental pollutants, such as methylene blue (MB) and Cu²⁺, due to its good dispersibility in both water and organic solutions and sufficient magnetic response for recovery. This study indicates that MCNT composites could simultaneously extract organic and inorganic substances in diverse environmental media. For example, MCNT composites were fabricated via an in-situ high-temperature decomposition method and then used this composite as the MSPE adsorbent for separating seven PAHs from aqueous samples [125]. In other research [126], magnetic carboxylic MWCNT composites enhanced by hollow carbon nanospheres (HCSs) (HCSs@Fe₃O₄-MWCNTs-COOH) were fabricated and used as MSPE adsorbents to simultaneously extract three polar herbicides from wheat flour samples (Fig. 7). This MWCNT magnetic composite could afford π - π electron-donor-acceptor interaction, hydrogen bonding, hydrophobic interaction, and electrostatic attraction for target analytes; therefore, the selectivity for the hydrophobic and aromatic herbicides was significantly improved. The established MSPE-HPLC-DAD approach had superior analytical performance, and LODs and recoveries in the range of 0.24–0.68 ng g⁻¹ and 88.8%–96.6%, respectively. Moreover, CNT-based composites can also effectively adsorb inorganic elements from

Table 3 Application of graphene-based composites for MSPE of pesticides, drug residues, endocrine disruptors, biological molecules and heavy metals

| Magnetic adsorbents | Analytes | Samples | Analytical techniques | LOD | Recovery | References |
|--|-----------------------------|----------------------------|-----------------------|----------------------------------|--------------|------------|
| 3D-G-Fe ₃ O ₄ | Organophosphorus pesticides | Fruiti juices | GC-NPD | 1.2–5.1 ng L ⁻¹ | 86.6–107.5 | [95] |
| Fe ₃ O ₄ @G-TEOS-MTMOS | Organophosphorus pesticides | Water samples | GC-mECD | 1.4–23.7 pg mL ⁻¹ | 83–105 | [96] |
| Fe ₃ O ₄ @G-CNPrTEOS | Organophosphorus pesticides | Cow milk | GC-mECD | 0.01–0.6 ng mL ⁻¹ | 82–94 | [97] |
| Fe ₃ O ₄ @SiO ₂ @GO-PEA | Organophosphorus pesticides | Fruit, vegetable and water | GC-NPD | 0.02–0.1 mg L ⁻¹ | 90.4–108.0 | [98] |
| Fe ₃ O ₄ @SiO ₂ -G | Organochlorine pesticides | Orange juices | GC-MS | 0.01–0.05 ng mL ⁻¹ | 73.8–105.4 | [99] |
| Fe ₃ O ₄ @G | Organochlorine pesticide | Tobacco | On-line GPC-GC-MS/MS | 0.01275–3.150 ng g ⁻¹ | 64–126 | [100] |
| Fe ₃ O ₄ @SiO ₂ -G | Organochlorine pesticide | Water | GC-μECD | 0.12–0.28 pg mL ⁻¹ | 80.8–106.3 | [101] |
| RGO/Fe ₃ O ₄ @Au | Organochlorine pesticide | Water | GC-MS | 0.4–4.1 ng L ⁻¹ | 69–114 | [102] |
| mSiO ₂ @Fe ₃ O ₄ -G | Pesticides | Water | HPLC-UV | 0.525–3.30 g L ⁻¹ | 77.5–113.6 | [103] |
| Fe ₃ O ₄ @PEI-RGO | Phenoxy acid herbicides | Rice | HPLC-DAD | 0.67–2 ng g ⁻¹ | 87.41–102.52 | [104] |
| Fe ₃ O ₄ @G | Sulfonamides | Milk | CE | 1.2–5.1 ng L ⁻¹ | 62.7–104.8 | [105] |
| Fe ₃ O ₄ @G | Sulfonamides | Wastewater | HPLC-DAD | 0.43–0.57 ng mL ⁻¹ | 89.1–101.7 | [106] |
| Fe ₃ O ₄ @G | Fluoroquinolones | Food | HPLC-DAD | 0.05–0.3 ng g ⁻¹ | 82.4–108.5 | [107] |

(continued)

Table 3 (continued)

| Magnetic adsorbents | Analytes | Samples | Analytical techniques | LOD | Recovery | References |
|--|--|-------------------------------|-------------------------------------|-------------------------------|------------|------------|
| Fe ₃ O ₄ @GO-ILs | Cephalosporins | Urine | HPLC-UV | 0.6–1.9 ng mL ⁻¹ | 84.3–101.7 | [108] |
| Magnetic ethylenediamine functionalized GO | Naproxen and ibuprofen | Biological and water matrices | HPLC-DAD | 0.03–0.1 ng mL ⁻¹ | 86.4–109.9 | [109] |
| GO/Fe ₃ O ₄ @PABT | Naproxen, diclofenac and ibuprofen | Urine | HPLC-DAD | – | 85.5–90.5 | [110] |
| Fe ₃ O ₄ @G-ILs | Fluoxetine | Urine and water | Spectrofluorometry and spectroscopy | 0.21 mg L ⁻¹ | 95.3–100.6 | [111] |
| Magnetic GO-PANI | Antidepressant | Urine and water | HPLC-UV | 0.4–1.1 ng mL ⁻¹ | 80.2–119.8 | [112] |
| Magnetic G @PDA@Zr-MOF | Bisphenols | Water | HPLC-UV | 0.1–1 mg L ⁻¹ | 64.8–92.8 | [113] |
| rGO-Fe ₃ O ₄ | Bisphenol A | Water | HPLC-UV | 0.01 mg L ⁻¹ | 84.8–104.9 | [114] |
| TET functionalized magnetic GO | Phenolic environmental estrogens | Water | HPLC-UV | 0.15–1.5 ng L ⁻¹ | 88.5–105.6 | [115] |
| (3DG)/ZnFe ₂ O ₄ | Bisphenol analogs | Water | HPLC-DAD | 0.05–0.18 ng mL ⁻¹ | 95.1–103.8 | [116] |
| Octyl-modified magnetic G | Fragrance allergens, musks, phthalates | Water | GC-MS | 0.29–3.2 ng L ⁻¹ | 83–105 | [117] |
| Fe ₃ O ₄ /GO | Co(II), Ni(II), Cu(II), Cd(II) and Pb(II) | Human urine, plasma | ICP-MS | 16–395 ng L ⁻¹ | 81–113 | [118] |
| GO-PAR@Fe ₃ O ₄ | Pb(II) | Food, water | ETAAS | 0.18 ng L ⁻¹ | 94.3–107 | [119] |
| Fe ₃ O ₄ @GO/2-PTSC | Hg(II) | Food, water | ICP-OES | 7.9 ng L ⁻¹ | 92.75–100 | [120] |
| MGO/SiO ₂ @coPPy-Th | Cu(II), Pb(II), Zn(II), Cr(III) and Cd(II) | Water | FAAS | 150–650 ng L ⁻¹ | 90–106 | [121] |

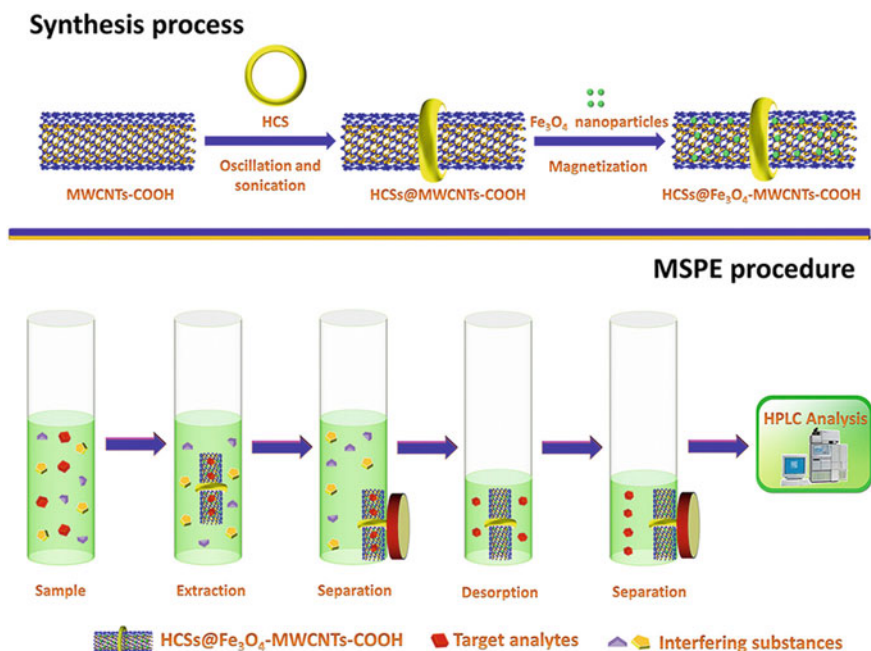


Fig. 7 The synthesis protocol and the proposed MSPE-HPLC-DAD procedure. Reprinted with permission from Li et al. [126]. Copyright (2018), Elsevier

environmental matrices. A magnetic MWCNT composite functionalized with thiol groups (CNTs-SH@Fe₃O₄) was fabricated as an MSPE adsorbent to remove Hg(II) from complex water samples [127]. The CNT-based composite afforded a large surface area of 200.21 m² g⁻¹, pore volume of 0.427 cm³ g⁻¹, and average pore size of 9.23 nm. The maximum adsorption capacity of CNTs-SH@Fe₃O₄ for Hg(II) was 172.4 mg g⁻¹, attributed to surface physical adsorption, reduction adsorption, and the Lewis acid-base interaction between the adsorbent and Hg(II). In addition, this CNT-based composite had good reusability, stability, and good selectivity toward Hg(II).

Other Carbon-Based Magnetic Composites

Some other carbon-based magnetic composites used for MSPE have also been reported, such as CNFs, CQDs, and g-C₃N₄. CNFs are fabricated from various stacking arrangements of G sheets with nonhollow cylindrical nanostructures. They can be used as advantageous adsorbents due to their high surface area, abundant edge sites, flexibility, and mechanical strength. However, CNFs adsorb analytes mainly via π - π interactions; therefore, the modification of CNFs to enhance their polarity and reduce their agglomeration is necessary. Sarafraz-Yazdi et al. [128] prepared a

magnetic CNF composite as an MSPE adsorbent through a chemical co-precipitation synthesis approach. The magnetic CNFs had a rough and highly porous structure, including spherical magnetic particles (about 20 nm), making them suitable candidates for application in MSPE extraction. In this research, three PAHs (anthracene, naphthalene, and fluorine) in environmental water samples were extracted using the magnetic CNFs and were determined via GC with flame-ionization detection. The LODs and recoveries ranged from 0.008 to 0.03 ng mL⁻¹ and 90.1%–100.9%, respectively. Furthermore, CQDs are zero-dimensional spherical NPs less than 10 nm and are mainly composed of graphene quantum dots (GQDs) and carbon quantum dots (CQDs). They can be used to extract pollutants from various environmental samples owing to their large contact area and specific photoluminescence properties [129]. For example, in one study, a magnetic GQD composite (Fe₃O₄/GQDs) was synthesized via a simple hydrothermal method to extract BPA from water samples. The Fe₃O₄/GQDs as an MSPE adsorbent exhibited higher adsorption efficiency for BPA than did Fe₃O₄/G, due to the Fe₃O₄/GQDs large surface-to-volume ratio and high polarity derived from the hydroxyl groups of GQDs [130]. As a new two-dimensional G analog, g-C₃N₄, mainly composed of carbon and nitrogen atoms, has superior characteristics, including thermal and chemical stabilities, good biocompatibility, unique photocatalytic activities, low friction coefficient, and easy surface modification. Moreover, g-C₃N₄ can be prepared via chemical vapor deposition, solid-state reaction, thermal decomposition, and solvothermal synthesis [131]. Magnetic composites based on g-C₃N₄ have been used as MSPE adsorbents owing to their adsorption mechanisms of hydrogen bonding interaction, electrostatic interaction, π - π conjugation, and hydrophobic interaction. Moreover, the lower aromatic content of g-C₃N₄ than that of G endows g-C₃N₄ with a higher extraction recovery for aromatic analytes. Furthermore, magnetic g-C₃N₄ was fabricated as an MSPE adsorbent for the extraction of PAHs in edible oil samples [132]. The established method exhibited excellent properties. The enrichment of targets could be realized within 10 min. The LOQs were less than 15.0%. The recoveries of PAHs for spiked soybean oil samples ranged from 91.0 to 124.1%, with RSDs less than 10.2%.

3 Solid-Phase Microextraction (SPME)

SPME is a well-established green solvent-free extraction technique integrating sampling, extraction, preconcentration, and sample introduction into a single step. It has attracted great interest and has been widely applied in various fields, such as biomedicine, food, forensic science, and environmental studies. The key for SPME is a thin layer of extracting phase, which is spread on a solid support to form different extraction devices, including fiber, in-tube device, stirrer, vessel wall, and disk. Among these, fiber is the most commonly used extraction device. Traditional SPME fibers, such as polydimethylsiloxane (PDMS), polyacrylate, polyethylene glycol, and divinylbenzene (DVB) fibers, have limitations in extraction capability. It is crucial to synthesize novel SPME adsorbents to enrich targets selectively and sensitively and

in a high-throughput manner [133]. Recent materials obtained from compositing the reported materials with other functional materials have excellent characteristics to reasonably overcome the challenges in sample pretreatment. In this work, composites based on MOFs, COFs, G, and MIPs as SPME fiber coatings are discussed.

3.1 MOFs-Based Composites

The first study using MOFs as SPME coating was performed by Cui et al. [134]. In this work, a thin film of MOF-199 was coated on the surface of SPME fiber via a hydrothermal procedure. The fiber provided wide linearity ($36\text{--}23,000\text{ ng L}^{-1}$) and low LODs ($8.3\text{--}23.3\text{ ng L}^{-1}$) for benzene homologs. The excellent efficiency of MOF-199 is attributed to its porous structure and large surface area, $\pi\text{--}\pi$ interactions between aromatic analytes, and Lewis acid sites of MOF-199 pores. Given that the MOFs are prone to collapse when used in humid environment, it is necessary to protect them or hybridize them with other functional materials, leading to better stability and better enrichment efficiency. For example, the MOF/GO composite has been used as a new fiber coating for the SPME of organochlorine pesticides (OCPs) [135]. This composite was prepared through the reaction between oxygen groups of GO and copper sites in MOF-199. The MOF-199/GO composite provided high porosity, large surface area, strong dispersive forces, and good mechanical and thermal stabilities (above $300\text{ }^{\circ}\text{C}$). Moreover, the prepared fiber was successfully applied to extract OCPs more than 140 times. In another work, considering the fascinating properties of both MOF and IL-functionalized graphene (ILG), researchers successfully immobilized MOF-5/ILG composite on etched stainless steel wire through in-situ solvothermal growth (Fig. 8). Owing to its high specific surface area ($820\text{ m}^2\text{ g}^{-1}$) and good adsorption capability, the MOF-5/ILG exhibited high enrichment capacity for chloramphenicol and thiamphenicol through $\pi\text{--}\pi$ and H-bonding interactions [136]. Furthermore, MOF@microporous organic network (MON) composite was prepared via a Sonogashira coupling reaction. The MOF@MON was successfully used to enrich PAHs in environmental water, food samples, and particulate matter (PM 2.5), and the results indicate that the combination of MOF and MON not only enhanced the hydrophobic properties of MOFs, but also improved the extraction capacity [137].

3.2 COFs-Based Composites

Due to their large adsorption capability, COFs have attracted attention in SPME applications in the past five years. Wang et al. successfully synthesized a novel COF (SNW-1) through a solvothermal method. Then, an SPME fiber was prepared via a covalent crosslinking between the SNW-1 nanocomposite and a silanol-functionalized stainless steel wire. The SPME fiber was used for the extraction of phenols in real honey

Fig. 8 Schematic demonstration of the in-situ solvothermal growth of MOF-5/ILG on etched stainless steel wire. Reprinted with permission from Wu et al. [136]. Copyright (2016), Elsevier



samples before detection through GC-MS. The results indicated that the established method was appropriate for the detection of the phenols in honey samples, and the SNW-1 fiber may have application potential for the extraction of more organic compounds in other samples [138]. Furthermore, an effective and stable nanocomposite consisting of GO and SNW-1 (rGO/SNW-1) was prepared. This composite was attached to the surface of stainless steel fiber through a quick inversion process. This robust and stable coating was applied for the headspace extraction of PAEs from water samples. The rGO/SNW-1 composite combined the excellent properties of SNW-1 and rGO, among which SNW-1 is N-rich, and rGO is full of hexagonal conjugated rings. Therefore, due to hydrogen binding and π -interaction, the coating had a high enrichment factor of PAEs. The rGO/SNW-1 fiber showed stability, reusability, and high extraction efficiency for targets [139].

Furthermore, the number of reported studies on COF application for SPME is relatively small. However, more COFs and COFs-based composites can be designed and prepared with higher surface area, good stability, and unique functional groups through the adjustment of the monomer and the frame structure. COFs and COFs-based composites have the potential to further improve the sensitivity and enhance the selectivity of self-made SPME coatings.

3.3 Graphene-Based Composites

Graphene (G) and its composites have also been widely used as SPME fiber coatings. G can be coated onto the surface of SPME fiber via covalent grafting and non-covalent wrapping, including direct immersion, chemical bonding method, sol-gel method, and electrochemical method. Moreover, G could be embedded in a polymer-based monolith for a novel multiple monolithic fiber [140]. In addition, G-based composites have a better specific adsorption capacity due to their combination of the advantages of G and other functional materials. As shown in Table 4, G-based composites have been widely used as SPME fibers for the analysis of various targets. Moreover, various functionalities have been introduced into the G/GO composites to establish more effective, selective, and environmental-friendly analytical methods. In one study, the GNC-Co composite, derived from ZIF-67-GO composite, was successfully prepared as a fascinating SPME fiber with enhanced performance. The research results showed that the GNC-Co composite had good adsorption properties for acenaphthylene, naphthalene, and fluorine [148]. Considering the excellent characteristics of both MOF and ILG, Wu et al. prepared a new SPME fiber through the in-situ solvothermal growth of MOF-5/ILG nanocomposite on etched stainless steel wire [136]. The MOF-5/ILG-coated fiber was used to enrich chloramphenicol and thiamphenicol from food (milk and honey) and biological samples (serum and urine). As the composite combined the properties of MOF and ILG, it exhibited high affinity to the antibiotics. Compared with the MOF-5-coated fiber, the MOF-5/ILG-coated fiber provided much higher enhancement factors, due to enhanced π - π and H-bonding interactions.

3.4 Other Carbon-Based Composites (CNTs)

CNTs are the most commonly used carbon materials in SPME. Originally, CNT-based SPME coatings were synthesized using commercial CNTs, including SWCNTs and MWCNTs, with no further treatment. The obtained coatings showed a better extraction effect toward hydrophobic organic targets than commercial SPME fibers (PDMS and PDMS/DVB). Moreover, the direct extraction of some organic polar and ionic compounds from aqueous solutions is challenging due to their hydrophilic nature. To enhance the extraction efficiency and selectivity of SPME coatings, CNTs are usually combined with other functional materials through chemical bonding or physical blending. The functional materials include ILs, polymers, chitosan, metal oxides, cyclodextrin, phenylboronic acid, and silicon dioxide. Their advantages can be successfully introduced into the composites, and the extraction capability of the modified CNTs is also improved [133]. A composite based on PBA-functionalized CNTs was prepared. This composite coating for SPME could effectively enrich carbohydrates in biofluids and semi-solid biotissues in vitro or in vivo, due to the extraction capability of CNT and the recognition function of PBA [149].

Table 4 Application of G-based composites as SPME fibers in various targets analysis

| Materials | Analytes | Samples | Analytical techniques | LOD | Recovery | References |
|---------------------------|----------------------------|-------------------------------------|-----------------------|--------------------------------|-------------|------------|
| rGO/SNW-1 | Phthalate esters | Cucumber solution and boiling water | GC-MS | 0.01–0.50 $\mu\text{g L}^{-1}$ | 80.5–111.0% | [139] |
| MOF-5/GO | Triazole fungicides | Fruits, vegetables | SPME-GC- μ ECD | 0.05–1.58 ng g^{-1} | 85.6–105.8% | [140] |
| ^a TPhP-MIPs/GO | Triphenyl phosphate | Environmental water samples | ^b GC-FPD | 0.04–0.12 ng mL^{-1} | 70–110% | [141] |
| MoS ₂ /RGO | Polychlorinated biphenyls | Milk | GC-MS | 0.05–0.09 ng mL^{-1} | – | [142] |
| ^c PANI/PPy/GO | Volatile organic compounds | Lung cell lines | GC-MS | 1.0–12 ng L^{-1} | – | [143] |
| ^d GO-PDMS | Triazoles | Environmental water samples | GC-ECD | 0.01–0.03 g L^{-1} | – | [144] |
| 3D-rGO-PANI | Ethion | Environmental water samples | NCD-IMS | 0.4 $\mu\text{g L}^{-1}$ | 84–98% | [145] |
| G-CNTs | Benzene homologues | Environmental water samples | GC-MS | 0.59–2.68 ng L^{-1} | 84.7–108.1% | [146] |
| ^e GO/POE | Phenols | River water | GC-MS | 0.12–1.36 ng L^{-1} | 81–113% | [147] |

^a TPhP: Triphenyl phosphate^b FPD: flame photometric detector^c PANI: polyaniline; PPy: polypyrrole^d PDMS: poly(dimethylsiloxane)^e POE: polyoxyethylene

In addition, CFs, g-C₃N₄ and carbon dots have been used as SPME coatings alone or combined with other materials. For example, in one study, the CFs@PPy composite obtained by combining polypyrrole with CFs exhibited better physico-chemical characteristics (such as large surface area, high efficiency, reproducibility, and reusability) than bare CFs and PPy fibers. Moreover, the CFs@PPy could be used as SPME adsorbent for the extraction and quantification of 2-PF from patients' breath and coffee samples. The results showed that the LOD was 0.05 ng mL⁻¹, and the fiber repeatability and fiber-to-fiber reproducibility (RSD%) were in the range of 3.2–4.1%. Therefore, the proposed fiber had great extraction performance for 2-pentylfuran [129]. In another research, a novel graphitic carbon nitride hybridized with copper oxide (g-C₃N₄/CuO) composite was prepared and was used as the coating of SPME for the first time. The coating was used to preconcentrate PAHs from water and soil samples. Compared with pristine g-C₃N₄ or CuO, the g-C₃N₄/CuO composite as the SPME coating provided the best adsorption affinity for PAHs.

4 Conclusion

The use of composites in sample preparation is an important trend since the composites combine the advantages of different functional materials. This chapter outlines the current states of various composites and their applications as adsorbents for SPE and SPME. As shown in the literature, MOFs, comprising metal ions and organic linkers, have attracted much attention owing to their ability to function as hosts. Moreover, MOFs can adsorb and separate target analytes from mixtures owing to their several extraordinary properties, such as large surface area, high porosity, and uniformly structured cavities. However, many MOFs still have some limits, especially due to the lack of durability in water and thermal stability. Composites prepared based on MOFs can keep the advantages of MOFs, improve their shortcomings and introduce excellent properties of other functional materials. Therefore, MOF-based composites have been widely used as an adsorbent in DSPE, column SPE, MSPE, and SPME, among others. Generally, the hydrophobicity of most COFs is high, which restricts their application in the adsorption of hydrophilic compounds. Therefore, the modification of COFs to improve their hydrophilicity is necessary. From this chapter, we know that COFs-based composites have also been widely used in SPE and SPME. The employment of G-based composites in sample pretreatment is a topic of growing interest since G possesses large surface area, large delocalized π -electron system, and controllable surface properties. The surface of G, GO, or rGO could be modified with other functional materials such as MOFs, ILs, MIPs, metal, or metal-oxide NPs to overcome the interlayer accumulation and improve the mechanical/thermal stability and the selectivity, thus enhancing the extraction efficiency of separation techniques for target analytes with different structures and properties. Meanwhile, other carbon-based composites and MIP-based composites also play important roles

in sample preparation involving column SPE, MSPE, DSPE, and SPME. Therefore, the development of tunable composite materials containing different functional materials opens up a large research window.

However, the extraction selectivity and specificity of these developed composites are not enough to meet the requirements of higher extraction capacity for each analyte in complex matrices with specific structures and physicochemical properties. The adsorption mechanism of composite materials to the target analytes is still derived from speculation. Clarifying the adsorption mechanism between composites and target analytes is beneficial for design and development of new strategies that can help researchers control the target/adsorbent interactions and enhance the physicochemical properties of composites; this can help prevent and reduce the background signal caused by non-specific binding. Therefore, more attention should be given to the adsorption mechanism between composites and analytes. Meanwhile, more composite materials with excellent properties should be developed based on the adsorption mechanism.

Acknowledgements We greatly appreciate the financial support provided by Shandong Provincial Natural Science Foundation, China (No. ZR2017PH044), National Natural Science Foundation of China (NSFC, No. 21777054), and the foundation of Linyi University (LYDX2016BS050).

References

1. B.H. Fumes, M.R. Silva, F.N. Andrade, C.E. Nazario, F.M. Lanças, *Trends Anal. Chem.* **71**, 9 (2015)
2. M. Sajid, M.K. Nazal, I. Ihsanullah, *Anal. Chim. Acta.* **1141**, 246 (2021)
3. M. Ghorbani, M. Aghamohammadhassan, H. Ghorbani, A. Zabihi, *Microchem. J.* **158**, 105250 (2020)
4. S.J. Yin, J. Zhao, F.Q. Yang, *J. Pharmaceut. Biomed.* **192**, 113675 (2021)
5. C. Calderilla, F. Maya, L.O. Leal, V. Cerda, *Trends Anal. Chem.* **108**, 370 (2018)
6. G. Marrubini, S. Dugheri, G. Cappelli, G. Arcangeli, N. Mucci, P. Appelblad, C. Melzi, A. Speltini, *Anal. Chim. Acta.* **1119**, 77 (2020)
7. V. Jalili, A. Barkhordari, A. Ghiasvand, *Microchem. J.* **157**, 104967 (2020)
8. X.J. Li, W. Ma, H.M. Li, Y. Bai, H.W. Liu, *Coordin. Chem. Rev.* **397**, 1 (2019)
9. Y.H. Gao, G. Liu, M.K. Gao, X.D. Huang, D.H. Xu, *Crit. Rev. Anal. Chem.* **50**(5), 472 (2020)
10. N. Li, J.J. Du, D. Wu, J.C. Liu, N. Li, Z.W. Sun, G.L. Li, Y.N. Wu, *Trends Anal. Chem.* **108**, 154 (2018)
11. J. Feng, J. Feng, X. Ji, C. Li, S. Han, H. Sun, M. Sun, *Trends Anal. Chem.* **137**, 116208 (2021)
12. J. Guo, S.J. Park, L.Y. Meng, X.H. Jin, *Carbon Lett.* **24**(1), 10 (2017)
13. M. Sun, J. Feng, Y. Bu, X. Wang, H. Duan, C. Luo, *Talanta* **134**, 200 (2015)
14. J. Feng, M. Sun, Y. Bu, C. Luo, *Talanta* **148**, 313 (2016)
15. J. Feng, M. Sun, Y. Bu, C. Luo, *J. Chromatogr. A* **1393**, 8 (2015)
16. J. Zhang, W. Li, W. Zhu, P. Qin, M. Lu, X. Zhang, Y. Miao, Z. Cai, *Chem. Commun.* **55**, 10019 (2019)
17. T.Y. Zhou, L. Ding, G.B. Che, W. Jiang, L. Sang, *Trends Anal. Chem.* **114**, 11 (2019)
18. H. Sun, J. Feng, S. Han, X. Ji, C. Li, J. Feng, M. Sun, *Microchim. Acta.* **188**, 189 (2021)
19. J. Feng, H. Maloko Loussala, S. Han, X. Ji, C. Li, M. Sun, *Trends Anal. Chem.* **125**, 115833 (2020)

20. H.M. Liu, P. Jin, F.C. Zhu, L. Nie, H.D. Qiu, Trends Anal. Chem. **134**, 116132 (2021)
21. I. Saeedi, P. Hashemi, Z. Ramezani, A. Badiei, Anal. Methods-UK **7**(24), 10185 (2015)
22. Q. Wu, H. Yuan, Y. Weng, Z. Sui, X. Zhang, Y. Hu, Z. Liang, L. Zhang, Y. Zhang, Chin. J. Chromatogr. **37**(8), 836 (2019)
23. M. Sun, S. Han, J. Feng, C. Li, X. Ji, J. Feng, H. Sun, Topics Curr. Chem. **379**(4), 24 (2021)
24. M. Sun, J. Feng, X. Ji, C. Li, S. Han, M. Sun, Y. Feng, J. Feng, H. Sun, J. Chromatogr. A **1642**, 462003 (2021)
25. N. Manousi, B. Gomez-Gomez, Y. Madrid, E.A. Deliyanni, G.A. Zachariadis, Microchem J. **152**, 104428 (2020)
26. A.R. Bagheri, M. Ghaedi, Arab. J. Chem. **13**, 5218 (2020)
27. D.K. Lu, C. Liu, M.H. Qin, J.J. Deng, G.Y. Shi, T.S. Zhou, Anal. Chim. Acta **1133**, 88 (2020)
28. C.D. Jia, Y.D. Mi, Z.K. Liu, W.F. Zhou, H.X. Gao, S.B. Zhang, R.H. Lu, Microchem. J. **153**, 104522 (2020)
29. Y. Zhang, Y.G. Zhao, N. Muhammad, M.L. Ye, Y. Zhu, J. Chromatogr. A **1618**, 460891 (2020)
30. E.V.S. Maciel, A.L. de Toffoli, E.S. Neto, C.E.D. Nazario, F.M. Lanças, Trends Anal. Chem. **119**, 115633 (2019)
31. G. Ma, M. Zhang, L. Zhu, H. Chen, X. Liu, C. Lu, J. Chromatogr. A **1531**, 22 (2018)
32. C. Lou, C. Wu, K. Zhang, D. Guo, L. Jiang, Y. Lu, Y. Zhu, J. Chromatogr. A **1550**, 45 (2018)
33. Y. Yan, J. Lu, C. Deng, X. Zhang, Talanta **107**, 30 (2013)
34. B. Arabsorkhi, H. Sereshti, Microchem. J. **140**, 241 (2018)
35. H. Fotovat, M. Khajeh, A.R. Oveisi, M. Ghaffari-Moghaddam, S. Daliran, Microchim. Acta. **185**, 469 (2018)
36. P.P. Yang, Q. Liu, J.Y. Liu, H.S. Zhang, Z.S. Li, R.M. Li, L.H. Liu, J. Wang, J. Mater. Chem. A **5**, 17933 (2017)
37. W.X. Li, L. Huang, D.D. Guo, Y.G. Zhao, Y. Zhu, J. Chromatogr. A **1571**, 76 (2018)
38. W.H. Ji, R.H. Sun, Y.L. Geng, W. Liu, X. Wang, Anal. Chim. Acta **1001**, 179 (2018)
39. K.Q. Jiang, Q.W. Huang, K. Fan, L.D. Wu, D.X. Nie, W.B. Guo, Y.J. Wu, Z. Han, Food Chem. **264**, 218 (2018)
40. P. Klongklaew, T. Naksena, P. Kanatharana, O. Bunkoed, Anal. Bioanal. Chem. **410**, 7185 (2018)
41. I. Vasconcelos, C. Fernandes, Trends Anal. Chem. **89**, 41 (2017)
42. W.K. Li, Y.P. Shi, Trends Anal. Chem. **118**, 652 (2019)
43. V.V. Tolmacheva, V.V. Apyari, E.V. Kochuk, S.G. Dmitrienko, J. Anal. Chem. **71**, 321 (2016)
44. A. Speltini, M. Sturini, F. Maraschi, A. Profumo, Trends Environ Anal. Chem. **10**, 11 (2016)
45. R. Ma, L. Hao, J. Wang, C. Wang, Q. Wu, Z. Wang, J. Sep. Sci. **39**, 3571 (2016)
46. F. Maya, C.P. Cabello, R.M. F., J.M. Estela, G.T. Palomino, V. Cerd, Trends Anal. Chem. **90**, 142 (2017)
47. J.P. Ma, G.G. Wu, S. Li, W.Q. Tan, X.Y. Wang, J.H. Li, L.X. Chen, J. Chromatogr. A **1553**, 57 (2018)
48. V. Georgakilas, M. Otyepka, A.B. Bourlinos, V. Chandra, N. Kim, K.C. Kemp, P. Hobza, R. Zboril, K.S. Kim, Chem. Rev. **112**, 6156 (2012)
49. A. Tadjarodi, A. Abbaszadeh, Microchim. Acta **183**, 1391 (2016)
50. S.H. Huo, X.P. Yan, Analyst **137**, 3445 (2012)
51. Y.F. Huang, M. Liu, Y.Q. Wang, Y. Li, J.M. Zhang, S.H. Huo, RSC Adv. **6**, 15362 (2016)
52. J. Ma, Z. Yao, L. Hou, W. Lu, Q. Yang, J. Li, L. Chen, Talanta **161**, 686 (2016)
53. X. He, W. Yang, S. Li, Y. Liu, B. Hu, T. Wang, X. Hou, Microchim. Acta **185**, 125 (2018)
54. S. Zhang, Z. Jiao, W. Yao, J. Chromatogr. A **1371**, 74 (2014)
55. M. Babazadeh, R. Hosseinzadeh-Khanmiri, J. Abolhasani, E. Ghorbani-Kalhor, A. Hassanpour, RSC Adv. **5**, 19884 (2015)
56. X. Chen, N. Ding, H. Zang, H. Yeung, R.S. Zhao, C. Cheng, J. Liu, T.W.D. Chan, J. Chromatogr. A **1304**, 241 (2013)
57. F. Du, Q. Qin, J. Deng, G. Ruan, X. Yang, L. Li, J. Li, J. Sep. Sci. **39**, 2356 (2016)
58. T. Khezeli, A. Daneshfar, RSC Adv. **5**, 65264 (2015)

59. X. Liu, Z. Sun, G. Chen, W. Zhang, Y. Cai, R. Kong, X. Wang, Y. Suo, J. You, *J. Chromatogr. A* **1409**, 46 (2015)
60. H. Su, Y. Lin, Z. Wang, Y.L. Wong, X. Chen, T.W. Chan, *J. Chromatogr. A* **1466**, 21 (2016)
61. S. Zhang, W. Yao, J. Ying, H. Zhao, *J. Chromatogr. A* **1452**, 18 (2016)
62. Y. Hu, Z. Huang, J. Liao, G. Li, *Anal. Chem.* **85**, 6885 (2013)
63. G.H. Wang, Y.Q. Lei, H.C. Song, *Anal. Methods* **6**, 7842 (2014)
64. Y. Wang, J. Xie, Y. Wu, X. Hu, *Microchim. Acta* **181**, 949 (2014)
65. S.E. Moradi, A.M. Haji Shabani, S. Dadfarnia, S. Emami, *Anal. Methods* **8**, 6337 (2016)
66. E. Ghorbani-Kalhor, R. Hosseinzadeh-Khanmiri, M. Babazadeh, J. Abolhasani, A. Hassanpour, *Can. J. Chem.* **93**, 518 (2015)
67. L.X. Chen, Q. Wu, J. Gao, H. Li, S.Q. Dong, X.F. Shi, L. Zhao, *Trends Anal. Chem.* **113**, 182 (2019)
68. N. Li, D. Wu, N. Hu, G. Fan, X. Li, J. Sun, X. Chen, Y. Suo, G. Li, Y. Wu, *J. Agric. Food Chem.* **66**, 3572 (2018)
69. N. Li, D. Wu, J. Liu, N. Hu, X. Shi, C. Dai, Z. Sun, Y. Suo, G. Li, Y. Wu, *Microchem. J.* **143**, 350 (2018)
70. R. Wang, Z. Chen, *Microchim. Acta* **184**, 1657 (2017)
71. L. Chen, M. Zhang, F. Fu, J. Li, Z. Lin, *J. Chromatogr. A* **1567**, 136 (2018)
72. Y. Li, C.X. Yang, X.P. Yan, *Chem. Commun.* **53**, 2511 (2017)
73. L. Chen, Y. He, Z. Lei, C. Gao, Q. Xie, P. Tong, Z. Lin, *Talanta* **181**, 296 (2018)
74. J.Y. Ren, X.L. Wang, X.L. Li, M.L. Wang, R.S. Zhao, J.M. Lin, *Anal. Bioanal. Chem.* **410**, 136 (2018)
75. G. Lin, C. Gao, Q. Zheng, Z. Lei, H. Geng, Z. Lin, H. Yang, Z. Cai, *Chem. Commun.* **53**, 3649 (2017)
76. C. Gao, G. Lin, Z. Lei, Q. Zheng, J. Lin, Z. Lin, *J. Mater. Chem. B* **5**, 7496 (2017)
77. L.X. Chen, X.Y. Wang, W.H. Lu, X.Q. Wu, J.H. Li, *Chem. Soc. Rev.* **45**, 2137 (2016)
78. S.Y. Huang, J.Q. Xu, J.T. Zheng, F. Zhu, L.J. Xie, G.F. Ouyang, *Anal. Bioanal. Chem.* **410**, 3991 (2018)
79. C.Y. Li, X.G. Ma, X.J. Zhang, R. Wang, Y. Chen, Z.Y. Li, *Anal. Bioanal. Chem.* **408**, 7857 (2016)
80. A. Azizi, F. Shahhoseini, C.S. Bottaro, *J. Chromatogr. A* **1610**, 460534 (2020)
81. M. Villar-Navarro, M.J. Martín-Valero, R.M. Fernández-Torres, M. Callejón-Mochón, M.Á. Bello-López, *J. Chromatogr. B* **1044**, 63 (2017)
82. B. Benedetti, M. Di Carlo, E. Magi, *Microchem. J.* **145**, 1199 (2019)
83. A. Masoumi, K. Hemmati, M. Ghaemy, *RSC Adv.* **55**, 49401 (2016)
84. S.S. Miao, M.S. Wu, H.G. Zuo, C. Jiang, S.F. Jin, Y.C. Lu, H. Yang, *J. Agric. Food. Chem.* **63**, 3634 (2015)
85. A. Bazmandegan-Shamili, S. Dadfarnia, A.M.H. Shabani, M. Saeidi, M.R. Moghadam, *Food. Anal. Methods* **9**, 2621 (2016)
86. M.J. Patiño-Roperro, M. Díaz-Álvarez, *J. Mol. Recognit.* **30**, 2593 (2017)
87. W.W. Yang, T. Muhammad, A. Yigaimu, K. Muhammad, L.X. Chen, *J. Sep. Sci.* **41**, 4185 (2019)
88. X.J. Kong, C. Zheng, Y.H. Lan, S.S. Chi, Q. Dong, H.L. Liu, C. Peng, L.Y. Dong, L. Xu, X.H. Wang, *Anal. Bioanal. Chem.* **410**, 247 (2018)
89. S.X. Wang, R.R. Ma, Y.Z. Mazzu, J.W. Zhang, W. Li, L. Tan, L.D. Zhou, Z.N. Xia, Q.H. Zhang, C.S. Yuan, *Food. Chem.* **326**, 126969 (2020)
90. H. Abdolmohammad-Zadeh, A. Zamani, Z. Shamsi, *J. Chromatogr. A* **1590**, 2 (2019)
91. A. Azzouz, S.K. Kailasa, S.S. Lee, A.J. Rascon, E. Ballesteros, M. Zhang, K.H. Kim, *Trends Anal. Chem.* **108**, 347 (2018)
92. S.Y. Di, T. Ning, J. Yu, P. Chen, H. Yu, J.H. Wang, H.C. Yang, S.K. Zhu, *Trends Anal. Chem.* **126**, 115864 (2020)
93. N. Li, H.L. Jiang, X.L. Wang, X. Wang, G.J. Xu, B.B. Zhang, L.J. Wang, R.S. Zhao, J.M. Lin, *Trends Anal. Chem.* **102**, 60 (2018)
94. T. Khezeli, A. Daneshfar, *Trends Anal. Chem.* **89**, 99 (2017)

95. S. Mahpishanian, H. Sereshti, *J. Chromatogr. A* **1443**, 43 (2016)
96. H.R. Nodeh, W.A.W. Ibrahim, M.A. Kamboh, M.M. Sanagi, *Chemosphere* **166**, 21 (2017)
97. H.R. Nodeh, W.A.W. Ibrahim, M.M. Sanagi, H.Y. Aboul-Enein, *RSC Adv.* **6**, 24853 (2016)
98. S. Mahpishanian, H. Sereshti, M. Baghdadi, *J. Chromatogr. A* **1405**, 48 (2016)
99. T. Sun, J. Yang, L. Li, X. Wang, X. Li, Y. Jin, *Chromatographia* **79**, 345 (2016)
100. Y.B. Luo, X. Li, X.Y. Jiang, B.D. Cai, F.P. Zhu, H.F. Zhang, Z.G. Chen, Y.Q. Pang, Y.Q. Feng, *J. Chromatogr. A* **1406**, 1 (2015)
101. H.R. Nodeh, W.A.W. Ibrahim, M.A. Kamboh, M.M. Sanagi, *RSC Adv.* **5**, 76424 (2015)
102. A. Mehdinia, S. Rouhani, S. Mozaffari, *Microchim. Acta* **183**, 1177 (2016)
103. X. Wang, H. Wang, M. Lu, X. Ma, P. Huang, X. Lu, X. Du, *J. Sep. Sci.* **39**, 1734 (2016)
104. N. Li, J. Chen, Y.P. Shi, *Anal. Chim. Acta* **949**, 23 (2017)
105. Z. Li, Y. Li, M. Qi, S. Zhong, W. Wang, A.J. Wang, J. Chen, *J. Sep. Sci.* **39**, 3818 (2016)
106. J. Wu, H. Zhao, R. Chen, C. Pham-Huy, X. Hui, H. He, *J. Chromatogr. B* **1029**, 106 (2016)
107. X. He, G.N. Wang, K. Yang, H.Z. Liu, X.J. Wu, J.P. Wang, *Food Chem.* **221**, 1226 (2017)
108. J. Wu, H. Zhao, D. Xiao, P.H. Chuong, J. He, H. He, *J. Chromatogr. A* **1454**, 1 (2016)
109. M. Ghorbani, M. Chamsaz, G.H. Rounaghi, *J. Sep. Sci.* **39**, 1082 (2016)
110. A.A. Asgharinezhad, H. Ebrahimzadeh, *J. Chromatogr. A* **1435**, 18 (2016)
111. E. Kazemi, A.M.H. Shabani, S. Dadfarnia, A. Abbasi, M.R.R. Vaziri, A. Behjat, *Anal. Chim. Acta* **905**, 85 (2016)
112. M. Ghorbani, M. Chamsaz, G.H. Rounaghi, M. Aghamohammadhasani, O. Seyedin, N.A. Lahoori, *Anal. Bioanal. Chem.* **408**, 7719 (2016)
113. X.Y. Wang, C.H. Deng, *Talanta* **144**, 1329 (2015)
114. D. Li, X. Ma, R. Wang, Y. Yu, *Anal. Bioanal. Chem.* **409**, 1 (2016)
115. X.H. Chen, S.D. Pan, M.J. Ye, X.P. Li, Y.G. Zhao, M.C. Jin, *J. Sep. Sci.* **39**, 762 (2016)
116. L. Wang, Z. Zhang, J. Zhang, L. Zhang, *J. Chromatogr. A* **1463**, 1 (2016)
117. K.V. Maidatsi, T.G. Chatzimitakos, V.A. Sakkas, C.D. Stalikas, *J. Sep. Sci.* **38**, 3758 (2015)
118. J. Sun, Q. Liang, Q. Han, X. Zhang, M. Ding, *Talanta* **132**, 557 (2015)
119. S. Akbarzade, M. Chamsaz, G.H. Rounaghi, *Anal. Methods* **10**, 2081 (2018)
120. A. Keramat, R. Zare-Dorabei, *Ultrason. Sonochem.* **38**, 421 (2017)
121. K. Molaei, H. Bagheri, A.A. Asgharinezhad, H. Ebrahimzadeh, M. Shamsipur, *Talanta* **167**, 607 (2017)
122. W.Q. Li, J. Zhang, W.L. Zhu, P.G. Qin, Q. Zhou, M.H. Lu, X.B. Zhang, W.D. Zhao, S.S. Zhang, Z.W. Cai, *Talanta* **208**, 120440 (2020)
123. J. Ahmad, S. Naeem, M. Ahmad, A.R.A. Usman, M.I. Al-Wabel, *J. Environ. Manag.* **246**, 214 (2019)
124. Y. Liu, L. Guo, H. Huang, J. Dou, Q. Huang, D. Gan, J. Chen, Y. Li, X. Zhang, Y. Wei, *J. Colloid. Interface. Sci.* **545**, 8 (2019)
125. A.I. Corps Ricardo, F.J. Guzman Bernardo, M. Zougagh, R.C. Rodriguez Martin-Doimeadios, A. Rios, *Anal. Bioanal. Chem.* **409**, 5125 (2017)
126. W.-K. Li, H.X. Zhang, Y.P. Shi, *Anal. Chim. Acta* **1011**, 40 (2018)
127. L. Fan, A. Zhou, L. Zhong, Z. Zhang, Y. Liu, *Chemosphere* **226**, 405 (2019)
128. A. Sarafraz-Yazdi, T. Rokhian, A. Amiri, F. Ghaemi, *New J. Chem.* **39**, 5621 (2015)
129. X. Shi, W. Wei, Z. Fu, W. Gao, C. Zhang, Q. Zhao, F. Deng, X. Lu, *Talanta* **194**, 809 (2019)
130. R. Mohammad-Rezaei, H. Razmi, V. Abdollahi, A.A. Matin, *Anal. Methods* **6**, 8413 (2014)
131. Y.Y. Zhang, G.L. Li, D. Wu, X.T. Li, Y.X. Yu, P.J. Luo, J. Chen, C.J. Dai, Y.N. Wu, *Trends Anal. Chem.* **121**, 115669 (2019)
132. H. Zheng, J. Ding, S. Zheng, G. Zhu, B. Yuan, Y. Feng, *Talanta* **148**, 46 (2016)
133. J. Zheng, J.L. Huang, Q. Yang, C.Y. Ni, X.T. Xie, Y.R. Shi, J.F. Sun, F. Zhu, G.F. Ouyang, *Trends Anal. Chem.* **108**, 135 (2018)
134. X.Y. Cui, Z.Y. Gu, D.Q. Jiang, Y. Li, H.F. Wang, X.P. Yan, *Anal. Chem.* **81**, 9771 (2009)
135. S. Zhang, Z. Du, G. Li, *Talanta* **115**, 32 (2013)
136. M. Wu, Y. Ai, B. Zeng, F. Zhao, *J. Chromatogr. A* **1427**, 1 (2016)
137. Y.Q. Jia, H. Su, Z.H. Wang, Y.L.E. Wong, X.F. Chen, M.L. Wang, T.W.D. Chan, *Anal. Chem.* **88**, 9364 (2016)

138. W.C. Wang, J.T. Wang, S.H. Zhang, P.L. Cui, C. Wang, Z. Wang, *Talanta* **161**, 22 (2016)
139. M.M. Khataei, Y. Yamini, M. Ghaemmaghami, *Microchim. Acta* **187**, 256 (2020)
140. X.D. Hou, S. Tang, J. Wang, *Trends Anal. Chem.* **119**, 115603 (2019)
141. Y.J. Jian, L.F. Chen, J. Cheng, X.L. Huang, L. Yan, H.B. Li, *Anal. Chim. Acta* **1133**, 1 (2020)
142. F.Y. Lv, N. Gan, Y.T. Cao, Y. Zhou, R.J. Zuo, Y.R. Dong, *J. Chromatogr. A* **1525**, 42 (2017)
143. J.H. Li, H. Xu, *Talanta* **167**, 623 (2017)
144. Z. Li, R.Y. Ma, G.J. Zhang, S.H. Zhang, C. Wang, Q.H. Wu, Z. Wang, *J. Sep. Sci.* **39**, 3171 (2016)
145. M. Heydari, M. Saraji, M.T. Jafari, *Talanta* **209**, 120576 (2020)
146. J.M. Cen, S.B. Wei, H.J. Nan, J.Q. Xu, Z.B. Huang, S.Q. Liu, Q.K. Hu, J. Yan, G.F. Ouyang, *Microchem. J.* **139**, 203 (2018)
147. Y. Liu, Y.F. Huang, G.S. Chen, J.L. Huang, J. Zheng, J.Q. Xu, S.Q. Liu, J.L. Qiu, L. Yin, W.H. Ruan, F. Zhu, G.F. Ouyang, *Anal. Chim. Acta* **1015**, 20 (2018)
148. F. Wang, Y. Zheng, J. Qiu, S. Liu, Y. Tong, F. Zhu, G.F. Ouyang, *Nanoscale* **10**, 10073 (2018)
149. G.S. Chen, J.L. Qiu, J.Q. Xu, X.A. Fang, Y. Liu, S.Q. Liu, S.B. Wei, R.F. Jiang, T.G. Luan, F. Zeng, F. Zhu, G.F. Ouyang, *Chem. Sci.* **7**, 1487 (2016)
150. M. Tabibpour, Y. Yamini, S.H. Ahmadi, A. Esrafil, Q. Salamat, *J. Chromatogr. A* **1609**, 460497 (2020)

Composite Materials for Ballistic Applications



Ali Imran Ayten and Mehmet Atilla Tasdelen

Abstract This chapter focus on the synthesis, analysis and modeling of composite materials used in ballistic applications. In this context, a brief introduction is made on the summary of ballistics and threat types in personal ballistics. The main components of the composites including fiber types and fabric structures are described in detail. Then, the ballistic impact mechanisms for textile and composite materials are discussed with failure mechanisms that occurred in the ballistic tests. Additionally, numerical simulation techniques and material models for ballistic fabrics and composite structures are presented with corresponding literature published in the last five years. Finally, final trends such as bio-inspired structures and adding novel soft energy absorbing materials into the ballistic structures are exemplarily offered.

Keywords Aramid fiber · Ballistic · Carbon fiber · Composites · Glass fiber

Nomenclature

| | |
|--------------|------------------------------------|
| AP | Armor piercing |
| BFD | Back face deflection |
| BNNSs | Boron nitride nanosheets |
| BNNTs | Boron nitride nanotubes |
| CFRC | Carbon fiber reinforced composites |
| CNTs | Carbon nanotubes |
| DoP | Depth of Penetration |
| E | Elastic modulus |
| EP | Epoxy |
| FMJ | Full metal jacket |
| FN | Flat nose |
| GNPs | Graphene platelets |

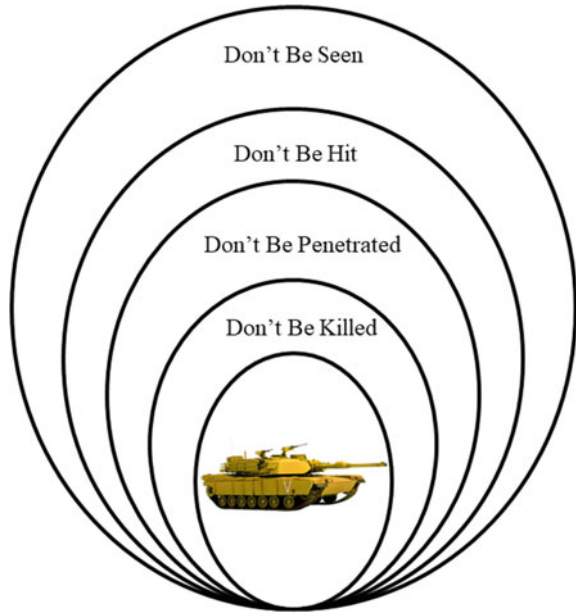
A. I. Ayten (✉) · M. A. Tasdelen
Department of Polymer Materials Engineering, Faculty of Engineering, Yalova University, 77200
Yalova, Türkiye
e-mail: aiayten@yalova.edu.tr

| | |
|---------------|--|
| JSP | Jacketed soft point |
| NIJ | National Institute of Justice |
| PEG | Poly(ethylene glycol) |
| PU | Polyurethane |
| PVA | Poly(vinyl acetate) |
| QI | Quasi-isotropic |
| QS-PST | Quasi-static punch shear test |
| RN | Round nose |
| SJHP | Semi jacketed hollow point |
| STF | Shear thickening fluid |
| UD | Unidirectional |
| UHMWPE | Ultra-high molecular weight polyethylene |

1 Introduction to Ballistics

Protection from ballistic threats such as knives, swords, pistols, or rifles has been one of the primary purposes since the earlier times of mankind. Various armors made from leather, fabric, iron, steel, wood, ceramic, and plastic were developed and used for this purpose. Identifying ballistic threats as a function of the type, distance, and location is vital for the development of armor and ballistic science. Figure 1 shows a general approach in ballistic science named as “survivability onion.” The outset surface of this “onion ring” may be related to radar-absorbing components, which provide attenuating electromagnetic waves while the penetration stage is entirely related to the design of body or vehicle armor material.

In terms of choosing protective armor depends on identifying the threat and selecting a material or combination of materials that will stop the potential ballistic threats. For instance, mobility is more critical in personnel armoring while it can be considered secondary important in vehicle armoring. Optimizing the relationship between protectiveness and the weight of armor structure is one of the main problems in ballistic science. The main requirements for optimization study in a ballistic structure are understanding the types of ballistic threats, the effects of fiber and fabric types used in armor structure, and the impact mechanisms that occurred in structure. This chapter consists of introducing the reader to the ballistic threats, fibers, and fabric types used in personnel ballistics, and ballistic impact mechanisms in armor structures. Finally, possible future trends in ballistic materials and structures are summarized.

Fig. 1 Survivability onion

2 Ballistic Threats

Threat types are important phenomena in ballistic science to understand their potential damages and take precautions to prevent such attacks. Armor structure shows critical differences depending on the ammo level which is defined in NIJ 0101.06 (National Institute of Justice) standard [1]. The flexible design may be enough for low-level ammo such as levels IIA (9 mm and 40 S&W), II (9 mm and 0.357 Magnum) and IIIA (0.357 SIG; 0.44 Magnum) [1] while the complex design may be needed for protection against the high level of threats. For this purpose, different classes of materials such as ceramics and metal plates having higher density are commonly used (Table 1).

The effect of threat types including II-A, II and III-A levels of shootings on the deformation of the aramid/epoxy composite sample were shown in Fig. 2. There was a linear relationship between the primary damage size and level of threats. Back face damage and deflection were affected by kinetic energy, front shape, and material of bullet. For instance, both 44 Magnum and 357 Magnum caused a perforation in aramid/epoxy laminated composite plate in Fig. 2. If the impacted area on the back face of the sample was compared, it could be seen that Magnum 44 caused the most damage size among all bullets because it had the most kinetic energy and bullet diameter than others.

There are several fiber-based materials, which are used against ballistic threats in the market. Para-aramid (commercially known as Kevlar[®] and Twaron[®]), ultra-high molecular weight polyethylene (UHMWPE) (commercially known as Dyneema),

Table 1 Body armor classifications according to NIJ 0101.06 standard [1]

| Level | Round | Caliber | Ammo type | Mass (g) | Minimum bullet velocity (m/s) |
|-------|-------|--------------|-----------|----------|-------------------------------|
| II-A | 1 | 9 mm | FMJ RN | 8 | 373 |
| | 2 | 0.40 | S&W FMJ | 11.7 | 352 |
| II | 1 | 9 mm | FMJ RN | 8 | 398 |
| | 2 | 0.357 Magnum | JSP | 10.2 | 436 |
| III-A | 1 | 0.357 SIG | FMJ FN | 8.1 | 448 |
| | 2 | 0.44 Magnum | SJHP | 15.6 | 436 |
| III | 1 | 7.62 mm | NATO FMJ | 9.6 | 847 |
| IV | 1 | 0.30 Caliber | M2 AP | 10.8 | 878 |

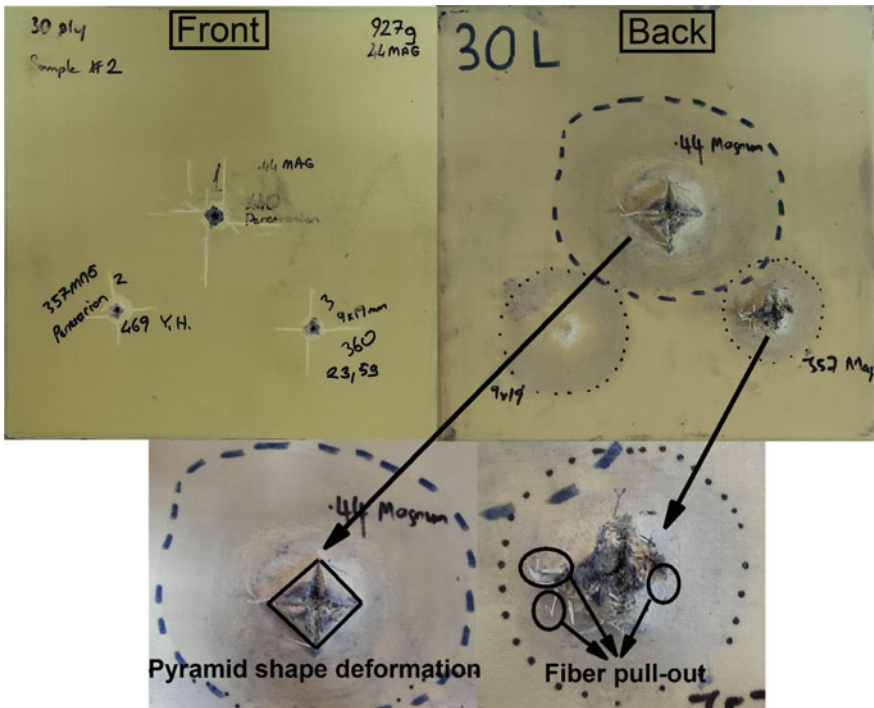


Fig. 2 Damage size and types of failure occurred in 30 layers of aramid/epoxy composite sample at the end of ballistic shot by 0.44 Magnum, 0.357 Magnum and 9 × 19 mm ammo

and S-2 glass fibers are frequently used fibers for ballistic applications. Details and related studies published in the last five years of these technical fibers are focused on the following sections.

3 Fiber Types for Ballistic Protection

3.1 Para-Aramid Fibers

Para-aramid fibers were firstly developed at DuPont in 1965; then it was commercially used as Kevlar[®] trade name. After that, Akzo company revealed their commercial aramid fiber for ballistic which is named Twaron[®]. Aramid structure contains long-chain synthetic poly-para-phenylene terephthalamide, which at least 85% of amide linkages are attached to two aromatic rings, as can be seen in Fig. 3. Perfect alignment of the polymer chain, which includes a para-oriented benzene ring, provides high strength due to its rod-like structure (Table 2).

Fig. 3 Chemical structure of poly(*p*-phenylene terephthalamide) (aramid)

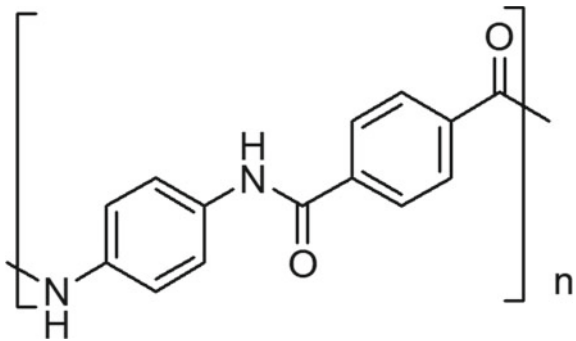


Table 2 Physical, thermal, and mechanical properties of commonly used para-aramid and high molecular weight polyethylene fibers

| Fiber types | Density (g/cm ³) | Tensile modulus (GPa) | Tensile strength (MPa) | Strain at failure (%) | Decomposition or melting temperature (°C) |
|--------------|------------------------------|-----------------------|------------------------|-----------------------|---|
| Kevlar 29 | 1.44 | 70 | 3300 | 4.2 | 550 |
| Kevlar 49 | 1.45 | 135 | 3300 | 2.8 | |
| Kevlar 129 | 1.45 | 99 | 3400 | 3.3 | |
| Kevlar KM2 | 1.44 | 70 | 3300 | 4 | |
| Twaron | 1.45 | 70 | 3100 | 2 | |
| Technora | 1.39 | 121 | 3000 | 4.4 | |
| Spectra 900 | 0.97 | 73 | 2400 | 2.8 | 150 |
| Spectra 1000 | 0.97 | 103 | 2830 | 2.8 | |
| Spectra 2000 | 0.97 | 124 | 3340 | 3 | |
| Dyneema | 0.97 | 87 | 2600 | 3.5 | |

Reprinted from Bilisik [2]. Copyright (2018), with permission from Elsevier

In ballistic science, the strategy is based on creating basic and practical solutions in present materials that are more applicable than discovering a novel material. Fiber modification is one of the featured solutions in the composite science such as impregnating shear thickening fluids (STF) into the fibers. There are numerous experimental and numerical studies about the effect of STF and its bullet-stopping mechanisms in the literature [2–25]. The introduction of STF not only improves the efficiency of aramid fabric against ballistic loading but also keeps the fabric's flexibility. Furthermore, the STF-impregnated fabric significantly increases friction between yarns providing more energy absorptions as well as better ballistic performance. Bajya et al. [24] studied the use of STF-impregnated soft armor panel design strategies against 9×19 mm ammunition with a velocity of 430 ± 15 m/s. Two different solutions containing silica particles having 100 and 500 nm diameters with poly(ethylene glycol) (PEG200) as the carrier fluid were independently prepared. The composite sample formed with silica particles having 500 nm diameter and aramid fabric showed less back face deflection (BFD) than other composite prepared by silica particles with 100 nm diameter. Also, the STF-impregnation process reduced the BFD value of samples by 2.5–2.8 mm while their areal densities remained at the same value. Because the shear thickening fluid improved the inter-yarn friction and yarn pull-out force values of fabrics, it contributed to the energy absorption property of the composite structure.

Wang et al. [26] used polyurethane (PU) as an adhesive to enhance inter-yarn adhesion in ballistic structure. The STF-impregnated aramid fabric, STF/aramid/PU composite and PU/aramid samples were compared under identical conditions. Among these samples, the STF/aramid/PU composite displayed highest energy absorption due to the better adhesion properties of PU compared to the STF/aramid and PU/aramid samples. Fiber modification can be also applied by the surface coating of fibers. For example, the surface of Twaron[®] 709 aramid fiber fabric coated by polyvinyl acetate (PVA) and the obtained sample was compared with uncoated form in terms of static and dynamic tests [27]. The results showed that thin PVA coating provided an extra polymer connection between yarns, and this caused an improvement in pull-out force. This synergetic effect also increased the ballistic limit of coated fabric twice and decreased the back face deflection value three times compared to the neat sample.

Chu et al. [28] have coated the Twaron[®] fabric using the sol-gel method by a coating in which TiO_2/ZnO composites are embedded to provide an improvement in inter-yarn friction without increasing the weight of fabric. After the sol-gel treatment, the inter-yarn friction was increased by 20%. On the other hand, the energy absorption rate was increased 35% in the ballistic test of eight layers of Twaron[®] fabric. In another study, ballistic performance of Kevlar[®] and basalt fabric reinforced hybrid thermoplastic composite armors were numerically and experimentally investigated [29]. The 2D plain woven and 3D angle interlock fabric structure with polypropylene matrix were tested. Armor structure having a non-symmetric stacking sequence was fully perforated at the velocities between 365 and 395 m/s, while the symmetric stacking sequence-structure exhibited penetration behavior. The stacking sequence did not affect the front face damage of composite samples. Multiple component STF

solutions containing carbon nanotube/polystyrene-ethyl acrylate based STF were also utilized to enhance the ballistic resistance of aramid fabrics [30]. The ballistic limit velocity of Kevlar was improved from 84.6 to 96.5 m/s using this STF solution. Additionally, the optimization study for carbon nanotubes concentration was also investigated and it was found that the optimum amount of carbon nanotubes in STF solution was 1%. At higher concentration, the carbon nanotubes caused agglomeration which would lower the ballistic performance.

3.2 Ultra-High Molecular Weight Polyethylene Fibers

Another ballistic material commonly used in protective equipment is UHMWPE, which has high strength and modulus. The chemical structure of UHMWPE contains extremely long and linear chains that are aligned in the same direction. Due to strong intermolecular interactions between long polyethylene chains, the load more effectively transferred to the polymer backbone. The gel-spinning process is used to produce the UHMWPE fiber consisting of a highly oriented molecular structure that provides toughness, chemical resistance, and abrasion. Because of its excellent mechanical properties and lowest density (only 0.97 g/cm³), UHMWPE fiber is one of the best choices for the lightweight ballistic applications. There are two commercially available UHMWPE fibers, namely, Dyneema[®] (DSM) and Spectra[®] (Honeywell) in the market. These fibers can absorb a large amount of kinetic energy, but they are weak against environmental conditions such as temperature ($T_m = 144\text{--}152\text{ }^\circ\text{C}$), moisture and water. On the other hand, the UHMWPE fibers show higher resistance to abrasion and chemicals along with good thermal degradation (+50 to +100 °C). The rigidity of the UHMWPE structure varies depending on temperature due to the nature of the polyethylene molecule [31, 32].

A comparative study about the ballistic performances of Dyneema[®] and Spectra[®] fabrics using 20 mm diameter copper and steel fragment simulating projectiles that have 400–1000 m/s striking velocities was conducted by Ćwik and coworkers [33]. It was noticed that the Dyneema HB26 sample had a slightly higher ballistic limit value than the Spectra 3124 sample. In addition to this, both samples presented similar ballistic performance at very high striking velocities such as 850 m/s and higher values.

In a recent study, the effect of hybridization in unidirectional laminate consisted of high-modulus UHMWPE yarn, woven fabric of high-modulus UHMWPE yarn and shear thickening fluid impregnated para-aramid woven fabric was also investigated by Mawkhliar and Majumdar [34]. Various samples with different configurations were prepared for ballistic tests. Noticeably, the positioning of unidirectional fabric at the strike face was more efficient than positioning woven fabrics at the strike face. Furthermore, the back face deflection value was reduced when backing layers were impregnated with STF.

3.3 Glass Fibers

Two types of glass fibers including low-cost general-purpose (E) and premium special-purpose (C, D, E, M, S, R, and ECR etc.) fibers are commercially available. The “E-glass fiber” is commonly used as thermal, electrical, and sound insulation. Its chemical composition contains varying amounts of silica, alumina, calcium oxide, and magnesium oxide. The special-purpose S-glass fiber includes 20% higher silica and three times more alumina contents than E-glass fiber. Tensile strength and Young’s modulus values of S-2 glass are 4890 MPa and 85.5 GPa, while these values of E-glass are 3445 MPa and 76 GPa, respectively. The S-2 type glass fiber is specially developed for ballistic applications. There are limited studies for the understanding of ballistic performance of S-2 glass-fiber reinforced composites in the literature.

A series of experimental and numerical studies to obtain progressive damage modeling of plain weave S-2 glass/SC-15 epoxy composites was done by Xiao and coworkers [35]. To investigate compression-shear and tension-shear dominated damage modes, the QS-PST were performed for 25.4 and 101.6 mm support span diameter values with different numbers of composite layers. Ls-Dyna MAT162 material model was used to calculate progressive damage and material degradation. Firstly, calibration of the material model was performed using experimental data of 22 plate layers for two-span diameters. Then, this calibrated model was applied to simulate the quasi-static punch behavior of composite plates having different thicknesses. The results were in good agreement with experimental data, and the composite samples showed delamination and fiber breakage due to the shear and tensile stresses.

In another study, Gama and Gillespie [36] investigated the impact, damage, and penetration behavior of thick section S-2 glass/SC15 epoxy composites. Impact tests having different velocities from 50 to 1000 m/s were performed, and numerical simulations were run to verify the material model. Due to the lack of erosion and softening parameters of composite materials, residual velocities obtained from the simulation did not match at the beginning of experimental data. After the calibration study by a set of numerical studies using strain parameters and softening parameters, the numerical model and experimental data became well-suited. It was also reported that shock compression and delamination behaviors during short time Phase I penetration of ballistic impact were observed while tension-shear dominated damage and large deformations occurred in long-time Phase II penetration.

The multi-hit performance of ballistic structures is also an important topic because serious degradation in the mechanical properties of materials may occur during the ballistic tests. Structural integrity of the composite is damaged after the first shot, then its protection performance was gradually reduced against the following shots. A numerical and experimental study using S-2 glass/SC15 epoxy thick-section composites was done to inform their single and multi-hit ballistic impact behaviors [37, 38]. Single hit ballistic tests were performed with 22 and 33 layers of composite plates for two different spans (8 and 16) of punch ratios (SPRs). Subsequently, four extra shots were fired to the different locations of test plates for $SPR = 16$. The results

showed that support span diameter had a slight effect on the ballistic limit velocity of samples in single-shot cases. On the other hand, the damage scenario in multiple impact cases was similar to single-shot cases except for extensive delamination that occurred after the extra shots.

In a recent study, epoxy matrix phase of glass-fiber reinforced composite was filled by the combination of either hybrid boron nitride nanosheets/carbon nanotubes (BNNs/CNTs) or hybrid boron nitride nanotubes/graphene nanoplates (BNNTs/GNPs) [39]. Two different projectiles with velocities of 76 and 134.3 m/s were used and it was found that the two modified composites with hybrid nanofillers had lower final velocities than the neat epoxy matrix composite. On the other hand, the BNNTs/GNPs modified epoxy matrix composite sample reduced the initial velocity of the projectile at the rate of 89.1%, while this value was found as 67% for the neat epoxy matrix specimen. As a result, the modification of neat epoxy matrix with nanofillers provided an average increase at the rate of 11.4% in terms of specific energy absorption.

3.4 Carbon Fibers

Carbon fiber reinforced composites (CFRC) are generally used in automotive, aircraft and sports industries because of their superior mechanical properties. However, there are few reports to determine the CFRC against ballistic threats in the literature. Recently, Reddy et al. [40] conducted a study on ballistic impact behavior of carbon/UHMWPE hybrid composites, which contains the different volumes of carbon and UHMWPE against 7.62×39 mm mild steel projectile having a velocity of 720–740 m/s. It was determined that specific absorbed energy value increased by increasing UHMWPE content. Additionally, the samples containing 75 and 100% carbon fibers were fully perforated, while the samples comprising 50, 75, and 100% UHMWPE fibers fully absorbed the kinetic energy of the bullets. Energy absorption values were similar for the samples containing 50, 75, and 100% UHMWPE fibers. Besides, the maximum deflection value was determined as 62 mm for 50% UHMWPE fibers configuration while it was 38 and 40 mm for the samples containing 75 and 100% UHMWPE fibers. In another study, numerical and experimental examinations of carbon/Kevlar 3D woven composites were done by Ahmed et al. [41] to determine its high-velocity impact behavior. The hybrid structure consisting of carbon fiber composite at the striking face and Kevlar—at the back face was the best composition in terms of energy absorption capability because Kevlar fibers performed large deformation before failure. The matrix cracking was dominant failure mechanism for carbon layers, whereas fiber pull-out and rupture were the main failure mechanism for Kevlar layers.

In a recent study, ballistic impact behavior of 3D braided carbon fiber reinforced composites was also monitored by two camera, C-scan, and digital microscope systems [42]. Upon ballistic tests with a velocity range of 115–172 m/s, the matrix cracking, fiber breakage and fiber bundle cracking damage mechanisms

were clearly observed. It was noted that there was a linear relationship between the absorbed energy and the initial velocity. A comparative study was recently performed by Heimbs et al. [43] to demonstrate the impact behaviors of glass, carbon and UHMWPE fibers reinforced composites using a Charpy pendulum, a drop weight and a ballistic impact with a gas gun. The carbon fiber reinforced composite performed the worst penetration resistance in all tests due to brittle nature of carbon fibers. The S-2 glass-fiber composite sample exhibited higher specific penetration resistance, but it had almost 2.5 times greater density than the UHMWPE fiber. Thus, the UHMWPE fiber reinforced composite was more suitable for the ballistic application, which requires high strength and stability and lightweight.

4 Fabric Types

4.1 Fabric Structures

Textile products, existing woven, knitted, and non-woven forms comprise high mechanical properties as well as high heat-, abrasion-, and moisture-resistant properties that are important end-user requirements for the ballistic industry. For instance, versatility is a key factor for aramid fabrics used in bullet-proof vests. Fabric characteristics such as woven or non-woven forms play a crucial role under loading on the ballistic behavior of the structure. Because the woven forms are generally used in ballistics, non-woven fabrics are out of the scope of this chapter. Figure 4 presents mostly used fabric structures including plain, twill and satin weaves in industrial applications.

The plain weave may be counted as the most common fabric structure among all other geometries due to its simple symmetrical array that is efficient against ballistic

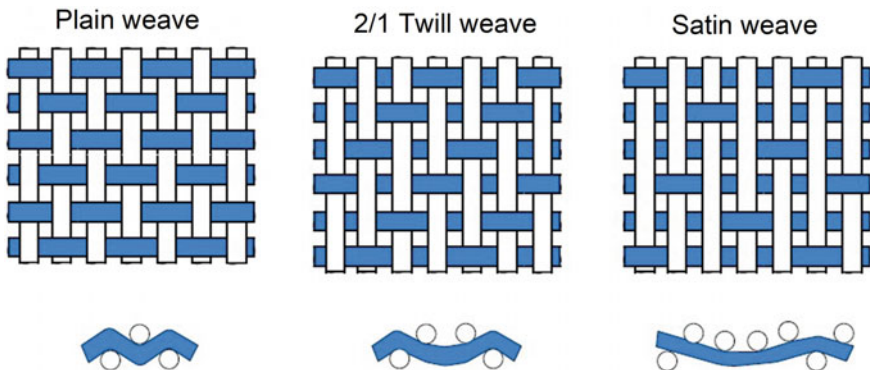


Fig. 4 Woven fabrics that are used in ballistic structures. Reprinted from Campbell [44]. Copyright (2004), with permission from Elsevier

loadings. Each filling yarns passes over and under the warp yarn. On the other hand, twill is the other common fabric structure with a specific weave pattern such as “Z twill”—twill right, “S-twill”—twill left. Filling yarns are passed over and under two or more warp yarns, and a characteristic pattern is obtained, as shown in Fig. 4. Main twill weaves may be classified as continuous twills, zigzag twills, rearranged twills, combination twills, broken twills. Satin weave is another basic fabric structure having interlacing points that are randomly distributed. Repeated number of weaves may be counted as 5, 6, 9, 11, 13 etc. When the applied stress waves onto fabric cannot regularly transfer to the other yarns, this distribution may have a negative effect in terms of the energy absorption characteristics [45].

In the literature, the plain weave type of aramid fabric is commonly used for ballistic applications [2–4, 12, 16, 17, 19, 47]. For example, a ballistic response of stitched woven fabrics against a projectile with a mass of 2 g, and a maximum velocity of 180 m/s was investigated by Zhou and coworkers [48]. The stitched samples exhibited four times more energy absorptions than those unstitched ones. More fiber failure damage mechanism was observed compared to yarn pull-out in stitched samples.

In a recent study, Arora et al. [23] performed an experimental study about the effectiveness of STF on different UHMWPE fabric structures such as woven plain, 2/2 twill, 3/1 twill, and 2×2 matt fabrics against 202 J. Neat form of plain weave fabric exhibited better performance in terms of energy absorption than twill weave structures. Conversely, the STF-impregnated form of plain weave fabric just absorbed 5% less impact energy than its neat form. However, the STF-impregnated twill and matt fabric structures displayed more energy absorption as 20% and 42%, respectively. In another study, the effect of fabric structure, thread density and yarn linear density in woven fabrics were systematically investigated [49]. Five types of fabrics were used throughout studies as plain, 2/1 twill, 3/1 twill, 5-end satin and 7-end satin, which have equal density, 174 Tex. The simulation results showed that the plain weave fabric demonstrated better energy absorption than other fabric structures. The plain weave fabric also displayed 34% more energy absorption than the 7-end satin weave structure, which revealed the worst performance because it has less interlacing point than others.

5 Ballistic Impact Mechanisms

Engineering materials are exposed to different types of loadings, including tension, compression, shear, quasi-static, and impact. It can be said that ballistic impact is the most complex phenomenon compared to other mechanical loadings. Because it has occurred at a millisecond period, and it is hard to understand what occurred during the impact stage. The main factors affecting ballistic impact response of materials are thickness, strength, toughness, and projectile properties. In addition, ballistic behavior of materials is significantly affected by various parameters such as weave

type and areal density of fabric structure, the impact velocity of the projectile, projectile geometry, contact angle between target and projectile except for material properties. Damage that occurred in composite structures against ballistic impact loadings can be divided as fiber and matrix damages. Fiber fracture and yarn pull-out may realize in fiber materials of composite structures, while matrix cracking and crushing may occur in the matrix phase. Additionally, a delamination damage between plies is particularly observed in the laminated composites due to the interlaminar stresses caused by the different material properties. Understanding the reasons behind the damage mechanisms is crucial in terms of designing the soft or hard ballistic structure. There are different approaches such as experimental, analytical, and numerical to analyze the ballistic impact mechanism of composite structures or fiber fabrics in the literature [8, 36, 49–55].

In order to determine the ballistic behavior of the composites, ballistic test setup consists of weapons, ammunition, firing range setup, optical sensors, and high-speed camera that capture the material responses against the bullets. There are three velocity sensors in a ballistic test setup, which two of them are in front of the target, and the other one is the back of the specimen. Thus, residual velocity can be measured if the bullet perforated to test sample and energy absorbed by the specimen can be determined using simple kinetic energy formula. A backing clay (Roma Plastilina No. 1) is used in the ballistic tests of soft samples to determine back face signature occurred in penetration case, which is caused by a bullet. If the back face deflection value of the sample is not exceeding 44 mm value, it can be said that this sample is successfully qualified in corresponding test level [1].

Recently, Gilson et al. [56, 57] conducted numerical and experimental studies on the ballistic response of Dyneema[®] HB80 composite. The 9 mm lead core/brass jacket bullets with an average kinetic energy of 605.37 J and 0.44 Magnum lead core/pure copper jacket bullet with an average kinetic energy of 1402.49 J and the Johnson-Cook material model were used for modeling the high rate of deformation of bullets. The fiber breaking, delamination and permanent back face deflection damages were observed in all samples. Ballistic impact mechanisms of textile materials and laminated composites are not comparable due to their divergent physical properties and structures. Below, the ballistic impacts occurred in these materials are presented, and their failure mechanisms are described.

5.1 Ballistic Impact on Textile Materials

Propagating impact waves must be clearly understood to interpret ballistic impact mechanisms in the fabrics. The deformation mechanism of the fabric deformation is similar to a single yarn under ballistic impact that is shown in Fig. 5. Herein, the transverse impacts are dominant in the center of yarn, while longitudinal loadings are dominant in vertically undeformed part of the yarn. Besides, the deformation profile of yarn at the center depends on the projectile geometry. If the projectile maintains a section area like Fig. 5, the stress waves occurring on the yarn have a

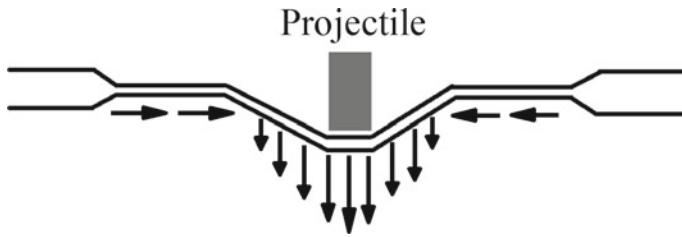


Fig. 5 Deformation behavior of a single yarn subjected to ballistic impact. Arrows at x-direction present longitudinal waves, while arrows at y-direction show transverse waves. Reprinted from Langston [58]. Copyright (2017), with permission from Elsevier

linear distribution. Stress wave distribution in the center of yarn would be parabolic in the case of the round nose projectile. Localized stress causes stress concentration in each of two distributions. This situation induces transverse waves getting spread to the other part of the yarn and deformed it [58].

In a recent study, the effect of ply orientation on ballistic performance of plain weave multi-ply fabrics having a number of different lay-up sequences such as $[0^\circ/0^\circ]$, $[0^\circ/15^\circ]$, $[0^\circ/30^\circ]$, $[0^\circ/45^\circ/0^\circ]$, $[0^\circ/0^\circ/45^\circ]$, $[0^\circ/0^\circ/0^\circ/0^\circ]$, and $[0^\circ/22.5^\circ/45^\circ/67.5^\circ]$ were investigated [59]. A novel clamp system was designed to prevent the slipping of fabrics due to the tension forces that occur during ballistic impact. As a result, the angled ply sequences exhibited better energy absorption at a rate of 15% than aligned plies.

5.2 Ballistic Impact in Laminated Composites

Laminated composites are also exposed to several types of loadings during ballistic impact. Penetration or perforation cases may occur throughout ballistic impacts depend on types of fiber and matrix materials, plate thickness, projectile mass, projectile shape, and projectile velocity. Recently, Reddy et al. [51] reported a study on the ballistic impact behavior of E-glass/phenolic composite in order to determine the effect of laminate thickness and projectile impact velocity parameters on the energy absorption. It was found that thicknesses of the layers directly influence the failure mechanisms as the damaged area increases with the increasing thickness. Tensile failure and delamination mechanisms were also observed in the laminates with higher thickness, conversely shear cutting damage of fibers was seen in the lower thickness.

Manufacturing method and thickness of the composite plates are critical parameters in terms of energy absorption capability of composite structure against ballistic impact. Nunes et al. [60] compared the different number of layers aramid/epoxy composite laminates which consist of 8, 13, 18, and 23 plain weave fabric layers. The samples consisted of 18 and 23 layers that were not perforated when using $9 \times$

19 mm ammo having an average kinetic energy of 595 J. It was revealed that vacuum infusion process for manufacturing thick laminates (12 mm) is equivalent to high-cost process such as autoclave and compression molding if high volume fraction and low void content can be achieved during the infusion process.

Haque and Gillespie Jr. [61] investigated the penetration behavior of Dyneema® HB26 laminated composite. Two types of projectiles including 16-grain right circular cylinders and 44 grain fragment simulating projectiles were used in the depth of penetration (DoP) tests. A new energy-based DoP model was developed to reduce experimental data needed to conduct numerical simulations. It is reported that this new DoP model can calculate the initial impact force and dynamic pressure.

5.3 Failure Mechanisms of Fabrics and Composites

Dynamic loadings resulting from suddenly happened events may cause unpredictable outcomes on the structure of materials. All engineering materials give different responses to the loadings, therefore the structural damage scenarios against ballistic impacts can be varied such as complete perforation and partial perforation. The complete perforation can be realized with two possibilities: (a) projectile has a residual velocity after it perforates the target or (b) the whole impact energy of the projectile is absorbed by the target. If the potential energy absorbed by the material is greater than the kinetic energy of the bullet, the partial perforation has occurred in the sample. In this case, the projectile cannot perforate the target, and it stops inside of the composite material. Several energy absorption mechanisms can be assessed for this type of damage [32].

- (a) Compression failure: Compression loading is applied to the target by the projectile, and highly localized compressive stress occurs in the contact region between target and projectile. This stress causes compressive strain up to the layer where the projectile proceeds. Local failure may occur below the projectile and surrounding impact zone in such cases.
- (b) Delamination and matrix cracking: Both longitudinal and transverse waves propagate along the radial direction during impact loading in woven fabric reinforced composite impact. The transverse waves will tend to create a cone at the backsides of the target, whereas the stress wave will decrease as the longitudinal wave propagates along with the yarns. The matrix tends to fail when the occurring strain exceeds the damage threshold strain of the given material in the vicinity of the point of impact. Typically, these damages persist until the complete perforation or complete projectile energy absorption happens. Figure 6 shows the damage mechanisms that occurred in the laminated composite sample in the cases of three different energy levels namely low, medium, and high. Herein, high energy impact causes penetration or perforation with delamination and fiber pull-out. Visible damage realizes in a few layers with low and medium velocity impacts, while delamination and fiber breakage may occur within the

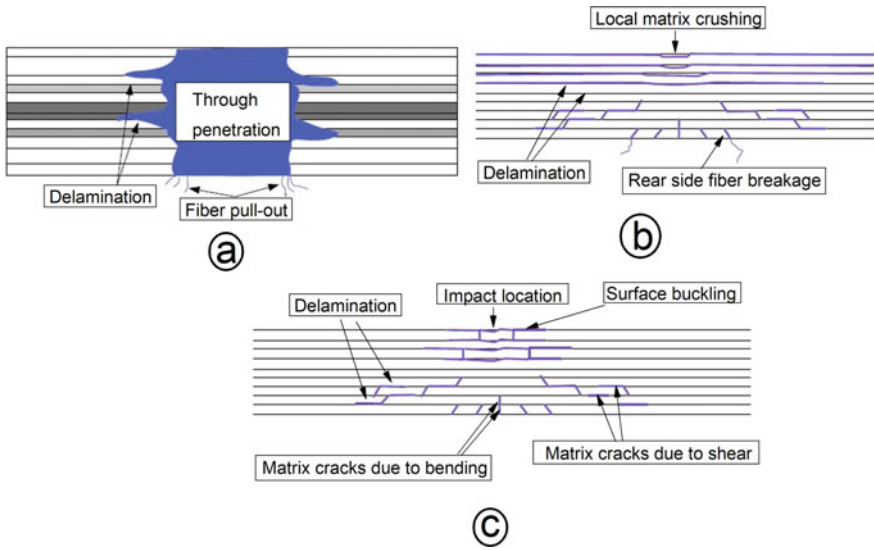
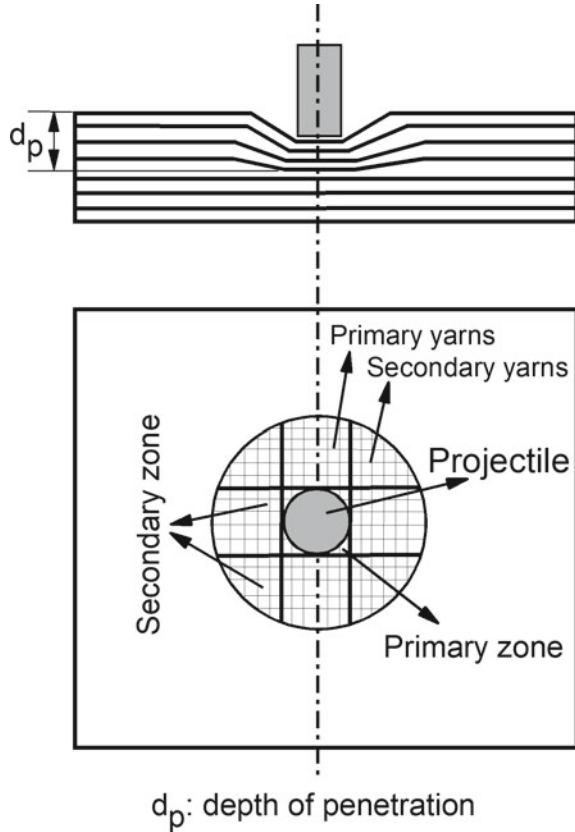


Fig. 6 Damage mechanisms that occur in laminated composite structures against impact loading, **a** high energy, **b** medium energy and **c** low energy. Reprinted from Andrew et al. [62]. Copyright (2019), with permission from Elsevier

structure. Matrix cracks occur in the bottom layers due to the bending stress while they are realized in the middle layers due to shear stress. This situation is risky because the composite structure becomes vulnerable to further loading [62].

- (c) Conical back face deflection: Initial velocity of the projectile is suddenly reduced when it hits the target. Therefore, a few layers fail due to the effect of the high kinetic energy of the projectile. The shear plugging mechanism is dominant during this phase. Then, the other layers help to absorb residual kinetic energy, and this causes conical deformation of the back layers. This shape may be pyramidal as in Fig. 2 because the formation of this cone is affected by the geometry of the bullet [51].
- (d) Deformation of primary and secondary yarns: Primary yarns are affected by the projectile impact firstly because the stress wave propagation continues in the fiber direction. This may be due to fiber failure if its strain value exceeds its failure strain value. On the other hand, secondary yarns in Fig. 7 help to absorb kinetic energy. Because the secondary yarns are out of the primary impact zone, they have limited contribution to absorbing kinetic energy compared to the primary yarns. Figure 8 presents the deformation of 36 layers of plain weave aramid fabrics subjected to ballistic impact by Magnum 44 bullet. The bullet could perforate to fabric structure until the 8th layer, and it stopped at the 9th layer forming a bullet shape at the surface. Fabric wrinkling was observed in each of the perforated layers due to the failure of these layers.

Fig. 7 Deformation mechanisms for 2D woven fabric target during ballistic impact. Side view (above) and front view (below). Reprinted from Shaktivish et al. [64], Copyright (2013), with permission from Elsevier



- (e) **Shear plugging:** This is one of the most important damage mechanisms during ballistic impact. When a projectile hits the laminated composite sample, it experiences shear loading due to the high velocity of the projectile. If the applied shear stress by the projectile to the sample is more than the maximum shear stress of the material, the sample is resisted toward this stress, and then it fails.
- (f) **Friction:** Also, the friction mechanism is an essential parameter that contributes to stopping the projectile. But its effect may be limited compared to other energy-absorbing mechanisms such as delamination, matrix cracking, shear plugging, etc. Nevertheless, the friction mechanism should be calculated when the simulations or experiments are performed. If the frictional resistance cannot overcome the stopping the projectile, the structure is instantly perforated [32].

In a recent work, penetration mechanisms of the beam samples made from laminated UHMWPE fabric having $[0^\circ/90^\circ]$ configuration were investigated [63]. Two-dimensional ballistic tests altering mass and fixed geometry or vice versa were examined. Firstly, back-supported and free-standing samples were exposed to impact using a square cross-sectional projectile having different masses. Progressive damage was

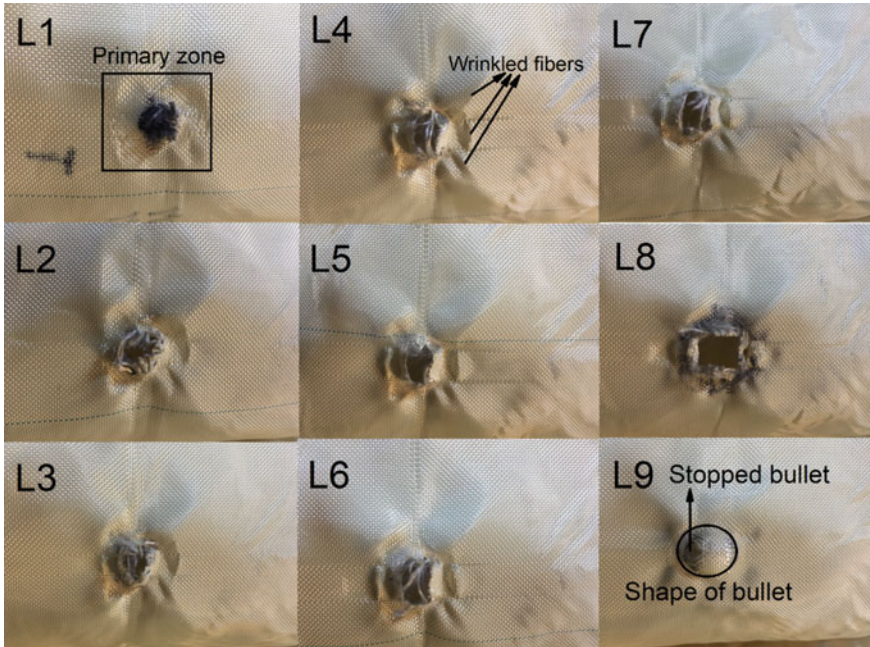


Fig. 8 Deformation of plain weave aramid fabric against Magnum 44 bullet having 1440 J kinetic energy value

observed in every case, and dynamic failure mode was similar to the quasi-static penetration test. Secondly, the projectile mass was constant, and its width changed. Either quasi-static penetration or dynamic impact tests, the geometry of projectile did not influence the damages. This indicated that shear damage at the edge of the projectile was not dominant in failure mechanisms. Tensile ply failure governed the failure process rather than membrane extension or shear failure in laminated UHMWPE.

Figure 2 shows a para-aramid/epoxy composite consisting of 30 layers of fabric exposed to ballistic impact by a 0.44 Magnum and 0.357 Magnum with 9×19 mm ammo. When the bullet hit the front face of the composite, the fibers at the back face were forced to stretch, while the fibers at the front face were forced to compress. These tension forces caused fiber to split and break. As can be seen in the back face of the test sample, the stress waves occurred due to the ballistic impact spread out into the layers, and this resulted in delamination of layers. Additionally, the delamination, fiber pull-out, and fiber breakage mechanisms were observed in the surrounding area where the bullet hit.

A quasi-static punch shear test (QS-PST) was developed to model different phases of ballistic impact phenomena [64]. This method has a simple test setup represented in Fig. 9 when it is compared to the ballistic test. Punch moves throughout vertical direction with a defined speed, and it perforates to laminated structure. The main parameter in this test method is the span to punch diameter ratio (D_s/D_p).

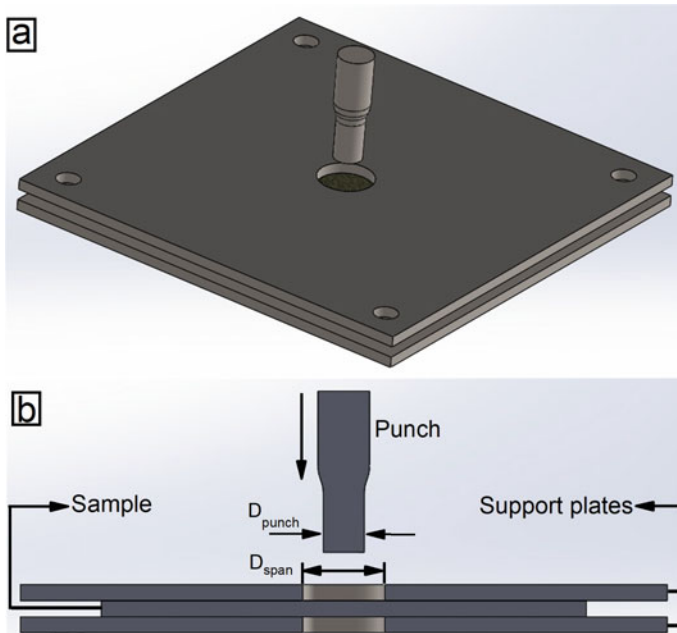


Fig. 9 QS-PST apparatus. **a** Isometric view, **b** section view

Ayten et al. [65] investigated the failure mechanisms of aramid/epoxy composites under shear loading. The different damage mechanisms including matrix cracking, fiber splitting, and fiber breakage were caused by the samples having various thicknesses at the end of QS-PST tests. When top views of samples were investigated, it could be seen that there was matrix cracking at the surrounding impact zone. On the other hand, fiber splitting and fiber breakage type of failure were dominant at the bottom surfaces of the samples because tensile stress occurred at the bottom of the composite plate when the punch applied compressive stress to the top layer.

5.4 Performance Parameters of Ballistic Materials Against Ballistic Impact Loading

Performance of ballistic materials is a two-way property that is related to target and threat properties. Therefore, fiber type, areal density of fabric, yarn properties, number of plies of the ballistic sample, woven/non-woven/2D/3D structure of the fabric have a great effect on the ballistic performance of materials. In addition, yarn-yarn friction, projectile-yarn friction, contact angle of the projectile to target are also important parameters for the ballistic impact behaviors of soft and hard samples.

In a recent report, ballistic performance and failure modes of soft armor panels consisting of woven fabric and unidirectional laminates were studied by Bajya and coworkers [46]. For this purpose, para-aramid and UHMWPE laminated samples were prepared and a 9 mm lead core bullet was used in the ballistic test with an average velocity of 430 m/s and the results were compared in terms of back face signature, bullet expansion, and perforation ratio parameters. All unidirectional samples made of the same type of material exhibited less back face deflection than the samples prepared by woven fabrics. Additionally, the unidirectional laminated UHMWPE samples showed less BFD value about 1–2 mm than the unidirectional laminated panels. By comparing the bullet expansion at the rate that is directly proportional to the energy absorption capability, it was found as 95.6–97.8% and 78.9–87.8% for the unidirectional laminated UHMWPE and para-aramid samples, respectively.

5.5 Numerical Modeling in Ballistic Fabric and Composite Structures

Commercial software based on finite element theory such as Ansys, Ls-Dyna, Abaqus, COMSOL, Pam-Crash, etc., make a great contribution to understanding the response of materials or structures under dynamic loadings if they are correctly modeled. There are several material models to define composite materials or fabrics in the commercial software. For instance, many material models in Ls-Dyna, such as MAT22, 26, 40, 54, 55, 58, 59, 116, 117, 118, 158, 161, 162, 249, etc., have been used to predict the damage behavior of composite materials. These material models can be used with different elements such as shell or solid structures. For example, Fig. 10 shows a numerical model containing 270,000 eight-node solid elements to analyze 30 layers of laminated composite with a dimension of 300 × 300 mm. The x- and y-axis symmetries were used to reduce solution time in this model. Each lamina has a thickness of 0.25 mm, and element dimensions of 0.5 × 0.5 × 0.25 mm.

Analysis software uses several criteria to calculate whether the failure occurs or not against applied loading as the initial condition. There are various failure criteria for composite materials such as maximum stress, Hoffman, Tsai-Wu, Tsai-Hill, Hashin, Chang-Chang, LaRC04, etc. For example, the MAT54 material model in Ls-Dyna uses the Chang-Chang failure criteria [66]. This failure criterion calculates the failure using the Eqs. (1–4).

$$\sigma_{11} > 0; e_f^2 = \left(\frac{\sigma_{11}}{X_t}\right)^2 + \beta \left(\frac{\sigma_{12}}{S_c}\right)^2 - 1; E_{11} = E_{22} = G_{12} = \nu_{12} = \nu_{21} = 0 \quad (1)$$

$$\sigma_{11} < 0; e_c^2 = \left(\frac{\sigma_{11}}{X_c}\right)^2 - 1; E_{11} = \nu_{12} = \nu_{21} = 0 \quad (2)$$

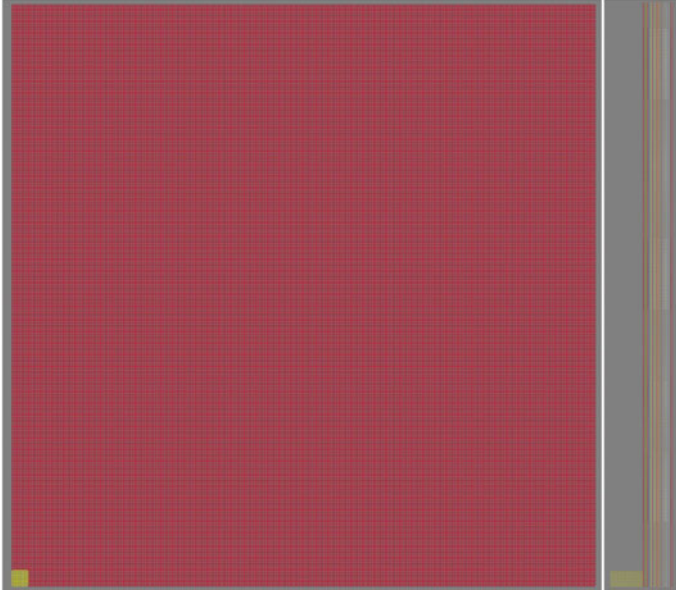


Fig. 10 A symmetrical numerical model for modeling the ballistic impact of laminated composite. Top view (at left) and side view (at right)

$$\sigma_{22} > 0; e_m^2 = \left(\frac{\sigma_{22}}{Y_t}\right)^2 + \beta \left(\frac{\sigma_{12}}{S_c}\right)^2 - 1; E_{22} = \nu_{21} = \nu_{12} = G_{12} = 0 \quad (3)$$

$$\sigma_{22} < 0; e_d^2 = \left(\frac{\sigma_{22}}{2S_c}\right)^2 + \left[\left(\frac{Y_c}{2S_c}\right)^2 - 1\right] \left(\frac{\sigma_{22}}{Y_t}\right) + \left(\frac{\sigma_{12}}{S_c}\right)^2 - 1;$$

$$E_{22} = \nu_{21} = \nu_{12} = G_{12} = 0 \quad (4)$$

where,

σ_{11} is the principal stress in longitudinal direction

σ_{12} is the shear stress in 1–2 plane

σ_{22} is the principal stress in transverse direction

e_c is the failure flag compressive fiber mode

e_d is the failure flag compressive matrix mode

e_f is the failure flag tensile fiber mode

e_m is the failure flag tensile matrix mode

β is the kinematic hardening parameter

S_c is the shear strength in 1–2 plane

X_t is the tensile strength in the longitudinal direction

X_c is the compressive strength in the longitudinal direction

Y_t is the tensile strength in the transverse direction

Y_c is the compressive strength in the transverse direction

ν_{12} is the poisson ratio in 1–2 plane

ν_{21} is the poisson ratio in 2–1 plane

E_{11} is the elastic modulus in the longitudinal direction

E_{22} is the elastic modulus in the transverse direction

G_{12} is the shear modulus in 1–2 plane.

Herein, the equations are used for the tensile and compressive fiber modes, and the tensile and compressive matrix modes. The failure of material occurs when one of the e_f , e_c , e_m , and e_d values is greater than or equal to zero.

The effects of inter-yarn friction and material properties on the ballistic impact behaviors of woven fabrics were numerically examined using ABAQUS software and shell element [67]. During the study, the toughness values of samples were kept constant and a sample having low longitudinal modulus and high failure strain demonstrated the less threshold friction level than the sample having high longitudinal modulus and lower failure strain. The enhanced inter-yarn friction level increased ballistic energy absorption in fabric strain energy mode, whereas it negatively affected energy absorption in kinetic energy mode until the threshold friction value. In another report, a comparative study about the ballistic penetration behaviors of stacked cross-plyed aramid fabrics and aramid fiber laminated panels were numerically and experimentally investigated using a projectile with a velocity of 550–600 m/s [68]. The PART_COMPOSITE card was utilized to define the thickness and ply orientation. The MAT58 (MAT_LAMINATED COMPOSITE FABRIC) material model was applied for laminate and fabric materials. As a result, the fabric samples absorbed more energy than laminated structures at a rate of 30%. A comparative numerical study about ballistic impact behavior of quasi-isotropic (angled) and aligned Dyneema[®] panels were also reported by Yuan and coworkers [69]. The fiber density and fabric thickness in the numerical model were similar to the real fabric. Cross-section of yarn contains 10 eight-node solid brick elements, whereas the single yarn consists of 130 elements. The 2, 3, and 4 plies quasi-isotropic panels showed better energy absorption than aligned panels about 6–8%, while the yarns in QI panels were weaker against perforation than aligned counterparts at an impact velocity 475 m/s.

In a recent study, 3D composite structures can also be modeled by a finite element method using continuum shell elements and Hashin failure criteria [41]. Additionally, cohesive surface contact with traction separation law for an estimate of the damage behavior at interply and interplay were utilized to model the hybrid structure. The z-yarn was modeled using a 3D axial connector element named CONN3D2 that provides a good approximation to experimental results.

Recently, Chocron et al. conducted a series of experimental and numerical studies on the impact behavior of 2D and 3D carbon fiber composites [70]. The composite components, fiber and matrix, were separately tested and modeled. *MAT_ORTHOTROPIC_ELASTIC and Mohr-Coulomb material models were used for both carbon fiber yarns and matrix materials, respectively. The fiber/matrix interface was also modeled with *MAT_COHESIVE_MIXED_MODE employing a bilinear mixed-mode traction separation law. The results indicated that the tensile properties of 2D and 3D composites were almost similar, while 3D composites presented better performance than 2D composites in terms of shear strength.

Nilakantan and Nutt [71] numerically studied the ballistic performance of single layer and multi-layered non-stitched woven aramid fabrics for different boundary conditions and ply orientations. The 0°, 15°, 30°, and 45° ply orientations were studied with 2 and 4 sides clamped configurations and the 0.22 caliber spherical steel projectile, which has a mass of 0.692 g was modeled and used throughout numerical studies. They determined that multi-layered configurations are more effective than single layer because they can transfer the stress waves applied onto them.

6 Future Trends

Increasing the energy absorption capability of the composites may be possible by changing the type of component materials or design strategies. Among them, the development of a novel design is more practical than using new materials that require lengthy synthesis and commercialization processes. In the literature, one of the most common approaches is bio-inspired design which is increasingly attracting researchers' interest [72–75]. In a recent study, a finite element model was proposed to predict the ballistic performance of the bio-inspired helical structure [75]. It was noticed that the bio-inspired helical structure gave rise to large delamination, which helped in the spreading of stress waves in the laminates.

In another study, shell structure of mantis shrimp crustaceans were mimicked using helicoidal laminates consisting of carbon fiber reinforced epoxy, Kevlar-reinforced epoxy and laminated polyethylene [76]. The carbon/epoxy composites having helical structure displayed the best performance against the small projectiles.

Another alternative in design may be the addition of a new type of material on to the back face or front face of the fabric layers. The additional material should not increase the weight of the whole structure, but it should provide to decrease in back face deflection or the number of penetrating layers. For example, Ayten and coworkers utilized silica-based crosslinked aerogels in the aramid fabrics to improve the ballistic efficiency [77]. The ballistic tests were performed using 44 Magnum ammo, which has a kinetic energy value of 1500 J. The addition of aerogels only increased the weight of the whole structure at a rate of 6.6%, whereas the number of penetrated fabric layers decreased by the rate of 72%.

Also, the addition of soft energy absorption materials to the armor structure is another design option for the improvement of ballistic performance of the materials.

A ballistic hybrid panel consisting of UHMWPE fabrics with nanoporous materials functionalized liquid as an energy absorption material and structure was designed by Liu and coworkers [78]. The hybrid panel demonstrated less back deflection at the rate of 6–17% when it is compared with the neat UHMWPE fabrics panel having the same areal density. This could be due to the contribution of the nanoporous materials functionalized liquid providing the flexibility of the structure.

7 Summary

Herein, a literature survey about the composite materials used in ballistic protection, especially in human protection was summarized with the publications published in the last few years. Firstly, a brief introduction was presented regarding the ballistic science and ballistic threats. Then, the type of fiber materials and fabric structures that are important factors for ballistic performance were explained in detail. Secondly, ballistic impact and failure mechanisms, and numerical modeling and material models for both fabric and composites structures were discussed with recently published articles. Finally, future trends in ballistic science such as bio-inspired structures and adding novel soft energy absorbing materials into the ballistic structures were presented.

References

1. Office of Law Enforcement Standards (OLEs) of the National Institute of Standards and Technology (NIST), *Ballistic Resistance of Body Armor NIJ Standard. 0101.06* (National Institute of Justice Office of Science and Technology, Washington, 2008), p. 55
2. J.L. Park, B.I. Yoon, J.G. Paik, T.J. Kang, Ballistic performance of p-aramid fabrics impregnated with shear thickening fluid; Part I—Effect of laminating sequence. *Text. Res. J.* **82**, 527–541 (2011). <https://doi.org/10.1177/0040517511420753>
3. B.-W. Lee, C.-G. Kim, Computational analysis of shear thickening fluid impregnated fabrics subjected to ballistic impacts. *Adv. Compos. Mater.* **21**, 177–192 (2012). <https://doi.org/10.1080/09243046.2012.690298>
4. J.L. Park, B.I. Yoon, J.G. Paik, T.J. Kang, Ballistic performance of p-aramid fabrics impregnated with shear thickening fluid; Part II—Effect of fabric count and shot location. *Text. Res. J.* **82**, 542–557 (2012). <https://doi.org/10.1177/0040517511420765>
5. Y. Park, Y. Kim, A.H. Baluch, C.-G. Kim, Empirical study of the high velocity impact energy absorption characteristics of shear thickening fluid (STF) impregnated Kevlar fabric. *Int. J. Impact Eng.* **72**, 67–74 (2014). <https://doi.org/10.1016/j.ijimpeng.2014.05.007>
6. A. Haris, H.P. Lee, T.E. Tay, V.B.C. Tan, Shear thickening fluid impregnated ballistic fabric composites for shock wave mitigation. *Int. J. Impact Eng.* **80**, 143–151 (2015). <https://doi.org/10.1016/j.ijimpeng.2015.02.008>
7. O.E. Petel, S. Ouellet, J. Loiseau, D.L. Frost, A.J. Higgins, A comparison of the ballistic performance of shear thickening fluids based on particle strength and volume fraction. *Int. J. Impact Eng.* **85**, 83–96 (2015). <https://doi.org/10.1016/j.ijimpeng.2015.06.004>

8. M. Fahool, A.R. Sabet, Parametric study of energy absorption mechanism in Twaron fabric impregnated with a shear thickening fluid. *Int. J. Impact Eng.* **90**, 61–71 (2016). <https://doi.org/10.1016/j.ijimpeng.2015.11.016>
9. E.E. Haro, A.G. Odeshi, J.A. Szpunar, The energy absorption behavior of hybrid composite laminates containing nano-fillers under ballistic impact. *Int. J. Impact Eng.* **96**, 11–22 (2016). <https://doi.org/10.1016/j.ijimpeng.2016.05.012>
10. A. Laha, A. Majumdar, Interactive effects of p-aramid fabric structure and shear thickening fluid on impact resistance performance of soft armor materials. *Mater. Des.* **89**, 286–293 (2016). <https://doi.org/10.1016/j.matdes.2015.09.077>
11. A. Laha, A. Majumdar, Shear thickening fluids using silica-halloysite nanotubes to improve the impact resistance of p-aramid fabrics. *Appl. Clay Sci.* **132–133**, 468–474 (2016). <https://doi.org/10.1016/j.clay.2016.07.017>
12. S. Gürgen, M.C. Kuşhan, The ballistic performance of aramid based fabrics impregnated with multi-phase shear thickening fluids. *Polym. Test.* **64**, 296–306 (2017). <https://doi.org/10.1016/j.polymertesting.2017.11.003>
13. M. Hasanzadeh, V. Mottaghtalab, M. Rezaei, H. Babaei, Numerical and experimental investigations into the response of STF-treated fabric composites undergoing ballistic impact. *Thin-Walled Struct.* **119**, 700–706 (2017). <https://doi.org/10.1016/j.tws.2017.07.020>
14. A. Khodadadi, G.H. Liaghat, A.R. Sabet, H. Hadavinia, A. Aboutorabi, O. Razmkhah, M. Akbari, M. Tahmasebi, Experimental and numerical analysis of penetration into Kevlar fabric impregnated with shear thickening fluid. *J. Thermoplast. Compos. Mater.* **31**, 392–407 (2017). <https://doi.org/10.1177/0892705717704485>
15. A. Majumdar, A. Laha, D. Bhattacharjee, I. Biswas, Tuning the structure of 3D woven aramid fabrics reinforced with shear thickening fluid for developing soft body armour. *Compos. Struct.* **178**, 415–425 (2017). <https://doi.org/10.1016/j.compstruct.2017.07.018>
16. A.F. Ávila, A.M. de Oliveira, S.G. Leão, M.G. Martins, Aramid fabric/nano-size dual phase shear thickening fluid composites response to ballistic impact. *Compos. Part A Appl. Sci. Manuf.* **112**, 468–474 (2018). <https://doi.org/10.1016/j.compositesa.2018.07.006>
17. Q. He, S. Cao, Y. Wang, S. Xuan, P. Wang, X. Gong, Impact resistance of shear thickening fluid/Kevlar composite treated with shear-stiffening gel. *Compos. Part A Appl. Sci. Manuf.* **106**, 82–90 (2018). <https://doi.org/10.1016/j.compositesa.2017.12.019>
18. V.A. Chatterjee, S.K. Verma, D. Bhattacharjee, I. Biswas, S. Neogi, Enhancement of energy absorption by incorporation of shear thickening fluids in 3D-mat sandwich composite panels upon ballistic impact. *Compos. Struct.* **225** (2019). <https://doi.org/10.1016/j.compstruct.2019.111148>
19. A. Khodadadi, G. Liaghat, S. Vahid, A.R. Sabet, H. Hadavinia, Ballistic performance of Kevlar fabric impregnated with nanosilica/PEG shear thickening fluid. *Compos. B Eng.* **162**, 643–652 (2019). <https://doi.org/10.1016/j.compositesb.2018.12.121>
20. S. Sen, N.B. Jamal M, A. Shaw, A. Deb, Numerical investigation of ballistic performance of shear thickening fluid (STF)-Kevlar composite. *Int. J. Mech. Sci.* **164** (2019). <https://doi.org/10.1016/j.ijmecsci.2019.105174>
21. D. Weerasinghe, D. Mohotti, J. Anderson, Incorporation of shear thickening fluid effects into computational modelling of woven fabrics subjected to impact loading: a review. *Int. J. Prot. Struct.* **11**, 340–378 (2019). <https://doi.org/10.1177/2041419619889071>
22. S. Arora, A. Majumdar, B.S. Butola, Soft armour design by angular stacking of shear thickening fluid impregnated high-performance fabrics for quasi-isotropic ballistic response. *Compos. Struct.* **233** (2020). <https://doi.org/10.1016/j.compstruct.2019.111720>
23. S. Arora, A. Majumdar, B. Singh Butola, Interplay of fabric structure and shear thickening fluid impregnation in moderating the impact response of high-performance woven fabrics. *J. Compos. Mater.* **54**, 4387–4395 (2020). <https://doi.org/10.1177/0021998320932991>
24. M. Bajya, A. Majumdar, B.S. Butola, S.K. Verma, D. Bhattacharjee, Design strategy for optimising weight and ballistic performance of soft body armour reinforced with shear thickening fluid. *Compos. Part B: Eng.* **183** (2020). <https://doi.org/10.1016/j.compositesb.2019.107721>

25. J. Qin, T. Wang, J. Yun, B. Guo, X. Shi, G. Zhang, Response and adaptability of composites composed of the STF-treated Kevlar fabric to temperature. *Compos. Struct.* **260** (2021). <https://doi.org/10.1016/j.compstruct.2020.113511>
26. X. Wang, J. Zhang, L. Bao, W. Yang, F. Zhou, W. Liu, Enhancement of the ballistic performance of aramid fabric with polyurethane and shear thickening fluid. *Mater. Des.* **196** (2020). <https://doi.org/10.1016/j.matdes.2020.109015>
27. A.V. Ignatova, O.A. Kudryavtsev, M.V. Zhikharev, Influence of surface polymer coating on ballistic impact response of multi-layered fabric composites: Experimental and numerical study. *Int. J. Impact Eng.* **144** (2020). <https://doi.org/10.1016/j.ijimpeng.2020.103654>
28. Y. Chu, M.D.R. Rahman, S. Min, X. Chen, Experimental and numerical study of inter-yarn friction affecting mechanism on ballistic performance of Twaron® fabric. *Mech. Mater.* **148** (2020). <https://doi.org/10.1016/j.mechmat.2020.103421>
29. A.K. Bandaru, S. Ahmad, N. Bhatnagar, Ballistic performance of hybrid thermoplastic composite armors reinforced with Kevlar and basalt fabrics. *Compos. Part A Appl. Sci. Manuf.* **97**, 151–165 (2017). <https://doi.org/10.1016/j.compositesa.2016.12.007>
30. S. Cao, H. Pang, C. Zhao, S. Xuan, X. Gong, The CNT/PSt-EA/Kevlar composite with excellent ballistic performance. *Compos. Part B: Eng.* **185** (2020). <https://doi.org/10.1016/j.compositesb.2020.107793>
31. Y. Yang, X. Chen, Investigation of failure modes and influence on ballistic performance of ultra-high molecular weight polyethylene (UHMWPE) uni-directional laminate for hybrid design. *Compos. Struct.* **174**, 233–243 (2017). <https://doi.org/10.1016/j.compstruct.2017.04.033>
32. M.A. Abtef, F. Boussu, P. Bruniaux, C. Loghini, I. Cristiani, Ballistic impact mechanisms—A review on textiles and fibre-reinforced composites impact responses. *Compos. Struct.* **223** (2019). <https://doi.org/10.1016/j.compstruct.2019.110966>
33. T.K. Ćwik, L. Iannucci, P. Curtis, D. Pope, Investigation of the ballistic performance of ultra high molecular weight polyethylene composite panels. *Compos. Struct.* **149**, 197–212 (2016). <https://doi.org/10.1016/j.compstruct.2015.11.009>
34. U. Mawkhlieng, A. Majumdar, Designing of hybrid soft body armour using high-performance unidirectional and woven fabrics impregnated with shear thickening fluid. *Compos. Struct.* **253** (2020). <https://doi.org/10.1016/j.compstruct.2020.112776>
35. J.R. Xiao, B.A. Gama, J.W. Gillespie, Progressive damage and delamination in plain weave S-2 glass/SC-15 composites under quasi-static punch-shear loading. *Compos. Struct.* **78**, 182–196 (2007). <https://doi.org/10.1016/j.compstruct.2005.09.001>
36. B.A. Gama, J.W. Gillespie, Finite element modeling of impact, damage evolution and penetration of thick-section composites. *Int. J. Impact Eng.* **38**, 181–197 (2011). <https://doi.org/10.1016/j.ijimpeng.2010.11.001>
37. B.Z. Haque, J.L. Harrington, J.W. Gillespie, Multi-hit ballistic impact on S-2 glass/SC15 thick-section composites: finite element analyses. *J. Strain Anal. Eng. Des.* **47**, 495–512 (2012). <https://doi.org/10.1177/0309324712456823>
38. B.Z. Haque, J.L. Harrington, J.W. Gillespie, Multi-hit ballistic impact on S-2 glass/SC15 thick-section composites: experiments. *J. Strain Anal. Eng. Des.* **47**, 480–494 (2012). <https://doi.org/10.1177/0309324712456797>
39. N. Domun, C. Kaboglu, K.R. Paton, J.P. Dear, J. Liu, B.R.K. Blackman, G. Liaghat, H. Hadavinia, Ballistic impact behaviour of glass fibre reinforced polymer composite with 1D/2D nanomodified epoxy matrices. *Compos. B. Eng.* **167**, 497–506 (2019). <https://doi.org/10.1016/j.compositesb.2019.03.024>
40. T.S. Reddy, P.R.S. Reddy, V. Madhu, Dynamic behaviour of carbon/ultra high molecular weight polyethylene (UHMWPE) hybrid composite laminates under ballistic impact. *J. Dyn. Behav. Mater.* (2021). <https://doi.org/10.1007/s40870-020-00275-3>
41. S. Ahmed, X. Zheng, D. Zhang, L. Yan, Impact response of carbon/Kevlar hybrid 3D woven composite under high velocity impact: experimental and numerical study. *Appl. Compos. Mater.* **27**, 285–305 (2020). <https://doi.org/10.1007/s10443-020-09809-3>
42. Y. Yang, L. Zhang, L. Guo, W. Zhang, J. Zhao, W. Xie, Dynamic response and research of 3D braided carbon fiber reinforced plastics subjected to ballistic impact loading. *Compos. Struct.* **206**, 578–587 (2018). <https://doi.org/10.1016/j.compstruct.2018.08.021>

43. S. Heimbs, T. Wagner, J.T. Viana Lozoya, B. Hoenisch, F. Franke, Comparison of impact behaviour of glass, carbon and Dyneema composites. *Proc. Inst. Mech. Eng. Part C: J. Mech. Eng. Sci.* **233**, 951–966 (2018). <https://doi.org/10.1177/0954406218764509>
44. F.C. Campbell, *Manufacturing Processes for Advanced Composites*, 1st edn. (Elsevier, New York, 2004), pp.52–53
45. B.A. Cheeseman, T.A. Bogetti, Ballistic impact into fabric and compliant composite laminates. *Compos. Struct.* **61**, 161–173 (2003). [https://doi.org/10.1016/s0263-8223\(03\)00029-1](https://doi.org/10.1016/s0263-8223(03)00029-1)
46. M. Bajya, A. Majumdar, B.S. Butola, S. Arora, D. Bhattacharjee, Ballistic performance and failure modes of woven and unidirectional fabric based soft armour panels. *Compos. Struct.* **255**, 112941 (2021). <https://doi.org/10.1016/j.compstruct.2020.112941>
47. Y.S. Lee, E.D. Wetzel, N.J. Wagner, The ballistic impact characteristics of Kevlar[®] woven fabrics impregnated with a colloidal shear thickening fluid. *J. Mater. Sci.* **38**, 2825–2833 (2003). <https://doi.org/10.1023/A:1024424200221>
48. Y. Zhou, H. Li, Z. Zhang, G. Li, Z. Xiong, M. Wang, Ballistic response of stitched woven fabrics with superior energy absorption capacity: experimental and numerical investigation. *Compos. Struct.* **261** (2021). <https://doi.org/10.1016/j.compstruct.2020.113328>
49. Y. Zhou, X. Chen, A numerical investigation into the influence of fabric construction on ballistic performance. *Compos. B Eng.* **76**, 209–217 (2015). <https://doi.org/10.1016/j.compositesb.2015.02.008>
50. K.S. Pandya, C.V.S. Kumar, N.S. Nair, P.S. Patil, N.K. Naik, Analytical and experimental studies on ballistic impact behavior of 2D woven fabric composites. *Int. J. Damage Mech.* **24**, 471–511 (2014). <https://doi.org/10.1177/1056789514531440>
51. P.R.S. Reddy, T.S. Reddy, V. Madhu, A.K. Gogia, K.V. Rao, Behavior of E-glass composite laminates under ballistic impact. *Mater. Des.* **84**, 79–86 (2015). <https://doi.org/10.1016/j.matdes.2015.06.094>
52. A.K. Bandaru, V.V. Chavan, S. Ahmad, R. Alagirusamy, N. Bhatnagar, Ballistic impact response of Kevlar[®] reinforced thermoplastic composite armors. *Int. J. Impact Eng.* **89**, 1–13 (2016). <https://doi.org/10.1016/j.ijimpeng.2015.10.014>
53. P. Kędzierski, R. Gieleta, A. Morka, T. Niezgodna, Z. Surma, Experimental study of hybrid soft ballistic structures. *Compos. Struct.* **153**, 204–211 (2016). <https://doi.org/10.1016/j.compstruct.2016.06.006>
54. L.H. Nguyen, T.R. Lässig, S. Ryan, W. Riedel, A.P. Mouritz, A.C. Orifici, A methodology for hydrocode analysis of ultra-high molecular weight polyethylene composite under ballistic impact. *Compos. Part A Appl. Sci. Manuf.* **84**, 224–235 (2016). <https://doi.org/10.1016/j.compositesa.2016.01.014>
55. R. Yahaya, S.M. Sapuan, M. Jawaid, Z. Leman, E.S. Zainudin, Measurement of ballistic impact properties of woven kenaf–aramid hybrid composites. *Measurement* **77**, 335–343 (2016). <https://doi.org/10.1016/j.measurement.2015.09.016>
56. L. Gilson, A. Imad, L. Rabet, F. Coghe, On analysis of deformation and damage mechanisms of DYNEEMA composite under ballistic impact. *Compos. Struct.* **253**, 112791 (2020). <https://doi.org/10.1016/j.compstruct.2020.112791>
57. L. Gilson, L. Rabet, A. Imad, F. Coghe, Experimental and numerical assessment of non-penetrating impacts on a composite protection and ballistic gelatine. *Int. J. Impact Eng.* **136** (2020). <https://doi.org/10.1016/j.ijimpeng.2019.103417>
58. T. Langston, An analytical model for the ballistic performance of ultra-high molecular weight polyethylene composites. *Compos. Struct.* **179**, 245–257 (2017). <https://doi.org/10.1016/j.compstruct.2017.07.074>
59. Y. Wang, X. Chen, R. Young, I. Kinloch, W. Garry, An experimental study of the effect of ply orientation on ballistic impact performance of multi-ply fabric panels. *Text. Res. J.* **86**, 34–43 (2015). <https://doi.org/10.1177/0040517514566110>
60. S.G. Nunes, W.F. de Amorim, A. Manes, S.C. Amico, The effect of thickness on vacuum infusion processing of aramid/epoxy composites for ballistic application. *J. Compos. Mater.* **53**, 383–391 (2018). <https://doi.org/10.1177/0021998318785702>

61. B.Z. Haque, J.W. Gillespie, Depth of penetration of Dyneema® HB26 hard ballistic laminates. *J. Thermoplast. Compos. Mater.* **36**(11), 089270572110185(2021). <https://doi.org/10.1177/08927057211018532>
62. J.J. Andrew, S.M. Srinivasan, A. Arockiarajan, H.N. Dhakal, Parameters influencing the impact response of fiber-reinforced polymer matrix composite materials: a critical review. *Compos. Struct.* **224** (2019). <https://doi.org/10.1016/j.compstruct.2019.111007>
63. J.P. Attwood, B.P. Russell, H.N.G. Wadley, V.S. Deshpande, Mechanisms of the penetration of ultra-high molecular weight polyethylene composite beams. *Int. J. Impact Eng.* **93**, 153–165 (2016). <https://doi.org/10.1016/j.ijimpeng.2016.02.010>
64. B.A. Gama, J.W. Gillespie, Punch shear based penetration model of ballistic impact of thick-section composites. *Compos. Struct.* **86**, 356–369 (2008). <https://doi.org/10.1016/j.compstruct.2007.11.001>
65. A.İ Ayten, B. Ekici, M.A. Taşdelen, A numerical and experimental investigation on quasi-static punch shear test behavior of aramid/epoxy composites. *Polym. Polym. Compos.* **28**, 398–409 (2019). <https://doi.org/10.1177/0967391119881554>
66. L.S.T. Corporation, *LS-Dyna Keyword user's Manual: volume II* (2016)
67. S. Ingle, C.S. Yerramalli, A. Guha, S. Mishra, Effect of material properties on ballistic energy absorption of woven fabrics subjected to different levels of inter-yarn friction. *Compos. Struct.* **266** (2021). <https://doi.org/10.1016/j.compstruct.2021.113824>
68. Q. Wei, B. Gu, B. Sun, Ballistic penetration damages and energy absorptions of stacked cross-ply composite fabrics and laminated panels. *Int. J. Damage Mech.* **29**, 1465–1484 (2020). <https://doi.org/10.1177/1056789520927074>
69. Z. Yuan, K. Wang, J. Qiu, Y. Xu, X. Chen, A numerical study on the mechanisms of Dyneema® quasi-isotropic woven panels under ballistic impact. *Compos. Struct.* **236** (2020). <https://doi.org/10.1016/j.compstruct.2020.111855>
70. S. Chocron, A.J. Carpenter, N.L. Scott, R.P. Bigger, K. Warren, Impact on carbon fiber composite: ballistic tests, material tests, and computer simulations. *Int. J. Impact Eng.* **131**, 39–56 (2019). <https://doi.org/10.1016/j.ijimpeng.2019.05.002>
71. G. Nilakantan, S. Nutt, Effects of ply orientation and material on the ballistic impact behavior of multilayer plain-weave aramid fabric targets. *Defence Technol.* **14**, 165–178 (2018). <https://doi.org/10.1016/j.dt.2018.01.002>
72. L. Amorim, A. Santos, J.P. Nunes, J.C. Viana, Bioinspired approaches for toughening of fibre reinforced polymer composites. *Mater.* **199**, 109336 (2021). <https://doi.org/10.1016/j.matdes.2020.109336>
73. P. Miranda, A. Pajares, M.A. Meyers, Bioinspired composite segmented armour: numerical simulations. *J. Mater. Res. Technol.* **8**, 1274–1287 (2019). <https://doi.org/10.1016/j.jmrt.2018.09.007>
74. A. Ghazlan, T. Ngo, P. Tan, Y.M. Xie, P. Tran, M. Donough, Inspiration from Nature's body armours—A review of biological and bioinspired composites. *Compos. Part B: Eng.* **205**, 108513 (2021). <https://doi.org/10.1016/j.compositesb.2020.108513>
75. M.R. Abir, T.E. Tay, H.P. Lee, On the improved ballistic performance of bio-inspired composites. *Compos. Part A Appl. Sci. Manuf.* **123**, 59–70 (2019). <https://doi.org/10.1016/j.compositesa.2019.04.021>
76. J.L. Liu, A.K. Singh, H.P. Lee, T.E. Tay, V.B.C. Tan, The response of bio-inspired helicoidal laminates to small projectile impact. *Int. J. Impact Eng.* **142** (2020). <https://doi.org/10.1016/j.ijimpeng.2020.103608>
77. A.İ Ayten, M.A. Taşdelen, B. Ekici, An experimental investigation on ballistic efficiency of silica-based crosslinked aerogels in aramid fabric. *Ceram. Int.* **46**, 26724–26730 (2020). <https://doi.org/10.1016/j.ceramint.2020.07.147>
78. X. Liu, M. Li, X. Li, X. Deng, X. Zhang, Y. Yan, Y. Liu, X. Chen, Ballistic performance of UHMWPE fabrics/EAMS hybrid panel. *J. Mater. Sci.* **53**, 7357–7371 (2018). <https://doi.org/10.1007/s10853-018-2055-4>

Additive Manufacturing for Complex Geometries in Polymer Composites



Juventino López-Barroso, Cynthia Graciela Flores-Hernández,
Ana Laura Martínez-Hernández, Gonzalo Martínez-Barrera,
and Carlos Velasco-Santos

Abstract This chapter focuses on reviewing different research related to additive manufacturing to generate complex geometries of polymer composites and their applications. As the Industry 4.0 takes off, the efforts to get smart manufacturing have become a critical topic for many countries in their national development strategies. Research has focused on the necessities of resource efficiency, creation, and innovation. In this sense, additive manufacturing plays a vital role in this new industrial revolution. This method has a significant advantage over traditional subtracting manufacture methods due to its ability to build complex geometries in polymer composites, generating the possibility to diversify their potential applications. Thus, this breakthrough technology can assist the construction of diverse composite materials for aerospace, aeronautics, marine, building, biomedical, and vehicle parts, among others. Thus, this chapter offers an introduction to additive manufacturing principles for polymeric composites with complex geometries for functional applications. Afterward, the investigations related to geometries in cores for sandwich structures in polymer composites are reviewed. Besides, cellular, auxetic, and other complex geometries properties and advances in polymer composites, and their focus to diverse possible applications such as building or biomedical materials are assessed and discussed. Finally, the future trends in polymer composites with complex geometries 3d printed are also analyzed.

Keywords 3D printed complex geometry · Cellular printed composites · Additive manufacturing · Complex structures · Polymers

J. López-Barroso · C. G. Flores-Hernández · A. L. Martínez-Hernández · C. Velasco-Santos (✉)
División de Estudios de Posgrado e Investigación, Tecnológico Nacional de México Campus
Querétaro, Santiago de Querétaro, Querétaro 76000, México
e-mail: cylaura@gmail.com

G. Martínez-Barrera
Facultad de Química, Universidad Autónoma del Estado de México, Estado de México,
Toluca 50210, México

Abbreviations

| | |
|--------------------------------|--|
| ISO | International Organization and Standardization |
| ASTM | American Society for Testing and Materials |
| AM | Additive Manufacturing |
| SM | Subtractive manufacturing |
| FDM | Fused deposition method |
| FFA | Fully functional assemblies |
| MagFill | Highly loaded magnetic compound |
| BVOH | Butenediol vinyl alcohol copolymer |
| PLA | Poly(lactic acid) |
| TPU | Thermoplastic Polyurethane |
| CNT | Carbon nanotubes |
| GDS | Gradient structures |
| B-rep | Boundary representation |
| F-rep | Function representation |
| RIM | Reverse imaging modeling |
| CT | Computed Tomography |
| Mri | Scanning Magnetic Resonance |
| CELLMAT | Cellular Architected Materials |
| CAD | Computer-Aided Design |
| 4D | Fourth dimension |
| 2D | Two dimensions |
| 3D | Third dimension |
| FEA | Finite Element Method |
| CAE | Computer-Aided Engineering |
| CAM | Computer-Aided Manufacturing |
| GD | Generative Design |
| AI | Artificial Intelligence |
| FRAM | Fiber-Reinforced Additive Manufacturing |
| TOP | Topology Optimization |
| STL | Standard Triangulation Language |
| FFF | Fused Filament Deposition |
| ABS | Acrylonitrile Butadiene Styrene |
| PCL | Polycaprolactone |
| HA | Hydroxyapatite |
| nHA | Nanohydroxyapatite |
| PA6-I | Polyamide 6-I |
| PETG | Poly-ethylene terephthalate glycol copolymer |
| PLGA | Polyglycolic acid |
| PUA | Poly-urethane acrylate |
| CaCO ₃ | Calcium carbonate |
| MWCNTs | Multiwalled Carbon Nanotubes |
| Fe ₃ O ₄ | Iron oxide |

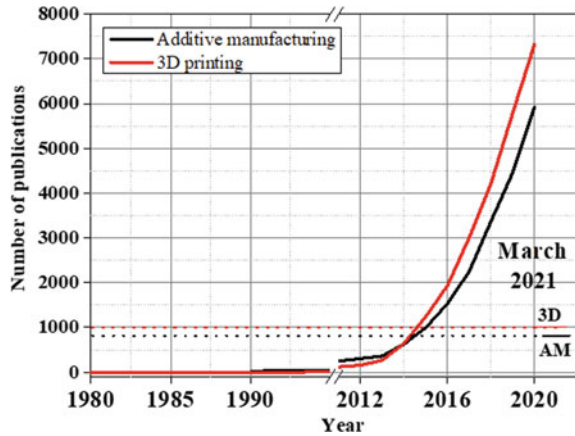
| | |
|--------------------|--|
| PA 12 | Polyamide 12 |
| CNF | Carbon Nanofibers |
| Poly(NIPAM)-4PBA | Poly(N-isopropyl acrylamide)-co-4-(acrylamidomethyl) phenylboronic acid) |
| PA | Polyamide |
| V_f | Volume Fraction |
| MCF | Milled Carbon Fiber |
| RGO | Reduced graphene oxide |
| UAV | Unmanned Aerial Vehicles |
| CFRCLSs | Continuous Fiber-Reinforced Lightweight Composite Structures |
| CFRCHSs | Continuous Fiber-Reinforced Composite Honeycomb Structures |
| CFFRP | Continuous Flax-Fibers Reinforced Composites |
| SMM | Shape Memory Materials |
| PED | Precision Extruding Deposition |
| SEM | Scanning Electron Microscopy |
| DIW | Direct Ink Writing |
| MHDS | Multi-Head Deposition System |
| ION | Iron Oxide Nanoparticles |
| mT | Militesla |
| UV | Ultraviolet |
| CaSiO ₃ | Wollastonite |
| LCE | Liquid Crystal Elastomer |
| SLA | Stereolithography |
| DLP | Digital Light Processing |
| CDLP | Continuous Digital Light Processing |
| CLIP | Continuous Liquid Light Processing |
| PEGDA | Poly(ethylene glycol) Poly(ethylene glycol) diacrylate |
| PEDOT: PSS | Poly(3,4-ethylene dioxathiophene)-poly(styrene sulfonate) |
| GNP | Graphene Nanoplatelets |
| GO | Graphene oxide |
| TPO | Diphenyl (2,4,6-trimethylbenzoyl) phosphine oxide |
| BNNP | Boron nitride nanoplatelets |
| PSP | Photosensitive Polymer |
| PCP | Polysilazane preceramic polymer |
| GelMA | Gelatin-methacryloyl |
| MPEG-PCL | Poly(ethylene glycol) - poly(3-caprolactone) |
| PtO ₂ | Platinum(IV) oxide |
| WO ₃ | Tungsten trioxide |
| phr | Parts Per Hundred |
| DMSO | Dimethyl Sulfoxide |
| MPLS | Mask Projection Stereolithography |
| UV-vis | Ultraviolet-Visible |
| SMP | Shape Memory Polymers |

| | |
|---|---|
| PDC | Polymer-Derived Composites |
| AgNO ₃ | Silver Nitrate |
| LEDs | Light-emitting diodes |
| <i>HASEL</i> | Electrohydraulic Tentacles Actuators |
| SLS | Selective Laser Sintering |
| TMPS | Triply periodic minimal surface |
| PHBV | Poly(3-hydroxybutyrate-co-3-hydroxyvalerate) |
| SWCNTs | Single-Walled Carbon Nanotubes |
| PVP | Polyvinylpyrrolidone |
| TEM | Transmission Electron Microscopy |
| H ₂ SO ₄ | Sulfuric Acid |
| HNO ₃ | Nitric Acid |
| AKM | Akermanite Ca ₂ Mg [Si ₂ O ₇] |
| μ-CT | Microcomputed Tomography |
| Silres MK | Polymethylsilsesquioxane Resin |
| (CH ₃ –SiO _{3/2}) _x | Ceramic Silicone Powder |
| SiC | Silicon carbide |
| SiCN | Silicon –Carbon–Nitrogen Ceramic |
| BN | Boron Nitride |
| PET | Polyethylene Terephthalate |
| MLA | Microlens Arrays |
| EFD | Electric-Field-Driven |
| PDMS | Polydimethylsiloxane |
| SHL | Sheet Lamination |
| LOM | Laminated Object Manufacturing |
| PVA | Polyvinyl Acetate |
| PI | Polyimide |
| EG | Ethylene Glicol |
| LIG | Laser Induced Graphene Foam |
| ZnO | Zinc oxide |
| μCOP | Microscale Continuous Optical |

1 Introduction

In the 80s, a novel manufacturing technique emerged [1, 2]. According to International Organization and Standardization (ISO) and American Society for Testing and Materials (ASTM) standards, the Additive Manufacturing (AM) consists of “a process of fabricating materials to make objects from 3D model data, usually layer upon layer” [3]. This is the argument due to 3D printing is called “additive” in contraposition of the “subtractive” manufacturing (SM) methods. In the subtractive methods, the final geometry comes after removing mass to an initial block [4]. Nowadays, AM plays a crucial role in making objects with the main objective focused on

Fig. 1 Publications per year in the web of science related to additive manufacturing and 3D printing. Based on the bibliometric analysis from the web of science until March 2021



“maximize product performance through the synthesis of shapes, sizes, hierarchical structures, and materials composition, subject to the capabilities of AM technologies” as Gibson et al. mentioned [5]. Then, in the Industry 4.0, the AM plays a vital role in the smart manufacturing and resource efficiency area [6–8]. Consequently, this topic’s research interest boosted drastically as the number of publications reflects (Fig. 1). According to Ligon et al. [2], until 2017, the number of publications per year was below 2500. For 2020, this number reached three times. One aspect where the AM impacts deeply is the capability of building high-complex geometries (theoretically any shape) with different kinds of materials [9–12].

This review aims to provide the advances and focus of research of polymeric printed composites with complex geometries. In the second section, the classification, and scenarios of the application of AM are exposed. Then in the third- and fourth-sections, topics related to complex geometry such as the design features, the customized geometry, and computer tools are commented. In the fifth section, the modifications to the AM methods are commented. Moreover, the printer devices and the issues in the printing process as material heterogeneity are analyzed. It is worthy to note that other techniques such as Binder Jetting and Direct Energy Deposition (focused mainly on metal applications) are only mentioned, but fall outside of the scope of this review, which principally focused on polymeric composites. The sixth section is an outlook of the applications of AM composite. The concluding remarks and trending of this innovative manufacturing are also discussed.

2 Additive Manufacturing for Complex Geometries

Based on the standard ASTM F2792-12a, there are more than 50 different AM techniques [13]. For that reason, there is necessary to define a basic understanding and fundamental principles like a general classification of AM categories. Regarding

this issue, the ISO/ASTM standard 52,900:2015 classifies the AM process according to the final formation object methodology in seven categories [14, 15]. In addition, Fig. 2 shows, a comparative table of technologies and some features of these seven AM categories (summarized by Gao et al. [16]).

- **Material Extrusion:** Process in which material is selectively dispensed (extruded) through a nozzle or orifice. Then this nozzle moves according to a well-defined pattern, depositing layers of material.
- **Powder bed fusion:** Process in which thermal energy selectively fuses regions of a powder bed, commonly a laser or electron beam acts as energy source.
- **Vat polymerization:** In this process, a liquid photopolymer contained in a vat cure in specific regions or part cross-section by light-activated polymerization.
- **Material jetting:** Process in which droplets of build material (including photopolymer and wax) are selectively deposited.
- **Binder jetting:** In this process a liquid bonding agent is selectively deposited to join powder materials to form a part section.
- **Sheet lamination:** Processes that bond sheets of material to form a part.

| CATEGORIES | TECHNOLOGIES | PRINTED "INK" | POWER SOURCE | STRENGTHS / DOWNSIDES |
|----------------------------|---|---|------------------------------|--|
| Material Extrusion | Fused Deposition Modeling (FDM) | Thermoplastics, Ceramic slurries, Metal pastes | Thermal Energy | <ul style="list-style-type: none"> • Inexpensive extrusion machine • Multi-material printing • Limited part resolution • Poor surface finish |
| | Contour Crafting | | | |
| Powder Bed Fusion | Selective Laser Sintering (SLS) | Polyamides /Polymer | High-powered Laser Beam | <ul style="list-style-type: none"> • High Accuracy and Details • Fully dense parts • High specific strength & stiffness • Powder handling & recycling • Support and anchor structure • Fully dense parts • High specific strength and stiffness |
| | Direct Metal Laser Sintering (DMLS) | Atomized metal powder (17-4 PH stainless steel, cobalt chromium, titanium Ti6Al-4V), ceramic powder | | |
| | Selective Laser Melting (SLM) | | | |
| | Electron Beam Melting (EBM) | | Electron Beam | |
| Vat Photopolymerization | Stereolithography (SLA) | Photopolymer, Ceramics (alumina, zirconia, PZT) | Ultraviolet Laser | <ul style="list-style-type: none"> • High building speed • Good part resolution • Overcuring, scanned line shape • High cost for supplies and materials |
| Material Jetting | Polyjet / Inkjet Printing | Photopolymer, Wax | Thermal Energy / Photocuring | <ul style="list-style-type: none"> • Multi-material printing • High surface finish • Low-strength material |
| Binder Jetting | Indirect Inkjet Printing (Binder 3DP) | Polymer Powder (Plaster, Resin), Ceramic powder, Metal powder | Thermal Energy | <ul style="list-style-type: none"> • Full-color objects printing • Require infiltration during post-processing • Wide material selection • High porosities on finished parts |
| Sheet Lamination | Laminated Object Manufacturing (LOM) | Plastic Film, Metallic Sheet, Ceramic Tape | Laser Beam | <ul style="list-style-type: none"> • High surface finish • Low material, machine, process cost • Decubing issues |
| Directed Energy Deposition | Laser Engineered Net Shaping (LENS) Electronic Beam Welding (EBW) | Molten metal powder | Laser Beam | <ul style="list-style-type: none"> • Repair of damaged / worn parts • Functionally graded material printing • Require post-processing machine |

Fig. 2 Comparison of AM methods according to the ISO/ASTM 52,900. Reprinted from Gao et al. [16]. Copyright (2015), with permission from Elsevier

- **Directed energy deposition:** Focused thermal energy is used to fuse materials by melting as they are being deposited. The term focused thermal energy means that an energy source (laser, electron beam, or plasma arc) is concentrated in melting the materials being deposited.

The different methods in AM allow wide application scenarios of AM are diverse, as Table 1 shows. The applications range from educational, medical, military, smart materials, metamaterials until emergent (such as in COVID 19 pandemic). The objects developed for these applications need components with specific design parameters, functionality, mechanical properties, and printability [17]. These parameters have been studied by applying artificial intelligence (AI) indicating in this way the degree of complexity acquired [18]. A complex system refers, how the components inside the system are related to each other [19]. Then, complexity alludes to the number of possible behaviors than a system could exhibit from its components relation [19]. In addition to this, complexity is a multifaceted concept depending on the context [20]. In this case, complexity refers to complicated 3D geometries based on parameters such as lattice patterns, the numbers of nodes and connections in a system, and the relationship between the process parameters and the performance indicators [20–22]. The geometry is a dare to build. In some cases, it is necessary to mimic a specific behavior in the application [23]; in these cases, the piece is achieved only by assembling a high number of parts after their individual manufacturing processing [24].

3 Complex Geometry

As it was mentioned AM methods are a versatile option for most shapes that can imagine even with high-complex designs. Complex geometries mean those structures with abrupt changes in shape, sharp internal corners, high internal porosity, enclosures, and undercuts, among others (Fig. 3) [81]. These geometries can be inspired in math like fractals [82] or numerical calculations [75, 83], biological systems [84, 85], cellular materials [83, 86, 87] or according to a specific necessity of design to acquire specific response [19–22, 88–90]. Without the AM, the conception of complex structures would be a labor-extensive procedure involving a particular manual skill or a specific tool [91]. Conformal cooling passages are directly incorporated in the design, machinery parts that need welding, brazing or assembled from many parts can be replaced by a one structure with high performance (as Fig. 3) [92, 93]. Nowadays, AM and subtractive manufacturing make a synergy to solve geometry complexity problems [94, 95]. In these systems, the hybrid technologies exploit a common platform assembled with additive and subtractive technologies.

Gibson et al. [81] point one of the main advantages of AM as “complexity for free”. As they mentioned, a simple cube fabricated by subtractive manufacturing involves more time and effort than a 3D printed complex anatomic model, both with the same enclosing volume. Also, AM can fabricate controlled porous structures for complex

Table 1 Literature review about some scenarios of AM

| | |
|-------------|--|
| Educational | Engineering education [25, 26] |
| Medical | Medical-surgical models [27–29] |
| | Scaffolds [30, 31] |
| | Tissue regeneration [17, 32–39] |
| | [40–43] |
| | Drug delivery [44, 45] |
| | COVID 19 [29, 46–48] |
| | Prosthetics [3, 27, 49, 50] |
| Mechanics | Metamaterials [51–54] |
| | Auxetic [55, 56] |
| | Structural [11, 57] |
| | Non-assembly [58] |
| | Mechanical properties [59–61] |
| Composites | Polymeric nanocomposites [62–65] |
| | Polymeric composites [9, 13, 66–70] |
| Optics | Nanophotonics and metaphotonics [71] |
| Energy | Carbon in energy-related applications [72] |
| Body armor | Ballistic protection [73, 74] |
| Microscale | Fourth dimension (4D) Microdevices [75] |
| | Machines [76] |
| Others | Actuators [77] |
| | Electromagnetic shielding [78] |
| | Smart materials [53, 79, 80] |

geometry composites, which is mandatory in some applications (Fig. 4) [99]. Other features that have impulse the AM technologies' development are adaptability and repeatability of the structures printed [89]. Moreover, the scrap can decrease by 90%, as Hodonou et al. [100] have mentioned for aircraft components machining.

Vicente et al. [94] have classified the printed structures based on the functionalities. This classification is based on fused deposition method (FDM), however it has been modified, considering complex structures are based on their functionality. Thus, complex geometries have been separated into four groups, as follows.

3.1 Fully Functional Assemblies (FFA)

This classification involves integrated circuits and assembly of multi-materials parts in one step. In most cases, they need a minimum of additional assembly steps after printing (Fig. 5a–c) [81, 91, 105]. For example, von Petersdorff-Campen et al. [106] reported the fabrication of a rotary blood pump with magnetic bearing and magnetic

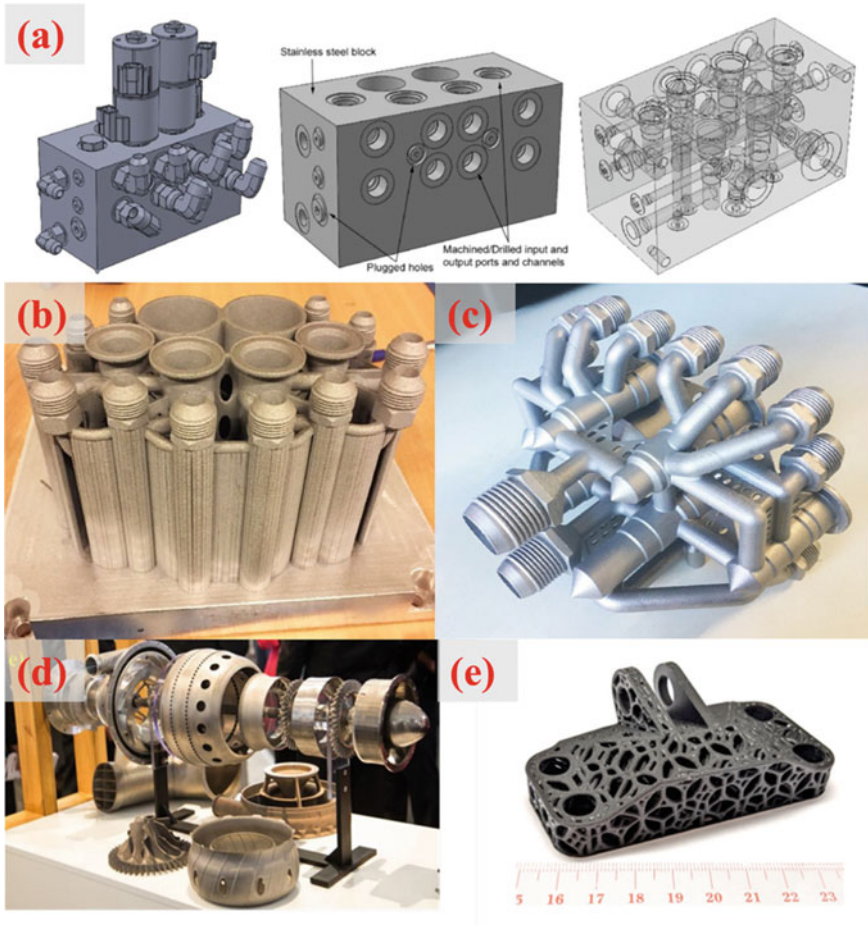


Fig. 3 a–c Redesign process of hydraulic manifold for and underground drilling rig; **a** conventional structure model from original manifold with many removable parts and drill holes; **b** AM manifold obtained with “substantial” amount of support material. Reprinted from Diegel et al. [96]. Copyright (2020), with permission from Elsevier. **d** Gas turbine engine fabricated by AM. Reprinted from Karayel and Bozkurt [97]. Copyright (2020), with permission from Elsevier **e** GE bracket with internal complex shape patterns instead of a solid structure. Reprinted from Woodward and Fromen [98]. Copyright (2021), with permission from Elsevier

drive coupling. In this work, housing and impeller were printed once a time by FDM using three different polymers. “MagFill” this filament is defined as highly loaded magnetic compound, and it was used to print the magnetic components. The polylactic acid (PLA) filament was used for the structures in which the magnets were embedded. Finally, the third polymer, a butenediol vinyl alcohol copolymer (BVOH), was both a support and separator of parts which were dissolved later. The functional



Fig. 4 AM fabricated complex geometries in different science fields **a** One process cycle printed continuous fiber composite. Reprinted from Hou et al. [101]. Copyright (2018), with permission from Elsevier. **b** Lung and vascular system printed by digital light processing (DLP) adapted from Kim et al. [90] under the terms of the Creative Commons CC license <https://creativecommons.org/licenses/>. **c** Double helical printed sample adapted from Scordo et al. [102] under the terms of the Creative Commons CC By 4.0. license <https://creativecommons.org/licenses/by/4.0/>. **d** Continuous lattice fiber ultra-light weight composites. Reprinted from Eichenhofer et al. [103]. Copyright (2017), with permission from Elsevier. **e** Light tower printed by direct ink writing DIW-DLP hybrid system, from printing to a functional device. Reprinted from Peng et al. [104]. Copyright (2021), with permission from Elsevier. **f** Diamond structure with 60% of porosity (from left to right) unit cell, ordered location Computer-Aided Design (CAD) model, printed high porous structure. Adapted from Rollo et al. [83] under the terms of the Creative Commons CC By 4.0. license <https://creativecommons.org/licenses/by/4.0/>

prototype demonstrated operation features of the maximum rotational speed of 1000 rpm, with a flow rate of 3 L min^{-1} and a pressure head of 6 mmHg. However, the authors reported some issues interchanging the filament, such as clean time and the contamination by the dispersing agent used in MagFill filament. Thus, they propose to use a multi-nozzle printer to solve those issues. Generally, the FFA assemblies do not require extra post-processing. However, if the post-processing is mandatory, it is minimum [91]. However, the dimensional accuracy of the individual components demands high control of printing parameters [107].

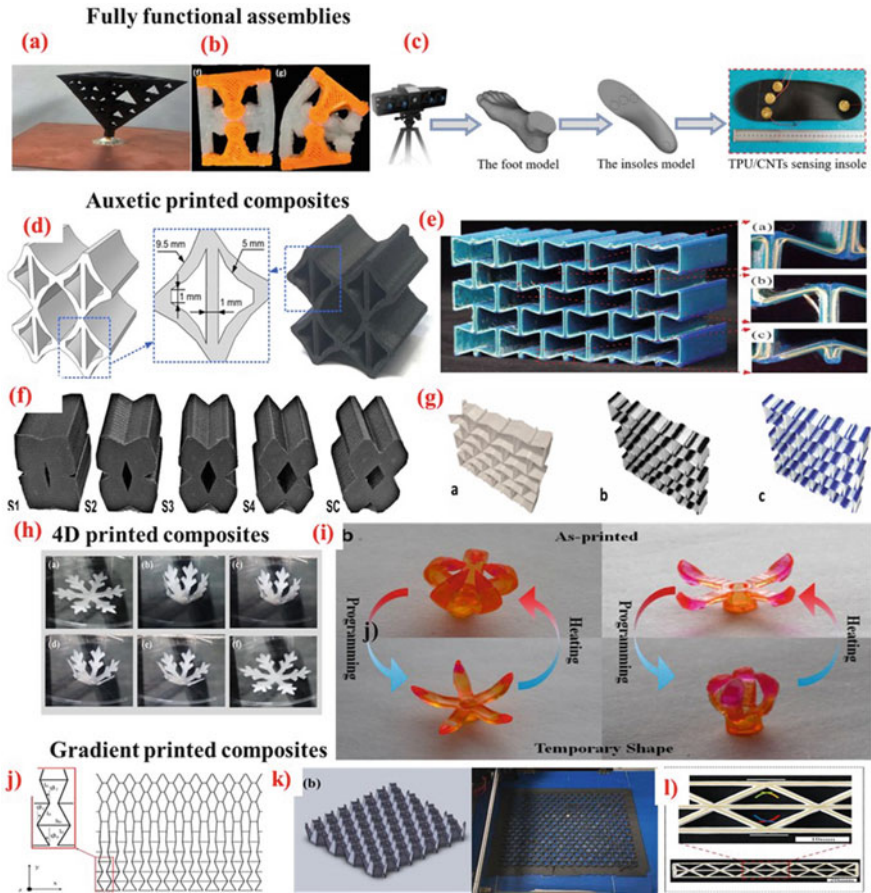


Fig. 5 Printed complex geometry composites: From a to c FFA **a** Sierpinski gasket 3D. Reprinted from Clower et al. [108]. Copyright (2020), with permission from Elsevier **b** Musculoskeletal joint. Reprinted from Hamidi et al. [105]. Copyright (2019), with permission from Elsevier **c** Thermoplastic Polyurethane (TPU)/carbon nanotubes (CNT) sensing insole process. Adapted from Zhuang et al. [109] under the terms of the Creative Commons CC license <https://creativecommons.org/licenses/>. Auxetic printed composites **d** Printed auxetic perforated structures. Reprinted from Chen et al. [110]. Copyright (2020), with permission from Elsevier. **e** Continuous carbon fiber-reinforced auxetic honeycomb. Reprinted from Quan et al. [111]. Copyright (2020), with permission from Elsevier. **f** Rotating perforated auxetic composites. Reprinted from Chen and He [110]. Copyright (2020), with permission from Elsevier. **g** 3D printed re-entrant composites (from left to right) PLA, PLA-Nylon, PLA-TPU. Reprinted from Johnston and Kazanci [112]. Copyright (2021), with permission from Elsevier. **h** Snowflake-like shape memory composite showing its different shape stages against a thermal stimulus. Reprinted from Jiang et al. [113]. Copyright (2021), with permission from Elsevier. **i** Multi-material gripper transition between printed and temporary shape and its process of grabbing an object. Adapted from Ge et al. [114] under the terms of the Creative Commons CC license <https://creativecommons.org/licenses/>. **j** Angle-graded topology. Reprinted from Boldrin et al. [115]. Copyright (2016), with permission from Elsevier. **k** Design and printed gradient honeycomb composite. Reprinted from Pei et al. [116]. Copyright (2020), with permission from Elsevier. **l** Lightweight cellular composite. Reprinted from Dong et al. [117]. Copyright (2021), with permission from Elsevier

3.2 4D Printed Structures

According to Spiegel et al. [75], 4D printed objects are those 3D printed with “life” incorporated. In other words, the properties change with time influenced by an external stimulus [118, 119] like a magnetic field [120], light [121], water [80], or heat interchange [104], among others. This application is focused principally (but not only) on changes in the functionality [122, 123] or the shape memory [85, 124]. Ahmed et al. [125] mentioned that 4D printing combines AM, smart material, and well-programed design. Zhafar and Zhao [74] indicate three fundamental concepts to “materialize” 4D printing process a) the preparation of stimulus-responsive composite; b) specific stimulus and particular response; and c) the length of time for the response.

Momeni and Ni 2020 [126] introduced the 4D printing laws and are summarized as follows:

1. Shape-Morphing Behavior in 4D Printed structures Has Its Origin in the “Relative expansion” Between Active and Passive Materials.
2. All multi-material 4D printed structures have four types of physics: mass diffusion, thermal expansion, molecular transformation, and organic growth considering 4D bioprinting or like-organic growth behavior in other 4D materials.
3. The time-dependent shape-morphing behavior in most multi-material 4D printed structures is governed by two “different types” of time constants (passive and active layers).

Sossou et al. [127] analyzed the design for the 4D printing. First, they asked about, what characteristics are necessary for 4D printing materials? Then, through questions like: is it enough one smart material to get the desired behavior? How can smart materials be combined to produce behavior? And if it is necessary for that combination, does a spatial arrangement behave according to the design? They assign to the modeling and simulation of the behaviors a particular relevance. From this point of view, design in 4D printing is not an intuitive task as happens in conventional material. The iterative design based on voxel modeling and rapid simulation offer designers a rapid test of the distribution of smart materials and their behavior upon external stimulus.

As it was mentioned by Zafar and Zhao [74] one key parameter in 4D printing is the material used, which receives, transmits, and processes the stimulus [79]. Then the material performs as an actuator, shape-morphing or changing the start structure in 4D printing. For these reasons, the election of a suitable material is essential for a successful final printed object. However, regularly a single material has some drawbacks to the entire application due to its physical limitations. For example, Ge et al. [114] mentioned limited mechanical properties, for instance poor deformation at break (10–25%) and applications where the operating temperature is higher than the polymer glass transition temperature. Selecting the adequate AM method and printing multi-material specimens as a polymeric composite with tuned properties can solve those mechanical and thermomechanical issues mentioned [74, 79].

According to Bajpai et al. [79], there are two basic requirements in 4D printing materials. The first is the autonomous shape memory as a response to external stimulus. The second one is printability, considering adequate resolution, printing without damage or degradation to polymer structure, adhesion, and interlayer behavior [59, 128]. Composites provide an alternative to 4D printing, as they extend the properties of polymers, overcome their limitations, and allow tailored properties without losing the printability to complex geometries [74, 79, 125, 129].

3.3 Gradient Structures (GDS)

The GDS can be defined as structure systematic gradual change from interior to exterior [130] or different lengths from the bottom to the top [116]. In other words are those materials with spatial variation of density and composition [16, 131]. GDS are commonly found in nature, like spongy trabecular structures, seashells, and plants that the AM can mimic as aperiodic structures [131, 132]. This kind of design in materials allows customizing and enhancing structural efficiency regarding the structures with uniform cells [133]. In general, GDS can classify as follows [131]:

- (a) Single-phase materials with gradual variations in density
- (b) Multi-phase materials with gradual variations in material composition
- (c) The combination of (a) and (b), in other words, density and composition simultaneously.

According to Li et al. [131], the design geometrical representation is the most fundamental step in conceptualizing GDS. They listed four main geometrical representations for GDS:

- Boundary representation (B-rep): is a method for representing shapes in terms of its surface boundaries, like vertices, edges, and faces [134].
- Function representation (F-rep): where a constructive object is defined with the help of set-theoretic operations on primitives [135].
- Constructive solid geometry: This representation generates topology geometries with smooth boundaries and parametric control [136].
- Spatial decomposition: A complex structure is decomposed by mathematically defined shape metrics (mesh) to quantify its structure [137].

These representations can define the complex geometries involved in GDS to conceptualize and fabricate 3D model data, depositing layers of material [136]. They have recently been developed, more computationally efficient, and geometrically flexible methodologies to design GDS.

- Reverse imaging modeling (RIM). In this case, computed tomography (CT) scanning magnetic resonance (MRI) obtained a detailed 3D voxel object from physical data [131]. In this case, we would suppose 3D scanner could include in this classification. However, the main difference between RIM and conventional scan 3D

models lies in their reconstruction method. In RIM, an algorithm is necessary in contrast to a 3D scan based on surface information [131, 138].

- Topology optimization: This consists of optimizing material distribution based on the analysis of loads, boundary conditions, and constraints by mathematical algorithms [131].
- Voxel-based methods: In this case, volumetric pixels are the base to represent 3D volume in analogous mode like 2D image such as bitmap [96, 137].

All mentioned representations are not exclusive of GDS. However, this complex geometry clearly shows the different scenarios used to represent printed structures in AM. The fabrication of complex geometries (intricate gradients) and highly specific properties, tuning the materials used by AM open the door to applications in different fields of science. For example, geological models, biomedical implants, energy-absorb systems, and so on [131].

3.4 Cellular Materials

It is worth noting the cellular architected materials (CELLMAT) could appear in the whole subclassifications. However, classifying these materials by function in a single division is not possible. For that reason, a special mention of CELLMAT is essential to include. As Schaedler et al. [11] define, the CELLMAT have a spatial distribution of voids and solid part. The cellular materials offer tunable properties materials with high performance, for example, high mechanical strength at low density [139] or low strength-large compressive ratio [99]. They can be classified as random (stochastics), ordered (periodic two dimensions), and ordered location (periodic three dimensions) specifically based on the cell shape, size, and distribution principally [11, 140].

One subclassification of CELLMAT is auxetic materials. Auxetic means that “may be increased” according to the Greek word “Auxetos” [56]. This term is related to the ratio between the transversal to a longitudinal strain called the Poisson ratio. Auxetic materials are characterized by a negative Poisson ratio [52]. For example, the deformation in negative Poisson’s ratio material increments dimensions in the transverse direction while stretched in longitudinal direction [24, 141]. In Fig. 5d-g are some auxetic 3D printed composites. Recently, re-entrant auxetic structures demonstrated a synergetic effect when keratin was added to the PLA matrix [7]. The geometry and the materials evidenced sound absorption properties, which can be applied in automotive or aeronautic vehicles.

Other authors mentioned open and close cell geometries in CELLMAT [87, 139]. Both differences lie if the structure is built by sheets, as Berger et al. [87] mentioned. Moreover, if the cell is on a sandwich panel can be classified as stochastic, 2D, which includes honeycomb and prismatic, and 3D periodic structures like truss or textile (Fig. 6) [142].

The conceptualization of the final structure in AM is the first step in the fabrication of complex geometries structures. In this step, the necessity of a clear idea of the

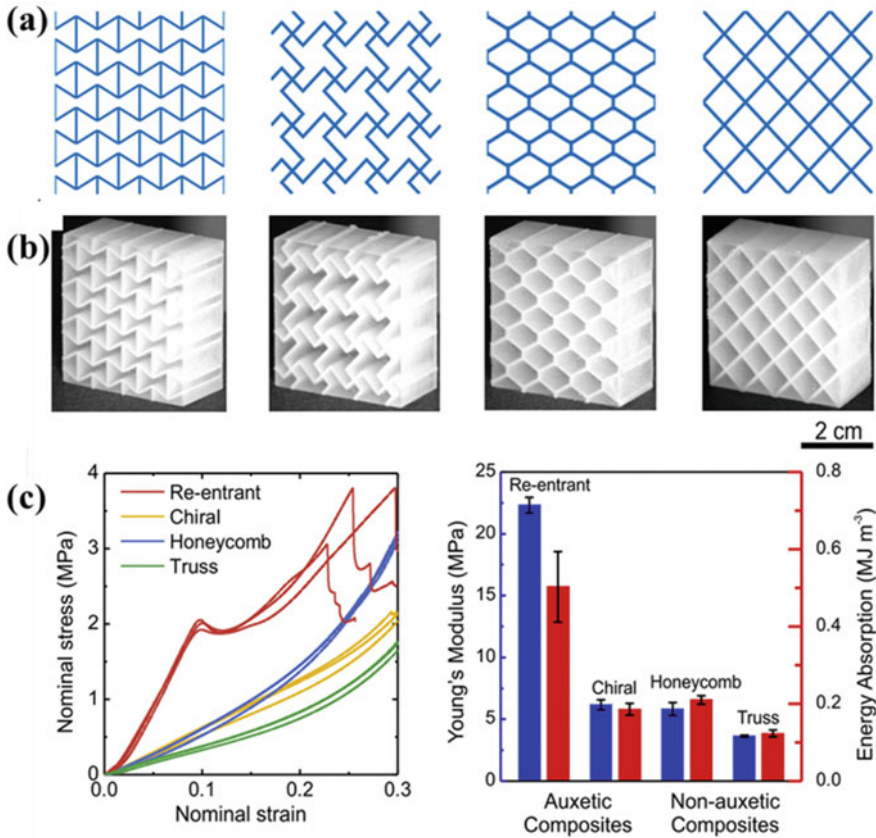


Fig. 6 **a** Cellular lattices with unit cells re-entrant honeycomb, chiral, honeycomb, and truss (from left to right). **b** 3d printed lattice composites. **c** Mechanical properties of 3d printed composites, stress-strain curve (left) and Young's modulus and energy absorption (right). Reprinted from Li et al. [142]. Copyright (2018), with permission from Elsevier

product is demanding [119]. Also, functionality and structure play an important role in describing the solution deeply in problems. The printed structure is conceptualized by a 3D CAD model previously the fabrication of the object [143]. In this step of AM process, the expertise of designers impacts the conception of the selected geometry. In some cases, the CAD model can be optimized through simulation by finite element method (FEA), then the model analyzed can be used or re-analyzed until the desired geometry [100]. For example, mimicking nature by fabricating combined cell structures with variation in size, orientation, cellular topology, and other parameters needs to overcome design issues in “adaptative” cell materials [133]. Thus, technical information like printing speed, the nozzle temperature, and onset parameters must be clearly defined before starting the printing process [119]. All these activities have been improved by developing design knowledge and technological tools, as it is commented as follows the following sections.

4 Design for AM Complex Geometries

Gao et al. [16] made a comparison between “traditional” subtractive manufacturing methods like (milling, cutting, and others) versus AM. Figure 7 shows a synthesized comparative analysis [16].

Figure 7 shows the opportunity to explore design concepts the AM offers, in comparison with the SM limits [5, 16]. However, innovative design concepts and developments must be manufacturable by the accurate AM process [5]. Thus, to reach this goal, it has been described two broad considerations for the AM. The first one, the “opportunistic” design, is related to the advantages and opportunities of the “clean sheet” conceptual design activity in AM. For example, customization, generative design, topology optimization, graded materials, and so on. The second one, the “restrictive” design, is related to the restrictions presented by AM process, such as understanding process constraints, design rules, and minimizing the costs.

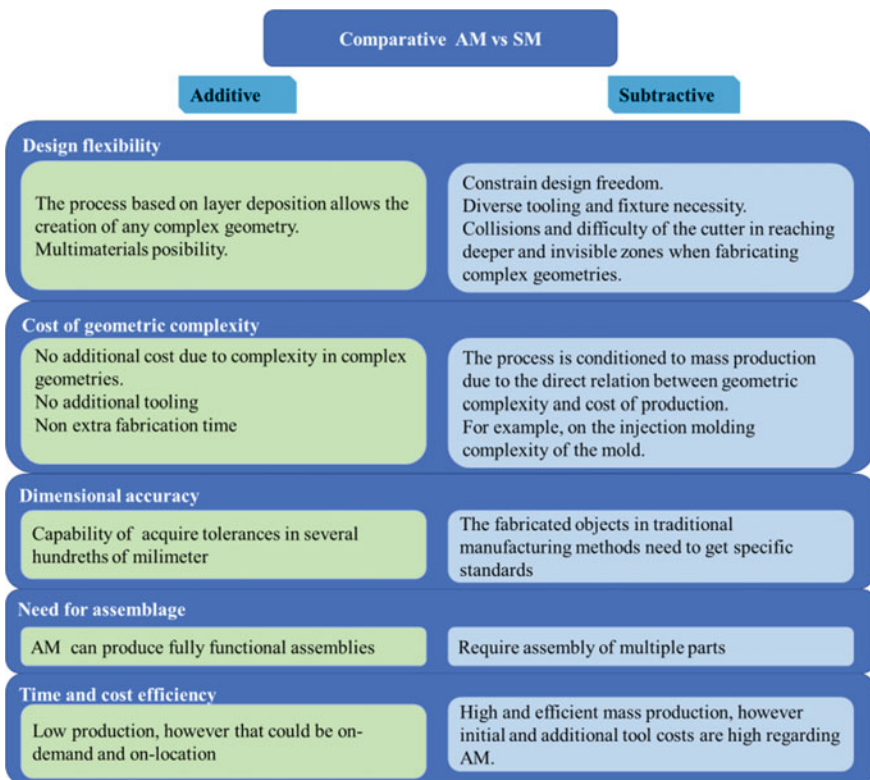


Fig. 7 Comparative analysis of the capabilities of AM versus SM

Regarding the opportunistic design, the sequential layer addition nature in AM provides unique capabilities compared to other manufacturing processes. enlisted as follows [5, 93]:

- Shape complexity: virtually any shape can be fabricated.
- Hierarchical complexity: multiple size scales can be involved in the design of complex geometries
- Functional complexity: the fabrication of functional multipart devices instead of single pieces is possible.
- Material complexity: single, combination, or composites materials can be processed. Shape complexity has been one of the most explored considering the relation between the layer added and the shape of layers. Moreover, it can exploit some advantages from the other capabilities mentioned [5]. In other words, shape complexity allows the production of complex geometries for efficient, lightweight, integrated products, compliant mechanisms, and other applications. Then, the shape complexity can be related to hierarchical complexity by a custom geometry for a patient, with material complexity as occur in multi-functional systems such as in smart actuators [144] or no tooling necessity Inasmuch as functional complexity allows FFA.

As it has been reviewed in this work, the AM has impacted different fields of science due to all possible geometries which could be fabricated. However, these geometries could not materialize considering the development of computer-aided tools. CAD/CAE/CAM tools refer to the Computer-Aided Design (CAD), Computer-Aided Engineering (CAE), and Computer-Aided Manufacturing (CAM) [145]. As these tools have been evolving, accurate, design, manufacturing, and simulations allow engineers and researchers to accomplish their tasks at higher performance levels.

4.1 CAD Tools

CAD tools have been used for designing sophisticated, complex geometries for either single parts or FFA. In the past, CAD tools were focused only on visualizing the model of the product that designers created. Now it is an active process that allows designers to modify, optimize, and create in the shaping process [146]. However, some challenges that CAD tools need to overcome are the geometry complexity principally when it is necessary supports [5]. Physically based materials representation refers to defining in the model the limits with adequate representation of the different materials used in concentration and distribution [5, 144]. Physically based property representation, this concept means a specific distribution of physical and mechanical properties must be represented and evaluated according to physical basis.

One interesting approach about CAD tools is incorporating novelty techniques such as generative design (GD) (Fig. 8a). GD is applied to optimize resources and goals, from urban arrangements to complex shapes inspired in biomorphic [146]. In

GD for structural design software, algorithms are used to generate a shape [136]. Thus, boundary conditions and some parameters according to the problem need to be defined, for example, the material or geometries to be retained from the original design, loads, and the manufacturing process. GD can generate many solutions in parallel for a further decision [136, 146]. In GD, the AI is integrated into the CAD tool. Then, the software recognizes patterns in data sets, and with proper training, the software can recognize patterns in new unknown data called machine learning. To make this recognition, the GD uses artificial neural networks [146].

Junk and Burkart [146] compared CAD software for GD, summarized in Table 2. As it can be noted, the software programs included in Table 2 are focused on the breakthrough GD. The authors compared important parameters such as storage capacity, connectivity, costs, and other important features in that research. However, there are alternatives of high-performance CAD tools such as Solidworks®, Rhino®, nTopology®, AutoCAD®, openSCAD®, Geomagic®, which are used in the creation of complex geometries where GD is not used.

4.2 CAE Tools

CAE tools is focused mainly on the simulation of engineering problems. This analysis is based on the FEA, which solves a problem by a discretization [149]. The mechanical analysis of structures, thermometallurgical-mechanical, hardening mechanical properties, topology optimization, and other physical studies can be performed [145, 150, 151]. In AM, the CAE tools have been applied to simulate the AM process and test obtained structures' properties [151]. Mainly, in complex geometries, this is focused on generating lightweight and high-performance configurations that are difficult to obtain with conventional ideas by topology optimization (TOP) [152]. The TOP is an advanced structural methodology that optimizes the material and shape configuration (Fig. 8b) [153]. Generally, the solutions show nearly fully stressed structures or constant strain energy [5].

The TOP analysis has been applied from the 90s decade. However, it was impractical until the revolution caused by the AM [154]. From the AM impact on manufacturing processes, the optimized parts obtained in TOP become manufacturable causing high specialized software demand. Table 3 lists some products that are used in the TOP.

Liu et al. [162] reviewed trajectory planning in AM as a critical step. The CAE software in these cases assists in planning and optimizing the trajectories, which are strongly linked with the structure behavior [153]. Thus, analyzing the initial design by numerical methods available in CAE software or using an additional optimization toolbox (as reported for a genetic algorithm) [163]. Optimization in the fiber direction, for example, in continuous FRAM, directly affects the anisotropy materials properties [153]. Then, the physical phenomena such as stiffness, strength, dynamics, or heat conduction affected by the optimized fiber orientation spatially would be compatible with an industrial application [153, 164, 165].

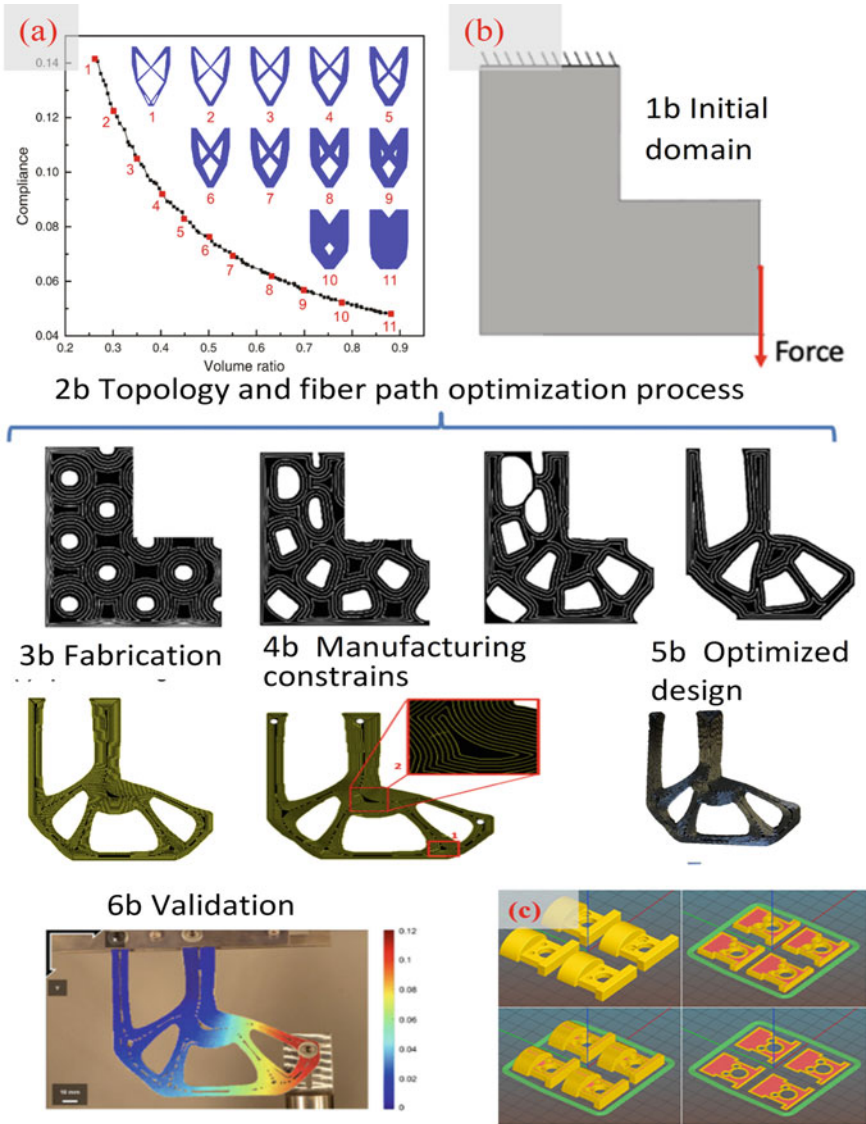


Fig. 8 Application of computer-aided tools in complex geometries **a** GD solutions for a beam cantilever problem, the black and red points show the entire population and the optimized solutions of problem respectively. Reprinted from Wang et al. [136]. Copyright (2021), with permission from Elsevier. **b** Design, testing, and manufacturing process of complex geometry continuous fiber-reinforced additive manufacturing (FRAM) with topology optimization (TOP). Reprinted from Fernandes et al. [147]. Copyright (2021), with permission from Elsevier. **c** A model representation of prototype using CAM software. Reprinted from Mikołajczyk [148]. Copyright (2019), with permission from Elsevier

Table 2 CAD tools for GD. Adapted from Junk and Burkart [146]. Copyright (2021), with permission from Elsevier

| Software | Provider | Origin | Connectivity | Storage |
|------------|-------------------|---------|--------------|---------|
| Fusion 360 | Autodesk | USA | Integrated | Cloud |
| CogniCAD | ParaMatters | USA | Stand-alone | Local |
| Solid Edge | Siemens | Germany | Integrated | Local |
| Creo 7.0 | PTC | USA | Integrated | Local |
| MSC Apex | MSC Software | USA | Stand-alone | Local |
| CATIA V6 | Dassault Systèmes | France | Integrated | Local |
| NX | Siemens | Germany | Integrated | Local |

Table 3 Software used for topology optimization in AM

| Company | Software product | References | Company | Software product | References |
|-------------------|--|------------|---------------------------------------|------------------------------|------------|
| Altair | OptiStruct, inspire, DesignThinking | [5, 154] | Siemens | Solid Edge Generative Design | [5, 154] |
| Ansys | Ansys Discovery AIM, Additive suite | | Vanderplaats Research and Development | GENESIS | |
| Autodesk | Autodesk Generative Design, Netfabb Ultimate | | Rhinoceros | Grasshopper TOpos | [155] |
| COMSOL | Optimization Module | | DTU Mechanical Engineering | TopOpt | [156] |
| Dassault Systèmes | Tosca Structure, Abaqus, Solidworks xDesign | | RMIT University | BESO2D | [157] |
| MSC | Patran/Nastran | | FEMtools | FEMtools 4 Optimization | [158] |
| nTopology | Element Free/Pro | | INTES | PERMANS TOPO module | [159] |
| ParaMatters | CogniCAD | | CAESS | CAESS ProTOP | [160] |
| PTC | Creo BMX | | Linköping University | Trinitas | [161] |

4.3 CAM Tools

Traditional CAD/CAM systems for SM can become complicated due to the programming necessities to accurately organize the shaping and finishing process [148]. In the CAM system for AM, that could be simpler than SM because most printers simplify this task with friendly user software. Furthermore, most CAM systems are mature technology. Hence AM can adopt and adapt this technology to its process [166, 167]. Hedrick et al. [166] summarized the process flow of AM using the CAM module as follows steps:

- Project setup: in this step, considerations such as a machine, process type, base material, material, and travel path strategy are involved.
- Travel path strategy/creation of Standard Triangulation Language (STL) file format (.stl) [149].
- Definition of the process of specific parameters such as speed/feed parameters, base heat input parameter, transient conditions, profile, and fill parameters. Moreover, a G-code generally is created to define all mentioned process-specific parameters [148].
- Travel path simulation/verification.
- Component printing.

The machine virtualization achieved by the CAM tools allows complex geometries to consider AM conditions and components of printers. Then, the suitable strategy of machine kinematics can be evaluated. Moreover, machine virtualization enables the prediction and prevention of collisions of printer components that could happen in the real process (Fig. 8c) [166, 167].

In CAM processes, not all software used in SM support AM [166]. However, there are great options to make a complete computer-aided analysis (CAD/CAE/CAM) such as Solidworks® and NX® from Dassault and Siemens brands, respectively. Other options of software that have CAD/CAM analysis are CAM Works®, Creo CAM®, and hyperMILL®. There are options which assist the creation of STL files [168] and software-focused principally on G-Code creation, and virtual AM process [169] as Table 4 listed.

5 Printing Complex Geometry Composites

5.1 Extrusion-Based Composites

Fused filament deposition (FFF) is a printing technology used to obtain composites with complex geometries [108, 112, 175–178]. A melted polymer with a dispersed second phase is extruded and deposited layer by layer following a CAD model in these additive manufacturing technologies. One of the main advantages of this printing method is its low cost and usability [179]. Hence, different kinds of materials can be extruded by this method [66, 178, 180–183]. This versatility lies in controlling essential parameters such as temperature, printing speed, and resolution [66, 184]. These reasons convert the material extrusion-based AM method to the most used to build complex geometries composites. In Table 5, there are some complex geometry composites obtained by AM extrusion-based method.

Estakhrianhighi et al. [175] reported a comparative study of 2D cellular materials to obtain recyclability and biodegradability lightweight structures. Honeycomb and Isomixed cellular wood composites were printed by FFF. Mechanical properties of these composites were compared to FEA simulated mechanical properties. Isomixed cellular composites showed better performance in the tensile modulus and

Table 4 Software used in CAM for AM

| Company | Software product | Reference | Company | Software product | Reference |
|-----------------------------|------------------|-----------|---|-------------------|-----------|
| <i>CAD/CAE/CAM Software</i> | | | | | |
| Dassault | Solidworks | [170] | Christophe Geuzaine-Jean-Francois Remacle | Gmsh | [168] |
| Siemens | NX | [171] | Autodesk | Tinkercad | |
| <i>CAD/CAM Software</i> | | | | | |
| HCL | CAM Works | [172] | Gina Häußge | OctoPrint | [169] |
| PTC | Creo CAM | [173] | Ultimaker | Cura | |
| Open Mind Technologies AG | hyperMILL | [174] | Corey Daniels | Slic3er | |
| <i>.STL files</i> | | | Raise3D | ideaMaker | |
| Autodesk | Meshmixer | [168] | CBD- Tech | ChiTuBox | |
| Blender | Blender | | Mango SAS | Lychee Slicer | |
| CNR | MeshLab | | Grid.Space | Kiri.Moto | |
| Slash | Slash | | MatterHackers Inc | MatterControl 2.0 | |
| Stéphane GINIER | SculptiGL | | G-Code Analyzer | G-Code Analyzer | |
| Digital Ocean-Jürgen Riegel | FreeCAD | | Autodesk | Fusion 360 | |
| | | | Digital Ocean | FreeCAD | |

Table 5 The extrusion-based AM complex geometry composites

| | | Extrusion-based method | | | | | | | |
|----------------------|--|--|---------------------------------------|---|---|-------|--|--|--|
| | | Fibers reinforcer | Added % | Geometry | Properties and applications studied | Refs. | | | |
| PLA | | Wood fibers | 10 wt. % | Hexagonal honeycomb-Isomixed cell | Improvements in mechanical performance | [175] | | | |
| ABS, PLA | | Graphene | 5–25% | Sierpinski tetrahedron | Antennas for wide band multifrequency | [108] | | | |
| PLA | | Colorfabb® bronze-fill, graphene, and carbon black | Information reserved by the fabricant | One-step printed device | Electronic circuits | [176] | | | |
| ABS | | TW-CON175BK® carbon-loaded material | Information reserved by the fabricant | Period p | Absorptivity more than 90% in 3.9–12 GHz band | [177] | | | |
| PLA | | Kevlar R | NA | Spline corrugated core | Compressive strength | [101] | | | |
| semi-crystalline PLA | | 300B–3000–40B carbon fiber bundles | NA | Honeycomb | Compressive strength | [185] | | | |
| PLA | | Iron (Protopasta) | (45%) ~ | Venus flytrap inspired architecture | Shape memory structure | [186] | | | |
| PLA | | RGO | 6 wt. % | Monolayer structure with tetragonal lines | 2D flexible circuits (600 S/cm) | [187] | | | |
| PCL | | HA | Ratio 6:4 powders | Kagome structure | Bio-scaffold | [188] | | | |
| PCL | | nHA | 3, 5 & 10% | Kagome structure | Bio-scaffold | [189] | | | |
| PCL | | nHA-Zinc oxide coating | 10 wt. % | Kagome structure | Bio-scaffold | [190] | | | |

(continued)

Table 5 (continued)

| | | Extrusion-based method | | | | | Refs. |
|-----------------------|--|---------------------------------------|---|--|--|--|-------|
| | Fibers reinforcer | Added % | Geometry | Properties and applications studied | | | |
| PP | Petlite | 30 vol % | Honeycomb | 300% improvement of Young's modulus in comparison of unreinforcement material | | | [191] |
| Polyamide 6-I (PA6-I) | Carbon fiber | 20% V_f | High curvature paths | Stress concentration by changing the geometry | | | [192] |
| PLA | Yarns of carbon fiber and polyamide 12 | > 50% | Chiral pyramidal lattice unit cell | Evaluation of continuous lattice fabrication process to produce high stiffness-light density cores | | | [103] |
| PLA | Flax fiber | ~ | Curved geometry composite | Improvement in compressive of composite printed in 5-axis 3d printer until 522% | | | [193] |
| PLA | Flax fiber | Range between 10.6–36.7 wt. % | Curved composites | Tensile and bending mechanical properties. Alternative natural reinforced materials | | | [194] |
| PLA | Carbon fiber | Four V_f ranging 42.15–51.92% | Tetrahedron, Kagome, Pyramidal, Octet-truss, circular grid, integral wing | Evaluate a free-hanging printing method | | | [195] |
| Polyester | Electrifi® Cupper | Information reserved by the fabricant | 3D HD | Microwave metamaterial permittivity ≈ 14.4 | | | [180] |
| PLA | Black Magic® Graphene | Information reserved by the fabricant | Microstrip antenna | Microwave antennas | | | [181] |
| PLA; PETG | Copper wire, CNT | Information reserved by the fabricant | Ball and socket | Synovial joint | | | [105] |

(continued)

Table 5 (continued)

| | | Extrusion-based method | | | | |
|---|----------------------------------|---------------------------------------|---|--|-------|--|
| | Fibers reinforcer | Added % | Geometry | Properties and applications studied | Refs. | |
| ABS | Microdiamonds | 37.5, 60 wt. % | Honeycomb, columnar arrangement, wing heat sinks | High-pressure, and high-temperature process Improvement $\approx 41.9\%$ in the elastic modulus of composite | [196] | |
| EPON Resin 862 | GNP-MCF | 7.6 wt. % MCF, 9.3 wt. t% GraNP | Heat sink | Thermal conductivity of $2 \text{ W m}^{-1} \text{ K}^{-1}$; modulus of 3000 MPa | [182] | |
| polylactide-co-glycolide (85:15) | Graphene | 60, 40, 20% Vol | “Macro” graphene; “Macro”-tube | Organ engineering | [197] | |
| Polypropilene | Microfibrillated cellulose | 20, 30, 40 wt. % | Transitibial prosthesis | At 30 wt. % of reinforcement, Young's modulus was twice than the matrix | [49] | |
| PLA | Carbon black | 25 wt. % | Holey geometry | Microwave shielding applications | [198] | |
| PLA-Black PLA | Proto pasta | Information reserved by the fabricant | A hexagon-shaped robotic claw, finger-like actuator and snake | Actuators based on shape memory materials | [122] | |
| PLA; PLA-Nylon; PLA-TPU | Dual-material cellular structure | ~ | Honeycomb Re-entrant Anti-tetrachiral | Improvements in the yield point of all dualmaterials. Until 452% in the case of the anti-tetrachiral and about 838% for honeycomb structures | [112] | |
| VeroWhitePlus®, TangoBlackPlus® Connex350 | Dual-material cellular structure | ~ | Dual-material auxetic metamaterial | They report an independent of the equivalent Young modulus | [141] | |
| PLA-TPU | Dual-material cellular structure | ~ | Nacre-like design Voronoi cells | Flexion test to know absorption energy capabilities | [84] | |

(continued)

Table 5 (continued)

| | | Extrusion-based method | | | | | | |
|---------------------------------------|--|---|---|---|--|-------|--|--|
| | | Fibers reinforcer | Added % | Geometry | Properties and applications studied | Refs. | | |
| PLA-TPU | | Dual-material cellular structure | ~ | Nacre-like design Voronoi cells | Drop weight impact improvements in comparison of monolithic structure | [179] | | |
| ABS-PLA ABS-TPU | | Dual-material cellular structure | ~ | Nacre-like design Voronoi cells | Transverse and dynamic loadings in finite element vs. experimental studies | [184] | | |
| VeroWhitePlus® and TangoBlackPlus® | | Dual-material cellular structure | ~ | Voronoi cells | Biomimetics composites | [199] | | |
| polyglycolic acid (PLGA) | | β -tricalcium phosphate (β -TCP) | 1 vol % | cartilage-bone layer | Bone scaffolds | [200] | | |
| LCE-PCL-Irgacure 819-acrilates | | Fumed SiO ₂ | 5 wt. % | Active hinge, closing box, gripper, hand for sign language | Soft robots | [201] | | |
| Poly-urethane acrylate (PUA) | | Fumed silica | 2–8 wt. % | Cuboids | Soft robots | [202] | | |
| Silres MK | | CaCO ₃ -AP40 glass | 80:20; 40:60 | Cylindrical and cubic porous scaffold | Porous scaffolds | [203] | | |
| Acrylamide | | Nanofibrillated cellulose-nanoclay | 0.8 wt % of cellulose and 10 wt. % nanoclay | <i>Erodium awn and Bauhinia seed pod</i> | Shape-morphing systems | [85] | | |
| Gelatin/Glycerol | | HA | 70 wt. % | A cross-sectional bone-like and other structures build by arranged cylindrical struts | Biomimetic composite scaffold | [204] | | |
| PCL | | HA-MWCNTs | 0–10 wt. % | High porous reticulated matrix | Porous scaffolds | [205] | | |
| PLA | | Fe ₃ O ₄ | 10, 15, 20 wt. % | Like-bone tissue shape | Magnetic shape recovery | [206] | | |
| Polyamide | | Aramid fibers | Continuous filament | Hinges | Flexural hinges for origami inspired structures | [207] | | |

(continued)

Table 5 (continued)

| | | Extrusion-based method | | | | | Refs. |
|--|---------------------------------------|--|---|---|--|-------|-------|
| | Fibers reinforcer | Added % | Geometry | Properties and applications studied | | | |
| Polyethylene terephthalate glycol (PETG) | Carbonyl iron particles | 15:85 relation | Gradient honeycomb | Electromagnetic shield | | [116] | |
| PA 12 | MWCNTs-Fe ₃ O ₄ | The blend was sprayed with relations 1:100 ml in distilled water and 5 wt.% for Fe ₃ O ₄ | 3D gradient honeycomb | Electromagnetic shield | | [208] | |
| Poly(NIPAM-4PBA) solution | 40% oxidized CNF | 7 wt. % | Honeycomb | Vascular like-channels | | [209] | |
| PLA | Carbon fiber | Continuous fiber | ψ-n-h configurations | Shape recovery composites | | [185] | |
| PLA | Kevlar R fiber | Continuous fiber | Auxetic honeycomb | Low-cost rapid manufacturing composites | | [111] | |
| FLX9860-Verowhite® | ~ | ~ | Square and triangular arrangements | Transformative composites | | [210] | |
| PLA | Keratin | 0.5, 0.75, and 1 wt. % | Re-entrant auxetic and honeycomb cells | Sound absorption | | [7] | |
| Nylon polymer | Short carbon fiber | 15 vol. % | Rotating squares, auxetic perforated structures | Lightweight auxetic structures | | [110] | |

tensile strength. However, toughness and the fracture strain were low regarding the honeycomb structures. The shortcomings in the AM process explained the diminishing impact properties and differences in the experimental-simulated properties. First, honeycomb printed composites showed higher values on the elastic modulus than the simulated samples. This result corresponds to the reduced stress concentration for the printed specimens due to the filleted corners, which are sharpened in simulation. Second, in the Isomixed composites, the printer's resolution was too low, causing deviation in the cell wall size. In contrast, Clower et al. [108] the successful generation of higher-order complex pre-fractal structures. In this case, the precision of the 3D printer for the X and Y-axis was ≈ 12.5 , Z-axis ≈ 0.4 all in μm . For a layer around 20–400 μm . The system applied exhibits a good layer resolution able to print the 3rd-order Sierpinsky tetrahedrons antennas.

Flowers et al. [176] reported modifying a 3D printer to build a printed high-pass filter LC circuit. The changes in the printer allowed the one-step fabrication device with individually printed materials components. This goal was reached by adapting a retractile mechanism (Dglass3D's Autolift retractable hot ends). The bushings integrated into this mechanism produce a retraction of nozzles if the filament is not extruded. There are some reports about using a commercial 3D printer with dual nozzles (Ultimaker) to fabricate nacre-like laminated composites [84, 179, 184]. The dual nozzles allow precise fabrication of complex geometries with Voronoi cell arrangement. The authors mentioned a preliminary trial-and-error study to get the suitable extrusion and nozzle parameters. They determine 0.4 mm of nozzle diameter and temperatures of 210 and 222°C for the PLA and TPU. Hence, quality production and adhesion obtained were proper. Moreover, each polymer's printing speed was 20 and 10 mm/s for PLA and TPU to balance the process's quality and efficiency. Other reports about multi-materials through modifications in the nozzle of the 3D printer had been reported for auxetic structures [112, 141] and others applications [122] of dual materials. Auxetic means that an auxetic cellular material behaves to a tensile load stretching in the transverse direction, which points to a negative Poisson coefficient [141].

Jonhston and Kazancı report about the shortcomings that originated in the dual FFF method [112]. They published some critical points related to the dual FFF. The first one is the adhesion between materials. This issue can solve by the loading parallel to the layers. Moreover, the dual FFF only allows printing one material at a time. Hence, poor interlocking among polymers triggers and promotes a failure. One solution was founded overlapping materials increase the union area in the polymeric components. Also, the warping and enclosure of the printed structures can diminish the air flow and keep the printing bed close to the polymers' glass transition temperature. The alternating use of nozzles in dual FFF generates strings because of the start and stop steps during the printing. To prevent the residual string formation, a slow retraction of the material solves the problem. Also, one nozzle's reactivation needs to create a small sacrificial structure, as the authors mentioned.

Fidan et al. [70] reviewed one of the most important aspects in complex geometries composites fabrication and FRAM. This key topic involves the flexibility of AM and the advantages of composite materials [70, 211, 212]. Fibers most utilized in

FRAM are short, continuous, and powder-based (latter can include nanomaterials). Goh et al. [213] mentioned that in short fiber, there is no necessary modification on FFF printer, also in continuous fiber, a small modification is required, even commercial options are available. Their relatively easy manipulation and prices short fibers have been used widely in additive manufacturing composites [13, 66–70, 211]. The FRAM composites with short fibers have captured the attention due to advantages like simplicity, customizability, and low cost [212]. In other words, the filament which contains the fibers can be customizable in the % of fiber content, fiber size, fiber distribution, and path design (Fig. 8a) [211, 214, 215]. Therefore, the flexibility in design and the capability of print complex 3D pieces open the possibilities to the universe of applications (Fig. 8c) [215].

New possibilities have emerged as a result of innovation in 3D printers, like the continuous fiber-reinforced composites [101, 111, 165, 185, 216]. In this FFF variation, printers use two nozzles to deposit polymer and fiber in each one (Fig. 9b) [215]. Mohammadzadeh and Fidan recently reported an increment until 2200% in the tensile strength of continuous FRAM composites [217]. This work extruded carbon, glass, Kevlar continuous fibers, and nylon matrix by Markforged printer. The mechanical tests showed that composites reinforced at 60% fiber had higher tensile strength than Aluminum 6061. Also, Mohammadzadeh and Fidan [218] reported the thermomechanical properties for continuous FRAM composites based on glass and carbon fibers in other research. In this approach, the storage modulus obtained in carbon fiber-reinforced composites was 64 times higher than the nylon matrix. Also, thermal conductivity and thermal capacity were improved, suggesting the potential in continuous FRAM composites in engineering applications.

Another example of complex geometries developed are corrugated structures [101]. In this research, an AM module is supported by a hybrid 3d printer and a 6-degree robotic freedom arm (MITSUBISHI RV-7F-1Q-S11). This assembly allows the synthesis of continuous fiber-reinforced lightweight composite structures (CFRCLSs). The panel-core structure was extruded in a single process. In other words, the panel is composed of a carbon-fiber structure that is heated and fused while the nozzle builds the core. Hence, when the extrusion of the wire is done, the panel is adhered to and solidified. In this study, the thickness and length of the unit cell were the critical parameters evaluated. The results evidence that the modulus and strength in compressive conditions were maximum at a layer thickness of 0.1 mm. When the layer thickness rises (0.3–0.5 mm), the response to compression decreases slightly. As the authors reported, the versatility of this additive manufacturing variation produced corrugated structures and heterogeneous lightweight sandwiches.

Zeng et al. [219] used a similar protocol to previous researches [111, 185] to obtain continuous fiber-reinforced composite honeycomb structures (CFRCHSs). These composites with shape recovery capacity were fabricated focus to develop new lightweight, intelligent systems in absorbing energy applications. The co-extrusion (two nozzles) process consists of feed continuously by two channels (fiber and polymer) converging in the extrusion head. Hence, the PLA and fiber are forced to pass through a high-temperature zone where the impregnation fiber succeeds.

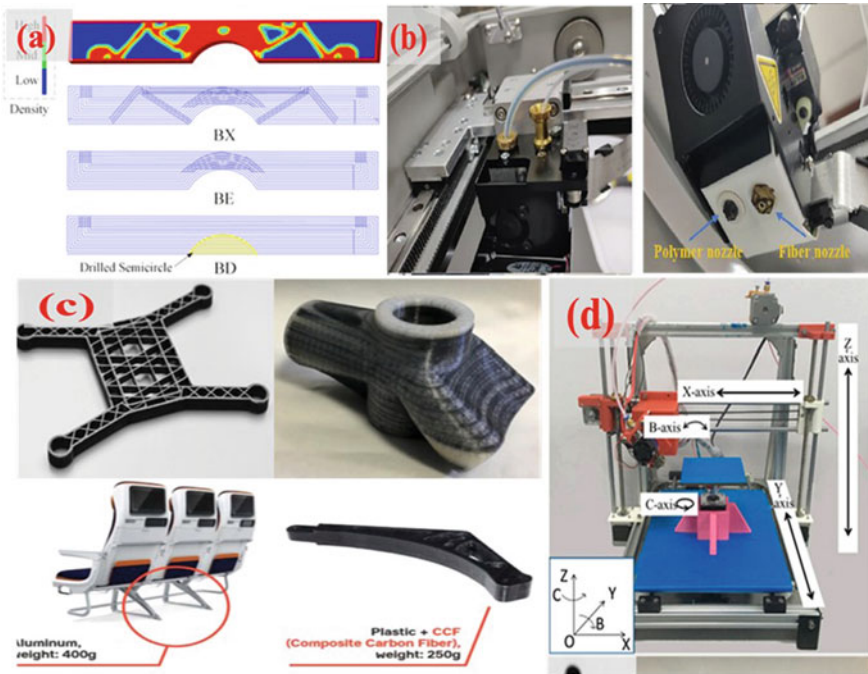


Fig. 9 **a** Analysis of load distribution and printing path in continuous fiber composite Reprinted from Li et al. [214]. Copyright (2020), with permission from Elsevier. **b** Upper and down views of Markforged nozzles for continuous FRAM composite, Reprinted from Prajapati et al. [215]. Copyright (2021), with permission from Elsevier. **c** Five-axis printer. Adapted from. Zhang et al. [194] under the terms of the Creative Commons CC By 4.0. license <https://creativecommons.org/licenses/by/4.0/>. **d** Applications of continuous fiber composites: Unmanned Aerial Vehicles (UAV) frame (left), bicycle lug (right), and aircraft seat printed support weight comparison metal and continuous fiber composite components. Reprinted from Zhuo et al. [216]. Copyright (2021), with permission from Elsevier

Then, applying tension in the fiber, both polymer and fiber are deposited. The mechanism reported does not involve a cut system. Consequently, printing paths need to be designed.

Other works reported manipulating printing parameters such as fiber orientation and printing speed [9, 103, 192–195, 220]. Moreover, the addition of two axes to the 3D cartesian printer allowed the rotation of the Y and Z-axis (Fig. 9d) [193, 194]. As the authors described, the added axis allows 0–180° rotation for the B-axis (rotation around Y-axis) and 360° completely free rotation for the C-axis (rotation around Z-axis). The continuous flax fibers reinforced composites (CFFRP) evidenced better mechanical performance than the unreinforced polymers and the upright and flat built orientation specimens [194].

Another important aspect of 3D printed composites is manipulating the final properties by tuning the printing parameters or using the residual stresses during the printing process [68]. Riley et al. [186] reported a shape memory recovery 3D printed

composite inspired in biological structure. The Venus flytrap-like composite with switchable multistability. The structure obtains its properties from the hierarchical effects at different length scales and shape memory recovery effect. Multistability refers to that the material has two or more states with the lowest strain energy. Shape memory materials (SMM) are generally built by complex geometry components, subject to high deformation. For that reason, some manufacturing methods have been developed to front these demands [221, 222]. Unfortunately, one of their biggest obstacles is the necessity of specific features in the equipment. In this shortcoming, additive manufacturing allows the synthesis of complex geometries and encodes multiple shapes in a structure. The glass transition temperature (T_g) acts as a key parameter to change the temporaries' shapes in these materials. In other words, the arbitrarily pre-strained polymeric chains in AM can modify the shape while the material is either heated or cooled.

One of the reasons for the success of the FDM AM method is the ability to make modifications. Cho et al. reported the printing of PCL and HA. The earlier report about these bio-scaffolds was about the development of a lab-made 3D printer [223]. The 3D Kagome structure proposed for tissue engineering needs interconnectivity, bio-compatible and bioresorbable materials at a small scale. For this reason, the extrude dispensing mechanism (Fig. 10) was developed to overcome this challenge. The precision extruding deposition (PED) allows the extrusion of high-viscosity materials in the order of $\approx 100 \mu\text{m}$ without pos-processing [188–190, 223]. Moreover, 3D Kagome cellular structures' strength and stiffness surpass the obtained by conventional methods like gas-foaming or phase-separation [223]. The printer (Fig. 3c) is conformed by a barrel, cartridge body, heating block, motor, screw, nozzle, gear set, and fans. Briefly, the PCL pellets melt at 80°C in the barrel. After the viscous blend is screwed at 70 rpm and $\approx 360 \text{ kPa}$ of air pressure flowing through a $\approx 50 \mu\text{m}$ nozzle diameter to build 3D Kagome cells. This system allows printing PCL-HA (HA size $\approx 50 \mu\text{m}$) [223], PCL-nHA (nHA size $< 200 \text{ nm}$) [188], and PCL-nHA with Zinc oxide coating [190].

The FDM composite printing process involves forcing a polymer-reinforcement blend (filament or powder) through an extruder barrel by a screw. This kind of material processing produces high shear stress. Hence, the stresses originated favors the dispersion of the reinforcements in composites [187, 191, 224]. Zhang et al. [187] reported the synthesis of 3D printed flexible circuits. In this work, the PLA and graphene were extruded two times. The first extrusion process was during the filament obtention. The second extrusion or flexible circuit fabrication consists of the process carried out in the 3D printer with the PLA-graphene filament. As the SEM micrographs of printed composites confirm, the graphene sheets reflect a lamellar arrangement. Hence the directional orientation of carbon sheets provides the improved electrical behavior in the nanocomposite. The extrusion process has been used to overcome some problems about particle dispersion.

Waheed et al. [196] coincide with other authors [187] about better features are obtained in the final 3D printed structure due to the better distribution. They printed Acrylonitrile Butadiene Styrene (ABS)-microdiamonds with a high-pressure and high-temperature system. The filament used was previously extruded six times in

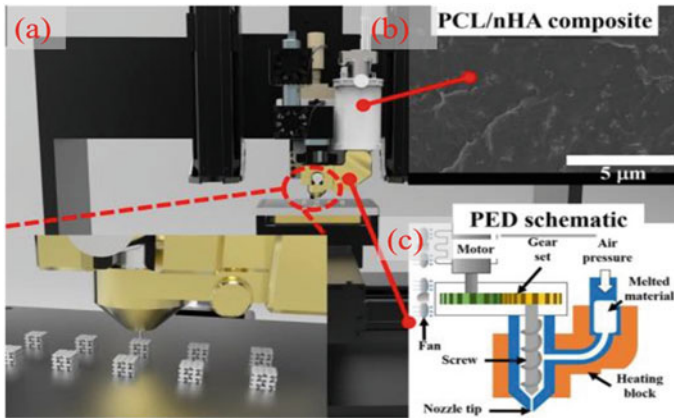


Fig. 10 **a** The single screw 3D-printer is coupled to the PED system. **b** scanning electron microscopy (SEM) image of printed bio-scaffold. **c** Schematic diagram of PED system. Adapted from Cho et al. [190] under the terms of the Creative Commons CC By 4.0. license <https://creativecommons.org/licenses/by/4.0/>

a filament extruder to decrease the filament's porosity. As the extrusion steps were carried out, the filament reflected a smooth appearance and was more compact than the incipient extrusion process. A couple of Titanium (Ti) gears designed by this research group provide the feed-retraction system in the 3D printer avoiding abrasion issues. The gears mechanism pushes the filament through six heaters coupled to melt the filament. Then the melted polymer is deposited by the nozzle to print heat dissipation complex structures.

6 Direct Ink Writing

The ink writing consists of the object's fabrication, such as high-complex composites, deposited from the nozzle over the power bed. Unlike conventional lithography or laser-based polymerization, the use of this variation of FDM offers the possibility of printing a broad range of materials [225]. The structured shape follows a CAD model, which generally is sliced to insert a G-code archive in the printed [183, 205].

In direct ink writing (DIW), the dispersion method of reinforcement considerably impacts the rheological behavior of inks. As some authors mentioned [226, 227], the shear thinning, yield strength, and storage modulus are the typical parameters that define an ink's printability. Chen et al. [226] reported mechanical properties in a TPU-silica nanoparticles reinforced composite. Tuning the pores in microscale and macroscale allowed changes in the density. The macroscale pores refer to the space assigned by the computer design. The microscale pores are those formed in the post-processing of composite. Two microscale pores were assigned a large-pore if the size is more than 20 μm and a small-pore under 5 μm. The adjustment in

the density by the hierarchical-porous structures reflects changes in the composites' mechanical behavior.

Highley et al. [228] reported the modification of a commercial 3D printer (X-truder, Quintessential Universal Building Device) mounting a syringe on a 3D printer. The modifications consist of coupling a worm gear to a lead screw to push the plunger in the syringe. Then, the G-code file obtained from the CAD model was used to guide the ink's printing patterns. Other authors reported the homemade modifications on the AM system to obtain a multichannel ink printing deposition [229, 230]. The multi-head deposition system (MHDS), as authors called [229], dispensed in temperature of barrel and syringe controlled. Moreover, each printing head's pressure and deposition speed were controlled by software developed by the research group. These customizations in the printer allowed the simultaneous deposition until four different inks (Fig. 11).

Another interesting modification to the printer in the DIW is the use of permanent magnets (20 mT). In this context, Tognato et al. [123] added iron oxide nanoparticles (ION) to the liquid hydrogel precursor. After, the self-assembly of ION was carried by the magnetic field applied at low intensity. Then, the stabilization of metallic nanoparticles happens as the temperature decreases. Finally, the crosslinking was accomplished by the exposition of ultraviolet (UV)-light of composite. The characterization of the printed structures revealed the formation of filaments with particles. As the authors mentioned, nanoparticles' concentration and the distance between

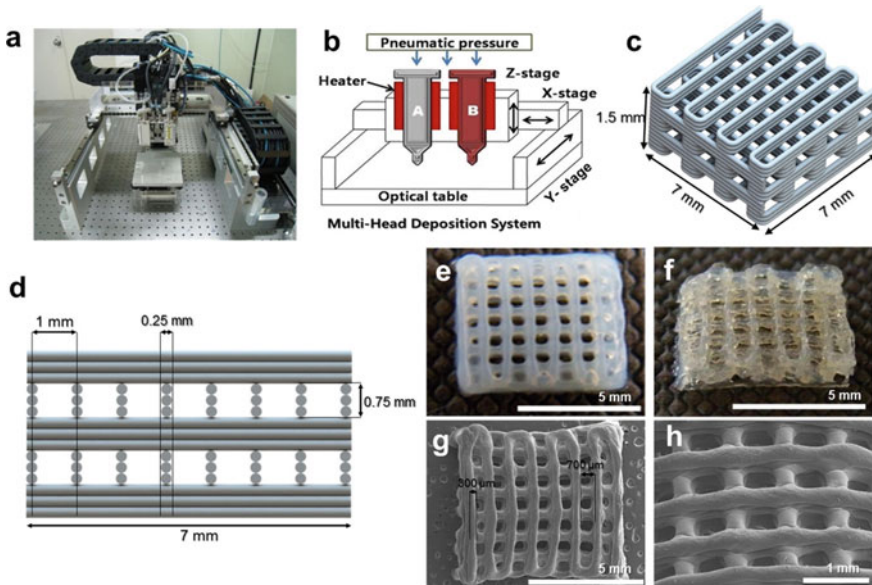


Fig. 11 a-b MHDS printer c-d Schematic diagram of DIW printed scaffolds and their dimensions. e-h Photography and SEM images of silk-gelatin constructs. Reprinted from Das et al. [229]. Copyright (2015), with permission from Elsevier

magnets influence the formation of the nanoparticulated filaments and spacing among them. Hence, the function of the physical barrier to align cells will change.

The use of DIW is useful in fabricating complex geometry scaffolds with high resolution and shape based on the anatomical specifications of patients [203, 205]. In combination with the possibility of the high-porosity, bioactivity, and stable mechanical structures acquired by AM, new specific designs have been developed. For instance, HA, (Multiwalled Carbon Nanotubes) MWNTs, and wollastonite (CaSiO_3) were used as reinforcement to prepare ink composites to build bio-scaffolds. In the case of HA and MWNTs as reinforcements of PCL (using a commercial printer, GmbH envision TEC 3-D), evidence well dispersion. As the authors mentioned, the dispersion observed in the SEM suggests a bonding among HA, MWNTs, and the PCL matrix [205].

The necessity of medical devices to change the shape, such as soft robotics, requires the development of new materials and modifying the manufacturing form. In the case of 4D applications, the AM has allowed the deposition of multiple materials. These printed structures have a complex geometry and the ability to change them by external stimuli. Roach et al. [201] reported the fabrication of 4D printed structures. They use the DIW method to print liquid crystal elastomer ink (LCE, based on (1,4-Bis-[4-(3-acryloyloxypropyloxy)benzoyloxy]-2-methylbenzene), RM27) at room temperature, conductive ink, and glassy polymer. Moreover, the pressure nozzle and speed printing were evaluated for their impact on the actuation characteristics. In this research, the photocuring process carried out immediately after the deposition was the key to retaining the shape and alignment in the LCE. In other words, the alignment of LCE mesogens created by shear forces in the DIW process was fixed by photopolymerization.

Another topic where DIW has impacted is biomimetic materials. The dynamic architectures obtained by DIW allow the imitation of natural motions like what happens in plants. For example, Gladman et al. [85] developed a 4D structure with shape changes when immersed in water. The composite architecture based on acrylamide and nanofibrils of cellulose produced a biocompatible hydrogel. As the authors mentioned, tuning parameters like filament size, orientation, and inter-filing spacing of composite ink could create complex architectures. For example, the *Dendrobium helix* and *Zantedeschia aethiopica* inspired biomimetic composites [85].

6.1 VAT Polymerization

VAT polymerization is a process to cure photo-sensitive polymer using a specific light source [231, 232]. This method has three main derivative curing methods. Stereolithography (SLA), digital light processing (DLP), and continuous digital light processing/continuous liquid light processing (CDLP/CLIP) [233]. In Table 6, there are some complex geometry composites obtained by VAT AM.

Table 6 VAT AM method for complex geometry composites

| SLA Matrix | Fibers, reinforcer | Added % | Geometry | Properties and applications studied | Refs. |
|--|---|------------------------------|---------------------------------------|--|-------|
| Pic 100 from EnvisionTEC | Single-layer GO | 0.2, 0.6% with two cure time | Triangular honeycomb | Improvements in the tensile strength until 62.2% | [234] |
| PEGDA | PEDOT:PSS | 5, 10, 15, 25, 35, 45 wt. % | Double helical structure | Conductive polymers | [102] |
| PEGDA- diphenyl (2,4,6-trimethylbenzoyl) phosphine oxide (TPO) | Prednisolone, Chloramphenicol, Caffeine, Paracetamol, Aspirin, Naproxen | 10% w/w | Ring shape poly pill | Drug deliver | [235] |
| Grey resin Formlabs® | GNP | 0.01–0.1 wt. % | Ocet-truss lattices | Mechanical and thermal improvements | [236] |
| PEGDA | GO | 0.3, 0.5 phr | Honeycomb, alveolar | Mechanical and electrical improvements | [237] |
| PSP resin (FLGPCL02) | BNNP | 0.5, 1.0% | Scaffolds with a gradient of porosity | Load bearing applications | [238] |
| 3,4-Epoxy cyclohexylmethyl-3,4-epoxy cyclohexane carboxylate | Quaternary ammonium modified HA | 2.5, 5, 10 wt. % | Dental bite prototype | Antimicrobial activity | [239] |
| DLP | | | | | |
| PEGDA | 2,4,6-trimethylbenzoyl 0.66 wt% Iracure 819, and 0.11 wt% | – | 2D thin films | Four different deformation modes, cylinder, spiral, bow-tie, cigar | [240] |

(continued)

Table 6 (continued)

| SLA | Matrix | Fibers, reinforcer | Added % | Geometry | Properties and applications studied | Refs. |
|-----|--|---|--|--|---|-------|
| | Polysilazane PCP | MWCNTs | 0.3 wt. % | Truss structures, honeycomb, and cubic 3D arrays | Ultra-light, high-strength and microwave absorbing properties | [86] |
| | Gelatin-methacryloyl (GelMA) | poly(ethylene glycol)-poly(3-caprolactone)(MPEG-PCL) nanoparticles loaded with XMU-MP-1 | 1% of Lithium phenyl-2,4,6-trimethyl-benzoylphosphinate with XMU-MP-1 (100 μ g/mL) | Flexible cylindrical shape with various wall thickness | 3D printed drug releasable conduit | [241] |
| | Ar3d-dlp405, TMTCTW acrylic based photocurable resin | MWCNTs | 0.3 wt. % | Hang structure spring, planar wave resistor, hollow structure truss, multi-materials arrays | Printed electronic devices | [242] |
| | DLP elastomer based on acrylates DLP plastic DIW-photocurable ink DIW liquid crystal elastomer DIW conductive silver ink | | Cylindrical lattice with 3 DIW primed rings embedded, single and multiple flower actuator crawler, and bi-stable lattice | DIW and DLP hybrid soft robots | | [104] |
| | FSL-C, and FSL-RED commercial resins, butyl acrylate, methyl acrylate, Jeffamine D-230, epoxy 44 Irgacure 819, isobornyl acrylate, dimethylamine, lauryl acrylate, vinyl pyrrolidone Ca-In-Sn liquid metal alloy | | Beam array, Kelvin lattice | Electronic devices | | [232] |
| | Polysilazane PCP Acrylic based formlabs resin | | Ceramic cuboid, honeycomb, and lattice | Mechanical and corrosion resistance | | [243] |
| | PEGDA | | Pt and iron oxide (Fe ₃ O ₄) | 8 \times 10 ⁸ and 4 \times 10 ⁸ mg mL ⁻¹ for Pt; 5 mg mL ⁻¹ for Fe ₃ O ₄ self-propelled microfish | Biorobotics with propulsion | [120] |

(continued)

Table 6 (continued)

| SLA | Matrix | Fibers, reinforcer | Added % | Geometry | Properties and applications studied | Refs. |
|-----|--|--------------------|---|---|--|-------|
| | Acrylic acid and PEGDA | | PTO ₂ -WO ₃ | Solution 36.37% w/w and 0.34% w/w Honeycomb | Kit-catalyst with structural complexity | [244] |
| | Acrylic acid and PEGDA | | Pt, Rh, and Pd | 0.46, 0.5, 0.5 wt. % Printed intricate tube with Pt, Rh, and Pd | Kit-catalyst with structural complexity | [244] |
| | Aliphatic acrylate-aliphatic urethane diacrylate | | trimethyl benzoyl diphenyl phosphine oxide-silver nanoparticles | 2 wt. %-solvent with 16.5% Soft actuators, conductive bucky balls | Soft and deformable structures | [124] |
| | Glycidyl methacrylate | | <i>B. mori</i> Cocoons silk | 10-30 w/v | Tissue engineering | [90] |
| | Silicone-urethane resin | | Ag particles | ~ | HASEL actuators Tentacle electrohydraulic structures | [245] |

6.1.1 Stereolithography

Stereolithography (SLA) is one of the most known methods of additive manufacturing. This rapid prototyping method consists principally in the obtention of 3D objects by photopolymerization [239]. In SLA, the chemical-physical process transforms the liquid monomer into a solid piece based on a CAD model [1]. The SLA allows obtaining exotic rigid metamaterials with high mechanical properties at low density [246]. However, the number of parameters involved in this method is at least 50, as was mentioned somewhere else [1].

Recently, Scordo et al. [102] reported the SLA synthesizing a double helix structure with mechanical and electrical conductivity. In this research, a 405 nm wavelength laser cured the layers deposited from top to bottom of CAD design. The polymer matrix was the photocurable poly(ethylene glycol) diacrylate (PEGDA) for this composite. The disperse phase was poly(3,4-ethylene dioxythiophene)-poly(styrene sulfonate) (PEDOT:PSS). Briefly, the process starts dissolving the radical photoinitiator (bis(2,4,6-trimethyl benzoyl) Phenylphosphineoxide, Irgacure 819) in the PEGDA by ultrasonic waves at 30 kHz. After the PEDOT:PSS and PEGDA and dimethyl sulfoxide (DMSO) were magnetic stirred at 600 rpm for 15 min. The concentrations vary from 5 wt. % until 45 wt. %. Despite the high load of PEDOT:PSS (45 wt. %), the photocurable feature of the matrix is not affected. However, a slight decrease in the PEGDA conversion was obtained. In addition, the authors highlighted the importance of the post-curing process, where the conversion reached more than 80%.

Generally, the SLA builds the piece in a top-bottom direction [102]. However, the variation in the process called mask projection stereolithography (MPLS) offers a bottom-up direction [234]. The MPLS project the light source through a pattern instead of concentrating it in a dot as in the vector scanning process. In a nutshell, the 3D model of an item is sectioned into 2D planes [247]. Each plane is converted into a mask image which is projected through the resin. Then, the final shape adopted in the polymer corresponds to the stacked mask images projected from the bottom of the polymer tank. This SLA variation offers advantages such as better surface quality and vertical resolution, a reduction in the amount of polymer and reinforcement, and, consequently, less contamination and material waste minimization. In addition, the process allows a coating process with minimum steps, which positively impacts the time fabrication consumption. Lin et al. [234] reported the synthesis of single-layer GO-reinforced composite by the MPLS technique. The printed nanocomposites were built with an arrangement of triangular honeycomb. The mechanical performance of GO-reinforced structures under compression reveals a shear slip plane like in crystalline metals.

Like the FDM, the SLA allows the printing of complex geometries with different materials. In the case of Robles-Martinez et al. [235] printed a multi-material pill by SLA. The idea focused on the production of personalized drugs was accomplished by the modification of the SLA printer. The authors identified three crucial steps to carry out to get the goal. These steps pause the printing process, raising and replacing the resin with different drug dissolution. However, the printer count with a

pause step, resin's interchange was not possible because the platform was kept in the pause position. The redesign of the software and some hand-made modifications in the printer allow building the customized multi-drug pills quickly. As Fig. 12 shows, the polypill is a compact multidiameter cylinder. Despite the ring, the shape does not represent a highly complex geometry like some others mentioned. The printing process's work opens the door to adjust these shapes to each patient's particular needs or other areas requiring multi-materials.

Markandan and Lai [236] and Chiappone et al. [237] reported the SLA complex-geometry nanocomposites reinforced with 2D carbon nanomaterials. In both cases, the dispersion of reinforcement was a challenge during the synthesis. On the one hand, ultrasonic waves dispersed the GO in water to avoid solvents [236]. Then, the simultaneous addition of two photoinitiators was necessary for the curing process to get both the best curing and the GO reduction. The authors evaluated the combinations using the ultraviolet-visible (UV-vis) spectroscopy technique to know the

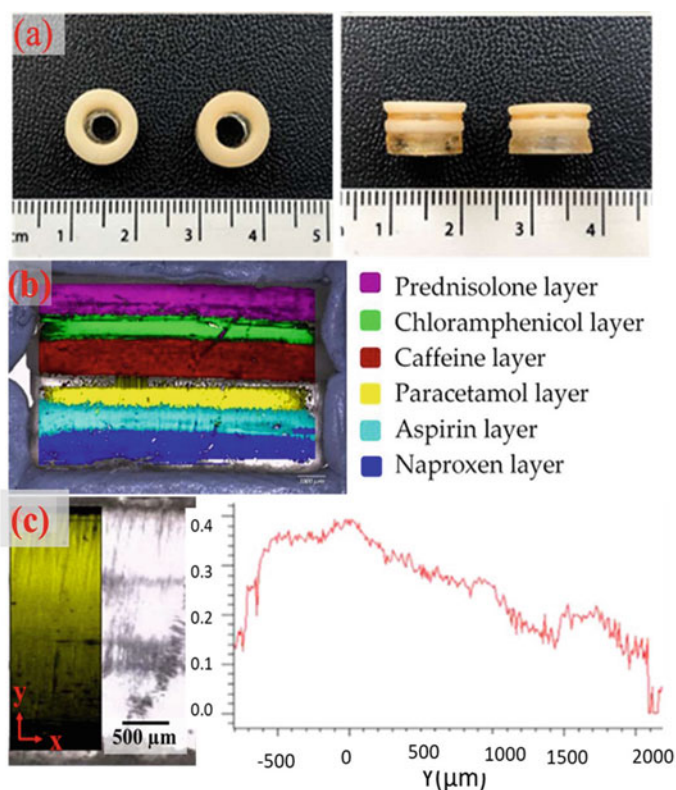


Fig. 12 a Ring shape six drugs polypill. The scale is in cm b Interfaces studied c Raman mapping of polypill showing the partial diffusion of paracetamol into adjacent layers. Adapted, and reprinted from Robles-Martinez et al. [235] under the terms of the Creative Commons CC By 4.0. license <https://creativecommons.org/licenses/by/4.0/>

best concentration in composites. One hour under ultraviolet (UV) radiation or 24 h in thermal treatments produces high absorbance, as the results reveal. As the authors inferred, the absorbance in the composites can reference the degree of reduction in the GO. Also, in the mechanical performance, composites exhibited higher rigidity than neat polymer. Besides, the samples with UV-radiation post-treatment showed the higher elastic modulus as their curves stress-strain evidenced. In contrast to the dispersion of 2D nanostructures with water, acetone in graphene nanoplatelets (GNP) diminishes the mechanical properties, as Markandan and Lai [236] reported. The GNP's dispersion was by ultrasound and acetone during 40 min previously the addition to the polymer. Then the GNP-polymer suspension of GNP was put in the oven for 12 h to evaporate the solvent. The nanocomposites printed with this formulation diminish their mechanical properties until 72.4%, in the case of Young's modulus. The authors explained this from the modifications that could happen in the polymeric matrix by the acetone, which negatively influences [248, 249]. The curing kinetics in the modified polymer inhibits the complete crosslinking, as other authors propose [238]. These changes in the reticulation and the remanent acetone (acting as stress concentrators) negatively impact the octet lattice composites [250]. As can be seen for these researchers, the pre- and post-processing in SLA play a vital role in printing composites. Despite the SLA advantages it could offer, these two steps described previously need to be carefully handled to apply AM successfully [251].

In the research of Bustillos et al. [238], observed a reduction in the compressive mechanical capabilities in the composite of BNNP in a photosensitive polymer (PSP). It is mentioned that the large surface area of BNNP originated UV-photons absorption during the printing process, blocking UV-rays. Therefore, a diminish in the crosslinking network in the matrix occurs. The inhomogeneity in the BNNP added system was reflected as low mechanical properties. However, the potential use of the BNNP needs to be improved by the accurate selection of dispersion method and optimum concentration of these nanomaterials.

6.1.2 The Digital Light Processing (DLP)

The Digital Light Processing/Digital Projection Lithography is an additive manufacturing method to polymerize a reactive light monomer using light. Contrasting to SLA (the light is concentrated in a spot), in DLP, the light is projected over a pattern [232, 252]. In other words, each layer is exposed to the projector. However, this method is faster regarding the SLA but is greatly dependent on the projector resolution [233]. Complex structures have been printed by the DLP like truss structures [86], honeycomb cells [86], micropatterns, and others [241].

The DLP has been used to synthesize shape-shifting structures, as Wang et al. [240] mentioned. In this work, 2D structures turn in 3D complex geometry, releasing the internal stresses generated in the printer during frontal photopolymerization (LightCrafter 6000, wavelength 405 nm). The shape-shifting structures were obtained through a grayscale bitmap projected in the resin during the irradiation time. Then, the attenuation effect assists the non-uniform photopolymerization in a combination

of photo absorbers added. After the polymerization, a hand-made removing residual monomer and post-curing under UV-light fixed the deformed shapes.

One of the most critical parameters to control in DLP is viscosity [232, 242, 253]. The higher viscosity after the addition of reinforcement turns into a barrier to some applications. In this context, Mu et al. [242] reported the printing of MWNTs composite with shape memory effect. First, they focused on finding the optimized concentration of MWNTs to get an accurate electrical property to shape memory polymers (SMP) and electrical circuits. The restricted flowability and consequently bubbles formation on the MWNTs-polymer were avoided using three dispersion steps involving ultrasonication and ball mill. The mixtures analysis points as 0.3 wt. % of MWNTs as the adequate concentration to be printed. Then a modified bottom-up DLP printer allowed the interchangeability of resin vats with multiple materials. As some authors mentioned, the use of bottom-up modification enhances this DLP variation's efficiency [114, 242].

Another drawback worth mentioning is the absorption of light by the reinforcement [86, 254]. In carbon materials, the light absorbed by the reinforcement triggers less crosslinking in the matrix network. As a result, there is a competition between CNT and a photoinitiator, which impacts the polymerization of the matrix [254]. This issue can be overcome by adding an excess photoinitiator or increasing the light intensity. Despite the drawbacks in polymeric composites originated for the light absorption of MWNTs, this property gives an advantage when printing ceramic composites. For instance, Xiao et al. [86] mention, the MWNTs can be used as low-reflectance and broadband absorbers to improve the DLP photocurable polysilazane preceramic polymer (PCP). Hence, the electronic properties of MWNTs regarding the plasmon resonance allow either the control of photocuring thickness or improvements in the printing precision.

As it was mentioned, DLP is a versatile method where different materials can be printed. 3D polymer-derived composites (PDC) are ceramic materials which fabrication involves the following steps. The synthesis of organic precursor, printing, and curing of a "green body" (which means a step previous to pyrolysis) and the pyrolysis to obtain the final ceramic structure [86, 136, 144–146, 243, 244, 255]. The use of DLP to fabrication of PDC allows not only the printing of complex geometries but also reaches chemical homogeneity by polymer derived. Moreover, the pyrolysis temperatures needed are relatively low. The fluidity and solubility in polymer-particles used in PDC allowed the preparation of fibers, films, even adhesives, and other forms for diverse applications [255].

Peng et al. [104] reported hybrid processing between DIW and DLP methods (Fig. 13). In this research, the DLP method contributes with a high speed and photocurable resolution matrix. The DIW can print functional materials. Both DIW and DLP make a synergy to realize multi-functional structures and devices in a single process. The hybrid printer consists of a top DLP system and a DIW system. The resolution is 30–100 μm in XY direction in DLP, and for the DIW component, the resolution ranges from 100 to 1540 μm . The main challenge in this system was the printing layer differences. One solution was indicating the DLP layers required to compensate the difference with one printed by DIW.

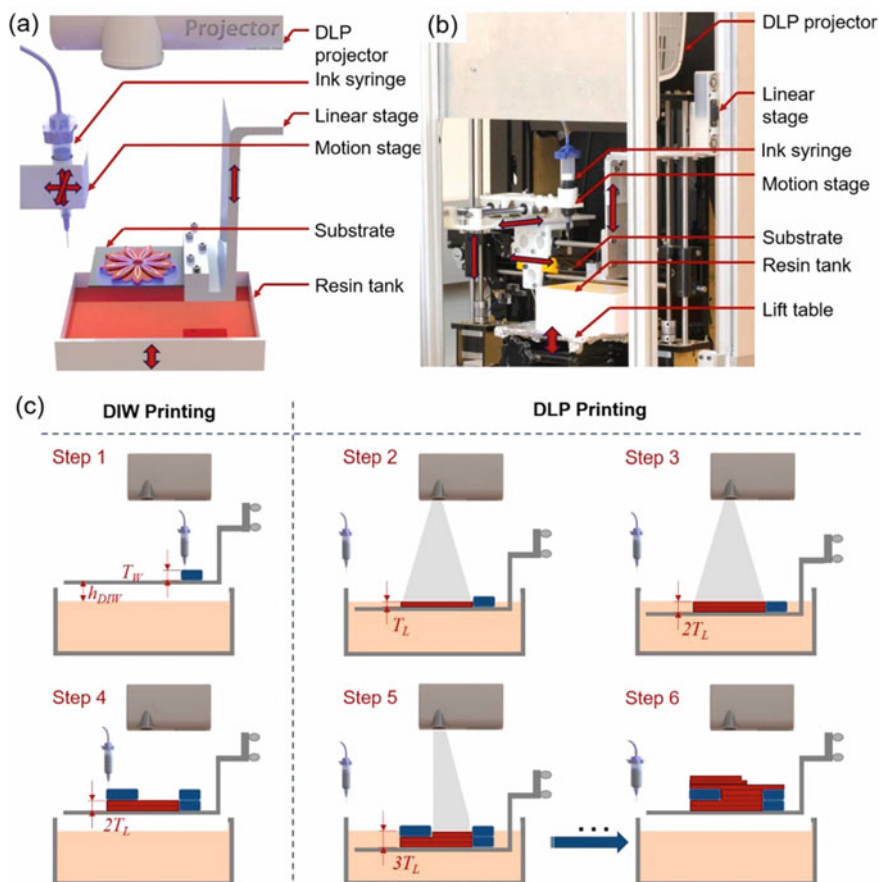


Fig. 13 a Schematic and b photography of hybrid DIW-DLP printer. c Schematic process of hybrid DIW-DLP printing. Reprinted from Peng et al. [104]. Copyright (2021), with permission from Elsevier

Looking for objects with high complex, tailored topology and functionality, the DLP can be an alternative or complementary method to the already exists [124, 144, 145, 148, 244, 255]. For, example the realization of polymer-metal nanoparticles composites. Related to this topic, Fantino et al. [256] reported the printing of silver nitrate (AgNO_3), polyethylene glycol diacrylate (PEGDA), and photoinitiators. The conjunction of monomers, metal salts, and photoinitiators trigger different reactions like the photoreduction of metal. During these reactions, the formation of both inorganic and organic phases provokes silver distribution until nano domains. In other words, the UV-radiation generates conductive silver nanoparticles during the DLP process. The UV-vis measurements evidenced the changes and kinetics during the formation silver nanoparticles. The results evidence an increment in the plasmon

of resonance as radiation time increase too which can be considered as evidence of nucleation and growth of silver nanoparticles.

6.1.3 Continuous Liquid Interface Production

CLIP is a variation on AM based on vat photopolymerization [2, 231]. This technology is based on the digital projection of light-emitting diodes (LEDs) through an oxygen-permeable window [233]. Then, the oxygen concentration in the bottom of the vat disrupts the radical polymerization creating a “dead zone” [2, 231, 232]. The illuminated area can be printed with high resolution and speed, with parts produced in minutes instead of hours.

CLIP is a relatively new technology that allows printing complex geometries such as electrohydraulic tentacles actuators (HASEL). O’Neill et al. [245] reported the fabrication of HASEL structures inspired by muscular hydrostats as elephant trunks or cephalopod tentacles. The muscular hydrostats consist of arrays of muscular fibers with a combination of orientations. These arrays change their forms when one point of the structure is compressed, keeping the volume constant. The authors mentioned that the speed (>100 mmh⁻¹), resolution (100 μ m layer heights), and the possibility to print elastomeric materials (with high permittivity) led to select this method.

6.2 Selective Laser Sintering

One method of additive manufacture is Selective Laser Sintering (SLS). In SLS, the printed final structure is built by sintering the polymer layer by layer to achieve a 3D object with arbitrary geometry [257–259]. One advantage of SLS is the relatively low cost which is not influenced even with intricate geometries [260]. However, SLS is a complex thermophysical process where the experience is necessary to adequate the optimum parameters [109]. Brighenti et al. [1] deposited thin layers of preheated materials sequentially by a laser beam. The laser melts and triggers the densification of the sintering polymer. As one layer is deposited, the platform adjusts the height until the predefined value [261]. In this AM technique coupled feeding system spreads the powder. Also, in the end, the excess of powder can recover to future deposition. In Table 7, there are some complex geometry composites obtained by SLS.

In the SLS, the method of the preparation of powder is the core of this technology [264]. The dispersion of reinforcement or filler and the interfacial binding force are the most critical parameters affected in the powder preparation [109]. The researchers used different methods to mix the components powder of composite. For example, Ronca et al. [262] obtained three different porous structures for piezoresistive applications. Before incorporating nanoreinforcement (graphene) into TPU powder, additional steps are needed to break the agglomerated nanoparticles. The graphene was sonicated in ethanol for 12 h to obtain homogeneous dispersion avoiding agglomerates. Then the TPU powder and graphene suspension were then mechanically stirred

Table 7 SLS AM complex geometry composites

| SLS | | | | | | |
|-----------------------------|---|---|--|---|-------|--|
| Matrix | Fibers, reinforcer | Added % | Geometry | Properties and applications studied | Refs. | |
| TPU | MWCNTs, MWCNTs-Graphene | 1% in the case of hybrid filler 70/30 | Diamond and Gyroid unit cells | Hybrid reinforcement to enhance piezoresistive properties | [83] | |
| Polyester-type polyurethane | Graphene | ~ | Triply periodic minimal surface (TMPS), Gyroid, diamond, Schwarz cells | Piezo resistive properties | [262] | |
| PHBV | AKM | 10–20 wt. % | High porous cubic structure | Scaffold-assisted tissue engineering | [263] | |
| TPU | SWCNTs | 1 wt. % | Gyroid, diamond, Schwarz cells | Piezo resistive properties | [264] | |
| PA 12 | HA | 5, 10, 15% | Cubical, shifted cubical, spherical, and shifted spherical | Bone tissue scaffold | [261] | |
| TPU | CNT | 0.25% | Human foot | Sensing insole | [109] | |
| Silres MK | (CH ₃ -SiO _{3/2}) _x | 40 g and 20 ml of solution of particles | 3D scaffold, with large overhangs, undercuts and cavities | Scaffold porosity until 93% | [265] | |
| PA | Chemical flame-retardant R [®] | Reserved by the fabricant | Air duct | Flame retardant polymer | [88] | |

for 4 h, the melt polymer had a high viscosity, and no stress was generated. Hence, the morphology of the dispersed phase does not deeply impact the process. As the results showed, the graphene-TPU complex structures were fabricated successfully, forming a percolation network, high pore interconnectivity.

Another printed carbon composite with a complex method was developed with a dispersion carried out by the wet ball milling process followed by an ultrasonication [264]. In the first step, single-walled carbon nanotubes (SWNTs) and polyvinylpyrrolidone (PVP) at adequate quantities were milled for 1 h. Then the dark dispersion and 2500 ml of anhydrous ethanol were ultrasonicated for 1 h at 40 W. The conditions selected, as the authors mentioned, avoid damage in the 1D reinforcement. Also, these conditions were applied to TPU powder adding MWNTs or graphene. In this case, the SWNTs percolation threshold appeared at 4 and 20-times fewer carbon nanomaterials regarding MWNTs and graphene. Authors attributed more minor hindrance due to the smaller diameters of SWNTs. Both the geometry of 2D and the size of MWNTs unfavored the diffusion of polymer melt and coalescence of nanoparticles.

Rollo et al. [83] continue a couple of works previously commented [262, 264]. The continued study is focused on the addition of MWNTs or MWNT-Graphene hybrid to the TPU polymer. Mechanical, electrical, and electromagnetic properties of composites are strongly related to the internal architecture and porosity of SLS printed structures. The SEM and transmission electron microscopy (TEM) showed for the samples with a porosity between 20–60% that the carbon nanoparticles keep the distribution (segregation). That feature allows the formation of a conductive network, which is a base of the percolation threshold. Also, the hybrid reinforcement 1D–2D reduces the coalescence issues observed when only 2D reinforcement was aggregated.

Recently, Zhuang et al. [109] reported the fabrication of pressure sensing insoles by SLS. In this work, the chemical functionalization assisted the dispersion of CNT in the TPU matrix powder. The CNT were immersed in sulfuric acid (H_2SO_4) and nitric acid (HNO_3) 3:1 ratio and magnetically stirred for 1h. After that, the process was similar to others works, where planetary milling and shear mixer incorporated the nanoparticles in TPU. Also, it was analyzed the laser power, scan spacing, layer thickness, and their levels to explain SLS composites' response. Their findings point to laser power as the most influential parameter in the piezoresistive response of printed materials. Furthermore, layer thickness and scan spacing impact the density and Z-dimensional precision, respectively. Hence the dispersion and printing method proposed in this work provides an effective way to synthesize pressure sensors.

Another study about SLS manufacture composites was developed by Dierman et al. [263]. In this study, Akermanite ($\text{Ca}_2\text{Mg}[\text{Si}_2\text{O}_7]$, AKM) particles and poly(3-hydroxybutyrate-co-3-hydroxyvalerate; PHBV) were the precursors composite. In this case, the background and characterization of PHBV scaffolds obtained by SLS revealed the piezoelectric, chemistry, and printability to use as supports for bone remodeling [266, 267]. Hence to enhance these properties, AKM addition was tested. The synthesis of AKM-PHBV scaffolds by SLS involves a previous mixing mechanically during 8 h. After, the SLS printer's modified chamber was filled with nitrogen

to keep the atmosphere with a low amount of oxygen (less than 5%). The results evidence well-dispersed particles as SEM, TEM, and microcomputed tomography (μ -CT) images showed. Consequently, the AKM exposition range is 7.1–8.6% and 14–15.3% in the case of 10 and 20 wt. % added particles. These percentages can translate into fast biodegradation and enhance osteogenesis due to the high exposition area of AKM particles.

As has been reviewed, SLS technology offers an AM solution to synthesize high-complex geometry composites. However, SLS can also be used as a previous step in fabricating complex ceramic geometries [268]. Zanchetta et al. [265] reported the fabrication of a 3D high porous scaffold based on polymethylsilsesquioxane resin (Silres MK) and the ceramic silicone powder $((\text{CH}_3 - \text{SiO}_{3/2})_x)$. The process consists of printing polymer and particles to obtain a predefined CAD design. Then, the pyrolysis at 1000 °C eliminates the polymer preform, and the ceramic remains as the final scaffold. Besides, the possibility of using this rapid prototyping method was mentioned with other particles (SiC, SiCN, and BN). However, some drawbacks like precision in the printing samples [88] for SLS and defects after the pyrolysis have not been solved yet.

6.3 Material Jetting

In this method, a liquid is deposited as a drop over a defined pattern. The solidification is carried on by cooling, evaporating the solvent, or through a chemical route [99]. Inkjet printing allows printing multi-materials in a specific pattern, mainly as conductive traces [269]. This feature has been exploited in 4D printing like expandable structural components, intelligent robots, flexible electronics, and others [270, 271]. In Table 8, there are some complex geometry composites obtained by the material jetting AM method.

Wagner et al. [207] reported the fabrication of hinges with origami folding structures. The origami structure was built alternating soft and rigid photopolymers on a Stratasys Connex3 Objet500 inkjet 3D printer. The auxetic response could trigger stress concentration in some regions of geometry. Hence, cuts and small gaps were

Table 8 Material jetting complex geometry composites

| Material jetting | | | | | |
|--|--------------------|---------|----------------|-------------------------------------|-------|
| Matrix | Fibers, reinforcer | Added % | Geometry | Properties and applications studied | Refs. |
| VeroWhitePlus Stratasys- Agilus30 Stratasys Ltd | ~ | ~ | Origami sheets | Flexural hinges | [207] |
| Beeswax | Fenofibrate | 5% w/w | Honeycomb | Drug delivery | [272] |

introduced to prevent this unfavorable condition. Furthermore, to prevent cured reaction differences, the structures were printed with a matte surface, also encapsulated in a shell hydrogel as support material. Other authors have reported printing origami structures for 4D structures to shape-programmable like self-folding mura ori design [129, 273].

Kyobula et al. [272] studied the relation between the load and released drug in adaptable, complex geometry. In this case, white beeswax and fenofibrate were printed in honeycomb arrays. The weight and diameter of tablets remained constant, but the changes were carried out in the height and dimensions of honeycomb cells. The preheated melt was printed in an inkjet printer (PiXDRO LP50, Meyer Burger) at 9 °C over a polyethylene terephthalate (PET) substrate. The traditional drug load and release have been done by different polymer formulations and barrier properties of materials, respectively. AM modifying the geometry and, consequently, the surface area can solve this medical therapeutic issue. In other words, the load and release drug tuning the surface area available instead of drug formulation influence positively both functionality and manufacturing process.

The aesthetic versatility of the inkjet printing method allowed the fabrication of smart and soft devices [274]. Also, no prefabrication or templates and composite-based inks allow inkjet printing to be relatively easy to apply for electronic applications. Moreover, the inkjet printer's features include mounting multiple cartridges, allowing print multiple materials and its layer intercalation [269]. For example, as it occurs in the fabrication of reconfigurable antennas [271]. In this research, two commercial polymers (Verowhite®-Tangoblack®) were printed according to CAD mode with intercalated zones. The sheet fabricated was according to simulated and optimized dipole antenna with fold-unfold ability as the environment temperature changes.

Recently the fabrication of flexible microdevices has been a topic of interest in academics and industry [275]. Despite the remarkable progress achieved, some challenges due to the differences in length and width direction scales remain. In the case of microlens arrays (MLA), which are used in digital cameras, medical devices, displays, and other applications, the electric-field-driven (EFD) jet printing allowed the fabrication of cylindrical MLA with controllable geometry and 100% fill factor. In this printing method, morphology, curvature, and fill factor are linked to the printing conditions. Consequently, geometry and fill factors for an extensive printed area can be adjusted by the abovementioned factors. Assisted printing of polydimethylsiloxane (PDMS) by EFD allows uniform and good curvature in MLA. In this assisted AM method, a high voltage is applied to the printer nozzle causing a charge redistribution on the substrate surface.

Furthermore, the polymer polarizes, forming a meniscus. As a result of the polarization, the Taylor cone is formed. Then a stable continuous jet formed is printed in thin lines, with the influence of gravity, surface tension, and material. Other circuits have been reported using the EFD assisted AM. For example, 4D stretchable heating circuits with fractal motifs [276]. In this work, a fractal-based Joule-heating circuit was developed using EFD assisted AM. As the author reported, complex 3D structures like a table with foldable active hinges and structures with double curvature

programmed by biaxial stretching were generated by programming the flat elements obtained. Flexible transparent electrodes (FTE) were fabricated by the EFD assisted AM method to print silver patterns and a posterior embedded PET process by roller-assisted hot embossed method [277]. Also, transparent glass heaters using EFD AM printing technique and UV-assisted micro-transfer process were reported [278].

6.4 Sheet Lamination

This method combines AM and SM where prefabricated layers (commonly called prepregs) are stacked and fused by the application of pressure, heat, adhesive, or ultrasonication [164, 213, 279, 280]. To obtain the desired shape, a cut process is necessary before or after the bonding step [281]. The sheet lamination (SHL) materials used are papers, metals, and composites [275]. Bhatt et al. [164] classify SHL in laminated object manufacturing (LOM) and ultrasonic consolidation. LOM is one of the oldest AM processes, which have been reported high-strength parts without post-processing and support are obtained [213]. However, in multi-materials and complex geometries applications, some issues have not been solved completely yet. To contribute to this field, the inclusion of some modifications such as milling improving [282], robots [164], and so on, adds to the LOM new capabilities manufacturing heterogeneous structures. Luong et al. [282] reported the application of LOM to obtain complex geometry graphene foams. They demonstrate the potential of LOM for industrial manufacturing of laser-induced graphene foam (LIG). In this case, the manufacturing system assisted by a laser and AM platform allows the fabrication of laminated foams graphene materials. Robotic manipulators increase the functional capabilities of AM process either in control of the platform of construction or as a multi-functional task (dispensing, cutting, inserting components) to build a complex geometry [164].

Chang et al. [283] reported the LOM process and ultrasonic vibration to fabricate carbon fiber-polyamide 6 reinforced composite. In this study, the ultrasonic consolidation and pressure over prepregs were carried on simultaneously by an ultrasonic vibration roller. In addition, hot-press postprocessing to some specimens was implemented. The results showed that the best performance in tensile and flexural tests of composites was acquired when ultrasonic-pressure and hot-press postprocessing were used. In addition, the analysis by computer tomography and fracture morphology, no distinguished boundaries between prepreg and delamination, respectively. These results indicate a better interfacial bonding between printed layers. Parandoush et al. [284] reported another modification in LOM. In this research, the addition of layers was assisted by a laser beam and consolidation roller to pressure the carbon fiber-polyamide 6 composites. As they reported, 2D cellular composites were developed, also functional 3D structures like a frame of a remote-control car. The frame replaces an Aluminum part maintaining rigidity. Another interesting approach of LOM for complex geometries was reported by Tao et al. [285]. They used polyvinyl acetate (PVA) and Poplar veneer. In this research, 2D Voronoi cellular

Table 9 Complex geometry composites formed by sheet lamination AM

| Sheet lamination | | | | | |
|------------------|-----------------------|---------------|--------------------------------|---|-------|
| Matrix | Fibers, reinforcement | Added percent | Geometry | Properties and applications studied | Refs. |
| PI-EG | LIG | ~ | Cubic high porous structures | ~ | [282] |
| Epoxy | Mylar | ~ | ~ | Ornithopter wing | [286] |
| PA 6 | CF | 60 wt. % | Gear, truss cell, and others | Interlaminar strength in ultrasonic consolidate composites | [283] |
| PA 6 | Continuous CF | 60 wt. % | 2D cellular composites | Flexural strength in laser and roller consolidate composite | [284] |
| PVA | Poplar veneer | ~ | 2D Voronoi cellular composites | Customizable wood products | [285] |

plies were piled vertical and with a certain deviation degree with respect to the first one. Then the resulting 3D objects with complex internal cavities could be used as sound absorbers and composites. In Table 9 there are some complex geometry composites obtained by the Sheet Lamination AM method.

7 Applications

7.1 Medical Field

AM technology is a powerful tool that has been used within the medical area for the fabrication of bone tissue engineering, artificial vessel stents, drug delivery, and rehabilitation [287–289]. For example, 3D bioprinting technology enables the fabrication of nerve canals to enhance peripheral nerves' regeneration. Nerve canals are considered the tool that repairs the injured peripheral nerve, which causes disability and mortality. Tao et al. [241] carried out hydrogel nanoparticle nerve canals, which can release drugs to facilitate peripheral nerve regeneration via the Hippo pathway. This research demonstrated 3D printed canals promoted recovery from injuries and demonstrated a promising clinical application.

On the other hand, there is a necessity to improve materials such as scaffolds in tissue engineering, which provide a temporary artificial matrix for cell growth. A scaffold must withstand the stresses and loads generated during in vitro or in vivo regeneration [290]. Therefore, AM offers an alternative and advantage, which can be used to produce scaffolds whose shape and size can be customized according to specific characteristics and requirements [291]. Cho et al. [190] developed a PCL and nHA scaffold through AM, with which they fabricated a kagome structure. The

scaffold 3D printed and coated with zinc oxide ZnO. The use of zinc ions serves to improve antibacterial activity. Scaffolds showed improvements in mechanical and antibacterial properties. Therefore, PCL/nHA-ZnO scaffold is an option for bone regeneration and surgical site infection prevention.

In the same context, the technology of alternative bone scaffold is an excellent alternative for the manufacture of bone substitutes. Kumaresan et al. [261] designed, manufactured, and analyzed porous scaffolds using additive manufacturing. The scaffolds were manufactured with the SLS with different configurations such as cubical pore, spherical pore, shifted cubical pore, shifted spherical pore. Besides, the research analyzed different types of biocompatible materials such as PA combined with HA, which favor the growth of bone tissue cells. The results reported in this research proved that the SLS method allows the manufacture of scaffolds with complex architectures and good quality. Also, it facilitates the mechanical resistance and accuracy of the scaffolds and offers control over the geometry according to the needs. The production of porous structured scaffolds could be applied as a replacement for fractured bones and in the regeneration of new bone.

In addition to good mechanical strength, the scaffolds and biomaterials manufactured and used in AM must mimic the typical physiological structure and natural tissue structure. Li et al. [200] designed both, multilayer cartilage, and bone composite scaffolds to simulate physiological full-thickness bone-cartilage structure. Therefore, they combined processing techniques to carry out their research, the cartilage layer was generated from thermally induced crystallization by a temperature gradient, and the bone layers were obtained by AM. The cell distribution, morphology, and proliferation results demonstrated its potential application to repair full-thickness joint defects in vivo. Production was also found to be easy, and a new alternative was proposed to repair joint defects [200].

Obtaining tissue scaffolds with unique characteristics through AM allows a significant advance in regenerative medicine. For example, vascular engineering would facilitate the production of 3D vascular scaffolds, which would have adequate blood circulation. Tsai et al. [209] prepared a boronate ester hydrogel. The preparation of the hydrogel was carried out from an N-isopropylacrylamide copolymer with pentafluorophenyl acrylate and polyvinyl alcohol. The development of a glucose-sensitive sacrificial hydrogel with self-healing capabilities, have demonstrated that it could be used to construct complicated and easily removable 3D structures, useful to fabricate applied biomimetic scaffolds in vascularized constructs. Therefore, the use of 3D printable hydrogels offers an excellent tool in biomedicine.

Improving biocompatibility in tissue engineering through complex constructions using (bio) AM technologies continues to be a challenge that must be solved in the medical area. For example, stimulus-sensitive hydrogels are an excellent option for the manufacture of cellular scaffolds, and their possible applications in soft robotics, to which development, function, and regeneration are attributed. Tognato et al. [123] studied a new method for manufacturing a cellularized anisotropic hybrid hydrogel through a process promoted by external stimuli such as the low-intensity magnetic field, temperature, and light-responsive. Their research reported the nanocomposite hydrogel could differentiate the C2C12 skeletal muscle cells in mature myotubes.

These results generate several possibilities of applying a hydrogel such as ink for AM, the development of new strategies of mechano-transduction activated at a distance for therapeutic approaches, and its potential to manufacture 3D biomimetic models (tissue engineering scaffolds) through soft robotics.

Accordingly, to the previous research described, DIW, among the AM methods, offers some advantages in developing biocompatible and conductive biomaterials, which give applications such as drug delivery, stem cell differentiation biosensors bone, cardiac and neuro tissue engineering, and regeneration. In this context, Jakus et al. [197] studied the potential of the manufacture of electrically conducting scaffolds with characteristics as small as 100 μm for tissue engineering applications. The composition of graphene and polylactide-co-glycolide was analyzed through in vitro and in vivo biocompatibility studies. Results confirmed that the application of graphene-based ink allows the possibility of the growth of adult mesenchymal stem cells and positive regulation of glial and neuron-specific genes, which could be considered for future applications in the regeneration of nerve tissues. Furthermore, in in vivo studies with graphene, it was demonstrated these polymer composites possess biocompatibility and the absence of accumulation of the nanomaterial in the kidney, liver, or spleen, which could be applied during surgical procedures such as nerve bundle wrapping.

Among AM techniques, SLA has excellent advantages in the development of scaffold geometries applied in tissue engineering. Bustillos et al. [238] manufactured scaffold geometries and dense rectangular structures of PSP resins and BNNP by SLA. The results of this investigation showed an improvement in damping behavior. Furthermore, the AM fabricated nanocomposites by SLA have proven to be an excellent alternative as a manufacturing technique. In addition, the AM fabricated nanocomposites by the SLA method are also a promising manufacturing technique in this field. Makvandi et al. [239] made a dental bite prototype by SLA. For the research, the authors took advantage of stereolithography's benefits through the photopolymerization of UV curable material to fabricate custom dental bites. The occlusal composite bite showed improvements in mechanical properties and antimicrobial capacity.

7.2 *Electronic Field*

Design and manufacture in electronics and other similar areas, such as three-dimensional chip stack architectures and flexible electronics, require materials with the higher power density and thermal control. Besides, the technological research area seeks low-cost, lightweight, and thermally conductive composite materials for effective heat dissipation in electronic devices [292]. On the other hand, AM technology offers the advantage of building complex structures for various applications and at a lower cost, allowing the manufacture of thermal devices such as heat exchangers, heat sinks, and hollow filters. Nguyen et al. [182] printed a heat sink using DIW. This work's main goal was to demonstrate the efficacy of the non-metallic composite

ink and direct writing approach. The ink used was an EPON 862 resin with a hybrid filler of milled carbon fiber and graphite nanoplatelets. Several designs with different patterns were made during the investigation and evaluated using thermal and mechanical techniques. The devices printed with the thermal ink demonstrated good thermal dissipation and the generation of a new study area. Manufacturing low-cost, high-performance thermal devices by DIW with lightness and resistance to corrosion would make it possible for developments in nanoelectronics and related areas. Fantino et al. [256] manufactured conductive structures in 3D, incorporating silver nitrate to PEGDA in the presence of suitable photoinitiators and exposing them to a digital light system. The production of parts with complex structures on a micrometer scale employing DLP printing and UV irradiation made it possible to obtain complex and light three-dimensional parts with electromagnetic properties. These results offer an alternative to producing 3D structures of metal-polymer composites, which could be found in application in the electronic device market.

Waheed et al. [196] created an ABS-microdiamonds composite filament to meet the needs of looking for thermally conductive and electrically insulating materials to manufacture electronic devices with complex structures through AM (Fig. 14). During the investigation, various conventional and nonconventional heat sinks, and the potential of incorporating synthetic high-pressure and high-temperature microdiamonds as fillers in ABS were tested. The results showed that heat sinks made using a fused deposition modeling printer increased thermal dissipation by 42%. Therefore, manufacturing heatsinks in three dimensions could decrease electronic devices' size, improve performance, and reduce manufacturing costs.

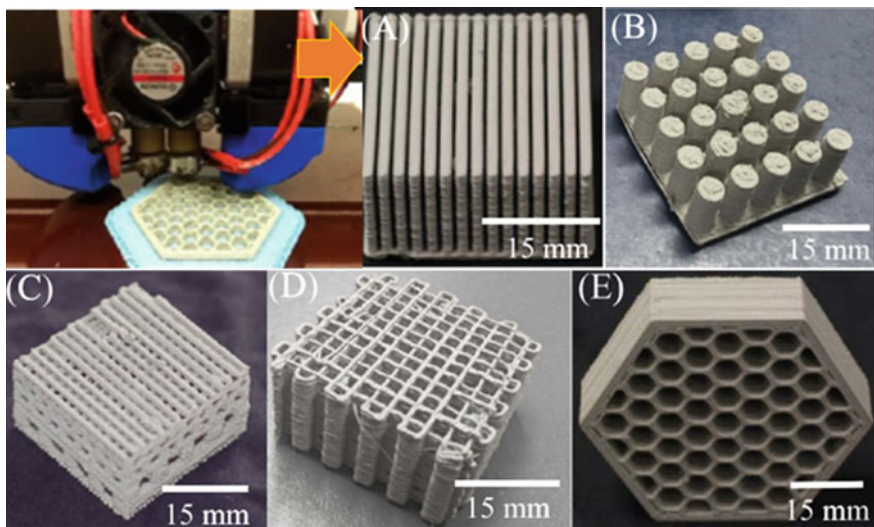


Fig. 14 Photographs of heat sinks fabricated of diamond-ABS composite by conventional and nonconventional AM. Reprinted from Waheed et al. [196]. Copyright (2019), with permission from Elsevier

7.3 Structural 3D Composites

AM is considered a manufacturing method with outstanding characteristics for creating new custom structures with a short production cycle and a high degree of automation [293]. The AM also modify or vary different characteristics in pieces, such as percentage of density, the thickness of the outer layer, and fill pattern. The selection of these characteristics notably influences the properties of the final product [294]. For example, the sandwich panel structure's design and application (which consists of two high-rigidity coatings and a low-density core panel). This structure is widely used in the aerospace, automotive, and military industries. Sandwich panel offers an advantage over other structures because it reduces weight and increases rigidity [61]. In this context, several investigations focused on studying and verifying the design of structures to modify and enhance mechanical properties. Specifically, Bollig et al. [294] studied the design and manufacture of 3D printed composites with toroidal geometry. PLA—Rustable Magnetic Iron filament (40 wt% of iron) was used to print the pieces. The experiments' design was based on varying the fill factor (20–100%) and the fill pattern (rectangular and honeycomb). The thickness of the outer layer for printed cores was kept constant (two layers). Thus, the construction of magnetic transformers could be achieved via FDM, and this manufacturing could be applied in the transmission and distribution of electric power. However, the study also reported many opportunity points to improve, during the manufacture of this material type, for instance: high filling factors, higher content of magnetic particles, and higher attraction.

Also, AM enables the fabrication of CFRCLSs. Such structures can be obtained in complex shapes through control of design and manufacture [295], which in the past was difficult to manufacture [296, 297]. For example, Hou et al. [101] manufactured and evaluated a lightweight sandwich structure based on a corrugated spline core. The lightweight sandwich structure specimen was 60 mm in length, 60 mm in width, and 15 mm in thickness. The materials used were continuous fiber-reinforced thermoplastic for the integrated manufacturing of CFRCLSs. The research results demonstrated that the design and processing parameters for the structure manufacture, such as printing speed of 100 mm/min and a hatch spacing of 1 mm, improve the resistance to compression compared to commercial structures produced by other methods. Thus, complex shapes productions by this technique were confirmed, and the possibility of increasing the applications of these structures in the aerospace industry, high-speed trains, ships, and among others.

On the other hand, other types of structures can be developed and have the purpose of improving their mechanical response through the combination of materials. Such as the architectures made from discontinuous fiber-reinforced composites. With this intention, Martin et al. [298] studied 3D magnetic printing to make light and strong composites. The research was based on designing microarchitectures from “concentric, layered, and the cholesteric structures. Besides, after verifying the creation of bioinspiration microarchitectures such as osteon, nacre, and peacock mantis shrimp.

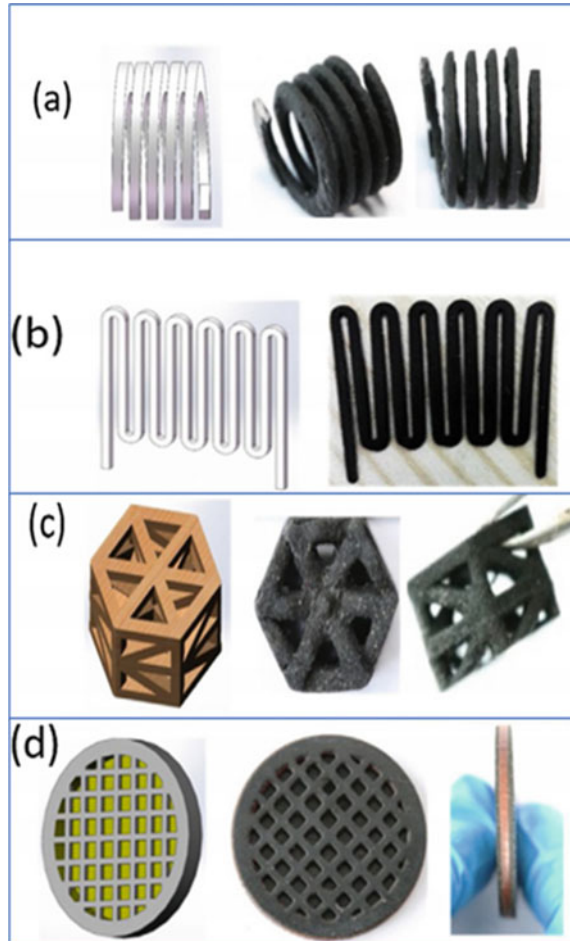
The printed composites demonstrated a mechanical dependence on the microarchitecture, which was verified through tests carried out such as hardness mapping and tensile tests. Also, the tensile tests applied on the printed pieces with "inspired by osteons" structures and in which the direction of the cracks was observed showed deflection during the propagation of the crack, associated with a higher toughness of fracture, this behavior is similar to the that occurs in human bone fractures. Therefore, the research analyzes and demonstrates, the architecture design can prevent and deflect crack propagation, which could be used to program failure mechanisms in different types of materials.

7.4 Other Applications

The design and manufacture of structures from conductive materials using AM technology have increased in recent years [299, 300]. Hybrid printing has even been used, where two or more AM technologies are integrated and combined, to print complex structures, such as the development of conductive parts within electrically insulating materials with multiple functions [301, 302]. For example, Mu et al. [242] developed complex conductive structures through DLP to develop capacitive sensors, smart structures with shape memory, and stretchable spring circuits (Fig. 15). The research analyzed the impression of different structures, flat and complex, spring type, wave-shaped resistance, and truss. In the research, other materials such as MWNTs were used. The electrical and mechanical results confirmed the method's effectiveness in manufacturing conductive parts, with good electrical properties and the versatility of creating different structures. Thus, it was demonstrated various possibilities in the design and manufacturing of geometrically complex structures such as conductive materials, which could be used as electrodes and connection cables applied in signal transfer, heating, and detection.

Another application is related to the term locomotion. The term "natural" locomotion in aquatic and aerial species within fluids has generated a topic of great interest in the scientific and technological area [303, 304]. Therefore, the technological area seeks to develop robotic devices with locomotive properties for use in the transport, delivery, and administration of medicines, as well as environmental decontamination, among others. Zhu et al. [120], taking advantage of the technology of rapid AM platform and microscale continuous optical printing (μ COP), designed and manufactured artificial hydrogel "micro fish" with biomimetic structures. The pieces produced based on PEGDA in the shape of a fish with functionalized nanoparticles had locomotive characteristics with high fidelity shapes and structures. So, the 3D printed micro fish demonstrated efficient propulsion and the ability to be magnetically guided. In this research, the digitized and μ COP technique played an important role in the manufacture of micro fish because it can construct a wide variety of complex 3D geometries. Also, structures can be printed in seconds, with high resolution, and with different magnitude orders. It even offers an improvement in manufacturing speed efficiency and does not require the use of harsh chemicals.

Fig. 15 Different types of DLP® 3D printed conductive structures of nanocomposite with pristine resins and MWCNTs, according to designed CAD models which are shown at the left side of the printed objects: **a** hang structured spring; **b** planar wave shape resistor; **c** hollow structure truss; and **d** capacitor with hollow structure. Reprinted from Mu et al. [242]. Copyright (2017), with permission from Elsevier



In addition, AM has worked to produce different electromagnetic components, which have been used in stealth technology, shielding, energy harvesting, and as a wave absorber [305]. Ren and Yin [177] manufactured a carbon-loaded ABS electromagnetic absorber. The construction was based on a cylindrical-dielectric resonator for microwave absorption. The conical shape design operating in the range of 3.9–12 GHz was made using FDM. The absorber exhibited high absorption under wide incidence angles and could be applied in microwave and stealth technology measurement.

On the other hand, Amaya et al. [7] studied the acoustic properties of auxetic pieces obtained by AM. Keratin-reinforced auxetic structures obtained from chicken feathers significantly improved acoustic absorption. As part of the research, the evaluation of the acoustic absorption coefficient was carried out by means of an electroacoustic experiment. The results obtained through the tests carried out were

attributed not only to the auxetic geometry but to the interactions between keratin materials and PLA. Therefore, the acoustic coefficient values obtained allow the manufacture of these auxetic structures with possible applications in the automotive and aeronautical industries.

Finally, multi-material AM has also been studied and applied. This technique allows the development of pieces with active heating zones and has inspired the manufacture of intelligent devices such as actuators [306–308]. Micalizzi et al. [122] studied the possibility of manufacturing shape memory actuators using dual extrusion multi-material printing. During the research, they developed three actuators, a hexagon-shaped robotic claw or gripper, a finger-shaped actuator made up of seven phalanges, and a kind of active snake. The results confirmed the advantages of AM given by minimizing post-processing and using additional heaters, such as resistors or thermal patches, as part of the structure of the device. Therefore, the research allows evaluating and validating the development of actuators generated by AM and offers an alternative for the engineering of complex actuators with shape memory.

8 Future Trends and Limitation Section

AM has evolved in recent years, allowing revolutionize manufacturing technology and expanding and solving problems in different areas and sectors. However, it still has some disadvantages, such as material selection, void formation, and manufacturing time. Besides, it exhibits other problems related to the lack of resolution and parts' limited design and construction. This could be compared with the evolution and development that computers have had because despite the years they continue to present advantages and disadvantages depending on the processor installed. Therefore, 3D printers may also present variations in their final products depending on the characteristics and models of each 3D equipment.

Different additive manufacturing processes currently trait to enter and test other materials. The range of materials includes polymers, metals, ceramics, and composites. The composites have been reinforced by different nanoparticles, fibers, and functional materials. Hence their use makes possible combinations, increasing, improving, and diversifying their properties and applications.

On the other hand, AM is also venturing into different manufacturing processes, allowing for the current inconveniences and challenges. This could be an advantage that additive manufacturing offers over traditional manufacturing processes. For example, FDM or FFF fusion printed materials are easy to obtain due to the easy handling of the equipment or the speed of printing. This allows these techniques to be used in many areas, from automotive to art or cooking. However, FDM printing can present parts with lower resolution and precision in complex or embossed designs compared to other techniques such as SLA and SLS.

Alternatively, VAT polymerization with the three main derivative curing methods: SLA, DLP, and CLIP diversifies the possibilities to develop complex structures due to the technique principles. For example, SLA structures have excellent advantages

in the development of scaffold geometries with high resolution. Besides, different materials can be used by modifying the printing system. However, the addition of other materials can cause curing problems associated with particle interference in some developments. This technique is more frequently used in the medical area related to the simplicity of the process, but diverse structures focused on other possible applications could be manufactured.

Finally, one of the most important advantages that AM offers, making this technique a highly competitive tool, is the manufacture of extraordinarily complex and customized parts. Besides, it provides various sectors in which it can be used and applied, ranging from personal use to academic and industrial (in its different sectors).

The development, innovation, and research of materials and methods around AM have evolved in the last decade, and different challenges have been overcome. However, it requires further research, and work. Mainly to position this manufacturing option on the already established methods. The growth and development of personalized pieces through three-dimensional printing has opened fields of research and application that were not contemplated or expected in the past. Consequently, this manufacturing method of 3D structures has many opportunity areas, its future looks like a promising solution in demanding society and technology challenges. As it was reviewed, the AM has the tendency will be able to change an endless number of areas, and it is contemplated that could be the solution to the development of unimaginable pieces for diverse applications, which will solve many of the current problems by some areas and sectors. Without a doubt, creativity and multidisciplinary research groups involved will be some of the keys for the constant and successful growth of this research field and the established technology.

9 Concluding Remarks

This work reviews and analyzes the research articles focused on complex geometries composites fabricated by AM. The reviewed literature explains the concept of complex geometry and the manufacturing possibilities in AM. Complex geometries composites fabricated by AM showed the significant impact of technologies as computer tools. Considering the deployment of computational tools (CAD/CAE/CAM), the design of complex geometries and progress in different application areas was analyzed. Another purpose of this book chapter is to analyze the modifications in the AM methods to fabricate complex geometries composites. The advances in manufacturing technologies evidence the flexibility of AM to build complex shapes. However, despite all progress in AM, there are still some challenges in fabricating complex geometries. For example, the design of optimized geometries and their manufacturability, large-scale printing, and multi-materials complex geometries need to overcome some limitations to get their maturity. Thus, the review realized would be useful as a guide to establish the bases and background of complex geometries in polymer composites

References

1. R. Brighenti, M.P. Cosma, L. Marsavina, A. Spagnoli, M. Terzano, *J. Mater. Sci.* **56**, 961 (2021)
2. S.C. Ligon, R. Liska, J. Stampfl, M. Gurr, R. Mülhaupt, *Chem. Rev.* **117**, 10212 (2017)
3. M. Revilla-León, M. Sadeghpour, M. Özcan, *Odontology* **108**, 331 (2020)
4. T. Sathish, M. D. Vijayakumar, and A. Krishnan Ayyangar, *Mater. Today Proc.* **5**, 14489 (2018).
5. I. Gibson, D. Rosen, B. Stucker, and M. Khorasani, *Design for Additive Manufacturing In: Additive Manufacturing Technologies*, Third ed. (Springer, 2021), pp. 555–607.
6. I. Paoletti, in *Customization 4.0. Springer Proceedings in Business and Economics*, ed. by S. Hankammer, K. Nielsen, F. Piller, G. Schuh, N. Wang (Springer, Cham, 2018), pp. 191–202.
7. V. Amaya-Amaya, M. de Icaza-Herrera, A.L. Martínez-Hernández, G. Martínez-Barrera, C. Velasco-Santos, *Mater. Lett.* **283**, 128757 (2021)
8. S.A.M. Tofail, E.P. Koumoulos, A. Bandyopadhyay, S. Bose, L. O’Donoghue, C. Charitidis, *Mater. Today* **21**, 22 (2018)
9. H. Zhao, X. Liu, W. Zhao, G. Wang, and B. Liu, *J. Phys. Conf. Ser.* **1213**, (2019).
10. A. Pham, C. Kelly, K. Gall, *J. Mater. Res.* **35**, 2547 (2020)
11. T.A. Schaedler, W.B. Carter, *Annu. Rev. Mater. Res.* **46**, 187 (2016)
12. G. Qi, B. Ji, L. Ma, *Mech. Adv. Mater. Struct.* **26**, 1298 (2019)
13. S.S. Alghamdi, S. John, N.R. Choudhury, N.K. Dutta, *Polymers* **13**, 753 (2021)
14. ISO, *Addit. Manuf. — Gen. Princ. — Terminol.* (2015).
15. I. Gibson, D. Rosen, B. Stucker, and M. Khorasani, in *Additive Manufacturing Technologies*, Third ed. (Springer, Cham, 2021), pp. 23–51.
16. W. Gao, Y. Zhang, D. Ramanujan, K. Ramani, Y. Chen, C. B. Williams, C. C. L. Wang, Y. C. Shin, S. Zhang, and P. D. Zavattieri, *CAD Comput. Aided Des.* **69**, 65 (2015).
17. S. Kyle, Z.M. Jessop, A. Al-sabah, I.S. Whitaker, *Adv. Healthc. Mater.* **1700264**, 1 (2017)
18. P. Jiao, A.H. Alavi, *Int. Mater. Rev.* **66**, 365 (2020)
19. A.F. Siegenfeld, Y. Bar-Yam, *Complexity* **2020**, 6105872 (2020)
20. M. Baumers, C. Tuck, R. Wildman, I. Ashcroft, R. Hague, *J. Ind. Ecol.* **21**, S157 (2017)
21. P. Stavropoulos, P. Foteinopoulos, A. Papapacharalampopoulos, *Appl. Sci.* **11**, 7743 (2021)
22. R. Chen, F. Imani, E. Reutzler, H. Yang, *IEEE Sensors Lett.* **3**, 1 (2019)
23. D. Gu, *Sci. Bull.* **61**, 1718 (2016)
24. X.T. Wang, Y.L. Chen, L. Ma, *J. Compos. Mater.* **52**, 3265 (2018)
25. B. Motyl, S. Filippi, *Int. J. Interact. Des. Manuf.* **15**, 103 (2020)
26. Y. Borgianni, L. Maccioni, P. Russo Spena, and M. K. Shunmugavel, *Proc. Int. Conf. Eng. Des. ICED 2019-Augus*, 629 (2019).
27. X. Chen, G. Chen, G. Wang, P. Zhu, C. Gao, *Adv. Eng. Mater.* **22**, 1 (2020)
28. J. Iwanaga, A.S. Dumont, R. S. Tubbs **34**, 108 (2020)
29. P.K.K. Arora, R. Arora, A. Haleem, H. Kumar, *Mater. Today Proc.* **38**, 466 (2021)
30. Y. Chen, W. Li, C. Zhang, Z. Wu, J. Liu, *Adv. Healthc. Mater.* **9**, 2000724 (2020)
31. I. Negut, G. Dorcioman, V. Grumezescu, *Polymers (Basel)*, **12**, 1 (2020)
32. H.W. Kang, S.J. Lee, I.K. Ko, C. Kengla, J.J. Yoo, A. Atala, *Nat. Biotechnol.* **34**, 312 (2016)
33. D.M. Junqueira, G.F. Gomes, M.E. Silveira, A.C. Ancelotti, *Appl. Compos. Mater.* **26**, 273 (2019)
34. M. Javid, A. Haleem, *Alexandria. J. Med.* **54**, 411 (2018)
35. D. Stanco, P. Urb, S. Tirendi, G. Ciardelli, J. Barrero, *Bioprinting* **20**, e00103 (2020)
36. Da. Chimene, Ki. Lennox, R. Kaunas, and A. K. Gaharwar, *Ann. Biomed* **44**, 2090 (2016).
37. M. Guvendiren, J. Molde, R.M.D. Soares, J. Kohn, *Physiol. Behav.* **176**, 139 (2017)
38. N. Hong, G. Yang, J. Lee, and G. Kim, *J. Biomed. Mater. Res. Part B* **444** (2017).
39. L. Moroni, J.A. Burdick, *Nat. Rev. Mater.* **3**, 21 (2018)
40. Q. Wang, G. Han, S. Yan, Q. Zhang, *Materials (Basel)*, **12**, 504 (2019)
41. F. You, B.F. Eames, X. Chen, *Int. J. Mol. Sci.* **18**, 8 (2017)

42. B.K. Gu, D.J. Choi, S.J. Park, M.S. Kim, C.M. Kang, C. Kim, *Biomater. Res.* **20**, 1 (2016)
43. A. Bandyopadhyay, S. Vahabzadeh, A. Shivaram **40**, 1162 (2015)
44. G. Chen, Y. Xu, P. Chi, L. Kwok, L. Kang, *Addit. Manuf.* **34**, 101209 (2020)
45. M. Albed Alhnan, O. Tochukwu Chijioko, S. Muzna, K.-W. Wan, W. Ahmed, and A. Basel, *Pharm. Res.* **33**, 1817 (2016).
46. R.C. Advincula, J.R.C. Dizon, Q. Chen, I. Niu, J. Chung, L. Kilpatrick, R. Newman, *MRS Commun.* **10**, 413 (2020)
47. N. Vordos, D.A. Gkika, G. Maliaris, K.E. Tilkeridis, A. Antoniou, D.V. Bandekas, A. Ch. Mitropoulos, *Saf. Sci.* **130**, 104870 (2020)
48. B.I. Oladapo, S.O. Ismail, T.D. Afolalu, D.B. Olawade, M. Zahedi, *Mater. Chem. Phys.* **258**, 123943 (2021)
49. E. Stenvall, G. Flodberg, H. Pettersson, K. Hellberg, L. Hermansson, M. Wallin, L. Yang, *Bioengineering* **7**, 1 (2020)
50. A.A. Zadpoor, *Int. J. Mol. Sci.* **18**, 1607 (2017)
51. M. Askari, D.A. Hutchins, P.J. Thomas, L. Astolfi, R.L. Watson, M. Abdi, M. Ricci, S. Laureti, L. Nie, S. Freear, R. Wildman, C. Tuck, M. Clarke, E. Woods, A.T. Clare, *Addit. Manuf.* **36**, 101562 (2020)
52. Z. Wang, C. Luan, G. Liao, J. Liu, X. Yao, J. Fu, *Adv. Eng. Mater.* **22**, 1 (2020)
53. Z. Jia, F. Liu, X. Jiang, and L. Wang, *J. Appl. Phys.* **127**, 150901 (2020).
54. S.C.L. Fischer, L. Hillen, C. Eberl, *Materials (Basel)*. **13**, 1 (2020)
55. H. Shams, K. Basit, M.A. Khan, S. Saleem, A. Mansoor, *Addit. Manuf.* **38**, 101777 (2021)
56. K.K. Saxena, R. Das, E.P. Calius, *Adv. Eng. Mater.* **18**, 1847 (2016)
57. G.D. Goh, S. Agarwala, G.L. Goh, V. Dikshit, S.L. Sing, W.Y. Yeong, *Aerosp. Sci. Technol.* **63**, 140 (2017)
58. K. Lussenburg, A. Sakes, and P. Breedveld, *Addit. Manuf.* **39**, 101846 (2021).
59. S. Sharafi, M.H. Santare, J. Gerdes, S.G. Advani, *Addit. Manuf.* **38**, 101830 (2021)
60. F. Korkees, J. Allenby, P. Dorrington, *Rapid Prototyp. J.* **26**, 699 (2020)
61. Q. Ma, M. R. M. Rejab, J. P. Siregar, and Z. Guan, *J. Compos. Mater.* **0**, 1 (2021).
62. R. Dermanaki Farahani and M. Dubé, *Adv. Eng. Mater.* **20**, 1 (2018).
63. J.Z. Manapat, Q. Chen, P. Ye, R.C. Advincula, *Macromol. Mater. Eng.* **302**, 1 (2017)
64. I. Khan, C.S. Kamma-Lorger, S.D. Mohan, A. Mateus, G.R. Mitchell, *Appl. Mech. Mater.* **890**, 113 (2019)
65. O. Oderinde, S. Liu, K. Li, M. Kang, H. Imtiaz, F. Yao, G. Fu, *Polym. Adv. Technol.* **29**, 1586 (2018)
66. S.D. Nath, S. Nilufar, *Polymers (Basel)*. **12**, 1 (2020)
67. T. Noraihan, A. Tuan, A.M. Abdullah, H. Akil, *Polym. Rev.* **59**, 589 (2019)
68. E.A. Papon, A. Haque, J. Reinf. Plast. Compos. **39**, 758 (2020)
69. X. Wang, M. Jiang, Z. Zhou, J. Gou, D. Hui, *Compos. Part B Eng.* **110**, 442 (2017)
70. I. Fidan, A. Imeri, A. Gupta, S. Hasanov, A. Nasirov, A. Elliott, F. Alifui-Segbaya, N. Nanami, *Int. J. Adv. Manuf. Technol.* **102**, 1801 (2019)
71. H.Y. Jeong, E. Lee, S.C. An, Y. Lim, Y.C. Jun, *Nanophotonics* **9**, 1139 (2020)
72. K. Fu, Y. Yao, J. Dai, L. Hu, *Adv. Mater.* **29**, 1603486 (2017)
73. Z. Benzait, L. Trabzon, *J. Compos. Mater.* **52**, 3241 (2018)
74. M.Q. Zafar, H. Zhao, *Met. Mater. Int.* **26**, 564 (2020)
75. C.A. Spiegel, M. Hippler, A. Münchinger, M. Bastmeyer, C. Barner-Kowollik, M. Wegener, E. Blasco, *Adv. Funct. Mater.* **30**, 1907615 (2020)
76. L. Tan, A.C. Davis, D.J. Cappelleri, *Adv. Funct. Mater.* **2020**, 2007125 (2020)
77. P. Martins, D.M. Correia, V. Correia, S. Lanceros-Mendez, *Phys. Chem. Chem. Phys.* **22**, 15163 (2020)
78. D. Wanasinghe, F. Aslani, G. Ma, D. Habibi, *Nanomaterials* **10**, 541 (2020)
79. A. Bajpai, A. Baigent, S. Raghav, C. Brádaigh, V. Koutsos, N. Radacsi, *Sustain.* **12**, 1 (2020)
80. A. Mitchell, U. Lafont, M. Hołyńska, C. Semprimoschnig, *Addit. Manuf.* **24**, 606 (2018)
81. I. Gibson, D. Rosen, and B. Stucker, in *Additive Manufacturing Technologies*, Second ed. (Springer, New York, 2015), pp. 245–268.

82. D. L. Kevin Noack, Martin Friedrich Eichenauer, *J. Ind. Des. Eng. Graph.* **14**, 35 (2019).
83. G. Rollo, A. Ronca, P. Cerruti, X. P. Gan, G. Fei, H. Xia, G. Gorokhov, D. Bychanok, P. Kuzhir, M. Lavorgna, and L. Ambrosio, *Polymers (Basel)*. **12**, (2020).
84. K. Ko, S. Jin, S.E. Lee, I. Lee, J.W. Hong, *Compos. Part B Eng.* **165**, 594 (2019)
85. A. Sydney Gladman, E. A. Matsumoto, R. G. Nuzzo, L. Mahadevan, and J. A. Lewis, *Nat. Mater.* **15**, 413 (2016).
86. J. Xiao, D. Liu, H. Cheng, Y. Jia, S. Zhou, M. Zu, *Ceram. Int.* **46**, 19393 (2020)
87. J.B. Berger, H.N.G. Wadley, R.M. McMeeking, *Nature* **543**, 533 (2017)
88. A. V. Borille, J. De Oliveira Gomes, and D. Lopes, *Rapid Prototyp. J.* **23**, 169 (2017).
89. C. Oztan, V. Coverstone, *Acta Astronaut.* **180**, 130 (2021)
90. S. H. Kim, Y. K. Yeon, J. M. Lee, J. R. Chao, Y. J. Lee, Y. B. Seo, M. T. Sultan, O. J. Lee, J. S. Lee, S. Il Yoon, I. S. Hong, G. Khang, S. J. Lee, J. J. Yoo, and C. H. Park, *Nat. Commun.* **9**, 1 (2018).
91. J. S. Cuellar, G. Smit, A. A. Zadpoor, and P. Breedveld, *Proc. Inst. Mech. Eng. Part H J. Eng. Med.* **232**, 962 (2018).
92. “What is Additive Manufacturing? | GE Additive.” <https://www.ge.com/additive/what-additive-manufacturing> (accessed Nov. 02, 2021).
93. I. Gibson, D. Rosen, and B. Stucker, in *Additive Manufacturing Technologies*. Second Ed. (Springer, Ney York, 2015), pp. 399–435.
94. C. M. S. Vicente, C. Jacinto, H. Carvalho, I. Ribeiro, L. Reis, M. Leite, P. Peças, R. Ribeiro, and S. Esteves, in *Additive Manufacturing Hybrid Processes for Composites Systems* edited by A. Torres Marques, S. Esteves, J. P. Pereira, and L. M. Oliveira (Springer, 2020), pp. 57–91.
95. G. Manogharan, R.A. Wysk, O.L.A. Harrysson, *Int. J. Comput. Integr. Manuf.* **29**, 473 (2016)
96. O. Diegel, J. Schutte, A. Ferreira, Y.L. Chan, *Addit. Manuf.* **36**, 101446 (2020)
97. E. Karayel, Y. Bozkurt, *J. Mater. Res. Technol.* **9**, 11424 (2020)
98. I.R. Woodward, C.A. Fromen, *Addit. Manuf.* **48**, 102386 (2021)
99. E. Uribe-Lam, C.D. Treviño-Quintanilla, E. Cuan-Urquizo, O. Olvera-Silva, *Mater. Manuf. Process.* **36**, 257 (2021)
100. C. Hodonou, M. Balazinski, M. Brochu, C. Mascle, *Int. J. Adv. Manuf. Technol.* **103**, 1509 (2019)
101. Z. Hou, X. Tian, J. Zhang, D. Li, *Compos. Struct.* **184**, 1005 (2018)
102. G. Scordo, V. Bertana, A. Balesio, R. Carcione, S.L. Marasso, M. Cocuzza, C.F. Pirri, M. Manachino, M.G. Gomez, A. Vitale, A. Chiodoni, E. Tamburri, L. Scaltrito, *Nanomaterials* **11**, 1 (2021)
103. M. Eichenhofer, J.C.H. Wong, P. Ermanni, *Addit. Manuf.* **18**, 48 (2017)
104. X. Peng, X. Kuang, D.J. Roach, Y. Wang, C.M. Hamel, C. Lu, H.J. Qi, *Addit. Manuf.* **40**, 101911 (2021)
105. A. Hamidi, Y. Tadesse, *Compos. Struct.* **210**, 250 (2019)
106. K. von Petersdorff-Campen, Y. Hauswirth, J. Carpenter, A. Hagmann, S. Boës, M. S. Daners, D. Penner, and M. Meboldt, *Appl. Sci.* **8**, 1275 (2018).
107. P. Schaechtl, B. Schleich, S. Wartzack, *Appl. Sci.* **11**, 1 (2021)
108. W. Clower, M. J. Hartmann, J. B. Joffrion, and C. G. Wilson, *Addit. Manuf.* **32**, 101024 (2020).
109. Y. Zhuang, Y. Guo, J. Li, Y. Yu, K. Jiang, H. Zhang, S. Guo, *Int. J. Adv. Manuf. Technol.* **112**, 2211 (2021)
110. Y. Chen, Q. He, *Compos. Struct.* **236**, 111859 (2020)
111. C. Quan, B. Han, Z. Hou, Q. Zhang, X. Tian, T.J. Lu, *Compos. Part B Eng.* **187**, 107858 (2020)
112. R. Johnston, Z. Kazancı, *Addit. Manuf.* **38**, 101783 (2021)
113. Y. Jiang, J. Leng, J. Zhang, *Addit. Manuf.* **38**, 101718 (2021)
114. Q. Ge, A.H. Sakhaei, H. Lee, C.K. Dunn, N.X. Fang, M.L. Dunn, *Sci. Rep.* **6**, 1 (2016)
115. L. Boldrin, S. Hummel, F. Scarpa, D. Di Maio, C. Lira, M. Ruzzene, C.D.L. Remillat, T.C. Lim, R. Rajasekaran, S. Patsias, *Compos. Struct.* **149**, 114 (2016)
116. Z. Pei, Y. Xu, F. Wei, T. Liu, D. Su, *J. Magn. Magn. Mater.* **493**, 165742 (2020)

117. K. Dong, H. Ke, M. Panahi-Sarmad, T. Yang, X. Huang, X. Xiao, *Mater. Des.* **198**, 109303 (2021)
118. H. Ding, X. Zhang, Y. Liu, S. Ramakrishna, *Int. J. Adv. Manuf. Technol.* **105**, 4633 (2019)
119. S. K. Melly, L. Liu, Y. Liu, and J. Leng, *Smart Mater. Struct.* **29**, 083001 (2020).
120. W. Zhu, J. Li, Y.J. Leong, I. Rozen, X. Qu, R. Dong, Z. Wu, W. Gao, P.H. Chung, J. Wang, S. Chen, *Adv. Mater.* **27**, 4411 (2015)
121. H.Y. Jeong, B.H. Woo, N. Kim, Y.C. Jun, *Sci. Rep.* **10**, 1 (2020)
122. S. Micalizzi, A. Díaz Lantada, and C. De Maria, *Smart Mater. Struct.* **28**, 105025 (2019).
123. R. Tognato, A.R. Armiento, V. Bonfrate, R. Levato, J. Malda, M. Alini, D. Eglin, G. Giancane, T. Serra, *Adv. Funct. Mater.* **29**, 1 (2019)
124. D.K. Patel, A.H. Sakhaei, M. Layani, B. Zhang, Q. Ge, S. Magdassi, *Adv. Mater.* **29**, 1 (2017)
125. A. Ahmed, S. Arya, V. Gupta, H. Furukawa, A. Khosla, *Polymer (Guildf)*. **228**, 123926 (2021)
126. F. Momeni, J. Ni, *Engineering* **6**, 1035 (2020)
127. G. Sossou, F. Demoly, H. Belkebir, H.J. Qi, S. Gomes, G. Montavon, *Mater. Des.* **175**, 107798 (2019)
128. D. G. Shin, T. H. Kim, and D. E. Kim, *Int. J. Precis. Eng. Manuf. - Green Technol.* **4**, 349 (2017).
129. C. Yuan, T. Wang, M. L. Dunn, and H. J. Qi, *Int. J. Precis. Eng. Manuf. - Green Technol.* **4**, 281 (2017).
130. L. Chen, T. Cao, R. Wei, K. Tang, C. Xin, F. Jiang, J. Sun, *Mater. Sci. Eng. A* **772**, 138661 (2020)
131. Y. Li, Z. Feng, L. Hao, L. Huang, C. Xin, Y. Wang, E. Bilotti, K. Essa, H. Zhang, Z. Li, F. Yan, and T. Peijs, *Adv. Mater. Technol.* **5**, 1900981 (2020).
132. J. Martínez, J. Dumas, and S. Lefebvre, *ACM Trans. Graph.* **35**, 44 (2016).
133. S. Li, Y. Xin, Y. Yu, Y. Wang, *Mater. Des.* **204**, 109664 (2021)
134. S. Farook Jilani and K. K. Chand, in *Int. Conf. Recent Trends Mech. Eng.* (2015), pp. 122–127.
135. A. Pasko, V. Adzhiev, A. Sourin, V. Savchenko, *Vis. Comput.* **11**, 429 (1995)
136. Z. Wang, Y. Zhang, A. Bernard, *Addit. Manuf.* **41**, 101952 (2021)
137. S. J. P. Callens, D. C. Tourolle né Betts, R. Müller, and A. A. Zadpoor, *Acta Biomater.* **130**, 343 (2021).
138. A. Haleem, M. Javaid, A. Goyal, T. Khanam, *J. Ind. Integr. Manag.* **5**, 2050007 (2020)
139. S.J. Yeo, M.J. Oh, P.J. Yoo, *Adv. Mater.* **31**, 1 (2019)
140. D. Bhate, C.A. Penick, L.A. Ferry, C. Lee, *Designs* **3**, 1 (2019)
141. K. Wang, Y.H. Chang, Y.W. Chen, C. Zhang, B. Wang, *Mater. Des.* **67**, 159 (2015)
142. T. Li, Y. Chen, X. Hu, Y. Li, L. Wang, *Mater. Des.* **142**, 247 (2018)
143. F. Valjak and N. Bojčetić, *Proc. Int. Conf. Eng. Des. ICED 2019-Augus*, 689 (2019).
144. S. Yuan, S. Li, J. Zhu, Y. Tang, *Compos. Part B Eng.* **219**, 108903 (2021)
145. P. Kyratsis, K. Kakoulis, A.P. Markopoulos, *Machines* **8**, 5 (2020)
146. S. Junk and L. Burkart, in *Procedia CIRP* (100), 577 (2021).
147. R.R. Fernandes, N. van de Werken, P. Koirala, T. Yap, A.Y. Tamijani, M. Tehrani, *Addit. Manuf.* **44**, 102056 (2021)
148. T. Mikolajczyk, T. Malinowski, L. Moldovan, H. Fuwen, I. Ciobanu, and I. Ciobanu, in *Procedia Manuf.* (2019), pp. 22–28.
149. S. Paul, *Meas. J. Int. Meas. Confed.* **178**, 109320 (2021)
150. I. Echeta, B. Dutton, R.K. Leach, S. Piano, *Addit. Manuf.* **47**, 102301 (2021)
151. S. Vyavahare, S. Teraiya, D. Panghal, S. Kumar, *Rapid Prototyp. J.* **26**, 176 (2020)
152. J. Zhu, H. Zhou, C. Wang, L. Zhou, S. Yuan, W. Zhang, *Chinese J. Aeronaut.* **34**, 91 (2021)
153. M.P. Schmidt, L. Couret, C. Gout, C.B.W. Pedersen, *Struct. Multidiscip. Optim.* **62**, 3105 (2020)
154. Engineering.com, “Generative Design and Topology Optimization: In-Depth Look at the Two Latest...” <https://www.engineering.com/story/research-report-generative-design-and-topology-optimization-in-depth-look-at-the-two-latest?resid=826> (accessed Nov. 07, 2021)

155. M. Europe, "tOpos | Food4Rhino," 2021. <https://www.food4rhino.com/en/app/topos> (accessed Nov. 07, 2021).
156. D. M. E. and D. Group, TopOpt Compute, (2018).
156. D. M. E. and D. Group, TopOpt Compute, "TopOpt," 2018. <https://www.topopt.mek.dtu.dk/?q=node/11> (accessed Nov. 07, 2021).
157. R. University, "BESO2D." <https://www.rmit.edu.au/research/centres-collaborations/centre-for-innovative-structures-and-materials/software> (accessed Nov. 07, 2021).
158. D. D. Solutions, "FEMtools Products Overview," 2021 <https://www.femtools.com/products/index.htm> (accessed Nov. 07, 2021).
159. I. G. Stuttgart, "PERMAS-TOPO Topology Optimization," 2021. http://www.intes.de/kategorie_permas/modules/optimization/topology_optimization/ (accessed Nov. 07, 2021).
160. C. D.o.o., "CAESS Topology Optimization," 2021. <https://www.caess.eu/> (accessed Nov. 07, 2021).
161. L. University, "Division of Solid Mechanics," 2019. http://www.solid.iei.liu.se/Offered_services/Trinitas/index.html (accessed Nov. 07, 2021).
162. G. Liu, Y. Xiong, L. Zhou, Compos. Commun. **27**, 100907 (2021)
163. Y. Yamanaka, A. Todoroki, M. Ueda, Y. Hirano, R. Matsuzaki, Open. J. Compos. Mater. **06**, 121 (2016)
164. P. M. Bhatt, A. M. Kabir, R. K. Malhan, B. Shah, A. V. Shembekar, Y. J. Yoon, and S. K. Gupta, Proc. - IEEE Int. Conf. Robot. Autom. 20–24-May, 2019, Montreal, Canada, 2800 (2019).
165. M. Mohammadzadeh, A. Imeri, I. Fidan, M. Elkelany, Compos. Part B Eng. **175**, 107112 (2019)
166. R.W. Hedrick, R.J. Urbanic, C.G. Burford, IFAC-PapersOnLine **28**, 2327 (2015)
167. H. González, I. Arrizubieta, A. Calleja, J. E. Industry, I. Arrizubieta, A. Calleja, E. Ruiz, and A. Lamikiz, 1 (2017).
168. F. Bedrich, "7 Free STL Editors: How to Edit & Repair STL Files All3DP," 2021. <https://all3dp.com/1/7-free-stl-editors-edit-repair-stl-files/> (accessed Nov. 07, 2021).
169. ALL3DP, "Best Free 3D Printing Software in 2021 | All3DP," 02/09/2021, 2021. <https://all3dp.com/1/best-free-3d-printing-software-3d-printer-program/#uvtools> (accessed Nov. 07, 2021).
170. "SOLIDWORKS." <https://www.solidworks.com/es> (accessed Jan. 20, 2022).
171. "NX | Siemens Software." <https://www.plm.automation.siemens.com/global/es/products/nx/> (accessed Jan. 20, 2022).
172. "CAM Software | CNC Programming Software | CAMWorks." <https://camworks.com/> (accessed Jan. 20, 2022).
173. "Software CAM Creo | PTC." <https://www.ptc.com/es/technologies/cad/cam-software> (accessed Jan. 20, 2022).
174. "CAD CAM | Sistema de software | hyperMILL | OPEN MIND." <https://www.openmind-tech.com/es/cam/hypermill.html> (accessed Jan. 20, 2022).
175. E. Estakhrianhaghighi, A. Mirabolghasemi, Y. Zhang, L. Lessard, A. Akbarzadeh, Adv. Eng. Mater. **22**, 1 (2020)
176. P.F. Flowers, C. Reyes, S. Ye, M.J. Kim, B.J. Wiley, Addit. Manuf. **18**, 156 (2017)
177. J. Ren, J.Y. Yin, Materials (Basel). **11**, 1249 (2018)
178. J. Saroia, Y. Wang, Q. Wei, M. Lei, X. Li, Y. Guo, K. Zhang, Int. J. Adv. Manuf. Technol. **106**, 1695 (2020)
179. K. Ko, S. Jin, S.E. Lee, J.W. Hong, Compos. Struct. **238**, 111951 (2020)
180. Y. Xie, S. Ye, C. Reyes, P. Sithikong, B.I. Popa, B.J. Wiley, S.A. Cummer, Appl. Phys. Lett. **110**, 181903 (2017)
181. U. Hasni, R. Green, A.V. Filippas, E. Topsakal, Microw. Opt. Technol. Lett. **61**, 734 (2019)
182. N. Nguyen, E. Melamed, J.G. Park, S. Zhang, A. Hao, R. Liang, Macromol. Mater. Eng. **302**, 1700135 (2017)
183. J. Ahmed, in *3D and 4D Printing in Biomedical Applications: Process Engineering and Additive Manufacturing*, edited by M. Maniruzzaman. (Wiley, 2018), pp. 239–271.
184. P. Tran, T.D. Ngo, A. Ghazlan, D. Hui, Compos. Part B Eng. **108**, 210 (2017)
185. C. Zeng, L. Liu, W. Bian, J. Leng, Y. Liu, Compos. Struct. **262**, 113626 (2021)

186. K.S. Riley, K.J. Ang, K.A. Martin, W.K. Chan, J.A. Faber, A.F. Arrieta, *Mater. Des.* **194**, 108888 (2020)
187. D. Zhang, B. Chi, B. Li, Z. Gao, Y. Du, J. Guo, J. Wei, *Synth. Met.* **217**, 79 (2016)
188. Y.S. Cho, M. Quan, S.H. Lee, M.W. Hong, Y.Y. Kim, Y.S. Cho, *Compos. Sci. Technol.* **184**, 107844 (2019)
189. Y.S. Cho, M. Quan, N.U. Kang, H.J. Jeong, M.W. Hong, Y.Y. Kim, Y.S. Cho, *Eur. Polym. J.* **134**, 109814 (2020)
190. Y.S. Cho, H.K. Kim, M.S. Ghim, M.W. Hong, Y.Y. Kim, Y.S. Cho, *Polymers (Basel)*. **12**, 2193 (2020)
191. M. Spoerk, J. Sapkota, G. Weingrill, T. Fischinger, F. Arbeiter, C. Holzer, *Macromol. Mater. Eng.* **302**, 1700143 (2017)
192. H. Zhang, J. Chen, D. Yang, *Addit. Manuf.* **38**, 101775 (2021)
193. H. Zhang, D. Liu, T. Huang, Q. Hu, H. Lammer, *I.O.P. Conf. Ser. Mater. Sci. Eng.* **782**, 8 (2020)
194. H. Zhang, D. Liu, T. Huang, Q. Hu, H. Lammer, *Materials (Basel)*. **13**, 1678 (2020)
195. S. Liu, Y. Li, N. Li, *Mater. Des.* **137**, 235 (2018)
196. S. Waheed, J.M. Cabot, P. Smejkal, S. Farajikhah, S. Sayyar, P.C. Innis, S. Beirne, G. Barnsley, T.W. Lewis, M.C. Breadmore, B. Paull, A.C.S. Appl. Mater. Interfaces **11**, 4353 (2019)
197. A.E. Jakus, E.B. Secor, A.L. Rutz, S.W. Jordan, M.C. Hersam, R.N. Shah, *ACS Nano* **9**, 4636 (2015)
198. P. Lambin, A. Liubimau, D. Bychanok, L. Vitale, P. Kuzhir, *Polymers (Basel)*. **12**, 2892 (2020)
199. Z. Jia, L. Wang, *Acta Mater.* **173**, 61 (2019)
200. Z. Li, S. Jia, Z. Xiong, Q. Long, S. Yan, F. Hao, J. Liu, Z. Yuan, *J. Biosci. Bioeng.* **126**, 389 (2018)
201. D.J. Roach, X. Kuang, C. Yuan, K. Chen, H.J. Qi, *Smart Mater. Struct.* **27**, 125011 (2018)
202. D. Kokkinis, M. Schaffner, A.R. Studart, *Nat. Commun.* **6**, 8643 (2015)
203. A. Zocca, H. Elsayed, E. Bernardo, C.M. Gomes, M.A. Lopez-Heredia, C. Knabe, P. Colombo, *J. Günster, Biofabrication* **7**, 025008 (2015)
204. D. Kim, J.U. Lee, G.H. Kim, *Addit. Manuf.* **36**, 101616 (2020)
205. E.M. Gonçalves, F.J. Oliveira, R.F. Silva, M.A. Neto, M.H. Fernandes, M. Amaral, M. Vallet-Regí, M. Vila, *J. Biomed. Mater. Res. - Part B Appl. Biomater.* **104**, 1210 (2016)
206. F. Zhang, L. Wang, Z. Zheng, Y. Liu, J. Leng, *Compos. Part A Appl. Sci. Manuf.* **125**, 105571 (2019)
207. M.A. Wagner, J.L. Huang, P. Okle, J. Paik, R. Spolenak, *Mater. Des.* **191**, 108643 (2020)
208. H. Younes, R. Li, S. E. Lee, Y. K. Kim, and D. Choi, *Synth. Met.* **275**, 116731 (2021).
209. Y. L. Tsai, P. Theato, C. F. Huang, and S. hui Hsu, *Appl. Mater. Today* **20**, 100778 (2020).
210. J. Li, S. Rudykh, *Compos. Part B Eng.* **172**, 352 (2019)
211. M. Mohammadzadeh, A. Gupta, I. Fidan, *J. Compos. Mater.* **55**, 3629 (2021)
212. A. Gupta, I. Fidan, S. Hasanov, A. Nasirov, *Int. J. Adv. Manuf. Technol.* **107**, 3185 (2020)
213. G.D. Goh, Y.L. Yap, S. Agarwala, W.Y. Yeong, *Adv. Mater. Technol.* **4**, 1800271 (2019)
214. N. Li, G. Link, T. Wang, V. Ramopoulos, D. Neumaier, J. Hofele, M. Walter, J. Jelonnek, *Compos. Part B Eng.* **182**, 107612 (2020)
215. A.R. Prajapati, H.K. Dave, H.K. Raval, *Mater. Today Proc.* **44**, 2102 (2021)
216. P. Zhuo, S. Li, I.A. Ashcroft, A.I. Jones, *Compos. Part B Eng.* **224**, 109143 (2021)
217. M. Mohammadzadeh, I. Fidan, *J. Manuf. Mater. Process.* **5**, 68 (2021)
218. M. Mohammadzadeh and I. Fidan, in *TMS 2020 149th Annu. Meet. Exhib. Suppl. Proc. The Minerals, Metals & Materials Series.* (Springer, Cham, 2020), pp. 321–328.
219. C. Zeng, L. Liu, W. Bian, J. Leng, and Y. Liu, *Addit. Manuf.* **38**, 101842 (2021)
220. H. Shiratori, A. Todoroki, M. Ueda, R. Matsuzaki, Y. Hirano, *Adv. Compos. Mater.* **29**, 247 (2020)
221. J.U. Schmied, H. Le Ferrand, P. Ermanni, A.R. Studart, A.F. Arrieta, *Bioinspir. Biomim.* **12**, 026012 (2017)
222. Y. Cui, M. Santer, *Compos. Struct.* **137**, 93 (2016)

223. S.H. Lee, Y.S. Cho, M.W. Hong, B.K. Lee, Y. Park, S.H. Park, Y.Y. Kim, Y.S. Cho, *Biomed. Mater.* **12**, 055003 (2017)
224. R. Ariño, E. Álvarez, M. Rigdahl, *J. Appl. Polym. Sci.* **133**, 42897 (2016)
225. G. Siqueira, D. Kokkinis, R. Libanori, M.K. Hausmann, A.S. Gladman, A. Neels, P. Tingaut, T. Zimmermann, J.A. Lewis, A.R. Studart, *Adv. Funct. Mater.* **27**, 1604619 (2017)
226. Q. Chen, P.F. Cao, R.C. Advincula, *Adv. Funct. Mater.* **28**, 1800631 (2018)
227. L.A.E. Müller, T. Zimmermann, G. Nyström, I. Burgert, G. Siqueira, *Adv. Funct. Mater.* **30**, 2002914 (2020)
228. C.B. Highley, C.B. Rodell, J.A. Burdick, *Adv. Mater.* **27**, 5075 (2015)
229. S. Das, F. Pati, Y.J. Choi, G. Rijal, J.H. Shim, S.W. Kim, A.R. Ray, D.W. Cho, S. Ghosh, *Acta Biomater.* **11**, 233 (2015)
230. J.H. Shim, J.Y. Kim, M. Park, J. Park, D.W. Cho, *Biofabrication* **3**, 034102 (2011)
231. L.Y. Zhou, J. Fu, Y. He, *Adv. Funct. Mater.* **30**, 2000187 (2020)
232. S. Deng, J. Wu, M.D. Dickey, Q. Zhao, T. Xie, *Adv. Mater.* **31**, 1903970 (2019)
233. M. Pagac, J. Hajnys, Q.P. Ma, L. Jancar, J. Jansa, P. Stefek, J. Mesicek, *Polymers (Basel)*. **13**, 1 (2021)
234. D. Lin, S. Jin, F. Zhang, C. Wang, Y. Wang, C. Zhou, G.J. Cheng, *Nanotechnology* **26**, 434003 (2015)
235. P. Robles-Martinez, X. Xu, S.J. Trenfield, A. Awad, A. Goyanes, R. Telford, A.W. Basit, S. Gaisford, *Pharmaceutics* **11**, 274 (2019)
236. K. Markandan, C.Q. Lai, *Compos. Part A Appl. Sci. Manuf.* **129**, 105726 (2020)
237. A. Chiappone, I. Roppolo, E. Naretto, E. Fantino, F. Calignano, M. Sangermano, F. Pirri, *Compos. Part B Eng.* **124**, 9 (2017)
238. J. Bustillos, D. Montero-Zambrano, A. Loganathan, B. Boesl, A. Agarwal, *Polym. Compos.* **40**, 379 (2019)
239. P. Makvandi, C. Esposito Corcione, F. Paladini, A. L. Gallo, F. Montagna, R. Jamaledin, M. Pollini, and A. Maffezzoli, *Polym. Adv. Technol.* **29**, 364 (2018).
240. J. Wang, N. Dai, C. Jiang, X. Mu, B. Zhang, Q. Ge, D. Wang, *Mater. Des.* **198**, 109381 (2021)
241. J. Tao, J. Zhang, T. Du, X. Xu, X. Deng, S. Chen, J. Liu, Y. Chen, X. Liu, M. Xiong, Y. Luo, H. Cheng, J. Mao, L. Cardon, M. Gou, Y. Wei, *Acta Biomater.* **90**, 49 (2019)
242. Q. Mu, L. Wang, C.K. Dunn, X. Kuang, F. Duan, Z. Zhang, H.J. Qi, T. Wang, *Addit. Manuf.* **18**, 74 (2017)
243. M. Wang, C. Xie, R. He, G. Ding, K. Zhang, G. Wang, D. Fang, *J. Am. Ceram. Soc.* **102**, 5117 (2019)
244. X. Wang, W. Guo, R. Abu-reziq, S. Magdassi, *Catalysts* **10**, 840 (2020)
245. M.R. O'Neill, E. Acome, S. Bakarich, S.K. Mitchell, J. Timko, C. Keplinger, R.F. Shepherd, *Adv. Funct. Mater.* **30**, 2005244 (2020)
246. Y. Jiang, Q. Wang, *Sci. Rep.* **6**, 34147 (2016)
247. C. Zhou, H. Ye, F. Zhang, *J. Comput. Inf. Sci. Eng.* **15**, 011003 (2015)
248. E. Pullicino, W. Zou, M. Gresil, C. Soutis, *Appl. Compos. Mater.* **24**, 301 (2017)
249. I. M.-G. Helena Varela-Rizo, Iluminada Rodriguez-Pastor, *J. Appl. Polym. Sci.* **116**, 2658 (2010).
250. S.H. Dickens, B.H. Cho, *Dent. Mater.* **21**, 354 (2005)
251. Q.A. Poutrel, Z. Wang, D. Wang, C. Soutis, M. Gresil, *Appl. Compos. Mater.* **24**, 313 (2017)
252. S.L. Sherman, O. Kadioglu, G.F. Currier, J.P. Kierl, J. Li, *Am. J. Orthod. Dentofac. Orthop.* **157**, 422 (2020)
253. X. Ding, R. Jia, Z. Gan, Y. Du, D. Wang, X. Xu, *Mater. Res. Express* **7**, 055304 (2020)
254. G. González, D. Baruffaldi, C. Martinengo, A. Angelini, A. Chiappone, I. Roppolo, C.F. Pirri, F. Frascella, *Nanomaterials* **10**, 1788 (2020)
255. S. Zakeri, M. Vippola, E. Levänen, *Addit. Manuf.* **35**, 101177 (2020)
256. E. Fantino, A. Chiappone, I. Roppolo, D. Manfredi, R. Bongiovanni, C.F. Pirri, F. Calignano, *Adv. Mater.* **28**, 3712 (2016)
257. L.C. Geng, X.L. Ruan, W.W. Wu, R. Xia, D.N. Fang, *Exp. Mech.* **59**, 913 (2019)
258. H. Mazhar, T. Osswald, D. Negrut, *Addit. Manuf.* **12**, 291 (2016)

259. S. Yuan, F. Shen, J. Bai, C.K. Chua, J. Wei, K. Zhou, *Mater. Des.* **120**, 317 (2017)
260. N. Bâlc, C. Vilău, *MATEC Web Conf.* **121**, 04002 (2017)
261. T. Kumaresan, R. Gandhinathan, M. Ramu, M. Ananthasubramanian, K.B. Pradheepa, J. Mech. Sci. Technol. **30**, 5305 (2016)
262. A. Ronca, G. Rollo, P. Cerruti, G. Fei, X. Gan, G.G. Buonocore, M. Lavorgna, H. Xia, C. Silvestre, L. Ambrosio, *Appl. Sci.* **9**, 864 (2019)
263. S.H. Diermann, M. Lu, M. Dargusch, L. Grøndahl, H. Huang, J. Biomed. Mater. Res. - Part B Appl. Biomater. **107**, 2596 (2019)
264. X. Gan, J. Wang, Z. Wang, Z. Zheng, M. Lavorgna, A. Ronca, G. Fei, H. Xia, *Mater. Des.* **178**, 107874 (2019)
265. E. Zanchetta, M. Cattaldo, G. Franchin, M. Schwentenwein, J. Homa, G. Brusatin, P. Colombo, *Adv. Mater.* **28**, 370 (2016)
266. S.H. Diermann, M. Lu, Y. Zhao, L.J. Vandi, M. Dargusch, H. Huang, J. Mech. Behav. Biomed. Mater. **84**, 151 (2018)
267. S.H. Diermann, M. Lu, G. Edwards, M. Dargusch, H. Huang, J. Biomed. Mater. Res. - Part A **107**, 154 (2019)
268. A. Zocca, P. Colombo, C.M. Gomes, J. Günster, *J. Am. Ceram. Soc.* **98**, 1983 (2015)
269. S. Kholghi Eshkalak, A. Chinnappan, W. A. D. M. Jayathilaka, M. Khatibzadeh, E. Kowsari, and S. Ramakrishna, *Appl. Mater. Today* **9**, 372 (2017).
270. R. Tao, L. Ji, Y. Li, Z. Wan, W. Hu, W. Wu, B. Liao, L. Ma, D. Fang, *Compos. Part B Eng.* **201**, 108344 (2020)
271. C.X. Liu, Y.J. Zhang, Y. Li, *Smart Mater. Struct.* **28**, 095020 (2019)
272. M. Kyobula, A. Adedeji, M.R. Alexander, E. Saleh, R. Wildman, I. Ashcroft, P.R. Gellert, C.J. Roberts, *J. Control. Release* **261**, 207 (2017)
273. A. Adeyeye, A. Eid, J. Hester, S.A. Nauroze, B. Tehrani, Y. Cui, M.M. Tentzeris, *Int. J. High Speed Electron. Syst.* **28**, 1940016 (2019)
274. G. Cai, S. Park, X. Cheng, A.L.S. Eh, P.S. Lee, *Sci. Technol. Adv. Mater.* **19**, 759 (2018)
275. H. Zhang, T. Qi, X. Zhu, L. Zhou, Z. Li, Y.F. Zhang, W. Yang, J. Yang, Z. Peng, G. Zhang, F. Wang, P. Guo, H. Lan, *A.C.S. Appl. Mater. Interfaces* **13**, 36295 (2021)
276. Y.F. Zhang, Z. Li, H. Li, H. Li, Y. Xiong, X. Zhu, H. Lan, Q. Ge, *A.C.S. Appl. Mater. Interfaces* **13**, 41414 (2021)
277. X. Zhu, M. Liu, X. Qi, H. Li, Y.F. Zhang, Z. Li, Z. Peng, J. Yang, L. Qian, Q. Xu, N. Gou, J. He, D. Li, H. Lan, *Adv. Mater.* **33**, 1 (2021)
278. X. Zhu, Q. Xu, H. Li, M. Liu, Z. Li, K. Yang, J. Zhao, L. Qian, Z. Peng, G. Zhang, J. Yang, F. Wang, D. Li, H. Lan, *Adv. Mater.* **31**, 2007772 (2019)
279. D. Zindani, K. Kumar, *Int. J. Light. Mater. Manuf.* **2**, 267 (2019)
280. G. Rasiya, A. Shukla, K. Saran, *Mater. Today Proc.* **47**, 6896 (2021)
281. I. Gibson, D. Rosen, B. Stucker, and M. Khorasani, in *Additive Manufacturing Technologies*, Third ed. (Springer, Cham, 2021), pp. 253–283.
282. D.X. Luong, A.K. Subramanian, G.A.L. Silva, J. Yoon, S. Cofer, K. Yang, P.S. Owuor, T. Wang, Z. Wang, J. Lou, P.M. Ajayan, J.M. Tour, *Adv. Mater.* **30**, 1707416 (2018)
283. B. Chang, P. Parandoush, X. Li, S. Ruan, C. Shen, R.A. Behnagh, Y. Liu, D. Lin, *Polym. Compos.* **41**, 4706 (2020)
284. P. Parandoush, C. Zhou, D. Lin, *Adv. Eng. Mater.* **21**, 1800622 (2018)
285. Y. Tao, Q. Yin, P. Li, *Polymers (Basel)*. **13**, 144 (2021)
286. P. M. Bhatt, M. Peralta, H. A. Bruck, and S. K. Gupta, in *Proceedings of the ASME 2018 13th Int. Manuf. Sci. Eng. Conf. Volume 1: Additive Manufacturing; Bio and Sustainable Manufacturing*. College Station, Texas, USA. June 18–22, 2018. V001T01A012. ASME
287. A.M. Cakmak, S. Unal, A. Sahin, F.N. Oktar, M. Sengor, N. Ekren, O. Gunduz, D.M. Kalaskar, *Polymers (Basel)*. **12**, 1962 (2020)
288. X.P. Tan, Y.J. Tan, C.S.L. Chow, S.B. Tor, W.Y. Yeong, *Mater. Sci. Eng. C* **76**, 1328 (2017)
289. M. Hassan, K. Dave, R. Chandrawati, F. Dehghani, V.G. Gomes, *Eur. Polym. J.* **121**, 109340 (2019)

290. C. Wang, W. Huang, Y. Zhou, L. He, Z. He, Z. Chen, X. He, S. Tian, J. Liao, B. Lu, Y. Wei, M. Wang, *Bioact. Mater.* **5**, 82 (2020)
291. L. E. Rojas-Martínez, C. G. Flores-Hernandez, L. M. López-Marín, A. L. Martínez-Hernandez, S. B. Thorat, C. D. Reyes Vasquez, A. E. Del Rio-Castillo, and C. Velasco-Santos, *Eur. Polym. J.* **141**, 110088 (2020).
292. N. Nguyen, A. Hao, J.G. Park, R. Liang, *Adv. Eng. Mater.* **18**, 1906 (2016)
293. Q. Zhang, F. Zhang, S.P. Medarametla, H. Li, C. Zhou, D. Lin, *Small* **12**, 1702 (2016)
294. L.M. Bollig, M.V. Patton, G.S. Mowry, B.B. Nelson-Cheeseman, *IEEE Trans. Magn.* **53**, 2300806 (2017)
295. R. Matsuzaki, M. Ueda, M. Namiki, T.K. Jeong, H. Asahara, K. Horiguchi, T. Nakamura, A. Todoroki, Y. Hirano, *Sci. Rep.* **6**, 23058 (2016)
296. Q. Wu, L. Ma, L. Wu, J. Xiong, *Compos. Struct.* **153**, 585 (2016)
297. H.Z. Jishi, R. Umer, W.J. Cantwell, *Mater. Des.* **91**, 286 (2016)
298. J.J. Martin, B.E. Fiore, R.M. Erb, *Nat. Commun.* **6**, 86641 (2015)
299. I. Cooperstein, M. Layani, S. Magdassi, *J. Mater. Chem. C* **3**, 2040 (2015)
300. J.O. Hardin, T.J. Ober, A.D. Valentine, J.A. Lewis, *Adv. Mater.* **27**, 3279 (2015)
301. E. MacDonald and R. Wicker, *Science* **353**, aaf2093–1 (2016).
302. Q. Mu, C.K. Dunn, L. Wang, M.L. Dunn, H.J. Qi, T. Wang, *Smart Mater. Struct.* **26**, 045008 (2017)
303. Y.H. Tan, R. Siddall, M. Kovac, *I.E.E.E. Robot. Autom. Lett.* **2**, 1304 (2017)
304. D. Zhang, G. Pan, L. Chao, and G. Yan, *Mod. Phys. Lett. B* **32**, (2018).
305. Y. Li, B. An, S. Jiang, J. Gao, Y. Chen, S. Pan, *Opt. Express* **23**, 17607 (2015)
306. A. Pentek, M. Nyitrai, A. Schiffer, H. Abraham, M. Bene, E. Molnar, R. Told, P. Maroti, *Crystals* **10**, 398 (2020)
307. Y. Mao, K. Yu, M. S. Isakov, J. Wu, M. L. Dunn, and H. Jerry Qi, *Sci. Rep.* **5**, 13616 (2015).
308. J. Wu, C. Yuan, Z. Ding, M. Isakov, Y. Mao, T. Wang, M.L. Dunn, H.J. Qi, *Sci. Rep.* **6**, 24224 (2016)

Eco/Friendly Polymer-Based Composites for Nuclear Shielding Applications



F. Akman, H. Ogul, M. R. Kaçal, H. Polat, K. Dilsiz, and O. Agar

Abstract In the last few decades, the challenges of ionizing radiation shielding have begun gaining attention of investigators in order to minimize the harmful effects of various radiations especially on workers who are interested in the outcome of a nuclear or radiological situation that requires protection. In this context, the presented chapter focuses on the shielding preparation, materials design, photon, and neutron shielding performances of polymer-based composites doped with bismuth nitrate in different weight ratios. Here, the photon attenuation behavior of the prepared composites is determined using a gamma spectrometer equipped with High Purity Germanium (HPGe) detector that covers a wide energy range varying from 0.060 to 1.408 MeV. Besides, the obtained experimental data are further compared with the results of theoretical (WinXCOM software) and Monte Carlo simulation (GEANT4). In addition, the fast neutron mass removal cross sections and the numbers of transmitted neutrons at different thickness and neutron energies are estimated with the

F. Akman (✉)

Vocational School of Social Sciences, Department of Property Protection and Security, Program of Occupational Health and Safety, Bingöl University, 12000 Bingöl, Türkiye
e-mail: fakman@bingol.edu.tr

Central Laboratory Application and Research Center, Bingöl University, 12000 Bingöl, Türkiye

H. Ogul

Department of Nuclear Engineering, Faculty of Engineering and Architecture, Sinop University, Sinop, Türkiye

Department of Physics and Astronomy, Faculty of Science, University of Iowa, Iowa City, IA, USA

M. R. Kaçal

Faculty of Arts and Sciences, Department of Physics, Giresun University, 28100 Giresun, Türkiye

H. Polat

Vocational School of Technical Sciences, Department of Architecture and Urban Planning, Bingöl University, 12000 Bingöl, Türkiye

K. Dilsiz

Faculty of Art and Science, Department of Physics, Bingöl University, 12000 Bingöl, Türkiye

O. Agar

Department of Physics, Karamanoğlu Mehmetbey University, Karaman, Türkiye

use of GEANT4 simulations by coding the elemental compositions of the fabricated composites. The results showed that the gamma attenuation was improved with the increase of BiNO dopant amount. Among the prepared samples, the sample with 20% BiNO concentration was found to be the best radiation shielding material. In addition to being used for the ionizing radiation shielding, such polyester composites can also be used as shielding absorbers for the low-energy ionizing radiation. In short, it is expected that the researchers and scientists in the fields of nuclear and medical physics will benefit from this chapter.

Keywords Gamma rays · Neutrons · Radiation shielding · GEANT4 · HPGc detector · WinXCOM

1 Introduction

Electromagnetic radiation is the form of waves or particles which makes the propagation or transmission of energy through the space or matter. Depending on its frequency or wavelength, it is classified into two stages namely ionizing and non-ionizing radiations. Whereas non-ionizing radiation does not ionize or excite the atoms, ionizing radiation can be absorbed and scattered by giving its energy to atoms of the interacting matter. In this study, high energetic ionizing radiation has been handled with a broad perspective because of its undesirable impacts on human and environment.

Ionizing radiations such as X- and gamma rays are emitted by excited or naturally radioactive nuclei which decay from upper to lower energy states [1, 2]. In addition, neutrons can be produced copiously in nuclear fission and fusion or from other nuclear reactions such as radioactive decay. These radiations have enough energy to release in any medium. The released photons can be widely used in various fields of our daily life for different applications. Especially, new health technologies and medical apparatuses utilizing ionizing radiation have led to major improvements in the diagnosis and treatment of diseases. The rising number of radiation facilities at institutes and hospitals, especially diagnostics and radiotherapy departments, and implementation of high energetic photons in patients' care can cause vital risks for both workers and electronic devices in the environment [3, 4]. Thus, the harmful impact of radiation increases on the human cells [5, 6], and the exposure to high radiation dosage badly affects the lifetime of the electronic devices that are used in these departments [7]. In addition, the exposure to high radiation dosage damages the mechanism of these electronics. In order to protect the human body and the environment from the possible damages, there are three well-known principal ways that must be taken into account, which are; shortening the duration time in the radiation environment, maximizing the distance to the radiation source, and the use of a shielding material that absorbs the radiation. Here it should be noticed that the amount of radiation received is directly proportional with the exposure time and inversely proportional with the square of the distance to the radiation source. Therefore, the exposure time should be short as much as possible, while the distance

to the radiation source must be long as much as possible. On the other hand, the last and most effective way used for radiation protection is the radiation absorber/attenuator that has a suitable thickness and material [8].

The shielding of any radiation source is considered as the most effective technique relative to time and distance. Therefore, lead (Pb) and thick concrete conventional absorbers—with high Z atomic number and density respectively—are quite appropriate to attenuate radiation intensities to the desired low an allowable radiation level. Even though the Pb or Pb-doped materials are often used for radiation shielding due to their capability on radiation attenuation, it should not be ignored that such materials have a crucial drawback such as their environmental toxicity. Besides, more disadvantages could be further listed as high cost, fragility, difficulties in manufacturing and heaviness for storage and difficulties in product transportation [9].

During the last decades, numerous studies on the utilization of various shielding materials such as glasses [10, 11], concretes [12, 13], some alloys [14–16], poly boron [17], ceramics [18], and various ores [19] have been reported using experimental, theoretical, and simulation techniques. Due to a number of advantages provided with the use of polymers, many research groups have attempted to develop different fillers to reinforce polymer composites as an effective shielding material that could replace with Pb [20–26]. It is a well-known fact that polymers offer various advantages such as low cost, low density, easiness to manufacture as well as practical for transportation from one point to others. Here, the polymer composite could be described as a combination of a variety of chemicals bonded with a matrix material that presents better features than the individual components. Hence, the utilization of polymer-based composites with excellent characteristics has been paid attention recently. The obtained results of previous published studies will be discussed in Sect. 2.

Micro content fabrication is a promising method to produce better radiation shielding materials as desired. Therefore, this research focuses on gamma and neutron radiation shielding performances of polymer composites incorporated with Bismuth (III) nitrate pentahydrate (BiNO) filler. The mass attenuation coefficients of pure and micro-BiNO doped composites have been estimated at different gamma energies varying from 0.060 to 1.408 meV using HPGc scintillation detector-based gamma spectrometer, as well as WinXCOM software and GEANT4 computer simulation code. Besides, fast neutron removal cross section values of the investigated composites have been calculated through the simulation code. The hypothesis of the present study is that the increasing of BiNO filler content should be proportional to a synergistic effect on nuclear-radiation shielding effectiveness. Thus, outcomes of all the shielding quantities are discussed with regard to increased BiNO filler content in polymer composites.

The gamma and neutron shielding properties of polyester resin-based composites reinforced with bismuth nitrate pentahydrate have not been studied before. In this study, the measurements were conducted at twenty-two different energies ranging from 0.060 to 1.408 meV to evaluate the gamma radiation attenuation properties of polyester-based composites reinforced with different weight ratios of $\text{Bi}(\text{NO}_3)_3 \cdot 5\text{H}_2\text{O}$. In this context, the parameters such as radiation protection efficiency, transmission factor, mass attenuation coefficient, linear attenuation coefficient, half value

layer, tenth value layer, mean free path, effective atomic number, and effective electron density were calculated to evaluate the gamma radiation shielding effect of the prepared polyester material. In order to evaluate the neutron attenuation characteristics of these composites, neutron mass removal cross sections and neutron transmissions in different thicknesses and energies were calculated using the GEANT4 simulation code.

2 Literature Review of Polymer Based Shielding Composites

Lead-based materials have been used for years, especially for the shielding of gamma rays, due to their cost and ease of processing. The preference for these materials is declining due to the known significant toxicity issue of lead, and it is a known fact that anyone working in the production, use, transportation, protection, or disposal of lead-containing materials is at risk. Therefore, in the field of radiation shielding applications, there have been significant efforts to search for alternative materials instead of lead-based materials. The researchers investigated many materials up to now, such as concrete, alloy, ceramic, glass, and soil in terms of radiation shielding using experimental, theoretical, or simulation techniques. It might be eventually concluded that some of these might be used as alternative shielding materials. It is expected that possible new alternative shielding materials have good properties such as cost, lightness, and durability. In recent years, the use and research of the composite materials have gained attention since the amount of material components can be adjusted as desired. Therefore, composite materials are thought to be a good alternative to lead-based shielding materials; therefore, studies on composites in the field of radiation shielding have accelerated, and the literatures on radiation shielding have gained momentum.

Akman et al. [27], for example, investigated the photon and neutron attenuation characteristics of BiBr_3 and PbSO_4 doped composites. They observed that the gamma attenuation properties of composites were increased with the increase of the dopant ratio, while their neutron attenuation properties were decreased. On another reported work, Yilmaz et al. [28] have developed an elastic composite material with silicone rubber base and doped with bismuth oxide and hexagonal boron nitride for use in attenuating both neutron and gamma rays and they managed to reduce 84.1% of the gamma radiation and 65.8% of the neutron radiation with those materials. Radiation shielding parameters such as linear and mass attenuation coefficients, half value layer, mean free path, tenth value layer, effective atomic number, and effective electron density were investigated by Kaçal et al. [29] for composites composed of unsaturated resin and different proportions of Li_2WO_4 in the photon energy range of 59.5–1408.0 keV. Besides, El-Khatib et al. [30] studied the neutron shielding properties of composites consisting of micro or nano-sized cadmium oxide and high-density polyethylene polymers and observed that the fast neutron fractions transmitted in

nanostructured composites was less. Akman et al. [31] investigated the gamma radiation attenuation properties of polyester composites with different ratios of CdTe at different photon energies varying from 59.5 to 1408.0 keV and noted that the gamma radiation attenuation properties of the material improved with increasing CdTe ratio. Alduhaibat et al. [32] determined the radiation shielding behavior of Fe₂O₃ and Al₂O₃ reinforced epoxy composites at 0.662, 1.173, and 1.333 MeV energies and reported that their radiation shielding properties were improved compared to unreinforced epoxy. Kalkornsuranee et al. [33] investigated the gamma radiation shielding properties of composites made of natural rubber, PbO, and Bi₂O₃ materials in the energy range of 223–662 keV and noted that the shielding properties of reinforced composites with respect to natural rubber improved. Gamma, X-ray, and neutron attenuation characteristics of composites obtained using open-cell aluminum foams with different pore sizes, epoxy resin and different compounds were investigated by Araz et al. [34]. They suggested that composites produced with WO₃ and Bi₂O₃ could be an alternative shielding material. More et al. [35] conducted a comprehensive literature study on polymers and composites containing polymers. For the presented materials, extensive data has been collected on their ability to attenuate gamma radiation and fast neutrons. Nunez-Briones et al. [36] investigated the X-ray attenuation characteristics of composites based on plasticized polyvinyl chloride and reinforced with bismuth (iii) oxide using X-ray tube in the voltage range 20–61 kV, and they reported that there is almost complete absorption for 50% Bi₂O₃ doped composite at 61 kV. Akman et al. [37] obtained the gamma radiation and electromagnetic shielding characteristics of FeCr reinforced and unsaturated polyester resin-based composites. Although they observed that the 15% FeCr doped composite had good gamma radiation attenuation properties, the 10% FeCr reinforced composite had good electromagnetic shielding properties. Quan et al. [38] determined the half value layer in the energy range of 33–118 keV to evaluate the X-ray attenuation characteristics of the composite consisting of ultrahigh molecular weight polyethylene (UHMWPE), polyester mesh (PM), cellulose nanofiber (CNF), and bismuth nanoparticles (nBi), and they noted that the composite is a good material for shielding low intensity X-rays. Kalkornsurapranee et al. [39] determined many shielding parameters to study the X- and γ -rays attenuation behavior of natural rubber-based composites reinforced with BaCO₃, Bi₂O₃ and BaSO₄. They reported that the produced composites are a better shielding material than commercial shielding materials such as window, serpentine, hematite, and ordinary concrete, and among the produced composites, the one reinforced with Bi₂O₃ is the best shielding material.

El-Khatib et al. [40] experimentally and theoretically investigated the radiation shielding properties of composite materials consisting of natural rubber, N220 block, and lead powder, and reported that the radiation shielding properties of composites increased with increasing Pb amount, especially at low energies. Adliene et al. [41] produced WO₃ and Na₂WO₄ doped composites containing polydimethylsiloxane, and Ta and Ta₂O₅ doped composites containing universal silicone and they investigated their X-ray attenuation properties. They reported that the composite containing 50% Ta or Ta₂O₅ could be used instead of lead in medical radiation shielding. Nikbin

et al. [42] investigated the effect of temperature on the radiations shielding properties of cement composites containing different proportions of nano-sized Bi_2O_3 and noted that there was a slight improvement in radiation shielding properties with increasing temperature. New hybrid composites were prepared by Zegaoui et al. [43] by compressing short glass/basalt hybrid fibers into both bisphend-A based dicyanate ester and benzoxazine resin mixtures and reported that they would be excellent radiation shielding materials. Cao et al. [44] investigated the gamma shielding physical and mechanical properties of composites, which they obtained using the fast ultraviolet curing method, made of poly methyl methacrylate and bismuth trioxide and they observed that with increasing bismuth trioxide ratio, gamma radiation shielding properties increased. Kaçal et al. [45] obtained various gamma attenuation characteristics of zinc doped polyester composites experimentally with the help of HPGe detector and theoretically using WinXCOM and MCNPX programs, and they reported that their shielding properties improved depending on the increasing amount of zinc. Turhan et al. [46] experimentally and theoretically determined parameters such as transmission factor, mass and linear attenuation coefficients, effective atomic number, exposure build-up factor, and energy absorption build-up factor to investigate the gamma radiation shielding properties of hematite-added polymer composites. They observed that the shielding properties deteriorated with increasing energy, but the shielding properties improved with the increasing amount of additives. The ionizing radiation shielding properties of polymer composites doped in different proportions with BaTiO_3 and CaWO_4 compounds were investigated by Akman et al. [47] at twenty-two different energies in the energy range of 59.5–1408.0 keV. It was observed that there was good agreement between the parameters determined both theoretically and experimentally and they noted that CaWO_4 doped composites would be better shielding material than the other. Ahmed et al. [48] produced silicon-based composites containing different proportions of tungsten and investigated their gamma radiation attenuation behavior. They reported 3.5% better shielding properties than commercially blended silicone/tungsten composite for 88.1% tungsten doped composite. Akman et al. [49] obtained many parameters such as mass attenuation coefficient, effective atomic number, and half value layer in the energy range of 59.5–1408.0 keV to investigate the radiation shielding properties of PbI_2 doped polyester composites and reported that the shielding properties improved with increasing the doping ratio. Olukotun et al. [50] calculated the gamma radiation shielding parameters of some clay-polyethylene composites containing recycled low-density polyethylene (LDPE) using the Monte Carlo simulation code, XCOM program, and Phy-X/PDS software in the energy range of 0.1–15 meV and they observed that as the LDPE ratio decreased and the clay ratio increased, the shielding properties improved. Körpınar et al. [51] tested the radiation shielding properties of composites made of poly (hydroxyethyl methacrylate-co-styrene) and WO_3 at 662, 1173, and 1332 keV photon energies, and they observed that the radiation shielding properties increased with the increasing amount of WO_3 . The gamma shielding attenuation characteristics of undoped and PbCl_2 -doped polyester composites were investigated by Özkalaycı et al. [52] at twenty-two different energies ($59.5 \leq E \leq 1408.0$ keV), and they reported that 20% PbCl_2 -doped composite showed 244% higher radiation shielding

efficiency than the undoped composite. Li et al. [53] produced a series of composites consisting of natural leather, La_2O_3 and Bi_2O_3 nanoparticles and studied their X-ray radiation shielding properties in the energy range of 20–120 keV. They noticed that composites have X-ray shielding capabilities between 10 and 65%. Intom et al. [54] investigated the radiation shielding properties of composites made of natural rubber and Bi_2O_3 using the Compton scattering technique and observed that the half value layer values decreased with increasing Bi_2O_3 concentration. As functional waves, paraffin and lead tungstate phase-shifting microcapsules and silicone rubber base composites were produced by Lau et al. [55], and they investigated their thermal, mechanical, and gamma radiation shielding characteristics. They reported that the shielding properties increased due to the increasing microcapsules in the composites. Sharma et al. [56] investigated the gamma radiation attenuation properties of polyester-based and BiClO reinforced composites with the use of experimental, theoretical, and simulation methods. They reported that the shielding feature improved depending on increasing BiClO ratio. Körpınar et al. [57] determined the gamma radiation shielding characteristics of composites reinforced with 10–50% tungsten (IV) oxide and poly (hydroxyethyl methacrylate) with a NaI(Tl) detector at 662, 1172, and 1332 keV energies. They noticed that the composite with 50% WO_3 content had the best shielding properties. Tekin et al. [58] investigated the gamma radiation attenuation behavior of lightweight composites produced using $\text{Na}_3\text{PO}_4 \cdot 12\text{WO}_3 \cdot \text{H}_2\text{O}$ and unsaturated polyester using experimental, theoretical, and simulation code. They noticed that there was good agreement between the experimental and theoretical results and the shielding properties improved with increasing the amount of doping. The gamma-ray attenuation characteristics of nine different polycarbonate-based composites reinforced with $\text{Bi}(\text{NO}_3)_3 \cdot 5\text{H}_2\text{O}$ (0.1 and 5% by weight) were evaluated by Mirji and Lobo [59] in the energy range of 303–1332 keV, and they reported that the shielding property increased with increasing doping ratio. El-Toony et al. [60] determined the shielding parameters to determine the gamma-ray attenuation properties of polyvinyl ester based and Pb_2O_3 nanoparticle doped composites. They reported that 86% shielding was achieved at photon energy of 662 keV. Tekin et al. [61] investigated the gamma radiation shielding characteristics of iron-reinforced and unsaturated polyester-based composites in different proportions with the help of experimental, theoretical, and simulation codes as well as charged particle interactions parameters, and neutron attenuation behaviors. They observed that the best composite was 20% Fe doped composite for charged particle, and gamma radiation attenuation characteristics, while 5% Fe doped composite had the best neutron attenuation.

El-Khatib et al. [62] investigated the gamma radiation properties of composites composed of nano and micro-sized cadmium oxide and high-density polyethylene in the energy range of 59.53–1408.01 keV and reported that nano-doped composites have better radiation shielding properties than micro-doped composites. Çağlar et al. [63] evaluated the gamma radiation shielding properties of $\text{Na}_2\text{Si}_3\text{O}_7/\text{BaO}$ composites with the aid of experimental, simulation code and WinXCOM program and observed that the gamma radiation shielding properties increased with increasing

amount of BaO. The composites consisting of different concentrations of high-density polyethylene (HDPE), borax, sand, and Portland cement were produced by Elwahab et al. [64] and investigated their neutron and gamma radiation attenuation properties. They observed that the composite consisting of 12.5% HDPE, 37.5% borax, 25% cement, and 25% sand had the highest neutron and gamma radiation attenuation properties. Muthamma et al. [65] produced poly (vinyl alcohol) based composites reinforced with bismuth oxide in different proportions between 10 and 50% and investigated their X- and γ -rays attenuation characteristics. They observed that the shielding properties increased with the increase of bismuth oxide ratio. Alavin and Tavakol-Anbaran [66] investigated the effect of particle size on gamma radiation shielding properties of composites containing different sizes of tungsten and light-density polyethylene-based composite materials. According to the calculated results with the simulation code, they reported that the gamma shielding properties improved with the decrease of the particle size and the increase of the dopant ratio.

Abunahel et al. [67] evaluated the X-ray attenuation feature of composites made of Bi_2O_3 and epoxy polyvinyl alcohol (PVA) at a voltage range of 23–100 kV, and suggested that composites with more than 12% additives can be used as radiation shields at 23 and 35 kV. Atashi et al. [3] produced composites obtained by mixing silicon rubber, tungsten, and bismuth oxide in different proportions and investigated their radiation shielding properties in the energy range of 122–964 keV. They reported that prepared composites compared to commercial composites had better gamma radiation attenuation properties. A series of composites consisting of micro- and nano-sized lead oxides and high-density polyethylene polymers were produced by Mahmoud et al. [68] and investigated their gamma radiation attenuation properties. They reported that composites made with lead oxides' nanoparticles have higher density than those made with microparticles. It was further found that the composites with nanoparticles are better radiation shielding materials than the commercial shielding materials. Güngör et al. [69] investigated the mechanical, thermal, and radiation shielding properties of composites consisting of ethylene propylene diene monomer (EPDM) rubber and bismuth trioxide and they obtained composite with 94% radiation shielding property with different thicknesses. Hou et al. [70] obtained composites made of basalt fiber, epoxy, and tungsten by hot-press process and investigated their mechanical and gamma radiation attenuation properties. They reported that the gamma radiation attenuation properties increased with the increasing amount of tungsten in the low-energy region. Verdipoor et al. [71] produced a series of composites using silicon resin-based micro and nano-sized WO_3 , PbO , and Bi_2O_3 molecules and investigated their gamma radiation attenuation properties. They reported that composites reinforced with nanoparticles could be a better shielding material. Gong et al. [72] investigated the neutron and gamma radiation attenuation characteristics of flexible composites based on methyl vinyl silicone rubber and reinforced with B_4C , PbO , and benzophenone. They found that the 2 mm thick composite had good neutron shielding ability and the 20 mm thick composite had good gamma shielding property. Poltabtim et al. [73] evaluated the gamma-ray attenuation behavior of composites based on ethylene propylene diene monomer rubber and reinforced with Fe_3O_4 , W_2O_3 , and Bi_2O_3 , and they observed

that their shielding properties increased with increasing metal oxide doping ratio. Bagheri et al. [74] investigated the gamma radiation shielding properties of composites composed of different proportions of unsaturated polyester, nano-clay, and PbO using NaI(Tl) detector and ^{192}Ir , ^{137}Cs , and ^{60}Co radioactive sources. They noticed that the radiation shielding properties improved due to increased PbO amount and that composites could be used as an alternative shielding material at low energies. Shik and Gholamzadeh [75] investigated the X-ray attenuation characteristics of emulsion of poly vinyl chloride based and nano/micro-sized composites reinforced with WO_3 , PbO, and Bi_2O_3 and noticed that the Bi_2O_3 nanoparticle-reinforced composite could be an alternative to the one reinforced with PbO.

Belgin et al. [76] studied the effect of particle size on radiation shielding in hematite and ilmenite doped polymer composites with different particle sizes and observed that the shielding property improved as the particle size decreased. Srinivasan and Samuel [77] investigated the ionizing radiation shielding properties of polyvinyl alcohol/iron oxide polymer composites containing five different concentrations of magnetite in the energy range of 15 keV–20 meV and noticed that the composite containing high Fe had a better radiation shielding property. Ambika et al. [24] evaluated the gamma-ray attenuation characteristics of isophthalie resin-based composites reinforced with different proportions of Bi_2O_3 using the open mold cast technique at 662 keV photon energy and noticed that their radiation shielding properties improved with the increasing Bi_2O_3 concentration. A review was conducted by Ambika et al. [78] to evaluate the gamma-ray attenuation behavior of unsaturated polyester resin-based composites reinforced with different proportions of Bi_2O_3 , and they reported that the shielding ability increased with increasing amount of Bi_2O_3 , especially at low energies. Azman et al. [79] produced Bi_2O_3 -PVA composites using nano and microparticles Bi_2O_3 and investigated their X-ray attenuation characteristics at different energies. They reported that the produced Bi_2O_3 -PVA composites using nano-sized are better radiation shielding materials than those produced using micro-sized. Huang et al. [26] produced a series of composites reinforced with carbon blacks and PbWO_4 powders and based on ethylene-propylene-diene and evaluated their gamma radiation shielding properties using HPGe detector and ^{155}Eu , ^{137}Cs , and ^{60}Co radioactive sources. They observed that radiation shielding properties improved with increasing PbWO_4 concentration. Chai et al. [80] investigated the X-ray attenuation behavior of composites doped with tungsten and bismuth (iii) oxide and methyl vinyl silicone rubber based between 48 and 185 keV energies and noticed that tungsten doped composite was a better shielding material at 87 keV. Erol et al. [81] produced a series of high-density polyethylene-based composites reinforced with wolfram carbide and boron carbide and determined the gamma radiation attenuation properties of these composites with the aid of Geiger-Müller detector and ^{137}Cs and ^{131}I radioactive sources. They reported that some composites showed a better shielding property than lead at various energies. Brief information on the above-mentioned composites has been tabulated in Table 1.

As can be seen from a comprehensive literature review, the gamma and neutron shielding properties of polyester resin-based composites reinforced with bismuth nitrate pentahydrate have not been studied before. The presented comprehensive

Table 1 Summary information on various composites in literature

| Materials | Type of detector | Radioactive sources | References |
|---|------------------|---|-----------------------|
| Composites containing tungsten (iv) oxide and poly (hydroxyethyl methacrylate) | NaI(Tl) | ^{137}Cs , ^{60}Co | Körpınar et al. [57] |
| Nano cadmium oxide/high-density polyethylene composites | HPGe | ^{241}Am , ^{133}Ba , ^{137}Cs , ^{60}Co , and ^{152}Eu | El-Khatib et al. [62] |
| $\text{Na}_2\text{Si}_3\text{O}_7/\text{BaO}$ composites | NaI(Tl) | ^{133}Ba , ^{241}Am , $^{99\text{m}}\text{Tc}$, ^{177}Lu , ^{192}Ir , and ^{137}Cs | Çağlar et al. [63] |
| Composites including unsaturated polyester, nano-clay, and PbO | NaI(Tl) | ^{192}Ir , ^{137}Cs , and ^{60}Co | Bagheri et al. [74] |
| Composites reinforced with carbon blacks and PbWO_4 powders | HPGe | ^{155}Eu , ^{137}Cs , and ^{60}Co | Huang et al. [26] |
| Polyethylene-based composites reinforced with wolfram carbide and boron carbide | Geiger-Müller | ^{137}Cs and ^{131}I | Erol et al. [81] |
| Composites including unsaturated polyester and $\text{Bi}(\text{NO}_3)_3 \cdot 5\text{H}_2\text{O}$ | HPGe | ^{241}Am , ^{152}Eu , ^{137}Cs , ^{133}Ba , ^{60}Co , ^{57}Co , ^{54}Mn , and ^{22}Na | This study |

study was conducted in the energy range of 0.060–1.408 meV (twenty-two different energies) using experimental, theoretical, and simulation code techniques in order to evaluate the gamma radiation attenuation properties of polyester-based composites reinforced with different ratios of $\text{Bi}(\text{NO}_3)_3 \cdot 5\text{H}_2\text{O}$. On this purpose, radiation protection efficiency, transmission factor, mass attenuation coefficient, linear attenuation coefficient, half value layer, tenth value layer, mean free path, effective atomic number, and effective electron density gamma radiation shielding parameters were determined by all three ways. In order to evaluate the neutron attenuation characteristics of these composites, neutron mass removal cross sections and neutron transmissions in different thickness and energies were calculated with the help of the GEANT4 simulation code.

3 Materials and Methods

3.1 Production of Polymer-Based Composites

Polymers are chain-shaped macromolecules made up of repeating units. Using polymers as a composite material provides a significant advantage to the users: having the ability of the material to be molded in complex segmented geometries without the need for extra processing. In essence, there are two important reasons that cause

the polymers to be used so widely. One reason is that the production of polymers is extremely easy and the other reason is that various combinations of composites can be made in the production using natural ways.

In this study, with a unit weight of 1.113 g/cm^3 TP 100 casting type polyester resin ($\text{C}_{16}\text{O}_7\text{H}_{14}$, $\text{MW} = 318.278 \text{ amu}$) purchased from Turkuaz polyester company was used in the production of composite materials. The composites were obtained using resin and mineral materials together. The curing or hardening process was initiated with the addition of hardener and accelerator to the resin. Methyl ethyl ketone peroxide (Mekp) ($\text{C}_8\text{O}_6\text{H}_{18}$, $\text{MW} = 210.254 \text{ amu}$) was used as a hardener and it initiated polymerization reaction, where the unit weight of Mekp used for preparation of the material is 1.17 g/cm^3 . Since Mekp has the facility of fast gelation and curing, it is appropriate to cure resins in combination with Mekp and Cobalt Octoate accelerator. In addition, the Cobalt Octoate (6%) ($\text{CoC}_{16}\text{H}_{30}\text{O}_4$, $\text{MW} = 345.389 \text{ amu}$) that has a unit weight of 0.885 g/cm^3 was used as an accelerator to cure unsaturated polyester resins at room temperature.

To prepare the composite material, polyester, Mekp, Cobalt Octoate, which were weighed precisely in accordance with the mixture design, were mixed for 300 s in the mixer for the production of polymer composite samples. After that, Bismuth (III) nitrate pentahydrate ($\text{Bi}(\text{NO}_3)_3 \cdot 5\text{H}_2\text{O}$) was added into the polymer matrix (formed in 5, 10, 15, and 20% by weight of the amount of polyester resin) as filling material, and the mixing was kept on for another 300 s. Then, the sample was poured into molds to harden. After being hard enough, the hardened samples were removed from the molds and cured in a suitable environment. A schematic view of the production steps for the prepared polymer sample was given in Fig. 1.

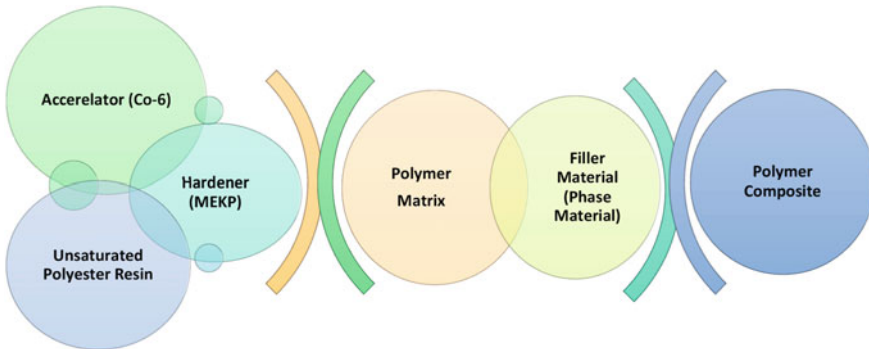


Fig. 1 Production scheme of polymer composites [58]

3.2 Radiation Shielding Performances

3.2.1 Theoretical Background

The photon beam with the initial intensity (I_0), which moves through the absorber, attenuates to the residual intensity (I). The relationship between the absorber, the initial, and the residual intensities are given by Lambert-Beer equation [82]:

$$\mu = -\frac{\ln \frac{I}{I_0}}{x} \quad (1)$$

where μ and x denote the linear attenuation coefficient (in cm^{-1}), and thickness (in cm) of the absorber respectively.

Based on estimating μ values, mass attenuation coefficients (μ_m) of the absorber can be calculated by dividing μ with its density (ρ) [83]:

$$\mu_m = \frac{\mu}{\rho} = \sum w_i \left(\frac{\mu}{\rho} \right)_i \quad (2)$$

Total atomic and electronic cross sections, the effective atomic number, and electron density can be derived through the result of Eq. 2. The total atomic cross section (σ_a , cm^2/atom) and electronic cross section (σ_e , $\text{cm}^2/\text{electron}$) can be described using the following relationships [84]:

$$\sigma_a = \frac{(\mu_m)}{N_A \sum_i \frac{w_i}{A_i}} \quad (3)$$

$$\sigma_e = \frac{1}{N} \sum_i \mu_{mi} \frac{f_i A_i}{Z_i} \quad (4)$$

where Z_i and f_i are respectively the atomic number and the fractional abundance of the i th element. Z_{eff} can be derived by dividing σ_e to σ_a as shown in Eq. (5).

$$Z_{\text{eff}} = \frac{\sigma_a}{\sigma_e} \quad (5)$$

Also, the electron density (N_E) defines the electron numbers per unit mass of the interacting absorber and is associated with Z_{eff} as below:

$$N_E = (n_{\text{tot}} N) \frac{Z_{\text{eff}}}{A_{\text{tot}}} \quad (6)$$

Half value layer (HVL) is described as the absorber's thickness at which the intensity of the photons after being attenuated is reduced to 50% relative to the initial intensity. HVL (cm) can be calculated with Eq. (7) [85]:

$$\text{HVL} = \frac{\ln 2}{\mu} \quad (7)$$

Mean free path (MFP) plays a significant role in calculation of the exponential shielding of gamma photon and gives shorter distance between two interactions [86]. It is estimated through the following equation:

$$\text{MFP} = \frac{1}{\mu} \quad (8)$$

The radiation protection efficiency (RPE) of any absorber can be obtained by using the following equation [87].

$$\text{RPE}(\%) = \left(1 - \frac{I}{I_0}\right) \times 100\% \quad (9)$$

The macroscopic effective removal cross section (Σ_R , cm^{-1}) is a term on the contingency of a neutron undergoing certain reaction per unit length when passing across absorber [88]. The following relationship is used in the calculation of Σ_R values.

$$\Sigma_R = \sum w_i \left(\Sigma_{R/\rho} \right)_i \quad (10)$$

3.2.2 Experimental Details

The shielding performances of the synthesized composites are assessed experimentally by means of μ/ρ employing an HPGe detector in conjunction with gamma spectrometer. The experimental setup and geometry of the tested material are shown in Fig. 2. The photo-peak energies and nuclear data emitted by radioactive point sources ^{241}Am , ^{152}Eu , ^{137}Cs , ^{133}Ba , ^{60}Co , ^{57}Co , ^{54}Mn , and ^{22}Na can be taken from Ref. [89]. The detailed information on experimental gamma systems can be found in Refs. [90–94]. The detected photo-peaks in data acquisitions were analyzed through MAESTRO software. Their net areas were determined with the help of the least-squares fitting method through the Origin 7.5 program (demo).

3.2.3 Monte Carlo Simulations

Monte Carlo simulations are useful tools for simulating experimental designs, which let researchers to assess the validity of experimental design and results. In addition to their contribution to experimental designs, they could also be key point to provide

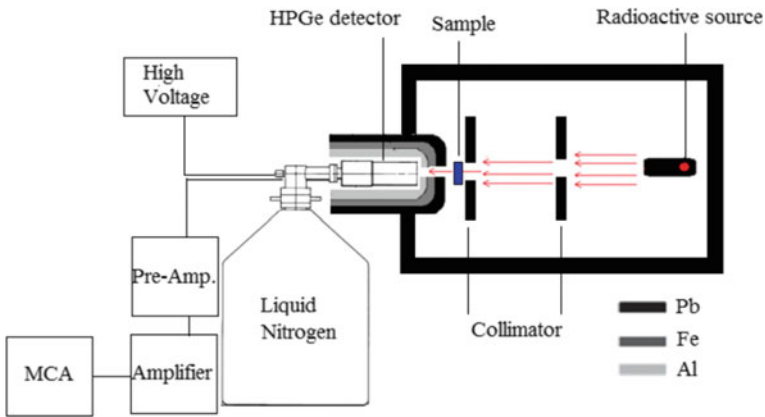


Fig. 2 Narrow beam transmission geometry of the experimental system

hints for physics events in the lack of experimental apparatus. Therefore, their use is very common in many fields of natural sciences, and have significant contribution to the quantitative probabilistic and sensitivity analyses. In this regard, variety of event generators are currently available to determine the radiation shielding characteristics of the materials, and GEANT4 simulation toolkit [95] computer programs were chosen in order to obtain the desired simulation results of this work. Both programs provide precise numerical values to understand a possible description of what happens during the particle passage through a matter.

European Center for Nuclear Research (CERN) has developed the GEANT4 simulation toolkit to allow the users model and build their own particle detectors. The program is a full set of libraries written in C++ and enables the researchers to simulate own particle detectors with desired particles. It sounds like the developed program is useful for particle experiments, but it is currently useful for many fields such as nuclear power reactors [96, 97], medical researches [98, 99], space science [100, 101], astrophysics [102, 103], radiation protection [104, 105], and so on, and these areas could be definitely extended. The biggest drawback of it could be considered as the fact that it is only accessible as computer-based program.

Since researchers do not have opportunity to perform experimental evaluation on the neutron shielding properties, GEANT4 simulation toolkit was utilized to have a complete discussion on radiation shielding ability of the proposed composite. On the first step, neutron removal cross sections of produced polyester composites were calculated separately using partial density of elements and their cross sections. Then, GEANT4 codes were simulated with 10000000 neutrons in order to assess the number of neutrons passing through the chosen material. The discussion on neutron shielding evaluation is focused on transmitted neutron numbers through the produced samples at different energies and thickness, mean free path, and neutron total macroscopic cross sections.

3.2.4 Theoretical Estimations

XCOM program is suitable to calculate mass attenuation coefficients or photon interaction cross sections for chosen mixture, compound or element in a wide gamma energy range from 1 to 100000 keV. The program was originally developed by Berger and Hubbell [106] and was transformed to the Windows platform in 2001 by taking the name of "WinXCOM". Contrast to GEANT4 simulation tool, WinXCOM is computer- and web-based program [107]. Besides, WinXCOM is not a simulation code. The chemical compositions of the proposed composites are previously given, and they were encoded in WinXCOM program. WinXCOM code uses the predefined tables by the developers of the code in Eq. 2 and provides mass attenuation coefficients of the user defined materials at desired energies. The code does not require any thickness or density of the material, which are mandatory information in GEANT4 simulation tool. Then, the user needs to calculate the remaining gamma attenuation parameters using the provided mass attenuation values. The numerical theoretical values of the considered gamma radiation attenuation parameters were further compared to the experimental results obtained via HPGe detector to verify the conducted experimental design.

4 Results and Discussions

4.1 Evaluation of Gamma Shielding Effect of the Material

Using environmentally friendly shielding materials is not only important to reduce the radiation effect, but also important in terms of their physical and chemical properties. Having no toxicity and not being heavy makes the polymers more advantageous materials. Because of this, research studies for having lightweight, durable, low-cost, and eco friendly alternative polymer materials that stop or attenuate radiation are increasing.

The interaction of radiation with a material can cause the radiation to be scattered, absorbed, or pass throughout the material without affected. Therefore, material type is very important to reduce the radiation intensity. Either the selected material can be found in the nature or it can be obtained as alloys or composites by mixing various elements. In this study, we test the radiation characteristics of a polymer composite which is obtained by the mixture of elements given in Table 2. As shown in the table, different amounts of BiNO were added into the sample to test the radiation protection effect of BiNO inside the material.

One way of testing the radiation shielding characteristics of the prepared composite material is to evaluate the linear attenuation coefficient (μ) that describes the fraction of the attenuated incident particles (photon, neutron, etc.) in a monoenergetic beam per unit of the material thickness. For this measurement, we used an HPGe detector with the radioactive sources that are defined in Sect. 3.2.2. Then, the

Table 2 Chemical content of the prepared composites

| Sample | Chemical content (%) | | | | | | ρ (g/cm ³) |
|--------------------|----------------------|---------|--------|---------|--------|--------|-----------------------------|
| | H | C | N | O | Co | Bi | |
| BiNO ₅ | 4.5416 | 56.9947 | 0.3920 | 36.0952 | 0.0271 | 1.9494 | 1.1455 |
| BiNO ₁₀ | 4.4349 | 54.5274 | 0.7500 | 36.5316 | 0.0260 | 3.7301 | 1.2034 |
| BiNO ₁₅ | 4.3371 | 52.2649 | 1.0783 | 36.9318 | 0.0249 | 5.3630 | 1.2753 |
| BiNO ₂₀ | 4.2471 | 50.1826 | 1.3805 | 37.3002 | 0.0239 | 6.8657 | 1.3212 |

test results were compared with the theoretical WinXCOM and GEANT4 simulation results. Figure 3 shows a comparison of experimental μ results with computer-based theoretical WinXCOM and a simulation based GEANT4 results. As shown in the figure, there is a consistency among the experimental, WinXCOM, and GEANT4 results for all BiNO-doped composites. There are only some small discrepancies between experimental and GEANT4 simulation results at low energies, but the experimental results are suitable to report the μ value of the prepared composites, since the discrepancy is decreasing at higher energies. Figure 3 also shows an exponential decrease of μ value almost at all energies except of the energies from 0.081 to 0.122 meV. This shows that the shielding property of the samples decreases with increasing energy and this property agrees with Lambert-Beer law. Since the cross section of the photoelectric effect is related to Z^{4-5} and $E^{3.5}$ in the low-energy region, the reduction of μ values at high energies are not as sharp as the reduction of μ values at low energies. The sharp decrease in μ value decreases with the increase in energy and having very close μ values for all polyester composites, especially at the energies from 0.662 to 1.408 meV, attributed to Compton scattering. Additionally, this physical behaviors systematically are consistent with the observed change in μ_m values reported by Sayyed et al. [108], Kacal et al. [109], and Kumar et al. [110]. The calculated μ values for the produced composites are given in Table 3. The experimental, theoretical, and simulated results in Table 3 illustrate that increasing BiNO concentration is proportional to the μ value of the sample because Bi ($Z = 83$) is a heavy material and preferred in gamma radiation shielding applications.

Another parameter that allows us to measure how a photon beam can penetrate a material is the mass attenuation coefficient (μ/ρ). The calculation of μ/ρ provides a definition of effective area per unit mass. Figure 4 shows the μ/ρ of the 5, 10, 15, and 20% BiNO doped composite samples. As shown in the figure, μ/ρ decreases with increasing energy. However, increasing BiNO concentration in the sample increases μ/ρ , and this shows that the shielding effect of the composite sample increases with the increase of BiNO concentration. In addition, experimental test results show consistency with WinXCOM and GEANT4 results. The experimental, WinXCOM, and GEANT4 results of μ/ρ for produced samples are given in Table 4.

Except for the linear attenuation and mass attenuation coefficients, the half value layer (HVL), the tenth value layer (TVL), and mean free path (MFP) are other essential measurements used to determine the photon attenuation effect of a material. While HVL is used to determine the thickness required to reduce the photon

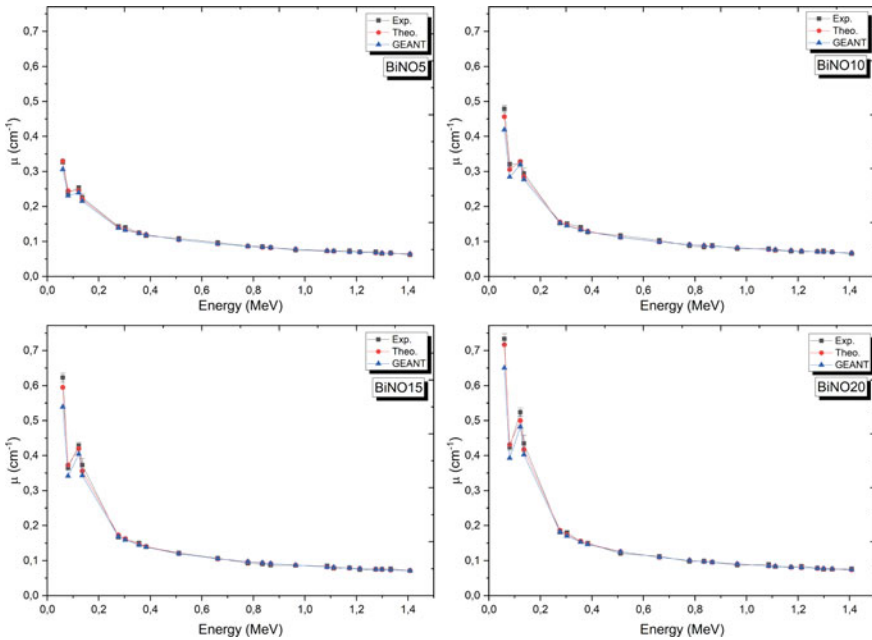


Fig. 3 A comparison of experimental, WinXCOM, and GEANT4 results of the linear attenuation coefficient for the prepared samples

intensity to one-half of the original value, TVL is used to determine the required thickness to reduce this intensity to a tenth of its original value. Finally, the MFP is the average distance traveled by a photon before it interacts with the atoms of the target material. The HVL, TVL, and MFP of the samples that consist of different BiNO doped concentrations by increasing energy are shown in Figs. 5, 6, and 7. As can be seen in the figures, these three essential values increase with increasing energy. The numerical results of HVL, TVL, and MFP for the four different samples are given in Tables 5, 6, and 7. The results in these tables show that HVL, TVL, and MFP values are highest for the sample that contains 5% BiNO, and they are lowest for the sample of 20% BiNO concentration. Comparing to other samples, the sample with 5% BiNO concentration has the lowest density, and the sample with 20% BiNO concentration has the highest density, so that having the highest (lowest) HVL, TVL, and MFP values for 5% BiNO (20% BiNO) concentration is an expected case. The current HVL, TVL, and MFP trends in photon energy region of 0.060–1.408 meV are in good agreement with the data published by Dong et al. [111] and, Akman and Kacal [112].

The remaining parameters that are necessary to understand the photon shielding effect clearly are the effective atomic number (Z_{eff}), effective electron density (N_E), radiation protection efficiency (RPE), and radiation transmission factor (TF). The definition of Z_{eff} for a composite is not similar to the definition of the one that for an atom. Providing a strong relationship with the nature of radiation interactions in the

Table 3 Experimental, theoretical, and GEANT results of μ (cm^{-1}) for produced polyester based composites

| Energy (MeV) | BiNO ₅ | | | BiNO ₁₀ | | | BiNO ₁₅ | | | BiNO ₂₀ | | |
|--------------|-------------------|-----------------|--------|--------------------|-----------------|--------|--------------------|-----------------|--------|--------------------|-----------------|--------|
| | Exp | WinX | GEANT | Exp | WinX | GEANT | Exp | WinX | GEANT | Exp | WinX | GEANT |
| | 0.060 | 0.3274 ± 0.0067 | 0.3298 | 0.3058 | 0.4790 ± 0.0099 | 0.4561 | 0.4190 | 0.6227 ± 0.0128 | 0.5948 | 0.5392 | 0.7335 ± 0.0152 | 0.7170 |
| 0.081 | 0.2388 ± 0.0050 | 0.2447 | 0.2308 | 0.3206 ± 0.0066 | 0.3055 | 0.2841 | 0.3659 ± 0.0075 | 0.3730 | 0.3420 | 0.4243 ± 0.0087 | 0.4309 | 0.3929 |
| 0.122 | 0.2540 ± 0.0057 | 0.2454 | 0.2391 | 0.3230 ± 0.0076 | 0.3285 | 0.3192 | 0.4280 ± 0.0095 | 0.4200 | 0.4045 | 0.5239 ± 0.0121 | 0.5001 | 0.4821 |
| 0.136 | 0.2253 ± 0.0107 | 0.2213 | 0.2154 | 0.2944 ± 0.0151 | 0.2853 | 0.2771 | 0.3732 ± 0.0192 | 0.3561 | 0.3432 | 0.4347 ± 0.0239 | 0.4175 | 0.4027 |
| 0.276 | 0.1427 ± 0.0046 | 0.1401 | 0.1385 | 0.1525 ± 0.0050 | 0.1553 | 0.1528 | 0.1669 ± 0.0060 | 0.1728 | 0.1690 | 0.1819 ± 0.0066 | 0.1864 | 0.1822 |
| 0.303 | 0.1404 ± 0.0035 | 0.1339 | 0.1325 | 0.1507 ± 0.0037 | 0.1470 | 0.1450 | 0.1612 ± 0.0038 | 0.1622 | 0.1591 | 0.1797 ± 0.0044 | 0.1738 | 0.1701 |
| 0.356 | 0.1252 ± 0.0026 | 0.1240 | 0.1231 | 0.1409 ± 0.0029 | 0.1343 | 0.1327 | 0.1504 ± 0.0031 | 0.1465 | 0.1442 | 0.1543 ± 0.0032 | 0.1555 | 0.1528 |
| 0.384 | 0.1163 ± 0.0041 | 0.1197 | 0.1190 | 0.1267 ± 0.0040 | 0.1291 | 0.1279 | 0.1392 ± 0.0047 | 0.1401 | 0.1385 | 0.1500 ± 0.0051 | 0.1482 | 0.1462 |
| 0.511 | 0.1086 ± 0.0022 | 0.1050 | 0.1049 | 0.1169 ± 0.0024 | 0.1118 | 0.1116 | 0.1220 ± 0.0025 | 0.1200 | 0.1194 | 0.1199 ± 0.0025 | 0.1256 | 0.1249 |
| 0.662 | 0.0971 ± 0.0020 | 0.0932 | 0.0935 | 0.1029 ± 0.0021 | 0.0985 | 0.0987 | 0.1067 ± 0.0022 | 0.1051 | 0.1052 | 0.1123 ± 0.0023 | 0.1095 | 0.1094 |
| 0.779 | 0.0866 ± 0.0023 | 0.0863 | 0.0866 | 0.0873 ± 0.0023 | 0.0910 | 0.0913 | 0.0926 ± 0.0024 | 0.0968 | 0.0969 | 0.0977 ± 0.0026 | 0.1006 | 0.1007 |
| 0.835 | 0.0857 ± 0.0021 | 0.0834 | 0.0838 | 0.0838 ± 0.0021 | 0.0879 | 0.0882 | 0.0902 ± 0.0022 | 0.0934 | 0.0936 | 0.0989 ± 0.0025 | 0.0971 | 0.0972 |
| 0.867 | 0.0829 ± 0.0032 | 0.0819 | 0.0822 | 0.0890 ± 0.0032 | 0.0863 | 0.0864 | 0.0871 ± 0.0031 | 0.0916 | 0.0917 | 0.0957 ± 0.0037 | 0.0952 | 0.0951 |
| 0.964 | 0.0751 ± 0.0017 | 0.0777 | 0.0779 | 0.0789 ± 0.0018 | 0.0818 | 0.0820 | 0.0859 ± 0.0019 | 0.0868 | 0.0871 | 0.0872 ± 0.0019 | 0.0901 | 0.0904 |
| 1.086 | 0.0727 ± 0.0019 | 0.0733 | 0.0735 | 0.0792 ± 0.0021 | 0.0770 | 0.0771 | 0.0851 ± 0.0022 | 0.0817 | 0.0817 | 0.0886 ± 0.0022 | 0.0847 | 0.0846 |
| 1.112 | 0.0727 ± 0.0016 | 0.0724 | 0.0725 | 0.0746 ± 0.0016 | 0.0761 | 0.0762 | 0.0780 ± 0.0017 | 0.0807 | 0.0808 | 0.0828 ± 0.0018 | 0.0836 | 0.0835 |
| 1.173 | 0.0735 ± 0.0015 | 0.0705 | 0.0705 | 0.0719 ± 0.0015 | 0.0740 | 0.0741 | 0.0794 ± 0.0017 | 0.0785 | 0.0785 | 0.0810 ± 0.0017 | 0.0813 | 0.0812 |
| 1.213 | 0.0701 ± 0.0032 | 0.0693 | 0.0694 | 0.0710 ± 0.0034 | 0.0727 | 0.0729 | 0.0739 ± 0.0034 | 0.0771 | 0.0772 | 0.0836 ± 0.0040 | 0.0799 | 0.0800 |
| 1.275 | 0.0704 ± 0.0015 | 0.0675 | 0.0679 | 0.0719 ± 0.0015 | 0.0709 | 0.0710 | 0.0751 ± 0.0016 | 0.0751 | 0.0752 | 0.0788 ± 0.0016 | 0.0778 | 0.0779 |
| 1.299 | 0.0654 ± 0.0025 | 0.0668 | 0.0669 | 0.0734 ± 0.0027 | 0.0702 | 0.0703 | 0.0754 ± 0.0027 | 0.0744 | 0.0745 | 0.0749 ± 0.0028 | 0.0770 | 0.0771 |

(continued)

Table 3 (continued)

| Energy (MeV) | BiNO ₅ | | | BiNO ₁₀ | | | BiNO ₁₅ | | | BiNO ₂₀ | | |
|--------------|-------------------|--------|--------|--------------------|--------|--------|--------------------|--------|--------|--------------------|--------|--------|
| | Exp | WinX | GEANT | Exp | WinX | GEANT | Exp | WinX | GEANT | Exp | WinX | GEANT |
| 1.333 | 0.0675 ± 0.0014 | 0.0659 | 0.0661 | 0.0702 ± 0.0015 | 0.0693 | 0.0693 | 0.0762 ± 0.0016 | 0.0734 | 0.0734 | 0.0750 ± 0.0016 | 0.0760 | 0.0761 |
| 1.408 | 0.0618 ± 0.0013 | 0.0641 | 0.0642 | 0.0646 ± 0.0013 | 0.0673 | 0.0673 | 0.0711 ± 0.0015 | 0.0713 | 0.0713 | 0.0765 ± 0.0016 | 0.0738 | 0.0739 |

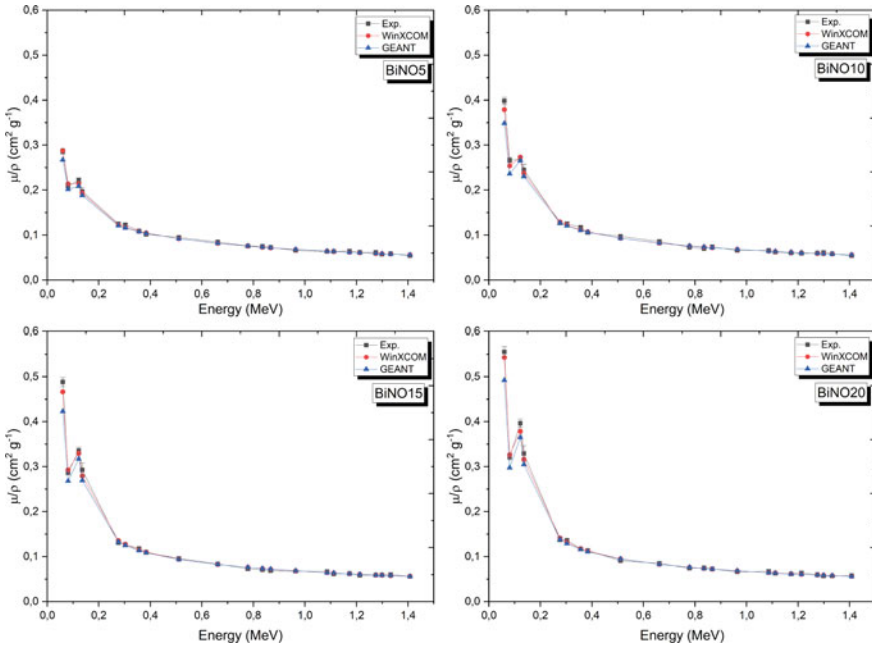


Fig. 4 A comparison of experimental, WinXCOM, and GEANT4 results of μ/ρ for produced polyester based composites

medium complicates the definition of Z_{eff} for a composite. Even though the Z_{eff} of the composites is not the equivalent to Z_{eff} of an atom, it is the Z_{eff} which is used for composites. N_E is the parameter that has a relationship with Z_{eff} , and the RPE is the parameter that decides the protection efficiency of the material. TF is proportional to the ratio of the transmitted and primary intensities. Here, we provide Z_{eff} and N_E values of the prepared polyester samples as shown in Figs. 8 and 9. As can be seen, the Z_{eff} and N_E decrease with increasing energy except for the energy ranges from 0.081 to 0.122 meV. The jump between 0.081 and 0.122 meV is a result of the K-edge absorption energy of Bi at 0.069 meV. Tables 8 and 9 show the experimental and theoretical results of Z_{eff} and N_E for 5, 10, 15, and 20% of BiNO concentration. Figure 10 shows the RPE values of the polyester composites doped with different amount of BiNO. As shown in the figure, RPE decreases with increasing energy and insertion of BiNO into the material increases the radiation protection ability of the material since the RPE increases with the addition of BiNO concentration. Figure 11 shows TF of the prepared samples at the energy range from 0.060 to 1.408 meV. As can be seen in the figure, TF increases with increasing energy, and increasing the concentration of BiNO in the sample partially decreases TF. The numerical results of RPE and TF for the prepared samples doped with 5, 10, 15, and 20% BiNO concentration are given in Table 10.

Table 4 Experimental, WinXCOM, and GEANT results of μ/ρ ($\text{cm}^2 \text{g}^{-1}$) for produced polyester based composites

| Energy (MeV) | BiNO ₅ | | | BiNO ₁₀ | | | BiNO ₁₅ | | | BiNO ₂₀ | | |
|--------------|-------------------|-----------------|--------|--------------------|-----------------|--------|--------------------|-----------------|--------|--------------------|-----------------|--------|
| | Exp | WinX | GEANT | Exp | WinX | GEANT | Exp | WinX | GEANT | Exp | WinX | GEANT |
| | 0.060 | 0.2858 ± 0.0059 | 0.2879 | 0.2670 | 0.3980 ± 0.0082 | 0.3790 | 0.3482 | 0.4883 ± 0.0101 | 0.4664 | 0.4228 | 0.5551 ± 0.0115 | 0.5427 |
| 0.081 | 0.2085 ± 0.0044 | 0.2136 | 0.2015 | 0.2664 ± 0.0055 | 0.2538 | 0.2361 | 0.2869 ± 0.0059 | 0.2925 | 0.2682 | 0.3212 ± 0.0066 | 0.3261 | 0.2974 |
| 0.122 | 0.2217 ± 0.0050 | 0.2142 | 0.2088 | 0.2684 ± 0.0063 | 0.2730 | 0.2653 | 0.3356 ± 0.0074 | 0.3294 | 0.3172 | 0.3965 ± 0.0091 | 0.3785 | 0.3649 |
| 0.136 | 0.1967 ± 0.0094 | 0.1932 | 0.1880 | 0.2446 ± 0.0126 | 0.2371 | 0.2303 | 0.2926 ± 0.0151 | 0.2792 | 0.2691 | 0.3290 ± 0.0181 | 0.3160 | 0.3048 |
| 0.276 | 0.1246 ± 0.0040 | 0.1223 | 0.1209 | 0.1267 ± 0.0042 | 0.1290 | 0.1270 | 0.1308 ± 0.0047 | 0.1355 | 0.1325 | 0.1377 ± 0.0050 | 0.1411 | 0.1379 |
| 0.303 | 0.1226 ± 0.0031 | 0.1169 | 0.1157 | 0.1252 ± 0.0031 | 0.1222 | 0.1205 | 0.1264 ± 0.0030 | 0.1272 | 0.1247 | 0.1360 ± 0.0033 | 0.1315 | 0.1287 |
| 0.356 | 0.1093 ± 0.0023 | 0.1083 | 0.1074 | 0.1171 ± 0.0024 | 0.1116 | 0.1103 | 0.1179 ± 0.0025 | 0.1149 | 0.1131 | 0.1168 ± 0.0024 | 0.1177 | 0.1156 |
| 0.384 | 0.1015 ± 0.0035 | 0.1045 | 0.1039 | 0.1052 ± 0.0034 | 0.1073 | 0.1063 | 0.1091 ± 0.0037 | 0.1099 | 0.1086 | 0.1135 ± 0.0038 | 0.1122 | 0.1107 |
| 0.511 | 0.0948 ± 0.0019 | 0.0917 | 0.0916 | 0.0971 ± 0.0020 | 0.0929 | 0.0927 | 0.0956 ± 0.0020 | 0.0941 | 0.0936 | 0.0907 ± 0.0019 | 0.0951 | 0.0945 |
| 0.662 | 0.0847 ± 0.0017 | 0.0813 | 0.0817 | 0.0855 ± 0.0018 | 0.0819 | 0.0820 | 0.0836 ± 0.0017 | 0.0824 | 0.0825 | 0.0850 ± 0.0017 | 0.0829 | 0.0828 |
| 0.779 | 0.0756 ± 0.0020 | 0.0753 | 0.0756 | 0.0725 ± 0.0019 | 0.0756 | 0.0759 | 0.0726 ± 0.0019 | 0.0759 | 0.0760 | 0.0740 ± 0.0019 | 0.0762 | 0.0762 |
| 0.835 | 0.0748 ± 0.0018 | 0.0728 | 0.0731 | 0.0696 ± 0.0018 | 0.0731 | 0.0733 | 0.0707 ± 0.0018 | 0.0733 | 0.0734 | 0.0749 ± 0.0019 | 0.0735 | 0.0736 |
| 0.867 | 0.0724 ± 0.0028 | 0.0715 | 0.0718 | 0.0739 ± 0.0026 | 0.0717 | 0.0718 | 0.0683 ± 0.0025 | 0.0719 | 0.0719 | 0.0725 ± 0.0028 | 0.0720 | 0.0720 |
| 0.964 | 0.0656 ± 0.0015 | 0.0679 | 0.0680 | 0.0656 ± 0.0015 | 0.0680 | 0.0681 | 0.0674 ± 0.0015 | 0.0681 | 0.0683 | 0.0660 ± 0.0015 | 0.0682 | 0.0684 |
| 1.086 | 0.0635 ± 0.0017 | 0.0640 | 0.0641 | 0.0658 ± 0.0017 | 0.0640 | 0.0641 | 0.0667 ± 0.0017 | 0.0641 | 0.0641 | 0.0671 ± 0.0017 | 0.0641 | 0.0640 |
| 1.112 | 0.0635 ± 0.0014 | 0.0632 | 0.0633 | 0.0620 ± 0.0013 | 0.0632 | 0.0633 | 0.0612 ± 0.0013 | 0.0633 | 0.0633 | 0.0627 ± 0.0013 | 0.0633 | 0.0632 |
| 1.173 | 0.0641 ± 0.0014 | 0.0615 | 0.0615 | 0.0597 ± 0.0013 | 0.0615 | 0.0616 | 0.0622 ± 0.0013 | 0.0615 | 0.0615 | 0.0613 ± 0.0013 | 0.0615 | 0.0615 |
| 1.213 | 0.0612 ± 0.0028 | 0.0605 | 0.0606 | 0.0590 ± 0.0028 | 0.0604 | 0.0606 | 0.0579 ± 0.0027 | 0.0604 | 0.0606 | 0.0633 ± 0.0030 | 0.0604 | 0.0606 |
| 1.275 | 0.0614 ± 0.0013 | 0.0589 | 0.0592 | 0.0597 ± 0.0012 | 0.0589 | 0.0590 | 0.0589 ± 0.0012 | 0.0589 | 0.0589 | 0.0597 ± 0.0012 | 0.0589 | 0.0589 |
| 1.299 | 0.0571 ± 0.0021 | 0.0583 | 0.0584 | 0.0610 ± 0.0022 | 0.0583 | 0.0584 | 0.0591 ± 0.0022 | 0.0583 | 0.0584 | 0.0567 ± 0.0021 | 0.0583 | 0.0583 |

(continued)

Table 4 (continued)

| Energy (MeV) | BiNO ₅ | | | BiNO ₁₀ | | | BiNO ₁₅ | | | BiNO ₂₀ | | |
|--------------|-------------------|--------|--------|--------------------|--------|--------|--------------------|--------|--------|--------------------|--------|--------|
| | Exp | WinX | GEANT | Exp | WinX | GEANT | Exp | WinX | GEANT | Exp | WinX | GEANT |
| 1.333 | 0.0589 ± 0.0012 | 0.0576 | 0.0577 | 0.0584 ± 0.0012 | 0.0575 | 0.0576 | 0.0598 ± 0.0012 | 0.0575 | 0.0576 | 0.0568 ± 0.0012 | 0.0575 | 0.0576 |
| 1.408 | 0.0539 ± 0.0011 | 0.0560 | 0.0560 | 0.0537 ± 0.0011 | 0.0559 | 0.0559 | 0.0557 ± 0.0011 | 0.0559 | 0.0559 | 0.0579 ± 0.0012 | 0.0559 | 0.0559 |

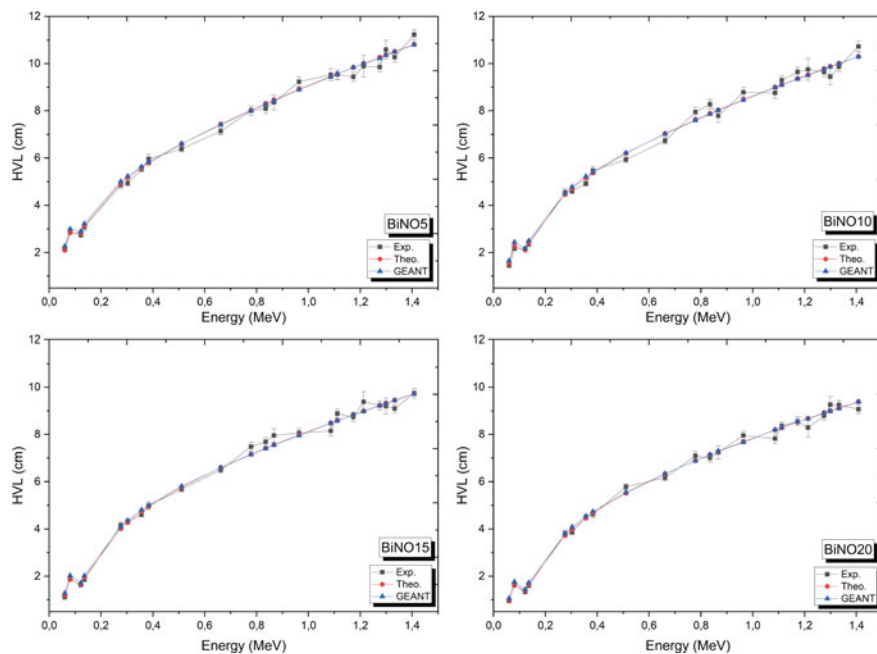


Fig. 5 HVL of the samples that are prepared with 5, 10, 15, and 20% BiNO doping concentrations

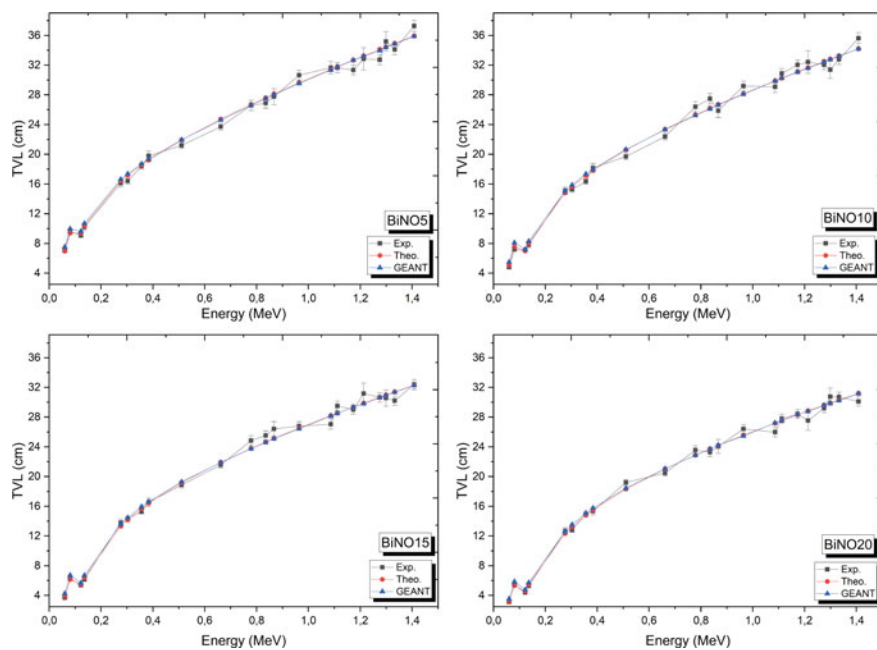


Fig. 6 TVL of the samples that are prepared with 5, 10, 15, and 20% BiNO doping concentrations

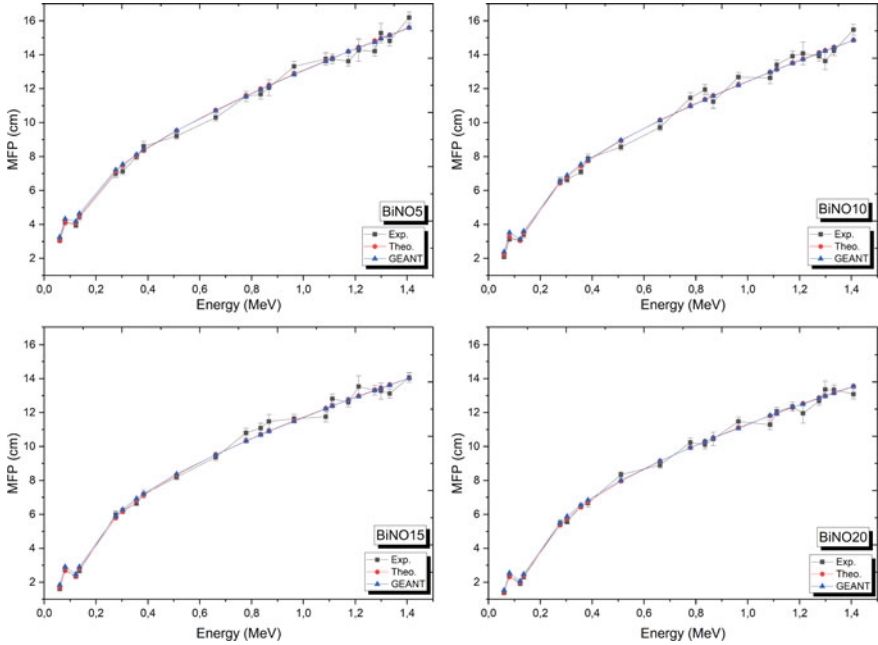


Fig. 7 MFP of the samples that are prepared with 5, 10, 15, and 20% BiNO doping concentrations

4.2 Evaluation of Neutron Shielding Effect of the Material

In addition to testing the gamma shielding ability of the material, the neutron shielding ability of the material was also performed to determine the total macroscopic cross section, mean free path, the effective removal cross section, and transmitted neutron numbers. All these parameters were calculated using mixture rule and GEANT4 simulation tool. In GEANT4 simulation code the thickness of the material was selected as 10 mm and 10,000,000 neutrons at 4.5 meV were bombarded on each sample. By doing so, the number of transmitted neutrons through the sample, MFP (mm), and neutron total macroscopic cross section (cm^{-1}) were obtained. Table 11 shows the theoretical results of effective removal cross section values for the produced polyester-based composites. MFP, total macroscopic cross section, and the number of transmitted neutrons for the prepared samples that doped with different BiNO concentration are given in Table 12. MFP and neutron transmission values of 20% BiNO concentration are lower compared to the MFP and neutron transmission values of 5, 10, and 15% BiNO concentration. This shows that both MFP values and the number of transmitted neutrons decrease with the increase of BiNO concentration. The results in Table 12 also show that effective removal cross section values of 20% BiNO concentration are higher than the effective removal cross section values of

Table 5 Experimental, theoretical, and GEANT results of HVL (cm) for produced polyester based composites

| Energy (MeV) | BiNO ₅ | | | BiNO ₁₀ | | | BiNO ₁₅ | | | BiNO ₂₀ | | |
|--------------|-------------------|--------|--------|--------------------|-------|-------|--------------------|-------|-------|--------------------|-------|-------|
| | Exp | WinX | GEANT | Exp | WinX | GEANT | Exp | WinX | GEANT | Exp | WinX | GEANT |
| 0.060 | 2.117 ± 0.043 | 2.102 | 2.267 | 1.447 ± 0.030 | 1.520 | 1.654 | 1.113 ± 0.023 | 1.165 | 1.286 | 0.945 ± 0.020 | 0.967 | 1.066 |
| 0.081 | 2.903 ± 0.061 | 2.833 | 3.003 | 2.162 ± 0.044 | 2.269 | 2.440 | 1.894 ± 0.039 | 1.858 | 2.027 | 1.634 ± 0.034 | 1.609 | 1.764 |
| 0.122 | 2.729 ± 0.062 | 2.824 | 2.899 | 2.146 ± 0.051 | 2.110 | 2.171 | 1.619 ± 0.036 | 1.650 | 1.714 | 1.323 ± 0.030 | 1.386 | 1.438 |
| 0.136 | 3.077 ± 0.147 | 3.132 | 3.218 | 2.354 ± 0.121 | 2.429 | 2.501 | 1.857 ± 0.096 | 1.946 | 2.020 | 1.594 ± 0.087 | 1.660 | 1.721 |
| 0.276 | 4.856 ± 0.156 | 4.946 | 5.005 | 4.546 ± 0.149 | 4.464 | 4.536 | 4.154 ± 0.148 | 4.012 | 4.101 | 3.811 ± 0.138 | 3.719 | 3.804 |
| 0.303 | 4.937 ± 0.123 | 5.175 | 5.231 | 4.599 ± 0.114 | 4.715 | 4.779 | 4.300 ± 0.102 | 4.274 | 4.358 | 3.856 ± 0.094 | 3.988 | 4.076 |
| 0.356 | 5.537 ± 0.115 | 5.589 | 5.632 | 4.918 ± 0.102 | 5.160 | 5.222 | 4.609 ± 0.096 | 4.732 | 4.806 | 4.492 ± 0.093 | 4.458 | 4.537 |
| 0.384 | 5.961 ± 0.208 | 5.789 | 5.823 | 5.473 ± 0.175 | 5.370 | 5.418 | 4.981 ± 0.169 | 4.946 | 5.003 | 4.620 ± 0.156 | 4.677 | 4.741 |
| 0.511 | 6.385 ± 0.131 | 6.600 | 6.606 | 5.931 ± 0.122 | 6.200 | 6.213 | 5.683 ± 0.117 | 5.778 | 5.805 | 5.782 ± 0.119 | 5.517 | 5.550 |
| 0.662 | 7.141 ± 0.146 | 7.439 | 7.410 | 6.736 ± 0.138 | 7.034 | 7.022 | 6.498 ± 0.134 | 6.595 | 6.590 | 6.171 ± 0.127 | 6.331 | 6.338 |
| 0.779 | 8.004 ± 0.210 | 8.035 | 8.008 | 7.944 ± 0.208 | 7.618 | 7.594 | 7.482 ± 0.196 | 7.161 | 7.150 | 7.093 ± 0.186 | 6.889 | 6.881 |
| 0.835 | 8.088 ± 0.199 | 8.309 | 8.272 | 8.276 ± 0.209 | 7.884 | 7.857 | 7.683 ± 0.191 | 7.418 | 7.403 | 7.005 ± 0.179 | 7.141 | 7.133 |
| 0.867 | 8.358 ± 0.325 | 8.465 | 8.430 | 7.792 ± 0.276 | 8.036 | 8.021 | 7.955 ± 0.287 | 7.564 | 7.558 | 7.240 ± 0.280 | 7.285 | 7.288 |
| 0.964 | 9.228 ± 0.205 | 8.915 | 8.894 | 8.787 ± 0.196 | 8.473 | 8.456 | 8.065 ± 0.178 | 7.983 | 7.954 | 7.952 ± 0.178 | 7.695 | 7.666 |
| 1.086 | 9.529 ± 0.250 | 9.457 | 9.434 | 8.755 ± 0.229 | 8.997 | 8.988 | 8.143 ± 0.211 | 8.485 | 8.480 | 7.821 ± 0.198 | 8.186 | 8.198 |
| 1.112 | 9.531 ± 0.205 | 9.571 | 9.558 | 9.295 ± 0.200 | 9.107 | 9.101 | 8.884 ± 0.191 | 8.590 | 8.581 | 8.367 ± 0.180 | 8.289 | 8.297 |
| 1.173 | 9.435 ± 0.199 | 9.837 | 9.833 | 9.643 ± 0.204 | 9.363 | 9.349 | 8.735 ± 0.184 | 8.834 | 8.833 | 8.554 ± 0.180 | 8.527 | 8.536 |
| 1.213 | 9.889 ± 0.455 | 10.009 | 9.992 | 9.756 ± 0.464 | 9.528 | 9.508 | 9.381 ± 0.432 | 8.992 | 8.975 | 8.288 ± 0.398 | 8.680 | 8.661 |
| 1.275 | 9.852 ± 0.205 | 10.271 | 10.215 | 9.646 ± 0.201 | 9.779 | 9.760 | 9.226 ± 0.192 | 9.231 | 9.222 | 8.791 ± 0.183 | 8.912 | 8.903 |
| 1.299 | 10.593 ± 0.397 | 10.371 | 10.361 | 9.446 ± 0.345 | 9.875 | 9.861 | 9.197 ± 0.335 | 9.322 | 9.309 | 9.258 ± 0.351 | 9.000 | 8.995 |

(continued)

Table 5 (continued)

| Energy (MeV) | BiNO ₅ | | | BiNO ₁₀ | | | BiNO ₁₅ | | | BiNO ₂₀ | | |
|--------------|-------------------|--------|--------|--------------------|--------|--------|--------------------|-------|-------|--------------------|-------|-------|
| | Exp | WinX | GEANT | Exp | WinX | GEANT | Exp | WinX | GEANT | Exp | WinX | GEANT |
| 1.333 | 10.268 ± 0.214 | 10.510 | 10.493 | 9.868 ± 0.205 | 10.009 | 9.995 | 9.093 ± 0.189 | 9.449 | 9.438 | 9.243 ± 0.192 | 9.124 | 9.104 |
| 1.408 | 11.222 ± 0.230 | 10.813 | 10.801 | 10.725 ± 0.220 | 10.299 | 10.298 | 9.750 ± 0.200 | 9.724 | 9.720 | 9.064 ± 0.186 | 9.390 | 9.386 |

Table 6 Experimental, theoretical, and GEANT results of TVL (cm) for produced polyester based composites

| Energy (MeV) | BiNO ₅ | | | BiNO ₁₀ | | | BiNO ₁₅ | | | BiNO ₂₀ | | |
|--------------|-------------------|---------------|--------|--------------------|---------------|--------|--------------------|---------------|--------|--------------------|---------------|--------|
| | Exp | WinX | GEANT | Exp | WinX | GEANT | Exp | WinX | GEANT | Exp | WinX | GEANT |
| | 0.060 | 7.033 ± 0.144 | 6.983 | 7.529 | 4.807 ± 0.099 | 5.048 | 5.495 | 3.698 ± 0.076 | 3.871 | 4.271 | 3.139 ± 0.065 | 3.211 |
| 0.081 | 9.642 ± 0.201 | 9.410 | 9.977 | 7.182 ± 0.147 | 7.537 | 8.106 | 6.293 ± 0.129 | 6.174 | 6.733 | 5.426 ± 0.111 | 5.344 | 5.861 |
| 0.122 | 9.065 ± 0.205 | 9.382 | 9.629 | 7.129 ± 0.168 | 7.009 | 7.213 | 5.380 ± 0.119 | 5.482 | 5.693 | 4.395 ± 0.101 | 4.604 | 4.776 |
| 0.136 | 10.221 ± 0.487 | 10.405 | 10.690 | 7.821 ± 0.402 | 8.069 | 8.310 | 6.170 ± 0.318 | 6.466 | 6.709 | 5.297 ± 0.291 | 5.515 | 5.718 |
| 0.276 | 16.132 ± 0.518 | 16.430 | 16.628 | 15.103 ± 0.496 | 14.827 | 15.067 | 13.798 ± 0.492 | 13.328 | 13.622 | 12.661 ± 0.457 | 12.354 | 12.637 |
| 0.303 | 16.401 ± 0.409 | 17.191 | 17.377 | 15.276 ± 0.377 | 15.664 | 15.876 | 14.285 ± 0.337 | 14.198 | 14.477 | 12.810 ± 0.314 | 13.249 | 13.541 |
| 0.356 | 18.394 ± 0.383 | 18.567 | 18.709 | 16.338 ± 0.340 | 17.141 | 17.347 | 15.310 ± 0.318 | 15.720 | 15.964 | 14.921 ± 0.310 | 14.810 | 15.072 |
| 0.384 | 19.801 ± 0.691 | 19.231 | 19.345 | 18.180 ± 0.581 | 17.838 | 17.998 | 16.545 ± 0.560 | 16.431 | 16.619 | 15.349 ± 0.517 | 15.536 | 15.749 |
| 0.511 | 21.212 ± 0.436 | 21.924 | 21.946 | 19.704 ± 0.405 | 20.595 | 20.641 | 18.878 ± 0.388 | 19.194 | 19.284 | 19.207 ± 0.394 | 18.328 | 18.438 |
| 0.662 | 23.722 ± 0.486 | 24.712 | 24.615 | 22.377 ± 0.460 | 23.366 | 23.328 | 21.585 ± 0.445 | 21.908 | 21.890 | 20.498 ± 0.421 | 21.031 | 21.053 |
| 0.779 | 26.587 ± 0.698 | 26.693 | 26.601 | 26.390 ± 0.692 | 25.306 | 25.226 | 24.855 ± 0.653 | 23.788 | 23.752 | 23.561 ± 0.617 | 22.885 | 22.859 |
| 0.835 | 26.868 ± 0.662 | 27.601 | 27.480 | 27.492 ± 0.693 | 26.191 | 26.100 | 25.521 ± 0.636 | 24.641 | 24.593 | 23.270 ± 0.594 | 23.723 | 23.695 |
| 0.867 | 27.764 ± 1.079 | 28.121 | 28.003 | 25.884 ± 0.918 | 26.696 | 26.644 | 26.425 ± 0.953 | 25.126 | 25.108 | 24.051 ± 0.931 | 24.199 | 24.209 |
| 0.964 | 30.655 ± 0.680 | 29.616 | 29.546 | 29.188 ± 0.651 | 28.146 | 28.090 | 26.791 ± 0.592 | 26.519 | 26.423 | 26.417 ± 0.591 | 25.563 | 25.466 |
| 1.086 | 31.655 ± 0.832 | 31.416 | 31.338 | 29.084 ± 0.760 | 29.886 | 29.858 | 27.051 ± 0.702 | 28.185 | 28.170 | 25.981 ± 0.656 | 27.193 | 27.233 |
| 1.112 | 31.662 ± 0.681 | 31.795 | 31.751 | 30.876 ± 0.664 | 30.252 | 30.231 | 29.511 ± 0.635 | 28.535 | 28.507 | 27.796 ± 0.597 | 27.534 | 27.562 |
| 1.173 | 31.343 ± 0.661 | 32.678 | 32.664 | 32.035 ± 0.676 | 31.103 | 31.058 | 29.018 ± 0.613 | 29.347 | 29.342 | 28.416 ± 0.598 | 28.325 | 28.357 |
| 1.213 | 32.850 ± 1.512 | 33.250 | 33.193 | 32.409 ± 1.542 | 31.652 | 31.586 | 31.164 ± 1.436 | 29.870 | 29.815 | 27.533 ± 1.321 | 28.834 | 28.771 |
| 1.275 | 32.727 ± 0.683 | 34.119 | 33.935 | 32.044 ± 0.668 | 32.487 | 32.422 | 30.649 ± 0.638 | 30.664 | 30.634 | 29.202 ± 0.608 | 29.606 | 29.575 |
| 1.299 | 35.188 ± 1.318 | 34.451 | 34.419 | 31.380 ± 1.147 | 32.804 | 32.759 | 30.552 ± 1.113 | 30.966 | 30.923 | 30.754 ± 1.166 | 29.899 | 29.880 |

(continued)

Table 6 (continued)

| Energy (MeV) | BiNO ₅ | | | BiNO ₁₀ | | | BiNO ₁₅ | | | BiNO ₂₀ | | |
|--------------|-------------------|--------|--------|--------------------|--------|--------|--------------------|--------|--------|--------------------|--------|--------|
| | Exp | WinX | GEANT | Exp | WinX | GEANT | Exp | WinX | GEANT | Exp | WinX | GEANT |
| 1.333 | 34.109 ± 0.711 | 34.915 | 34.857 | 32.782 ± 0.682 | 33.249 | 33.203 | 30.205 ± 0.629 | 31.388 | 31.354 | 30.705 ± 0.638 | 30.309 | 30.244 |
| 1.408 | 37.278 ± 0.765 | 35.921 | 35.880 | 35.628 ± 0.731 | 34.212 | 34.208 | 32.390 ± 0.664 | 32.301 | 32.290 | 30.110 ± 0.618 | 31.194 | 31.178 |

Table 7 Experimental, theoretical, and GEANT results of MFP (cm) for produced polyester based composites

| Energy (MeV) | BiNO ₅ | | | BiNO ₁₀ | | | BiNO ₁₅ | | | BiNO ₂₀ | | |
|--------------|-------------------|---------------|--------|--------------------|---------------|--------|--------------------|---------------|--------|--------------------|---------------|--------|
| | Exp | WinX | GEANT | Exp | WinX | GEANT | Exp | WinX | GEANT | Exp | WinX | GEANT |
| | 0.060 | 3.054 ± 0.063 | 3.033 | 3.270 | 2.088 ± 0.043 | 2.192 | 2.386 | 1.606 ± 0.033 | 1.681 | 1.855 | 1.363 ± 0.028 | 1.395 |
| 0.081 | 4.188 ± 0.087 | 4.087 | 4.333 | 3.119 ± 0.064 | 3.273 | 3.520 | 2.733 ± 0.056 | 2.681 | 2.924 | 2.357 ± 0.048 | 2.321 | 2.545 |
| 0.122 | 3.937 ± 0.089 | 4.074 | 4.182 | 3.096 ± 0.073 | 3.044 | 3.132 | 2.336 ± 0.052 | 2.381 | 2.472 | 1.909 ± 0.044 | 1.999 | 2.074 |
| 0.136 | 4.439 ± 0.212 | 4.519 | 4.643 | 3.397 ± 0.175 | 3.504 | 3.609 | 2.679 ± 0.138 | 2.808 | 2.914 | 2.300 ± 0.126 | 2.395 | 2.483 |
| 0.276 | 7.006 ± 0.225 | 7.135 | 7.221 | 6.559 ± 0.215 | 6.439 | 6.544 | 5.993 ± 0.214 | 5.788 | 5.916 | 5.498 ± 0.198 | 5.365 | 5.488 |
| 0.303 | 7.123 ± 0.178 | 7.466 | 7.547 | 6.634 ± 0.164 | 6.803 | 6.895 | 6.204 ± 0.147 | 6.166 | 6.287 | 5.563 ± 0.136 | 5.754 | 5.881 |
| 0.356 | 7.989 ± 0.166 | 8.064 | 8.125 | 7.096 ± 0.148 | 7.444 | 7.534 | 6.649 ± 0.138 | 6.827 | 6.933 | 6.480 ± 0.134 | 6.432 | 6.546 |
| 0.384 | 8.599 ± 0.300 | 8.352 | 8.401 | 7.895 ± 0.252 | 7.747 | 7.817 | 7.186 ± 0.243 | 7.136 | 7.218 | 6.666 ± 0.225 | 6.747 | 6.840 |
| 0.511 | 9.212 ± 0.189 | 9.521 | 9.531 | 8.557 ± 0.176 | 8.945 | 8.964 | 8.198 ± 0.168 | 8.336 | 8.375 | 8.342 ± 0.171 | 7.960 | 8.007 |
| 0.662 | 10.302 ± 0.211 | 10.732 | 10.690 | 9.718 ± 0.200 | 10.148 | 10.131 | 9.374 ± 0.193 | 9.515 | 9.507 | 8.902 ± 0.183 | 9.134 | 9.143 |
| 0.779 | 11.547 ± 0.303 | 11.593 | 11.553 | 11.461 ± 0.301 | 10.990 | 10.956 | 10.794 ± 0.283 | 10.331 | 10.315 | 10.232 ± 0.268 | 9.939 | 9.928 |
| 0.835 | 11.669 ± 0.288 | 11.987 | 11.934 | 11.939 ± 0.301 | 11.375 | 11.335 | 11.084 ± 0.276 | 10.701 | 10.681 | 10.106 ± 0.258 | 10.303 | 10.291 |
| 0.867 | 12.058 ± 0.469 | 12.213 | 12.161 | 11.241 ± 0.399 | 11.594 | 11.571 | 11.476 ± 0.414 | 10.912 | 10.904 | 10.445 ± 0.404 | 10.510 | 10.514 |
| 0.964 | 13.313 ± 0.295 | 12.862 | 12.832 | 12.676 ± 0.283 | 12.224 | 12.199 | 11.635 ± 0.257 | 11.517 | 11.475 | 11.473 ± 0.257 | 11.102 | 11.060 |
| 1.086 | 13.748 ± 0.361 | 13.644 | 13.610 | 12.631 ± 0.330 | 12.979 | 12.967 | 11.748 ± 0.305 | 12.241 | 12.234 | 11.283 ± 0.285 | 11.810 | 11.827 |
| 1.112 | 13.750 ± 0.296 | 13.809 | 13.789 | 13.409 ± 0.288 | 13.138 | 13.129 | 12.816 ± 0.276 | 12.393 | 12.380 | 12.071 ± 0.259 | 11.958 | 11.970 |
| 1.173 | 13.612 ± 0.287 | 14.192 | 14.186 | 13.913 ± 0.294 | 13.508 | 13.488 | 12.602 ± 0.266 | 12.745 | 12.743 | 12.341 ± 0.260 | 12.301 | 12.315 |
| 1.213 | 14.267 ± 0.657 | 14.440 | 14.416 | 14.075 ± 0.670 | 13.746 | 13.718 | 13.535 ± 0.623 | 12.972 | 12.948 | 11.958 ± 0.574 | 12.522 | 12.495 |
| 1.275 | 14.213 ± 0.296 | 14.818 | 14.738 | 13.917 ± 0.290 | 14.109 | 14.081 | 13.311 ± 0.277 | 13.317 | 13.304 | 12.682 ± 0.264 | 12.858 | 12.844 |
| 1.299 | 15.282 ± 0.572 | 14.962 | 14.948 | 13.628 ± 0.498 | 14.247 | 14.227 | 13.269 ± 0.483 | 13.448 | 13.430 | 13.356 ± 0.506 | 12.985 | 12.977 |

(continued)

Table 7 (continued)

| Energy (MeV) | BiNO ₅ | | BiNO ₁₀ | | BiNO ₁₅ | | BiNO ₂₀ | |
|--------------|-------------------|---------------|--------------------|---------------|--------------------|---------------|--------------------|---------------|
| | Exp | GEANT WinX | Exp | GEANT WinX | Exp | GEANT WinX | Exp | GEANT WinX |
| 1.333 | 14.813 ± 0.309 | 15.163 | 14.237 ± 0.296 | 14.440 | 13.118 ± 0.273 | 13.632 | 13.335 ± 0.277 | 13.163 |
| 1.408 | 16.190 ± 0.332 | 15.600 | 15.473 ± 0.318 | 14.858 | 14.067 ± 0.289 | 14.028 | 13.077 ± 0.268 | 13.547 |
| | | | | 14.856 | 14.023 | 14.023 | | 13.541 |

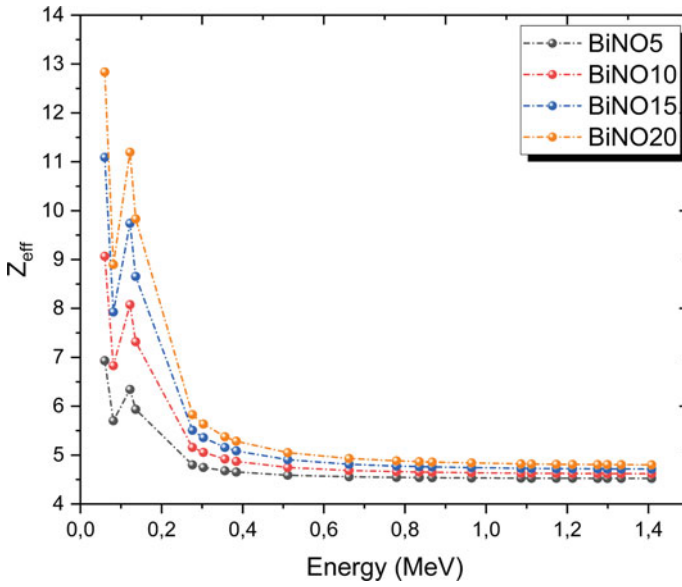


Fig. 8 Z_{eff} of the produced polyester-based composites as a function of energy

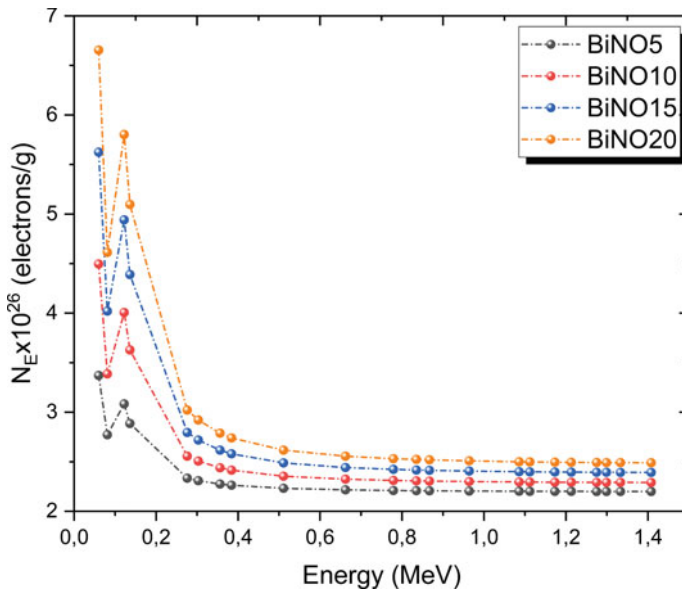


Fig. 9 N_E of the produced polyester-based composites as a function of energy

Table 8 Experimental and theoretical results of Z_{eff} for produced polyester based composites

| Energy (MeV) | BiNO ₅ | | BiNO ₁₀ | | BiNO ₁₅ | | BiNO ₂₀ | |
|--------------|-------------------|--------|--------------------|--------|--------------------|---------|--------------------|---------|
| | Exp | WinX | GEANT | Exp | WinX | GEANT | Exp | WinX |
| 0.060 | 6.8828 ± 0.1414 | 6.9322 | 9.5233 ± 0.1962 | 9.0679 | 11.6095 ± 0.2392 | 11.0898 | 13.1298 ± 0.2714 | 12.8360 |
| 0.081 | 5.5656 ± 0.1162 | 5.7029 | 7.1681 ± 0.1472 | 6.8298 | 7.7760 ± 0.1591 | 7.9263 | 8.7623 ± 0.1798 | 8.8982 |
| 0.122 | 6.5639 ± 0.1485 | 6.3421 | 7.9419 ± 0.1874 | 8.0785 | 9.9274 ± 0.2200 | 9.7419 | 11.7271 ± 0.2697 | 11.1945 |
| 0.136 | 6.0424 ± 0.2880 | 5.9354 | 7.5498 ± 0.3883 | 7.3178 | 9.0699 ± 0.4671 | 8.6546 | 10.2372 ± 0.5617 | 9.8325 |
| 0.276 | 4.8895 ± 0.1569 | 4.8010 | 5.0624 ± 0.1662 | 5.1564 | 5.3214 ± 0.1899 | 5.5091 | 5.6872 ± 0.2053 | 5.8284 |
| 0.303 | 4.9768 ± 0.1241 | 4.7481 | 5.1824 ± 0.1279 | 5.0544 | 5.3258 ± 0.1258 | 5.3585 | 5.8273 ± 0.1427 | 5.6345 |
| 0.356 | 4.7219 ± 0.0982 | 4.6780 | 5.1606 ± 0.1074 | 4.9190 | 5.2969 ± 0.1101 | 5.1586 | 5.3367 ± 0.1107 | 5.3765 |
| 0.384 | 4.5191 ± 0.1577 | 4.6531 | 4.7795 ± 0.1528 | 4.8709 | 5.0524 ± 0.1711 | 5.0875 | 5.3493 ± 0.1802 | 5.2847 |
| 0.511 | 4.7435 ± 0.0975 | 4.5895 | 4.9624 ± 0.1019 | 4.7476 | 4.9870 ± 0.1024 | 4.9049 | 4.8176 ± 0.0989 | 5.0486 |
| 0.662 | 4.7476 ± 0.0973 | 4.5575 | 4.8929 ± 0.1006 | 4.6858 | 4.8856 ± 0.1007 | 4.8134 | 5.0583 ± 0.1040 | 4.9302 |
| 0.779 | 4.5627 ± 0.1199 | 4.5446 | 4.4694 ± 0.1172 | 4.6608 | 4.5714 ± 0.1200 | 4.7764 | 4.7423 ± 0.1241 | 4.8823 |
| 0.835 | 4.6643 ± 0.1150 | 4.5403 | 4.4324 ± 0.1118 | 4.6525 | 4.5997 ± 0.1146 | 4.7641 | 4.9610 ± 0.1267 | 4.8664 |
| 0.867 | 4.5967 ± 0.1786 | 4.5383 | 4.7943 ± 0.1700 | 4.6485 | 4.5242 ± 0.1631 | 4.7581 | 4.8886 ± 0.1892 | 4.8585 |
| 0.964 | 4.3795 ± 0.0971 | 4.5331 | 4.4728 ± 0.0998 | 4.6384 | 4.6949 ± 0.1037 | 4.7432 | 4.6829 ± 0.1048 | 4.8393 |
| 1.086 | 4.4939 ± 0.1181 | 4.5281 | 4.7566 ± 0.1243 | 4.6289 | 4.9275 ± 0.1279 | 4.7292 | 5.0461 ± 0.1275 | 4.8212 |
| 1.112 | 4.5465 ± 0.0978 | 4.5274 | 4.5340 ± 0.0975 | 4.6275 | 4.5707 ± 0.0983 | 4.7270 | 4.7730 ± 0.1025 | 4.8183 |
| 1.173 | 4.7188 ± 0.0995 | 4.5260 | 4.4901 ± 0.0948 | 4.6247 | 4.7762 ± 0.1008 | 4.7227 | 4.7972 ± 0.1009 | 4.8127 |
| 1.213 | 4.5804 ± 0.2108 | 4.5254 | 4.5152 ± 0.2148 | 4.6232 | 4.5244 ± 0.2084 | 4.7205 | 5.0369 ± 0.2416 | 4.8098 |
| 1.275 | 4.7170 ± 0.0984 | 4.5246 | 4.6852 ± 0.0977 | 4.6215 | 4.7201 ± 0.0983 | 4.7178 | 4.8726 ± 0.1015 | 4.8062 |
| 1.299 | 4.4295 ± 0.1659 | 4.5244 | 4.8307 ± 0.1766 | 4.6209 | 4.7808 ± 0.1742 | 4.7169 | 4.6715 ± 0.1771 | 4.8051 |

(continued)

Table 8 (continued)

| Energy (MeV) | BiNO ₅ | | BiNO ₁₀ | | BiNO ₁₅ | | BiNO ₂₀ | |
|--------------|-------------------|--------|--------------------|--------|--------------------|--------|--------------------|--------|
| | Exp | WinX | GEANT | Exp | WinX | GEANT | Exp | WinX |
| 1.333 | 4.6310 ± 0.0965 | 4.5241 | 4.6862 ± 0.0975 | 4.6203 | 4.9007 ± 0.1020 | 4.7160 | 4.7419 ± 0.0985 | 4.8038 |
| 1.408 | 4.3592 ± 0.0894 | 4.5239 | 4.4359 ± 0.0910 | 4.6195 | 4.7016 ± 0.0964 | 4.7146 | 4.9748 ± 0.1021 | 4.8019 |

Table 9 Experimental and theoretical results of $N_E \times 10^{26}$ (electrons g^{-1}) for produced polyester based composites

| Energy (MeV) | BiNO ₅ | | BiNO ₁₀ | | BiNO ₁₅ | | BiNO ₂₀ | |
|--------------|-------------------|--------|--------------------|--------|--------------------|--------|--------------------|--------|
| | Exp | WinX | GEANT | Exp | WinX | GEANT | Exp | WinX |
| 0.060 | 3.3467 ± 0.0687 | 3.3707 | 4.7220 ± 0.0973 | 4.4962 | 5.8890 ± 0.1213 | 5.6254 | 6.8069 ± 0.1407 | 6.6546 |
| 0.081 | 2.7062 ± 0.0565 | 2.7730 | 3.5542 ± 0.0730 | 3.3864 | 3.9444 ± 0.0807 | 4.0207 | 4.5427 ± 0.0932 | 4.6131 |
| 0.122 | 3.1916 ± 0.0722 | 3.0838 | 3.9378 ± 0.0929 | 4.0055 | 5.0357 ± 0.1116 | 4.9416 | 6.0797 ± 0.1398 | 5.8036 |
| 0.136 | 2.9381 ± 0.1401 | 2.8861 | 3.7434 ± 0.1925 | 3.6284 | 4.6008 ± 0.2369 | 4.3901 | 5.3073 ± 0.2912 | 5.0975 |
| 0.276 | 2.3775 ± 0.0763 | 2.3345 | 2.5101 ± 0.0824 | 2.5567 | 2.6993 ± 0.0963 | 2.7945 | 2.9484 ± 0.1064 | 3.0217 |
| 0.303 | 2.4199 ± 0.0603 | 2.3087 | 2.5696 ± 0.0634 | 2.5061 | 2.7015 ± 0.0638 | 2.7182 | 3.0211 ± 0.0740 | 2.9211 |
| 0.356 | 2.2960 ± 0.0478 | 2.2746 | 2.5588 ± 0.0533 | 2.4390 | 2.6869 ± 0.0558 | 2.6167 | 2.7667 ± 0.0574 | 2.7874 |
| 0.384 | 2.1974 ± 0.0767 | 2.2625 | 2.3698 ± 0.0757 | 2.4151 | 2.5629 ± 0.0868 | 2.5807 | 2.7733 ± 0.0934 | 2.7398 |
| 0.511 | 2.3065 ± 0.0474 | 2.2316 | 2.4605 ± 0.0505 | 2.3540 | 2.5297 ± 0.0520 | 2.4881 | 2.4976 ± 0.0513 | 2.6173 |
| 0.662 | 2.3085 ± 0.0473 | 2.2160 | 2.4260 ± 0.0499 | 2.3233 | 2.4782 ± 0.0511 | 2.4416 | 2.6224 ± 0.0539 | 2.5560 |
| 0.779 | 2.2186 ± 0.0583 | 2.2098 | 2.2161 ± 0.0581 | 2.3110 | 2.3189 ± 0.0609 | 2.4229 | 2.4585 ± 0.0644 | 2.5312 |
| 0.835 | 2.2680 ± 0.0559 | 2.2077 | 2.1977 ± 0.0554 | 2.3069 | 2.3332 ± 0.0581 | 2.4166 | 2.5719 ± 0.0657 | 2.5229 |
| 0.867 | 2.2351 ± 0.0869 | 2.2067 | 2.3772 ± 0.0843 | 2.3049 | 2.2949 ± 0.0827 | 2.4136 | 2.5344 ± 0.0981 | 2.5188 |
| 0.964 | 2.1295 ± 0.0472 | 2.2042 | 2.2177 ± 0.0495 | 2.2999 | 2.3815 ± 0.0526 | 2.4060 | 2.4278 ± 0.0543 | 2.5088 |
| 1.086 | 2.1851 ± 0.0574 | 2.2018 | 2.3585 ± 0.0616 | 2.2952 | 2.4995 ± 0.0649 | 2.3989 | 2.6161 ± 0.0661 | 2.4995 |
| 1.112 | 2.2107 ± 0.0475 | 2.2014 | 2.2481 ± 0.0484 | 2.2944 | 2.3185 ± 0.0499 | 2.3978 | 2.4745 ± 0.0531 | 2.4980 |
| 1.173 | 2.2945 ± 0.0484 | 2.2008 | 2.2263 ± 0.0470 | 2.2930 | 2.4228 ± 0.0512 | 2.3956 | 2.4870 ± 0.0523 | 2.4951 |
| 1.213 | 2.2272 ± 0.1025 | 2.2004 | 2.2388 ± 0.1065 | 2.2923 | 2.2950 ± 0.1057 | 2.3945 | 2.6113 ± 0.1253 | 2.4936 |
| 1.275 | 2.2936 ± 0.0478 | 2.2001 | 2.3231 ± 0.0484 | 2.2915 | 2.3943 ± 0.0498 | 2.3931 | 2.5261 ± 0.0526 | 2.4917 |
| 1.299 | 2.1538 ± 0.0807 | 2.1999 | 2.3952 ± 0.0876 | 2.2912 | 2.4251 ± 0.0883 | 2.3927 | 2.4218 ± 0.0918 | 2.4911 |

(continued)

Table 9 (continued)

| Energy (MeV) | BiNO ₅ | | BiNO ₁₀ | | BiNO ₁₅ | | BiNO ₂₀ | |
|--------------|-------------------|--------|--------------------|-----------------|--------------------|-----------------|--------------------|-----------------|
| | Exp | WinX | GEANT | WinX | Exp | WinX | GEANT | Exp |
| 1.333 | 2.2518 ± 0.0469 | 2.1998 | 2.3236 ± 0.0484 | 2.4859 ± 0.0517 | 2.2909 | 2.4859 ± 0.0517 | 2.3922 | 2.4584 ± 0.0511 |
| 1.408 | 2.1197 ± 0.0435 | 2.1997 | 2.1994 ± 0.0451 | 2.3849 ± 0.0489 | 2.2905 | 2.3849 ± 0.0489 | 2.3915 | 2.5791 ± 0.0529 |

WinX

WinX

WinX

WinX

WinX

WinX

WinX

WinX

WinX

WinX

WinX

WinX

WinX

WinX

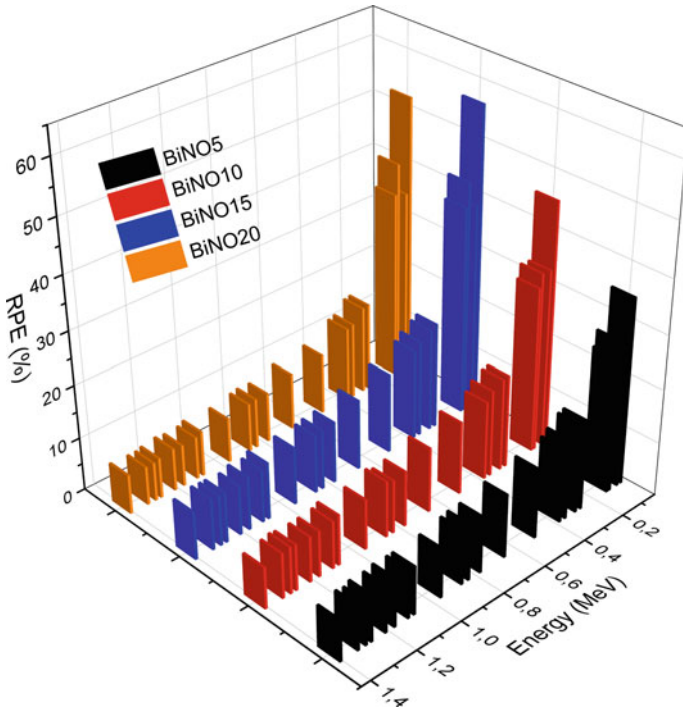


Fig. 10 RPE of the produced polyester samples as a function of energy

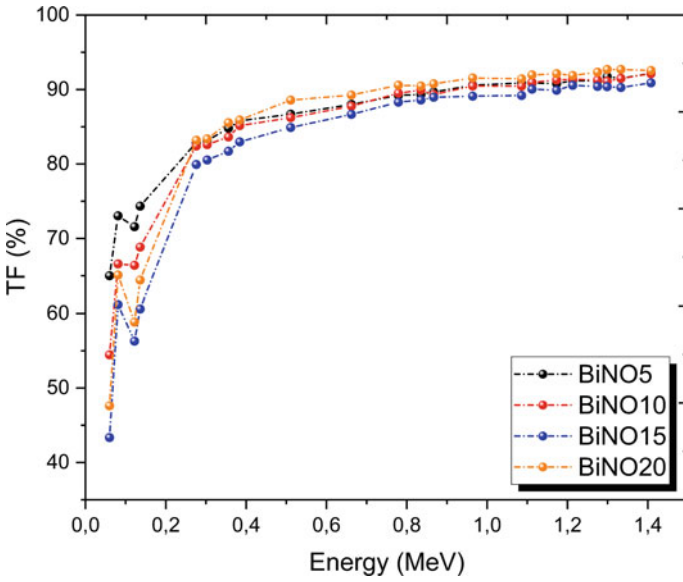


Fig. 11 TF of the produced polyester samples as a function of energy

Table 10 Experimental values of RPE (%) and TF (%) for produced polyester based composites

| Energy (MeV) | BiNO ₅ | | BiNO ₁₀ | | BiNO ₁₅ | | BiNO ₂₀ | |
|--------------|-------------------|--------------|--------------------|--------------|--------------------|--------------|--------------------|--------------|
| | RPE (%) | TF (%) | RPE (%) | TF (%) | RPE (%) | TF (%) | RPE (%) | TF (%) |
| 0.060 | 35.01 ± 0.16 | 64.99 ± 0.30 | 45.53 ± 0.23 | 54.47 ± 0.27 | 56.65 ± 0.28 | 43.35 ± 0.21 | 52.39 ± 0.27 | 47.61 ± 0.25 |
| 0.081 | 26.97 ± 0.16 | 73.03 ± 0.44 | 33.41 ± 0.16 | 66.59 ± 0.31 | 38.80 ± 0.17 | 61.20 ± 0.26 | 34.90 ± 0.16 | 65.10 ± 0.30 |
| 0.122 | 28.42 ± 0.30 | 71.58 ± 0.76 | 33.61 ± 0.42 | 66.39 ± 0.83 | 43.70 ± 0.42 | 56.30 ± 0.54 | 41.14 ± 0.47 | 58.86 ± 0.67 |
| 0.136 | 25.66 ± 1.11 | 74.34 ± 3.22 | 31.16 ± 1.48 | 68.84 ± 3.26 | 39.40 ± 1.87 | 60.60 ± 2.88 | 35.58 ± 1.82 | 64.42 ± 3.29 |
| 0.276 | 17.13 ± 0.43 | 82.87 ± 2.08 | 17.58 ± 0.46 | 82.42 ± 2.14 | 20.07 ± 0.59 | 79.93 ± 2.36 | 16.81 ± 0.51 | 83.19 ± 2.50 |
| 0.303 | 16.87 ± 0.25 | 83.13 ± 1.24 | 17.40 ± 0.25 | 82.60 ± 1.20 | 19.45 ± 0.24 | 80.55 ± 1.01 | 16.63 ± 0.23 | 83.37 ± 1.18 |
| 0.356 | 15.19 ± 0.09 | 84.81 ± 0.48 | 16.37 ± 0.09 | 83.63 ± 0.48 | 18.28 ± 0.10 | 81.72 ± 0.46 | 14.46 ± 0.08 | 85.54 ± 0.47 |
| 0.384 | 14.19 ± 0.41 | 85.81 ± 2.45 | 14.84 ± 0.37 | 85.16 ± 2.12 | 17.04 ± 0.47 | 82.96 ± 2.27 | 14.08 ± 0.38 | 85.92 ± 2.33 |
| 0.511 | 13.31 ± 0.06 | 86.69 ± 0.41 | 13.78 ± 0.06 | 86.22 ± 0.40 | 15.10 ± 0.07 | 84.90 ± 0.40 | 11.42 ± 0.05 | 88.58 ± 0.41 |
| 0.662 | 11.99 ± 0.05 | 88.01 ± 0.40 | 12.24 ± 0.06 | 87.76 ± 0.42 | 13.34 ± 0.07 | 86.66 ± 0.43 | 10.74 ± 0.05 | 89.26 ± 0.42 |
| 0.779 | 10.77 ± 0.18 | 89.23 ± 1.52 | 10.48 ± 0.18 | 89.52 ± 1.52 | 11.69 ± 0.20 | 88.31 ± 1.50 | 9.41 ± 0.16 | 90.59 ± 1.53 |
| 0.835 | 10.67 ± 0.15 | 89.33 ± 1.29 | 10.08 ± 0.15 | 89.92 ± 1.38 | 11.40 ± 0.17 | 88.60 ± 1.32 | 9.53 ± 0.15 | 90.47 ± 1.44 |
| 0.867 | 10.34 ± 0.34 | 89.66 ± 2.99 | 10.67 ± 0.31 | 89.33 ± 2.62 | 11.04 ± 0.33 | 88.96 ± 2.67 | 9.23 ± 0.31 | 90.77 ± 3.01 |
| 0.964 | 9.41 ± 0.09 | 90.59 ± 0.87 | 9.52 ± 0.09 | 90.48 ± 0.89 | 10.89 ± 0.10 | 89.11 ± 0.84 | 8.44 ± 0.08 | 91.56 ± 0.92 |
| 1.086 | 9.13 ± 0.16 | 90.87 ± 1.55 | 9.55 ± 0.16 | 90.45 ± 1.52 | 10.80 ± 0.18 | 89.20 ± 1.48 | 8.58 ± 0.13 | 91.42 ± 1.41 |
| 1.112 | 9.13 ± 0.07 | 90.87 ± 0.72 | 9.03 ± 0.07 | 90.97 ± 0.72 | 9.94 ± 0.08 | 90.06 ± 0.71 | 8.04 ± 0.06 | 91.96 ± 0.72 |
| 1.173 | 9.22 ± 0.06 | 90.78 ± 0.61 | 8.71 ± 0.06 | 91.29 ± 0.62 | 10.10 ± 0.07 | 89.90 ± 0.61 | 7.87 ± 0.05 | 92.13 ± 0.60 |
| 1.213 | 8.81 ± 0.37 | 91.19 ± 3.78 | 8.62 ± 0.37 | 91.38 ± 3.94 | 9.44 ± 0.39 | 90.56 ± 3.76 | 8.11 ± 0.35 | 91.89 ± 4.01 |
| 1.275 | 8.84 ± 0.05 | 91.16 ± 0.54 | 8.71 ± 0.05 | 91.29 ± 0.54 | 9.59 ± 0.06 | 90.41 ± 0.52 | 7.67 ± 0.04 | 92.33 ± 0.54 |
| 1.299 | 8.25 ± 0.26 | 91.75 ± 2.91 | 8.89 ± 0.27 | 91.11 ± 2.79 | 9.62 ± 0.29 | 90.38 ± 2.75 | 7.30 ± 0.23 | 92.70 ± 2.99 |

(continued)

Table 10 (continued)

| Energy (MeV) | BiNO ₅ | | BiNO ₁₀ | | BiNO ₁₅ | | BiNO ₂₀ | |
|--------------|-------------------|--------------|--------------------|--------------|--------------------|--------------|--------------------|--------------|
| | RPE (%) | TF (%) | RPE (%) | TF (%) | RPE (%) | TF (%) | RPE (%) | TF (%) |
| 1.333 | 8.50 ± 0.05 | 91.50 ± 0.54 | 8.52 ± 0.05 | 91.48 ± 0.53 | 9.73 ± 0.06 | 90.27 ± 0.52 | 7.31 ± 0.04 | 92.69 ± 0.52 |
| 1.408 | 7.81 ± 0.04 | 92.19 ± 0.42 | 7.87 ± 0.04 | 92.13 ± 0.42 | 9.10 ± 0.04 | 90.90 ± 0.41 | 7.45 ± 0.03 | 92.55 ± 0.42 |

other samples. Therefore, inserting more BiNO into the sample provides a better neutron shielding property. Besides, the sample thickness and increasing the energy would also be effective on the neutron transmission. Because of this, the neutron transmission was tested at different energies using the samples that have different thicknesses. Figure 12 shows a comparison of transmitted neutron numbers with the neutron energy and the absorber thickness. As can be seen in the figure, neutron transmission increases with increasing energy, and the transmission decreases, while the absorber's thickness increases. The transmitted neutron numbers for different thicknesses at 4.5 meV are given in Table 13. Figure 13 shows the neutron transmission of the prepared samples with 10 mm thickness at seven different energies. As shown in the figure, transmission number is proportional to the energy, but increasing the BiNO concentration in the sample reduces the neutron transmission. The neutron transmission numbers for different BiNO doped samples at seven different energies are given in Table 14.

5 Summary

In this study, gamma and neutron attenuation features of composites obtained by the mixture of unsaturated polyester with 5, 10, 15, and 20% BiNO concentration were analyzed. Then, the obtained results were compared by theoretical and simulation results that were respectively obtained by WinXCOM and GEANT4 computer programs. The results showed that both gamma and neutron attenuation were achieved by inserting more BiNO into the sample. Among the prepared samples, the sample with 20% BiNO concentration was found to be the best radiation shielding material. In addition to being used for ionizing radiation shielding, such polyester composites can also be used as shielding absorbers as well as low-energy ionizing radiation. The obtained composite samples are advantageous compared to concrete because they are lightweight materials and their storage and transport operations can be easily applied. Because these composites reduce ionizing radiation to a level safe for humans, they can be used in hospitals as well as to be used to shield reactors. All these features of the unsaturated polyester samples show that the samples are very useful and practical to be used as radiation shielding materials.

Table 11 Effective removal cross section values for produced polyester based composites

| Element | BiNO ₅ ($\rho = 1.1455 \text{ g cm}^{-3}$) | | BiNO ₁₀ ($\rho = 1.2034 \text{ g cm}^{-3}$) | | BiNO ₁₅ ($\rho = 1.2753 \text{ g cm}^{-3}$) | | BiNO ₂₀ ($\rho = 1.3212 \text{ g cm}^{-3}$) | |
|---------|---|-------------------------------------|--|-------------------------------------|--|-------------------------------------|--|-------------------------------------|
| | Partial density | $\Sigma_R \text{ (cm}^{-1}\text{)}$ | Partial density | $\Sigma_R \text{ (cm}^{-1}\text{)}$ | Partial density | $\Sigma_R \text{ (cm}^{-1}\text{)}$ | Partial density | $\Sigma_R \text{ (cm}^{-1}\text{)}$ |
| H | 0.052024 | 0.031110 | 0.053370 | 0.031915 | 0.055311 | 0.033076 | 0.056113 | 0.033555 |
| C | 0.652874 | 0.032774 | 0.656183 | 0.032940 | 0.666534 | 0.033460 | 0.663013 | 0.033283 |
| N | 0.004490 | 0.000201 | 0.009026 | 0.000404 | 0.013752 | 0.000616 | 0.018239 | 0.000817 |
| O | 0.413471 | 0.016746 | 0.439621 | 0.017805 | 0.470991 | 0.019075 | 0.492810 | 0.019959 |
| Co | 0.000310 | 0.000006 | 0.000313 | 0.000006 | 0.000318 | 0.000006 | 0.000316 | 0.000006 |
| Bi | 0.022330 | 0.000230 | 0.044888 | 0.000462 | 0.068394 | 0.000704 | 0.090710 | 0.000934 |
| Total | 1.145500 | 0.081067 | 1.203400 | 0.083533 | 1.275300 | 0.086938 | 1.321200 | 0.088555 |

Table 12 Neutron total macroscopic cross sections (cm^{-1}), mean free paths (mm), and number of transmitted neutrons of 10 mm thickness sample and 10^7 neutrons at 4.5 meV for produced polyester based composites

| Sample | Total macroscopic cross section | Mean free path | Number of transmitted neutrons |
|--------------------|---------------------------------|---------------------|--------------------------------|
| BiNO ₅ | 0.13116 | 4.8941 ± 0.2887 | 8770806 |
| BiNO ₁₀ | 0.13498 | 4.8911 ± 0.2887 | 8737375 |
| BiNO ₁₅ | 0.14043 | 4.8857 ± 0.2887 | 8689840 |
| BiNO ₂₀ | 0.14291 | 4.8796 ± 0.2883 | 8668338 |

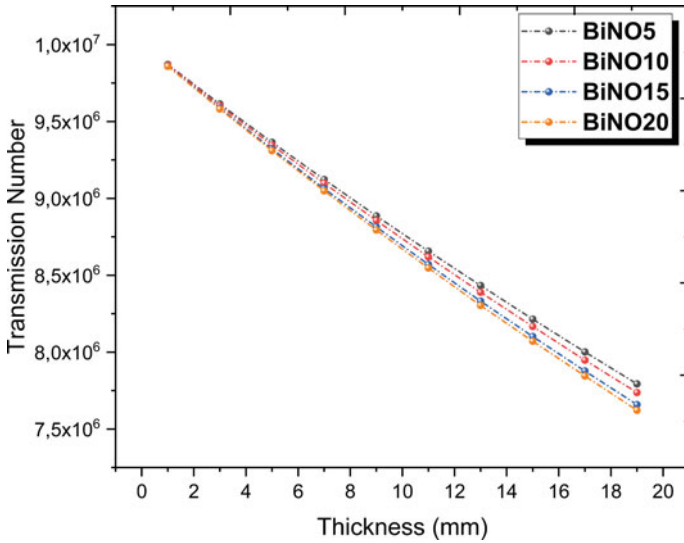


Fig. 12 Neutron transmission at 4.5 meV for the produced polyester samples that have different thicknesses

Table 13 Neutron transmission number for different thickness polyester-based composites and 10^7 neutrons at 4.5 meV

| Sample | 1 mm | 3 mm | 5 mm | 7 mm | 9 mm |
|--------------------|---------|---------|---------|---------|---------|
| BiNO ₅ | 9870430 | 9614064 | 9364781 | 9122425 | 8886020 |
| BiNO ₁₀ | 9866129 | 9602652 | 9346938 | 9097987 | 8856005 |
| BiNO ₁₅ | 9860632 | 9586791 | 9322011 | 9063194 | 8814276 |
| BiNO ₂₀ | 9858939 | 9580890 | 9310655 | 9049000 | 8794437 |
| | 11 mm | 13 mm | 15 mm | 17 mm | 19 mm |
| BiNO ₅ | 8656265 | 8432986 | 8214706 | 8001543 | 7793321 |
| BiNO ₁₀ | 8619678 | 8389208 | 8166435 | 7948184 | 7737594 |
| BiNO ₁₅ | 8570241 | 8331918 | 8101229 | 7877493 | 7658069 |
| BiNO ₂₀ | 8546730 | 8303897 | 8070757 | 7845223 | 7621981 |

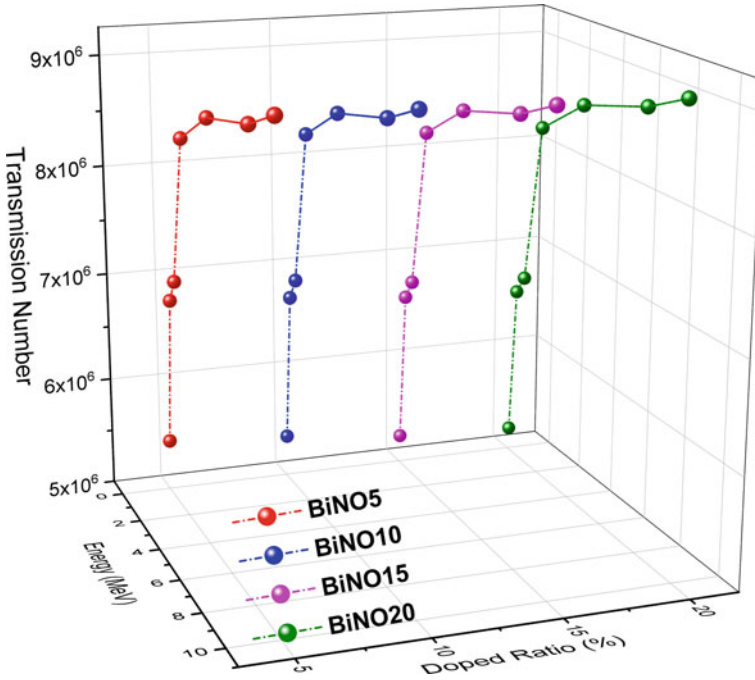


Fig. 13 Neutron transmission at seven different energies for the produced polyester samples that have 10 mm thickness

Table 14 Neutron transmission number for 10 mm thickness polyester-based composites and 10^7 neutrons at different energies

| Sample | 0.1 meV | 0.5 meV | 1 meV | 2 meV | 4.5 meV | 8 meV | 10 meV |
|--------------------|---------|---------|---------|---------|---------|---------|---------|
| BiNO ₅ | 5474438 | 6847487 | 7069319 | 8428088 | 8770806 | 8951806 | 9150398 |
| BiNO ₁₀ | 5390221 | 6771097 | 6980224 | 8389597 | 8737375 | 8926977 | 9125332 |
| BiNO ₁₅ | 5265482 | 6672761 | 6863268 | 8329953 | 8689840 | 8890242 | 9087910 |
| BiNO ₂₀ | 5215410 | 6622921 | 6801662 | 8300265 | 8668338 | 8878607 | 9072016 |

References

1. F. Akman, *Appl. Radiat. Isotopes* **115**, 295 (2016)
2. F. Akman, *Can. J. Phys.* **94**(7), 679 (2016)
3. P. Atashi, S. Rahmani, B. Ahadi, A. Rahmati, *J. Mater. Sci.-Mater. El.* **29**(14), 12306 (2018)
4. S.A.M. Issa, A.M. Ali, G. Susoy, H.O. Tekin, Y.B. Saddeek, R. Elsaman, H.H. Smailly, H. Algarni, *Ceram. Int.* **46**(12), 20251 (2020)
5. O. Agar, Z.Y. Khattari, M.I. Sayyed, H.O. Tekin, S. Al-Omari, M. Maghrabi, M.H.M. Zaid, I.V. Kityk, *Results Phys.* **12**, 101 (2019)
6. M.I. Sayyed, A. Kumar, H.O. Tekin, R. Kaur, M. Singh, O. Agar, M.U. Khandaker, *Prog. Nucl. Energ.* **118**, 103118 (2020)
7. A. Kahraman, E. Yilmaz, *Radiat. Phys. Chem.* **139**, 114 (2017)

8. C. Eke, O. Agar, C. Segebade, I. Boztosun, *Radiochim. Acta* **105**(10), 851 (2017)
9. M.I. Sayyed, H.O. Tekin, O. Kılıçoğlu, O. Agar, M.H.M. Zaid, *Results Phys.* **11**, 40 (2018)
10. B. Aygün, E. Şakar, E. Cinan, N.Y. Yorgun, M.I. Sayyed, O. Agar, A. Karabulut, *Radiat. Phys. Chem.* **174**, 108897 (2020)
11. G. Sathiyapriya, K. Marimuthu, M.I. Sayyed, A. Askin, O. Agar, *J. Non-Cryst. Solids* **522**, 119574 (2019)
12. B. Aygün, E. Şakar, O. Agar, M.I. Sayyed, A. Karabulut, V.P. Singh, *Prog. Nucl. Energ.* **133**, 103645 (2021)
13. O. Agar, *Radiochim. Acta* **106**(12), 1009 (2018)
14. F. Akman, M.I. Sayyed, M.R. Kaçal, H.O. Tekin, *J. Alloy Compd.* **772**, 516 (2019)
15. F. Akman, M.R. Kaçal, M.I. Sayyed, H.A. Karataş, *J. Alloy Compd.* **782**, 315 (2019)
16. O. Agar, M.I. Sayyed, F. Akman, H.O. Tekin, M.R. Kaçal, *Nucl. Eng. Technol.* **51**(3), 853 (2019)
17. R. Biswas, H. Sahadath, A.S. Mollah, M.F. Huq, *J. Radiat. Res. Appl. Sci.* **9**(1), 26 (2016)
18. M.I. Sayyed, F. Akman, A. Kumar, M.R. Kaçal, *Results Phys.* **11**, 1100 (2018)
19. B. Oto, N. Yıldız, F. Akdemir, E. Kavaz, *Prog. Nucl. Energ.* **85**, 391 (2015)
20. R. Li, Y. Gu, G. Zhang, Z. Yang, M. Li, Z. Zhang, *Compos. Sci. Technol.* **143**, 67 (2017)
21. M.S. Hossain, M.B. Uddin, M. Razzak, A.M.S. Chowdhury, R.A. Khan, *Radiat. Eff. Defect. S* **172**(11–12), 904 (2017)
22. Q. Li, Q. Wei, W. Zheng, Y. Zheng, N. Okosi, Z. Wang, M. Su, *ACS Appl. Mater. Int.* **10**(41), 35510 (2018)
23. N.I. Cherkashina, V.I. Pavlenko, A.V. Noskov, *Radiat. Phys. Chem.* **159**, 111 (2019)
24. M.R. Ambika, N. Nagaiah, V. Harish, N.K. Lokanath, M.A. Sridhar, N.M. Renukappa, S.K. Suman, *Radiat. Phys. Chem.* **130**, 351 (2017)
25. R. Li, Y. Gu, Y. Wang, Z. Yang, M. Li, Z. Zhang, *Mater. Res. Express* **4**(3), 035035 (2017)
26. W. Huang, W. Yang, Q. Ma, J. Wu, J. Fan, K. Zhang, *J. Radioanal. Nucl. Ch.* **309**(3), 1097 (2016)
27. F. Akman, M.R. Kacal, H. Polat, G. Aktas, A. Gultekin, O. Agar, *J. Phys. Chem. Solids* **152**, 109978 (2021)
28. S.N. Yılmaz, İ.K. Akbay, T. Özdemir, *Radiat. Phys. Chem.* **180**, 109316 (2021)
29. M.R. Kacal, K. Dilsiz, F. Akman, H. Polat, *Radiat. Phys. Chem.* **179**, 109257 (2021)
30. A.M. El-Khatib, M.S. Hamada, M.T. Alabsy, Y.M. Youssef, M.A. Elzaheer, M.S. Badawi, M. Fayez-Hassan, Y.N. Kopateh, I.N. Ruskov, M.I. Abbas, *Radiat. Phys. Chem.* **180**, 109245 (2021)
31. F. Akman, H. Ogul, M.R. Kaçal, H. Polat, K. Dilsiz, O. Agar, *Prog. Nucl. Energy* **131**, 103608 (2021)
32. M.J.R. Aldhuhaibat, M.S. Amana, N.J. Jubier, A.A. Salim, *Radiat. Phys. Chem.* **179**, 109183 (2021)
33. E. Kalkornsuranee, S. Intom, N. Lehman, J. Johns, S. Kothan, K. Sengloyluan, W. Chaiphaksa, J. Kaewkhao, Mechanical and gamma radiation shielding properties of natural rubber composites: effects of bismuth oxide (Bi_2O_3) and lead oxide (PbO). *Mater. Res. Innov.* **26**(1), 8–15 (2022). <https://doi.org/10.1080/14328917.2020.1853383>
34. A. Araz, E. Kavaz, R. Durak, *Radiat. Phys. Chem.* **182**, 109382 (2021)
35. C.V. More, Z. Alsayed, M.S. Badawi, A.A. Thabet, P.P. Pawar, *Polymeric composite materials for radiation shielding: a review. Environ. Chem. Lett.* **19**, 2057–2090 (2021). <https://doi.org/10.1007/s10311-021-01189-9>
36. A.G. Nunez-Briones, R. Benavides, E. Mendoza-Mendoza, M.E. Martinez-Pando, H. Carrasco-Abrego, C. Kotzian, F.R. Saucedo-Zendejo, L.A. Garcia-Cerda, *Radiat. Phys. Chem.* **179**, 109198 (2021)
37. F. Akman, I. Ozkan, M.R. Kaçal, H. Polat, S.A.M. Issa, H.O. Tekin, O. Agar, *Appl. Radiat. Isotopes* **167**, 109470 (2021)
38. J. Quan, H. Wang, J. Yu, Y. Wang, J. Zhu, Z. Hu, *Compos. Sci. Technol.* **201**, 108500 (2021)
39. E. Kalkornsurapranee, S. Kothan, S. Intom, J. Johns, S. Kaewjaeng, C. Kedkaew, W. Chaiphaksa, T. Sareein, J. Kaewkhao, *Radiat. Phys. Chem.* **179**, 109261 (2021)

40. A.M. El-Khatib, A.S. Doma, M.S. Badawi, A.E. Abu-Rayan, N.S. Aly, *Mater. Res. Express* **7**, 105309 (2020)
41. D. Adliene, L. Gilys, E. Griskonis, *Nucl. Instrum. Meth. B* **467**, 21 (2020)
42. I.M. Nikbin, A. Rafiee, S. Dezhampannah, S. Mehdipour, R. Mohebbi, H.H. Moghadam, A. Sadrumontazi, *J. Mater. Res. Technol.* **9**(5), 11135 (2020)
43. A. Zegaoui, M. Derradji, A. Medjahed, H.A., Ghouti, W. Cai, W. Liu, A.Q. Dayo, J. Wang, Y. Liu, *Polym-Plast. Technol. Mater.* **59**(3), 311 (2020)
44. D. Cao, G. Yang, M. Bourham, D. Moneghan, *Nucl. Eng. Technol.* **52**, 2613 (2020)
45. M.R. Kaçal, H. Polat, M. Oltulu, F. Akman, O. Agar, H.O. Tekin, *Appl. Phys. A* **126**, 205 (2020)
46. M.F. Turhan, F. Akman, H. Polat, M.R. Kaçal, İ Demirkol, *Prog. Nucl. Energy* **129**, 103504 (2020)
47. F. Akman, M.R. Kaçal, N. Almousa, M.I. Sayyed, H. Polat, *Prog. Nucl. Energy* **121**, 103257 (2020)
48. B. Ahmed, G.B. Shah, A.H. Malik, Auranzeb, M. Rizwan, *Appl. Radiat. Isotopes* **155**, 108901 (2020)
49. F. Akman, H. Ogul, M.R. Kaçal, H. Polat, K. Dilsiz, M.F. Turhan, *Appl. Phys. A* **126**, 301 (2020)
50. S.F. Olukotun, S.T. Gbenu, O.F. Oladejo, M.I. Sayyed, S.M. Tajudin, A.a. Amosun, O.G. Fadodun, M.K. Fasasi, *Radiat. Phys. Chem.* **177**, 109079 (2020)
51. B. Körpınar, B.C. Öztürk, N.F. Çam, H. Akat, *Prog. Nucl. Energy* **126**, 103424 (2020)
52. F. Özkalayci, M.R. Kaçal, O. Agar, H. Polat, A. Sharma, F. Akman, *J. Phys. Chem. Solids* **145**, 109542 (2020)
53. Q. Li, R. Zhong, X. Xiao, J. Liao, X. Liao, B. Shi, *ACS Appl. Mater. Int.* **12**, 54117 (2020)
54. S. Intom, E. Kalkornsurance, J. Johns, S. Kaewjaeng, S. Kothan, W. Hangtong, W. Chaiaphaksa, J. Kaewkhao, *Radiat. Phys. Chem.* **172**, 108772 (2020)
55. L. Lou, Z. He, Y. Li, Y. Zhou, C. Lin, Z. yang, J. Fan, K. Zhang, W. Yang, *Int. J. Energ. Res.* **44**, 7674 (2020)
56. A. Sharma, M.I. Sayyed, O. Agar, M.R. Kaçal, H. Polat, F. Akman, *Mater. Chem. Phys.* **241**, 122330 (2020)
57. B. Körpınar, B.C. Öztürk, N.F. Çam, H. Akat, *Mater. Chem. Phys.* **239**, 121986 (2020)
58. H.O. Tekin, M.R. Kaçal, S.A.M. Issa, H. Polat, G. Susoy, F. Akman, O. Kilicoglu, V.H. Gillette, *Mater. Chem. Phys.* **256**, 123667 (2020)
59. R. Mirji, B. Lobo, *J. Radioanal. Nucl. Ch.* **324**, 7 (2020)
60. M.M. El-Toony, Gh. Eid, H.M. Algarni, T.F. Alhuwaymel, E.E. Abel-hady, *Radiat. Phys. Chem.* **168**, 108538 (2020)
61. H.O. Tekin, F. Akman, S.A.M. Issa, M.R. Kaçal, O. Kilicoglu, H. Polat, *J. Phys. Chem. Solids* **146**, 109604 (2020)
62. A.M. El-Khatib, M.I. Abbas, M.A. Elzاهر, M.S. Badawi, M.T. Alabsy, G.A. Alharshan, D.A. Aloraini, *Sci. Rep.-Uk* **9**, 16012 (2019)
63. M. Çağlar, H. Kayacık, Y. Karabul, M. Kılıç, Z.G. Özdemir, O. İçelli, *Prog. Nucl. Energy* **117**, 103119 (2019)
64. N.R.A. Elwahab, N. Helal, T. Mohamed, F. Shahin, F.M. Ali, *Mater. Chem. Phys.* **233**, 249 (2019)
65. M.V. Muthamma, S.G. Bubbly, S.B. Gudennavar, K.C.S. Narendranath, *J. Appl. Polym. Sci.* **136**(37), 47949 (2019)
66. H. Alavian, H. Tavakoli-Anbaran, *Prog. Nucl. Energy* **115**, 91 (2019)
67. B.M. Abunahel, I.S. Mustafa, N.Z.N. Azman, *Appl. Phys. A* **124**, 828 (2018)
68. M.E. Mahmoud, A.M. El-Khatib, M.S. Badawi, A.R. Rashad, R.M. El-Sharkawy, A.A. Thabet, *Radiat. Phys. Chem.* **145**, 160 (2018)
69. A. Güngör, İ.K. Akbay, D. Yaşar, T. Özdemir, *Prog. Nucl. Energy* **106**, 262 (2018)
70. Y. Hou, M. Li, Y. Gu, Z. Yang, R. Li, Z. Zhang, *Polym. Compos.* **39**(S4), E2106 (2018)
71. K. Verdipoor, A. Alemi, A. Mesbahi, *Radiat. Phys. Chem.* **147**, 85 (2018)
72. P. Gong, M. Ni, H. Chai, F. Chen, X. Tang, *Nucl. Eng. Technol.* **50**, 470 (2018)

73. W. Poltabtim, E. Wimolmala, K. Saenboonruang, *Radiat. Phys. Chem.* **153**, 1 (2018)
74. K. Bagheri, S.M. Razavi, S.J. Ahmedi, M. Kosari, H. Abolghasemi, *Radiat. Phys. Chem.* **146**, 5 (2018)
75. N.A. Shik, L. Gholamzadeh, *Appl. Radiat. Isotopes* **139**, 61 (2018)
76. E.E. Belgin, G.A. Aycik, *J. Radioanal. Nucl. Ch.* **311**, 1953 (2017)
77. K. Srinivason, E.J.J. Samuel, *J. Med. Phys.* **42**, 273 (2017)
78. M.R. Ambika, N. Nagaiah, S.K. Suman, *J. Appl. Polym. Sci.* **134**(13), 44657 (2017)
79. N.Z.N. Azman, N.F.L. Musa, N.N.A.N.A. Razak, R.M. Ramli, I.S. Mustafa, A.A. Rahman, N.Z. Yahaya, *Appl. Phys. A* **122**, 818 (2016)
80. H. Chai, X. Tang, M. Ni, F. Chan, Y. Zhang, D. Chen, Y. Qiu, *J. Appl. Polym. Sci.* **133**(10), 43012 (2016)
81. A. Erol, I. Poca, E. Yanbay, O.A. Ersöz, F.Y. Lambrecht, *Radiat. Prot. Environ.* **39**, 3 (2016)
82. M.I. Sayyed, F. Akman, I.H. Geçibesler, H.O. Tekin, *Nucl. Sci. Tech.* **29**, 144 (2018)
83. F. Akman, I.H. Geçibesler, M.I. Sayyed, S.A. Tijani, A.R. Tufekci, I. Demirtas, *Nucl. Eng. Technol.* **50**(6), 944 (2018)
84. F. Akman, R. Durak, M.F. Turhan, M.R. Kaçal, *Appl. Radiat. Isotopes* **101**, 107 (2015)
85. N.S. Prabhu, V. Hegde, A. Wagh, M.I. Sayyed, O. Agar, S.D. Kamath, *J. Non-Cryst. Solids* **515**, 116 (2019)
86. D.K. Gaikwad, M.I. Sayyed, S.S. Obaid, S.A.M. Issa, P.P. Pawar, *J. Alloy. Compd.* **765**, 451 (2018)
87. A. Kumar, *Radiat. Phys. Chem.* **136**, 50 (2017)
88. A.M. El-Khayatt, *Ann. Nucl. Energy* **37**(2), 218 (2010)
89. The Lund/LBNL Nuclear Data Search (Version 2.0, February 1999). <http://nuclcardata.nuclear.lu.se/toi/>. Accessed 19 Mar. 2021
90. I. Boztosun, H. Dapo, S.F. Özmen, Y. Çeçen, M. Karakoç, A. Çoban, A. Cesur, T. Caner, E. Bayram, G.B. Keller, B. Küçük, A. Güvendi, M. Derman, D. Kaya, *Turk. J. Phys.* **38**(1), 1 (2014)
91. O. Agar, I. Boztosun, M.E. Korkmaz, S.F. Özmen, *Radiat. Prot. Dosim.* **162**(4), 630 (2014)
92. I. Boztosun, H. Dapo, M. Karakoç, S.F. Özmen, Y. Çeçen, A. Çoban, T. Caner, E. Bayram, T.R. Saito, T. Akdoğan, V. Bozkurt, Y. Kuçuk, D. Kaya, M.N. *Eur. Phys. J. Plus* **130**(9), 185 (2015)
93. F. Akman, O. Agar, M.R. Kaçal, M.I. Sayyed, *Nucl. Sci. Tech.* **30**(7), 110 (2019)
94. F. Akman, I.H. Geçibesler, A. Kumar, M.I. Sayyed, M.H.M. Zaid, *Results Phys.* **12**, 94 (2019)
95. S. Agostinelli et al., *Nucl. Instrum. Meth. A* **506**, 250 (2003)
96. L. Russell, A. Buijs, G. Jonkmans, *Ann. Nucl. Energy* **71**, 451 (2014)
97. S. Ozturk, A. Adiguzel, V. Ozcan, N. Unel, *Turk. J. Phys.* **41**(1), 41 (2017)
98. A.U. Khan, E.A. Simiele, R. Lotey, L.A. Dewerd, P. Yadav, Development and evaluation of a GEANT4-based Monte Carlo Model of a 0.35 T MR-guided radiation therapy (MRgRT) linear accelerator. *Med. Phys.* **8**(4), 1967–1982 (2021). <https://doi.org/10.1002/mp.14761>. PMID: 33555052
99. L. Grevillot, D.J. Boersma, H. Funchs, A. Aitkenhead, A. Elia, M. Bolsa, C. Winterhalter, M. Vidal, S. Jan, U. Pietrzyk, L. Maigne, D. Sarrut, *Med. Phys.* **47**(8), 3675 (2020)
100. E. Daly, H. Evans, F. Lei, F. Longo, S. Magni, R. Nartallo, P. Nieminen, M.G. Pia, P.R. Truscott, in *Advanced Monte Carlo for Radiation Physics, Particle Transport Simulation and Applications*. ed. by A. Kling, F.J.C. Barão, M. Nakagawa, L. Távora, P. Vaz (Springer, Berlin, Heidelberg, 2001), p.401
101. M. Lund, T. Jevremovic, *Acta Astronaut.* **165**, 219 (2019)
102. C.N. Shingledecker, S. Incerti, A. Ivlev, D. Emfietzoglou, I. Kyriakou, A. Vasyunin, P. Caselli, *Astrophys. J.* **904**(2), 189 (2020)
103. L.Q. Qi, G. Li, Y.P. Xu, J. Zhang, Y.J. Yang, L.Z. Sheng, S. Basso, R. Campana, Y. Chen, A. De Rosa, G. Pareschi, P.F. Qiang, A. Santangelo, G. Sironi, L.M. Song, D. Spiga, G. Tagliaferri, J. Wang, J. Wilms, Y. Zhang, F.J. Lu, *Nucl. Instrum. Meth. A* **963**, 163702 (2020)
104. Y. Al-Hadeethi, M.I. Sayyed, M. Nune, *Ceram. Int.* **47**(3), 3988 (2021)

105. I. Kebaili et al., Gamma-ray shielding parameters of lithium borotellurite glasses using Geant4 code. *Appl. Phys. A* **126**(7), 1 (2020)
106. M.J. Berger, J.H. Hubbell, *XCOM: Photon Cross Sections Database* (National Institute of Standards and Technology, Gaithersburg, MD 20899, USA, 1987). <http://physics.nist.gov/xcom>. Accessed 19 Mar. 2021
107. L. Gerward, N. Guilbert, K. Jensen, H. Levring, *Radiat. Phys. Chem.* **71**, 653 (2004)
108. M.I. Sayyed, O. Agar, A. Kumar, H.O. Tekin, D.K. Gaikwad, S.S. Obaid, *Chem. Phys.* **529**, 110571 (2020)
109. M.R. Kacal, F. Akman, M.I. Sayyed, *Radiochim. Acta* **107**(2), 179 (2019)
110. A. Kumar, D.K. Gaikwad, S.S. Obaid, H.O. Tekin, O. Agar, M.I. Sayyed, *Prog. Nucl. Energ.* **119**, 103047 (2020)
111. M.G. Dong, O. Agar, H.O. Tekin, O. Kilicoglu, K.M. Kaky, M.I. Sayyed, *Compos. Part B-Eng.* **165**, 636 (2019)
112. F. Akman, M.R. Kaçal, *J. Radiol. Oncol.* **2**, 47 (2018)

Mechanical and Tribological Behavior of Hybrid Polymer and Hybrid Sandwich Composites



Vasavi Boggarapu, Raghavendra Gujjala, Syam Prasad, Shakuntala Ojha, and Om Prakash Mingu

Abstract The present chapter addresses the mechanical and tribological behavior of advanced particulate, hybrid polymer and hybrid sandwich composites. Different fillers such as egg shell, arhar, graphitic carbon nitride (g-C₃N₄), and titanium dioxide (TiO₂) were added to epoxy resin to prepare the variety of composites. The experiments were carried out on universal testing machine, erosion and pin-on-disc apparatus to assess the mechanical and tribological behavior, respectively. The influence of parameters such as fiber orientation, filler size and content, and fiber volume fraction were discussed. Nano egg shell particulate composites have shown superior mechanical and erosion properties when compared to micron particles. The notable breakthroughs in terms of mechanical strength and erosion resistance were observed with 2 wt.% activated carbon than 4 wt.% biochar and 10 wt.% raw arhar fillers. Hybrid polymer composites with 12 layered bi-directional glass fiber filled with 2 wt.% g-C₃N₄ nano particles have been more beneficial compared to conventional composites. In contrast to hybrid polymer composites, novel hybrid sandwich composites prepared with glass fiber and TiO₂ have shown altered material characteristics in a single composite sample as confirmed from erosion wear test.

Keywords Hybrid polymer composites · Fillers · Glass fiber · Mechanical strength · Erosion · Abrasive wear

V. Boggarapu

School of Mechanical Engineering, VIT-AP University, Amaravati, Andhra Pradesh, India

R. Gujjala (✉)

Department of Mechanical Engineering, National Institute of Technology, Warangal, Telangana, India

e-mail: raghavendra.gujjala@nitw.ac.in

S. Prasad

Department of Physics, National Institute of Technology, Warangal, Telangana, India

S. Ojha · O. P. Mingu

Department of Mechanical Engineering, Kakatiya Institute of Technology and Science, Warangal, Telangana, India

1 Introduction

The significance of materials in present world comprehends a fact that a considerable amount of research is being progressed in applying the new materials for varied applications. The worldwide composites market was assessed at \$89.04 billion in 2019 and is required to extend at a rate of 7.6% from the years 2020–2027. Nowadays the market is significantly determined by expanding interest for lightweight materials in different sectors. Expanding interest for composites in automobiles is foreseen in the growth of the market over the estimated period. Rising fuel costs have set off the requirement for efficient fuel vehicles. Composites are most widely used as the substitution for aluminum, wood, and steel due to their higher strength to weight proportion.

From the past decades, widespread studies have been reported by numerous researchers on the polymer matrix composites to develop innovative materials for various engineering applications [1]. Advanced polymer composite materials provide a prospect to achieve beneficial effects in terms of economy and overall performance. Improvement in the structural and mechanical characteristics of polymer matrix composites is achieved with the addition of reinforcements like fibers and fillers. Fibers like carbon, glass, sisal, Kevlar, jute, etc., increase the strength and stiffness of polymers [2–4]. Greater than 90% of polymer composite materials presently are reinforced with either glass or carbon fibers. It is due to their broad applications in various engineering sectors. Glass fiber (GF) consists of many fine fibers of glass. GF reinforced composites are highly erosion resistive when compared to unfilled glass/epoxy composites. Polymer composites consisting of continuous fibers possess higher elastic modulus. Many investigations have been carried out on the geometry of various fiber and filler types [5, 6]. The advancement in composite materials has improved their performance with the addition of two or more reinforcements in a solitary polymer matrix, which are often referred to as hybrid composite materials. Reinforcements are the discontinuous phases present in the continuous phase of a composite. A discontinuous phase is termed as hybrid reinforcement which is hard and robust compared to continuous phase (matrix). Hybrid composite materials offer a great diversity toward material properties. They provide the designer to acquire the desired properties by choosing the appropriate reinforcements incorporated in the single resin.

In hybrid composites one among the reinforcement possess low elastic modulus and of less cost such as GF or Kevlar, while the other have high modulus such as carbon fiber (CF) or boron fiber. Thus, composite obtained due to hybridization of GF and CF will exhibit high strength and resistance toward damages. Additionally, hybrid composite shows high strength, fracture toughness, fatigue resistance and simultaneously cut the weight/overall cost [7]. The mechanical performance of hybrid composites are directly influenced by the size and content of reinforcement particles. Antil et al. [8] reported the effect of SiC particulate on the strength of hybrid polymer composites. The tensile strength shows a direct proportionality to weight fraction of filler and inverse proportionality to the grit size. Compared to

traditional composites, the better strength is achieved with hybrid. Besides, reinforcement addition reduces the wear but increase in grit size of SiC promotes the wear of composite. The interface between fiber and matrix is one of the most critical factors in development of composites. Weak interface leads to the early failure of composite structure under high loading. Interfacial strength of composites is comprehended through interlaminar shear strength analysis (ILSS). In this context, Nayak et al. [9] evaluated the impact of nano TiO_2 and Al_2O_3 particles on the mechanical strength of GF composites. Presence of nano fillers in the matrix has shown improvement in ILSS and strain than unfilled composites. Nano fillers help the interface bonding among fibers and matrix. However, addition of fillers beyond a saturation limit results in decrement of ILSS due to agglomeration. Fiber length plays a key role in deciding the performance of composites. In this regard, Rezaei et al. [10] studied the influence of fiber length on the thermo-mechanical properties of carbon fiber reinforced polymer composite and found that composites with longer carbon fibers exhibited better properties than short carbon fiber reinforced composites. Thermogravimetric analysis (TGA) results confirm the improvement in degradation temperature with the increase of fiber length. As mentioned by Bryk [11], the incorporation of filler particles in polyalkane enhances the thermal stability of polymeric matrices.

Therefore it is essential to understand the relationship between the material structural properties and its mechanical responses [12, 13]. Epoxy is extensively used as the matrix material in polymer composites. It offers excellent mechanical, tribological, and also thermal properties. Further strengthening of epoxy resins can be attained with the inorganic fillers [14] like TiO_2 (titania), ZrO_2 (zirconia), SiO_2 (silica), Al_2O_3 (alumina), iron-mud, fly ash, granite dust, copper slag, clay, etc. Generally, filler particles size, and their interfacial adhesion influence the matrix properties remarkably. The uniform dispersion of inorganic particles in organic epoxy resin, and their compatibility are essential to attain the overall performance of hybrid composites. Fillers can be dispersed by various methods and processing environments which are classified under ex-situ and in-situ processes. In the ex-situ process, inorganic filler particles were mixed in the resin by mechanical means, whereas the in-situ process involves the filler particles synthesis within the polymer resin [15]. Concerning the environmental pollution, from past decades, the biological wastes were modified as useful products in terms of fillers in composite materials [16]. Such composite materials were often referred to as biocomposites. Many bio-wastes such as rice husk, bamboo, coconut shell, crab shell, jute, arhar fiber, fiber coir, corn cob, etc., were used as reinforcement with epoxy matrix. One of the significant wastes produced worldwide is due to eggshells owing to their substantial production requirements. Eggshells are rich in calcium carbonate (CaCO_3) content, which could be a partial replacement to cement [17]. Additionally, they were used with epoxy resin as micron, or nano-sized particles offer thermal resistance, mechanical strength, and resistance to moisture. In South Asian countries, the majority of the population relies on agriculture. The leftover yield from the crop is burned or utilized as firewood, which causes air pollution. Such wastage can be modified into useful products that can generate additional economy to the farmers. Research is promoted toward the utilization of agricultural wastage in the development of composites, preparation

of biochar, and activated carbon [18–20]. Concerning this, the chapter attempts to present the performance of biocomposites with the eggshell, and agricultural waste of arhar fiber particles.

Polymer matrix composites have extended their applications in structural components for aerospace and automobile industries due to their high strength combined with enhanced anisotropic properties. This combination was tailored by numerous researchers to acquire desired properties. Such advanced composites were explored for structural and tribological applications. The metal-based components such as cams, gears, seals, etc., [21] were now substituted with various hybrid polymer composites due to their self-lubricating property. In general, tribology deals with wear and friction, which are inter-related to each other. There are different types of wear such as adhesive wear, abrasive wear, corrosive wear, erosive wear, fatigue wear, etc. Among the aforementioned wear types, abrasive and erosive are the significant wear losses experienced by most of the materials. Abrasive wear constitutes about 63% of total wear cost [22]. This wear occurs due to the hard particles or asperities penetration into the soft surfaces under the influence of normal contacting pressure. Upon imposition of tangential motion, the material from softer surface was removed via micro-ploughing, micro-cracking, and micro-cutting. The resulting worn out surfaces were identified by scars and grooves. Abrasive wear is categorized as two-body and three-body abrasive wear based upon contacting environment. Two-body abrasive wear arises whenever the harder surface removes away material from softer surface. Besides, two-body abrasion alters to three-body abrasion once the wear debris acts as an abrasive amid interacting surfaces. In gear and bearing applications, components having low frictional coefficient and wear rate were preferred when slide against the counter surfaces. Keeping in view, huge work has been cited in the scientific community on polymer composites with the inclusion of fiber/s or fillers that reduce dry friction and wear [23–27].

Generally, fiber reinforced composites are operated in a dusty environment; therefore, it is essential to comprehend the erosion wear of such composites. The erosion wear occurs by the continuous impact of airborne sharp solid particles moving at different impingement angles and velocities onto a surface, where the exposed surface experiences a severe degradation. Various researchers have published the erosion behavior of different polymer matrix composites. The discussion was mainly done about the testing parameters viz. impact velocity, geometry and nature of erodent, impingement angle, erodent mass flow rate, etc., and composite characteristics such as type of fiber, filler type their contents. In this context, Boggarapu et al. [28] had presented a detailed review of the influence of different testing parameters on the erosion wear behavior of polymer matrix composites, where different failure mechanisms were also discussed. To achieve the ideal material properties for particular applications, it is necessary to understand the performance of fiber reinforced composites (FRPs) with varied fiber content at distinct loading conditions. Erosion wear of FRPs with varying fiber content showed that the addition of brittle fibers to any polymer matrix enhances the erosion resistance [29]. Jagannatha [30] had prepared a hybrid composite comprised of carbon and glass fibers in an epoxy matrix.

The fabricated composites possess high hardness, which enriches the erosion resistance. Few researchers had developed hybrid composites with the addition of various fillers in a single matrix. Nayak et al. [9] had examined the influence of Al_2O_3 and TiO_2 particles on the mechanical strength of glass fiber epoxy composites. Response surface methodology was adopted to determine the optimum filler loading to obtain better strength. Filler particles are categorized as macro, micro, and nano-based upon their size. Generally, nanoparticles reinforced polymer composites show better erosion resistance than macro and micro under similar load conditions. It is mainly due to their high degree of contact with the matrices, which is called “nano-effect” [31]. Al-Zubaidi et al. [32] had prepared glass/epoxy hybrid composites filled with various volume fractions of micro and nano TiO_2 particles. The erosion rate was found to be higher for micro composites than nano. Both the composites had shown peak erosion rate at 30° impact angle, which indicates that the fabricated hybrid composites are semi-ductile. Similar erosion trend with micro and nano Al_2O_3 particles filled glass/epoxy hybrid composites were reported by Ahmedizat et al. [33]. Pani et al. [34] had incorporated the iron-mud as a filler particulate in glass/epoxy hybrid composites. The studies proved the effective utilization of industrial wastage in improving the erosion wear resistance. Hence it is vital to understand the effect of fillers and fibers on tribological behavior of hybrid polymer composites which has to be tested in the laboratory. For many engineering and industrial applications, a proper understanding of tribological behavior along with mechanical properties of composite materials is essential [35].

This chapter mainly discourses the fabrication and performance of advanced composites in terms of mechanical and tribological strength. Firstly, the particulate filled epoxy composites were discussed followed by hybrid polymer composites. The available research on hybrid composites focused on determining the material property. The composites exhibited solo material property in a single composite sample, whereas, no study is available on obtaining the varied material properties in a single composite. Therefore, an attempt was made to fabricate and study the nature of novel hybrid sandwich type composites, which are able to exhibit distinct material properties in a solo composite sample.

2 Materials and Fabrication Process

2.1 Raw Materials

The raw materials used in the preparation of various composite samples were tabulated (Table 1).

Table 1 Properties of raw materials

| Constituents in composite samples | | | Density (g/cc) | Major element | Refs. |
|-----------------------------------|------------------|---------------------------------|----------------|-------------------------|-------|
| Reinforcements | Filler particles | Egg shell particles | 1.950 | CaCO ₃ (94%) | [36] |
| | | Arhar fiber particles | 0.5193 | Carbon (63.61%) | [37] |
| | | g-C ₃ N ₄ | 2.74 | Nitrogen (61.56) | [38] |
| | | TiO ₂ | 3.7 | – | – |
| | Fiber | E-Glass | 2.25 | SiO ₂ (54%) | – |
| Matrix | Resin | LY 556-Epoxy | 1.15–1.20 | – | – |
| Hardener | – | HY 951 | 1.20–1.25 | – | – |

2.2 Fabrication of Composite Samples

2.2.1 Preparation of Particulate Composite Samples

The particulate composites were produced using two different filler particles i.e. egg shell particles and arhar fiber particles. Raw particles were subjected to ball milling to attain the micron and nano sizes. In contrary to traditional composites, the composite samples differ in their fabrication procedure. Firstly, the filler particles were mixed in epoxy resin using mechanical stirrer and then subjected to ultra-sonication to achieve the uniform distribution. The mixture was poured into the molds, which are then placed upon mechanical shaker for the even dispersal across the mold thickness. In addition, mechanical shaking also removes the entrapped air-bubbles present in the mixture. The composites were left out for curing at room temperature. Once the samples had reached semi-solid state, they were covered with cellulose acetate sheets followed by placement of deadweight above the mold. This avails the removal of leftover air bubbles (if any) in the composite samples. Finally, cured samples were cut according to American Society for Testing and Materials (ASTM) standards for mechanical and tribological testing.

2.2.2 Manufacturing of Hybrid Polymer Nanocomposite Samples

The hybrid polymer composites comprising of bi-directional glass fiber with the addition of graphitic carbon nitride (g-C₃N₄) particles were prepared by hand lay-up technique as shown in Fig. 1. The wt.% of g-C₃N₄ nano-sized filler particles were varied from 0 to 3 and the size distribution of filler particles ranges from 300 to 800 nm. Initially, g-C₃N₄ was prepared by the calcination of Melamine at 500 °C as presented in Fig. 2. Most of the researchers have adopted hand lay-up methodology in the development of hybrid composites. Besides, there exist few other methods such

as resin transfer molding, filament winding, pultrusion, etc., which are able to give much accurate results than hand lay-up. Yet they were not extensively implemented concerning cost of the processes.

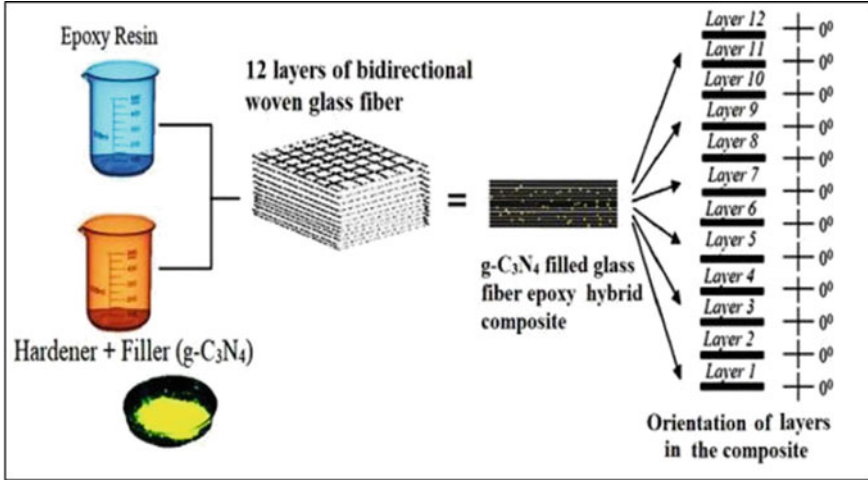


Fig. 1 Preparation of 12 layered bi-directional glass fiber hybrid composite. Reprinted from Naidu et al. [39], with permission from John Wiley and Sons. Copyright (2019)

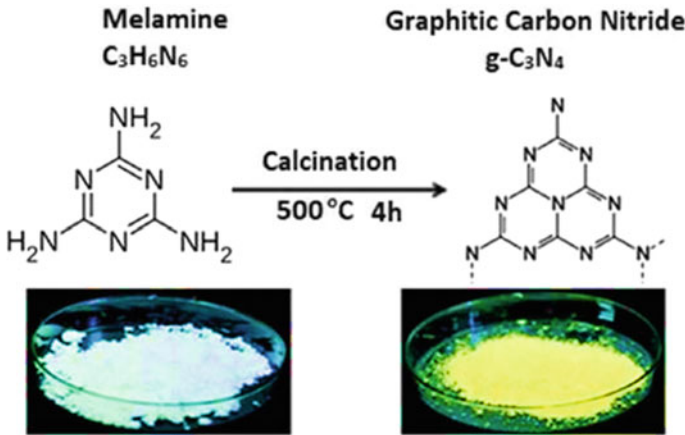


Fig. 2 Production of g-C₃N₄ particles from Melamine. Reprinted from Naidu et al. [39], with permission from John Wiley and Sons. Copyright (2019)

2.2.3 Fabrication of Novel Hybrid Sandwich Composite Samples

Titania (TiO_2) has a widespread application in various industries due to its substantial chemical and physical properties. It is capable of modifying the material structures, which provides a good scope in developing high performance, resilient, multi-functional, and eco-friendly composite materials. Keeping in view, TiO_2 particles are used to develop novel hybrid sandwich type via hand lay-up method. Ex-situ process was adopted for the dispersion of filler particles. A fixed weight percentage of glass fiber (4 layers) and TiO_2 filler particles (1 wt.%) was added to the epoxy resin according to “Rule of mixture”. Hardener and epoxy were maintained in the 1:10 ratio by weight. The constituents were mixed using mechanical stirrer to ensure the uniform dispersion and prevent air bubbles entrapment. The fabrication process of hybrid sandwich composites differs from the conventional hybrid composites. Firstly, 4 layers of glass fiber and a mixture of pure epoxy with hardener were added to half the mold volume and left for curing at room temperature (RT) for 12 h. Subsequently, other half volume of the mold was added with epoxy mixed with filler particles and cured for next 48 h. For ease of distinguishing, the sample is represented as C4. To fabricate another type of hybrid sandwich composite C5, the entire volume of the mold is divided into three portions. The top and bottom portions comprise of two layers of glass fiber with epoxy respectively. Whereas, the mid portion consists of pure epoxy dispersed with the filler particles. In the manufacturing of C5, the successive portion of a mold is filled with the constituents after ensuring the preceding portion to be cured properly. The effectiveness of hybrid sandwich composites was compared with hybrid composite sample C3, pure epoxy C1, and traditional composite sample C2. The hybrid composite C3 encompasses of glass fiber, filler particles, and epoxy resin. While, the sample C2 represents four layered glass fiber epoxy composite. The representation of fabricated composites is shown in Fig. 3.

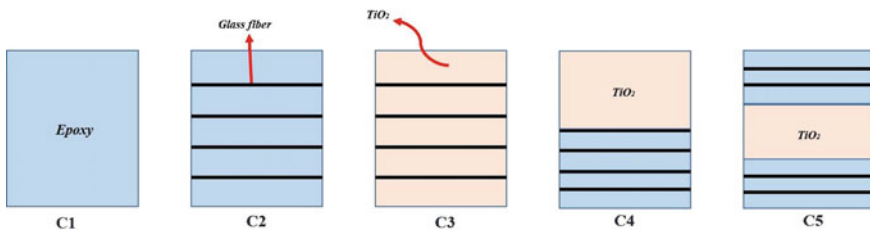


Fig. 3 Representation of composite samples

3 Experimental Methods

3.1 Mechanical Testing

The tensile strength of the composite samples was evaluated according to ASTM D 3039-76 standards. The flexural test was carried out adopting ASTM D 790. Both the experiments were performed on Universal testing machine (UTM). The tensile and flexural strength were evaluated using Eqs. (1) and (2) respectively. To predict the accurate mechanical strength, the average value for at least five identical samples was considered for all types of composites.

$$\text{Tensile Strength} = \frac{P}{A} \quad (1)$$

$$\text{Flexural Strength} = \frac{3FL}{2bd^2} \quad (2)$$

Here P = Maximum load on the sample, A is the cross-sectional area, F = Ultimate load at the failure, L = Length of the span, and b, d = Width and thickness of the sample respectively.

3.2 Tribological Testing

3.2.1 Erosion Test

Following the ASTM G76 standards [40], erosion wear test of fabricated samples was performed using erosion testing apparatus as shown in Fig. 4 [37]. The apparatus mainly comprises of air compressor, and a conveyor belt to feed the abrasive particles. It controls the flow of abrasive and air particles that mix in the accelerating chamber. The necessary air pressure, along with the abrasive particles, is continuously fed by a conveyor belt into the mixing chamber. Table 2 provides the experimental parameters (fixed and controlled) selected for the erosion wear test. Before and after each test, composite samples were properly cleaned with acetone followed by air drying. This removes the silica sand particles from the surface. The samples were weighed with well-calibrated electronic balance afore and after the erosion test. In case of hybrid sandwich composites, the material behavior of C4 and C5 samples was assessed by increasing the erosion testing time, whereas, the erosion time is static for particulate and hybrid polymer composites. The erosive wear rate was demonstrated as $\Delta W_1 / \Delta W_2$. Here ΔW_1 indicates the weight loss in the sample, and ΔW_2 represents the total weight of erodent particles used.

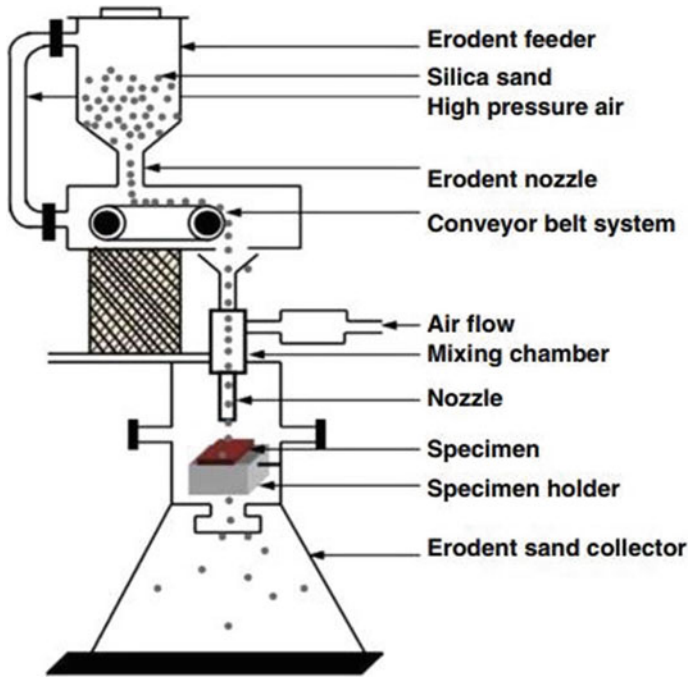


Fig. 4 Schematic view of erosion wear testing apparatus. Reprinted from Prakash et al. [37], with permission from John Wiley and Sons. Copyright (2017)

Table 2 Experimental parameters chosen for erosion test

| Fixed parameters | | Controlled parameters | |
|--|--------------------------|--------------------------------------|-----------------|
| Parameter | Specification | Parameter | Specification |
| Erodent | Silica sand | Impingement angle (α°) | 30, 45, 60, 90 |
| Erodent size (μm) and shape | 200 ± 50 and angular | Impact velocity (m/s) (V1, V2, V3) | 101, 119, 151 |
| Feed rate of erodent (g/min) | 2 ± 0.02 | Time interval of erosion test | t_1, t_2, t_3 |
| Temperature ($^\circ\text{C}$) | RT, 35 ± 2 | | |

3.2.2 Abrasive Wear Test

The two-body abrasive wear was performed on pin-on-disc testing apparatus. The cylindrical pin samples having a cross-sectional area of $12 \text{ mm} \times 30 \text{ mm}$ were fixed in a sample holder and rotated against a circular steel disc of cross-sectional $165 \text{ mm} \times 8 \text{ mm}$ at 150 rpm. To evaluate the three-body abrasive wear, the steel disc is provided with an abrasive paper of altered grit size. The wear rate and frictional coefficient at various loading conditions were calculated for every test on all the pin samples.

Before and after each test, composite samples were properly cleaned with acetone to remove wear debris from the surface. Wear loss of pin samples were measured with well-calibrated electronic balance of ± 0.0001 gm accuracy. To ensure the good interfacial contact with counter surface, the samples were initially polished against emery paper. The abrasive wear rate was determined from Eq. (3).

$$\text{Wear rate} = \frac{\Delta W}{\rho \times L} \quad (3)$$

Here L represents the sliding distance, ρ is the density of the sample, and ΔW is the weight loss in the sample.

4 Advanced Particulate Composites

4.1 Mechanical Testing

Concerning the mechanical strength of composites, it is essential to evaluate the optimal filler content to achieve the better characteristics. Hence, the experiments were performed with varying filler weight fractions. A study presented by Panchal et al. [41] have considered 4, 8, 12 wt.% of the micron sized egg shell filler particles in epoxy resin. The sample as shown in Fig. 5a was tested on UTM to predict the mechanical behavior. The higher tensile strength was reported on composite sample with 4 wt.% of filler content. This is due to the uniform distribution of fillers particles when a maximum filler loading of 4% is achieved, which contributes to higher tensile strength compared to other filler contents. A decrease in strength with increasing filler weight fraction was observed from Fig. 5b. The reason may be due to filler particles agglomeration in the matrix that weakens the interfacial bonding and results in failure. Compared to pure epoxy, the particulate composites exhibited higher strength owing to strong bonding between amine/carbonyl reactive group among egg shell particles and epoxy. The authors have further extended the work on nano-sized egg shell particles incorporated in epoxy resin [36]. From Figs. 5b to 6 it was evident that tensile strength of nanocomposites was higher than that of micron size composites.

Nanoparticles offer high surface to volume ratio in the matrix phase of composites. The interaction area between nano filler and matrix is higher than that in traditional composite materials due to which superior properties were established. From Fig. 6, the tensile and flexural strength of 2 wt.% particulate filled composites is higher. Beyond which a steady decrease in mechanical strength have been noticed. As the content of nano filler increases, they aggregate, and produce surface defects, which lead to permanent failure. Hence, the content of nano filler in the matrices has substantial effect on mechanical strength. It was observed from both studies that, the strength obtained with 2 wt.% of nano filler was higher than 4 wt.% micron filler.

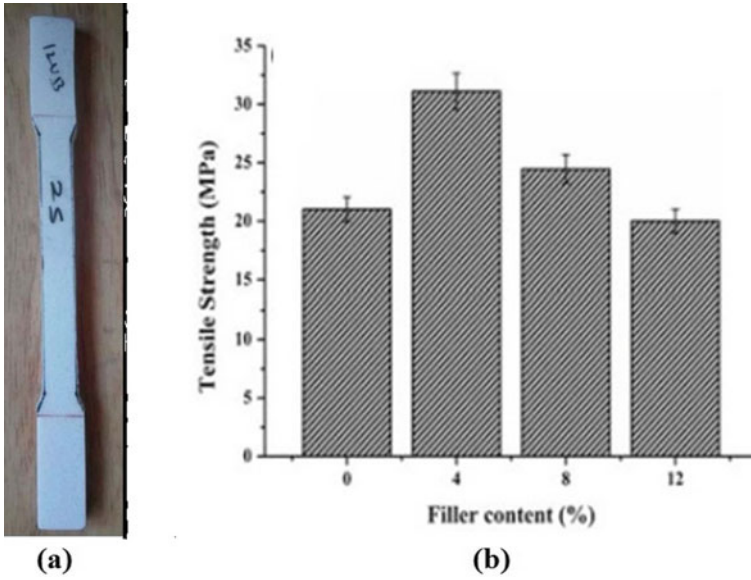


Fig. 5 a Tensile test sample. b Tensile strength of micron size egg shell particulate filled epoxy composites. Reprinted from Panchal et al. [41], with permission from Springer Nature. Copyright (2020)

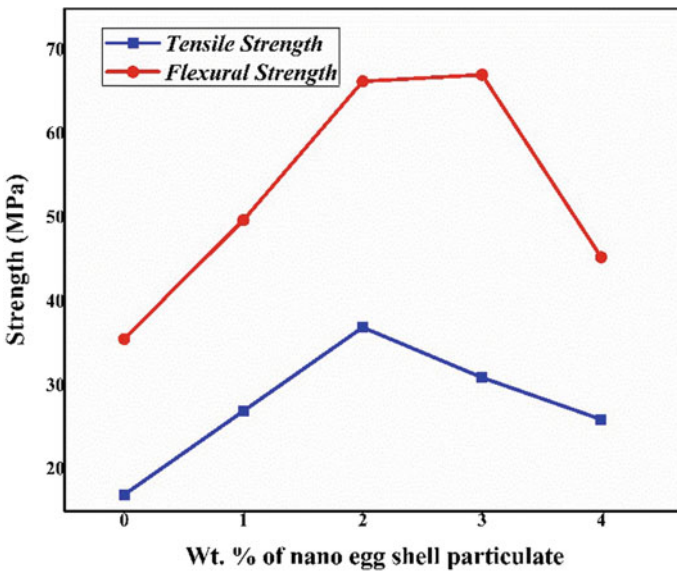


Fig. 6 Mechanical strength of nano egg shell particulate reinforced epoxy composites

Evaluation of mechanical properties is crucial in deciding the application of composites. In addition, the properties of materials degrade under the influence of liquid media due to their plasticity behavior. In this context, Prakash et al. [42] have presented the effect of different liquid media on the strength of arhar particulate filled epoxy composites as seen in Fig. 7a. The filler contents chosen in the epoxy were 5, 10, and 15 wt.%. Addition of filler up to 10 wt.% increased the tensile strength of bare epoxy as displayed in Fig. 7b. Thereafter, the decrement in strength was noticed due to inadequate bonding between matrix and reinforcement.

The mechanical properties of the composites in saline water medium has shown greater degradation. As the saline water medium contains sodium, and chlorine ions that react with the composite samples, leading to material degradation. In contrary, the composite samples immersed in kerosene medium have shown less degradation toward mechanical strength. The hydrocarbons present in the kerosene show a least effect toward interfacial bonding energy, which promotes the retention of composite strength. This study can be implemented in the design of storage tanks for kerosene with the utilization of particulate/hybrid polymer composites. Furthermore, the composites immersed in mineral water have shown deterioration of properties due to reduction of frictional coefficient in the medium. A detailed review on degradation of mechanical properties of polymer composites under different liquid media was presented by Chowdary et al. [43]. The further analysis on arhar fiber was presented

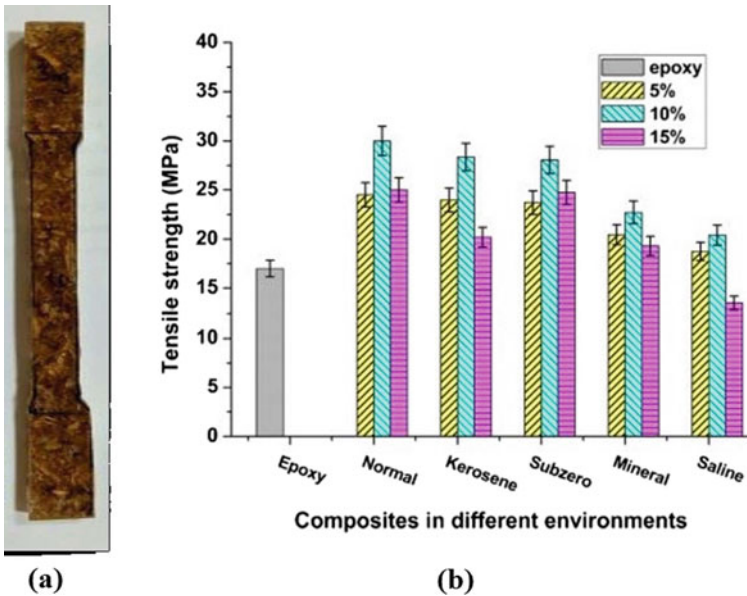


Fig. 7 a Tensile test sample. b Tensile strength of arhar fiber/epoxy composites under distinct liquid media. Reprinted from Prakash et al. [42], with permission from Springer Nature. Copyright (2017)

by Prakash et al. [44]. Activated carbon was synthesized from raw arhar fiber particulate by pyrolysis and chemical activation techniques. The detailed procedure had been reported by Prakash et al. [45]. Characterization of activated carbon particles have shown porous structure.

The nano-sized activated carbon (AC) was used as filler material in epoxy composites with varying content. The fabricated samples as shown in Figs. 8a and 9a were subjected to mechanical testing to evaluate their strength. Figures 8b and 9b display the tensile and flexural strength of composite samples with varying filler content respectively. It was noticed that 2 wt.% of AC filler exhibited higher mechanical strength. The comparison among the studies [42, 44] reveals the greater tensile strength with the AC filled composites than raw arhar composites. This is due to the high thermal stability of AC than the raw arhar material. Moreover, the porous morphology of AC particle promotes the better interfacial bonding with the matrix when compared to raw arhar particles. In addition to AC, an attempt was made to synthesize the biochar (BC) from raw arhar fiber particulate through pyrolysis method. The organic materials are rich in carbon content which can be derived in the form of AC and BC which are widely utilized in filtration applications. Furthermore, they have potential in engineering applications when used as fillers in composite materials. The BC was added to epoxy resin at various weight fractions. Figures 10a and 11a represent the composite samples for tensile and flexural testing. From Fig. 10b, it was observed that tensile strength of the composite sample comprising of 4 wt.% BC filler content has shown high compared to the other ones. Increase in strength is due to the mobility of epoxy into the pores presented on the surface of filler particle, which forms the mechanical interlocking. The strength is also due to the presence of biochar particles which possess high carbon content combined with high hardness. The filler content beyond 4% leads to the decrement of strength due to poor wettability of filler particles with the epoxy resin. As a result stress concentrated regions increase, which causes the early failure of the material.

Figure 11b indicates the flexural strength of composites, where the sample of 4 wt.% filler content showed the highest flexural strength. This is due to strong bonding between the epoxy resin and biochar particulate. The similar results were observed for bamboo biochar polymer composite materials, as reported by Ho et al. [46].

From the above observations it can be concluded that composite samples with AC possess higher mechanical strength than BC and raw arhar particulate filled composites. The reason is due to the surface morphology exhibited by filler particles as shown in Fig. 12. AC has porous structure which promotes the acceleration of epoxy particles inside it forming the mechanical interlocking that leads to enhancement of strength. Whereas BC particles having pore size less than AC and raw arhar particles have no porous structure. Therefore the strength of raw arhar filled epoxy composites were less than BC and AC filled composite samples. Due to the improved properties of above mentioned fillers, Panchal et al. [47] used activated carbon and egg shell particulate to fabricate silica based composite filter for water purification applications.

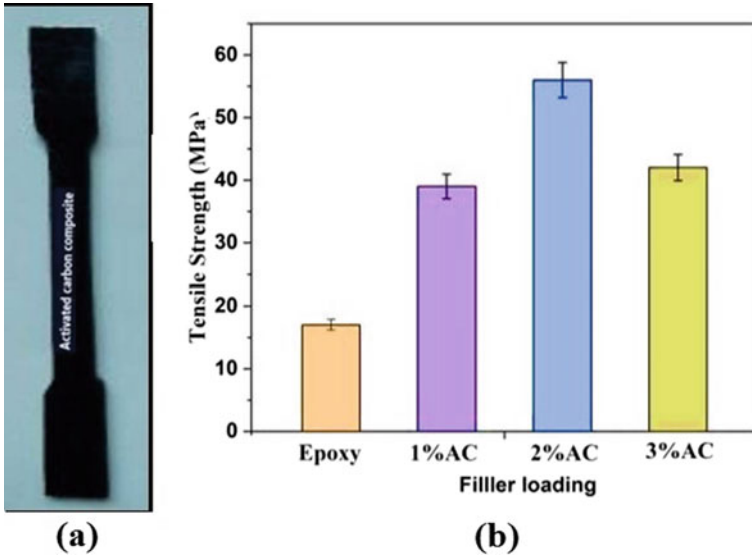


Fig. 8 a Tensile test sample of AC/epoxy porous nano composite. b Tensile strength of AC/epoxy porous nano composites. Reprinted from Prakash et al. [44], with permission from John Wiley and Sons. Copyright (2020)

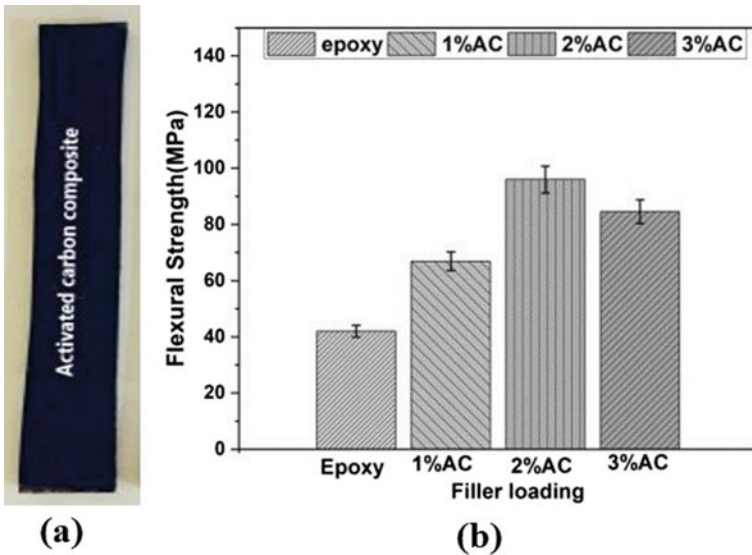


Fig. 9 a Flexural test sample. b Flexural strength of AC/epoxy composites. Reprinted from Prakash et al. [44], with permission from John Wiley and Sons. Copyright (2020)

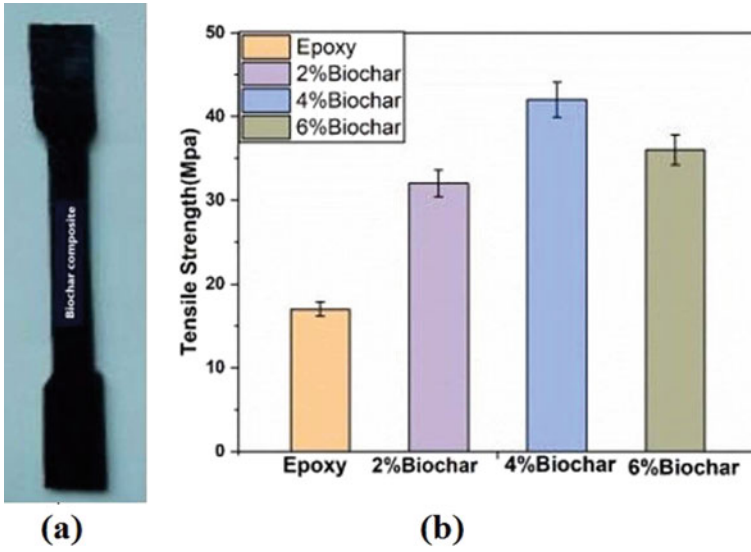


Fig. 10 a Tensile test sample. b Tensile strength of biochar filled epoxy composites

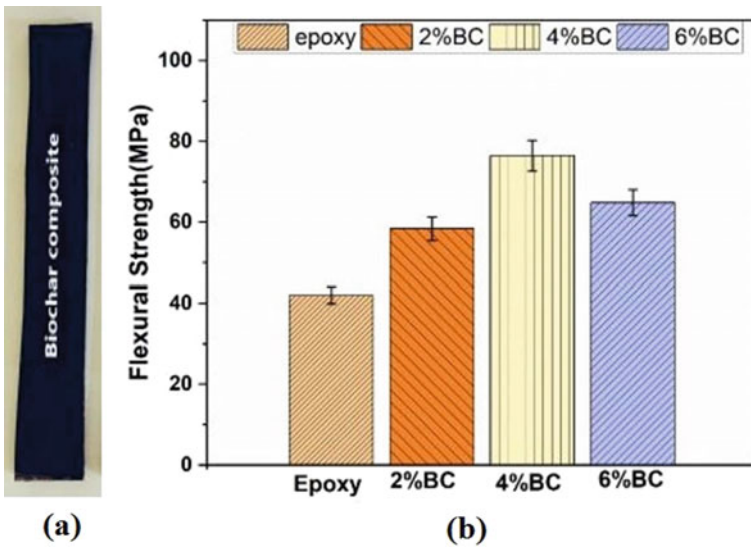


Fig. 11 a Flexural test sample. b Flexural strength of biochar filled epoxy composites

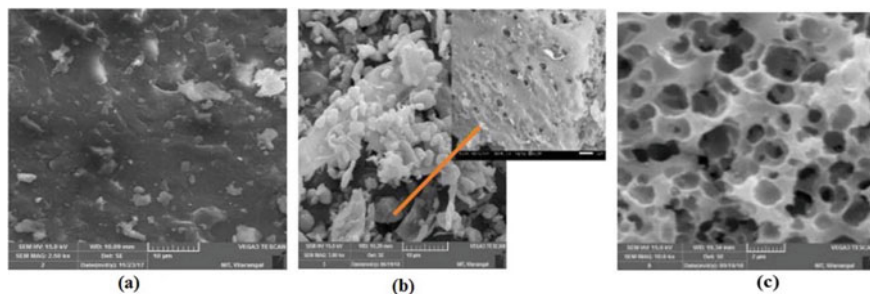


Fig. 12 Surface morphology of **a** Raw arhar particles. **b** Biochar. **c** Activated carbon

4.2 Erosion Wear Test Results

In general thermoplastic-based matrix composites erode in ductile fashion, whereas thermoset composites exhibit brittle erosion. Hence erosion performance of polymer matrix composites is categorized as brittle and ductile. Though, the mentioned classification is not ultimate, because the erosion wear performance depends upon parameters of the experiment. It also depends on the composition of the target surface. Impingement angle is one of the crucial parameters in determining erosion behavior. Ductile materials show maximum erosion at low impingement angles ($15^\circ < \alpha < 30^\circ$). In contrary brittle materials erode at the normal impact angle of 90° [48]. A study on erosion wear of 4, 8, 12 wt.% of micron sized egg shell particulate reinforced epoxy composites was reported by Panchal et al. [49]. Erosion performance was evaluated at different environmental conditions i.e. mineral water, kerosene, and saline water.

Erosion rate of the composites at dry condition has shown least compared to other conditions. The samples immersed in saline environment were highly affected by the erodent particles which exhibit high erosion rate. The reason may be due to the reaction of sodium and chlorine ions on composite samples which results in material degradation. Figures 13 and 14 represent the erosion wear rate of composites at dry and saline conditions respectively. Regardless of environmental conditions, 4 wt.% of egg shell particles filled composites are highly resistive toward erosion compared to other egg shell contents. Exceeding 4 wt.% shows an increased erosion rate due to the agglomeration of filler particles in the composite sample. Besides, unboiled egg shell particles exhibited higher erosion resistance than the boiled egg shell particles. The reason may be due to the decrease of egg shells strength after heating. All the composite samples exhibited high erosion at 60° , which indicates that material nature is semi-brittle. The further research on erosion wear of nano-sized egg shell particulate filled epoxy composite is found in [36].

The erosion resistance of 2 wt.% filled eggshell nanoparticulate composites was higher compared to other filler contents. Above 2 wt.% filler content, the erosion wear increases due to the improper bond between matrix and reinforcement. Agreeing with [42], the composites have also shown high erosion rate at 60° impingement angle as

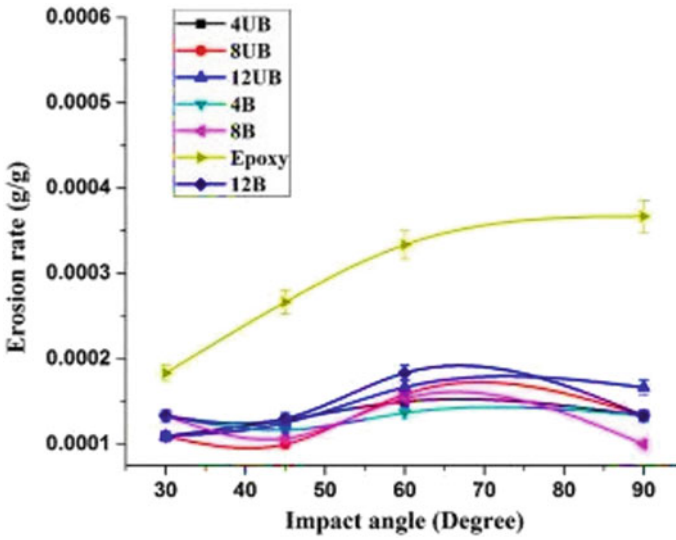


Fig. 13 Erosion rate of egg shell filled epoxy composites at dry condition, where (UB) in the legend refers to unboiled, and (B) refers to boiled eggshells filler. Reprinted from Panchal et al. [49], with permission from Springer Nature. Copyright (2017)

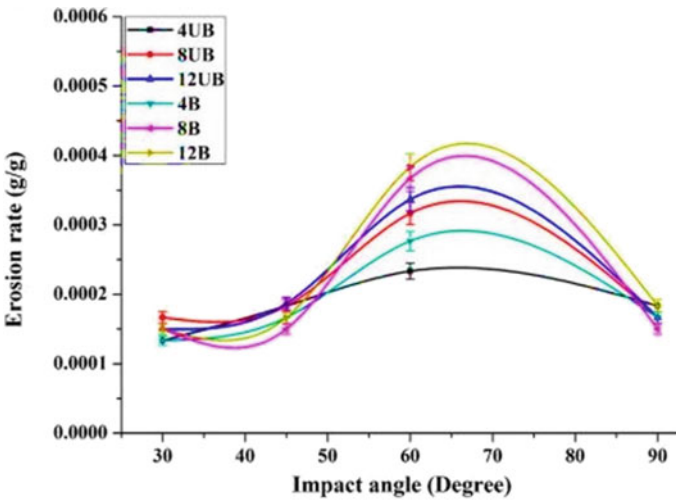


Fig. 14 Erosion rate of egg shell filled epoxy composites at saline condition, where (UB) in the legend refers to unboiled, and (B) refers to boiled eggshells filler. Reprinted from Panchal et al. [49], with permission from Springer Nature. Copyright (2017)

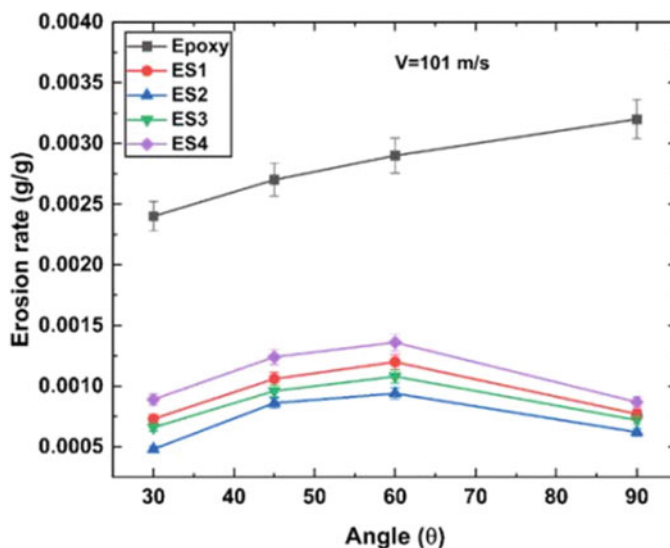


Fig. 15 Erosion rate of nano-sized egg shell particles filled epoxy composites [36]

shown in Fig. 15. Moreover, the erosion rates of nano filler composites were reported to be lower than the micron filler composite samples. Similar to the micron filler, the nano-sized egg shell filled composites have shown high erosion in saline environment as discussed in [50].

Prakash et al. [37] have investigated the erosion of arhar particles filled epoxy composites at varied weight fraction. The samples were exposed to different environmental conditions. It was observed that composites exhibit high erosive wear in saline condition as seen from Fig. 16a. Irrespective of filler content, the composites have shown greater erosion rate at a 60° impingement angle depicting the semi-brittle behavior. On the contrary, samples exhibited semi-ductile nature at sub-zero condition having high erosion at impingement angle of 45°. Besides, the erosion rate at 10 wt.% of filler is lower, beyond which the increment in wear was noticed as shown in Fig. 16b. This may be due to particles agglomeration that decreases the erosion resistance of composites. Keeping in view of mechanical strength, the activated carbon and biochar filled epoxy composites were further analyzed to predict their erosion behavior. The erosion testing was conducted at an impact velocity of 101 m/s at varying impingement angles. The peak erosion was reported at 45° impingement angle as seen in Fig. 17, which illustrates the semi-ductility behavior. When compared to BC particles filled composites, the AC particulate samples have shown lower erosion wear. This may be due to the surface morphology of AC particle which promotes the good mechanical locking with epoxy particles. Besides, 2 wt.% AC and 4 wt.% BC filler content composites exhibited greater erosion resistance compared to other filler contents. The erosion results were in agreement with the mechanical strength of composites.

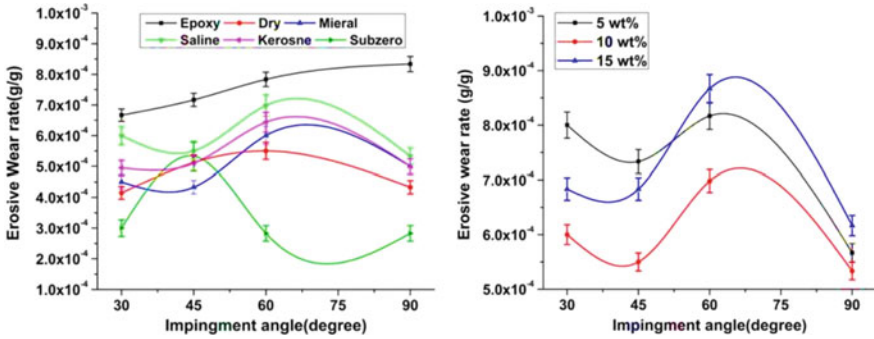


Fig. 16 Erosion wear of arhar particulate filled epoxy composites. a At distinct environmental conditions (10 wt.% arhar particulate). Reprinted from Prakash et al. [37], with permission from John Wiley and Sons. Copyright (2017). b With varying filler content in saline water

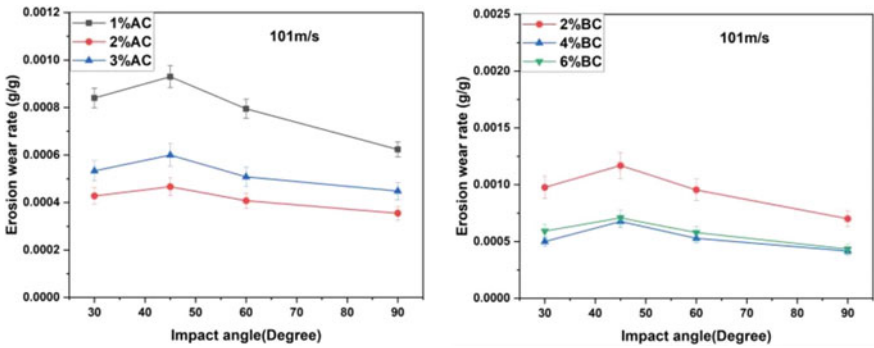


Fig. 17 Erosion wear of a AC. b BC particulate filled epoxy composites

4.3 Abrasive Wear Test Results

Owing to the superior mechanical and erosion properties, AC filled epoxy composites were evaluated for abrasive wear rate. The samples were prepared according to the required dimensions for testing apparatus which were shown in Fig. 18 [51]. Abrasive papers of different grit sizes were placed on the disc of testing apparatus to facilitate the three-body abrasion. Figure 19 depicts the wear rate of the composites at different loading conditions as reported by Prakash et al. [51]. The wear rate of 1 wt.% AC filled composites have shown high irrespective of loading conditions. While 2 wt.% AC composites displayed least wear among all the composite samples. The AC possesses graphitic and porous structure which acts as lubricant, resulting in the enhanced wear resistance. Furthermore, increment in filler content increases the wear rate due to poor bonding between epoxy and filler particles. Figure 19 also confirms the steady decrease in wear rate of the samples with the increase in grit size of emery paper. As the grit size changes from P180 to P800, the abrasive particles

Fig. 18 AC particulate filled epoxy composite samples for abrasive wear test. Reprinted from Prakash et al. [51], with permission from Elsevier. Copyright (2021)



alter their size from 75 to 25 μm . It is evident that nature of the particles changed from coarser to finer. Whenever the samples are subjected to larger coarser particles, the material loss will be higher due to ploughing and cutting actions. Besides, the large sized particles provide insufficient contact with the sample. As a result, the higher stresses were developed at the contact interface leading to greater wear rate. Minimal wear rate was observed on P800 grit abrasive paper at all loading conditions due to the presence of finer particles. The results were in agreement with the studies reported by Samantrai et al. [52] and Suresha et al. [53]. Irrespective of abrasive environment, the wear rate of all the composite samples increases with the increase of loading from 5 to 15 N. The reason may be due to the increased pressure on the contact surface which accelerates the abrasive particles to penetrate inside it causing the material loss. The material removal is mainly due to the ploughing action. The worn out surfaces show deep grooves which indicate the abrasive wear. The optimal condition for minimum wear rate was 10 N on a P800 grit abrasive paper for 2 wt.% of AC particulate filled epoxy composites.

5 Hybrid Polymer Composites

5.1 Mechanical Testing

Primarily, it is necessary to understand the performance of glass fiber epoxy composites prepared in bi- and multi-directions without the addition of filler particles in terms of their strength. Concerning this, Raghavendra et al. [54] have reported on mechanical behavior of bi- and multi-directional glass/epoxy composites. The comparison among bi- and multi-directional fibers in terms of tensile and flexural strength was presented in the study. It was evident from Fig. 21 that, the flexural strength is higher than tensile strength irrespective of fiber orientation. Uniform stress distribution

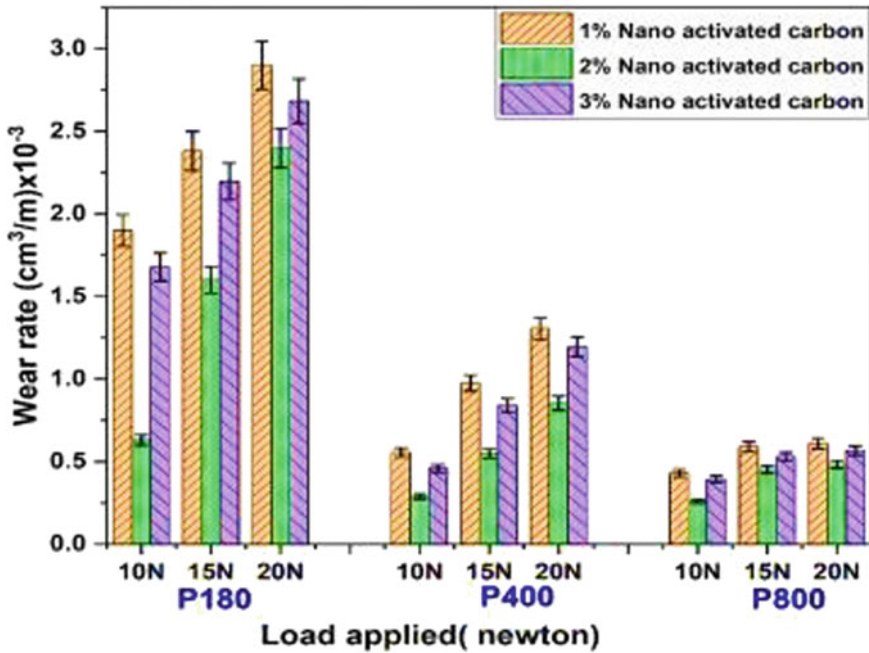


Fig. 19 Abrasive wear of AC filled epoxy composites at different loading conditions Reprinted from Prakash et al. [51], with permission from Elsevier. Copyright (2021)

is observed across the cross-section of composite sample while tested for tensile strength. On the contrary, flexural sample exhibits non-linearity in stress distribution which results in increased flexural strength compared to tensile. In addition, increment in the number of glass fiber layers leads to the increase in strength of composites linearly. However, beyond 12 layers the strength has been reduced. The reason may be the poor wettability of the matrix with the increase of fiber volume fraction. The tensile and flexural strengths of bi-directional composites have shown higher than those of the multi-directional samples. In bi-directional glass fiber composites, every layer is capable of holding the axial load. But then, only one layer out of six layers in multi-direction glass fiber composite samples was able to carry the axial load, which results in the reduction of strength. Thus, it was concluded from the study that bi-directional glass fibers with 12 layers can be adopted to attain the beneficial effects of composites. The results are in agreement with the studies reported by GuruRaja et al. [55] and Al-Hasani [56] (Fig. 20).

The conclusion derived from this research was adopted to study the performance of glass fiber reinforced hybrid composites with the addition of $g-C_3N_4$ nano particles. In the fabrication of hybrid composites it is crucial to understand the optimal range of filler weight percentage to attain the better characteristics. Concerning the composite samples comprised of 0–5 wt.% $g-C_3N_4$ and pure epoxy which were fabricated by hand lay-up method. The developed samples were subjected to tensile and flexural

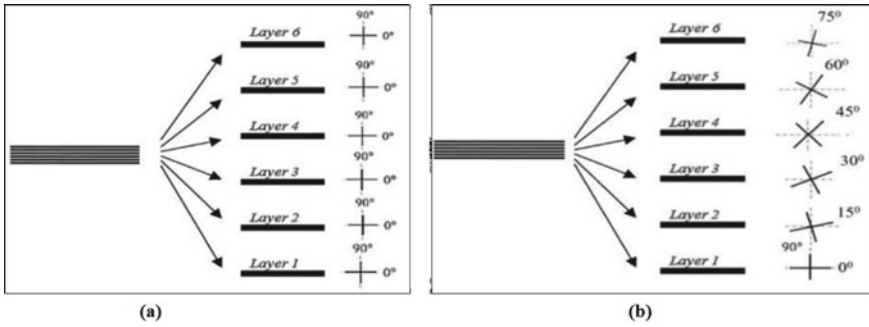


Fig. 20 Sample 6 layered; **a** bi-directional, and **b** multi-directional glass fiber composites. Reprinted from Raghavendra et al. [54], with permission from IOP Publishing, Ltd. Copyright (2014)

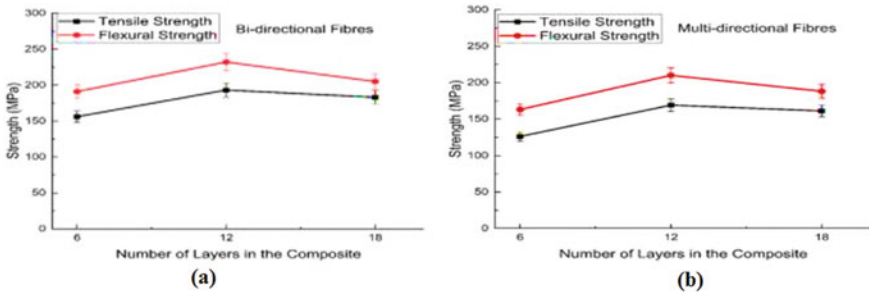


Fig. 21 Tensile and Flexural strength of bi-directional (a), and multi-directional (b) glass/epoxy composites. Reprinted from Raghavendra et al. [54], with permission from IOP Publishing, Ltd. Copyright (2014)

testing to access their mechanical behavior. It was evident from Fig. 22 that, the strength of composites increases with the $g-C_3N_4$ content until 2 wt.% beyond which the decrement was observed. The loss in the strength of composite samples at high filler content is due to the agglomeration of particles in the epoxy resin. Furthermore, the flexural strength of composites was higher than the tensile strength regardless of $g-C_3N_4$ volume fraction. Keeping in mind, the further study on hybrid composites was carried out adopting the wt.% of $g-C_3N_4$ between 1 and 3 and the 12 layered bi-directional glass fiber composites with inclusion of $g-C_3N_4$ nano particles were fabricated. The wt.% of filler particles varied from 1 to 3 with an increment of 0.5. The composites were prepared using hand lay-up at the room temperature. The strength of fabricated composite samples was predicted by tensile and flexural analysis. A gradual increase in the tensile strength was observed with the increase of $g-C_3N_4$ content from 0 to 2 wt.%. The drop in strength of composites beyond 2 wt.% is evident from Fig. 23. The increase in tensile strength from 0 to 2 wt.% of filler is by 46%, which indicates clearly that the enhancement is due to the presence of nano

particles. The filler particles promote the distribution of applied load between the epoxy and glass fibers effectively, which improves the strength of composites [53].

Besides, the frictional force between matrix and glass fiber increases with filler content, which also leads to the enrichment of composite strength. In contrary, the addition of filler content above 2 wt.% decreases the bonding force between the constituents as displayed in Fig. 24. Increased filler particles were unable to adhere with the epoxy and glass fibers, which led to formation of non-bonded zones. Due to the growth of these adhesive forces, the flexural strength of composites was reported to be higher than the tensile strength. The composite sample consisting of 2.5 wt.% filler content has shown higher flexural strength, which is 28% more than that of composite with 0 wt.% filler. Thus, the hybridization of 12 layered bi-directional glass

Fig. 22 Tensile and flexural strength of g-C₃N₄ reinforced epoxy composite samples

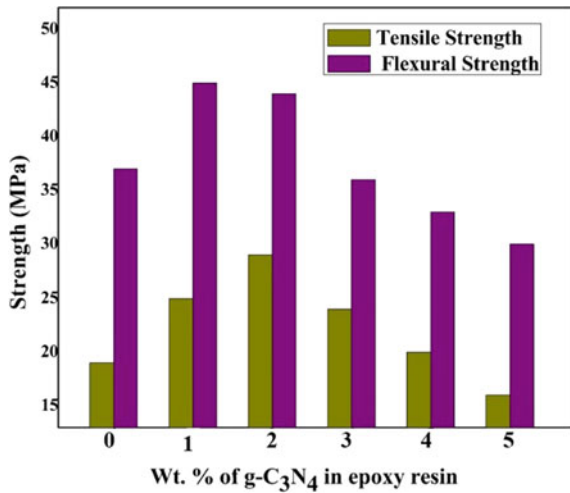
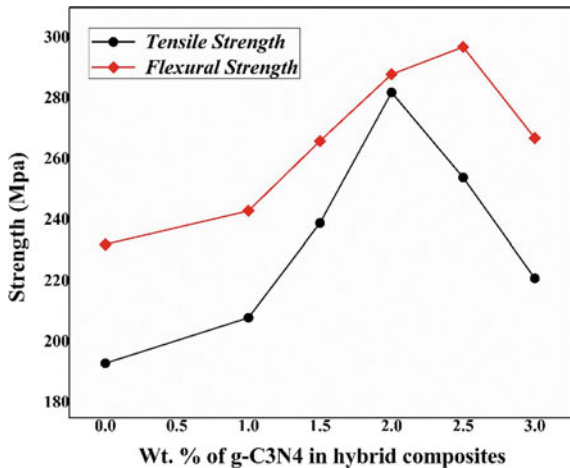


Fig. 23 Tensile and flexural analysis of 12 layered bi-directional glass fiber hybrid composites



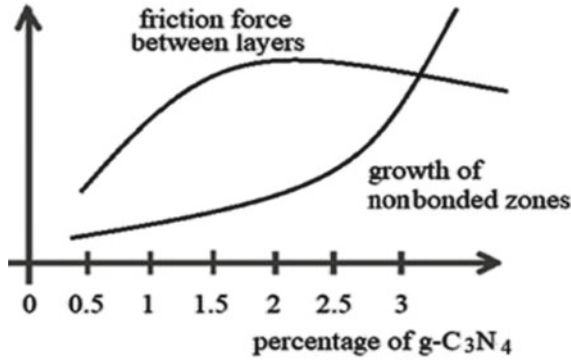


Fig. 24 Frictional force and non-bonded zones with the increase of filler content in hybrid composites

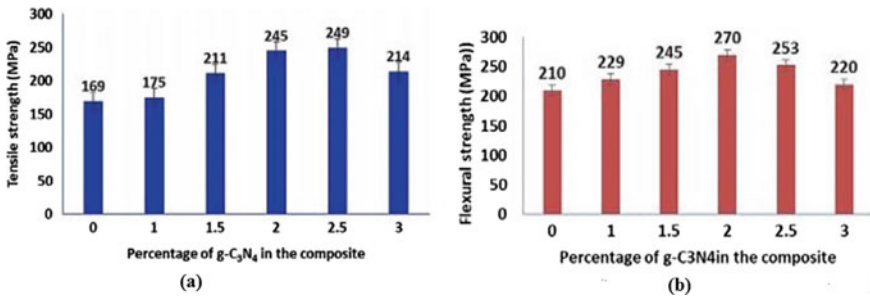


Fig. 25 Tensile and Flexural analysis of 12 layered multi-directional glass fiber hybrid composites. Reprinted from Naidu et al. [39], with permission from John Wiley and Sons. Copyright (2019)

fibers with 2 wt.% of g-C₃N₄ filler particles yields composites of better mechanical strength. Additionally, the work reported on 12 layered multi-directional glass hybrid composites by Naidu et al. [39] has shown analog mechanical behavior, which is in agreement with the results depicted in Fig. 25.

5.2 Erosion Wear Test

In addition to the mechanical analysis, it is essential to understand the erosion behavior of fabricated composite samples. Erosion wear is affected by several parameters such as impingement angle, impact velocity, nature of erodent, geometry of erodent particles, orientation of fibers, and content of filler particles. For the purpose of concise, the research [38] was focused on two parameters viz. impingement angle and impact velocity. Moreover, erosion of polymer composites depends upon nature

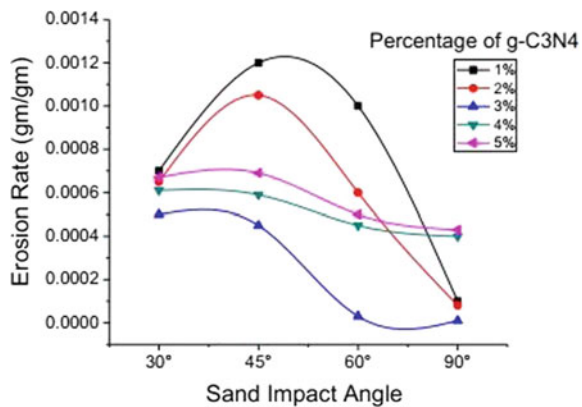
of matrix (thermoplastic or thermoset), brittleness of reinforcements, and interfacial bonding between matrix and reinforcements.

In general, the erosion wear resistivity of polymer composites enhances with the incorporation of both fiber and filler particles. A study on erosion behavior of bi-directional and multi-directional oriented glass fiber composites with varying the number of layers was reported by Naidu et al. [38]. The effect of impact angle on the erosion rate was evaluated on the composite samples. It was observed that glass fiber reinforced composites exhibit semi-ductility nature with maximum erosion at 45° . The composite sample with 12 layers has showed the best erosion resistivity, which was also in agreement with the mechanical analysis. Thus, the study concludes that fiber orientation has negligible effect on erosion wear.

Raghavendra et al. [57] have presented the erosion performance of epoxy resin composites with the addition of g-C₃N₄ filler at varied weight fractions. From Fig. 26, it was perceived that composites having 1 wt.% and 3 wt.% of filler particles exhibit highest and lowest wear respectively. Beyond 3 wt.%, the erosion rate steadily increases due to the weak interaction force between epoxy and g-C₃N₄. The nature of composites is termed as semi-ductile with peak erosion between 45° and 60° impingement angles. Besides, the addition of brittle filler particles has increased the erosion resistance of pure epoxy. From the aforementioned studies, it was concluded that the glass-fiber with 12 layers and (1–3) wt.% g-C₃N₄ filler content can yield better results in terms of erosion rate. Thus, further hybridization of glass fiber with g-C₃N₄ was developed through hand lay-up and their erosion wear behavior was evaluated.

Figures 27 and 28 represent the erosion rate of bi-directional and multi-directional hybrid glass fiber composites. Erosion test is conducted at different impingement angles and impact velocities at room temperature. Irrespective of fiber orientation, the peak erosion was shown at 60° sand impact angle which confirms the semi-ductility nature. At 30° impingement angle the erosion wear was observed to be low. The 0 wt.% NIL (pure epoxy sample) of g-C₃N₄ exemplifies the pure epoxy reinforced with glass fiber alone where the erosion rate was reported to be higher.

Fig. 26 Erosion behavior of g-C₃N₄ reinforced epoxy composites. Reproduced from Naidu and Raghavendra [57] under the terms and conditions of the Creative Commons Attribution 3.0 licence. <https://creativecommons.org/licenses/by/3.0/>



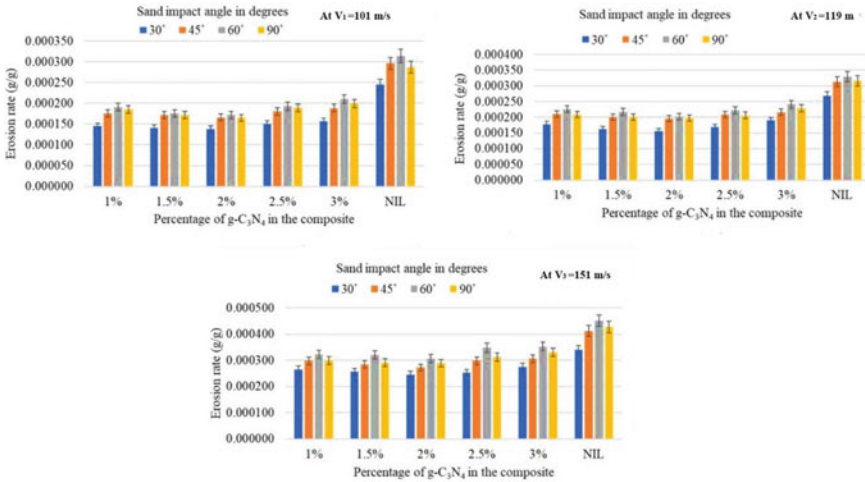


Fig. 27 Erosion wear rate of 12 layered bi-directional glass fiber hybrid composites at different impact velocities

Whereas, the addition of $\text{g-C}_3\text{N}_4$ particles has shown a decreasing trend of erosion wear. The erosion wear trend of composite samples comprising 1–2 wt.% of $\text{g-C}_3\text{N}_4$ has displayed decrement fashion. Beyond 2 wt.%, wear of the hybrid composites gradually increases due to the agglomeration of particles in the epoxy resin that weaken the interfacial bonding. Thus, it confirms that filler content has a substantial effect on erosion wear of hybrid composites. In addition, impingement angle also plays an important role in erosion behavior. Although erosion wear is least affected by impact velocity, it was observed that increasing the impact velocity leads to exponential increase of erosion rate in all the composite samples. Examination of fiber orientation reveals that the bi-directional glass fiber layered composites displayed lower erosion rate compared to multi-directionally oriented glass fiber composite samples. It was concluded from this study that hybrid composite of 12 layered glass fiber with 2 wt.% of $\text{g-C}_3\text{N}_4$ content exhibits the high erosion resistivity.

6 Hybrid Sandwich Composite Testing

6.1 Erosion Wear Test

6.1.1 Effect of Impingement Angle on Erosion Wear

The fabricated hybrid composites had neither responded in a ductile manner nor in brittle. This material behavior is named as semi-ductile/semi-brittle. Ductility of composites is lost with the integration of glass fiber and TiO_2 filler particles whose

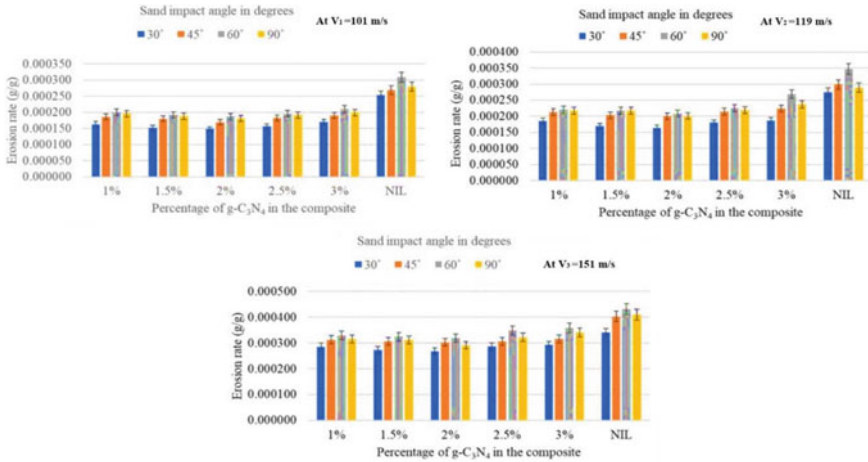


Fig. 28 Erosion wear rate of 12 layered multi-directional glass fiber hybrid composites at different impact velocities

nature is brittle. Figure 29a–c indicate the effect of impingement angle on erosion performance of composite samples subjected to different impact velocities. The composite C1 being pure epoxy whose nature is brittle, the maximum erosion wear occurred at 90° impingement angle. It was evident that glass fiber epoxy composites with and without the addition of filler particles (C3 and C2) exhibited semi-ductile and semi-brittle nature with peak erosion at 30° and 60° impingement angles, respectively. At 30° and 60° impingement angles, hybrid composite C3 have shown high and low erosion wear rate respectively, which indicates the semi-ductility nature. The interfacial bonding between the elements of the composite at 60° is good enough to give better erosion resistance when compared to other angles. Moreover, the erosion wear resistance of pure epoxy has been improved with the inclusion of glass fiber and TiO₂ particles. When compared to C2, the composite C3 exhibits lower erosion wear. The reason is that elements present in TiO₂ are harder than epoxy resin that enriches the hardness of composite thereby lowering the erosive wear.

The hybrid sandwich composite sample C4 has different constituents at varied volume fractions. During the time interval *t*₁, the top portion is subjected to erosion until it gets completely eroded and reaches the next portion of the sample. In the first time interval, C4 exhibited high erosion rate at 90° impingement angle due to the presence of brittle filler particles (TiO₂). In subsequent time interval *t*₂, the second portion of composite sample is subjected to erosion and a peak in erosion wear rate was observed at 60° impingement angle. Thus it was evident that the composite sample had altered its nature from brittle to semi-brittle irrespective of impact velocity as shown in Fig. 30a. To evaluate the material behavior of C5, the sample is subjected to three different erosion time intervals of *t*₁, *t*₂, *t*₃. The sand particles are made to impact from the top portion and progressed until erodent reaches the bottom portion. Each portion was subjected to erosion at varied time duration.

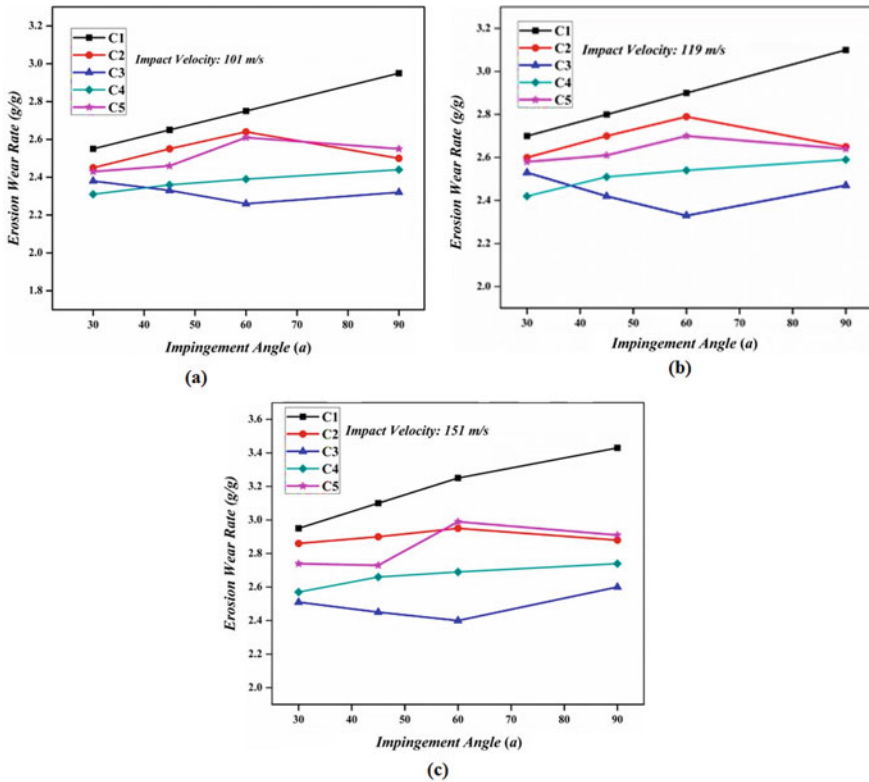


Fig. 29 Effect of impingement angle on erosion wear behavior of composite samples at impact velocity of **a** 101 m/s, **b** 119 m/s, **c** 151 m/s

To obtain the erosion behavior, Fig. 30b was plotted between impingement angle and erosion wear rate at varied time intervals. It was observed from Fig. 30b that the composite C5 exhibited erosion wear rate peak at 60°, 90° and 30° impingement angles during t_1 , t_2 , and t_3 time intervals, respectively. This showed a variation in material property from semi-brittle to brittle and finally to semi-ductility nature. The semi-brittle nature is due to the presence of glass fiber at the top portion of the sample. Since TiO_2 particles are at the mid portion of the composite, the nature is brittle. Although the third portion of C5 possesses semi-ductility behavior it exhibited maximum erosion rate at 30°. The reason may be the acceleration of TiO_2 particles into the bottom portion of composite sample due to their density differences. Besides, the addition of new constituents upon the cured layer may lead to its partial melting which causes the filler particles to penetrate to the bottom portion. In this work, the erosion time intervals for C4 and C5 composites were dissimilar as the volume fraction of constituents in each sample was different. The composites C1–C3 have a solitary nature whereas the developed hybrid sandwich composites C4 and C5 possessed altered behavior in a single sample. Impingement of erodent particles

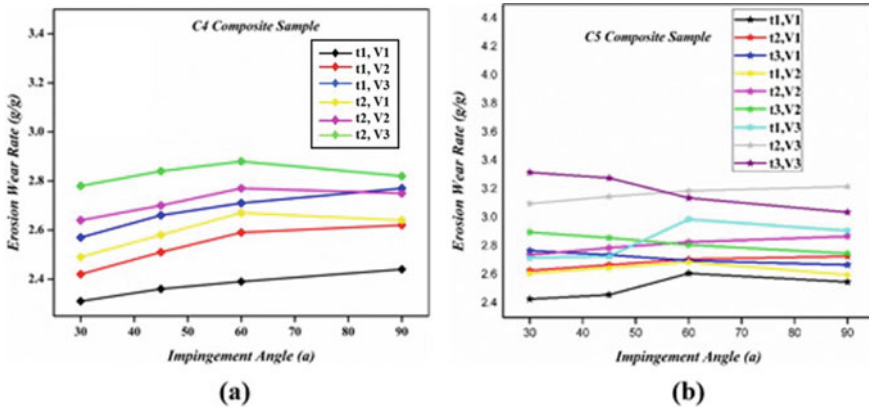


Fig. 30 Erosion wear behavior of a C4 composite sample, b C5 composite sample

causes the temperature rise of target material surface, which softens the matrix. Due to the impact, the kinetic energy of silica sand particles gets transferred to composite specimens, where material loss takes place with crater formation. The results indicate that hybrid composites (C3–C5) show lower erosion wear compared with other composites (C1 and C2) irrespective of impact velocity. It is apparent from our study that erosion wear rate strongly depends on the impingement angle.

6.1.2 Effect of Impact Velocity on Erosion Wear

Erosion wear rate of fabricated composite samples at various impact velocities was shown in Fig. 31. The erosion rate concerning impact velocity varies exponentially for all composite samples. With the increase of impact velocity, the kinetic energy of erodent particles gets increased. High energy particles impact the target surface, which leads to higher material loss. In any erosion wear test, the influence of impact velocity dominates the effect of other test parameters like erodent particle size, impingement angle, etc. The presence of reinforcements (fiber and filler) in the matrix aids in the absorption of kinetic energy that lowers the plastic deformation. Besides, the inclusion of filler particles in the composite samples considerably lowers the material loss. Addition of TiO₂ particles to glass fiber epoxy composites reduces the porosity with enhanced micro-hardness, which leads to the enhancement of erosion resistance. Such hybrid composites have prospective usage to wear allied applications.

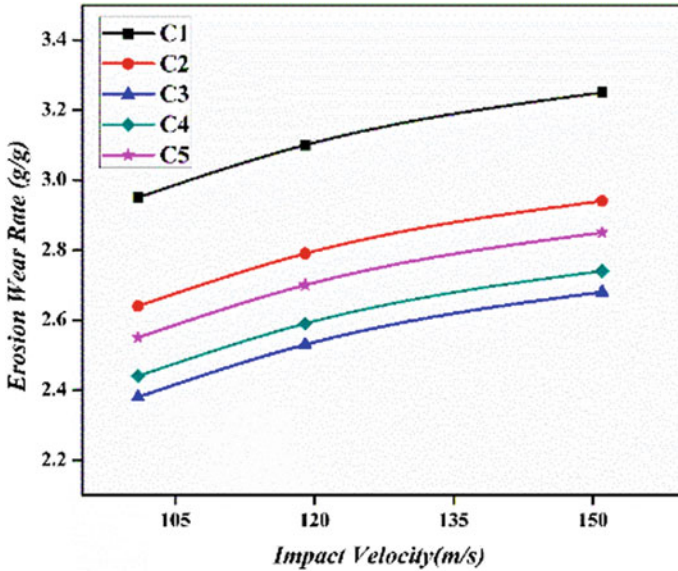


Fig. 31 Effect of impact velocity on erosion wear behavior of composite samples

7 Conclusions

The following conclusions were drawn from this chapter:

- The size of filler particles is vital in enhancing the composite properties. In this context, nano egg shell particles added to polymer composites exhibited superior mechanical and erosion properties when compared to micron particles.
- It was observed that the improved performance of polymer composites when arhar biomass particles converted in the form of biochar and activated carbon rather than raw arhar particulates.
- The remarkable breakthroughs in terms of mechanical strength and erosion resistance were observed with 2 wt.% AC filler rather than 4 wt.% BC and 10 wt.% raw arhar fillers.
- Hybrid polymer composites with 12 layered bi-directional glass fiber filled with 2 wt.% g-C₃N₄ nano particles have been more beneficial compared to conventional composites.
- The research results depict the improvement in mechanical and tribological performance of composites with the increase of reinforcement(s) content up to the saturation limit beyond which the strength decreases due to particles agglomeration.
- In contrast to hybrid polymer composites, novel hybrid sandwich composites comprising of glass fiber and TiO₂ have shown altered material characteristics in a single composite sample as confirmed from erosion wear test.

References

1. J.K. Nelson, Nano dielectrics-the first decade and beyond, in *Proceedings of International Symposium on Electrical Insulating Materials* (Niigata, Japan, 2014). 109/ISEIM.2014.6870707
2. B. Song, T. Wang, L. Wang, H. Liu, X. Mai, X. Wang, N. Wang, Y. Huang, Y. Ma, Y. Lu, E.K. Wujcik, Z. Guo, Interfacially reinforced carbon fiber/epoxy composite laminates via in-situ synthesized graphitic carbon nitride (g-C₃N₄). *Compos. Part B: Eng.* **158**, 259–268 (2019). <https://doi.org/10.1016/j.compositesb.2018.09.081>
3. S.J. Park, M.K. Seo, T.J. Ma, R. Lee, Effect of chemical treatment of Kevlar fibers on mechanical interfacial properties of composites. *J. Colloid. Interface Sci.* **252**, 249–255 (2002). <https://doi.org/10.1006/jcis.2002.8479>
4. G. Raghavendra, S. Ojha, S.K. Acharya, S.K. Pal, Jute fiber reinforced epoxy composites and comparison with the glass and neat epoxy composites. *J. Compos. Mater.* **48**, 2537–2547 (2014). <https://doi.org/10.1177/0021998313499955>
5. E. Manias, G. Polizos, H. Nakajima, M.J. Heidecker, in *Flame Retardant Polymer Nano Composites*, eds. by A.B. Morgan, C.A. Wilkie (Wiley, 2007), pp. 31–66
6. E. Manias, A. Touny, L. Wu, K. Strawhecker, B. Lu, T.C. Chung, Polypropylene/montmorillonite nano composites. Review of the synthetic routes and materials properties. *Chem. Mater.* **13**(10), 3516–3523 (2001). <https://doi.org/10.1021/cm0110627>
7. S.N.A. Safri, M.T.H. Sultan, M. Jawaid, K. Jayakrishna, Impact behaviour of hybrid composites for structural applications: a review. *Compos. Part B: Eng.* **133**, 112–121 (2018). <https://doi.org/10.1016/j.compositesb.2017.09.008>
8. P. Antil, S. Singh, A. Manna, Effect of reinforced SiC particulates of different grit size on mechanical and tribological properties of hybrid polymer matrix composites. *Mater. Today Proc.* **5**(2), 8073–8079 (2018). <https://doi.org/10.1016/j.matpr.2017.11.493>
9. R.K. Nayak, K.K. Mahato, B.C. Routara, B.C. Ray, Evaluation of mechanical properties of Al₂O₃ and TiO₂ nano filled enhanced glass fiber reinforced polymer composites. *J. Appl. Polym. Sci.* **133**(47), 44274 (2016). <https://doi.org/10.1002/app.44274>
10. F. Rezaei, R. Yunus, N.A. Ibrahim, Effect of fiber length on thermo mechanical properties of short carbon fiber reinforced polypropylene composites. *Mater. Des.* **30**(2), 260–263 (2009). <https://doi.org/10.1016/j.matdes.2008.05.005>
11. M.T. Bryk, *Degradation of Filled Polymers: high Temperature and Thermo-Oxidative Processes* (Ellis Horwood, New York, 1991), p. 71. <https://doi.org/10.1002/pi.4990280220>
12. D.P.R. Thirumalai, B. Madsen, H.L. Toftegaard, C.M. Markussen, Mechanics of functional materials and structures, in *Proceedings of 3rd Asian Conference on Mechanics of Functional Materials and Structures (ACMFMS 2912)* (Indian Institute of Technology, 2012), pp. 469–472
13. A. Jafari, H. Ashrafi, M. Bazli, T. Ozbakkaloglu, Effect of thermal cycles on mechanical response of pultruded glass fiber reinforced polymer profiles of different geometries. *Compos. Struct.* **223**, 110959 (2019). <https://doi.org/10.1016/j.compstruct.2019.110959>
14. M. Hussain, Y. Oku, A. Nakahira, K. Niihara, Effects of wet ball-milling on particle dispersion and mechanical properties of particulate epoxy composites. *Mater. Lett.* **26**(3), 177–184 (1996). [https://doi.org/10.1016/0167-577X\(95\)00223-5](https://doi.org/10.1016/0167-577X(95)00223-5)
15. G. Polizos, E. Tuncer, I. Sauers, D.R. James, A.R. Ellis, K.L. More, Electrical and mechanical properties of titanium dioxide nanoparticle filled epoxy resin composites. *AIP Conf. Proc.* **1219**, 41–46 (2010). <https://doi.org/10.1063/1.3402331>
16. S. Ahmed, S. Ikram, Chitosan & its derivatives: a review in recent innovations. *Int J Pharm. Sci. Res. (IJPSR)* **6**(1), 14–30 (2015). [https://doi.org/10.13040/IJPSR.0975-8232.6\(1\).14-30](https://doi.org/10.13040/IJPSR.0975-8232.6(1).14-30)
17. A.A. Jhatial, S. Sohu, M.J. Memon, N.U.K. Bhatti, Memon, Eggshell powder as partial cement replacement and its effect on the workability and compressive strength of concrete. *Int. J. Adv. Appl. Sci.* **6**(9), 71–75 (2019). <https://doi.org/10.21833/ijaas.2019.09.011>
18. K. Srinivas, A.L. Naidu, M.V.A.R. Bahubalendruni, A review on chemical and mechanical properties of natural fiber reinforced polymer composites. *Int. J. Perform. Eng.* **13**, 56–68 (2017). <https://doi.org/10.23940/ijpe.17.02.p8.189200>

19. A. Demirbas, Effects of temperature and particle size on bio-char yield from pyrolysis of agricultural residues. *J. Anal. Appl. Pyrolysis* **72**, 243–248 (2004). <https://doi.org/10.1016/j.jaap.2004.07.003>
20. M.A. Yahya, Z. Al-Qodah, C.W.Z. Ngah, Agricultural bio-waste materials as potential sustainable precursors used for activated carbon production: a review. *Renew. Sustain. Energy Rev.* **46**, 218–235 (2015). <https://doi.org/10.1016/j.rser.2015.02.051>
21. S.W. Zhang, State-of-the-art of polymer tribology. *Tribol. Int.* **31**(1–3), 49–60 (1998). [https://doi.org/10.1016/s0301-679x\(98\)00007-3](https://doi.org/10.1016/s0301-679x(98)00007-3)
22. B. Suresha, S. Kishore, S. Seetharamu, P.S. Kumaran, Investigations on the influence of graphite filler on dry sliding wear and abrasive wear behaviour of carbon fabric reinforced epoxy composites. *Wear* **267**(9–10), 1405–1414 (2009). <https://doi.org/10.1016/J.WEAR.2009.01.026>
23. U.K. Dwivedi, N. Chand, Influence of wood flour loading on tribological behavior of epoxy composites. *Polym. Compos.* **29**, 1189–1192 (2008). <https://doi.org/10.1002/pc.20548>
24. S. Suresh, D. Sudhakara, Investigation of mechanical and tribological properties of red mud-reinforced particulate polymer composite. *J. Bio-Tribo-Corros.* **5**, 87 (2019). <https://doi.org/10.1007/s40735-019-0279-8>
25. P. Mishra, S.K. Acharya, Anisotropy abrasive wear behavior of bagasse fiber reinforced polymer composite. *Int. J. Eng. Sci. Technol. IJEST* **2**(11), 104–112 (2010). <https://doi.org/10.4314/ijest.v2i11.64558>
26. M. Aslan, M. Tufan, T. Küçükömeroğlu, Tribological and mechanical performance of sisalfilled waste carbon and glass fibre hybrid composites. *Compos. Part B: Eng.* **140**, 241–249 (2018). <https://doi.org/10.1016/J.COMPOSITESB.2017.12.039>
27. S.W. Koh, B.C. Yang, H.J. Kim, J.D. Kim, Study on abrasive wear behaviour of a carbon fiber composites. *J. Korea Soc. Power Syst. Eng.* **10**(1), 46–51 (2006). <http://www.koreascience.or.kr/article/JAKO200621138245861.page>
28. V. Boggarapu, R. Gujjala, S. Ojha, A critical review on erosion wear characteristics of polymer matrix composites. *Mater. Res. Express.* **7**(2), 022002 (2020). <https://doi.org/10.1088/2053-1591/ab6e7b>
29. M. Choudhary, T. Singh, M. Dwivedi, A. Patnaik, Waste marble dust-filled glass fiber-reinforced polymer composite Part I: physical, thermo mechanical, and erosive wear properties. *Polym. Compos.* **40**(10), 4113–4124 (2019). <https://doi.org/10.1002/pc.25272>
30. T.D. Jagannatha, G. Harish, Mechanical properties of carbon/glass fiber reinforced epoxy hybrid polymer composites. *Int. J. Mech. Eng. Rob. Res.* **4**(2), 131–137(2015). <http://www.ijmerr.com/uploadfile/2015/0421/20150421101601643.pdf>
31. A.J. Crosby, J.Y. Lee, Polymer nanocomposites: The “nano” effect on mechanical properties. *Polym. Rev.* **47**(2), 217–229 (2007). <https://doi.org/10.1080/15583720701271278>
32. A.B. Al-Zubaidi, A.A. Al-Tabbakh, S.R. Ahmed, A. Achour, Erosion wear and hardness of glass fiber/epoxy with nano and micro TiO₂ hybride composites, in *Special Issus: 1st Scientific International Conference, College of Science* (Al-Nahrain University, 2017, Part I, 2018), pp. 43–51. <https://doi.org/10.22401/ANJS.00.1.06>
33. S.R. Ahmedizat, A.B. Al-Zubaidi, A.A. Al-Tabbakh A. Achour, A.A. Hamead, Comparative study of erosion wear of glass fiber/epoxy composite reinforced with Al₂O₃ nano and micro particles. *Mater. Today: Proc.* **20**(4), 420–427 (2020). <https://doi.org/10.1016/j.matpr.2019.09.158>
34. B. Pani, P. Chandrasekhar, S. Singh, Investigation of erosion behaviour of an iron-mud filled glass-fibre epoxy hybrid composite. *Bull. Mater. Sci.* **42**(5), 217 (2019). <https://doi.org/10.1007/s12034-019-1894-1>
35. A.P. Harsha, U.S. Tewari, Tribo performance of polyaryletherketone composites. *Polym. Test.* **21**(6), 697–709 (2002). [https://doi.org/10.1016/S0142-9418\(01\)00145-3](https://doi.org/10.1016/S0142-9418(01)00145-3)
36. M. Panchal, G. Raghavendra, A.R. Reddy, M. Omprakash, S. Ojha, Experimental investigation of mechanical and erosion behavior of eggshell nano particulate epoxy biocomposite. *Polym. Compos.* **29**(7), 897–908 (2021). <https://doi.org/10.1177/0967391120943454>

37. M.O. Prakash, G. Raghavendra, M. Panchal, S. Ojha, B.A. Reddy, Effects of environmental exposure on tribological properties of Arhar particulate/epoxy composites. *Polym Compos* **39**(9), 3102–3109 (2018). <https://doi.org/10.1002/pc.24316>
38. P.P. Naidu, G. Raghavendra, S. Ojha, Comparison of erosion wear of bidirectional and multi-directional oriented glass fibre epoxy composites. *Mater. Sci. Forum* **969**, 157–162 (2019). <https://doi.org/10.4028/www.scientific.net/MSF.969.157>
39. P.P. Naidu, G. Raghavendra, S. Ojha, B. Paplal, Effect of g-C₃N₄ nanofiller as filler on mechanical properties of multidirectional glass fiber epoxy hybrid composites. *J. Appl. Polym. Sci.* **137**(9), 48413 (2020). <https://doi.org/10.1002/app.48413>
40. P.S. Latha, M.V. Rao, V.K. Kumar, G. Raghavendra, S. Ojha, S.R. Inala, Evaluation of mechanical and tribological properties of bamboo–glass hybrid fiber reinforced polymer composite. *J. Ind. Text.* **46**(1), 3–18 (2016). <https://doi.org/10.1177/1528083715569376>
41. M. Panchal, G. Raghavendra, M. Om prakash, S. Ojha, B. Vasavi, *Innovative Product Design and Intelligent Manufacturing Systems*, eds. by B.B.V.L. Deepak, D.R.K. Parhi, P.C. Jena. Lecture Notes in Mechanical Engineering (Springer, Singapore, 2020), pp. 389–397
42. M.O. Prakash, G. Raghavendra, M. Panchal, S. Ojha, P.S.C. Bose, Influence of distinct environment on the mechanical characteristics of Arhar fiber polymer composites. *Silicon* **10**(3), 825–830 (2018). <https://doi.org/10.1007/s12633-016-9536-3>
43. M.S. Chowdary, G. Raghavendra, M.N. Kumar, S. Ojha, M.O. Prakash, A review on the degradation of properties under the influence of liquid medium of hybrid polymer composites. *SN Appl. Sci.* **2**(10), 1–12 (2020). <https://doi.org/10.1007/s12633-016-9536-3>
44. M.O. Prakash, R. Gujjala, M. Panchal, Ojha, Mechanical characterization of arhar biomass based porous nano activated carbon polymer composites. *Polym. Compos.* **41**(8), 3113–3123 (2020). <https://doi.org/10.1002/pc.25602>
45. M.O. Prakash, G. Raghavendra, S. Ojha, M. Panchal, Characterization of porous activated carbon prepared from Arhar stalks by single step chemical activation method. *Mater. Today: Proc.* **39**(4), 1476–1481 (2021). <https://doi.org/10.1016/j.matpr.2020.05.370>
46. M.P. Ho, K.T. Lau, H. Wang, Hui, Improvement on the properties of polylactic acid (PLA) using bamboo charcoal particles. *Compos. Part B: Eng.* **81**, 14–25 (2015). <https://doi.org/10.1016/j.compositesb.2015.05.048>
47. M. Panchal, G. Raghavendra, M. Omprakash, S. Ojha, Fabrication and characterization of silica based ceramic composite for filtration applications. *Silicon* **13**, 1951–1960 (2021). <https://doi.org/10.1007/s12633-020-00595-y>
48. V.K. Srivastava, Effects of wheat starch on erosive wear of E-glass fibre reinforced epoxy resin composite materials. *Mater. Sci. Eng. A* **435–436**, 282–287 (2006). <https://doi.org/10.1016/j.msea.2006.07.144>
49. M. Panchal, G. Raghavendra, M.O. Prakash, S. Ojha, Effects of environmental conditions on erosion wear of eggshell particulate epoxy composites. *Silicon* **10**(2), 627–634 (2018). <https://doi.org/10.1007/s12633-016-9505-x>
50. M. Panchal, G. Raghavendra, P.S. kumar Reddy, M. Om prakash, P. Srikar, Study of moisture absorption and its effect on erosion wear behavior of eggshell nano particulate epoxy composite. *Mater. Today: Proc.* **33**(8), 5746–5750 (2020). <https://doi.org/10.1016/j.matpr.2020.06.501>
51. M.O. Prakash, G. Raghavendra, S. Ojha, and. Kumar, Investigation of tribological properties of biomass developed porous nano activated carbon composites. *Wear* **466–467**, 203523 (2020). <https://doi.org/10.1016/j.wear.2020.203523>
52. S. Samantrai, G. Raghavendra, S. Acharya. Effect of carbonization temperature and fibre content on the abrasive wear of rice husk char reinforced epoxy composite. *Proc. Inst. Mech. Eng. Part J: J. Eng. Tribol.* **228**(4), 463–469 (2014). <https://doi.org/10.1177/1350650113516435>
53. B. Suresha, B.N. Ravi Kumar, Two-body abrasive wear behavior of particulate filled polyamide66/polypropylene nano composites. *J. Appl. Polym. Sci.* **119**, 2292–2301 (2011). <https://doi.org/10.1002/app.32909>

54. G. Raghavendra, P.P. Naidu, S. Ojha, B. Vasavi, M. Pachal, S.K. Acharya, Effect of bi-directional and multi-directional fibers on the mechanical properties of glass fiber-epoxy composites. *Mater. Res. Express* **6**(11), 115353 (2019). <https://doi.org/10.1088/2053-1591/ab529a>
55. M.N. GuruRaja, A.N. HariRao, Hybrid effect on tensile properties of carbon/glass angle ply composites. *J. Adv. Mater.* **2**(3), 36–41 (2013). <https://doi.org/10.11648/j.am.20130203.13>
56. E.S. Al-Hasani, Study of tensile strength and hardness property for epoxy reinforced with glass fiber layers. *Eng. Technol. J.* **25**(8), 988–997 (2007). <https://www.iasj.net/iasj?func=article&aId=25940>
57. P.P. Naidu, G. Raghavendra, Erosion behaviour of graphitic carbon nitride (g-C₃N₄) reinforced epoxy composites. *IOP Conf. Ser.: Mater. Sci. Eng.* **577**, 012144 (2019). <https://doi.org/10.1088/1757-899X/577/1/012144>

Nanocomposites Based on Conducting Polymers and Nanomaterials Derived from Natural Polymers



Alessandra Alves Correa, Ana Carolina Correa,
Kelcilene Bruna Ricardo Teodoro, José Manoel Marconcini,
and Lucia Helena Mascaro

Abstract There is a growing increase in the study of intrinsically conducting polymers as well as conducting polymer composites. Conducting polymers are well known for their electrical conduction properties, and therefore have great potential in technological applications. However, these materials have limitations in processing and mechanical properties. In order to overcome these limitations, conducting polymers can be combined with nanomaterials from renewable resources, such as cellulose, starch, alginate, chitosan, and others, resulting in nanocomposites with superior properties. These nanostructures from natural polymers (in the morphology of particles, fibers, or nanocrystals) have emerged as an alternative to reinforce synthetic polymers, being a sustainable and inexpensive material. This chapter will discuss an introduction about conducting polymers, natural polymers, and composites; types of composites and technological applications.

Keywords Conducting polymers · Natural polymers · Composites · Technological applications

A. A. Correa · A. C. Correa · J. M. Marconcini
Department of Materials Engineering, Center for Exact Sciences and Technology, PPCEM,
Federal University of São Carlos (UFSCar), São Carlos, SP, Brazil
e-mail: jose.marconcini@embrapa.br

A. A. Correa · A. C. Correa · K. B. R. Teodoro · J. M. Marconcini
Nanotechnology National Laboratory for Agriculture, Embrapa Instrumentação, São Carlos, SP,
Brazil

L. H. Mascaro (✉)
Department of Chemistry, Center for Exact Sciences and Technology, PPGQ, Federal University
of São Carlos (UFSCar), São Carlos, SP, Brazil
e-mail: lmascaro@ufscar.br

1 Introduction

1.1 *Conducting Polymers: Polyaniline, Polypyrrole, and Polythiophene*

Polymers, whose name comes from the Greek: poly (many) and mers (parts), are macromolecules that have high molecular mass resulting from the polymerization reaction between smaller structures, the so-called monomers.

Natural polymers are macromolecules that provide part of the structural and tissue support in animal organisms, the most known are collagen, proteins, chitosan, and DNA. In the case of plant organisms, there are cellulose, lignin, starch, latex, among others, known as natural polymers. Biodegradable polymers from fossil or renewable sources can also be synthesized in the laboratory through chemical reactions [1].

For a long time, the attempt to attribute electrical properties to conventional polymers was made with the incorporation of impurities such as carbon black, metallic fibers, or carbon to polymeric matrices. The incorporation of impurities was intended to assign a charge to these materials and, consequently, electrical conductivity. Thus, such polymers came to be called extrinsic conducting polymers [2].

Subsequently, a new class of conductive materials was studied, which are the intrinsic conducting polymers. These polymers conduct electrical current without the incorporation of conductive charges [2]. This new class of materials was discovered in 1976, in the laboratory of Prof. Hideki Shirakawa, where a faulty procedure of synthesis of polyacetylene resulted in a new material. The synthesis error was the excessive addition of the catalyst used in the reaction [3]. Subsequent studies by Shirakawa, MacDiarmid, and Heeger showed that the conductivity of this film was increased after doping with iodine vapor [4].

The fundamental characteristic for a polymer to be an electronic conductor is the existence of conjugated double bonds, which allows the removal or addition of electrons with ease, thus leading to the occurrence of electron flow through the material. The redox process in conducting polymers leads to formation of delocalized charges, whose charge balance is carried out by the incorporation of counter ions to the polymeric chain, which are called dopants [2, 5].

Unlike doping in inorganic semiconductors, where the dopant is incorporated in the crystalline structure of the material in a very small proportion, in intrinsically conducting polymers the dopant is located in neighborhoods of polymer chains in much larger quantities [2].

In this way, many researchers became interested in the study of conducting polymers, discovering new polymers, or modifying others already known. Because of these researches, the polymers that were previously considered as insulating materials started to compete with conductive materials, being then used in several technological applications.

There are several conducting polymers, however polyaniline (PAni), polypyrrole (PPy), and polythiophene (PT) and their derivatives form the vast majority of conducting polymers and have many technological applications.

Polyaniline is the most promising polymer because of its good environmental stability, controllable electrical properties, and low cost of monomer [6]. The first study with aniline appeared in 1862 [7], later it was discovered that octamers of aniline exist in different oxidation states [8]. At the beginning of the second decade of the twentieth century, its various oxidation states were described. Polyanilines represent a class of polymers, whose basic chemical composition is given by a general formula represented in Fig. 1a. The formula is composed of y and $(1 - y)$ repetitive units of the reduced and oxidized species, respectively. The value of y can vary between 1 for the completely reduced polymer (containing only amine nitrogens) and 0, in the case of the completely oxidized polymer (containing only imine nitrogens). The oxidation states are well defined, ranging from the totally reduced form (leucoemeraldine, $y = 1$) (yellow), partially oxidized (protoemeraldine, $y = 0.75$) (light green), semi oxidized (emeraldine, $y = 0.50$) (green), partially reduced (nigraniline, $y = 0.25$) (blue) to completely oxidized (pernigraniline, $y = 0$) (violet). While polyaromatics are conducting in the oxidized state, polyaniline is better conducting when in medium oxidized states (emeraldine and protoemeraldine), in which it undergoes protonation doping [2, 9–11].

Polyaniline can be synthesized by chemical and electrochemical methods. Chemical synthesis has the advantages of production of a polymer with high molar mass and of high purity, which can be obtained directly in the doped state. The disadvantage of chemical synthesis is the need for additional isolation and purification

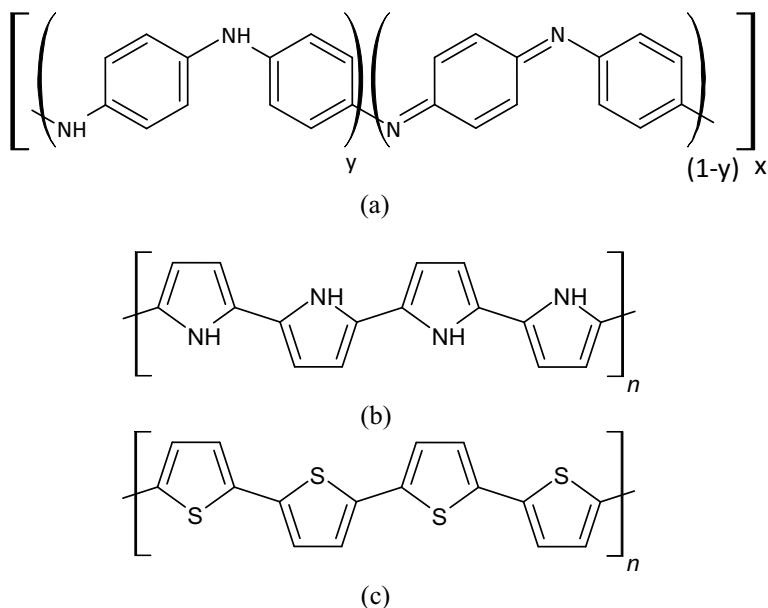


Fig. 1 Structural conducting polymer formula. **a** polyaniline, showing reduced (y) and oxidized ($1-y$) forms. **b** polypyrrole. **c** polythiophene

steps and the use of large amounts of solvents and other reagents. Polyaniline can also be synthesized through an electrochemical route providing thin films in a single step and a much lower consumption of reagents. This methodology allows obtaining films directly on the surface of an electrode. The disadvantage of electrochemical synthesis is obtaining a low molecular weight polymer and the amount of material is limited by the dimensions of the electrode [12, 13].

Chemical synthesis of polyaniline can be performed using various types of oxidizing agents such as $(\text{NH}_4)_2\text{S}_2\text{O}_8$, H_2O_2 , $\text{K}_2\text{Cr}_2\text{O}_7$, and KIO_3 , MnO_2 , Cr_2O_4 , etc., with $(\text{NH}_4)_2\text{S}_2\text{O}_8$ being the most widely used oxidizing agent [14, 15]. The polymerization temperature affects the molecular weight and conductivity of the polyaniline [16, 17]. The decrease in the temperature range, for example, from 5 until 20 °C to -5 until -3 °C leads to an increase in molecular weight from 1.3 to 1.6 g mol^{-1} , and in conductivity from 11 to 18 S cm^{-1} . This is due to the suppression of unwanted reactions at low temperatures [16]. It is also possible to obtain polyaniline with suitable characteristics, that is, high molar mass and good conductivity through chemical synthesis at room temperature [18].

The electrochemical polymerization of polyaniline occurs by anodic oxidation of aniline on an inert electrode such as platinum, gold, conductive glass, and glassy carbon [15]. The most used electropolymerization methods are controlled current and potential. The electrolyte is an acidic solution (HCl , H_2SO_4 , HNO_3 , HBF_4 , HClO_4 , CF_3COOH), and the concentration of anions influences the electrodeposition rate and the type of anion in the polymer morphology [19, 20].

The major problem with conducting polymers is their insolubility and, therefore, the difficulty in processing these materials. To solve this problem, polar functional groups and long alkyl groups, chemically linked to the polymer backbone, were introduced. Thus, polyanilines substituted in the ortho position of the aromatic ring by alkyl and alkoxy groups have been prepared using both chemical and electrochemical methods [21].

Among the polyaniline derivatives, the most important are poly(*o*-methoxyaniline) (POMA), poly(*o*-ethoxyaniline) (POEA) and polyaniline sulfonated. These polymers are soluble in various solvents such as dimethylformamide, acetonitrile, chloroform, dichloromethane, acetic and sulfuric acids, etc. These polyaniline derivatives can be processed by conventional methods [21].

Polypyrrole is one of the conductive polymers that have attracted most of the attention of researchers, because of its high conductivity, chemical stability, and relatively simple synthesis. The polymer chains of PPy are composed of aromatic units containing nitrogen atoms, linked by means of carbon atoms. Like other conductive polymers, PPy has high electrical conductivities and good oxidative stability [21]. Figure 1b shows the structural polypyrrole formula.

Polypyrrole was first synthesized in 1916 by the oxidation of pyrrole in hydrogen peroxide (H_2O_2), giving rise to an amorphous powder called "black pyrrole". In 1968, it was synthesized, electrochemically, by the French nuclear physicist Attilio Dall'olio in a solution of sulfuric acid. However, only in 1979 that PPy films grown electrochemically by American A. F. Diaz received some attention due to their better conductivity, adhesion to the substrate, and stability. In 1973 the Italian chemist Gian

Piero Gardini was the first to obtain PPy by chemical synthesis. PPy was obtained in both studies and was an insoluble and infusible black powder due to its inter and intramolecular interactions and also to the formation of cross-links [21–23].

There are two main routes to synthesize PPy: with chemical polymerization and electrochemistry. The first allows a large-scale production at low cost, favors the preparation of blends with other polymers and processability. Using the electrochemical synthesis, with in situ polymerization it is possible to obtain great electrical conductivity, but large-scale production is limited by the electrode area and the properties of the produced film can be controlled during preparation. Although the final product is the same, and the polymerization mechanisms are similar, the polymer morphology depends on the synthesis route.

Polypyrrole can be prepared by oxidizing the monomer using chemical oxidants and will produce a black powder. Chemical oxidants that are widely used are aqueous or anhydrous FeCl_3 , other salts of iron (III), and copper (II). It is also possible to use halogens and organic electron acceptors as oxidants for PPy. The yield and conductivity of the produced PPy are affected by a variety of factors, among which are the choices of solvent and oxidant, initial pyrrole/oxidant ratio, reaction time, temperature, etc. [24].

The choice of solvent is limited, as it must be compatible with the monomer and the oxidizing agent. The pyrrole synthesis can be performed in both aqueous and non-aqueous media. Some researchers have investigated the effect of various solvents on polypyrrole conductivity produced by chemical synthesis. The authors concluded that for methanol, ethanol, water, pentanol, octanol, and ethylene glycol, the synthesized polypyrrole exhibited conductivity greater than 90 S.cm^{-1} , while for synthesis in the presence of tetrahydrofuran, chloroform, and acetonitrile, it exhibited conductivity less than 20 S.cm^{-1} and even lower for dimethylformamide [25, 26].

The electrochemical route produces good quality films. The counter ion has a considerable influence on conductivity, solubility, morphology, and mechanical properties of the polypyrrole. Electrochemical synthesis of polypyrrole can be performed in different ways: potentiostatic [27, 28], galvanostatic [29], potentiodynamic [30], and pulsed one [31]. The mechanical properties of the films, their morphology and electrochemical behavior depend on the preparation conditions, including the nature of solvent, pH of the electrolyte, the purity, and concentration of the initial monomer, and the nature and concentration of electrolytic salt [27–31].

Studies have been carried out to develop polypyrrole derivatives in order to discover more stable and more reversible systems in aqueous media so that they can be used in technological applications. Soluble polypyrroles can be prepared by the introduction of flexible side chains. The most well-known polypyrrole derivatives are *n*-methyl, *n*-phenyl, *n*-methoxy-phenyl, 3-methyl, 3,4-dimethyl, *n*-ethyl, and *n*-propyl pyrrole. However, conductivity of these derivatives is always less than that of pure polypyrrole [21, 32].

Polythiophenes have a five-membered heterocyclic ring containing a sulfur atom and the aromatic units are linked by means of carbon atoms. Figure 1c shows the structural polythiophene formula.

Polythiophenes are materials of great interest due to their ease of chemical and electrochemical synthesis, stability, and processability [33]. The thin polymeric films of polythiophene are blue in the doped (oxidized) state and red in the undoped form [34]. The great advantage of this material in relation to other conjugated polymers is the ease of chemical synthesis and the relative ease of functionalization of its side chains. Polythiophene can be obtained by either chemical or electrochemical synthesis.

The first synthesis of polythiophene was carried out in 1833 and an insoluble dark material was obtained. However, until 1980 a well-defined material was not obtained. First controlled syntheses of polythiophene were obtained in 1980 [35, 36], and from then on a large number of works on the synthesis and properties of polythiophenes were carried out.

Polythiophenes are insoluble in organic solvents due to their rigid backbone. To solve the problem of solubility and processability, flexible side chains were introduced at the 3-and/or 4-position of the aromatic ring, thus, poly (alkylthiophenes) are extensively studied [21].

Polythiophene can be synthesized chemically using a chemical oxidizer. The most common method is using a Grignard derivative and a catalyst. Another well-known method is to use iron (III) trichloride (FeCl_3) as the oxidizing agent and chloroform as the solvent under anhydrous conditions [21].

The electrochemical synthesis of polythiophene was carried out for the first time in 1981. Despite the mechanism not being fully understood, it is generally proposed that polymerization occurs via coupling of two cationic radicals formed by oxidation of the monomer [37]. In electrochemical synthesis, the polymer is deposited on the electrode in conductive oxidized form. This main method has the advantages of obtaining stable, homogeneous, and high conductivity films. Commonly used dopants include lithium, tetraalkyl ammonium tetrafluoroborate, hexafluorophosphate, and those used as solvents include acetonitrile, tetrahydrofuran, and dichloromethane. The electrodes are usually platinum, gold, or indium tin oxide (ITO)/glass [21].

Chemical and electrochemical synthesis methods can also be used for the synthesis of polythiophene derivatives. These derivatives are soluble in several types of solvents in addition to exhibiting good processability, they can be used in conjunction with other polymers forming composites [21, 37].

As the conductive polymers have different characteristics: simple synthesis, acceptable environmental stability, electronic, and mechanical features, beneficial optical, researchers have largely considered them for diverse applications. Some of the applications of conducting polymers include rechargeable batteries, electrochromic display devices, sensors, light-emitting diodes, catalysis, adsorption of pollutants photovoltaic devices, transistors, electromagnetic shielding against electromagnetic interferences, and printed electronic circuits [38–49].

1.2 *Examples of Nanomaterials Based on Natural Polymers*

The raw materials used to obtain conventional polymers, such as polyethylene and polypropylene are non-renewable fossil materials. Alternatives such as recycling plastics and replacing conventional synthetic polymers by natural, biobased or biodegradable polymers have been widely studied due to the intense focus on the use of biological resources by a wide range of industries.

Basically, a polymer is synthesized by joining, via covalent bonds, small molecules, or substances (called monomers) into a larger molecule, by chemical processes of addition or condensation polymerization. The polymer is called “natural” when its monomers are obtained from nature (plants or animals) [50, 51].

Biopolymers are natural polymers produced by the cells of living organisms. The prefix “bio” means they are biodegradable materials produced by living organisms [52]. Biopolymers can be classified in three main classes, according to the monomers forming their structure: polynucleotides, polypeptides, and polysaccharides.

Briefly, polynucleotides (such as ribonucleic acid (RNA), and desoxyribonucleic acid (DNA)) are polymers composed of at least 13 nucleotide monomers. They give the necessary instructions for a cell to perform its function. The sequence of the nucleotides is what determines the instruction for a specific cell. In industry, polynucleotides are used for biomedical purposes, such as gene therapy and DNA sequencing [50].

Polypeptides and proteins are formed by amino acids, including collagen, actin, and fibrin. Polysaccharides are polymeric carbohydrates in linear or branched chains, such as starch, cellulose, and alginate.

But there are also a wide variety of materials derived from renewable resources, such as vegetable oils, sugars, starch, natural fibers, resins, proteins, etc., and produced by synthetic chemistry, resulting in biodegradable biopolymers, such as some polyesters, which degrades by exposure to bacteria in soil, compost, or marine sediment [52].

Below are summarized some of the most studied biopolymers, divided into groups according to the monomers, in polysaccharides, polypeptides, and biodegradable polyesters.

1.2.1 **Polysaccharides**

Polysaccharides are the most abundant renewable resource in the world. Depending on their function, they can be: storage polysaccharides (such as starch and glycogen), structural polysaccharides (such as cellulose and chitin), and gel forming polysaccharides (such as alginic acid and mucopolysaccharides) [50].

Starch

Starch is a form of carbohydrate (a basic food group), it is used to store energy in the tissues of plants and is widely available, found in the grains, cereal, and potatoes [51–54]. Starch is a semi-crystalline polymer, composed of glucose monomers polymerized by condensation.

The pure form of starch is an odorless and tasteless white powder, which consists of two types of glucose molecules: amylose and amylopectin. The concentration of each varies with the source and type of starch, but it is around 20–25 wt.% amylose and 75–80 wt.% amylopectin [50, 52]. Amylose is a water-soluble linear polysaccharide composed of (1–4)- α -d linked glucopyranosyl in a wobbled helix configuration, while amylopectin with α -(1–6) branches. While amylopectin is made up of (1–4)- α -d- linked glucopyranose chains, presenting branched configuration, with branching occurring after every 28–30 glucose units, making it more susceptible to hydrolysis and degradation, it has more regions exposed [50–52]. Although the composition of amylose and amylopectin varies for each source of starch, the observed microstructure of the starch granules is practically the same, regardless of the source [50, 53–58].

Starch is generally insoluble in water and alcohol, but it can be irreversibly dissolved in water if it is heated, in the process known as gelatinization. Starch in gel or thermoplastic, present poor mechanical properties due to its sensitivity to moisture, but by incorporating fibers or nanofibers (mainly from vegetal sources), the mechanical and barrier properties of starch products can be improved. In this way, as it is biodegradable and renewable, it is used for many applications including adhesives, paper, clothing, pesticides, cosmetics, plastic packaging, pharmaceutical tablets and even oil-drilling fluids [50, 52, 54].

Starch nanocrystals can be isolated by acid hydrolysis under mild conditions using hydrochloric or sulfuric acid. The amorphous regions of the starch granules are preferentially attacked and hydrolyzed by acid than the crystalline regions, resulting in starch nanocrystals with high crystallinity and platelet morphology [59]. These starch nanocrystals can be surface modified to improve interfacial adhesion with polymers, including conducting polymers, to obtain high performance starch nanocrystal-filled materials.

Cellulose

Cellulose is the most abundant biopolymer on the Earth, it is found in the plant cell walls, making up about half of the biomass of photosynthetic organisms [52, 54]. The polysaccharides present in the plant cell wall are mainly cellulose, hemicelluloses, and lignin [53]. Cellulose is a fibril component of plant cells, and the purest form of natural cellulose is the cotton, containing almost 99% cellulose in its structure [60]. Cellulose is a semi-crystalline polysaccharide, also composed of glucose molecules, but its structure is made by repeating β -(1 \rightarrow 4)-D-glucopyranose units. Hydrogen

bonding and Van der Waals forces join the glucan chains side by side to form cellulose microfibrils, which can be stacked together to form cellulose crystals [52].

The cellulose chains are neatly packed to form compact microfibrils, which are stabilized by inter- and intramolecular hydrogen bonds, making their crystals completely insoluble in water and in most organic solvents [60]. As a result, it can be chemically modified into ether, ester, and acetal derivatives. Six crystalline structures of cellulose were found: cellulose I, cellulose II, cellulose III₁, cellulose III₂, cellulose IV₁ and cellulose IV₂. Cellulose I is the crystalline structure found in nature. Cellulose II can be obtained from cellulose I by mercerization (treatment with NaOH) or regeneration (solving cellulose I in some solvent, followed by precipitation in water). Celluloses III₁ and III₂ are obtained from celluloses I and II treated with liquid ammonia or amines. Celluloses IV₁ and IV₂, respectively, are obtained from celluloses III₁ and III₂ after heated in glycerol at 206 °C [57, 60, 61].

Cellulose has been used in the form of nanofibrils from various sources like coir, banana, sugarcane bagasse, hemp, softwood, and hardwood pulps. Cellulose nanofibrils (CNF) are obtained by mechanical grinding or high-pressure fluidization of cellulose fibers in order to open the bunches and expose the fibrils [52, 62]. In this way, CNF consists of fibrils with (lengths of several μm) and thin diameter of 5–20 nm, resulting in high aspect ratio (length/diameter – L/D) nanofibrils. If it is at low concentration in suspension, it is possible to obtain a transparent gel-like material, which can be used to produce homogeneous, biodegradable, and environmentally safe films for various applications [63].

Cellulose nanocrystals (CNC), also called cellulose whiskers, present a rod-like aspect and high crystallinity, with diameters ranging from 5–70 nm and lengths from 100 nm up to a few microns. CNC can be obtained by the acid hydrolysis of lignocellulosic materials, such as vegetable fibers. The chemical process starts with the removal of superficial polysaccharides followed by cleavage, and destruction of amorphous fractions of cellulose, remaining the most crystalline part, and the cellulose nanocrystals [64].

In addition to plants, many other microorganisms are known to produce cellulose, such as fungi, bacteria, and algae. The cellulose produced by microbial strains is pure, that is, they do not have hemicellulose, lignin, or any other component present in plants.

Bacterial cellulose (BC) was first reported by A. J. Brown in 1886, in which it was synthesized by *Acetobacter xylinum* or *Gluconobacter xylinum*, known as *Bacterium aceti* [65]. During biosynthesis, bacteria utilize carbon sources from the medium to polymerize β -1,4-glucan chain, which will be crystallized into microfibrils, which will form bundles, and later ribbons, forming a thick, gelatinous film at the air-liquid interface in the static culture medium [65], thus resulting in a three-dimensional network of cellulose nanofibers with 10–100 nm in diameter and length in microns [65].

In this way, bacterial cellulose (BC) presents high purity and crystallinity, excellent mechanical properties, high water holding capacity, and large surface area, which makes it suitable for various applications, such as tissue engineering, drug delivery, food application, and in obtaining polymer nanocomposites. And by adding

inorganic or organic fillers to BC, it can be applied in areas such as sensing and thermoresponsive materials, biomedical device fabrications, etc. [65].

Hemicelluloses

Hemicelluloses refer to a mixture of low molecular weight polysaccharides, which are closely associated with cellulose and lignin in plant tissues. The fraction of hemicellulose in plants consists of polysaccharides with a lower degree of polymerization than cellulose, containing some types of sugars such as D-xylopyranose, D-glycopyranose, D-galactopyranose, L-arabinofuranose, D-manopyranose and D-glycopyranoseluronic acid, and smaller amounts of other sugars. Due to the absence of crystallinity, its low molecular mass, and its irregular and branched configuration, the polysaccharides absorb water easily. This fact contributes to swelling, internal mobility, and increased fiber flexibility, in addition to increasing the specific area, or fiber connection [53].

The combination of cellulose and hemicellulose, the largest portion of carbohydrates in the plant, is called holocellulose, corresponding to 65–70% of the dry weight of the plant. Hemicelluloses make up about 20–30% of dry plant biomass. Holocellulose, being formed by cellulose and hemicellulose, is rich in hydroxyl groups, responsible for the absorption of moisture and hydrogen bonds [50].

Hemicelluloses have the potential to be hydrolyzed mainly by enzymes into fermentable sugars for applications such as in second-generation ethanol production.

Lignin

Lignin is an amorphous, aromatic macromolecule, with rather complex structures, distributed over the secondary cell wall, with high concentration in the middle of the coverslip. It is associated with cellulose and hemicellulose in the composition of lignocellulosic materials. It is a hydrophobic material with a three-dimensional structure, highly branched, which can be classified as a polyphenol, which consists of an irregular arrangement of several phenylpropane units that may contain hydroxyl and methoxy groups as substituents in the phenyl group.

The functions of lignin in plants are, among others, to increase the rigidity of the cell wall, to unite the cells to each other, to reduce the permeability of the cell wall to water, and to protect them against microorganisms (being essentially phenolic, the lignin acts as a fungicide).

Lignin is considered a waste material from industrial processes of pulp and paper production and of ethanol production, but it is about 20–30.5% of cellulosic biomass [50]. It has been used as a fuel for burning in heating boilers, as reinforcement in polymeric composites [66].

Other Polysaccharides

Pectin is one of the main components found in fruit, and vegetables, it is found in the primary cell wall of plants. Pectin consists of chains of 300–1,000 galacturonic acid units bonded by $1\alpha \rightarrow 4$ linkages D-galacturonic acid units. This complex anionic polysaccharide is a water-soluble polymer, that presents good biodegradability which promotes its use for designing pectin films [50, 67]. Their functional groups such as carboxylic acid and hydroxyls allow covalent bonds of pectin to other biomolecules and proteins. Thus, it can be used to encapsulate metal nanoparticles, for example, to avoid their aggregation, expanding the possibilities of applications, whether in the health area, such as drug delivery, antioxidant, or antimicrobial activity; or increasing the electrochemical performance of sensors, in which electrode modified with pectin can immobilize enzymes and maintain electron transfer properties [68]. Pectin can also be hydrolyzed in alkaline media to improve interfacial features, electrical and optical properties in polyaniline/graphene composites [69].

Glycogen is a storage polysaccharide, presenting high branched molecules. It is present in the cytoplasm of animal cells, serving as the main storage form for glucose, and it is important for the body metabolism [50]. Hussain and coworkers [70] used glycogen as a natural polymer in the fabrication of hydrogels. They introduced Fe^{3+} ions to create ionic and metal-ligand interaction with functional groups of polymer chains of hydrogel. This hydrogel presented good mechanical properties, capability to transfer electrons and convert electrical energy to mechanical or chemical energy, making these hydrogels suitable for various applications, such as electrodes, conductors, actuators, capacitors, sensors, etc.

Chitin is a natural polysaccharide, similar in structure to cellulose, except for the hydroxyl groups of cellulose chain that are substituted by acetamido group. Chitin is synthesized by large number of living organisms, such as insects, lobsters, shells of crabs and shrimps, or in the cell walls of fungi and yeast. Chitin exists as ordered crystalline microfibrils, it is insoluble in water and other organic solvent [50, 52, 57].

Due to the semi-crystalline structure of chitin microfibrils, they can be treated with acid to produce whisker-shaped nanoparticles, which can be incorporated into polymers to obtain nanocomposites [57]. These chitin nanowhiskers can be used with ZnO nanoparticles and PANi to obtain nanocomposites via solution casting method to be applied as disposable ethanol sensor [71]. Chitin can be also applied in films and gel forming, chelation of metal ions, and formation of polyoxysalts.

Chitosan is obtained from the deacetylation of chitin, it is a cationic polysaccharide that can form polyelectrolyte complexes with other polysaccharides. Chitosan is especially applied in biotechnology because of its biocompatibility and bioactivity, stimulating a beneficial response from the body. It is widely used as transdermal drug delivery (mucoadhesives), and attractive as controlled delivery systems, due to its insolubility in neutral and alkali media, and its solubility in acidic media [50, 52, 57]. Chitosan also presents antimicrobial functions. And due to its good film forming property, it can be used as a coating on various surfaces to improve the permeability of moisture and other vapors, but it is possible to improve barrier properties using nanoclays incorporated into chitosan [50].

Hyaluronic acid (HA), also called hyaluronan, is a high molecular weight (105–107 Da) naturally occurring biodegradable polymer. HA is composed of disaccharides (β -1, 4-d-glucuronic acid (known as uronic acid) and β -1,3-N-acetyl-D-glucosamide) forming an unbranched chain of non-sulfated glycosaminoglycan. HA is a polyanion important in tissue development and cell proliferation. It is responsible for maintaining the viscoelasticity of biofluids controlling tissue hydration and water transport [72]. HA has been used in certain biomedical applications; for instance, in combination with alginate it is used in surgical applications for wound healing [50], potential agent of therapeutic intervention in osteoarthritis, development of cartilage, the maintenance of the synovial fluid, as lubricant and shock absorber, preventing bacterial adhesion to dental implants, intraocular lenses, catheters, etc. [72]. The incorporation of conductive PEDOT-HA nanoparticles in a chitosan/gelatin matrix can produce porous electroactive scaffolds for nerve tissue regeneration, as proposed by Wang [73], where 8% of PEDOT-HA, in addition to being biocompatible, promoted an increase in electrical and mechanical properties and decreased porosity, water absorption, and biodegradation [73].

Alginates are linear long chains, anionic and hydrophilic heteropolysaccharides. They are found within the cell walls of brown algae like *Laminaria* sp., *Lessonia* sp., *Macrocystis* sp., which belong to the family Phaeophyceae. Alginates provide flexibility and strength. They usually exist in association with other cations (mainly sodium and calcium) as sodium alginate and calcium alginate. They were traditionally used as stabilizing agent in ice cream, but they also can be used to develop delivery systems for cationic polyelectrolytes and proteoglycans through simple electrostatic interactions due to their pH dependent anionic nature [50, 72]. Alginate nanoparticles can be formed mainly based on two methods: the complexation method and the water/oil emulsification coupled with the gelling of the alginate emulsion droplet. Using mild conditions and without organic solvents, the preparation of alginate nanoparticles makes them viable both for trapping sensitive materials and for use in pharmaceutical and food products. In this way, alginate nanoparticles can be used in the drug delivery and immobilization of enzymes. However, the development of environmentally friendly processes to obtain these nanoparticles with controlled size distribution, mechanical and chemical properties, and scalable for industrial production, is still a challenge to be overcome [74].

1.2.2 Polypeptides or Proteins

Polypeptide refers to a linear polymer composed of amino acids, whose peptide (or amide) bonds occur between the carboxyl group of one amino acid and the amine group of another, releasing a molecule of water. A polypeptide with more than seventy amino acids is called a protein and it can be classified according to their shape, size, solubility, composition, and function.

Silks are types of protein synthesized by various insects in nature, such as silkworms, spiders, mites, and beetles. But silks are mainly derived from domesticated *Bombyx mori* silkworm cocoons. Their main components are about 70% silk fibroin

(fibrous protein) and around 30% silk sericin (globular proteins), in which fibroin constitutes the core of silk, and sericin is a glue-like layer coating the core [50]. When silk fibroin and sericin are completely separated, the pure silk fibroin is a biocompatible macromolecule which can be used in different biomedical applications, while sericin can lead to the allergic reactions and cytotoxicity problems [67, 75]. Sericin is usually removed from fibroin when they are placed in a boiling alkaline solution. After removal of sericin, silk fibroin fibers can be dissolved in aqueous solution with chaotropic agents. After dialysis, an aqueous solution of purified, transparent silk fibroin is obtained that can serve as a base for a variety of materials in the form of films, hydrogels, scaffolds, and nanofibers [76]. Because of the silk fibroin presents biocompatibility, slow biodegradability, good mechanical strength, and elasticity, making it suitable for surgical sutures, drug delivery, nanostructured scaffolds, artificial tendons, and coatings for metallic medical implants. And recent works have applied it in photonics, bioelectronics [77].

Zein is a hydrophobic prolamin protein, it is a byproduct of corn processing, and it has thermoplastic properties. It is soluble in alcohol and has potential for application as films coatings [50]. Zein nanoparticles can be prepared by liquid-liquid dispersion in 90% isopropyl alcohol followed by addition of deionized water under vigorous stirring at room temperature. For purification, the suspension is centrifuged; the precipitate is washed with water and lyophilized [78].

Gluten is a byproduct of the processing of wheat starch, and it is a mixture of several proteins, mainly gliadin and glutenin, along with globulin and albumin that make up about 8–15% of the dry mass of the wheat grain [50, 79]. Gluten can be used to make bread and to form films (properties can be changed by adding some plasticizer such as glycerol or changing pH) [50]. Gluten films can be used as substrates for the deposition of metallic nanoparticles, or for the synthesis of conductive polymers, such as polypyrrole, and can be applied in the most diverse uses given to flexible and electrically conductive films.

Collagen is the most abundant protein in human; it is the primary structure of vertebrates, found in bones, muscles, skin, and tendons. It makes up the connective tissue present in the skin of human beings, giving to skin its strength and structure, and collagen also carries out the replacement of dead skin cells [52]. Collagen has a triple-helical structure made of three polypeptide chains [50, 77]. The presence of cross-linking in mature collagen chains makes it difficult to dissolve in a wide range of solvents, which limits its processability, but gives it good mechanical properties such as tensile strength and elasticity so that it maintains the whole body together [77]. It is a nontoxic, biodegradable, and biocompatible material, which makes it suitable for many medical, pharmaceutical, and cosmetical applications. In recent studies, as many biological materials, enzymatic degradation by collagenase makes them suitable as substrates in transient, flexible, and biodegradable electronics [77].

Gelatin is a biomaterial based on animal proteins; it is usually obtained by partial hydrolysis of type I collagen. There are mainly two types of gelatin: Type A is obtained by acid hydrolysis of collagen and has 18.5% of nitrogen; Type B is obtained by alkaline hydrolysis and has 18% of nitrogen and no amide groups [50, 52, 77]. Gelatin presents many functional groups as $-\text{NH}_2$, $-\text{SH}$, and $-\text{COOH}$, which makes

its modification possible with biomolecules and nanoparticles, depending on the application [52]. Gelatin has been used in pharmaceutical formulation, cell culture, and tissue engineering, besides for weight loss; for treating bone diseases such as rheumatoid arthritis, and osteoporosis; for improving hair and skin quality [52]. Gelatin is widely applied in foods, pharmaceuticals, and cosmetics for its viscoelastic properties to act as gelling agent, thickener, or stabilizer [50, 80]. Gelatin can also be used in electronic devices, such as sensors, providing a stable matrix for the immobilization of enzymes such as urease [77].

1.2.3 Polyester

The main known polyesters in nature are cutin, suberin, and polyhydroxyalkanoates. But there are also sugar-based biopolymers, in which the most common, and widely researched is poly(lactic acid) (PLA). The raw material for the monomer of PLA is lactic acid, obtained from lactose, and extracted from natural sources such as potatoes, sugarcane, corn, and wheat. Another biopolymer produced by microorganisms is poly(hydroxybutyrate) produced by carbon assimilation from glucose [54]. Moreover, this chapter will also cover some biodegradable polymers that can be used as a substrate or modified for application as conductive polymers, such as polycaprolactones (PCL) and polyvinyl acetates (PVAc). There is also a brief introduction to natural rubber (polyisoprene), the latex from rubber trees, a highly electrical insulating material.

Polyhydroxyalkanoates

Polyhydroxyalkanoates (PHAs) are intracellular biopolymers, complexes microbologically synthesized by many bacteria. They act as carbon and energy storage granules. According to the number of carbon atoms in each monomer PHAs can be divided into two groups: the short chain length PHAs (scl-PHAs) with C3–C5 atoms; and the medium chain length PHAs (mcl-PHAs) with C6–C14 atoms; but there are some organisms that can produce copolymers with both scl and mcl monomers (scl-mcl-PHAs) [81]. They are composed of β -hydroxy fatty acids, where the R group changes from methyl to tridecyl, forming poly(hydroxybutyrate), poly(hydroxyvalerate), polyhydroxyhexanoate, and poly(hydroxyalkanoates) [50, 72, 82]. They all are biodegradable, because they can be degraded and metabolized by microorganisms and by enzymes; biocompatible, as they do not generate toxic byproducts; and some of them are piezoelectric, which stimulate cell growth [81]. Due to high cost of producing these polymers, polyhydroxyalkanoates are currently used only for special medical applications.

Poly hydroxybutyrate (PHB) is the simplest and most common scl-PHAs. It is highly crystalline, brittle, stiff, and piezoelectric, with a melting temperature $T_m = 173\text{--}180\text{ }^\circ\text{C}$, glass transition temperature T_g around $5\text{ }^\circ\text{C}$, tensile strength of 40 MPa, and elongation at break of 6% [72, 81]. Due to its high crystallinity and

brittleness, it is difficult to be a useful thermoplastic polymer. In this way, based on PHB, many copolymers can be synthesized, such as poly (hydroxybutyrate-co-hydroxyvalerate) (PHBV), by copolymerization with hydroxyvalerate by feeding the bacteria with propionic acid; poly (hydroxybutyrate-co-hydroxyhexanoate) (PHBH); poly (hydroxybutyrate-co-hydroxyoctanoate) [72]. PHB is biocompatible and biodegradable by ester bonds hydrolysis in aerobic media, moreover, it has piezoelectric properties making it suitable for drug delivery, tissue engineering, and orthopedic applications.

Poly(3-hydroxybutyrate-co-3-hydroxyvalerate) (PHBV) is a copolymer of hydroxybutyrate with random segments of hydroxyvalerate. PHBV is also produced by bacterial process, but it is thermoplastic linear aliphatic polyester [52]. The concentration of valerate in the copolymer can cause variation in the time necessary for complete degradation, from few weeks to several years. In general, PHBV is biodegradable, water resistant, nontoxic, and biocompatible, being produced from glucose and propionate by the recombinant *Escherichia coli* strains [52]. PHBV can be applied in many medical devices which enhance cell adhesion, migration, proliferation, and differentiation functions, especially dental, orthopedic, and skin surgery. Besides bioresorbable surgical sutures, biodegradable screws and plates for cartilage and bone fixation, substrate for tissue engineering, wound coverings, etc. [52, 81].

The mcl-PHAs such as poly(3-hydroxyhexanoate) and poly(3-hydroxyoctanoate) are thermoplastic elastomers with T_m around 40 and 60 °C and T_g ranging between -50 and -25 °C. If compared to scl-PHAs (as PHB), these mcl-PHAs present lower crystallinity, but higher flexibility, softness, and thermal stability. Their elastomeric behavior increases with the size of the side chain. They are also biodegradable, water resistant, and biocompatible, and as other PHAs, they could be utilized in medical applications [81].

Poly(lactic Acid (PLA)

Poly(lactic acid or polylactide (PLA) is one of the most promising biopolymers, it is a linear thermoplastic aliphatic polyester, derived from renewable resources, such as corn starch, tapioca roots, chips, or sugarcane [52]. As lactic acid it presents a chiral carbon. PLA exists in three stereochemical forms: poly(l-lactide), poly(d-lactide), and poly(dl-lactide) (meso-lactide) [82].

PLA is first obtainable by an ionic polymerization of lactide (the cyclic dimer of lactic acid, obtained by a combined process of oligomerization and cyclization). The PLA can be prepared by (1) ring-opening polymerization of the ring-formed dilactide, using a catalyst, (2) polycondensation of lactic acid and polylactide, while removing the reaction water, using drying agents, or (3) polycondensation and linking of lactic acid monomers [52, 83]. There is an increasing interest in microbial fermentative production of lactic acid, due to the low price of lactic acid sources (whey, maize, sugarcane and cassava bagasse, potato, wheat, tapioca, or sugar in pure form); high production rate and yield; low production temperature and energy consumption; little or no byproduct formation, and this process do not need further pretreatment [82].

PLA can be processed like all other thermoplastic polymers by extrusion, injection molding, blow molding, thermoforming, or fiber spinning, and the products can also be recycled after use or hydrolyzed back into lactic acid, which could be re-introduced into the polymerization process of PLA [83]. It is a hydrophobic polyester, but soluble in chloroform, dichloromethane, etc. Their properties depend on the molecular weight, crystallinity, and proportion of co-monomers. PLA is highly crystalline, and higher molecular weight leads to higher T_g and T_m , as well as, tensile strength and elastic modulus, but smaller elongation to break [52].

In this way, PLA is a versatile polymer, with high transparency, high molecular weight, good processability, and water resistant, besides recyclable and compostable. That is why it has been shown the highest commercial potential and it is produced in large scale for lots of applications, including medical devices [82], food packaging, disposable cups and cutlery, substrates for sensors and electronic devices, scaffolds for tissue engineering, among others.

Poly(ϵ -Caprolactone) (PCL)

PCL is a semi-crystalline, thermoplastic, and biodegradable polyester. PCL is resistant to water, oil, solvent, but it is soluble in chloroform, dichloromethane, benzene, toluene, etc. The PCL is hydrophobic, which makes cells adhesion and proliferation difficult [52]. PCL is synthesized by ring-opening polymerization of ϵ -caprolactone in the presence of a catalyst. It presents high flexibility, low melting point (around 60 °C), and good compatibility with many other polymers. In materials applications, PCL can be used as a polymeric plasticizer, as an additive to improve impact resistance, as a ductile phase with rigid biopolymers as PLA, to improve the mechanical resistance of the blend, among others [58]. In biomedical field, as PCL is biocompatible, it is used for various long-term implantable biomaterials. In physiological conditions, PCL degrades by hydrolysis of its ester linkages, slower than PLA [52].

Polyvinyl Acetate (PVAc)

Polyvinyl acetate (PVAc) is a polyvinyl ester, a synthetic thermoplastic polymer, produced by the polymerization of vinyl acetate monomer. PVAc has a general formula of $-[RCOOCH_2CH_2]-$ and is found as an aqueous solution with 50–55% solids. Polyvinyl alcohol is produced by controlled reaction of hydrolysis of polyvinyl acetates. In addition to the application of PVAc as a wood glue, it also can be used in various fields, such as biomedical, synthesis of metal nanoparticles, sensing activity [52], polymeric nanocomposites of PVAc and cellulose nanocrystals to improve mechanical properties [84], among others.

1.2.4 Polyisoprenes

Latex is a kind of natural rubber collected from rubber trees, but it can also be prepared artificially by building up long chains of styrene molecules [51]. Polyisoprenes are natural rubbers with thermosetting properties, and they are classified into two types, cis and trans, giving different properties to the polyisoprene formed. The cis-polyisoprene is more widely available, it is the type produced by the rubber tree *Hevea brasiliensis*, the main commercial source of polyisoprene, the cis-isomer presents elasticity, due to its non-linear and somewhat spiral spatial structure. The trans-isomer presents a linear structure, which results in high rigidity, electrical and thermal insulation, low coefficient of thermal expansion, and some alkali and acid resistance [50]. After cured, polyisoprenes are not biodegradable. Natural rubber is mainly used in the manufacture of tires, in particular for heavy vehicles; footwear components, elastomeric springs, supports and shock absorbers, seals, pharmaceutical articles, carpets and floors, etc.

2 Conducting Polymer-Natural Polymers Nanocomposites

As previously mentioned, intrinsically conducting polymers, such as polyaniline, polypyrrole, polythiophene among others, have been attracting the attention of numerous research groups due to the great potential in technological applications. However, these materials have limitations in processing and mechanical properties. To compensate for these limitations, conducting polymers are incorporated into insulating materials. Nanocomposites based on conducting polymers associated to nanostructures from natural polymers comprise an emerging class of novel materials. The literature presents a broad range of these nanocomposites, and the outstanding properties obtained have ensued in a growing number of researches which cover different scientific fields. In this section we discuss some examples of nanocomposites based on conducting polymers and nanomaterials derived from natural polymers, their fabrication and applications, which are summarized in Table 1 as well.

The deposition of the conducting polymer in a flexible matrix, such as bacterial cellulose, can result in a material with the processability, mechanical properties, and biocompatibility of the insulating matrix associated with the optical, magnetic, and electrical properties of the conducting polymer.

A composite is formed by the union of two or more distinct materials, consisting of a matrix (continuous phase) and a reinforcement (dispersed phase), with significantly different chemical and physical properties. The resulting material is a superior product compared to its initial precursors. The preparation of some types of composite will always aim to improve some singularity of the material, such as making it lighter, stronger or even cheaper than those existing in the market. Within the category of composite materials there are nanoscale materials, which are nanocomposites. These materials are also made up of two phases, however, at least one of them must

Table 1 Some recent papers reporting nanocomposites based on conducting polymers and natural polymers

| Natural Polymer | Conducting polymer* | Application | Refs. |
|-----------------|---------------------|--|------------|
| Lignin | PEDOT | Electrochemical supercapacitor | [115, 116] |
| Lignin | PPy | Electro-Fenton process for dye removal | [117] |
| Natural Rubber | PAni | Electrical sensor | [118] |
| | | Conductive membranes | [119] |
| PLA | P3HT | p–n diodes | [120] |
| Chitosan | PEDOT:PSS | Cardio tissue engineering scaffolds | [121] |
| Chitosan | PAni | Adsorption and degradation of pollutants | [122] |
| Chitin | PAni | Gas Sensor | [71] |
| Cellulose | PPy | Flexible humidity and temperature sensor | [123] |
| | | Neural tissue engineering scaffolds | [124] |
| | | Glucose biosensor | [125] |
| | | Electrically conductive nanopaper | [126] |
| Cellulose | PAni | Gas Sensor | [127] |
| | | Screen-printed electrode modification | [130] |
| | | Adsorption of pollutants | [132] |
| Cellulose | PVdF | Membrane for lithium ion battery | [128] |
| | | Energy storage | [129] |
| Cellulose | P3HT | Flexible electronic applications | [131] |
| Alginate | PEDOT:PSS | Flexible electronic applications | [133] |
| Alginate | PPy | Tissue engineering | [134] |
| Alginate | PAni | Adsorption of pollutants | [135] |
| Pectin | P3DPA | Electrically controlled release | [136] |
| Dextrin | PPy | Antioxidant and antibacterial materials | [137] |
| Dextrin | PAni | Antioxidant and adsorption of pollutants | [138] |

* Description of conducting polymers abbreviations: PEDOT = poly(3,4-ethylene dioxythiophene), PPy = polypyrrole, PAni = polyaniline, P3HT = poly(3-hexylthiophene) (P3HT), PSS = poly(styrene sulfonic acid), PVdF = poly(vinylidene fluoride) (PVDF), P3DPA = poly(3-methoxydiphenylamine)

have a nanometric dimension from 1 to 100 nm. In nanocomposites, the increase in resistance will occur due to interactions at the atomic or molecular level [85].

Nanocomposites based on conducting polymers coated cellulose nanofibers are of scientific and industrial interest due to their unique properties. Among cellulose nanofibers, bacterial nanocellulose has been employed as flexible scaffolds for conductive polymer nanocomposites, especially because of its biocompatibility, low density, high surface-to-mass ratio, flexibility, high tensile strength, and crystallinity [86–88].

The chemical polymerization of conductive polymers functionalized with cellulose has been studied by different methods for obtaining nanocomposites. The most used methodology is the polymerization of the aniline monomer in the presence of cellulose using ammonium persulfate as a starting agent for various applications using the combination of these materials [89]. Much research is being done where PANi and cellulose are used [90–92]. The presence of cellulose in the composite structure provides improvements in the mechanical properties of conducting polymers [87, 91].

Researchers incorporated polypyrrole in the presence of hydrated bacterial cellulose by oxidative chemical polymerization, using ferric chloride (FeCl_3) as an oxidizing agent [93]. Conductive membranes of bacterial cellulose (CB) and polyaniline doped with dodecylbenzene sulfonic acid (DBSA) were produced by chemical oxidative polymerization in situ of aniline in the presence of hydrated bacterial cellulose. The polymerization was carried out with ammonium persulfate, as an oxidizing agent, and different amounts of dodecylbenzene sulfonic acid (DBSA). The experiment showed that the highest electrical conductivity achieved was in the order of $10^{-4} \text{ S cm}^{-1}$ with a molar ratio of DBSA/aniline of 1.5. According to the authors, this condition provided a better penetration of the PANi.DBSA chains among the CB nanofibers. The increase in the amount of DBSA resulted in a decrease in the electrical conductivity of the CB/PAni.DBSA mixtures obtained. The conductivity values for the nanocomposites containing the DBSA/aniline molar ratio of 1.0, 1.5, and 4.0 were: 5.78×10^{-6} , 1.88×10^{-4} , and 1.61×10^{-4} , respectively. The largest amount of DBSA avoids the penetration of the polyaniline chains inside the bulk material [86].

Another work presented the synthesis of polyaniline in the presence of bacterial cellulose, forming conductive nanocomposites (PANi/CB) from the in situ oxidative chemical polymerization, using ammonium persulfate as an oxidant. The authors observed that the PANi nanoparticles deposited on the cellulose surface form a continuous nanolayer along the cellulose nanofibers, increasing the thermal stability of the nanocomposite. The results indicated that CB is activated by acids and the intermolecular hydrogen bonds are broken, thus facilitating the coating of cellulose nanofibers by PANi. The electrical conductivity of the nanocomposites reached a value of $5.0 \times 10^{-2} \text{ S.cm}^{-1}$ [94].

Polymeric nanocomposites of bacterial cellulose and PANi were produced from the oxidative chemical polymerization of aniline. Ammonium persulfate was used as an oxidizing agent and hydrochloric and p-toluenesulfonic (p-TSA) acids as protonating agents. The results showed that the bacterial cellulose was completely coated with polyaniline, forming a membrane with the properties of both components. The oxidizing agent and functionalized protonic acid had a significant effect on the electrical conductivity and thermal stability of the nanocomposites. The nanocomposites of CB/PAni.p-TSA showed higher electrical conductivity and protonation than the samples of CB/PAni.HCl. This result showed that p-TSA causes an increase in the degree of protonation of PANi [95].

Conducting polymers and bacterial nanocellulose nanocomposites can be obtained through in situ pyrrole, aniline oxidative polymerization, or interfacial polymerization in the presence of nanocellulose hydrogels using ammonium persulfate or iron III chloride hexahydrate ($\text{FeCl}_3 \cdot 6\text{H}_2\text{O}$) as oxidizing agents [96, 97].

The PANi/bacterial cellulose nanocomposite was produced by interfacial polymerization, with a single conductive surface, presenting a surface resistivity of $40.1 \Omega \cdot \text{cm}$. This PANi/bacterial cellulose nanocomposite is able to conduct electricity and can be used as a flexible electrode material with potential battery applications [98].

Cellulose can act by stabilizing the PANi, making it easier to form continuous conductive network and also allowing the formation of a conductive structure with less conductive components. Recent studies indicate that the cellulose -OH group can bond with the PANi-NH group by strong hydrogen bonds [99, 100].

The polyaniline/cellulose nanofibers were also synthesized by the polymerization of the aniline monomer in the presence of nanocellulose, where composites with thermal resistance and superior electrical conductivity were obtained, when compared with pure polyaniline [101].

The effect of the functionalization of cellulose nanowhiskers with polyaniline was evaluated for epoxy coatings. The synthesis was carried out by the polymerization of polyaniline in emerald salt in the presence of cellulose nanowhiskers, where the thermal, chemical, and morphological properties of the samples were evaluated. The results of the morphological analysis showed that the cellulose nanowhiskers present good dispersion in the polymeric matrix without formation of agglomerates [102].

Studies carried out the characterization of the materials cellulose/polyaniline and the proposal for possible applications for synthesized materials, such as use of a cellulose/PANi composite for the removal of dyes present in residues [103], a route methodology for manufacture of flexible supercapacitors [104]. These studies, combined with many others involving conductive polymers and cellulose demonstrate the potential for application for such materials.

Some authors presented the fabrication of gel polymer electrolytes based on sulfonated bacterial cellulose/polyaniline nanocomposite with an ionic conductivity of $5.2 \times 10^{-3} \text{ S} \cdot \text{cm}^{-1}$ [105].

The polyaniline/cellulosic fiber nanocomposite was prepared by chemical oxidation polymerization. The prepared composites were characterized by Fourier transform infrared, thermal gravimetric analysis, and their morphology was investigated using field emission scanning electron microscope to elucidate the mechanism of conductivity decay of the paper nanocomposite. In this work the effect of surfactant type, mass ratio of fibers/aniline, and time of polymerization on conductivity of polyaniline/cellulose fibers nanocomposites were evaluated [106].

Some researchers developed a novel method to prepare bacterial cellulose/polyaniline nanocomposites via the chemical grafting of polyaniline onto epoxy-modified bacterial cellulose [107].

A study of the structure-property relationship in the bacterial cellulose/polyaniline nanocomposite aerogels has been found in the literature using both experimental and density functional theory simulation. The authors studied the presence/absence

of cetyltrimethylammonium bromide on the morphology, dielectric, and rheological properties of bacterial cellulose/polyaniline nanocomposite. The density functional theory simulation results showed that the main interfacial interaction between bacterial cellulose and aniline monomer is forming hydrogen bonds [108].

Hosseini and Mousavi prepared bacterial cellulose/polyaniline nanocomposite aerogels with different morphology in the presence of sodium dodecylbenzenesulfonate and sodium dodecyl sulfate and the nanocomposite obtained was used as bioadsorbent for removal of hexavalent chromium [109]. These novel nanocomposites may have prosperous applications in various fields such as flexible electronic devices and antistatic and electromagnetic materials.

Razak and collaborators reported an effective method of fabricating a conductive and highly porous scaffold material made up of polylactic acid and conducting polyaniline. The work investigated the effects of polyaniline addition on the properties of polylactic acid scaffold prepared using freeze extraction. This conductive scaffold may open up opportunities for use in biomedical applications, for example in the tissue regeneration of skin, cartilage, blood vessel, and cardiac valve [110].

There are many papers reporting on polyaniline and its nanocomposites, describing advantages and properties, from structure, synthesis, physicochemical properties to their potential in biomedical applications. Biodegradable polymers improve the mechanical properties of polyaniline [111].

Some authors studied the preparation of polylactic acid/polyaniline/nanocrystalline cellulose nanocomposite film and observed that polylactic acid was wrapped with polyaniline particles, and nanocrystalline cellulose nanocomposite was uniformly distributed on the surface of nanocomposite films. The nanocomposite films exhibited an electrical conductivity of values up to $2.16 \text{ S}\cdot\text{m}^{-1}$. The presence of nanocrystalline cellulose nanocomposite exerted a significantly positive effect on the mechanical strength of the nanocomposite films. The nanocomposite film can be used as a biobased electrically conductive material [112].

Lignin/polyaniline nanocomposite was prepared by adding kraft lignin for the synthesis of polyaniline. The nanocomposite was used as an adsorbent material to remove hexavalent chromium and showed excellent efficiency in removing chromium [113]. Nanocomposite of polyaniline/sodium alginate was synthesized and the nanocomposite was an efficient adsorbent for the removal of both cationic and anionic dyes from water at different pH values [114].

2.1 Nanocomposites—Thin Films

Conducting polymers are commonly applied in electrical and optoelectronic devices as thin films deposited onto a substrate surface. A thin film comprises a set of particles connected with the next neighbors to substrates, such as electrodes, being its thickness ranging around several micrometers [139, 140]. As a consequence of the advances of nanoscience and nanotechnology, the techniques and composition of

these films became more sophisticated, including nanostructured materials in techniques such as drop-casting, spin and dip coating, lithography, electropolymerization, inkjet printing, spray techniques, layers deposition by Langmuir–Blodgett (LB), and layer-by-layer (LBL), among others [141, 142].

Razalli and coworkers [130] modified screen printed electrodes with a nanocomposites based on PANi and (CNC). In this work, the nanocomposite PANi/CNC was produced by in situ chemical oxidative polymerization of aniline, using a simple procedure that consisted of the mixture of CNC aqueous suspension and aqueous solution of aniline (monomer) and posterior addition of the oxidizing agent ammonium persulfate, which led to the rise of the typical color green of green emeraldine PANi. The electrode modification was performed by drop-casting of PANi/CNC aliquots onto screen printed electrodes and left to dry at room temperature.

Nanostructured thin films based on natural polymers associated to conducting polymers are involved in important recent researches, such as the work presented by Ajjan and coworkers [115], which combines lignin to PEDOT to fabricate bionanocomposites for a sustainable organic electrode material for application as an electrochemical supercapacitor. The PEDOT/Lignin nanocomposites were chemically synthesized by two routes: (i) inclusion of lignin in chemical oxidative polymerization of EDOT, and (ii) via electrochemical polymerization of EDOT, using a EDOT/lignin initial ratio of 3: 2. The PEDOT polymerization could be followed by naked-eye, as long the reaction media have their color changed from brownish to deep blue. Transmission electron microscopes (TEM) micrography showed that the chemically synthesized PEDOT/Lignin nanocomposite was constituted of aggregates of various tangles formed by PEDOT rich inner part and a lignin rich outer part, with average size of 200–400 nm. Thin films of the PEDOT/Lignin nanocomposites were fabricated by drop-casting of nanocomposite suspensions onto glass substrate and onto prior polished glassy carbon electrodes. The morphological characterization of the nanocomposites surface revealed a granular-spongy morphology. Aggregates were formed in samples with high content of PEDOT and more compact structures with a slightly granular surface were obtained by electropolymerization. Comparing both synthetic routes, the authors verified that the electrochemical polymerization gives rise to a more homogeneous surface than the chemically polymerized one. The authors point out that, in this work, lignin act as a polyanion, behaving both as a dopant and dispersing agent. Meanwhile, lignin presents insulating nature, leading the combination with conducting materials to contribute to charge transport, whereas the PEDOT performs the charge transport to the lignin moiety, where the energy storage occurs due to reversible reduction–oxidation conversion of hydroquinone/quinone redox couple.

The inclusion of natural polymers in LBL films has been also explored aiming at advanced functionalities. The main principle involved in LBL technique involves the alternating exposure of a substrate of positively and negatively charged polymeric materials in such way, as schematically illustrated in Fig. 2a1. The substrate is successively immersed in solutions containing polycations and polyanions, interspersed with washing steps [143]. This image also represents a possible arrangement of the positively charged materials in the LBL film. An example of LBL film built

up by combination of conducting polymer and natural polymer nanostructures is shown in Fig. 2a2, which refers to an Atomic force microscopy (AFM) topography images of single PAH/CNC bilayer [143]. Using the LBL approach, Cena et al. [118] developed self-assembled thin films of PANi and natural rubber nanoparticles (NR) by LBL technique for potential application as electrical sensor. The morphological analysis of the separated material indicated the spherical shape of NR nanoparticles, while the PANi forms a compact and dense film. In the aforementioned work, PANi presents the positively charged species, while the NR constitutes the negative, once it is chemically constituted by polymer chains of cis-1,4-polyisoprene surrounded by proteins, lipids, and long chains of fatty acid, and shows a stable configuration under $\text{pH} > 5.0$. The morphological analysis was performed by Atomic Force Microscopy (AFM), and the topography of the 10 bilayers PANi/NR thin film demonstrated an irregular surface, evidencing globular particles stemming from NR nanoparticles, nevertheless, the authors report a decreasing on roughness occurred as consequence of the increase of the adsorbed material.

2.2 Nanocomposites—Nanofibers

Nanofiber fabrication techniques represent another recent route widely applied to obtain thin films and promote nanostructure for electrodes. Today, many nanofiber fabrication techniques are known, including electrospinning, solution blow spinning, wet-spinning, microfluidic spinning, among others, being each one able to provide architectures with a series of features stemming from their specific morphologies, which propitiate suitable properties for certain applications [145]. In case of electrode modification, electrospinning stands out as the main exploited technique since it leads to the formation of mats rich in pores and channels, conferring a high surface area, as well as the ability to include materials from different chemical nature, allowing functionalization and biomolecules immobilization [144].

In essence, nanofiber formation by electrospinning occurs by the stretching of a drop and subsequent ejection of polymer solution as result of electrical forces applied on it [145, 146]. The solvent is volatilized and the nanofibers are collected in a rotating collector, or directly deposited onto substrates. The scheme of an electrospinning apparatus and its components are displayed in Fig. 2b1 [144]. Conducting polymers combined with polymers conventionally used in spinning techniques (such as polyamides, poly(lactic acid), cellulose acetate, chitosan, etc.) have enabled the production of conducting nanofibers with distinctive properties. In general, the conducting polymers properties do not allow the fiber formation without support of these conventional polymers, due to their low molecular weight which hamper the required entanglement to fiber formation, besides the low solubility in most organic solvents used in spinning procedures [147]. In this way, blends containing conducting polymers are greatly used, as demonstrated in the research of Bhute and coworkers [128], in which the authors fabricated a membrane based on PVdF/cellulose acetate (CA) electrospun nanofibers for application as component of lithium ion battery.

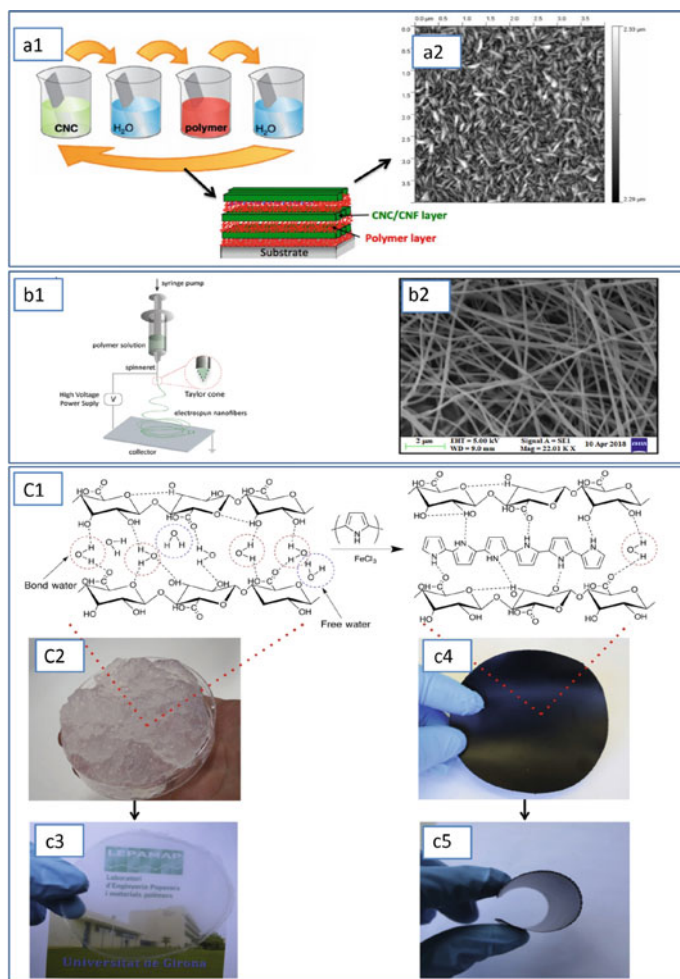


Fig. 2 Examples of conducting polymers and natural polymers nanocomposites produced by different techniques and compositions. First, we present an example of nanocomposite fabricated by LBL technique, which is a generically experimental setup illustrated in **a1**. Adapted with permission from Martin and Jean [143]. Copyright (2014), Walter De Gruyter. **a2** presents the topography obtained by AFM of a self-assembled LBL thin film based on a single bilayer of PAH/CNC. Adapted with permission from Martin and Jean [143]. Copyright (2014), Walter De Gruyter. **b1** A schematic representation of an electrospinning apparatus. Adapted with permission from Mercante et al. [144]. Copyright (2017), Elsevier. **b2** SEM image of a uniform and bead-free nanofiber-based PVdF/CA membrane. Adapted with permission from Bhute and Kondawar [128]. Copyright (2019), Elsevier. **c1** The intermolecular interactions existent between CNF chains and the interaction mechanism between CNF and PPy after the in situ chemical polymerization (FeCl₃ as oxidant agent). **c2** and **c3** The physical aspect of neat CNF gel and sheet, respectively, while **c4** and **c5** demonstrate the CNF/PPy conductive nanopaper and its flexibility. Adapted with permission from Lay et al. [126]. Copyright (2016), Elsevier

The nanofiber fabrication was performed in a procedure in which silver doped titania nanoparticles (AgTiO_2) were incorporated in electrospinning solution of (PVdF)/CA, using N,N-dimethylformamide (DMF) and acetone (7:3 V/V) as solvent. PVdF/CA nanofibers characterization, made to compare with PVdF/CA- AgTiO_2 , revealed, by SEM images, the formation of uniform, bead-free nanofibers, whose average diameter was 160 nm (Fig. 2b2). The high porosity of the interconnected network of nanofibers enhanced properties such as electrolyte uptake in liquid electrolyte and gelatinization efficiency. Moreover, the authors also assign these improvements to the predominant amorphous nature of the polymeric matrix, given by the absence of sharp peaks and the presence of broader peaks on XRD pattern, which also facilitates migration through the matrix, enhancing the ionic conductivity. Besides the environmental friendliness of cellulose acetate, the author also highlight that this polymer was chosen because it presents interesting properties to lithium ion battery separator, such as its hydrophilicity, superior thermal stability, chemical stability, and thermal stability, and to suppress the crystalline nature and enhance the ionic conductivity of the final nanocomposite.

The research of Serrano et al. [120] shows the development of nanofibers based on biopolymer (PLA) and p-type semiconducting polymer P3HT, and its application in electronic devices fabrication, as p-n diodes. The PLA was used in this work to provide mechanical support to P3HT, as discussed before, but an interesting novelty of this work is related to the ability to form nanofibers under a very low concentration of commercial PLA (5 wt.%, $60,000 \text{ g}\cdot\text{mol}^{-1}$), due to the lack of enough viscosity and poor entanglement of the chains. It was verified that the addition of the right amount of P3HT enabled the formation of long and thin nanofibers, whose diameters ranged from 100 nm to 4 μm .

Nanocomposites based on natural polymers and conducting polymers have also been successfully applied in biomedical fields. Adebil et al. [121] showed the performance of an electrically conductive scaffold based on chitosan and PEDOT:PSS conductive scaffolds with suitable mechanical properties for cardiac tissue engineering. Chitosan is widely explored for biological applications and for tissue engineering, however, it suffers from a lack of enough mechanical and electrical properties required for this purpose. It could be overcome by the introduction of 0.3, 0.6, and 1 wt.% of PEDOT:PSS, providing a 100-fold increase in conductivity, placing the fabricated scaffold in the semiconducting range and close values attributed to native neural tissue in gray and white matter, mimicking physical properties of cardiac tissue. The same concentration of the conducting polymer also led to improvements in tensile strength ($\sim 9 \text{ MPa}$), which is ascribed to reduced nanofiber diameters obtained for nanocomposite as well as to chemical interactions among components. It is well-known that an increase of polymer solution conductivity results in thinner nanofibers, being the main factor that influences the diameter, facilitating the pulling of polymeric jet toward the collection. It can be demonstrated that in this work, 1 wt.% PEDOT:PSS content resulted in 30–40% reduction of fiber diameter.

2.3 Nanocomposites—Conductive Nanopapers and Flexible Substrates

The interest in developing novel flexible and lightweight electronics has arisen from over the past several years in order to overcome drawbacks related to conventional substrates of metal foils, plastic substrates, and glasses. Zhang et al. [148] listed the main disadvantages associated with them:

- (i) Poor mechanical stability: active materials deposited on substrates surfaces cannot adhere firmly, and even small architectures can tear or crack when handling, bending, or stretching;
- (ii) Challenges over integration and interconnection: multilayered surface-modified components can just be connected by cutting, drilling, or by external connections, which turns the multifunctional integration more difficult;
- (iii) Limited surface area: when the substrate surface top is functionalized, it hampers the exploration of interior architectures.

Wright and coworkers [134] demonstrated the preparation of a nanocomposite based on alginate and PPy with potential application as flexible electronic substrate and cell adhesive, and subsequently, it can be used to configure bioelectronic devices capable of establishing communication between biological systems and electronic devices. In situ polymerization of PPy was performed by adding pyrrol monomers at alginate 2% solution, and sodium persulfate was used as the sole oxidant in this synthesis, justifying its easy removal after alginate gelation. The final mixture was used to produce cast films and hydrogels, by crosslinking using calcium carbonate. Focusing exclusively on Alginate/PPy cast films, the authors verified that the films prepared under $\text{pH} > 4$ were easily bent without any damage, while the other samples of the generated films were quite brittle. They also observed that the increase of PPy concentration generated materials mechanically fragile, with hindered ability to be applied in most potential applications. Moreover, under low PPy concentrations, the nanocomposite showed properties similar to alginate, except for the enhanced electrical conductivity, since alginate is an insulating material.

Among the flexible substrates, conducting materials related to papers and nanopapers has enabled the development of an area of extensive research over the past few decades, revealing to be an interesting trend as substrates for components of energy devices. Moreover, paper-based devices can also be used in biomedical applications, since they are “ASSURED”; which is a criteria established by World Health Organization, where ASSURED represents the benchmark criteria: affordable, sensitive, specific, user-friendly, rapid and robust, equipment-free and deliverable to end-users, for identifying the most appropriate diagnostic tests for resource-constrained settings [149]. With outstanding mechanical, biocompatible, flexible, and adaptable conductive properties, cellulose could bridge the world between nature biomaterials and flexible bioelectronics [150].

Nanopapers are usually defined as a sheet exclusively made of nanocellulose [77, 151]. As cellulose is inherently nonconductive, nanocomposites from a combination of nanocellulose and various types of conducting materials have resulted in very interesting research, as well as conducting polymers. Due to nanocelluloses dimensions, if the pack was dense enough, the interstices would be much lower than the visible light wavelength, avoiding light scattering, giving to the nanopapers properties of high optical transparency [151]. Because of this, a growing trend is the use of these novel materials as substrates for optoelectronics components, as they provide high flexibility, lightweight, lower cost, and biodegradability, which are advantageous features over conventional substrates, such as glass and plastic. In this way, Lay and coworkers [126] prepared nanopapers based on cellulose nanofibrils (CNF) and coated with PPy, whose schematic representation can be found in Fig. 2c1. The CNF was obtained from pine pulp as a transparent gel, shown in Fig. 2c2, consisting of a long web-like structure. The sheet obtained from neat CNF is also transparent, as shown in Fig. 2c3. To this gel were added pyrrole solutions of different concentrations, and slowly mixed with iron chloride (III), an oxidant agent, driving to the in situ polymerization of PPy. The addition of around 20% of PPy allowed the fabrication of CNF/PPy nanopapers with high transparency, high flexibility, and also high mechanical performance, which can be seen in Fig. 2c4, c5.

3 Technological Applications of Conducting-Natural Polymers Composites

Nanocomposites based on conducting polymers associated to nanostructures from natural polymers have found successful applications in versatile fields such as sensors, biosensors, medical applications, energy storage devices, catalysis, adsorption of pollutants, etc. [115–138].

The union between natural polymer and conducting polymer, to form a nanocomposite, can take place in two different ways: mixture of natural polymer with conducting polymer [110, 112], or mixture of natural polymer with the conducting polymer monomer [105–108]. In the second case, the conducting polymer is synthesized in the presence of the natural polymer. These two forms of synthesis are shown in Fig. 3a.

3.1 *Sensors and Biosensors*

A chemical sensor can be defined as a transducer device that converts information or changes in the species or substance under study, commonly referred to as analyte, into a signal that contains qualitative and/or quantitative information about that analyte. In the case of polymer-based chemical sensors, the changes are related to factors

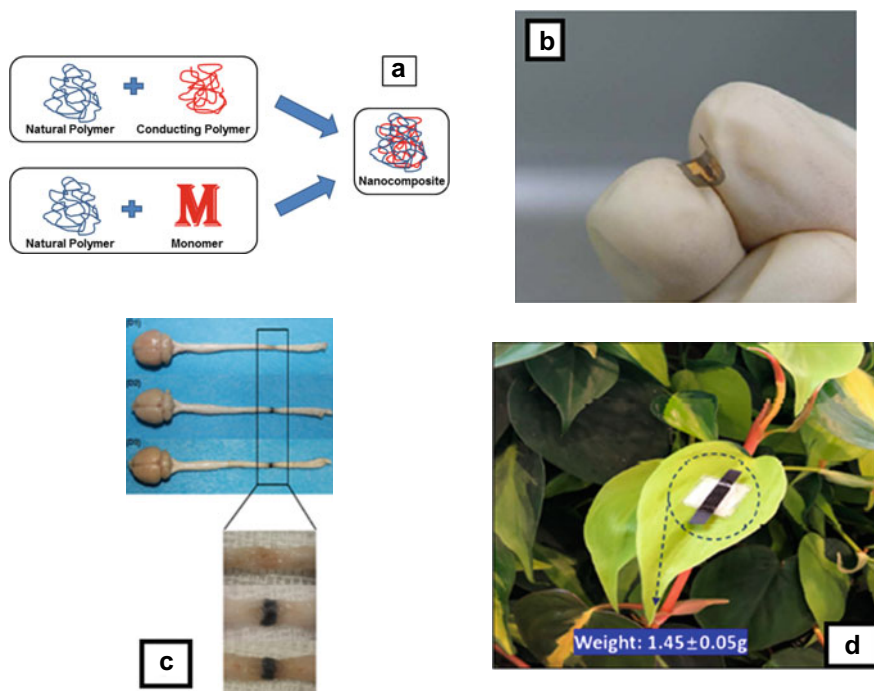


Fig. 3 **a** Representation of the forms of nanocomposite synthesis. **b** Flexible humidity and temperature sensor based on cellulose and polypyrrole. Adapted with permission from Mahadeva et al. [123]. Copyright (2011), Elsevier. **c** Implantation of the PPy/PLA nanofibrous scaffold in host spinal cord tissue. Adapted from Raynald et al. [175] under the terms and conditions of the Creative Commons CC BY license. <https://creativecommons.org/licenses/>. **d** Flexible solid-state supercapacitor based on PEDOT/cellulose showing the lightweight characterization. Adapted with permission from Li et al. [200]. Copyright (2020) ACS

such as changes in polarity, electrochemical behavior, and variation of concentration of the analyte, and the response can be detected by measuring the electrical, electrochemical, or optical properties, such as conductivity, potential difference, and frequency [152–154].

Thus, a chemical sensor is a device that transforms chemical information into a signal that can be measured. Signal generation occurs when analyte molecules interact with the sensory layer through physical and chemical processes that cause changes, typically in electrical or optical properties, which are detected by an appropriate transducer and converted into an output electrical signal. This obtained signal is processed using pattern recognition methods and analytical data are displayed [154].

Sensors can be classified in several ways: according to the nature of the analyte, or the quantity to be measured (pH, humidity, liquid, and gas sensors), the nature of the

sensory species (chemical and biological sensors), transduction principle (potentiometric, amperometric, voltammetric, conductometric sensors, etc.), measured property (resistivity, capacitance, reflectance, etc.), molecular recognition mechanism (microbiological, enzymatic, immunosensory sensors, etc.), selectivity (specific and semi-specific) [153].

Mahadeva and coworkers prepared a biodegradable and flexible nanocomposite based on cellulose and polypyrrole and this material was used as a flexible humidity and temperature sensor. The authors observed that the capacitance of flexible sensor increased with increasing the humidity and temperature [123]. The image of this sensor can be seen in Fig. 3b.

Bano and coworkers prepared bionanocomposites involving polypyrrole, tin oxide, and chitin. The authors studied the photocatalytic degradation process by monitoring decolorization and degradation of Rhodamine B dye solution. The prepared materials were also tested in the application as a sensor. The sensor was used in the detection of methanol via cyclic voltammetry. The bionanocomposites of polypyrrole-tin oxide-chitin showed good sensing properties as compared to pure tin oxide nanoparticles. The synthesized nanocomposites were found to be effective for wider concentration range of methanol [155]. The synthesis and photoelectrocatalytic response scheme, and also sensor measurements are presented in Fig. 4.

Biological sensors or biosensors are chemical sensors although are often treated separately. A biosensor can be defined as a chemical sensor that detects biological materials such as enzymes, DNA, and antibodies, or uses them in its sensory layer [156].

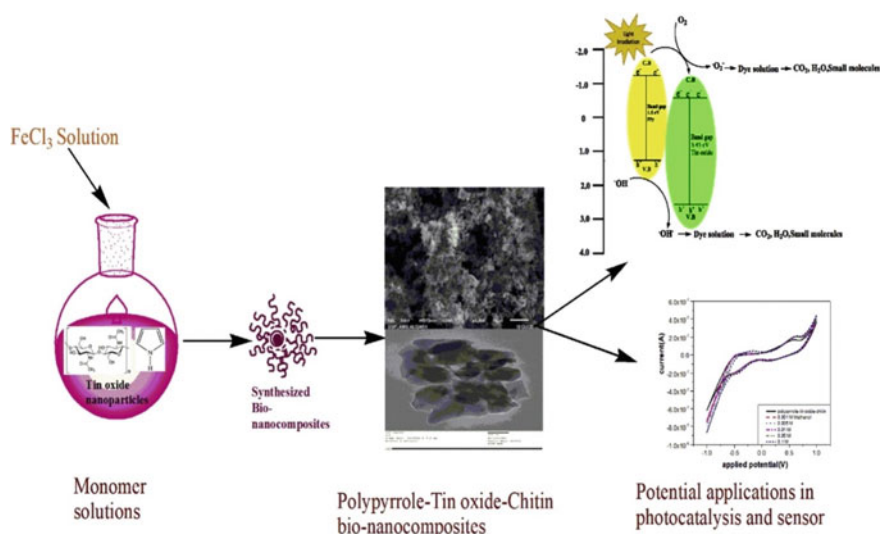


Fig. 4 The synthesis and photoelectrocatalytic response scheme of the bionanocomposite as a sensor for methanol detection. Adapted with permission from Bano et al. [155]. Copyright (2019), Elsevier

Table 2 Some recent papers reporting nanocomposites based on conducting polymers and natural polymers for sensor and biosensor application

| Natural polymer | Conducting polymer | Application | Refs. |
|-----------------|--------------------|--|-------|
| Chitin | PPy | Methanol sensor | [155] |
| Chitin | PAni | Gas sensor | [71] |
| Cellulose | PAni | Sensor for detection of ammonia | [157] |
| | | Touch sensor | [165] |
| | | Biosensor | [167] |
| Cellulose | PEDOT | Amperometric sensing of nitrite | [159] |
| Natural rubber | PPy | Strain sensor | [160] |
| Alginate | PEDOT:PSS | Wearable sensor applications | [161] |
| Alginate | PPy | Mechanical sensor | [162] |
| Chitosan | PAni | Gas sensor | [164] |
| Chitosan | PPy | Optical urea biosensing | [166] |
| Pectin | PAni | Amperometric glucose biosensor | [168] |
| Cellulose | PPy | Glucose and H ₂ O ₂ sensor | [158] |
| | | Pressure sensor | [163] |
| | | Strain sensor | [169] |
| | | Glucose Biosensor | [125] |
| | | Flexible humidity and temperature sensor | [123] |
| PLA | PEDOT:PSS | Gas Sensor | [170] |
| Starch | PAni | Cholesterol sensor | [171] |

Sensors using conducting polymer-natural polymer nanocomposites can be low-cost tools for qualification or quantification of a large number of chemical and biological substances in applications ranging from quality control to food and beverages in pharmaceutical industries, clinical diagnosis, and substance detection, which are summarized in Table 2.

3.2 Medical Applications

In recent years, research on the incorporation of conducting polymer on supports consisting of a network of nanofibers polymeric activities is being directed, especially in biomedical area, to applications in tissue growth and regeneration, release controlled drug, biomechanical, and biological sensors. In this way, conducting polymer-natural polymer nanocomposites are applied in the study of tissue engineering.

Central nervous system diseases caused by neurodegenerative disorders such as the spinal cord and brain injury are a group that result from the loss of neurons and

axons in the brain or spinal cord [172]. The central nervous system has difficulty to repair its damaged tissue, and then the regeneration of tissue has been studied [173]. Tissue engineering is concerned with the replacement or regeneration of cells, tissues (the focus of tissue engineers), or organs to restore normal biological function [174]. Different types of biomaterials, either of natural or of synthetic origin, have been developed as inductive microenvironment for neural regeneration.

Infection caused by microbes entails problems in human life. Many works have been developed to prepare new antimicrobial agents to fight pathogens. The demand for new materials with these properties has been great. In this sense, conducting polymer-natural polymer nanocomposites have been studied.

Inflammation, heart disease, cancer, and premature aging can be caused by free radical intermediates. Antioxidant materials are compounds that prevent the oxidation of other materials. These materials have an important role in tissues as a health protective factor and reduce the risk of the chronic diseases [111].

Raynald and coworkers prepared polypyrrole/polylacticacid nanocomposite and nanofibrous scaffold was grafted into a complete transected spinal cord to promote nerve regeneration and to recover nerve conduction. This material can inhibit scar tissue formation and induce the axonal regeneration and myelination in the lesion area and was tested in rats [175]. Figure 3c presents the image of implantation of the PPy/PLA nanofibrous scaffold in host spinal cord tissue.

Cellulose hydrogels were fabricated from a cellulose solution and then used as a template for in situ synthesis of PANi via limited interfacial polymerization in a natural phytic acid solution to obtain one conductive side in the hydrogel. The structure and properties of the PANi/cellulose composite hydrogels were characterized. The composite presented excellent guiding capacity for the sciatic nerve regeneration of rats without any extra treatment [176]. The photograph of the PANi/cellulose composite hydrogels, image of the cross-section of the conductive side, the schema of the hierarchical micro-nano-structured PANi embedded in cellulose matrix, and intraoperative photograph of the PANi/cellulose composite hydrogels showing reconstruction of the sciatic nerve at 3 months after surgery are shown in Fig. 5 [176].

Some recent papers reporting nanocomposites based on conducting polymers and natural polymers for medical application are presented in Table 3.

3.3 Energy Storage Devices

The traditional use of fossil fuels to supply the energy needs of the world presents well-known problems. These problems range from the scarcity of natural resources to environmental concerns about pollution, mainly due to the emission of carbon dioxide (CO₂). In this way, fossil fuels have been gradually replaced by renewable energy resources, such as wave and tidal energy, solar, wind, and hydroelectric [194]. These new technologies are a convenient alternative for the supply of energy with less environmental impact. These new technologies can supply residential, industrial, and

Fig. 5 **a** Photograph of the PANi/cellulose composite hydrogels. **b** TEM image of the cross-section of the PANi/cellulose composite hydrogels of the conductive side. **c** The schema of the hierarchical micro-nano-structured PANi embedded in cellulose matrix. **d** Intraoperative photographs of the PANi/cellulose composite hydrogels after 3 months after surgery. Adapted with permission from Xu et al. [176]. Copyright (2016), ACS

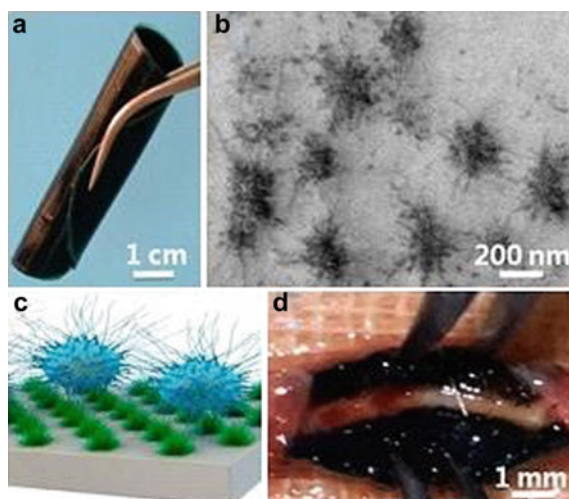


Table 3 Some recent papers reporting nanocomposites based on conducting polymers and natural polymers for medical application

| Natural polymer | Conducting polymer | Application | Refs. |
|-----------------|--------------------|--------------------------------------|-------|
| Alginate | PPy | Tissue engineering | [134] |
| PLA | PPy | Nanofibrous scaffold | [175] |
| Cellulose | PAni | Nerve regeneration | [176] |
| | | Drug delivery | [181] |
| Starch | PAni | Antioxidant activity | [178] |
| Chitosan | PAni | Antimicrobial activity | [177] |
| | | Antimicrobial therapy | [179] |
| | | Antibacterial activity | [180] |
| Pectin | PAni | Drug delivery | [182] |
| Pectin | PPy | Antibacterial activity | [183] |
| PLA | PPy | Bioactive electroconductive scaffold | [184] |
| | | Tissue engineering | [186] |
| PLA | PAni | Tissue engineering | [185] |
| Cellulose | P3HT | Tissue engineering | [187] |
| Chitosan | PPy | Antivirulence drug | [188] |
| Cellulose | PEDOT:SDS | Wound dressing | [189] |
| Chitosan | PEDOT:PSS | Tissue engineering | [121] |
| Chitosan | PEDOT | Tissue engineering | [190] |
| Alginate | PEDOT:PSS | Neuroprosthetics | [191] |
| Alginate | PAni | Tissue engineering | [192] |
| Several | PPy | Biomedical applications | [193] |

transportation consumption. However, the generation of electricity from renewable resources varies, as it depends on climatic conditions. Thus, it generates the need for new technologies that allow the use of the full potential of these resources in order to meet the demand for energy on a regular basis [194].

The development of technologies that enable the use of renewable energy on a continuous basis has been the motivation of several researches. Thus, energy conversion and storage devices have been proposed as something of interest with the main objective of achieving a balance between generation and demand for energy. These devices will allow demand to be met when needed, managing energy through an intelligent distribution network to, in the near future, supply power to remote locations and decentralize the energy supply system [194, 195].

Among the energy storage devices, the two most important are supercapacitors and batteries. Supercapacitors, also called electrochemical capacitors, stand out for properties such as high charge/discharge speed, good stability, and high power density. Supercapacitors can be defined as devices that combine the behavior of capacitors and batteries. The batteries have high energy density (Wh/g) and low power density (W/kg) characteristics and the capacitors have high power density and low energy density. Energy density is the ability of the device to supply power for long periods of time, and power density is the supply of large amounts of energy for short periods of time. Batteries have a high energy density, as they allow the supply of the same for long periods, while the capacitors provide a high power density, as they provide a large amount of energy for short periods of time [194, 195]. Many studies have been directed to develop new materials that increase the efficiency of supercapacitors and batteries.

Conducting polymers are a promising candidate for materials used in energy storage. These materials are highly conductive and can store and distribute energy through electrochemical doping reactions, leading to a high power and energy density. A conducting polymer can be used for supercapacitors because it exhibits high theoretical capacitance, low cost, easy synthesis, controllable electrical conductivity, and environmental stability [196]. Joining the natural polymer into a conductive polymer improves the mechanical properties allowing for flexible materials.

Fuel biocells are bioelectrochemical devices that convert chemical energy into electrical energy, where enzymes and/or microorganisms are used in bioanodes and biocathodes, catalyzing the oxidation of fuels and the reduction of oxidizing agents, respectively. This system is characterized as a non-polluting and silent technology. Fuel biocell is an alternative to conventional fuel cells based on metal catalysts, which switch to biological fuel cells or biofuel cells. This device employs enzymes (enzymatic biofuel cell) or microorganisms (microbial fuel cell) as catalyst instead of the traditional noble metal catalysts. These devices constitute a system that can directly transform chemical energy into electricity through reactions involving biochemical steps. In general, traditional fuel cells use noble metal catalysts to generate electrons from fuel oxidation (typical fuels are hydrogen or small organic molecules such as methanol, ethanol, and glutaraldehyde, among others). After the oxidation step, an external circuit transfers the electrons to the cathode side where the electrons react with an oxidant molecule (usually oxygen), and generate electrical work as well as

water and heat. There are many types of basic fuel cells, depending on the type of electrolyte and operation temperature [197–199].

Li and coworkers prepared a PEDOT/cellulose nanocomposite and this material was used as a flexible solid-state supercapacitor. PEDOT/cellulose nanocomposite is sufficiently conductive to function as current collector. The supercapacitor kept 77% capacitance after 1000 cycles. The supercapacitor exhibited a lightweight of 1.45 g and is represented in Fig. 3d [200].

Tan and coworkers prepared the composites of polyaniline/pristine graphene – bacterial cellulose as electrodes for all-solid-state supercapacitors with high performance. First, a mixture of pristine graphene and bacterial cellulose was made as substrate. Subsequently, PANi was deposited via in situ polymerization on the substrate surface. The composite had a high capacitance per unit area of $3.65 \text{ F}\cdot\text{cm}^{-2}$ at current density of $5 \text{ mA}\cdot\text{cm}^{-2}$, and the electrode was produced with different shapes without fracture. The supercapacitor was flexible and exhibited excellent capacitance per unit area of $1389 \text{ mF}\cdot\text{cm}^{-2}$, energy density of $9.80 \text{ mW}\cdot\text{h}\cdot\text{cm}^{-3}$, and 89.8% retention of its initial capacitance after 5000 cycles at a current density of $2 \text{ mA}\cdot\text{cm}^{-2}$. Figure 6 presents the composite synthesis scheme and photograph of the composite as well as bending and cutting into different shapes [201].

Thus, there is a possibility of obtaining a wide variety of nanocomposite materials for application in energy storage devices. Table 4 shows some nanocomposites used for this purpose.

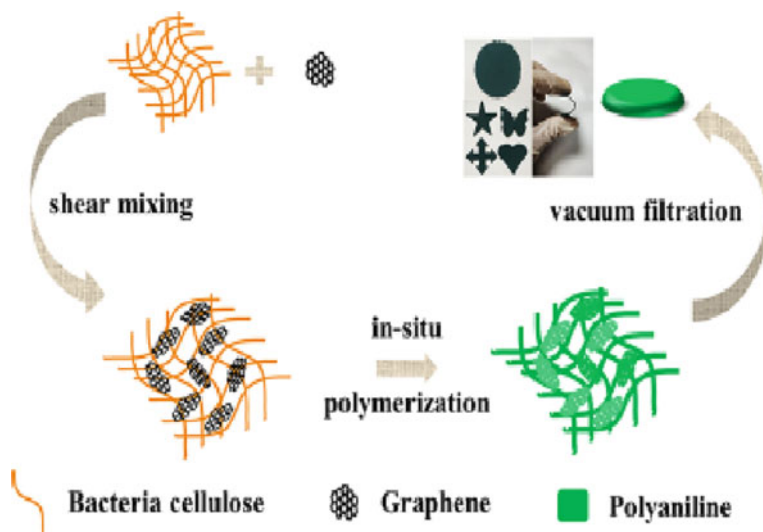


Fig. 6 Schematic illustration of the synthesis of the polyaniline/pristine graphene – bacterial cellulose composite, and photograph of the composite, as well as bending and cutting into different shapes. Adapted with permission from Tan et al. [201]. Copyright (2021), ACS

Table 4 Some recent papers reporting nanocomposites based on conducting polymers and natural polymers for energy storage devices

| Natural polymer | Conducting polymer | Application | Refs. |
|-----------------|--------------------|---------------------|-----------------|
| Cellulose | PEDOT | Supercapacitor | [200] |
| | | Fuel cell | [216] |
| Cellulose | PAni | Supercapacitor | [201, 202, 209] |
| | | Microbial fuel cell | [211, 214, 217] |
| | | Fuel cell | [218] |
| Chitosan | PAni | Supercapacitor | [203] |
| Alginate | PAni | Supercapacitor | [204] |
| PLA | PAni | Supercapacitor | [205] |
| PLA | PPy | Supercapacitor | [206] |
| Alginate | PPy | Supercapacitor | [208] |
| Chitosan | PAni | Fuel cell | [212] |
| Alginate | PAni | Microbial fuel cell | [215] |
| Cellulose | PPy | Supercapacitor | [207, 210] |
| | | Microbial fuel cell | [213] |
| | | Biofuel cell | [219] |

4 Final Remarks

The search for materials that have electrical conductivity but that have good mechanical properties leads to the study of nanocomposites. Various types of natural polymers, conducting polymers, preparation of nanocomposites, and some of their applications have been reported in this chapter. There is a very extensive class of natural polymers and they are of great interest due to their low cost and obtaining them from renewable sources. Conducting polymers are generally applied in electrical and optoelectronic devices. So, the union of the two types of polymers allows to obtain different properties when compared with the original materials. There are many techniques for obtaining these nanocomposites, for example, drop-casting, spin and dip coating, lithography, electropolymerization, inkjet printing, spray techniques, layers deposition by Langmuir–Blodgett (LB), and layer-by-layer (LBL), among others. These nanocomposites have promising properties, which allow them to be used in various technological applications, such as sensors, biosensors, tissue engineering, dressings, drugs, capacitors, biofuel cells, and others. Many combinations and preparation routes need to be explored in order to enable further studies.

Acknowledgements This study was financed in part by the Coordenação de Aperfeiçoamento de Pessoal de Nível Superior – Brazil (CAPES) – Finance Code 001 (Proc. 88887.362974/2019-00 and 88887.362968/2019-00), FAPESP (proc. 2013/07296-2 and 2017/11986-5). The authors would like to thank to financial support given by SisNANO (CNPq/382244/2020-6), MCTI, FINEP, and Embrapa AgroNano research network.

References

1. S. Bhatia, in *Drug delivery Systems*. (Springer, Cham, 2016). https://doi.org/10.1007/978-3-319-41129-3_3
2. A.G. MacDiarmid, Synthetic metals: a novel role for organic polymers. *Synth. Met.* **125**, 11–22 (2002). [https://doi.org/10.1016/s0379-6779\(01\)00508-2](https://doi.org/10.1016/s0379-6779(01)00508-2)
3. H. Shirakawa, E.J. Louis, A.G. MacDiarmid, C.K. Chiang, A.J. Heeger, Synthesis of electrically conducting organic polymers: halogen derivatives of polyacetylene, (CH)_x. *J. Chem. Soc.*, 578–580 (1977). <https://doi.org/10.1039/c39770000578>.
4. C.K. Chiang, M.A. Drury, S.C. Gaul, A.J. Heeger, E.J. Louis, A.G. MacDiarmid, Y.W. Park, H. Shirakawa, Synthesis of highly conducting films of derivatives of polyacetylene, (CH)_x. *J. American Chem. Soc.*, 1013–1015 (1978). <https://doi.org/10.1021/ja00471a081>.
5. T.F. Otero, J.G. Martinez, J. Arias-Pardilla, Biomimetic electrochemistry from conducting polymers. A review artificial muscles, smart membranes, smart drug delivery and computer/neuron interfaces. *Electrochim. Acta*, **84**, 112–128 (2012). <https://doi.org/10.1016/j.electacta.2012.03.097>.
6. S.Y. Park, M.S. Cho, H.J. Choi, *Curr. Appl. Phys.* **4**, 581–583 (2004). <https://doi.org/10.1016/j.cap.2004.01.020>
7. H. Letheby, XXIX.—On the production of a blue substance by the electrolysis of sulphate of aniline. *J. Chem. Soc.*, **15**(0), 161–163 (1862). <https://doi.org/10.1039/js8621500161>.
8. A.G. Green, A.E. Woodhead, CCXLIII.—Aniline-black and allied compounds. Part I. *J. Chem. Soc., Trans.*, **97**(0), 2388–2403 (1910). <https://doi.org/10.1039/ct9109702388>.
9. W.S. Huang, B.D. Humphrey, A.G. MacDiarmid, Polyaniline, a novel conducting polymer. Morphology and chemistry of its oxidation and reduction in aqueous electrolytes. *J. Chem. Soc., Faraday Trans. 1* **82**(8), 2385 (1986). <https://doi.org/10.1039/f19868202385>.
10. A.G. MacDiarmid, A.J. Epstein, Synthetic metals: A novel role for organic polymers. *Makromol. Chem., Macromol. Symp.* **51**(1), 11–28 (1991). <https://doi.org/10.1002/masy.19910510104>.
11. J.E. de Albuquerque, L.H.C. Mattoso, R.M. Faria, J.G. Masters, A.G. MacDiarmid, Study of the interconversion of polyaniline oxidation states by optical absorption spectroscopy. *Synth. Met.* **146**(1), 1–10 (2004). <https://doi.org/10.1016/j.synthmet.2004.05.019>
12. L.H.C. Mattoso, Polianilinas: síntese, estrutura e propriedades. *Quim. Nova* **19**(4), 388–399 (1995)
13. E.S. Medeiros, J.E. Oliveira, N. Consolin-Filho, L.G. Paterno, L.H.C. Mattoso, Uso de Polímeros Condutores em Sensores. Parte 1: Introdução aos Polímeros Condutores. *Revista Eletrônica de Materiais e Processos*, **7.2**, 62–77 (2012)
14. A. Pron, F. Genoud, C. Menardo, M. Nechtschein, The effect of the oxidation conditions on the chemical polymerization of polyaniline. *Synth. Met.* **24**, 193–201 (1988). [https://doi.org/10.1016/0379-6779\(88\)90257-3](https://doi.org/10.1016/0379-6779(88)90257-3)
15. E.M. Geniès, A. Boyle, M. Lapkowsky, C. Tsintavis, Polyaniline: a historical survey. *Synth. Met.* **36**, 139–182 (1990). [https://doi.org/10.1016/0379-6779\(90\)90050-U](https://doi.org/10.1016/0379-6779(90)90050-U)
16. M. Abe, A. Ohtani, Y. Umemoto, S. Akizuki, M. Ezoe, H. Higuchi, K. Nakamoto, A. Okuno, Y. Noda. Soluble and High Molecular Weight Polyaniline. *J. Chem. Soc., Chem. Commun.*, 1736–1738 (1989). <https://doi.org/10.1039/C39890001736>
17. P.N. Adams, P.J. Laughlin, A.P. Monkman, Low temperature synthesis of high molecular weight polyaniline. *Polymer* **37**(15), 3411–3417 (1996). [https://doi.org/10.1016/0032-3861\(96\)88489-8](https://doi.org/10.1016/0032-3861(96)88489-8)
18. J. Stejskal, R.G. Gilbert, Polyaniline. Preparation of a conducting polymer (IUPAC Technical Report). *Pure Appl. Chem.*, **74**(5), 857–867 (2002). <https://doi.org/10.1351/pac200274050857>.
19. B. Wang, J. Tang, F. Wang, Electrochemical polymerization of aniline. *Synth. Met.* **18**(1–3), 323–328 (1987). [https://doi.org/10.1016/0379-6779\(87\)90899-X](https://doi.org/10.1016/0379-6779(87)90899-X)

20. G. Zotti, S. Cattarin, N. Comisso, Cyclic potential sweep electropolymerization of aniline. *J. Electroanal. Chem. Interf. Electrochem.* **239**(1–2), 387–396 (1988). [https://doi.org/10.1016/0022-0728\(88\)80293-6](https://doi.org/10.1016/0022-0728(88)80293-6)
21. W.J. Feast, J. Tsibouklis, K.L. Pouwer, L. Groenendaal, E.W. Meijer, Synthesis, processing and material properties of conjugated polymers. *Polymer* **37**(22), 5017–5047 (1996). [https://doi.org/10.1016/0032-3861\(96\)00439-9](https://doi.org/10.1016/0032-3861(96)00439-9)
22. G.B. Street, R.H. Geiss, S.E. Lindsey, A. Nazzari, P. Pfluger, Conducting Polymers Derived from Pyrrole. In: P. Reineker, H. Haken, H.C. Wolf (eds) *Organic Molecular Aggregates*. Springer Series in Solid-State Sciences, vol 49. Springer, Berlin, Heidelberg (1983). https://doi.org/10.1007/978-3-642-82141-7_24
23. S.C. Rasmussen, Conjugated and Conducting Organic Polymers: The First 150 Years. *Chem. Plus. Chem* **85**(7), 1412–1429 (2020). <https://doi.org/10.1002/cplu.202000325>
24. T.V. Vernitskaya, O.N. Efimov, Polypyrrole: a conducting polymer; its synthesis, properties and applications. *Russ. Chem. Rev.* **66**(5), 443–457 (1997). <https://doi.org/10.1070/rc1997v066n05abeh000261>
25. S. Machida, S. Miyata, A. Techagumpuch, Chemical synthesis of highly electrically conductive polypyrrole. *Synth. Met.* **31**(3), 311–318 (1989). [https://doi.org/10.1016/0379-6779\(89\)90798-4](https://doi.org/10.1016/0379-6779(89)90798-4)
26. P.C. Wang, Z. Huang, A.G. MacDiarmid, Critical dependency of the conductivity of polypyrrole and polyaniline films on the hydrophobicity/hydrophilicity of the substrate surface. *Synth. Met.* **101**(1–3), 852–853 (1999). [https://doi.org/10.1016/s0379-6779\(98\)01329-0](https://doi.org/10.1016/s0379-6779(98)01329-0)
27. A.F. Diaz, J.I. Castillo, J.A. Logan, W.Y. Lee, Electrochemistry of conducting polypyrrole films. *J. Electroanal. Chem. Interf. Electrochem.* **129**(1–2), 115–132 (1981). [https://doi.org/10.1016/s0022-0728\(81\)80008-3](https://doi.org/10.1016/s0022-0728(81)80008-3)
28. E.L. Kupila, J. Kankare, Electropolymerization of pyrrole: Effects of pH and anions on the conductivity and growth kinetics of polypyrrole. *Synth. Met.* **55**(2–3), 1402–1405 (1993). [https://doi.org/10.1016/0379-6779\(93\)90258-x](https://doi.org/10.1016/0379-6779(93)90258-x)
29. M. Yamaura, K. Sato, T. Hagiwara, Effect of counter-anion exchange on electrical conductivity of polypyrrole films. *Synth. Met.* **41**(1–2), 439–442 (1991). [https://doi.org/10.1016/0379-6779\(91\)91102-g](https://doi.org/10.1016/0379-6779(91)91102-g)
30. B.S. Kim, W.H. Kim, S.N. Hoier, S.M. Park, Electrochemistry of conductive polymers XVI. Growth mechanism of polypyrrole studied by kinetic and spectroelectrochemical measurements. *Synth. Met.* **69** (1–3), 455–458 (1995). [https://doi.org/10.1016/0379-6779\(94\)02527-6](https://doi.org/10.1016/0379-6779(94)02527-6)
31. M.S. Kiani, G.R. Mitchell, The role of the counter-ion in the preparation of polypyrrole films with enhanced properties using a pulsed electrochemical potential. *Synth. Met.* **48**(2), 203–218 (1992). [https://doi.org/10.1016/0379-6779\(92\)90062-n](https://doi.org/10.1016/0379-6779(92)90062-n)
32. G. Zotti, G. Schiavon, A. Berlin, G. Pagani, Electrochemical polymerization of 3-alkylthiopyrroles. *Synth. Met.* **28**(1–2), 183–186 (1989). [https://doi.org/10.1016/0379-6779\(89\)90518-3](https://doi.org/10.1016/0379-6779(89)90518-3)
33. J.B. Chang, V. Liu, V. Subramanian, K. Sivula, C. Luscombe, A. Murphy, J. Liu, J.M.J. Fréchet, Printable polythiophene gas sensor array for low-cost electronic noses. *J. Appl. Phys.* **100**(1), 014506 (2006). <https://doi.org/10.1063/1.2208743>
34. E. Aslan, P. Camurlu, L. Toppare, Synthesis and electrochromic properties of a symmetric polythiophene derivative: decanedionic acid bis-(2-thiophene-3-yl-ether)ester and its copolymer with thiophene. *J. Macromol. Sci. A* **42**(4), 451–462 (2005). <https://doi.org/10.1081/ma-200054346>
35. T. Yamamoto, K. Sanechika, A. Yamamoto, Preparation of thermostable and electric-conducting poly(2,5-thienylene). *J. Polym. Sci., Polym. Lett. Ed.* **18**(1), 9–12 (1980). <https://doi.org/10.1002/pol.1980.130180103>
36. J.W.P. Lin, L.P. Dudek, Synthesis and properties of poly(2,5-thienylene). *J. Polym. Sci.: Polym. Chem. Ed.*, **18**(9), 2869–2873 (1980). <https://doi.org/10.1002/pol.1980.170180910>
37. J. Roncali, Conjugated poly(thiophenes): synthesis, functionalization, and applications. *Chem. Rev.* **92**(4), 711–738 (1992). <https://doi.org/10.1021/cr00012a009>

38. Y. Chen, A review of polyaniline based materials as anodes for lithiumion batteries IOP Conf. Series: Mater. Sci. Eng., **677**, 022115–022120 (2019). <https://doi.org/10.1088/1757-899X/677/2/022115>.
39. F.M. Kelly, L. Meunier, C. Cochrane, V. Koncar, Polyaniline: Application as solid state electrochromic in a flexible textile display. *Displays* **34**(1), 1–7 (2013). <https://doi.org/10.1016/j.displa.2012.10.001>
40. A. Manzoli, C. Steffens, R.T. Paschoalin, A.A. Correa, W. Alves, F. Leite, P. Herrmann, Low-Cost gas sensors produced by the graphite line-patterning technique applied to monitoring banana ripeness. *Sensors* **11**(6), 6425–6434 (2011). <https://doi.org/10.3390/s110606425>
41. S. Ahn, M.H. Park, S.H. Jeong, Y.H. Kim, J. Park, S. Kim, H. Kim, H. Cho, C. Wolf, M. Pei, H. Yang, T.W. Lee, Fine control of perovskite crystallization and reducing luminescence quenching using self-doped polyaniline hole injection layer for efficient perovskite light-emitting diodes. *Adv. Funct. Mater.* **29**, 1807535–1807542 (2019). <https://doi.org/10.1002/adfm.201807535>
42. K. Hiraoka, Y. Kusumoto, I. Ikezoe, H. Kajii, Y. Ohmori, Properties of polymer light-emitting transistors with Ag-nanowire source/drain electrodes fabricated on polymer substrate. *Thin Solid Films* **554**, 184–188 (2014). <https://doi.org/10.1016/j.tsf.2013.08.021>
43. M. Qiu, Y. Zhang B. Wen, Facile synthesis of polyaniline nanostructures with effective electromagnetic interference shielding performance. *J. Mater. Sci.: Mater. Electronics*, **29**(12), 10437–10444 (2018). <https://doi.org/10.1007/s10854-018-9100-6>.
44. J. Wen, Y. Tian, C. Hao, S. Wang, Z. Mei, W. Wu, J. Lu, Z. Zheng, Y. Tian, Fabrication of High Performance Printed Flexible Conductors by Doping of Polyaniline Nanomaterials into Silver Paste. *J. Mater. Chem. C*, **7**, 1188–1197 (2019). <https://doi.org/10.1039/c8tc05391j>
45. T.K. Das, S. Prusty, Review on conducting polymers and their applications. *Polymer Plast. Tech. Eng.* **51**(14), 1487–1500 (2012). <https://doi.org/10.1080/03602559.2012.710697>
46. S. Tajik, H. Beitollahi, F.G. Nejad, I.S. Shoaie, M.A. Khalilzadeh, M.S. Asl, Q.V. Le, K. Zhang, H.W. Jang, M. Shokouhimehr, Recent developments in conducting polymers: applications for electrochemistry. *RSC Adv.* **10**, 37834–37856 (2020). <https://doi.org/10.1039/d0ra06160c>
47. L.A. Fard, R. Ojani, J.B. Raouf, E.N. Zare, M.M. Lakoura, Poly (pyrrole-co-aniline) hollow nanosphere supported Pd nanoflowers as high-performance catalyst for methanol electrooxidation in alkaline media. *Energy* **127**, 419–427 (2017). <https://doi.org/10.1016/j.energy.2017.03.159>
48. J. Hosseini, E.N. Zare, D. Ajloo, Experimental and theoretical calculation investigation on effective adsorption of lead(II) onto poly(aniline-co-pyrrole) nanospheres. *J. Mol. Liq.* **296**, 111789 (2019). <https://doi.org/10.1016/j.molliq.2019.111789>.
49. E.N. Zare, A. Motahari, M. Sillanpää, Nanoadsorbents based on conducting polymer nanocomposites with main focus on polyaniline and its derivatives for removal of heavy metal ions/ dyes: A review. *Environ. Res.* **162**, 173–195 (2018). <https://doi.org/10.1016/j.envres.2017.12.025>
50. O. Olatunji, Classification of Natural Polymers, in *Natural Polymers*. Cham: Springer International Publishing, 1–17 (2016). https://doi.org/10.1007/978-3-319-26414-1_1.
51. Natural Polymers (2021). Available at: <https://byjus.com/chemistry/natural-polymers> (accessed Mar. 01, 2021).
52. S. Mohan, O. Oluwafemi, N. Kalarikkal, S. Thomas, S.P. Songca, in *Recent Advances in Biopolymers*. (InTech, 2016), pp. 47–72. <https://doi.org/10.5772/62225>.
53. V. Kulkarni, K. Butte, S. Rathod, Natural polymers – A comprehensive review. *Int. J. of Res. Pharm. Biom. Sci.* **3**(4), 1597–1613 (2012)
54. P. Bhagabati, in *Sustainable Nanocellulose and Nanohydrogels from Natural Sources*. A volume in Micro and Nano Technologies, ed. by F. Mohammad, H. A. Al-Lohedan, M. Jawaid, (Elsevier, 2020), pp. 197–216. <https://doi.org/10.1016/b978-0-12-816789-2.00009-2>
55. R. Parker, S.G. Ring, Aspects of the Physical Chemistry of Starch. *J. Cereal Sci.* **34**, 1–17 (2001). <https://doi.org/10.1006/jcrs.2000.0402>

56. V.B. Carmona, A.C. Corrêa, J.M. Marconcini, L.H.C. Mattoso, Properties of a Biodegradable Ternary Blend of Thermoplastic Starch (TPS), Poly(ϵ -Caprolactone) (PCL) and Poly(Lactic Acid) (PLA). *J. Polym. Environ.* **23**(1), 83–89 (2015). <https://doi.org/10.1007/s10924-014-0666-7>
57. F.Z. Benabid, F. Zouai, Natural polymers: Cellulose, Chitin, Chitosan, Gelatin, Starch, Garrageenan, Xylan and Dextran. *Algerian Journal of Natural Products* **4**(3), 348–357 (2016). <https://doi.org/10.5281/zenodo.199036>
58. A.C. Correa, V.B. Carmona, J.A. Simão, L.H.C. Mattoso, J.M. Marconcini, Biodegradable blends of urea plasticized thermoplastic starch (UTPS) and poly(ϵ -caprolactone) (PCL): Morphological, rheological, thermal and mechanical properties. *Carbohydr. Polym.* **167**, 177–184 (2017). <https://doi.org/10.1016/j.carbpol.2017.03.051>
59. N. Lin, J. Huang, P.R. Chang, D.P. Anderson, J. Yu, Preparation, Modification, and Application of Starch Nanocrystals in Nanomaterials: A Review. *J. Nanomat.*, (2011), 573687 (2011). <https://doi.org/10.1155/2011/573687>.
60. A.C. Corrêa, E.M. Teixeira, L.A. Pessan, L.H.C. Mattoso, Cellulose nanofibers from curaua fibers. *Cellulose* **17**(6), 1183–1192 (2010). <https://doi.org/10.1007/s10570-010-9453-3>
61. K. Müller, C. Zollfrank, M. Schmid, Natural Polymers from Biomass Resources as Feedstocks for Thermoplastic Materials. *Macromol. Mater. Eng.* **304**(5), 1–17 (2019). <https://doi.org/10.1002/mame.201800760>
62. S.J. Eichhorn, S.S. Rahateka, S. Vignolini, A.H. Windle, New horizons for cellulose nanotechnology. *Philos. Trans. A Math. Phys. Eng. Sci.*, **376**(2112), 20170200 (2018). <https://doi.org/10.1098/rsta.2017.0200>.
63. P. Claro, A. Campos, A. Corrêa, V. Rodrigues, B. Luchesi, L. Silva, G. Tonoli, L. Mattoso, J. Marconcini, Curaua and eucalyptus nanofiber films by continuous casting: mixture of cellulose nanocrystals and nanofibrils. *Cellulose*, **26**(4) (2019). <https://doi.org/10.1007/s10570-019-02280-9>.
64. A.C. Corrêa, V.B. Carmona, J.A. Simão, F. Galvani, J.M. Marconcini, L.H.C. Mattoso, Cellulose nanocrystals from fibers of Macauba (*Acrocomia Aculeata*) and Gravata (*Bromelia Balansae*) from Brazilian Pantanal. *Polymers* **11**(11), 1785–1800 (2019). <https://doi.org/10.3390/polym11111785>
65. M.K. Poddar, P.K. Dikshit, Recent development in bacterial cellulose production and synthesis of cellulose based conductive polymer nanocomposites. *Nano Select*, 1–24 (2021). <https://doi.org/10.1002/nano.202100044>.
66. A. Diop, K. Adjalle, B. Boens, D. Montplaisir, S. Barnabé, Synthesis and characterization of lignin-melamine-formaldehyde resin. *J. Thermoplast. Compos. Mater.* **30**(9), 1255–1266 (2016). <https://doi.org/10.1177/0892705716632856>
67. A. Taqi, L. Muthiac, I. Stamatina, Physical and barrier properties of apple pectin/cassava starch composite films incorporating *Laurus nobilis* L. oil and oleic acid, *J. Food Process. Preserv.* **38**, 1982–1993 (2014). <https://doi.org/10.1111/jfpp.12174>.
68. M. Nemiwal, T.C. Zhang, D. Kumar, Pectin modified metal nanoparticles and their application in property modification of biosensors. *Carbohydr. Polym. Tech. Appl.* **2**(25), 100164 (2021). <https://doi.org/10.1016/j.carpta.2021.100164>
69. A. Alipour, M.M. Lakouraj, R. Ojani, M.N. Roudbari, M.J. Chaichi, A. Nemati, Electrochemical and chemiluminescence properties of polyaniline/pectin hybrid nanocomposites based on graphene and CdS nanoparticles. *Polym. Test.* **76**, 490–498 (2019). <https://doi.org/10.1016/j.polymertesting.2019.04.013>
70. I. Hussain, X. Ma, Y. Luo, Z. Luo, Fabrication and characterization of glycogen-based elastic, self-healable, and conductive hydrogels as a wearable strain-sensor for flexible e-skin. *Polymer* **210**, 122961 (2020). <https://doi.org/10.1016/j.polymer.2020.122961>
71. R.S. Andre, D.M. dos Santos, L.A. Mercante, M.H.M. Facure, S.P. Campana-Filho, L.H.C. Mattoso, D.S. Correa, Nanochitin-based composite films as a disposable ethanol sensor. *J. Environ. Chem. Eng.* **8**(5), 104163 (2020). <https://doi.org/10.1016/j.jece.2020.104163>
72. S. Doppalapudi, S. Katiyar, A.J. Domb, W. Khan, in *Advanced Polymers in Medicine*, ed. by F. Puoci (Springer, Cham, 2015). <https://doi.org/10.1007/978-3-319-12478-0>.

73. S. Wang, S. Guan, Z. Zhu, W. Li, T. Liu, X. Ma, Hyaluronic Acid Doped-Poly(3,4-Ethylenedioxythiophene)/Chitosan/Gelatin (PEDOT-HA/Cs/Gel) Porous Conductive Scaffold for Nerve Regeneration. *Mater. Sci. Eng. C* **71**, 308–316 (2017). <https://doi.org/10.1016/j.msec.2016.10.029>
74. J.P. Paques, E. Linden, C.J.M. Rijn, L.M.C. Sagis, Preparation methods of alginate nanoparticles. *Adv. Colloid Interface Sci.* **209**, 163–171 (2014). <https://doi.org/10.1016/j.cis.2014.03.009>
75. S. Vandghanooni, M. Eskandani, Electrically conductive biomaterials based on natural polysaccharides: Challenges and applications in tissue engineering. *International Int. J. Biol. Macromol.* **141**, 636–662 (2019). <https://doi.org/10.1016/j.ijbiomac.2019.09.020>
76. Z. Xu, L. Shi, M. Yang, L. Zhu, Preparation and biomedical applications of silk fibroin-nanoparticles composites with enhanced properties - A review. *Mater. Sci. Eng. C* **95**, 302–311 (2019). <https://doi.org/10.1016/j.msec.2018.11.010>
77. S. Pradhan, A.K. Brooks, V.K. Yadavalli, Nature-derived materials for the fabrication of functional biodevices. *Mater. Today Bio.* **7**, 100065 (2020). <https://doi.org/10.1016/j.mtbio.2020.100065>
78. R.G. Aswathy, B. Sivakumar, D. Brahatheeswaran, T. Fukuda, Y. Yoshida, T. Maekawa, D.S. Kumar, Biocompatible fluorescent zein nanoparticles for simultaneous bioimaging and drug delivery application. *Adv. Nat. Sci.: Nanosci. Nanotechnol.* **3**(2), 025006–025013 (2012). <https://doi.org/10.1088/2043-6262/3/2/025006>
79. S. Kim, Processing and properties of gluten/zein composite. *Bioresour. Technol.* **99**, 2032–2036 (2008). <https://doi.org/10.1016/j.biortech.2007.02.050>
80. L.S.F. Leite, C.M. Ferreira, A.C. Corrêa, F.K.V. Moreira, L.H.C. Mattoso, Scaled-up production of gelatin-cellulose nanocrystal bionanocomposite films by continuous casting. *Carbohydr. Polym.* **238**, 116198–116206 (2020). <https://doi.org/10.1016/j.carbpol.2020.116198>
81. B. Panchal, A. Bagdadi, I. Roy, in *Advances in Natural Polymers: Composites and Nanocomposites*. A volume in *Advanced Structured Materials*, ed. by S. Thomas, P. M. Visakh, A. P. Mathew, 397–421 (Springer, Berlin Heidelberg, 2013). https://doi.org/10.1007/978-3-642-20940-6_12
82. C. Ingraio, and V. Siracusa, in *Biodegradable and Biocompatible Polymer Composites: Processing, Properties and Applications, a volume in Woodhead Publishing Series in Composites Science and Engineering*, ed. by N. G. Shimpi (Woodhead Publishing, 2018) pp. 401–418. <https://doi.org/10.1016/B978-0-08-100970-3.00014-6>
83. A. Hassan, and H. Balakrishnan, in *Advances in Natural Polymers: Composites and Nanocomposites*. A volume in *Advanced Structured Materials*, ed. by S. Thomas, P. M. Visakh, A. P. Mathew (Springer Berlin Heidelberg, 2013), pp. 361–396. https://doi.org/10.1007/978-3-642-20940-6_11
84. J. Sapkota, S. Kumar, C. Weder, E.J. Foster, Influence of Processing Conditions on Properties of Poly (Vinyl acetate)/Cellulose Nanocrystal Nanocomposites. *Macromol. Mater. Eng.* **300**, 562–571 (2015). <https://doi.org/10.1002/mame.201400313>
85. H.P.S.A. Khalil, A.H. Bhat, A.F.I. Yusra, Green composites from sustainable cellulose nanofibrils: A review. *Carbohydr. Polym.* **87**(2), 963–979 (2012). <https://doi.org/10.1016/j.carbpol.2011.08.078>
86. J.A. Marins, B.G. Soares, K. Dahmouche, S.J.L. Ribeiro, H. Barud, D. Bonemer, Structure and properties of conducting bacterial cellulose-polyaniline nanocomposites. *Cellulose* **18**(5), 1285–1294 (2011). <https://doi.org/10.1007/s10570-011-9565-4>
87. D. Müller, C.R. Rambo, L.M. Porto, W.H. Schreiner, G.M.O. Barra, Structure and properties of polypyrrole/bacterial cellulose nanocomposites. *Carbohydr. Polym.* **94**, 655–662 (2013). <https://doi.org/10.1016/j.carbpol.2013.01.041>
88. S. Khan, M. Ul-Islam, M.W. Ullah, Y. Kim, J.K. Park, Synthesis and characterization of a novel bacterial cellulose–poly(3,4-ethylenedioxythiophene)–poly(styrene sulfonate) composite for use in biomedical applications. *Cellulose* **22**(4), 2141–2148 (2015). <https://doi.org/10.1007/s10570-015-0683-2>

89. A.M. Youssef, M.A. El-Samahy, M.H.A. Rehim, Preparation of conductive paper composites based on natural cellulose fibers for packaging applications. *Carbohydr. Polym.* **89**(4), 1027–1032 (2012). <https://doi.org/10.1016/j.carbpol.2012.03.044>
90. Z. Mo, Z. Zhao, H. Chen, G. Niu, H. Shi, Heterogeneous preparation of cellulose–polyaniline conductive composites with cellulose activated by acids and its electrical properties. *Carbohydr. Polym.* **75**(4), 660–664 (2009). <https://doi.org/10.1016/j.carbpol.2008.09.010>
91. L.H.C. Mattoso, E.S. Medeiros, D.A. Baker, J. Avloni, D.F. Wood, W.J. Orts, Electrically Conductive Nanocomposites Made from Cellulose Nanofibrils and Polyaniline. *J. Nanosci. Nanotechnol.* **9**(5), 2917–2922 (2009). <https://doi.org/10.1166/jnn.2009.dk24>
92. A. Shalini, R. Nishanthi, P. Palani, V. Jaisankar, One pot synthesis, characterization of polyaniline and cellulose/polyaniline nanocomposites: application towards in vitro measurements of antibacterial activity. *Mater. Today Proc.* **3**(6), 1633–1642 (2016). <https://doi.org/10.1016/j.matpr.2016.04.053>
93. D. Müller, C.R. Rambo, D.O.S. Recouvreur, L.M. Porto, G.M.O. Barra, Chemical in situ polymerization of polypyrrole on bacterial cellulose nanofibers. *Synth. Met.* **161**, 106–111 (2011). <https://doi.org/10.1016/j.synthmet.2010.11.005>
94. W.L. Hu, S. Chen, Z. Yang, L. Liu, H. Wang, Flexible Electrically Conductive Nanocomposite Membrane Based on Bacterial Cellulose and Polyaniline. *J. Phys. Chem. B* **26**, 8453–8457 (2011). <https://doi.org/10.1021/jp204422v>
95. B.H. Lee, H.J. Kim, H.S. Yang, Polymerization of aniline on bacterial cellulose and characterization of bacterial cellulose/polyaniline nanocomposite films. *J. Curr. Appl. Phys.* **12**, 75–80 (2012). <https://doi.org/10.1016/j.cap.2011.04.045>
96. D. Müller, J.S. Mandelli, J.A. Marins, B.G. Soares, L.M. Porto, C.R. Rambo, G.M.O. Barra, Electrically conducting nanocomposites: preparation and properties of polyaniline (PAni)-coated bacterial cellulose nanofibers (BC). *Cellulose* **19**, 1645 (2012). <https://doi.org/10.1007/s10570-012-9754-9>
97. H.J. Lee, T.J. Chung, H.J. Kwon, H.J. Kim, W.T.Y. Tze, Fabrication and evaluation of bacterial cellulose-polyaniline composites by interfacial polymerization. *Cellulose* **19**(4), 1251–1258 (2012). <https://doi.org/10.1007/s10570-012-9705-5>
98. Z. Lin, Z. Guan, Z. Huang, New Bacterial Cellulose/Polyaniline Nanocomposite Film with One Conductive Side through Constrained Interfacial Polymerization. *Ind. Eng. Chem. Res.* **52**(8), 2869–2874 (2013). <https://doi.org/10.1021/ie303297b>
99. X. Shi, L. Zhang, J. Cai, G. Cheng, H. Zhang, J. Li, X. Wang, A Facile Construction of Supramolecular Complex from Polyaniline and Cellulose in Aqueous System. *Macromol.* **44**(12), 4565–4568 (2011). <https://doi.org/10.1021/ma2009904>
100. Z. Zhou, X. Zhang, C. Lu, L. Lan, G. Yuan, Polyaniline-decorated cellulose aerogel nanocomposite with strong interfacial adhesion and enhanced photocatalytic activity. *RSC Adv.* **4**(18), 8966–8972 (2014). <https://doi.org/10.1039/c3ra46441e>
101. Y. Kaitsuka, N. Hayashi, T. Shimokawa, E. Togawa, H. Goto, Synthesis of Polyaniline (PANI) in Nano-Reaction Field of Cellulose Nanofiber (CNF), and Carbonization. *Polymers* **8**(2), 40 (2016). <https://doi.org/10.3390/polym8020040>
102. C. Borsoi, A.J. Zattera, C.A. Ferreira, Effect of cellulose nanowhiskers functionalization with polyaniline for epoxy coatings. *Appl. Surf. Sci.* **364**, 124–132 (2016). <https://doi.org/10.1016/j.apsusc.2015.12.140>
103. M. Abbasian, P. Niroomand, M. Jaymand, Cellulose/polyaniline derivatives nanocomposites: Synthesis and their performance in removal of anionic dyes from simulated industrial effluents. *J. Appl. Polymer Sci.* **134**(39), 45352–45362 (2017). <https://doi.org/10.1002/app.45352>
104. W. Zheng, R. Lv, B. Na, H. Liu, T. Jin, D. Yuan, Nanocellulose-mediated hybrid polyaniline electrodes for high performance flexible supercapacitors. *J. Mater. Chem. A* **5**(25), 12969–12976 (2017). <https://doi.org/10.1039/c7ta01990d>
105. L. Yue, Y. Xie, Y. Zheng, W. He, S. Guo, Y. Sun, T. Zhang S. Liu, Sulfonated bacterial cellulose/polyaniline composite membrane for use as gel polymer electrolyte. *Compos. Sci. Tech.* **145**, 122–131 (2017). <https://doi.org/10.1016/j.compscitech.2017.04.002>

106. H. Sharifi, S.M. Zabihzadeh, M. Ghorbani, The application of response surface methodology on the synthesis of conductive polyaniline/cellulosic fiber nanocomposites. *Carbohydr. Polym.* **194**, 384–394 (2018). <https://doi.org/10.1016/j.carbpol.2018.04.083>
107. G. Fei, Y. Wang, H. Wang, Y. Ma, Q. Guo, W. Huang, D. Yang, Y. Shao, Y. Ni, Fabrication of bacterial cellulose/polyaniline nanocomposite paper with excellent conductivity, strength and flexibility. *ACS Sustainable Chem. Eng.* **7**, 8215–8225 (2019). <https://doi.org/10.1021/acssuschemeng.8b06306>
108. H. Hosseini, S.M. Mousavi, Influence of surfactant and molarity on the properties of bacterial cellulose/polyaniline: Experimental and density functional theory. *Carbohydr. Polym.* **250**, 116903–116913 (2020). <https://doi.org/10.1016/j.carbpol.2020.116903>
109. H. Hosseini, S.M. Mousavi, Bacterial cellulose/polyaniline nanocomposite aerogels as novel bioadsorbents for removal of hexavalent chromium: Experimental and simulation study. *J. Clean. Prod.* **278**, 123817–123829 (2021). <https://doi.org/10.1016/j.jclepro.2020.123817>
110. S.I.A. Razak, F.N. Dahli, I.F. Wahab, M.R.A. Kadir, I.I. Muhamad, A.H.M. Yusof, H. Adeli, A Conductive polylactic acid/polyaniline porous scaffold via freeze extraction for potential biomedical applications. *Soft Mater.* **14**(2), 78–86 (2016). <https://doi.org/10.1080/1539445x.2016.1149078>
111. E.N. Zare, P. Makvandi, B. Ashtari, F. Rossi, A. Motahari, G. Perale, Progresses in conductive polyaniline-based nanocomposites for biomedical applications: a review. *J. Med. Chem.* **63**(1), 1–22 (2020). <https://doi.org/10.1021/acs.jmedchem.9b00803>
112. X. Wang, Y. Tang, X. Zhu, Y. Zhou, X. Hong, Preparation and characterization of polylactic acid/polyaniline/nanocrystalline cellulose nanocomposite films. *Int. J. Biol. Macromol.* **146**, 1069–1075 (2020). <https://doi.org/10.1016/j.ijbiomac.2019.09.233>
113. J.H. Seo, C.S. Choi, J.H. Bae, H. Jeong, S.H. Lee, Y.S. Kim, Preparation of a lignin/polyaniline composite and its application in Cr(VI) removal from aqueous solutions. *BioResources* **14**(4), 9169–9182 (2019). <https://doi.org/10.15376/biores.14.4.9169-9182>
114. D. Majhi, B.N. Patra, Polyaniline and sodium alginate nanocomposite: a pH-responsive adsorbent for the removal of organic dyes from water. *RSC Adv.* **10**(71), 43904–43914 (2020). <https://doi.org/10.1039/D0RA08125F>
115. F.N. Ajjan, N. Casado, T. Rebiş, A. Elfwing, N. Solin, D. Mecerreyes, O. Inganäs, High performance PEDOT/Lignin biopolymer composites for electrochemical supercapacitors. *J. Mater. Chem. A* **4**(5), 1838–1847 (2016). <https://doi.org/10.1039/c5ta10096h>
116. Y. Wu, J. Wang, X. Qiu, R. Yang, H. Lou, X. Bao, Y. Li, Highly efficient inverted perovskite solar cells with sulfonated lignin doped PEDOT as hole extract layer. *ACS Appl. Mater. Interfaces* **8**(19), 12377–12383 (2016). <https://doi.org/10.1021/acsmi.6b00084>
117. H. Huang, C. Han, G. Wang, C. Feng, Lignin combined with polypyrrole as a renewable cathode material for H₂O₂ generation and its application in the electro-fenton process for azo dye removal. *Electrochim. Acta* **259**, 637–646 (2018). <https://doi.org/10.1016/j.electacta.2017.11.014>
118. C.R. Cena, L.F. Malmonge, J.A. Malmonge, Layer-by-Layer thin films of polyaniline alternated with natural rubber and their potential application as a chemical sensor. *J. Polym. Res* **24**(1), 1–7 (2016). <https://doi.org/10.1007/s10965-016-1170-7>
119. G. Dognani, A.A. da Silva, F.C. Cabrera, F.L. Faita, C.A.T. Saénz, I.H. Bechtold, A. E. Job, D.L.S. Agostini, Electrospun natural rubber fibers-based flexible conductive membranes. *Rev. Mater.* **25**(3), 1–9 (2020). <https://doi.org/10.1590/s1517-707620200003.1116>
120. W. Serrano, A. Meléndez, I. Ramos, N.J. Pinto, Poly(lactic acid)/Poly(3-hexylthiophene) composite nanofiber fabrication for electronic applications. *Polym. Int* **65**(5), 503–507 (2016). <https://doi.org/10.1002/pi.5081>
121. A. Abedi, M. Hasanzadeh, L. Tayebi, Conductive nanofibrous chitosan/PEDOT:PSS tissue engineering scaffolds. *Mater. Chem. Phys.* **237**, 121882 (2019). <https://doi.org/10.1016/j.matchemphys.2019.121882>
122. Y. Zhang, H. Xu, M. Chen, P. Chen, G. Gou, Y. Chen, Simultaneous adsorption and degradation tetracycline and heavy metals using polyaniline/chitosan to loading nanoscale zero-valent iron. *Phys. Chem. Liq.* **60**(3), 351–368 (2022). <https://doi.org/10.1080/00319104.2021.1972298>

123. S.K. Mahadeva, S. Yun, J. Kim, Flexible humidity and temperature sensor based on cellulose-polypyrrole nanocomposite. *Sens. Actuators, A*, **165**(2), 194–199 (2011). <https://doi.org/10.1016/j.sna.2010.10.018>.
124. J. Thunberg, T. Kalogeropoulos, V. Kuzmenko, D. Hägg, S. Johannesson, G. Westman, P. Gatenholm, In situ synthesis of conductive polypyrrole on electrospun cellulose nanofibers: scaffold for neural tissue engineering. *Cellulose* **22**(3), 1459–1467 (2015). <https://doi.org/10.1007/s10570-015-0591-5>
125. C. Esmaili, M.M. Abdi, A.P. Mathew, M. Jonoobi, K. Oksman, M. Rezayi, Synergy effect of nanocrystalline cellulose for the biosensing detection of glucose. *Sensors* **15**(10), 24681–24697 (2015). <https://doi.org/10.3390/s151024681>
126. M. Lay, J.A. Méndez, M. Delgado-Aguilar, K.N. Bun, F. Vilaseca, Strong and electrically conductive nanopaper from cellulose nanofibers and polypyrrole. *Carbohydr. Polym.* **152**, 361–369 (2016). <https://doi.org/10.1016/j.carbpol.2016.06.102>
127. L. Yang, X. Xu, M. Liu, C. Chen, J. Cui, X. Chen, K. Wu, D. Sun, Wearable and flexible bacterial cellulose/polyaniline ammonia sensor based on a synergistic doping strategy. *Sensors Actuat. B-Chem.* **334**, 129647 (2021). <https://doi.org/10.1016/j.snb.2021.129647>
128. M.V. Bhute, S.B. Kondawar, Electrospun poly(vinylidene fluoride)/cellulose acetate/AgTiO₂ nanofibers polymer electrolyte membrane for lithium ion battery. *Solid State Ion.* **333**, 38–44 (2019). <https://doi.org/10.1016/j.ssi.2019.01.019>
129. M. Salado, S. Lanceros-Mendez, E. Lizundia, Free-standing intrinsically conducting polymer membranes based on cellulose and poly(vinylidene fluoride) for energy storage applications. *Eur. Polym. J.* **144**, 110240 (2021). <https://doi.org/10.1016/j.eurpolymj.2020.110240>.
130. R.L. Razalli, M.M. Abdi, P.M. Tahir, A. Moradbak, Y. Sulaiman, L.Y. Heng, Polyaniline-modified nanocellulose prepared from semantan bamboo by chemical polymerization: preparation and characterization. *RSC Adv.* **7**(41), 25191–25198 (2017). <https://doi.org/10.1039/c7ra03379f>
131. O.A.T. Dias, S. Konar, A.L. Leão, M. Sain, Flexible electrically conductive films based on nanofibrillated cellulose and polythiophene prepared via oxidative polymerization. *Carbohydr. Polym.* **220**, 79–85 (2019). <https://doi.org/10.1016/j.carbpol.2019.05.057>
132. L. Wang, S. Chen, P. Wu, K. Wu, J. Wu, G. Meng, J. Hou, Z. Liu, X. Guo, Enhanced optical absorption and pollutant adsorption for photocatalytic performance of three-dimensional porous cellulose aerogel with BiVO₄ and PANI. *J. Mat. Res.* **35**(10), 1316–1328 (2020). <https://doi.org/10.1557/jmr.2020.40>
133. J. Guo, Y. Yu, H. Wang, H. Zhang, X. Zhang, Y. Zhao, Conductive polymer hydrogel microfibers from multiflow microfluidics. *Small* **15**(15), 1–7 (2019). <https://doi.org/10.1002/sml.201805162>
134. C.J. Wright, B.Z. Molino, J.H.Y. Chung, J.T. Pannell, M. Kuester, P.J. Molino, T.W. Hanks, Synthesis and 3D printing of conducting alginate–polypyrrole ionomers. *Gels* **6**(2), 1–12 (2020). <https://doi.org/10.3390/gels6020013>
135. M. Maqbool, H.N. Bhatti, S. Sadaf, M.M. AL-Anazy, M. Iqbal, Biocomposite of polyaniline and sodium alginate with *Oscillatoria* biomass: a potential adsorbent for the removal of basic blue 41. *J. Mat. Res. Tech.*, **9**(6), 14729–14741 (2020). <https://doi.org/10.1016/j.jmrt.2020.10.017>
136. S. Mongkolkitikul, N. Paradee, A. Sirivat, Electrically controlled release of ibuprofen from conductive poly(3-Methoxydiphenylamine)/crosslinked pectin hydrogel. *Eur. J. Pharm. Sci.* **112**, 20–27 (2018). <https://doi.org/10.1016/j.ejps.2017.10.043>
137. E.N. Zare, M.M. Lakouraj, M. Mohseni, Biodegradable polypyrrole/dextrin conductive nanocomposite: Synthesis, characterization, antioxidant and antibacterial activity. *Synth. Met.* **187**, 9–16 (2014). <https://doi.org/10.1016/j.synthmet.2013.09.045>
138. E.N. Zare, M.M. Lakouraj, Biodegradable polyaniline/dextrin conductive nanocomposites: synthesis, characterization, and study of antioxidant activity and sorption of heavy metal ions. *Iran Polym. J.* **23**, 257–266 (2014). <https://doi.org/10.1007/s13726-014-0221-3>
139. K. Wasa, M. Kitabatake, H. Adachi, in *Thin Film Materials Technology: Sputtering of Compound Materials* (William Andrew Publishing, 2004), pp. 1–16. <https://doi.org/10.30919/esmm5f970>.

140. E. Empting, M. Klopotek, A. Hinderhofer, F. Schreiber, M. Oettel, Lattice gas study of growth scenarios and transitions between them: role of substrate. *Phys. Rev. E* **103**(2), 23302 (2020). <https://doi.org/10.1103/PhysRevE.103.023302>
141. R. Rathanasamy, S. Sahoo, J.H. Lee, A.K. Das, M. Somasundaram, S.K. Palaniappan, S. Sivaraj, Carbon-based multi-layered films for electronic application: a review. *J. Electron. Mater.* **50**, 1845–1892 (2021). <https://doi.org/10.1007/s11664-020-08724-4>
142. D.S. Correa, E.S. Medeiros, J.E. Oliveira, L.G. Paterno, L.H.C. Mattoso, Nanostructured conjugated polymers in chemical sensors: synthesis, properties and applications. *J. Nanosci. Nanotechnol.* **14**, 1–19 (2014). <https://doi.org/10.1166/jnn.2014.9362>
143. C. Martin, B. Jean, Nanocellulose/polymer multilayered thin films: tunable architectures towards tailored physical properties. *Nord. Pulp. Pap. Res. J.* **29**(1), 19–30 (2014). <https://doi.org/10.3183/npprj-2014-29-01-p019-030>
144. L.A. Mercante, V.P. Scagion, F.L. Migliorini, L.H.C. Mattoso, D.S. Correa, Electrospinning-based (bio)sensors for food and agricultural applications: a review. *Trends Anal. Chem.* **91**, 91–103 (2017). <https://doi.org/10.1016/j.trac.2017.04.004>
145. D.M. dos Santos, D.S. Correa, E.S. Medeiros, J.E. Oliveira, L.H.C. Mattoso, Advances in functional polymer nanofibers: from spinning fabrication techniques to recent biomedical applications. *ACS Appl. Mater. Interfaces* **12**(41), 45673–45701 (2020). <https://doi.org/10.1021/acsami.0c12410>
146. A.L. Yarin, Coaxial electrospinning and emulsion electrospinning of core-shell Fibers. *Polym. Adv. Technol.* **22**(3), 310–317 (2011). <https://doi.org/10.1002/pat.1781>
147. T. Blachowicz, A. Ehrmann, Conductive electrospun nanofiber mats. *Materials* **13**, 152 (2020). <https://doi.org/10.3390/ma13010152>
148. Y. Zhang, L. Zhang, K. Cui, S. Ge, X. Cheng, M. Yan, J. Yu, H. Liu, Flexible electronics based on micro/nanostructured paper. *Adv. Mater.* **1801588**, 1–39 (2018). <https://doi.org/10.1002/adma.201801588>
149. F. Arduini, L. Micheli, V. Scognamiglio, V. Mazzaracchio, D. Moscone, Sustainable materials for the design of forefront printed (bio)sensors applied in agrifood sector. *TrAC - Trends Anal. Chem.* **128**, 115909 (2020). <https://doi.org/10.1016/j.trac.2020.115909>
150. Q. Sun, B. Qian, K. Uto, J. Chen, X. Liu, T. Minari, Functional biomaterials towards flexible electronics and sensors. *Biosens. Bioelectron.* **119**, 237–251 (2018). <https://doi.org/10.1016/j.bios.2018.08.018>
151. M. Golmohammadi, E. Morales-Narváez, T. Naghdi, A. Merkoçi, Nanocellulose in sensing and biosensing. *Chem. Mater.* **29**(13), 5426–5446 (2017). <https://doi.org/10.1021/acs.chemmater.7b01170>
152. J. Janata, A. Bezegh, Chemical sensors. *Anal. Chem.* **60**(12), 62–74 (1988). <https://doi.org/10.1021/ac00163a004>
153. A. Hulanicki, S. Glab, F. Ingman, Chemical sensors: definitions and classification. *Pure Appl. Chem.* **63**(9), 1247–1250 (1991). <https://doi.org/10.1351/pac199163091247>
154. B. Adhikari, S. Majumdar, Polymers in sensor applications. *Prog. Polym. Sci.* **29**(7), 699–766 (2004). <https://doi.org/10.1016/j.progpolymsci.2004.03.002>
155. S. Bano, N. Ahmad, S. Sultana, S. Sabir, M.Z. Khan, Preparation and study of ternary polypyrrole-tin oxide-chitin nanocomposites and their potential applications in visible light photocatalysis and sensors. *J. Environ. Chem. Eng.* **7**, 103012–103024 (2019). <https://doi.org/10.1016/j.jece.2019.103012>
156. M. Gerard, Application of conducting polymers to biosensors. *Biosens. Bioelectron.* **17**(5), 345–359 (2002). [https://doi.org/10.1016/s0956-5663\(01\)00312-8](https://doi.org/10.1016/s0956-5663(01)00312-8)
157. L. Yang, L. Yang, S. Wu, F. Wei, Y. Hu, X. Xu, L. Zhang, D. Sun, Three-dimensional conductive organic sulfonic acid co-doped bacterial cellulose/polyaniline nanocomposite films for detection of ammonia at room temperature. *Sensors Actuat. B Chem.* **323**, 128689–128698 (2020). <https://doi.org/10.1016/j.snb.2020.128689>
158. S. Uzunçar, N. Özdoğan, M. Ak, Amperometric Detection of Glucose and H₂O₂ using Peroxide selective Electrode based on carboxymethylcellulose/polypyrrole and prussian blue nanocomposite. *Mater. Today Commun.* **21**, 101839 (2021) <https://doi.org/10.1016/j.mtc.2020.101839>.

159. G. Xu, S. Liang, J. Fan, G. Sheng, X. Luo, Amperometric sensing of nitrite using a glassy carbon electrode modified with a multilayer consisting of carboxylated nanocrystalline cellulose and poly(diallyldimethyl ammonium) ions in a PEDOT host. *Microchim. Acta* **183**(6), 2031–2037 (2016). <https://doi.org/10.1007/s00604-016-1842-3>
160. A.P. Tjahyono, K.C. Aw, J. Travas-Sejdic, A novel polypyrrole and natural rubber based flexible large strain sensor. *Sens. Actuators B Chem.* **166–167**, 426–437 (2012). <https://doi.org/10.1016/j.snb.2012.02.083>
161. M. Wang, Q. Gao, J. Gao, C. Zhu, K. Chen, Core-shell PEDOT: PSS/SA composite fibers via a single-nozzle technique enables wearable sensor applications. *J. Mater. Chem. C* (2020). <https://doi.org/10.1039/c9tc05527d>
162. K. Ren, Y. Cheng, C. Huang, R. Chen, Z. Wang, J. Wei, Self-healing conductive hydrogels based on alginate, gelatin and polypyrrole serve as repairable circuit and mechanical sensor. *J. Mater. Chem. B.* **7**(37), 5704–5712 (2019). <https://doi.org/10.1039/c9tb01214a>.
163. M. Luo, M. Li, Y. Li, K. Chang, K. Liu, Q. Liu, Y. Wang, Z. Lu, X. Liu, D. Wang, In-situ polymerization of PPY/cellulose composite sponge with high elasticity and conductivity for the application of pressure sensor. *Compos. Commun.* **6**, 68–72 (2017). <https://doi.org/10.1016/j.coco.2017.10.001>
164. M.M. Ayad, N.A. Salahuddin, I.M. Minisy, W.A. Amer, Chitosan/polyaniline nanofibers coating on the quartz crystal microbalance electrode for gas sensing. *Sens. Actuators B Chem.* **202**, 144–153 (2014). <https://doi.org/10.1016/j.snb.2014.05.046>
165. I. Ragazzini, I. Gualandi, S. Selli, C. Polizzi, M.C. Cassani, D. Nanni, F. Gambassi, F. Tarterini, D. Tonelli, E. Scavetta, B. Ballarin, A simple and industrially scalable method for making a PANI-modified cellulose touch sensor. *Carbohydr. Polym.* **254** 117304 (2021). <https://doi.org/10.1016/j.carbpol.2020.117304>.
166. S.K. Shukla, O. Parlak, S. Shukla, S. Mishra, A.P.F. Turner, A. Tiwari, Self-reporting micellar polymer nanostructures for optical urea biosensing. *Ind. Eng. Chem. Res.* **53**(20), 8509–8514 (2014). <https://doi.org/10.1021/ie5012799>
167. A. Jasim, M.W. Ullah, Z. Shi, X. Lin, G. Yang, Fabrication of bacterial cellulose/polyaniline/single-walled carbon nanotubes membrane for potential application as biosensor. *Carbohydr. Polym.* **163**, 62–69 (2017). <https://doi.org/10.1016/j.carbpol.2017.01.056>
168. B. Thakur, C.A. Amarnath, S.N. Sawant, Pectin coated polyaniline nanoparticles for an amperometric glucose biosensor. *RSC Adv.* **4**(77), 40917–40923 (2014). <https://doi.org/10.1039/c4ra05264a>
169. X. Xu, S. Wu, J. Cui, L. Yang, K. Wu, X. Chen, D. Sun, Highly stretchable and sensitive strain sensor based on polypyrrole coated bacterial cellulose fibrous network for human motion detection. *Compos. Part. B-Eng.* **221**, 108665 (2021). <https://doi.org/10.1016/j.compositesb.2021.108665>
170. Q. Zhang, X. Wang, J. Fu, R. Liu, H. He, J. Ma, M. Yu, S. Ramakrishna, Y. Long, Electrospinning of Ultrafine Conducting Polymer Composite Nanofibers with Diameter Less than 70 nm as High Sensitive Gas Sensor. *Materials* **11**(9), 1744 (2018). <https://doi.org/10.3390/ma11091744>
171. V. Gautam, K.P. Singh, V.L. Yadav, Polyaniline/MWCNTs/starch modified carbon paste electrode for non-enzymatic detection of cholesterol: application to real sample (cow milk). *Anal. Bioanal. Chem.* **410**(8), 2173–2181 (2018). <https://doi.org/10.1007/s00216-018-0880-6>
172. A. Manzari-Tavakoli, R. Tarasi, R. Sedghi, A. Moghimi, H. Niknejad, Fabrication of nanochitosan incorporated polypyrrole/alginate conducting scaffold for neural tissue engineering. *Sci. Rep.* **10**, 22012 (1–10) (2020). <https://doi.org/10.1038/s41598-020-78650-2>.
173. H. Amani, H. Kazerouni, H. Hassanpoor, A. Akbarzadeh, H. Pazoki-Toroudi, Tailoring synthetic polymeric biomaterials towards nerve tissue engineering: a review. *Artif. Cells Nanomed. Biotechnol.* **47**(1), 3524–3539 (2019). <https://doi.org/10.1080/21691401.2019.1639723>
174. B. Dhandayuthapani, Y. Yoshida, T. Maekawa, D.S. Kumar, Polymeric scaffolds in tissue engineering application: a review. *Int. J. Polym. Sci.* **2011**, 1–19 (2011). <https://doi.org/10.1155/2011/290602>

175. B. Raynald, X. Shu, J. Liu, H. Zhou, J. Huang, X. Wang, C. Sun, Y. Qin, An, Polypyrrole/poly(lactic acid) nanofibrous scaffold cotransplanted with bone marrow stromal cells promotes the functional recovery of spinal cord injury in rats. *CNS Neurosci. Ther.* **25**(9), 951–964 (2019). <https://doi.org/10.1111/cns.13135>
176. D. Xu, L. Fan, L. Gao, Y. Xiong, Y. Wang, Q. Ye, A. Yu, H. Dai, Y. Yin, J. Cai, L. Zhang, Micro-nano-structured Polyaniline Assembled in Cellulose Matrix Via Interfacial Polymerization for Applications in Nerve Regeneration. *ACS Appl. Mater. Interfaces* **8**(27), 17090–17097 (2016). <https://doi.org/10.1021/acsami.6b03555>
177. X. Zhao, P. Li, B. Guo, P.X. Ma, Antibacterial and conductive injectable hydrogels based on quaternized chitosan-graft-polyaniline/oxidized dextran for tissue engineering. *Acta Biomater.* **26**, 236–248 (2015). <https://doi.org/10.1016/j.actbio.2015.08.006>
178. J.P. Saikia, S. Banerjee, B.K. Konwar, A. Kumar, Biocompatible novel starch/polyaniline composites: Characterization, anti-cytotoxicity and antioxidant activity. *Colloids Surf. B: Biointerfaces* **81**(1), 158–164 (2010). <https://doi.org/10.1016/j.colsurfb.2010.07.005>
179. R. Dong, X. Zhao, B. Guo, P.X. Ma, Self-healing conductive injectable hydrogels with antibacterial activity as cell delivery carrier for cardiac cell therapy. *ACS Appl. Mater. Interfaces* **8**(27), 17138–17150 (2016). <https://doi.org/10.1021/acsami.6b04911>
180. J. Qu, X. Zhao, Y. Liang, Y. Xu, P.X. Ma, B. Guo, Degradable conductive injectable hydrogels as novel antibacterial, anti-oxidant wound dressings for wound healing. *Chem. Eng. J.* **362**, 548–560 (2019). <https://doi.org/10.1016/j.cej.2019.01.028>
181. S. Li, A. Jasim, W. Zhao, L. Fu, M.W. Ullah, Z. Shi, G. Yang, Fabrication of pH-electroactive Bacterial Cellulose/Polyaniline Hydrogel for the Development of a Controlled Drug Release System. *ES Mater. Manuf.* **1**, 41–49 (2018). <https://doi.org/10.30919/esmm5f120>
182. M.S.A. Hamzah, A. Austad, S.I.A. Razak, N.H.M. Nayan, Tensile and wettability properties of electrospun polycaprolactone coated with pectin/polyaniline composite for drug delivery application. *Int. J. Struct. Integr.* **10**(5), 704–713 (2019). <https://doi.org/10.1108/IJSI-04-2019-0033>
183. A.M. Kumar, A.Y. Adesina, M.A. Hussein, S.A. Umoren, S. Ramakrishna, S. Saravanan, Preparation and characterization of Pectin/Polypyrrole based multifunctional coatings on TiNbZr alloy for orthopaedic applications. *Carbohydr. Polym.*, **242**, 116285 (2020). <https://doi.org/10.1016/j.carbpol.2020.116285>
184. F. Imani, R. Karimi-Soflou, I. Shabani, A. Karkhaneh, PLA electrospun nanofibers modified with polypyrrole-grafted gelatin as bioactive electroconductive scaffold. *Polymer* **218**, 123487 (2021). <https://doi.org/10.1016/j.polymer.2021.123487>
185. P.T. Bertuoli, J. Ordoño, E. Armelin, S. Pérez-Amodio, A.F. Baldissera, C.A. Ferreira, J. Puiggalí, E. Engel, L.J. del Valle, C. Alemán, Electrospun Conducting and Biocompatible Uniaxial and Core-Shell Fibers Having Poly(lactic acid), Poly(ethylene glycol), and Polyaniline for Cardiac Tissue Engineering. *ACS Omega* **4**(2), 3660–3672 (2019). <https://doi.org/10.1021/acsomega.8b03411>
186. J. Zhou, Y. Wang, L. Cheng, Z. Wu, X. Sun, J. Peng, Preparation of polypyrrole-embedded electrospun poly(lactic acid) nanofibrous scaffolds for nerve tissue engineering. *Neural. Regen. Res.* **11**(10), 1644–1652 (2016). <https://doi.org/10.4103/1673-5374.193245>
187. F. Zha, W. Chen, L. Hao, C. Wu, M. Lu, L. Zhang, D. Yu, Electrospun cellulose-based conductive polymer nanofibrous mats: composite scaffolds and their influence on cell behavior with electrical stimulation for nerve tissue engineering. *Soft Matter* **16**(28), 6591–6598 (2020). <https://doi.org/10.1039/d0sm00593b>
188. F. Khan, P. Manivasagan, D.T. Nguyen Pham, J. Oh, S.-K. Kim, Y.-M. Kim, Antibiofilm and antivirulence properties of chitosan-polypyrrole nanocomposites to *Pseudomonas aeruginosa*. *Microb. Pathog.*, **128**, 363–373 (2019). <https://doi.org/10.1016/j.micpath.2019.01.033>
189. X. Fu, J.K., Wang, A.C. Ramírez-Pérez, C. Choong, G. Lisak, Flexible conducting polymer-based cellulose substrates for on skin applications. *Mater. Sci. Eng. C*, **108**, 110392 (2020). <https://doi.org/10.1016/j.msec.2019.110392>
190. S. Wang, S. Guan, W. Li, D. Ge, J. Xu, C. Sun, T. Liu, X. Ma, 3D culture of neural stem cells within conductive PEDOT layer-assembled chitosan/gelatin scaffolds for neural tissue

- engineering. *Mater. Sci. Eng. C* **93**, 890–901 (2018). <https://doi.org/10.1016/j.msec.2018.08.054>
191. L. Ferlauto, A.N. D'Angelo, P. Vagni, M.J.I. Airaghi Leccardi, F.M. Mor, E.A. Cuttaz, M. Heuschkel, L. Stoppini, D. Ghezzi, Development and Characterization of PEDOT:PSS/Alginate Soft Microelectrodes for Application in Neuroprosthetics. *Front. Neurosci.*, **12**, 648 (2018). <https://doi.org/10.3389/fnins.2018.00648>.
 192. Z. Atoufi, P. Zarrintaj, G.H. Motlagh, A. Amiri, Z. Bagher, S.K. Kamrava, A novel bio electro active alginate-aniline tetramer/agarose scaffold for tissue engineering: synthesis, characterization, drug release and cell culture study. *J. Biomater. Sci. Polym. Ed.* **28**(15), 1617–1638 (2017). <https://doi.org/10.1080/09205063.2017.1340044>
 193. E.N. Zare, T. Agarwal, A. Zarepour, F. Pinelli, A. Zarrabi, F. Rossi, M. Ashrafizadeh, A. Maleki, M. Shahbazi, T.K. Maiti, R.S. Varma, F.R. Tay, M.R. Hamblin, V. Mattoli, P. Makvandi, *Appl. Mater. Today* **24**, 101117–101152 (2021). <https://doi.org/10.1016/j.apmt.2021.101117>
 194. A. González, E. Goikolea, J.A. Barrena, R. Mysyk, Review on supercapacitors: Technologies and materials. *Renew. Sust. Energ. Rev.* **58**, 1189–1206 (2016). <https://doi.org/10.1016/j.rser.2015.12.249>
 195. Z. Lin, E. Goikolea, A. Balducci, K. Naoi, P.L. Taberna, M. Salanne, G. Yushin, P. Simon, Materials for supercapacitors: When Li-ion battery power is not enough. *Mater. Today* **21**(4), 419–436 (2018). <https://doi.org/10.1016/j.mattod.2018.01.035>
 196. L.M. Santino, S. Acharya, J.M. D'Arcy, Low-temperature vapour phase polymerized polypyrrole nanobrushes for supercapacitors. *J. Mater. Chem. A* **5**(23), 11772–11780 (2017). <https://doi.org/10.1039/c7ta00369b>
 197. C. Lamy, A. Lima, V. LeRhun, F. Delime, C. Coutanceau, J.-M. Léger, Recent advances in the development of direct alcohol fuel cells (DAFC). *J. Power Sources* **105**(2), 283–296 (2002). [https://doi.org/10.1016/s0378-7753\(01\)00954-5](https://doi.org/10.1016/s0378-7753(01)00954-5)
 198. X. Cheng, Z., Shi, N. Glass, L. Zhang, J. Zhang, D. Song, Z. Liu, H. Wang, J. Shen, A review of PEM hydrogen fuel cell contamination: Impacts, mechanisms, and mitigation. *J. Power Sources*, **165**(2), 739–756 (2007). <https://doi.org/10.1016/j.jpowsour.2006.12.012>.
 199. M. J. Cooney, V. Svoboda, C. Lau, G. Martin, S.D. Minteer, Enzyme catalysed biofuel cells. *Energy Environ. Sci.*, **1**(3), 320. <https://doi.org/10.1039/b809009b>.
 200. B. Li, H. Lopez-Beltran, C. Siu, K.H. Skorenko, H. Zhou, W.E. Bernier, M.S. Whittingham, W.E. Jones Jr., Vapor Phased Polymerized PEDOT/Cellulose Paper Composite for Flexible Solid-State Supercapacitor. *ACS Appl. Energy Mater.* **3**, 1559–1568 (2020). <https://doi.org/10.1021/acsaem.9b02044>
 201. H. Tan, D. Xiao, R. Navik, Y. Zhao, Facile Fabrication of Polyaniline/Pristine Graphene–Bacterial Cellulose Composites as High-Performance Electrodes for Constructing Flexible All-Solid-State Supercapacitors. *ACS Omega* **6**, 11427–11435 (2021). <https://doi.org/10.1021/acsomega.1c00442>
 202. R. Liu, L. Ma, S. Huang, J. Mei, J. Xu, G. Yuan, Polyaniline/graphene/bacterial cellulose flexible electrodes for supercapacitor. *New J. Chem.* **41**(2), 857–864 (2017). <https://doi.org/10.1039/c6nj03107b>
 203. M.G. Hosseini, E. Shahryari, A novel high-performance supercapacitor based on chitosan/graphene oxide-MWCNT/polyaniline. *J. Colloid Interface Sci.* **496**, 371–381 (2017). <https://doi.org/10.1016/j.jcis.2017.02.027>
 204. Y. Li, X. Zhao, Q. Xu, Q. Zhang, D. Chen, Facile preparation and enhanced capacitance of the polyaniline/sodium alginate nanofiber network for supercapacitors. *Langmuir*, **27**(10), 6458–6463 (2011). <https://doi.org/10.1021/la2003063>.
 205. Q. Wang, H. Wang, P. Du, J. Liu, D. Liu, P. Liu, Porous polylactic acid/carbon nanotubes/polyaniline composite film as flexible free-standing electrode for supercapacitors. *Electrochim. Acta* **294**, 312–324 (2019). <https://doi.org/10.1016/j.electacta.2018.10.108>
 206. W. Nie, L. Liu, Q. Li, S. Zhang, J. Hu, X. Yang, X. Ding, A wearable fiber-shaped supercapacitor based on a poly(lactic acid) filament and high loading polypyrrole. *RSC Adv.* **9**(33), 19180–19188 (2019). <https://doi.org/10.1039/c9ra02171j>

207. L. Ma, R. Liu, H. Niu, M. Zhao, Y. Huang, Flexible and freestanding electrode based on polypyrrole/graphene/bacterial cellulose paper for supercapacitor. *Compos. Sci. Technol.* **137**, 87–93 (2016). <https://doi.org/10.1016/j.compscitech.2016.10.027>
208. H. Huang, J. Yao, Y. Liu, X. Tuo, Y. Da, X. Zeng, L. Li, 3D Nanostructured Polypyrrole/Sodium Alginate Conducting Hydrogel from self-assembly with High Supercapacitor Performance. *J. Macromol. Sci. B* **56**(8), 532–540 (2017). <https://doi.org/10.1080/00222348.2017.1342951>
209. H. Wang, E. Zhu, J. Yang, P. Zhou, D. Sun, W. Tang, Bacterial Cellulose Nanofiber-Supported Polyaniline Nanocomposites with Flake-Shaped Morphology as Supercapacitor Electrodes. *J. Phys. Chem. C* **116**(24), 13013–13019 (2012). <https://doi.org/10.1021/jp301099r>
210. F. Wang, H.J. Kim, S. Park, C.D. Kee, S.J. Kim, I.K. Oh, Bendable and flexible supercapacitor based on polypyrrole-coated bacterial cellulose core-shell composite network. *Compos. Sci. Tech.* **128**, 33–40 (2016). <https://doi.org/10.1016/j.compscitech.2016.03.012>
211. E.C.A. Trindade, R.V. Antônio, R. Brandes, L. Souza, G. Neto, V.M.M. Vargas, C.A. Carminnatti, D.O.S. Recouvreux, Carbon fiber-embedded bacterial cellulose/polyaniline nanocomposite with tailored for microbial fuel cells electrode. *J. Appl. Polymer Sci.* **49036**, 1–9 (2020). <https://doi.org/10.1002/app.49036>
212. V. Vijayakumar, D. Khashtgir, Hybrid composite membranes of chitosan/sulfonated polyaniline/silica as polymer electrolyte membrane for fuel cells. *Carbohydr. Polym.* **179**, 152–163 (2018). <https://doi.org/10.1016/j.carbpol.2017.09.083>
213. Y. Wang, Q. Wen, Y. Chen, C. Lin, J. Zheng, W. Li, Conductive polypyrrole-carboxymethyl cellulose-titanium nitride/carbon brush hydrogels as bioanodes for enhanced energy output in microbial fuel cells. *Energy*, 117942 (2020). <https://doi.org/10.1016/j.energy.2020.117942>
214. M. Mashkour, M. Rahimnejad, M. Mashkour, F. Soavi, Electro-polymerized polyaniline modified conductive bacterial cellulose anode for supercapacitive microbial fuel cells and studying the role of anodic biofilm in the capacitive behavior. *J. Power Sources* **478**, 228822 (2020). <https://doi.org/10.1016/j.jpowsour.2020.228822>
215. Y. Wang, Q. Wen, Y. Chen, H. Zheng, S. Wang, Enhanced performance of microbial fuel cell with polyaniline/sodium alginate/carbon brush hydrogel bioanode and removal of COD. *Energy* **202**, 117780 (2020). <https://doi.org/10.1016/j.energy.2020.117780>
216. E. Mitraha, M. Vagin, A. Sjöstedt, M. Berggren, K.M.O. Håkansson, M.P. Jonsson, X. Crispin, PEDOT-cellulose gas diffusion electrodes for disposable fuel cells. *Adv. Sustain. Syst.*, **12**(3), 1900097 (2019). <https://doi.org/10.1002/adsu.201900097>
217. M. Mashkour, M. Rahimnejad, M. Mashkour, Bacterial cellulose-polyaniline nanobiocomposite: A porous media hydrogel bioanode enhancing the performance of microbial fuel cell. *J. Power Sources* **325**, 322–328 (2016). <https://doi.org/10.1016/j.jpowsour.2016.06.063>
218. S. Rogalsky, J.F. Bardeau, S. Makhno, N. Babkina, O. Tarasyuk, T. Cherniavska, I. Orlovska, N. Kozyrovska, O. Brovko, New proton conducting membrane based on bacterial cellulose/polyaniline nanocomposite film impregnated with guanidinium-based ionic liquid. *Polymer* **142**, 183–195 (2018). <https://doi.org/10.1016/j.polymer.2018.03.032>
219. M. Kizling, K. Stolarczyk, J.S.S. Kiat, P. Tammela, Z. Wang, L. Nyholm, R. Bilewicz, Pseudocapacitive polypyrrole-nanocellulose composite for sugar-air enzymatic fuel cells. *Electrochem. Commun.* **50**, 55–59 (2015). <https://doi.org/10.1016/j.elecom.2014.11.008>

Mechanical and Sliding Wear Performance of ZA27-Gr Alloy Composites for Bearing Applications: Analysis Using Preference Selection Index Method



Ashiwani Kumar and Mukesh Kumar

Abstract In this chapter, the sliding wear and mechanical performance of Gr-ZA-27 alloy composites are investigated following ASTM standards. Taguchi methodology is used in designing sliding wear experiments, and the same methodology is used for parametric optimization. In order to comprehend the associated wear mechanisms responsible for surface damage, surface micrograph studies employing scanning electron microscopy (SEM) are conducted. Furthermore, the rank of designed compositions is evaluated using Preference Selection Index (PSI), and decision-making technique. The physical and mechanical characteristics of alloy composites with reinforcement are found to be improved, including void content (1.33–2.50), hardness (107–171 HV), compressive strength (406–496 MPa), flexural strength (300–490 MPa), tensile strength (290–428 MPa), impact strength (22.76–64 J), and sliding wear performance. It is found that the AGr-6 alloy composite showed to optimize the overall physical, mechanical, and sliding wear performance. The evaluation of performance data using the PSI and decision-making tool reveals that the order of material composition that optimizes the required performance is AGr-6 > AGr-4 > AGr-2 > AGr-0. As both decisions are attained, decision-making technologies like PSI can be applied to these challenges of material selection.

Keywords ZA-27 alloy · Graphite powder · Dry sliding wear · Mechanical properties · Preference Selection Index method (PSI)

A. Kumar (✉)

Department of Mechanical Engineering, Feroze Gandhi Institute of Engineering and Technology, Raebareli 229316, U.P., India
e-mail: ashi15031985@gmail.com

M. Kumar

Department of Mechanical Engineering, Malaviya National Institute of Technology, Jaipur 302017, Rajasthan, India

1 Introduction

ZA-27 alloy is a typical monolithic material that is employed in automobile company. This material is used for bearing material application and it shows outstanding characterizations such as fluidity, castability, mechanical properties and wear resistance. Tribological-based properties are being opted into consideration for different applications such as piston material, cylinder and aerospace/automobile industry [1, 2]. Raju et al. [3] investigated the mechanical characteristics of Silicon-carbide (SiC)-ZA27 alloy. It was found that the increase in weight percentage of reinforcement improves the mechanical properties (such as hardness, tensile strength, impact strength, and compressive strength) of composites. The improvement in mechanical properties is due to the effect of ceramic reinforced based alloy matrix. Dalmis et al. [4] investigated the impact of inclusion of Gr nano powder particles on the mechanical and physical characterization of ZA-27 alloy composites. It is found that the hardness and tensile strength diminish as the filler content increases. The ductility of composite increases with the increases in Gr content. It may be attributed to the improvement in mechanical characteristics because of the strong bonding between matrix and reinforcement. Ranganath et al. [5] studied the mechanical properties and fractography characteristics of TiO₂ reinforced ZA27 alloy based composite. It was observed that mechanical properties such as Young's modulus, ultimate tensile strength, yield strength, and hardness increase with the increase in TiO₂ content. Sharma et al. [6] investigated the influence of short glass fibres on the mechanical properties of cast ZA-27 alloy composites. It was found that the mechanical characteristics such as tensile strength, hardness, and Young's modulus improve with the increase in filler content. Alaneme et al. [7] studied the mechanical and wear behaviour performance of Steel chips reinforced ZA27 alloy based composites. It was found that increasing the weight percentage of reinforcement improved the composites' hardness and wear resistance. Girisha et al. [8] and Baradeswaran et al. [9] examined the effects of composites reinforced with graphite and the ZA-27 alloy. It was found that the increase in filler content resulted in better mechanical and tribological qualities. Kumar and Kumar [10] evaluated the mechanical and sliding wear performance improvement as the filler content rises. Similar findings are published by Ashiwani and Mukesh [11] and Kumar et al. [12]. It is noticed that the impendence of Gr reinforced ZA27 alloy composite indicated increased wear resistance of investigated composites with the increasing Gr content. In their study of the impact of AA7075SiC/Marble Dust/Graphite Hybrid alloy composites on their mechanical and sliding performance, Kumar et al. [13] discovered that the performance of the mechanical and sliding wear improved as the filler content increased. Using the PSI approach, Kumar et al. [14] determined the ranking performance of the composite by analysing the effects of Al₂O₃/SiC on the mechanical and wear performance of the AA2024 alloy. For the mechanical and sliding performance of particle filled alloy composite, similar results have been reported by other researchers [15–17]. The unit cost approach and digital logic method, which are used to analyze the performance of materials, were covered by Maleque et al. [18]. Similar outcomes have been reported

by Maniya [19] and Kumar [20], who proposed utilizing the presence selection index approach to choose the content and rank it in terms of preference. For the purpose of choosing materials for certain applications, design engineers can benefit from this strategy.

The mechanical and sliding wear performance of graphite-filled ZA27 alloy composites is covered in this chapter. Using decision-making tools and PSI techniques, the ranking of manufactured composite materials was carried out. Decision-making technologies such as PSI could be applied in such material selection issues because both decisions are tuned.

2 Materials and Methodology

2.1 Materials, Design and Fabrication Procedure

The ZA-27 alloy was obtained from Bharat Aerospace Metals in Mumbai, India, as rods with the following composition: aluminium (25–28 wt.%), Copper (1.0–2.5 wt.%), Magnesium (0.01–0.02 wt.%), Iron (~0.075 wt.%), lead (~0.006 wt.%), Tin (~0.003 wt.%), and the rest is Zinc wt.%. While Graphite particulates (99 μm) were procured from Savita Scientific Pvt. Ltd. Jaipur. The four alloy compositions (AGr-0, AGr-2, AGr-4, and AGr-6) were fabricated using a high vacuum casting method.

The precise fabrication process is as follows:

- The ZA-27 metal long rods that were measured out were cleaned and cut into little pieces. The tiny bits were melted using a high vacuum induction furnace inside a graphite crucible. The amount that had melted was maintained at 870°C for 20 minutes. After that, the temperature was decreased to between 430 and 660 °C (the alloy's solidus and liquid temperature). The quantities of reinforcements were separately preheated at 300 °C for 3 h.
- Magnesium powder (2 wt%) was added to the molten metal in order to increase the Gr phase's wettability.
- A completely automatic magnetic stirrer (made of stainless steel; speed: 280 rpm; time: 10 min.) was employed to ensure that the graphite phase was added uniformly to the melt.
- The mixture was placed into a stationary 150 × 90 × 10 mm³ cast iron mould and allowed to solidify to 30 °C in air for at least 45 min.
- The specimens were cut using a wire Electric Discharge Machine (EDM) in accordance with ASTM standards, and their dimensions were then polished with sandpaper in various sizes.

2.2 Physical and Mechanical Characterization

The physical characteristics of the Gr-reinforced ZA-27 alloy composite, including its actual density, theoretical density and vacancy fraction are investigated. The void fraction was determined using the water displacement method utilising the Archimedes principle approach and the ASTM D792 standard, and the experimental density of planned composite specimens was calculated. Using Eq. 1 [21], it was possible to calculate density of samples by using the rule of mixture:

$$\rho_c = \frac{1}{\left(\frac{W_p}{\rho_p}\right) + \left(\frac{W_m}{\rho_m}\right)} \quad (1)$$

where W stands for the weight fraction, p for the phase of particles and m for the phase of the matrix. ρ_p and ρ_m represent densities of the particulates and matrix phases respectively.

Using Eq. 2 [17], the voids fraction of planned composite samples was calculated.

$$\text{Void fraction} = \frac{\text{Theoretical } (\rho_t) - \text{Experimental } (\rho_e)}{\text{Theoretical } (\rho_t)} \quad (2)$$

The proposed composite of hardness was evaluated by using hardness tester (ASTM E92 standard; Walter Uhl testing tester). Specimens were tested for hardness under a 180 g load for 15 s. Each sample indentation is held using a diamond indenter. Vickers hardness was calculated using Eq. 3 using the average of the five measurements taken five times for each specimen of the specified composite.

$$\text{HV} = 1.854 \frac{L}{D} \quad (3)$$

where D is the indenter's diagonal dimension (in mm) and L is the applied load (in g).

The UTM equipment (ASTM: E-8) was used to performed tensile tests on composite specimens while parameters such as the specimen's (flat shape) dimensions of $160 \times 10 \times 10 \text{ mm}^3$ and the cross-head speed of 2 mm/s were chosen. An ASTM E-290 universal testing machine was used to conduct a flexural experiment on composite samples. Selected parameters, including (specimen dimension = $50 \times 10 \times 10 \text{ mm}^3$; span length = 40 mm; cross-head speed = 2 m/s), were carried out in accordance with the (ASTM E- 290) standard. Using Eq. 4 [12], the flexural strength (F) was calculated.

$$F = \frac{3PL}{2bt^2} \quad (4)$$

where P is the load (kg), b is the specimen's width (mm), t is the sample's thickness (mm) and L is the sample's span length (mm).

On impact tester equipment (executed in accordance with ASTM E-23) the composite specimen (impact strength) was completed, and the machine settings were chosen as follows: specimen size = $64 \times 12.8 \times 3.2 \text{ mm}^3$; depth of notch = 10.2 mm. The ASTM E9-09 compression tester was used to determine the compressive strength of the composite specimen, and the compression test on UTM was carried out with the following parameters: specimen size = $10 \times 10 \times 10 \text{ mm}^3$, span length = 0.5 mm, speed = 2 m/s.

2.3 Multi-Specimen Dry Sliding Wear Tribo-Meter

Multi-specimen Tribo-tester apparatus was used to measure the friction and tribological performance. Figure 1 presents an image of this apparatus, with required specifications of a revolving disc made of 62 HRC hardened steel, a specimen with dimensions of $14 \times 9 \times 10 \text{ mm}^3$, a load given to a fixed specimen in a vertical direction, and other details. A fixed load of 20 N and sliding velocities of 1, 1.25, 1.5, and 1.75 m/s were chosen as the steady state wear performance condition parameters. On the Tribo-tester, the analysis of sliding behaviour (five repetitions of 700 m each; constant disc track diameter = 40 mm) was done, and the composite wear rate was also acquired. Every test result was measured in an environmental setting. Following this, samples were taken using various sizes of abrasive paper, such as (200–600 grit), for a brief period of time to remove debris particles and collected material, which were taken for sampling, and regularly cleaned samples with alcohol.

The experimental design employed the Taguchi orthogonal array, with the parameters and their levels stated in Table 1. Each sample was then cleaned. Prior to this, the pin-type sample was weighed using an Electronic Balance Machine (EBM) with a $1 \times$

Fig. 1 Multi-specimen tribometer (Model: TR-705 of Ducom Instruments)



10⁻³ mg precision. The equipment was used to gather and analyse the experimentally recorded value on wear rate and coefficient of friction. As a result, Table 2 includes the experimental specific wear rate numerical values. Following Eq. 5 led to the development of a novel alloy composite with particular wear rates (Ws) [23].

$$W_s = \frac{\Delta m}{\rho \times v_s \times t \times f_n} \tag{5}$$

where Δm = mass loss (g); density (ρ); the sliding velocity (v_s); the test duration (t); and the normal load (f_n).

Table 1 Working range of selected parameters

| Control parameter | Level | | | | | Units |
|----------------------|-------|------|------|------|--|-------|
| | I | II | III | IV | | |
| Normal load (A) | 10 | 20 | 30 | 40 | | N |
| Filler content (B) | 0 | 2 | 4 | 6 | | % |
| Sliding velocity (C) | 1 | 1.25 | 1.50 | 1.75 | | m/s |
| Sliding distance (D) | 700 | 1400 | 2100 | 2800 | | M |

Table 2 Experimental response table for L16 orthogonal array layout

| Sample number | Normal load (N) | Filler content (wt.%) | Sliding distance (m) | Sliding velocity (m/s) | Specific wear rate (mm ³ /Nm) | S/N ratio (dB) |
|---------------|-----------------|-----------------------|----------------------|------------------------|--|----------------|
| 1 | 10 | 0 | 700 | 1 | 0.000188300 | 74.5030 |
| 2 | 10 | 2 | 1400 | 1.25 | 0.000193836 | 74.2513 |
| 3 | 10 | 4 | 2100 | 1.5 | 0.000265287 | 71.5257 |
| 4 | 10 | 6 | 2800 | 1.75 | 0.000163827 | 75.7123 |
| 5 | 20 | 0 | 1400 | 1.5 | 0.000337371 | 69.4378 |
| 6 | 20 | 2 | 700 | 1.75 | 0.000371519 | 68.6004 |
| 7 | 20 | 4 | 2800 | 1 | 0.000360625 | 68.8589 |
| 8 | 20 | 6 | 2100 | 1.25 | 0.000196592 | 74.1287 |
| 9 | 30 | 0 | 2100 | 1.75 | 0.000118559 | 78.5213 |
| 10 | 30 | 2 | 2800 | 1.5 | 0.000191144 | 74.3728 |
| 11 | 30 | 4 | 700 | 1.25 | 6.63218E-05 | 83.5669 |
| 12 | 30 | 6 | 1400 | 1 | 8.19135E-05 | 81.7329 |
| 13 | 40 | 0 | 2800 | 1.25 | 0.000125534 | 78.0248 |
| 14 | 40 | 2 | 2100 | 1 | 0.000115763 | 78.7286 |
| 15 | 40 | 4 | 1400 | 1.75 | 0.000116063 | 78.7061 |
| 16 | 40 | 6 | 700 | 1.5 | 0.00018021 | 74.8844 |

2.4 Experimental Design and Surface Morphology Studies

A useful tool for optimizing a variety of control parameters, including the load, sliding velocity, filler content and sliding distance, as well as an examination of the sliding wear behaviour of specified composites, was the thorough Taguchi design technique. The signal-to-noise (S/N) ratio derived from the experimental data of proposed composite utilizing (Eq. 6) represents the performance qualities in this approach. So, using the lower-the-better (LB) features approach, the wear rate performance was examined. The various input parameters are shown in Table 1 together with their quantified values.

The experiment's Taguchi design (L16 orthogonal array) used the wear rate as the output parameter. In terms of Eq. 6, the S/N ratio with the lower-the-best characteristic is expressed. Analysis of variance (ANOVA) is also carried out in order to rank the relevance of input characteristics on output performance (such as Wear rate).

$$\frac{S}{N} = -10 \log \frac{1}{N} \sum Y^2 \quad (6)$$

where N = number of observations, and Y = observed data measurement.

The behaviour of a SEM micrograph of worn-out surfaces is examined using a field emission scanning electron microscope (FESEM; FEI Nova Nano SEM 450, USA) in order to comprehend the wear process of developed composite.

2.5 Preference Selection Index Method Algorithm

Design engineers can use the PSI technique as a methodical, scientific methodology or instrument to choose the best material for a certain application. When there is a conflict in assessing relative significance of qualities, which is the PSI method's weakness, this methodology can be helpful. The next phases represent the precise PSI computing processes [24–28].

Step 1: The structure of decision problem: For PSI, data entry is necessary, for example, to compile all material choices and selection criteria for a certain application. This strategy aids in determining the objective. According to some academics, the typical decision-making problem's hierarchical structure makes it possible to understand the issue clearly. The primary goal should be at the top of the hierarchy, followed by the ranking criteria for evaluation and finally the alternatives/options. Thus, Fig. 2 [29, 30] depicts the hierarchical structure of the problem.

Step 2: Formulating the decision matrix: A multi-alternative (say m-alternatives) and multi-criteria (say n-criteria) formulation of the issue is used. Additionally, the model also expresses the decision matrix's product (for example, the matrix D of order $m \times n$ order).

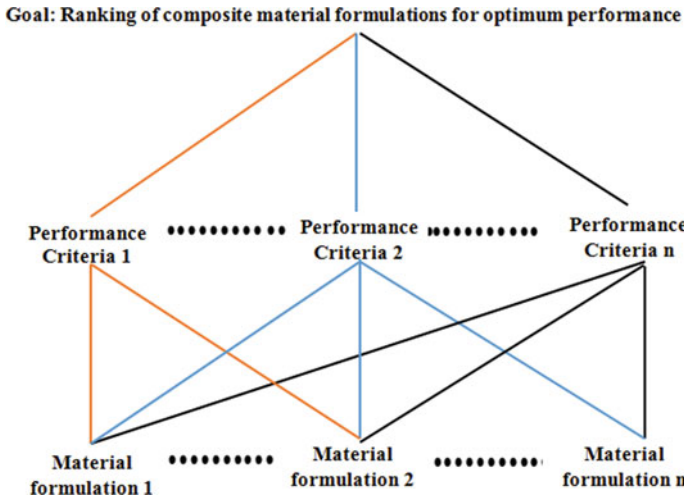


Fig. 2 Hierarchical structure of the problem

$$\begin{matrix}
 C_1 & C_2 & \cdots & C_n \\
 A_1 & \begin{bmatrix} p_{11} & p_{12} & \cdots & p_{1n} \end{bmatrix} \\
 A_2 & \begin{bmatrix} p_{21} & p_{22} & \cdots & p_{2n} \end{bmatrix} \\
 \vdots & \begin{bmatrix} \vdots & \vdots & \ddots & \vdots \end{bmatrix} \\
 A_m & \begin{bmatrix} p_{m1} & p_{m2} & \cdots & p_{mn} \end{bmatrix}
 \end{matrix}
 \quad \text{where } C_1, C_2, \dots, C_n \text{ are the } n\text{-criteria and } A_1, A_2, \dots, A_m \text{ are the } m\text{-alternatives}$$

The element p_{ij} is the performance value of the i th alternative (A_i) with respect to the j th attribute (C_j), where $i = 1, 2, \dots, m$ and $j = 1, 2, \dots, n$.

Step 3: Normalization of the decision matrix: Normalization is the process of transforming the decisive data range of 0 to 1 and is needed in order to transform performance rating with the various data measurement units into a compatible unit. In order to compute all criteria in unitless, and to facilitate inter-attribute comparisons, the above matrix entries are normalized (using the principle below). Thus, find out normalized matrix is R_{ij} .

(i) If the expectation is *larger-the-better*, then the performance of the original attribute can be normalized as follows: (Eq. 7).

$$R_{ij} = \frac{x_{ij}}{x_j^{max}} \tag{7}$$

(ii) If the expectation is *smaller-the-better*, then the performance of the original attribute can be normalized as follows: (Eq. 8).

$$R_{ij} = \frac{x_j^{min}}{x_{ij}} \tag{8}$$

where x_{ij} are the measures of the attribute ($i = 1, 2, 3, \dots, m$, and $j = 1, 2, 3, \dots, n$).

Step 4: Computation of preference variation value (PV_j): The normalized matrix R_{ij} , is used to measure preference variation value (PV_j) for each criterion with the concept of sample variance using the following Eq. 9:

$$PV_j = \sum_{i=1}^N (R_{ij} - R_j)^2 \tag{9}$$

where R_j is the mean of normalized values of criteria j i.e. $R_j = \frac{1}{n} \sum_{i=1}^N R_{ij}$

Step 5: Computation of overall preference value (ψ_j): The overall preference value (ψ_j) of every criterion is calculated using the following 10:

$$\Psi_j = \frac{\Phi_j}{\sum_{j=1}^n \Phi_j} \tag{10}$$

where $\Phi_j = 1 - \sum PV_j$, is the deviation in the preference value of each criterion. For consistency, the sum of overall preference values for all the criteria should be unity i.e. $\sum \Psi_j = 1$.

Step 6: Computation of Preference Selection Index (I_i): The preference selection index (I_i) for each alternative is measured using the following Eq. 11:

$$I_i = \sum_{j=1}^n (R_{ij} \times \Psi_j) \tag{11}$$

Step 7: The computed values of preference selection index (I_i): The computed values of preference selection index (I_i) are used to rank the alternatives according to their descending order, i.e. highest to lowest I_i value is used to rank the alternatives from first to last and then making related interpretations or recommendations.

3 Result and Discussion

3.1 Physical and Mechanical Characteristics

3.1.1 Effect of Filler on Voids Content and Density of developed Composite

Figure 3 shows the impact of graphite on the amount of voids in a Zinc Aluminium (ZA-27) alloy composite filled with 0, 2, 4, and 6 wt% filler, respectively. For the planned composites of both theoretical and experimental densities, the results of the void fraction experiment are obtained. While the void fraction of the intended

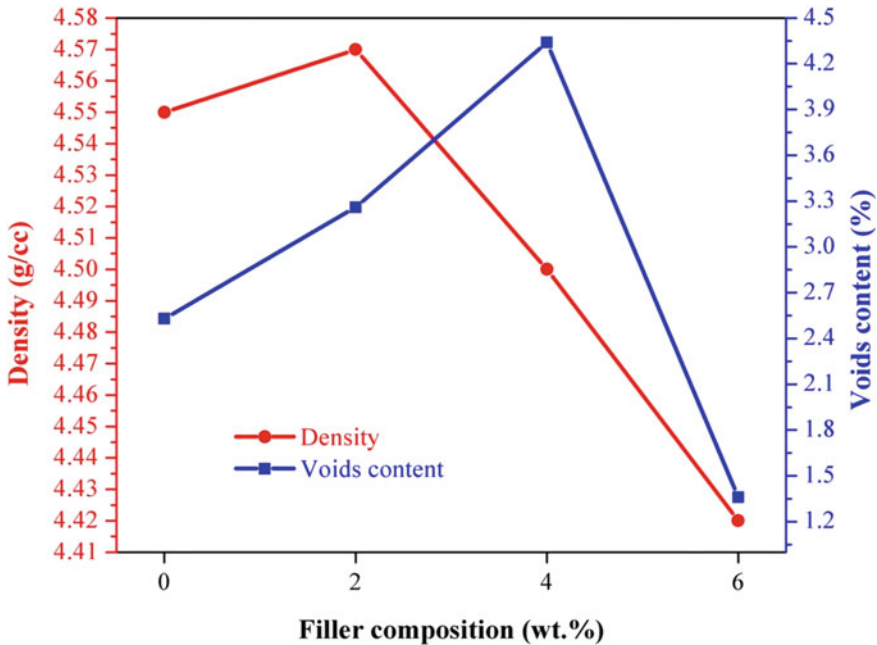


Fig. 3 Effect of Gr on the density and the voids content of alloy composite

alloy composites is gradually improving due to an increase in reinforcement, the void fraction of the 6 wt.% Gr-ZA-27 alloy composite is on the decline. Due to the perfect blending of the reinforcement and the composite matrix, the greater weight percentage of void contents appears to be minor and may rely on the shape and size of the individual particle.

The change in density and void content with rise in graphite content of filled ZA-27 alloy composite was presented in Fig. 3. It has been noticed that increasing the graphite component causes the density of the designed composite to drop. The added 2 weight per cent Gr-reinforced ZA-27 alloy composite has a density of 4.42 g/cc, compared to the 4.55 g/cc of the pure alloy composite. A further addition is a 4.30 g/cc (4 wt.%) gr powder. Adding 6.0% Gr powder again reduces the base alloy's density by 3.6% to 4.36 g/cc. It should be observed that the composite's density falls as a result of Gr particles' decreased weight relative to the base alloy. With an increase in rice/Sic powder particle, the density of the composite falls [12, 31].

3.1.2 Effect of Filler on Hardness

Figure 4 depicts the effect of graphite on the hardness of the designed alloy composites. It has been found that adding more reinforcement increases the hardness of planned alloy composites. When compared to unfilled alloy composite, the ZA 27-6

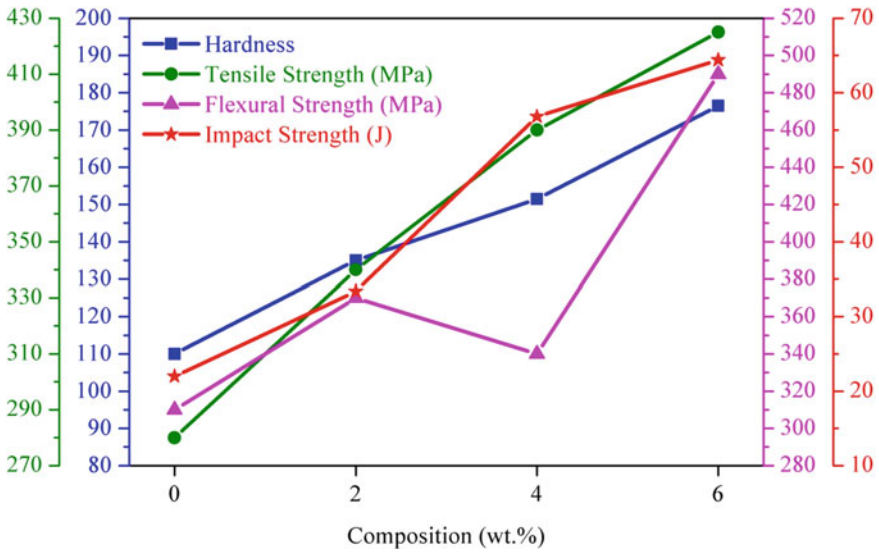


Fig. 4 Effect of Gr on the mechanical characteristics of alloy composite

wt.% Gr alloy composite exhibits greater hardness. The graph reveals that the clean alloy composite has a hardness of 107 HV. Hardness of alloy composite increases (135 HV) with the addition of 2 weight per cent graphite powder. Once more, adding 4 wt.% and 6 wt.% of graphite powder to a pristine alloy composite results in an increase in hardness to 157 HV and 171 HV, respectively. Similar results are reported by Dali et al. [32], who found that incorrectly mixed graphite reinforced with matrix caused the graphite-reinforced ZA-27 alloy composites to grow with increasing Gr content. According to Sharma et al. [33], enhancements in addition to graphite-reinforced particles boost the composite’s hardness by enhancing the bonding strength and load-bearing capability of the matrix and reinforcement. According to Rajmohan et al. [34], adding mica boosted the composite’s hardness, which enhanced the produced composite’s mechanical capabilities.

3.1.3 Effect of Filler on Flexural Strength

The change in flexural strength on the graphite-filled ZA-27 alloy composite is depicted in Fig. 4. It has been found that adding an additional 2 wt.% of graphite reinforcement increased the flexural strength of the specified specimen. The flexural strength was then decreased by the inclusion of an additional 2 wt% Gr content. The trend of increased flexural strength was maintained by increasing the graphite content to 4 and 6 wt.%. As a result, this may be the proper particle dispersion, and the right casting procedure is what created the strongest binding. Therefore, increasing the graphite concentration increases the flexural strength of specified specimens. As

the amount of distortion of the material reduces, an increase in ductility may be the cause of the rise in flexural strength. Therefore, this is the interfacial bonding strength between the matrix and the reinforcement that is the strongest. These findings are in perfect accordance with other research in this field [35].

3.1.4 Effect of Filler on Tensile Strength

Figure 4 shows the effect of graphite particles on the tensile strength of an alloy composite made of zinc and aluminium (ZA-27). By use of the software-based computerized UTM Machine, the tensile strength of the specified composite was computed. It has been found that increasing the graphite content produces better results in terms of tensile strength. The improvement in composite's hardness and strength is what causes the planned specimens' increased tensile strength, and the addition of graphite increases tensile strength while reducing elongation [36]. The intended specimen is found to have a tensile strength of 290 MPa at 0% Gr reinforcement. The designed specimen has a tensile strength of 340 MPa after being further strengthened with a 2 wt.% Gr component. Tensile strengths of 395 and 428 MPa are obtained by increasing the Gr content in the composite sample to 4 and 6 wt.%, respectively. Similar findings reported by Ramnath et al. [22] found that the base alloy matrix and Gr particles had a strong connection, increasing the tensile strength of the planned composite specimen. It should be emphasized that the base material's matrix and filler both significantly contribute to the composite's improved specimen strength.

3.1.5 Effect of Filler on Impact Strength

Figure 4 illustrates graphite particles effect on the impact resistance of the ZA-27 alloy composite. The impact strength of the composite obtained by the Izod experiment is observed to rise as the weight percentage of graphite is increased. The intended composite specimen has an impact strength of 23.56 J at 0% Gr content. Once more, increasing the reinforcement content to 2, 4, and 6 wt.% raises the composite's impact strength to 33.5, 58.5, and 64 J, respectively. When compared to base alloy matrix, the developed composite's maximum impact strength at 6 wt.% Gr is lower. Similar conclusions made by Ozden et al. demonstrated that better resistance ability was the reason why impact strength increased. As the particle size and hot extrusion ratio are increased, the composite's impact strength somewhat improves. Due to temperature's influence, the impact strength is also increased [32].

3.1.6 Effect of Filler on Compressive Strength

The effect of graphite powder filler on compressive strength of ZA-27 alloy composite is depicted in Fig.5. It is found from the graph that the compressive strength of filled

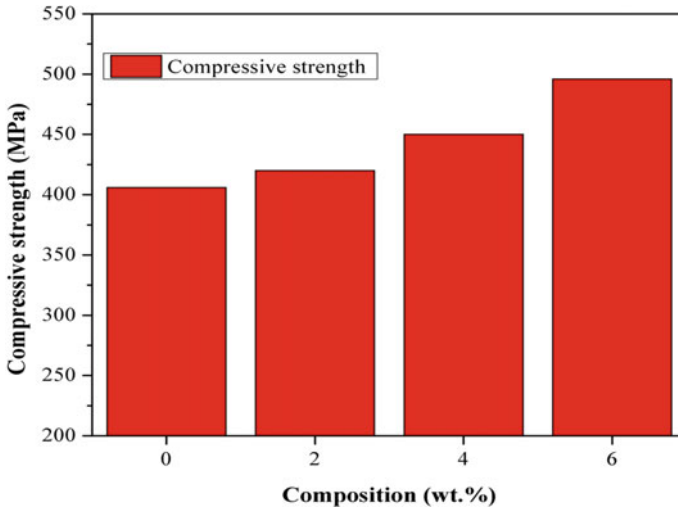


Fig. 5 Influence of Gr on the compressive strength of alloy composite

designed composite is larger than that of unfilled alloy composite. The compressive strength of designed specimen increases with the increase of graphite content. The compressive strength of unfilled alloy composite (at 0 wt. % Gr content) is 406 MPa. Addition of Gr content to 2 wt.% and 4 wt.% increases the compressive strength to 420 MPa and 450 MPa respectively. The higher compressive strength value of designed composite is 496 MPa at 6 wt.% Gr content.

The compressive strength of designed composite which gradually increases with the increase in graphite content may cause the growth of hard ceramic particles that stop the movement of modified crack and dislocation levels as outcome result of size of Gr network. Also, the strengthening mechanism of dispersion is likely to be continued even at higher temperature [12].

3.2 Steady State-Specific Wear Condition

Figure 6 displays a plot of the specific wear rate of an unfilled alloy and its specified composites with varying graphite contents against sliding velocity. The specific wear rate reduces as the sliding velocity increases, as shown in Fig. 6. The figure also demonstrates the specific wear rate of the designed composite drops as the graphite content is increased; it is discovered to be lower at a graphite content of 6 wt.% than that of other designed composites with different graphite content percentages. Therefore, the material with 0% composite has the highest specific wear rate. The production of the lubricating tribo-layer, porosity, fissures, and the abrasion process are few examples of possible causes for the decrease in specific wear rate with the

addition of graphite content [8]. That is, the addition of the graphite reinforcement may serve as a thick layer of solid lubricant between the mating surfaces. The precise wear rate behaviour is in line with the patterns noticed by a small number of academics and materialists [37, 38].

Figure 7 illustrates the sliding velocity effects on the coefficient of friction of composites made of Gr-reinforced Zinc-Aluminum alloys. The coefficient of friction (COF) increases with increasing sliding velocity and decreases with increasing graphite content. It was discovered that, when compared to the specified weight percentage of the composite, the 0 wt.% Gr-reinforced Zinc-Aluminum alloy composite exhibits the highest value of (μ), which is 0.93 at the value of 1.78 m/s of sliding velocity. According to the figure, the 6 wt.% Gr-ZA-27 produced composite has the lowest coefficient of friction (μ), in the group. This could be explained by the potential that the unyielding action of the cutting tool increases the coefficient of friction (COF), which, if it happens, can harm the material’s surface over deep grooves or scratches. The material deformation between the flat specimen and spinning disc may also be a contributing factor to the higher coefficient of friction. The greatest material loss is produced at the highest sliding velocity and highest friction. [12, 39].

Figure 8 shows the impact of altering the normal load (10–40) N on the specific wear rate of Gr-filled Zinc-Aluminum alloy composites under a constant test condition (slide distance = 700 m; sliding speed = 1 m/s). It was found that adding graphite causes the specific wear rate of specified Gr-ZA-27 alloy composites to decrease while increasing applied load. It forms a thin layer of graphite coating on the upper section of the counter surfaces, stopping sub-surface contact during sliding, when employed as a solid lubricant in sliding tests. The order of the specified wear rates is

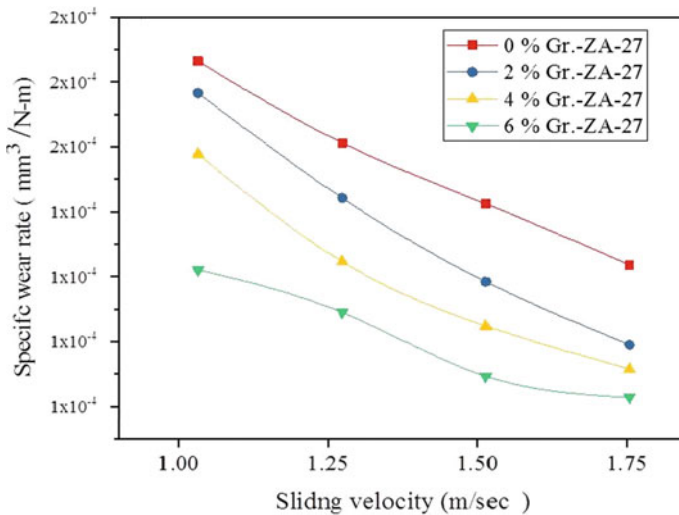


Fig. 6 Effect of sliding velocity on the specific wear rate of alloy composite

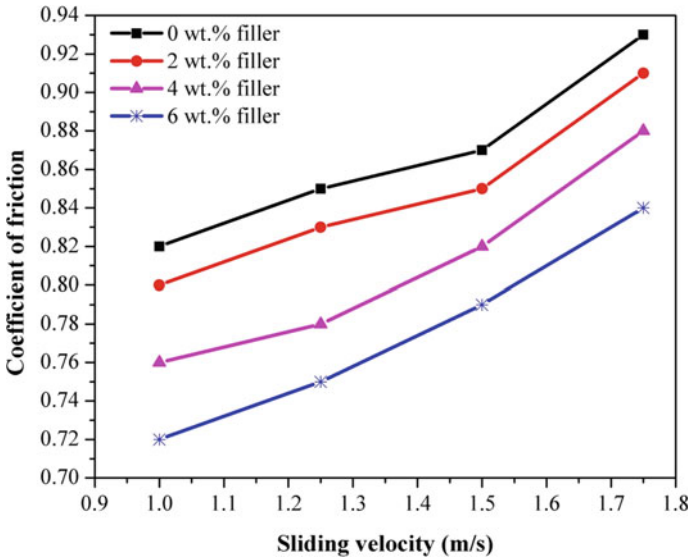


Fig. 7 Effect of sliding velocity on the coefficient of friction of alloy composite

0 wt.% GR-ZA27 > 2 wt.% GR-ZA27 > 4 wt.% GR-ZA27 > 6 wt.% GR-ZA27. The Zinc-Aluminum matrix and graphite content, which exhibit strong adhesion bonding conditions between the matrix and filler content, may be responsible for the good wear performance of 6 wt.% GR-ZA27 alloy composite. Due to the high porosity, the hardness of the manufactured alloy composite diminishes, which accounts for the rise in the alloy composite’s specific wear rate as the normal load is increased. Numerous scientists and researchers have reported findings that are similar [41, 42].

The influence of the variation of the normal load (10–40) N on COF(μ) of Gr-filled Zinc-aluminum composites is shown in Fig. 9. It is clear that the value of the (COF) rises as the normal load rises; this indicates that the trend of the COF value remains consistent between 10 and 20 N of applied load at the various weight percentages of filler content. The COF value then increased in the load range (30–40) N, rising from roughly 0.29 to 0.31 for the 0 wt.% of Gr-filled ZA-27 alloy composite, indicating that it has the best values when compared to the other alloy composites that were investigated. The planned alloy composite’s COF order is as follows: 0 wt.% Gr-ZA-27 > 2 wt.% Gr-ZA-27 > 4 wt.% Gr-ZA-27 > 6 wt.% Gr-ZA-27. This may be caused by the emergence of a mechanical layer and the sliding disintegration of asperities debris particles. With increasing applied load, it is seen that the alloy composites with 6 wt% Gr-filled Zinc-aluminum (ZA-27) exhibit the lowest friction. This is caused by a variety of wear mechanisms and thermal softening beneath the worn-out surface as a result of temperature rise [4]. It should be noticed that this specially constructed composite minimizes the friction coefficient of the composite and minimizes contact between the pin and the disc. This leads to the conclusion that adding graphite content to unfilled alloy enhances wear behaviour, engineered

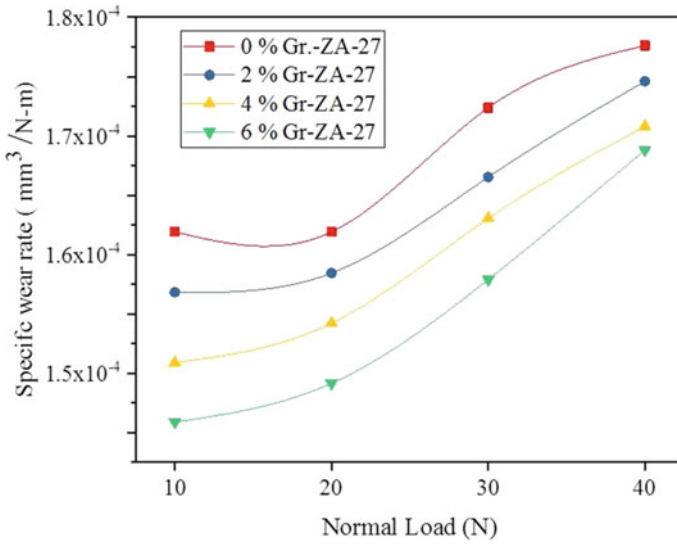


Fig. 8 Effect of normal load on the specific wear rate of alloy composite

composites perform considerably better than matrix alloy, and wear and friction coefficients fall as graphite content is increased [35].

Figure 10 shows the effect of sliding distance of a Gr-reinforced ZA-27 alloy composite on the specific wear rate. It has been found that as sliding distance increases, the specific wear rate of specified composites also increases. It's possible that an increase in reaction time and disc rotation leads to an increase in the sliding surface contact area, which in turn increases the specific wear rate. The following

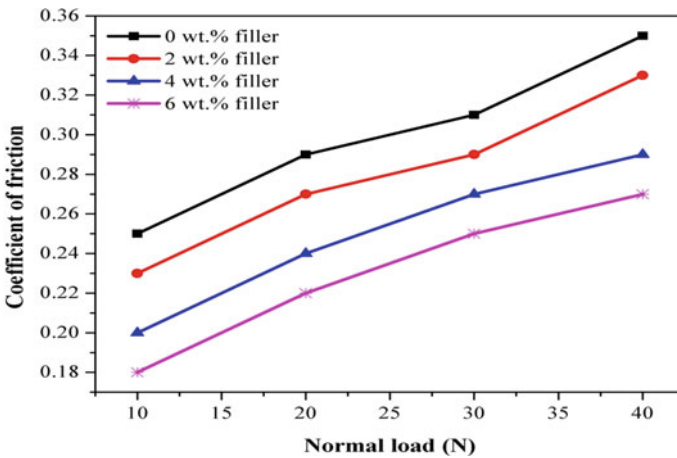


Fig. 9 Effect of normal load on the coefficient of friction of alloy composite

is the order of the specific wear rate: 0 wt. % Gr-ZA-27 > 2 wt.% Gr-ZA-27 > 4 wt.% Gr-ZA-27 > 6 wt.% Gr-ZA-27. It was evident from the graph that the specific wear rate of the composite was the smallest at a sliding distance of just 700 m, and it increases in the whole range. In comparison to specified alloy composites, the specific wear rate of the unfilled alloy composite is often higher. Because the sliding disk's bottom section is steady, the particles are broken, and exhausted debris particles pass through the counter surface.

The effect of increasing sliding distance (700–2800) m on COF (μ) of Gr-filled Zinc-aluminum (ZA-27) alloy composites is shown in Fig. 11. The COF(μ) value decreases when the alloy composite's Gr (0–6% wt%) content is increased. The COF value of the designed composite displays the higher at 0 weight per cent. At 2 wt.% Gr powder reinforced ZA-27 alloy composite, COF value was reduced. However, the decline in wear rate trend indicates damage to the alloy composite and reduction in the micrograph structure. Specific grain sizes, and grain shape distribution are also supportive of wear attributes. It was found that for alloy composite, the COF magnitude was smaller at a lower sliding distance. With increasing sliding distance for the Gr-filled Zinc-Aluminum alloy composite, the COF of the material gradually improves. This may be due to grain expansion and an increase in hardness [12, 43].

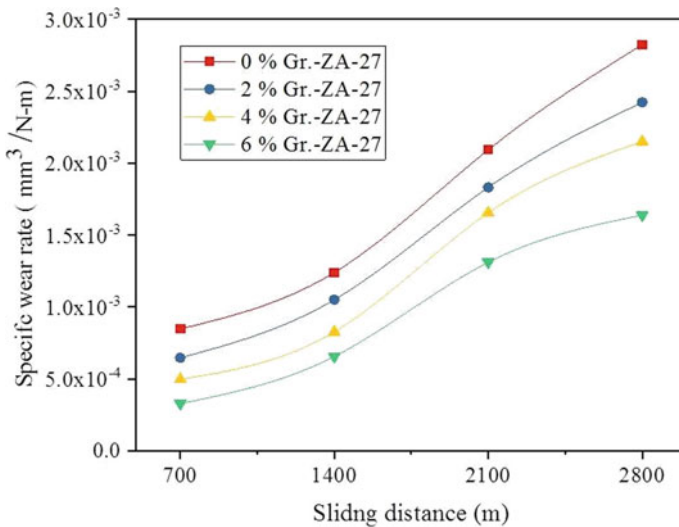


Fig. 10 Effect of the sliding distance on the specific wear rate

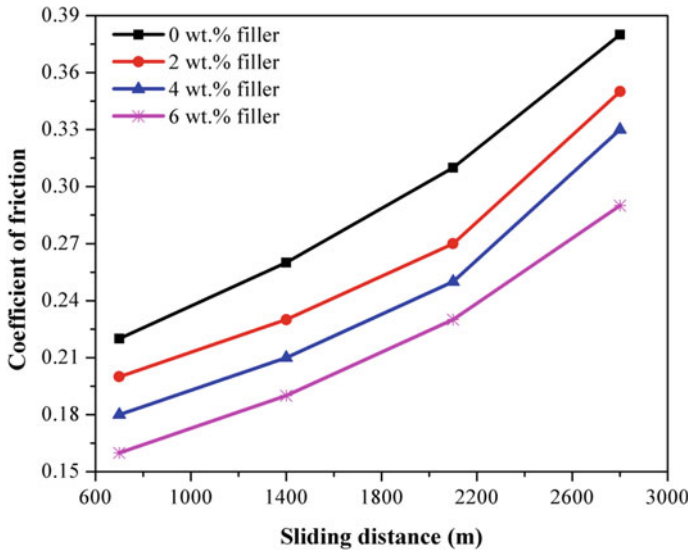
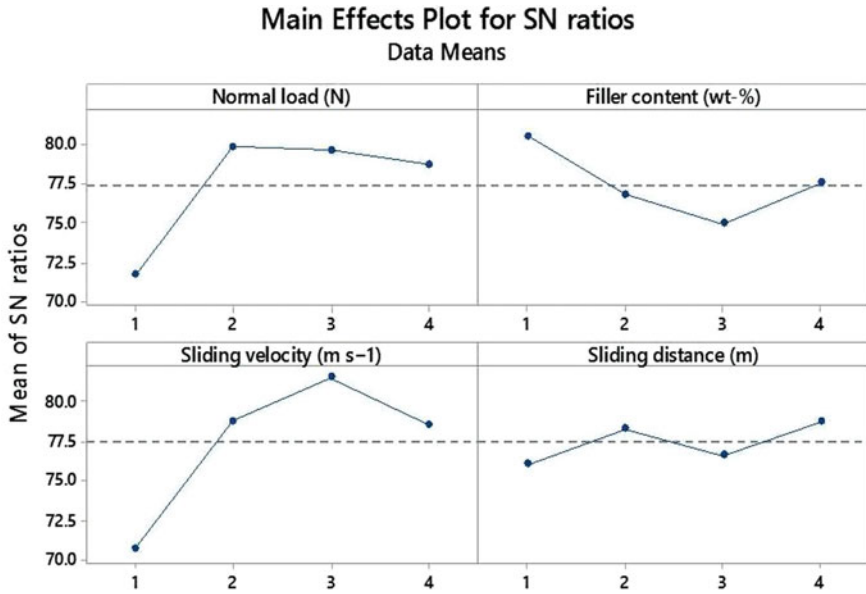


Fig. 11 Effect of the sliding distance on the coefficient of friction

3.3 Analysis of Experimental Results by Taguchi Experimental Design

The robustness and signal-to-noise (S/N) ratio is estimated using the Taguchi method, which is a very useful part of a parametric design. In this strategy, the words “signal” and “noise” refer to the desired outcome, which in this case is wear rate, and the unwanted background, respectively. The values for the S/N ratio shown in Table 2 are the average of two replications. The composites that were created and filled with graphite have an overall mean S/N ratio of 75.25 dB. The MINITAB 14 programme is used to analyse the Taguchi data. Before using this model as a forecast for performance estimation, any test must take into account the proper interactions between the control parameters. However, a composite factorial design was used to measure the interaction impact.

Figure 12 shows how control factors affect wear rate in the appropriate ways. The order of importance of the control parameters for composites, from normal load (L) to reinforcement or filler content (R), to sliding velocity (V), to sliding distance (SD) [44, 45], is given below.



Signal-to-noise: Smaller is better

Fig. 12 Influence of control parameters on signal-to-noise ratio (S/N)

3.4 Analysis of Variance (ANOVA) and Effect of Control Parameters

The wear rate of the composite was the control parameter that was observed using ANOVA, along with its percentage share in the calculation of the response. The research was done using 5% (level of significance). Normal load (41.81%), reinforcement or filler content (22.98%), sliding velocity (14.55%) and sliding distance (11.53%) are the results of the ANOVA, in that order (see Table 3). The order of key control parameters demonstrates their ability to fully regulate the wear system’s whole mechanism.

3.5 Surface Morphology

Graphite-reinforced Zinc aluminium (ZA-27) alloy composite SEM micrographs for sliding wear (stationary state condition; Taguchi DOE; L16 orthogonal array) at varied load (10–40) N are shown in Fig. 13(a-d). Due to the lowest stress (10 N) and slowest sliding speed (1 m/sec), delaminations are seen in the SEM picture of the sample (0 wt.% Gr-ZA-27 Gr) in Fig. 13a. The delamination may result from insufficient frictional heating of the counter face and substantial material removal

Table 3 Wear rate of response of ANOVA table for S/N ratios

| Source | DF | Seq SS | Adj SS | Adj MS | F | P | P (%) |
|----------------------|----|---------|---------|--------|------|-------|-------|
| Normal load (L) | 4 | 1300.72 | 1226.63 | 340.46 | 7.87 | 0.019 | 41.81 |
| Filler content (F) | 4 | 651.06 | 648.73 | 120.86 | 5.08 | 0.188 | 22.98 |
| Sliding velocity (V) | 4 | 641.13 | 685.85 | 187.52 | 6.67 | 0.115 | 14.55 |
| Sliding distance (D) | 4 | 2472.72 | 1462.89 | 362.48 | 8.19 | 0.016 | 11.53 |
| Error | 8 | 504.33 | 534.35 | 64.47 | | | 15 |
| total | 24 | 5569.96 | | | | | 100 |

Standard deviation (S) = 8.24402 R^2 (R-Sq) = 90.54% Adjusted R^2 (R-Sq (adj)) = 80.93% (DF = Degrees of freedom, Seq SS = Sequential sums of squares, Adj SS = Adjusted sums of squares, Adj MS = Adjusted mean squares, F = Variance, P = Probability)

from the sample surface, and it happens at low load and slow sliding velocity [43]. Shallow grooves can be seen on the surface of the sample (2 wt% Gr-ZA-27 Gr) in the SEM image of the sample in Fig. 13b under a normal load of 20 N. In steady state sliding tests, heat is produced at the interface of the materials' surfaces when the two flat pieces are rubbed together because of friction. As a result of the surface's mellowing, wear particles are impaired and shallow composite grooves develop [46]. The SEM picture of the sample (4 wt.% Gr-ZA-27 Gr) with a normal load of 30 N is shown in Fig. 13c. Debris particles (PD) can be seen on the worn-out surface when using an increase in load. This is due to the fact that friction at the interface generates heat, which causes the wear particles to degrade and the surface to mellow [47]. The ploughing mechanism is generated due to the highest content of plastic deformation, as can be seen in the SEM micrograph of sample (6 wt% Gr-ZA-27 Gr) for sliding wear with normal load 40 N in Fig. 13d. Numerous researchers [48–55] obtained similar results.

3.6 Ranking Optimization Using PSI Method

In this research chapter, the PSI method is used to analyse the decision matrix (D), which has four composite specimens (AGR0, AGR2, AGR4 and AGR6) as alternatives and performance criteria that are provided in Table 4. The following are the step-by-step calculations:

Step 1: The evaluated performance data are organized in the form of decision matrix shown in Table 5.

Step 2: The decision matrix has been normalized as per the algorithm, as shown in Table 6.

Step 3–7: Table 7 displays the final ranking order of alloy composites determined using the technique along with the intermediate calculations.

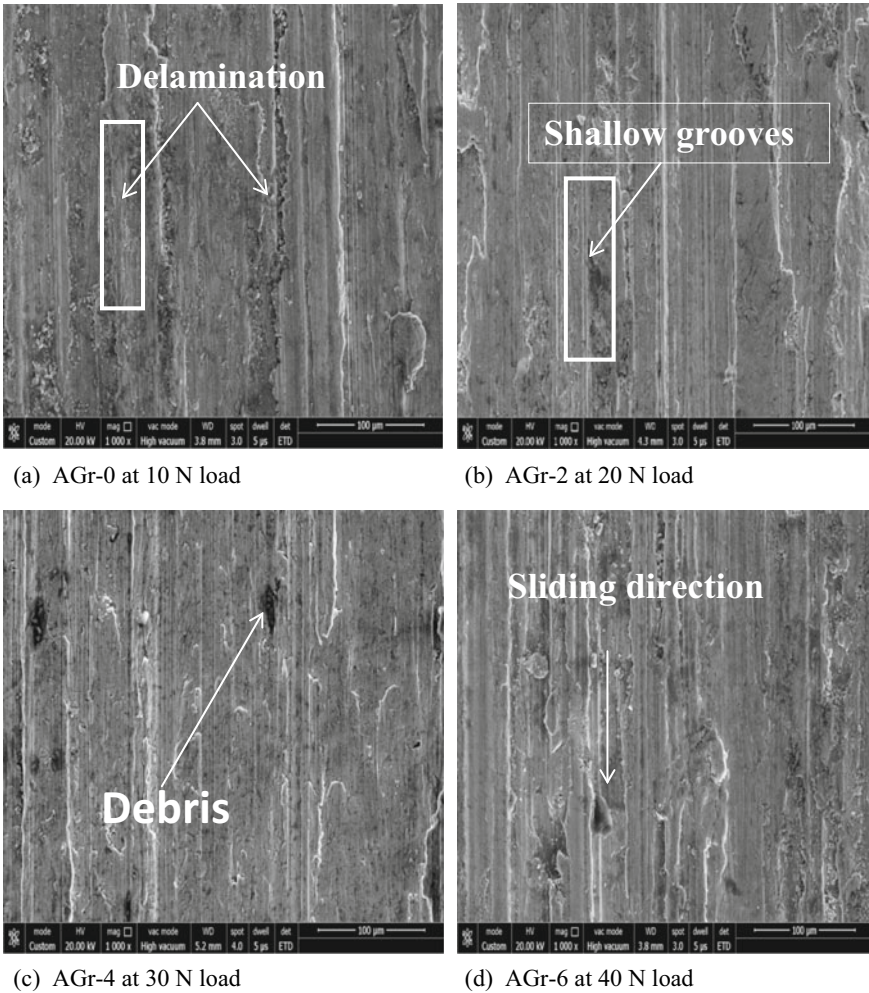


Fig. 13 SEM micrographs of graphite-reinforced ZA-27 alloy composite samples for sliding wear at varying load (10–40) N

4 Conclusions

High vacuum casting was used to create the alloy composite ZA-27-GR. UTM and multi-specimen tester machines were used to analyse the mechanical and tribological characteristics of alloy composites made of ZA-27-GR. PSI Method was used to analyse the ranking order.

The following points serve as the conclusion:

1. The physical and mechanical characterization like (Voids content (VC); Hardness (H); Impact strength (IM); Flexural strength (FS); Density (D)) of

Table 4 Descriptions of the selection criteria applied in this case study

| Sr. no | Performance criteria | Preference |
|--------|--|------------|
| 1 | Tensile strength (MPa) | Maximum |
| 2 | Flexural strength (MPa) | Maximum |
| 3 | Impact strength (J) | Maximum |
| 4 | Hardness (HRB) | Maximum |
| 5 | Compressive strength | Maximum |
| 6 | Density (g/cc) | Minimum |
| 7 | Void content (%) | Minimum |
| 8 | Specific wear rate (mm ³ /Nm) | Minimum |
| 9 | COF | Minimum |

Table 5 Decision matrix

| | Material alternatives | 0% | 2% | 4% | 6% |
|------|--|-------|------|------|------|
| PC's | Property ↓ | | | | |
| PC-1 | Tensile strength (MPa) | 290 | 340 | 395 | 428 |
| PC-2 | Flexural strength (MPa) | 300 | 363 | 342 | 490 |
| PC-3 | Impact strength (J) | 22.76 | 33.5 | 58.5 | 64 |
| PC-4 | Hardness (HRB) | 107 | 135 | 151 | 171 |
| PC-5 | Compression strength (MPa) | 406 | 420 | 450 | 496 |
| PC-6 | Experimental density (g/cc) | 4.55 | 4.57 | 4.5 | 4.42 |
| PC-7 | Voids content (%) | 2.53 | 3.26 | 4.36 | 1.36 |
| PC-8 | Specific wear rate at sliding distance (mm ³ /Nm) | 2.8 | 2.5 | 1.8 | 1.4 |
| PC-9 | Coefficient of friction at sliding distance | 0.19 | 0.28 | 0.35 | 0.55 |

Table 6 Normalization of the decision matrix

| Material Alternatives → PC's ↓ | 0% | 2% | 4% | 6% | Mean |
|-----------------------------------|------|------|------|------|------|
| PC-1 | 0.67 | 0.78 | 0.91 | 1.00 | 0.84 |
| PC-2 | 1.00 | 0.87 | 0.82 | 0.65 | 0.83 |
| PC-3 | 1.00 | 0.91 | 0.78 | 0.62 | 0.82 |
| PC-4 | 1.00 | 0.95 | 0.88 | 0.76 | 0.90 |
| PC-5 | 0.82 | 0.85 | 0.91 | 1.00 | 0.89 |
| PC-6 | 0.97 | 0.97 | 0.98 | 1.00 | 0.98 |
| PC-7 | 0.54 | 0.42 | 0.31 | 1.00 | 0.57 |
| PC-8 | 0.50 | 0.56 | 0.78 | 1.00 | 0.71 |
| PC-9 | 1.00 | 0.68 | 0.54 | 0.35 | 0.64 |

Table 7 Ranking of the composites

| Material alternatives | 0% | 2% | 4% | 6% |
|----------------------------|--------|--------|--------|--------|
| PC's ↓ | | | | |
| PC-1 | 0.0906 | 0.1050 | 0.1159 | 0.0773 |
| PC-2 | 0.1009 | 0.0946 | 0.0757 | 0.1161 |
| PC-3 | 0.1030 | 0.0879 | 0.0697 | 0.1134 |
| PC-4 | 0.1141 | 0.1055 | 0.0913 | 0.1198 |
| PC-5 | 0.1028 | 0.1101 | 0.1214 | 0.994 |
| PC-6 | 0.1196 | 0.1215 | 0.1237 | 0.1202 |
| PC-7 | 0.0374 | 0.0280 | 0.0896 | 0.0482 |
| PC-8 | 0.0585 | 0.0813 | 0.1046 | 0.0523 |
| PC-9 | 0.0649 | 0.0519 | 0.0330 | 0.0956 |
| Preference Selection Index | 0.79 | 0.79 | 0.82 | 0.84 |
| Preference ranking | 4 | 3 | 2 | 1 |

composite decrease with increment in Gr (0–6 wt. %) reinforcement, while the Tensile strength and compressive strength of composite shows an increasing in trend.

2. The ZA-27-Gr alloy composites under study with the base alloy at steady state sliding, wear parameters as normal load (10–40 N), sliding velocity (1-1.75 m/s) and sliding distance (700-2800 m) show the predominant wear resistance performance, thus they could be broadly utilized for bearing material application.
3. The specific wear rate of ZA-27-Gr alloy composites decreases with the increase in sliding velocity (1–1.75 m/s) under the steady state wear test irrespective of the reinforcement. The wear rate order is (0 wt.% Gr –ZA-27 > 2 wt.%Gr-ZA-27 > 4 wt.%Gr-ZA-27 > 6 wt.% Gr-ZA-27). Also, the coefficient of friction increases with the increase in filler content with the order: 0 wt.% Gr-ZA-27 > 2 wt.% Gr-ZA-27 > 4 wt. % Gr-ZA-27 > 6 wt. % Gr-ZA-27 across the entire sliding velocity range.
4. Specific wear rates of Gr-reinforced ZA-27 alloy composite decrease with increasing the normal load (10–40 N) under the steady state wear test. The specific wear rate order is: 0 wt.% Gr –ZA-27 > 2 wt.% Gr-ZA-27 > 4 wt.% Gr-ZA-27 > 6 wt.% Gr-ZA-27. Also, the coefficient of friction decreases with increasing filler content with the order : 0 wt.% Gr-ZA-27 > 2 wt.% Gr-ZA-27 > 4 wt.% Gr-ZA-27 > 6 wt.% Gr-ZA-27 across the entire range of the normal load.
5. Under the steady state wear test, the specific wear rates of Gr-reinforced ZA-27 alloy composite rise with increasing sliding distance (700–280 m), regardless of the reinforcement. Additionally, as filler content increases, the coefficient of friction falls in the following order: 0 wt.% Gr-ZA-27 > 2 wt.% Gr-ZA-27 > 4 wt.% Gr-ZA-27 > 6 wt.% SiC-Gr-ZA-27 across the entire range of sliding distance.

6. Using the design of experiment (DOE) Taguchi approach, the total average for (S/N) proportions for specific wear rate of composites was determined to be 75.25 db. Normal load > filler content > sliding velocity > sliding distance is the whole hierarchy of the critical factors affecting the reduction of wear rate. At a 5% significance level, the ANOVA method is used to corroborate the same results.
7. The priority order of performance criteria is as follows: Tensile Strength (TS) ~ Flexural Strength (FS) ~ (ImpactStrength) ~ (Compressive Strength) ~ Hardness (HVR) > Density (D) > Voids Content (VC) > Wear (W) ~ Coefficient Of Friction.
8. The PSI technique assigns the highest ranking to the alloy composites that have been manufactured and have a uniformly mixed base alloy and particle reinforcement because of their superior qualities. The analysis of performance by PSI method depicted the ranking order AGR6 > AGR4 > AGR2 > AGR0.
9. The PSI approach can be utilized to successfully develop a better composite formulation composition when there are conflicting performance objectives.
10. The analysis of wear data and SEM micrographs of composites made of 6 wt.% Gr-ZA-27 alloy demonstrates their superior wear performance when compared to other composites, making them suitable for use as tribological applications.

Acknowledgements The authors express their truthful gratitude to the Department of Mechanical Engineering of MNITJaipur-302017, Rajasthan, INDIA for their all kinds of financial as well also the miscellaneous infrastructural support. In addition, the authors thank the Institute's Advanced Research Lab for Tribology and Material Research Centre for their assistance and facilities with the experimental and characterization work.

References

1. S.S. Owoeye, D.O. Folorunso, B. Oji, S.G. Borisade, *Int. J. Adv. Manuf. Tech.* **170**, 760 (2018)
2. S.C. Tjong, Z.Y. Ma, *Mater. Sci. Eng.* **29**, 49 (2000)
3. S.A.B. Raju, K.C. Hemanth, S.I.N. Jayasimha, *Proc. Int. Conf. Eng. Sci. Tech. ICCTEST - 2017*, 228–232s, (2017)
4. R. Dalmis, H. Cuvalci, A. Canakci, O. Guler, *Adv. Compos. Lett.* **25**(2), 37 (2016)
5. G. Ranganath, S.C. Sharma, M. Krishna, *Wear* **251**, 1408 (2001)
6. S.C. Sharma, K.H.W. Seah, B.M. Satish, B.M. Girish, *Mater. Des.* **17**(6), 245 (1996)
7. K.K. Alaneme, K.O. Adeoye, S.K. Oke, *Leon. Electro. J.* **29**, 1 (2016)
8. B.M. Girisha, K.R. Prakash, B.M. Satisha, *Mater. Sci. Eng. A.* **530**, 382 (2011)
9. A. Baradiswaran, A.E. Perumal, *Int. J. Compos. Part B.* **54**, 146 (2013)
10. A. Kumar, M. Kumar, *Mater. Today Proc.* **27**, 2617 (2019)
11. A. Kumar, M. Kumar, *Mater. Today. Proc.* **27**, 2667 (2019)
12. A. Kumar, A. Patnaik, I.K. Bhat, *J. Powder Metallur.* **60**, 371 (2017)
13. A. Kumar, M. Kumar, B. Pandey, *SILICON* **14**(5), 2051 (2022)
14. M. Kumar, S. Bhashkar, N.K. Shakyawal, A. Kumar, *Materialwiss. Werkstofftech.* **51**, 1662 (2020)
15. A. Kumar, V. Kukshal, V.R. Kiragi, *Mater. Today Proc.* **44**, 4349 (2021)
16. A. Kumar, V. Kumar, A. Kumar, B. Nahak, R. Singh, *Mater. Today. Proc.* **44**, 4542 (2021)

17. A. Kumar, M. Kumar, A. Patnaik, M.J. Pauer, A. Pandey, A. Kumar, V. Gautam, *Mater. Today Proc.* **44**, 4784 (2021)
18. M.A. Maleque, S. Dyuti, M.M. Rahman, *Proc. Worl. Congr. Eng.* **1**, 2078 (2010)
19. K. Maniya, M.G. Bhatt, *Mater. Des.* **31**, 1785 (2010)
20. M. Kumar, A. Kumar, *Mater. Today Proc.* **27**, 20120 (1972)
21. B.D. Agarwal, L.J. Broutman, in *Analysis and Performance of Fiber Composites*, 2nd edn. (Jhon. Wiley Sons, 1990), pp. 440–442
22. R. Kumar, K. Kiran, V.S. Sreebalaji, *Measure.* **102**, 142 (2017)
23. S.S. Kumar, M. Devaiah, *Ceram. Int.* **38**, 1139 (2012)
24. S. Gangwar, A. Patnaik, I.K. Bhat, *SILICON* **8**, 601 (2016)
25. D. Petkovic, M. Madic, M. Radovanovic, V. Gecevska, *Facta. Univ. Ser. Mech. Eng.* **15**, 97 (2017)
26. R. Attri, S. Grover, J. King, *Saud. Univ. Eng. Sci.* **27**, 207 (2015)
27. K. Jha, S. Chamoli, Y.K. Tyagi, H.O. Maurya, *Mater. Today Proc.* **5**, 3353 (2018)
28. R. Khorshidi, A. Hassani, *Mater. Des.* **52**, 999 (2013)
29. M. Panahi, H. Gitinavard, *J. Sustain. Min.* **16**, 207 (2018)
30. K. Mesran, R.D. Tampubolon, R.D. Sianturi, F.T. Waruwu, *Sci. Tech.* **3**, 230 (2017)
31. S.Y. Jian, S.J. Tao, X.R. Huang, *Adv. Mater. Res.* **1078**, 290 (2014)
32. H. Abdizadeh, R. Ebrahimifard, M.A. Baghchesara, *Compos. Part B.* **56**, 217 (2014)
33. X. Li, C. Guo, X. Liu, *Prog Nat Sci.* **24**, 478 (2014)
34. S.C. Sharma, B.M. Girish, R. Kamath, B.M. Satis, *Wear* **219**, 162 (1998)
35. T. Rajmohan, K. Palanikumar, S. Ranganathan, *Trans. Nonferrous Met. Soc.* **23**, 2509 (2013)
36. A. Baradeswaran, A.E. Perumal, *Compos. Part B.* **56**, 472 (2014)
37. B.V. Ramnath, C. Elanchezhian, M. Jaivignesh, *Mater. Desi.* **58**, 332 (2014)
38. S. Ozden, R. Ekici, N. Nair, *Compos A Appl S.* **38**, 484 (2007)
39. J.U. Ejjioforand, R.G. Reddy, *J. Miner. Proc.* **49**, 31 (1997)
40. B.P. Krishanand, P.K. Rohatgi, *Meter. Technol.* **11**, 41 (1984)
41. L.I. Xuan, G. Chao, L. Xiaokai, *Mater. Int.* **24**, 472 (2014)
42. S. Baskaran, V. Anandakrishnan, M. Duraiselvam, *Mater. Des.* **60**, 184 (2014)
43. A.K. Mondal, S. Kumar, *Wear* **267**, 458 (2009)
44. H. Chi, L. Jiang, G. Chen, *Mater. Des.* **87**, 960 (2015)
45. K. Nirajan, P.R. Lakshminarayanan, *Mater. Des.* **47**, 167 (2015)
46. S.A. Alidokhta, A.A. Zadeh, H. Assadi, *Wear* **305**, 291 (2013)
47. H.R. Manohara, T.M. Chandrashekharaiah, K. Venkateswarlu, S.A. Kori, *Tribol. Int.* **51**, 54 (2012)
48. C.S. Ramesh, R. Keshavamurthy, B.H. Channabasappa, *Tribol. Int.* **43**, 623 (2010)
49. J.C. Walker, W.M. Rain, H. Jones, *Wear* **259**, 577 (2005)
50. E. Naveena, S. Ilangovan, *Mater. Today: Proc.* **22**, 2704 (2020)
51. O. Savas, *Mater. Today Communi.* **23**, 100 (2020)
52. T. Sathis, S. Karthick, *J. Mater. Sci. Technol.* **9**(3), 3481 (2020)
53. S. Arif, B. Jamil, M. Sheikh, *Engg. Sci. Tech. Int. J.* **23**, 674 (2020)
54. X. Li, M. Sosa, U. Olofesson, *Wear* **340**, 31 (2015)
55. T.S. Kran, M.P. Kumar, S. Basarajappa, B.M. Viswanatha, *Mater. Des.* **63**, 294 (2014)

Mechanical and Tribological Aspects of Aluminium Alloy Composites for Gear Application—A Review



Ashiwani Kumar and Mukesh Kumar

Abstract This chapter highlights the mechanical and tribological aspects of aluminium alloy composites that may act as a better substitute as a Gear material. It elaborately discusses the impact of mechanical properties (like hardness, impact strength, fracture toughness, etc.), material selection factors (like particulate reinforcement type, proportion, size, geometry, etc.), and tribological factors (like sliding velocity, sliding distance, load, etc.) of such aluminium alloy composites on the sliding performance of Gear. The specific results indicate that selection of particulate reinforcement type, proportion, size, and geometry leads to improvement of the mechanical characteristics of aluminium alloy matrix, which further enhances their sliding wear tribological performance, thereby, justifying their suitability for Gear application. The scholars have to investigate the appropriate mix design specific to certain Gear applications. A carefully designed and tested aluminium alloy composite could be a better alternative for a higher benefit-to-cost ratio.

Keywords Mechanical properties · Sliding wear · Tribology · Aluminum alloy · Alloy composites · Gears

1 Introduction

In our automotive dependent world, where fossil-fuel resources are depleting, cost and fuel economy are significant concerns of consumers when buying a car. Friction is a major concern to vehicle efficiency because it absorbs nearly 10% of the input energy. It has investigated that the use of metal alloy composite for bevel gear, and the life strip of bevel gear is analyzed through stress [1]. This matrix is used in

A. Kumar (✉)

Mechanical Engineering Department, Feroze Gandhi Institute of Engineering and Technology, Raebareli 229316, U.P., India
e-mail: ashi15031985@gmail.com

M. Kumar

Mechanical Engineering Department, Malaviya National Institute of Technology, Jaipur 302017, Rajasthan, India

aerospace and automobile industries and improved characteristics, i.e. modulus of elasticity, microhardness, tensile strength, and wear resistance of particulate filled aluminum alloy composite [2–5]. Moreover, Savaskan et al. [6] had investigated the effects of nickel reinforcement on the small scale structure of a material, mechanical, and wear behavior of zinc aluminium alloy composite. They reported that the friction of composites slowly decreases after the increase in addition of nickel filler content in metal matrix composite. Further, Qua et al. [7] have studied the tribological characteristics of aluminum 6061 alloy, and found that they were improved using the surface compositing techniques with sub-micro-size ceramic particles and friction stir processing. The surface compositing technique was used in an alloy of wrought aluminum (6061-T651) with various sub-micro-sized particles. Thakur et al. [8] who had investigated the influence of varying amount of Ti reinforcement on mechanical properties and microstructure of aluminium alloy composite where Ti particulates were produced by the disintegrated melt deposition (DMD) processing technique followed by hot extrusion. The authors found that the mechanical properties such as elastic modulus, ultimate tensile strength, and yield strength increased, but ductility decreased with the addition of Ti particulates in the Al matrix.

Further, Jiménez et al. [9] studied the behavior of dry wear of NiAl₃-reinforced mechanically alloyed aluminium with different microstructure. They compared the wear resistance of both nickel-containing materials (MA Al–NiS and MA Al–Ni S₂), under variable situations with that of the nickel-free mechanically alloyed aluminum obtained by a traditional sintering cycle. Zhou et al. [10] found that properties and microstructure of in situ created MgAl₂O₄ spinel whisker reinforced aluminum matrix composite. MgAl₂O₄ spinel whisker reinforced composite was fabricated in situ by a powder metallurgy technique in an Al matrix. The hot extruded MgAl₂O₄/Al composite rods were obtained with high relative density. Both Hardness and softening temperature of composites are also increased with increasing content of MgAl₂O₄ whisker. The hardness was measured through Vickers microhardness tests, and the mechanism of the reinforcement effect of in situ generated MgAl₂O₄ spinel whisker was deduced. Further, Mobasherpour et al. [11] had investigated the influence of nano-sized Al₂O₃ filler on the behavior of mechanically synthesized 7075 aluminum alloy composite. The nano-composite powders were characterized by scanning electron microscope (SEM), transmission electron microscope (TEM), and X-ray diffraction (XRD). They found that the role of nano-sized alumina particles is to increase the crystallite size, lattice strain, density and the hardness, ultimate tensile strength of 7075 aluminum alloy with increasing nano-Al₂O₃ weight percentage at the expense of tensile ductility.

Wang et al. [12] had studied the microstructure and mechanical properties of (Al, Cr)₃Ti based alloy with various Al additions, where this mechanically alloyed composite was fabricated by hot isostatic pressing (HIP). The manufacturing processes are as given: (i) cubic L12 ordered structure with Al₆₇Ti₂₅Cr₈ powders was formed by mechanical alloying and annealing process, (ii) X% Al–Al₆₇Ti₂₅Cr₈ composites were produced by HIP, where X changes from 5 to 20 in steps of 5. Then, the mechanical properties and microstructure of (Al, Cr)₃Ti based alloy were

determined. Sabatini et al. [13] applied plasma electrolytic oxidation (PEO) technique for the surface treatment of wrought AA7075 aluminium alloy and A356 cast alloy to improve wear resistance under sliding and abrasive wear conditions. The performances of the two alloys were compared and the wear behavior of the PEO coatings on these two substrates was determined under condition of micro-scale abrasion (with both SiC and Al₂O₃ particles) and dry sliding conditions. Further, Venkataraman and Sundararajan [14] had investigated the wear behavior and sliding friction of aluminum (Al), aluminum alloy 7075 (Al 7075) and SiC_p reinforced aluminum matrix composites (Al-SiC), where they used dry sliding wear conditions, and the characterization was performed using Electron probe micro analysis (EPMA), Energy dispersive X-ray analysis (EDS), and SEM techniques. They concluded that the presence of thin and hard mechanically mixed layer (MML) provides the best wear resistance even though the coefficient of friction will stay high. The disadvantage of providing aluminum-metal matrix composites (AMC's) usually the relatively high cost of manufacturing of the reinforcement materials. These composites were synthesized by cost effective techniques that can be used for various important applications, and (AMCs) with Particulate reinforcement of their isotropic properties and lower cost are attracting researchers. The stir casting process is a liquid state process for manufacturing AMCs at industrial scale, and this method is easier than other techniques.

Metal aluminum gears have been replaced by plastic gears because of their functionality and cost advantages. The use of plastics and composites raises sustainability issues because of the depletion of non-renewable petroleum resources and the pollution that is generated. The limitations of composite aluminum alloy gears relative to conventional gears are that aluminum alloy composite gears are cheaper relative to conventional gear. Composites of aluminum alloy are light in weight relative to metal counterpart. Composite gear can be designed for its strength, hardness, and stiffness. Composites may be brittle hence less efficient under the influence of working environment.

Therefore, the present chapter summarizes the mechanical and tribological characteristics that were observed, and accordingly, different the ories showed the effect of this parameter on tribological state. Moreover, the wear behavior of aluminum alloy metal matrix composite may be realized by analyzing the effect of all these factors on tribological mechanisms encountered by morphology of worn surface composites.

2 Mechanical Characteristics of Metal Alloy Composites

The effect of refractory alloying conditions on mechanical properties of Ni–Al had been investigated by Liu, and Horton [15], where the authors used the fabrication techniques; melting, drop forging, and hot extrusion. Moreover, Subramanian et al. [16] studied the effect of adding aluminum to titanium nitride (TiN) matrix on corrosion resistance and properties of titanium aluminum nitride films coated on AISI 316

stainless steel, silicon wafer, and low carbon steel by reactive dc magnetron sputtering. The XRD, transmission electron microscope-selected area electron diffraction (TEM-SAED) patterns and X-ray Photoelectron Spectroscopy (XPS) analyses were used to determine the AlNi film microstructure. Mechanical properties like hardness and yield strength have increased with adding the Al reinforcement in the composite matrix.

Zheng et al. [17] had investigated the mechanical properties and microstructure of magnesium matrix composites reinforced with aluminum borate whiskers. They investigated the compatibility of the aluminium alloy composite whisker with molten magnesium alloys, and developed more cost effective magnesium matrix composites fabricated by squeeze casting technique. When the volume fraction was more constant than hardness, elastic modulus and tensile strength of the composites are increased. When the volume fractions was constant, elongation was decreased. Magnesium matrix composites are widely used for aerospace fields, and defense industry. Yu et al. [18] investigated the effect of coating Al_2O_3 reinforcing particles on the interface, and mechanical properties of 6061 alloy aluminum matrix composites. This study was performed to enhance the interfacial properties of the squeeze casting Al_2O_3 powder reinforced 6061Al composites. The comparison of the mechanical properties of coated Al_2O_3 /6061Al composite with those of uncoated particles showed that the mechanical properties of coated Al_2O_3 /6061Al composite are better. The elongation, ultimate tensile strength, and yield strength are increased as a result of coating Al_2O_3 reinforcing particles. Safavi et al. [19] had investigated that the influence of Al content on the mechanical properties and cold workability of Fe-33Ni-15Co alloy. They found that ductility and toughness decrease with increasing Al content reinforcement in the matrix composite. Thakur et al. [20] studied the effect of varying amounts of Ti reinforcement on the mechanical properties and microstructure of Al based composite, which was fabricated by the disintegrated melt deposition (DMD) processing technique followed by hot extrusion. They found that the mechanical properties such as ultimate tensile strength, yield strength, and elastic modulus increased, but ductility decreased with adding Ti particulates in the Al matrix.

Bhingole et al. [21] had studied the processing, microstructure, and behavior of ultrasonically processed in situ MgO- Al_2O_3 -MgAl₂O₄ distributed magnesium alloy composites. Microstructure of the composites was characterized for the uniformity in the distribution of reinforcement particles. Further, it was found that the mechanical properties such as hardness, yield strength, and strain-hardening exponent grow with the mixing of filler contents in matrix composite and related to mechanical properties. The dry sliding wear behavior was also evaluated over a range of loads, and the operating wear mechanisms are analyzed. Mordyuk et al. [22] studied the evaluation of the wear resistance of Al-6Mg alloy plates after reinforcement of sub-surface layers with QC Al₆₃Cu₂₅Fe₁₂ particles by the ultrasonic impact treatment (UIT). XRD and SEM represented that the layers of 40–50 μm thickness were produced by process which contain homogeneously dispersed fine (0.5–3 μm) or coarse (15

μm) particles, with the values of volume fractions 9% and 22%, respectively. It was also found that microhardness is affected by grain/crystallite size of the matrix alloy composite.

Stein et al. [23] studied first the effect of the multi-walled carbon nanotubes (MWCNT) concentration on the mechanical properties of carbon nanotubes (CNT)/AA5083 composites and compared their results with analytical models. Second they studied the reinforcement with MWCNT and single-walled carbon nanotubes (SWCNT). They determined the optimal content of CNT in order to achieve enhanced mechanical properties of AA5083 aluminium alloy matrix composites. Merhy et al. [24] investigated the Crack growth of A356-T7 aluminum alloy under thermo-mechanical fatigue loading. The important variables generating the fatigue crack propagation and relative contributions were calculated. He et al. [25] reported that the $\text{Al}_2\text{O}_3\text{-CeO}_2/\text{Ni}$ -base alloy composite coatings prepared on aluminum alloy 7005 which were prepared by plasma spray. They investigated the mechanical performance, wear properties, and microstructure of the composite coatings, and improved the wear resistance of Ni-base alloy coatings. Akbari et al. [26] had studied the fracture behavior and mechanical properties of nanometric Al_2O_3 particle-reinforced aluminium alloy (A356) composite, and focused on the parameters of vortex method. Nano- Al_2O_3 particles were milled separately with the powders of copper and aluminum then incorporated into aluminum alloy and used to fabricate A356/1.5 vol. % nano- Al_2O_3 composites.

Lee et al. [27] investigated the high temperature impact properties and microstructural evolution of 6061-T₆ aluminum alloy. The deformation behavior of 6061-T₆ alloy was determined at strain rates in the range $1 \times 10^3\text{--}5 \times 10^3 \text{ s}^{-1}$, and temperatures range 100–350 °C using a compressive split-Hopkinson pressure bar (SHPB). Karakulak et al. [28] studied the influence of nickel content on the hardness and microstructure of the Al–Cu–SiC composite alloys. They found that the wear properties of Al–Cu–SiC–xNi composite alloys which were determined under dry sliding conditions were affected. The hardness increased with the increase of nickel content, but the wear resistance reached a maximum with Ni addition at 1 wt.%Ni. The corrosion behavior of Al–Cu–SiC–xNi composite alloys was investigated using potentiodynamic polarization, impedance spectroscopy, and chronoamperometric methods, and corrosion resistance was improved with the increase of Ni content. Zhao et al. [29] investigated the development of silicon carbide (SiC) nano-particulate reinforced AlON composites through the change of SiC content. And it was determined that with increasing addition of SiC particles up to 8 wt.%, the relative density, hardness, Young's modulus, flexural strength, and fracture toughness all increased moderately, but when the addition of SiC nano-particles reached 12 wt.% all of these mechanical properties decreased. Skan et al. [30] studied the influence of silicon content on the tribological and mechanical properties of monotectoid-based zinc–aluminum–silicon alloys. The tensile strength and hardness of the alloys were found to increase with the addition of filler silicon content in the matrix. They found that friction coefficient and wear rate of the alloys decrease with the increase in silicon content up to 2 wt. % Si. It was also found that the wear behavior of the Zn–Al–Si alloys correlates strongly with their hardness, tensile strength, and friction coefficient. Jiménez et al.

[31] studied the dry wear of NiAl₃-reinforced mechanically alloyed aluminum with different microstructure. They compared the tribological resistance of both nickel-containing materials (MA Al–NiS and MA Al–Ni S₂), under variable conditions, where the nickel-free mechanically alloyed aluminum, MA Al S, was obtained using a traditional sintering cycle and used as a reference.

Savaşkan et al. [6] investigated the influence of nickel addition on the mechanical properties and microstructure, lubricated friction, and wear behavior of Al–40Zn–3Cu alloy, and determined the most suitable alloy composition (with nickel addition) for their tribological applications. They also found that the wear volume of the alloys exhibited a gradual decrease following an initial increase with increasing percentage of nickel. Qu et al. [32] improved the tribological properties of aluminum 6061 alloy using surface compositing with sub-micro-size ceramic particles through friction stir processing. They applied the surface compositing technique in a wrought aluminum alloy (6061-T651) with two different sub-micro-size ceramic particles and characterized of the processed composite surface. Chen et al. [33] investigated the room temperature mechanical properties of Al–8.5Fe–1.3V–1.7Si/15 vol. % SiC_p composite sheet (where the subscript p refers to particulates) produced using a spray deposition (SD)-rolling process. They determined the micro-structures, density, and rigidity. Joel Hemanth [34] studied the influence of presence of nano particulates ZrO₂ particulates in Al matrix, and the effect of its increasing amount on the mechanical response and microstructure of standard LM 13 Al alloy. They found that the presence of nano-ZrO₂ particles in the Al matrix significantly improves hardness, strength, and fracture toughness, but slightly reduces the ductility. Also they observed that the thermal and electrical tests developed on the composite indicate that both electrical resistance and thermal conductivity decreased with increasing the reinforcement content.

Yar et al. [35] studied the mechanical properties and microstructure of aluminum alloy matrix composite with nano-particle MgO as the reinforcement, where reinforced A356.1 alloy was fabricated by stir casting method. Nano-particle MgO, wrapped in aluminum foil, was incorporated into the molten metal, at various temperatures. Simultaneous stirring of molten metal at constant stirring rate was also employed. Reinforcement content and optimum casting temperature were found by investigating mechanical properties and microstructure. Onat [36] investigated the mechanical properties, micro structural features, and dry sliding wear properties of Al–4.5Cu–3 Mg/15 vol. % SiC_p matrix composites, synthesized by squeeze casting technique. The improvement of dry sliding wear characteristics of Al–4.5Cu–3 Mg matrix composites reinforced with SiC particles at different loads and speeds has been investigated. Tang [37] studied the mechanical/thermal stress intensification for mode II crack tip: Fracture initiation behavior of steel, titanium, and aluminum alloys. Also, how the thermal stress affects the fracture behavior, and in what cases the heat flow enhances or retards the crack propagation are analyzed and discussed.

Panagopoulos et al. [38] studied the surface mechanical behavior of Ni–P–fly ash coatings containing various amounts of Fe, and deposited by electroless deposition technique on zincate coated 5083 wrought aluminium alloy substrates. They found

that these coatings higher hardness and roughness compared to Ni–P/zincate coatings, and the frictional coefficient of Ni–P–fly ash/zincate coating/stainless steel is less than that of 5083 aluminium alloy/stainless steel. Abdizadeh et al. [39] have investigated that the effects of sintering temperature and content of zircon on some mechanical and physical properties, such as microstructure, morphology, yield strength, compression strength, elongation, and density of an aluminium/zircon silicon oxide (Al/ZrSiO₄) composite produced by powder metallurgy techniques.

Sajjadi et al. [40] have investigated the behavior of mechanical aluminum alloys reinforced by micro and nano hard particles such as aluminium oxide and silicon carbide. The nano and micro composites were synthesized by two techniques; stir-casting and compo-casting. The structure was determined by optical (OP) microscope and scanning electron microscope (SEM). Further, they also studied the mechanical properties like yield, compression, and ultimate tensile strength of the composite and found that they increase with increasing aluminium oxide percentage because of the increasing load stress. Further, Liu et al. [41] had studied the aluminum matrix composites reinforced with various percentages of multi-walled carbon nanotubes produced by friction stir processing (FSP) technique. The microstructure was determined by the optical microscope (OM), transmission electron microscope (TEM), and SEM. It was found that the microhardness and tensile strength of MWCNTs/Al composites gradually increase with increasing MWCNT content, but the elongation decreases. Zhou et al. [10] had studied the properties and microstructure of in situ produced magnesium aluminates (MgAl₂O₄) spinel whisker reinforced aluminum matrix composites, which were produced using the powder metallurgy technique. The as-prepared composites were hot extruded and magnesium aluminates/aluminum composite rods with more relative density were obtained. Hardness and softening temperature of the composites were increased with increasing the content of magnesium aluminates whisker. The hardness, thermal behaviors are determined by Vickers microhardness test and coefficient of thermal expansion (CTE) measurements respectively, while wear resistance was determined by abrasive wear tests. The mechanism of the reinforcement effect of in situ generated MgAl₂O₄ spinel whisker was determined too.

Pengting et al. [42] had studied a new Al–3Ti–1B–0.2C master alloy which was prepared by the melt reaction method. They investigated the grain refining performance of the master alloy on the A356 alloy. The mechanical properties of aluminium alloy A356 including the ultimate tensile strength, yield strength, and elongation had been improved with the addition of the master alloy. The master alloy showed high grain refining efficiency and stability. It could be used for industrial application such as cast aluminum alloys. Further, Selvam et al. [43] had studied the effect of fly ash content on the mechanical properties and microstructure of AA6061/fly ash aluminum metal matrix composites (AMCs). Aluminum alloy AA6061 filled with fly ash particles was fabricated by the combocasting method. The microstructures of the (AMCs) were analyzed using SEM. The microhardness and tensile strength of the AMCs increased with the addition of fly ash particles in metal matrix composite, and higher ultimate tensile strength (UTS) was obtained compared to unreinforced AA6061 alloy. Mobasherpour et al. [11] studied the effect of nano-size aluminium

oxide filler on the mechanical behavior of synthesis 7075 aluminum alloy composites by mechanical alloying. The nano-composite powders were characterized by SEM, TEM, and XRD. They investigated the role of alumina hard nano-sized particle reinforcement on the crystallite size, lattice strain, density, hardness, and mechanical properties, and found that the ultimate tensile strength and hardness of the Al 7075 nano-Al₂O₃ tend to increase with increasing nano aluminium oxide volume content at the expense of tensile ductility.

Hamid et al. [44] had studied the surface mechanical properties and microstructure of electrodeposited Ni coating on aluminium alloy composite Al 2014. The authors modified the surface of Al 2014 using electrochemical deposition of Ni, and concluded that electrochemical deposition combined with heat treatment can be used to enhance the surface mechanical properties of aluminium alloys. They also determined the electrochemical conditions and the heat treatment method under which compact, uniform, and adherent Ni coatings can be obtained on aluminium alloy Al 2014. Moreover, Zhang et al. [45] had investigated the mechanical properties and microstructure of multiphase coating deposited by plasma nitriding GB-5083 aluminum alloy coated by Ti. The authors developed this method to manufacture multiphase coatings containing both nitride and intermetallic on GB-5083 aluminium alloy to harden its surface properties. Their method consists of two steps, i.e. producing pure Ti film on the GB-5083 aluminium substrate, and post plasma nitriding the Ti coated substrate. Furthermore, Arik [46] had studied the influence of the process of mechanical alloying on mechanical properties of aluminum-based composite materials reinforced with α - silicon nitride (α -Si₃N₄). The mixture of Al and α -Si₃N₄ powders was prepared using two different methods, namely; mechanical alloying, and conventional mixing. The effect of some variables, such as sintering temperatures, the amount of silicon nitride, and the preparation of the starting powders on the mechanical properties of the produced Al matrix composite materials were observed and investigated.

Further, Wang et al. [47] had studied the mechanical properties and microstructure of (Al,Cr)₃Ti based alloy with various Al additions. The composites were manufactured by hot isostatic pressing (HIP). The manufacturing technique used by these authors to fabricate (Al,Cr)₃Ti based alloys by additions of Al was (mechanical alloying (MA) + hot isostatic pressing (HIP)). The followed processes are given as (i) cubic L12 ordered structure (Al,Cr)₃Ti. which was made by mechanical alloying and annealing process, (ii) Al-(Al, Cr)₃Ti composites which were fabricated by HIP. The mechanical properties and microstructure of (Al,Cr)₃Ti based alloy were determined. Panagopoulos et al. [48] investigated the mechanical behavior of Zn-Fe alloy coated mild steel samples. The ultimate tensile strength of Zn-Fe coated mild steel was less than that of the bare mild steel. The ductility of Zn-Fe coated mild steel was found to decrease significantly with increasing Fe content in the coating.

Devaraju et al. [49] found that the effect of filler particles and rotational speed on the mechanical properties and wear of aluminum alloy 6061-T6/(SiC + Al₂O₃) surface hybrid composites. These hybrid composites were synthesized by the use of friction stir processing (FSP), and Taguchi method was used to obtain the optimum

rotational speed and volume percentage of filler particles for improving the mechanical properties and wear of the surface hybrid composites. The filler particles (i.e. SiC and Al_2O_3) decreased in size ($\sim 5 \mu\text{m}$) than the as received particles size, and the wear resistance at optimum condition improved. The mechanical properties and wear were found to be correlated with microstructures and worn micrographs [50]. Further, Zheng et al. [51] had studied that mechanical properties and microstructure of aluminum alloy matrix composites reinforced with Fe-based metallic glass particles. This composite was synthesized by the powder metallurgy method.

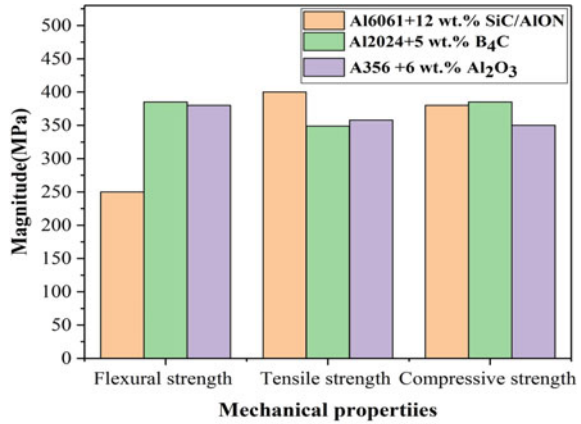
Zadeh et al. [52] had investigated the structural and mechanical characterization of aluminium based composite which was reinforced with heat treated aluminium oxide particles. The aluminium oxide particles were heated at 1000°C , and x-ray diffraction (XRD) was used to characterize the structure of Al_2O_3 during heat treatment. Scanning electron microscope (SEM) was used to determine the size and shape of the Al_2O_3 grains. The compression strength of the aluminum with 1 wt.% aluminum oxide was found to increase while adding Al_2O_3 heat treated particles to A356 metal matrix.

Taleghani et al. [53] had investigated the mechanical and microstructural characterization of 7075 aluminum alloy consolidated from a premixed powder using cold compaction and hot extrusion. To avoid the effects of microstructural differences between various parts of the extrudates, all of the samples were cut from the center of each extruded rod [54]. The extruded samples were characterized using SEM and XRD techniques. Ozdemir et al. [55] had investigated the effect of forging on the properties of particulate-silicon carbide reinforced aluminum-alloy composites. The mechanical properties of these composites reinforced with particulate SiC were investigated under foundry conditions. The effects on the mechanical properties after forging were found to increase with yield strength, and improvement of tensile strength, but ductility decreased with the addition of the particulate reinforced SiC in the metal matrix composites up to an optimum reinforcement volume fraction.

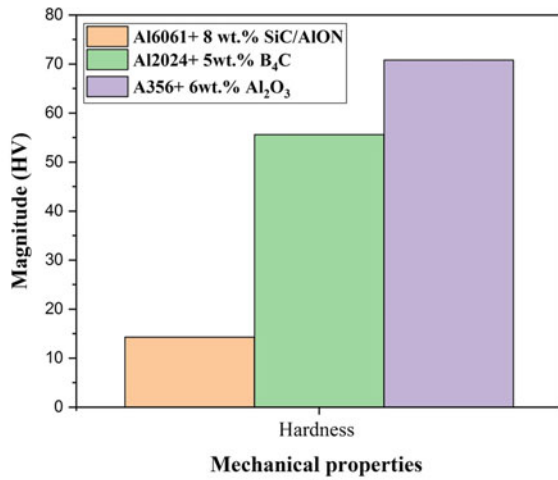
Chou et al. [56] had investigated the effects of the composition on the homogenized analysis and physical properties. In addition, the microstructure and uniform properties analysis of the composites are observed. The aluminum alloy composites A356, 6061, and 1050 are infiltrated into the porous aluminum oxide (Al_2O_3) performs which were formed by sintering, by squeeze casting to make $\text{Al}_2\text{O}_3/\text{A356}$, $\text{Al}_2\text{O}_3/6061$, and $\text{Al}_2\text{O}_3/1050$ composites.

Figure 1a, b and Table 1 show a summary of the mechanical properties and the effects of various fillers on mechanical properties of aluminium composites from literature. It is found that the 12 wt.% SiC/AlON tensile strength is higher than other fillers of composite. The 5 wt.% B_4C flexural and compressive strength is maximum compared to other particulate fillers. Hardness of composites increases with increasing various filler contents. Hardness of composite is higher at 6 wt.% Al_2O_3 compared to other reinforcements. Similar results were reported by various materialists [6, 22, 36]. Therefore, this chapter shows that the mechanical properties of metal matrix composite were improved by reinforcements.

Fig. 1 Comparative studies of mechanical properties of aluminum alloy composite. **a** Flexural, tensile, and compressive strengths. **b** Hardness [19, 29, 33]



(a)



(b)

3 Tribological Behavior

3.1 Effect of Wear Parameters

3.1.1 Normal Load

Zhiqiang et al. [57] had discovered that wear loss of both the aluminium alloy matrix as well as composite samples increase with increasing the applied load. The authors had found that the frictional coefficient of the composite specimen is less than that of the aluminium alloy matrix upto a load of 65 N and vice versa. At a load of 50 N, the transition of the tribological conditions of aluminium alloy matrix takes place,

Table 1 Comparative studies on mechanical properties of aluminum alloy composite [19, 29, 33]

| Composition | Hardness (HV) | Flexural strength (MPa) | Tensile strength (MPa) | Compressive strength (MPa) |
|--|---------------|-------------------------|------------------------|----------------------------|
| Al6061 + 0% SiC/AlON | 13.5 | 300 | 325 | 225 |
| Al6061 + 4% SiC/AlON | 13.8 | 330 | 350 | 300 |
| Al6061 + 8% SiC/AlON | 14.3 | 400 | 375 | 337 |
| Al6061 + 12% SiC/AlON | 10.5 | 250 | 400 | 380 |
| Al2024 + 0%B ₄ C | 20.4 | 400 | 250 | 270 |
| Al2024 + 1%B ₄ C | 28.7 | 430 | 270 | 290 |
| Al2024 + 2%B ₄ C | 35.8 | 456 | 290 | 310 |
| Al2024 + 3%B ₄ C | 46.9 | 500 | 330 | 350 |
| Al2024 + 5% B ₄ C | 55.6 | 525 | 349 | 385 |
| A356 + 0% Al ₂ O ₃ | 25.7 | 275 | 350 | 290 |
| A356 + 2% Al ₂ O ₃ | 29.4 | 325 | 340 | 310 |
| A356 + 4% Al ₂ O ₃ | 38.9 | 360 | 356 | 320 |
| A356 + 6% Al ₂ O ₃ | 70.8 | 380 | 358 | 350 |

while wear resistance of the composite specimen was improved in comparison to that of the alloy specimens. At this condition, the wear loss rises suddenly for the metal alloy matrix composite. Therefore, the AMCs reinforced with 9 wt.% SiC possess greater wear resistance than the matrix alloy [58]. These results were also found by Rajeev et al. [59] who had investigated the wear of aluminium composites reinforced with 15 wt.% silicon carbide contents and found that specific wear rate increases as the normal load increases in the range 60 N–120 N. During the manufacturing of composite specimens, aluminum alloy gets in SiC particles and coefficient of friction decreased with the increase in the applied load value of up to 98 N and this condition was assigned to the presence of trio layers within a specific normal load.

Similar findings were reported by Baradeswarm et al. and Ravindran et al. [60, 61]. The increase in the wear rate with increasing load may be related to the more plastic deformation of wear surface under highest load. Kumar and Dhiman [62] had observed different wear mechanism during the analysis of hybrid composite and

unreinforced alloy under condition of sliding wear (for a load range of 20–60 N). The transitional load was also reported by the researchers for all the specimens. They have also found that the hybrid composites showed higher wear resistance than those of the alloy matrix over the complete range of the applied load. Rajmohan et al. [63] and Radhika et al. [64] had found that the wear rate improved with a growing applied load value for all of the composite samples. The wear performance of hybrid composite has been analyzed by the analysis of variance technique, and it shows the effect of very important controllable parameters. In these investigations the load has been observed as a significant contributor in wear behavior of composites. It was found that the wear mechanism of the particulate reinforced hybrid composite is different from the adhesion to pure abrasion with the improvement of the normal load value. Furthermore, Umanath et al. [65] found that wear rate of the composite increases with increasing load from 40 to 60 N. The authors found that the decrease of the load decreases the force of friction, and increasing the load, reduces the hardness and increases the wear rate.

Further, Murakami et al. [66] investigated the wear properties and friction when sliding against aluminum alloy 5052 pin samples during unlubricated conditions at 823 K in air. Si_3N_4 –8 mass % Al_2O_3 –6 mass% Y_2O_3 , AISI 52,100 steel, ZrO_2 –3 mol.% Y_2O_3 , WC-6 mass% Co were chosen as disk materials, because they were used as sliding materials. Moreover, the worn surfaces of the disk and pin samples were observed by scanning electron microscopy (SEM). Howell and Ball [67] had studied the sliding wears of alloys with particulate-reinforced against friction materials. They reported that the effect of contact pressure, and sliding velocity on the friction and wear mechanisms occurs at the sliding interface. Rao et al. [68] studied the influence of heat treatment on the sliding wear of aluminum alloy (Al–Zn–Mg) hard particle composite. They reported that during varying applied load and sliding speed, where the authors emphasized on variables like wear rate, temperature rise, coefficient of friction, and seizure pressure. The sliding wear of 7009 alloy, especially compared to 7009 alloy with silicon carbide composite was missing even though it has good strength for use as airplane structural sheets, and armor materials. Daoud and Khair [69] studied the influence of speed and load on the wear and frictional behavior of brake rotor fabricated from alloy A359 with 20 Vol. % SiC particle composites sliding against the automobile friction material. The dry wear behavior and sliding friction were determined in a pin-on-disc apparatus. The composite was prepared by the use of the stir casting technique. The wear debris and worn surfaces were checked for their chemical characterization and morphology using SEM provided with energy dispersive X-ray (EDX) analyzer. Ramesh et al. [70] had investigated wear behavior and friction of nickel phosphorus (Ni–P) coated silicon nitride (Si_3N_4) reinforced Al6061 alloy composites. Dry sliding friction and wear tests were examined using pin-on-disk apparatus. Al6061–Ni–P– Si_3N_4 composites exhibited reduced wear rate and coefficient of friction compared to the matrix alloy, but increased wear resistance.

Jha et al. [71] had studied the sliding wear behavior of aluminum syntactic foam (ASF), where they made a comparison with the wear behavior of 10 wt.% silicon carbide (SiC) particle-reinforced aluminum matrix composite (AMC). The experiment was performed under dry and lubrication conditions using the pin-on-disc

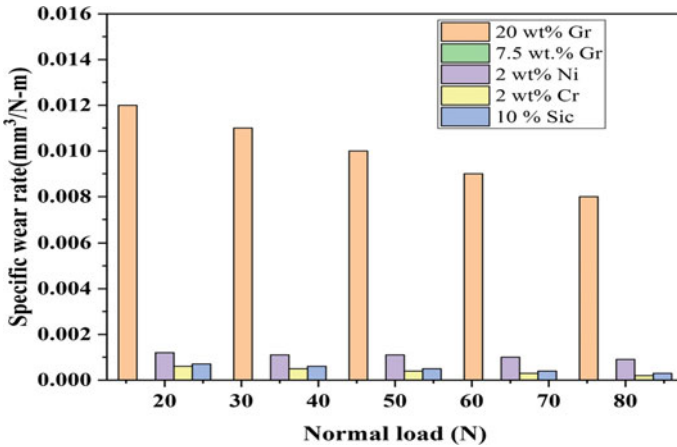


Fig. 2 Comparative studies of influence of normal load and reinforcement type on specific wear rate [57–65]

machine. And tribological properties such as wear rate, the frictional coefficient, and the frictional heating were determined and discussed. It was reported that wear rate, friction coefficient, and temperature rise of (ASF) were smaller than those of (AMC) in both dry and lubricated conditions. Moreover, Zhu et al. [72] had studied the dry sliding friction and wear characteristics of in situ composites (Al₃Zr + α-Al₂O₃)/Al at high temperature, using of the pin-on-disc machine. The wear resistance of the composites was found to be increasing by the increase of the reinforcement volume fraction. Figure 2 shows the influence of load on specific wear rate of aluminum alloy composite, and it was found that various reinforcements show different specific wear rates with load. It was found that 20 wt.% Gr specific wear rate is good compared to the other fillers. Summarizing the effect of applied normal load on the tribological behavior of aluminum alloy composites, it could be said that wear mechanism of composites acts by different load dependent zones. This area was further investigated to be based upon the interaction of applied normal load with several other variables [48–72]. Further, normal load has been found by almost all the researchers, giving details about the safe loading conditions and working areas for an individual composite.

3.1.2 Sliding Velocity

Zhiqiang et al. [57] investigated the effects of sliding velocity on weight loss and frictional coefficient of silicon particles reinforced aluminum matrix composites and noted increasing trend with increasing the sliding speed. Ravindran et al. [61] also found that the wear loss of powder metallurgy based Al 2024/5 wt. % SiC/x wt.% Gr (x = 0, 5, 10) composites was decreasing with increasing sliding velocity (up to a transition velocity of 5 m/s). Therefore, the Al 2024/5 wt.% SiC/5 wt.% Gr

composite showed smallest wear loss among all specimens of the composite. The authors [61] made analysis of variance (ANOVA) table to determine the order of significant factors and their interactions and found that the sliding speed effect on the wear behavior was 12.43%, and the effect of sliding speed on frictional coefficient was 8.86%. The reduction in wear of the composites may be related to the presence of solid lubricant (graphite) particles in the composites, which form a tribo-layer on the wear contact surfaces. Kumar and Dhiman [62] had also found that the specific wear rate of unreinforced alloy (Al 7075) and composite (Al 7075/7 wt.% SiC/3 wt.% Gr) reduced with increasing the sliding speed (up to 4 m/s) for few normal load conditions (20–40 N). Therefore, the specific wear rate of both materials was changed, i.e. the weight loss increased with sliding speed. But, under more loads (40–60 N), the unreinforced alloy seized at a speed of 6 m/s due to the combination of abrasion and delaminating wear, when severe wear was reported on the composite (without a seizure). However, the transitional speed of 4 m/s was reported, beyond which the wear raised rapidly for all specimens.

Further, Ramachand and Radhakrishna [73] had studied the effect of fly ash reinforcement on corrosive behavior, sliding wear, and slurry erosive wear of aluminum matrix composite and the aluminum alloy composites which were synthesized by the use of the liquid metallurgy route. However, the sliding wear of the metal matrix composite were obtained by various parameters like normal load, percentage fly ash, and track velocity, and sliding wear behavior was investigated using pin-on-disc wear testing machine. The worn surfaces are observed using scanning electron microscope and it was observed that wear resistance of fly ash reinforced material increased with increasing fly ash content, but decreases with increasing the normal load, track velocity. Corrosion wear had increased with the addition of particulate reinforced fly ash of the composite. Also it was observed that the magnitudes of wear and frictional force increase with increasing the normal load and sliding velocity. These findings are consistent with the those obtained by Lee et al. [74] had investigated dry sliding wear of the micro-arc oxidation (MAO) coating applied on aluminum matrix composites A356/20 vol.% SiC_p composites with and without surface coating. The samples were tested using pin-on-disc wear test apparatus in the temperature range 25–180 °C with different sliding velocities, and applied load. The authors studied the feasibility of more improvement of wear behavior for alloy composites by MAO coating technique. The variation of wear rate with the applied load and sliding speed for uncoated and MAO-coated specimens were tested at room temperature for constant sliding distance of 1500 m. It was observed that the wear rate increases with increasing applied load and sliding speedy regardless coating thickness.

Figure 3 shows the influence of sliding velocity on specific wear rate of aluminum alloy composite with various types and quantities of reinforcements. It is reported that the 15 wt.% SiC of specific has the best wear rate than other fillers, and the lowest wear rate is that of the 2 wt.% Co filler. Similar studies are reported by various researchers in above literature [57–62].

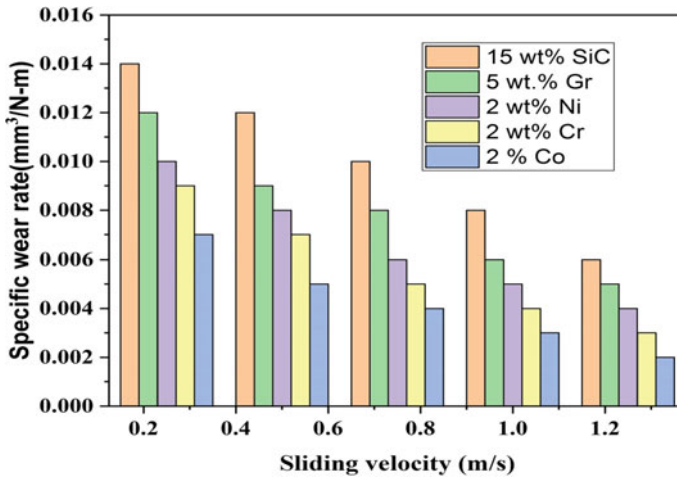


Fig. 3 Comparative studies of the effect of sliding velocity on specific wear rate for different types and quantities of fillers [57–62]

It has been uncovered from the literature review that the kind of counterpart and load variation may outcome in conflicting outcomes [57, 59, 63, 64]. From these investigates, it is not possible to get a general relationship between the wear of composites and sliding velocity (0–5 m/s). In general, one can say that as the surface of wear track comes in contact with the counter face during initial run-in-period, the wear rate of aluminium alloy composite has also increased. Yet, the wear rate obeys decreasing pattern with enhanced velocity. It may be related to temperature increase and tribo-layer formation (based on interaction with other variables) up to the transition limit. Moreover, the tribo-layers are divided and metal-to-metal contact begins. At larger sliding speed, more frictional heat was generated which causes localized melt and more plastic deformations. These factors contribute to remove materials from the wear surface, and the wear tracks have been clearly noticed in some of the examinations [63, 64].

3.1.3 Sliding Distance

The weight loss was approximately linearly related with the sliding distance, which is the repeated trend followed by wear type characterized by tribo-chemical reaction, mainly when oxidation of the matrix occurs. The wear resistance increases with increasing the sliding distance owing to shear force, and micro-cutting by the hard asperities of the counter face material, then the matrix alloy will deform and when the sliding distance increases, frictional heat between pin and disk surface also increases. The wear rate increases with increasing the sliding distance because of the increase of temperature and cracking of the composite specimen [57–60].

Ravindran et al. [61] have investigated the wear loss and frictional coefficient of Al 2024–5 wt.% SiC- x wt.% Gr ($x = 0, 5, 10$) composites increase with increasing sliding distance. By using ANOVA they found that sliding distance had the largest influence on wear loss, with percent of significance ($p = 57.12\%$).

Further, Kumar and Dhiman [62] had investigated sliding wear behaviors of the hybrid composite and 7075 aluminium alloy at small speed (2–6 m/s) and small load (20–60 N) combinations. They reported that for combination of small speed (2–4 m/s), and small loads (20–40 N), the specific wear rate follows a reducing trend with increasing the sliding distance in the range 2000–4000 m. According to them this may be related to initial association between the two surfaces through large number of sharp asperities and the contact between the two surfaces was made by these points.

Toptan et al. [75] had reported the effects of B_4C volume fraction, sliding velocity, sliding distance, and applied load on dry sliding wear behavior of aluminium alloy matrix composites reinforced with 15 and 19 vol.% B_4C_p which were fabricated by squeeze casting route at 850 °C under low vacuum. In their study, they used a general full factorial experimental design. The authors determined the effects of the mentioned factors and interactions on the average frictional coefficient values, and value of wear rate combine in composite specimens and counter materials. Regarding the sliding distance, they reported that the frictional coefficient and wear rates increased with increasing the value of sliding distance. Moreover, they reported that the values of frictional coefficient were almost linearly increasing during sliding distance. Further, Sarmadi et al. [76] had also studied the influence of graphite content on the value of frictional coefficient, and wear loss for metal composites and Copper–graphite composites, which were synthesized by the use of friction stir processing technique. The friction and wear behavior of the composites were tested by a pin-on-disc tribometer. In Fig. 13 of Ref. [76] the wear weight loss was plotted versus sliding distance in the range 0–1000 m for specimens of different graphite content, and the figure shows that wear weight loss increases with the increase in sliding distance.

Basavarajappa et al. [77] had studied the influence of sliding speed, sliding distance, and normal load on dry sliding wear behavior of the Al/SiC_p and Al/SiC_p–Gr composites, which were fabricated by liquid metallurgy route, where the Taguchi experiments were used for collecting data. An orthogonal array and analysis of variance were utilized to get the percentage of influence of various parameters on dry sliding wear of the composites and the alloy composites with particulate SiC and graphite (Gr) particles [78]. It was observed that graphite particles were effective factors in increasing dry sliding wear resistance of Al/SiC_p composite. Baskaran et al. [79] had investigated the sliding wears behavior of in situ casted aluminium alloy AA7075 reinforced with 4 wt.% and 8 wt.% tin carbide TiC fabricated by the use of reactive in situ casting technique, where Taguchi technique was used. The wear behavior was obtained using a pin-on-disc tribometer machine, and they examined the significance of the effect of filler percentage, sliding velocity, sliding distance, and load on the sliding wear behavior of the fabricated composites using ANOVA analysis. They found that load and sliding velocity with percentage contributions of

50.09% and 31.26% respectively are the most effective, on sliding wear behavior, while sliding distance is insignificant with very small percentage contributions.

Also Kiran et al. [80] had investigated the parameters that influence the wear behavior of heat treated zinc alloy (ZA-27), and zinc alloy/silicon carbide-germanium (ZA-27/9SiC-3Gr) by Taguchi technique. Zinc based alloy and composite particulate with SiC_p (9 wt. %) and Gr (3 wt. %) were manufactured by stir casting method, and wear behavior was analyzed using a pin-on-disc apparatus. The influence of various parameters likes, sliding speed, load, and sliding distance on wear behavior were determined using analysis of variance (ANOVA), and wear mechanism of the worn surface was analyzed using scanning electron microscopy. They found that load is the most important parameter in causing wear in the case of the alloy followed by sliding distance, then sliding speed. Similarly for composites the most significant is the load, followed by sliding speed, and sliding distance.

Further, Jin et al. [81] had investigated the friction and wear characteristics of Mg₂B₂O₅ whisker reinforced aluminium 6061Al matrix composite produced by power ultrasonic-stir casting process. The ball-on-disk wear testing machine was used under dry sliding conditions. It was reported that the wear rate of the Mg₂B₂O₅ whiskers coated with ZnO reinforced aluminum matrix composites was the smallest among the materials. They reported that the frictional coefficients of the matrix and composites were gradually decreasing and remained stable with the increase in the sliding distance and sliding time. Jiang et al. [82] had studied the friction and wear properties of in situ synthesized aluminium oxide reinforced alloy composites. These composites were manufactured by powder metallurgy and in situ reactive synthesis method. The influence of various parameters sliding speed, load, and long-time continuous friction on friction and wear properties of Al-5% Si-Al₂O₃ composites were studied. The authors found that the frictional coefficient and wear loss increased with the increase of the sliding distance. Alidokhta et al. [83] had investigated the microstructure and wear behavior of friction stir processed cast aluminum alloy (A356), where the composites were synthesized using friction stir process, and dry sliding wear tests were performed on a pin-on-disc apparatus. They observed that the wear mass loss increases with increasing sliding distance, and the extent of wear is significantly lower in friction stir processed A356 when compared with the as-cast A356. The wear rate was found to decrease with sliding distance, but it is larger in the case of as-cast A356.

Baradeswaran and Elaya Perumal [84] had investigated the influence of graphite on the tribological and mechanical behavior of Al 7075 composites under dry sliding conditions. The composites were synthesized using liquid casting method. They evaluated the optimum amount of graphite added in Al 7075 for the minimum wear rate. In addition to other results they reported that the wear mass loss decreases with the increase in sliding distance, while wear rate increases with increasing sliding distance. Thangarasu et al. [85] have reported the effect of TiC particles of various volume fractions on dry sliding wear behavior and microstructure of AMCs. TiC were used as reinforcement to make AMCs due to its hardness and its elastic modulus. These composites were produced by the use of friction stir processing (FSP) method. The microstructure of AA6082/TiC AMCs was examined by the

optical spectroscopy and the scanning electron microscope (SEM), and sliding wear behavior was performed by using a pin-on-disk apparatus. Their data in Fig. 5a shows that the weight loss approximately increases with the increase of sliding distance but in two stages (before 500 m, and after 500 m), while Fig. 5b in their work shows that the rate of wear fluctuates and shows maxima and minima with sliding distance.

On the other side, Radhika et al. [64] had reported a reduction in the wear rate as well as the frictional coefficient within selected values of sliding distance, which may be related to the presence of hard alumina particles, which produce abrasion resistance. The researchers had reported various regions while considering the effect of sliding distance on wear behavior of the composite.

Figure 4 shows a comparative plot of sliding distance and several particulates on the specific wear rate of aluminum alloy composite. It was found that the specific wear rate decreases with the increasing the sliding distance. The SiC_p reinforcement wear rate is higher than those of the other reinforcing particulates. These results are also dependent on the interaction of sliding distance with other parameters. As the numerical values of another variable change, wear performance of the composites changes too. The abrasion was the normal mechanism which had been reported for the composites with an increasing distance. The research [64] also disclosed that sliding distance is the most influential variable with contribution of 46.8%, and the contribution of sliding distance to the friction coefficient is (50%). As far as the influence of sliding distance on the tribological behavior of aluminum alloy composite is concerned, some of the investigators had found initial-run-in period during the wear investigations [61, 62]. However, some had found the initial-run-in stage for the AMCs [57, 59, 64]. However, the contradiction in outcomes may be a remark to the interaction of sliding distance with other variables.

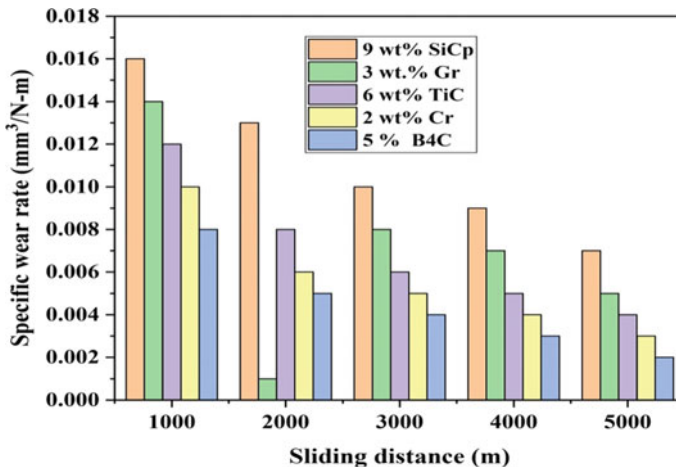


Fig. 4 Comparative studies of influence of sliding distance, and different reinforcements on specific wear rate of aluminum alloy composite [75–94]

3.2 Influence of Material Factors of Metal Alloy Composite

3.2.1 Influence of Reinforcement Type of Metal Alloy Composite

Aluminium composites reinforced with ceramic phases like Al_2O_3 or SiC have performed well tribological properties [57, 59]. Some investigators [95, 96] had reported that a critical load survives during dry sliding conditions above which a ceramic dependent composite offers small change in wear resistance differentiate to a non-filled sample, while others [96, 97] had reported that hard ceramics can actually increase the wear rate of mating counterface due to their abrasive action, and therefore can decrease the overall wear resistance of the tribo-system. In this respect, the discovery of Al-composite reinforced with smooth phases were also of great interest. These authors [97, 98] had also reported that the intermetallic fillers such as Ni–Al and Ni_3Al enhance the wear resistance of Al-alloys (similar as that of SiC reinforced composite). Furthermore, it also helps in decreasing the wear of counterface simultaneously. Walker et al. [99] had prepared aluminium alloy matrix composites reinforced with 15 vol.% Ni_3Al intermetallic particles which gave superior wear resistance to the monoliths at loads 42 and 91 N.

Pan et al. [100] showed that Al 2124 + SiC exhibits more wear resistances than the Al 2124. The flow of alloy matrix around the fillers had been noticed by Wang et al. [98] too.

3.2.2 Influence of Reinforcement Content of Metal Alloy Composite

It had been recognized that the more volume fraction of hard ceramic filler improves the wear resistance of discontinuously reinforced aluminum (DRA) through abrasion, fretting, and sliding, except under few situations, through the wear rate for reinforced and unreinforced Al-matrices are alike (e.g. for a particular range of applied normal load and sliding velocity) [101]. Further, Rajeev et al. [59] for Al–Si– SiC_p composites found that the tribology loss and frictional coefficient of the composites decrease with increasing SiC_p contents from 6 wt.% to 18 wt.%. Dwivedi [102] found that the increase in Si-contents in cast Al–(4–20%) Si–0.3% Mg composites increases the resistance for thermal softening and also increases the ability to support the oxide film surface. Silicon addition to pure aluminium improves wear and seizure resistance, because silicon is an anti-adhesion agent [103]. Baradeswaran et al. [60] have investigated the composites (AA7075 + Al_2O_3) and found that wear rates and frictional coefficient decrease as the Al_2O_3 reinforcement content increases up to 6 wt.%, after which it begins increasing. The differences of wear rate and frictional coefficient with Al_2O_3 reinforcement contents were analyzed in the range 0–8 wt.% at different load conditions for 1200 m sliding distance. The wear resistance of the composites was increasing with addition of the Al_2O_3 particle content. It may be related to the cause that the particles of Al_2O_3 were much harder and stronger than the aluminium composite. Further, Ravindran et al. [61] had observed the effect of filler contents

of solid lubricant particles (for constant contents of SiC grains) in 2024 aluminium alloy with 5 wt.% SiC and x wt.% Gr ($x = 0, 5, \text{ and } 10$) composites. They reported that the lowest wear loss, and coefficients of friction are those of the composites with 5 wt.% graphite content, which was due to the self-lubricating effect of graphite. Their results showed that wear of hybrid composites first decrease with increasing Gr content up to 5 wt.%, then it increases for the 10 wt.% Gr content. Gautam et al. [104] found that there was decrease in ductility of Cu–4Cr–4G composites at larger particle content caused by hot forging, which may be related to the ease of fragmentation of metal particles from the matrix, and so contributing in increasing the volume loss. Savas and Bican [105] studied the properties of dry sliding friction and wear of the ternary Al–25Zn–3Cu and quaternary Al–25Zn–3Cu–(1–5)Si alloys. They reported that the steady state values of the frictional coefficient and temperature of the alloys was continuously increasing with increasing the silicon content, while the wear volume of the alloys increased with increasing the silicon content up to 3%, then the trend was reversed.

Wang and Rack [106] have elaborated a statistical wear model depending on the fact that the filler distributions are not perfectly homogeneous. By this model they reported that the wear rate of the unreinforced component varies exponentially with nominal reinforcement volume fraction. The experiments were performed on the SiC_w 2124 Al composite/17–4 PH steel system, and the results confirmed the validity of the theoretical model.

Moreover, Diler and Ipek [107] found that the volume fraction and particle sizes of matrix and reinforcement are effective on the wear behavior of Al–SiC_p composites, where wear loss decreases with the increase in the volume fraction up to a point (17.5 Vol.%), and volume fraction is the most significant factor for wear behavior, then the particle size of reinforcement and matrix, in addition, the interaction between volume fraction when it is high, and particle size of reinforcement has negative effect on the wear resistance. Also, they found that hardness increases with increasing volume fraction, and according to Archard's adhesive wear theory, the improve in wear resistance is related to the increase in hardness of the material. Moreover, wear loss depends on hardness of material according to Archard's theory too. The wear resistance is associated with hardness of material as given in the following formula [108];

$$V = \frac{r \times e \times q}{h} \quad (1)$$

where V is the volume of material, r is the wear coefficient, e is the sliding distance, q is the applied normal load, and h is the bulk hardness of the material.

The effect of the other variables (load, velocity, particle size, etc.) can also be simultaneously investigated to get exact understanding of the wear behavior of AMCs under increasing volume percentage [53].

3.2.3 Influence of Particle Size of Metal Alloy Composite

According to Hutchings et al. [109], and Zum Gahr [110] the removal of ceramic particles is a role of interface property of reinforcement and the matrix alloy as it keeps the ejection of reinforcing particles from the wear surface. As the interface bonding is strong to keep the whole particles in an alloy, while the composite is expected to give more wear resistance even under severe tribological conditions. The authors had investigated the ceramic particle size with regard to the depth/width of tribological groove produced by the counterpart that may be used to predict the possibility of ejection of the reinforcement particles from the wear surface during abrasive action. When the ceramic particle size (reinforcement) is less than the depth/width of the grooves, the reinforcement ceramic particles did not offer any resistance against the abrasive action. In the same context, some authors such as Mondal et al. [111] had investigated the critical abrasive size above which the composite can suffer of smaller wear resistance in comparison with the pure alloy.

Some researchers [112–114] found that AMCs suffer from the greater wear rate compared to the alloy at a load value of 7 N with 80 mm abrasive when the size of the SiC particle was within the range of 50 and 80 μm . The composites wear was found to be based on the contact of abrasives with the matrix. The number of fillers in the nominal region was varying with the size and proportion of the reinforcement. On the other side, Kumar and Balasubramanian [115] had developed a mathematical model to study the influence of reinforcement size and volume fraction on the abrasive wear behavior of AA7075Al/SiC_p P/M composites. They observed that the coarser the SiC_p articles the lower the abrasion and vice versa. That is reinforcement SiC_p particles of large size are expected to remain embedded in the matrix until it can no longer support them. So, in general for the taken range of particle size (which is about 40–150 μm), and volume fraction (which is 5%–25%), the coarser particle size and large volume fraction give larger abrasive resistance. Therefore, coarser particles give good protection to the matrix below sliding conditions. In the same context, Lee et al. [116] found for powder metallurgy (P/M) aluminium alloy 6061 matrix composites reinforced with silicon carbide particles (SiC_p) that when the composites contain the same amount of SiC_p particles, the wear rates decrease with increasing the size of SiC_p. Hence according to Yılmaz and Buytoz [117] the aluminium alloy composites which were reinforced with larger size of SiC_p particles are more effective against abrasive wear than the ones reinforced with smaller size SiC_p particles. This agrees with the findings of Diler and Ipek [107] who had found that for a particular range of volume fraction (12.5–17.5 vol%), the composites reinforced with fine particles show less better wear resistance as compared to those reinforced with coarse particles. Their idea of their investigations was that the increase in size of reinforcing particulate may be utilized or detrimental according to the operative mechanisms. However, a simple rule respecting the influence of reinforcement particles size on the wear characterization of composite can not be inferred [106–116]. Finally, it can be said that the interactions between various variables (i.e. reinforcement particle size, volume percentage) have considerable effect on the wear resistance of AMCs as well as their main effects.

4 Scope for Future Research Work

The research work thus far in the development of metal powder particulate filled metal fabricated alloy composites has decorated certain areas for future research.

1. Variety of al alloys exists for the commercial application for the gear fabrication. Different grades of aluminium alloy can be used to fabricate gears with the addition of the same filler material used in the existing work.
2. Mechanical alloying can be used to fabricate the gear made up of composite materials. Powder technology is one of the existing methods to enhance the property of the gear.
3. The performance of the gear material can further be enhanced by addition of other filler material.
4. The tribological property of the powder reinforced composite material can be further improved by addition of solid lubricating particles.
5. The failure of gears was majorly caused by various factors like misalignment, over loading, dirt and rust, error in manufacturing, and improper material section or fabrication.

5 Conclusions

In this chapter, a literature overview on mechanical and tribological aspects of aluminum alloy composites for gear application is made. The following are the salient observations:

1. Wear mechanism is the prominent wear associated with automobile and aerospace industry and comes out to be a severe problem resulting in gear worn surface damage of components thereby alternating the working performance and bring large economic loss.
2. Parameter like reinforcement size, normal load, sliding velocity, sliding distance and composition, etc., are the factor affecting the specific wear rate.
3. Though much work had been reported on various dry sliding wear and friction characteristics of metals, alloys and homogeneous materials, comparatively less had been reported on the sliding wear and friction performance of metal matrix composite for gear.
4. Reinforcement of MMC can improve wear behavior and friction properties.
5. It was found by number of researchers that the reinforcement with particulates like Al, SiC, ZnO, and Al₂O₃ increases hardness, resistance, and sliding wear characteristics of aluminium composite materials.
6. Theoretical models help in predicting and analyzing sliding wear behavior of metal composites.

Acknowledgements The authors express their gratitude to the Department of Mechanical Engineering of MNIT Jaipur-302017, Rajasthan, INDIA for their all kinds of financial as well as other miscellaneous infrastructural support.

References

1. Fu. Mingwang, and B. Shang, *J. Mater. Process. Tech.* 53, 511(1995).
2. R. Dwivedi, *SAE Tech.* 1, 940 (1995)
3. B. Neitzel, M. Barth, M. Matic, *SAE Tech.* 1, 940 (1995)
4. T. Zeuner, P. Stojanov, P.R. Saham, H. Ruppert, *Mater. Sci. Tech.* 14(8), 57 (1998)
5. R. Dwivedi, *SAE Tech.* 8, 950 (1995)
6. T. Savaşkan, Y. Alemdağ, *Wear* 268, 565 (2010)
7. J. Qua, H. Xu, Z. Feng, D. Alan Frederick, A.Linan, and H. Heinrich, *Wear* 271, 1940(2011).
8. S.K. Thakur, M. Gupta, *J. Compos. Appl. Sci. Mgf.* 38(3), 1010 (2007)
9. A.E. Jiménez, M.D. Bermúdez, J. Cintasand, E.J. Herrera, *Wear* 266, 255 (2009)
10. Y. Zhou, Z. Yu, N. Zhao, C. Shi, E. Liu, X. Du, C. He, *Mater. Des.* 46, 724 (2013)
11. I. Mobasherpour, A.A. Tofigh, M. Ebrahimi, *Mater. Chem. Phys.* 138, 535 (2013)
12. S. Wang, P. Guo, L. Yang, F. Zhao, Y. Wang, *J. Mater. Des.* 30, 704 (2009)
13. G. Sabatini, L. Ceschini, C. Martini, J.A. Williams, I.M. Hutchings, *J. Mater. Des.* 31, 816 (2010)
14. B. Venkataraman, G. Sundararajan, *Wear* 245, 22 (2000)
15. C.T. Liu, and J.A. Horton, *Mater. Sci. Eng. A* 192/193,170 (1995).
16. B. Subramanian, R. Ananthakumar, M. Jayachandran, *Vacuum* 85, 601 (2010)
17. M. Zheng, K. Wu, H. Liang, S. Kamado, Y. Kojima, *Mater. Lett.* 57, 558 (2002)
18. Z. Yu, G. Wu, L. Jiang, D. Sun, *Mater. Lett.* 59(18), 2281 (2005)
19. M. Safavi, S.M. Abbasi, R. Mahdavi, *J. Iron Steel. Res. Int.* 19(2), 67 (2012)
20. S. Thakur, M. Gupta, *Compos. Part. A* 38(3), 1010 (2007)
21. P.P. Bhingole, G.P. Chaudhari, S.K. Nath, *Compos. Part. A* 66, 209 (2014)
22. B.N. Mordiyuk, G.I. Prokopenko, V. Milman, M.O. Iefimov, K.E. Grinkevych, A.V. Sameljuk, I.V. Tkachenko, *Wear* 319(1–2), 84 (2014)
23. J. Stein, B. Lenczowski, E. Anglaret, N. Frety, *Carbon* 77, 44 (2014)
24. E. Merhy, L. Remy, H. Maitournam, L. Augustins, *Eng. Fract. Mech.* 110, 99 (2013)
25. L. He, Y. Tan, X. Wang, T. Xu, X. Hong, *Appl. Sur. Sci.* 314, 760 (2014)
26. M.K. Akbari, O. Mirzaee, H.R. Baharvandi, *Mater. Des.* 46, 199 (2013)
27. W.S. Lee, Z.C. Tang, *Mater. Des.* 58, 116 (2014)
28. E. Karakulak, R. Yamanoğlu, U. Erten, A. Zeren, S. Zor, M. Zeren, *Mater. Des.* 59, 33 (2014)
29. X.J. Zhao, L.R. Xiao, Z.W. Zhao, L. Guo, H.Q. Ru, N.Zhang, and D.L. Chen, *Ceram. Int.* 40, 14295 (2014).
30. T.S. Skan, A. Aydnir, *Wear* 257, 377 (2004)
31. A.E. Jiménez, M.D. Bermúdez, J. Cintas, E.J. Herrera, *Wear* 266(1–2), 255 (2009)
32. J. Qu, H. Xu, Z. Feng, D.A. Frederick, L. An, H. Heinrich, *Wear* 271, 1940 (2011)
33. Z.H. Chen, Y.Q. He, H.G. Yan, Z.G. Chen, X.J. Yin, G. Chen, *Mater. Sci. Eng. A* 461, 180 (2007)
34. J. Hemanth, *Mater. Sci. Eng. A* 507(1–2), 110 (2009)
35. A. Yar, M. Montazerian, H. Abdizadeh, H.R. Baharvandi, *J. Alloys. Compd.* 484, 400 (2009)
36. A. Onat, *J. Alloys. Compd.* 489, 119 (2010)
37. X.S. Tang, *Theor. Appl. Fract. Mech.* 50,105 (2008)
38. C.N. Panagopoulos, E.N. Georgiou, *Appl. Surf. Sci.* 255, 6499 (2009)
39. H. Abdizadeh, M. Ashuri, P.T. Moghadam, A. Nouribahador, H.R. Baharvandi, *Mater. Des.* 32(8–9), 4417 (2011)

40. S.A. Sajjadi, H.R. Ezatpour, M.T. Parizi, *Mater. Des.* **34**, 106 (2012)
41. Q. Liu, L. Ke, F. Liu, Huang, and L. Xing, *Mater. Des.* **45**, 343 (2013).
42. P. Li, S. Liu, L. Zhang, X. Liu, *Mater. Des.* **47**, 522 (2013)
43. J. Selvam, D.S. Smart, I. Dinahran, *Mater. Des.* **49**, 28 (2013)
44. A. Ul-Hamid, A. Quddus, F.K. Al-Yousef, A.I. Mohammed, H. Saricimen, L.M. Al-Hadhrami, *Surf. Coat. Technol.* **205**, 2023 (2010)
45. F.Y. Zhang, M.F. Yan, *Surf. Coat. Technol.* **253**, 268 (2014)
46. H. Arik, *Mater. Des.* **29**(9), 1856 (2008)
47. S. Wang, P. Guo, L. Yang, F. Zhao, Y. Wang, *Mater. Des.* **30**(3), 704 (2009)
48. C.N. Panagopoulos, E.P. Georgiou, P.E. Agathocleous, K.I. Giannakopoulos, *Mater. Des.* **30**(10), 4267 (2009)
49. A. Devaraju, A. Kumar, A. Kumaraswamy, B. Kotiveerachari, *Mater. Des.* **51**, 331 (2013)
50. C. Wang, K. Deng, Y. Bai, *Materials* **12**, 1190 (2019)
51. R. Zheng, H. Yang, T. Liu, K. Ameyama, C. Ma, *Mater. Des.* **53**, 512 (2014)
52. M. Zadeh, O. Mirzaee, P. Saidi, *Mater. Des.* **54**, 245 (2014)
53. M.A. Taleghani, E.M. Navas, J.M. Torralba, *Mater. Des.* **55**, 674 (2014)
54. A.S. Mukasyan, K.V. Manukyan, in *Micro and Nano Technologies, Nanomaterials Synthesis*, ed. by Y.B. Pottathara, S. Thomas, N. Kalarikkal, Y. Grohens, V. Kokol (Elsevier, 2019), pp. 85–120,
55. I. Ozdemir, U. Cocen, K. Oene, *Compos. Sci. Technol.* **60**(3), 411 (2000)
56. S.N. Chou, H. Lu, D. Lii, *Compos. Ceram. Int.* **35**, 7 (2009)
57. S. Zhiqiang, Z. Di, L. Guobin, *Mater. Des.* **26**(5), 454(2005).
58. J. Singh, and A. Chauhan, *Ceram. Int.*, **42**(1), 56(2016)
59. V.R. Rajeev, D.K. Dwivedi, S.C. Jain, *Tribol. Int.* **43**(8), 1532 (2010)
60. A. Baradeswaran, A. Elayaperumal, F.R. Issac, *Proced. Eng.* **64**, 973 (2013)
61. P. Ravindran, K. Manisekar, R. Narayanasamy, P. Narayanasamy, *Ceram. Int.* **39**(2), 1169 (2013)
62. R. Kumar, S. Dhiman, *Mater. Des.* **50**, 351 (2013)
63. T. Rajmohan, K. Palanikumar, S. Ranganathan, *Trans. Non. ferr. Met. Soc.* **23**(9), 2509 (2013)
64. N. Radhika, R. Subramanian, S. Prasat, J. Miner. Mater. Charact. Eng. **10**, 427 (2011)
65. K. Umanath, K. Palanikumar, S.T. Selvamani, *Compos. B* **53**, 159 (2013)
66. T. Murakami, S. Kajiino, S. Nakano, *Tribol. Int.* **60**, 45 (2013)
67. G.J. Howell, A. Ball, *Wear* **181–183**, 379 (1995)
68. R.N. Rao, S. Das, D.P. Mondal, A.G. Dixit, *Tribol. Int.* **43**(1–2), 330 (2013)
69. A. Daoud, M.T. Khair, *Tribol. Int.* **43**(3), 544 (2010)
70. C.S. Ramesh, R. Keshavamurthy, B.H. Channabasappa, S. Pramod, *Tribol. Int.* **43**, 623 (2010)
71. N. Jha, A. Badkul, D.P. Mondaland S. Das, *Tribol. Int.* **44**(3), 220 (2011).
72. H. Zhu, C. Jar, J. Song, J. Zhao, J. Li, Z. Xie, *Tribol. Int.* **48**, 78 (2012)
73. M. Ramachandra, K. Radhakrishna, *Wear* **262**(11–12), 1450 (2007)
74. J.M. Lee, S.B. Kang, J. Han, *Wear* **264**, 75 (2008)
75. F. Toptan, I. Kerti, L.A. Rocha, *Wear* **290**, 74 (2012)
76. H. Sarmadi, A.H. Kokabi, S.M. Seyed Reihani, *Wear* **304**, 1 (2013).
77. S. Basavarajappa, G.Chandramohan, and J. Paulo Davim, *Mater. Des.* **28**, 1393 (2007).
78. N. Miloradović, R. Vujanac, B. Stojanović, A. Pavlović, *Compos. Struct.* **264**, 113658 (2021)
79. S. Baskaran, V. Anandkrishnan, M. Duraiselvam, *Mater. Des.* **60**, 184 (2014)
80. T.S. Kiran, M. Prasanna Kumar, S. Basavarajappa, and B.M. Viswanatha, *Mater. Des.* **63**, 294 (2014).
81. P.P. Jin, G. Chen, L.I. Han, J. Wang, *Trans. Nonferrous. Met. Soc. China* **24**(1), 49 (2014)
82. X. Jiang, N.J. Wang, D.U. Zhu, *Trans. Nonferrous. Met. Soc. China.* **24**(7), 2352 (2014)
83. S.A. Alidokhta, A.A. Zadeh, S. Soleymani, T. Saeid, H. Assadi, *Mater. Charact.* **63**, 90 (2012)
84. A. Baradeswaran, E. Perumal, *Compos. Part. B.* **56**, 472 (2014)
85. A. Thangarasu, N. Murugan, I. Dinaharan, *Proced. Eng.* **97**, 590 (2014)
86. M. Lieblich, J. Corrochano, J. Ibáñez, V. Vadillo, J.C. Walker, *Wear* **309**, 126 (2014)
87. R. Hashemi, G. Hussain, *Wear* **324**, 45 (2015)

88. F. Wang, S. Zhang, J. Mater. Process. Technol. **182**(1–3), 122 (2007)
89. H. Arik, Y. Ozcatlbaz, M. Turker, Mater. Des. **27**(9), 799 (2006)
90. R.N. Rao, S. Das, Mater. Des. **32**(2), 1066 (2011)
91. D.P. Mondal, S. Das, R.N. Rao, M. Singh, Mater Sci Eng. A **402**, 307 (2005)
92. D.K. Dwivedi, T.S. Arjun, P. Thakur, H. Vaidya, K. Singh, J. Mater. Process. Technol. **152**, 323 (2004)
93. H. Dan, C. Wei-ping, Z.S. yang, and H.E. Xian, Trans. Nonferrous Met .Soc. China **20**, 54 (2010).
94. J. Lan, J. Yan, Y.U. Liang, S.U. Nan, D.Y. Dong, Trans. Nonferrous Met. Soc. China **22**(12), 2913 (2012)
95. T. Miyajima, S. Sasajama, T. Honda, Y. Fuwa, Y. Iwai, Tribol. **7**(1), 24 (2012)
96. T. Miyajima, Y. Iwai, Wear **255**, 606 (2003)
97. Y. Wang, W.M. Rainforth, H. Jones, M. Lieblich, Mater. Sci. Forum. **396–402**, 1473 (2002)
98. Y. Wang, W.M. Rainforth, H. Jones, M. Lieblich, Wear **251**, 1421 (2001)
99. J.C. Walker, J.M. Rainforth, H. Jones, Wear **259**(1–6), 577 (2005)
100. Y.M. Pan, M.E. Fine, H.S. Cheng, Scr. Meter. **24**, 1341 (1990)
101. A.P. Sannino, H.J. Rack, Wear **189**, 1 (1995)
102. D.K. Dwivedi, Mater. Sci. Eng. A **382**(1–2), 328 (2004)
103. R.A. Somi, B.B.N. Pramila, K.K.S. Murthy, S.K. Biswas, Wear **171**(1–2), 115 (1994)
104. R.K. Gautam, S. Ray, S.C. Sharma, S.C. Jain, R. Tyagi, Wear **271**, 658 (2011)
105. T. Savaskan, O. Brian, Tribol. Lett. **40**, 327 (2010)
106. A. Wang, H.J. Rack, Acta. Metall. Mater. **40**, 2301 (1992)
107. E.A. Diler, R. Ipek, Compos. B: Eng. **50**, 371 (2013)
108. J. F. Archard, in *ASME Wear Control Handbook*, ed. by M. B. Peterson and W. O. Winer (American Society of Mechanical Engineers, New York, 1980), pp. 35 - 80.
109. I.M. Hutchings, S. Wilson, and A.T. Alpas, in *Comprehensive Composite Materials*, ed. by Anthony Kelly and Carl Zweben (Elsevier Science Ltd., 2000), pp. 501–519
110. K.H. Zum Gahr, *Microstructure and Wear of Materials*, (Elsevier, 1987), p.465
111. D.P. Mondal, S. Das, Tribol. Int. **39**(6), 470 (2006)
112. M. Singh, D.P. Mondal, O.P. Modi, A.K. Jha, Wear **253**, 357 (2002)
113. R.K. Singh, A. Telang, S. Das, Trans. Nonferrous Met. Soc. China **30**(1), 65 (2020)
114. D.P. Mondal, S. Das, A.K. Jha, A.H. Yegneswaran, Wear **223**, 131 (1998)
115. S. Kumar, V. Balasubramanian, Tribol. Int. **43**, 414 (2010)
116. H-L. Lee, W-H. Lu, and S.L-I. Chan, Wear **159**, 223(1992).
117. O. Yilmaz, S. Buytoz, Compos. Sci. Technol. **61**, 2381 (2001)

Microcavity Mediated Light Emissions from Plasmonic and Dielectric Composites



Xianguang Yang, Jiahao Yan, and Baojun Li

Abstract Surface plasmons and Mie resonances of plasmonic and dielectric microcavities provide powerful platforms for enhancing exciton-exciton coupling and energy transfer at micro- and nano-scale. In this chapter, we report the light emission when quantum dots are coupled to the surface plasmon and Mie resonance of gold spheres and silicon particles, respectively. For gold microcavity, whispering-gallery-mode emission of quantum dots mediated by plasmon was realized. For silicon microcavity, Mie resonance suppressed emission blinking of quantum dots was realized. These two types of plasma and dielectric composites are expected to make the optical confinement exceed the diffraction limit, and hold extensive application prospects in nanophotonics.

Keywords Surface plasmon · Mie resonances · Quantum dots

1 Introduction

Advanced composites consist of metallic and semiconductor particles have been successfully fabricated by different methods [1–4]. Micro- and nano-scale integration of micro-nano metals with semiconductors is highly important because the advantages of each of these two materials combine in this composite. The local surface plasmon of metal particles makes the light field concentration reach the sub-wavelength dimension, which is well below the limit of light diffraction [5–9]. Semiconductor nanocrystals (QDs) could be used as a vigorous component with large light gain and powerful optical absorption/emission, compensating the intrinsic loss of metallic plasma microcavity [4]. Compact devices with metal–semiconductor composites have been well reported, including photonic detectors [3, 10,

X. Yang (✉) · J. Yan · B. Li (✉)

Guangdong Provincial Key Laboratory of Nanophotonic Manipulation, Institute of Nanophotonics, Jinan University, Guangzhou 511443, China
e-mail: xianguang@jnu.edu.cn

B. Li

e-mail: baojunli@jnu.edu.cn

[11], photonic modulators [12], photovoltaic cells [13, 14], nanoscale lasers [15–17] also. Light confinement in micro- and nano-scale cavities has aroused people's interest because it can enhance the light-matter interactions. Single-particle plasmonic microcavity is interesting because it supports a high Purcell factor (F), which is caused by a small mode volume (V) [16, 18]. Whispering-gallery-modes (WGMs), which are derived from the total internal reflection of the light wave propagating circumferentially around the microcavity, makes the optical research based on plasma microcavity of great significance. However, when the cavity diameter decreases, the WGM radiation loss will also increase as the weakness effect for total internal reflection [19, 20]. Fortunately, the surface plasmons can propagate around the equator of plasmonic cavity, making it to be as a potential candidate for high-density integrated devices. In this chapter, we report a gold sphere plasmonic microcavity for WGM emission of quantum dots first. The quantum-dots-coated gold sphere composite was well synthesized through electrostatic interactions. The polarization- and size-related WGM emissions have been well investigated. The physical mechanism of decay kinetics behind the emission process of WGM was experimentally investigated using fluorescence spectroscopy in time-resolved mode. Moreover, the spatial interference pattern was experimentally observed and explained. In the following, we will introduce the case of dielectric counterparts.

The scattering and absorption of light waves by micro-nano particles with sizes smaller than wavelength of light have already emerged as an attractive research topics in micro-nano photonics. Over the decades, they have a variety of properties and applications, like biological markers, single-photon emissions, light-emitting diodes, etc. For metallic particles, the free electrons oscillate around the surface of the particle with the same frequency of incidence as the incident light. Surface plasmons will be locally generated as long as the condition for optical resonance is reached. The local surface plasmon resonance is largely related to their shapes, sizes, and the surrounding materials [21]. The light energy of incident radiation would be transferred to free electrons with the realization of local surface plasmon resonance, which would maximize the oscillation amplitude of the light field and finally enhance the local electric field [6]. Although the diffraction limit can be fundamentally broken by the enhanced optical field, the metal ohmic losses due to the high imaginary refractive index limit their practical applications. To overcome the ohmic losses, all-dielectric particles with low optical absorption and high refractive index appear as substitutes [22, 23]. Mie scattering theory points out that compared with metal particles with high absorption and high thermal effect, dielectric particles could make a strong response to the magnetic field generated by light waves, thus fundamentally limiting the optical field to micro-nano scale, without heating issues [24, 25]. Furthermore, because dielectric particles could be made with germanium, silicon and their compounds, they are naturally compatible with semiconductor technology [26, 27]. In addition, micro-nano Si particles show magnetic dipolar resonances contrast to the electric dipolar resonances [28, 29]. In particular, in the visible range, we can see strong magnetic dipole resonance in spherical silicon particle with a diameter ranging from 100 to 200 nm [26]. The magnetic dipole resonance of silicon particles originates from the displacement current cycle, which is different from that of

plasma particles [28]. Microscopically, the displacement current is due to the polarization of silicon atoms. Hence, all-dielectric silicon particles could be applied as a micro cavity with low loss of magnetic scattering for optical spectroscopy and field localization [30, 31].

Herein we demonstrate that it is possible to utilize the magnetic dipole resonance of Si particles to control the visible emission of quantum dots, which is a new channel. In silicon particles, electric dipole resonance using laser excitation and magnetic dipole resonance using quantum dot photoluminescence were achieved. For the photoluminescence of quantum dots, these two kinds of resonance would produce a synergistic effect. Specifically, the energy transfer between the silicon magnetic dipole and the quantum dot exciton is more helpful by the latter, thus stabilizing the sub-wavelength limitation of photoluminescence. The stable quantum-dot-emission is conducive to the development of many applications, such as light-emitting diodes, single-photon sources, biological tracking, etc. Particularly, the quantum dots were directly connected to the silicon particles through surface interactions. For the hybrid system consisting of quantum dots and metals, the distance between them needs precise design to control the quenching effects [32, 33]. The distance design always increases the fabrication cost and complication. For quantum dots near the metal surface, fluorescence quenching always occurs because of the presence of coupling of higher-order dark modes, but this is avoidable for silicon particles due to the absence of dark mode support [34]. Mismatch between wave-vectors is caused by the absence of surface patterns at the high wave-vectors. A variety of low-loss and low-cost applications can be provided by our all-dielectric hybrid system.

2 Plasmonic Composites

Gold spheres appended with amine groups ($-\text{NH}_2$) and quantum dots (quantum yield of 30%) appended with carboxy groups ($-\text{COOH}$) were commercially available from NanoSeedz (Hong Kong) and Zkwy Bio-Tech (Beijing) companies, respectively. In order to coat quantum dots on gold balls, an effective method is as follows: First, the solution of gold balls added with amine (concentration is about 9.5×10^9 particles/mL) and the solution of quantum dots added with carboxyl (molar concentration is about 4×10^{-6} M/L) were adjusted to pH of ~ 4 and pH of ~ 10 , respectively, to prepare polycationic and polyanionic particles. Second, the gold sphere solution was slowly dropped into the quantum dot solution and gently shaken to assemble quantum dots on the gold sphere surface. When the pale haziness occurs, the drop-wise addition of gold sphere solution could be stopped. Through a series of experiments, the resulted pH of mix suspension was about 7.5–7.8 and homogeneous coating of quantum dots was realized. Good control over the number of quantum dots coated on a single gold sphere could be achieved by means of adjusting the concentration and reaction time.

Optical characterization: Micro spectrophotometer (CRAIC, USA) was used to characterize the optical properties of quantum-dots-coated gold spheres. Quantum dot coated gold spheres were pumped by a continuously working 365 nm wavelength

laser. The photoluminescence signal was collected with an objective (100X, NA of 0.95) and then directed by the dichroic mirror and the 365 nm long pass filter. The filtered photoluminescence signal is separated by a beam splitter, and then input to a CCD camera for imaging, and input to a spectrometer for spectrum presentation. Furthermore, one linear polarizer for polarization selection was effectively inserted into the optical path between the CCD camera and the microscope objective.

Confocal Raman microscopy (Horiba) was used to record the time trajectories of the photoluminescence emission intensity. A continuous wave laser at 532 nm wavelength via 100 objective (NA of 0.9) was used to excite the dielectric composite sample. Representative power density of excitation laser for the emission measurements is set to be of $10 \mu\text{W}/\mu\text{m}^2$. The photoluminescence emission signal was collected under the same objective lens, followed by continuous detection with a photodiode through long pass optical filter and a dichroic beam splitter. The forward scattering spectrum of the monocrystalline silicon particles was measured using a dark-field scattering optical microscope equipped with a monochromator, a quartz-halogen-tungsten lamp, and a charge-coupled device (SSD). For dielectric composites, a broadband white light is obliquely incident onto it at a 50° incidence angle and the scattered light is then efficiently collected with an objective in the dark-field.

Typical transmission electron microscopy (TEM) micrographs of gold spheres with a diameter of 470 nm and TEM micrographs of individual quantum-dots-coated gold sphere with a diameter of 490 nm were shown in Fig. 1a, b, respectively. High resolution TEM micrographs of quantum dots were shown in Fig. 1c. The coated quantum dots (ensembles of quantum dots indicated with red arrows) had an average diameter of ~ 5 nm, and approximately two layers of quantum dots were coated on the gold sphere, where the inner layer served as dielectric space to avoid quenching effects. Figure 1d shows the characterization of energy-dispersive X-ray spectrum (EDS), and the optical absorption and photoluminescence spectra of CdSe/ZnS core-shell quantum dots were shown in the inset. The EDS results confirm that the existence of element Au at 30.25 wt.%, Cd at 0.06 wt.%, Se at 0.43 wt.%, Zn at 0.96 wt.%, and S at 0.41 wt.%.

A linear polarizer was inserted between the CCD camera for polarization selection and the microscope objective as previously mentioned to study the polarization properties of light emitted from quantum-dots-coated gold spheres. A 490-nm-diameter well-positioned quantum-dots-coated gold sphere was used for experimental testing. The emission directions of photoluminescence signals from individual quantum dots coated around gold spheres are perpendicular to the surface of gold sphere. The crossing angle of the axial direction of the optical polarizer with the direction of photoluminescence signal emission is the definition of polarization angle (θ). The photoluminescence intensity of light signal will exhibit an oscillation phenomenon around the minimum and maximum with the continuous change of polarization angle (θ). The dark-field photoluminescence micrographs of quantum-dots-coated gold sphere excited by 365-nm-wavelength laser with 10-mW-power were shown in Fig. 2 at different θ values of -90° , -70° , -50° , -30° , -10° , and 10° , respectively. When the polarization angle was varied from 90° to 10° , the photoluminescence intensity of the light signal was enhanced.

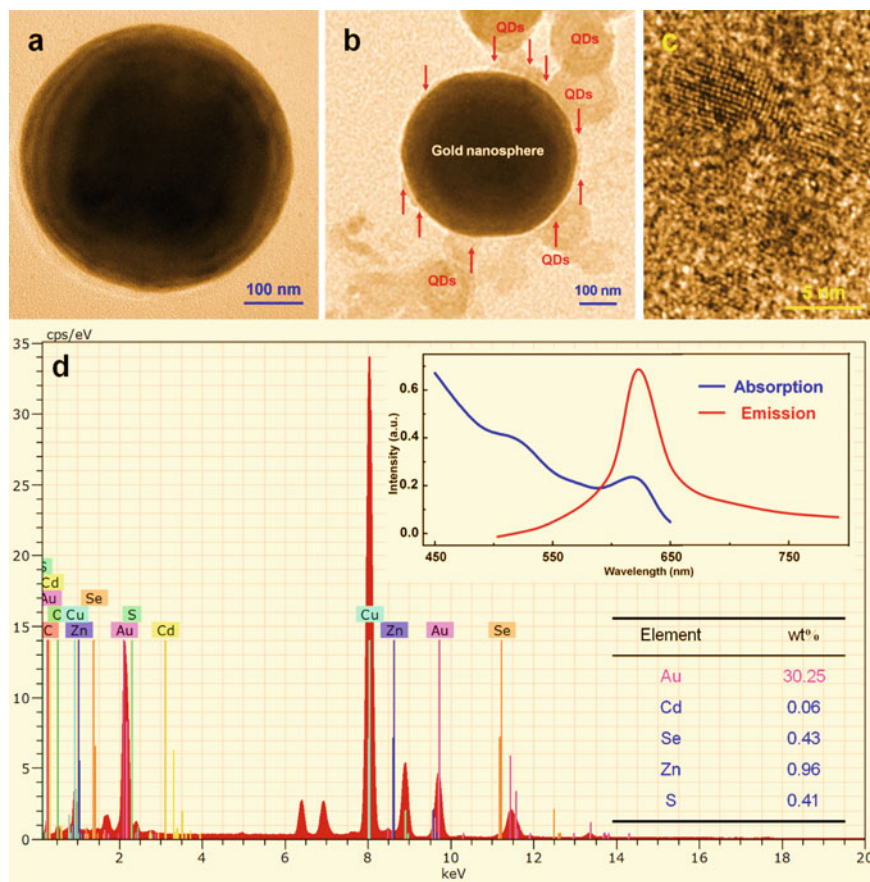


Fig. 1 TEM micrographs, EDS analysis, and optical properties. **a** TEM micrograph of a typical 470-nm-diameter gold sphere. **b** TEM micrograph of quantum-dots-coated gold sphere with diameter of ~490 nm. Quantum dots are indicated with red arrows. **c** The high resolution TEM micrograph of quantum dots. **d** EDS spectrum of quantum-dots-coated gold sphere shown in **(b)**. Inset: The optical absorption and photoluminescence spectra of CdSe-ZnS quantum dots. Reprinted with permission from Yang et al. [35], with permission from American Chemical Society. Copyright (2015)

Figure 3a presents θ -related photoluminescence intensity of the optical signals. The intensity distribution of photoluminescence can be described by the sine equation $I = I_1 \cdot \cos(2\theta) + I_0$, in which I_1 and I_0 are two fitting parameters. The maximum light intensity appears at $\theta = 10^\circ$ and the minimum light intensity appears at $\theta = -90^\circ$, corresponding to the emission polarization parallel to and perpendicular to the extinction direction of the gold sphere, respectively. The oscillation period is 180° , which is independent on the size of gold sphere. It is similar to the case in plasmonic structure with quantum dots [36]. Liquid-nitrogen-cooled spectrometer was equipped with optical microscopy for measuring the photoluminescence spectra

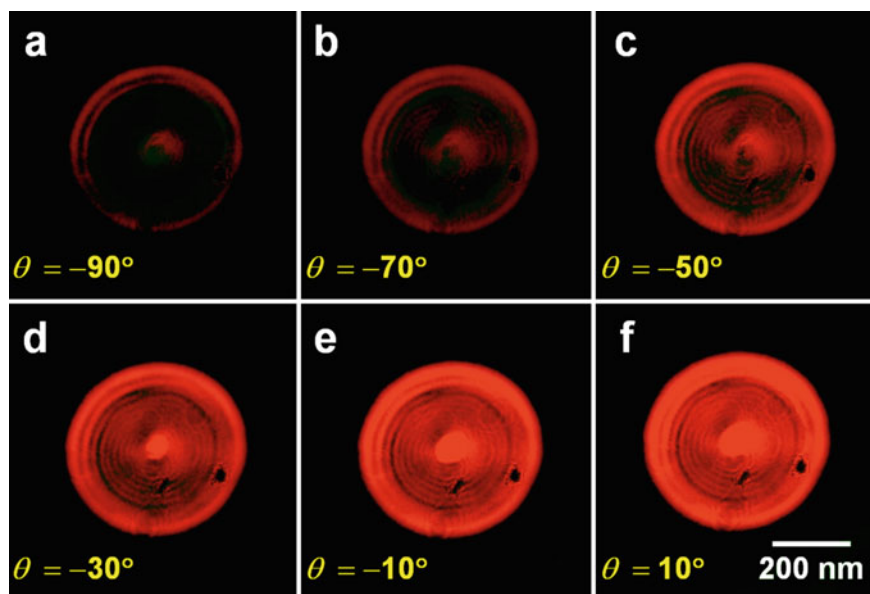


Fig. 2 Polarization-related light emission in plasmonic composites. Optical micrographs of quantum-dots-coated gold sphere excited by 365-nm-wavelength laser with 10-mW-power at distinctive polarization angle (θ) of **a** -90° , **b** -70° , **c** -50° , **d** -30° , **e** -10° , and **f** 10° . Scale bar of 100 nm is applicable to (**a–e**), but the scale bar for (**f**) is shown in lower right part of the image Reprinted with permission from Yang et al. [35], with permission from American Chemical Society. Copyright (2015)

from the studied quantum-dots-coated gold sphere. The emission spectrum (blue line) of the quantum-dots-coated gold sphere and that of the quantum dots solution (red dotted line) are shown in Fig. 3b, which contains five narrow bands, giving the WGM characteristics. The maximum peak of WGM emission is in good agreement with that of solution emission, which is consistent with previous work [37]. Three different sizes of quantum-dots-coated gold spheres were prepared and studied for studying size dependent WGM emission, and the results are shown in Fig. 3c. Because of the WGM characteristics, the photoluminescence spectra of quantum-dots-coated gold spheres with diameters of 800 nm, 550 nm, and 490 nm show similar narrow bands, but the positions of discrete peaks are blue-shifted due to the diameter increase. Since the spectral differences of many quantum-dots-coated gold spheres have been measured experimentally, this illustrates that the measured blue shift is not only present for some particular sample, but is universal. In fact, the observation of photoluminescence signals from the quantum-dots-coated gold spheres requires the recombination process of photo-active electron–hole pairs, generating emitted photons with one particular WGM mode energy, where the energy density of the particular WGM mode is non-zero along the spatial location of the quantum dot [38]. In experiment, the photoluminescence signals of quantum-dots-coated gold spheres were measured, in which the quantum dot size and composition were the same, the

wavelength, intensity, and polarization of the excitation light were the same, and the surrounding medium and experimental temperature were the same. Therefore, the blue shifts of the observed photoluminescence peak are mainly caused by the change of WGM mode density and near-field coupling intensity, which can be assumed. The boundary conditions of light propagation around the plasmonic microchambers were altered by the quantum dot coating on the surface of the gold sphere. Meanwhile, the spatial distribution of coated-quantum-dots changes their local orientations with respect to the radial direction of the plasmonic microcavity, because the distribution of the electromagnetic field is spatially related.

To investigate the decay kinetics of radiative emission process in the quantum-dots-coated gold sphere, the photoluminescence decay spectra of the quantum

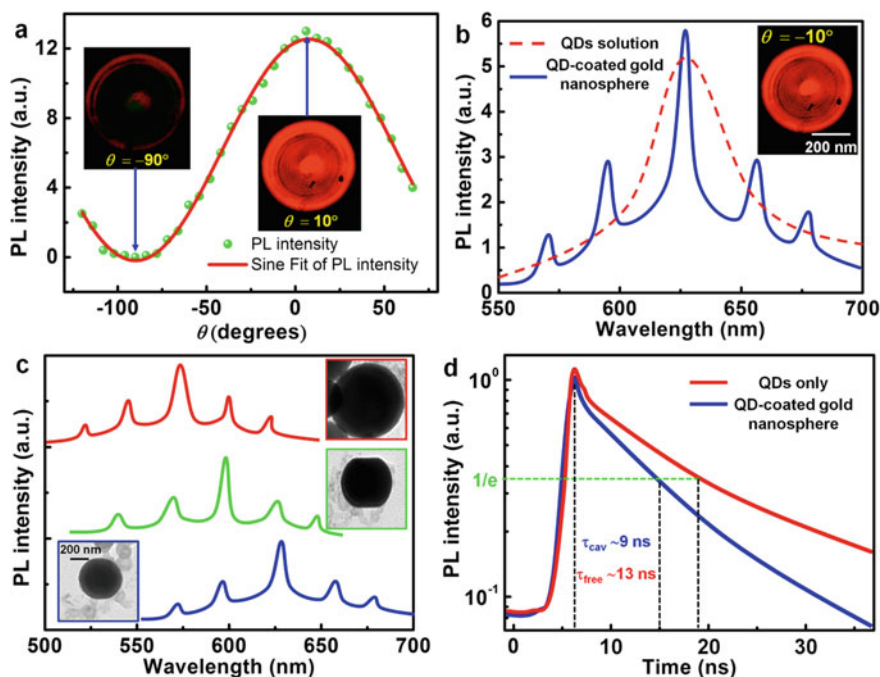


Fig. 3 Optical Spectroscopy analysis. **a** Polarization-related photoluminescence intensity. The red line is best-fitted with sine curve. Insets show the optical micrographs of quantum-dots-coated gold sphere with $\theta = -90^\circ$ and $\theta = 10^\circ$, respectively. **b** WGM spectrum of quantum-dots-coated gold sphere (blue line), and the emission spectrum of quantum dots solution (dotted red line). The peak intensity profile of WGM spectrum agrees well with that of solution emission. **c** WGM emission spectra of three quantum-dots-coated gold spheres with diameters of 490 nm (blue), 550 nm (green), and 800 nm (red). Insets: The corresponding TEM micrographs with the same scale bar of 200 nm. **d** Photoluminescence decay spectra of quantum-dots-coated gold sphere (blue line), and the quantum dots solution (red line), giving the lifetime of 9 and 13 ns, respectively. Reprinted with permission from Yang et al. [35], with permission from American Chemical Society. Copyright (2015)

dots with and without gold sphere (470-nm-diameter) were measured by 405-nm-wavelength pulsed laser excitation at 130-mW-power. The 1 MHz of repetition rate (interval of pulse-to-pulse, 1000 ns) was applied to make sure that the complete photoluminescence decay process re-excites the quantum dots before the next laser pulse, and then preventing the multiple excitations. The pump intensity was approximately 130 nJ/cm^2 for each pulse. The photoluminescence decay spectra of quantum-dots-only solution (red line) and the quantum-dots-coated gold sphere (blue line) were shown by Fig. 3d. The decay is a multi-exponential process. The photoluminescence decay at least includes plasma quenching, plasma enhancement, and intrinsic attenuation. The decay lifetimes of the quantum dot coated gold sphere and quantum-dots-only solution were about ~ 9 and ~ 13 ns, respectively, which were extracted from the $1/e$ value. Compared with the decay lifetime of quantum-dots-only solution, when the gold sphere exists, the decay lifetime was shortened from 13 to 9 ns, indicating that the radiation emission rate increases. This suggests that the localized field intensity increases with the presence of gold sphere. Since the radiative decay life of quantum-dots-only is larger than that of an emitted photon coupled to a microcavity, the experiments also demonstrated the enhancement of spontaneous radiation. Therefore, the near-field interaction between the radiative emission of the coated quantum dots and the localized optical field around the gold sphere is verified due to the shortened photoluminescence decay lifetime. Using the Purcell factor to describe the modulation of spontaneous radiation [39]:

$$F = \tau_{free}/\tau_{cav} = 3Q(\lambda_c/n)^3/(4\pi^2 \cdot V_{eff}) \quad (1)$$

where the effective mode volume (V_{eff}) can be estimated by the size of the light spot and gold sphere. The quality factor (Q) of plasmonic microcavity can be calculated from Fig. 3b. The refractive index (n) can be estimated from core-shell structures [40]. Consequently, the Purcell factor was calculated to be of 1.51. Additionally, the Purcell factor can also be obtained by lifetime, where $F = (\tau_{free}/\tau_{cav}) = 1.44 = (13\text{ns})/(9\text{ns})$. The little difference between these two calculations comes from the fact that lifetimes are just taken by $1/e$ value. Theoretically, by analyzing the numerical calculation of the field distribution, it could be known that the WGM mode with high-Q is strongly confined around the circular rings [41].

We also investigated the spatial distribution of photoluminescence intensity in the quantum-dots-coated gold sphere. Under laser excitation, photoluminescence light spots were experimentally observed and shown in Fig. 4a, d with the clear interference patterns, indicating the high-quality spatial coherence of the photoluminescence signals. The distribution of photoluminescence intensity along the X axis is shown in Fig. 4b. In addition, Fig. 4c shows an enlarged view of the green area of Fig. 4b, indicating that the photoluminescence intensity has oscillatory behavior along the X axis from 200 to the maximum and minimum values of 300 nm. For comparison, Fig. 4e shows the distribution of photoluminescence intensity along the X axis. Further, Fig. 4f shows an enlarged view of the green region of Fig. 4e, indicating that the photoluminescence intensity has the oscillating behavior of maximum and minimum values from 400 to 600 nm along the X axis. Experimentally, the change

in the spatial part of the oscillatory behavior is relatively dependent on the change in polarization angle. For example, when the polarization angle (θ) changed from -50° to -10° , the corresponding spatial section of the oscillation behavior gradually changed from 200 ~ 300 nm to 400 ~ 600 nm. It can be proposed that this relationship may be correlated to the spatial orientation of coated-quantum-dots, which is sensitive to polarization direction. The spatial orientation of coated quantum dots would change with the change of polarization direction, which in turn would change the spatial distribution of the coherent light signal from each quantum dot. Hence, the spatial section of the oscillation resulting from the spatial interference emitted by coherent light will change simultaneously. In general, the observed photoluminescence intensity distribution is very consistent with the optical micrograph and the theoretical model of the previously reported work [42].

3 Dielectric Composites

The fabrication method of Si particles hybrid with quantum dots (Si-QDs) is schematically illustrated with three steps in Fig. 5. Colloidal CdSe-ZnS core-shell quantum dots were used which are fluorescent, semiconducting, and have solution processing capability. Figure 5a, b show transmission electron microscope (TEM) images of monodisperse quantum dots with an average diameter of 6 nm and scanning electron microscope (SEM) images of silicon particles with an average diameter of 160 nm, respectively. Colloidal nano-crystals have large specific surface area and surface energy, so that quantum dots can be connected with silicon particles through surface adsorption. The silicon particles hybrid with quantum dots are named as Si-QDs. The homogeneous distribution of quantum dots on silicon particles was realized by controlling the concentration and ratio of the two kinds of colloids through a series of experiments. The images of the as prepared silicon quantum dots are shown in Fig. 5c, in which about 65% of silicon particles were mixed with quantum dots. For Si-QDs, monolayer quantum dots were connected on the surface of silicon particles, and its average diameter is approximately 172 nm. Because quantum dots have a small enough size compared with the size of silicon particles, it could be calculated that the number of connected quantum dots is about 2.2×10^3 . The projected area of single quantum dots onto Si surface is considered as the square area with 6 nm side length.

The normalized spectra of core-shell CdSe-ZnS quantum dots relative to the experimentally measured photoluminescence and absorption spectra are represented by red and green curves in Fig. 6a, respectively. The absorption intensity at 532-nm-wavelength (excitation laser) is of 0.4. The photoluminescence peak is located at the wavelength value around 650 nm, while the full width at half maximum (FWHM) is approximately 20 nm. Experimentally measured scattering spectra of silicon particles are shown in the blue curve in Fig. 6a, showing three maxima, which are denoted by MDR, EDR, and QR, respectively. MDR refers to magnetic dipole resonance, which has an FWHM of 70 nm near the wavelength of 650 nm. EDR refers to

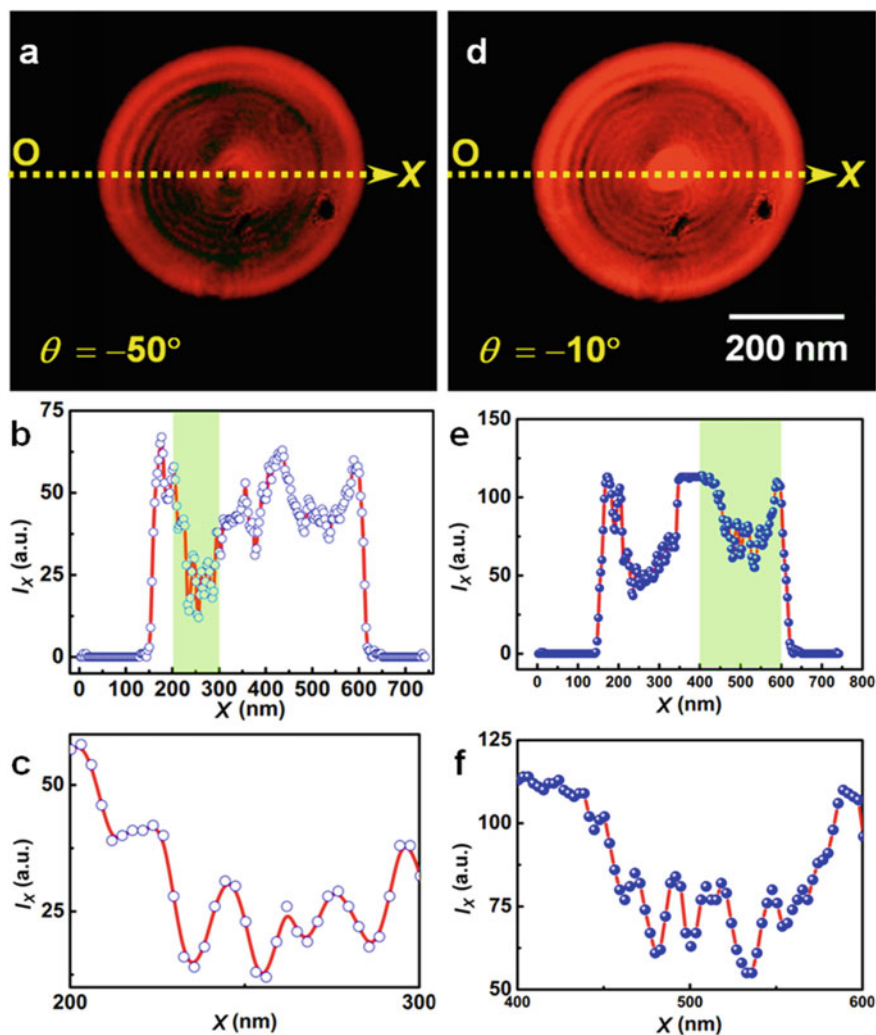


Fig. 4 Photoluminescence intensity distribution and interference patterns. **a** Optical micrograph of quantum-dots-coated gold sphere at polarization angle of $\theta = -50^\circ$. **b** Photoluminescence intensity distribution along the X axis in **(a)**. **c** Enlarged view of green area in **(b)**. **d** Optical micrograph of quantum-dots-coated gold sphere at polarization angle of $\theta = -10^\circ$. **(d)** and **(a)** have the same scale. **e** Photoluminescence intensity distribution along the X axis in **(d)**. **(f)** Enlarged view of green area in **(e)**. The distribution of photoluminescence intensity along the X axis was measurable using the histogram tool in Adobe Photoshop software. Reprinted with permission from Yang et al. [35], with permission from American Chemical Society. Copyright (2015)

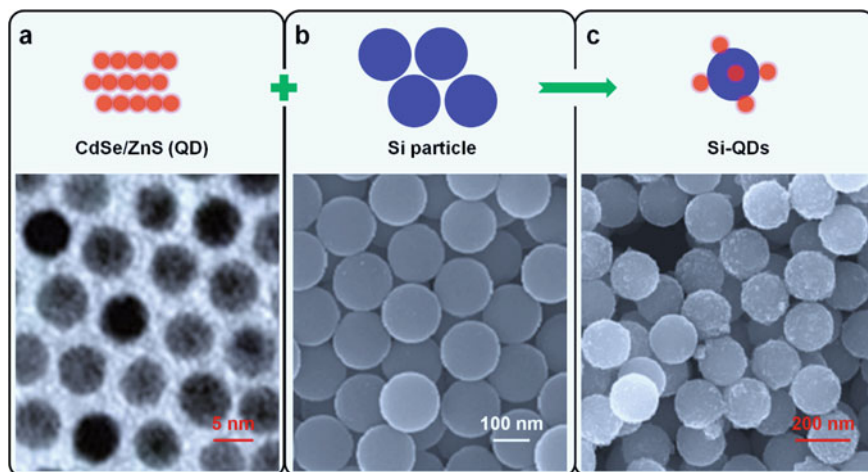


Fig. 5 Schematic illustration of the preparation principle of Si-QDs (hybridizing silicon particles with quantum dots). **a** A schematic of core-shell CdSe/ZnS quantum dots with a TEM micrograph. **b** A schematic of Si particles with SEM micrograph. **c** A schematic of Si-QDs with SEM micrograph. Reprinted with permission from Yang et al. [43], with permission from American Chemical Society. Copyright (2017)

electric dipole resonance, which is located near the wavelength of 525 nm and has an FWHM of 120 nm. In terms of scattering intensity, MDR is twice as high as EDR, which indicates that MDR is stronger than EDR. QR refers to quadrupole resonance, including magnetic quadrupole resonance and electric quadrupole resonance. Compared with MDR and EDR, the intensity of QR is negligible (its intensity is less than 0.2). Moreover, the quantum-dot-emission and the MDR are spectrally overlapped for energy transfer, while the excitation laser wavelength is approaching the EDR center. In order to study the forward scattering, a single silicon particle with a diameter of 160 nm is numerically calculated. When electromagnetic radiation was incident on a single silicon particle, the all-dielectric silicon particle with low light absorption could be used as a low-loss scattering microcavity with Mie resonance. Magnetic dipole, electric dipole and quadrupole make main contribution to the far-field scattering intensity. Scattering spectra were calculated by finite difference time domain (FDTD) using FDTD solutions 8.6 (lumerical solutions) software. Fully matched layer (PML) boundary condition was adopted, the three-dimensional size was set to 0.5 μm , 0.5 μm , 1.5 μm , and the mesh size of overlap zone was set to 5 nm. The dielectric constant of silicon could be obtained from palik. Silicon particles were irradiated using an electromagnetic plane wave with linear polarization in the visible range (400–700 nm), and the forward scattering was collected by a two-dimensional frequency domain field via a power monitor positioned approximately 200 nm below the center of the particles. Figure 6b presents the calculated forward scattering spectra of silicon particles as well as the near-field EDR and MDR distributions. The calculated EDR and MDR bands were located near the wavelength

values around 530 nm and 651.5 nm with 125 nm and 75 nm FWHM, respectively. MDR intensity was approximately twice as high as EDR, and QR intensity was low. Overall, the calculated results agree well with the experiments.

The photoluminescence decay spectra of quantum dots and Si-QDs were characterized to investigate the decay kinetics of the photoluminescence process, as shown in Fig. 6c. Quantum dots with a lifetime of 24 ns were shown in red attenuation spectrum and silicon quantum dots with a lifetime of 8 ns were shown in blue attenuation spectrum. In dielectric composites of silicon quantum dots, the quantum yield and excitation rate of quantum dots are affected by silicon particles. For excitation, the incident laser beam can be absorbed by quantum dots and can excite the EDR of Si particles. The localized field generated by EDR can be coupled to the quantum dots,

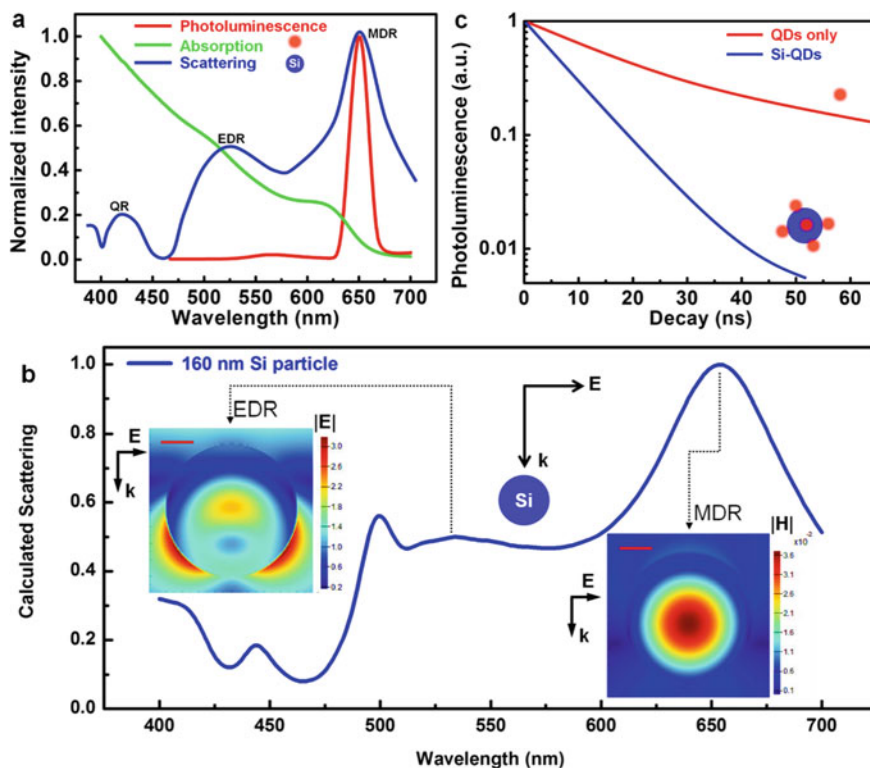


Fig. 6 Spectroscopic analysis and near-field distribution. **a** The red and green curves represent the normalized photoluminescence and absorption spectra of quantum dots, respectively. The blue curve represents the forward scattering spectrum of silicon particles. Magnetic dipole resonance and electric dipole resonance are respectively referred to as EDR and MDR. Quadrupole resonance is referred to as QR. **b** Calculated scattering spectrum of Si particle and the near-field distributions of EDR and MDR modes. The scale is 40 nm. **c** The red and blue curves represent the photoluminescence decay spectra of quantum-dots-only and Si-QDs, respectively. Reprinted from Yang et al. [43], with permission from American Chemical Society. Copyright (2017)

resulting in an enhanced excitation rate. In the process of emission, silicon particle microcavity can change the quantum yield through the modification of decay rates for radiative and non-radiative emissions. Modification of radiative decay results from the changing of local density of electromagnetic states, which is caused by silicon particle. The modification of non-radiative decay can be attributed to MDR excitation with quantum-dots-emission, which leads to the resonance transfer of energy to silicon particles. Considering that quantum dots are in direct contact with silicon particles, resonance energy transfer is the main reason for the decrease of quantum yield. The product of quantum yield and excitation rate determines the total intensity of photoluminescence. Increasing the excitation rate can compensate for the decreased quantum yield, which explains the same intensity of quantum dots and silicon quantum dots (see subsequent experimental results).

The photoluminescence intensity of silicon quantum dots using 10-ms-binning as a function of time is shown in Fig. 7a, and the intensity distribution is shown by a blue histogram with a mean of 250 and a variance of 3.2. As a comparison, Fig. 7b presents the photoluminescence intensity of quantum dots as a function of time, and the intensity distribution is shown by the red histogram with a mean value of 247 and a variance of 6.5. In order to study the difference between Fig. 7a, b, the corresponding curves of power spectrum relative to frequency of logarithmic scale silicon quantum dots and pure quantum dots were obtained by Fourier transform, which were shown in Fig. 7c, d. Background noise was shown by green traces. Intensity fluctuations of ensemble emissions were displayed by histograms. For quantum-dots-only, the emission fluctuates around 247 due to the fluorescence flicker (intermittent) of each quantum dot. [44]. The absence of dark period in ensemble emission can be attributed to the collective accumulation of fluorescence emitted by each quantum dot. In the emission of a single quantum dot, the dark state and bright state always correspond to the charged state and uncharged state of the quantum dot, respectively. The decay rates of radiative and non-radiative processes determine the quantum yield of uncharged quantum dots, with the lifetime of non-radiative decay being about 10–100 ns. For charged quantum dot, Auger recombination is the main contribution for non-radiative decay, giving the blinking fluorescence from single quantum dot. Auger recombination with a time scale of 0.1ns can not emit photoluminescence signal, but it can reduce the quantum yield of dark period, which is due to its pushing excess charge to a higher energy level. For silicon quantum dots, since the blinking of individual quantum dots was largely suppressed, the emission fluctuation of the ensemble quantum dots was well improved. The silicon particles can increase both radiative and non-radiative decay. The greatly increased decay rate is sufficient to compete with Auger recombination. At the same time, the reduction of Auger recombination can also lead to the suppression of blinking. Core-shell engineering was always used for suppression in blinking [44]. In this chapter, MDR mode in Si particle plays a significant role for the suppression of blinking. The hole wave function would be confined to the quantum dot by the excitation of MDR mode, and then the electron wave function would be delocalized to the surface of silicon particles. Therefore, reducing the overlap of hole and electron wave function is beneficial to reduce Auger recombination.

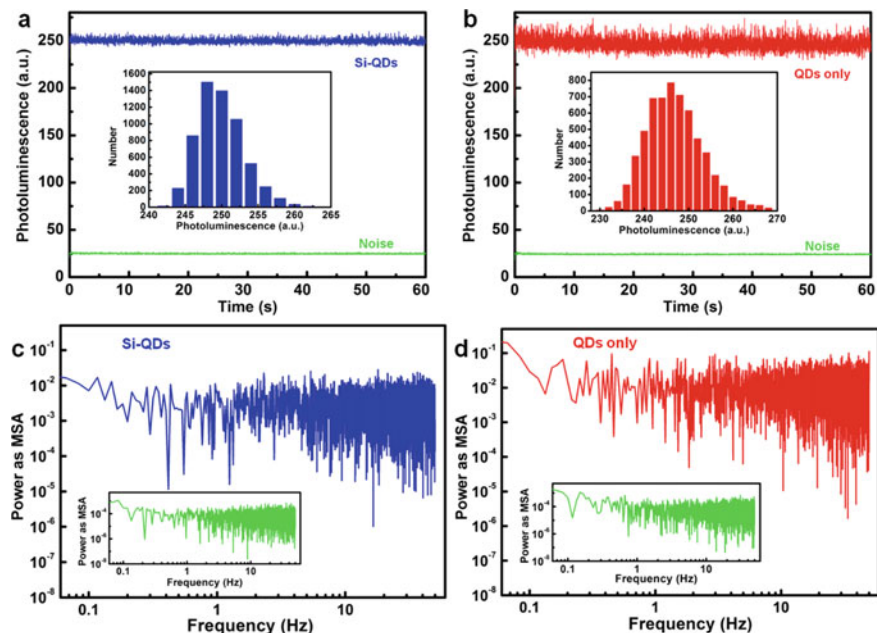


Fig. 7 Photoluminescence intensity versus time, and the intensities distributions are for (a) Si particles hybrid with quantum dots (Si-QDs), and (b) quantum-dots-only. The particle sizes of Si-QDs and Si particle are 172 and 160 nm, respectively. The background intensities of noise are green traces. Power spectra versus frequency are for (c) Si-QDs and (d) quantum-dots-only. The power spectrum of the noise traces is shown in the inset. Reprinted from Yang et al. [43], with permission from American Chemical Society. Copyright (2017)

To make sure that the fluctuation is from ensemble emission, five different ensembles of quantum dots were chosen arbitrarily to measure time traces. Figure 8 shows the obtained time traces and intensity distribution. Five results of fluctuation and distribution are similar to those in Fig. 7b, though their mean intensities are different. The different mean values can be attributed to an arbitrarily chosen set of five quantum dots, and they contain different numbers of quantum dots. Thus, fluorescence blinking induced fluctuations of ensemble emission are unavoidable to limit their device applications, especially suitable for display and lighting equipment requiring stable and homogeneous emission. In this chapter, we realize stable emission in the ensemble quantum dots doped with silicon particles, which provides an effective solution to related problem. In order to further verify the effectiveness of this effective solution, five different Si-QDs samples were randomly selected to measure the time traces, and the results are shown in Fig. 9. The measurements show that the fluctuation of the ensemble emissions were well refined and were similar to those in Fig. 7a. Since surface adsorption is the approximate connection between quantum dots and silicon particles, the number of quantum dots connected to silicon particles varies from particle to particle. The mean intensities of the Si-QDs was dependent on the

number of connected quantum dots, and the optimization of the connection process by chemical coupling could well control the number of connected quantum dots.

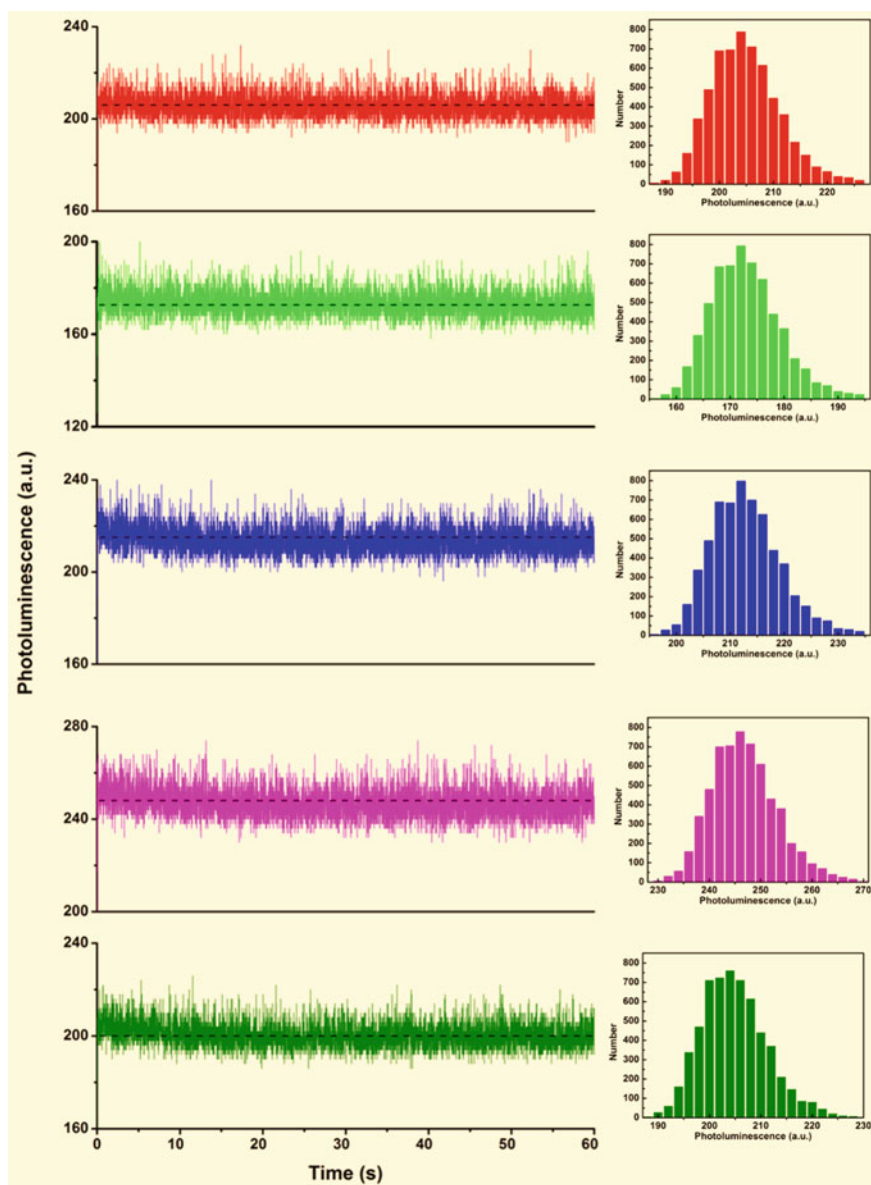


Fig. 8 Time traces and intensity distributions from five samples of ensemble quantum dots. Reprinted from Yang et al. [43], with permission from American Chemical Society. Copyright (2017)

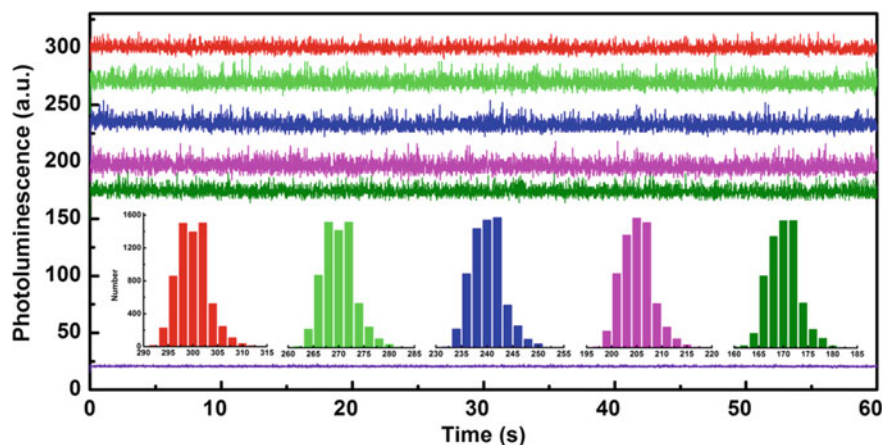


Fig. 9 Time traces and intensity distributions from five samples of ensemble Si-QDs. Reprinted from Yang et al. [43], with permission from American Chemical Society. Copyright (2017)

To study the temperature effects on quantum dots emission, the local temperature around 160 nm diameter silicon particles dispersed in water was calculated numerically when the laser with wavelength of 532 nm and power of $10 \mu\text{W}/\mu\text{m}^2$ was incident. The light heating was mainly generated by MD (magnetic dipole) mode excitation. The calculated temperature difference between Si-QDs and pure quantum dots is approximately 0.8 K, which can be neglected for influencing the quantum dots emission. Magnetic quadrupole (MQ) mode is too weak to be considered and MQ-induced heating could not provide optical heats to the temperature of quantum dots on the surface of Si particle. Thus, temperature difference within 1 K and the emission difference of quantum dots measured at 300 K room temperature can be ignored, which benefits their device applications in integrated photonics and optoelectronics [45–53].

To study the fluctuation behaviors after continuous excitation, Fig. 10 gives a time-dependent function of photoluminescence emission intensity within eighteen hours under continuous excitation at 532 nm wavelength for representative Si-QDs. The results obtained show that even after eighteen hours of continuous laser excitation, the well-improved fluctuation of photoluminescence emission can be maintained.

4 Applications

Typical applications of microcavity mediated light emissions from different plasmonic and dielectric composites are also reported recently. For example, we prepared hexagonal Cu_2Te microdiscs using a chemical vapor deposition method with gate as tellurium source, meanwhile, a layer by layer growth model was proposed to

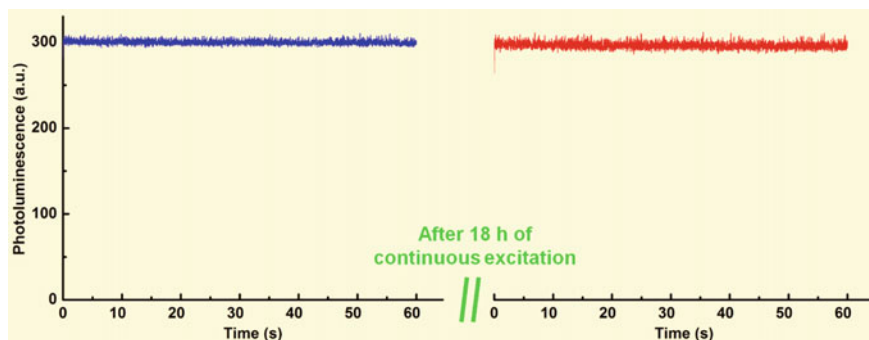


Fig. 10 Emission intensity of Si-QDs versus time with continuous 532-nm-wavelength laser excitation. Reprinted from Yang et al. [43], with permission from American Chemical Society. Copyright (2017)

explain the epitaxial growth mechanism of Cu_2Te hexagonal structures with orthogonal phases [54]. And semiconductor materials Cu_2Te hexagonal microdiscs were demonstrated to have great potential in red light laser and nonmetal SERS applications. Because of the abundant nonmetal plasma materials and low cost, it is expected to be an alternative to noble metals in laser and SERS applications. We prepared Er/W thin films by magnetically sputtering erbium and tungsten, and successfully prepared high-quality erbium-doped WS_2 nanosheets on silicon substrates by a chemical vapor deposition sulfurization method. The same conditions were used for testing, and the results show that the photoelectrochemical current of erbium-doped WS_2 nanosheets and that of pristine WS_2 nanosheets are 200 times higher than that of the latter. At the same time, under the influence of the erbium-doped WS_2 nanosheet's reasonable structural arrangement and its enhanced photoelectrical performance, the resistance between it and the electrolyte decreases nearly 20 times [55]. High quality erbium-doped WS_2 nanosheets are expected to be an alternative to noble metals and exhibit great potential in high-performance photoelectrochemical applications.

In addition, we pulled out the organic-inorganic hybrid nano-waveguide from the organic PVP matrix doped with MoS_2 quantum dots by physical pulling method. In the 55° intersection angle cross geometry, the asymmetric route of light energy is obtained, which destroys the symmetry of evanescent field coupling, and the nano-waveguide excited by nano-fiber asymmetrically couples the excitation signal along two opposite directions. At the same time, due to the energy dissipation related to self-absorption, two different colors of light emission are finally collected at the end of nano-waveguide. Nano-red, green, and blue signals are mixed in nano-waveguide to produce color emission [56]. This study shows potential applications in the fields of color displays, optical routing of photonic circuits and devices, and output coupling of laser emission. We have written a review of monolayer MoS_2 , focusing on the characteristics of monolayer MoS_2 and their applications in nanoscale photonics and optoelectronics. In the review, we first characterize the materials of monolayer

MoS₂, then explore its exciton modes and related properties. In the aspect of application, the latest progress in the research of nanoscale laser source, the integration of MoS₂ with nanowire or supersurface, and the PL of monolayer MoS₂ manipulated by plasma nanostructure and all dielectric hypersurfaces are introduced. We urgently need to improve the quantum yield in monolayer MoS₂ so that it can be better used in practical luminescence [57]. This review is necessary and meaningful. It shows that monolayer MoS₂ has great application potential in the basic physics and device applications of nanophotonics and optoelectronics. We report a nonmetallic plasma WSe₂/WO_{3-x} active system supported by environmentally friendly and highly conductive Ag/cellulose paper electrode. Using the air thermal annealing technology, p-WO_{3-x} dopant in WSe₂ was enriched, and the electrocatalytic behavior and photoreponse in near-infrared (NIR) region were significantly improved. Compared with the original electrocatalyst based on WSe₂, the thermally annealed WSe₂/WO_{3-x} shows enhanced electrocatalytic hydrogen evolution reaction. The results are a great progress in photo-enhanced electrocatalysis. It is believed that this study has a good application prospect in commercial hydrogen production [58]. This work reveals the development of nonmetallic plasma electrocatalysts and shows that they have great application prospects in biodegradable and photosensitive electrodes. We propose a single-layer fast response code-like nano-router similar to QR code, which can be used for full-color optical routing of image sensors at pixel level. The nano-router achieves high optical efficiency and negligible color distortion. Compared with various structural color technologies and optical routing technologies, it has low cost and simple structure that is easy to realize while maintaining high performance. At the same time, using the same nanometer outer layer and through multi-objective optimization method, robust polarization insensitivity and signal enhancement of more than 60% are obtained in all three primary color bands [59]. This nano-router can be used not only in ISs field, but also in the development of image sensors, photovoltaic devices, and color displays. We effectively collected and simply removed carbon nanotubes (CNT) dispersed in suspension by using tapered fiber tips. The temperature gradient produced by the photothermal effect of 1550 nm laser on water and the thermal convection produced push CNT to the fiber tip and make it adhere, which is confirmed in our simulation results. At the same time, the microscopic morphology of the collected CNT clusters is explained by simulating the velocity distribution [60]. CNT has great application prospects in biology and medicine. In order to avoid negative effects, it is very important to remove the remaining CNT. This work is expected to open up a new way for CNT removal. We successfully prepared WS₂: Er nanosheets by using rare earth doping strategy, and achieved simultaneous up-conversion and down-conversion luminescence from visible light to near-infrared region suitable for light detection. The WS₂/Si (WS₂:Er/Si) heterojunction infrared photodetector was successfully prepared by magnetic co-sputtering W:Er film on P-type Si substrate and sulfurizing it into WS₂: Er nanoplate/Si heterojunction, which has high photoelectric performance and stability [61]. Integrating silicon and two-dimensional nanomaterials expands the family of two-dimensional functional nanomaterials, making it more possible in application fields. This work

proves the potential integration of 2D nanowires on silicon platform, and erbium-doped WS_2 nanosheets have great potential in the development of high-performance IR photodetectors. We propose a broadband spectral modulation scheme for space light, which uses double epsilon-near-zero (ENZ) limitation of electric solution in silicon-insulator-silicon (SIS) capacitor based on deep nanometer. This study demonstrates that the dual ENZ mode scheme in the SIS structure facilitates the implementation of photo modulation of the electrical addressing space from the near-infrared (NIR) to mid-infrared (MIR) region due to its utilization of extended spectral bandwidth, large modulation depth and high speed switching. In similar TCO/Si-based SIS structures, the proposed scheme is expected to realize broadband high-speed spatial optical modulation on a fully integrated silicon platform [62]. Our research group will continue to explore new materials and physics in the field of microcavity mediated light emission, and enrich its potential in device application.

5 Conclusion

Plasmonic composite consists of quantum dots, and gold spheres have been fabricated by electrostatic interaction. Such composites make it possible to systematically study the emission properties of WGM as a function of polarization and size effects. The obtained results show that when the polarization angle is $\sim 10^\circ$, the photoluminescence intensity is the strongest and the WGM is the maximum. Due to the increase of the size, the positions of the WGM peak have a blue shift. Time-resolved decay kinetics shows that the photoluminescence lifetime is reduced from 13 to 9 ns before and after the quantum dot is combined with the gold sphere, and the emissivity is increased. Furthermore, the observed interferograms were analyzed in terms of the spatial distribution of the photoluminescence intensities. This kind of plasma composite material provides an effective tactics for the fabrication of active plasmonic microcavities for intense WGM emission devices and light concentration. Meanwhile, dielectric composite based on the high refractive index silicon particles hybrid with core-shell CdSe-ZnS quantum dots via surface interaction were used for achieving stable emission. The silicon microcavity with a diameter of 160 nm displays EDR and MDR modes near 525 nm and 650 nm, which the laser and emission wavelength of quantum dots at 532 nm, respectively. The energy transfer induced by MDR is resonantly effective for the coupling of quantum dot ensemble emission. By suppressing the emission of each quantum dot by scintillation, the emission fluctuation of the whole quantum dot can be improved. It could be believed that the all-dielectric composite may provide long-term and stable emitting source for metal-free photonic devices. Overall, these two classes of plasmonic and dielectric composites may realize the light confinement beyond diffraction limits and offer various applications in integrated nanophotonics.

Acknowledgements We thank the Guangdong Basic and Applied Basic Research Foundation (Grant. 2023A1515030209), the Research Projects from Guangzhou (Grant. 2023A03J0018), the

Fundamental Research Funds for the Central Universities (Grant. 21623412), and the National Natural Science Foundation of China (Grants. 11804120 and 61827822) for their financial support.

References

1. R. Costi, A.E. Saunders, U. Banin, *Angew. Chem. Int. Ed.* **49**, 4878 (2010)
2. B.P. Khanal et al., *ACS Nano* **6**, 3832 (2012)
3. P. Fan et al., *Nat. Photonics* **6**, 380 (2012)
4. U. Banin, Y. Ben-Shahar, K. Vinokurov, *Chem. Mater.* **26**, 97 (2013)
5. M. Pelton, J. Aizpurua, G. Bryant, *Laser Photonics Rev.* **2**, 136 (2008)
6. J.A. Schuller et al., *Nat. Mater.* **9**, 193 (2010)
7. B. Gjonaj et al., *Nat. Photonics* **5**, 360 (2011)
8. O. Hess et al., *Nat. Mater.* **11**, 573 (2012)
9. Z. Fang, X. Zhu, *Adv. Mater.* **25**, 3840 (2013)
10. G. Konstantatos, E.H. Sargent, *Nat. Nanotechnol.* **5**, 391 (2010)
11. P. Berini, *Laser Photonics Rev.* **8**, 197 (2014)
12. D. Pacifici, H.J. Lezec, H.A. Atwater, *Nat. Photonics* **1**, 402 (2007)
13. H.A. Atwater, A. Polman, *Nat. Mater.* **9**, 205 (2010)
14. Q. Gan, F.J. Bartoli, Z.H. Kafafi, *Adv. Mater.* **25**, 2385 (2013)
15. R.F. Oulton et al., *Nature* **461**, 629 (2009)
16. M. Noginov et al., *Nature* **460**, 1110 (2009)
17. C.-Y. Wu et al., *Nano Lett.* **11**, 4256 (2011)
18. X. Meng, A.V. Kildishev, K. Fujita, K. Tanaka, V.M. Shalaev, *Nano Lett.* **13**, 4106 (2013)
19. S.-H. Kwon, *Opt. Express* **20**, 24918 (2012)
20. J. Ward, O. Benson, *Laser Photonics Rev.* **5**, 553 (2011)
21. K.L. Kelly, E. Coronado, L.L. Zhao, G.C. Schatz, *J. Phys. Chem. B* **107**, 668 (2003)
22. U. Zywietz, A.B. Evlyukhin, C. Reinhardt, B.N. Chichkov, *Nat. Commun.* **5**, 3402 (2014)
23. P. Dmitriev et al., *Nanoscale* **8**, 5043 (2016)
24. Q. Zhao, J. Zhou, F. Zhang, D. Lippens, *Mater. Today* **12**, 60 (2009)
25. C.M. Soukoulis, M. Wegener, *Nat. Photonics* **5**, 523 (2011)
26. A.I. Kuznetsov, A.E. Miroshnichenko, Y.H. Fu, J. Zhang, B. Luk'yanchuk, *Sci. Rep.* **2**, 492 (2012)
27. B. García-Cámara, R. Gómez-Medina, J.J. Sáenz, B. Sepúlveda, *Opt. Express* **21**, 23007 (2013)
28. A.B. Evlyukhin et al., *Nano Lett.* **12**, 3749 (2012)
29. Y.H. Fu, A.I. Kuznetsov, A.E. Miroshnichenko, Y.F. Yu, B. Luk'yanchuk, *Nat. Commun.* **4**, 1527 (2013)
30. M.K. Schmidt et al., *Phys. Rev. Lett.* **114**, 113902 (2015)
31. I. Staude et al., *ACS Photonics* **2**, 172 (2015)
32. A. Delga, J. Feist, J. Bravo-Abad, F. Garcia-Vidal, *Phys. Rev. Lett.* **112**, 253601 (2014)
33. A. Samanta, Y. Zhou, S. Zou, H. Yan, Y. Liu, *Nano Lett.* **14**, 5052 (2014)
34. M. Decker, I. Staude, *J. Opt.* **18**, 103001 (2016)
35. X. Yang, D. Bao, B. Li, *J. Phys. Chem. C* **119**, 25476 (2015)
36. Q.Z. Zhu, S.P. Zheng, S.J. Lin, T.R. Liu, C.J. Jin, *Nanoscale* **6**, 7237 (2014)
37. D.E. Gomez, I. Pastoriza-Santos, P. Mulvaney, *Small* **1**, 238 (2005)
38. A. Chiasera et al., *Laser Photonics Rev.* **4**, 457 (2010)
39. Y. Gu et al., *Nano Lett.* **12**, 2488 (2012)
40. J. Xu, J. Xia, J. Wang, J. Shinar, Z. Lin, *Appl. Phys. Lett.* **89**, 133110 (2006)
41. R.G. Neuhauser, K.T. Shimizu, W.K. Woo, S.A. Empedocles, M.G. Bawendi, *Phys. Rev. Lett.* **85**, 3301 (2000)
42. M.V. Artemyev, U. Woggon, R. Wannemacher, H. Jaschinski, W. Langbein, *Nano Lett.* **1**, 309 (2001)

43. X. Yang, Y. Li, B. Li, *ACS Photonics* **4**, 2669 (2017)
44. A.L. Efros, D.J. Nesbitt, *Nat. Nanotechnol.* **11**, 661 (2016)
45. X. Yang, Y. Liu, H. Lei, B. Li, *Nanoscale* **8**, 15529 (2016)
46. X. Yang, D. Bao, B. Li, *RSC Adv.* **5**, 60770 (2015)
47. X. Yang, Y. Li, Z. Lou, Q. Chen, B. Li, *A.C.S. Appl. Energy Mater.* **1**, 278 (2018)
48. X. Yang, R. Xu, D. Bao, B. Li, *A.C.S. Appl. Mater. Interfaces* **6**, 11846 (2014)
49. X. Yang, D. Bao, Y. Zhang, B. Li, *ACS Photonics* **3**, 1256 (2016)
50. X. Yang, B. Li, *ACS Macro Lett.* **3**, 1266 (2014)
51. X. Yang, B. Li, in *Asia Communications and Photonics Conference (OSA, 2017)*, pp. Su2C.5
52. X. Yang, B. Li, in *Proc. of SPIE* **10622**, 106220B (2018)
53. X. Yang, B. Li, in *Plasmonics*. ed. by T. Gric (IntechOpen, London, 2018), p.21
54. Q. Li, H. Rao, X. Ma, H. Mei, Z. Zhao, W. Gong, A. Camposeo, D. Pisignano, X. Yang, *Adv. Opt. Mater.* **10**, 2101976 (2022)
55. Q. Li, H. Rao, X. Yang, Z. Guo, W. Gong, X. Ma, B. Li, *J. Phys. Chem. C* **126**, 9293 (2022)
56. X. Yang, L. Wen, J. Yan, Y. Bao, Q. Chen, A. Camposeo, D. Pisignano, B. Li, *J. Phys. Chem. Lett.* **12**, 7034 (2021)
57. X. Yang, B. Li, *Nanophotonics* **9**, 1557 (2020)
58. P.M. Pataniya, X. Yang, B. Li, D. Kanichkandy, C.K. Sumesh, *Int. J. Energy Res.* **46**, 12073 (2022)
59. M. Chen, L. Wen, D. Pan, D.R.S. Cumming, X. Yang, Q. Chen, *Nanoscale* **13**, 13024 (2021)
60. X. Yang, R. Xu, L. Wen, Z. Lou, Q. Chen, B. Li, *Fundam. Res.* **2**, 59 (2022)
61. Q. Li, H. Rao, H. Mei, Z. Zhao, W. Gong, A. Camposeo, D. Pisignano, X. Yang, *Adv. Mater. Interfaces* **9**, 2201175 (2022)
62. L. Wen, X. Nan, J. Li, D.R.S. Cumming, X. Hu, Q. Chen, *Opto-Electron. Adv.* **5**, 200093 (2022)

Fabrication and Application of Graphene-Composite Materials



Manish Srivastava, Bharti Mehlawt, Anamika Srivastava,
and Nirmala Kumari Jangid

Abstract In recent years, the research on the preparation and categorization of the composites from graphene is increasing widely as graphene has so many interesting properties. The amazing characteristics of graphene occur because of the stretched series of π conjugation that results in high charge mobility, high conductivity, and high Young's Modulus value. Due to these attractive properties, graphene has gained a lot of attention. Graphene also has some interesting properties in the biomedical field such as drug delivery, tissue engineering, biosensors, etc. The in-vivo and in-vitro study of graphene-based materials is an interesting subject for research. Graphene polymers can also be used for filler matter. These can be classified into two categories—(a) graphene-non-conducting polymer composites; (b) graphene-conducting polymer composites. The nanocomposite of the graphene-based polymer has three morphological states—(a) phase-separated micro composites; (b) intercalated nanocomposites; (c) exfoliated nanocomposites. Various techniques such as sol-gel process, in-situ polymerization, microwave-assisted process, electrochemical processes, etc. are used to prepare the composites of graphene. This chapter highlights some main findings related to graphene polymers that can be used as electrochemical devices and have applications in the fields of coatings, solar cells, light-emitting diodes (LEDs), sports equipment, aircrafts. The development of graphene in the form of nanofiller has been proved as a new source of the production of low-cost and high-performance composites for a wide range of applications.

Keywords Graphene · Graphene oxide · Graphene/conducting and non-conducting polymer composites · Polymer graphene/polymer nanocomposites · Fabrication methods · Applications

M. Srivastava (✉)

Department of Chemistry, University of Allahabad, Uttar Pradesh, Prayagraj, India
e-mail: sagermanish1@gmail.com

B. Mehlawt

Department of Environmental Science, Banasthali Vidyapith, Banasthali, Rajasthan, India

A. Srivastava · N. K. Jangid

Department of Chemistry, Banasthali Vidyapith, Banasthali, Rajasthan, India

1 Introduction

Graphene comprises of hexagonal structures of carbon atoms. It is a two-dimensional atomic crystal and an allotrope of carbon, or it may be referred to as a building block of the allotropes based on carbon. Graphene can form zero-dimensional, one-dimensional and three-dimensional structures. Zero-dimensional fullerenes can be formed by wrapping; one-dimensional carbon nanotubes can be formed by rolling, and three-dimensional graphite can be formed by stacking [1]. There are some important terminologies that are necessary to understand along with graphene [2].

Graphene layer—the graphene layer can be considered as a structured unit of a thick & single sheet that is arranged in hexagonal manner with sp^2 hybridization along with carbon materials.

Graphene oxide (GO)—It can be represented as another form of graphene which is of single layer and formed by modification in chemical structure by exfoliation or oxidation. This material has very high oxygen content.

Reduced graphene oxide (rGO)—rGO is that form of graphene oxide which is produced in reduction manner by the process of photo thermal, photo chemical, microwave, chemical, or bacterial methods for reducing the content of oxygen.

Graphene nanosheet—Nanosheet is a single sheet that is arranged in hexagonal manner with sp^2 bonding and atoms of carbon. These atoms are not basic element of the carbon material, but they are suspended free or can adhere to a foreign substrate.

When the sheets are drifted on one another, the bond length of carbon atoms in graphene is about 0.142 nm and the inter-planar spacing is 0.335 nm. There are 2 atoms in single-layer graphene or monolayer graphene while there are 4 atoms in bi-layers cell. The strong backbone of the lattice structure is formed by the in-plane sigma bonding [3 bonds/atom] of graphene. Graphene can keep a very high density of electric current. The high thermal conductivity of more than 3000 W mK^{-1} and electron movement of $2.5 \times 10^5 \text{ cm}^2 \text{ V}^{-1} \text{ s}^{-1}$ at room temperature is also presented by it. Graphene has a tensile strength of $130 \pm 10 \text{ GPa}$ and a very high elastic modulus of about 1 TPa. Graphene has a very fascinating property of zero-gap or semi-metallic semiconductor.

An optical transmittance of about 97.7% is shown by graphene. It also reveals high flexibility and impermeability to gases [3]. A high specific area of $2630 \text{ m}^2 \text{ g}^{-1}$ is represented by graphene which is significant for biomedical applications [4].

Researchers have concluded that the derivative of graphene is bio-compatible, and represents less cytotoxicity in several cells, but the results are still questionable [5, 6]. The viability of a cell can be decreased by enhancing the concentration of graphene, and its contact time. But the reports of literature claimed that the functionalized graphene materials are less toxic than the non-functionalized ones and present improved biocompatibility. Also, it has been noticed that the harmful effect of the fillers can be decreased when incorporated in biomaterials [7]. Though there is a limitation of graphene that it can get agglomerate because of tough van der Waals force. Graphene is hardly dissolved in aqueous or organic solution that contains ions, salts, or proteins [8].

Though, the performance of authentic graphene composites is still low as compared to the claimed property of graphene. The failure of graphene utilization in new technology can be due to the reduced presentation of graphene instead of its ideal performance. So, it is hard to say that graphene can be predicted as a new technical source or can be used as an increment or advantage in the further work. Although this assumption does not have a clarified answer, we try to explain some *main difficulties and challenges* which must be resolved to develop the possible advantages from graphene composites.

- **The size of flakes in graphene composites**

To attain better mechanical strength in composites, mechanical stress should be applied to the polymer composites which have to be transmitted to the sheets of graphene by the polymer matrices. When a load is applied to the composites, it starts to distort the polymer matrix around the sheets of graphene. Due to this distortion, shear forces start to build up at the end of the flakes that generate the strain inside the graphene [9]. The strain goes on increasing till the strain at flake becomes equal to the strain of matrices. The degree of reinforcement is equal to the length of flakes when graphene is sufficiently long along with the direction of load. On the other hand, if flake size is small, there is not enough length for a shear force to build up the considerable strain or stress in the graphene. Therefore, mechanical enforcement cannot be given to the composites by a small length flake, despite its high elastic modulus. This critical concern of length can be mainly noticed in conventional fiber composites [10].

Raman microscopy can be used to measure the strain of the grapheme composite materials. For grapheme composite materials the most favorable length of 30 μm would be desired for best reinforcement properties. Critically, the length is one order of magnitude longer than the normal length of the graphene attained via exfoliated graphene by ultrasound or shear. By in-situ Raman dimensions, it is feasible to estimate the interfacial shear stress of the graphene-polymer interface which is estimated to be about 10% of that of the polymer-carbon interfaces; as for carbon fiber. The cause behind the low shear stress value of composites is that atomic flat graphene does not have functional groups and defects for chemical interactions. So, there is a requirement of the route that can create highly functionalized and larger sheets.

- **Strong but flexible**

The single and defect less sheet of graphene has a young's modulus of ≈ 1 TPa and tensile strength of ≈ 100 GPa. Therefore, graphene may be considered preferably as the strongest material known, still not the stiffest, as both carbine & diamond that have higher modulus. Though it is established that graphene can be transferred from single sheet to macro-scale purposes, still it cannot out-perform steel (Young's modulus ≈ 200 GPa & strength ≈ 1 GPa, respectively). The defects and aggregation on graphene are responsible for this low performance. The lattice of graphene that is formed by sp^2 bond has exceptional mechanical properties because of high stability. Any changes in angle or length can be opposed by these bonds and on straining; a very high energy is yielded. On the contrary, if a graphene sheet is bended, it does not

lead to any deformation in the bonds. So, a very small amount of energy is required for bending as compared to stretching which required high energy [11, 12].

Because of the flexibility and strength, graphene could also resist high pressure difference and hence act as a different gas-separation barrier. Single graphene sheet can be suspended onto silicon microchambers. If there is a pressure difference between the internal cavity and external area, the sheets could uphold the pressure up to 90 kPa for several hours by bulging inward or outward the combination of flexibility and strength plays a key role in producing suspended multi-layer graphene membrane which can withstand the effect of high speed micro-bullets [12]. It is demonstrated that the precise penetrating energy for a multilayer graphene is about ten times greater than the macroscopic steel sheet [13]. By atomistic modeling, the mechanical behavior of graphene and related characteristics of structure & geometry of chemical bonding has also been studied deeply. But still there are no practical ways for complete exploitation of mechanical properties of graphene [14].

• Processing of Graphene Sheets in Composites

The automatic mechanical breakdown of sheets in graphene materials is one of the major concerns. The billions of graphene sheets are fixed in the polymer matrix to form a macroscopic composite which may rupture further because of poor interactions of matrices & graphene. It can cause sheet pull out or bad dispersal of sheet into the matrix, and can form huge aggregates which may be proved as a defect in the material [15]. Due to this reason, the usual performance of macroscopic composite is of the level of two orders inferior to the nanoscopic graphene. To create the composites, the most challenging or promising step is to process the sheet of graphene into polymer [16]. Because of the presence of strong π - π interactions & planar shape, the sheets would be likely to reaggregate or stack over one another. Due to this issue of reaggregation or to make sure for the significant mechanical property, the uniform distribution of sheets in matrices should be promoted [17]. Recently co-extrusion, simple mechanical mixing, blending, and three roll milling type of techniques are used for dispersing the graphene in matrix. Though the most favorable condition depends on the polymer matrix, and type of graphene used. By these means, the sheet of graphene can be diffused into monomers & then the polymer chain is increased directly from the sheet's surface and ensures better-dispersing properties of sheets in the matrices, very less aggregation and the higher interaction level [18].

Despite all these difficulties, graphene has great interest in many fields.

1.1 Importance of Graphene Composites

Graphene has very significant type of properties like its flexibility, strength, conductivity, and very light weight. The very effective way to harness its significant potential is to join or merge the graphene with accessible products—so-called composite materials.

Table 1 Properties of graphene oxide and reduced graphene oxide [27]

| Properties | GO | rGO |
|------------------------------|--|--|
| Fracture strength | 120 MPa | – |
| Thermal conductivity | 2000 W m ⁻¹ K for pure 600 W m ⁻¹ K on Si/SiO ₂ | 0.14–0.87 W m ⁻¹ K |
| Electrical conductivity | 10 ⁻¹ S/cm | 200–35,000 S/cm |
| Charge carrier concentration | – | – |
| Young's modulus | 220 GPa | – |
| Room temperature. mobility | – | – |
| Optical transmittance | – | Depends 60–90% on the synthesizing method and reducing agent |

These composites have a lot of importance in various fields such as:

- Graphene composite can work as a high performance photo catalyst [19].
- These composites can be used as dye adsorbents [20].
- They are used as electrode materials for energy storage [21].
- Graphene composites have a huge importance in lithium-ion batteries.
- They can be used as electrochemical biosensors [22].
- The composites may be very important in heavy metal removal [23].
- The importance of graphene composites as thermal conductors can be proved useful.
- The composites are recently proved as useful for making photovoltaic wire [24].
- Graphene composites are used to form corrosion resistant coatings.
- Graphene-based polymer composites are important as compared to neat polymers as they show better thermal, electrical, mechanical, gas barrier, and flame retardant properties [25].
- It is also noticed that graphene composites have better electrical & mechanical importance as compared to other filler-based composites [26] (Table 1).

1.2 Graphene-Composite Materials

“The 3-scotch tape method” is a process for the synthesis of graphene which was evolved by Novoselov and Geim. High-grade graphene is produced from this method which can be observed by Atomic force microscopy (AFM) & Raman spectroscopy, but production on large scale from this process is not appropriate. Therefore, this method could not be applied for the preparation of composites. Five noble winning techniques can be used for graphene synthesis [28, 29]; chemical reduction of graphite derivatives [30, 31], chemical vapor deposition [32, 33], organic synthesis technique, epitaxial growth [34–36], and “Unzipping” of Carbon Nanotubes (CNTs) [37, 38]. From these techniques, chemical reduction of graphene derivatives is

Table 2 Classification of graphene-composite materials

| Graphene-based composites | | Second component | References |
|-------------------------------|------------------------------------|------------------------|------------|
| Graphene-Polymer composites | | Polymer | [46–48] |
| Graphene-inorganic composites | Graphene/Metal composite | Metal | [49–51] |
| | Graphene/Carbon composite | Carbon building blocks | [52–54] |
| | Graphene/ Metal compound composite | Metal compounds | [55–57] |
| | Graphene/ Nonmetal composite | Nonmetals | [58, 59] |

evolved as the widely used method for the synthesis of graphene composites. This approach has been widely used as it produces modified graphene in a large quantity and used for its functionalization for suitable function. In recent times, mostly graphene composites use reduced graphene oxide (rGO), which is a derivative of graphene and can be obtained by chemical reduction of graphene oxide and its exfoliation. For the synthesis of graphite oxide, the modified Hummers' method is the widely used method where graphite is treated with strong mineral acids. Graphite is easy to exfoliate as its oxidation can demolish the sp^2 hybridization which can enhance interlayer separation & weaken the Vander Waal's force between the layers. Various reducing agents can be used for the reduction of graphene oxide to reduce graphene oxide such as hydroquinone [39], sodium borohydride [40, 41], and hydrazine hydrate. Mostly hydrazine is used. Some other eco-friendly chemicals are also used for reduction as tea, sodium citrate, alcohols, etc. [42–45] (Table 2).

2 Classification of Graphene-Composite Materials

The composites of graphene can be classified into two groups—(1) Graphene-polymer composite and (2) Graphene-inorganic material composite.

2.1 Graphene/Polymer Composite

As like CNT in polymers, graphene can also be used as filler matter. This can be subdivided into 2 types—(a) Graphene conducting polymer composite and (b) Graphene non-conducting polymer composites. The composites of Graphene and polymer are some kinds of hybrid materials of graphene nanosheets and polymers. The properties like mechanical strength, electrical conductivity, and thermal conductivity are improved within these composites [60]. Solution mixing is an easy and basic process for the synthesis of composites. The affinity of graphene and polymer can be achieved

by better dispersion. Graphene oxide can be easily dispersed in water because of its oxygen functionality. But reduced graphene oxide had to be sonicated in water to achieve good dispersion before being mixed into aqueous solution of a polymer as it is less soluble. In-situ polymerization method is another technique for synthesis [61–65]. Graphene/polyaniline composite was synthesized by the process of in-situ polymerization [66]. Various graphene-polymer composites are developed because of their low cost, and more production of graphene oxide and reduced graphene oxide. There is no tension of entanglement in graphene oxide and reduced uniform distribution and preventing restacking in graphene sometimes becomes a crucial process. This happens because restacking sometimes can reduce its effectiveness to become filler for composites [67].

Graphene oxide has insulating properties which can limit its applications in conductive polymers composites. However, the conductivity of graphene oxide can be increased by reduction. The in-situ reduction in polymer solution can restore the conductivity and can also prevent restacking. Graphene also possesses strong mechanical properties.

2.2 Graphene/Inorganic Composite

During the last decade, nanostructures and nanoparticles have got so much attention for research due to their interesting properties. For more improving properties, various nanoparticles of metal oxides, metals, and inorganic compounds have been incorporated with graphene in a structure of composite. MnO₂ [68], Au, Ni [69], NiO [70], Co₃O₄ [71], ZnO, Fe₃O₄, Ag [72], Rh [73], Ru, TiO₃, etc.

Graphene-inorganic composites can be further distinguished as graphene-carbon composites, graphene-metal composites, graphene-metal compound composites. Metals such as Sn, Cu, Co, bimetals and alloys are used for fabricating inorganic composites. The integration of carbon nanotubes and graphene exhibits fascinating properties. These composites provide high surface area, and more electrical and thermal conductivity, mechanical strength.

The combination of graphene with metal compound like hydroxides, oxides, selenides, clay, sulphides, inorganic salt, etc. can form great composites. There are various uses of graphene resulting from these compounds like as in electron transfer.

For instance, the composite formed by C₃H₄-graphene has been reported as a catalyst with high performance which can activate molecular O₂ in saturated alkanes to oxidize the secondary C-H bonds [74]. Generally, the fabrication of graphene-inorganic nanostructures is divided into two groups—in-situ hybridization and ex-situ hybridization.

2.2.1 Ex-Situ Hybridization

This method is much easier to work than in-situ techniques. Generally, prepared nanoparticles and graphene are mixed in solutions. Surface modification of graphene & nanocrystals is approved for improved mixing. But this is not a usual process. In this procedure, the mechanism implicated is p–p stacking by some involving molecule. For absorbing nanocrystals, the role of adhesive layers is played by the p–p stacking. From various examples, mercaptan capped CdS nanoparticles [75] and 2-mercaptopyridine modified gold nanoparticles are effectively added to reduced graphene oxide that has many functions e.g., surface-enhanced Raman spectroscopy, in catalysis, etc. On the other hand, for connecting nanocrystals, modified graphene can also be used. For example, adhesive polymer Nafion coated rGO has been used to prepare rGO = TiO₂ composites, or bovine-serum albumin (a biopolymer) has been employed to modify rGO for the fabrication of silver, palladium, or platinum nanoparticle/graphene composites. Other than p–p stacking, which is a noncovalent interaction, covalent interaction has also been used to prepare composites. For this purpose, graphene oxide is used in place of reduced graphene oxide, because many oxygen groups have been contained in graphene oxide that are used to link with another functional group. To synthesize graphene composites & inorganic nanocrystals, electrostatic interactions can also be used. In electrostatic interaction, the ionized functional groups that are negatively charged are exploited to assemble positively charged nanoparticles on them. rGO = Fe₃O₄ composite can be prepared by this process [75, 76].

2.2.2 In-Situ Hybridization

To achieve even surface for nanocrystal on reduced graphene oxide is not easy in ex-situ technique. The in-situ method can control the nucleation site of reduced graphene oxide by modification of surface that provides an even surface site.

The most accepted process for growing nanostructure on graphene is the chemical-reduction process. By in-situ process, the chemical reducing components such as ascorbic acid, sodium borohydride, and amines can reduce the precursor of noble metals like K₂PtCl₄, H₂PdCl₆, and AgNO₃. Sodium borohydride (NaBH₄) can be used to reduce HAuCl₄ in an octa-decyl-amine suspension of reduced graphene oxide for synthesizing nanocrystals of the composite of graphene. By chemical-reduction process, anisotropic nanostructure beside the nanoparticle is also formed. The preparation of nanostructures based on the composite of graphene can also be done by the photochemical reduction technique. Here, bright gold nano-dots are grown on reduced graphene oxide surface modified by thiol with the in-situ reduction of HAuCl₄ in light irradiation [75]: Along with metal particles, metal oxides like MnO₂, SnO₂ can also be prepared on the surface of graphene oxide using in-situ technique. Metal oxide and metal nanoparticle can be synthesized on reduced graphene oxide using an in-situ microwave radiation method. This technique has a limitation that it does not provide excellent allocation or management of size. This drawback

can be conquered by joining the process of microwave-assisted synthesis and ionic-assisted dispersion. In the altered process, the composites of Rh/rGO and Ru/rGO through narrow range allocation of Rh & Ru nanoparticles were prepared. Nowadays, an electrochemical process is utilized to prepare graphene-inorganic nanocomposites. There are two parts of this technique; firstly, the sheets of graphene are collected on the electrode after the electrochemical process in which the electrode grafted with graphene is immersed in the suspension of electrolytes. When electro-potential is applied to the metals which are noble or highly pure like platinum, gold, platinum-gold alloy, they were diminished electro-chemically [77]. The oxide of metals can also be prepared by this process. MnO_2 -rGO composites can be prepared using the in-situ technique of electrodeposition of γ MnO_2 nano-flowers on the electrodes of reduced graphene oxide. Firstly, the suspension of reduced graphene oxide is filtered by vacuum to prepare the paper of the graphene oxide. Then the paper is used as an electrode in the desired form for electrodeposition of MnO_2 . rGO-GO can also be used to synthesize the nanoparticles of silver along with that of Pt and Au by electrodepositions. The single-walled carbon nanotubes (SWCN) of Ag act as a cathode for donating electrons to reduce the ions of metals and for the nucleation as it is less negative than the redox potential of Pt and Au. Graphene oxide has functional groups that contain oxygen, so it offers more sites for nucleation as compared to the reduced graphene oxide that does not contain the oxygen-containing functional group. In the in-situ techniques that are used to prepare the composites of graphene metal oxides, the sol-gel process is widely used for the preparation of nanostructured SiO_2 , and TiO_2 at the surface of reduced graphene oxide [78]. The hydroxide functional group present at the surface of rGO-GO has an important function and behaves as a nucleation site of the nanoparticles. Zhu et al. [79] also synthesized the composites of silica on graphene oxide with the hydrolysis process of tetramethyl orthosilicate (TMOS) followed by the dispersion of graphene oxide in water or ethanol, by placing the film of composites in the vaporizing atmosphere of hydrazine hydrate for a full night for the reduction of graphene oxide. That film acts as a transparent conductor and shows very little percolating properties (Table 3).

3 Fabrication and Characterization of Graphene-Composite Materials

Graphene composites can be synthesized by various methods. Some of which are shown in Fig. 1 and described in the following sub-sections.

Table 3 Different types of graphene/inorganic nanostructured composite materials

| Composite | Route | Property measured | Applications | References |
|---|--|--|--|------------|
| CdSe/rGO | CVD ¹ growth of CdSe NP with Cd and Se shot as precursors on GRO prepared by thermal annealing | Photoinduced current response with time | Optoelectronics | [80] |
| ZnS/graphene | Thermal CVD growth of single-crystalline ZnS on graphene using ZnS powder as precursors | CL ² spectra | Cathodoluminescence | [81] |
| Cu/rGO; Ru/rGO; Rh/rGO | In-situ reduction by microwave | Catalytic activity in hydrogenation reaction | Catalysis | [82] |
| Fe ₃ O ₄ /GO or rGO | Hydrolysis with FeCl ₃ or redox reaction using FeCl ₃ , FeCl ₂ and NaOH | Charge/discharge cyclic performance and magnetometry | Li-ion battery, magnetic composite, and drug carrier | [83] |
| ZnO/rGO; Cu ₂ O/rGO | In-situ electrochemical deposition | Current voltage under the sunlight | Photovoltaics | [83] |
| MnO ₂ /GO or FGS ³ | Reaction b/w C and KMnO ₄ | Cyclic voltgram and galvanostatic charge/discharge | Supercapacitor, Li-ion battery | [84] |
| CdS/rGO | Hydrothermal rxn. With dimethyl sulfoxide, GO and Cd (CH ₃ COO) ₂ | Time-resolved fluorescence decay | Optoelectronics | [85, 86] |
| NiO/rGO | By sputtering | Current voltage | Nanocapacitor | [87] |
| SnO ₂ /FGS | In-situ redox reaction with SnCl ₂ and H ₂ O ₂ | Galvanostatic charge/discharge | Li-ion battery | [88] |
| Ag/GO or rGO | Ex-situ by π - π stacking via bovine-serum albumin or in-situ reduction by NaBH ₄ , or electroless deposition | Raman spectroscopy | As substrate in Surface-enhanced Raman spectroscopy (SERS) | [89] |
| Pt or Pd on GO or rGO | Ex-situ, π - π stacking via bovine-serum albumin, or in-situ reduction by microwave and H ₂ PdCl ₄ with HCOOH, ascorbic acid | Cyclic voltgram | Electro catalysis | [90] |
| SiO ₂ /rGO or FGS | Electrostatic interaction via C ₆ H ₁₇ NO ₃ Si or hydrolysis by TEOS ⁴ | Electrical conductivity | Transparent conductor | [91] |
| CNT/graphene | CNT was grown on grapheme by CVD using Ni or Co as catalyst | – | – | |

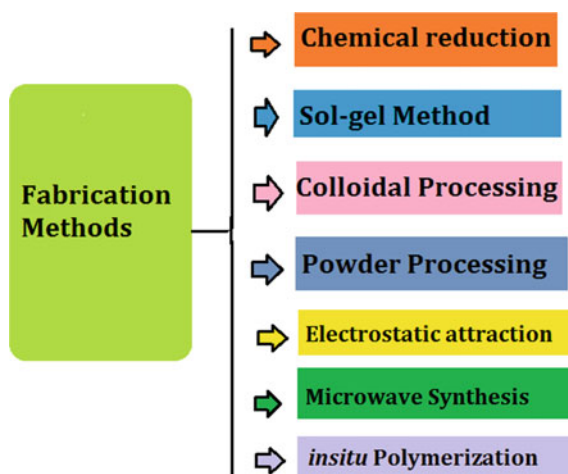
(continued)

Table 3 (continued)

| Composite | Route | Property measured | Applications | References |
|---|--|---|---|------------|
| CdSe/ CVD-graphene | Electrochemical deposition | – | Optoelectronics | [90, 91] |
| TiO ₂ /rGO | Ex-situ, noncovalent adhesion via nafion or self-assembly of TiO ₂ nanorods on rGO. In-situ template hydrolysis with TiCl ₃ or C ₁₆ H ₃₆ O ₄ Ti | Cyclic photocatalytic degradation | Li-ion battery, photovoltaics, photocatalysis | [91] |
| Au/rGO or GO | Ex-situ, π - π stacking via bovine-serum albumin, or in-situ reduction by NaBH ₄ , sodium citrate, ascorbic acid, or microwave | Raman spectroscopy and Catalytic activity | Catalysis, Surface-enhanced Raman spectroscopy, plasmonic | [91] |
| Co ₃ O ₄ /rGO or GO | Reduction of Co (OH) ₂ /GO at 450-degree Celsius. Reaction of urea Co (NO ₃) ₂ in microwave | Cyclic voltgram, specific capacitance, galvanostatic charge/discharge | Li-ion battery, supercapacitor | [88] |
| SnO ₂ /rGO | ALD ⁵ on grapheme of SnO ₂ with SnCl ₄ and H ₂ O as precursors | Galvanostatic charge/discharge | Li-ion battery | [88] |

¹ CVD: Chemical vapor deposition; ² CL: Cathodoluminescence; ³ FGS: Functionalized graphene sheets; ⁴ TEOS: Tetraethylorthosilicate; ⁵ ALD: Atomic layer deposition

Fig. 1 Various methods to fabricate graphene composites materials



3.1 *In-Situ Polymerization/Crystallization*

In this process, a solution of monomer or multiple monomers has been mixed and then polymerized. The sheets of graphene are converted into liquid and then an appropriate initiator is put in that solution. Both radiation and heat can initiate the process of polymerization [92]. Crystallization or in-situ polymerization is a low-cost heating process that has good optical properties and a very high molding ability [93]. For better quick dispersion in the solution of monomers and composites, the functionalization of the sheets of graphene is done. Through the intercalation of monomers, the layered structure of graphene is exfoliated in nanoplates and a polymer matrix with well-dispersed graphene is then produced [94]. In the process of in-situ polymerization, firstly the graphene flakes are dissolved into prepolymers or monomers and polymerization is then carried out that leads to the precipitation or crystallization of composites having better-dispersing properties and very strong connection between the filler and the matrix. For increasing the ability of the components in a system, this process lets the polymer grafted with fillers with or without functionalization. Though the viscosity of the system is increased in this process that can reduce the processing and loading fraction of the composite through the means of in-situ polymerization synthesis, the graphene-based filler dispersion of a high level can be attained without any exfoliation step. In this process, the monomer is dispersed between the layers of graphene and then the polymerization is followed for isolating the layers. This technique is utilized to test graphene-polymer composites and is called intercalation polymerization [95]. Graphene is intercalated by Styrene, isoprene or (monomer) and an alkali metal. Graphene sheets that are negatively charged are then used for polymerization. Throughout this process, the fabricated filler and the matrix have built up covalent linking between them. On the other hand, this process can also prepare various other polymers like polypyrrole, polyethylene, and methyl methacrylate (PMMA) by noncovalent linking. As compared to graphite, graphene oxide has a large space that supports the intercalation of layers either by polymers or monomers. Direct insertion of hydrophilic molecules is supported via polar functional groups by taking polymer or monomer in an increased quantity. Graphene has a functional group that contains oxygen that offers enough dynamic sites and then a bond is formed with secondary filler or matrix. This bond considerably improves the characteristics of the composite. A far-reaching study has been carried out for producing nanocomposite that is based on the epoxy group. Here fillers are primarily dissolved in the resin following curing and hardening [96]. Various composites have been synthesized by this method like PANI-GO, PANI-GO/PANI-graphene, and graphene nanosheet/carbon nanotube/polyaniline [97, 98]. Ma and his co-workers prepared composites of PI/GO [Polyimide-graphene oxide] by in-situ polymerization [99]. Dreyer et al. have declared that in the process of polymerization, there are two purposes served by graphene oxide [100, 101]. Firstly, this catalyzed the dehydrative polymerization, and then the left carbon in the catalyst of graphene oxide whereas the residual carbon from the GO catalyst experienced dehydrogenation all through the reaction and acted as an additional component to the composite.

3.2 Chemical Reduction

Graphene derivatives such as graphene oxide (GO) platelets have a surface rich in reactive functional groups, and numerous techniques have been developed to develop covalent linkages between GO platelets and polymers. For example, both grafting-to and grafting-from methods are introduced for the attachment of a wide range of polymers. Polymer brushes have been fabricated in a controlled manner by adding an ATRP-compatible monomer (such as styrene, butyl acrylate, or methyl methacrylate) and a source of copper iodide. Similar studies using such ATRP-based methods have reported an increased scope of monomer reactivity [102]. Significant improvements in thermal and mechanical properties have been reported for polymer-grafted chemically modified graphene (CMG) platelets into a polymer matrix as compared to the neat matrix polymer [103]. In some polymers, covalent linkage between GO platelets and the matrix is developed during polymerization without performing any prior functionalization. In the case of epoxy matrix composite, curing with an amine hardener may lead to the incorporation of GO platelets directly into the cross-linked network [104]. Xu et al. grafted polyamide brushes to GO platelets through condensation reactions between carboxylic acid groups of GO platelets and amine-containing monomers [105].

3.3 Sol–Gel Methods

The ceramics or glass composites of graphene are synthesized by the sol–gel process. In this method, a precursor is prepared that goes through the process of condensation for growing a material that has well-dispersed graphene. Firstly, with the help of ultrasonication, a suspension that remains stable and has well-dispersed graphene is prepared. Then the hydrolysis process is promoted, and gel is formed by adding a catalyst [acidic water]. This process is mainly used for synthesizing nanocomposite of silica and CNT-silica [106, 107].

3.4 Colloidal Processing

Colloidal processing is used to prepare ceramic suspensions based on colloidal chemistry. This technique is also utilized to fabricate graphene–ceramic mixtures by mixing graphene colloidal suspensions and ceramic powders. Generally, that same solution is favored for making suspension for obtaining consistent dispersion. This mixing is done by the process of ultrasonication or magnetic stirring. The modification of the surface of graphene and matrix is also required in colloidal processing. This can be attained by creating an electric charge in between ceramics and graphene using surfactant [hetero coagulation] or direct functionalization [108, 109].

3.5 Powder Processing

CNT-ceramic composites with different matrix-like zirconia, borosilicate glass, silica, alumina, etc. are usually made from this process [110, 111]. The deagglomeration of CNT or graphene i.e., of filler matter is done by ultrasonication of the particles followed by the addition of ceramic to the solution. This can also be done by conventional ball milling to produce slurry of composite. Kun and his co-workers used NMP/ethanol that acts as a dispersing medium to prepare ceramic-graphene composite. Powder processing is a simple technique to produce well-dispersed composite of graphene [112].

3.6 Microwave-Assisted Synthesis of Metal/Graphene Composites

An effective method to heat for processing the reactions is the utilization of microwave radiation which is a better option for carrying out the reactions [113]. In 1986, the process of microwave-assisted synthesis for organic nanomaterials was first reported [114]. The utilization of microwave radiations for inorganic synthesis is at primary stage until now and will take time for its complete utilization [115, 116]. There is an increasing interest for using microwave radiations in the field of nanotechnology or nano-science. Small particulate matter can be created by the microwave synthesis process. This process also reduces the order of magnitude by time for a chemical reaction [117]. Graphene was used in the fabrication of grapheme nanosheets using chitosan under the microwave radiations [118, 119]. The particles of chitosan were grafted on the layer of graphene and at the same time the sheet of graphene oxide was reduced to graphene [120]. Under the strength of electric field, the nanocomposite grafted by chitosan exhibits ER (Electrorheological properties) behavior. Microwave-assisted process is also used to prepare dry water-free ER system that consists of polyionic liquid particles [121, 122].

3.7 Electrostatic Attraction

As functional groups are present naturally in graphene oxide, it has negative electric charge. So, a simplistic electrostatic attraction-based approach is used for preparing various nanocomposites of graphene oxide [123–125]. Yin et al. [126] used electrostatic attraction approach for synthesizing the titania microspheres enclosed with graphene oxide. The titania microspheres wrapped with graphene oxide is more polarized than pure titania microsphere. Goswami and co-workers [127] used electrostatic attraction to graft polar graphene oxide sheet on the modified silica surface. Initially the silica particles reacted with 3-aminopropyltrimethoxysilane for 10–12 h

for introducing amine group which resulted in the positive charged surface [128]. The solution of silica particles mixed with the sheets of graphene oxide to get silica particles enclosed with graphene oxide-sheets. The ER (Electrorheological properties) behavior for the geometrical effect on the particles was estimated because the aspect ratio has an optimistic position in enhancing the ER characteristics. The better ER presentation was detected by the material that had high aspect ratio. The high ER efficacy is demonstrated by dielectric properties, mechanical stability, and low resistance.

4 Fabrication of Advanced Graphene Materials

4.1 Quantum Dots of Graphene

4.1.1 Fabrication of Quantum Dots of Graphene

Considering edge effects and quantum confinement of nano-graphene, its new derivatives have been evolved. Nanosheets of graphene having a lateral dimension below 100 nm and multi-layered stacks of graphene together are termed, graphene quantum dots [129]. Because of their flexible bandgap and fluorescence stability, they are of keen interest [130]. Fabrication of these quantum dots requires alteration of graphene oxide and reduced graphene oxide via bottom-up and top-down approaches which include microwave-assisted thermal treatment, high-power ultrasonication, hydrothermal, and liquid-phase exfoliation [131, 132]. Lu and co-workers reported the eco-friendly one-pot hydrothermal process for the fabrication of quantum dots (90 min) using black C [133]. By making use of H_2O_2 they can be made efficiently photo-stable and biologically compatible. Wang and co-workers demonstrated a single-step, one-pot hydrothermal procedure to fabricate quantum dots by making use of rice husk biomass. With the help of light-emitting quenchers, these quantum dots sensed iron's 3p orbital [134]. A derivative of graphene is too diverse and involves varied fabrication processes and for fabricating graphene oxide, reduced graphene oxide, or quantum dots of graphene there is no "standard" procedure. It opens gates for many exclusive prospects.

4.2 Graphene and Derived Nanofiller

4.2.1 Fabrication of Graphene and Derived Nanofiller

Because of the simple method of preparation, tunable property and wide application conductive polymer composites (CPCs) are of great interest. For synthesizing

conductive polymer composites from non-conducting polymers, conducting fillers are inserted into them. They increase the conductivity of the material. This is known as an electrical percolation threshold (Pc). Both theoretically and experimentally it was found that with an increase in filler aspect ratio electrical percolation threshold decreases. So, by employing large aspect ratio conducting fillers then conducting networks in a matrix can be synthesized [135]. Graphene composites possess great mechanical properties, extraordinary thermal conductivity, and higher electron portability at room temperature. For corresponding to electrical conductivity polymer composites a 3-D network is used. Wu and co-workers used a hot press method for the preparation of polystyrene composites having a three-dimensional network [136]. Chen and co-workers fabricated an excellent conducting composite film with the help of three-dimensional graphene foam via template-assisted chemical vapor deposition method [137].

4.2.2 Significance of Graphene and Derived Nanofiller

As a nanofiller, graphene is preferred over other common nanofillers like exfoliated graphite, sodium montmorillonite, carbon nanotube, and carbon nanofiber, and because of higher aspect ratio, great surface area, low coefficient of thermal expansion, tensile strength (TS), electrical and thermal conductivity, transparency, flexibility, and shielding ability [138].

4.2.3 Applications of Graphene and Derived Nanofiller in Energy and Electronics

Because of extraordinary microelectronic chips, they require high-power densities and high conductivity, which are issued as thermal pads, heat spreaders, and thermal interface materials. Graphene and derived nanofillers are necessary compounds for thermal packaging and are responsible for maintaining a great relationship between metal sinks and chips [139]. The most important characteristic of graphene is the very high electrical conductivity.

Conductive polymer composites are synthesized by inserting graphene in the polymer matrix. Various polymers specifically polyvinyl chloride, polyvinyl alcohol, polymethyl methacrylate, polyethylene, polyamide, and polystyrene worked as matrices to fabricate graphene composites. They generally demonstrate a non-linear improvement of the electrical conductance as a means of concentration of filler. They can be used to make sensors, solar cells, etc.

4.3 Graphene Aerogels (GAs)

Several procedures including chemical-reduction methods [140, 141], hydrothermal methods [142, 143], resorcinol (R), and formaldehyde (F) sol-gel chemistry methods [144, 145] were suggested for the preparation of aerogels and monolithic aerogels on basis of graphene oxide. The chemical-reduction method was found to be the most appropriate one since it is an eco-friendly and low-cost method. This method requires low temperature without the need for a binder. Worsley and co-workers [146] observed high electrical conductivity of 1×10^2 S/m, a large specific surface area of $548 \text{ m}^2\text{g}^{-1}$, and pore volumes ($2.96 \text{ cm}^3/\text{g}$), making these materials viable candidates for use in energy storage, catalysis, and sensing applications.

4.4 Hybrid Graphene/Microfiber Composites

An encouraging progress is being made on current graphene-based composites through the use of hybrid fillers that consist of an inorganic material and graphene-based materials. The hybrid combination gives advantages such as synergistic effects between the fillers, or final properties resulting from preservative. The hybridization process will come across few drawbacks of filler, and the progress of its interaction with the host matrix depends on its working parameters. Multifunctionality plays an important role in manufacturing hybrid composites since combined properties of diverse fillers correspond to a substance having a different set of properties as opposed to properties of individually fabricated materials.

In addition, the value of the ultimate product can be increased by making use of fine microscale reinforcements like C and glass fibers having lower levels of graphene, where stress moves from micro to nano-scale reinforcement, hence improving the final properties.

Hybridization of graphene materials and the rest of the inorganic group showed outstanding properties on an atomic or nano, or can be synergized with integration. Hybrid graphene and other two-dimensional structures maintained the electronic properties and specifically, the bandgap of grapheme could be altered. The zero-band gap of graphene is unsuccessful in semiconductor materials, but it is useful for its composites that can help in the manufacture of graphene-based electronics. The tuned band gap of grapheme with hexagonal boron nitride (h-BN) is 5.8 eV. In-plane alteration of h-boron nitride on grapheme (64% C) broadens band gap up to 4 eV. Opposite to it, adding carbon to h-boron nitride increases electric conductivity, which acts as an insulating agent in pristine form. The inductive band gap in graphene can effectively fabricate field-effect transistors of graphene/boron nitride films having $190\text{--}2000 \text{ cm}^2\text{V}^{-1} \text{ s}^{-1}$ carrier mobilities. Cross-linking of graphene via chemicals and h-boron nitride composites could efficiently store energy. The (h-BN) Supercapacitors of graphene or boron nitride have specific capacitance of 240 F/g. The bond formed between graphene and individual fillers affect the resulting physical and

chemical characteristics of synthesized reinforced composites. To improve the efficiency among fillers various procedures were followed like solution blending, functionalization via chemicals, mechanical mixing, alternate growth, and many more. Aggregation of graphene takes place because of higher specific surface area and van der Waals interaction. The ornament of graphene is preferred since it avoids aggregation with other nanomaterials. Graphene's reactive sites got improved because of its functionalization which further improved its bond formation capability with the rest of the nanomaterials and finally led to the advancement of less significant covalent bonding between the matrix of host and hybrid filler.

The functioning of multiwalled carbon nanotubes established effective bonds between multi-graphene platelets and fillers. The two-dimensional filler i.e., multi-graphene platelets and one-dimensional filler i.e., multiwalled carbon nanotubes combine to form a three-dimensional structure having a higher surface area. Thermal conductivity of functionalized multiwalled carbon nanotube showed enlargement of > 50% in comparison to pristine hybrid filler.

4.5 Graphene Bioactive Composites

Various biosensors which depend on graphene for different sensing purposes consist of separate standards for electrochemical and optical signals. Because of its fast response, high sensitivity, excellent electrochemical properties, straightforward operation, and low cost, graphene is used as a probable competitor for biomolecule discovery. Bai and co-workers [147] reported the synthesis of thin highly reduced graphene oxide film and reported their high electro-catalytic activity.

In comparison to the exposed electrode, noteworthy enlargement in the rate of electron transmission of graphene-based electrodes has been obtained. Zhu and co-workers [148] accounted for superior electro-catalytic progress of (N-doped graphene) N-graphene toward reduction of H_2O_2 in comparison to graphene, which is responsible for the occurrence of N- containing groups, O- functional groups, and structural defects. GO possess fluorescence over a broad range of wavelengths i.e., 200–1200 nm and it successfully quenched the light-emitting property of other fluorescing dyes.

5 Applications of Graphene/Polymer Composite Materials

5.1 Structural Reinforcement Materials

At the low graphene loading, these materials can be used in transport that requires lightweight & high strength because of improved mechanical strength of the polymer matrix. In general, the utilization of graphene and its derivatives increases the tendency to improve the mechanical properties of conventional fiber-reinforced

polymer composite systems. GO could also be utilized to alter the surface of the carbon fibers or to provide improved properties to carbon fiber-polymer composite [149, 150]. When graphene oxide is initiated at low load (approx. at 5.0 wt. %) into the surface fiber, properties like tensile properties, interlaminar shear strength (IFSS), and interfacial shear strength (ILSS) are improved. Additionally, the use of both graphene & carbon fiber produces the result of thermoplastic composites [151]. These materials of better qualities can look up the reliability, cost-effectiveness & safety of fiber emphasized polymer composites which are the matter of interest in the marine, automotive, aerospace, sports, wind energy industries, and biomedical. The derivatives of graphene & the graphene itself have been used to strengthen the fibers of polymers by melting and solution mixing techniques [152, 153]. For generating a very short pulse in fiber laser or to demonstrate its ability to absorb as a broadband absorber, a membrane is prepared from electro spun graphene-PVA fibers which has revealed its tendency as an adsorbent & as efficient photonic material. PVA-based and rigid composite fibers were prepared by the hybridization of wrinkled reduced graphene oxide flakes [154]. These fibers made by hybridization were shaped into high-modulus helical springs and showed gravimetric toughness of $\sim 1000 \text{ Jg}^{-1}$, where this value is far exceeding spider dragline silk (165 Jg^{-1}) and Kevlar (78 Jg^{-1}). Recently, graphene nanoribbon (GNR)-carbon composite nanofibers have been synthesized by electrospinning method using poly (acrylonitrile), that contains graphene oxide nanoribbons (GONRs), carbonizing and successive twisting. In the process of electrospinning, the graphene oxide nanoribbons are leaning in an electrified thin liquid jet by the side of the axis of the fiber, whereas the carbonization of the polymer matrices increases the electrical and mechanical properties of the composites. This type of nanofibers composites can be approached for reinforcement of lightweight composites and high-performance electrodes for fiber-shaped solar cells, capacitors, secondary batteries, and fuel cells that includes elastic electronic device.

Since graphene has more thermal stability & a different type of structure, it can also provide another option for slowing down conventional flames as it can work as a barrier in the transfer of gases into the zone of flame and retards their combustion. The nature of the flame of epoxy composites that contains GO, Ethylene glycol (EG), CrGO, and organic phosphate functionalized graphene oxide was investigated and with the help of micro combustion calorimeter that both functionalized graphene oxide (FGO)-epoxy composite & CrGO-epoxy composite is superior to GO-epoxy composites in flame retardant properties and shows that when there is a loading of 5 wt.% CrGO and 5 wt.% FGO, the highest reduction is 43.9% & 27.3% respectively in peak-heat release rate. The possible outcomes of graphene-polymer composites as flame retardants were investigated in earlier period [155, 156]. Moreover, with low loading fractions (0.25%), increase in temperature of decomposition (60°C), increase in modulus ($>200\%$), and increases in the strength of compression of reduced graphene oxide with thermal stability of the sheets in the form of polymers. These graphene foams are multifunctional and light weighted and hence can be used in construction, packaging applications, and construction [157–160]. The permeation of gas by a polymer composite can be reduced by the inclusion of graphene and its derivative [161]. Wide applications in packaging materials can be suggested by

the grouping of light absorption & barrier properties of a graphene-PS composite and neat PS composite [162]. The mechanical strengthening of graphene-polymer composite combined with protective outcome of graphene besides the friction force and the effect of graphene suppression presents its function as resistant materials [92].

5.2 Sensors

Temperature Sensing, and damage & strain sensing are the two main types of response from a sensor of graphene-polymer composites [163–167]. The channel between local conductive networks is the main thing that affects the conductivity of graphene-polymer composite. So, if there is a change in the distance of channeling of a local network, the conductivity is also changed. This change in conductivity can be observed and used for sensing [168]. To design strain sensors, the derivatives of graphene are insulated in the polymer matrices [169–171]. The direct and easy energy impulse can be provided to electrical and mechanical domains by piezoresistive effect. In this effect, the conducting network of conductive composite alters due to external pressure which results in variation of resistance. Piezoresistive materials have so many functions in wearable electronics, smart textiles, movement sensors, and health monitoring [172]. The composites of graphene-PDMS are synthesized from direct chemical vapor deposition by 3-D graphene-foam nano structures [173]. It is concluded that these composites show high electrical conductivity ($\sim 10 \text{ Scm}^{-1}$) at a low load ($\sim 0.5 \text{ wt.}\%$) of graphene. The different kind of properties and structure of these composites shows high potential for foldable, stretchable, and flexible conductors. In the same way, Zhang et al. used pre-stretched polydimethylsiloxane (PDMS) films coated with graphene ribbons or sheets & the buckling structures are prepared when the film gets released by strain [174]. The resistance of the ruffled graphene-PDMS composite gets changed due to strain. There is a decrement in the resistance from 5 to 3 k Ω with an increment in strain from 0–20%. The conductivity of polymer composites is extensively affected by temperature [92, 175–179]. So self-regulated heaters, over current protectors, and temperature sensors, can be utilized by this property. It was examined by Mahmoud et al. [180] that conductivity depends on both fillers loading & temperature. They observed the outcome of temperature on conductivity of graphene-rubber composite by filling them with different loads that range from 1 to 5%. When the quantity of graphene nanoparticles increases in the rubber matrices, the path between the layers is decreased and as a result, the conductivity is increased. Graphene & its derivatives are capable to functionalize as energy transfer in some contexts because they have a mixture of mechanical, electrical, optical, and thermal properties. Cheng et al. observed the enhanced effect of mechanical properties by graphene-PU composite [181, 182]. It was estimated that the composites contained approximately 1.0 wt.% sulfonated graphene, showed repeated operations, and could remarkably contract & raise a 21-g weight of 3 cm with 0.21 force when exposed to infrared (IR) light. In addition, the energy density of more than 0.33 J/g could be checked, the composite of graphene polymer would

also be researched for electrical and mechanical operators and hence used for several purposes like micro-robotics, microscopic pumps, artificial muscles, and switches [183]. As graphene has negative thermal expansion coefficient and high conductivity, it presents itself as a new material for electromechanical operators as compared to traditional devices. Several mechanical and electrical composite drivers or operators of better characteristics would be formed by incorporating the derivatives of graphene into polymers [184–186]. For instance, Liang et al. [187] synthesized a bimorph operator from graphene-polydiacetylene and got a great movement using a curvature of approximately 0.37 cm^{-1} under a current density of 0.74 A/mm^2 , and produced high actuation stress of more than 160 MPa/g at an applied direct current density of 0.29 A/mm^2 . These composites exhibited a large life cycle of reversible swings beneath alternating currents at large frequencies up to 200 Hz .

5.3 Wastewater Treatment

Graphene composites have applications in environmental safety and protection. Since graphene has low effective contact with molecules of water as it is hydrophobic and so results in bad absorption quality for heavy metals from water. But it was estimated that hydrophilic property can be achieved within a modified form of graphene by which heavy metals can be absorbed. The complex reactions are caused in heavy metals by the grouping of oxygen-containing groups present with high surface area within graphene oxide. The contaminants available in wastewater, especially the noble metals are photo degraded by photo catalyst that is activated by ultraviolet (UV) radiation [188]. In the mechanism of photodegradation by UV, the electrons get excited by UV radiation from the valence band to the conduction band for generating holes & photogenerated electrons in the valence band. As these electrons get dispersed on the surface, they degrade the various pollutants present on the surface by reacting with them [189]. Reduced graphene oxide gets precipitated easily in the suspension because of its stability & solubility which is a major problem that needs to be resolved [190, 191]. Guo et al. [192] formed silver and gold nanoparticles of reduced graphene oxide hybrids from chitosan that acts as stabilizing and reducing agent. The study revealed that at low temperatures, chitosan can effectively reduce graphene oxide & their adsorption on graphene oxide nanosheets which formed stable reduced graphene oxide solution. These stable hybrids have many purposes for the protection of the environment. Sung-Suh et al. [193] described the disintegration of RhB by the photo-induced heating of suspended graphene sheets in the presence of intense UV radiation. The following steps are engaged in the decaying process of Rhodamine B (RhB). The sheets are deoxygenated in the absence of the photocatalyst hybrids based on graphene and are produced on the sheet for growth of nanoparticles, and selective nucleation in the presence of graphene oxide, the RhB molecule is decomposed. Also, the sheets of graphene in any hybrid material act as a catalyst and not as a reactant. The adsorption capacity of synthetic organic compounds from GO and GNS was also estimated which was then compared with

carbon nanotubes in the availability of natural organic matters (biphenyl, dyes, and phenanthrene) [194]. Good absorption quality was revealed by graphene as compared to carbon nanotubes that characterize the less compact structure. As a result, it was concluded that graphene could be a great choice as an adsorbent to remove organic pollutants from wastewater [192, 195].

5.4 Biomedical Applications

Graphene has extraordinary characteristics that offer several important applications. Biomedical application from nanocomposites of graphene polymer is one of them [196, 197]. In 2008, the very first report was published about the biomedical applications of graphene [198, 199]. After that graphene and its derivatives had been used for various biological purposes such as cancer therapy, bioimaging, gene delivery, and drug delivery.

5.4.1 Drug Delivery

There is a strong interaction between aromatics areas in sheets of graphene & hydrophobic drugs, so it is very interesting to use graphene in drug delivery. Improved anticancer activity by the use of PEGylated nano-graphene oxide as a nano-carrier has been made by Pei group [200] for loading various types of anticancer drugs through nanocovalent physisorption. The photoluminescent characteristics & in-vitro cellular uptake capacity have also been assessed [201, 202]. Polyvinyl alcohol (PVA) grafted graphene oxide, and CNT filled by CPT (Calprotectin) formed complex CNT-PVACPT & GO-PVA-CPT were compared & estimated for checking their abilities to kill cancer cells [203]. Pan et al. [204] functionalized the sheets of graphene with poly (N-isopropyl acrylamide) [PNI-PAM] [205]. These sheets have higher ability to bind CPT at high loading ratio (18.5 wt. %). Also, these sheets were harmless.

The efficient loading of a drug can be utilized by the beneficial effect of the delocalized surface of the π electron that is present in graphene with a two-dimensional structure. This loading is done by π - π stacking & hydrophobic interactions. Moreover, graphene has more surface area and high density that permits biofunctionalization by both noncovalent & covalent modification of surface. Good behavior of graphene can replace the other materials used for bioactivity as in tissue-engineered scaffolds, biosensors, bio grafts, drug delivery, etc. [206, 207].

5.4.2 Gene Delivery

The acquired and inborn diseases can be treated well by the gene therapy [208, 209]. In gene therapy, PEI [polyethyleneimine] has been identified as “gold standard” among all the polyelectrolytes. It has a better proton sponge effect and a strong

binding capability with nucleic acid. But it also has bad biocompatibility and more cytotoxicity that limits its further use for gene therapy purposes. Liu et al. [210] prepared nano-carrier from modified polyethyleneimine (PEI) graphene oxide for DNA transfection [211–213].

Chitosan is a naturally occurring polysaccharide that has many bio-applications in tissue engineering, gene delivery, and drug delivery. It acts as a good pharmaceutical agent as it is biodegradable, bio-compatible, and antibacterial [214, 215]. Bao et al. [216] delivered CPT drug in cancer cells of human & reported the DNA using the nano-carrier formed of chitosan functionalized graphene oxide [217]. Zhang et al. [218] estimated that the gene delivery by graphene oxide nano-carrier directed the increased anticancer efficiency.

Kim and his workers [219] installed a cationic polymer, PEI [polyethyleneimine], which is a nonviral vector for gene delivery that estimated the progress in graphene oxide-based effective gene delivery

5.4.3 Cancer Therapy

In the field of biomedicine, cancer can also be treated through graphene and graphene-polymer composites. Lan and his co-workers [220] reported that [NGO-PEG] polyethylene glycol functionalized graphene oxide showed less or no toxicity in cells. Liu et al. [221] performed a research on multifunctionalization of graphene and graphene oxide for controlled release and targeted delivery of anticancer drugs.

Markovic & his co-workers [222] reported membrane depolarization and found that oxidative stress was engaged in graphene-mediated photo-thermal killing of cancer cells resulting in necrotic and apoptotic death of cell [223, 224].

Tian et al. [225] loaded the chlorin e6 (ce6) using a photo-sensitizer molecule through π - π stacking on polyethylene glycol-graphene oxide and this was used in the cancer therapy. In-vitro hepatocarcinoma was diagnosed and treated by Shen and co-workers [226] through graphene oxide nanocomposite [GO-PEG-FA/Gd/DOX].

6 Conclusion

The composites that emerged from the interaction of graphene and polymers can be represented as one of the most advanced developments in technology. Although there are several difficulties and challenging perspectives of graphene composites, which have to be noticed for assessing their complete potential, their importance, main properties, fabrication methods, applications, challenges, and overcoming were overviewed. However, this technology is yet in an early stage of development, an increasing curiosity, and enormous possibilities of work will become apparent. The graphene of high quality is still not prepared and transferred in cost-effective way. The thermal, mechanical, and electrical properties of graphene are viable for electrical &

thermal-induced composites, electrical sensors, electronic circuits, and transparent and flexible electrodes for displays and solar cells, etc.

In place of conventional nanofillers, graphene fillers can be proved as beneficial for the matrices because they have good electrical and thermal conductivity, high aspect ratio, and high surface area. It is stated earlier that various attempts must be made for preparing graphene composites. Though there are several advancements made in this field, extensive research is still required for further development and basic understanding. Regardless of the various combinations of matrix, and the composites of different shapes, sizes, chemistry and properties, all graphene composites share same features somewhere along with the characterization, processing, and fundamentals. Therefore, the vital key for preparing advanced composites is the engineering of the graphene-polymer interaction. It is important to develop an understanding related to the properties of the interface or interfacial region, surface chemistry, and arrangement of the constituents for further work in this field. This description also emphasizes some main applications related to biomedical field such as ultra-miniaturized low-cost sensors for analyzing urine and blood. The conducting polymers may be used as electrochemical devices and have great applications in coatings, solar cells, light-emitting diodes (LEDs), etc. Some other commercial uses of graphene-polymer composites are in sports equipment, car parts, aircrafts, plastic containers, light weight tanks, medicinal plants, and wind turbines. The development of graphene in the form of nanofiller has been proved as a new source of the production of low cost, lightweight, and high performance composites for a wide range of applications.

It is expected that a wide range of new composites of various polymers (thermosetting, thermoplastic, commodity polymers) and graphene elements of various sizes, shapes, and functionalities will be published in near future. As for example, the innovative molecular design of polymeric surfactants, which can avoid the issue of dispersion and solubility in polymers, and the film-forming capability of graphene, have not yet been discovered.

Nevertheless, we are far away in terms of understanding the mechanism of the enhancement effect in graphene composites.

References

1. K.S. Novoselov, S.V. Morozov, T.M.G. Mohinddin, L.A. Ponomarenko, D.C. Elias, R. Yang, I.I. Barbolina, P. Blake, T.J. Booth, D. Jiang, J. Giesbers, E.W. Hill, A.K. Geim, *Phys. Stat. Sol. (b)* **244**(11), 4106 (2007)
2. H.P. Boehm, R. Setton, E. Stumpp, *Pure Appl Chem.* **66**(9), 189 (1994)
3. K.S. Novoselov, V.I. Fal'ko, L. Colombo, P.R. Gellert, M.G. Schwab, K. Kim, *Nature* **490**, 192 (2012)
4. S. Goenka, V. Sant, S. Sant, *J. Control Release* **173**, 75 (2013)

5. A.M. Pinto, I.C. Gonçalves, F.D. Magalhães, J. Colloids. Surf. B. Biointerfaces. **111**, 188 (2013)
6. Y. Zhang, T.R. Nayak, H. Hong, W. Cai, J. Nanoscale. **4**, 3833 (2012)
7. S.P. Lonkar, Y.S. Deshmukh, A.A. Abdala, J. Nano. Research. **8**, 1039 (2015)
8. I. W. Frank, D. M. Tanenbaum, A. M. van der Zande, and P. L. McEuen, *J. Journal of Vacuum Science & Technology B*. **25**, 2558 (2007).
9. W.H. Roos, J. Methods Mol. Biol. **783**, 251 (2011)
10. J.H. Zou, Z.Q. Ye, B.Y. Cao, J. Chem. Phys. **145**(13), 134705 (2016)
11. V. Singh, D. Joung, L. Zhai, S. Das, S.I. Khondaker, S. Seal, Prog. Mater. Sci. **56**(8), 1178 (2011)
12. R.R. Nair, P. Blake, A.N. Grigorenko, K.S. Novoselov, T.J. Booth, T. Stauber, N.M.R. Peres, A.K. Geim, Science **320**, 1308 (2008)
13. V.G. Kravets, A.N. Grigorenko, R.R. Nair, P. Blake, S. Anissimova, K.S. Novoselov, A.K. J. Geim, Phys. Rev. B. **81**, 155413 (2010)
14. F. Wang, M. Hamdi, J.I.E.E. Commun, Lett. **12**, 206 (2008)
15. F. Rana, P.A. George, J.H. Strait, J. Dawlaty, S. Shivaraman, M. Chandrashekar, M.G. J. Spencer, Phys. Rev. B. **79**, 115447 (2009)
16. S. Park, R.S. Ruoff, Nat. Nanotechnol. **4**, 217 (2009)
17. D.C. Elias, R.R. Nair, T.M.G. Mohiuddin, S.V. Morozov, P. Blake, M.P. Halsall, A.C. Ferrari, D.W. Boukhalvalov, M.I. Katsnelson, A.K. Geim, K.S. Novoselov, Science **323**(5914), 610 (2009)
18. F. Bonaccorso, Z. Sun, T. Hasan, A.C. Ferrari, Nat. Photonics. **4**, 611 (2010)
19. X. Ma, H. Tao, K. Yang, L. Feng, L. Cheng, X. Shi, Y. Li, L. Guo, Z. Liu, Nano Res. **5**, 199 (2012)
20. A.-J. Shen, D.-L. Li, X.-J. Cai, C.-Y. Dong, H.-Q. Dong, H.-Y. Wen, G.-H. Dai, P.-J. Wang, Y.-Y. Li, J. Biomed. Mater. Res. A. **100A**, 2499 (2012)
21. V.C. Sanchez, A. Jachak, R.H. Hurt, A.B. Kane, Chem. Res. Toxicol. **25**, 15 (2011)
22. A. Bianco, Angew. Chem., Int. Ed. Engl. **52**, 4986 (2013).
23. H. Ren, C. Wang, J. Zhang, X. Zhou, D. Xu, J. Zheng, S. Guo, J. Zhang, ACS Nano **4**, 7169 (2010)
24. C.-H. Lu, C.-L. Zhu, J. Li, J.-J. Liu, X. Chen, H.-H. Yang, Chem. Commun. **46**, 3116 (2010)
25. Y. Wang, Z. Li, D. Hu, C.-T. Lin, J. Li, Y. Lin, J. Am. Chem. Soc. **132**, 9274 (2010)
26. Y. Xu, Q. Wu, Y. Sun, H. Bai, G. Shi, ACS Nano **4**, 7358 (2010)
27. A.T. Smith, A.M. LaChance, S. Zeng, B. Liu, L. Sun, Nano materials science. **1**(1), 31 (2019)
28. A.V. Titov, P. Král, R. Pearson, ACS Nano **4**, 229 (2009)
29. K.S. Novoselov, A.K. Geim, S.V. Morozov, D. Jiang, Y. Zhang, S.V. Dubonos, I.V. Grigorieva, A.A. Firsov, Science **306**, 666 (2004)
30. S. Stankovich, D.A. Dikin, R.D. Piner, K.A. Kohlhaas, A. Kleinhammes, Y. Jia, Y. Wu, S.T. Nguyen, R.S. Ruoff, Carbon **45**, 1558 (2007)
31. S. Park, R.S. Ruoff, Nat. Nanotech. **4**, 217 (2009)
32. A. Reina, X. Jia, J. Ho, D. Nezich, H. Son, V. Bulovic, M.S. Dresselhaus, J. Kong, Nano Lett. **9**, 30 (2009)
33. C. Mattevi, H. Kim, M. Chhowalla, J. Mater. Chem. **21**, 3324 (2011)
34. W.A. de Heer, C. Berger, X. Wu, P.N. First, E.H. Conrad, X. Li, T. Li, M. Sprinkle, J. Hass, M.L. Sadowski, M. Potemski, G. Martinez, Solid State Commun. **143**, 92 (2007)
35. P.W. Sutter, J.-I. Flege, E.A. Sutter, Nature Mater. **7**, 406 (2008)
36. S. Shivaraman, R. A. Barton, X. Yu, J. Alden, L. Herman, M. Chandrashekar, J. Park, P. L. McEuen, J. M. Parpia, H. G. Craighead, and M. G. Spencer, *Nano Lett.* **9**, 3100, (2009).
37. D.V. Kosynkin, A.L. Higginbotham, A. Sinitskii, J.R. Lomeda, A. Dimiev, B.K. Price, J.M. Tour, Nature **458**, 872 (2009)

38. L. Jiao, L. Zhang, X. Wang, G. Diankov, H. Dai, *Nature* **458**, 877 (2009)
39. G. Wang, J. Yang, J. Park, X. Gou, B. Wang, H. Liu, J. Yao, *J. Phys. Chem. C* **112**, 8192 (2008)
40. J. Shen, Y. Hu, M. Shi, X. Lu, C. Qin, C. Li, M. Ye, *J. Chem. Mater.* **21**, 3514 (2009)
41. H.-J. Shin, K.K. Kim, A. Benayad, S.-M. Yoon, H.K. Park, I.-S. Jung, M.H. Jin, H.-K. Jeong, J.M. Kim, J.-Y. Choi, Y.H. Lee, *Adv. Funct. Mater.* **19**, 1987 (2009)
42. D. R. Dreyer, S. Murali, Y. Zhu, R. S. Ruoff, and C. W. Bielawski, *J. Mater. Chem.* **21**, 3443 (2011)
43. Z. Zhang, H. Chen, C. Xing, M. Guo, F. Xu, X. Wang, H.J. Gruber, B. Zhang, J. Tang, *J. Nano Res.* **4**, 599 (2011)
44. Y. Wang, Z. Shi, J. Yin, *A.C.S. Appl. Mater. Interfaces* **3**, 1127 (2011)
45. V. Eswarajah, S.S.J. Aravind, S. Ramaprabhu, *J. Mater. Chem.* **21**, 6800 (2011)
46. S. Stankovich, D. A. Dikin., G. H. Dommett., K.M. Kohlhaas, E.J. Zimny, E. A. Stach, E. A., & R.S. Ruoff. *Nature*, **442**, 282 (2006).
47. J. Liang, Y. Huang, L., Zhang, Y., Wang, Y., Ma, T., Guo, & Y., Chen. *Advanced Functional Materials*, **19**(14), 2297 (2009).
48. M.A. Rafiee, J. Rafiee, Z. Wang, H.H. Song, Z.Z. Yu, N. Koratkar, *ACS Nano* **3**, 3884 (2009)
49. R. Muszynski, B. Seger, P.V. Kamat, *J. Phys. Chem. C* **112**(14), 5263 (2008)
50. G., Goncalves, P. A., Marques, C.M. Granadeiro, H.I., Nogueira, M.K. Singh, J., Gracio, *Chemistry of Materials*, **21**(20), 4796 (2009).
51. X. Huang, S. Li, Y. Huang, S. Wu, X. Zhou, S. Li, S.H. Zhang, *Nat. Commun.* **2**(1), 1 (2011)
52. J.K. Wassei, K.C., Cha, V.C. Tung, Y. Yang, R.B. Kaner, *J. Mater. Chem.* **21**(10), 3391 (2011).
53. S. Das, R. Seelaboyina, V. Verma, I. Lahiri, J.Y. Hwang, R. Banerjee, W. Choi, *J. Mater. Chem.* **21**(20), 7289 (2011)
54. X.C. Dong, B. Li, A. Wei, X.H. Cao, M.B. Chan-Park, H. Zhang, L.J. Li, W. Huang, P. Chen, *Carbon* **49**, 2944 (2011)
55. T.T. Baby, R. Sundara, *J. Phys. Chem. C* **115**(17), 8527 (2011)
56. P. Wang, Y. Zhai, D. Wang, S. Dong, *Nanoscale* **3**(4), 1640 (2011)
57. H. Y. Koo, H.J. Lee, H. A. Go, Y.B. Lee, T.S. Bae, J.K. Kim, W.S. Choi. *Graphene-Based Multifunctional Iron Oxide Nanosheets with Tunable Properties. Chemistry—A European Journal* **17**(4), 1214 (2011).
58. Y. Cao, X. Li, I.A. Aksay, J. Lemmon, Z. Nie, Z. Yang, J. Liu. *Phys. Chem. Chem. Phys.* **13**(17), 7660 (2011)
59. H. Wang, Y. Yang, Y. Liang, J.T. Robinson, Y. Li, A. Jackson, H. Dai, *Nano Lett.* **11**(7), 2644 (2011)
60. J. Du, H.M. Cheng, *Macromol. Chem. Phys.* **213**(10–11), 1060 (2012)
61. A. Yu, P. Ramesh, M. E. Itkis, E. Bekyarova, R. C. Haddon, *J. Phys. Chem. C* **111**, 7565 (2007).
62. X. Xiao, T. Xie, Y.-T. Cheng, *J. Mater. Chem.* **20**, 3508 (2010)
63. M.A. Rafiee, J. Rafiee, I. Srivastava, Z. Wang, H. Song, Z.-Z. Yu, N. Koratkar, *Small* **6**, 179 (2010)
64. X. Zhou, T. Wu, B. Hu, G. Yang, B. Han, *Chem. Commun.* **46**, 3663 (2010)
65. K. Zhang, L.L. Zhang, X.S. Zhao, J. Wu, *Chem. Mater.* **22**, 1392 (2010)
66. D.-W. Wang, F. Li, J. Zhao, W. Ren, Z.-G. Chen, J. Tan, Z.-S. Wu, I. Gentle, G.Q. Lu, H.-M. Cheng, *ACS Nano* **3**, 1745 (2009)
67. H. Kim, A.A. Abdal, C.W. Macosko, *Macromolecules* **43**(16), 6515 (2010)
68. S. Chen, J. Zhu, X. Wu, Q. Han, X. Wang, *ACS Nano* **4**, 2822 (2010)
69. H. Wang, J.T. Robinson, G. Diankov, H. Dai, *J. Am. Chem. Soc.* **132**, 3270 (2010)
70. J.Y. Son, Y.-H. Shin, H. Kim, H.M. Jang, *ACS Nano* **4**, 2655 (2010)
71. Q. Wu, Y. Xu, Z. Yao, A. Liu, G. Shi, *ACS Nano* **4**, 1963 (2010)
72. X. Zhou, X. Huang, X. Qi, S. Wu, C. Xue, F. Y. C. Boey, Q. Yan, P. Chen, H. Zhang, *J. Phys. Chem. C* **113**, 10842 (2009)
73. D. Marquardt, C. Vollmer, R. Thomann, P. Steurer, R. M. lhaupt, E. Redel, and C. Janiak, *Carbon* **49**, 1326 (2011)
74. S. Bai, X. Shen, *RSC Adv.* **2**(1), 64 (2012)

75. M. Feng, R. Sun, H. Zhan, Y. Chen, *Nanotechnology* **21**, 075601 (2010)
76. J. Huang, L. Zhang, B. Chen, N. Ji, F. Chen, Y. Zhang, Z. Zhang *Nanoscale* **2**, 2733 (2010).
77. S. Sun, L. Gao, Y. Liu, *Appl. Phys. Lett.* **96**, 083113 (2010)
78. J. Liu, S. Fu, B. Yuan, Y. Li, Z. Deng, *J. Am. Chem. Soc.* **132**, 7279 (2010)
79. Y. Zhu, S. Murali, W. Cai, X. Li, J.W. Suk, J.R. Potts, R.S. Ruoff, *Adv. Mater.* **22**, 3906 (2010)
80. R. Muszynski, B. Seger, P.V. Kamat, *J. Phys. Chem. C* **112**, 5263 (2008)
81. X. Huang, X. Zhou, S. Wu, Y. Wei, X. Qi, J. Zhang, F. Boey, H. Zhang, *Small* **6**, 513 (2010).
82. D. Wang, R. Kou, D. Choi, Z. Yang, Z. Nie, J. Li, L.V. Saraf, D. Hu, J. Zhang, G.L. Graff, J. Liu, M.A. Pope, I.A. Aksay, *ACS Nano* **4**, 1587 (2010)
83. M. Du, T. Yang, K. Jiao, *J. Mater. Chem.* **20**, 9253 (2010)
84. C. Fu, Y. Kuang, Z. Huang, X. Wang, N. Du, J. Chen, H. Zhou, *Chem. Phys. Lett.* **499**, 250 (2010)
85. S. Liu, J. Wang, J. Zeng, J. Ou, Z. Li, X. Liu, S. Yang, *J. Power Sources* **195**, 4628 (2010)
86. Y. Hu, H. Zhang, P. Wu, H. Zhang, B. Zhou, C. Cai, *J. Phys. Chem. Chem. Phys.* **13**, 4083 (2011)
87. Q. Cheng, J. Tang, J. Ma, H. Zhang, N. Shinya, L.-C. Qin, *Carbon* **49**, 2917 (2011)
88. H.C. Choi, M. Shim, S. Bangsaruntip, H. Dai, *J. Am. Chem. Soc.* **124**, 9058 (2002)
89. Y.-B. Tang, C.-S. Lee, J. Xu, Z.-T. Liu, Z.-H. Chen, Z. He, Y.-L. Cao, G. Yuan, H. Song, L. Chen, L. Luo, H.-M. Cheng, W.-J. Zhang, I. Bello, S.-T. Lee, *ACS Nano* **4**, 3482 (2010)
90. G. Zhou, D.-W. Wang, F. Li, L. Zhang, N. Li, Z.-S. Wu, L. Wen, G. Q. (Max) Lu, H.-M. C. Cheng, *Mater.* **22**, 5306 (2010)
91. S. Watcharotone, D.A. Dikin, S. Stankovich, R. Piner, I. Jung, G.H.B. Dommett, G. Evmenenko, S.-E. Wu, S.-F. Chen, C.-P. Liu, S.T. Nguyen, R.S. Ruoff, *Nano Lett.* **7**, 1888 (2007)
92. J.R. Potts, D.R. Dreyer, C.W. Bielawski, R.S. Ruoff, *Polymer* **52**, 5 (2011)
93. S.N. Tripathi, P. Saini, D. Gupta, V. Choudhary, *J. Mater. Sci* **48**, 6223 (2013)
94. V. Singh, D. Joung, L. Zhai, S. Das, S.I. Khondaker, S. Seal, *Prog. Mater. Sci.* **56**, 1178 (2011)
95. D. G. Papageorgiou, I.A. Kinloch, R.J. Young, *Prog. Mater. Sci.* **90**, 75 (2017)
96. M.A. Rafiee, I. Srivastava, Z. Wang, H. Song, Z.Z. Yu, N. Koratkar, *Small* **6**, 179 (2010)
97. X. Yan, J. Chen, J. Yang, Q. Xue, P. Miele, A.C.S. *Appl. Mater. Interfaces.* **2**, 2521 (2010)
98. J. Yan, T. Wei, Z. Fan, W. Qian, M. Zhang, X. Shen, F. Wei, *J. Power Sources* **195**, 3041 (2010)
99. L. Ma, G. Wang, J. Dai. *High performance polymers* **29**, 02 (2016)
100. D.R. Dreyer, K.A. Jarvis, P.J. Ferreira, C.W. Bielawski, *Polym. Chem.* **3**, 757 (2012)
101. D.R. Dreyer, K.A. Jarvis, P.J. Ferreira, C.W. Bielawski, *Macromolecules* **44**, 7659–7667 (2011)
102. M. Fang, K. Wang, H. Lu, Y. Yang, S. Nutt, *J. Mater. Chem.* **20**, 1982 (2010)
103. R.K. Layek, S. Samanta, D.P. Chatterjee, A.K. Nandi, *Polymer* **51**, 5846 (2010)
104. H. Yang, F. Li, C. Shan, D. Han, Q. Zhang, L. Niu, A. Ivaska, *J. Mater. Chem.* **19**, 4632 (2009)
105. Z. Xu, C. Gao, *Macromolecules* **43**, 6716 (2010)
106. C. Zheng, M. Feng, X. Zhen, J. Huang, H. Zhan, *J. Non-Cryst. Solids.* **354**, 1327 (2008)
107. Z. Hongbing, C. Wenzhe, W. Minquan, Zhengchan, Z. Chunlin., *J. Chem. Phys. Lett.* **382**, 313 (2003).
108. J. Cho, F. Inam, M.J. Reece, Z. Chlup, I. Dlouhy, M.S. Shaffer, A.R. Boccaccini, *J. Material Science.* **46**, 4770 (2011)
109. J.A. Lewis, *J. Am. Ceram. Soc.* **83**, 2341 (2000)
110. F. Inam, H. Yan, M.J. Reece, T. Peijs, *Nanotechnology* **19**, 195710 (2008)
111. Y. Yang, Y. Wang, W. Tian, Z.-q. Wang, , Y. Zhao, L.Wang, H-m. Bian, *Mater. Sci. Eng. A.* **508**, 161 (2009).
112. P. Kun, O. Tapasztó, F. Weber, C. Balázs, *Ceram. Int.* **38**, 211 (2012)
113. C. Wiles, P. Watts, in *Green Processes, Volume 7: Green Synthesis*, ed. by C.-J. Li. in *Handbook of Green Chemistry* (John Wiley & Sons, 2014), pp.159–210
114. C. Qi, Y.-J. Zhu, X.-Y. Zhao, B.-Q. Lu, Q.-L. Tang, J. Zhao, F. Chen, *Chemistry-A. European Journal.* **19**, 981 (2013)

115. C. Qi, Y.-J. Zhu, B.-Q. Lu, X.-Y. Zhao, J. Zhao, F. Chen, J. Wu, *Chemistry-A. European Journal* **19**, 5332 (2013)
116. S.L. Suib, in *Microwave Heating as a Tool for Sustainable Chemistry*, ed. by N.E. Leadbeater (CRC Press, 2010), p. 207
117. C. Yansheng, Z. Zhida, L. Changping, L. Qingshan, Y. Peifang, U. Welz-Biermann, *Green Chem.* **13**, 666 (2011)
118. C. Tan, X. Huang, H. Zhang, *Mater. Today* **16**, 29 (2013)
119. H.M.A. Hassan, V. Abdelsayed, S.K. Abd El Rahman, K.M. AbouZeid, J. Turner, M.S. El-Shall, S.I. Al-Resayes, A.A. El-Azhary, *J. Mater. Chem.* **19**, 3832 (2009)
120. H. Zhang, X. Xu, P. Gu, C. Li, P. Wu, C. Cai, *Electrochim. Acta* **56**, 7064 (2011)
121. A.R. Siamaki, A.E.R.S. Khder, V. Abdelsayed, M.S. El-Shall, B.F.J. Gupton, *J. Catal.* **279**, 1 (2011)
122. L. Xue, Z. Lin, *J. Chem. Soc. Rev.* **39**, 1692 (2010)
123. V.K. Ponnusamy, V. Mani, S.-M. Chen, W.-T. Huang, J.-F. Jen, *Talanta* **120**, 148 (2014)
124. S. Lee, C.-M. Yoon, J.-Y. Hong, J. Jang, *J. Mater. Chem. C* **30**, 6010 (2014)
125. L. Huo, F.-H. Liao, J.-R. Li, *Compos. Sci. Technol.* **71**, 1639 (2011)
126. J. Yin, Y. Shui, Y. Dong, X. Zhao, *Nanotechnology* **25**, 045702 (2014)
127. S. Goswami, T. Brehm, S. Filonovich, M. Teresa Cidade, *Smart Materials and Structures* **23**(10), 105012 (2012).
128. L. Li, G. Wu, G. Yang, J. Peng, J. Zhao, J.-J. Zhu, *Nanoscale* **5**, 4015 (2013).
129. C. Cheng, S. Li, A. Thomas, N.A. Kotov, R. Haag, *Chem. Rev.* **117**(3), 1826 (2017)
130. J.P. Melo, P.L. Ríos, P. Povea, C. Morales-Verdejo, M.B. Camarada, *ACS Omega* **3**(7), 7278 (2018)
131. P. Tian, L. Tang, K.S. Teng, S.P. Lau, *Materials Today Chemistry* **10**, 221 (2018)
132. Q. Lu, C. Wu, D. Liu, H. Wang, W. Su, H. Li, Y. Zhang, S. Yao, *Green Chem.* **19**(4), 900 (2017).
133. W. Wang, Z. Wang, J. Liu, Y. Peng, X. Yu, W. Wang, Z. Zhang, L. Sun, *Ind. Eng. Chem. Res.* **57**(28), 9144 (2018)
134. W. Bauhofer, J.Z. Kovacs, *Compos. Sci. Technol.* **69**, 1486 (2009)
135. C. Wu, X. Huang, G. Wang, L. Lv, G. Chen, G. Li, P. Jiang, *Adv. Func. Mater.* **23**, 506513 (2013)
136. Z. Chen, C. Xu, C. Ma, W. Ren, H.M. Cheng, *Adv. Mater.* **25**, 1296 (2013)
137. X. Wang, L. Zhi, K. Mulle, *Nano Letter.* **8**, 323 (2008)
138. G.A. Slack, *Phys. Rev.* **127**, 694 (1962)
139. W. Chen,; L. Yan, *Nanoscale* **3**(8), 3132 (2011).
140. X. Zhang, Z. Sui, B. Xu, S. Yue, Y. Luo, W. Zhan, B. Liu, *J. Mater. Chem.* **21**(18), 6494 (2011)
141. Y. Xu, K. Sheng, C. Li, G. Shi, *ACS Nano* **4**(7), 4324 (2010)
142. S.T. Nguyen, H.T. Nguyen, A. Rinaldi, N.P.V. Nguyen, Z. Fan, H.M. Duong, *Colloids Surf A* **414**, 352 (2012)
143. M.A. Worsley, P.J. Pauzauskie, S.O. Kucheyev, J.M. Zaugg, A.V. Hamza, J.H. Satcher, T.F. Baumann, *Acta Mater* **57**(17), 5131 (2009)
144. M.A. Worsley, T.Y. Olson, J.R.I. Lee, T.M. Willey, M.H. Nielsen, S.K. Roberts, P.J. Pauzauskie, J. Biener, J.H. Satcher, T.F. Baumann, *J. Phys. Chem. Lett.* **2**(8), 921 (2011)
145. S. Longo, M. Mauro, C. Daniel, P. Musto, G. Guerra, *Carbon* **77**, 896 (2014)
146. M.A. Worsley, P.J. Pauzauskie, T.Y. Olson, J. Biener, J.H. Satcher Jr., and T. F. Baumann *J. Am. Chem. Soc.* **132**(40), 14067 (2010)
147. Y-F. Bai, Y.-F. Zhang, A.-W. Zhou, H.-W. Li, Y. Zhang, J. H. Luong, H.-F. Cui, *Nanotechnology* **25** (40), 405601 (2014).
148. W. Zhu, Z. Zhang, W. Chai, Q. Zhang, D. Chen, Z. Lin, J. Chang, J. Zhang, C. Zhang, Y. Hao, *Chem. Sus. Chem.* **12**(10), 2318 (2019)
149. D.R. Dreyer, S. Park, C.W. Bielawski, R.S. Ruoff, *J. Chem. Soc. Rev.* **39**, 228 (2010)
150. S-Y. Huang, G-P, Wu, C-M., Chen, Y. Yang, S-C. Zhang, C-X., Lu. *Carbon* **52**, 613 (2013).

151. X. Zhang, X. Fan, C. Yan, H. Li, Y. Zhu, X. Li, L. Yu, A.C.S. Appl. Mater. Interfaces **4**, 1543 (2012)
152. X. Yang, Z. Wang, M. Xu, R. Zhao, X. Liu, Mater. Des. **44**, 74 (2013)
153. Q. Bao, H. Zhang, J.-X. Yang, S. Wang, D.Y. Tang, R., Jose, S. Ramakrishna, C.T. Lim, K.P. Loh, *Advanced Functional Materials* **20**, 782 (2010).
154. M. K. Shin, B. Lee, S.H. Kim, J.A. Lee, G.M. Spinks, S., Gambhir, G.G. Wallace, M.E. Kozlov, R.H. Baughman, S.J. Kim, *Nat. Commun.* **3**, 650 (2012).
155. H. Matsumoto, S. Imaizumi, Y. Konosu, M. Ashizawa, M. Minagawa, A. Tanioka, W., Lu, J.M. Tour, *ACS Appl. Mater. Interfaces* **5**, 6225 (2013).
156. Y. Guo, C. Bao, L. Song, B. Yuan, Y. Hu, *Ind. Eng. Chem. Res.* **50**, 7772 (2011)
157. A.L. Higginbotham, J.R. Lomeda, A.B., Morgan, J.M., Tour, *ACS Appl. Mater. Interfaces* **1**, 2256 (2009).
158. S. Liu, H. Yan, Z. Fang, H. Wang, *Compos. Sci. Technol.* **90**, 40 (2014)
159. R. Verdejo, F. Barroso-Bujans, M. A, Rodriguez-Perez, J. A. de Sajab, M.A. Lopez-Manchado. Functionalized graphene sheet filled silicone foam nanocomposites. *J. Mater. Chem.* **18**, 2221, (2008).
160. V. Eswaraiyah, V. Sankaranarayanan, S. Ramaprabhu, *Macromol. Mater. Eng.* **296**, 894 (2011)
161. R.M. Hodlur, M.K. Rabinal, *Compos. Sci. Technol.* **90**, 160 (2014)
162. B. Shen, W. Zhai, D. Lu, W. Zheng, Q. Yan, *Polym. Int.* **61**, 1693 (2012)
163. O.C. Compton, S. Kim, C. Pierre, J.M. Torkelson, S.T. Nguyen, *Adv. Mater.* **22**, 4759 (2010)
164. S.S. Kandannur, M.A. Rafiee, F. Yavari, M. Schrammeyer, Z.-Z. Yu, T.A. Blanchet, N. Koratkar, *Carbon* **50**, 3178 (2012)
165. W. Cai, Y. Huang, D. Wang, C. Liu, Y. Zhang, *Journal of Applied Polymer Science.* **131**(3), (2014). <https://doi.org/10.1002/app.39778>
166. L.M. Chiacchiarelli, L.M. Rallini, M. Monti, M. Puglia, D. Kenny, J.M. Torre, *Compos. Sci. Technol.* **80**, 73 (2013)
167. X. Du, I. Skachko, A. Barker, E.Y. Andrei, *Nat. Nanotechnol.* **3**, 491 (2008)
168. V. Gonçalves, L. Brandão, A. Mendes, *Polym. Testing* **37**, 129 (2014)
169. C. Hou, T. Huang, H. Wang, H. Yu, Q. Zhang, Y. Li, *Sci. Rep.* **3**, 3138 (2013)
170. J. Kuang, L. Liu, Y. Gao, D. Zhou, Z. Chen, B. Han, Z. Zhang, *Nanoscale* **5**, 12171 (2013)
171. K.K. Sadasivuni, D. Ponnamma, S. Thomas, Y. Grohens, Evolution from graphite to graphene elastomer composites. *Prog. Polym. Sci.* **39**, 749 (2014)
172. F.R. Al-Solamy, A.A. Al-Ghamdi, W.E. Mahmoud, *Polymers Advanced Technologies.* **23**, 478 (2012)
173. J.S. Kim, J.H. Yun, I. Kim, S.E. Shim, *J. Ind. Eng. Chem.* **17**, 325 (2011)
174. T. Yamada, Y. Hayamizu, Y. Yamamoto, Y. Yomogida, A. Izadi-Najafabadi, D.N. Futaba, K. Hata, *Nat. Nanotechnol.* **6**, 296 (2011)
175. Z. Chen, W. Ren, L. Gao, B. Liu, S. Pei, H.-M. Cheng, *Nature Mater.* **10**, 424 (2011)
176. C. Wang, X. Han, P. Xu, X. Zhang, Y. Du, S. Hu, J. Wang, X. Wang, *Appl. Phys. Lett.* **98**, 072906 (2011)
177. K. Dai, Y.-C. Zhang, J.-H. Tang, X. Ji, Z.-M. Li, *J. Appl. Polym. Sci.* **125**, E561 (2012)
178. C.A, Hewitt, A.B. Kaiser, M. Craps, R. Czerw, S. Roth, D.L. Carroll, *Synthetic Metals* **165**, 56 (2013).
179. A. Rybak, G. Boiteux, F. Melis, G. Seytre, *Compos. Sci. Technol.* **70**, 410 (2010)
180. W.E. Mahmoud, A.A. Al-Ghamdi, *Polym. Int.* **61**, 51 (2012)
181. H.K. Cheng, N.G. Sahoo, Y.P. Tan, Y. Pan, H. Bao, L. Li, S.H. Chan, J. Zhao, A.C.S. Appl. Mater. Interfaces. **4**, 2387 (2012)
182. J. Syurik, O.A. Ageev, D.I. Cherednichenko, B.G. Konoplev, A. Alexeev, *Carbon* **63**, 317 (2013)
183. S. Ansari, C. Rahima, M.N. Muralidharan, *Polym.-Plast. Technol. Eng.* **52**, 1604 (2013)
184. J. Liang, Y. Xu, Y. Huang, L. Zhang, Y. Wang, Y. Ma, F. Li, T. Guo, Y. Chen, *The Journal of Physical Chemistry C.* **113**, 9921 (2009)
185. Y. Huang, J. Liang, Y. Chen, *J. Mater. Chem.* **22**, 3671 (2012)

186. M.S. Ramasamy, S.S. Mahapatra, H.J. Yoo, Y.A. Kim, J.W. Cho, *Journal of Materials Chemistry A* **2**, 4788 (2014)
187. J. Liang, L. Huang, N. Li, Y. Huang, Y. Wu, S. Fang, J. Oh, M. Kozlov, Y. Ma, F. Li, R. Baughman, Y. Chen, *ACS Nano* **6**(5), 4508 (2012)
188. J. Kim, J.-H. Jeon, H.-J. Kim, H. Lim, I.K. Oh, *ACS Nano* **8**, 2986 (2014)
189. Y. Lian, Y. Liu, T. Jiang, J. Shu, H. Lian, M. Cao, *J. Phys. Chem. C* **114**, 9659 (2010)
190. Z. Li, Y. Wang, A. Kozbial, G. Shenoy, F. Zhou, R. McGinley, P. Ireland, B. Morganstein, A. Kunkel, S.P. Surwade, *Nat Mater.* **12**, 925 (2013)
191. G.Z. Kyzas, E.A. Deliyanni, K.A. Matis, *J. Chem. Technol. Biotechnol.* **89**(2), 196 (2014)
192. Y. Guo, X. Sun, Y. Liu, W. Wang, H. Qiu, J. Gao, *Carbon* **50**, 2513 (2012)
193. H.M. Sung-Suh, J.R. Choi, H.J. Hah, S.M. Koo, Y.C. Bae, *J. Photochem. Photobiol., A* **163**, 37 (2004)
194. J. Paredes, S. Villar-Rodil, M. Fernández-Merino, L. Guardia, A. Martínez-Alonso, J. Tascón, *J. Mater. Chem.* **21**, 298 (2011)
195. L. Guardia, S. Villar-Rodil, J. Paredes, R. Rozada, A. Martínez-Alonso, J. Tascón, *Carbon* **50**, 1014 (2012)
196. O.G. Apul, Q. Wang, Y. Zhou, T. Karanfil, *Water Res.* **47**, 1648 (2013)
197. Z. Liu, J.T. Robinson, X. Sun, H. Dai, H. Dai, *J. Am. Chem. Soc.* **130**, 10876 (2008)
198. K. Yang, J. Wan, S. Zhang, Y. Zhang, S.-T. Lee, Z. Liu, *ACS Nano* **5**, 516 (2010)
199. Y. Yang, Y.-M. Zhang, Y. Chen, D. Zhao, J.-T. Chen, Y. Liu, *Chem. Eur. J.* **18**, 4208 (2012)
200. X. Pei, Z. Zhu, Z. Gan, J. Chen, X. Zhang, X. Cheng, Q. Wan, J. Wang, *Sci Rep.* **10**, 2020 (2017)
201. K. Yang, S. Zhang, G. Zhang, X. Sun, S.-T. Lee, Z. Liu, *Nano Lett.* **10**, 3318 (2010)
202. Z. Liu, J.T. Robinson, X. Sun, H. Dai, *J. Am. Chem. Soc.* **130**(33), 10876 (2008)
203. X. Sun, Z. Liu, K. Welsher, J.T. Robinson, A. Goodwin, S. Zaric, H. Dai, *Nano Res.* **1**(3), 203 (2008)
204. Y. Pan, H. Bao, N.G. Sahoo, T. Wu, L. Li, *Adv. Func. Mater.* **21**(14), 2754 (2011)
205. N.G. Sahoo, H. Bao, Y. Pan, M. Pal, M. Kakran, H.K.F. Cheng, L. Li, L.P. Tan, *Chem. Commun.* **47**(18), 5235 (2011)
206. Y. Pan, H. Bao, N.G. Sahoo, T. Wu, L. Li, *Advan. Funct. Mater.* **21**(14), 2754 (2011)
207. A. Yu, P. Ramesh, X. Sun, E. Bekyarova, M.E. Itkis, R.C. Haddon, *Adv. Mater.* **20**, 4740 (2008)
208. S. Ganguli, A.K. Roy, D.P. Anderson, *Carbon* **46**, 806 (2008)
209. H. Li, J. Chen, S. Han, W. Niu, X. Liu, G. Xu, *Talanta* **79**, 165 (2009)
210. S. Liu, D. Zhou, J. Yang, H. Zhou, J. Chen, T. Guo, *J. Am. Chem. Soc.* **139**(14), 5102 (2017)
211. S.-S. Li, K.-H. Tu, C.-C. Lin, C.-W. Chen, M. Chhowalla, *ACS Nano* **4**, 3169 (2010)
212. L. Valentini, M. Cardinali, S.B. Bon, D. Bagnis, R. Verdejo, M.A. Lopez Manchado, J.M. Kenny, *J. Mater. Chem.* **20**, 995 (2010).
213. T.G. Park, J.H. Jeong, S.W. Kim, *Adv. Drug. Deliv. Rev.* **58**(4), 467 (2006)
214. T.-H. Kim, H.-L. Jiang, D. Jere, I.-K. Park, M.-H. Cho, J.-W. Nah, Y.-J. Choi, T. Akaike, C.-S. Cho, *Progr. Polym. Sci.* **32**, 726 (2007)
215. L. Feng, S. Zhang, Z. Liu, *Nanoscale* **3**(3), 1252 (2011)
216. H. Bao, Y. Pan, Y. Ping, N.G. Sahoo, T. Wu, L. Li, J. Li, L.H. Gan, *Small* **7**(11), 1569 (2011)
217. B. Chen, M. Liu, L. Zhang, J. Huang, J. Yao, Z. Zhang, *J. Mater. Chem.* **21**, 7736 (2011)
218. L. Zhang, J. Xia, Q. Zhao, L. Liu, Z. Zhang, *Small* **6**(4), 537 (2010)
219. Y.H. Kim, J.H. Park, M. Lee, Y.-H. Kim, T.G. Park, S.W. Kim, *J. Control. Release.* **103**(1), 209 (2005)
220. M.Y. Lan, Y.B. Hsu, M.C. Lan, J.P. Chen, Y.J. Lu, *Int. J. Nanomedicine* **15**, 7569 (2020).
221. C.C. Liu, J.J. Zhao, R. Zhang, H. Li, B. Chen, L.L. Zhang, H. Yang, *Am. J. Transl. Res.* **9**(12), 5197 (2017)
222. Z.M. Markovic, L.M. Harhaji-Trajkovic, B.M. Todorovic-Markovic, D.P. Kepić, K.M. Arsin, S.P. Jovanović, A.C. Pantovic, M.D. Dramićanin, V.S. Trajkovic, *Biomaterials* **32**(4), 1121 (2011)

223. L. Zhang, Z. Lu, Q. Zhao, J. Huang, H. Shen, Z. Zhang, *Small* **7**(4), 460 (2011)
224. H. Kim, R. Namgung, K. Singha, I.-K. Oh, W.J. Kim, *Bioconjug. Chem.* **22**(12), 2558 (2011)
225. B. Tian, C. Wang, S. Zhang, L. Feng, Z. Liu, *ACS Nano* **5**(9), 7000 (2011)
226. A.-J. Shen, D.-L. Li, X.-J. Cai, C.-Y. Dong, H.-Q. Dong, H.-Y. Wen, G.-H. Dai, P.-J. Wang, Y.-Y. Li, *J. Biomed. Mater. Res.* **100A**, 2499 (2012)

Sustainable Grinding Performances of Nano SiC Reinforced Al Matrix Composites Under Minimum Quantity Lubrication (MQL)



A. Nandakumar, T. Rajmohan, and S. Vijayabhaskar

Abstract Nanoparticles filled lubricants demonstrate reduced wear and coefficient of friction due to their improved physical, thermal, and heat transfer capabilities. The process of grinding plays a crucial role in attaining enhanced precision in dimensions and superior surface finish. Thus, it becomes essential in increasing the surface finish and the grinding rate for economic production. In this chapter, the effect of nano titanium dioxide (TiO_2) filled Cashew nutshell Oil on the sustainable grinding process of Aluminium matrix composites reinforced with nano silicon carbide (SiC) is being investigated under the lubrication of Cashew nutshell Oil and SAE20W40 oil. All the experiments were performed using a cylindrical grinding machine with a horizontal spindle, employing Response Surface Methodology (RSM). To enhance the surface quality during the grinding of composites with Minimum Quantity Lubrication (MQL), the main process variables considered were wt.% of nano SiC, work-piece speed, wheel speed, and depth of cut. The grinding performance is improved by adding Nano TiO_2 into Cashew nutshell Oil, which enhances the lubrication and cooling effect by allowing the nanoparticles to diffuse more effectively and trapped within the contact zone.

Keywords Grinding · Minimum Quantity Lubrication (MQL) · Nano TiO_2 · NanoSiC particles · Cutting force · Surface roughness

A. Nandakumar · T. Rajmohan (✉) · S. Vijayabhaskar
Department of Mechanical Engineering, Sri Chandrasekharendra Saraswathi Viswa Maha
Vidyalaya, Enathur, Kanchipuram 631561, India
e-mail: rajmohanscsmv@yahoo.com

A. Nandakumar
e-mail: nandakumar.a@kanchiuniv.ac.in

1 Introduction

The application of Metal Matrix Nano Composites (MMNCs) is experiencing a growing trend in the automotive and aeronautical sectors [1]. MMNCs are distinguished by their exceptional physical and mechanical properties across a broad temperature spectrum. In addition to aircraft technologies, Metal Matrix Composites (MMC) are presently employed in the fuselage manufacturing and jet engines, while their utilization in the automotive industry is experiencing rapid growth. Moreover, their mechanical, electrical, and thermal properties have led to a significant increase in their electronics industrial applications [2]. The continuous fiber-reinforced MMCs were incapable of attaining their entire potential as engineered materials for aeronautical applications, which can be possibly accomplished by discontinuously reinforced metals, due to their diverse functional properties as well as high structural efficiency and isotropic characteristics [3]. The Nano SiC reinforced magnesium exhibits an insignificant increment in the wear rate in comparison with plain alloys. Additionally, the coefficient of friction decreases as the average load and volume fraction of reinforcement increases [4]. When the weight percentage of Al_2O_3 nanoparticles was increased in the A356 composite, it resulted in improved hardness and compressive strength of the aluminium alloy nanocomposites. However, the porosity of the nanocomposites also increased [5]. Achieving defect-free components with the improved surface finish and required dimensions is crucial when machining aluminium hybrid metal matrix composites in a cost-effective manner successfully. A vital part is being performed by the grinding process in attaining high-quality surface finishes and long-lasting machining results. Utilizing a single grinding operation can prove to be an economic alternative as it eliminates the need for preceding conventional machining procedures [6].

Even though several ceramic reinforcements are chosen for Metal Matrix Composites, SiC has gained considerable attention because of its exceptional characteristics such as dimensional stability, wear resistance, robustness, high specific strength, and high rigidity [7]. The optimized parameters of the ultrasonic processing based on numerical simulation significantly improved the microstructure and mechanical characteristics of AZ91D magnesium composites with SiC nanoparticles reinforcement [8]. The incorporation of SiC nanoparticles resulted in enhanced mechanical characteristics such as increased yield strength and tensile strength, while maintaining the ductility of the nanocomposite [9, 10]. Industries face substantial challenges while machining composites reinforced with SiC, primarily due to the abrasive nature of the reinforcements and the presence of non-homogeneous and anisotropic structures. The major problem encountered during the machining of MMC is the tool's premature wear caused by the collapse of precipitates [11]. In comparison with the alumina wheel, the silicon carbide wheel provided a superior surface finish. The hardness of the composites has a significant impact on the surface roughness of the machined surface [12]. In terms of improved surface finish, low grinding forces, and low binding, open structure grinding wheels and conventional abrasives have provided superior performance in comparison with super-abrasives among the various types

of grinding wheels [13]. Developing quantitative analytical models is crucial in progressing sustainable product design and manufacturing. These models enable a deeper understanding of the integral sustainability components within the machining process, thereby emphasizing their essential role in developing ecofriendly products [14].

MQL grinding, employing vegetable oil, demonstrated superior performance over flood grinding in terms of a reduced grinding wheel wear, coefficient of friction, and specific grinding energy [15]. When compared to dry grinding and fluid cooling methods, MQL grinding significantly decreases tangential forces by utilizing a lubricant that surrounds the grinding wheel. This lubrication facilitates improved grain slippage at the interface amidst the workpiece and the tool [16]. The MQL-based machining process operates at an accelerated pace, utilizing a minimal quantity of cutting fluid ranging from 10 to 150 ml/h. This fluid is circulated in the machining region through vapor technique [17]. Achieving sustainable manufacturing in green machining involves a series of steps aimed at implementing economic and ecofriendly green machining methods. These steps are essential for formulating technologies that are both consistent with sustainability principles and economically viable [18]. The machining process employing cutting fluids is one of the primary environmental concerns. It is estimated that cutting fluids account for over 15% of machining costs [19]. The main purpose served by cutting fluid should increase the machining performances along with some of the ample requirements like non-fire hazard, non-toxic, non-smoke, unarmful to operators' health, and easy disposal [20]. The biodegradable cutting fluids like soybean oil, coconut oil, sesame oil, sunflower oil, canola oil, castor oil, etc., that are eco-friendly can opt over mineral-based cutting fluids [21].

The nano-cutting fluid is considered to be an original conception, in which Nano-sized particles are suspended in cutting fluid, to meet up the lubricating challenge during machining. Numerous investigations proved that the nanofluids exhibit a notably greater convective coefficient of heat transfer [22]. The incorporation of carbon nanotubes into nanofluid during the grinding, resulted in enhanced surface properties, including reduction in the formation of micro cracks and surface roughness [23]. Grinding is considered as one of the best recognizable machining methods which develops high specific energy genuine [24]. The conventional cutting fluids are being substituted with nano filled lubricants in grinding to conquer biological and cost-effectiveness issues [25].

Grinding forces and surface roughness are reduced as the grinding speed increases. In the case of Al/SiC composites, employing a high grinding speed with an Al₂O₃ grinding wheel at specific parameters (feed rate of 200 mm/min and depth of cut below 50 μm) allows for achieving superior surface integrity [26]. With a diamond wheel of 3000 grit, grinding depths of 0.5 mμ and 1 mμ on Al₂O₃/SiC reinforced Al metal matrix composites, resulted in the formation of ductile streaks. Remarkably, minimal subsurface damage was observed during fine grinding with the diamond wheel, with only rare instances of cracked particles [27]. In the case of cylindrical grinding using Al₂O₃ grinding wheel on aluminium metal matrix composites, it was observed that increasing the depth of cut and feed led to higher surface roughness and increased occurrence of damaged surfaces [28]. In MQL-assisted grinding of

EN31 steel, a significant reduction in surface roughness was achieved, reaching as low as 43% [29]. The introduction of fluid can improve the process efficiency and product quality effectively [30].

The machining of Ti-6Al-4 V utilizing MQL assisted by ultrasonic vibration involves using coolant that employs vegetable oil. Ultrasonic MQL grinding demonstrates reduced grinding forces and enhanced surface quality in contrast to traditional MQL grinding methods [31]. The dry grinding of glass fiber reinforced plastic using a cubic boron nitride (CBN) wheel achieved a superior material removal rate alongside minimal surface roughness [32]. Under different machining conditions, the MQL method is applied in the grinding process of Inconel 718 alloy. The most important aspect for efficient grinding performance is the cooling atmosphere [33]. The Laser irradiation technique was used for revealing the grinding and thermal behaviors [34]. Employing TiO₂ nano-cutting fluid even at lesser quantity of nanoparticles resulted in a significant decrease in grinding forces, while a higher concentration of nanoparticles was observed to enhance surface finish [35]. Improved grinding wheel life and a perceptible decrease in grinding force were accomplished by the inclusion of MoS₂ nanoparticles to the vegetable oil-based lubricant. The grinding temperature significantly decreases with MQL when compared to that of dry grinding [36]. MQL grinding of ductile iron SAE D-7003 and steel SAE 4340 resulted in a smoother surface compared to fluid grinding and notably superior to dry grinding [37].

Fiber-reinforced SiC matrix composites that were grinded using MQL with the outsized nanoplatelets were more efficient than the smaller nanoplatelets in tumbling the surface roughness, specific energy, and grinding forces [38]. The use of graphene nanoplatelets-based lubricants led to maximum reduction of energy consumption and the least coefficient of friction along with the growth in grinding wheel's consumption (G-ratio of grinding wheel) on Inconel 718 [39]. As the concentration of nanoparticles increases, the process efficiency improves. The nanolubricants based on paraffin and soybean performed best for cast iron and steel [40].

The incorporation of paraffin oil and diamond nanoparticles into a nano-fluid resulted in substantial reductions of surface roughness and grinding forces in contrast to pure MQL and dry grinding [41]. By employing ultrasonic processing, a composite material was successfully produced by incorporating Al₂O₃ and SiC nanoparticles into an A356 matrix. This fabrication technique yielded significant enhancements in mechanical characteristics, including ductility, yield strength, and tensile strength [42]. The maximum reinforcement for mechanical properties in metal matrix nanocomposites is achieved by the inclusion of straight carbon nanotubes (CNTs) into the matrix, whereas, the elastic modulus is greatly impacted by the non-straight shape and dispersion of CNTs [43, 44].

The increased surface area of the alumina nanoparticles in the A356 aluminum alloy composite resulted in an increased porosity level. The fracture surface of the composite revealed more dimples of different sizes which confirm high ductility of the nanocomposite [45]. When exposed to a NaCl solution, the corrosion resistance of MMNCs is inversely proportional to the size of Al₂O₃ and SiC nano-particles. Furthermore, a rise in the volume fraction of nano-particles above 3 vol. % leads to an

escalation in the corrosion rate of the MMNCs [46]. The inclusion of SiC nanoparticles to the nanocomposites leads to a reduction in the coefficient of thermal expansion, thereby ensuring high dimensional stability. The addition of nano SiC particles to the nanocomposites results in a reduction in the coefficient of thermal expansion, thereby ensuring high dimensional stability [47]. In aluminium matrix composites, the addition of Al_2O_3 nanoparticles exceeding 4 vol.% resulted in a decrease in the particle strengthening effect which can be associated with the decreased number of effective nanoparticles produced by agglomeration [48]. For the grinding of Ni-based alloy, the combined CNT/MoS₂ hybrid nanoparticles exhibit superior lubrication compared to individual nanoparticles. While the diameter of the nanoparticles has a slight impact on reducing the tangential grinding force similar to that of the peak grinding temperature [49].

When compared with pure water MQL grinding, the utilization of water-based Al_2O_3 nano-fluid in MQL grinding demonstrates notable advantages including a significant decrease in surface roughness, improved surface morphology of the ground material, reduced grinding forces, and temperature [50]. Numerous researchers have validated the noticeable improvement achieved in performance through MQL machining, yielding significant outcomes in comparison to dry machining. The cutting force and cutting temperature reductions occur at nozzle distance ranging from 6–9 mm and an input air pressure of 0.4 MPa [51]. The enhanced lubrication and cooling effects of MQL system improve 20–25% of the tool life on machining of MMC [52]. The MQL flow rate, cutting speed, and feed rate are most prominently influenced factors to reveal the cutting force [53].

The application of MQL grinding results in a substantial decrease in both the specific energy and frictional coefficient, applicable to both soft and hardened steel. This improvement can be attributed to the grit sharpness retention and effective lubrication within the contact region [20]. The wear mechanisms of the coated cemented carbide tool under MQL condition are analyzed and it is found that the abrasion and adhesion are the most leading tool wears under various cutting parameters [54]. During the milling process of hardened AISI 4140 steel using the MQL system, various factors such as tool life, tool wear, surface quality, etc., are significantly benefited and effectively decreased the chip-tool interface temperature [55]. In MQL cooling system is to be very efficient to reduce the fine particles emission and remove fine dust in the working condition [56]. In MQL conditions, the decrease in temperature at cutting zone results in improvement of tool life and yields superior results in comparison with dry machining [57].

The utilization of experimental design allows for the identification of the individual impacts of factors and their complex interrelationships [58]. The optimal response is obtained by the use of RSM [59]. An RSM based D-optimal design with four factors was employed to investigate the performances of drilling on hybrid metal matrix composites. D-optimal design based on RSM was utilized in predicting the oil-film pressure in journal bearing, employing several bio-lubricants based on nanomaterials for lubrication purposes. The accuracy of D-optimal standardization method is found to be superior to the conventional standardization method

in finding the error [60]. By employing the D-optimal design of experiment technique, statistical analyses were conducted, and a mathematical model was derived to determine spring-back within the experimental variable domain [61]. An analysis of variance (ANOVA) was carried out to assess the impacts of machining factors on constraints and validate the suitability of the developed mathematical model [62]. The geometric properties of a workpiece are controlled and calculated by DOE and RSM methods while reducing the experimental work [63].

A careful examination of the existing literature reveals a limited amount of research conducted on the sustainability of grinding in MMC i.e., manufacturing processes focused on energy efficiency. As a result, this chapter addresses this research gap by exploring different environmentally conscious machining techniques, specifically MQL with vegetable-based cutting fluids and cutting fluids filled with nanoparticles. Furthermore, the chapter evaluates the performance of environment friendly machining in terms of surface finish and cutting force. A cylindrical grinding machine with horizontal spindle is used to conduct the experiments. The process parameters like weight percentage of nano SiC, wheel speed, depth of cut, and workpiece speed were taken into consideration. The cutting forces and surface roughness were predicted by developing second-order mathematical models based on D-optimal design.

2 Materials and Methods

2.1 Materials

The Nanocomposites were fabricated using SiC nanoparticles obtained from M/S US Research Nanomaterials Inc, USA and aluminium billet procured from M/s Micro Fine chemicals, India. Vacuum-based solidification process was employed in the fabrication of SiC nanoparticles reinforced aluminium composites [11]. Nano TiO₂, cashew nut-based vegetable oil, and SAE20W40 acquired from M/s Ganapathy traders, India were used. The nanotubes exhibited a mean length of 10–30 μm and diameter ranging from 10–20 nm. The nanofluid is prepared by dispersing 10 g of nano TiO₂ in 500 ml cashew nut-based vegetable oil through Ultrasonic processing. The property measurements were conducted after allowing the prepared samples to rest 24 h. For determining the nanoparticle morphology and size, scanning electron microscopy (SEM) analysis was conducted using a Quanta FEG 200 instrument from Japan.

Figure 1 indicates that the nanoparticles exhibit a predominantly spherical morphology, confirming their conformity to the specified size range. Experimental tests were conducted to evaluate the properties of fluids mixed with nano TiO₂. The obtained results were then compared with those of cashew nutshell oil and SAE20W40, the comparative data are provided in Table 1.

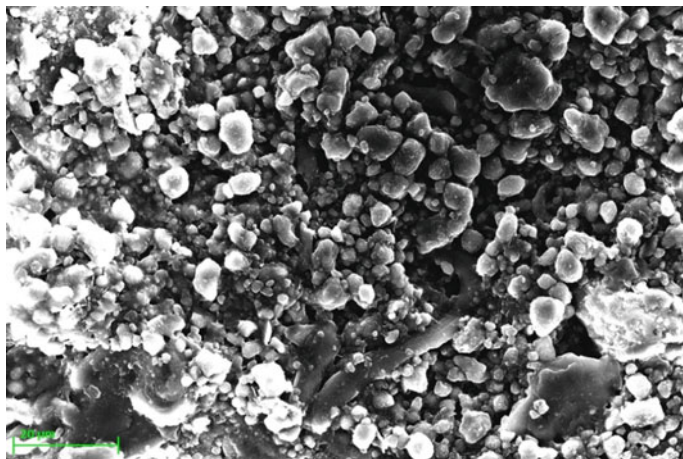


Fig. 1 SEM image of nano TiO₂

Table 1 Rheological properties of the lubricants

| Properties | SAE20W40 | Vegetable oil (Cashew nutshell oil) | Vegetable oil (Cashew nutshell oil + TiO ₂) |
|--|----------|--|---|
| Flashpoint (°C) [ASTM D92] | 200 | 214.27 | 190.2 |
| Thermal Conductivity Watt/mK | 0.152 | 0.161 | 0.169 |
| Viscosity @100 °C (cSt) [ASTM D445] | 15.2 | 15.48 | 16 |
| Viscosity index [ASTM D2270] | 120 | 126 | 158 |

The analysis of rheological properties revealed a significant enhancement in the performance of cashew nut-based vegetable oil filled with nano TiO₂. This improvement can be attributed to the nanofluid's improved heat dissipation capabilities [43].

Al matrix composites reinforced with nano SiC of dimensions 300 mm length and 20 mm diameter were fabricated using the gravity die casting method. Figure 2 presents the microstructure of the fabricated samples.

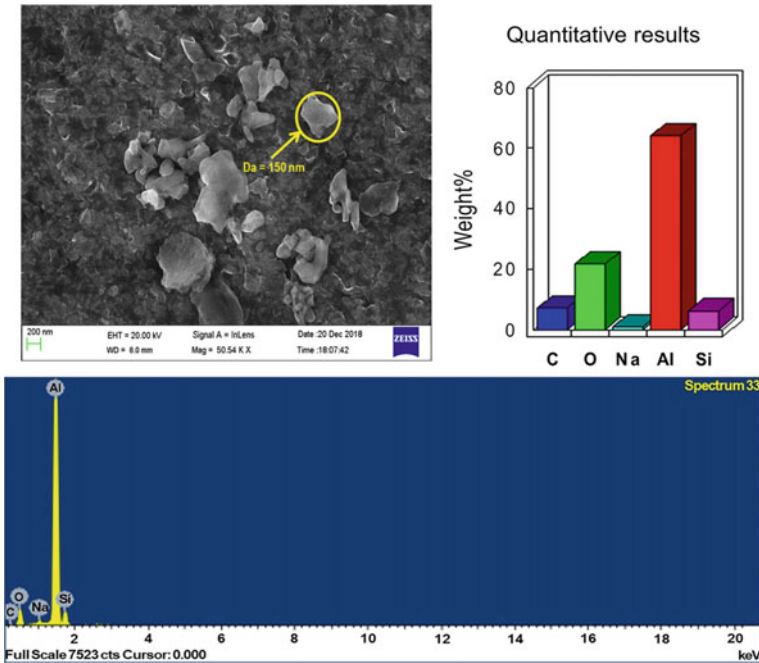


Fig. 2 SEM image and EDAX analysis of fabricated specimen

2.2 Experimental Design and Procedure

The surface roughness (SR) in grinding of composites based on MQL was examined using a D-optimal design based on RSM to model and analyze the experimental data. The scheme of the design is presented in Table 2.

After conducting pilot experiments and analyzing relevant literature, five parameters were selected and varied at three levels each [59]. A cylindrical grinding machine with horizontal spindle (HMT make, Model G13P) was employed to

Table 2 Grinding parameters and their levels

| Sl. No | Parameters | Notation | Unit | Levels | | |
|--------|--|----------|---------------|-----------|----------|-----------------------------|
| | | | | 1 | 2 | 3 |
| 1 | Wheel speed | n | rpm | 900 | 1200 | 1500 |
| 2 | Depth of cut | d | μm | 10 | 20 | 30 |
| 3 | Workpiece speed | v | rpm | 80 | 150 | 270 |
| 4 | wt. % nano SiC in the workpiece material | w | % | 1 | 2 | 3 |
| 5 | Type of MQL | – | – | SAE 20W40 | VEG. OIL | VEG. OIL + TiO ₂ |

perform the grindability study experiments. The cylindrical specimens of aluminium matrix composites reinforced with nanoparticles were subjected to grinding using the selected Al_2O_3 grinding wheel (AA60K5V8) in this investigation.

The wheel is dressed with a single point diamond dresser at the end of each experiment. Figure 3 illustrates the schematic arrangement of the experimental setup.

Instead of the standard lubricant setup, the MQL setup was employed, with the flow of MQL being regulated by an adjuster knob. The nozzle was placed about 35 mm from the boundary between the workpiece and the grinding wheel, and the lubricant was supplied at a flow rate of 40 ml/h. The surface finish of the machined surface was measured using a contact stylus instrument with 4 mm evaluation length, 0.8 mm cut-off length, and 2 mm tip radius. Measurements were taken at six distinct points normal to the cutting path, and the average of these readings was calculated as the recorded response.

The tangential grinding force (F_t) was determined by measuring the power of the grinding wheel motor using a Variable Frequency Drive (VFD) and applying the equation,

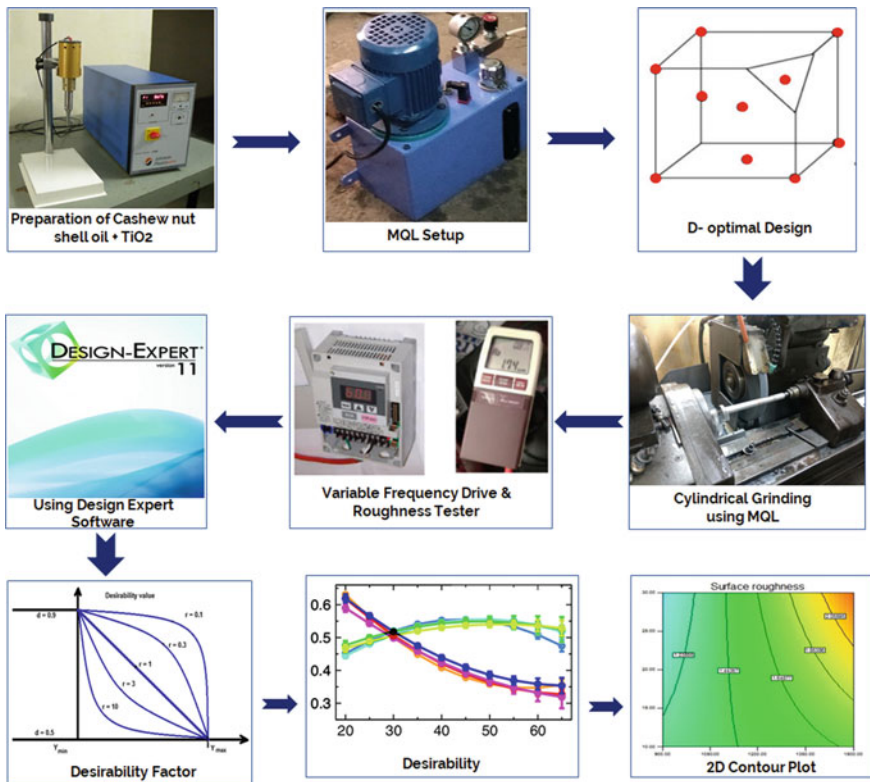


Fig. 3 Schematic arrangement of experimental setup

$$F_t = P.94535/V_s \quad (1)$$

where P is the power of the grinding wheel motor, and V_s is the wheel speed.

To enable speed variation, grinding wheel motor is connected with a Variable Frequency Drive (VFD). By altering the motor frequency, which remains at a constant speed, the wheel's speed can be adjusted. The power used for the operation is measured, and the tangential grinding force (F_t) is calculated by multiplying it with the wheel speed (V_s) and a predetermined constant. The power (P) can be calculated using the equation: $P = (F_t.V_s)/94535$. This power equation is applicable when using the unit of kilowatts for power and newtons for force. The experimental results are presented in Table 3.

3 Results and Discussions

3.1 Comparison of Tribological Performances of SAE20W40, Cashew Nutshell Oil, and Nano TiO₂ Filled Cashew Nutshell Oil

Figure 4 illustrates the use of a functional equipment called the four-ball tribometer TR-30L-IAS, which was utilized to perform the tribological study.

During the tribological study conducted using a four-ball tribometer, the test lubricant was heated to a temperature of 75 °C while applying a standard load of 148 N and maintaining a rotational speed of approximately 1200 rpm [59]. The image of the wear scar and corresponding diameter on the ball surface were measured using dedicated image capture software. The results from the tribological study are presented below.

The wear scar diameter observed in TiO₂-filled cashew nutshell oil is significantly smaller in comparison with cashew nutshell oil and SAE20W40. The wear scar image of cashew nutshell oil mixed with TiO₂ from Fig. 5 clearly demonstrates a clearer, more circular, and smoother appearance.

The coefficient of friction for three different lubricating oils, namely cashew nut-based vegetable oil, cashew nut-based vegetable oil mixed with TiO₂, and SAE20W40 are recorded as 0.0898, 0.0780, and 0.1015 respectively. The analysis reveals that cashew nut-based vegetable oil mixed with TiO₂ exhibits the lowest coefficient of friction in comparison with cashew nut-based vegetable oil and SAE20W40. The addition of nanoparticles to the cashew nut-based vegetable oil increases its viscosity, resulting in an increased oil film thickness that reduces the contact between the surfaces of the balls.

Table 3 Results of the experiments

| Sl. No | Material | Wheel speed (V_s) rpm | Depth of cut μm | Workpiece speed rpm | MQL | Surface roughness (RS) μm | Cutting force N |
|--------|-------------|---------------------------|----------------------------|---------------------|----------------------------|--------------------------------------|-----------------|
| 1 | 3% nano SiC | 1500 | 30 | 270 | VEG OIL + TiO ₂ | 1.64 | 37.45 |
| 2 | 1% nano SiC | 900 | 10 | 80 | VEG OIL + TiO ₂ | 1.16 | 52.96 |
| 3 | 1% nano SiC | 1500 | 30 | 270 | VEG OIL | 1.6 | 37.14 |
| 4 | 3% nano SiC | 1500 | 10 | 270 | VEG OIL | 2.41 | 37.03 |
| 5 | 3% nano SiC | 900 | 10 | 80 | SAE 20/40 | 1.41 | 53.38 |
| 6 | 1% nano SiC | 1500 | 10 | 270 | VEG OIL + TiO ₂ | 0.82 | 37.55 |
| 7 | 3% nano SiC | 1500 | 10 | 150 | SAE 20/40 | 1.11 | 37.13 |
| 8 | 3% nano SiC | 900 | 10 | 270 | VEG OIL + TiO ₂ | 0.83 | 52.75 |
| 9 | 1% nano SiC | 1500 | 30 | 80 | VEG OIL + TiO ₂ | 0.95 | 37.14 |
| 10 | 3% nano SiC | 900 | 20 | 270 | SAE 20/40 | 1.48 | 53.11 |
| 11 | 1% nano SiC | 900 | 30 | 270 | VEG OIL + TiO ₂ | 0.58 | 52.54 |
| 12 | 1% nano SiC | 900 | 30 | 150 | SAE 20/40 | 1.1 | 52.54 |
| 13 | 1% nano SiC | 1500 | 20 | 80 | SAE 20/40 | 2.48 | 37.24 |
| 14 | 1% nano SiC | 900 | 10 | 270 | VEG OIL | 2.54 | 52.54 |
| 15 | 3% nano SiC | 900 | 30 | 270 | VEG OIL | 0.87 | 52.75 |
| 16 | 1% nano SiC | 1500 | 10 | 80 | VEG OIL | 1.45 | 36.93 |
| 17 | 2% nano SiC | 1200 | 30 | 150 | SAE 20/40 | 1.74 | 54.38 |
| 18 | 3% nano SiC | 1200 | 20 | 150 | VEG OIL | 1.98 | 52.49 |

(continued)

Table 3 (continued)

| Sl. No | Material | Wheel speed (V_s) rpm | Depth of cut μm | Workpiece speed rpm | MQL | Surface roughness (RS) μm | Cutting force N |
|--------|-------------|---------------------------|----------------------------|---------------------|----------------------------|--------------------------------------|-----------------|
| 19 | 3% nano SiC | 1500 | 10 | 80 | VEG OIL + TiO ₂ | 0.84 | 24.83 |
| 20 | 3% nano SiC | 900 | 30 | 80 | VEG OIL + TiO ₂ | 1.02 | 52.96 |
| 21 | 1% nano SiC | 900 | 10 | 270 | SAE 20/40 | 0.89 | 52.75 |
| 22 | 2% nano SiC | 900 | 20 | 150 | VEG OIL + TiO ₂ | 0.9 | 52.75 |
| 23 | 1% nano SiC | 900 | 30 | 80 | VEG OIL | 2.19 | 52.75 |
| 24 | 3% nano SiC | 1500 | 30 | 80 | VEG OIL | 1.97 | 39.09 |
| 25 | 1% nano SiC | 1500 | 30 | 270 | SAE 20/40 | 2.07 | 36.93 |
| 26 | 1% nano SiC | 1200 | 20 | 150 | VEG OIL | 2.2 | 52.17 |
| 27 | 2% nano SiC | 1500 | 20 | 150 | VEG OIL + TiO ₂ | 1.12 | 35.07 |
| 28 | 2% nano SiC | 1200 | 15 | 150 | SAE 20/40 | 1.13 | 52.64 |
| 29 | 2% nano SiC | 900 | 10 | 80 | VEG OIL | 1.11 | 53.15 |
| 30 | 1% nano SiC | 1200 | 10 | 80 | SAE 20/40 | 2.4 | 52.01 |
| 31 | 1% nano SiC | 900 | 30 | 270 | VEG OIL + TiO ₂ | 0.77 | 52.96 |
| 32 | 3% nano SiC | 1500 | 10 | 270 | VEG OIL | 1.32 | 37.65 |
| 33 | 3% nano SiC | 1500 | 10 | 150 | SAE 20/40 | 2.02 | 31.6 |
| 34 | 3% nano SiC | 1500 | 10 | 80 | VEG OIL + TiO ₂ | 1.05 | 37.14 |
| 35 | 3% nano SiC | 900 | 30 | 270 | VEG OIL | 1.15 | 52.75 |



Fig. 4 Four-ball wear tester for tribological study



Fig. 5 Tribological performance of SAE20W40, veg. oil, and Veg. oil + TiO₂ using four-ball wear tester

3.2 Development of RSM Based D-optimal Design Models

Response Surface Method (RSM) is an optimization technique, ruling the best set of factor levels to attain performance. RSM is used to find the first and second-order response surface models and the steepest ascent direction to optimize the response. In the present investigation, the interaction of the qualitative parameters with quadratic effects of the quantitative parameters is examined for models using D-optimal design. D-optimal designs are created to decrease the generalized variance of the estimated regression coefficients. Designs that are D-optimal have been exposed to be nearly optimal for several other criteria that have been planned as well [63].

In numerous RSM applications, the association among the response and the independent variables is unknown. Therefore, an initial estimation is sought to determine the actual functional association among the set of independent variables involved

Table 4 Model for cutting force

| Sl. No | Type of MQL system | 2FI* model for cutting force |
|--------|---|---|
| 1 | SAE 20W40 | $-34.17015817 + 2.025307399w + 0.17559284n - 0.174358632d - 0.034140933v - 0.000855875wn + 0.054260311wd + 0.00240328wv + 0.000167673nd + 1.25877E-05nv - 0.000596958dv - 0.539060645w^2 - 8.62179E-05n^2 + 0.001554197d^2 + 6.09565E-05v^2$ |
| 2 | Vegetable oil (Cashew nut shell Oil) | $-36.4919234 + 1.968939669w + 0.178095052n - 0.235380715d - 0.031037011v - 0.000855875wn + 0.054260311wd + 0.00240328wv + 0.000167673nd + 1.25877E-05nv - 0.000596958dv - 0.539060645w^2 - 8.62179E-05n^2 + 0.001554197d^2 + 6.09565E-05v^2$ |
| 3 | Cashew nut shell oil + TiO ₂ | $-33.52179178 + 0.901474909w + 0.174498643n - 0.192324176d - 0.020835496v - 0.000855875wn + 0.054260311wd + 0.00240328wv + 0.000167673nd + 1.25877E-05nv - 0.000596958dv - 0.539060645w^2 - 8.62179E-05n^2 + 0.001554197d^2 + 6.09565E-05v^2$ |

*2FI: Two-factor interaction

and the predicted (dependent) response y . In RSM, a commonly used approach is to employ a second-order model.

$$y = \beta_0 + \beta_1x_1 + \beta_2x_2 + \beta_{12}x_1x_2 + \beta_{11}x_1^2 + \beta_{22}x_2^2 + \varepsilon \tag{2}$$

where the variables x_1 and x_2 represent the input factors or independent variables, while x_1^2 and x_2^2 represent the quadratic terms. The term, x_1x_2 represents the interaction term and ε represents the error of the model. β_0 represents the constant term, β_1 and β_2 denote the linear coefficients, β_{12} represents the interaction coefficient, β_{11} and β_{22} are the quadratic coefficients.

The current study presents the mathematical model that relates surface roughness and cutting force for various MQL systems, including, cashew nutshell oil, cashew nutshell oil + nano TiO₂, and SAE20W40. The specific mathematical relationships between these variables are given in Tables 4 and 5.

3.3 Examination of the Quadratic Mathematical Model

To analyze the collected data and fit a second-order polynomial with the experimental data, the design matrix was created with Design-Expert 8.0. The model’s performance was assessed employing various statistical measures, including the sequential F test, lack-of-fit test and further fitness procedures. The evaluation of the significant input parameters was carried out employing ANOVA. The validation of the responses was

Table 5 Model for surface roughness

| Sl. No | Type of MQL system | 2FI model for surface roughness |
|--------|---|---|
| 1 | SAE 20W40 | +3.41649-0.60166w-1.03568E-003n-0.057805d-5.68605E-003v + 3.00791E-004wn + 5.17856E-04wd + 7.10615E-004wv + 7.01641E-005nd + 2.17196E-006nv-1.09733E-004dv |
| 2 | Vegetable oil (Cashew nut shell oil) | +5.03283-0.64055w-2.34765E-003n-0.072703d-2.31354E-003v + 3.00791E-004wn + 5.17856E-004wd + 7.10615E-004wv + 7.01641E-005nd + 2.17196E-006nv-1.09733E-004dv |
| 3 | Cashew nut shell oil + TiO ₂ | +3.17974-0.36561w-2.15397E-003n-0.062034d-1.62670E-003v + 3.00791E-004wn + 5.17856E-004wd + 7.10615E-004wv + 7.01641E-005nd + 2.17196E-006nv-1.09733E-004dv |

carried out by applying a natural log transformation. If the Prob. > F-value—where Prob. refers to probability—varies from 0.05 to 0.1, the model terms are significant at times based on the condition. Moreover, the model with two-factor interaction (2FI) has been chosen for SR owing to extensive curvature. Tables 6 and 7 demonstrate the ANOVA table for SR and cutting force correspondingly.

The significant factors of the model include the MQL type, depth of cut, wheel speed, interaction between wheel speed and depth of cut, and interaction between MQL type and wheel speed. The model is considered significant based on the F-value of 2.43. The R-Squared value approaching 1 indicates desirable outcomes

Table 6 ANOVA for surface roughness

| Source | Sum of squares | df* | Mean Square | F Value | p-value Prob. > F | |
|-------------|----------------|-------|-------------|---------|-------------------|-----------------|
| Model | 8.23 | 20.00 | 0.41 | 2.43 | 0.0469 | Significant |
| Lack of fit | 1.29 | 9.00 | 0.14 | 0.66 | 0.7251 | Not significant |
| Pure error | 1.09 | 5.00 | 0.22 | | | |
| Cor total | 10.61 | 34.00 | | | | |

* df: degrees of freedom

Table 7 ANOVA for cutting force

| Source | Sum of Squares | df | Mean Square | F Value | p-value Prob. > F | |
|-------------|----------------|-------|-------------|---------|-------------------|-----------------|
| Model | 2509.29 | 24.00 | 104.55 | 11.37 | 0.0002 | Significant |
| Lack of fit | 0.62 | 5.00 | 0.12 | 0.01 | 1.0000 | Not significant |
| Pure error | 91.34 | 5.00 | 18.27 | | | |
| Cor total | 2601.25 | 34.00 | | | | |

for the responses. Additionally, the variations among Pred R-squared and Adj R-squared were limited referring to the adequate transaction among the output and input factors of the models. The signal to noise ratio calculated through Adeq-precision considerably more significant than 4 is preferred. The “lack-of-fit” is not significant compared to the pure error, which is favorable. The β_0 values for the cashew nutshell oil + nano TiO₂ MQL system are higher than the other two MQL systems. The β_0 value represents the average response value of all the experiments and serves as the reference point for the model [55]. The β_0 values rely on important grinding factors examined in the investigation, as well as experimental anomalies including machine vibrations, surface finish, and environmental conditions. The MQL system reinforced composites with cashew nutshell oil + nano TiO₂ exhibit improved performance, as indicated by the coefficient β_0 and the experimental outcomes. If the associated variables increase, the performances of the composites increase when the coefficient value is greater than 0, whereas the inverse effect is observed when it is lesser than 0.

3.4 Multi-Response Optimization of Grinding Parameters Based on Desirability Analysis

In the present investigation, the desirability function approach is employed in the multi-response optimization of grinding parameters. The simultaneous optimization technique is one of the useful approaches in multi-response optimization. In this method, the individual responses are initially predicted using regression techniques. Subsequently, each predicted response is converted into a desirability value. Then, the overall desirability, i.e., the performance metric is obtained, combining individual desirability through the geometric mean. According to this proposed approach, the optimization of a process with both ordinal response and quantitative variables would involve four steps: (i) calculation of a desirability index for every quantitative response variable individually, (ii) determination of desirability indices for the dispersion effect and location effect of every ordinal response variable, (iii) calculation of an overall desirability index, and (iv) optimization of the overall desirability index.

The optimization analysis in this study is performed through the DESIGN-EXPERT[®] software. Table 8 represents the goal set, weight, the importance of the factors, and upper and lower limits used.

Various best solutions are attained in this approach based on desirability. While the solution having high desirability is chosen and given in Table 9.

The desirability value falls within the range of 0–1, indicating how closely the response aligns with the desired result. The optimization analysis revealed that the preferred settings for reducing surface roughness and cutting force are as follows: MQL Type = VEG. OIL + TiO₂, workpiece speed = 80 rpm, wt. % Nano SiC = 1, depth of cut = 10 μ m, and wheel speed = 1500 rpm.

Table 8 Constraints used in desirability analysis

| Name | Goal | Lower limit | Upper limit | Lower weight | Upper weight | Importance |
|-------------------------------------|-------------|-------------|-----------------------------|--------------|--------------|------------|
| Wt. % Nano SiC | Is in range | 1 | 3 | 1 | 1 | 3 |
| Wheel speed (rpm) | Is in range | 900 | 1500 | 1 | 1 | 3 |
| Depth of cut (μm) | Is in range | 10 | 30 | 1 | 1 | 3 |
| Workpiece speed (rpm) | Is in range | 80 | 270 | 1 | 1 | 3 |
| MQL type | Is in range | SAE 20/40 | VEG. OIL + TiO ₂ | 1 | 1 | 3 |
| Surface roughness (μm) | Minimize | 0.58 | 2.48 | 1 | 1 | 3 |
| Cutting force (N) | Minimize | 24.83 | 54.38 | 1 | 1 | 3 |

Table 9 Results of desirability analysis

| Wt. % Nano SiC | Wheel speed (rpm) | Depth of cut (μm) | Workpiece speed (rpm) | MQL type | Surface roughness (μm) | Cutting force (N) | Desirability |
|----------------|-------------------|--------------------------------|-----------------------|-----------------------------|-------------------------------------|-------------------|--------------|
| 1.04 | 1500 | 10.09 | 80 | VEG. OIL + TiO ₂ | 0.579 | 34.53383 | 0.8195 |
| 1.05 | 1500 | 10.08 | 80.02 | VEG. OIL + TiO ₂ | 0.582196944 | 34.52054 | 0.819 |
| 1.12 | 1500 | 10 | 80.01 | VEG. OIL + TiO ₂ | 0.589040002 | 34.4575 | 0.8191 |

3.5 Confirmation Experiments

Validation experiments were performed to verify the accuracy of the developed model, and the corresponding details are presented in Table 10.

All the experiments were continual for 2 times, and the mean of the results is considered. The developed model is considered as the appropriate model for improving the performance of grinding of MMCs since the predicted values and the experimental results are closer with each other.

3.6 Effect of Grinding Parameters on Responses

Figure 6 displays the 3D contour plots illustrating the fitted 2FI models for surface roughness across various parameters of grinding.

Table 10 Confirmation experiments and results

| | Optimal machining parameter | |
|-------------------------------------|---|--------------|
| | Prediction | Experimental |
| Setting level | wheel speed = 1500 rpm Depth of cut = 10 mm wt. % Nano SiC = 1 Work piece speed = 80 rpm MQL Type = VEG. OIL + TiO ₂ | |
| Cutting force (N) | 34.5 | 35.85 |
| Surface roughness (μm) | 0.585 | 0.625 |

The prominent factor that influences the surface roughness is the wheel velocity. The maximum chip thickness corresponds to a decrease in the increase of the wheel velocity, providing justification for the significant impact on the surface roughness by the wheel velocity. The presence of reinforcement particles has a notable effect over the surface quality of aluminium composites in grinding. Regardless of the grinding conditions, a rise in the wt. % of SiC nanoparticles results in a reduction in surface roughness. Furthermore, the inclusion of nano SiC into the Al matrix leads to improvements in tensile strength, heat resistance, and hardness [64]. The increase in feed rate or cutting depth was observed to cause an increase in both grinding surface roughness and residual compressive stress. On the other hand, an increase in grinding speed exhibited a positive result on reducing surface roughness [26]. The workpieces subjected to MQL conditions showed superior surface finish in contrast to wet and dry conditions. Furthermore, a rise in extreme chip thickness for various cooling environments led to a reduction in specific energy consumption [65]. An enhancement in surface finish was observed as the concentration of nanoparticles increased. With varying cooling conditions, the specific energy decreased as the maximum chip thickness increased. The results of the experiment demonstrated that increasing the weight percentage of Nano SiC tends to a decrease the surface roughness. The composites hardness had a significant impact on surface roughness, resulting in an improved surface finish during MMNC grinding [66].

Figure 7 illustrates the 2D contour plots of the 2FI models developed to analyze the relationship between grinding parameters and cutting force.

Tool life is a crucial parameter that tends to decrease as the depth of cut and cutting force increase because of elevated stress and increased collision between the tool and workpiece. The advancement of the tool at a rapid rate and vibrations contribute to the generation of higher cutting force, which consequently tends to rise the surface roughness [67]. Based on the experiments, it was observed that increasing the wheel speed and workpiece speed resulted in decreasing the tangential grinding forces. Conversely, an increase in tangential grinding force and surface roughness was observed as the depth of cut increases [68]. The utilization of cutting fluid with nanoparticles, despite lower proportions nanoparticle concentrations, resulted in a substantial decrease in grinding forces [35]. The implementation of MQL in

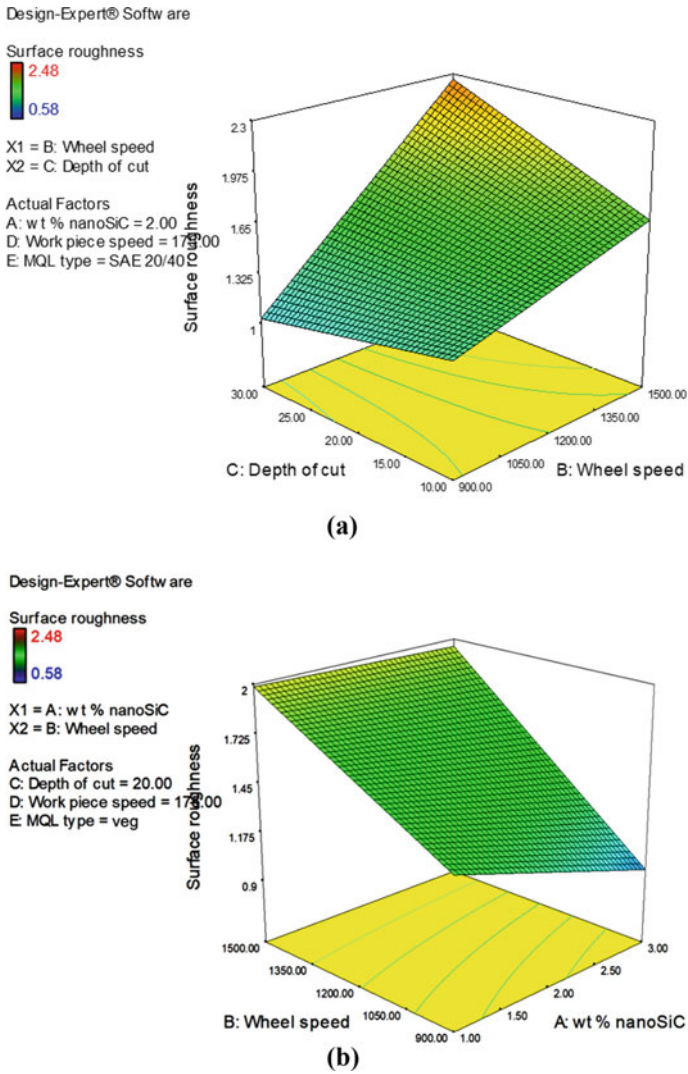


Fig. 6 3D contour plots for surface roughness on different MQL system. **a** Roughness with depth of cut and Wheel speed. **b** Roughness with Wheel speed and wt.% nano SiC

grinding operations decreased specific grinding energy and grinding forces. Consequently, there was an increase in the G-ratio and a decrease in wheel wear [37]. When compared with dry and wet grinding, MQL grinding demonstrates a significant reduction in tangential forces. This can be attributed to the existence of lubricant surrounding the grinding wheel, which facilitates improved grain slipping at the interface between the tool and the workpiece [20]. Cashew nutshell oil + nano TiO₂ based MQL exhibits superior performance due to the lubricant’s ability to effectively

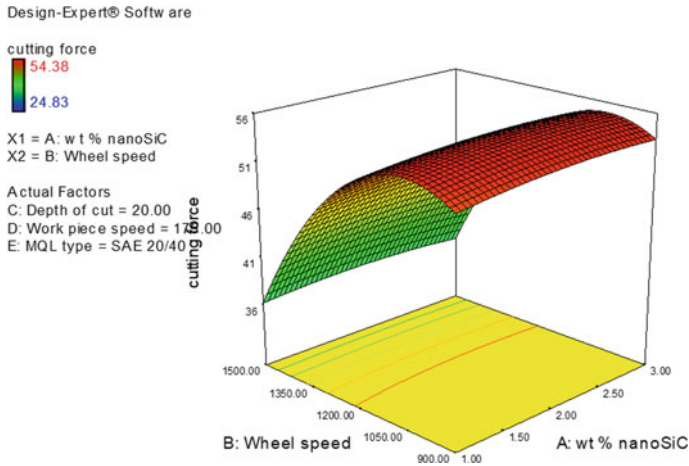


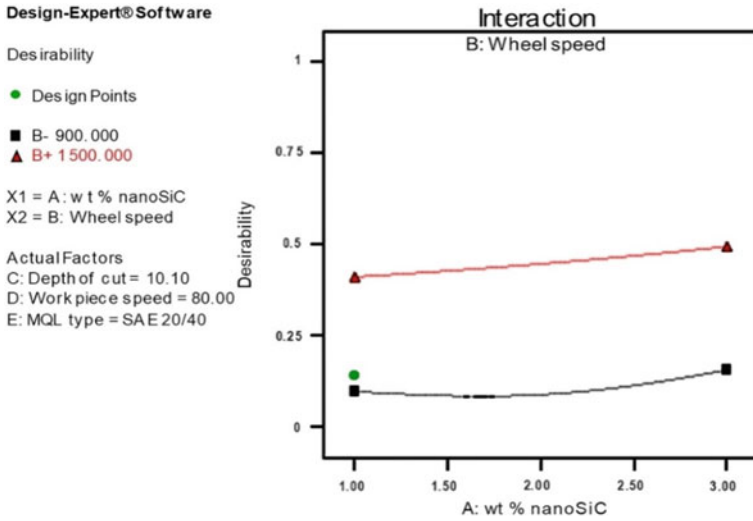
Fig. 7 2D contour plots for cutting force on different MQL system

penetrate the contact zone flanked by the grinding wheel and the workpiece interface [25].

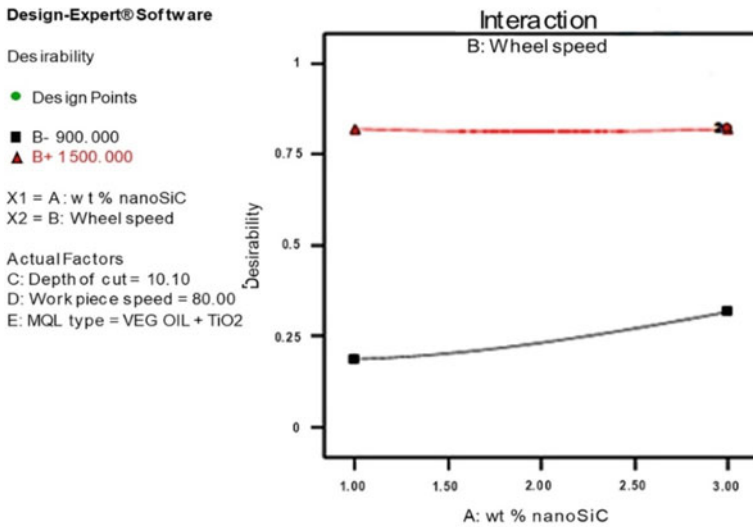
3.7 Effect of MQL Systems on the Desirability

The impact of various MQL systems on the desirability approach was shown in Fig. 8. The experimental outcomes demonstrate that the use of nanofluid MQL leads to a substantial reduction in grinding forces, resulting in enhanced surface quality. The utilization of TiO_2 in MQL systems demonstrates enhanced performance attributed to the improved load-bearing capacity and reduced friction in components. Nanofluid revealed better tribological and thermophysical properties by decreasing tool wear, cutting zone temperature, surface roughness, and cutting forces [69]. The temperature at cutting zone is decreased, whereas the heat extraction capability is increased with the increase in the density, viscosity, and thermal conductivity of fluid owing to the increase in nanoparticle volume concentration [70].

Peng [71] demonstrated various mechanisms that contribute to the reduction of friction and wear when nanoparticles are added to conventional cutting fluids. These mechanisms include the concentration of compressive stress caused by nanoparticles, the sewing effect, the formation of a surface protective film, and the rolling action of nano-sized spherical particles. Consequently, the incorporation of nanoparticles in MQL systems enhances the overall performance of sustainable grinding processes.



(a)



(b)

Fig. 8 Interaction plots for different MQL systems on the desirability **a** SAE 20/40, **b** Veg. oil + TiO₂

3.8 Surface Morphology of the Machined Surface

The utilization of SEM enables the observation and analysis of the surface morphology of the machined surface. Micrographs captured from SEM are depicted in Fig. 9. During the examination, it was observed that the surface finish of the workpiece was poor, and there were visible marks left by the grinding wheel. These undesirable effects can be attributed to the utilization of a grinding wheel with a high depth of cut [68]. No defects or cracks were detected on the cylindrical ground surfaces when employing minimum depth of cut and feed, high workpiece, and wheel velocities [28]. The fragmentation of Al_2O_3 grains from the grinding wheel and their subsequent attachment on the workpiece were observed as a consequence of increased cutting force and depth of cut. The micrograph clearly shows the disintegration and removal of nano SiC particles from the surface [11]. The dissimilarity in thermal expansion between Al and SiC nanoparticles induce heat generation, leading to the development of microcracks on the machined surface.

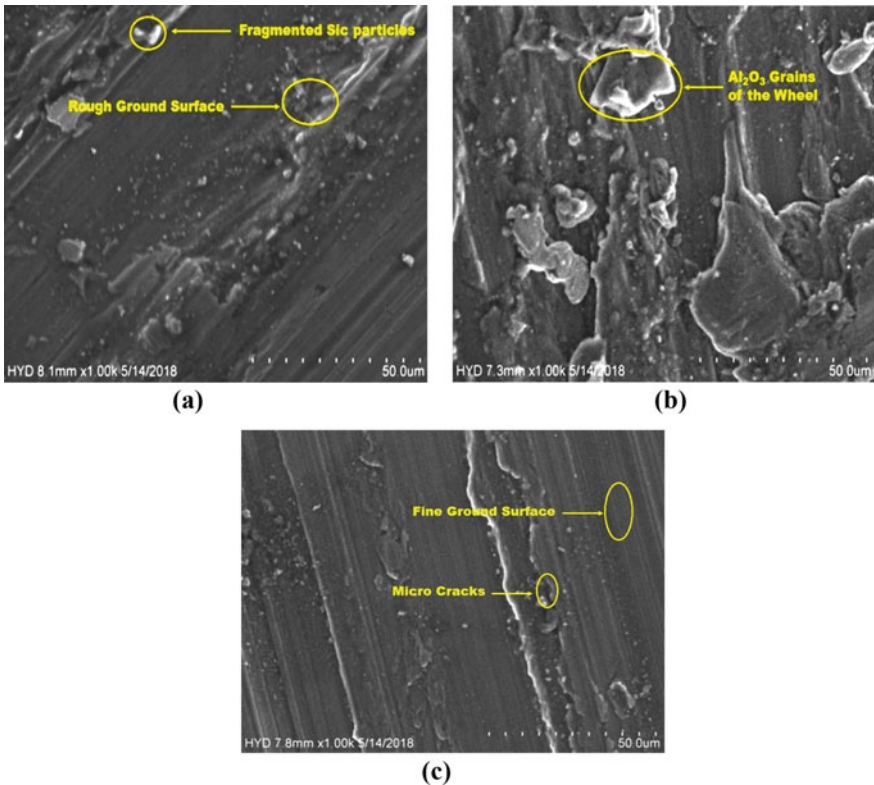


Fig. 9 SEM images of machined surface at: **a** $v = 270$ rpm, $d = 30$ μm , $n = 1500$ rpm, $w = 1\%$, and SAE20W40. **b** $v = 270$ rpm, $d = 30$ μm , $n = 1500$ rpm, $w = 3\%$, and Veg. oil. **c** $v = 270$ rpm, $d = 30$ μm , $n = 1500$ rpm, $w = 3\%$, and SAE20W40

3.9 Surface Roughness Analysis Using Atomic Force Microscopy (AFM)

Atomic force microscopy (AFM) analysis is the preferred method for precise quantitative measurement of nanoscale surface roughness and visualization of surface nanotexture in nanocomposites [23]. Figure 10 displays the corresponding 3D AFM analysis of surfaces machined with cashew nutshell oil, cashew nutshell oil + nano TiO₂, and SAE20W40.

The utilization of nano TiO₂ as a lubricating oil in MMNC caused reduction in the mean surface roughness from 226.5 nm to 108.3 nm. The incorporation of carbon nanotubes into the nano-fluid used for the grinding process exhibited enhancements in surface characteristics, including surface roughness and mitigation of microcracks [23]. The AFM analysis confirms the enhanced surface quality of MMNC when nano TiO₂ is employed in MQL system.

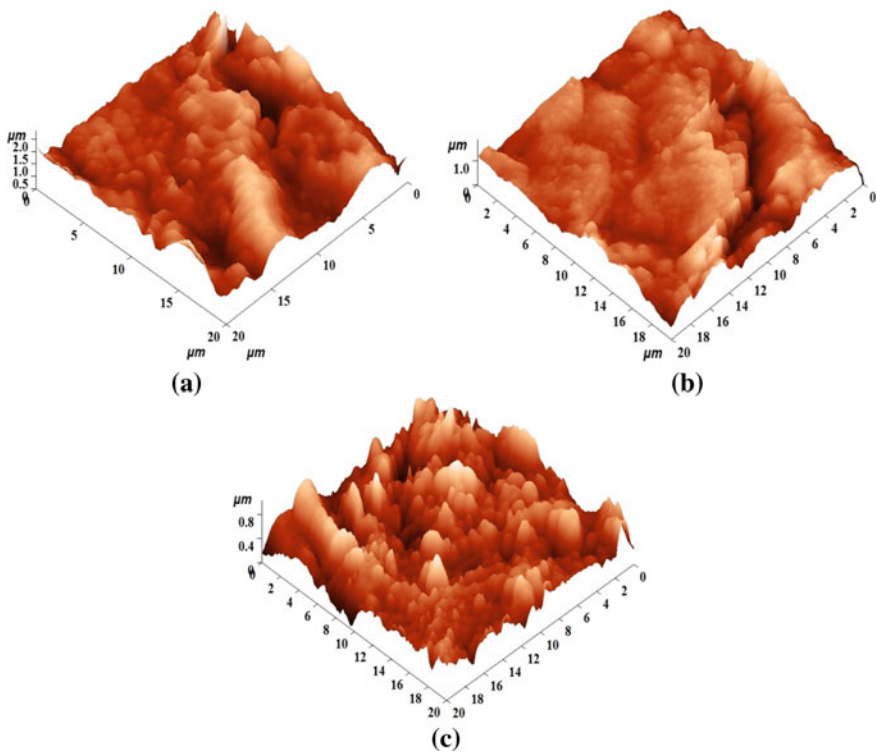


Fig. 10 AFM Analysis of the machined surface under **a** SAE20W40, **b** Veg. oil, and **c** Veg. oil + TiO₂

3.10 Surface Morphology of Grinding Wheel Surface

SEM is employed to examine and evaluate the grinding wheel surface morphology. Figure 11 demonstrates the micrographs obtained through SEM. During this observation, the abrasive grains exhibit larger and more pointed shapes after the dressing process compared to their initial state. These properties contribute to a reduction in the area of contact among the workpiece and the abrasive grains, resulting in improved efficiency. Moreover, large apertures are features of excellent cutting capability. The grinding wheel surface retains nano-fluids, with the crack networks resembling micro-reservoirs capable of temporarily storing these fluids [72]. This unique characteristic allows micro-reservoirs, characterized by high porosity, to deliver significant volumes of nano-fluids containing TiO_2 nanoparticles within the grinding region. The presence of nano-fluids on the surfaces of abrasive grains facilitates the formation lubricating film with TiO_2 nanoparticles by means of chemical and physical reactions. The present protective film effectively hinders the formation of wear flats and facilitates their removal from the abrasive grains.

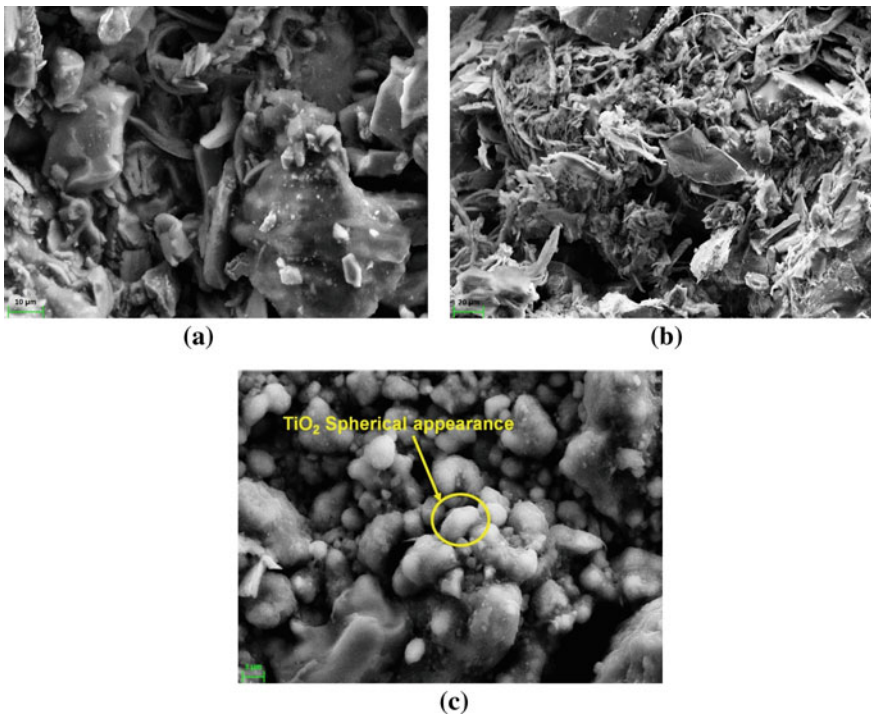


Fig. 11 SEM images of grinding wheel surface under **a** SAE20W40, **b** veg. oil, and **c** veg. oil + TiO_2

4 Conclusions

Based on the analysis of experimental data obtained from the cylindrical grinding of SiC nanoparticles reinforced Al matrix composites with different MQL conditions, the following conclusions can be derived:

- In the grinding process, the application of the MQL method proved to be a cost-effective approach. This MQL method facilitated the oil mist dispersion within the machining region, significantly reduced the frictional coefficient and tangential forces.
- The 2FI model for surface roughness and cutting force was carried out relating the dominant grinding factors like wheel speed, depth of cut, weight percentage of SiC nanoparticles, and work piece speed matched with experimental data at 95% confidence level.
- The surface roughness of the machined surface is primarily influenced by important factors like the wheel speed, depth of cut, and MQL type.
- Desirability analysis based on RSM is performed to improve the sustainable grinding parameters of nano SiC reinforced composites. The optimization results indicated that the following parameters are preferred for decreasing the surface roughness and cutting force: wheel speed = 1500 rpm, depth of cut = 10 μm , weight percentage of SiC nanoparticles = 1%, workpiece speed = 80 rpm, and MQL type = VEG OIL + TiO₂.
- MQL systems utilizing nano fluid caused reduction in both cutting forces and surface roughness. The incorporation of Nano TiO₂ into cashew nutshell oil further enhanced performance by improving the lubrication and cooling effect. This improvement can be attributed to the increased diffusion and entrapment of Nano TiO₂ at the contact zone.
- The utilization of Veg oil filled with nano TiO₂ as a lubricating oil in MMNC resulted in reduction of the average surface roughness from 226.5 nm to 108.3 nm.

References

1. S. Vijayabhaskar, T. Rajmohan, Experimental investigation and optimization of machining parameters in WEDM of Nano-SiC particles reinforced magnesium matrix composites. *SILICON* **11**, 1701–1716 (2019). <https://doi.org/10.1007/s12633-017-9676-0>
2. J.W. Kaczmar, K. Pietrzak, W. Włosiński, *J. Mater. Process. Technol.* **106**, 58 (2000)
3. S.P. Rawal, *JOM* **53**, 14 (2001)
4. L. Poovazhagan, K. Kalaichelvan, T. Sornakumar, *Mater. Manuf. Process.* **31**, 1275 (2015)
5. S.M. Suresh, D. Mishra, A. Srinivasan, R. M. Arunachalam, R. Sasikumar, *ARPN J. Eng. Appl. Sci.* **6**, 94 (2011)
6. A. Kumar Singh, A. Kumar, V. Sharma, P. Kala, *J. Cleaner Prod.* **269**, 121875 (2020)
7. T. Rajmohan, K. Palanikumar, S. Prakash, *Compos. Part B - Eng.* **50**, 297 (2016)
8. S. Song, X. Zhou, L. Li, W. Ma, *Ultrason. Sonochem.* **24**, 43 (2015)
9. X.J. Wang, N.Z. Wang, L.Y. Wang, X.S. Hu, K. Wu, Y.Q. Wang, Y.D. Huang, *Mater. Design.* **57**, 638 (2014)

10. G. Cao, H. Konishi, X. Li, Mater. Sci. Eng. A. **486**, 357 (2008)
11. T. Rajmohan, K. Palanikumar, Int. J. Adv. Manuf. Technol. **64**, 249 (2013)
12. J. Hankel, S. Jäger, S. Weber, J. Cleaner Prod. **263**, 121501 (2020)
13. A.D. Ilio, A. Paoletti, Int. J. Mach. Tool Manuf. **40**, 173 (2000)
14. Y. Kaynak, T. Lu, I.S. Jawahir, Mach. Sci. Technol. **18**(2), 149 (2014)
15. Y. Wang, C. Li, Y. Zhang, M. Yang, B. Li, D. Jia, Y. Hou, C. Mao, J. Clean Prod. **127**, 487 (2016)
16. T. Tawakoli, M. J. Hadad, M. H. Sadeghi, A. Daneshi, S. Stöckert, A. Rasifard, Int. J. Mach. Tool Manu. **49**, 924 (2009)
17. W. Grzesik, *Advanced Machining Processes of Metallic Materials: Theory, Modelling and Applications*, 1st edn. (Elsevier, 2008), pp. 226–245
18. M.F. Rajemi, P.T. Mativenga, A. Aramcharoen, J. Clean Prod. **18**, 1059 (2010)
19. S. Arumugam, G. Sriram, T. Rajmohan, K. Sivakumar, Energ. Source Part A. **38**, 300 (2016)
20. A. Nandakumar, T. Rajmohan, IOP Conference Series: Materials Science and Engineering **390**(1), 012033 (2018)
21. D.N. Rao, R.R. Srikant, P. I. Mech. Eng. B – J. Eng. **220**, 1803 (2006)
22. D. Wen, Y. Ding, Int. J. Heat Mass Transf. **48**, 5181 (2004)
23. S. Prabhu, B.K. Vinayagam, Int. J. Adv. Manuf. Tech. **60**, 149 (2012)
24. A. Nandakumar, T. Rajmohan, S. Vijayabhaskar, SILICON **11**, 2987 (2019)
25. C. Mao, Mater. Manuf. Process. **23**, 436 (2013)
26. F.H. Sun, X. K. Li, Y. Wang, M. Chen, Key Eng. Mater. **304–305**, 261 (2006)
27. Z.W. Zhong, Int. J. Adv. Manuf. Technol. **21**, 79 (2003)
28. C. Thiagarajan, R. Sivaramakrishnan, S. Somasundaram, ARPN J. Eng. Appl. Sci. **6**, 14 (2011)
29. H. Masoumi, S.M. Safavi, M. Salehi, Mater. Manuf. Process. **29**, 321 (2014)
30. S. Majumdar, Mater. Manuf. Process. **33**, 1459 (2018)
31. R. Madarkar, Manuf. Process. **33**, 1445 (2017)
32. P. Chockalingam, K.C. Kuang, T.R. Vijayaram, Mater. Manuf. Process. **28**, 1071 (2013)
33. D. De Oliveira, R.B. Da Silva, R.V. Gelamo, Wear **426–427**, 1371 (2019)
34. A. Mohammed, J. Folkes, X. Chen, Mater. Manuf. Process. **27**, 395 (2012)
35. J.C. Lopes, M. V. Garcia, R. S. Volpato, H. J. de Mello, F. S. F. Ribeiro, L. E. de Angelo Sanchez, K. de Oliveira Rocha, L. D. Neto, P. R. Aguiar, E. C. Bianchi, Int. J. Adv. Manuf. Technol. **106**, 2205 (2020)
36. D. Setti, S. Ghosh, P.V. Rao, Int. J. Mech. Mechatron. Eng. **6**, 10 (2012)
37. F.S.F. Ribeiro, J. C. Lopes, M. V. Garcia, L. E. de Angelo Sanchez, H. J. de Mello, P. R. de Aguiar, E. C. Bianchi, Int. J. Adv. Manuf. Technol. **107**, 4415 (2020)
38. H. Adibi, H. Esmaeili, S.M. Rezaei, Int. J. Adv. Manuf. Technol. **95**, 3753 (2017)
39. H. Fukushima, L.T. Drzal, in *Proceedings of the 17th Annual Conference of the American Society for Composites*, (Purdue University, 2002). pp. 21–23
40. P. Kalita, J. Manuf. Process. **14**, 160 (2012)
41. P. -H. Lee, T. S. Nam, C. Li, S. W. Lee, in *International Conference on Manufacturing Automation* (Hong Kong, IEEE, 2010), pp. 44–49
42. X. Liu, S. Jia, L. Nastac, Int. J. Metal Cast. **8**, 51 (2014)
43. S. Prabhu, B.K. Vinayagam, Sadhana **35**, 747 (2010)
44. Y. Su, Int. J. Adv. Manuf. Technol. **83**, 2083 (2016)
45. A. Mazahery, M. Ostadshabani, J. Compos. Mater. **45**, 2579 (2011)
46. T.S. Mahmoud, E.Y. El-Kady, Corros. Eng. Sci. Technol. **47**, 45 (2012)
47. M. P. Reddy, R. A. Shakoor, G. Parande, V. Manakari, F. Ubaid, A. M. A. Mohamed, M. Gupta, Prog. Nat. Sci-Mater. **27**, 606 (2017)
48. Y.C. Kang, S.L.I. Chan, Mater. Chem. Phys. **85**, 438 (2004)
49. Y. Zhang, C. Li, D. Jia, D. Zhang, X. Zhang, Int. J. Mach. Tool Manuf. **99**, 19 (2015)
50. C. Mao, X. Tang, H. Zou, X. Huang, Z. Zhou, Int. J. Precis. Eng. Manuf. **13**, 1745 (2012)
51. C. Mao, J. Zhang, Y. Huang, H. Zou, X. Huang, Z. Zhou, Mater. Manuf. Process. **28**, 436 (2013)
52. E.A. Rahim, H. Dorairaju, Measurement **123**, 213 (2018)

53. S. Chinchani, S.K. Choudhury, *Measurement* **55**, 536 (2014)
54. M. Mia, *Measurement* **122**, 380 (2018)
55. M. Mia, *Measurement* **121**, 249 (2018)
56. M. Mia, *Measurement* **129**, 156 (2018)
57. V. Songmene, J. Kouam, A. Balhoul, *Measurement* **114**, 398 (2018)
58. R. Viswanathana, S. Ramesh, V. Subburam, *Measurement* **120**, 107 (2018)
59. T. Rajmohan, *Particul. Sci. Technol.* **37**, 21 (2019)
60. S. Baskar, G. Sriram, S. Arumugam, *Energ. Source. Part A* **40**, 1583 (2018)
61. T. Rajmohan, K. Palanikumar, S. Ranganathan, T. Nonferr, *Metal. Soc.* **23**, 2509 (2013)
62. M.E. Khamneh, M. Askari-Paykani, H. Shahverdi, S. M. M. Hadavi, M. Emami, *Measurement* **88**, 278 (2016)
63. A. Laouissi, M. A. Yallese, A. Belbah, S. Belhadi, A. Haddad, *Int. J. Adv. Manuf. Technol.* **101**, 523 (2019)
64. T. Rajmohan, K. Palanikumar, M. Kathirvel, T. Nonferr, *Metal. Soc.* **22**, 1286 (2012)
65. P. Lakshmanan, K. Kalaichelvan, T. Sornakumar, *Mater. Manuf. Process.* **31**, 1275 (2015)
66. P.S.P. Anand, N. Arunachalam, L. Vijayaraghavan, *Mater. Manuf. Process.* **33**, 634 (2017)
67. L. Fu, X. Yang, L.L. Wang, *Measurement* **46**, 3173 (2013)
68. S. Jeevanantham, *Int. J. Appl. Eng. Res.* **12**, 2963 (2017)
69. C. Thiagarajan, *ARPJ, J. Eng. Appl. Sci.* **6**, 14 (2011)
70. J. Sharma, B.S. Sidhu, *J. Clean. Prod.* **66**, 619 (2014)
71. D. Peng, *Tribol. Int.* **4**, 911 (2009)
72. A.K. Tiwari, P. Ghosh, J. Sarkar, *J. Environ. Res. Dev.* **7**, 768 (2012)

Waste-Based Zeolites and their Advanced Composites for Wastewater and Environmental Remediation Applications



Niladri Shekhar Samanta, Piyal Mondal, and Mihir K. Purkait

Abstract The drinking water crisis has shaped into a major threat for the human race nowadays due to heavy and unwanted wastage of water for different purposes. To overcome such issues, the treatment of wastewater through several techniques for removing unwanted pollutants has proved to be beneficial. Adsorption being an efficient technique utilizes a physical and chemical process to remove harmful metal ions, anions, and chemical pollutants from the wastewater. Various synthetic and natural adsorbents were utilized by researchers for studying the adsorption process. Zeolite nowadays has been explored as a very eminent material for carrying out adsorption studies for wastewater treatment. This chapter discusses the preparation techniques of zeolite by both conventional and advanced techniques. The utilization of various industrial waste sources for preparing zeolite has been mainly focused on in this chapter. Moreover, the synthesis of various advanced zeolite-based composites is described along with their specific utilization toward environmental remediation applications. This chapter also points out the recent advancements and future scope of advanced zeolite composite materials which can prove to be more efficient in remediation-based applications.

Keywords Zeolite · Adsorption · Dye removal · Metal removal · Waste reuse · Wastewater treatment

N. S. Samanta · M. K. Purkait (✉)
Centre for the Environment, Indian Institute of Technology Guwahati, Guwahati,
Assam 781039, India
e-mail: mihir@iitg.ac.in

N. S. Samanta
e-mail: s.niladri@iitg.ac.in

P. Mondal · M. K. Purkait
Department of Chemical Engineering, Indian Institute of Technology Guwahati, Guwahati,
Assam 781039, India
e-mail: piyal@iitg.ac.in

1 Introduction

The normal environmental processes are adversely affected by the contamination of physical and biological components of the earth. Mostly the pollution is found to occur through air and water. In recent global concern, water and air pollution are expanding rapidly because of access to population and industrialization. Water is being contaminated enormously by industrial effluent and municipal sewage water. On the other hand, the air is being contaminated by industrial hazardous gas or gas mixture. Therefore, the accumulation of large quantities of harmful organic and inorganic contaminants may pose a severe threat to the environment and human health, and remediation is required. The two major techniques of remediation are the removal of pollutants from soils or aquatic systems, or the reduction of their mobility and/or in situ stability. In order to attain such objectives several materials and techniques were utilized to treat water systems [1]. Zeolites were first utilized as adsorbents in industrial separations and purifications due to their distinctive porous characteristics, extraordinary physicochemical properties (e.g. extreme ion-exchange capacity, high crystallinity, regular nanometric cavities). It is also concluded that zeolites are crystalline aluminosilicates with open three-dimensional framework structures made up of AlO_4 and SiO_4 tetrahedra connected together by sharing all of their oxygen atoms to produce regular intra-crystalline voids and channels with molecular dimensions [2–5]. The framework structure may comprise connected cages, cavities, or channels large enough for tiny molecules to pass through. These features make them excellent candidates for heavy metal removal as well as gas separation processes. A recent study also revealed that zeolites can be employed as water softeners. Notably, the same properties have also been observed in synthetic zeolites. The characteristics like molecular sieve, crystallinity, and phase purity can be modified for the hybrid zeolite fabrication to get high ion-exchange removal. Nowadays, the removal efficiency over zeolite has become of great interest to researchers. Also, zeolites are non-toxic, inexpensive, and extensively distributed in nature. Besides, synthetic zeolite composite has an efficient role in waste removal with better adsorption capacity, stability, and durability than commercially available zeolite.

Several studies have been committed for synthesizing zeolite-composite hybrid sorbents where zeolite was composed with other material or used as a support for sorption studies. Researchers have also been devoted to zeolite blended zeolite-membrane composite, namely, mixed matrix membranes (MMM) like material synthesis for gas separation and hazardous material removal from waste-loaded industrial effluent. It was observed that zeolite composite can exchange a higher amount of Cd^{2+} , Pb^{2+} , and Cu^{2+} compared to unmodified zeolite [6].

This chapter deals with advanced zeolite synthesis using various preparation techniques such as hydrothermal treatment, two-step hydrothermal treatment, fusion-facilitated hydrothermal treatment, microwave-assisted technique, ball milling, and solvent-free synthesis with their significant advantages and disadvantages. A review of zeolite uses for various heavy metals and cationic dye removal from industrial effluent, and for organic and greenhouse gas separation from a gas mixture was presented in this chapter.

2 Zeolite and Synthesis Methods

2.1 Zeolite Minerals

Natural or synthetic zeolites are a distinctive class of inorganic oxides, comprising crystalline, and microporous aluminosilicates. However, in recent years the mesoporous zeolite such as ITQ-37, zeolite Y, ZSM-5, etc., have been effectively synthesized. This aluminosilicate framework carries cages and open channels, where water, cations, and sorbed particles may settle and react. The superior ion exchange and adsorption characteristics of zeolite minerals are extremely useful for color removal, desiccants, detergents, and other industrial purposes [7, 8]. Zeolites can also be acidic that leads to catalytic cracking, synthesis of hydrocarbon, and isomerization. In addition, the well-defined pore structure in the zeolite framework offers suitable stability of the zeolite mineral. However, there are limited zeolites that are still sensitive to salts and pH, which can be utilized for specific applications.

There are two classes of zeolites: Natural and synthetic zeolite. Natural zeolite is formed of hydrated aluminosilicates having a three-dimensional tetrahedral network, where oxygen atoms are shared with T atoms, where T is Si or Al atom. The arrangements of atoms construct a large pore system, and this significant characteristic allows zeolites to have several adsorption applications such as cation exchange through intra-crystalline sites. Internal structure cavities and channels of zeolite are internally connected by molecular dimensions, where ion-exchange phenomena are being carried out by compensation cations [9].

2.2 Zeolite Synthesis Methods

The synthesis of zeolite through the crystallization mechanism provides a significant specific structure and functionality that makes it more important for industrial application. The synthesis mechanism and development of the zeolite network are now progressing consistently. The fabrication of zeolite is a complicated process. The steps of the process involve the dissolution of silicate and aluminate to form an aluminosilicate complex, the continuous formation of gel-solid, and corresponding solution phase, nucleation, and crystal growth of the zeolite. In the crystallization process, any solid phase should not exist during the solid-phase transformation mechanism, nor any liquid stage directly connected to the nucleation of zeolite crystals. However, in the gel-solid phase, only the aluminosilicate framework will be reorganized under fixed conditions. The X-ray diffraction revealed the relationship between time and zeolite crystallization [10]. In 1966, Kerr et al. [11] demonstrated the crystallization of zeolite through a liquid-phase transformation process. They observed that gel transformed into zeolite crystal in the liquid phase transformation treatment when aluminosilicate gel is getting dissolved into aqueous NaOH.

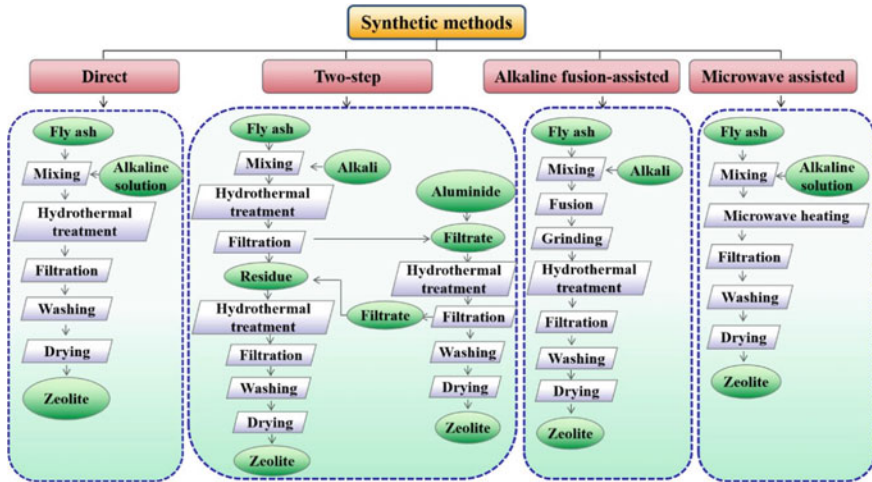


Fig. 1 Typical flowcharts for the synthesis methods of zeolites from Si and Al-rich CFA. Reproduced from Ren et al. [12] under the terms and conditions of the Creative Commons Attribution 4.0 License (CC BY 4.0) (<https://creativecommons.org/licenses/by/4.0/>)

It was proven that waste materials namely circulating fluidized bed fly ash (CFA), blast furnace slag (BFS), biomass ash (e.g. rice husk, sugarcane bagasse, palm oil mill fly ash) are comprising of silica and alumina as main components which can be utilized as starting materials for zeolite fabrication under various conventional or non-conventional treatment. Also, so many methods involved for zeolite synthesis are as follows: two-step followed by hydrothermal treatment, fusion-facilitated alkaline hydrothermal treatment, direct hydrothermal, Microwave irradiation hydrothermal process, Fusion-assisted ultrasonic hydrothermal, Microwave hydrothermal treatment with pulverization process, Molten-slat method, Ball milling, solvent-free synthesis. In this chapter, the zeolite synthesis from various wastes using the aforementioned methods has been discussed along with their advantages and disadvantages. The synthesis of zeolites using CFA as the raw material has been shown in Fig. 1.

2.2.1 Direct Hydrothermal Method

Zeolite-like materials can be synthesized from direct hydrothermal treatment by dissolving waste CFA in an aqueous alkaline solution. Querol et al. [13] demonstrated zeolite synthesis with 14 kinds of Spanish coal fly ash having different chemical and physical properties to examine the zeolite properties such as crystallinity, phase purity, and particle size. It was also reported that the aluminum-silicate glass content of CFA-based zeolite has shown the greatest efficiency for industrial applications. The CFA comprises two active substances quartz and glass which are very potential

for zeolite synthesis, however, mullite has very low activity in zeolite synthesizing [13]. Izidoro et al. [14] have also demonstrated the formation of zeolite using five different Brazilian CFA under hydrothermal treatment. This study also confirmed that precursor material comprising more than 70% of SiO_2 and Al_2O_3 leads to the greatest ion-exchange capability. The obtained findings suggest that valuable elements of CFA play a crucial role in the synthesis of zeolites. The zeolite synthesis varies with different variables such as alkaline condition and Si/Al molar ratio, which are also discussed by Inada et al. [15]. High silica-rich CFA with low alkaline concentration can produce zeolite P, where the addition of Si takes a major role in zeolite P formation. The zeolite P class has the typical oxide formula: $\text{M}_2/n.\text{O}.\text{Al}_2\text{O}_3.1.80\text{--}5.00\text{SiO}_2.5\text{H}_2\text{O}$ where M is an n-valent cation, normally an alkali metal. Zeolite type P is utilized to create environmentally friendly detergents because they have superior water-softening capabilities than zeolite type A (zeolite type A is synthetic, hydrous, alkali aluminosilicates, with exceptionally advantageous structural channels and cavities. As a selective sorbent for drying gases and liquids, the cubic framework structure is often utilized.). These findings conclude that the formation of a type of zeolite and its physiochemical properties could be influenced by added Si or Al source. However, crystallization time and temperature have a potential effect on zeolite shape and durability.

2.2.2 Two-Step Hydrothermal Synthesis Technique

In 1999, Hollman et al. [16] first synthesized pure zeolite from CFA via a two-step synthesis method. To form pure crystalline zeolite (> 99%) from CFA the extracted Si was blended with an aqueous NaOH solution. Furthermore, the resulting solid residue can be converted into zeolite through the conventional method. Pure zeolite exhibits a high cation-exchange capacity (CEC) toward wastewater treatment that is two times of zeolite-CFA blended material. The effect of drainage during synthesis and the high temperature on CFA-based zeolite synthesis has been reported by Moriyama et al. [17]. They also revealed that the best synthesis was carried out with 0.88–1.10 L/Kg of liquid/solid and 2.5–3.5 mol/L of NaOH concentration. The zeolite produced in the pilot plant using the conventional method showed a higher CEC. The effects of NaOH molar concentration on the dissolution of silica during zeolite synthesis through the conventional hydrothermal route has been deliberated by Wang et al. [18]. This study also revealed that narrow-shape zeolite A can be obtained by increasing NaOH concentration during a small crystallization period. Czuma et al. [19] have found zeolite type-P1 of chemical formula $(\text{Na}_6\text{Al}_6\text{Si}_{10}\text{O}_{32}.12\text{H}_2\text{O})$ from waste fly ash through a two-step hydrothermal method. They employed the hydrothermally synthesized zeolite for SO_2 capture from exhaust gases. The highest sorption capacity for SO_2 was found to be 0.45 mmol/g over the synthesized zeolite P1. It can be seen from the above section that two-step hydrothermally synthesized zeolite can be utilized for hazardous gas removal and other environmental remediations. The process has advantages in that it shortens the treatment time, consumes less electrical energy, and lowers the preparation cost of zeolite. However, this process can be

modified by adjusting the fly ash and NaOH concentrations. In addition, changing the temperature range can also be employed to examine any changes in morphological and crystalline behavior.

2.2.3 Fusion-Facilitated Alkaline Hydrothermal Treatment

To enhance the quality and yield of zeolitic materials the alkaline fusion-assisted hydrothermal synthesis method was employed. Two main parts exist in this method; first, the alkali material, and second, the melted mixture.

In 1993 Shigemoto et al. [20] first revealed the zeolite X synthesis through the fusion-based hydrothermal method in the presence of alkali material. The zeolite was produced with 62% crystallinity. In the year of 1996, Berggaut and Singer [21] demonstrated the mechanism involved in this method. They also reported that the reaction carried out at (170–180) °C is endothermic and produces sodium aluminosilicate. Also, they proposed that zeolite can be converted further by mixing water with aluminosilicate gel. It was also proposed that adding a little amount of water to the CFA and NaOH mixture can produce zeolite before the melting process. The CFA conversion and types of zeolite formation that were affected by NaOH concentration were investigated by Rayalu et al. [22]. The researchers also invented that, a tiny amount of aluminum silicate was extracted from CFA by adding a lower concentration of NaOH, which was not favorable to the zeolite synthesis. The double alkali method for zeolite synthesis is highly operative rather than the single alkali approach [23]. Sivalingam and Sen [24] prepared Zeolite X which is characterized by the formula $\text{NaAlSi}_{1.23}\text{O}_{4.46}\cdot 3.07\text{H}_2\text{O}$. It comprises 76% crystallinity with 88% yield. The adsorption capacity of crystal violet ($\text{C}_{25}\text{N}_3\text{H}_{30}\text{Cl}$) which is a triarylmethane dye was 99.62%, over synthesized zeolite, which is relatively better than commercial zeolite X. On the contrary, Gao et al. [25] prepared value-added zeolite-carbon composite from synthetic CFA waste using a combination process of calcination-carbonization under an elevated temperature ranging from (600–850) °C followed by the conventional hydrothermal method. The resulting composite material exhibited a significant adsorptive capacity toward electromagnetic waves and water vapors, which suggested that the prepared composite can be employed as a building material for flooring or wall with water vapor sorption abilities. As shown in the preceding section, a fusion-based hydrothermal method produces outstanding zeolite characteristics, such as large surface area and crystallinity. However, it's also noticeable that the higher temperature required in this technique may consume higher electricity costs. As a consequence, more research is needed to upgrade the conventional techniques in zeolite synthesis.

2.2.4 Microwave-Assisted Method

Zeolite synthesis from CFA raw waste using microwave-assisted hydrothermal treatment has been demonstrated by Querol et al. [26]. The microwave-facilitated

hydrothermal process can produce zeolite with the same quality in a shortening time range compared with the traditional hydrothermal treatment. It was also evidenced by Tanaka et al. [27] that, single-phase zeolite A—where zeolite A belongs to the aluminosilicate molecular sieves family, and characterized by the formula $\text{NaAlSi}_{1.1}\text{O}_{4.2}\cdot 2.25\text{H}_2\text{O}$ was derived from CFA as a silica source through this technique which takes a short crystallization time. Inada et al. [28] reported that the yield percent of zeolite synthesized from fly ash was highly affected by microwave irradiation and the corresponding mechanism was investigated during zeolite crystallization. They revealed that the zeolitization process was improved effectively by the microwave irradiation method. The authors also showed that zeolite crystal growth can be inhibited by successive microwave radiation, and zeolite formation benefited from early microwave heating. In this regard, Salman et al. [29] initiated zeolite A synthesis through a microwave treatment strategy. The study also suggested that the obtained Linde-type zeolite A has a higher crystalline phase and sorption capacity toward industrial wastewater treatment. Anuwattana et al. [30] synthesized ZSM-5 from acid-treated cupola slag, carried out in a conventional microwave-assisted hydrothermal process at (130–200) °C. The enhancement rate of ZSM-5 that was noticed at 150 °C under microwave heating methodology was 4 times higher than conventional heating. Zeolite ZSM-5 having a particle diameter of 3 μm when treated with conventional heating treatment, while microwave crystallization produced ZSM-5 particles of diameter 0.3 μm. In a recent study, Inada et al. [28] obtained P1-type zeolite from CFA as starting material using the microwave (MW) irradiation method. The obtained zeolite was used for $(\text{NH}_4)^+$ removal where the maximum cation-exchange capacity (CEC) was estimated to be 200 meq/100 g. This section indicates that using the microwave method to synthesize zeolites, the activation time is considerably decreased while the NaOH molarity and Si/Al ratio remain within the necessary range.

2.2.5 Fusion-Assisted Ultrasonic (US) Hydrothermal Treatment

Ultrasonic irradiation treatment enhances the Si and Al dissolution factor to form amorphous aluminosilicate that has a great impact on Si-O-Al bond strength at solid particle-gel phase interphase, increases the degree of crystallinity, and improves the polycondensation reaction rate [31]. Hydroxy sodalite (HSOD) like material was synthesized from silica-rich coal fly ash (CFA) as source material using an ultrasound-assisted hydrothermal method. Meanwhile, Musyoka et al. [32] demonstrated zeolite A synthesis from silica as a starting material by ultrasound-facilitated hydrothermal treatment. They also tried to report that, ultrasound energy before the hydrothermal method influences zeolite phase purity, degree of crystallinity, and decreases the new phase formation time from 2 to 1 h. Bukhari et al. [33] recognized zeolite synthesis under sonication using coal fly ash extracted chemically, and also investigated the process parameters involved in the direct ultrasound irradiation method in the reacting mixture.

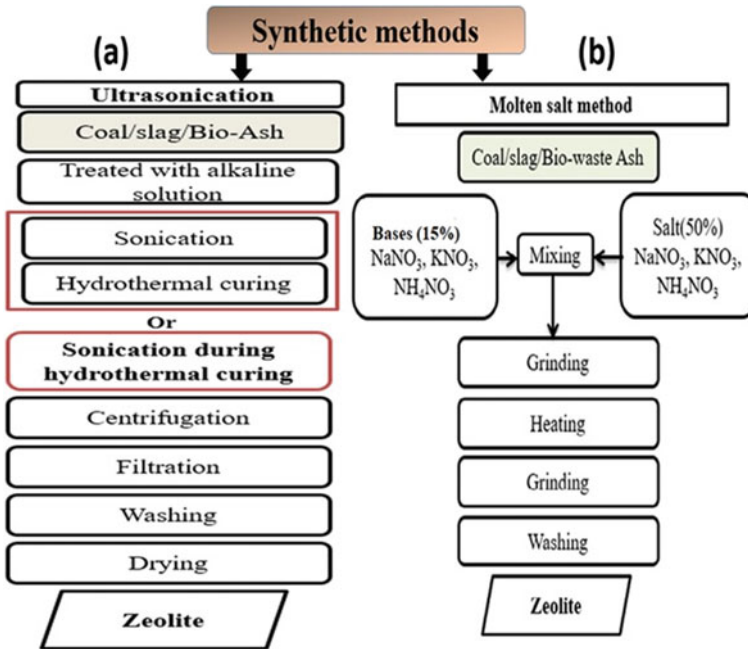


Fig. 2 Synthetic methods of zeolite. **a** The ultrasonic treatment for zeolite synthesis and **b** the steps involved in the molten-salt method

Dere et al. [34] focused on alkali fusion-assisted ultrasonic treatment for the synthesis of zeolite type-X using CFA as a waste source. The presence of ultrasonic energy in the ultrasonic coupled hydrothermal method reduced the treatment time from 24 to 1 h and was also explored. The novel approach also revealed that the resulted zeolite X has a CEC of 495.33 meq/100 g which is very similar to the commercially available zeolite X. Vaičiukyniene et al. [35] and co-workers have depicted the benefit of using ultrasonic treatment strategy on fabricated zeolite A using by-product silica as precursor material. In this study, the reaction was carried out at room temperature using a 20 kHz ultrasound signal to obtain zeolite type A. This section reported zeolite production through fusion-facilitated US treatment. However, zeolite synthesis via fusion with low temperature and high pressure irrespective of size and shape has not been studied yet. Hence, the researchers can exploit this gap (Fig. 2).

2.2.6 Molten-Salt Method

Park et al. [36] have demonstrated the formation of the zeolite-like material using mineral wastes under molten environments without adding any water. Usually, the solid mixture comprising 0.7 g fly ash, 0.3 g base, and 1 g salts is ground into

a fine dust. Therefore, the powder was heated at $(350 \pm 5) ^\circ\text{C}$ to get a molten state for different synthesis periods. Then the molten sample was taken out and kept at room temperature for cooling, and the resulting conglomerated product was washed with 50 ml of deionized water for seven times to extract unwanted bases and salts. In this typical experiment NaOH, KOH, or NH_4F were appointed as bases and KNO_3 , NaNO_3 , or NH_4NO_3 as salts. Employing this technique they prepared hydroxyl-sodalite zeolite with different CEC of 206 and 144 meq/100 g, respectively. The above survey conveyed that a high concentration of salt is required in zeolite synthesis. Therefore, further study may be carried out on various types of zeolite synthesis by reducing the salt amount.

2.2.7 Microwave (MW) Hydrothermal Treatment with Pulverization Process

Fukasawa et al. [37] demonstrated the zeolite synthesis with NaOH-composed fly ash under a hydrothermal synthesis process followed by microwave heating at $100 ^\circ\text{C}$. In this typical experiment, 2 g fly ash and 2 M of aqueous NaOH solution were taken as precursor materials to prepare the slurry. Thereafter, the obtained slurry was heated at an elevated temperature by microwaves. Then, the amount of 60 g zirconia beads having a particle diameter of 2 mm were successfully mixed with processed slurry to pulverize the fly ash. The zeolite synthesis temperature was fixed at $100 ^\circ\text{C}$ with a proportional–integral–derivative (PID) controller equipped with a microwave heating reactor. The thermal treatment continued for 4 h at atmospheric pressure ($1.013 \times 10^5 \text{ Pa}$) with 100 rpm rotational speed. The influence of zirconia beds in the pulverization process for zeolite fabrication was also brightly investigated. Four experimental conditions in zeolitization are as follows: (i) non-pulverized: the produced slurry was treated under hydrothermal treatment for 4 h without the addition of beads; (ii) pre-pulverized: here the slurry was pulverized for 4 h with beads, followed by filtration to remove the beads from slurry and then the filtrated slurry was treated with the conventional hydrothermal reaction for 4 h; (iii) pulverized: in this process, zirconia beds composed with slurry and treated hydrothermally; and (iv) partially pulverized: for the first hour the beads assisted slurry was hydrothermally treated, once the hydrothermal reaction is over, the beads were extracted by sieve facilitated filtration process, and the filtrated slurry was sent to hydrothermal treatment for 3 h. The hydrothermal treatment period was set at 4 h for the aforementioned four conditions. The slurry was cooled down at room temperature after hydrothermal treatment. Using a Buchner funnel the resulted powder was segregated from the hydrothermal solution, washed with distilled water, and dried at $120 ^\circ\text{C}$ for overnight. It is evident from the above section that the zeolite was produced under high pressure followed by rigorous treatment, therefore, the synthesis time was enhanced. Hence, attention needs to be paid to zeolite synthesis with minimal pressure and temperature that reduces the synthesis time for zeolite production.

2.2.8 Ball Milling, Solvent-Free Synthesis

Zeolites like mordenite and ZSM-5 were approached through template-free and solvent-free methods without adding any crystal seed. The entire reaction was performed with a mechanochemical pathway, i.e. ball milling process. In this typical experiment, 5.03 mmol $\text{Na}_2\text{SiO}_3 \cdot 9\text{H}_2\text{O}$, 24 mmol SiO_2 , 0.98 mmol $\text{Al}_2(\text{SO}_4)_3 \cdot 18\text{H}_2\text{O}$, and NaOH were used as silica, alumina source, and an additive. The above solid mixture was finely ground by a ball mill at a high rotational speed of 1400 rpm for 25 min and 50 min. Thereafter, the solid mixture was placed into a Teflon-lined autoclave, where the hydrothermal reaction would take place at 180 °C for 24, 48, and 72 h. To summarize this study, the solid mixture was mixed physically without using a grinder. The product sample was washed frequently using H_2O followed by drying at 80 °C to remove the by-product salts. This synthesis study has also explored the effects of Si, Al, and Na ratios, alkaline concentration, heating, and grinding time on the final product in zeolitization process. The prepared samples were kept at 550 °C for 6 h to investigate the thermal stability. To determine the zeolite phase effect the ratio of precursor materials Si and Al was adjusted. Consequently, the ball milling process revealed that the ZSM-5 and mordenite zeolites were formed without any organic template at 50 min. The significant role of Na has been demonstrated and it was confirmed that a higher molar ratio of $\text{Na}_2\text{O}/\text{Al}_2\text{O}_3$ in the range 7–9 formed a crystalline phase, whereas an amorphous phase was found at a lower ratio [38]. The ball milling process has several advantages and produces a variety of zeolite structures with diverse properties when compared to other treatments. As a result, more research may be conducted on the various zeolite synthesis methods that use a solvent-free ball milling process. Figure 3 depicts the solvent-free ball milling synthesis technique for zeolite production.

As mentioned before, this chapter focuses on zeolite preparation from Si and Al-rich waste sources such as coal fly ash (CFA), blast furnace slag (BFS), bagasse fly ash (BFA), and others using various methods. From the chapter, it was also clearly seen that numerous studies have been focused on synthetic waste-based zeolite production through conventional techniques such as hydrothermal or fusion-facilitated hydrothermal treatment. However, a few research was carried out on the preparation of synthetic waste-based zeolite by novel methods like microwave (MW) and ultrasonic (US) irradiation, solvent-free ball milling synthetic techniques that offer more advantages rather than other traditional techniques which required high temperature and time. Hence, these techniques are not an economically acceptable option for zeolite synthesis. Hence, future research can be focused on zeolite fabrication from waste with a low-cost energy technique to minimize the zeolite cost. So, it needs to be paid attention to the advanced zeolite synthesis and potential applications for industrial scaling up. The major advantages and disadvantages of all methods are summarized in Table 1.

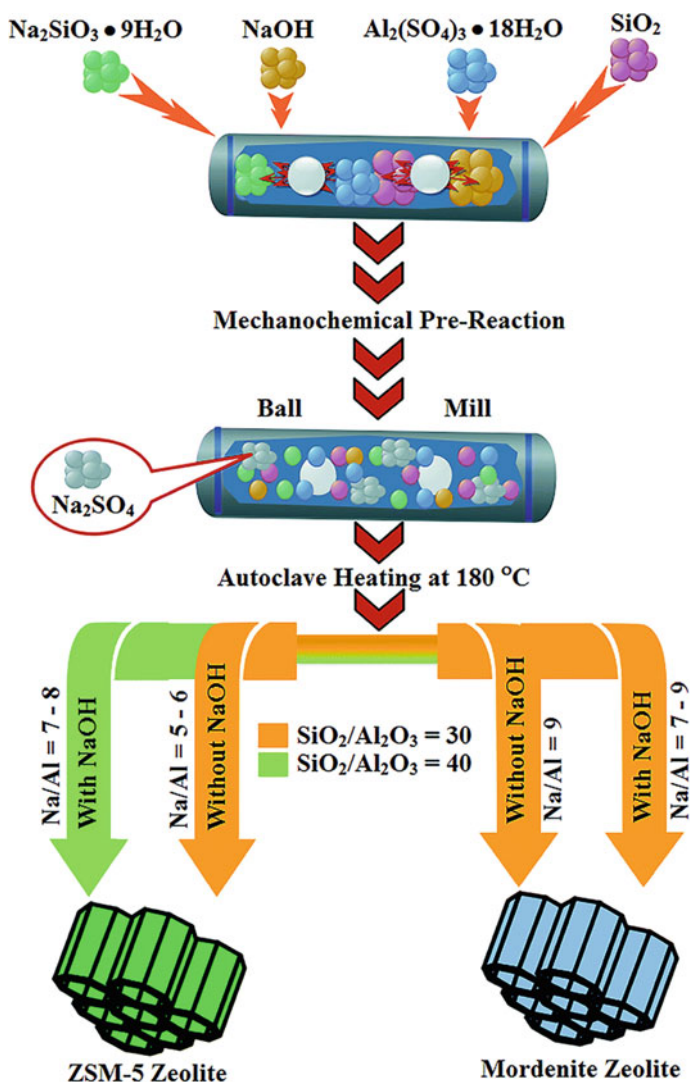


Fig. 3 The solvent-free ball milling synthesis methodology for zeolite formation. Reproduced from Narayan et al. [39] under the terms and conditions of the Creative Commons Attribution-NonCommercial 3.0 Unported License (CC BY-NC 3.0). <https://creativecommons.org/licenses/by-nc/3.0/>

Table 1 Advantages and disadvantages of zeolite synthesis techniques

| Zeolite synthesis technique | Advantages | Disadvantages/limitations |
|--|---|---|
| Direct hydrothermal method | <ul style="list-style-type: none"> Parameters have effects on the zeolite synthesis in order to achieve high crystallinity, and homogeneity | <ul style="list-style-type: none"> Less purity present in the obtained zeolite Exhibits less Al dissolution A time-consuming process, and requires high temperatures for zeolite synthesis |
| Two-step hydrothermal method | <ul style="list-style-type: none"> Enhanced degree of crystallinity, and phase purity of the final product | <ul style="list-style-type: none"> High operational cost and low selectivity of pure zeolite are major disadvantages |
| Alkaline fusion-assisted hydrothermal method | <ul style="list-style-type: none"> Allows a substantial amount of silicate and aluminosilicate, which enhances the zeolite yield | <ul style="list-style-type: none"> Energy squandering technique |
| Microwave (MW)-assisted Method | <ul style="list-style-type: none"> Accelerates the dissolution rate of SiO₂ and Al₂O₃ Reduces crystallization period Excellent selectivity toward zeolite formation | <ul style="list-style-type: none"> Industrial scaling up for zeolite production is a major drawback |
| Fusion-assisted ultrasonic (US) hydrothermal treatment | <ul style="list-style-type: none"> Better crystallinity of zeolite can be achieved Enhanced nucleation rate, resulting in a higher crystal growth rate Less time taking synthesis technique | <ul style="list-style-type: none"> Zeolite production on an industrial scale is a major disadvantage |
| Molten-salt method | <ul style="list-style-type: none"> Less amount of NaOH and KOH is required A significant temperature is required for zeolite fabrication The technique exhibits low elemental loss Obtained zeolites have high purity, low pH value, and high alkali contents | <ul style="list-style-type: none"> Salt occlusion occurred during the process that may interrupt the adsorption process |
| Microwave (MW) hydrothermal treatment with pulverization process | <ul style="list-style-type: none"> Reduces the synthesis time | |
| Ball milling, solvent-free synthesis | <ul style="list-style-type: none"> Requires negligible quantity of water Several zeolite structures can be generated | <ul style="list-style-type: none"> Milling friction may enhance the local temperature |

3 Zeolite Properties

3.1 Zeolite Structure

Zeolites are inorganic, crystalline, microporous-hydrated aluminosilicate minerals constructed from interlinked tetrahedrons of alumina (AlO_4) and silica (SiO_4). In this three-dimensional tetrahedral framework, oxygen is shared with two tetrahedral atoms (T-O-T) mainly Al and Si. Figure 4 represents the steps involved in forming secondary building units (SBUs) from a tetrahedral primary unit in the LTA (zeolite A) formation.

Whereas T refers to Al and Si atoms in the zeolite cage, it has also been reported that the presence of Al^{3+} and Si^{4+} in the zeolite framework creates a negative charge that will be compensated by balancing cation-charge in additional framework locations, positioned at zeolite pores or cages of the structure. In the zeolite network, the tetrahedron has been considered the primary building unit, located in secondary building units (SBUs), having up to 16 T-atoms (Fig. 4).

3.2 Adsorption and Ion-Exchange Phenomena

The transformation and distribution of solutes between particles and a fluid phase interface will occur in both adsorption and ion-exchange phenomena. Two types of adsorbents exist, synthetic and natural, with crystalline or amorphous phases. Several studies have been involved in the preparation of activated carbon, silica gel, activated alumina, and molecular sieve-supported zeolite synthesis for commercial or industrial applications.

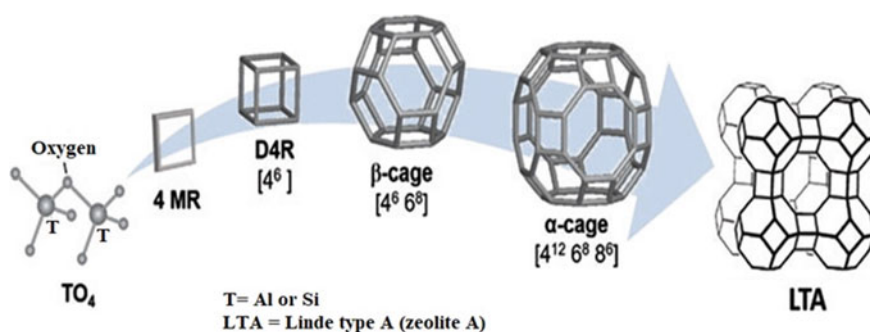


Fig. 4 The steps involved in the formation of secondary building units (SBUs) from a tetrahedral primary unit in the LTA (zeolite A) formation. Reproduced with permission from Schwanke et al. [40]. Copyright (2019), Springer Nature

In general, a polymeric solid can diffuse as the ion exchange takes place in the fluid phase. In ion exchange, ions of positive charge in some cases (cations) and negative charge in others (anions) from the fluid replace dissimilar ions of the same charge initially in the solid. Bound functional groups of different charges were shown by the ion exchanger. The bound sulfonic acid groups; frequently, phosphonic, carboxylic, phosphinic, and so on belong to cation-exchange resins, appearing in an ion exchanger [41].

3.2.1 Adsorption Phenomena in Zeolites

In general, adsorption phenomena take place at liquid–liquid interfaces, gas–liquid interfaces, and detergency, as in foam fractionation with the depletion of reactant molecules.

Liquid–solid and gas–solid interfaces are the common adsorption mechanism, where selective diffusion of solute molecules will be conducted between the fluid–solid phases. Highly porous solids with a large internal area per unit volume allow the solute molecules to pass through the pore channel where adsorption phenomena will take place. The adsorption process is classified into two types, namely physical adsorption and chemical adsorption. The physisorption or physical adsorption process is caused by the intermolecular force of adsorbates and adsorbents molecules that are also known as the van der Waals force, on the contrary, chemisorption or chemical adsorption is achieved by substantial sharing of electrons between adsorbate and adsorbent surface to form a covalent or ionic bond [42]. For wastewater treatment, adsorption techniques have become more popular in recent decades due to their efficient pollutant removal capacity. Especially, most of the adsorbents are inexpensive and readily available. The advantages of the adsorption process are as follows: clean operation, sludge-free, and perfect pollutants removal from diluted waste solution.

For adsorption treatment, zeolite is the most prominent inorganic adsorbent. Attractive properties like high cation-exchange selectivity, high resistance to ionizing radiation, temperature, and outstanding affinity to the environment turn it into the most valuable material. Hence, in modern technologies zeolites are extensively utilized as a molecular sieve, and particularly as catalysts and adsorbents. In addition, a modified zeolite structure could be employed to obtain specific performance and excellent cation uptake capacity in water processing through an ion-exchange mechanism. Zeolite mineral, specifically clinoptilolite has conducive ion-exchange behavior toward nuclear wastewater, acid mine drainage wastewater, industrial and municipal wastewater treatment which contains certain cations [43].

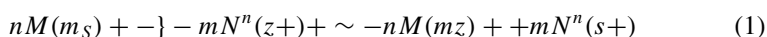
3.2.2 Ion-Exchange Phenomena in Zeolites

Ion-exchange phenomena depend on aqueous solution concentration, solid and aqueous phase composition.

Generally, ion-exchange equilibrium takes place between two or more phases. The liquid is one of them which interchange two or more cations or anions, bounded strongly with each phase. The term ion-exchange capacity (meq/g) is defined by the number of ions exchanged by a solid adsorbent which also depends on the exchanger's skeletal characteristics.

Zeolite shows a negative charge due to the presence of tetrahedron elements like Al in a three-dimensional framework. With the presence of the alkaline medium, the aluminum-rich synthesized zeolite contains a high amount of alkaline cations usually Na^+ , which is a charge-balancing ion that can be exchanged by adding other cations under ion-exchange phenomena. A maximum cation-exchange capacity can be possessed by aluminium-rich ($\text{Si}/\text{Al} = 1$) zeolite. Commercial or synthetic zeolites such as zeolite A, zeolite X, zeolite P have a notably different crystalline structure and pore size which leads to a great impact on selective removal of Ca, Mg, or both. It was also committed that small pores and window (0.42 and 0.3 nm), content zeolite A and P has a good affinity toward Ca removal, but less uptake capacity for Mg. It was also demonstrated that it will require a relatively large pore (0.75 nm) aided zeolite X for Mg removal [44]. The mixture of different zeolites is used when waste or synthetic solution contains both cations.

The cation-exchange reaction can be expressed by the following Eqn.



In this equation m and n denote valances in exchanging cation, where subscripts s and z and M and N are zeolite and solution phase, respectively. Table 2 illustrates various types of synthesized zeolites and their several characteristics.

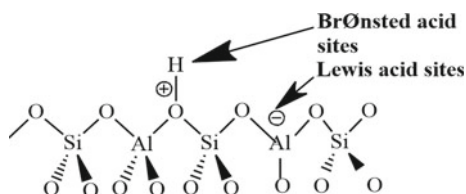
3.2.3 Cations and Acidity in Zeolites

The zeolite framework consists of Al^{3+} and Si^{4+} ions. The units possess a net charge of -1 by replacing Al^{3+} ions. This negative charge will be neutralized by a cation, for example, Na^+ . In a zeolite structure, the number of alumina tetrahedrons is equal to the number of cations. Theoretically, the zeolite becomes a gigantic polyacid (forming H-X, H-ZSM-5) when Na^+ ions are replaced by H^+ ions. Figure 5 shows the structure of an acidic site with H^+ on a Si-O-Al bridge. The Bronsted acid site in zeolite structure is known as a proton donor and the acid strength relies on the number of additional aluminum ions in the surroundings and the proton's local environment.

Table 2 Represents the synthesized typical zeolites and their various characteristics with the chemical formula

| Sl. no. | Zeolite types | Chemical formula | Characteristics | | | | | References |
|---------|------------------|--|------------------|-------------|-----------------|------------------------------|---------------------|--------------|
| | | | Si/Al mole ratio | pH in water | CEC (meq/100 g) | Thermal stability (Relative) | Textural properties | |
| 1 | Zeolite A | $\text{NaAlSi}_3\text{O}_8 \cdot 2.25\text{H}_2\text{O}$ | 1.00 | 10.05 | 556 | High | Cubical | [45, 45, 45] |
| 2 | Zeolite X | $\text{NaAlSi}_3\text{O}_8 \cdot 3.07\text{H}_2\text{O}$ | 1.24 | 9.84 | 440 | High | Octahedral | [45–47] |
| 3 | Zeolite Y | $\text{NaAlSi}_3\text{O}_8 \cdot 4.46\text{H}_2\text{O}$ | 2.66 | 7.41 | 240 | High | Octahedral | [45–47] |
| 4 | Zeolite 4A | $\text{Na}_{12}\text{Al}_4\text{Si}_4\text{O}_{20} \cdot 12\text{H}_2\text{O}$ | 1.00 | 10.05 | 556 | High | Cubical | [45–47] |
| 5 | Zeolite P1 | $\text{Na}_6\text{Al}_6\text{Si}_6\text{O}_{32} \cdot 12\text{H}_2\text{O}$ | 1.67 | 10.08 | 429 | High | Diamond/cubical | [45–48] |
| 6 | Phillipsite | $\text{K}_2\text{Al}_2\text{Si}_3\text{O}_{10} \cdot \text{H}_2\text{O}$ | 1.65–2.23 | 13.3–13.7 | – | Medium | Rod shape | [49] |
| 7 | K-Chabazite | $\text{K}_2\text{Al}_2\text{Si}_3\text{O}_{10} \cdot \text{H}_2\text{O}$ | 1.43–4.18 | – | – | High | Rhombohedral | [47] |
| 8 | Zeolite F linde | $\text{KAlSi}_3\text{O}_8 \cdot 1.5\text{H}_2\text{O}$ | 3.3 | – | – | High | Sphere type | [48] |
| 9 | Analcime | $\text{NaAlSi}_2\text{O}_6 \cdot \text{H}_2\text{O}$ | >1 | – | – | High | Cubic | [46] |
| 10 | Hydroxy sodalite | $\text{Na}_{1.08}\text{Al}_2\text{Si}_{1.68}\text{O}_{7.44} \cdot 1.8\text{H}_2\text{O}$ | 1.1–1.9 | – | – | High | Coral like | [50] |

Fig. 5 Structure of a solid acid where H^+ ion is placed on the Si-O-Al bridge



4 Preparation of Zeolites from Wastes

4.1 Industrial or Plant Waste

4.1.1 Coal Fly Ash (CFA)

Commonly, coal is classified based on carbon content: hard coal (anthracite, bituminous) forms 53% of total coal, and low-grade coal forms 47% (lignite and sub-bituminous) of total coal reserves. Figure 6 illustrates the coal fly ash (CFA), emitted from a power plant industry [51]. From a survey, 5–20% of ash can be produced from the coal burn industry, which comprises CFA (85–95%), and coal bottom ash (CBA) (5–15 wt.%). Usually, CFA is produced in a coal combustion reactor in solid or wet form. A large number of research articles reviews on CFA, types of CFA, their characteristics, composition, and zeolite have been published including a deep review on CFA-based zeolite and nanoporous zeolite synthesis for waste materials and hazardous gaseous elements removal, Querol et al. [52].

Belviso et al. [53] invented a new conventional route, i.e. ultrasonication process to prepare zeolite X with a nominal temperature (25 °C). The crystallinity and phase purity of the resulted zeolite influenced by ultrasonic treatment was confirmed from x-ray diffraction (XRD) and scanning electron microscope (SEM) analysis. Cardoso et al. [54] prepared zeolite P1 from purified silica as starting material using CFA

Fig. 6 The coal fly ash (CFA). Reproduced with permission from Hui et al. [51]. Copyright (2021), Elsevier



as a waste source in a high-pressurized reactor during the hydrothermal process. The prepared adsorbent showed a high removal efficiency toward heavy metals such as copper, nickel, arsenic, and a significant amount of ammonium. Using the same treatment methodology Prasad et al. [55] derived NaA zeolite from CFA. Many authors have also synthesized spherical and smooth zeolite X that can be used in the adsorption process using NaOH-facilitated fly ash. Bandura et al. [41] synthesized Na-P1zeolite using Si and Al-rich CFA using the conventional hydrothermal route, and the BTX sorption from the gas mixture was performed over fabricated zeolite. Murayama et al. [42] have also utilized the same strategy for zeolite synthesis. Selective Y-type zeolite was derived from CFA as the waste source using conventional hydrothermal treatment at 50 °C for 48 h. Zhao et al. [43] also tried to investigate the effect of synthesis parameters like aging time, temperature, Si/Al ratio, and crystalline structure on CEC capacity with synthesized zeolite.

4.1.2 Iron Steel Industry Slag or Blast Furnace Slag (BFS)

Any steel industry emits a huge amount of slag that comprises several inorganic oxides such as CaO, Al₂O₃, SiO₂, P₂O₅, etc. Out of them Al₂O₃ and SiO₂ are very essential compounds in the zeolite-making process. Many research articles have elucidated the synthesis process and type of zeolite formation using various steel waste sources namely BFS, Linz-Donawitz (LD)-slag, and electric arc furnace slag (EAFS) [56]. Liu et al. [57] synthesized spherical crystal-shaped hydroxycancrinite zeolite using BFS as silica–alumina source under hydrothermal treatment and the affecting parameters such as alkaline dose, crystallization temperature, and time were also observed in this study. Synthesis of Zeolite types A and X was reported by Kuwahara et al. [44] from hazardous solid waste source BFS. An excellent selectivity toward water adsorption of 247 and 333 mg/g was reported over prepared zeolites, respectively. Using BFS highly riched in silica and alumina Liu et al. [44] derived zeolite P under hydrothermal treatment to capture cations from wastewater. Kotoulas and his team examined the adsorbed NH⁴⁺ recovery using a desorption column over 0.71–1.0 mm-sized granular zeolite minerals [58]. The investigation also revealed that the highest ammonium recovery was found to be 4.39%. Nevertheless, it is well known that the zeolite's uptake capacity cannot be entirely recovered in operating loops. In contrast, Murakami et al. [59] attempted to prepare zeolite A from BFS after calcium extraction. The zeolite synthesis was carried out under hydrothermal treatment at high temperatures. They also suggested that the XRD pattern confirmed the attainment of Na-P1 phases at the Si/Al ratio of 5/3. Li et al. [60] tried to synthesize hydroxy sodalite (HSOD) and NaA zeolite from electric arc furnace (EAF) slag as a precursor. The influence of SiO₂/Al₂O₃ molar ratio, H₂O/Na₂O molar ratio, hydrothermal temperature, and time on crystallization, and phase purity was also invented systematically.

The preceding section elaborates on specific zeolite production using CFA and steel slag as initial raw materials using standard methods. Therefore, it's possible that different zeolite structures can be created using existing methods to utilize synthetic solid wastes.

4.2 Biomass Ash

4.2.1 Rice Husk Ash (RHA)

In the earth's crust silica is the most abundant inorganic oxide. Nowadays silica is synthesized in a predominant order for its use toward technological applications which makes it a more valuable chemical compound. Rice husk sawdust is an agricultural residue that can be converted into valuable end products. Silica is the most proficient chemical that can be extracted from rice husk ash (RHA) using the solvent extraction method (Fig. 7) at elevated temperature [61]. Londeree et al. [62] proposed zeolite A synthesis using rice husk ash as the starting material. NaOH comprised fusion reaction was carried out at 100 °C. The effecting parameters like NaOH addition, reaction time, and temperature, Si/Al ratio to zeolite crystallization were also studied. The hydrothermal reaction was employed under the following reaction conditions: NaOH concentration 2–6M; Si/Al ratio = 1.7–2.8; temperature = (50–80) °C; reaction time = (0–48) h. Several studies have reported the silica extraction from RHA by acid leaching treatment to avail the pure silica that can be used in the zeolite-making process.

Wajima et al. [63] used acid-leached silica to form NaA zeolite under hydrothermal reaction. The influence of the Si/Al ratio was observed and at fixed Si/Al ratio the

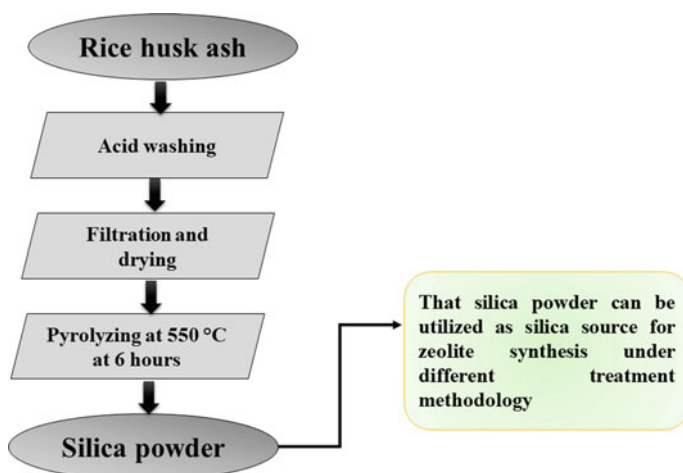


Fig. 7 Silica extraction from rice husk using the solvent extraction method

zeolite crystallinity was high, in the range of 98–100%. Crystalline NaA zeolite was derived from RHA for potential adsorbent to remove fluoride from aqueous solution, as reported by Mukherjee et al. [64]. The highest adsorption capacity was noted at 22.83 mg/g over fabricated NaA zeolite. Mohamed et al. [65] synthesized highly crystalline zeolite-Y in sodium form (NaY) using an acid-extracted silica source from rice husk. They also observed that NaP type zeolite was formed without aging in zeolitization process. A new type zeolite SUZ-4 was synthesized by Worathanakul et al. [66] from RHA solid waste under conventional hydrothermal treatment with different RHA/Si molar ratios, as following 0:100, 50:50, 70:30, 90:10, and 100:0. It was also confirmed that the zeolite phase increased with an increasing amount of RHA used. Husk et al. [67] demonstrated square tablet type aluminosilicate zeolite L with a particle size of 210 nm, synthesized under hydrothermal treatment from RHA. In addition, the investigation of the synthesis of zeolite type ZSM-5 and ZSM-48 was studied at different reaction conditions using extracted silica sources from rice husk [18, 68]. The crystal growth of ZSM-5 and ZSM-48 zeolites were also evaluated with RHA/Si ratio, crystallizing time, and temperature. On the contrary, Zhang et al. [69] derived ZSM-5 zeolite from high silica content rice husk by solvent-free solid-phase conversion method to enhance its economic value and recovery rate. A comparative study of zeolite synthesis also has been performed by the authors. The specific surface area of the resulting zeolite from hydrothermal synthesis was 320 m²/g with a sharp crystalline shape, comparable to the solid-phase conversion method (304 m²/g).

4.2.2 Palm Oil Mill Fly Ash (POMFA)

The palm oil industry generates a huge amount of solid palm oil mill fly ash (POMFA), as shown in Fig. 8, which contains around 39% silica. By alkaline extraction of fly ash followed by sol-gel precipitation method synthetic amorphous silica (SAS) can be synthesized. The POMFA comprises 39% silica, 30% carbon, and other inorganic chemicals, hence silica can be extracted from [68]. Davina et al. [70] confirmed Na-P1 zeolite after alkali extraction assisted sol-gel method using raw fly ash waste as silica source at 120 °C for 8 h. The zeolite synthesis was investigated with different Si/Al ratios of 8 and 11. An 85% yield of zeolite-13X has been prepared from POMFA using a conventional hydrothermal route with NaOH-fused fly ash at a high temperature of 600 °C. Acid activation was performed with prepared zeolite-13X in order to increase CO₂ uptake capacity. The prepared zeolite showed a CO₂ adsorption capacity of 6.42 mol CO₂/kg at a pressure and temperature of 403 kPa and 32 °C, respectively [71]. Utama et al. [72] produced high purity silica as zeolite synthesis starting material by sol-gel precipitation method using POMFA as a waste source. Zeolite ZSM-5 has been successfully prepared using highly pure extracted silica and the crystalline phase was confirmed by XRD analysis. Nurdin et al. [73] proposed zeolite formation from silica and alumina rich POMFA using ultrasound irradiation treatment methodology at 80 °C.

Fig. 8 Palm oil mill fly ash (POMFA). Reproduced with permission from Tangchirapat et al. [74]. Copyright (2007), Elsevier



4.2.3 Sugarcane Bagasse Fly Ash (SCBFA)

Sugar mills can produce a large amount of sugarcane bagasse that is a hazardous solid waste. However, a great amount of denominated sugarcane bagasse ash (SCBA) could be produced after the combustion of sugarcane bagasse in boilers, as depicted in Fig. 9. Purnomo et al. [75] demonstrated the synthesis of highly pure and regular Na-A, and Na-X zeolite using low-cost bagasse fly ash (BFA) by fusion-assisted hydrothermal treatment. In every zeolitization treatment, Si/Al ratio is the preliminary step for the required zeolite type that is treated under hydrothermal reaction. Parameters like pH, NaOH concentration, crystallization time, and temperature affect the zeolite synthesis process. Adjusting pH during zeolite synthesis is an important factor because zeolite has a high tendency to dissolve in concentrated alkaline solutions. It's obvious that higher porosity and ion-exchange capacity are influenced by higher purity and smaller size of zeolite particles that are processed under low-temperature hydrothermal synthesis. The synthesis of zeolite type-P was reported by Thuadajj et al. [76] using sugarcane bagasse waste ash using refluxing method with varying NaOH concentration from 2.5 to 3 M at 100 °C. A cation-exchange capacity of 351 meq/100 g was found for the synthesized zeolite P1 sample. Oliveira et al. [77] prepared sugarcane-based zeolite type-A which was used as a low-cost adsorbent for heavy metal removal from wastewater. In this work, the zeolite synthesis was carried out under NaOH-facilitated hydrothermal treatment. They also reported that further addition of Al isopropoxide resulted in enhanced zeolite structure, and phase purity that leads to high Cu^{2+} uptake capacity (142 mg/g). Moisés et al. [78] fabricated zeolite-NaA from bagasse solid waste extracted silica as starting material under hydrothermal process at 80 °C for (72–160) hours.

They also reported that prepared NaA zeolite can be utilized for potential application of ion exchange or adsorption experiments. Different types of synthesized zeolites and their applications in wastewater treatment, as well as environmental remediation, are listed in Table 3.

Fig. 9 Sugarcane bagasse fly ash (SBFA). Reproduced with permission from Batool et al. [79]. Copyright (2020), Springer Nature



Table 3 Various types of zeolites and their application in wastewater treatment as well as environmental remediation

| Sl. no. | Zeolite types | Application | Adsorption capacities | References |
|---------|---------------|----------------------------|-----------------------|------------|
| 1 | Zeolite A | Fe ³⁺ removal | 27.55 mg/g | [4] |
| 2 | Zeolite P1 | NH ⁴⁺ | 2.9 meq/g | [54, 80] |
| 3 | Zeolite 4A | NH ⁴⁺ | 4.5 meq/g | [54] |
| 4 | Zeolite X | Dye removal | 44.07 mg/g | [81] |
| 5 | Zeolite X | Heavy metal removal | 400 meq/100 g | [82] |
| 6 | Zeolite P1 | Pb ²⁺ removal | 400 meq/100 g | [82] |
| 7 | Zeolite P1 | NH ⁴⁺ removal | 20 mg/g | [83] |
| 8 | Zeolite X | NH ⁴⁺ removal | 5 meq/g | [83] |
| 9 | Zeolite P1 | Zn ²⁺ removal | 420 meq/100 g | [84] |
| 10 | Zeolite 4A | As (V) removal | 5.3 meq/g | [84] |
| 11 | Zeolite X | CO ₂ adsorption | 225 mg/g | [85] |
| 12 | Zeolite Y | SO ₂ adsorption | 21.9 mg/g | [86] |
| 13 | Zeolite P1 | p-Xylene removal | 0.58 mg/g | [87] |
| 14 | Sodalite | Hg removal | 75 mg/g | [88] |
| 15 | Zeolite Y | SO ₂ adsorption | 21.9 mg/g | [89] |

According to the literature review, several forms of zeolites derived from biomass ash may be used to minimize wastewater toxicity by eliminating heavy metals such as Ni²⁺, Cu²⁺, Fe³⁺, and others, while also reducing greenhouse gas emissions and lowering health risks. Because of zeolite's interesting properties, it may be feasible to make unique zeolitic minerals from biomass waste, which may be utilized for several purposes ranging from heavy metal removal to biological applications.

5 Zeolite Composites for Environmental Remediation Applications

Due to good removal efficiency, simple operation, and wide adaptability the adsorption method is highly used toward pollutants removal namely, cations, organic dyes, and the harmful gaseous agents from the environment. For this purpose, zeolite has been used as a solid-based adsorbent for wastewater as well as gas separation processes. Nowadays, a group of researchers is developing and investigating the feasibility of zeolite composites as materials for exclusion of heavy metals, dyes, and hazardous gases. Moreover, utilization of industrial slags (e.g. CFA, BFS), and biomass ash (e.g. rice husk, bagasse ash, palm oil mill ash) to produce zeolite and zeolite composite has become a field of great interest, which may lead to environmental remediation and cost estimation on an industrial scale. Therefore, in recent years, the synthesis of the advanced zeolite-composite materials, and their interaction with metals and other harmful components have attracted readers [90]. In our point of view, the combination of microporous zeolite with mesoporous geopolymer (which is non-crystalline, amorphous, and inorganic aluminosilicates that form long-range, covalently linked networks) matrix showed good durability or uniaxial strength, and unique pore size distribution which exhibited a significant impact on toxic ions, dyes, as well as pollutant gas removal for environmental remediation. Therefore, the zeolite-geopolymer matrix may be considered an acceptable candidate for adsorption studies. In a recent study, Minelli et al. [91] prepared a geopolymer-zeolite matrix by incorporating zeolite 13X into an aqueous metakaolin solution. The obtained composite was applied for CO₂ capturing applications.

5.1 Cation Removal

Katsuki et al. [92] derived Na-A or Na-X zeolite/porous carbon composites materials under hydrothermal treatment mixing of NaOH with carbonized rice husk silica followed by NaAlO₂ addition and crystallization process. The crystallization process was carried out at 90 °C for 2 to 6 h varying with SiO₂/Al₂O₃, H₂O/Na₂O, and Na₂O/SiO₂ molar ratios in two-step zeolitization. The NH₄⁺ cation-exchange experiments were investigated on prepared Na-A and Na-X zeolite/porous carbon samples with cation-exchange capacity of 506 meq/100 g and 317 meq/100 g, respectively. A new type of zeolite SUZ-4 was hydrothermally synthesized using bagasse fly ash as a waste feedstock at a SiO₂:Al₂O₃ ratio of 21.2 under autogenous pressure. The SUZ-4/Cu composite material was prepared by incorporating different copper and SUZ-4 zeolite weight ratios of 2.3, 2.5, 3.3, and 5.5 using the aqueous ion-exchange method, as stated by Worathanakul et al. [66]. This work also reveals the effect of the silica/alumina ratio and thermal stability on the synthesized composite materials. The SiO₂/Al₂O₃ ratios of 32.4 and 16.3 indicate the co-existence of mordenite and merlinotie phases in synthesized SUZ-4. In addition, the thermal stability of prepared

samples was tested at various temperatures in the range of (400–700) °C. Katsuki and co-workers [93] prepared a novel ZSM-5 zeolite/porous carbon composite hybrid adsorbent using carbonized rice husk as a silica source under microwave followed by hydrothermal treatment at (140–160) °C. Jha et al. [94] successfully produced Na-X and Na-A zeolites from CFA waste. The CFA was fused at 700 °C with NaOH followed by a hydrothermal reaction in the N₂ atmosphere. Uptake experiments of Ni²⁺, Cu²⁺, Cd²⁺, and Pb²⁺ metals were performed using porous activated carbon-supported Na-X and Na-A zeolites. Synthesized composite showed the highest equilibrium uptake capacity for Pb²⁺ from the aqueous solution of 2.65 mmol/g. By taking the same experimental methodology and raw materials Miyake et al. [95] prepared Na-A and Na-X zeolites. They also elucidated the influence of process parameters such as crystallization temperature, presence and absence of unburned carbon on the chemical conversion of coal fly ash into composite materials in this work. It was investigated that, the crystallization process was effective when activated carbon was added before NaOH fusion treatment for Na-X synthesis, whereas the addition of carbon before hydrothermal treatment was ineffective. A composite of amorphous hydrated iron oxide and synthetic zeolite type P1 (Na P1) was formed, where the zeolite was prepared from coal fly ash. The obtained new composite material Na-P1 zeolite/Fe₂O₃ has shown a greater phosphate uptake capacity of 1543 mmol/kg where synthetic zeolite shows only 287 mmol/kg uptake capacity for the same component [54]. CFA-based synthetic NaA zeolite was used as a support to prepare nano zerovalent iron and nickel bimetallic composite materials for the potential removal of cationic and anionic heavy metals from wastewater. Parameters such as pH, time, temperature, initial concentration, coexisting metals, and loading ability were also studied. The nano zerovalent iron and nickel–zeolite composite (nZVI/Ni@FZA) possessed higher heavy metals uptake capacity than nZVI@FZA and FZA. The adsorption capacity toward Cr (VI) and Cu (II) was 48.31 and 147.06 mg/g, respectively, revealed from adsorption isotherm results. Reduced graphene oxide-zeolite (ZrGO) composite was prepared with synthetic zeolite using fly ash as silica source, according to Soni et al. [96]. The spherical-shaped zeolite-GO composite was prepared under UV exposure ($\lambda = 254$ nm). The highest arsenic removal capacity was found to be 0.04923 mg/g over synthesized zeolite-composite material.

5.2 Dye Removal

Dyes are used extensively in paint, paper, plastic, textile, and tannery industries. It is estimated that 700,000 tons of dyes are produced annually and approximately 15% of total production is discharged into wastewater. In recent years several types of dye removal techniques have been revealed namely oxidation, catalytic degradation, and biodegradation. These processes are not being used in dye removal due to some major drawbacks like synthesis time and high operational cost. Low cost, facile operation, and insensitivity to toxic elements are existing in the adsorption process, which makes it more attractive toward dye removal from wastewater. At present

time dye removal studies by utilizing sludge, fruit peels, and husk-based composite adsorbents are rising effectively [97].

A mesoporous type and high surface area zeolite-activated carbon (Z-AC) composite adsorbent was prepared utilizing palm oil mill ash as a feedstock. The ash was chemically facilitated with NaOH for fusion at high temperatures and hydrothermally treated to get the zeolite. The adsorption study for methylene blue (MB) was performed with synthesized Z-AC composite using batch method varying with temperature from (30–50) °C. The highest uptake capacity of the synthesized composite was 285.71 mg/g at 50 °C for MB [97]. They also proposed the synthesis of palm oil fly ash zeolite/chitosan (Z-AC/C) composite for MB and acid blue 29 (AB29) removal study. The composite material was prepared under hydrothermal treatment with activated NaOH used as a mineralizing agent followed by beading with chitosan. At 50 °C the maximum adsorption capacity of Z-AC/C was 199.20 and 270 mg/g for MB and AB29, respectively. Lin et al. [98] prepared a highly effective zeolite/hydrous iron oxide (ZFA/HIO) and zeolite/hydrous zirconia (ZFA/HZ) composite using CFA-based synthetic zeolite for MB adsorption studies. The adsorption studies were performed at different pH wherever an increasing adsorption trend was observed with pH ranging from 3 to 6. Tauanov et al. [99] derived mesoporous type zeolite Na-P1 having a specific surface area of 246 m²/g from CFA to make zeolite-silver (Ag-ZFA) nanocomposite. The zeolite was prepared by conventional hydrothermal treatment for heavy metal (Hg²⁺) removal from wastewater. The adsorption capacity of the resulting zeolite composite was measured to be 7.69 mg/g. Employing the same treatment methodology, Shui et al. [100] prepared a low-cost novel zeolite-carbon composite with a specific surface area of 660 m²/g for ammonia-nitrogen (NH⁴⁺-N) and MB removal. The uptake capacity for MB and NH⁴⁺-N was 15.49 and 498.61 mg/g, respectively, over the synthesized adsorbent. It was also observed that zeolite-geopolymer has insensitivity toward dye removal. Pimaraska et al. [101] showed the effective adsorptive capacity for dye removal using zeolite and TiO₂ incorporated geopolymer matrix. The presence and absence of TiO₂ in geopolymer composite were examined from the methylene blue adsorption result. They reported that geopolymer composite with 40% TiO₂-zeolite shows 99.1% MB removal, however the removal was decreased to 92.5% with 40% zeolite without TiO₂ doping.

5.3 Harmful-Gas Removal

The zeolite has uniform microporosity, catalytic activity, selective adsorption, and ion-exchange properties that lead to the different catalytic and separation processes. The advanced zeolite composite material synthesis may possess a better thermal, mechanical durability, and adsorption capacity rather than only synthetic zeolite. So, zeolite composites are getting more attraction toward different gas or heavy metal removal studies. In recent years various researchers have explored the use of zeolite

composites for gas adsorption and storage purpose, and thus it is very useful toward environmental remediation applications.

In advanced research, the NaA/glass/mullite and hollow aluminosilicate microsphere composite were revealed by Vereshchagina et al. [102]. The porous composite was synthesized with CFA-derived silica facilitated with 2.5M of NaOH under hydrothermal treatment. At a fixed Si/Al ratio of 1.18 cenosphere zeolite shape was observed by SEM images. They also reported that the prepared composite may be highly effective on He and H₂ gas adsorption. Faghihian et al. [80] demonstrated a new magnetic-zeolite composite type adsorbent prepared by conventional chemical co-precipitation strategy by incorporating Fe²⁺ and Fe³⁺ into zeolite A support. Table 4 presents different zeolite-composite materials and their structural properties.

An alternative activated carbon-zeolite composite (ACZC) material was synthesized under the hydrothermal treatment in which activated carbon was composed in octahedral-shaped zeolite-13X. A comparative adsorption study was established for synthetic zeolite 13X and ACZC toward CO₂/N₂ separation experiment with different temperatures (10, 30, and 50 °C). The CO₂ uptake capacity percent increased for ACZC by about 8.57% compared to z-13X, whereas the adsorption capacity increased from 13.22 to 16.25 mg/g for all temperatures (10, 30, and 50 °C) [107]. A catalytic characteristic TiO₂/nano zeolite composite was proposed by Catala et al. [83]. Here, they employed two approaches, i.e. incorporating zeolite in the synthesized TiO₂ medium, and vice versa. Both prepared samples (ZSM-5/TiO₂ and TiO₂/ZSM-5) were addressed for Photocatalytic activity in the oxidation of propene in the gas phase.

It is apparent from the literature that different types of zeolite composites manufactured from waste can be utilized to mitigate the toxic metal concentration from wastewater. However, the recovery of used zeolite composites for re-utilization is scarce. Hence, future investigation can be carried out to find a sustainable method to recover the used zeolite which may reduce the quantity and cost of zeolite for adsorption study.

6 Zeolite-Composites Membrane for Environmental Remediation Applications

Heavy metals like copper, zinc, lead, are present in many industrial effluents. In addition, harmful gases (such as CO₂, SO₂), and dyes (like methylene blue, MO, AB29) are continuously departing from several industries and contact with surface water or air directly or indirectly which may provide a bad impact on the human body. Several treatment techniques namely ion exchange, chemical precipitation, adsorption, and coagulation precipitation are proposed to reduce the toxic metal from wastewater and gaseous pollutant removal from the exhaust gas. Separating dyes, and heavy metal, from aqueous solution by a membrane and membrane-composite

Table 4 Zeolite composites and their structural properties

| Sl. no. | Zeolite composite | Specific surface area (m ² /g) | Textural properties | References |
|---------|--|---|--|------------|
| 1 | Zeolite/Activated carbon | 615.406 | Porous and loose texture | [103] |
| 2 | Zeolite/chitosan | 82.96 | Feathery protruding grooves | [97] |
| 3 | Zeolite/hydrous metal oxide | 196.7 | Coarse, porous, and uneven | [54] |
| 4 | Zeolite/Activated carbon | 660 | Serried spheres | [100] |
| 5 | Geopolymer/zeolite | 437.60 | Agglomerated octahedral particles | [28] |
| 6 | Zeolite/silver | 260 | Needle-like | [54] |
| 7 | Zeolite/glass shell | 131, 332 (with and without agitation) | Cubic-like crystals | [19] |
| 8 | Zeolite/Activated carbon | 656 | Angular and slit shape | [54] |
| 9 | TiO ₂ /zeolite | 28.32 | Rough surface and non-uniform | [68] |
| 10 | Zeolite/magnetic | – | Homogenous morphology | [91] |
| 11 | TiO ₂ /nanozeolite | 234 | – | [54] |
| 12 | Zeolite/porous carbon | 171 | Chamfered-edge shape | [104] |
| 13 | Cu/SUZ-4 | 341–398 | Needle-shaped crystals | [68] |
| 14 | Zeolite/Activated carbon | – | Agglomerated | [81] |
| 15 | Geopolymer/zeolite | 17–36 | Sphere and irregular shape was observed | [68] |
| 16 | Zeolite/Fe ₂ O ₃ | 161.5 | – | [81] |
| 17 | Zeolite/reduced graphene | – | Spherical particles | [105] |
| 18 | 4A-zeolite/polyvinyl acetate (PVA) | – | Dispersed finely through the polymer matrix | [54] |
| 19 | Chitosan/PVA/zeolite | | Rough and porous surface | [81] |
| 20 | ZIF-8/polyethyleneimine (PEI) | – | Leaf-like structures | [82] |
| 21 | MFI-zeolite/membrane | – | – | [82] |
| 22 | Zeolite/ceramic membrane | – | Ceramic supports are roofed with a dense film of zeolite | [87] |
| 23 | Zeolite/polysulfone (PSF) | – | Finger-like microvoids were formed | [81] |

(continued)

Table 4 (continued)

| Sl. no. | Zeolite composite | Specific surface area (m ² /g) | Textural properties | References |
|---------|--|---|---|------------|
| 24 | Al ₂ O ₃ -NaA zeolite/membrane | – | Cubic shapes scattered on hollow fiber membrane | [82] |
| 25 | ZIF/polyvinylidene fluoride (PVDF) | – | The functional layer was observed | [106] |

materials, is rising attractively due to its mechanical and thermal stability, and level of removal efficiency. A huge number of articles have been published on waste removal utilizing zeolite embedded membrane composite [84].

6.1 Cation Removal

Zhu et al. [85] have prepared a uniform and narrow size Al₂O₃-NaA zeolite composite membrane synthesized from solid waste coal fly ash used for lead (Pb²⁺) removal from synthetic wastewater with a removal efficiency of 99.9% at 0.1 MPa. In this typical experiment hydrothermally synthesized NaA zeolite was incorporated in the Al₂O₃ hollow fiber support to prepare Al₂O₃-NaA zeolite composite hollow fiber membrane maintaining the Si/Al ratio of 1.07. A zeolite imidazolate framework-based thin-film polymer composite membrane was synthesized by Li et al. [87]. The prepared zeolite-polymer film composite was used for desalination with a removal efficiency of 50–75%. Kumar et al. [88] prepared analcime zeolite-ceramic composite membrane using in situ hydrothermal crystallization process for chromium exclusion from wastewater. The chromium (VI) removal experiment was performed using the prepared composite membrane, where 84% chromium removal was achieved at an applied pressure of 207 kPa with a CEC of 1.84 meq/100 g. They also explored the influence of zeolite coating on ceramic support. From this study, it was evident that the multiple numbers of zeolite coating reduce the membrane pore size, porosity, and permeability rate. Habiba et al. [108] used an electrospinning method to fabricate a novel advanced chitosan/polyvinyl alcohol (PVA)/zeolite nanofibrous composite membrane. In this typical experiment, chitosan was composed with hydrolyzed NaOH, and thereafter the mixture was blended with 1% zeolite with the presence of different aqueous PVA ratios. The resulting composite membrane film has shown a significant impact on the chemical and mechanical stability when it was kept in distilled water, acidic and basic media for 20 days. Metal ions such as Cr (VI), Fe (III), and Ni (II) removal study was performed over the prepared composite membrane. The adsorption capacity for Cr (VI), Fe (III), and Ni (II) was 0.17, 0.11, and 0.03 mmol/g, respectively. The involvement of zeolite nano-particles in membrane matrix and its effect on ion uptake capacity has also been studied. The importance of nano-sized zeolite embedded membrane composite was elucidated by Yurekli et al. [109]. The hydrothermally synthesized pure Na-X zeolite was dispersed on PSF membrane

film during phase inversion process. The membrane pore radius was enlarged after the addition of nano type zeolite crystallites that enhance the permeability rate and removal efficiency of lead and nickel ions. At the end of 60 min the lead and nickel uptake capacity was found to be 682 and 122 mg/g, respectively, over the prepared hybrid membrane.

6.2 Dye Removal

The presence of zeolite framework in the membrane matrix provides high surface area, porosity, ion-exchange capacity, and enhances the durability of the composite membrane. Numerous studies have been conducted on dye removal for wastewater treatment using different zeolite-membrane composite materials.

Baheri et al. [110] modified polyvinyl alcohol (PVA) membrane by composing zeolite-4A powder in the membrane material. The prepared zeolite-4A/PVA composite mixed matrix membrane (MMM) was efficient for dye removal with a maximum adsorption capacity of 41.08 mg/g. NaY blended carbonaceous membrane composite was fabricated by Priyadarshini et al. [111] for Methyl Orange (MO) and Rhodamine-B (RB) rejection. The prepared NaY zeolite-carbonaceous membrane composite achieved the highest removal rate (95.5%) toward MO, and (94%) for RB using the same composite material. It is apparent that zeolite imidazolate framework incorporated hybrid membrane has a higher affinity toward methyl blue (MB) rejection. MB rejection was found to be 99.6% and 98.4% by utilizing Zeolite imidazolate (ZIF-8)-polyethyleneimine (PEI) and nanoconfined Zeolite imidazolate-polymer membrane composite, respectively. Yang et al. [112] synthesized ZIF-8/PEI-HPAN composite membrane under chelation-assisted interfacial reaction (CAIR). Membrane content of ZIF-8/PEI material provided good surface hydrophilicity and super wettability nature that enhanced congo red (CR) dye rejection by about 99.2% at normal atmospheric conditions. They also reported that the composite membrane matrix showed better stability at high pressure and temperatures where the removal efficiency obtained was about 84%. Habiba et al. [113] also proposed congo red and MO removal over chitosan/PVA/zeolite composite membrane with a removal rate of 94% and 83%, respectively. The findings also reported that for Cr (VI) the adsorption capacity of prepared zeolite composite was estimated to be 450 mg/g. Thermal analysis revealed the composite stability in acidic and basic media.

6.3 Harmful-Gas Removal

In recent years, indoor air is polluted by a wide number of pollutants such as SO₂, CO₂, NO₂, CO, CH₄ or by their mixture such as CO₂/CH₄, CO/air, CO/N₂ which are emitted profusely from biogas industry, oil and natural gas industry, or many

chemical extraction process industries with different concentration levels. Zeolite membrane showed the best possibility toward gas-phase separations. Hence, zeolite-membranes composite has been targeted for gas separation from the gas mixture from a trace concentration level to a normal range [114].

Liu et al. [103] examined the H₂S removal by a low-cost novel TiO₂/zeolite-composite material that was synthesized by the ultrasonic-calcination process. The obtained composite membrane was performed with the result of highest H₂S capture and lowest SO₂ emission, compared with a single zeolite adsorbent. The highest H₂S removal was found at 0.13 mmol/g over TiO₂/zeolite composite membrane. An alumina and stainless steel tubular shape supported MFI-zeolite membrane preparation and its utilization in organic gas (n-hexane) separation from n-hexane/air gas mixture was investigated by Aguado et al. [115]. Table 5 shows the zeolite composites and their utilization for environmental remediation.

The membrane has been studied extensively for various purposes. However, a comprehensive understanding of membrane fouling, their recovery, and re-utilization, are not studied yet. However, research is still going on to fix that problem. Therefore, the researcher can exploit this gap in research for enriching and fulfilling the collective knowledge of mankind.

The said zeolite composite membrane was fabricated by direct liquid-phase hydrothermal synthesis. The highest removal rate of n-hexane was observed at 0.01 g/m²h. A porous tubular α -alumina-supported zeolite-A membrane was synthesized by a conventional hydrothermal treatment which showed a suitable hydrophobic nature for binary gas separation. The prepared zeolite-composite membrane was highly stable at temperature range (35–200) °C in a period of 4 months. Separation factors include molecular size, and affinity to the pore wall, which were also illustrated in this study. The zeolite-nanocomposite, zeolite-blended ceramic, and polymeric membranes utilized for gas separation, toxic metal removal from polluted water, and cationic dye removal are depicted in Fig. 10.

7 Recent Advancements and Future Outlook

Recently, many research works are dealing with geopolymer-zeolite composite material as a hybrid adsorbent. In the process of geo-polymerization, metakaolin and CFA are commonly used as aluminosilicate precursors. Anhydrous aluminosilicate metakaolin can be produced by thermal decomposition of kaolin, which is natural clay comprised of kaolinite mineral [Al₂Si₂O₅(OH)₄], and a significant amount of quartz with other minerals. Hence, converting the CFA into a geopolymer in a sustainable way to dispose of this by-product is a promising route for the reuse of synthetic waste. Other industrial by-products viz. slag, red mud, and biomass fly ash containing a high amount of alumina and silica also can be used as starting materials for geopolymer synthesis.

This type of hybrid composites provides advantageous properties to the zeolite network such as high porosity, surface area, and adsorption capacity, where the

Table 5 Various types of Zeolite composites and their applications in environmental remediation

| Sl. no. | Zeolite-composite types | Pollutant removal application | Adsorption capacities | References |
|---------|--|--|--|------------|
| 1 | Zeolite/Activated carbon | Dye removal | 285.71 mg/g | [97] |
| 2 | Zeolite/chitosan | Dye removal | 270.27 mg/g | [101] |
| 3 | Zeolite/hydrous metal oxide | Dye removal | 80.12 mg/g | [98] |
| 4 | Zeolite/Activated carbon | Dye removal | 498.61 mg/g | [100] |
| 5 | Geopolymer/zeolite | Dye removal | 99.1% | [101] |
| 6 | Zeolite/silver | Mercury removal | 7.69 mg/g | [89] |
| 7 | Zeolite/Activated carbon | CO ₂ /N ₂ separation | 6.5, 2.6 mmol/kg for CO ₂ and N ₂ , respectively | [107] |
| 8 | TiO ₂ /zeolite | H ₂ S removal | 0.06 mmol/g | [103] |
| 9 | Zeolite/magnetic | Cs ⁺ , Sr ²⁺ removal | 1.51, 1.87 meq/100 g for Cs ⁺ , Sr ²⁺ , respectively | [80] |
| 10 | TiO ₂ /Nanozeolite | Propene removal | 0.0153 mmol/g | [83] |
| 11 | Zeolite/porous carbon | NH ₄ exchange | 506 meq/100 g | [92] |
| 12 | Zeolite/Activated carbon | Pb ²⁺ removal | 2.65 mmol/g | [116] |
| 13 | geopolymer/zeolite | Co(II) removal | 134.24 mg/g | [117] |
| 14 | zeolite/Fe ₂ O ₃ | Cation removal | 1543 mmol/kg | [118] |
| 15 | Zeolite/reduced graphene | Arsenic(III) removal | 0.049.23 mg/g | [119] |
| 16 | 4A-zeolite/PVA | Dye removal | 41.08 mg/g | [110] |
| 17 | Chitosan/PVA/zeolite | Dye removal | 450 mg/g | [108] |
| 18 | ZIF-8/PEI | Dye removal | 99.2% | [112] |
| 19 | Zeolite/ceramic membrane | Cr(VI) removal | 84% | [88] |
| 20 | Zeolite/PSF | Pb, Ni removal | 682, 122 mg/g | [109] |
| 21 | Al ₂ O ₃ -NaA zeolite/membrane | Pb(II) removal | 99.9% | [85] |
| 22 | ZIF/PVDF | Dye removal | 99.8% | [87] |

geopolymer serves as a durable and strong support to zeolite. Therefore, the composite can be used in bulk with the membrane in separation and pervaporation experiments. These composite materials contain mesoporous and macroscopic pore sizes that are connected internally and distributed to the multiscale number of pores [84].

For years, synthetic zeolites have been studied, but more research is needed, including the production of several types of zeolites and their composites from various synthetic wastes using advanced techniques, their real-life application in

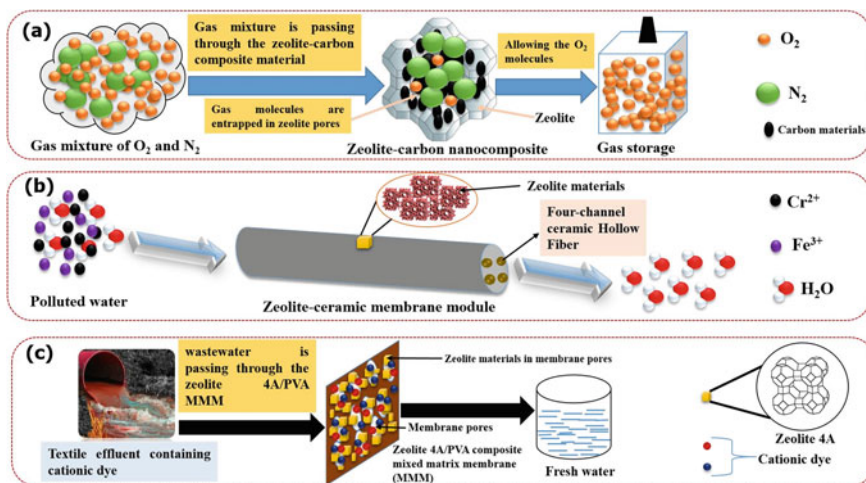


Fig. 10 Schematic of; **a** O₂ recovery from O₂ and N₂ gas mixture using zeolite-carbon nanocomposite, **b** toxic metal removal from polluted water by zeolite embedded ceramic membrane, and **c** cationic dye removal from textile effluent using zeolite 4A/PVA mixed matrix membrane (MMM)

water treatment as well as wastewater treatment, and hazardous gas removal from industrial exhaust gas in the commercial scale. Therefore, the following future scopes are required, comprising:

1. In order to further improve greater adsorption capacity, purity, and selectivity, more investigation should be conducted to parameters for zeolite type X and Y, A, P1 production from Si and Al enriched fly ash or biomass ash.
2. To investigate the long-term effect of zeolite addition, zeolite/pollutants concentration should be optimized.
3. Further study can be extended to the possibility of using waste-based zeolite and zeolite composite such as zeolite-carbon, zeolite-Fe in the fertilizer industry by diminishing toxic metals from soil.

Future studies should explore demanding pure phase zeolite formation for environmental and agricultural applications in a profound way that can be sustainable economically and environmentally.

8 Conclusion

Over the past few years, the explosive development of zeolite synthesis and characterization has been examined. The inherent porous structure and functionalities within the zeolite framework lead to versatile applications ranging from adsorption, catalysis, and separation to sensing and drug delivery appliances for environmental

remedy. In recent, few numbers of modern synthesized routes such as microwave-assisted hydrothermal treatment, ultrasonic irradiation, molten-salt method, and solvent-free ball milling have been explored to demonstrate zeolite formation from Si or Al riched-waste or by utilizing $Na_2O \cdot Al_2O_3$ and Na_2SiO_3 as precursor materials, while conventional hydrothermal and two-step hydrothermal treatments have been explored from past decades. In addition, methods like molten-salt and solvent-free ball milling synthesis have also been adapted for the zeolite synthesis. However, only a few methods are readily available to fabricate zeolite-composite hybrid materials namely direct hydrogel or hydrothermal-assisted hydrogel synthesis. Using these treatment strategies powdered zeolite composites or polymeric zeolite composites can be produced.

Recent studies also focused on conventional synthesis, development, and flexibilities toward a zeolite-like novel material synthesis which will mark a good sign for adsorption and separation studies. In the past 3–5 years many achievements have been obtained using the zeolite imidazolate framework (ZIF) due to the presence of abundant functionalities like zeolite material to the researchers. Therefore, fabrication, development, and utilization of ZIF and its composite material from mineral wastes could open an alternative and new approach for the mass treatment of wastewater and gas separation as well as for environmental remedy.

References

1. P. Misaelides, Application of natural zeolites in environmental remediation: A short review. *Microporous Mesoporous Mater.* **144**, 15–18 (2011). <https://doi.org/10.1016/j.micromeso.2011.03.024>
2. N.S. Samanta, P.P. Das, P. Mondal, U. Bora, M.K. Purkait, Physico-chemical and adsorption study of hydrothermally treated zeolite A and FAU-type zeolite X prepared from LD (Linz-Donawitz) slag of the steel industry. *Int. J. Environ. Anal. Chem.* **00**, 1–23 (2022). <https://doi.org/10.1080/03067319.2022.2079082>
3. N. Shekhar, P.P. Das, P. Mondal, M. Changmai, M.K. Purkait, Journal of the Indian Chemical Society Critical review on the synthesis and advancement of industrial and biomass waste-based zeolites and their applications in gas adsorption and biomedical studies. *J. Indian Chem. Soc.* **99**, 100761 (2022). <https://doi.org/10.1016/j.jics.2022.100761>
4. N.S. Samanta, S. Banerjee, P. Mondal, Anweshan, U. Bora, M.K. Purkait, Preparation and characterization of zeolite from waste Linz-Donawitz (LD) process slag of steel industry for removal of Fe³⁺ from drinking water. *Adv. Powder Technol.* **32**, 3372–3387 (2021). <https://doi.org/10.1016/j.apt.2021.07.023>
5. S. Dhara, N.S. Samanta, R. Uppaluri, M.K. Purkait, High-purity alkaline lignin extraction from *Saccharum ravannae* and optimization of lignin recovery through response surface methodology. *Int. J. Biol. Macromol.* **234**, 123594 (2023). <https://doi.org/10.1016/j.ijbiomac.2023.123594>
6. S.K. Dentel, A.I. Jamrah, D.L. Sparks, orption and cosorption of 1,2,4-trichlorobenzene and tannic acid by organo-clays, *Water Research*, **32**, 3689–3697 (1998). [https://doi.org/10.1016/S0043-1354\(98\)00148-1](https://doi.org/10.1016/S0043-1354(98)00148-1)
7. P.P. Das, Anweshan, M.K. Purkait, Treatment of cold rolling mill (CRM) effluent of steel industry. *Sep. Purif. Technol.* **274**, 119083 (2021). <https://doi.org/10.1016/j.seppur.2021.119083>

8. G.M. Evans, J.C. Furlong, *Environmental biotechnology: theory and application*, 2nd edn. Environ. Biotechnol. Theory. Appl. (John Wiley & Sons, Ltd, 2010), pp.1–11. <https://doi.org/10.1002/9780470975152>
9. B. Prasad, K. Sangita, B.K. Tewary, Reducing the hardness of mine water using transformed fly ash. *Mine Water Environ.* **30**, 61–66 (2011). <https://doi.org/10.1007/s10230-010-0130-4>
10. Report of the New England Association of Chemistry Teachers, *J. Chem. Educ.* **31**, 328 (1954). <https://doi.org/10.1021/ed031p328>
11. G.T. Kerr, G.T. Kerr, Chemistry of Crystalline Aluminosilicates. I. Factors Affecting the Formation of Zeolite A, *J. Phys. Chem.* **70**, 1047–1050 (1966). <https://doi.org/10.1021/j100876a015>
12. X. Ren, R. Qu, S. Liu, H. Zhao, W. Wu, H. Song, C. Zheng, X. Wu, X. Gao, Synthesis of zeolites from coal fly ash for removal of harmful gaseous pollutants: a review, aerosol air. Qual. Res. **20**, 1127–1144 (2020). <https://doi.org/10.4209/aaqr.2019.12.0651>
13. X. Querol, J.C. Umana, A. Alastuey, C. Bertrana, A. Lopez-Soler, F. Plana, Physicochemical characterization of Spanish fly ashes, *Energy Sources*, **21**(10), 883–898 (1999). <https://doi.org/10.1080/00908319950014263>
14. J.D.C. Izidoro, D.A. Fungaro, F. S. D. Santos, S. Wang, Characteristics of Brazilian coal fly ashes and their synthesized zeolites, *Fuel Processing Technology* **97**, 38–44 (2012). <https://doi.org/10.1016/j.fuproc.2012.01.009>
15. M. Inada, Y. Eguchi, N. Enomoto, J. Hojo, Synthesis of zeolite from coal fly ashes with different silica-alumina composition. *Fuel* **84**, 299–304 (2005). <https://doi.org/10.1016/j.fuel.2004.08.012>
16. G.G. Hollman, G. Steenbruggen, M. Janssen-Jurkovičová, Two-step process for the synthesis of zeolites from coal fly ash. *Fuel* **78**, 1225–1230 (1999). [https://doi.org/10.1016/S0016-2361\(99\)00030-7](https://doi.org/10.1016/S0016-2361(99)00030-7)
17. R. Moriyama, S. Takeda, M. Onozaki, Y. Katayama, Large-scale synthesis of artificial zeolite from coal fly ash with a small charge of alkaline solution **84**, 1455–1461 (2005). <https://doi.org/10.1016/j.fuel.2005.02.026>
18. Y. Wang, T. Du, H. Jia, Z. Qiu, Y. Song, Synthesis, characterization and CO₂ adsorption of NaA, NaX and NaZSM-5 from rice husk ash. *Solid State Sci.* **86**, 24–33 (2018). <https://doi.org/10.1016/j.solidstatesciences.2018.10.003>
19. N. Czuma, P. Baran, W. Franus, P. Zabierowski, K. Zarebska, Synthesis of zeolites from fly ash with the use of modified two-step hydrothermal method and preliminary SO₂ sorption tests. *Adsorpt. Sci. Technol.* **37**, 61–76 (2018). <https://doi.org/10.1177/0263617418810607>
20. N. Shigemoto, K. Shirakami, S. Hirano, H. Hayashi, Preparation and characterization of zeolites from coal ash. *Japan: N. p.* 5, 484–492 (1992). <https://www.osti.gov/etdweb/biblio/7045960>
21. V. Berkgaot, A. Singer, High capacity cation exchanger by hydrothermal zeolitization of coal fly ash **10**, 369–378 (1996)
22. S. Rayalu, S.U. Meshram, M.Z. Hasan, Highly crystalline faujasitic zeolites from flyash. *J. Hazard. Mater.* **77**, 123–131 (2000). [https://doi.org/10.1016/S0304-3894\(00\)00212-0](https://doi.org/10.1016/S0304-3894(00)00212-0)
23. L. Yang, X. Qian, P. Yuan, H. Bai, T. Miki, F. Men, H. Li, T. Nagasaka, Green synthesis of zeolite 4A using fly ash fused with synergism of NaOH and Na₂CO₃. *J. Clean. Prod.* **212**, 250–260 (2019). <https://doi.org/10.1016/j.jclepro.2018.11.259>
24. S. Sivalingam, S. Sen, Optimization of synthesis parameters and characterization of coal fly ash derived microporous zeolite X. *Appl. Surf. Sci.* **455**, 903–910 (2018). <https://doi.org/10.1016/j.apsusc.2018.05.222>
25. N.F. Gao, S. Kume, K. Watari, Zeolite-carbon composites prepared from industrial wastes: (II) evaluation of the adaptability as environmental materials. *Mater. Sci. Eng. A.* **404**, 274–280 (2005). <https://doi.org/10.1016/j.msea.2005.05.090>
26. X. Querol, A. Lo, J.M. Andre, R. Juan, P. Ferrer, C.R. Ruiz, A fast method for recycling fly ash: microwave-assisted zeolite synthesis **31**, 2527–2533 (1997)
27. H. Tanaka, A. Fujii, S. Fujimoto, Y. Tanaka, Microwave-assisted two-step process for the synthesis of a single-phase Na-A zeolite from coal fly ash. *Adv. Powder Technol.* **19**, 83–94 (2008). <https://doi.org/10.1163/156855208X291783>

28. M. Inada, H. Tsujimoto, Y. Eguchi, N. Enomoto, J. Hojo, Microwave-assisted zeolite synthesis from coal fly ash in hydrothermal process **84**, 1482–1486 (2005). <https://doi.org/10.1016/j.fuel.2005.02.002>
29. S.S. Bukhari, J. Behin, H. Kazemian, S. Rohani, Conversion of coal fly ash to zeolite utilizing microwave and ultrasound energies: a review. *Fuel* **140**, 250–266 (2015). <https://doi.org/10.1016/j.fuel.2014.09.077>
30. R. Anuwattana, P. Khummongkol, Conventional hydrothermal synthesis of Na-A zeolite from cupola slag and aluminum sludge. *J. Hazard. Mater.* **166**, 227–232 (2009). <https://doi.org/10.1016/j.jhazmat.2008.11.020>
31. A.D. Sontakke, M.K. Purkait, Fabrication of ultrasound-mediated tunable graphene oxide nanoscrolls, *Ultrason. Sonochem.* **63**, 104976 (2020). <https://doi.org/10.1016/j.ultsonch.2020.104976>
32. N.M. Musyoka, L.F. Petrik, E. Hums, Ultrasonic assisted synthesis of zeolite A from coal fly ash using mine waters (acid mine drainage and circumneutral mine water) as a substitute for ultra pure water. *IMWA* 423–428 (2011)
33. S. S. R. Bukhari, *Microwave and Ultrasound Assisted Zeolitization of Coal Fly Ash*. The University of Western Ontario, 2016
34. O. Dere, O. Sabriye, A novel synthesis method of zeolite X from coal fly ash: alkaline fusion followed by ultrasonic-assisted synthesis method. *Waste Biomass Valoriz.* **10**, 143–154 (2019). <https://doi.org/10.1007/s12649-017-0050-7>
35. D. Vaičiukyniene, A. Kantautas, V. Vaitkevičius, L. Jakevičius, Ž. Rudžionis, M. Paškevičius, Effects of ultrasonic treatment on zeolite NaA synthesized from by-product silica. *Ultrason. Sonochem.* **27**, 515–521 (2015). <https://doi.org/10.1016/j.ultsonch.2015.06.001>
36. M. Park, C. Lyeal, W. Taik, M. Chul, J. Choi, N. Ho, Molten-salt method for the synthesis of zeolitic materials I. Zeolite Form. *Alkaline Molten-Salt Syst.* **37**, 81–89 (2000)
37. T. Fukasawa, A. Horigome, A.D. Karisma, N. Maeda, A.-N. Huang, K. Fukui, Utilization of incineration fly ash from biomass power plants for zeolite synthesis from coal fly ash by microwave hydrothermal treatment. *Adv. Powder Technol.* **29**, 450–456 (2018). <https://doi.org/10.1016/j.apt.2017.10.022>
38. M.H. Nada, S.C. Larsen, E.G. Gillan, Mechanochemically-assisted solvent-free and template-free synthesis of zeolites ZSM-5 and mordenite. *Nanoscale Adv.* **1**, 3918–3928 (2019). <https://doi.org/10.1039/c9na00399a>
39. S. Narayanan, P. Tamizhdurai, V.L. Mangesh, C. Ragupathi, P. Santhana krishnan, A. Ramesh, Recent advances in the synthesis and applications of mordenite zeolite—review. *RSC Adv.* **11**, 250–267 (2021). <https://doi.org/10.1039/D0RA09434J>
40. A.J. Schwanke, R. Balzer, S. Pergher, Microporous and mesoporous materials from natural and inexpensive sources microporous and mesoporous materials from natural and inexpensive sources, in *Handbook of Ecomaterials*, ed. by L. Martínez, O. Kharissova, B. Kharisov (Springer, Cham, 2017), pp. 1–22. https://doi.org/10.1007/978-3-319-48281-1_43-1
41. L. Bandura, R. Panek, M. Rotko, W. Franus, Synthetic zeolites from fly ash for an effective trapping of BTX in gas stream. *Microporous Mesoporous Mater.* **223**, 1–9 (2016). <https://doi.org/10.1016/j.micromeso.2015.10.032>
42. N. Murayama, H. Yamamoto, J. Shibata, Mechanism of zeolite synthesis from coal fly ash by alkali hydrothermal reaction. *Int. J. Miner. Process.* **64**, 1–17 (2002). [https://doi.org/10.1016/S0301-7516\(01\)00046-1](https://doi.org/10.1016/S0301-7516(01)00046-1)
43. X.S. Zhao, G.Q. Lu, H.Y. Zhu, Effects of ageing and seeding on the formation of zeolite Y from coal fly ash. *J. Porous Mater.* **4**, 245–251 (1997). <https://doi.org/10.1023/A:1009669104923>
44. Y. Kuwahara, T. Ohmichi, T. Kamegawa, K. Mori, H. Yamashita, A novel conversion process for waste slag: synthesis of a hydrotalcite-like compound and zeolite from blast furnace slag and evaluation of adsorption capacities. *J. Mater. Chem.* **20**, 5052–5062 (2010). <https://doi.org/10.1039/c0jm00518e>
45. M.W. Munthali, M.A. Elsheikh, E. Johan, N. Matsue, Proton adsorption selectivity of zeolites in aqueous media: effect of Si/Al ratio of zeolites, *Molecules* **19**, 20468–20481 (2014). <https://doi.org/10.3390/molecules191220468>

46. E. Cataldo, L. Salvi, F. Paoli, M. Fucile, G. Masciandaro, D. Manzi, C.M. Masini, G.B. Mattii, Application of zeolites in agriculture and other potential uses: a review. *Agronomy* **11**, 1–14 (2021). <https://doi.org/10.3390/agronomy11081547>
47. P. Kabwadza-corner, M.W. Munthali, E. Johan, N. Matsue, Comparative study of copper adsorptivity and selectivity toward Zeolites, *American Journal of Analytical Chemistry*, **5**, 395–405 (2014). <https://doi.org/10.4236/ajac.2014.57048>
48. H. Methods, P. Tayraukham, N. Jantarit, N. Osakoo, Synthesis of pure phase NaP2 zeolite from the gel of NaY by conventional and microwave-assisted (2020)
49. P.Y. He, Y.J. Zhang, H. Chen, Z.C. Han, L.C. Liu, One-step synthesis of rod-shaped phillip-site using circulating fluidized bed fly ash and its application for removal heavy metal. *Ferroelectrics* **547**, 51–58 (2019). <https://doi.org/10.1080/00150193.2019.1592483>
50. M.K. Naskar, D. Kundu, M. Chatterjee, Coral-like hydroxy sodalite particles from rice husk ash as silica source. *Mater. Lett.* **65**, 3408–3410 (2011). <https://doi.org/10.1016/j.matlet.2011.07.084>
51. T. Hui, H.J. Sun, T.J. Peng, Preparation and characterization of cordierite-based ceramic foams with permeable property from asbestos tailings and coal fly ash. *J. Alloys Compd.* **885**, 160967 (2021). <https://doi.org/10.1016/j.jallcom.2021.160967>
52. N. Moreno, X. Querol, F. Plana, J.M. Andres, M. Janssen, H. Nugteren, Pure zeolite synthesis from silica extracted from coal fly ashes. *J. Chem. Technol. Biotechnol.* **77**, 274–279 (2002). <https://doi.org/10.1002/jctb.578>
53. C. Belviso, State-of-the-art applications of fly ash from coal and biomass: a focus on zeolite synthesis processes and issues. *Prog. Energy Combust. Sci.* **65**, 109–135 (2018). <https://doi.org/10.1016/j.peccs.2017.10.004>
54. A.M. Cardoso, A. Paprocki, L.S. Ferret, C.M.N. Azevedo, M. Pires, Synthesis of zeolite Na-P1 under mild conditions using Brazilian coal fly ash and its application in wastewater treatment. *Fuel* **139**, 59–67 (2015). <https://doi.org/10.1016/j.fuel.2014.08.016>
55. K. Sangita, B. Prasad, G. Udayabhanu, Synthesis of zeolite from waste fly ash by using different methods. *Asian J. Chem.* **28**, 1435–1439 (2016). <https://doi.org/10.14233/ajchem.2016.19682>
56. Deepti, A. Sinha, P. Biswas, S. Sarkar, U. Bora, M.K. Purkait, Utilization of LD slag from steel industry for the preparation of MF membrane. *J. Environ. Manage.* **259**, 110060 (2020). <https://doi.org/10.1016/j.jenvman.2019.110060>
57. W. Liu, T. Aldahri, S. Ren, C.C. Xu, S. Rohani, B. Liang, C. Li, Solvent-free synthesis of hydroxycancrinite zeolite microspheres during the carbonation process of blast furnace slag. *J. Alloys Compd.* **847**, 156456 (2020). <https://doi.org/10.1016/j.jallcom.2020.156456>
58. A. Kotoulas, D. Agathou, I.E. Triantaphyllidou, T.I. Tatoulis, C.S. Akratos, A.G. Tekerekopoulou, D. V. Vayenas, Zeolite as a potential medium for ammonium recovery and second cheese whey treatment. *Water (Switzerland)* **11** (2019). <https://doi.org/10.3390/w11010136>
59. T. Murakami, Y. Sugano, T. Narushima, Y. Iguchi, C. Ouchi, Recovery of calcium from BF slag and synthesis of zeolite a using its residue. *ISIJ Int.* **51**, 901–905 (2011). <https://doi.org/10.2355/isijinternational.51.901>
60. Y. Li, T. Peng, W. Man, L. Ju, F. Zheng, M. Zhang, M. Guo, Hydrothermal synthesis of mixtures of NaA zeolite and sodalite from Ti-bearing electric arc furnace slag. *RSC Adv.* **6**, 8358–8366 (2016). <https://doi.org/10.1039/c5ra26881h>
61. T. Wajima, Synthesis of zeolite from blast furnace slag using alkali fusion with addition of EDTA. *Adv. Mater. Res.* **1044–1045**, 124–127 (2014). <https://doi.org/10.4028/www.scientific.net/AMR.1044-1045.124>
62. D.J. Londeree, Silica-Titania composites for water treatment. *Univ. Florida.* **53**, 62 (2002)
63. T. Wajima, O. Kiguchi, K. Sugawara, T. Sugawara, Synthesis of zeolite-A using silica from rice husk ash. *J. Chem. Eng. Japan.* **42**, 61–66 (2009). <https://doi.org/10.1252/jcej.08we139>
64. S. Mukherjee, S. Barman, G. Halder, Fluoride uptake by zeolite NaA synthesized from rice husk: isotherm, kinetics, thermodynamics and cost estimation. *Groundw. Sustain. Dev.* **7**, 39–47 (2018). <https://doi.org/10.1016/j.gsd.2018.03.003>

65. R.M. Mohamed, Rice husk ash as a renewable source for the production of zeolite NaY and its characterization 48–53 (2015). <https://doi.org/10.1016/j.arabjc.2012.12.013>
66. P. Worathanakul, P. Kongkachuichay, SUZ-4 zeolite synthesis derived from rice husk ash (2016)
67. R. Husk, J. Wong, E. Ng, F. Adam, Microscopic investigation of nanocrystalline zeolite I synthesized from rice husk ash **808**, 805–808 (2012). <https://doi.org/10.1111/j.1551-2916.2011.04995.x>
68. B. Jha, D.N. Singh, ChemInform abstract: a review on synthesis, characterization and industrial applications of flyash zeolites (2012). <https://doi.org/10.1002/chin.201225227>
69. C. Zhang, S. Li, S. Bao, Sustainable synthesis of ZSM-5 zeolite from rice husk ash without addition of solvents. *Waste Biomass Valoriz.* **10**, 2825–2835 (2019). <https://doi.org/10.1007/s12649-018-0356-0>
70. V. Davina, P.S. Utama, E. Saputra, S. Bahri, Zeolite Na-P1 derived from palm oil mill fly ash: synthesis and characterization. *J. Phys. Conf. Ser.* **1351**, 12103 (2019). <https://doi.org/10.1088/1742-6596/1351/1/012103>
71. A. Kongnoo, S. Tontisirin, P. Worathanakul, C. Phalakornkule, Surface characteristics and CO₂ adsorption capacities of acid-activated zeolite 13X prepared from palm oil mill fly ash. *Fuel* **193**, 385–394 (2017). <https://doi.org/10.1016/j.fuel.2016.12.087>
72. P.S. Aman, E. Utama, Saputra, high purity silica from palm oil mill fly ash for catalyst ZSM-5 zeolite synthesis. *Appl. Sci. Technol.* **1**, 267–272 (2017)
73. S.A. Khairuddin, S. Nurdin, H.A.M. Sukri, C.C.Wooi, Characterization and optimization of palm industry ash waste (PIAW) derived zeolites using central composite design (CCD). *Journal* **1**, 27–33 (2018)
74. W. Tangchirapat, T. Saeting, C. Jaturapitakkul, K. Kiattikomol, A. Siripanichgorn, Use of waste ash from palm oil industry in concrete **27**, 81–88 (2007). <https://doi.org/10.1016/j.wasman.2005.12.014>
75. C.W. Purnomo, C. Salim, H. Hinode, Synthesis of pure Na–X and Na–A zeolite from bagasse fly ash. *Microporous Mesoporous Mater.* **162**, 6–13 (2012). <https://doi.org/10.1016/j.micromeso.2012.06.007>
76. P. Thuadaij, P. Mukda, Synthesis and characterization of zeolite derived from Buriram sugarcane bagasse ash and Narathiwat kaolinite **8**, 320–326 (2016)
77. J.A. Oliveira, F.A. Cunha, L.A.M. Ruotolo, Synthesis of zeolite from sugarcane bagasse fly ash and its application as a low-cost adsorbent to remove heavy metals. *J. Clean. Prod.* **229**, 956–963 (2019). <https://doi.org/10.1016/j.jclepro.2019.05.069>
78. M.P. Moisés, C.T.P. da Silva, J.G. Meneguín, E.M. Giroto, E. Radovanovic, Synthesis of zeolite NaA from sugarcane bagasse ash. *Mater. Lett.* **108**, 243–246 (2013). <https://doi.org/10.1016/j.matlet.2013.06.086>
79. F. Batool, A. Masood, M. Ali, Characterization of sugarcane bagasse ash as pozzolan and influence on concrete properties. *Arab. J. Sci. Eng.* **45**, 3891–3900 (2020). <https://doi.org/10.1007/s13369-019-04301-y>
80. H. Faghihian, M. Moayed, A. Firooz, M. Iravani, Comptes rendus chimie evaluation of a new magnetic zeolite composite for removal of Cs⁺ and Sr²⁺ from aqueous solutions: kinetic, equilibrium and thermodynamic studies. *Comptes Rendus Chim.* **17**, 108–117 (2014). <https://doi.org/10.1016/j.crci.2013.02.006>
81. W. Chunfeng, L.I. Jiansheng, W. Lianjun, S.U.N. Xiuyun, Adsorption of dye from wastewater by zeolites synthesized from fly ash: kinetic and equilibrium studies *, *Chinese. J Chem. Eng.* **17**, 513–521 (2009). [https://doi.org/10.1016/S1004-9541\(08\)60239-6](https://doi.org/10.1016/S1004-9541(08)60239-6)
82. X. Ji, M. Zhang, Y. Wang, Y. Song, Y. Ke, Y. Wang, Immobilization of ammonium and phosphate in aqueous solution by zeolites synthesized from fly ashes with different compositions. *J. Ind. Eng. Chem.* **22**, 1–7 (2015). <https://doi.org/10.1016/j.jiec.2014.06.017>
83. J. Fernández-Catalá, M. Sánchez-Rubio, M. Navlani-García, Á. Berenguer-Murcia, D. Cazorla-Amorós, Synthesis of TiO₂/nanozeolite composites for highly efficient photocatalytic oxidation of propene in the gas phase. *ACS Omega* **5**, 31323–31331 (2020). <https://doi.org/10.1021/acsomega.0c04793>

84. V.K. Gupta, S. Agarwal, T.A. Saleh, Synthesis and characterization of alumina-coated carbon nanotubes and their application for lead removal. *J. Hazard. Mater.* **185**, 17–23 (2011). <https://doi.org/10.1016/j.jhazmat.2010.08.053>
85. L. Zhu, J. Ji, S. Wang, C. Xu, K. Yang, M. Xu, Removal of Pb(II) from wastewater using Al₂O₃-NaA zeolite composite hollow fiber membranes synthesized from solid waste coal fly ash. *Chemosphere* **206**, 278–284 (2018). <https://doi.org/10.1016/j.chemosphere.2018.05.001>
86. R. Panek, M. Wdowin, W. Franus, D. Czarna, L.A. Stevens, H. Deng, J. Liu, C. Sun, H. Liu, C.E. Snape, Fly ash-derived MCM-41 as a low-cost silica support for polyethyleneimine in post-combustion CO₂ capture. *J. CO₂ Util.* **22**, 81–90 (2017). <https://doi.org/10.1016/j.jcou.2017.09.015>
87. T. Li, Y. Ren, D. Wu, W. Zhang, M. Shi, C. Ji, L. Lv, M. Hua, W. Zhang, A novel water-stable two-dimensional zeolitic imidazolate frameworks thin-film composite membrane for enhancements in water permeability and nanofiltration performance. *Chemosphere* **261**, 127717 (2020). <https://doi.org/10.1016/j.chemosphere.2020.127717>
88. R.V. Kumar, A.K. Basumatary, A.K. Ghoshal, G. Pugazhenth, RSC Advances Performance assessment of an analcime-C zeolite—ceramic composite membrane by removal of Cr (VI) from aqueous solution, 6246–6254 (2015). <https://doi.org/10.1039/c4ra14527e>
89. M. Wdowin, M. Macherzyński, R. Panek, J. Górecki, W. Franus, Investigation of the sorption of mercury vapour from exhaust gas by an Ag-X zeolite. *Clay Miner.* **50**, 31–40 (2015). <https://doi.org/10.1180/claymin.2015.050.1.04>
90. D. Geopolymers, A. Contain, N. Zeolites, Reexamination of existing results. *Society*, 3075–3085 (2005)
91. M. Minelli, E. Papa, V. Medri, F. Miccio, P. Benito, F. Doghieri, E. Landi, Characterization of novel geopolymer—zeolite composites as solid adsorbents for CO₂ capture. *Chem. Eng. J.* **341**, 505–515 (2018). <https://doi.org/10.1016/j.cej.2018.02.050>
92. H. Katsuki, S. Komarneni, Journal of solid state chemistry synthesis of Na-A and/or Na-X zeolite/porous carbon composites from carbonized rice husk. *J. Solid State Chem.* **182**, 1749–1753 (2009). <https://doi.org/10.1016/j.jssc.2009.04.022>
93. H. Katsuki, S. Furuta, T. Watari, S. Komarneni, ZSM-5 zeolite/porous carbon composite: conventional- and microwave-hydrothermal synthesis from carbonized rice husk. *Micro-porous Mesoporous Mater.* **86**, 145–151 (2005). <https://doi.org/10.1016/j.micromeso.2005.07.010>
94. V.K. Jha, M. Nagae, M. Matsuda, M. Miyake, Zeolite formation from coal fly ash and heavy metal ion removal characteristics of thus-obtained Zeolite X in multi-metal systems. *J. Environ. Manage.* **90**, 2507–2514 (2009). <https://doi.org/10.1016/j.jenvman.2009.01.009>
95. M. Miyake, Y. Kimura, T. Ohashi, M. Matsuda, Preparation of activated carbon—zeolite composite materials from coal fly ash **112**, 170–177 (2008). <https://doi.org/10.1016/j.micromeso.2007.09.028>
96. R. Soni, D.P. Shukla, *Chemosphere* synthesis of fly ash based zeolite-reduced graphene oxide composite and its evaluation as an adsorbent for arsenic removal. *Chemosphere* **219**, 504–509 (2019). <https://doi.org/10.1016/j.chemosphere.2018.11.203>
97. W.A. Khanday, F. Marrakchi, M. Asif, B.H. Hameed, Journal of the Taiwan institute of chemical engineers mesoporous zeolite—activated carbon composite from oil palm ash as an effective adsorbent for methylene blue. *J. Taiwan Inst. Chem. Eng.* **70**, 32–41 (2017). <https://doi.org/10.1016/j.jtice.2016.10.029>
98. L. Lin, Y. Lin, C. Li, D. Wu, H. Kong, Synthesis of zeolite/hydrous metal oxide composites from coal fly ash as efficient adsorbents for removal of methylene blue from water. *Int. J. Miner. Process.* **148**, 32–40 (2016). <https://doi.org/10.1016/j.minpro.2016.01.010>
99. Z. Tauanov, P.E. Tsakiridis, S.V. Mikhailovsky, V.J. Inglezakis, Synthetic coal fly ash-derived zeolites doped with silver nanoparticles for mercury (II) removal from water. *J. Environ. Manage.* **224**, 164–171 (2018). <https://doi.org/10.1016/j.jenvman.2018.07.049>
100. Z. Shui, L. Yao, X. Pu, L. Yang, W. Jiang, X. Jiang, Synthesis of a novel zeolite—activated carbon composite using lithium—silicon-powder waste for ammonia-nitrogen and methylene blue removal (2020). <https://doi.org/10.1021/acs.iecr.0c00617>

101. K.P. Id, N. Sethhaya, M. Thala, P. Chindaprasirt, geopolymer/zeolite composite materials with adsorptive and photocatalytic properties for dye removal, 1–20 (2020). <https://doi.org/10.1371/journal.pone.0241603>
102. T.A. Vereshchagina, S.N. Vereshchagin, N.N. Shishkina, O.A. Mikhaylova, L.A. Solovoyov, A.G. Anshits, Microporous and mesoporous materials one-step fabrication of hollow aluminosilicate microspheres with a composite zeolite/glass crystalline shell. *Microporous Mesoporous Mater.* **169**, 207–211 (2013). <https://doi.org/10.1016/j.micromeso.2012.11.010>
103. C. Liu, R. Zhang, S. Wei, J. Wang, Y. Liu, M. Li, R. Liu, Selective removal of H₂S from biogas using a regenerable hybrid TiO₂/zeolite composite. *Fuel* **157**, 183–190 (2015). <https://doi.org/10.1016/j.fuel.2015.05.003>
104. B. Baheri, R. Ghahremani, M. Peydayesh, M. Shahverdi, T. Mohammadi, matrix membrane adsorbents: preparation. *Res. Chem. Intermed.* **42**, 5309–5328 (2016). <https://doi.org/10.1007/s11164-015-2362-1>
105. S.K. Brown, M.R. Sim, M.J. Abramson, C.N. Gray, Concentrations of volatile organic compounds in indoor air—a review. *Indoor Air* **4**, 123–134 (1994). <https://doi.org/10.1111/j.1600-0668.1994.t01-2-00007.x>
106. N.A. Ibrahim, M.D.H. Wirzal, N.A.H. Nordin, N.S. Abd Halim, Development of Polyvinylidene fluoride (PVDF)-ZIF-8 Membrane for wastewater treatment. *IOP Conf. Ser. Earth Environ. Sci.* **140**, 12021 (2018). <https://doi.org/10.1088/1755-1315/140/1/012021>
107. M. Rostami, M. Mofarahi, R. Karimzadeh, D. Abedi, Preparation and characterization of activated carbon-zeolite composite for gas adsorption separation of CO₂/N₂ system. *J. Chem. Eng. Data* **61**, 2638–2646 (2016). <https://doi.org/10.1021/acs.jced.6b00374>
108. U. Habiba, A.M. Afifi, A. Salleh, B.C. Ang, Chitosan/(polyvinyl alcohol)/zeolite electrospun composite nanofibrous membrane for adsorption of Cr⁶⁺, Fe³⁺ and Ni²⁺. *J. Hazard. Mater.* **322**, 182–194 (2017). <https://doi.org/10.1016/j.jhazmat.2016.06.028>
109. Y. Yurekli, Removal of heavy metals in wastewater by using zeolite nano-particles impregnated polysulfone membranes. *J. Hazard. Mater.* **309**, 53–64 (2016). <https://doi.org/10.1016/j.jhazmat.2016.01.064>
110. B. Baheri, R. Ghahremani, M. Peydayesh, M. Shahverdi, T. Mohammadi, Dye removal using 4A-zeolite/polyvinyl alcohol mixed matrix membrane adsorbents: preparation, characterization, adsorption, kinetics, and thermodynamics. *Res. Chem. Intermed.* **42**, 5309–5328 (2016). <https://doi.org/10.1007/s11164-015-2362-1>
111. A. Priyadarshini, S. Wei, P. Jin, L. Hong, Zeolite Y-carbonaceous composite membrane with a pseudo solid foam structure assessed by nano filtration of aqueous dye solutions. *J. Memb. Sci.* **567**, 146–156 (2018). <https://doi.org/10.1016/j.memsci.2018.09.025>
112. L. Yang, Z. Wang, J. Zhang, Highly permeable zeolite imidazolate framework composite membranes fabricated via a chelation-assisted interfacial reaction. *J. Mater. Chem. A* **5**, 15342–15355 (2017). <https://doi.org/10.1039/C7TA03244G>
113. U. Habiba, T.A. Siddique, T. Chin, A. Salleh, B. Chin, A.M. Afifi, Synthesis of chitosan/polyvinyl alcohol/zeolite composite for removal of methyl orange, Congo red and chromium (VI) by flocculation/adsorption. *Carbohydr. Polym.* **157**, 1568–1576 (2017). <https://doi.org/10.1016/j.carbpol.2016.11.037>
114. H.J. Salonen, A.-L. Pasanen, S.K. Lappalainen, H.M. Riuttala, T.M. Tuomi, P.O. Pasanen, B.C. Bäck, K.E. Reijula, Airborne concentrations of volatile organic compounds, formaldehyde and ammonia in Finnish office buildings with suspected indoor air problems. *J. Occup. Environ. Hyg.* **6**, 200–209 (2009). <https://doi.org/10.1080/15459620802707835>
115. S. Aguado, A.C. Polo, P. Bernal, J. Santamar, Removal of pollutants from indoor air using zeolite membranes **240**, 159–166 (2004). <https://doi.org/10.1016/j.memsci.2004.05.004>
116. V.K. Jha, M. Matsuda, M. Miyake, Sorption properties of the activated carbon-zeolite composite prepared from coal fly ash for Ni²⁺, Cu²⁺, Cd²⁺ and Pb²⁺ **160**, 148–153 (2008). <https://doi.org/10.1016/j.jhazmat.2008.02.107>
117. M. Kr, P. Ro, Geopolymer-zeolite composites : a review **230** (2019). <https://doi.org/10.1016/j.jclepro.2019.05.152>

118. J. Xie, Z. Wang, D. Wu, H. Kong, Synthesis and properties of zeolite/hydrated iron oxide composite from coal fly ash as efficient adsorbent to simultaneously retain cationic and anionic pollutants from water. *Fuel* **116**, 71–76 (2014). <https://doi.org/10.1016/j.fuel.2013.07.126>
119. R. Soni, D.P. Shukla, Synthesis of fly ash based zeolite-reduced graphene oxide composite and its evaluation as an adsorbent for arsenic removal. *Chemosphere* **219**, 504–509 (2019). <https://doi.org/10.1016/j.chemosphere.2018.11.203>
120. W. Liu, T. Aldahri, C. Xu, C. Li, S. Rohani, *Journal of Environmental Chemical Engineering* Synthesis of sole gismondine-type zeolite from blast furnace slag during CO₂ mineralization process. *J. Environ. Chem. Eng.* **9** (2021) 104652. <https://doi.org/10.1016/j.jece.2020.104652>

Advanced Composites for Drug Adsorption



Thaís Strieder Machado, Brenda Isadora Soares Damin, Giovana Marchezi, Larissa Crestani, and Jeferson Steffanello Piccin

Abstract The increase in world population and the high consumption of medicines have caused an inadequate disposal and release of medicines in surface and underground waters. Besides, these compounds are persistent in wastewaters. Recent studies reported the efficiency in removing pharmaceutical products present in the ecosystem through the development of adsorbent composites. Thus, the advancement of composite materials has stood out as an alternative, which is evolving and improving, using two or more raw materials to combine physical, chemical, or mechanical properties and obtain a desired product. Moreover, the use of byproducts or agro-industrial residues to compose the use of raw materials has been highlighted, which may reduce the total cost of the development of advanced composites. The adsorption technique combined with the development of these composites allows testing on a laboratory scale the efficiency of these composites. Therefore, the operational conditions obtained through isothermal and kinetic experimental data are crucial for the success of the technique. This chapter aims to present the state of the art in composite materials developed to the removal of drugs through the adsorption technique. For this, the classification of composites was described, the adsorption technique principles were addressed, and a bibliometric analysis was carried out to satisfy the advancement of composite materials in the state of the art.

Keywords Bibliometric analysis · Medicines · Pharmaceutical compounds · Materials · Organic · Inorganic · Operational conditions

T. S. Machado (✉) · J. S. Piccin

Postgraduate Program in Civil and Environmental Engineering, Faculty of Engineering and Architecture, University of Passo Fundo, Passo Fundo/RS, Brazil
e-mail: thaiis.strieder@hotmail.com

B. I. S. Damin · J. S. Piccin

Postgraduate Program in Food Science and Technology, Faculty of Agronomy and Veterinary Medicine, University of Passo Fundo, Passo Fundo/RS, Brazil

G. Marchezi · L. Crestani · J. S. Piccin

Chemical Engineering Course, Faculty of Engineering and Architecture, University of Passo Fundo, Passo Fundo/RS, Brazil

1 Introduction

The availability of drinking water is threatened due to the increased contamination from industrial activities and population growth, combined with long-term droughts [1, 2]. It is known that a significant number of emerging contaminants have contributed to point and diffuse pollution, favoring the contamination of surface and underground water resources [3]. Different classes of medicines, pharmaceutical compounds, dyes, surfactants, industrial chemicals, agrochemicals, and micro-nano plastics stand out among emerging contaminants [3].

Most of the emerging contaminants do not have specific legislation for the disposal in water resources. However, it is known that they are found in micrograms or nanograms in the ecosystem and that they are not completely removed by conventional water and effluent treatment systems, such as coagulation, flocculation, decantation, and filtration [4, 5].

One of the categories of emerging contaminants is drugs and their intermediate compounds, since, even in small concentrations, there is no clear evidence of toxicity and side effects for living beings that these components can cause [6]. This category includes pharmaceutical compounds consumed with or without medical prescription, for human or veterinary use, food supplements, in addition to the inappropriate disposal of medicines out of expiration date and the excretion of active compounds in urine and feces [4, 7].

In this way, new studies of water and effluent treatment techniques to remove emerging contaminants have emerged. One of the techniques that can be used is adsorption, since it allows the removal of small dissolved concentrations of contaminants in liquid media, which does not occur when conventional methods of treatment are applied, and because of that a wide range of adsorbents can be used and developed [1, 8, 9]. In adsorption, the operational conditions are crucial for the success of the technique, such as pH, temperature, flow rate, mass, and bed height, which are verified from batch and fixed-bed assays.

Allied to this, composites are a trend of the adsorbent materials for application in adsorption processes, as they aim at the compilation of materials with different promising characteristics, to synthesize a new material with unique characteristics and, thus, being able to increase the efficiency and selectivity of the process. Composite materials have superior properties compared to an individual material that would be in their composition.

Physical, chemical, and thermal modifications can be proposed in the matrix phase and in the dispersed phase of the composite materials. But for this, it is necessary to have adequate control in the development of composites, considering the specificities and limitations of each organic and inorganic material, to achieve the desired enhancement. For an unconventional adsorbent, the ideal situation is that it offers high adsorption capacities, high efficiency to remove several emerging contaminants, is renewable, applicable to industrial effluents, and has a low cost [10, 11], along with sustainability of the development process.

Thus, this chapter aims to present the state of the art in composite materials developed for drug removal through the adsorption technique. For this, the classification of composites was described, the adsorption technique principles were addressed, and a bibliometric analysis was carried out to satisfy the advancement of composite materials in the state of the art.

2 Classifications of Composites

2.1 Composite Definitions and Classifications

Materials are classified according to three basic categories: metals, ceramics, and polymers. Thus, each material has different properties and, so, a wide range of applications in different segments [12]. The performance of a material is linked to its mechanical and thermal properties. Mechanical properties of materials refer to a material response to an applied force, and thermal properties refer to a material response to the application of heat [13]. Mechanical properties are associated with stiffness, strength, ductility, and toughness. Thermal properties are associated with the heat capacity and thermal conductivity of a material [12, 13].

Metals have high density, thermal stability, are corrosion resistant, and are moderately easy to mold and join. Ceramic materials are very rigid but fragile and difficult to mold. Furthermore, they feature thermal stability and are resistant to corrosion and abrasion. Polymeric materials have low density, weak mechanical properties, and lack thermal stability, however, they are easily manufactured and bonded together [12, 14].

The surface area and porosity of materials are also important characteristics and are associated with mechanical properties. When there is a high surface area, there is a tendency for particles to agglomerate and directly affect the mechanical properties of materials [15]. Porosity is defined as the volume fraction of pores, the size, shape, and distribution of the pores. The total porosity includes the surface porosity and internal porosity which are the pores connected and those not connected to the surface, respectively [13]. In this sense, a larger distribution of pores on the surface and the increase in the size of these pores leads to an increase in the surface area [13, 16]. For the composite formation which includes the combination of different materials, the pores of which can be partially occupied by the agglomeration of the particles. Thus, a composite material tends to have a different surface area from its source materials, and it can be larger or smaller.

From these three basic categories, composite materials are derived, as shown in Fig. 1. Composites, commonly called composite materials, are made up of two or more materials linked together by their interfaces and that form large and continuous regions. The constituent materials must have significantly different physical or chemical properties and when combined produce a material with unique and different characteristics from the original materials [12, 16, 17]. According to Callister and

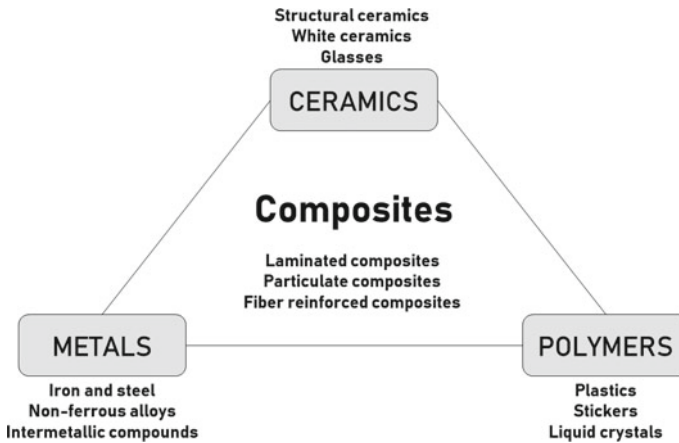


Fig. 1 Main subclasses of the three basic materials and composites

Rethwisch [13], the composite is a multiphase material whose properties are a synergistic combination of the properties of the phases that constitute them. With this, the materials combine and contribute synergistically with their characteristics to improve the properties of the final product, called the composite of interest.

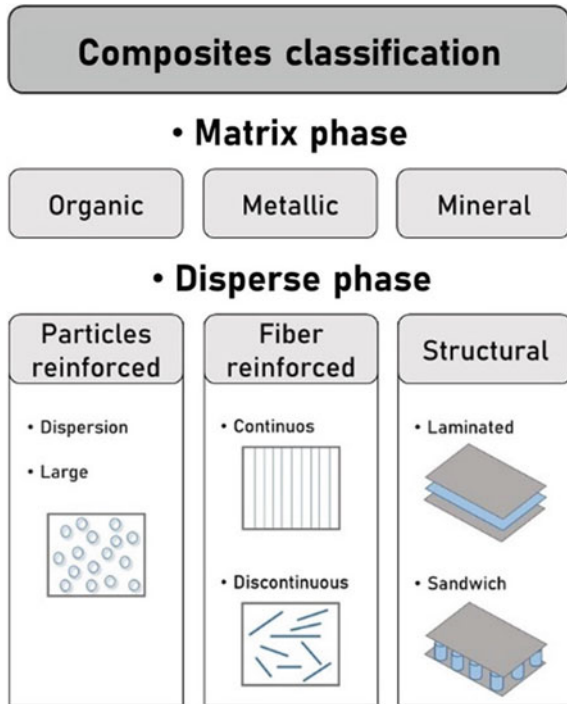
The composites have two phases, the matrix phase, and the dispersed phase. The matrix phase, known as the “binder”, is the continuous phase and includes metallic, non-metallic, or polymeric materials. It presents specific physical and mechanical properties such as ductility, formability, and thermal conductivity. The dispersed phase, known as “reinforcement” or “filling”, is the phase involved by the matrix and has low thermal expansions, high strength, and high rigidity, it can be a fibrous material such as glass or an organic fiber, among others [18]. The reinforcement phase is generally stronger and more rigid than the matrix phase, as it carries the load applied to the material. At least one representative from each phase is required to create a compound [18–20].

In this sense, the property of composite material will depend on the characteristics and geometry of the constituents, orientation, and distribution of the reinforcements, nature, and quality resulting from the reinforcement-matrix interface. Composites can be classified according to the nature of their constituents and according to the types and distribution of reinforcements [12, 13]. Figure 2 shows a schematic flowchart of these two types of classifications.

2.1.1 The Matrix Phase

Composites of organic classification are those that have as their matrix phase a polymer with dispersed reinforcement of carbon, glass, or metal fibers. The matrix determines the maximum service temperature, since it softens, melts, or degrades at a much lower temperature than the reinforcement, and because of this, thermosets

Fig. 2 Classification of composites



and thermoplastics are the two main types of polymers for the formation of these composites [13, 21, 22].

Thermosets have a 3D molecular structure that decomposes at high temperatures, and can be retained in a partially cured condition for a long period of time. Thermoplastics have a one- or two-dimensional molecular structure and melt at high temperatures. However, as an advantage over thermosets, they are soft at high temperatures, reversible, and their original properties can be restored by cooling [13, 16]. In this sense, typical thermosetting matrices are epoxy, polyester, polyamide, and vinyl ester, whereas the commonly used thermoplastics are polyethylene, polystyrene, and polyetheretherketone materials [12, 18, 23]. Organic matrix composites can be used in a low-temperature range, between 200 and 300 °C [12, 23].

The metallic composites are formed mainly by matrices of aluminum, magnesium, copper, and titanium, with reinforcement of mineral or metallic fibers, being able to be dispersed ceramic-like oxides and carbides or dispersed metallic like tungsten and molybdenum [24]. The metallic materials for having high rigidity and abrasive structures are attractive for the formation of composites. The metal composite reinforced with fibers or metallic particles is highly compatible and, if combined with heat-resistant metals, can withstand high temperatures. Carbon steel fibers are used to reinforce metallic matrices to withstand temperatures up to 300 °C [12, 19].

Mineral matrix composites are ceramic reinforced with metallic, mineral, or polymeric fibers or particles. Mineral composites can be used in a high-temperature range,

up to 1000 °C [12]. The main properties of these composites are lightness, rigidity, resistance to oxidation and deterioration at high temperatures, and susceptibility to brittle fracture, however, they are more resistant than conventional ceramic materials [13]. Among these composites are metal oxides, graphene oxides, and silicon carbide, which have a high degree of a bonding between matrix and reinforcement.

2.1.2 The Dispersed Phase

Composites can be classified by the form of distribution of their constituents, in this case, the reinforcement constituents. The classification according to the dispersed phase is subdivided into fibrous, particulate, or structural, as shown in Fig. 2. According to Callister and Rethwisch [13], the particles are a portion of a solid with three equal dimensions and the fibers are thin and elongated materials, like filaments.

In the dispersed phase reinforced with particles, charge transfer occurs from the matrix phase to the dispersed phase. The particle reinforcements do not have standard shapes, they can be of any geometry, regular or irregular, and their arrangement is randomly oriented, resulting in homogeneous and isotropic mechanical properties [12]. Particulate composites are more commonly made of a polymeric and mineral matrix, such as cement (mineral matrix) reinforced with gravel (particulate), to increase the hardness of the material. Particulate reinforced composites find applications where high levels of wear resistance are required. The advantage of particulate reinforced composites is their low cost and ease of production and conformation [12, 19, 25].

Fibrous composites are the most common and have the advantage of the high strength of the fiber combined with the low density of the matrix. The properties of these composites are the result of the adhesion intensity between matrix and reinforcement, the direction in which the load is applied in relation to the direction of the fibers, and the arrangement and orientation of the fibers. The behavior of the properties of these composites varies between a general anisotropy and a quasi-isotropy. Anisotropy is when a given property varies according to its direction in the material, and isotropy is when the material has the same physical properties in all its directions [13, 14, 23]. High adhesion between the two phases gives good mechanical resistance and a high fragility; this is due to the efficient transfer of charge from the matrix to the fibers. Low adhesion results in low mechanical resistance, as the adsorbed energy increases during the fiber pullout process [12, 13, 16].

The fibers can be classified as continuous (long) or discontinuous (short). When the manufacturing process ensures that the fibers are aligned, the anisotropy of the properties appears. The long fibers are usually arranged unidirectionally or bidirectionally and the short fibers are arranged irregularly. The preferred orientation in the case of continuous fiber composites is unidirectional for each layer [12]. Fiber-reinforced composites are very common in several processes, such as in the production of concretes, mortars, structures, and parts of automotive, marine, and aircraft vehicles [12, 19].

The structural classification can be by sandwich or laminated form and its formation occurs with alternating layers of different materials such as metals, glass, fabrics, or papers impregnated with polymers. The properties of these composites depend, in addition to the constituents, on the geometric design [13].

Within these classifications, there is the possibility of combining materials on a nanoscale that results in the formation of a new material called nanocomposite. Nanocomposites are generally classified as non-intercalated, laminated, and exfoliated, and the increase in their resistance occurs through interactions at the atomic or molecular level. These composites started to occupy a very important and promising space in several areas, more intensely in the area of biomedical and engineering [19, 26].

Therefore, composite materials are used in a wide range of applications in different segments. For example, they are used in the structure of automobiles and aircrafts [27, 28], the nautical area [29], civil construction [14], electronics [30], the medical and biomedical fields [31], and various sectors of engineering, chemistry, and the environment. In this sense, much research has started to develop new manufacturing techniques to increase the productivity and efficiency of these composites [19]. Besides, the appearance of emerging contaminants in the environment has become a focus of research since the mid-1990s [32]. The removal of these contaminants can be carried out by several methods, including the adsorption technique using composite materials.

Gelatin and activated carbon materials were developed as a non-toxic, biocompatible, and low-cost composite by Hayeeye et al. [33], to adsorb heavy metals and organic substances. Chitosan and carbon-based composite materials, including magnetic chitosan and chitosan combined with graphene oxide, carbon nanotubes, biochar, and activated carbon, as well as silica/chitosan compounds, are described in the study by Alves et al. [8]. These composites are applied in the removal of various heavy metal ions, including Cr(VI), Pb(II), Cd(II), Cu(II), and in different cationic and anionic dyes. Zhou et al. [26] developed Nano-MnO₂-biochar composites and determined the adsorption properties of Cu(II) using isothermal and kinetic studies.

3 General Concepts of the Adsorption Technique in Liquid Medium

Adsorption is a physical-chemical phenomenon that consists of the mass transfer of a fluid, which can be liquid or gas, to a solid surface in a heterogeneous system [9, 34–37]. In this chapter, only the liquid adsorption technique will be approached. In this technique, the solid phase is known as adsorbent and the molecule of interest, present in the liquid phase, is called adsorbate [36, 38].

In the adsorption mechanism, due to the imbalance of forces, the adsorbate is attracted to the surface of the adsorbent and, consequently, the degrees of freedom and the surface-free energy are reduced [39]. The transfer of the adsorbate from

the liquid to the solid phase continues until the equilibrium is reached, between the amount of adsorbate attached to the adsorbent and the amount of adsorbate remaining in the solution [38].

Compared to other unit operations, adsorption in liquid medium has some advantages [1, 34, 37, 40–43]:

- (a) Low energy consumption;
- (b) Environmentally friendly;
- (c) Easy implementation and operation;
- (d) Many materials can be used as adsorbents and can be regenerated, then reused several times, making the adsorption process a low-cost operation;
- (e) It is an efficient technique, because it can remove or recover all the adsorbate from the solution;
- (f) In some cases, adsorption can also be selective.

However, studies must be performed to the correct dimensioning and understanding of the adsorption system, determining parameters of speed, capacities, nature, and adsorption mechanisms, in addition to the development of new adsorbent materials [44].

3.1 Physical and Chemical Adsorption and Factors that Influence This Phenomenon

The nature of the adsorption phenomenon depends on the bonding strength between the molecules that are being adsorbed and the adsorbent [35]. There are two types of adsorption: physical adsorption and chemical adsorption.

In physical adsorption, the intermolecular forces of attraction of the molecules in the fluid phase and on the surface of the adsorbent are greater than the attractive forces between the molecules of the fluid itself [45]. Thus, in the case of physical adsorption relatively weak, and spontaneously reversible forces, which mainly involve Van der Waals forces, cause the fluid molecules to adhere on the surface of the solid adsorbent, establishing a balance between the adsorbed fluid and the remaining fluid phase [36, 46]. In this type of adsorption, no bond is broken or created. Therefore, the chemical nature of the adsorbate is not changed [36]. In addition, as it occurs on the entire surface of the adsorbent, it is considered non-localized adsorption [35]. In this case, the adsorption energies are in the range of 5–40 kJ/mol [47].

Chemical adsorption involves the electrons replacement or sharing between the molecules of the fluid phase and the surface of the adsorbent, resulting in a new chemical bond, which is stronger than the physical adsorption [1, 35, 38]. It is important to note that not all molecules in the fluid can be chemically adsorbed, only those capable of binding to active sites, so it is said to be localized [35]. The adsorption energies are in the range of 40–800 kJ/mol [47].

Usually, the adsorption phenomenon is the result of a combination of the types of forces involved between chemical and physical adsorption. Thus, several factors

influence the adsorption process, such as: nature of the adsorbent and the adsorbate, and the operating conditions [35].

Mechanical properties (tensile and compression strength, stiffness, ductility, and toughness) [42], chemical properties (water-insoluble solid) [47, 48], and physical properties (surface area and pore volume) [49] are able to make the adsorbent more stable, expanding its application. Thus, the adsorbent surface area and porosity determine how much area will be available for adsorption, in addition to assisting in the choice of the adsorbent, since, it depends on the size of the pores available in the material [48, 50].

The quantity, type, and location of functional groups on the adsorbent surface directly affect the adsorption capacity, since they are directly responsible for the chemical or physical bonding process between the adsorbent and the adsorbate [35]. One of the ways to evaluate the types of available groups in the aqueous solution is through pH, which determines the degree of chemical species distribution. Thus, the ideal pH will depend on the type of the evaluated adsorbate, which is $\text{pH} > 7$ favoring the adsorption of organic bases and $\text{pH} < 7$ favoring the adsorption of organic acids [35, 48]. To evaluate the present groups on the surface of the adsorbent material, zero charge point determination may be used [51], which will infer in the presence of anions or cations.

The temperature mainly affects the adsorption rate constant [35]. An increase in temperature during the adsorption process can cause an increase in the kinetic energy and in the mobility of the adsorbate species, and also, it can cause an increase in the intraparticle diffusion rate of the adsorbate [52].

3.2 Adsorption Isotherm

The adsorption isotherm is a relationship between the amount of adsorbate retained in the adsorbent material and the amount of adsorbate that remained in the liquid phase, with the two phases at a certain temperature and in dynamic equilibrium [38, 50]. Therefore, the isotherm provides the measure of equilibrium [53]. In addition, it is important in the optimization of the use of adsorbents, in the reliable prediction of adsorption parameters and in the analysis of data through its suitability for different mathematical models [47, 54].

The adsorption equilibrium data are evaluated using physical-mathematical models of isotherms. The isotherm models observed in the literature for the prediction of the drugs by composites are: Dubinin-Radushkevich [55], Freundlich [56], Hill [57], Langmuir [58], Liu et al. [59], Redlich-Peterson [60], Sips [61], and Temkin [62]. These models are shown in Table 1. The appropriate adjustment of these equations to the experimental data provides information about the maximum adsorption capacity of the adsorbent material (q_{max}), the nature of the adsorption and the possible interaction mechanisms between the adsorbate and the adsorbent [9, 35].

Furthermore, in liquid phase adsorption, isotherm curves are important due to [38]:

Table 1 Isothermal models applied for the prediction of drug adsorption by composites

| Isothermal models | Equations | Parameters | References |
|----------------------|--|---|-------------------------------|
| Dubinin-Radushkevich | $q_e = q_{DR} \times \exp(-K_{DR} \times \varepsilon^2)$ | q _e : equilibrium adsorption capacity (mg/g); q _{DR} : Dubinin-Radushkevich constant (L/mg); K _{DR} : constant associated to the adsorption free energy (kJ/mol); ε: potential of Polainy (J/mol) | Dubinin and Radushkevich [55] |
| Freundlich | $q_e = K_F \times C_e^{\frac{1}{n_F}}$ | K _F : Freundlich equilibrium constant ((mg/g)(L/mg) ^{1/n_F}); C _e : supernatant concentration at equilibrium (mg/L); 1/n _F : heterogeneity factor | Freundlich [56] |
| Hill | $q_e = \frac{q_{max} \times C_e^{n_H}}{K_H + C_e^{n_H}}$ | q _{max} : maximum adsorption capacity of the monolayer (mg/g); n _H : coefficient of cooperativity of the bond interaction; K _H : Hill equilibrium constant (L/mg) | Hill [57] |
| Langmuir | $q_e = \frac{q_{max} \times K_L \times C_e}{1 + K_L \times C_e}$ | K _L : Langmuir equilibrium constant (L/mg) | Langmuir [58] |
| Liu | $q_e = \frac{q_{max} \times (K_G \times C_e)^{n_L}}{1 + (K_G \times C_e)^{n_L}}$ | K _G : Liu equilibrium constant (L/mg); n _L : exponent of Liu (dimensionless) | Liu et al. [59] |
| Redlich-Peterson | $q_e = \frac{K_{RP} \times C_e}{1 + a_{RP} \times C_e^{\beta_{RP}}}$ | K _{RP} and a _{RP} : Redlich-Peterson equilibrium constants (L/g or mg/L); β _{RP} : exponent of Redlich-Peterson (dimensionless) | Redlich and Peterson [60] |

(continued)

Table 1 (continued)

| Isothermal models | Equations | Parameters | References |
|-------------------|--|---|-------------|
| Sips | $q_e = \frac{K_S \times q_{max} \times C_e^{ns}}{1 + K_S \times C_e^{ns}}$ | K_S : Sips equilibrium constant (L/mg); ns: exponent of Sips (dimensionless) | Sips [61] |
| Temkin | $q_e = \frac{R \times T}{b_t} \times \ln(K_t \times C_e)$ | R: universal gas constant (8.314 J/mol K); T: temperature (K); b_t : related to the maximum bond energy; K_t : Temkin adsorption constant (L/mg) | Temkin [62] |

- (a) Possibility of obtaining the greatest adsorption capacity of an adsorbent in different experimental conditions;
- (b) Acquisition of information about the energetic, steric, and affinity points of view;
- (c) From the shape of the isothermal curve it is possible to understand the mechanism of interaction between adsorbent and adsorbate;
- (d) Identification of thermodynamic adsorption parameters, such as Gibbs free energy change (ΔG°), standard enthalpy change (ΔH°), and standard entropy change (ΔS°), these parameters are fundamental to verify the spontaneity and nature of the adsorption.

3.3 Adsorption Kinetics

The kinetic study of adsorption provides information about the speed that the adsorbate is retained on the surface of the adsorbent material, and about the factors that influence the adsorption rate [47, 63]. In addition, it provides information about the mass transfer mechanisms [47].

The mechanisms of mass transfer consist of a few steps that explain the passage of the contaminant from the sinus of the solution to the adsorbent material [63, 64]. Among these mechanisms, the following can be highlighted [63, 64]:

- (a) Transport of the contaminant molecules to the adsorbent external surface;
- (b) Movement of the contaminant molecules through the adsorbent interface, the adsorption is governed by convection at the external sites of the adsorbent;
- (c) Migration of the molecules in the solution to the adsorbent internal pores, by diffusion;
- (d) Adsorption of contaminant molecules at the available adsorption sites.

Generally, the first and the last steps of the adsorption are relatively quick, by making the mass transfer into the adsorbent composite to be governed by the mass

transfer at its interface and inside. Homogeneous solid diffusion models (HSDM) [65] and linear driving force [66, 67] describe these two mechanisms. The model of Weber and Morris [68] is a physical-mathematical simplification of the HSDM model that serves to evaluate mass transfer steps. However, in the case of emerging contaminants removal by adsorbent composites, pseudo-reactive models have been applied in the study of adsorption rates. In this case, the models of Elovich [69], fractional order [70], pseudo-first order [71], and pseudo-second order [72, 73] are included. The mass transfer and reaction models are shown in Table 2.

3.4 *Fixed-Bed Adsorption*

Batch adsorption assays are used in the preliminary choice of the adsorbent, providing data such as the maximum amount of adsorption, speed, and favorable conditions of the process. However, these assays are limited to the treatment of small volumes of liquid and are not able to provide data for the dimension of continuous treatment systems [74]. Thus, fixed-bed systems (column) are an alternative, as they allow the treatment of large volumes of effluents [75]. In addition, this system allows the operation of regeneration cycles, so, through the use of an appropriate effluent solution, the adsorbent can be regenerated and reused [75, 76].

Fixed-bed adsorption is influenced by several dynamic conditions, such as pH of the input solution, initial contaminant concentration, initial flow rate, bed height, and mass, as these being the objects of pilot scale studies [77]. In addition, one of the most important elements associated with the design of a fixed-bed adsorption column is the description of the mass transfer rate of the adsorbent, which can be obtained through the rupture curves [78, 79]. This essay can predict the saturation point of the adsorption column according to the feeding conditions, obtaining a relation between the ratio of the output concentration and the concentration of the feed and the time [76, 79]. Through the rupture curve at the equilibrium point it is possible to determine parameters such as total time, useful time, useful height, and saturation capacity [78].

At the beginning of the fixed-bed adsorption process, most of the mass transfer occurs close to the entrance of the bed, where the liquid phase comes into contact with the adsorbent [53, 79]. In this system, the concentration of the adsorbate in the liquid and solid phases varies in space and time. Thus, the concentration of the adsorbate in the liquid phase exponentially decays with the distance traveled in the bed for a certain time, being retained in the adsorbent material [79]. After a period of time, the adsorbent at the entrance of the bed is saturated, and most of the mass transfer takes place inside the bed, until the effluent concentration is equal to the effluent concentration in the column [53, 79]. Thus, fixed-bed adsorption assays are used to determine operational parameters and to satisfy the expansion of the process.

Table 2 Kinetic models applied for the prediction of drug adsorption by composites

| Kinetic models | Equations | Parameters | References |
|--|---|--|---------------------------------|
| <i>Mass transfer models</i> | | | |
| Homogeneous diffusion solid model (HSDM) | $\frac{\partial q_r}{\partial t} = D_s \times \left(\frac{\partial^2 q_r}{\partial r^2} + \frac{2\partial q_r}{r\partial r} \right)$ | $\partial q_r/\partial t$: rate of change of the adsorbate concentration in the solid phase with time in a position of the particle (mg/g/min); $\partial q_r/\partial r$: gradient of adsorbate concentration in the solid phase along the particle radius (mg/g/m); D_s : diffusivity in the solid (m ² /min) | Crank [65] |
| Linear driving force | $\frac{\partial q}{\partial t} = k_f \times a_p \times (C - C_i)$ | $\partial q/\partial t$: rate of change in the adsorbate concentration in the solid phase by unit of time (mg/g/min); k_f : mass transfer coefficient in the stagnant film (m/min); a_p : specific area of the adsorbent particles by volume unit (m ² /g); C : adsorbate concentration in the liquid phase (mg/m ³); C_i : adsorbate concentration in the liquid phase at the solid/liquid interface (mg/m ³) | Qiu et al. [66] and Cooney [67] |
| Weber and Morris | $q_t = k_{int} \times t^{0.5} + C$ | q_t : adsorption capacity in the time (mg/g); k_{int} : intraparticle diffusion coefficient (mg/g/min); t : time (min); C : constant that is linked with the resistance to diffusion (mg/g) | Weber and Morris [68] |

(continued)

Table 2 (continued)

| Kinetic models | Equations | Parameters | References |
|------------------------|--|---|--------------------------------------|
| <i>Reaction models</i> | | | |
| Elovich | $q_t = \frac{1}{a} \times \ln(1 + (a \times b \times t))$ | a: initial adsorption rate (mg/g/min); b: desorption constant (mg/g) | Elovich and Larionov [69] |
| Fractional order | $q_t = q_e \times \{1 - \exp[-(k_{AV} \times t)]^{n_{AV}}\}$ | q _e : equilibrium adsorption capacity (mg/g); k _{AV} : Avrami kinetic constant (min ⁻¹); n _{AV} : fractional order of reaction related to the adsorption mechanism | Avrami [70] |
| Pseudo-first order | $q_t = q_1 \times (1 - \exp(-k_1 \times t))$ | q ₁ : theoretical value of the adsorption capacity (mg/g); k ₁ : pseudo-first order rate constant (min ⁻¹) | Lagergren [71] |
| Pseudo-second order | $q_t = \frac{t}{\left(\frac{1}{k_2 \times q_2^2}\right) + \left(\frac{t}{q_2}\right)}$ | k ₂ : pseudo-second order rate constant (g/mg/min); q ₂ : theoretical value of the adsorption capacity (mg/g) | Ho and Mckay [72], Ho and Mckay [73] |

3.5 Development of Adsorbent Composites Used in Adsorption

In order to develop a suitable adsorption system, the choice of the adsorbent material is one of the fundamental aspects [38]. A good adsorbent must have the following characteristics: low cost, availability, efficiency, high surface area and pore volume, mechanical and chemical stability, ease of desorption and reuse, fast kinetics, and mainly, high adsorption capacity [80].

Often, the use of only one component in the adsorbent formulation does not present satisfactory characteristics of adsorption. In this way, composite materials are alternatives, as they consist in two or more components with different characteristics from the unique constituents [13]. Composites are generally stronger and more stable, of lower density or less cost than basic materials [16].

Examples of adsorbent composites include: nanocomposites, metal matrix composites, polymer matrix, ceramic matrix, organic–inorganic composites, magnetic, and hybrid composites [19].

The composites production has been widespread in the adsorption area due to the need of adsorbents with better removal characteristics for emerging contaminants [81]. In addition, it is interesting to highlight that materials of residual origin, degradable, or low cost can be used in the formulations of composite materials.

4 Composite Materials for Drug Adsorption: Bibliometric and Systematic Review

The bibliometric analysis and the systematic review provide a transparent and reproducible process for selecting studies, extracting data and analyzing results in a given topic [82, 83]. This research methodology allows to approach a large number of records and to identify the main trends in a given scope of interest, composing an overview of the latest advances reported in the state of the art through a qualitative and quantitative assessment.

Thus, in order to understand scientific articles that addressed the scope of composite materials for drug adsorption, bibliometric analysis was carried out through the academic database of Science Direct. The database was consulted on February 10, 2021. The methodological procedures adopted to meet the research focus, took place after the study of keywords on the subject and the operators used by the database [82, 84].

The words used for the search were composed of “adsorption AND composite AND (drug OR medicine OR pharmaceutical)”, using English as the exclusive language for the search in title, abstracts, and keywords in the category of research articles starting with the year 2015. Afterward, the articles were refined through the title, highlights, summary, and keywords that understood the intended scope.

The search in the database resulted in 304 research articles. Of these, 87 articles were selected in the screening to compose the study's bibliographic portfolio. The others were disregarded as they focused on studies that did not address the intended scope. Articles that approached preliminary adsorption assays were considered, which could have their parameters extracted for analysis and confection of the tables. In addition, for some selected articles, the extracted data was standardized for the units of analysis. Thus, Tables 3 and 4 were made for batch and fixed-bed assays, respectively, which show all selected studies. The year 2020 presented the largest number of publications with 26 articles, and the year 2021 already had 11 articles up to the date of the research. In addition, Fig. 3 shows the main drugs evaluated in the adsorption studies.

It is observed from Tables 3 and 4, trends for syntheses of composites based on chitosan, biochar, activated carbon, graphene oxide, carbon nanotubes, clay, silica, and metal-organic compounds for the drug removal using the adsorption processes in liquid medium, real effluent, or water resource sampling. Allied to this, in Fig. 4 the applications of adsorbent composites were schematized. The incorporation of these materials for the development of composites is an efficient way to improve and enhance the physical, chemical, and mechanical properties. Subsequently, in items 4.1 and 4.2, some main studies are discussed, which comprehend materials of organic and inorganic origins commonly used and identified with the aid of the bibliometric analysis for the development of new composites. In addition, the main characteristics of the materials are presented.

Each composite has specificities, and is also influenced by operating conditions of the adsorption process, resulting in the adsorption capacities or removals obtained in each study, and presented in Tables 3 and 4. This demonstrates the wide range of possibilities for composites and conditions for drug removal, which can still be developed and evaluated.

The pHs that stood out in the batch adsorption studies (Table 3) were pH 5 and 6, while in fixed bed (Table 4) the highlighted pH was 7. The pH influences the distribution of chemical species in the adsorbent and the adsorbate structures, inducing the type of interactions between them, such as electrostatic attractions, π -ion bonds, and ion-dipole interaction. To evaluate the effect of pH on the surface charge of the adsorbent, it is necessary to characterize the zero charge point [51]. Commonly, at $\text{pH} > 7$, negative charges are observed on the surface of the adsorbent materials, when this occurs, there is a preference for contaminants with cationic groups. On the other hand, at $\text{pH} < 7$, the surface of the adsorbent is positively charged, having greater interaction by anionic molecules of the adsorbate. Another point that must be taken into account is the ionization constant of the drugs, as it will imply the load of the contaminant molecule and its precipitation, influencing the removal. Thus, the natural pH of the solution can be maintained or changed to favor the adsorption, given the knowledge of the charges of the adsorbent material and the contaminant.

The temperature that stood out in batch adsorption studies (Table 3) was 25 °C and in fixed-bed studies (Table 4) was 20 °C. The temperature affects the speed of diffusion of the adsorbate molecules, making it possible to determine the adsorption thermodynamics through temperature ranges, and thus evaluate possible adsorption

Table 3 Adsorbent composites and operational conditions used in the adsorption of drugs through batch assay

| Adsorbent composite | Drug | Operational conditions | | | q _{max} (mg/g) | References |
|--|----------------------------|------------------------|------------------|----------------------|-------------------------|--------------------------|
| | | pH | Temperature (°C) | Concentration (mg/L) | | |
| Magnetic (MnFe ₂ O ₄)/chitosan/diphenylureaformaldehyde | Tetracycline | 6.0 | 25 | 5–250 | 172.12 ^a | Ahamad et al. [87] |
| Iron nanoparticles/chitosan | Diclofenac sodium | 5.0 | 30 | 0.10–0.70 | 0.50 ^d | ALOfthman et al. [88] |
| Bentonite/chitosan/activated carbon/magnetic (Fe ₃ O ₄) | Atenolol | – | 30 | 0.5–40 | 15.60 ^a | Arya and Philip [89] |
| | Ciprofloxacin | | | | 39.10 ^a | |
| | Gemfibrozil | | | | 24.80 ^a | |
| O-carboxymethyl-N-laurylchitosan/magnetic (γ-Fe ₂ O ₃) | Ibuprofen | 7.0 | 25 | 5–75 | 395.00 ^b | Chahm and Rodrigues [90] |
| Chitosan hydrogels/nano-graphene oxide/genipin | Diclofenac sodium | – | Room temperature | 0.01 | 2.00 [*] | Feng et al. [91] |
| Magnetite/chitosan/poly(sodium 4-styrenesulfate) positive | Tetracycline hydrochloride | 3.7 | 25 | 125–755 | 66.66 ^b | Filho et al. [92] |
| | Sodium cromoglycate | 6.6 | | 12–90 | 76.85 ^b | |
| Magnetite/chitosan/poly(sodium 4-styrenesulfate) negative | Tetracycline hydrochloride | 3.7 | | 12.5–755 | 93.33 ^b | |
| | Sodium cromoglycate | 6.6 | | 12–90 | 23.05 ^b | |
| Magnetic (γ-Fe ₂ O ₃)/crosslinked chitosan | Norfloxacin | 5.0 | 30 | 10–35 | 8.55 ^a | Huang et al. [93] |
| Starch/chitosan/MOF (UiO-66-COOH) | Sulfamilamide | 3.0 | – | 10–160 | 70.20 ^a | Jia et al. [94] |
| Chitosan/waste coffee-grounds | Caffeine | 6.0 | 25 | 2 | 8.21 [*] | Lessa et al. [95] |
| | Acetaminophen | | | | 7.52 [*] | |

(continued)

Table 3 (continued)

| Adsorbent composite | Drug | Operational conditions | | | q _{max} (mg/g) | References |
|--|-------------------------------|------------------------|------------------|----------------------|-------------------------|---------------------------|
| | | pH | Temperature (°C) | Concentration (mg/L) | | |
| Magnetic (Fe ₃ O ₄)/ amine-functionalized chitosan | Acetylsalicylic acid | | | | 9.92* | |
| | Metamizol | | | | 6.29* | |
| Genipin-crosslinked chitosan/ graphene oxide-SO ₃ H | Diclofenac sodium | 4.5 | 30 | 20–1000 | 469.48 ^a | Liang et al. [96] |
| | Tetracycline | 7.0 | 40 | 20–200 | 500.68 ^a | Liu et al. [97] |
| Chitosan/TiO ₂ | Ibuprofen | 6.0 | 35 | 1–10 | 160.83 ^a | |
| | Metronidazole | – | – | 0.1–10 | 5.90 ^d | Neghi et al. [98] |
| Polyvinyl alcohol/chitosan supported TiO ₂ | | | | | 5.10 ^d | |
| | | | | | | |
| Chitosan/magnetic (Fe ₃ O ₄) | Diclofenac sodium | 4.0 | 25 | 20–200 | 196.00 ^a | Zhang et al. [99] |
| | Tetracycline hydrochloride | | 35 | | 67.10 ^a | |
| MOF (ZIF-8)/chitosan | Tetracycline | 8.0–9.0 | 20 | 40–500 | 495.04 ^a | Zhao et al. [100] |
| | Norfloxacin | 3.0 | 25 | 20–150 | 165.00* | Zhou et al. [86] |
| Aromatic rings-functionalized chitosan/magnetic (Fe ₃ O ₄) | Tylosin | 4.0 | | | 134.00* | |
| | Diclofenac sodium | 6.0 | | | 151.00* | |
| Activated carbon/magnetic (Fe ₃ O ₄) | Ceftriaxone | 3.0 | 25 | 10–100 | 28.93 ^a | Badi et al. [101] |
| Activated carbon/Fe(II) and Fe(III) oxides | Metformin hydrochloride | 5.8 | 45 | 1–25 | 18.74 ^a | Çavuşoğlu et al. [102] |

(continued)

Table 3 (continued)

| Adsorbent composite | Drug | Operational conditions | | | References |
|---|-------------------|------------------------|------------------|----------------------|---------------------------|
| | | pH | Temperature (°C) | Concentration (mg/L) | |
| Multiwalled carbon nanotubes/Fe(II) and Fe(III) oxides | | 35 | | 14.59 ^a | Dang et al. [103] |
| | | 45 | | 26.17 ^a | |
| Graphene nanoplatelets/Fe(II) and Fe(III) oxides | | | | | |
| Titanate nanotubes/activated carbon fiber | Diclofenac | 7.0 | 0–80 | 86.96 ^a | Dang et al. [103] |
| Magnetic (NiFe ₂ O ₄)/activated carbon | Ibuprofen | 2.0 | 0–100 | 261.35 ^b | Frohlich et al. [104] |
| | Ketoprofen | | | 97.75 ^b | |
| MgAl/activated carbon with layered double hydroxides | Diclofenac sodium | 5.5 | 5–200 | 2114.43 ^a | Lins et al. [105] |
| Activated carbon/TiO ₂ | Diclofenac | – | 5–50 | 105.30 ^a | Mouchtari et al. [106] |
| | Carbamazepine | | | 153.80 ^a | |
| | Sulfamethoxazole | | | 125.00 ^a | |
| Waste polyethylene terephthalate/activated carbon | Cephalexin | Natural | 15–55 | 21.27 ^a | Rai and Singh [107] |
| | | | | 71.42 ^a | |
| Waste polyethylene terephthalate/activated carbon/magnetic (FeCl ₃) | | | | | |
| Magnetic (CuFe ₂ O ₄)/activated carbon | Tetracycline | 6.8 | 100–700 | 384.62 ^a | Saygılı and Saygılı [108] |
| Activated carbon/TiO ₂ | Salicylic acid | 3.0 | Room temperature | 990.00 ^b | Taoufik et al. [109] |
| | Ciprofloxacin | 6.0 | 10–250 | 286.60 ^c | |

(continued)

Table 3 (continued)

| Adsorbent composite | Drug | Operational conditions | | | q _{max} (mg/g) | References |
|--|----------------------------|------------------------|------------------|----------------------|-------------------------|---------------------------|
| | | pH | Temperature (°C) | Concentration (mg/L) | | |
| Biochar/montmorillonite | Ciprofloxacin | 5.0–6.0 | 25 | 10–250 | 167.36 ^c | Ashiq et al. [111] |
| Montmorillonite/biochar | Tetracycline | 7.0 | – | 0.25–50 | 25.98 ^a | Borthakur et al. [112] |
| Natural red earth/biochar | | | | | 17.50 ^a | |
| Metal/biochar | Methylene blue | 3.0 | – | 24 | 9.19 [*] | Cho et al. [113] |
| | Para-chlorobenzoic acid | 5.0 | | 0.2 | 0.03 [*] | |
| Biochar/montmorillonite | Atenolol | 8.0 | 25 | 25–200 | 86.86 [*] | Fu et al. [114] |
| Magnetic (CuZnFe ₂ O ₄)/biochar | Sulfamethoxazole | 7.0 | 25 | 1–80 | 212.80 ^a | Heo et al. [115] |
| Biochar/nano-hydroxyapatite | Tylosin | 6.0 | 35 | 20 | 67.03 ^a | Li et al. [116] |
| Bentonite/zeolites/biochar/cockleshell/portland cement | Atenolol | 7.0 | – | 2.5 | 0.12 ^a | Mojiri et al. [117] |
| | Ciprofloxacin | | | | 0.13 ^a | |
| | Diazepam | | | | 0.13 ^a | |
| ZnAl/biochar | Acetaminophen | 5.0 | 25 | 25–125 | 1108.43 [*] | Moreno-Pérez et al. [118] |
| | Ketoprofen | | | | 1081.35 [*] | |
| | Ibuprofen | | | | 1032.81 [*] | |
| MgAl/layered double hydroxide supported on biochar | Diclofenac sodium | 5.65 | 60 | 50–1000 | 168.04 ^b | Santos et al. [85] |
| Nanosheets (MoS ₂)/biochar nanocomposite | Tetracycline hydrochloride | 4.0 | 45 | 10–400 | 699.30 ^a | Zeng et al. [119] |

(continued)

Table 3 (continued)

| Adsorbent composite | Drug | Operational conditions | | | References |
|--|-----------------------------|------------------------|------------------|----------------------|---------------------------|
| | | pH | Temperature (°C) | Concentration (mg/L) | |
| Graphene oxide/nano-hydroxyapatite | Aureomycin hydrochloride | 5.5 | 20 | – | Anirudhan et al. [120] |
| Nano-zinc oxide/graphene oxide/nanocellulose | Ciprofloxacin hydrochloride | 5.5 | 20 | – | Anirudhan and Deepa [121] |
| Graphene oxide/cellulose | Flupentixol | 5.3 | 21.5 | 47.8 | Balsubramani et al. [122] |
| Graphene oxide/magnetite | Chlorpheniramine | 5.0 | – | 120 | Chen et al. [123] |
| Three-dimensional graphene oxide/L-ascorbic acid | Diclofenac sodium | 6.0 | 30 | 100–400 | Hiew et al. [124] |
| Magnetite/graphene oxide | Phenazopyridine | 6.0 | 25 | 0.25–14 | Karimi-Maleh et al. [125] |
| Non-covalent functionalized graphene oxide with an organic gelator | Ciprofloxacin | 7.0 | – | 10 | Ly et al. [126] |
| Graphene oxide/imidazolium based ionic liquid | Sulfamethoxazole | 6.3 | 25 | 5–25 | Ogunleye et al. [127] |
| Nitrogen-doped reduced graphene oxide/magnetic (Fe ₃ O ₄) | Norfloxacin | 6.8 | 25 | 10–60 | Peng et al. [128] |
| | Ketoprofen | | | 468.00 ^a | |
| Graphene oxide/MOF (MIL-101 (Cr)) | Naproxen | 7.0 | 25 | 10–50 | Sarker et al. [129] |
| | Ketoprofen | | | 140.00 ^a | |
| Functional polyaniline/multiwalled carbon nanotube | Meloxicam | 2.0 | 25 | 0.025–2 | Dutra et al. [130] |

(continued)

Table 3 (continued)

| Adsorbent composite | Drug | Operational conditions | | | q _{max} (mg/g) | References |
|--|--------------------|------------------------|------------------|----------------------|-------------------------|------------------------|
| | | pH | Temperature (°C) | Concentration (mg/L) | | |
| Tannery wastes-derived gelatin/carbon nanotubes | Diclofenac sodium | 8.15 | 25 | 37.5–300 | 20.57 ^a | Rigueto et al. [131] |
| Commercial gelatin/carbon nanotubes | | | | | 26.97 ^a | |
| Bismuth tungstate/raphitic carbon nitride/multiwall carbon nanotube | Ceftriaxone sodium | 4.0 | Room temperature | 10–100 | 19.57 ^a | Shi et al. [132] |
| Polymer/magnetic carbon nanotubes | Metformin | 10.0 | – | 5–100 | 80.00 ^a | Toudeshki et al. [133] |
| Montmorillonite/pyridine monomers of poly-4-vinylpyridin-co-styrene 50% | Gemfibrozil | – | – | 0–12 | 1.60 [*] | Kohay et al. [134] |
| | Diclofenac sodium | | | 0–161 | 15.90 [*] | |
| Montmorillonite/pyridine monomers of poly-4-vinylpyridin-co-styrene 100% | Gemfibrozil | | | 0–12 | 0.75 [*] | |
| | Diclofenac sodium | | | 0–161 | 27.04 [*] | |
| Magnetic (Fe ₃ O ₄)/montmorillonite | Enrofloxacin | 6.8 | 25 | – | 162.91 ^a | Peng et al. [135] |
| Zeolite/molybdenum disulfide/cobalt disulfide | Tetracycline | 3.0 | 20 | 200 | 817.60 [*] | Liu et al. [136] |
| Surfactant/phillipsite modified with cetylpyridinium chloride | Diclofenac sodium | 7.4 | 30 | 50–500 | 47.05 ^a | Marković et al. [137] |
| | | | | | 56.20 ^a | |
| Surfactant/phillipsite modified with hexadecyltrimethyl ammonium bromid | | | | | | |
| Zinc (II)/hydroxyapatites | Tetracycline | 5.0 | 25 | 1–2500 | 168.46 ^a | Oliveira et al. [138] |

(continued)

Table 3 (continued)

| Adsorbent composite | Drug | Operational conditions | | | q _{max} (mg/g) | References |
|--|-------------------------------|------------------------|------------------|----------------------|-------------------------|---------------------------------|
| | | pH | Temperature (°C) | Concentration (mg/L) | | |
| Natural zeolites (Clinoptilolite)/ cationic surfactants (Cetylpyridinium chloride) | Diclofenac sodium | 6.5 | Room temperature | 2–100 | 35.00 ^a | Smiljanic et al. [139] |
| | Ketoprofen | | | | 13.60 ^a | |
| Silica/alumina | Metformin | 9.0 | 20 | 5–250 | 45.70 ^b | Alhajjar et al. [140] |
| Silica/zirconia | Ampicillin | – | – | 20 | 20.00 [*] | Catauro et al. [141] |
| Silica/magnetite/N1-(3 trimethoxisilylpropyl) diethylenetriamine | Ibuprofen | 6.0 | 25 | 10–250 | 72.60 ^a | Kittappa et al. [142] |
| Amine grafted pumice/silica | Ibuprofen | 7.0 | – | 2–10 | 26.82 ^a | Mohseni-Bandpei et al. [143] |
| Iron oxide/silica | Acetylsalicylic acid | – | Room temperature | 100–500 | 7.08 ^a | Teo et al. [144] |
| Silica/polyelectrolytes | Ibuprofen | 5.5 | Room temperature | 1–41 | 1666.00 ^a | Varga et al. [145] |
| Porous silica fibers/polyacrylonitrile/ polymethylmethacrylate | Metoprolol tartate | – | Room temperature | 50,000 | 225.00 [*] | Zhang et al. [146] |
| Wool/MOF (ZIF-8 (Zn)) | 2-naphthol | – | 30 | 0–5000 | 391.10 ^a | Abdelhameed and Emam [147] |
| Wool/MOF (ZIF-64 (Co)) | | – | | | 371.20 ^a | |
| MOF (UiO-66)/polydopamine/ bacterial cellulose | Aspirin | 3.0–4.0 | 45 | 20–200 | 176.55 ^a | Cui et al. [148] |
| | Tetracycline hydrochloride | | | | 210.31 ^a | |
| MOF (Bimetallic ZIF (Co and Zn))/ activated carbon | Amodiaquine | 5.4 | 25 | 50–300 | 1039.27 [*] | Pan et al. [149] |

(continued)

Table 3 (continued)

| Adsorbent composite | Drug | Operational conditions | | | q _{max} (mg/g) | References |
|---|-----------------|------------------------|------------------|----------------------|-------------------------|-----------------------|
| | | pH | Temperature (°C) | Concentration (mg/L) | | |
| Eutectic solvents/magnetic (Fe ₃ O ₄)/MOF (MUIO-66-NH ₂) | Ofloxacin | 5.0 | 25 | 0.2–1.6 | 50.00a | Wei et al. [150] |
| | Mefenamic acid | – | – | – | 52.91 ^a | |
| Nickel/MOF (74 (Ni)) | Ibuprofen | – | Room temperature | 475 | 4.10 [*] | Xu et al. [151] |
| Tonic liquids/MOF (ZIF-8) | Oxytetracycline | 8.0 | 25 | 10–50 | 69.50 ^a | Yohannes et al. [152] |
| MOF (MIL-101(Cr))/graphene aerogel | Phenacetin | 4.0 | – | 2–40 | 232.50 ^a | Zhou et al. [153] |
| | Naproxen | – | – | 1–60 | 333.30 ^a | |
| MOF (MIL-101(Cr))/chitosan | Benzoic acid | 4.08 | – | 20–80 | 66.55 ^a | Zhuo et al. [154] |
| | Ibuprofen | 4.27 | – | – | 103.20 ^a | |
| | Ketoprofen | 4.23 | – | – | 156.50 ^a | |
| | Benzoic acid | 4.08 | – | – | 36.50 ^a | |
| MOF (MIL-101(Cr))/sodium alginate | Ibuprofen | 4.27 | – | – | 62.60 ^a | |
| | Ketoprofen | 4.23 | – | – | 130.60 ^a | |
| | Ibuprofen | 7.0 | 20 | 0.01–0.08 | 0.07 ^a | |
| Iron nanocomposite/carboxymethylcellulose | Pantoprazole | 7.0 | 20 | 0.01–0.07 | 0.05 ^a | Ali et al. [155] |
| Iron nanocomposite/carboxymethylcellulose | Pantoprazole | 7.0 | 20 | 0.01–0.07 | 0.05 ^a | Ali et al. [156] |

(continued)

Table 3 (continued)

| Adsorbent composite | Drug | Operational conditions | | | q _{max} (mg/g) | References |
|--|----------------------|------------------------|------------------|----------------------|-------------------------|---------------------------|
| | | pH | Temperature (°C) | Concentration (mg/L) | | |
| Polyethyleneimine-functionalized sodium alginate/cellulose nanocrystal/polyvinyl alcohol core-shell microspheres | Diclofenac sodium | 4.5 | 30 | 100–1000 | 418.41 ^a | Fan et al. [157] |
| Egg albumin/polyethyleneimine functional | Diclofenac sodium | 6.0 | – | 10–300 | 232.50 ^a | Godiya et al. [158] |
| Cellulosic sisal/sisal-poly | Ibuprofen | 5.0 | 40 | 10–50 | 19.45 ^a | Khadir et al. [159] |
| Luffa cylindrica/polypyrrole | Ibuprofen | 5.0 | 25 | 10–100 | 19.16 ^a | Khadir et al. [160] |
| Poly (styrene-divinyl benzene-glycidylmethacrylate) | Ibuprofen | 4.0 | – | 50 | 2168.90 ^a | Li et al. [161] |
| Polypyrrole/cellulose fiber | Diclofenac potassium | 6.0 | Room temperature | 0.25–1.5 | 213.74 ^a | Pires et al. [162] |
| Polysiloxanes/sewage sludge | Diclofenac | 7.0 | 25 | 5–500 | 41.43 ^b | Reis et al. [163] |
| | Nimesulide | 9.0 | | | 26.12 ^b | |
| Carbon sphere/polyaniline | Diclofenac sodium | 5.5 | 25 | 100–500 | 430.54 ^a | Xu et al. [164] |
| Carbon sphere/layered double hydroxides | | | | | 528.78 ^a | |
| | | | | | 618.16 ^a | |
| Iron nanocomposite/ionic liquid double hydroxides | Propranolol | 9.0 | 20 | 0.01–0.07 | 0.11 ^a | Ali et al. [165] |
| Sewage sludge/fish waste | Sulfamethoxazole | 4.5 | 30 | 1–100 | 16.97 ^a | Nielsen and Bandosz [166] |
| | Trimethoprim | 7.6 | | | 43.84 ^a | |

(continued)

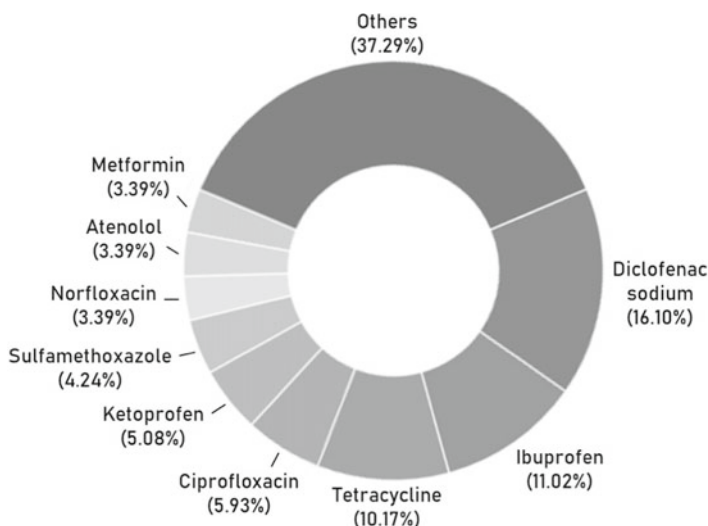
Table 3 (continued)

| Adsorbent composite | Drug | Operational conditions | | | q _{max} (mg/g) | References |
|---|------------------------------|------------------------|------------------|----------------------|--|--------------------|
| | | pH | Temperature (°C) | Concentration (mg/L) | | |
| Bismuth oxychloride/bismuth oxyiodide | Hydroxyphenylacetic acid | – | 25 | 5–80 | 20.01 ^a | Wang et al. [167] |
| Magnetic (Fe ₃ O ₄)/β-cyclodextrin/activated charcoal/alginate | Norfloxacin Ciprofloxacin | 5.0 | 35 | 5–45 | 2.55 ^d 3.12 ^d | Yadav et al. [168] |

Legend q_{max}, maximum adsorption capacity; ^aLangmuir isothermal model [58]; ^bSips isothermal model [61]; ^cHill isothermal model [57]; ^dq_e experimental adsorption capacity; MOF, metal-organic framework

Table 4 Adsorbent composites and operational conditions used in the adsorption of drugs through fixed bed

| Adsorbent composite | Drug | Column specifications | | Operational conditions | | | | | | Removal (%) | References |
|---------------------------|-------------------|-----------------------|---------------|------------------------|---------------|-----------------|-----|------------------|----------------------|-------------|-----------------------------|
| | | Height (mm) | Diameter (mm) | Flow rate (mL/min) | Bed mass (mg) | Bed height (mm) | pH | Temperature (°C) | Concentration (mg/L) | | |
| Fe/graphene | Tetracycline | 100 | 6.6 | 1.2 | 50 | – | 5.0 | 23 | 25 | 76.46 | Alatalo et al. [169] |
| Silica/alumina | Metformin | 100 | 6.0 | 2.0 | – | 36.3 | 9.0 | 20 | 50 | 86.30 | Hethnawi et al. [77] |
| Bentonite/cationic starch | Atenolol | 210 | 20.0 | 10.0 | 1500 | – | 7.0 | 20 | 5 | 100 | Lozano-Morales et al. [170] |
| | Sulfamethoxazole | | | | | | 6.5 | | | 100 | |
| | Diclofenac sodium | | | | | | 7.0 | | | 100 | |



Legend: Others, comprise gemfibrozil, ceftriaxone, acetylsalicylic acid, tylosin, naproxen, 2-naphthol, pantoprazole, propranolol, aureomycine hydrochloride, flupentixol, ampicillin, chlorpheniramine, methylene blue, para-chlorobenzoic acid, aspirin, meloxicam, salicylic acid, sodium cromoglycate, sulfanilamide, phenazopyridine, caffeine, acetaminophen, metamizol, diazepam, carbamazepine, metronidazole, trimethoprim, amodiaquine, enrofloxacin, diclofenac potassium, cephalixin, nimesulide, hydroxyphenylacetic acid, ofloxacin, mefenamic acid, oxytetracycline, metoprolol tartate, phenacetin and benzoic acid.

Fig. 3 Main compounds of the drugs evaluated for removal through the adsorption process using composites

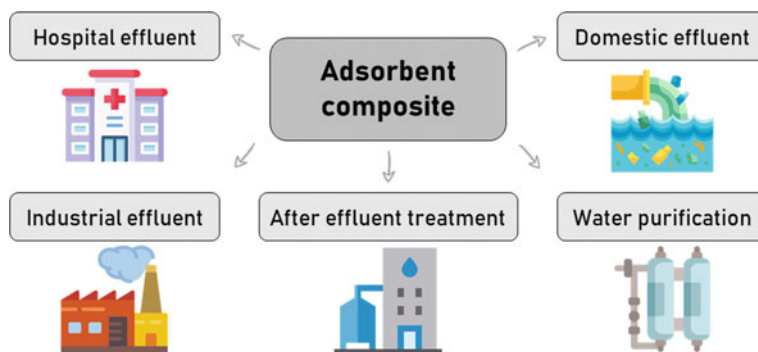


Fig. 4 Use of adsorbent composites for drug removal

mechanisms. Furthermore, through the thermodynamic parameters, it is possible to identify whether the process occurs spontaneously or with energy aid. Thus, if there is more release of energy to the external medium than absorption, it has an exothermic character ($\Delta H^\circ < 0$), for example, in the study of Santos et al. [85] in the adsorption of diclofenac sodium with the MgAl composite and double hydroxide in

layers supported by biochar, using the temperature range of 30–60 °C, was obtained an increase in the adsorption capacity from 135.83 mg/g at 30 °C to 168.04 mg/g at 60 °C using the Sips model. On the other hand, the endothermic character ($\Delta H^\circ > 0$) is favored when energy absorption occurs, needing a supply of external energy of the system, as is the case of Zhou et al. [86] who studied aromatic rings-functionalized chitosan magnetic front composite, and evaluated the adsorption of diclofenac sodium in the temperature range of 15–35 °C, in which the adsorption capacity increased with decreasing temperature, reaching a q_{\max} of 438.60 mg/g at 15 °C and 262.20 mg/g at 35 °C by the Langmuir model.

Through the operational conditions of pH and temperature, it was possible to verify that the most used conditions for the removal of drugs by the composites developed in the studies are close to the natural ones, such as pH close to 7 and temperatures around 25 °C. This favors applications, making the process more sustainable compared to assays that demand extreme temperature and pH ranges, resulting in greater energy consumption and effluent generation.

4.1 Development of Composites with Organic Materials

Generally, for the synthesis of the composite, the environmental aspects of the materials are taken into account through the sustainability of the processes. Therefore, there is an interest in the use of materials of natural origins, renewable, waste, and biopolymers, to introduce more economical adsorbents into the adsorption process.

One of the biopolymers highlighted is chitosan (poly β -1,4-D-glucosamine), obtained from the chitin deacetylation process. Generally, in the deacetylation process are used alkaline solutions that will define the degree of deacetylation of the chitosan or the proportions of deacetylated and acetylated units. The chitosan is a cationic biopolymer, present in crustacean shells (fish residues), insect exoskeletons, and in the microorganism's cell wall, with recognized adsorption capacity of organic compounds, due to the presence of amine (NH_3^+) and hydroxyl (OH^-) groups in its molecule [8, 87, 95, 97, 171, 172]. The presence of these chemical groups is influenced by the degree of deacetylation of the biopolymer, because the higher the degree, the greater the proportion of NH_3^+ groups.

However, chitosan can have properties that limit the application in adsorption processes. As an example, the solubility in weak organic acids, low porosity, low surface area (in the range of 2–30 m²/g), low mechanical resistance, and low thermal resistance [47, 173, 174]. These deficiencies can be circumvented through the development of composites, as achieved successfully in studies of Filho et al. [92], Zhao et al. [100], Ahamad et al. [87], Liang et al. [96], and Zhou et al. [86]. Just as Liu et al. [97], who developed a magnetic adsorbent composite with cross-linked chitosan with genipin and graphene oxide, and when evaluated in the adsorption of tetracycline at pH 7 and at 40 °C, was obtained q_{\max} equal to 500.68 mg/g by the Langmuir model, through a predominantly endothermic process. Ahamad et al. [87] developed a magnetic composite with chitosan, diphenylurea, and formaldehyde,

which presented a surface area of $442.6 \text{ m}^2/\text{g}$ and a pore volume of $0.74 \text{ cm}^3/\text{g}$. This material, when evaluated in tetracycline adsorption at pH 6 at $25 \text{ }^\circ\text{C}$, presented a q_{max} of 172.12 mg/g by the Langmuir model, through Van der Waals forces, π - π stacking interactions, and hydrogen bonds.

Activated carbon and biochar are similar, solid, and rich in carbon. They are obtained from biomasses of vegetable origin or solid residues, processed by means of pyrolysis, and under oxygen limited atmosphere [175, 176]. Briefly, they are products obtained by the thermal decomposition of the organic material. The main difference between biochar and activated charcoal is that biochar is the product obtained directly from the pyrolysis process and activated charcoal is biochar after an activation process. These products can also be used for soil corrections and activated carbon, due to its selective properties, has noble applications in gases and liquids. Moreover, the cost of producing biochar is lower than the activated carbon [8, 110].

Activated carbon and biochar have a high potential to adsorb contaminants due to the wide availability of biomass, favorable physical, chemical, and thermal surface characteristics, in addition to high surface area and adjustable porous structure [108, 175], contributing to high drug adsorption capacities [105, 108, 109]. However, may contain limitations that come by the biomass after pyrolysis [177], which requires an adequate choice to not limit the adsorptive properties in the development of composites. In addition to the pyrolytic temperature, the residence time and the thermal conversion technology can also interfere with the desired properties. Another important aspect to be considered is that the activated carbon and powdered biochar are difficult to separate from the aqueous solution due to their small particle sizes [178, 179], which can be overcome using magnetic materials to facilitate separation through a magnetic field [101, 115]. In addition, activated carbon and biochar may have low regeneration capacity after an adsorption process [1], making it difficult to use them on a large scale.

The high adsorption capacities of activated carbon and biochar can be observed in the studies of Lins et al. [105], Taoufik et al. [109], and Zeng et al. [119]. Lins et al. [105] synthesized an activated carbon of bovine bone with anionic clays (layered hydroxide composed of Mg and Al) to remove diclofenac sodium, reaching q_{max} of 2114.43 mg/g by the Langmuir model at pH 5.5 and at $30 \text{ }^\circ\text{C}$, through a multi-molecular process. This composite developed presented a surface area of $151.25 \text{ m}^2/\text{g}$, superior to that of activated charcoal from bovine bone that presented $94.38 \text{ m}^2/\text{g}$. Taoufik et al. [109] applied commercial activated carbon composites coated with TiO_2 in the adsorption of salicylic acid and obtained a q_{max} of 990 mg/g by the Sips model at pH 3 and at room temperature, through Van der Waals forces and π - π interactions. The material had a surface area of $580 \text{ m}^2/\text{g}$ and a pore volume of $0.57 \text{ cm}^3/\text{g}$, indicating that the presence of TiO_2 did not modify the area and the pore volume of the activated carbon. Zeng et al. [119], used rice straw to produce the biochar and added nanosheets of molybdenum disulfide (MoS_2) for the development of the composite with a surface area of $176.8 \text{ m}^2/\text{g}$ and pore volume of $0.084 \text{ cm}^3/\text{g}$, both larger than that of the biochar. The composite presented a q_{max} of 699.30 mg/

g through the Langmuir model for tetracycline adsorption at pH 4 at 45 °C, highlighting the pore filling mechanisms, hydrogen bonds, electrostatic interactions, and π - π .

Graphene oxide is a nanomaterial produced by the oxidation and exfoliation of graphite through chemical processes [1, 180, 181]. It has several applications due to its favorable characteristics, such as excellent chemical, thermal, electrical, and mechanical properties [180, 181]. In addition, they have numerous functional groups rich in oxygen in their structure, such as phenol, hydroxyl, and epoxy groups, mainly at the basal plane and carboxylic acid groups at the edges [121, 180]. Due to the large specific area of approximately 2630 m²/g, and the other characteristics, graphene oxide becomes an effective adsorbent for removing contaminants [1, 121, 180].

However, graphene oxide has some limitations as a tendency to agglomerate in aqueous solution reducing the surface area and high colloidal stability, making its recovery more difficult [97, 121, 122, 128]. Thus, studies have been carried out with the incorporation of graphene oxide into other materials to improve its characteristics and performance in view of the adsorption of various contaminants, such as drugs. For example, Balasubramani et al. [122] studied the composite graphene oxide and cellulose for the removal of flupentixol, obtaining q_{\max} by the Langmuir model of 131.36 mg/g at pH 5.3 and at 21.5 °C, having as mechanisms hydrogen bonds, hydrophobic and π - π interactions. The composite presented surface area of 195 m²/g and pore volume of 0.124 cm³/g, the surface area value being higher than that of the graphene oxide of 187 m²/g, in view of the composition of graphene oxide and cellulose.

Likewise, Peng et al. [128] developed a magnetic nanocomposite of reduced graphene oxide and doped with nitrogen, with a surface area of 38.2 m²/g. This area is smaller than that of reduced graphene oxide doped with nitrogen of 58.3 m²/g, due to the addition of the magnetic compound (iron oxide), which occupied part of the available pores. This composite was studied for adsorption of norfloxacin and ketoprofen at pH 6.8 and at 25 °C, finding q_{\max} of 158.10 and 468 mg/g, respectively, by the Langmuir model, having as mechanisms hydrogen bonds, hydrophobic and π - π interactions.

Carbon nanotubes are composed of graphite sheets in the shape of a seamless hollow cylinder, with a diameter in the order of a nanometer, their properties depend on how these sheets are arranged, on the diameters and lengths of the tubes and on the morphology or nanostructure [182, 183]. The two main types are single-walled and multiwalled, the first characterized by being a single layer of rolled graphite and the second by having several concentric layers of graphite, forming a tube with different diameters [182, 183]. Carbon nanotubes have excellent mechanical, thermal, and electrical properties that, combined with their low density, can be used to reinforce composites, obtaining a rigid and resistant nanomaterial [183]. Furthermore, due to their structure being highly porous, hollow and with a large surface area, they are attractive for the adsorption of contaminants, presenting strong interaction with several inorganic and organic molecules [130, 184, 185].

Nonetheless, carbon nanotubes have negative aspects for application in liquid medium, due to their low dispersion, with a tendency to agglomerate, and their small

particle size making it difficult to separate [1, 102, 132, 184]. Thus, carbon nanotube-based composites are being developed, such as for example Shi et al. [132] developed an adsorbent composite of bismuth tungstate implanted on graphitic carbon nitride and multiwall carbon nanotube. This composite was studied for the adsorption of ceftriaxone sodium at pH 4 and at room temperature, obtaining a q_{\max} of 19.57 mg/g by the Langmuir model, through electrostatic interactions and hydrogen bonds.

Dutra et al. [130] produced a functional polyaniline and multiwalled carbon nanotube composite, being efficient for removing meloxicam at pH 2 and at 25 °C, obtaining a q_{\max} of 218.98 mg/g by the Langmuir model, through chemical adsorption by π - π interactions and hydrogen bonds. Rigueto et al. [131] elaborated two composites with carbon nanotubes and different sources of gelatin for the removal of diclofenac sodium, obtaining a q_{\max} of 26.97 mg/g for a composite with commercial gelatin and 20.57 mg/g for a composite with gelatin derived from tannery wastes, both by the Langmuir model at pH 8.15 and at 25 °C. The possible mechanisms involved in the adsorption by composites were π - π interactions and hydrogen bonds. The nanotube used by Rigueto et al. [127] contained a surface area of 132.99 m²/g.

4.2 Development of Composites with Inorganic Materials

Clay minerals, also known as clays, make important contributions to the adsorption of drugs, according to Tables 3 and 4. Clays are composed of hydrated aluminum and iron silicates, with hydrophilic nature, high surface areas, no toxic, layered structures, possibility of expansion and are available in abundance, therefore, a low-cost material [11, 89, 112, 186]. In addition, montmorillonite, kaolinite, and illite clays have chemical and mechanical stability, favoring their use as adsorbents.

Clays have a very varied constitution that directly influences the adsorption processes through their surface charge, and can be distributed in cations and anions, such as, for example, Ca^{2+} , Mg^{2+} , H^+ , K^+ , NH_4^+ , Na^+ , SO_4^{2-} , PO_4^{3-} , Cl^- , NO_3^- [112, 186]. Thus, the development of composites with clays has been proposed to improve their limited properties, for example, restricted conditions to cationic contaminants, difficulty in separating from the aqueous medium due to fine particles, and even to expand the adsorption spectrum for multi-components [89, 111, 114]. As an example, Ashiq et al. [110] synthesized a composite with bentonite and urban solid waste biochar for adsorption of ciprofloxacin at pH 6 and at 25 °C, obtaining a q_{\max} of 286.60 mg/g by the Hill model, principally by electrostatic interactions. As well as Peng et al. [135] used a composite of magnetic montmorillonite in the adsorption of enrofloxacin at pH 6.8 and at 25 °C, obtaining q_{\max} of 162.91 mg/g by the Langmuir model, through electrostatic interactions. This composite developed presented a surface area of 64.78 m²/g and pore volume of 0.206 cm³/g.

The materials from the silica that have an amorphous structure are stimulating a growing interest for the removal of drugs, due to their relevant properties [77, 146, 187–189]. These properties include high surface area, high pore size (micropores and/or mesopores), low toxicity, chemical inertness, thermal stability and in

an acid medium, the abundant repertoire of functional groups on the surface that can be adapted for excellent selectivity in relation to a specific contaminant and relatively low production cost [144, 188, 190–192]. In addition, silica can be easily functionalized due to its hydroxyl groups [8].

Hydrophobic silica materials are highly efficient in the removal of organic compounds soluble in aqueous solutions, and hydrophilic materials are more effective in eliminating sparingly water-soluble contaminants [193, 194]. Due to materials with silica present a more robust structure, can be commonly used to satisfy this condition in more fragile materials. Furthermore, depending on the method of obtaining the silica material, this material may require modifications to the improvement of the functional groups, as they may present weak interactions with drug compounds [144]. In the study of Mohseni-Bandpei et al. [143], was applied a silica aerogel derived from pumice grafted with amine, with a surface area of 407 m²/g and pore volume of 1.05 cm³/g, for adsorption of ibuprofen at pH 7, obtaining a q_{\max} of 26.82 mg/g by the Langmuir model. The main adsorption mechanisms of ibuprofen were hydrogen bonds, hydrophobic and electrostatic interactions. Hethnawi et al. [77] evaluated the adsorption of metformin in a fixed-bed column using amorphous silica and an alumina composite, produced by the sol–gel method, and achieved a removal of 86.30% of the drug compound through electrostatic interactions. The composite presented a surface area of 470 m²/g and pore volume of 0.35 cm³/g.

An advanced class of hybrid crystalline porous materials is metal-organic frameworks (MOFs), which are made up of metal ions (inorganic species) and coordinated organic ligands [151, 152, 195]. In addition to the high porosity (0.14–1 cm³/g), these structures have a high surface area (100–3400 m²/g), thermal, mechanical, and chemical stability, as well as ease of functionalization, which makes them potential adsorbents [150, 153]. Examples of MOFs are zirconium-based (Zr) structures, such as UiO-66 and UiO-66-COOH, zeolitic imidazole structures, such as ZIF-8 and ZIF-64, and materials from the Lavoisier Institute, such as MIL-101 [150, 152, 153, 195]. Second Burtch et al. [195], most MOFs show sensitivity to moisture/water and low support in acidic or basic media, limiting their application. Moreover, as they are powdered and, consequently, of reduced size, they present difficulties in separating the aqueous solution and regenerating, which may result in secondary pollution [100, 151, 153].

In view of the limitations of MOFs, it is necessary to develop alternatives to overcome them, such as incorporating MOFs in other materials combining properties. An example is the adsorbent composite with bimetallic zeolitic-imidazolate framework (zinc and cobalt) and magnetic carbon developed by Pan et al. [149], with surface area of 514 m²/g and pore volume of 0.31 m³/g. This composite under conditions of pH 5.4 and at 25 °C, an experimental q_{\max} of 1039.27 mg/g was obtained, from the adsorption of amodiaquine, under combinations of electrostatic interactions and hydrogen bonds.

Another example is the study of Zhao et al. [100] who produced a composite ZIF-8 and chitosan for the removal of tetracycline in aqueous solution. This material presented surface area of 221.4 m²/g, having Langmuir-modeled q_{\max} of 495.04 mg/g at a pH between 8 and 9 and at 20 °C, with adsorption mechanism by electrostatic and

π - π interactions and hydrogen bonds. Zhou et al. [153] developed a composite with MIL-101 (Cr) and graphene aerogel for the adsorption of phenacetin and naproxen at pH = 4, obtaining a q_{\max} of 232.50 and 333.30 mg/g, respectively, through the Langmuir model. This composite presented surface area of 372.31 m²/g and pore volume of 0.18 cm³/g, this area being smaller than that of MIL-101 (Cr) (3311.88 m²/g), due to the addition of graphene in the material, agglomerating in the MOF structure.

Likewise, Cui et al. [148] studied an adsorbent composite of UiO-66, poly-dopamine and bacterial cellulose to remove aspirin and tetracycline, obtaining q_{\max} of 176.55 and 210.31 mg/g, respectively, by the Langmuir model at 45 °C and pH between 3 and 4. The adsorption process was different for both drugs, being physical adsorption by π - π and electrostatic interactions for aspirin, and chemical adsorption for tetracycline by Zr-N coordination binding, π - π and electrostatic interactions. The surface area of this adsorbent material was 454 m²/g.

As noted, many materials are difficult to separate from the aqueous solution, needing modifications for successful application. Thus, several studies are incorporating magnetic materials in their matrices, as can be seen in Table 3, the most common being the magnetite (Fe₃O₄), iron oxides (II) and (III) [86, 87, 90, 102, 122, 125]. This facilitates the separation of the medium through the use of a magnetic field, making it faster and more efficient. Furthermore, the magnetic means offered a potential to improve other properties of base materials, such as chemical stability, recyclability, and functionality [102, 122, 123, 135].

5 Conclusion and Future Perspectives

The new generation adsorbent composites must be synthesized by increasing the surface area, size, and volume of pores, searching for greater selectivity, efficiency, and economy, considering their environmental sustainability, for the removal of emerging contaminants, as is the case of drugs. In conjunction to this, one of the biggest challenges for composites technologies is to find substitutes for the rapid decrease in non-renewable natural resources. It is encouraged, for the industrial exploration of adsorbent composites to become a reality, the use of less aggressive solvents and the implementation of non-thermal technologies.

There is a great need to develop adsorbent materials with applicability in various experimental conditions. In addition, the challenges in the conception of hybrid adsorbents (organic and inorganic) are the capacity to control the morphology and the size of the particles, and also in how to obtain a homogeneous distribution in all the material matrix. Bearing in mind that the amount of incorporation of organic portions in inorganic materials is still limited, which opens the way for further investigations. This demands modifications with caution to catch up the desired physical, chemical, and mechanical properties in adsorbent composites.

Allied to this, the advancement in the field of adsorbent composites opens possibilities for applications in other areas, as is the case for the development of sensors, membranes, catalysts, drugs release, and loading.

Acknowledgements The authors would like to thank the Coordination for the Improvement of Higher Education Personnel (CAPES - Finance Code 001), National Council for Scientific and Technological Development (CNPQ - Proc. 405311/2016-8) and the University of Passo Fundo (UPF).

References

1. A.C. Sophia, E.C. Lima, Removal of emerging contaminants from the environment by adsorption. *Ecotoxicol. Environ. Saf.* **150**, 1–17 (2018). <https://doi.org/10.1016/j.ecoenv.2017.12.026>
2. S. Agarwal, I. Tyagi, V.K. Gupta, M. Sohrabi, S. Mohammadi, A.N. Golikand, A. Fakhri, Iron doped SnO₂/Co₃O₄ nanocomposites synthesized by sol-gel and precipitation method for metronidazole antibiotic degradation. *Mater. Sci. Eng., C.* **70**, 178–183 (2017). <https://doi.org/10.1016/j.msec.2016.08.062>
3. V. Geissen, H. Mol, E. Klumpp, G. Umlauf, M. Nadal, M.V.D. Ploeg, S.E.A.T.M.V. Zee, C.J. Ritsema, Emerging pollutants in the environment: a challenge for water resource management. *Int Soil Water Conserv. Res.* **3**, 57–65 (2015). <https://doi.org/10.1016/j.iswcr.2015.03.002>
4. C.C. Montagner, C. Vidal, R.D. Acayaba, Emerging contaminants in aquatic matrices in Brazil: current scenario and analytical, ecotoxicological and regulatory aspects. *New Chem.* **40**, 1094–1110 (2017). <https://doi.org/10.21577/0100-4042.20170091>. (in Portuguese)
5. D.M. Bila, M. Dezotti, Endocrine disruptors in the environment: effects and consequences. *New Chem.* **30**, 651–666 (2007). <https://doi.org/10.1590/S0100-40422007000300027>. (in Portuguese)
6. M. Patel, R. Kumar, K. Kishor, T. Misra, C.U. Pittman Jr., D. Mohan, Pharmaceuticals of emerging concern in aquatic systems: chemistry, occurrence, effects, and removal methods. *Chem. Rev.* **119**, 3510–3673 (2019). <https://doi.org/10.1021/acs.chemrev.8b00299>
7. N. Politakis, A. Belavgeni, I. Efthimiou, N. Charalampous, C. Kourkouta, S. Dailianis, The impact of expired commercial drugs on non-target marine species: a case study with the use of a battery of biomarkers in hemocytes of mussels. *Ecotoxicol. Environ. Saf.* **148**, 160–168 (2018). <https://doi.org/10.1016/j.ecoenv.2017.10.021>
8. D.C.S. Alves, B. Healy, L.A.A. Pinto, T.R.S.J. Cadaval, C.B. Breslin, Recent developments in chitosan-based adsorbents for the removal of pollutants from aqueous environments. *Molecules* **26**, 1–45 (2021). <https://doi.org/10.3390/molecules26030594>
9. A.A. Basheer, New generation nano-adsorbents for the removal of emerging contaminants in water. *J. Mol. Liq.* **261**, 583–593 (2018). <https://doi.org/10.1016/j.molliq.2018.04.021>
10. G. Crini, E. Lichtfouse, L.D. Wilson, N. Morin-Crini, in *Green Adsorbents for Pollutant Removal*, ed. by G. Crini, E. Lichtfouse. Volume 18 in *Environmental Chemistry for a Sustainable World* (Springer, Cham, 2018), pp. 23–71. https://doi.org/10.1007/978-3-319-92111-2_2
11. G. Crini, Non-conventional low-cost adsorbents for dye removal: a review. *Bioresour. Technol.* **97**, 1061–1085 (2006). <https://doi.org/10.1016/j.biortech.2005.05.001>
12. H. Altenbach, J. Altenbach, W. Kissing, in *Mechanics of Composite Structural Elements*, 1st edn. (Springer, Heidelberg, 2004), pp. 1–14
13. W.D. Callister, D.G. Rethwisch, in *Materials Science and Engineering—An Introduction*, 10th edn. (LTC, Rio de Janeiro, 2021), pp. 503–541 (in Portuguese)
14. D. Gay, S.V. Hoa, S.W. Tsai, in *Composite Materials: Design and Applications*, 3rd edn. (CRC Press, New York, 2003), pp. 3–16

15. D. Kralova, M. Slouf, M. Klementova, R. Kuzel, I. Kelnar, Preparation of gram quantities of high-quality titanate nanotubes and their composites with polyamide 6. *Mater. Chem. Phys.* **124**, 652–657 (2010). <https://doi.org/10.1016/j.matchemphys.2010.07.029>
16. M.M Dawoud, H.M. Saleh, in *Characterizations of Some Composite Materials*, ed by H. Saleh, M. Koller (IntechOpen, London, 2018), pp. 3–12. <https://doi.org/10.5772/intechopen.80960>
17. Z. Hashin, Analysis of composite materials—A survey. *J. Appl. Mech.* **50**, 481–505 (1983). <https://doi.org/10.1115/1.3167081>
18. R.-M. Wang, S.-R. Zheng, Y.-P. Zheng, in *Polymer Matrix Composites and Technology*, 1st edn. (Woodhead Publishing, Cambridge, 2011), pp. 1–25. <https://doi.org/10.1533/9780857092229.1>
19. D.K. Rajak, D.D. Pagar, R. Kumar, C.I. Pruncu, Recent progress of reinforcement materials: a comprehensive overview of composite materials. *J. Mater. Res. Technol.* **8**, 6354–6374 (2019). <https://doi.org/10.1016/j.jmrt.2019.09.068>
20. D. Kumlutaş, I.H. Tavman, M.T. Çoban, Thermal conductivity of particle filled polyethylene composite materials. *Compos. Sci. Technol.* **63**, 113–117 (2003). [https://doi.org/10.1016/S0266-3538\(02\)00194-X](https://doi.org/10.1016/S0266-3538(02)00194-X)
21. Z.-M. Dang, J.-K. Yuan, J.-W. Zha, T. Zhou, S.-T. Li, G.-H. Hu, Fundamentals, processes and applications of high-permittivity polymer-matrix composites. *Prog. Mater. Sci.* **57**, 660–723 (2012). <https://doi.org/10.1016/j.pmatsci.2011.08.001>
22. B.C. Ray, Temperature effect during humid ageing on interfaces of glass and carbon fibers reinforced epoxy composites. *J. Colloid Interf. Sci.* **298**, 111–117 (2006). <https://doi.org/10.1016/j.jcis.2005.12.023>
23. L.A. Carlsson, D.F. Adams, R.B. Pipes, in *Experimental Characterization of Advanced Composite Materials*, 4th edn. (CRC Press, Boca Raton, 2014), pp. 11–34
24. W.H.J. Hunt, Metal matrix composites. *Comprehen. Compos. Mater.* **6**, 57–66 (2000). <https://doi.org/10.1016/B0-08-042993-9/00134-0>
25. Y. Gan, D. Solomon, M. Reinbolt, Friction stir processing of particle reinforced composite materials. *Materials* **3**, 329–350 (2010). <https://doi.org/10.3390/ma3010329>
26. L. Zhou, Y. Huang, W. Qiu, Z. Sun, Z. Liu, Z. Song, Adsorption properties of Nano-MnO₂-Biochar composites for copper in aqueous solution molecules. *Molecules* **22**, 1–13 (2017). <https://doi.org/10.3390/molecules22010173>
27. S. Fan, C. Yang, L. He, Y. Du, W. Krenkel, P. Greil, N. Travitzky, Progress of ceramic matrix composites brake materials for aircraft application. *Rev. Adv. Mater. Sci.* **44**, 313–325 (2016)
28. X. Wang, W.S. Liu, X. Lu, P.S Lee, Dodecyl sulfate-induced fast faradaic process in nickel cobalt oxide-reduced graph it oxide composite material and its application for asymmetric supercapacitor device. *J. Mater. Chem.* **22**, 23114–23119 (2012). <https://doi.org/10.1039/c2jm35307e>
29. Y.L. Young, Fluid-structure interaction analysis of flexible composite marine propellers. *J. Fluids Struct.* **24**, 799–818 (2008). <https://doi.org/10.1016/j.jfluidstructs.2007.12.010>
30. Y. Zhou, M. Zhang, Z. Guo, L. Miao, S.-T. Han, Z. Wang, X. Zhang, H. Zhang, Z. Peng, Recent advances in black phosphorus-based photonics, electronics, sensors and energy devices. *Mater. Horiz.* **4**, 997–1019 (2017). <https://doi.org/10.1039/c7mh00543a>
31. E.L. Steinberg, E. Rath, A. Shlaifer, O. Chechik, E. Maman, M. Salai, Carbon fiber reinforced PEEK Optima-a composite material biomechanical properties and wear/debris characteristics of CF-PEEK composites for orthopedic trauma implants. *J. Mech. Behav. Biomed. Mater.* **17**, 221–228 (2013). <https://doi.org/10.1016/j.jmbbm.2012.09.013>
32. V.B.K. Yaah, S. Ojala, H. Khallok, T. Laitinen, M. Selent, H. Zhao, R. Sliz, S.B. Oliveira development and characterization of composite carbon adsorbents with photocatalytic regeneration ability: application to diclofenac removal from water. *Catalysts* **11**, 1–22 (2021). <https://doi.org/10.3390/catal11020173>
33. F. Hayeeye, Q.J.Y., M. Sattar, W. Chinpa, O. Sirichote, Adsorption of Pb²⁺ ions from aqueous solutions by gelatin/activated carbon composite bead form. *Adsorpt. Sci. Technol.* **36**, 355–371 (2018). <https://doi.org/10.1177/026361741769300>

34. J. Ma, M. Yang, F. Yu, J. Zheng, Water-enhanced removal of ciprofloxacin from water by porous graphene hydrogel. *Sci. Rep.* **5**, 1–10 (2015). <https://doi.org/10.1038/srep13578>
35. R.F. Nascimento, A.C.A. Lima, C.B. Vidal, D.Q. Melo, G.S.C Raulino, *Adsorption: Theoretical Aspects and Environmental Applications*, 2nd edn. (University Press, Fortaleza, 2014) pp. 256 (in Portuguese)
36. A.S. Foust, L.A. Wenzel, C.W. Clump, L. Maus, L.B. Andersen, *Principles of Unit Operations*, 2nd edn. (LTC, Rio de Janeiro, 1982), pp. 682 (in Portuguese)
37. G. Gopal, S.A. Alex, N. Chandrasekaran, A. Mukherjee, A review on tetracycline removal from aqueous systems by advanced treatment techniques. *RSC Adv.* **10**, 27081–27095 (2020). <https://doi.org/10.1039/D0RA04264A>
38. J.S. Piccin, T.R.S. Cadaval Jr, L.A.A. Pinto, G.L. Dotto, in *Adsorption Processes for Water Treatment and Purification*, ed. by A. Bonilla-Petriciolet, D.I. Mendoza-Castillo, H.E. Reynel-Ávila (Springer, Switzerland, 2017), pp. 19–48. https://doi.org/10.1007/978-3-319-58136-1_2
39. M. Suzuki, *Fundamentals of Adsorption*, 1st edn. (Elsevier, Amsterdam, 1993), p. 798
40. D.D. Do, *Adsorption Analysis: Equilibria and Kinetics*, 1st edn. (Imperial College Press, London, 1998), pp.11–48
41. P. Pal, A. Pal, Treatment of real wastewater: kinetic and thermodynamic aspects of cadmium adsorption onto surfactant-modified chitosan beads. *Int. J. Biol. Macromol.* **131**, 1092–1100 (2019). <https://doi.org/10.1016/j.ijbiomac.2019.03.121>
42. M.Z. Afzal, X.-F. Sun, J. Liu, C. Song, S.-G. Wang, A. Javed, Enhancement of ciprofloxacin sorption on chitosan/biochar hydrogel beads. *Sci. Total. Environ.* **639**, 560–569 (2018). <https://doi.org/10.1016/j.scitotenv.2018.05.129>
43. B. Noroozi, G.A. Sorial, H. Bahrami, M. Arami, Equilibrium and kinetic adsorption study of a cationic dye by a natural adsorbent-Silkworm pupa. *J. Hazard. Mater.* **139**, 167–174 (2007). <https://doi.org/10.1016/j.jhazmat.2006.06.021>
44. D. Kavitha, C. Namasivayam, Experimental and kinetic studies on methylene blue adsorption by coir pith carbon. *Bioresour. Technol.* **98**, 14–21 (2007). <https://doi.org/10.1016/j.biortech.2005.12.008>
45. A. Claudino, Dissertation, Federal University of Santa Catarina, 2003 (in Portuguese)
46. R. Ciola, *Fundamentals of Catalysis*, 1st edn. (Moderna, São Paulo, 1981), pp. 378 (in Portuguese)
47. G. Crini, P.M. Badot, Application of chitosan, a natural aminopolysaccharide, for dye removal from aqueous solutions by adsorption processes using batch studies: a review of recent literature. *Prog. Polym. Sci.* **33**, 399–447 (2008). <https://doi.org/10.1016/j.progpolymsci.2007.11.001>
48. J.S. Piccin, M.L.G. Vieira, J.O. Gonçalves, G.L. Dotto, L.A.A. Pinto, Adsorption of FD&C Red No. 40 by chitosan: isotherms analysis. *J. Food Eng.* **95**, 16–20 (2009). <https://doi.org/10.1016/j.jfoodeng.2009.03.017>
49. N.F. Cardoso, Dissertation, Federal University of Rio Grande do Sul, 2010 (in Portuguese)
50. N.F. Cardoso, E.C. Lima, I.S. Pinto, C.V. Amavisca, B. Royer, R.B. Pinto, W.S. Alencar, S.F.P. Pereira, Application of cupuassu shell as biosorbent for the removal of textile dyes from aqueous solution. *J. Environ. Manag.* **92**, 1237–1247 (2011). <https://doi.org/10.1016/j.jenvman.2010.12.010>
51. G. Newcombe, R. Hayes, M. Drikas, Granular activated carbon: importance of surface properties in the adsorption of naturally occurring organics. *Colloids Surf., A.* **74**, 275–286 (1993). [https://doi.org/10.1016/0927-7757\(93\)80271-F](https://doi.org/10.1016/0927-7757(93)80271-F)
52. R.S. Jimenez, S.M. Dal Bosco, W.A. Carvalho, Removal of heavy metals from aqueous effluents by natural scolecite zeolite—influence of temperature and pH in the adsorption of systems monoelementary. *New Chem.* **27**, 734–738 (2004). <https://doi.org/10.1590/S0100-40422004000500011>. (in Portuguese)
53. S. Ray, G. Das, in *Process Equipment and Plant Design*, ed. by S. Ray, G. Das (Elsevier, 2020), pp. 351–384. <https://doi.org/10.1016/B978-0-12-814885-3.00012-9>

54. J. Gao, J. Chen, X. Li, M. Wang, X. Zhang, F. Tan, S. Xu, J. Liu, Azide-functionalized hollow silica nanospheres for removal of antibiotics. *J. Colloid Interf. Sci.* **444**, 38–41 (2015). <https://doi.org/10.1016/j.jcis.2014.12.054>
55. M.M. Dubinin, L.V. Radushkevich, The equation of the characteristic curve of the activated charcoal. *Proc. Acad. Sci. USSR Phys. Chem. Sect.*, **55**, 331–337 (1947)
56. H.M.F. Freundlich, Over the adsorption in solution. *J. Phys. Chem.* **57**, 385–471 (1906)
57. T.L. Hill, Statistical mechanics of multimolecular adsorption. *Int. J. Chem. Phys.* **14**, 263–267 (1946). <https://doi.org/10.1063/1.1724129>
58. I. Langmuir, The adsorption of gases on plane surfaces of glass, mica and platinum. *J. Am. Chem. Soc.* **40**, 1361–1403 (1918). <https://doi.org/10.1021/ja02242a004>
59. Y. Liu, H. Xu, S.-F. Yang, J.-H. Tay, A general model for biosorption of Cd²⁺, Cu²⁺ and Zn²⁺ by aerobic granules. *J. Biotechnol.* **102**, 233–239 (2003). [https://doi.org/10.1016/S0168-1656\(03\)00030-0](https://doi.org/10.1016/S0168-1656(03)00030-0)
60. O.J.D.L. Redlich, D.L. Peterson, A useful adsorption isotherm. *J. Phys. Chem.* **63**, 1024 (1959). <https://doi.org/10.1021/j150576a61>
61. R. Sips, On the structure of a catalyst surface. *J. Chem. Phys.* **16**, 490–495 (1948). <https://doi.org/10.1063/1.1746922>
62. M.I. Temkin, Adsorption equilibrium and the kinetics of processes on nonhomogeneous surfaces and in the interaction between adsorbed molecules. *Zh. Fiz. Chim.* **15**, 296–332 (1941)
63. J.S. Piccin, L.A. Ferris, M. Cooper, M. Gutterres, Dye adsorption by leather waste: mechanism diffusion, nature studies, and thermodynamic data. *J. Chem. Eng. Data* **58**, 873–882 (2013). <https://doi.org/10.1021/je301076n>
64. W.J. Weber, E.H. Smith, Simulation and design models for adsorption processes. *Environ. Sci. Technol.* **21**, 1040–1050 (1987). <https://doi.org/10.1021/es00164a002>
65. J. Crank, *The Mathematics of Diffusion*, 2nd edn. (Oxford Clarendon Press, Oxford, 1975), p.421
66. H. Qiu, L. Lv, B.-C. Pan, Q.-J. Zhang, W.-M. Zhang, Q.-X. Zhang, Critical review in adsorption kinetic models. *J. Zhejiang Univ., Sci., A.* **10**, 716–724 (2009). <https://doi.org/10.1631/jzus.A0820524>
67. D.O. Cooney, *Adsorption Design for Wastewater Treatment* (CRC Press, Florida, 1998), p.208
68. W.J. Weber, J.C. Morris, Kinetics of adsorption on carbon from solution. *J. Sanit. Eng. Div.* **89**, 31–60 (1963)
69. S.Y. Elovich, O.G. Larinov, Theory of adsorption from nonelectrolyte solutions on solid adsorbents. *Russ. Chem. Bull.* **11**, 191–197 (1962). <https://doi.org/10.1007/BF00908016>
70. M. Avrami, Kinetics of phase change I. General theory. *J. Chem. Phys.* **7**, 1103–1112 (1939). <https://doi.org/10.1063/1.1750380>
71. S. Lagergreen, Zur Theorie der sogenannten Gelöster de adsorção Stoffe. *Zeitschr f Chem und Ind der Kolloide* **2**, 174–175 (1907). <https://doi.org/10.1007/BF01501332>
72. Y.S. Ho, G. McKay, The kinetics of sorption of divalent metal ions onto sphagnum moss peat. *Water Res.* **34**, 735–742 (2000). [https://doi.org/10.1016/S0043-1354\(99\)00232-8](https://doi.org/10.1016/S0043-1354(99)00232-8)
73. Y.S. Ho, G. McKay, Pseudo-second order model for sorption processes. *Process Biochem.* **34**, 451–465 (1999). [https://doi.org/10.1016/S0032-9592\(98\)00112-5](https://doi.org/10.1016/S0032-9592(98)00112-5)
74. V.K. Gupta, S.K. Srivastava, D. Mohan, S. Sharma, Design parameters for fixed bed reactors of activated carbon developed from fertilizer waste for the removal of some heavy metal ions. *Waste Manag.* **17**, 517–522 (1998). [https://doi.org/10.1016/S0956-053X\(97\)10062-9](https://doi.org/10.1016/S0956-053X(97)10062-9)
75. C.E. Borba, R. Guirardello, E.A. Silva, M.T. Veit, C.R.G. Tavares, Removal of nickel(II) ions from aqueous solution by biosorption in a fixed bed column: experimental and theoretical breakthrough curves. *Biochem. Eng. J.* **30**, 184–191 (2006). <https://doi.org/10.1016/j.bej.2006.04.001>
76. P. Lodeiro, R. Herrero, M.E.S. Vicente, Batch desorption studies and multiple sorption-regeneration cycles in a fixed-bed column for Cd(II) elimination by protonated *Sargassum muticum*. *J. Hazard. Mater.* **137**, 1649–1655 (2006). <https://doi.org/10.1016/j.jhazmat.2006.05.003>

77. A. Hethnawi, M. Alnajjar, A.D. Manasrah, A. Hassan, G. Vitale, R. Jeong, N.N. Nassar, Metformin removal from water using fixed-bed column of silica-alumina composite. *Colloids Surf., A*. **597**, 124814 (2020). <https://doi.org/10.1016/j.colsurfa.2020.124814>
78. H.A.S. Neto, H.L. Garcia, R.G.O. Araujo, C.A.B. Garcia, Fixed bed column adsorption applied to the preconcentration of cadmium in water samples. *Sci. Plena*. **14**, 1–10 (2018). <https://doi.org/10.14808/sci.plena.2018.064208>
79. A.D. Luz, Dissertation, Federal University of Santa Catarina, 2009 (in Portuguese)
80. A.E. Rodrigues, *Simulated Moving Bed Technology: Principles, Design and Process Applications*, 1st edn. (Elsevier, Amsterdam, 2015), pp. 304. <https://doi.org/10.1016/C2013-0-19564-5>
81. M.R. Berber, Current advances of polymer composites for water treatment and desalination. *J. Chem.* **2020**, 1–19 (2020). <https://doi.org/10.1155/2020/7608423>
82. R. Merli, M. Preziosi, A. Acampora, How do scholars approach the circular economy? A systematic literature review. *J. Cleaner Prod.* **178**, 703–722 (2018). <https://doi.org/10.1016/j.jclepro.2017.12.112>
83. D. Denyer, D. Tranfield, in *The SAGE Handbook of Organizational Research Methods*, ed. by D. Buchanan, A. Bryman (SAGE Publications, Oliver's Yard, London, 2009), pp. 671–689
84. Elsevier, How do I use the new advanced search? (2021). https://service.elsevier.com/app/answers/detail/a_id/25974/c/10545/supporthub/sciencedirect/. Accessed 10 Feb 2021
85. G.E.S. Santos, A.H. Ide, J.L.S. Duarte, G. McKay, A.O.S. Silva, L. Meili, Adsorption of anti-inflammatory drug diclofenac by MgAl/layered double hydroxide supported on *Syagrus coronata* biochar. *Powder Technol.* **364**, 229–240 (2020). <https://doi.org/10.1016/j.powtec.2020.01.083>
86. X. Zhou, C. Dong, Z. Yang, Z. Tian, L. Lu, W. Yang, Y. Wang, L. Zhang, A. Li, J. Chen, Enhanced adsorption of pharmaceuticals onto core-brush shaped aromatic rings-functionalized chitosan magnetic composite particles: effects of structural characteristics of both pharmaceuticals and brushes. *J. Cleaner Prod.* **172**, 1025–1034 (2018). <https://doi.org/10.1016/j.jclepro.2017.10.207>
87. T. Ahamad, Ruksana, A.A. Chaudhary, M. Naushad, S.M. Alshehri, Fabrication of MnFe₂O₄ nanoparticles embedded chitosan-diphenylureaformaldehyde resin for the removal of tetracycline from aqueous solution. *Int. J. Biol. Macromol.* **134**, 180–188 (2019). <https://doi.org/10.1016/j.ijbiomac.2019.04.204>
88. Z.A. ALOthman, A.Y. Badjah, O.M.L. Alharbi, I. Ali, Synthesis of chitosan composite iron nanoparticles for removal of diclofenac sodium drug residue in water. *Int. J. Biol. Macromol.* **159**, 870–876 (2020). <https://doi.org/10.1016/j.ijbiomac.2020.05.154>
89. V. Arya, L. Philip, Adsorption of pharmaceuticals in water using Fe₃O₄ coated polymer clay composite. *Microporous Mesoporous Mater.* **232**, 273–280 (2016). <https://doi.org/10.1016/j.micromeso.2016.06.033>
90. T. Chahm, C.A. Rodrigues, Removal of ibuprofen from aqueous solutions using O-carboxymethyl-N-laurylchitosan/ γ -Fe₂O₃. *Environ. Nanotechnol. Monit. Manag.* **7**, 139–148 (2017). <https://doi.org/10.1016/j.enmm.2017.03.001>
91. Z. Feng, K. Odelius, M. Hakkarainen, Tunable chitosan hydrogels for adsorption: property control by biobased modifiers. *Carbohydr. Polym.* **196**, 135–145 (2018). <https://doi.org/10.1016/j.carbpol.2018.05.029>
92. E.D.S. Filho, E.L. Brito, D.O. Nogueira, J.L.C. Fonseca, Thermal degradation and drug sorption in hybrid interpolyelectrolyte particles. *Colloids Surf., A*. **610**, 125894 (2021). <https://doi.org/10.1016/j.colsurfa.2020.125894>
93. M. Huang, T. Zhou, X. Wu, J. Mao, Adsorption and degradation of norfloxacin by a novel molecular imprinting magnetic Fenton-like catalyst. *Chin. J. Chem. Eng.* **23**, 1698–1704 (2015). <https://doi.org/10.1016/j.cjche.2015.08.030>
94. X. Jia, B. Zhang, C. Chen, X. Fu, Q. Huang, Immobilization of chitosan grafted carboxylic Zr-MOF to porous starch for sulfanilamide adsorption. *Carbohydr. Polym.* **253**, 117305 (2021). <https://doi.org/10.1016/j.carbpol.2020.117305>

95. E.F. Lessa, M.L. Nunes, A.R. Fajardo, Chitosan/waste coffee-grounds composite: an efficient and eco-friendly adsorbent for removal of pharmaceutical contaminants from water. *Carbohydr. Polym.* **189**, 257–266 (2018). <https://doi.org/10.1016/j.carbpol.2018.02.018>
96. X.X. Liang, A.M. Omer, Z.-H. Hu, Y.-G. Wang, D. Yu, X.-K. Ouyang, Efficient adsorption of diclofenac sodium from aqueous solutions using magnetic amine-functionalized chitosan. *Chemosphere* **217**, 270–278 (2019). <https://doi.org/10.1016/j.chemosphere.2018.11.023>
97. Y. Liu, R. Liu, M. Li, F. Yu, C. He, Removal of pharmaceuticals by novel magnetic genipin-crosslinked chitosan/graphene oxide-SO₃H composite. *Carbohydr. Polym.* **220**, 141–148 (2019). <https://doi.org/10.1016/j.carbpol.2019.05.060>
98. N. Neghi, M. Kumar, D. Burkhalov, Synthesis and application of stable, reusable TiO₂ polymeric composites for photocatalytic removal of metronidazole: removal kinetics and density functional analysis. *Chem. Eng. J.* **359**, 963–975 (2019). <https://doi.org/10.1016/j.cej.2018.11.090>
99. S. Zhang, Y. Dong, Z. Yang, W. Yang, J. Wu, C. Dong, Adsorption of pharmaceuticals on chitosan-based magnetic composite particles with core-brush topology. *Chem. Eng. J.* **304**, 325–334 (2016). <https://doi.org/10.1016/j.cej.2016.06.087>
100. R. Zhao, T. Ma, S. Zhao, H. Rong, Y. Tian, G. Zhu, Uniform and stable immobilization of metal-organic frameworks into chitosan matrix for enhanced tetracycline removal from water. *Chem. Eng. J.* **382**, 122893 (2020). <https://doi.org/10.1016/j.cej.2019.122893>
101. M.Y. Badi, A. Azari, H. Pasalari, A. Esrafil, M. Farzadkia, Modification of activated carbon with magnetic Fe₃O₄ nanoparticle composite for removal of ceftriaxone from aquatic solutions. *J. Mol. Liq.* **261**, 146–154 (2018). <https://doi.org/10.1016/j.molliq.2018.04.019>
102. F.C. Çavuşoğlu, Ş.S. Bayazit, M.S. Secula, B. Cagnon, Magnetic carbon composites as regenerable and fully recoverable adsorbents: performance on the removal of antidiabetic agent metformin hydrochloride. *Chem. Eng. Res. Des.* **168**, 443–452 (2021). <https://doi.org/10.1016/j.cherd.2021.01.034>
103. C. Dang, F. Sun, H. Jiang, T. Huang, W. Liu, X. Chen, H. Ji, Pre-accumulation and in-situ destruction of diclofenac by a photoregenerable activated carbon fiber supported titanate nanotubes composite material: Intermediates, DFT calculation, and ecotoxicity. *J. Hazard. Mater.* **400**, 123225 (2020). <https://doi.org/10.1016/j.jhazmat.2020.123225>
104. A.C. Fröhlich, E.L. Foletto, G.L. Dotto, Preparation and characterization of NiFe₂O₄/activated carbon composite as potential magnetic adsorbent for removal of ibuprofen and ketoprofen pharmaceuticals from aqueous solutions. *J. Cleaner Prod.* **229**, 828–837 (2019). <https://doi.org/10.1016/j.jclepro.2019.05.037>
105. P.V.S. Lins, D.C. Henrique, A.H. Ide, J.L.S. Duarte, G.L. Dotto, A. Yazidi, L. Sellaoui, A. Erto, C.L.P.S. Zanta, L. Meili, Adsorption of a non-steroidal anti-inflammatory drug onto MgAl/LDH-activated carbon composite—Experimental investigation and statistical physics modeling. *Colloids Surf., A* **586**, 124217 (2020). <https://doi.org/10.1016/j.colsurfa.2019.124217>
106. E.M.E. Mouchtari, C. Daou, S. Rafqah, F. Najjar, H. Anane, A. Piram, A. Hamade, S. Briche, P. Wong-Wah-Chung, TiO₂ and activated carbon of *Argania Spinosa* tree nutshells composites for the adsorption photocatalysis removal of pharmaceuticals from aqueous solution. *J. Photochem. Photobiol., A* **388**, 112183 (2020). <https://doi.org/10.1016/j.jphotochem.2019.112183>
107. P. Rai, K.P. Singh, Valorization of Poly (ethylene) terephthalate (PET) wastes into magnetic carbon for adsorption of antibiotic from water: characterization and application. *J. Environ. Manag.* **207**, 249–261 (2018). <https://doi.org/10.1016/j.jenvman.2017.11.047>
108. G.A. Saygılı, H. Saygılı, Pharmaceutical analysis by a novel spinel ferrite nanocomposite derived from a biomaterial-based activated carbon. *J. Pharm. Biomed. Anal.* **179**, 112957 (2020). <https://doi.org/10.1016/j.jpba.2019.112957>
109. N. Taoufik, A. Elmchaouri, F. Anouar, S.A. Korili, A. Gil, Improvement of the adsorption properties of an activated carbon coated by titanium dioxide for the removal of emerging contaminants. *J. Water Process. Eng.* **31**, 100876 (2019). <https://doi.org/10.1016/j.jwpe.2019.100876>

110. A. Ashiq, N.M. Adassooriya, B. Sarkar, A.U. Rajapaksha, Y.S. Ok, M. Vithanage, Municipal solid waste biochar-bentonite composite for the removal of antibiotic ciprofloxacin from aqueous media. *J. Environ. Manage.* **236**, 428–435 (2019). <https://doi.org/10.1016/j.jenvman.2019.02.006>
111. A. Ashiq, B. Sarkar, N. Adassooriya, J. Walpita, A.U. Rajapaksha, Y.S. Ok, M. Vithanage, Sorption process of municipal solid waste biochar-montmorillonite composite for ciprofloxacin removal in aqueous media. *Chemosphere* **236**, 124384 (2019). <https://doi.org/10.1016/j.chemosphere.2019.124384>
112. P. Borthakur, M. Aryafard, Z. Zara, R. David, B. Minofar, M.R. Das, M. Vithanage, Computational and experimental assessment of pH and specific ions on the solute solvent interactions of clay-biochar composites towards tetracycline adsorption: implications on wastewater treatment. *J. Environ. Manage.* **283**, 111989 (2021). <https://doi.org/10.1016/j.jenvman.2021.111989>
113. D.-W. Cho, K. Yoon, Y. Ahn, Y. Sun, D.C.W. Tsang, D. Hou, Y.S. Ok, H. Song, Fabrication and environmental applications of multifunctional mixed metal-biochar composites (MMBC) from red mud and lignin wastes. *J. Hazard. Mater.* **374**, 412–419 (2019). <https://doi.org/10.1016/j.jhazmat.2019.04.071>
114. C. Fu, H. Zhang, M. Xia, W. Lei, F. Wang, The single/co-adsorption characteristics and microscopic adsorption mechanism of biochar-montmorillonite composite adsorbent for pharmaceutical emerging organic contaminant atenolol and lead ions. *Ecotoxicol. Environ. Saf.* **187**, 109763 (2020). <https://doi.org/10.1016/j.ecoenv.2019.109763>
115. J. Heo, Y. Yoon, G. Lee, Y. Kim, J. Han, C.M. Park, Enhanced adsorption of bisphenol A and sulfamethoxazole by a novel magnetic CuZnFe₂O₄-biochar composite. *Bioresour. Technol.* **281**, 179–187 (2019). <https://doi.org/10.1016/j.biortech.2019.02.091>
116. Z. Li, M. Li, T. Zheng, Y. Li, X. Liu, Removal of tylosin and copper from aqueous solution by biochar stabilized nano-hydroxyapatite. *Chemosphere* **235**, 136–142 (2019). <https://doi.org/10.1016/j.chemosphere.2019.06.091>
117. A. Mojiri, J. Zhou, M. Vakili, H.V. Le, Removal performance and optimisation of pharmaceutical micropollutants from synthetic domestic wastewater by hybrid treatment. *J. Contam. Hydrol.* **235**, 103736 (2020). <https://doi.org/10.1016/j.jconhyd.2020.103736>
118. J. Moreno-Pérez, P.S. Pauletto, A.M. Cunha, Á. Bonilla-Petriciolet, N.P.G. Salau, G.L. Dotto, Three-dimensional mass transport modeling of pharmaceuticals adsorption inside ZnAl/biochar composite. *Colloids Surf., A* **614**, 126170 (2021). <https://doi.org/10.1016/j.colsurfa.2021.126170>
119. Z. Zeng, S. Ye, H. Wu, R. Xiao, G. Zeng, J. Liang, C. Zhang, J. Yu, Y. Fang, B. Song, Research on the sustainable efficacy of g-MoS₂ decorated biochar nanocomposites for removing tetracycline hydrochloride from antibiotic-polluted aqueous solution. *Sci. Total. Environ.* **648**, 206–217 (2019). <https://doi.org/10.1016/j.scitotenv.2018.08.108>
120. T.S. Anirudhan, J.R. Deepa, A.S. Nair, Fabrication of chemically modified graphene oxide/nano hydroxyapatite composite for adsorption and subsequent photocatalytic degradation of aureomycin hydrochloride. *J. Ind. Eng. Chem.* **47**, 415–430 (2017). <https://doi.org/10.1016/j.jiec.2016.12.014>
121. T.S. Anirudhan, J.R. Deepa, Nano-zinc oxide incorporated graphene oxide/nanocellulose composite for the adsorption and photo catalytic degradation of ciprofloxacin hydrochloride from aqueous solutions. *J. Colloid Interf. Sci.* **490**, 343–356 (2017). <https://doi.org/10.1016/j.jcis.2016.11.042>
122. K. Balasubramani, N. Sivarajasekar, S. Muthusaravanan, K. Ram, M. Naushad, T. Ahamad, G. Sharma, Efficient removal of antidepressant Fluoxetine using graphene oxide/cellulose nanogel composite: Particle swarm algorithm based artificial neural network modelling and optimization. *J. Mol. Liq.* **319**, 114371 (2020). <https://doi.org/10.1016/j.molliq.2020.114371>
123. W.-H. Chen, J.-R. Huang, C.-H. Lin, C.-P. Huang, Catalytic degradation of chlorpheniramine over GO-Fe₃O₄ in the presence of H₂O₂ in water: the synergistic effect of adsorption. *Sci. Total. Environ.* **736**, 139468 (2020). <https://doi.org/10.1016/j.scitotenv.2020.139468>

124. B.Y.Z. Hiew, L.Y. Lee, K.C. Lai, S. Gan, S. Thangalazhy-Gopakumar, G.-T. Pan, T.C.-K. Yang, Adsorptive decontamination of diclofenac by three-dimensional graphene-based adsorbent: response surface methodology, adsorption equilibrium, kinetic and thermodynamic studies. *Environ. Res.* **168**, 241–253 (2019). <https://doi.org/10.1016/j.envres.2018.09.030>
125. H. Karimi-Maleh, M. Shafieizadeh, M.A. Taher, F. Opoku, E.M. Kiarri, P.P. Govender, S. Ranjbari, M. Rezapour, Y. Orooji, The role of magnetite/graphene oxide nano-composite as a high-efficiency adsorbent for removal of phenazopyridine residues from water samples, an experimental/theoretical investigation. *J. Mol. Liq.* **298**, 112040 (2020). <https://doi.org/10.1016/j.molliq.2019.112040>
126. M. Lv, L. Yan, C. Liu, C. Su, Q. Zhou, X. Zhang, Y. Lan, Y. Zheng, L. Lai, X. Liu, Z. Ye, Non-covalent functionalized graphene oxide (GO) adsorbent with an organic gelator for co-adsorption of dye, endocrine-disruptor, pharmaceutical and metal ion. *Chem. Eng. J.* **349**, 791–799 (2018). <https://doi.org/10.1016/j.cej.2018.04.153>
127. D.T. Ogunleye, S.O. Akpotu, B. Moodley, Adsorption of sulfamethoxazole and reactive blue 19 using graphene oxide modified with imidazolium based ionic liquid. *Environ. Technol. Innov.* **17**, 100616 (2020). <https://doi.org/10.1016/j.eti.2020.100616>
128. G. Peng, M. Zhang, S. Deng, D. Shan, Q. He, G. Yu, Adsorption and catalytic oxidation of pharmaceuticals by nitrogen-doped reduced graphene oxide/Fe₃O₄ nanocomposite. *Chem. Eng. J.* **341**, 361–370 (2018). <https://doi.org/10.1016/j.cej.2018.02.064>
129. M. Sarker, J.Y. Song, S.H. Jung, Adsorptive removal of anti-inflammatory drugs from water using graphene oxide/metal-organic framework composites. *Chem. Eng. J.* **335**, 74–81 (2018). <https://doi.org/10.1016/j.cej.2017.10.138>
130. F.V.A. Dutra, B.C. Pires, T.A. Nascimento, K.B. Borges, Functional polyaniline/multiwalled carbon nanotube composite as an efficient adsorbent material for removing pharmaceuticals from aqueous media. *J. Environ. Manag.* **221**, 28–37 (2018). <https://doi.org/10.1016/j.jenvman.2018.05.051>
131. C.V.T. Rigueto, M. Rosseto, M.T. Nazari, B.E.P. Ostwald, I. Alessandretti, C. Manera, J.S. Piccin, A. Dettmer, Adsorption of diclofenac sodium by composite beads prepared from tannery wastes-derived gelatin and carbon nanotubes. *J. Environ. Chem. Eng.* **9**, 105030 (2021). <https://doi.org/10.1016/j.jece.2021.105030>
132. X. Shi, A. Karachi, M. Hosseini, M.S. Yazd, H. Kamyab, M. Ebrahimi, Z. Parsaee, Ultrasound wave assisted removal of Ceftriaxone sodium in aqueous media with novel nano composite g-C₃N₄/MWCNT/Bi₂WO₆ based on CCD-RSM model. *Ultrason. Sonochem.* **68**, 104460 (2020). <https://doi.org/10.1016/j.ultsonch.2019.01.018>
133. R.M. Toudeshki, S. Dadfarnia, A.M.H. Shabani, Surface molecularly imprinted polymer on magnetic multi-walled carbon nanotubes for selective recognition and preconcentration of metformin in biological fluids prior to its sensitive chemiluminescence determination: Central composite design optimization. *Anal. Chim. Acta* **1089**, 78–89 (2019). <https://doi.org/10.1016/j.aca.2019.08.070>
134. H. Kohay, I.I. Bilkis, Y.G. Mishael, Effect of polycation charge density on polymer conformation at the clay surface and consequently on pharmaceutical binding. *J. Colloid Interf. Sci.* **552**, 517–527 (2019). <https://doi.org/10.1016/j.jcis.2019.05.079>
135. G. Peng, T. Li, B. Ai, S. Yang, J. Fu, Q. He, G. Yu, S. Deng, Highly efficient removal of enrofloxacin by magnetic montmorillonite via adsorption and persulfate oxidation. *Chem. Eng. J.* **360**, 1119–1127 (2019). <https://doi.org/10.1016/j.cej.2018.10.190>
136. J. Liu, H. Lin, Y. He, Y. Dong, E.R.G.Y. Menzembere, Novel CoS₂/MoS₂@Zeolite with excellent adsorption and photocatalytic performance for tetracycline removal in simulated wastewater. *J. Cleaner Prod.* **260**, 121047 (2020). <https://doi.org/10.1016/j.jclepro.2020.121047>
137. M. Marković, A. Daković, D. Krajišnik, M. Kragović, J. Milić, A. Langella, B. Gennaro, P. Cappelletti, M. Mercurio, Evaluation of the surfactant/phillipsite composites as carriers for diclofenac sodium. *J. Mol. Liq.* **222**, 711–716 (2016). <https://doi.org/10.1016/j.molliq.2016.07.127>

138. C. Oliveira, A.L.M. Oliveira, L. Chantelle, R. Landers, S. Medina-Carrasco, M.D.M. Orta, E.C.S. Filho, M.G. Fonseca, Zinc (II) modified hydroxyapatites for tetracycline removal: Zn (II) doping or ZnO deposition and their influence in the adsorption. *Polyhedron* **194**, 114879 (2021). <https://doi.org/10.1016/j.poly.2020.114879>
139. D. Smiljanić, B. Gennaro, F. Izzo, A. Langella, A. Daković, C. Germinario, G.E. Rottinghaus, M. Spasojević, M. Mercurio, Removal of emerging contaminants from water by zeolite-rich composites: a first approach aiming at diclofenac and ketoprofen. *Microporous Mesoporous Mater.* **298**, 110057 (2020). <https://doi.org/10.1016/j.micromeso.2020.110057>
140. M. Alnajjar, A. Hethnawi, G. Nafie, A. Hassan, G. Vitale, N.N. Nassar, Silica-alumina composite as an effective adsorbent for the removal of metformin from water. *J. Environ. Chem. Eng.* **7**, 102994 (2019). <https://doi.org/10.1016/j.jece.2019.102994>
141. M. Catauro, F. Barrino, G.D. Pogetto, M. Milazzo, I. Blanco, S.V. Cipriotti, Structure, drug absorption, bioactive and antibacterial properties of sol-gel SiO₂/ZrO₂ materials. *Ceram. Int.* **46**, 29459–29465 (2020). <https://doi.org/10.1016/j.ceramint.2020.03.167>
142. S. Kittappa, M. Jang, M. Ramalingam, S. Ibrahim, Amine functionalized magnetic nano-composite materials for the removal of selected endocrine disrupting compounds and its mechanism study. *J. Environ. Chem. Eng.* **8**, 103839 (2020). <https://doi.org/10.1016/j.jece.2020.103839>
143. A. Mohseni-Bandpei, A. Eslami, H. Kazemian, M. Zarrabi, T.J. Al-Musawi, A high density 3-aminopropyltriethoxysilane grafted pumice-derived silica aerogel as an efficient adsorbent for ibuprofen: characterization and optimization of the adsorption data using response surface methodology. *Environ. Technol. Innov.* **18**, 100642 (2020). <https://doi.org/10.1016/j.eti.2020.100642>
144. H.T. Teo, W.R. Siah, L. Yuliati, Enhanced adsorption of acetylsalicylic acid over hydrothermally synthesized iron oxide-mesoporous silica MCM-41 composites. *J. Taiwan Inst. Chem. Eng.* **65**, 591–598 (2016). <https://doi.org/10.1016/j.jtice.2016.06.006>
145. N. Varga, M. Benkő, D. Sebők, G. Bohus, L. Janovák, I. Dékány, Mesoporous silica core-shell composite functionalized with polyelectrolytes for drug delivery. *Microporous Mesoporous Mater.* **213**, 134–141 (2015). <https://doi.org/10.1016/j.micromeso.2015.02.008>
146. R. Zhang, R. Xie, D. Liu, X. Jia, Q. Cai, X. Yang, Nanoporous fibers built with carbon-bound SiO₂ nanospheres via electrospinning and calcination. *Mater. Des.* **130**, 231–238 (2017). <https://doi.org/10.1016/j.matdes.2017.05.073>
147. R.M. Abdelhameed, H.E. Emam, Design of ZIF(Co & Zn)@wool composite for efficient removal of pharmaceutical intermediate from wastewater. *J. Colloid Interf. Sci.* **552**, 494–505 (2019). <https://doi.org/10.1016/j.jcis.2019.05.077>
148. J. Cui, X. Xu, L. Yang, C. Chen, J. Qian, X. Chen, D. Sun, Soft foam-like UiO-66/Polydopamine/Bacterial cellulose composite for the removal of aspirin and tetracycline hydrochloride. *Chem. Eng. J.* **395**, 125174 (2020). <https://doi.org/10.1016/j.cej.2020.125174>
149. Y. Pan, Q. Ding, B. Li, X. Wang, Y. Liu, J. Chen, F. Ke, J. Liu, Self-adjusted bimetallic zeolitic-imidazolate framework-derived hierarchical magnetic carbon composites as efficient adsorbent for optimizing drug contaminant removal. *Chemosphere* **263**, 128101 (2021). <https://doi.org/10.1016/j.chemosphere.2020.128101>
150. X. Wei, Y. Wang, J. Chen, F. Xu, Z. Liu, X. He, H. Li, Y. Zhou, Adsorption of pharmaceuticals and personal care products by deep eutectic solvents-regulated magnetic metal-organic framework adsorbents: performance and mechanism. *Chem. Eng. J.* **392**, 124808 (2020). <https://doi.org/10.1016/j.cej.2020.124808>
151. T. Xu, X. Hou, S. Liu, B. Liu, One-step synthesis of magnetic and porous Ni@MOF-74(Ni) composite. *Microporous Mesoporous Mater.* **259**, 178–183 (2018). <https://doi.org/10.1016/j.micromeso.2017.10.014>
152. A. Yohannes, J. Li, S. Yao, Various metal organic frameworks combined with imidazolium, quinolinium and benzothiazolium ionic liquids for removal of three antibiotics from water. *J. Mol. Liq.* **318**, 114304 (2020). <https://doi.org/10.1016/j.molliq.2020.114304>
153. Y. Zhou, J. Xu, N. Lu, X. Wu, Y. Zhang, X. Hou, Development and application of metal-organic framework@GA based on solid-phase extraction coupling with UPLC-MS/MS for

- the determination of five NSAIDs in water. *Talanta* **225**, 121846 (2021). <https://doi.org/10.1016/j.talanta.2020.121846>
154. N. Zhuo, Y. Lan, W. Yang, Z. Yang, X. Li, X. Zhou, Y. Liu, J. Shen, X. Zhang, Adsorption of three selected pharmaceuticals and personal care products (PPCPs) onto MIL-101(Cr)/natural polymer composite beads. *Sep. Purif. Technol.* **177**, 272–280 (2017). <https://doi.org/10.1016/j.seppur.2016.12.041>
155. I. Ali, Z.A. AL-Othman, A. Alwarthan, Synthesis of composite iron nano adsorbent and removal of ibuprofen drug residue from water. *J. Mol. Liq.* **219**, 858–864 (2016). <https://doi.org/10.1016/j.molliq.2016.04.031>
156. I. Ali, Z.A. AL-Othman, O.M.L. Alharbi, Uptake of pantoprazole drug residue from water using novel synthesized composite iron nano adsorbent. *J. Mol. Liq.* **218**, 465–472 (2016). <https://doi.org/10.1016/j.molliq.2016.02.088>
157. L. Fan, Y. Lu, L.-Y. Yang, F. Huang, X.-K. Ouyang, Fabrication of polyethylenimine-functionalized sodium alginate/cellulose nanocrystal/polyvinyl alcohol core-shell microspheres ((PVA/SA/CNC)@PEI) for diclofenac sodium adsorption. *J. Colloid Interf. Sci.* **554**, 48–58 (2019). <https://doi.org/10.1016/j.jcis.2019.06.099>
158. C.B. Godiya, S. Kumar, Y. Xiao, Amine functionalized egg albumin hydrogel with enhanced adsorption potential for diclofenac sodium in water. *J. Hazard. Mater.* **393**, 122417 (2020). <https://doi.org/10.1016/j.jhazmat.2020.122417>
159. A. Khadir, M. Motamedi, M. Negarestani, M. Sillanpää, M. Sasani, Preparation of a nano bio-composite based on cellulosic biomass and conducting polymeric nanoparticles for ibuprofen removal: kinetics, isotherms, and energy site distribution. *Int. J. Biol. Macromol.* **162**, 663–677 (2020). <https://doi.org/10.1016/j.jbiomac.2020.06.095>
160. A. Khadir, M. Negarestani, A. Mollahosseini, Sequestration of a non-steroidal anti-inflammatory drug from aquatic media by lignocellulosic material (*Luffa cylindrica*) reinforced with polypyrrole: study of parameters, kinetics, and equilibrium. *J. Environ. Chem. Eng.* **8**, 103734 (2020). <https://doi.org/10.1016/j.jece.2020.103734>
161. W. Li, L. Huang, D. Guo, Y. Zhao, Y. Zhu, Self-assembling covalent organic framework functionalized poly(styrene-divinyl benzene-glycidylmethacrylate) composite for therapid extraction of non-steroidal anti-inflammatory drugs in wastewater. *J. Chromatogr. A* **1571**, 76–83 (2018). <https://doi.org/10.1016/j.chroma.2018.08.019>
162. B.C. Pires, F.V.A. Dutra, T.A. Nascimento, K.B. Borges, Preparation of PPy/cellulose fibre as an effective potassium diclofenac adsorbent. *React. Funct. Polym.* **113**, 40–49 (2017). <https://doi.org/10.1016/j.reactfunctpolym.2017.02.002>
163. G.S. Reis, C.H. Sampaio, E.C. Lima, M. Wilhelm, Preparation of novel adsorbents based on combinations of polysiloxanes and sewage sludge to remove pharmaceuticals from aqueous solutions. *Colloids Surf., A.* **497**, 304–315 (2016). <https://doi.org/10.1016/j.colsurfa.2016.03.021>
164. H. Xu, S. Zhu, M. Xia, F. Wang, Rapid and efficient removal of diclofenac sodium from aqueous solution via ternary core-shell CS@PANI@LDH composite: experimental and adsorption mechanism study. *J. Hazard. Mater.* **402**, 123815 (2021). <https://doi.org/10.1016/j.jhazmat.2020.123815>
165. I. Ali, Z.A. Alothman, A. Alwarthan, Uptake of propranolol on ionic liquid iron nanocomposite adsorbent: kinetic, thermodynamics and mechanism of adsorption. *J. Mol. Liq.* **236**, 205–213 (2017). <https://doi.org/10.1016/j.molliq.2017.04.028>
166. L. Nielsen, T.J. Badosz, Analysis of sulfamethoxazole and trimethoprim adsorption on sewage sludge and fish waste derived adsorbents. *Microporous Mesoporous Mater.* **220**, 58–72 (2016). <https://doi.org/10.1016/j.micromeso.2015.08.025>
167. X. Wang, W. Bi, P. Zhai, X. Wang, H. Li, G. Mailhot, W. Dong, Adsorption and photocatalytic degradation of pharmaceuticals by BiOCl_xI_y nanospheres in aqueous solution. *Appl. Surf. Sci.* **360**, 240–251 (2016). <https://doi.org/10.1016/j.apsusc.2015.10.229>
168. S. Yadav, A. Asthana, A.K. Singh, R. Chakraborty, S.S. Vidya, M.A.B.H. Susan, S.A.C. Carabineiro, Adsorption of cationic dyes, drugs and metal from aqueous solutions using a polymer composite of magnetic/β-cyclodextrin/activated charcoal/Na alginate: Isotherm,

- kinetics and regeneration studies. *J. Hazard. Mater.* **409**, 124840 (2021). <https://doi.org/10.1016/j.jhazmat.2020.124840>
169. S.-M. Alatalo, E. Daneshvar, N. Kinnunen, A. Meščeriakovas, S.K. Thangaraj, J. Jänis, D.C.W. Tsang, A. Bhatnagar, A. Lähde, Mechanistic insight into efficient removal of tetracycline from water by Fe/graphene. *Chem. Eng. J.* **373**, 821–830 (2019). <https://doi.org/10.1016/j.cej.2019.05.118>
170. V. Lozano-Morales, I. Gardi, S. Nir, T. Undabeytia, Removal of pharmaceuticals from water by clay-cationic starch sorbents. *J. Cleaner Prod.* **190**, 703–711 (2018). <https://doi.org/10.1016/j.jclepro.2018.04.174>
171. J.M.N. Santos, C.R. Pereira, L.A.A. Pinto, T. Frantz, É.C. Lima, E.L. Foletto, G.L. Dotto, Synthesis of a novel CoFe₂O₄/chitosan magnetic composite for fast adsorption of indigotine blue dye. *Carbohydr. Polym.* **217**, 6–14 (2019). <https://doi.org/10.1016/j.carbpol.2019.04.054>
172. D. Rahangdale, A. Kumar, Chitosan as a substrate for simultaneous surface imprinting of salicylic acid and cadmium. *Carbohydr. Polym.* **202**, 334–344 (2018). <https://doi.org/10.1016/j.carbpol.2018.08.129>
173. M. Vakili, M. Rafatullah, B. Salamatinia, A.Z. Abdullah, M.H. Ibrahim, K.B. Tan, Z. Gholami, P. Amouzgar, Application of chitosan and its derivatives as adsorbents for dye removal from water and wastewater: a review. *Carbohydr. Polym.* **113**, 115–130 (2014). <https://doi.org/10.1016/j.carbpol.2014.07.007>
174. G. Crini, Recent developments in polysaccharide-based materials used as adsorbents in wastewater treatment. *Prog. Polym. Sci.* **30**, 38–70 (2005). <https://doi.org/10.1016/j.progpolymsci.2004.11.002>
175. X. Tan, Y. Liu, G. Zeng, X. Wang, X. Hu, Y. Gu, Z. Yang, Application of biochar for the removal of pollutants from aqueous solutions. *Chemosphere* **125**, 70–85 (2015). <https://doi.org/10.1016/j.chemosphere.2014.12.058>
176. J. Lehmann, S. Joseph, in *Biochar for Environmental Management: Science and Technology*. ed. by J. Lehmann, S. Joseph (Earthscan, London, 2009), p. 448
177. X.-F. Tan, Y.-G. Liu, Y.-L. Gu, Y. Xu, G.-M. Zeng, X.-J. Hu, S.-B. Liu, X. Wang, S.-M. Liu, J. Li, Biochar-based nano-composites for the decontamination of wastewater: a review. *Bioresour. Technol.* **212**, 318–333 (2016). <https://doi.org/10.1016/j.biortech.2016.04.093>
178. T. Liao, T. Li, X. Su, X. Yu, H. Song, Y. Zhu, Y. Zhang, La(OH)₃ modified magnetic pineapple biochar as novel adsorbents for efficient phosphate removal. *Bioresour. Technol.* **263**, 207–213 (2018). <https://doi.org/10.1016/j.biortech.2018.04.108>
179. B. Chen, Z. Chen, S. Lv, A novel magnetic biochar efficiently sorbs organic pollutants and phosphate. *Bioresour. Technol.* **102**, 716–723 (2011). <https://doi.org/10.1016/j.biortech.2010.08.067>
180. V.B. Mohan, K. Lau, D. Hui, D. Bhattacharyy, Graphene-based materials and their composites: a review on production, applications and product limitations. *Compos. B* **142**, 200–220 (2018). <https://doi.org/10.1016/j.compositesb.2018.01.013>
181. Y. Zhu, S. Murali, W. Cai, X. Li, J.W. Suk, J.R. Potts, R.S. Ruoff, Graphene and graphene oxide: synthesis, properties, and applications. *Adv. Mater.* **22**, 3906–3924 (2010). <https://doi.org/10.1002/adma.201001068>
182. A. Aqel, K.M.M.A. El-Nour, R.A.A. Ammar, A. Al-Warthan, Carbon nanotubes, science and technology part (I) structure, synthesis and characterization. *Arabian J. Chem.* **5**, 1–23 (2012). <https://doi.org/10.1016/j.arabjc.2010.08.022>
183. E.T. Thostenson, Z. Ren, T. Chou, Advances in the science and technology of carbon nanotubes and their composites: a review. *Compos. Sci. Technol.* **61**, 1899–1912 (2001). [https://doi.org/10.1016/S0266-3538\(01\)00094-X](https://doi.org/10.1016/S0266-3538(01)00094-X)
184. B. Sarkar, S. Mandal, Y.F. Tsang, P. Kumar, K. Kim, Y.S. Ok, Designer carbon nanotubes for contaminant removal in water and wastewater: a critical review. *Sci. Total Environ.* **612**, 561–581 (2018). <https://doi.org/10.1016/j.scitotenv.2017.08.132>
185. X. Ren, C. Chen, M. Nagatsu, X. Wang, Carbon nanotubes as adsorbents in environmental pollution management: a review. *Chem. Eng. J.* **170**, 385–410 (2011). <https://doi.org/10.1016/j.cej.2010.08.045>

186. R. Srinivasan, Advances in application of natural clay and its composites in removal of biological, organic, and inorganic contaminants from drinking water. *Adv. Mater. Sci. Eng.* **2011**, 1–17 (2011). <https://doi.org/10.1155/2011/872531>
187. P.N.E. Diagboya, E.D. Dikio, Silica-based mesoporous materials; emerging designer adsorbents for aqueous pollutants removal and water treatment. *Microporous Mesoporous Mater.* **266**, 252–267 (2018). <https://doi.org/10.1016/j.micromeso.2018.03.008>
188. T.M. Budnyak, I.V. Pylypchuk, V.A. Tertykh, E.S. Yanovska, D. Kolodynska, Synthesis and adsorption properties of chitosan-silica nanocomposite prepared by sol-gel method. *Nanoscale Res. Lett.* **10**, 1–10 (2015). <https://doi.org/10.1186/s11671-014-0722-1>
189. Q. Gao, H. Zhu, W.-J. Luo, S. Wang, C.-G. Zhou, Preparation, characterization, and adsorption evaluation of chitosan-functionalized mesoporous composites. *Microporous Mesoporous Mater.* **193**, 15–26 (2014). <https://doi.org/10.1016/j.micromeso.2014.02.025>
190. P.N. Diagboya, B.I. Olu-Owolabi, K.O. Adebowale, Microscale scavenging of pentachlorophenol in water using amine and triphosphosphate-grafted SBA-15 silica: batch and modeling studies. *J. Environ. Manag.* **146**, 42–49 (2014). <https://doi.org/10.1016/j.jenvman.2014.04.038>
191. M.Z. Momčilović, M.S. Randelović, A.R. Zarubica, A.E. Onjia, M. Kokunešoski, B.Z. Matović, SBA-15 templated mesoporous carbons for 2,4-dichlorophenoxyacetic acid removal. *Chem. Eng. J.* **220**, 276–283 (2013). <https://doi.org/10.1016/j.ccej.2012.12.024>
192. M.L.N. Perdigoto, R.C. Martins, N. Rocha, M.J. Quina, L. Gando-Ferreira, R. Patrício, L. Durães, Application of hydrophobic silica based aerogels and xerogels for removal of toxic organic compounds from aqueous solutions. *J. Colloid Interface Sci.* **380**, 134–140 (2012). <https://doi.org/10.1016/j.jcis.2012.04.062>
193. H. Liu, W. Sha, A.T. Cooper, M. Fan, Preparation and characterization of a novel silica aerogel as adsorbent for toxic organic compounds. *Colloids Surf., A.* **347**, 38–44 (2009). <https://doi.org/10.1016/j.colsurfa.2008.11.033>
194. L.W. Hrubesh, P.R. Coronado, J.H. Satcher Jr., Solvent removal from water with hydrophobic aerogels. *J. Non-Cryst. Solids* **285**, 328–332 (2001). [https://doi.org/10.1016/S0022-3093\(01\)00475-6](https://doi.org/10.1016/S0022-3093(01)00475-6)
195. N.C. Burtch, H. Jasuja, K.S. Walton, Water stability and adsorption in metal-organic frameworks. *Chem. Rev.* **114**, 10575–10612 (2014). <https://doi.org/10.1021/cr5002589>

Advances in Manufacturing and Processing of Discontinuous Particle-Reinforced Titanium Matrix Composites (TMCs)



Yaya Wu, Bingliang Liu, Siyu Ren, Run Miao, Liqiang Wang, Weijie Lu, and Lechun Xie

Abstract Titanium matrix composites (TMCs) have a high specific strength, specific stiffness, high modulus, corrosion resistance, and high-temperature resistance, so they are widely used in aerospace, weaponry, shipbuilding and other fields. However, TMCs are difficult to process using traditional technology, and the discontinuous TMCs mainly rely on in-situ synthesis technology to prepare. This chapter introduces the main preparation technologies of discontinuous particle-reinforced TMCs, including the technologies of powder metallurgy (PM), mechanical alloying (MA), self-propagating high-temperature synthesis (SHS), and rapid solidification processing (RSP). In additive manufacturing of TMCs, selective laser melting (SLM) can prepare mixed ex-situ/in-situ reinforced TMCs, which can realize the rapid and near-final forming of high-performance complex parts. Direct laser deposition (DLD) can be used to prepare in-situ reinforced TMCs, which provides new possibilities for the preparation of TMCs. TMCs are processed by heat treatment or electropulsing treatment (EPT), which can modify and optimize their microstructure. By modifying the structure and the phase content of TMCs, the performance of TMCs can be improved.

Keywords Titanium matrix composites (TMCs) · Microstructure · Heat treatment · Synthesis · Additive manufacturing.

Y. Wu and B. Liu contribute equally in this chapter.

Y. Wu · B. Liu · S. Ren · R. Miao · L. Xie (✉)

Hubei Key Laboratory of Advanced Technology for Automotive Components, Wuhan University of Technology, Wuhan 430070, P.R. China

e-mail: xielechun@whut.edu.cn

Hubei Collaborative Innovation Center for Automotive Components Technology, Wuhan University of Technology, Wuhan 430070, P.R. China

L. Wang · W. Lu

State Key Laboratory of Metal Matrix Composites, School of Materials Science and Engineering, Shanghai Jiao Tong University, No. 800 Dongchuan Road, Shanghai 200240, P.R. China

1 Introduction

1.1 Titanium Matrix Composites (TMCs)

Titanium and titanium alloys have been widely used in aerospace, petrochemical and military industries because of their excellent properties, but their Young's modulus and wear resistance are not as good as steel. In order to further improve the mechanical properties of titanium and titanium alloys, researchers introduced some hard particles or fibers to obtain better mechanical properties [1]. This type of composite material formed by introducing ceramic reinforcements into titanium alloys is called titanium matrix composites (TMCs) [2]. TMCs show higher specific strength, high-temperature resistance, anti-corrosion performance, non-magnetism, excellent abrasion resistance, anti-oxidation, and so on. TMCs are mainly used in impellers, support blocks, and key components for aerospace, unmanned submarine pressure shells, high-performance forgings for new-generation combat vehicles, etc. They are the most potential structural material for high-efficiency aeroengine [3].

The performance of TMCs mainly depends on the characteristics, content, and distribution of matrix and reinforcement, and there are obvious differences in the performance of TMCs with different processing methods. According to different types of reinforcements, it can be divided into continuous fiber-reinforced TMCs and discontinuous particle-reinforced TMCs. Fiber can significantly improve the mechanical properties and wear resistance of TMCs, while particle reinforcement can refine the microstructure of matrix, effectively hinder the movement of dislocations, and improve the service life of the material. This work will be focused on the discussion of discontinuous particle-reinforced TMCs. Particle reinforcements include metal ceramics (TiB, TiC, B₄C, SiC, TiB₂, etc.), oxides (Al₂O₃, Zr₂O₃, R₂O₃, R is the rare earth element, etc.), and intermetallic compounds (TiAl, Ti₃Al, Ti₅Si₃, etc.). In addition, there are some other reinforcements such as B, C, carbon nanotube (CNT), nanodiamond, graphene (GR), and so on [4].

Although TMCs show good properties, there are still some limitations. For example, the uneven distribution of reinforcements could lead to the agglomeration of reinforcements, and the reinforcements could not be bonded to matrix firmly. Besides, the interface between reinforcement and matrix could be unstable, which would result in crack nucleation. Therefore, in order to overcome the limitations of TMCs, many researchers have proposed the methods of heat treatment, which can improve the strength and fracture toughness of TMCs by refining the matrix grain, and the reinforcement can prevent crack propagation, prolonging the propagation path and increasing the absorbed impact energy [5].

Table 1 Comparison of mechanical properties of some TMCs and corresponding matrix. Reprinted with permission from Huang et al. [6]. Copyright (2009), Elsevier

| Materials | Elastic Modulus/ MPa | Yield Strength/MPa | Tensile Strength/ MPa | Elongation/% |
|---------------|-------------------------|--------------------|--------------------------|--------------|
| Ti | 108 | 367 | 474 | 8.3 |
| TiC/Ti | 140 | 444 | 573 | 1.9 |
| TiC+TiB/Ti | 137 | 690 | 757 | 2.0 |
| Ti-6Al-4V | 120 | 868 | 950 | 9.4 |
| TiC/Ti-6Al-4V | – | 944 | 999 | 2.0 |
| TiB/Ti-6Al-4V | 121 | 1000 | 1107 | 7.0 |

1.2 Advantages of TMCs

Compared with titanium alloy, TMCs show high specific strength, superior high-temperature performance and can serve for a long time at 600 °C high temperature and –250 °C low temperature. It has broad application prospects in emerging fields such as aerospace, space technology and weaponry. The addition of reinforcement improves the overall performance of the titanium matrix. The stable reinforcement can effectively strengthen the matrix and significantly improve the tensile strength of the matrix. Moreover, the existence of reinforcements can prevent the oxidation of raw materials and improves the oxidation resistance of composites. Table 1 shows the comparison of the mechanical properties of some TMCs with the corresponding matrix [6].

It can be seen from Table 1 that after the reinforcement is introduced, the elastic modulus, yield strength and tensile strength of the overall material have been significantly improved, but the plasticity is reduced. The addition of reinforcement can refine the grains, but the brittle reinforcement particles are often incompatible with the elastic–plastic deformation of the matrix, which reduces the elongation of TMCs. The steady-state creep rates of TMCs are much lower than those of matrix, which are closely related to the content, distribution and shape of reinforcements. The high-temperature creep deformation of TMCs is mainly caused by intragranular dislocation slip, climbing and grain boundary slip. The influence of the matrix on the creep properties of TMCs is also very important. The creep performance of the lamella structure is better than that of the dual-state structure and the equiaxed structure. The larger the β grains and α lamellae in the matrix, the better the creep resistance of TMCs.

1.3 Applications of TMCs

As important strategic structural material in the country, TMCs have broad application prospects due to their high specific modulus and strength, as well as excellent

high-temperature performance. They are effective materials for solving and eliminating many safety hazards [4]. TMCs have been used in the wings, support beams, stiffeners, and fuselage skin of the space shuttle. Figure 1 shows the TMCs gears developed by Spectronics (SP) Company for Air Force Fighters [7]. Figure 2 shows the TMC pneumatic grille for a certain aerospace device [8]. It has high-temperature performance, including strength, creep resistance, and oxidation resistance. It can replace high-temperature alloy components to reduce weight.

In the manufacturing of automobile industry, TMCs can be used as engine cylinder liner, piston, engine cylinder block, chassis, drive shaft, brake disc, etc. For example, the engine crankshaft needs to bear a huge load during the whole driving cycle of vehicle. Meanwhile, in order to reduce the mass of vehicle, the crankshaft must be reduced as much as possible on the basis of maintaining a certain bearing capacity, and TMCs fully meet the requirements. TiB-reinforced Ti-7Mo-4Fe-2Al-2V composite was prepared by powder metallurgy and successfully applied to the

Fig. 1 SiC fiber-reinforced TMC equipment developed by American Spectronics Company for Air Force Fighter. Reprinted with permission from Hayat et al. [7]. Copyright (2019), Elsevier

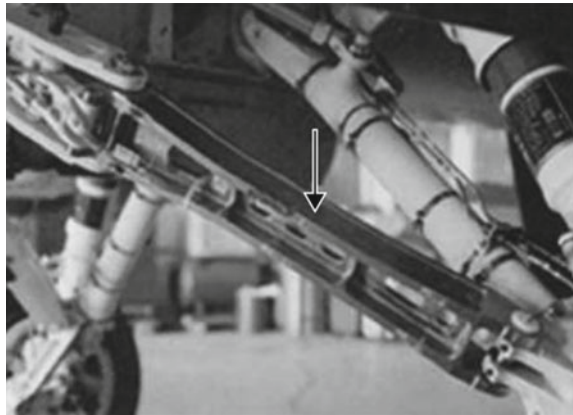
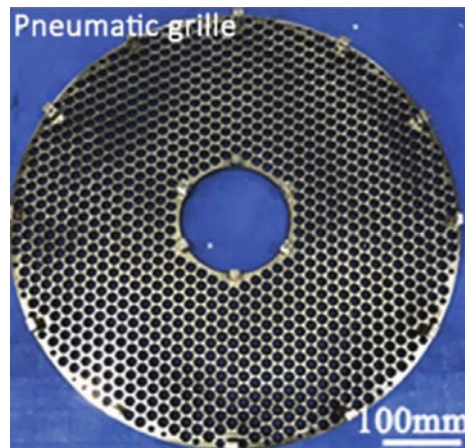


Fig. 2 TMC pneumatic grille for a certain aerospace device. Reprinted with permission from Huang et al. [8]. Copyright (2020), Elsevier



intake and exhaust valves of the Toyota engine. Even missile fins and efficient rocket thrusters were made by TMCs. The TiC-reinforced TMCs developed by Dynamet Technology Inc. have been used to manufacture hemispherical missile shells [9].

TMCs also play an important role in the field of medicine. At present, metal biomaterials are mainly used in dentures, artificial head segments, internal fixators, cardiac stents, artificial blood vessels, etc. Titanium alloy has become a popular metal biomaterial because of its low density, low Young's modulus, and high biocompatibility. However, its low Young's modulus is still much higher than human bone, so the bone around the implant will be absorbed and lead to loosening. This phenomenon is called "stress shielding effect" in biology [10]. TMCs with porous structures can replace bulk materials, which are considered for joint replacement surgery and bone transplantation. The introduction of porous structure can reduce the Young's modulus and weight of materials relative to bulk materials. In addition, the modulus of porous structure is easy to operate, and the growth of bone cells can be improved compared with solid structure [11–13]. Bioactive materials could be coated on the titanium matrix, which shows both the characteristics of titanium and active materials. It shows good biocompatibility and can maintain its own strength and toughness. Therefore, TMCs still have a lot of development space in the medical field.

At present, the cost of TMCs preparation is high, in order to promote TMCs in future industrial applications, the subsequent processing technology and improvement process need to be investigated further.

2 Processing of Discontinuous Particle-Reinforced TMCs

2.1 *Synthesis of Discontinuous Particle-Reinforced TMCs*

Discontinuously discontinuous particle-reinforced TMCs can be divided into additive method and in-situ synthesis process, according to the way of reinforcement. The additive method is to use a granular or powdered ceramic reinforcing phase to be added to the titanium matrix. The bonding between the matrix and the reinforcement produced by the additive method is not compatible, and the size of reinforcements is limited by the powder, so it has not been received significant attention. In-situ synthesis method is the chemical reaction between the elements in the raw materials to form reinforcements. The in-situ manufacturing of discontinuous particle-reinforced TMCs enhances the stability of interface between matrix and reinforcement, the distribution of particles in the matrix is uniform and stable, and the mechanical properties are excellent. The composite material produced by in-situ technology shows high specific strength and high modulus, as well as excellent oxidation resistance and wear resistance [14]. Commonly used in-situ processing additives are TiB_2 , B_4C , Cr_3C_2 , and Si_3N_4 .

2.2 *In-Situ Processing Technique*

The main preparation methods for preparing discontinuously reinforced TMCs by in-situ method include powder metallurgy, fusion casting method, exothermic diffusion method, mechanical alloying, self-propagating high-temperature synthesis, rapid solidification technology, reactive hot pressing, and various melting and casting technologies. In powder metallurgy, the uniform dispersion and mixing of powder are the key points. And they determine the final properties of TMCs. Sometimes, surface coatings can be applied to enhance or ensure uniform dispersion [15]. In powder metallurgy, depending on whether the additive reacts with the matrix, the reinforcement can be incorporated into the matrix by two methods, namely, the additive method and the in-situ synthesis method [7]. Carbon nanotube-reinforced TMCs prepared by powder metallurgy showed better wear resistance and mechanical properties [16]. The TMCs with carbon nanotubes (CNT) and graphite as reinforcements were prepared by powder metallurgy and hot extrusion. In the microstructure, it was observed that the formed TiC particles were present in the Ti matrix and showed a uniform distribution in TMC [17]. Carbon nanotubes (CNT) and pure titanium powder have been synthesized to TMCs by powder metallurgy, and hot extrusion was originally used for grain refinement meanwhile [18]. Powder metallurgy was used to prepare TMCs reinforced with TiC particles and TiB whiskers formed in-situ. And TiB whiskers showed good alignment [19]. The Ti-6Al-4V alloy produced by powder sintering and in-situ press forging could form a new twin-crystal structure with ultra-fine layered α and β . This twin-crystal alloy was superior to other Ti-6Al-4V alloys reported so far and their composite materials under tension and compression conditions [20]. Spark plasma sintering (SPS), hot isostatic pressing (HIP), and reactive hot pressing (RHP) represented by powder metallurgy showed controllable and uniform distribution of reinforcements and high production efficiency. The common SPS process is putting the reinforcement powder and titanium powder into the mold, and then energizing and pressurizing to realize the rapid compaction of the powder and the in-situ reaction to generate TMCs. The hybrid carbon network in multi-walled carbon nanotubes (MWCNs) prepared by SPS could improve the strengthening efficiency [21, 22].

TMCs reinforced with 5 wt.% graphene oxide exhibited the largest nano hardness (4.79 GPa) and elastic modulus (163.7 GPa) at 1473 K [23]. TiNi matrix composites prepared by sintering 1 vol.% multi-walled carbon nanotubes (MWCNs) with Ti and Ni elemental powders have a slight decrease in average friction coefficient [24]. TiAl/Ti-2Al-C (4, 8, 12, 16, and 20 wt.%) composites were prepared in-situ by high-energy ball milling of TiH₂, Al, and C powders and then hot-press sintering at 1473 K. While the milling time increased, the average particle size of the powder decreased first and then increased [25]. With the increase of graphene oxide content and sintering temperature, the content of TiC increases, which improves the mechanical properties of TMCs [26].

The melting and casting method is putting the base titanium alloy and the additional source into a melting and casting furnace, and then heating to a molten state, and

the additional source and the base react to form reinforcements [27]. The induction skull melting (ISM) and the vacuum consumable arc smelting technology (VAR) in the casting method require the advantages of simple equipment, mass production, low cost, and easy manufacture of large and complex structural parts [28]. The exothermic diffusion method (XDTM) is to mix the reinforcement powder with the matrix powder [29], so that the two powders undergo an exothermic reaction under the conditions of higher than the matrix, but lower than the melting point of the reinforcement to produce sub-microscopic reinforcement. The resulting reinforcements are granular, flake-like, or whisker-like. The mechanical alloying (MA) method is to use a ball mill to crush powder with a certain mass ratio, and then to prepare TMCs through processes such as forming and sintering. Li et al. [30] prepared $\text{TiB}_2/\text{Ti}-4.5\text{Fe}-6.8\text{Mo}-1.5\text{Al}$ by MA and SPS methods. With the prolonged milling time, the particle size of powder decreased and the number of that increased, and the microstructure of the sintered sample is more uniform. The advantage of MA process is that the reinforcements are evenly distributed, but Ti tends to absorb hydrogen and oxygen in the ball mill and become brittle. Therefore, this process has problems such as low production efficiency and expensive equipment.

The self-propagating high-temperature synthesis (SHS) uses the heat generated by the chemical reaction of the raw materials to further promote the chemical reaction. Once the reaction occurs, it will continue until the reaction is complete. The SHS method shows the advantages of simple process and easy automation. TMCs could be prepared with high reinforcement. However, the theoretical density of reinforcements prepared by this technology is only about 50%, and post-processing of TMCs is required to obtain excellent properties. Lagos et al. [31] obtained TiC/Ti through SHS. In order to control the size of reinforcement and improve the compatibility of reinforcement with the matrix, more Ti than equal atomic TiC was introduced in the reaction, and SPS was used for consolidation. Rapid solidification technology (RST) uses a cooling rate of more than 10^3-10^4 K/s during the melt solidification process to make the material own better mechanical and physical properties. The RST can refine the grain size, change the microstructure, and enhance the solid solubility [32]. RST becomes a potential manufacturing technology for processing discontinuously particles reinforced TMCs. The RST greatly modified the shape of TiB phase [33]. Traditional ingot metallurgy and rapid solidification technology were used to produce the refined Al-TiC composite and introduce the dispersion hardening of reinforcement phase [34].

There are other methods for in-situ synthesis of TMCs, such as combustion-assisted casting is also called combustion-assisted synthesis (CAS) [35], which combines combustion synthesis with traditional casting metallurgy methods to synthesize TMCs in-situ. The ceramic reinforcements in TMCs are generated in-situ by the exothermic reaction between the reactants during the melting process. Such methods have been used in the work of in-situ synthesis of TiC/Ti via TiC, TiB/Ti via TiB, and (TiB+TiC)/Ti via Ti-B4C. The direct reaction synthesis (DRS) method is to directly add reaction powder or compacted reaction powder to molten metal [36], and the ceramic reinforcement is directly generated in-situ through the exothermic reaction between the reactants or between the reactants and the molten

metal. Besides, the assisted synthesis method (FAS) is that adding the fluoride salt containing the reinforcement element to the molten base metal during stirring and generating the reinforcement in-situ through an exothermic reaction [37]. At the same time, the stirring is stopped after the reaction is completed and the metal lump containing the fluoride salt product is removed. The reaction spontaneous infiltration method (RSI) is to place a titanium alloy metal ingot by the mixed powder of the reactants in the crucible, and then put them into the furnace together, and heat to a certain temperature for a certain period of time [38]. This process is used to generate reinforcements in-situ, this method can be used to prepare TMCs with high ceramic content. In recent years, researchers have shown that plasma can also be used as a chemical reactor to produce in-situ TMCs [7].

2.3 Additive Manufacturing on TMCs

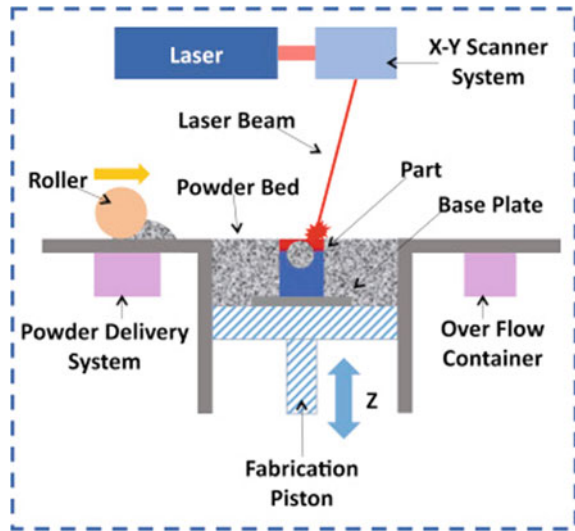
For TMCs, the lower thermal conductivity and higher chemical affinity greatly affect the processability of TMC [39], and the traditional manufacturing processes such as sintering and mechanical alloying show high production costs and long production cycles. Compared with traditional manufacturing methods, additive manufacturing (AM) can produce parts with complex shapes, and has the characteristics of short production cycle, high design flexibility, and high degree of customization. For the amplitude modulation of metal materials, laser is generally selected as energy. At present, the most popular research fields are selective laser melting (SLM) and direct laser deposition (DLD).

2.3.1 Selective Laser Melting (SLM) on TMCs

SLM adopts powder bed technology. The laser beam selectively melts the powder according to the machining path to form a micro-molten pool. After rapid cooling, the solid contour of the current layer is formed. The whole part can be processed through repeated cycles of powder spreading, melting, and solidification [40]. The schematic is shown in Fig. 3. Regarding the preparation of TMCs by SLM, the relevant research is usually carried out from the aspects of the type and content of the reinforcement phase, the adjustment of processing parameters, etc.

A large number of studies showed that TMC prepared by SLM showed higher hardness and wear resistance than unreinforced titanium alloy after adding B [41], TiC [42, 43], B₄C [44], and TiB₂ [45, 46]. The microhardness of TiC/Ti parts was increased to 566 HV_{0.2}, the average friction coefficient was reduced to 0.25, and the wear rate was reduced to $4 \times 10^{-16} \text{ m}^3/(\text{Nm})$ [43]. Cai et al. [45] used SLM to prepare in-situ synthesized TiB/Ti-6Al-4V alloy-based nano-TMC. The nano hardness of TMC was as high as 6.0 GPa, which was much higher than that of the traditional sintered material. The wear amount of sample without TiB was about twice that of the sample containing 3% TiB₂. Regarding the strengthening mechanism, B, TiB₂ and

Fig. 3 Schematic diagram of SLM technology. Reprinted with permission from Thompson et. al [40]. Copyright (2015), Elsevier



B_4C would react with titanium matrix to form TiB and TiC in-situ. The reinforcement would induce fine grain strengthening, dispersion strengthening, and solid solution strengthening in the composites. Therefore, compared with titanium alloys, TMCs prepared by SLM show higher hardness and wear resistance. The strengthening effect was related to the content of reinforcements. When the TiB_2 content increased to 7.5 wt.%, due to the strengthening and hardening effect of TiB_2 and in-situ generated TiB particles and the refinement of Ti matrix, as shown in Fig. 4, the hardness of the composite prepared by SLM increased by 68.6% and the wear resistance increased by 32.6% [46]. However, it is noticed that the larger reinforcements content, the higher hardness of TMCs. When the content of TiC was more than 17.5 wt.%, the densification of nano- TiC reinforcement was insufficient and disappeared, which reduced the hardness and wear resistance of TMCs [42].

Compared with the traditional processes, such as powder metallurgy and casting, TMCs prepared by SLM also show good properties. The yield strength, the ultimate compressive strength, and the maximum strain of 8.35 vol.% TiB/Ti were (1103 ± 20) MPa, (1421 ± 47) MPa, and $(17.8 \pm 3.2)\%$ respectively [47], the strength was higher than that of Cp-Ti, but the plasticity decreased. The ultimate tensile strength and elongation of 3 wt.% $TiC/Ti-6Al-4V$ were 1564.5 MPa and 3.7% [48], similarly, compared with $Ti-6Al-4V$, the strength increased and the plasticity decreased. The comparison of mechanical properties of titanium materials prepared by different processes is shown in Table 2.

In addition, different reinforcements will also affect the structure and properties of TMCs prepared by SLM. Kang et al. [52] used the mixed powder of CpTi and CrB_2 as raw materials to prepare TiB reinforced near α -Ti composites by SLM. Due to the formation of TiB and near α -Ti phase, the hardness and wear resistance of titanium can be improved. Liu et al. [53] proposed a new process for doping carbon

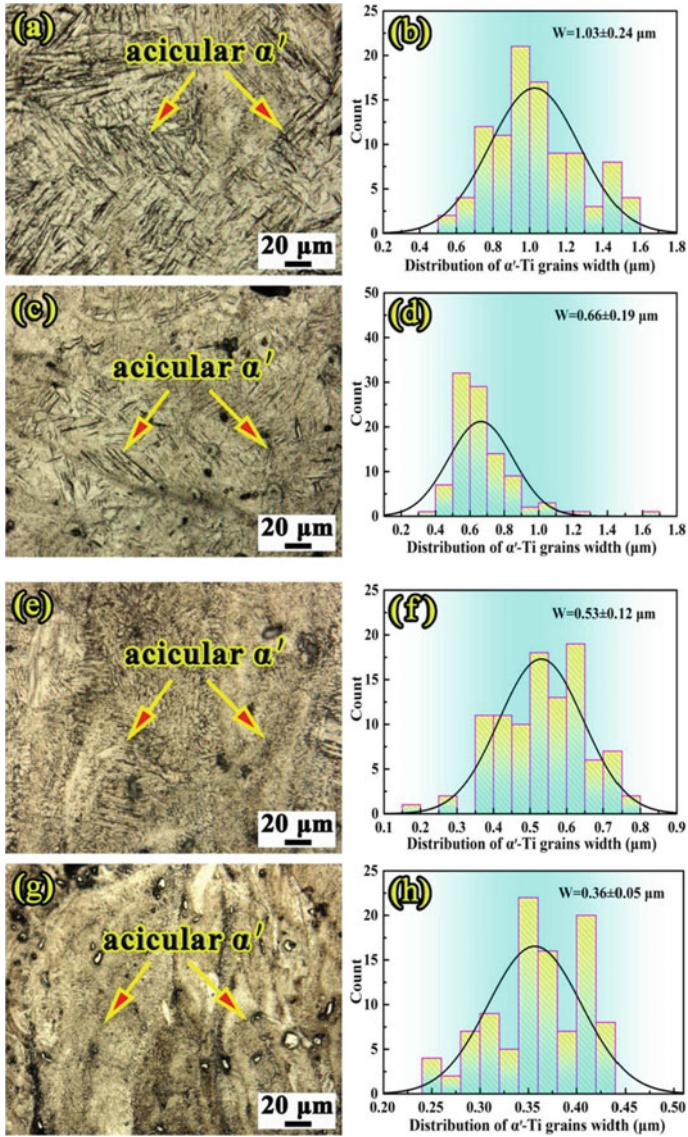


Fig. 4 Optical microscopy images of SLM-produced CPTi and TMCs specimens. **a** 0 wt.% TiB_2 ; **b** distribution of α' -Ti grains width in (a); **c** 2.5 wt.% TiB_2 ; **d** distribution of α' -Ti grains width in (c); **e** 5 wt.% TiB_2 ; **f** distribution of α' -Ti grains width in (e); **g** 7.5 wt.% TiB_2 ; **h** distribution of α' -Ti grains width in (g). Reprinted with permission from Jin et al. [46]. Copyright (2021), Elsevier

Table 2 Comparison of mechanical properties of titanium materials prepared by different processes

| Material | Process | Yield strength (MPa) | Ultimate compressive strength (MPa) | Ultimate tensile strength (MPa) | Maximum strain (%) | Elongation (%) | Reference |
|------------------------|-------------------|----------------------|-------------------------------------|---------------------------------|--------------------|----------------|-----------|
| Cp-Ti | SLM | 560 ± 5 | 1136 ± 15 | - | 51 ± 3.5 | - | [47] |
| Ti-6Al-4V | SLM | 964 | - | 1008 | - | 7 | [49] |
| 8.35 vol. % TiB/Ti | SLM | 1103 ± 20 | 1421 ± 47 | - | 17.8 ± 3.2 | - | [47] |
| 5 vol. % TiB/Ti | Powder metallurgy | 1200 | 1420 | - | 8.5 | - | [47] |
| 10 vol. % TiB/Ti | Powder metallurgy | 1400 | 1650 | - | 5.5 | - | [47] |
| 3 wt. % TiC/Ti-6Al-4V | SLM | - | - | 1564.5 | - | 3.7 | [48] |
| 5 vol. % TiC/Ti-6Al-4V | Cast | 900.7 ± 14.2 | - | 1005.2 ± 9.0 | - | 3.6 ± 0.2 | [50] |
| TiB/Ti | SLM | 1103 ± 20 | - | 1421 ± 47 | - | - | [51] |
| TiB/Ti | Cast | 815 ± 19 | - | 1434 ± 29 | - | - | [51] |
| TiB/Ti(25% porosity) | Powder metallurgy | 318 ± 32 | - | 510 ± 44 | - | - | [51] |
| TiB/Ti(29% porosity) | Powder metallurgy | 243 ± 19 | - | 414 ± 40 | - | - | [51] |
| TiB/Ti(36% porosity) | Powder metallurgy | 204 ± 13 | - | 310 ± 9 | - | - | [51] |

nanotubes (CNTs) into spherical Ti-6Al-4V powders. Unlike ball-milled powders, there is no coarse dendritic TiC. Due to the synergistic enhancement of the bridging enhancement of TiC nanosheets and the transfer of load from the matrix to the residual CNTs, the mechanical properties of CNTs/TiC-reinforced TMC are better than those of TiC-reinforced TMC, and the yield strength and elongation are up to 1162 MPa and 3.2%, respectively. 2 wt.% graphene/Ti-6Al-4V composites prepared by SLM obtained higher microhardness (432.03 HV_{0.2}), lower friction coefficient (0.3453), higher tensile strength (1276 MPa) and higher elongation (5.90%) [54]. Sitek et al. [55] using AlN as the reinforcement phase, the porosity of obtained TMC is between 7% and 17.5%, and the cross-sectional hardness is greater than that of 700 HV_{0.2}.

Another important factor influencing the performance of TMCs is SLM processing parameters. The study by Kang et al. [52] indicated that the parts obtained by high and low scanning speeds showed the higher hardness and lower wear rate, and the needle-like TiBw were formed at low scanning speed (1000 mm/s). Xia et al. [56] prepared B₄C/Ti composites, which showed that the high hardness about 577.1 HV_{0.2} was obtained due to the fine TiB and TiC reinforcements at lower laser power. With the increase of laser power, B and C elements have sufficient energy and a large amount of diffusion, in-situ whisker TiB phase and granular TiC phase obviously grew and the microhardness decreased. Energy density refers to the amount of energy used per unit volume of powder material. It is used to optimize the SLM process, taking into account laser power (P), scanning speed (v), layer thickness (t) and scanning distance (h). The formula is shown as follows [39, 57]:

$$E = \frac{P}{v \cdot h \cdot t} \quad (1)$$

Liu et al. [58] used SLM to prepare TiB₂-TiB-Ti TMC, and found that the size and proportion of TiB phase were affected by laser energy density, and the proportion of needle-like TiB phase was increased with the increase of laser energy density, as shown in Fig. 5. Pan et al. [59] replaced the traditional premixing method with electrode induction melting gas atomization technology, and the Ti-TiB₂ material had micron network structure and micron-nanometer TiBw at grain boundary. The rapid solidification in the SLM process made the TiBw further refined to the nanometer level, and the TMC showed excellent strength ($\sigma_b = 851$ MPa) and good ductility ($\delta = 10.2\%$).

Compared with other processes, such as arc melting, the microstructure of TMCs prepared by SLM was much finer [44]. However, the rapid melting, cooling and cyclic heating in the manufacturing process could accumulate a lot of residual stress. Li et al. [60, 61] carried out a heat treatment on TiB/Ti-6Al-4V prepared by SLM and showed that after heat treatment at 850 °C, the comprehensive mechanical properties of samples were improved, the yield strength was enhanced to 1345 MPa, and the fracture strain increased from 17.6% to 31.3%. With the increase of temperature, the microstructure was coarsened, and a stable ($\alpha+\beta$) biphasic matrix was obtained.

As mentioned earlier, TMC prepared by SLM shows unique structural characteristics and excellent mechanical properties. However, in order to obtain high-quality

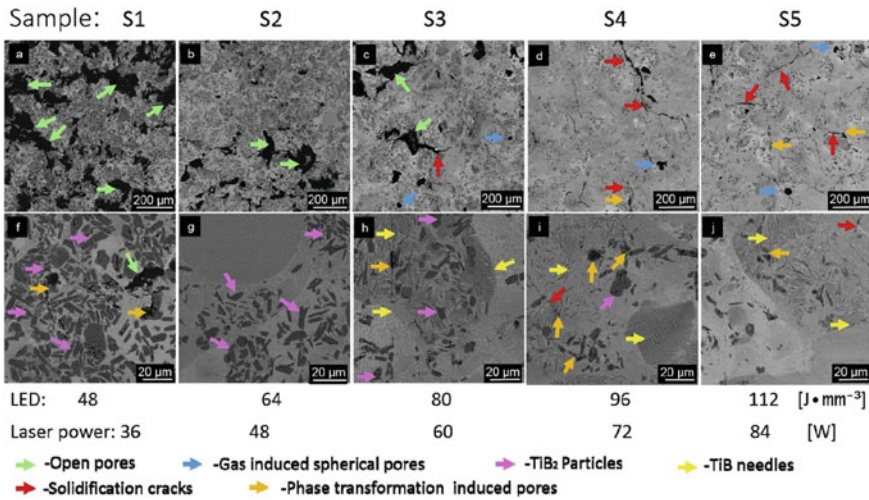


Fig. 5 Microstructure variation with laser energy density. Reprinted with permission from Liu et al. [58] Copyright (2020), Elsevier

parts, it is necessary to consider the type and content of reinforcements and the corresponding laser processing parameters. In addition, appropriate powder pretreatment, auxiliary processing technology during molding and post-molding heat treatment could improve the properties of the material to a certain extent. With the continuous development and maturity of SLM, it presents a huge development space in the preparation of complex structural parts with both precision and high-performance requirements.

2.3.2 Direct Laser Deposition (DLD) on TMCs

DLD is currently one of the important methods of laser AM. Compared with SLM, DLD technology uses coaxial powder feeding technology to complete the transportation of raw materials, and realize the manufacture of parts through layer deposition. At present, the research on manufacture of TMCs by DLD is focused on the influence of type, content, and processing parameters of reinforcements. Boron is very effective for grain refinement and texture weakening. The grain refinement effect of TiB is that TiB can be used as the heterogeneous nucleation center of β -Ti fine-grain and transformed into fine equiaxial crystal α -Ti in the remaining liquid titanium [62, 63]. Other studies showed that when the addition of B reached 0.08 wt.%, the average length and aspect ratio of α phase in the crystal decreased by 43% compared with Ti-6Al-4V, the transverse and longitudinal ultimate tensile strength of the material reached 1108 MPa and 1062 MPa, respectively, and the elongation decreased to 9.05% and 10.58%, respectively [64, 65]. For TiC-TMC prepared by DLD, TiC particles could strengthen the grain boundary and improve the stability of TiC/Ti-6Al-4V

[66]. The primary TiC could provide heterogeneous nucleation for the Ti phase and restrict its free growth, and the α -Ti grains tended to be refined [67]. When the TiC content exceeded 5 vol.%, a typical dendritic primary TiC phase may be produced in the TiC/Ti-6Al-4V structure [68–70]. Figure 6 shows the microstructure of different TiC contents. Different TiC content could also show different properties. The ultimate tensile strength of 5 vol.% TiC/Ti-6Al-4V was nearly 12.3% higher than that of Ti-6Al-4V matrix, and the microhardness of 50 vol.% TiC/Ti-6Al-4V reached 736.7 HV [69]. However, a high proportion of TiCp was disadvantageous to the tensile properties of TMC, and the tensile strength and elongation of 50 wt.% TiC/Ti-6Al-4V were only 515.5 MPa and 1.83%, respectively.

Besides, the wear resistance and oxidation resistance of TMCs prepared by DLD method were studied. Zhao et al. [71] formed TiC in-situ by adding graphene. This kind of composite material formed a mechanical mixed layer on the worn surface

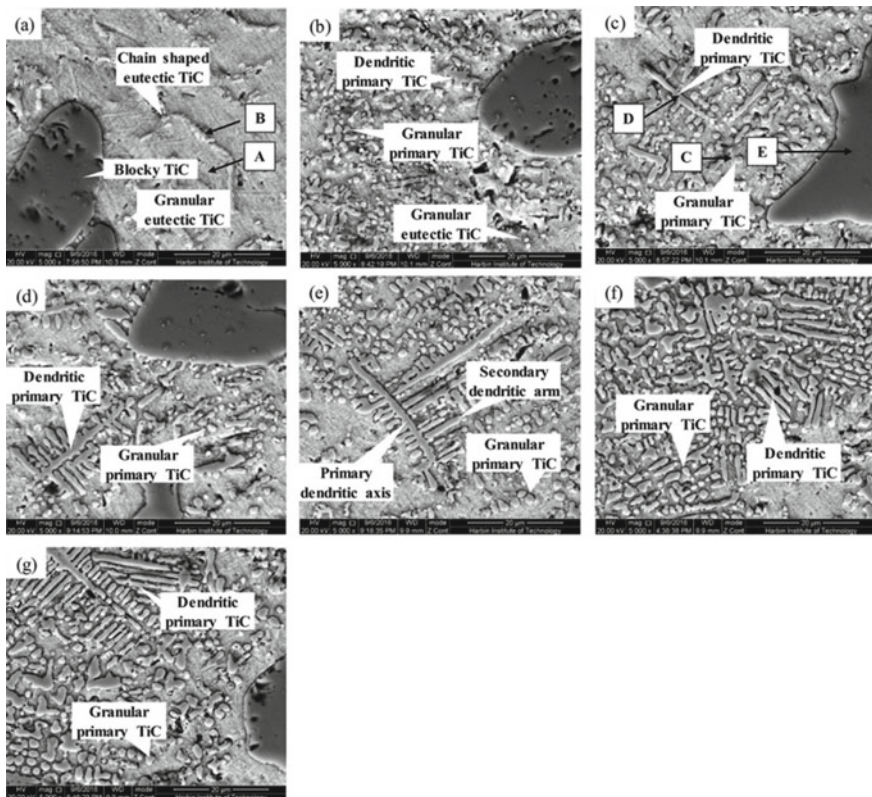


Fig. 6 Microstructure of functionally graded TiCp/Ti-6Al-4V composite with increasing the TiC volume fraction in different positions: **a** 5 vol.% TiCp/Ti-6Al-4V, **b** 10 vol.% TiCp/Ti-6Al-4V, **c** 15 vol.% TiCp/Ti-6Al-4V, **d** 20 vol.% TiCp/Ti-6Al-4V, **e** 30 vol.% TiCp/Ti-6Al-4V, **f** 40 vol.% TiCp/Ti-6Al-4V, **g** 50 vol.% TiCp/Ti-6Al-4V. Reprinted with permission from Li et al. [69]. Copyright (2018), Elsevier

of the composite under the action of friction heat, which protected the matrix and reduced the contact. Because of the self-lubricating property of graphene/graphite, it is easy to effectively reduce the friction force. Traxel et al. [63] prepared Ti/B₄C+BN composite materials through DLD. Compared with other particle-reinforced TMCs and pure titanium, this new composite material owned excellent yield strength and wear resistance, and comparable oxidation characteristics. Figure 7 shows the oxidation mass of each material, and the mass increased at 700 °C was equivalent to IMI-834 and Ti₃Al [39, 63]. Although the strength and hardness of TMCs prepared by DLD were improved compared to titanium alloys, but the plasticity was reduced. Generally, a suitable heat treatment method could be used to balance the plasticity and other properties. After heat treatment under 950 °C for 10 h, the limit tensile strength of the prepared TiC/Ti-6Al-4 V dropped from 1225.5 MPa to 1202.2 MPa. However, the elongation of composite was increased from 1.31% to 3.95% after heat treatment. And a large number of large-size cracks appeared on the fracture of TMCs after heat treatment at 1150 °C (in Fig. 8), and the plasticity of the material was deteriorated [70].

Processing technology is also an important factor affecting the preparation of TMCs from DLD. Ogunlana et al. [72] investigated the melting of Ti-6Al-4V and 20 wt.% B₄C under different powers, and when the laser power was 2000 W, the TMC showed the highest hardness of (445 ± 61) HV, and the wear amount and wear rate were the lowest, as 35.2 × 10⁻³ mm³ and 6.42 × 10⁻⁴ mm³/Nm respectively while the laser power was 800 W. Hu et al. [73, 74] indicated that using reasonable laser power could obtain three-dimensional quasi-continuous network (3DQCN) microstructure

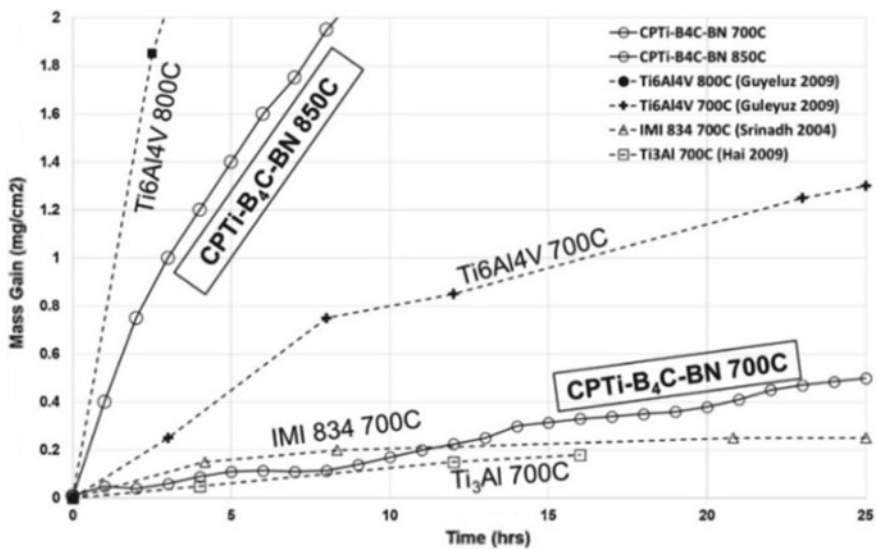


Fig. 7 Oxidation mass increase graph of CPTi-B4C-BN and other materials. Reprinted with permission from Traxel and Bandyopadhyay [63]. Copyright (2020), Elsevier

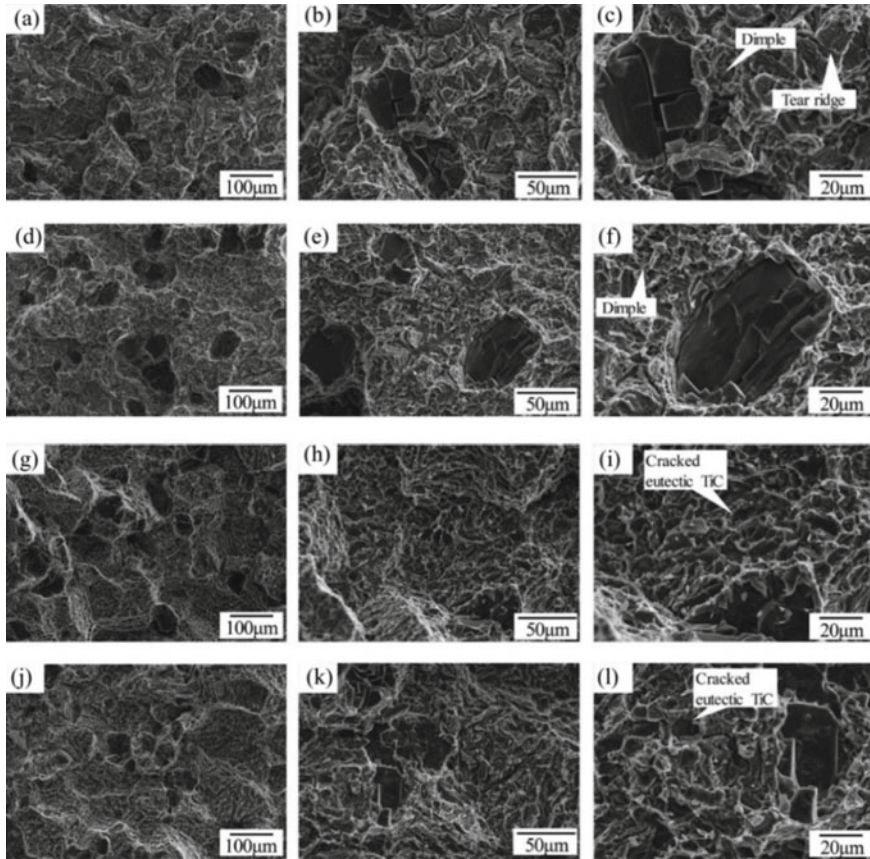


Fig. 8 Tensile fractography of as-deposited and heat-treated composites with 5% TiC volume fraction: **a–c** as-deposited composites; **d–f** composites after heat treating at 950 °C for 10 h; **g–i** composites after heat treating at 1050 °C for 10 h; **j–l** composites after heat treating at 1150 °C for 10 h. Reprinted with permission from Wang et al. [70]. Copyright (2018), Elsevier

in TiB-Ti composite, which is shown in Fig. 9. In this work, the increase in laser power made the average toughness of the material increased from 201 J/mm³ to 320 J/mm³, which was related to the formation of 3DQCN. With the increase of laser power, the contents of unfused TiC and fusion defects were obviously reduced, and heterogeneous nucleation was relatively easy. And the higher laser energy density was also beneficial to the diffusion of carbon in ultra-fine intermetallic compounds [67].

Besides the above parameters, the processing parameters and powder materials should be considered necessary during DLD. The type, content, and size of powder, and the laser power and scanning speed would directly affect the performance of TMCs. Zhang et al. [75] mentioned that the reaction product formed around the unreacted B₄C was relatively thin, resulting in poor performance of TMCs. Ning

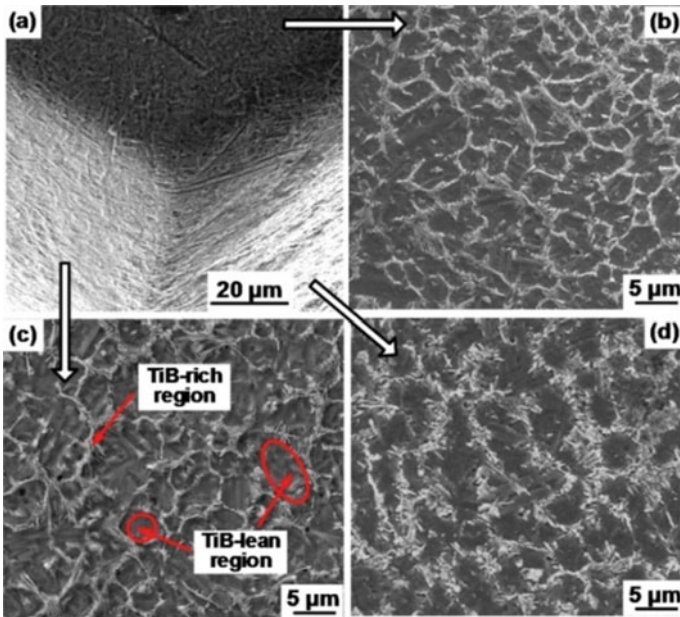


Fig. 9 Scanning electron microscope (SEM) analysis of **a** a stereo corner image taken from the fabricated part, and detailed 3DQCN microstructures of the **b** top side, **c** left side, and **d** right side. Reprinted with permission from Hu et al. [73]. Copyright (2018), Elsevier

et al. [76] used ultrasonic vibration during the laser deposition process, and the smaller TiB whisker was obtained and the porosity was significantly reduced. These whiskers were distributed along the grain boundary, and the dispersion was uniform, and the finer microstructure would hinder the movement of dislocations, thereby improving the properties.

When it comes to DLD technology, its advantages in the preparation of gradient composites is not ignored. Many researchers have studied the microstructure and properties of TiC gradient composites prepared by DLD [77]. By adjusting process parameters and changing Ti/TiC feed ratio in real time, gradient composites without a clear interface in each layer were obtained, and the microstructure was changed smoothly [78]. With the increase of TiC, Young's modulus increased, and the hardness continuously increased from 300 to 700 HV [69, 77]. Ti/TiAl functionally gradient materials have also been studied. Ti-47Al-2.5V-Cr/Ti-6Al-2Zr-Mo-V functionally gradient materials prepared by DLD showed a longitudinal tensile strength of about 1198.8 MPa and elongation of about 0.4%, which were typical brittle fracture [79]. In conclusion, by setting reasonable process parameters varying with composition, DLD technology can obtain crack-free gradient materials with stable changes in microstructure and mechanical properties. It can be seen that there is no essential difference between DLD and SLM. In the process of preparing TMCs, the processing parameters are closely related to the type and size of the matrix and reinforcements.

Controlling the properties of materials by heat treatment after molding is also an important way to obtain better properties of TMCs. However, different from SLM, the powder feeding mode of DLD makes it easy to change the type and content of reinforcements in TMCs, which has a great application prospect in the preparation of gradient composites.

3 Treatment of TMCs

3.1 Heat Treatment of TMCs

There are many heat treatment methods of TMCs, like the solid solution and aging. The properties and morphology of TMCs are closely related to microstructure, treating temperature, time, and cooling rate. If the solution temperature is lower than β transition temperature, some primary α phase would be retained. But if the solution temperature is higher than the β transition temperature, all primary α phases would undergo phase transformation in a certain time, and the microstructure after heat treatment no longer contains the primary α phase. Thus, under low treating temperatures, original microstructure of TMCs will significantly influence its morphology after heat treatment.

For TMCs, the solution temperature is generally in the upper $\alpha + \beta$ phase region or higher than β transition temperature. Under such high temperatures, β phase transformation occurs in the matrix during the solution process. Solid solution is usually followed by rapid cooling modes such as water cooling (water quench) or oil cooling. Due to the lack of diffusion of alloying elements caused by rapid cooling rate, the β phase transformed in the solution treatment undergoes a martensitic transformation in the form of non-diffusion transformation and converts into a needle-shaped martensitic phase. As shown in Fig. 10, with the increase of solution temperature, the content and size of the primary α phase gradually decreased, and the content of martensite gradually increased [80]. The aging temperature is generally low, between 400 °C and 800 °C, followed by air cooling. During the aging treatment after solid solution, martensite is an unstable transition phase, which would decompose and produce fine $\alpha + \beta$ phases, resulting in dispersion strengthening effect and improving the strength and hardness of TMCs [81].

The solution and aging temperature show a significant effect on the strength and plasticity of TMCs. As shown in Fig. 11a, with the increase of solution temperature, the strength first increased and then decreased, while the plasticity showed a downward trend, which was caused by the increase of martensite content in the transformed β microstructure [82–85]. The volume fraction of the transformed β phase in the whole matrix increased with the rising solution temperature, which was beneficial to the strength but sacrificing ductility. When the solution temperature increased more, α colonies would grow into a larger size, which could lead to a decrease in strength. With the increase of aging temperature, martensite decomposed completely

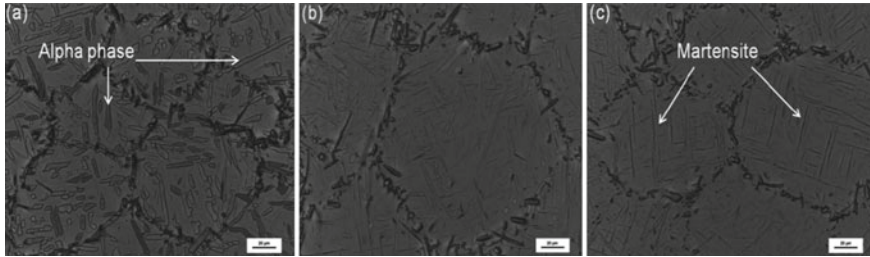


Fig. 10 The microstructures of 3.5vol% TiB_w/Ti-6.5Al-2Zr-1Mo-1V composite with different heating temperature: **a** 1000 °C; **b** 1005 °C; **c** 1010 °C. Reprinted with permission from Zhang et al. [80]. Copyright (2017), Elsevier

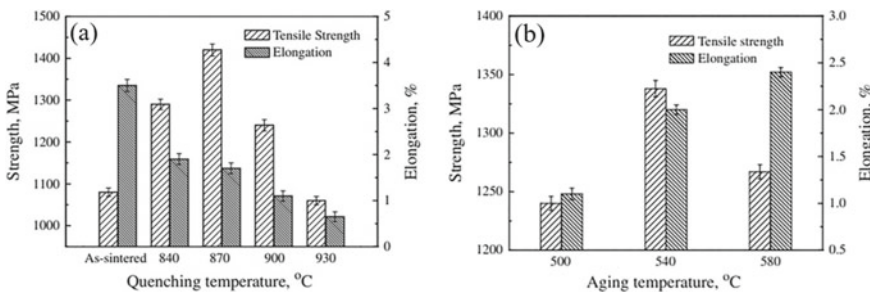


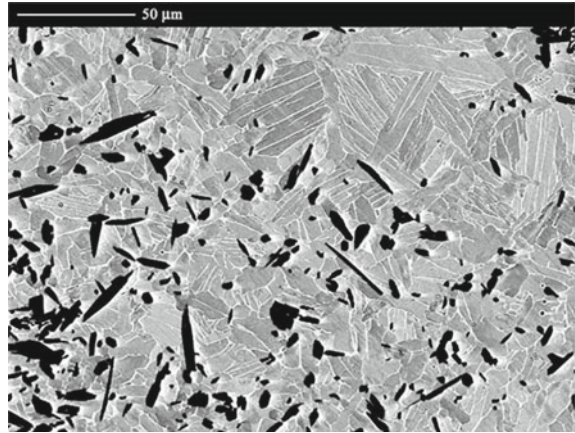
Fig. 11 Variations of tensile strength and elongation of 5 vol.% TiB_w/Ti-6Al-4V composite with different treating temperatures: **a** increasing quenching temperatures followed by aging at 500 °C; **b** increasing aging temperatures after water quenching at 900 °C. Reprinted with permission from Huang et al. [82]. Copyright (2012), Elsevier

into $\alpha + \beta$ phase, leading to a larger size and higher volume fraction. The coarsening $\alpha + \beta$ phase was unfavorable to the strength and hardness but could improve the plasticity, as shown in Fig. 11b.

Reinforcements can not only significantly reduce the size of matrix during the fabrication or hot deformation of TMCs, but also inhibit the grain growth and promote the spheroidization of α phase during the heat treatment. Li et al. [60] compared Ti-6Al-4 V with TMCs after specific heat treatment, and discovered that the grains didn't coarsen obviously, and α -Ti was almost equiaxed. This phenomenon was further illustrated in Fig. 12. Equiaxed and refined lamellar crystals were observed in the whisker-rich region, while the matrix structure in the whisker-free region was composed of larger lamellar crystals, which was caused by the Zener pinning effect of the dispersed reinforcement phase [85].

Compared with the complex phase transformation of matrix, the change of reinforcements in heat treatment is not so significant due to its thermal stability. Different elements of reinforcements show different effects on the microstructure and properties of TMCs after heat treatment. For example, TiC can be dissolved in a solid solution to a certain extent, and the dissolved C elements cause the lattice distortion

Fig. 12 Details in backscattered electron imaging of the duplex matrix microstructure of TiB/Ti-6Al-4V composite heat-treated at 1400 °C for 1 h. Reprinted with permission from Gorsse and Miracle [85]. Copyright (2003), Elsevier



and solid solution strengthening, and Fig. 13 shows the TiC particles with reduced size due to dissolution in the matrix after heat treatment. TiB coarsens significantly after heat treatment in TiB-reinforced TMCs, and the coarsening is caused by a small amount of TiB dissolving at high temperature, then precipitating and growing on the neighboring larger TiB. So the size of TiB increases but the number decreases, which can reduce the TiB clusters [86]. Hu et al. [87] found that TiB whiskers were sensitive to the thermal condition and the aspect ratio decreased with the increase of solution time.

It is worth noting that under the same heat treatment conditions, the tensile strength of TMCs is higher than that of the titanium alloy, which indicates that TiC, TiB, and rare earth oxides show good thermal stability and stress bearing effect, which effectively strengthen the material and improves the deformation resistance. Based on the variation of microstructure and properties of TMCs during heat treatment, the microstructure control and properties optimization of TMCs can be realized by setting reasonable heat treatment parameters.

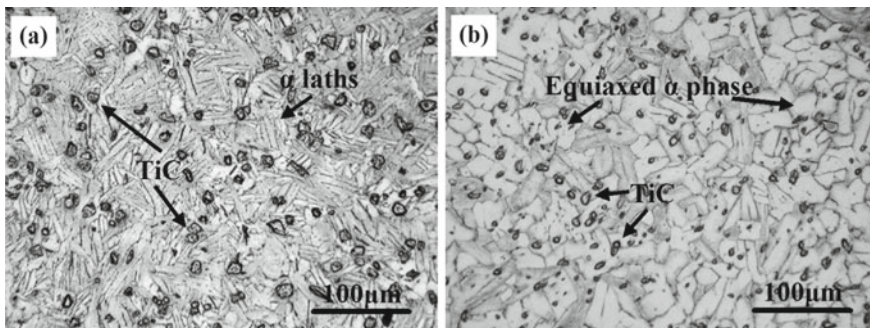


Fig. 13 Optical microscopy of the composite **a** before and **b** after heat treatment. Reprinted with permission from Qi et al. [86]. Copyright (2016), Elsevier

3.2 *Electro-Pulsing Treatment (EPT) of TMCs*

Traditional heat treatment methods, such as solid solution and aging, can adjust the structure of TMCs and improve the strength and plasticity, but they often require high-energy consumption, long time, and sometimes high pressure, vacuum and other harsh conditions. Electro-pulsing treatment (EPT) uses high-density current to interact with materials in a very short time. Instantaneous thermoelectric coupling can repair defects, promote phase transformation and improve plasticity, and effectively inhibit grain growth and surface oxygen absorption. It shows the advantages of short treatment time and low energy consumption.

Studies indicated that although the TiNi particle dispersion composite prepared by electric pulse sintering method had segregation on the particle surface, the change of the particle itself was suppressed. Some workers conducted an auxiliary electric pulse low-temperature diffusion connection test on Ti(C, N)-based cermet and 40Cr steel, and found that the interface formation was divided into four stages: physical contact of surface, melting of the intermediate layer, formation of the diffusion-reaction layer and solidification. That indicates that the EPT can promote the interface connection of the composite material [88].

EPT can adjust the local microstructure of the material in a short time by high-density pulse current to improve the material performance [89]. Figure 14 shows the stress-strain curves of TA15 (Ti-6Al-2Zr-1Mo-1V) alloy and ZA22 (Zn-22%Al-2.2%Cu) alloy under different pulse current densities [90, 91]. The influence mechanism of EPT on the microstructure and properties of metal materials mainly focuses on the thermal effect, athermal effect, and the coupling effect of thermal and athermal effects of the electric pulse. The thermal effect mechanism is attributed to the rapid accumulation of the energy of scattered electrons flow by the crystal lattice under the action of an electric pulse, which leads to a rapid increase of temperature in material, due to the asynchronous temperature rise and thermal expansion. The expansion lags behind the temperature rise, which creates a huge thermal pressure stress in the material. The athermal effect is attributed to the selective effect of the electric pulse: the pulse current preferentially passes through the high local strain area with small resistance or near the defect that is easy to induce transformation nucleation, causing the structure variation around the defect in a very short time. Compared with traditional heat treatment methods, EPT does not require the overall heat transfer process and can achieve targeted treatment of local high strain areas and defect areas. Therefore, the advantages of EPT could be used to specifically optimize the overall performance of TMCs.

A significant effect of EPT is to promote the healing of microcracks and other defects. Self-healing in metals is intrinsically difficult because they do not have the ability to probe and identify damage, and their atomic mobility or diffusivity is so low and the melting points are so high that a healing process is difficult to activate. Hosoi et al. [92] found that the high-density current field formed at the crack tip promoted the region near the crack heated rapidly, resulting in the hot compressive

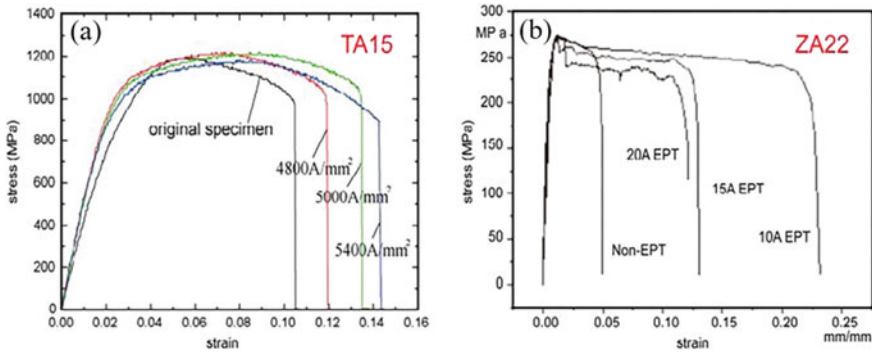


Fig. 14 Stress-strain curves of TA15 alloy (a), and ZA22 alloy (b), under different pulse current densities. a Reprinted with permission from Wang and Song [90]. Copyright (2009), Elsevier, b Reprinted with permission from Zhu et al. [91]. Copyright (2009), Elsevier

stress, and a healing effect on the crack. Figure 15 shows the healing of crack in the sample before and after EPT.

The coupling of thermal and athermal effects of high-density current can promote recrystallization, which has been reported in many literatures. Figure 16 shows the schematic diagram of defect repair and recrystallization respectively [93]. Figure 17 shows the dislocation distribution of cold-rolled copper before and after EPT and annealing treatment respectively. The dislocation density decreases and climbs to the grain boundary [94]. Lu et al. [95] found that under the same treatment temperature, the plastic deformation ability of Al₃Ti after EPT is higher than that of traditional heat treatment, because of the dislocation movement.

Besides the EPT, there is another useful treatment method of electro-shocking treatment (EST). Compared to EPT, EST can handle bulk specimens and large components and can achieve the targeted processing on local area rapidly [96–99]. Xie et al. [100] found that the EST method can refine TiB reinforced to the nanometer level,

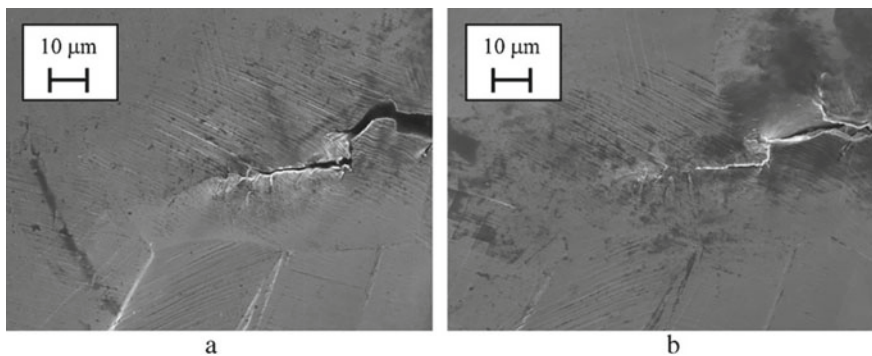


Fig. 15 Images of the fatigue cracks in specimen: a before and b after the application of EPT. Reprinted with permission from Hosoi et al. [92]. Copyright (2012), Elsevier

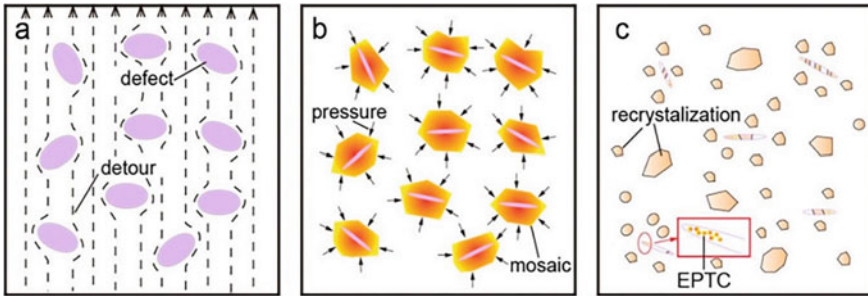


Fig. 16 Schematic diagram of defect healing and recrystallization: **a** plastic deformation to form defects and defective areas of the current bypass; **b** the formation of pressure around the metal defects; **c** healing defects, recrystallization, and high-energy EPT cladding (EPTC). Reprinted with permission from Song and Wang [93]. Copyright (2008), Elsevier

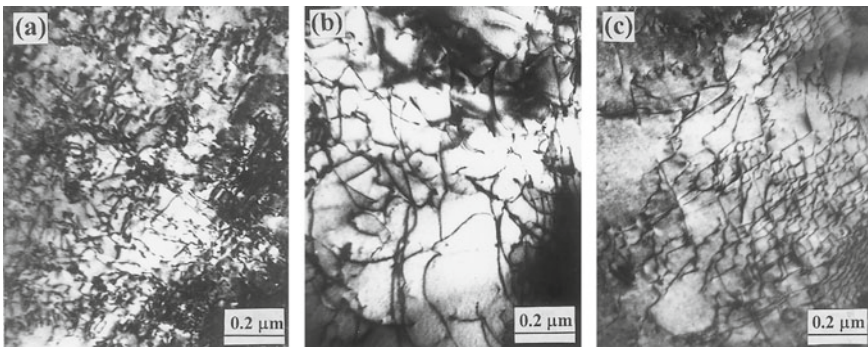


Fig. 17 Transmission electron microscope (TEM) image of brass strip under different treatment conditions: **a** cold-rolled, **b** high-current density electropulsing (HDE) treatment, and **c** annealing treatment. Reprinted with permission from He et al. [94]. Copyright (2000), Elsevier

fracture strain increased from 24.18% to 25.37%. The principle of EST is a technique similar to EPT but it shows considerable advantages including higher current density and continuous and stable pulse current. At present, the research of EST is less and is still in its infancy.

4 Conclusions

TMCs show the higher specific modulus and specific strength, more excellent high-temperature performance, and creep resistance than titanium alloys, which is one of the most important materials in aerospace, weaponry, and other fields. Some important preparation technologies and post-treatment methods were summarized in this chapter. Some important results were obtained.

- (1) Many synthetic methods can be used to prepare TMCs. The synthesis of discontinuous particles reinforced TMCs includes powder metallurgy, fusion casting method, exothermic diffusion method, mechanical alloying, self-propagating high-temperature synthesis process, rapid solidification technology, reactive hot pressing, and various melting and casting technologies. The reinforcement in powder metallurgy could be incorporated into matrix in two ways: ex-situ and in-situ processing. During the process of preparation, the matrix, the reinforcements, and the reaction parameters are needed to be chosen and considered according to the temperature and reinforcements content.
- (2) TMCs could be prepared by AM, which was a new technology. Two kinds of important AM technologies of SLM and DLD were discussed. In the process of preparing TMC by SLM, the type and content of reinforcements and the corresponding laser processing parameters should be considered. Powder pretreatment before molding, auxiliary processing technology during molding, and heat treatment after molding could modify the properties of TMCs. DLD made it easy to change the type and content of reinforcements in TMC, however, the porosity should be avoided and the combination properties should be improved further.
- (3) The heat treatments of TMC include solution, aging, and annealing. According to the phase transition of TMC, by setting reasonable heat treatment parameters, the best match between strength and plasticity could be obtained. During the heat treatment process, the effect of reinforcements on TMC was very obvious. Under the same heat treatment conditions, the tensile properties of TMC were improved because of the good thermal stability and load-bearing capacity of reinforcements.
- (4) EPT was a useful method for modification of the structure and properties of TMCs. However, there were relatively few studies on EST with higher energy. Due to the addition of reinforcements, the structure of TMCs included complex phases and reinforcing mechanisms. Therefore, it was of great theoretical significance to discuss the effect of EST on the variation of substrate, reinforcements, and interfaces, and the performance of TMCs.

Acknowledgements This work was financially supported by National Natural Science Foundation of China (Grant No. 52271135, No. 51975441), Major Research Plan of the National Natural Science Foundation of China (Grant No. 92266102), Natural Science Foundation of Hubei Province (Grant No. 2022CFB492), Knowledge Innovation Program of Wuhan -Basic Research (No. 2022010801010174), “Chu Tian Scholar” project of Hubei Province (CTXZ2017-05), Overseas Expertise Introduction Project for Discipline Innovation (B17034) and Innovative Research Team Development Program of Ministry of Education of China (IRT_17R83).

References

1. D.K. Ammisetti, S.S.H. Kruthiventi, in 3rd International E-Conference on Frontiers in Mechanical Engineering and NanoTechnology ((ICFMET)Electr. Network, 2020), pp. 9730
2. Lv., Weijie, *Progr. Mater. China* **29**, 41 (2010)
3. C. Zhenzhong, J. Yezhuang, C. Liqing, *Aeroengine* **04**, 40 (2006)
4. L. Shifeng, S. Xi, X. Tong, Ma., Ning, W. Yan, W. Liqiang, *J. Aerosp. Mater.* **40**, 77 (2020)
5. Y. Jianhui, X. Shulong, Y. Chen, X. Lijuan, W. Xiaopeng, Z. Dongdong, *Mater. Sci. Eng. A* **729**, 21 (2018)
6. L.J. Huang, L. Geng, A.B. Li, F.Y. Yang, H.X. Peng, *Scripta Mater.* **60**, 996 (2009)
7. M.D. Hayat, H. Singh, Z. He, P. Cao, *Compos. A Appl. Sci. Manuf.* **121**, 418 (2019)
8. L. Huang, Q. An, L. Geng, S. Wang, S. Jiang, X. Cui, R. Zhang, F. Sun, Y. Jiao, X. Chen, C. Wang, *Adv. Mater.* **33**, 2000688 (2021)
9. S.C. Tjong, Y.-W. Mai, *Compos. Sci. Technol.* **68**, 583 (2008)
10. L.-C. Zhang, H. Attar, *Adv. Eng. Mater.* **18**, 463 (2016)
11. E. Sallica-Leva, A.L. Jardini, J.B. Fogagnolo, *J. Mech. Behav. Biomed. Mater.* **26**, 98 (2013)
12. H. Attar, L. Löber, A. Funk, M. Calin, L.C. Zhang, K.G. Prashanth, S. Scudino, Y.S. Zhang, J. Eckert, *Mater. Sci. Eng., A* **625**, 350 (2015)
13. X.Y. Cheng, S.J. Li, L.E. Murr, Z.B. Zhang, Y.L. Hao, R. Yang, F. Medina, R.B. Wicker, *J. Mech. Behav. Biomed. Mater.* **16**, 153 (2012)
14. T. Saito, *JOM* **56**, 33 (2004)
15. L. Huang, L. Geng, *Discontinuously reinforced titanium matrix composites* (Springer, 2017), pp.1–15
16. K.S. Munir, P. Kingshott, C. Wen, *Crit. Rev. Solid State Mater. Sci.* **40**, 38 (2015)
17. S. Li, B. Sun, H. Imai, T. Mimoto, K. Kondoh, *Compos. A Appl. Sci. Manuf.* **48**, 57 (2013)
18. S. Li, B. Sun, H. Imai, K. Kondoh, *Carbon* **61**, 216 (2013)
19. S. Li, K. Kondoh, H. Imai, B. Chen, L. Jia, J. Umeda, Y. Fu, *Mater. Des.* **95**, 127 (2016)
20. L. Kang, Y. Cai, X. Luo, Z. Li, X. Liu, Z. Wang, Y. Li, C. Yang, *Scripta Mater.* **193**, 43 (2021)
21. K.S. Munir, Y. Zheng, D. Zhang, J. Lin, Y. Li, C. Wen, *Mater. Sci. Eng. A* **696**, 10 (2017)
22. L. Wei, X. Liu, Y. Gao, X. Lv, N. Hu, M. Chen, *Mater. Des.* **197**, 109261 (2021)
23. L. Wei, X. Liu, S. Zheng, N. Hu, M. Chen, X. Lv, *Mater. Chem. Phys.* **269**, 124763 (2021)
24. X. Feng, J.H. Sui, W. Cai, A.L. Liu, *Scripta Mater.* **64**, 824 (2011)
25. L. Wei, J. Liu, X. Wu, X. Liu, X. Lv, Y. Liu, *J. Alloy. Compd.* **813**, 152200 (2020)
26. J. Liu, N. Hu, X. Liu, Y. Liu, X. Lv, L. Wei, S. Zheng, *Nanoscale Res. Lett.* **14**, 114 (2019)
27. J. Wang, X. Guo, J. Qin, D. Zhang, W. Lu, *J. Mater. Sci.* **50**, 5674 (2015)
28. Y. Han, J. Le, M. Fang, L. Wang, W. Lv, *Adv. Mater. China* **39**, 945 (2020)
29. E. Zhang, Z. Songyan, Z. Zhu, *J. Mater. Sci.* **35**, 5989 (2000)
30. Y.Y. Li, F.W. Zhu, Z.L. Qiao, in *Applied Mechanics and Materials* (Trans. Tech. Publ., 2018), pp. 41–46
31. M. Lagos, I. Agote, G. Atxaga, O. Adarraga, L. Pambaguian, *Mater. Sci. Eng., A* **655**, 44 (2016)
32. L.E. Collins, *Can. Metall. Q.* **25**, 59 (1986)
33. Z. Fan, A. Miodownik, L. Chandrasekaran, M. Ward-Close, *J. Mater. Sci.* **29**, 1127 (1994)
34. X. Tong, H. Fang, *Metall. Mater. Trans. A.* **29**, 875 (1998)
35. S. Ranganath, M. Vijayakumar, J. Subrahmanyam, *Mater. Sci. Eng. A* **149**, 253 (1992)
36. D. Davoodi, R. Miri, A.H. Emami, M. Tayebi, S. Salahshour, *Int. J. Refract. Metal Hard Mater.* **88**, 105175 (2020)
37. Z. Li, D. Chen, H. Wang, E.J. Lavernia, A. Shan, *J. Mater. Res.* **29**, 2514 (2014)
38. L. Chen, J. Guo, J. Wang, Y. Xu, J. Bi, *Rare Metal Mater. Eng.* **35**, 29 (2006)
39. H. Attar, S. Ehtemam-Haghighi, D. Kent, M.S. Dargusch, *Int. J. Mach. Tools Manuf.* **133**, 85 (2018)
40. S.M. Thompson, L. Bian, N. Shamsaei, A. Yadollahi, *Addit. Manuf.* **8**, 36 (2015)
41. P.K. Verma, S. Warghane, U. Nichul, P. Kumar, A. Dhole, V. Hiwarkar, *Mater. Character.* **172**, 110848 (2021)

42. D. Gu, G. Meng, C. Li, W. Meiners, R. Poprawe, *Scripta Mater.* **67**, 185 (2012)
43. D. Gu, G. Zhang, *Virtual Phys. Prototyp.* **8**, 11 (2013)
44. E. Fereiduni, A. Ghasemi, M. Elbestawi, *Mater. Des.* **184**, 108185 (2019)
45. C. Cai, C. Radoslaw, J.L. Zhang, Q. Yan, S.F. Wen, B. Song, Y.S. Shi, *Powder Technol.* **342**, 73 (2019)
46. J. Jin, S. Zhou, Y. Zhao, Q. Zhang, X. Wang, W. Li, D. Chen, L.-C. Zhang, *Opt. Laser Technol.* **134**, 106644 (2021)
47. H. Attar, M. Bönisch, M. Calin, L.-C. Zhang, S. Scudino, J. Eckert, *Acta Mater.* **76**, 13 (2014)
48. M. Tang, L. Zhang, N. Zhang, *Mater. Sci. Eng., A* **814**, 141187 (2021)
49. M. Shunmugavel, A. Polishetty, G. Littlefair, *Proc. Technol.* **20**, 231 (2015)
50. Z. Wei, L. Cao, H. Wang, C. Zou, *Mater. Sci. Technol.* **27**, 1321 (2011)
51. H. Attar, M. Bönisch, M. Calin, L.C. Zhang, K. Zhuravleva, A. Funk, S. Scudino, C. Yang, J. Eckert, *J. Mater. Res.* **29**, 1941 (2014)
52. N. Kang, P. Coddet, Q. Liu, H. Liao, C. Coddet, *Addit. Manuf.* **11**, 1 (2016)
53. Y. Liu, S. Li, R. Misra, K. Geng, Y. Yang, *Scripta Mater.* **183**, 6 (2020)
54. K. Lin, Y. Fang, D. Gu, Q. Ge, J. Zhuang, L. Xi, *Adv. Powder Technol.* **32**, 1426 (2021)
55. R. Sitek, M. Szustecki, L. Zrodowski, B. Wysocki, J. Jaroszewicz, P. Wisniewski, J. Mizera, *Materials* **13**, 2218 (2020)
56. M. Xia, A. Liu, Z. Hou, N. Li, Z. Chen, H. Ding, *J. Alloy. Compd.* **728**, 436 (2017)
57. H. Attar, M. Calin, L. Zhang, S. Scudino, J. Eckert, *Mater. Sci. Eng. A* **593**, 170 (2014)
58. L. Liu, T. Minasyan, R. Ivanov, S. Aydinyan, I. Hussainova, *Ceram. Int.* **46**, 21128 (2020)
59. D. Pan, X. Zhang, X. Hou, Y. Han, M. Chu, B. Chen, L. Jia, K. Kondoh, S. Li, *Mater. Sci. Eng., A* **799**, 140137 (2021)
60. H. Li, D. Jia, Z. Yang, X. Liao, H. Jin, D. Cai, Y. Zhou, *Mater. Sci. Eng., A* **801**, 140415 (2021)
61. H. Li, D. Jia, Z. Yang, Y. Zhou, *J. Alloy. Compd.* **836**, 155344 (2020)
62. X. Meng, J. Min, Z. Sun, W. Zhang, H. Chang, Y. Han, *Compos. B Eng.* **212**, 108667 (2021)
63. K.D. Traxel, A. Bandyopadhyay, *Addit. Manuf.* **31**, 101004 (2020)
64. A. Xue, X. Lin, L. Wang, J. Wang, W. Huang, *Mater. Des.* **181**, 107943 (2019)
65. A.T. Xue, L.L. Wang, X. Lin, J. Wang, J. Chen, W.D. Huang, *J. Laser Appl.* **32**(10), 012007 (2020)
66. L. Zhang, Z. Zhao, P. Bai, W. Du, *Mater. Lett.* **290**, 129449 (2021)
67. C. Yu, X. Liu, Y. Li, C. Song, G. Ma, F. Niu, D. Wu, *Int. J. Mech. Sci.* **205**, 106595 (2021)
68. S. Liu, Y.C. Shin, *Mater. Des.* **136**, 185 (2017)
69. L. Li, J. Wang, P. Lin, P. Lin, H. Liu, *Ceram. Int.* **43**(18), 16638 (2017)
70. J.D. Wang, L.Q. Li, C.W. Tan, H. Liu, P.P. Lin, *J. Mater. Process. Technol.* **252**, 524 (2018)
71. Z. Zhao, L. Zhang, P. Bai, W. Du, S. Wang, X. Xu, Q. Dong, Y. Li, B. Han, *Acta Metallurg. Sin. (English Letters)* **34**, 1317 (2021)
72. M.O. Ogunlana, E.T. Akinlabi, M.F. Erinsho, *Stroj Vestn-J Mech E* **63**, 363 (2017)
73. Y.B. Hu, W.L. Cong, X.L. Wang, Y.C. Li, F.D. Ning, H. Wang, *Compos. Part B Eng.* **133**, 91 (2018)
74. Y. Hu, B. Zhao, F. Ning, H. Wang, W. Cong, *Mater. Lett.* **195**, 116 (2017)
75. Y. Zhang, J. Sun, R. Vilar, *J. Mater. Process. Technol.* **211**, 597 (2011)
76. F.D. Ning, Y.B. Hu, W.L. Cong, *Rapid Prototyp. J.* **25**, 581 (2019)
77. J. Zhang, Y. Zhang, W. Li, S. Karnati, F. Liou, J.W. Newkirk, *Rapid Prototyp. J.* **24**, 677 (2018)
78. Y. Zhang, Z. Wei, L. Shi, M. Xi, *J. Mater. Process. Technol.* **206**, 438 (2008)
79. H. Qu, P. Li, S. Zhang, A. Li, H. Wang, *Mater. Des.* **31**, 574 (2010)
80. R. Zhang, D.J. Wang, L.J. Huang, S.J. Yuan, *Mater. Sci. Eng., A* **679**, 314 (2017)
81. M. Hussein, M. Azeem, A.M. Kumar, N. Al-Aqeeli, N. Ankah, A. Sorour, *J. Mater. Eng. Perform.* **28**, 1337 (2019)
82. L.J. Huang, H.Y. Xu, B. Wang, Y.Z. Zhang, L. Geng, *Mater. Des.* **36**, 694 (2012)
83. B. Wang, L.J. Huang, L. Geng, *Mater. Sci. Eng., A* **558**, 663 (2012)
84. Z. Zhang, J. Qin, Z. Zhang, Y. Chen, W. Lu, D. Zhang, *Mater. Des.* **31**, 4269 (2010)

85. S. Gorsse, D.B. Miracle, *Acta Mater.* **51**, 2427 (2003)
86. J.Q. Qi, Y.W. Sui, Y. Chang, Y.Z. He, F.X. Wei, Q.K. Meng, Z.J. Wei, *Mater. Charact.* **118**, 263 (2016)
87. Z.Y. Hu, Z.H. Zhang, Q. Song, S.P. Yin, H. Wang, X.Y. Li, *Mater. Sci. Forum* **960**, 135 (2019)
88. C. Zhang, K. Zhang, G. Wang, *Mater. Lett.* **63**, 2153 (2009)
89. Y. Sheng, Y. Hua, X. Wang, X. Zhao, L. Chen, H. Zhou, J. Wang, C.C. Berndt, W. Li, *Materials* **11**, 185 (2018)
90. Z. Wang, H. Song, *J. Alloy. Compd.* **470**, 522 (2009)
91. Y.H. Zhu, S. To, W.B. Lee, X.M. Liu, Y.B. Jiang, G.Y. Tang, *Mater. Sci. Eng. A* **501**, 125 (2009)
92. A. Hosoi, T. Nagahama, Y. Ju, *Mater. Sci. Eng. A* **533**, 38 (2012)
93. H. Song, Z.-J. Wang, *Mater. Sci. Eng. A* **490**, 1 (2008)
94. G. He, B. Wang, X. Guo, F. Yang, J. Guo, B. Zhou, *Mater. Sci. Eng. A* **292**, 183 (2000)
95. Z. Lu, C. Guo, P. Li, Z. Wang, Y. Chang, G. Tang, F. Jiang, *J. Alloy. Compd.* **708**, 834 (2017)
96. L. Xie, C. Liu, Y. Song, H. Guo, Z. Wang, L. Hua, L. Wang, L.-C. Zhang, *J. Market. Res.* **9**, 2455 (2020)
97. L. Xie, H. Guo, Y. Song, C. Liu, Z. Wang, L. Hua, L. Wang, L.-C. Zhang, *Mater. Charact.* **161**, 110137 (2020)
98. C. Liu, L. Xie, D. Qian, L. Hua, L. Wang, L.-C. Zhang, *Mater. Des.* **198**, 109322 (2021)
99. W. Wu, Y. Song, Z. Wang, S. Ning, L. Hua, *J. Mater. Sci.* **55**, 2245 (2020)
100. L. Xie, Y. Wu, Y. Yao, L. Hua, L. Wang, L.-C. Zhang, W. Lu, *Mater. Charact.* **180**, 111395 (2021)

Metal-Based Electrical Contact Materials



Temel Varol and Onur Güler

Abstract Electrical contact materials (ECMs) are widely used as relays, low voltage circuit breakers, switches, and contactors in the electrical power systems, machinery, and automotive industries to ensure efficient operation and stopping of energy-generating and transmission vehicles. These materials are responsible for the conduction of electrical current between stationary and moving parts. The efficiency of ECMs depends on the electrical and thermal conductivities, hardness, wear resistance, and chemical stability. Metals such as Cu, Ag, and Au can be used as ECMs due to high electrical and thermal conductivity properties. Although Cu has a high electrical and thermal conductivity, one of the most critical disadvantages of Cu is its easy oxidation and poor wear resistance, even at low temperatures. Ag has high electrical and thermal conductivities with excellent oxidation resistance, but its high price and low wear resistance are major obstacles for ECMs. In order to overcome these problems, researchers are working on different and novel production methods, original alloy, and composite types. Despite the fact that the first preferred method for preparing ECMs is powder metallurgy, it requires a large number of devices and shaping molds, such as mixers, and mechanical or hydraulic presses with a long production process. Moreover, ECMs produced by powder metallurgy method may exhibit joint errors such as gapping and separation due to joining methods such as soldering and diffusion. The most effective method for the the fabrication of ECMs in the future is the additive manufacturing (AM) technique, although it is still early for commercial manufacturers. AM is an advanced manufacturing technology that enables the production of complex-shaped parts in layers, unlike traditional manufacturing methods. Using this method, ECMs can be produced to have faster, equivalent, or better properties than their counterparts produced by conventional methods. Moreover, the researchers focused their work on composite ECMs as an alternative to conventional parts because wear resistance can be increased using ECMs without a significant reduction of electrical and thermal conductivities. The purpose of this chapter is to identify application areas, environmental effects, economic value, performance requirements, and production methods of ECMS. In addition,

T. Varol (✉) · O. Güler

Department of Metallurgical and Materials Engineering, Engineering Faculty, Karadeniz Technical University, Trabzon, Türkiye
e-mail: tvarol@ktu.edu.tr

the research findings on on metal-based ECMs are discussed with the support of the literature.

Keywords Electrical contact materials · Electrical contact performance · Cu · Ag · Metal-based contacts

1 Introduction to Electrical Contact Materials

ECMs are advanced engineering materials that ensure the efficient operation of devices by providing current transmission in electrical and electronic systems. These materials are metal-based parts used to open and close electrical circuits at any time by sliding or constant contact motion. Today, contact materials are used to control electrically powered devices wherever electricity is an indispensable element of life and work life. ECMs are widely used in industrial applications such as contactors (Fig. 1a) that act as electromagnetic switches in high-current circuits, as relays (Fig. 1b) that act as a switch in devices that draw high current using low currents, as electrical switches (Fig. 1c) that activate or block the electrical current, as electrical fuses (Fig. 1d) that prevent overloading of the elements of devices operating in alternating and direct current, as voltage regulators (Fig. 1e) that prevent electronic circuit and devices from deteriorating by balancing voltage fluctuations and as connectors (Fig. 1f) that provide current connections. Contactors known as large power switches allow electric motors and electric vehicles to be remotely controlled by cable. When they are used with thermal relays, they protect devices and facilities against overload currents. Contactors not only open and close the circuit to which it belongs under nominal current but also prevent certain over currents.

When the usage areas shown in Fig. 1 are examined, it is understood that ECMs are widely used in all areas of our lives. Current examples of ECMs are motor contactors used in electric cars, relays, switches and connectors, contactors, and relays that provide driving control in high-speed trains, automatic door contactors and relays, contactors and relays in the signaling system, contact strips used as current transmission element in electric train lines, wind contactors and voltage regulators used in energy power conversion systems, contactors in power transmission panels on machines, and contactors and fuses in current distribution panels in our homes and offices.

ECMs are exposed to different electrical, thermal, mechanical, and chemical effects during opening–closing and short circuits. Since there is continuous on–off movement in the contacts, an electric arc occurs over time and the electric arc causes the contacts to oxidize and decrease conductivity. As seen in Fig. 2, as soon as the coil in the control circuit is fed, a magnetic field is formed and the contacts are closed. With the closing of the contacts, current flow is ensured so that the devices operate. The arc occurs during the start or interruption of the current transition during the operation of the contacts. As a result of high temperature and high-current density, wear occurs on the surface of the contact material. Therefore, in order for a contact

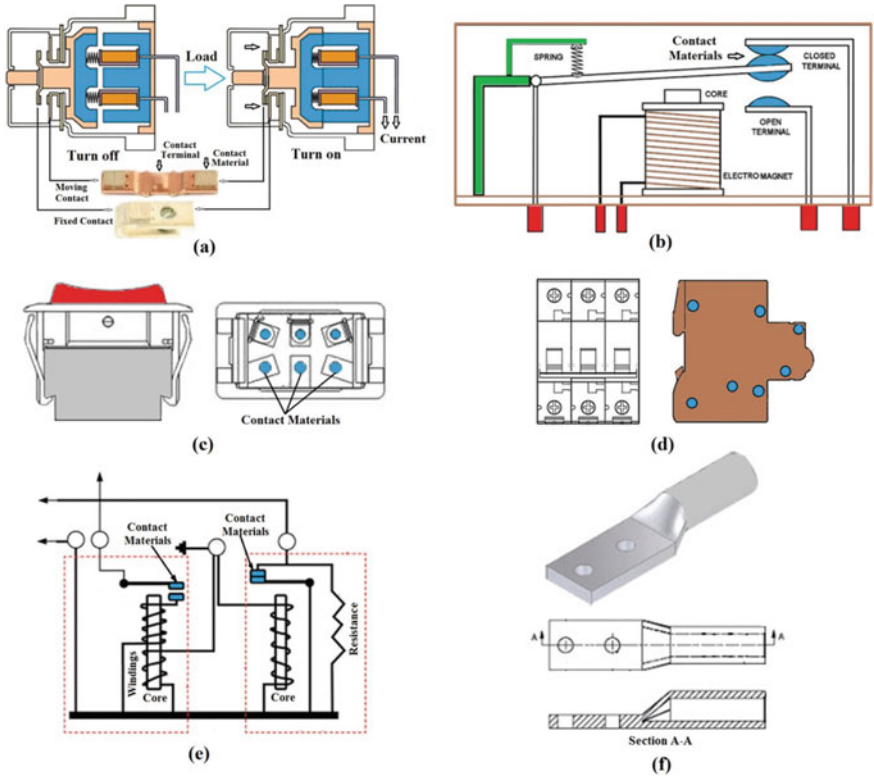


Fig. 1 Usage areas of ECMs; **a** contactors, **b** relays, **c** electrical switches, **d** electrical fuses, **e** voltage regulators, and **f** connectors

material to operate efficiently, the material must have high electrical and thermal conductivities, high melting temperature, high corrosion, and arc erosion resistance.

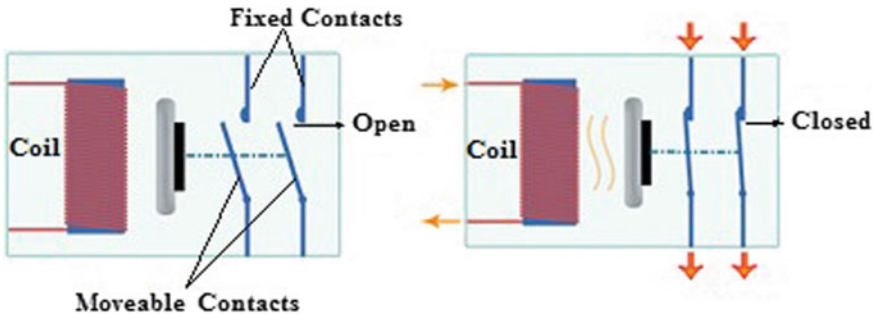


Fig. 2 Working principle of electrical contacts

The fact that ECMs are used in critical technologies such as electric cars and renewable energy sources increases the importance of these materials. As it is known, since the development of internal combustion engines, automobile technology has had to use fossil or hydrocarbon-based fuels such as gasoline, diesel, liquefied petroleum gas (LPG), and processed products in order to provide the necessary movement or thrust in the vehicles. Since the automobile prices are at reasonable levels today, the number of existing internal combustion engine cars in traffic is quite high and these vehicles constitute the majority sources of the harmful gases emitted to the environment in the cities. All pollutants that pollute the environment and are thrown into the atmosphere; 65% of carbon monoxide, 55% of nitrogen oxides, and 45% of hydrocarbons are caused by exhaust emissions of vehicles using gasoline and diesel fuel. The release of these harmful gases poses serious hazards to human health and the environment [1, 2]. Vehicle-induced exhaust emissions, which significantly increase global warming, are increasing in line with the increase in the number of fossil fuel-based vehicles in the world. Table 1 shows the number of vehicles produced by the top eight countries in 2016 and 2017 [3].

As can be seen from Table 1, millions of new vehicles are launched every year and the negative effects of harmful gas emissions on global warming and human health are constantly increasing. The most important solution developed for the end of the consumption of fossil fuels which have harmful effects on the environment and human health is the widespread use of electric vehicles. In many countries, the number of people driving electric cars is constantly increasing due to its low maintenance cost and economic and environmental benefits as well as its effectiveness in reducing carbon emissions. 40% of the total number of vehicles owned by Norway are electric vehicles and Norway ranks first in the world with this feature. The exemptions granted by the Norwegian government to the sale of electric vehicles, transportation tax, and parking fees play an important role in Norway's leadership in the number of electric vehicles [4, 5].

Table 1 Top eight countries in terms of ranking and the number of fabricated cars [3]

| Ranking | | | | Country | Production | |
|------------|------------|---------|---------|-------------|------------|------------|
| World 2016 | World 2017 | EU 2016 | EU 2017 | | 2016 | 2017 |
| 1 | 1 | | | China | 28,118,794 | 29,015,434 |
| 2 | 2 | | | USA | 12,180,301 | 11,189,985 |
| 3 | 3 | | | Japan | 9,204,813 | 9,693,746 |
| 4 | 4 | 1 | 1 | Germany | 5,746,808 | 5,645,581 |
| 5 | 5 | | | India | 4,519,341 | 4,782,896 |
| 6 | 6 | | | South Korea | 4,228,509 | 4,114,913 |
| 7 | 7 | | | Mexican | 3,600,365 | 4,068,415 |
| 8 | 8 | 2 | 2 | Spain | 2,156,356 | 2,848,335 |

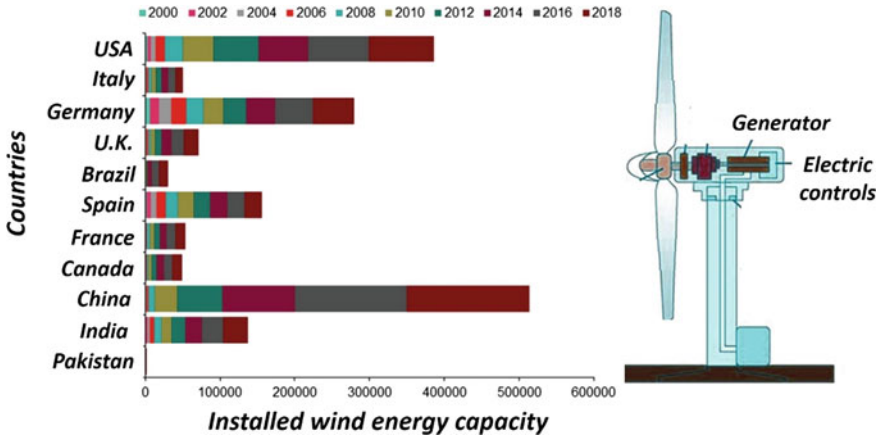


Fig. 3 Installed wind energy capacity. Reprinted from Nazir et al. [12], with permission from Elsevier. Copyright (2019)

Moreover, renewable energy resources are the best alternative to fossil fuels in electricity and energy production [6–8]. Wind energy is of significant importance among renewable energy resources due to potential in energy generation, market value, wide application range, and economic friendly attributes of wind energy (Fig. 3) [9–11]. It should be noted that wind power generation was produced by more than 17% in 2017 extending to 1120 TWh or 4.4% of the total global electricity generation. It is accounted for more than the total electricity generation in Russia, as Russia is the fourth-largest power producer in the world [12–14].

The properties of ECMs, which are used in electrical motors in electrical cars and the turbine generators in wind turbines that convert kinetic energy into electrical energy, significantly affect energy efficiency. In order to ensure the efficient use of electrical energy in electric cars and to produce electricity efficiently in renewable energy sources such as wind energy, the ECMs used in electric vehicle engines and turbine generator engines must have low cost, high electrical and thermal conductivity, high corrosion and arc erosion resistance. It should be noted that improvements in the properties of ECMs will minimize the energy losses and will enable the electric vehicles to be used more efficiently, and to go further with the same energy. Thus, fossil fuel-based impurities causing global warming can be minimized due to the greater preference of electric vehicles by users. Also, improvements in the properties of ECMs used in the turbine generators will reduce energy losses and will provide more production of clean energy, so destructive effects of fossil fuel-based impurities on humans and the environment (cancer, global warming, and climate change) can be minimized.

2 Performance Requirements of Electrical Contact Materials

Even though the ECMs are conductive materials, the heating occurs due to the resistance during the current transmission. The heat causes the regional melts and the contacts to be welded together, thus preventing the efficient exchange of current. Therefore, the ECMs must have good electrical conductivity. Because of low electrical conductivity values of oxides, which are formed as a result of regional melts during the operation of ECMs, the transmission of the electric current becomes more difficult, the electrical resistance increases, the heating of the contacts increases, and finally, the electrical current is not transmitted. Therefore, metals (Ag and Au), which do not tend to form oxides, are used in the fabrication of ECMs despite the high cost. The electrical and thermal properties of some metals are listed in Table 2.

2.1 IACS (*The International Annealed Copper Standard*)

The most important reason why metallic materials are used as ECMs is their electrical and thermal conductivities, easy processability, and accessibility. As seen in Table 2, Ag having the highest electrical conductivity (106 IACS) and thermal conductivity (419 W/mK) in metallic materials is the main material used in the production of ECMs and significantly increases the cost of contact materials due to its high cost. In addition, Ag prevents oxide formation with its high oxidation resistance and ensures the continuity of electrical conductivity, preventing all oxide-based negativities (decreasing conductivity, heat increase, welding, and material loss). With these superior features, Ag successfully continues its duty as an ECM but significantly increases the cost of the product. Therefore, it is important to reduce the cost of Ag contact materials.

ECMs are under the influence of mechanical wear, heat, oxide formation, and arc erosion (Figs. 4 and 5) during contact operation, and these influential factors prevent

Table 2 The electrical and thermal properties of some conductive metals [15]

| Metal | Electrical conductivity (IACS) | Thermal conductivity (W/mK) | Density (g/cm ³) | Melting point (°C) |
|-------|--------------------------------|-----------------------------|------------------------------|--------------------|
| Cu | 100 | 394 | 8.96 | 1080 |
| Ag | 106 | 419 | 10.49 | 960 |
| Au | 76 | 297 | 19.3 | 1064 |
| Al | 61 | 222 | 2.7 | 660 |
| Zn | 27 | 113 | 7.14 | 420 |
| Cr | 13 | 67 | 7.19 | 1907 |

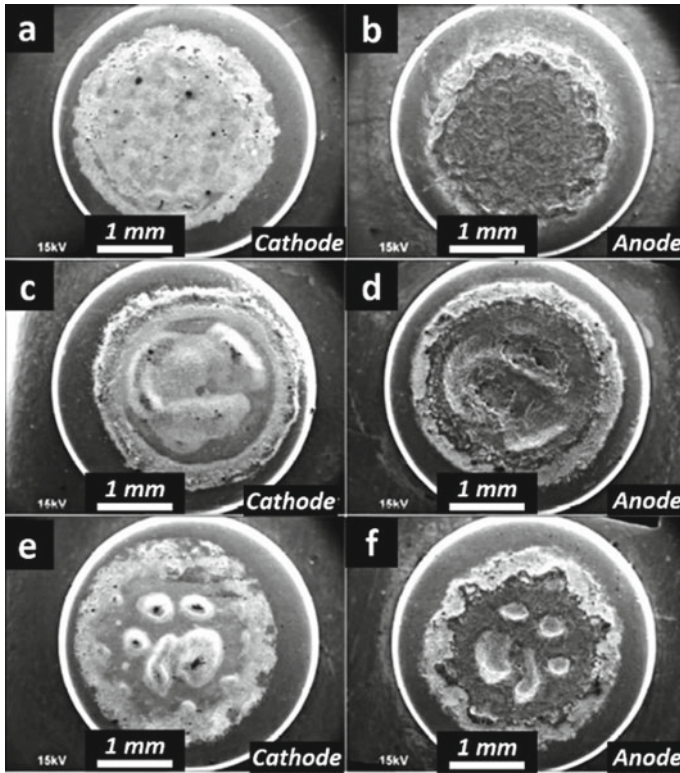


Fig. 4 Two-dimensional macro-morphologies of ECMs after arc erosion; **a, b** Ag/ZnO; **c, d** Ag/CuO; and **e, f** Ag/CdO. Reprinted from Wu et al. [16], with permission from the Nonferrous Metals Society of China, and Elsevier

ECMs from working efficiently, or in other words, they negatively affect the contact performance of ECMs.

The electrical conductivity and mechanical properties of ECMs affect the contact resistance. High contact resistance causes heating in the contacts. The increase in temperature in the contact materials causes spot and regional melting, causing welding and arc erosion. The contact resistance, which is very important in circuit breakers and miniature circuit breakers, should be low to prevent thermal overload during the contact cycle. The contact resistance of ECMs depends on the surface properties of the contact material such as surface hardness and elastic compliance, surface texture, and surface morphology. Figure 6 shows the contact surface morphologies of Ag-SnO₂ contact materials under contact cycles.

Mechanical wear prevents contact of surfaces due to the material loss over time and the damaged contact surface causes the current to be transmitted from certain areas rather than being transmitted across the entire surface. Therefore, the regional melts with the formation of the nozzle are observed on the contact surface. Consequently,

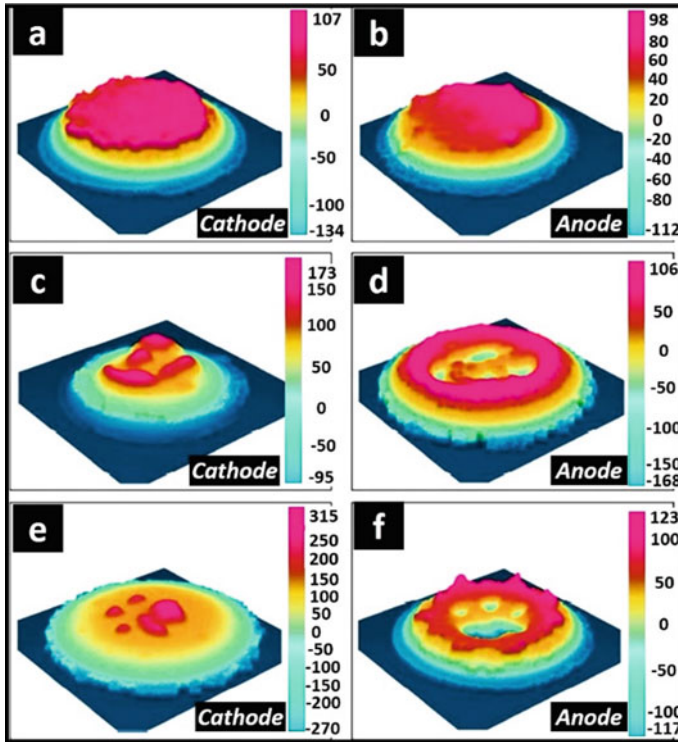


Fig. 5 Three-dimensional morphologies of ECMs after arc erosion; **a, b** Ag/ZnO, **c, d** Ag/CuO, and **e, f** Ag/CdO. Reprinted from Wu et al. [16], with permission from the Nonferrous Metals Society of China, and Elsevier

the contact materials become susceptible to weld each other. Therefore, the ECMs must have sufficient hardness. Although the upper and lower contacts appear to be in full contact, microscopic studies have shown that the surfaces are not fully in contact and that there are multiple points of contact or regional contacts (Fig. 7). It should be noticed that as the wear losses increase, the number of contact points between the contacted surfaces decreases, and therefore, heating of the contacts and melting of the zones occur, and as a result, arc erosion occurs. Figure 8 shows the wear surfaces formed in ECMs conducting current.

The arc causes the heating of the ECMs in a short period of time and the separation of the material from the surfaces in the form of rupture and breakings due to the regional melts. Then the transfer of the material from the surfaces to each other occurs, and finally, the ECMs become unusable due to welding of the surfaces to each other (Fig. 9 and 10).

During the opening and closing of the contacts, the softening and adhesion during the weld formation and current transmission, and the electrical wear (arc erosion) caused by material transfer from one contact to another have a significant effect on

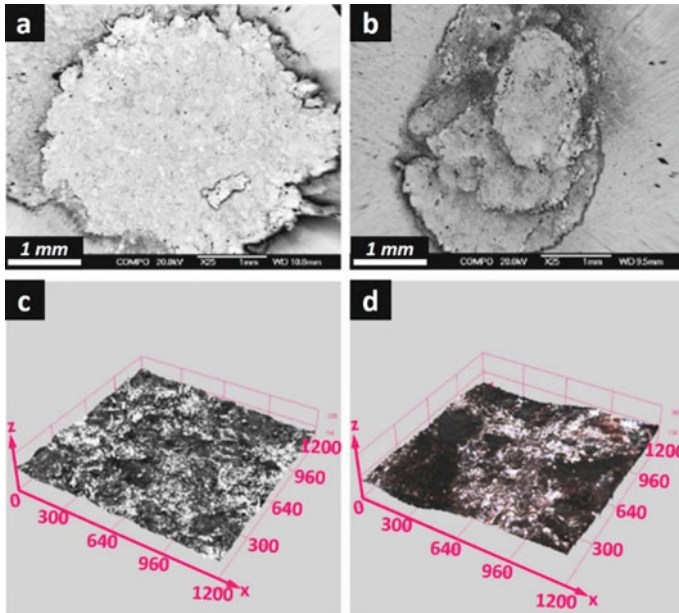


Fig. 6 Contact surface scanning electron microscope (SEM) images of Ag–SnO₂ samples after arc erosion: **a** Ag–15SnO₂, and **b** Ag–30SnO₂. Scanning laser microscope (SLM) images of **c** Ag–15SnO₂, and **d** Ag–30SnO₂. Reprinted from Wang et al. [17], with permission from Elsevier. Copyright (2015)

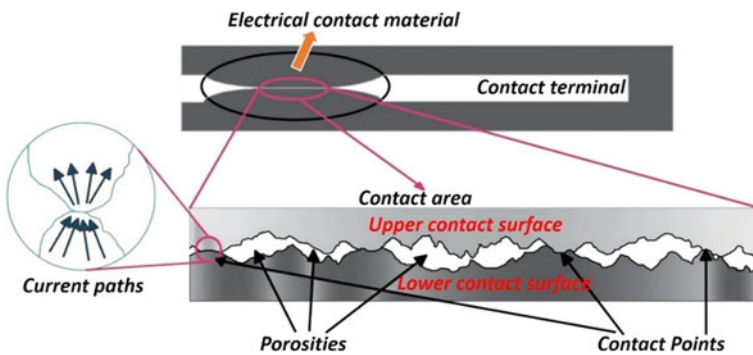


Fig. 7 Surface interactions in ECMs

the service life and performance of the contacts. If the arc erosion that starts with the bridge formation continues, material transfer occurs from the anode contact to the cathode contact, and the material transfer from the cathode to the anode occurs. Therefore, the contact performance of ECMs is directly dependent on arc erosion resistance and consequently material transfer. In addition, another phenomenon that greatly affects contact performance is the resource formation which can be defined

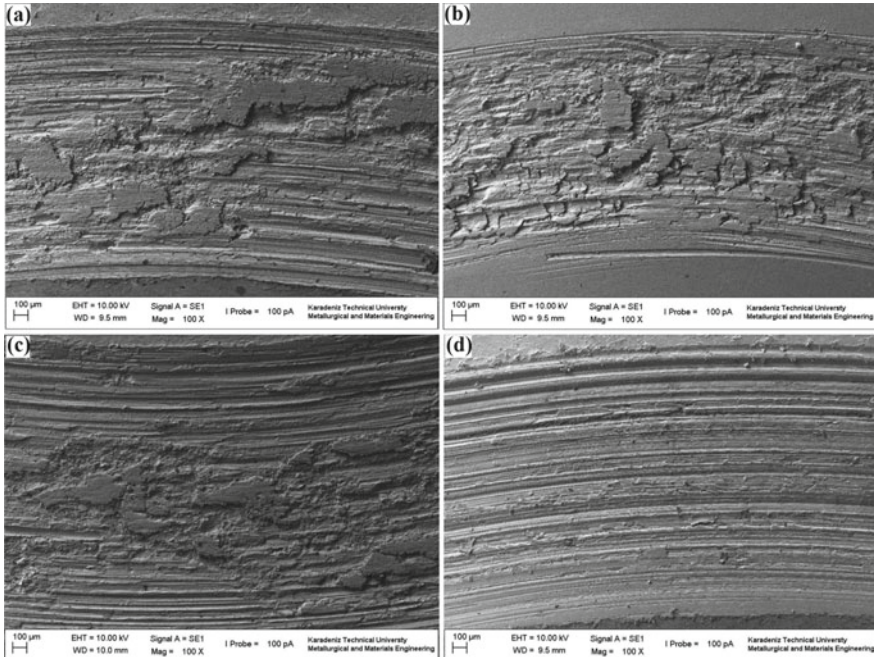


Fig. 8 SEM images of wear surfaces of Cu-graphite ECMs; **a** Cu-0.5 wt.% graphite, **b** Cu-1 wt.% graphite, **c** Cu-2 wt.% graphite, and **d** Cu-5 wt.% graphite composites [18]

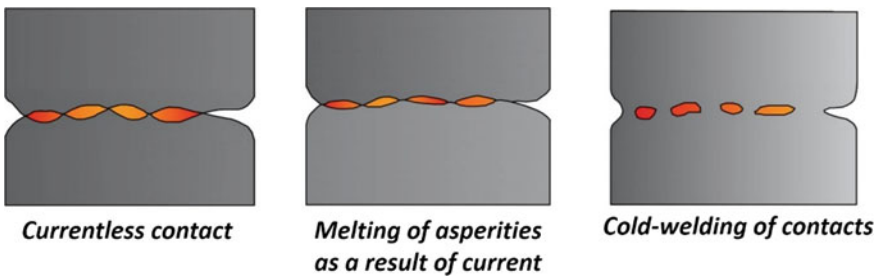


Fig. 9 Welding process during contact cycle

as the adhesion of electrical contacts to each other during operation. As a result of the arc caused by the rebound of the contacts, metal melting occurs in the contact areas and this molten metal causes the contacts to be welded to each other. On the other hand, welding can also be seen as a result of short-term heavy current passing from contact pairs in closed position. The high energy concentration that occurs in small contact areas causes regional melting and thus resource formation. The occurrence of all these conditions adversely affects the contact performance [19–22].

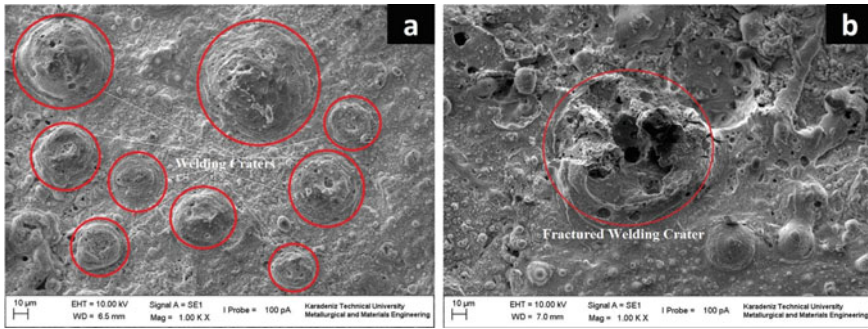


Fig. 10 The welding craters on the the surface of ECMs; **a** multi-welding crater formation and **b** fractured welding crater by arc erosion [18]

In the context of the the above explanations, ECMs must have the following properties:

- (1) High electrical conductivity [For easy transfer of electric current]
- (2) High thermal conductivity [For easy transfer of heat that will occur within the contact]
- (3) Moderate hardness [To minimize mechanical wear losses, and increase contact area, so as to reduce contact resistance]
- (4) High oxidation resistance [Maintaining electrical and thermal conductivity and preventing arc formation]
- (5) Low contact resistance and hence high oxidation resistance [For the prevention of heat increase, welding and breaks]
- (6) Simple and inexpensive production [for low cost] [18].

3 Metal-Based Electrical Contact Materials

The use of metal-based ECMs is provided by the selection of materials that are suitable for the desired areas. Ag metal, which has the highest electrical conductivity, is alloyed with different metals and can be used in contacts that require high hardness, especially in areas that require more electric voltage power. In this context, the most commonly used metal-based materials are pure Ag, Cu, and gold as metals, Ag-nickel, Ag-Cu, Ag-Cu-Ni alloys, Ag-Cd, Ag-Pd, Ag-Fe, Ag-Au, Ag-Au-Pt, Ag-Au-Pd-Pt-Cu-Zn, Ag-Pd-Cu-Pt-Ni alloys as metal-based contacts [20, 23]. However, Cu metal or its alloys has often been found suitable for use due to the high costs that limit the use of pure Ag and gold metals. However, although pure Cu metal has the highest electrical conductivity after Ag, its properties such as low wear resistance and hardness have led researchers to the need to alloy such pure metals [24]. Nagasawa and Kato stated that when compared to the wear rates of pure Cu metal and Cu-Sn and Cu-Cr-Zr alloys, the alloys mentioned under a current of 10 A showed up to 3–4 times lower wear rate than pure Cu [25].

In addition, the coatings with high hardness can be used without reducing electrical conductivity values much. Li et al. Investigated contact performance by modifying the pure Cu surface with the CrB/Cr₃C₂ layer by laser modification. According to the results obtained, the electrical conductivity of this hard layer was determined as approximately 92% IACS, while the rate of wear decreased by 80% compared to pure Cu. In this context, Fig. 11 presents the SEM image of the worn surface of pure Cu and the modified surface. As can be seen, the modified surface showed very smooth and shallow grooves than that of pure Cu [26].

On the other hand, it is frequently used because Ag has the highest electrical and thermal conductivity among metals. However, it is usually alloyed with elements such as copper, palladium, or platinum, due to the low hardness of Ag, wear resistance, and tendency to form films such as sulfide and chloride. Although alloying elements cause some decrease in electrical conductivity, they can form alloys with high hardness, oxidation resistance, and wear resistance. Hardness and electrical conductivity values of some Ag alloys are given in Table 3 [21, 27, 28].

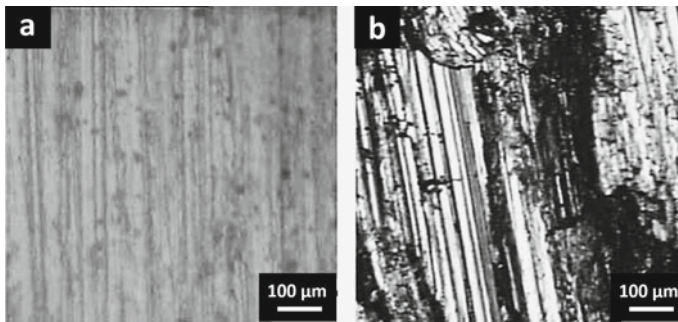


Fig. 11 SEM images of the worn surface belonging to the **a** modified Cu surface and **b** pure Cu. Reprinted from Li et al. [26], with permission from Elsevier. Copyright (2011)

Table 3 Hardness and electrical conductivity values of electrical contact alloys [28]

| Material | Hardness (HR) | Electrical conductivity (% IACS) |
|--------------|---------------|----------------------------------|
| Ag (99.9%) | 30 | 105 |
| 92.5Ag-7.5Cu | 65 | 88 |
| 90Ag-10Cu | 70 | 85 |
| 72Ag-28 Cu | 79 | 84 |
| 97Ag-3Pt | 45 | 45 |
| 97Ag-3Pd | 45 | 58 |
| 90Ag-10Pd | 63 | 27 |
| 40Ag-60Pd | 65 | 8 |
| 90Ag-10Au | 57 | 40 |
| 25Ag-75 Au | 50 | 17 |

In addition to increasing the hardness and wear resistance of the alloys, the decrease in the electrical conductivity values directed the researchers to the hard alloy coatings applied on Cu plates. Accordingly, Ni and Co reinforced gold alloy coatings (NiHG and CoHG, respectively) [29], nickel-phosphorus [30], and amorphous gold-nickel alloy film [31] coatings are mentioned in the literature. Togasaki et al. [31] determined that gold-nickel amorphous alloy films increased the hardness of soft gold samples approximately 5 times (Fig. 12). On the other hand, these amorphous films have almost the same contact resistance as that of traditional CoHG as seen in Table 4.

Lin et al. [32] produced the Ag-nickel alloy ECMs using nickel plates and nickel particles and determined that the anti-arc performance of nickel particle-containing alloys is superior to others. The fact that the distribution of nickel particles with Ag was quite better than that of the plate shape directly affected the contact performance. The hardness and electrical conductivity values obtained are given in Table 5. In addition, the post-test surface images of Ag-nickel alloy contacts containing nickel plates and particles are shown in Fig. 13.

Just as the shape of the alloying elements affects the contact performance of the contact materials, the addition of different alloying elements is also effective in obtaining high-performance contact materials. In this regard, Weichan et al. [33]

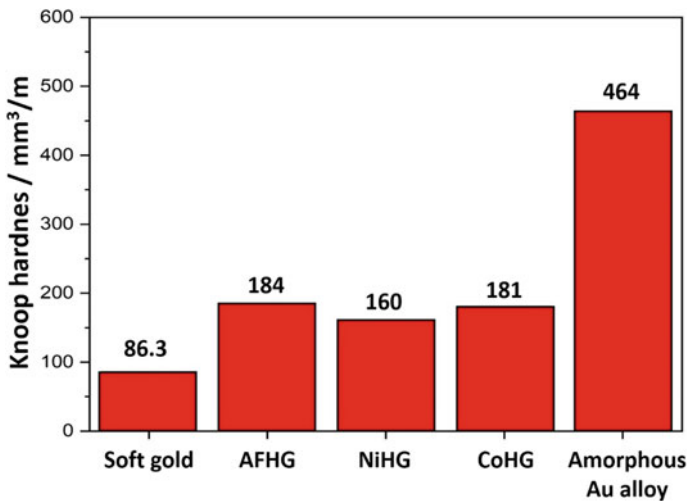


Fig. 12 Hardness of gold and hardened gold samples (*AFHG* describes additive-free hardened gold). Redrawn after Togasaki et al. [31]

Table 4 Contact resistance of CoHG and novel amorphous Au-Ni alloy

| Material | CoHG | Au-Ni alloy |
|--------------------|---------|-------------|
| Contact resistance | 2.16 mΩ | 2.21 mΩ |

Table 5 Nickel shape effect on the electrical contact properties of Ag–Ni alloys

| Material | Hardness (MPa) | Electrical conductivity (% IACS) |
|-------------------|----------------|----------------------------------|
| Ag–Ni (plates) | 104 | 91.4 |
| Ag–Ni (particles) | 117 | 76.0 |

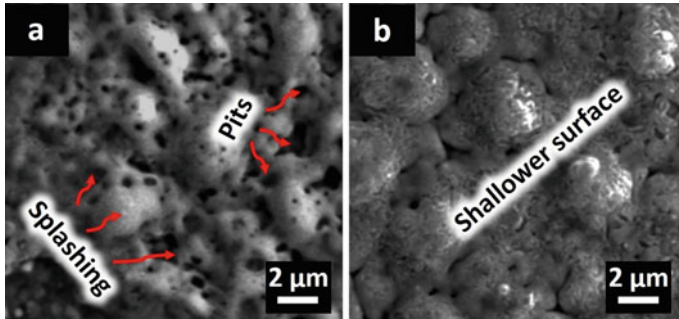
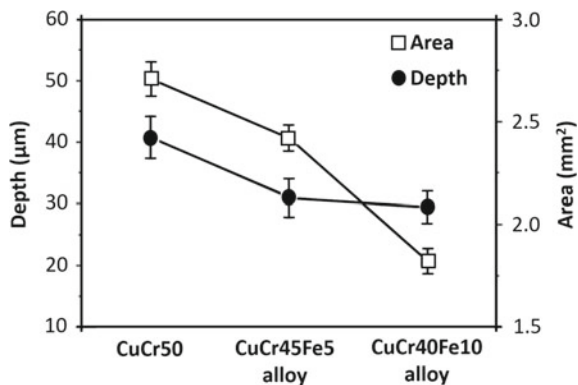


Fig. 13 SEM images of the arc surface of Ag–Ni (plates) and Ag–Ni (particles) electrical contact alloys. Reprinted from Lin et al. [32], with permission from Elsevier. Copyright (2016)

examined the performance of the contacts obtained by adding Fe alloying element to CuCr alloys in different contents. When they examined the contact performance of CuCr alloys with 5 wt.% and 10 wt.% Fe element additives, they observed a decrease in the area and depth of the arc erosion with different contents of Fe as can be observed in Fig. 14.

In ECMs, properties such as electrical conductivity, hardness, and wear resistance are critical features that directly affect the lifetime of the contacts. Therefore, materials with high mechanical properties as well as high electrical conductivity are in great demand in the production of ECMs [34]. Generally, it is ensured that metals frequently used in ECMs such as Ag and Cu are alloyed with different elements to

Fig. 14 Alloy element effect on the arc surface properties of contacts. Reprinted from Weichan et al. [33], with permission from Elsevier. Copyright (2011)



enhance the mechanical properties. However, the alloying process causes a critical decrease in the electrical conductivity values of the materials. Contrary to the increase in mechanical properties, the reason for the decrease in the electrical conductivity values is that the dissolved solids and precipitates during alloying prevent the electron movements [35]. Therefore, the production and development of composite materials using high electrical conductivity and thermal conductivity metals as matrixes such as Ag, Cu, and Cu alloys have been frequently the subject of research by researchers [36–38]. The wear resistance of the contacts has been significantly increased by using hard additives such as alumina [39], silicon carbide [40], lubricant such as graphite [41], and carbon nanotubes [42] in the production of these composite materials. Bera et al. [43] measured the electrical conductivity and hardness values of Cu-10Cr-3Ag alloys compared to those of Cu-10Cr-3Ag/5 wt.% Al₂O₃ composites. They determined that the properties of composites improved as seen in Table 6. As it can be understood from the table, with the addition of additives, the hardness of the composites increased by 35% compared to the alloy, while the electrical conductivity value decreased slightly.

Chang et al. [44] examined the contact performance of composites produced by adding materials such as W and C to CuCr alloys. According to their results, they found that W and C additives had no significant effect on electrical conductivity but had a considerable effect on hardness. Accordingly, while the hardness and electrical conductivity values of CuCr alloys and CuCr-W-C composites are given in Table 7, the arc erosion area of the composite was expanded by almost five times. Besides, while numerous pits formed regionally on the arc erosion surface of the alloy, the erosion zones on the composite surface were spread over almost the entire surface and only a few pits were seen.

The use of composites in which pure metals with high electrical and thermal conductivity are used as matrices is also indicated as the electrical contact material. In this context, cadmium oxide and tin oxide particles are often used as additives for Ag matrix composites. However, the negative effect of cadmium on the environment and human health and the low wettability of tin oxide directed the researchers to use different additives [45]. Carbon-based additives are used especially in contact materials made of Ag matrix composites. It has been reported that carbon-based additives increase the lifetime of the contact materials during the operation of the contact because of their anti-welding and natural lubrication properties. In this context, Jiang et al. [46] examined the properties of Ag matrix composites containing different carbon derivatives, such as hardness, electrical conductivity, and arc erosion resistance, which affect the contact performance. Some of the features they have obtained are given in Table 8. The highest conductivity value (37.6 m/($\Omega \cdot \text{mm}^2$)) was obtained from Ag/carbon nanotubes (CNTs) composites while the lowest hardness value (119.5 HV) was belonging to these composites as seen in Table 8. Ag-CNTs composites with the highest electrical conductivity showed a flatter erosion surface and shallower pits.

The effect of Y₂O₃ fiber weight ratio effect on the electrical contact performance of Ag matrix composites was investigated by Yang et al. [47]. When the contribution of Y₂O₃ ratio to the composite composition is 5% by weight, the hardness values of

Table 6 Some properties of Cu-10Cr-3Ag alloys and Cu-10Cr-3Ag/5 wt.% Al₂O₃ composites [43]

| Material | Temperatures of sintering (°C) | Theoretical density (%) | Electrical conductivity (% IACS) | Hardness (HV) |
|---|--------------------------------|-------------------------|----------------------------------|---------------|
| Cu-10Cr-3Ag | 800 | 92 | 32 | 305 ± 5 |
| Cu-10Cr-3Ag/5wt.%Al ₂ O ₃ | 800 | 96 | 25 | 413 ± 5 |

Table 7 Electrical conductivity and hardness of CuCr alloys and Cu-Cr-W-C composites [44]

| Material | Electrical conductivity (% IACS) | Hardness (HV) |
|---------------|----------------------------------|---------------|
| Cu50-Cr50 | 24.7 | 83.4 |
| Cu-Cr-W1-C0.5 | 24 | 140.7 |

Table 8 The properties of some different electrical contact composite materials [46]

| Composition | Content of carbon (wt.%) | Electrical conductivity (m/(Ω mm ²)) | Hardness (HV50) |
|-----------------|--------------------------|--|-----------------|
| Ag-Carbon black | 5 | 18.0 | 168.9 |
| Ag-CNTs | 5 | 37.6 | 119.5 |
| Ag-Graphite | 5 | 31.8 | 180.4 |
| Ag-Diamond | 5 | 25.9 | 159.5 |

these composites increased by almost 2 times, while the electrical conductivity values decreased only by 10% compared to Ag materials without additives (Table 9). Also, as can be seen from Fig. 15, although the electrical conductivity values decreased, the deformation with small splashing in the arc region was much less than that of Ag materials without reinforcement.

On the other hand, materials with enhanced contact performance can be produced using a graded composite structure. Zhang et al. [48] studied the graded composite design shown in Fig. 16 to compare with traditional composites. They used W-WC core-shell particle doped Cu matrix composites to form a layer with high wear and erosion resistance without decreasing the electrical conductivity values of the contact areas much.

They determined that the electrical conductivity and hardness values of conventional Cu-W composites were about 56.90% IACS and 181 HB, respectively, while those of the new design Cu/W-WC graded composites were about 46.55% IACS and 216 HB respectively. In addition, when they examined the arc erosion surfaces of conventional and newly graded composites, it was observed that the arc erosion craters on the surface of the novel-designed composites spread over the entire surface, creating shallow pitting (Fig. 17) [48].

Some interesting results in the investigation of copper matrix composites used in ECMs are also reported in the literature. According to this, when Koppad et al. investigated the thermal and electrical conductivity properties of powder Cu-MWCNTs (multiwalled carbon nanotubes) composites, they found a decrease in the electrical

Table 9 Hardness and electrical conductivity values of Ag and Ag-Y2O3 composites [47]

| Material composition | Electrical conductivity (% IACS) | Hardness (×10 ² N mm ⁻²) |
|---------------------------------------|----------------------------------|---|
| Unreinforced Ag | 106.03 ± 0.13 | 168.9 |
| Ag-5%wt.Y ₂ O ₃ | 96.38 ± 0.11 | 119.5 |

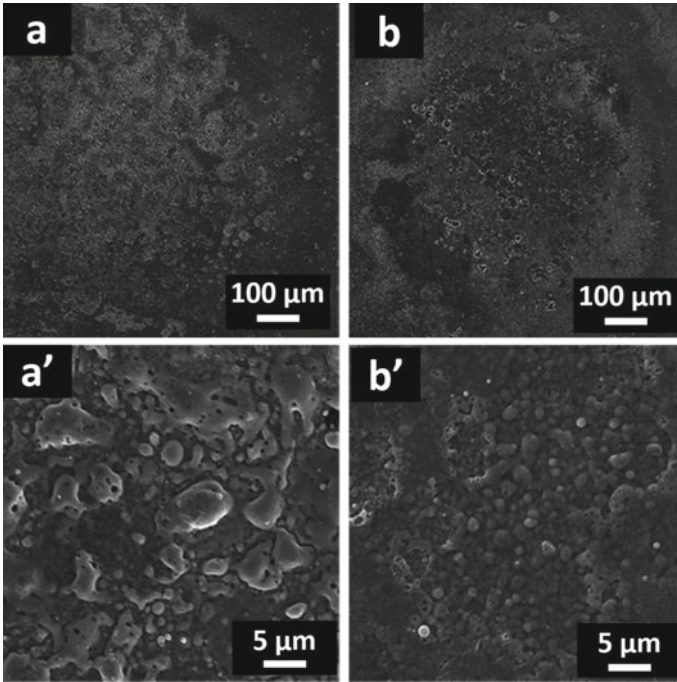


Fig. 15 Arc erosion surfaces of Ag with (a) low and (a') high magnification and Ag-5Y₂O₃ with (b) low and (b') high magnification. Reprinted from Yang et al. [47], with permission from Elsevier. Copyright (2019)

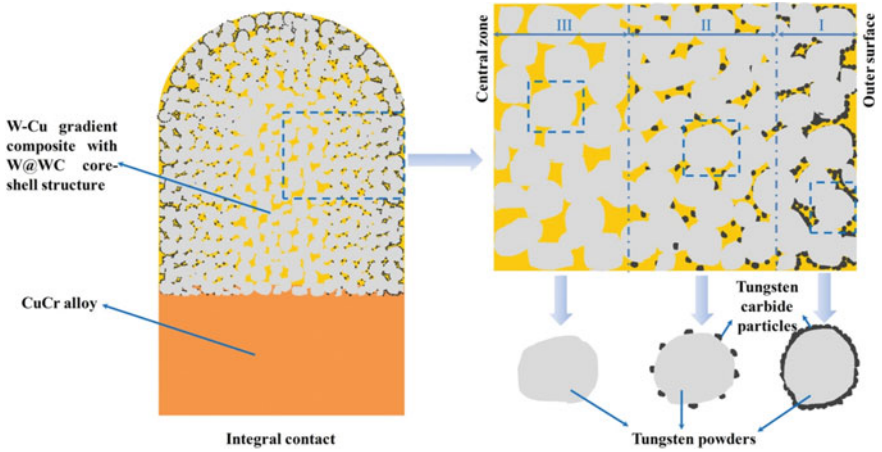


Fig. 16 New W-Cu gradient composite design with the use of W-WC core-shell structure. Reprinted from Zhang et al. [48], with permission from Elsevier. Copyright (2017)

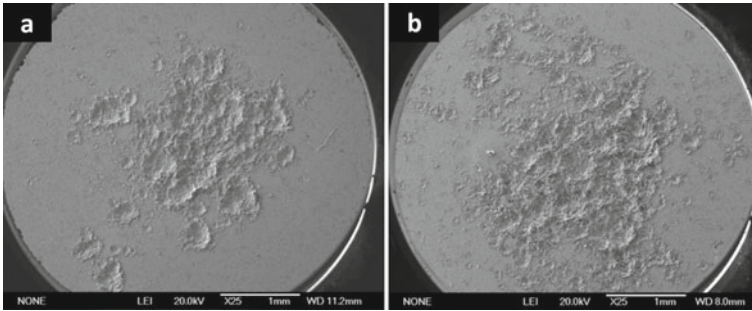


Fig. 17 Arc erosion surface of conventional Cu-W and novel Cu/W-WC gradient composites. Reprinted from Zhang et al. [48], with permission from Elsevier. Copyright (2017)

and thermal conductivity values of the composites with the increase of multiwalled carbon nanotubes (MWCNTs) weight ratio. They emphasized that the reason for this decrease in electrical and thermal conductivity values is, respectively, grain refinement (because of MWCNTs) and thermal resistance occurring at the matrix-reinforced interface [49]. Mallikarjuna et al. stated that the electrical conductivity properties of Cu-CNTs-SiC hybrid nanocomposites exhibit a similar behavior. As the CNT ratio increases, a serious decrease in the electrical conductivity values has been detected. They also emphasized that reinforcement materials trigger grain refinement [50]. In another study, they found that as the CNT ratio increased in Cu-Sn matrix composites, although the electrical conductivity of the materials decreased, the wear and friction coefficient values decreased significantly [51]. They also reported that Cu-MWCNTs-SiC hybrid composites exhibit similar behavior and these composites have improved wear resistance [42].

As a result, the properties of composite structures used in the production of ECMs depend on many parameters. These can be matrix and additive morphology, reinforcement ratios, production methods of materials, parameters used in the production method, and so on. Therefore, composite materials have become indispensable for electrical contacts, with the advantage of using different production methods and matrix-reinforcement structures, depending on the areas of use of ECMs and the desired properties.

4 Fabrication Methods of Electrical Contact Materials

4.1 Casting

Conventional fabrication steps of ECMs start with the production of ingot metals using the casting method as shown in Fig. 18. In the second step, the metal ingots are subjected to annealing process and they are turned into cylindrical cross-section

and large diameter wires by hot extrusion method. In step 3, these wires are reduced to the desired diameter by the wire drawing method and made ready for the production of electrical contact material. In the 4th step, the wires are cut to the required dimensions, pressed into the molds and converted into the desired design. In the the last step, ECMs are combined with the contact terminal with joining methods such as soldering, making them ready for use. Terminal materials, , in which ECMs are combined, are also produced using the same process (sheet metal cutting instead of wire drawing). Each of these fabrication stages requires expensive device investments, skilled labor and includes rather long production processes. Moreover, the fabrication of composite contact materials with high wear resistance is not possible using conventional manufacturing methods.

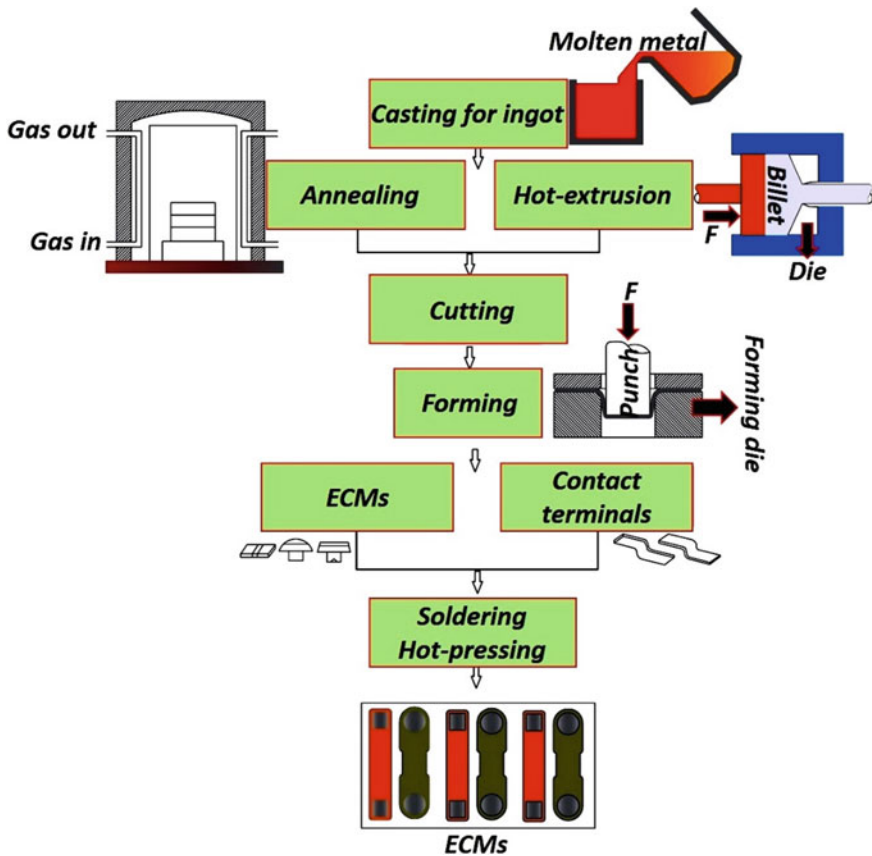


Fig. 18 Conventional electrical contact material production steps for ECMs

4.2 Powder Metallurgy

Another method used in the fabrication of ECMs is the powder metallurgy technique. Contact and contact terminal fabrication stages by powder metallurgy method involve mixing or milling metal powders with lubricants and binders, compacting by pressing, removing the binders and lubricants from the structure, sintering and the joining of the contact and contact terminal, such as soldering or diffusion. This method requires a large number of devices and shaping molds, such as mixers, mechanical or hydraulic presses, lubricant and binder removal furnaces, and sintering furnaces, and this method requires a long production process as it involves numerous production steps (Fig. 19). In addition, contact materials produced by powder metallurgy method may exhibit joint errors such as gapping and separation due to joining methods such as soldering and diffusion. However, this method has significant advantages over the casting methods in terms of the production of composite contact materials. The most important advantage of the powder metallurgy method is the low processing temperature compared with casting methods. That is why undesired phases between the matrix phase and the reinforcement phase are eliminated. Moreover, reinforcement particles are also well-distributed in the metal matrix. Another significant feature is the ability to produce near-net-shape parts which are cost-effective [52, 53].

In this context, powder metallurgy methods are used in the production of copper matrix composites, which are frequently preferred especially for ECMs. However, since the wettability of ceramic-based additives in metal matrix is bad, it affects the properties of composites negatively. Therefore, more dense structures can be obtained by applying processes such as hot forging after powder metallurgy processes [54]. Nevertheless, inhomogeneous particle distribution, wettability, and interfacial problems, especially in the structure of nanoscale particle-reinforced metal matrix composites, are frequently encountered difficulties in powder metallurgy methods. Therefore, it is clear that different methods are needed to minimize the problems caused by reinforcement particles that directly affect the physical and mechanical properties of copper matrix composites used in the production of ECMs [55].

4.3 Internal Oxidation Process

Another traditional method used to manufacture metal matrix composites, which is frequently used in the production of ECMs, is the internal oxidation method. Compared to methods such as powder metallurgy and casting methods, this method has some important advantages. For example, the use of this method in the production of particle-reinforced metal matrix composites allows the particles to be better dispersed in the matrix. Contamination formation on the matrix and particle reinforcement interface is minimized or even eliminated in this method. Since ECMs are

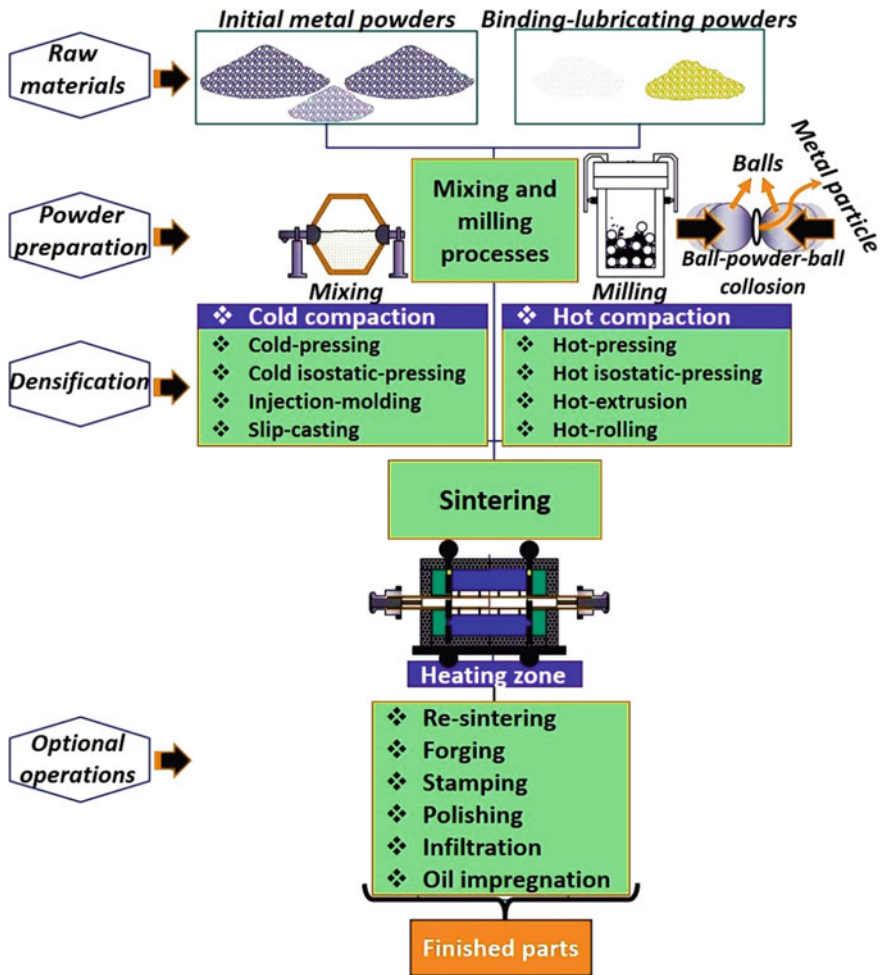


Fig. 19 Fabrication stages of powder metallurgy method

desired to have high electrical conductivity, obtaining the structure free from impurities at the interfaces demonstrates the advantage of this method [56]. As shown in Fig. 20, metal matrix composite ECMs with enhanced properties are produced by providing oxygen diffusion on the surface of metal or metal alloys, thanks to the oxide homogeneously distributed throughout the structure [57].

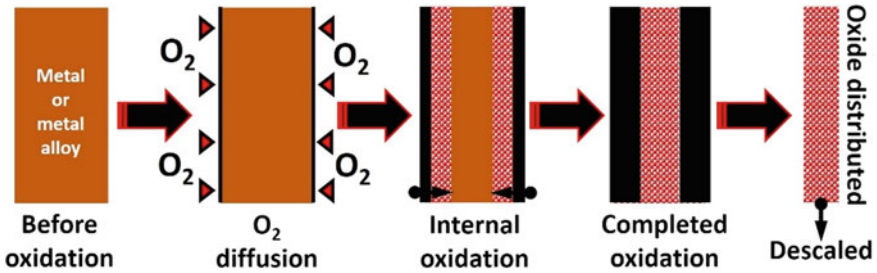


Fig. 20 Internal oxidation process. Reproduced from Han et al. [57], under the Creative Commons Attribution 4.0 International License. <http://creativecommons.org/licenses/by/4.0/>

4.4 Infiltration Process

The infiltration method is another method often used in the production of ECMs. In this method, which is common to use, metals or alloys with lower melting points are filled into the pores of the compacts. This method is considered advantageous since the porosity and particle distribution in the structure directly affect the electrical and mechanical properties of ECMs [58]. Besides, in the production of metal matrix composites with diamond particles, especially in areas where electrical and thermal conductivity are important, the ability of the metal matrix to wet the reinforcing diamond is very low. At this point, filling the pores in the process provided by infiltration can increase the wettability by adding different alloying elements to the structure. Thus, in this method, particles such as diamonds are filled into a mold and placed on the metal or metal alloy. After the residual air in the mold is evacuated by vacuum, it is heated to a temperature above the melting point of the metal or metal alloy. Thus, the molten metal settles in the pores between the diamond particles in the mold [59]. A Schematic representation of the infiltration method is given in Fig. 21.

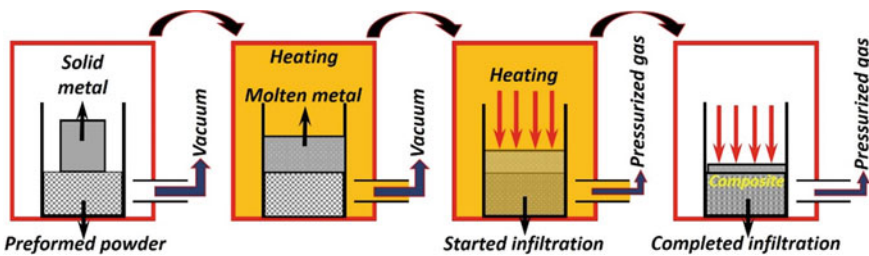


Fig. 21 Infiltration process [60]

5 New Methods for the Fabrication of Electrical Contact Materials

5.1 Development of Powder Properties

The porosity frequently encountered in ECMs produced from a ceramic-based particulate additive composite is due to the fact that the additive particles are not sufficiently homogeneously dispersed in the matrix. Therefore, the conventional powder metallurgy method used in the production of composite ECMs imposes some restrictions. Even though mechanical milling processes are applied to mix metal matrix powders homogeneously with ceramic-based particles, the wettability of ceramic particles with metal matrix powders is very poor. This causes the ceramic particles to agglomerate in the matrix structure [52]. Recently, some innovations have been made in composite powder production during the preparation of powders and homogeneous composites have started to be produced in the powder metallurgy method. For example, ceramic-based particle-reinforced and metal matrix composite powders produced by co-precipitation method have been produced. Then, ECMs were produced from these powders by powder metallurgy process. According to the results obtained, it is determined that the products with a very homogeneous distribution of matrix-additive material have very low porosity, high hardness, and electrical conductivity. It has been stated that the co-precipitation method is a very simple method and very useful in terms of getting results in a short time (according to mechanical milling, etc.) [61].

Liu et al. [62] produced Cu-doped SnO₂ particles with with co-precipitation method to prevent the problem of ceramic particle agglomeration in the production of conventional Ag/SnO₂ electrical contact composites. The wettability between Ag and SnO₂ particles is significantly increased thanks to Cu. The homogeneity in the microstructure has been determined that the composite contacts have low porosity, high electrical conductivity, and hardness. In addition, the arc erosion resistance of these contact materials developed with a new method has increased considerably. While the visual figure about how the new method improves the performance of the contact was given in Fig. 22, the data of the contacts developed with the new method were given in Table 10. As seen from Fig. 22, due to the low wettability between SnO₂ and Ag, and low density of SnO₂, SnO₂ particles tend to accumulate at the edges of the melting Ag pool during the arc. However, Cu-doped SnO₂ particles show low dispersion under the same conditions. Thanks to the inductive effect of Cu, growth has been observed in preferential direction. This resulted in homogeneous nanoneedle formation. In addition, material loss due to arc erosion of conventional Ag/SnO₂ and new Ag/SnO₂ materials is shown in Table 10.

Although Koppad et al. used traditional powder metallurgy and hot forging methods in the production of composites with Cu matrix and multiwalled carbon nanotubes (MWCNTs) reinforcement, while they coated MWCNTs with electroless Ni in the production of a group of composites, they did not use a coating in the other group. As a result of the study, they determined that the reinforcement particles of the

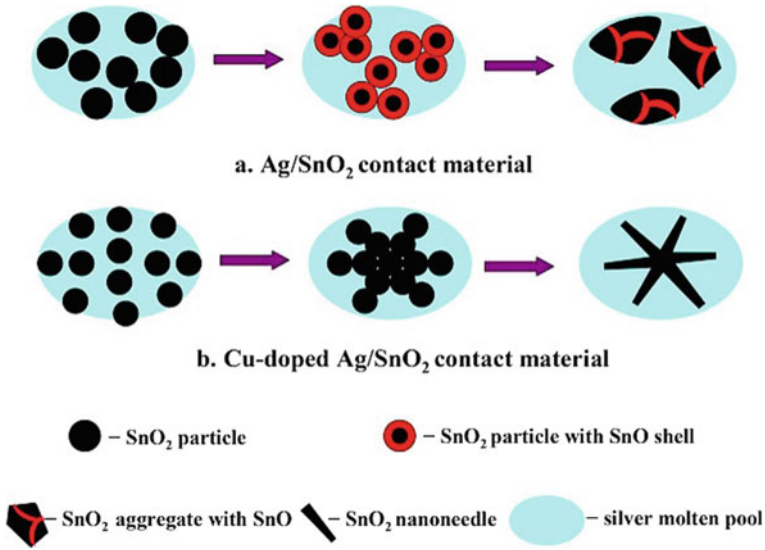


Fig. 22 Nonhomogeneous distribution of SnO₂ in the traditional Ag/SnO₂ and homogenous distribution of SnO₂ in novel Ag/SnO₂ composites during arcing. Reprinted from Liu et al. [62], with permission from Elsevier. Copyright (2019)

Table 10 The parameters of Ag/SnO₂ and Cu-doped Ag/SnO₂ composites [62]

| Composition | Density (g/cm ³) | Electrical conductivity (% IACS) | Hardness (HV) | Material loss (mg) |
|------------------------------|------------------------------|----------------------------------|---------------|--------------------|
| Ag/SnO ₂ | 9.23 | 56.5 | 131.3 | ~1.3 |
| Cu-doped Ag/SnO ₂ | 9.61 | 66.0 | 122.4 | ~0.5 |

interface formed by electroless Ni coating at the copper-MWCNTs interface spread more homogeneously in the matrix. Thus, they found that the strength of composites increased significantly [63].

Another new method that can be applied during the preparation of powders used in the production of ECMs before powder metallurgy and hot pressing processes is the electroless coating. In this method, electrical contact material can be produced using only layered metal powders against the risk of poor distribution of ceramic particles in the matrix. In addition, it is considered a cheap and fast method using very low amounts of Ag. Güler et al. [64] studied layered materials produced by hot pressing using Ag on Cu powders by electroless coating method and then nickel on this Ag layer with the same method. The new contact materials were produced by hot pressing, and compacting these 3-layered metal powders. The Ag layer coated on Cu powders increased the oxidation resistance and electrical conductivity of Cu. In addition, the outermost nickel layer significantly increased the hardness of the

contacts, while the electrical conductivity values did not decrease much. In addition, when contact materials produced by the use of layered metal powders are subject to wear, these new materials can be defined as self-renewal contact materials. Nickel layer will be resistant to wear resistance by coming back from the substrates over time to the nickel layer around each powder grain. The visual showing the production stages in brief is given in Fig. 23. Besides, comparing the properties of some conventional composites with those of these layered powders produced from layered powders, the usability of the materials obtained by this new production method can be seen as electrical contact material (Table 11).

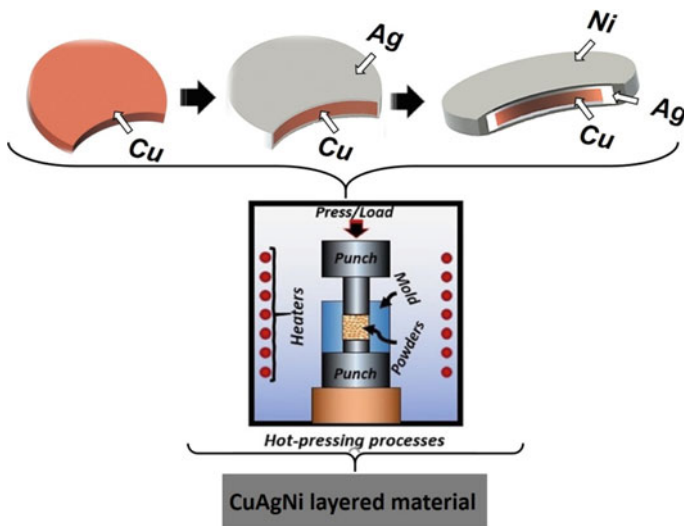


Fig. 23 New ECMs with layered metallic powders [64]

Table 11 Some properties of new layered materials comparing with some data in literature [64]

| Material | Hardness (HB) | Electrical conductivity (% IACS) | Oxidation resistance |
|--|---------------|----------------------------------|----------------------|
| CuAgNi layered materials | 125 | 76 | Very good |
| Al ₂ O ₃ -Cu/(35%)W(5%)Cr [65] | 126 | 62 | – |
| Al–Al ₂ O ₃ -coated Cu [66] | 119 | – | – |
| Ag-0.5Ag-doped graphene [45] | 75 | 98 | – |
| Cu-3 wt.% ZrO ₂ [67] | 117 | 72 | – |
| Cu-15 wt.% W [68] | 98 | 78 | – |
| Cu-5 wt.% B ₄ C [69] | 55 | 3.5 | – |

5.2 Equal Channel Angular Pressing (ECAP)

On the other hand, in many powder metallurgy methods used in the production of ECMs, the sample size may vary, and high sintering temperature and pressure may be required especially in obtaining Ag matrix composites. These situations make it difficult to control processes. In this case, the use of ECAP method, which can be produced without changing the shape of the materials, has attracted attention of researchers in ECMs. In this method, it is possible to produce homogenously distributed composites together with a very ultrafine-grained microstructure by providing severe plastic deformation without changing the shape of the materials. Since the material in the mold is subjected to direct sliding without compression, high pressing forces are not required in this method compared to powder metallurgy methods such as extrusion and hot pressing [70]. Wang and his colleagues [71] have worked on obtaining the contact material composite structure that is preferentially oriented with the rotary die system in the ECAP method. They produced fine-grained and oriented Ag/Ti₃AlC₂ 10 wt.% composites obtained by this method. Firstly, Ag and Ti₃AlC₂ powders were mixed by milling and pressing, followed by sintering to obtain the bulk composite samples. Bulk composites enclosed in an Al container were then taken into the rotating mold of the ECAP system, and 8 passes (extrusion) were performed. In the movement of the upper punch, the sample was extruded from the left horizontal path and 1 pass was completed. The mold was then turned 90° clockwise to restore it, but in this case, the sample head settled down and the process was repeated. The 8 passes operations were carried out in this way. Normal direction, transverse direction, and press direction were named ND, TD, and PD, respectively. The process is shown in Fig. 24 [71].

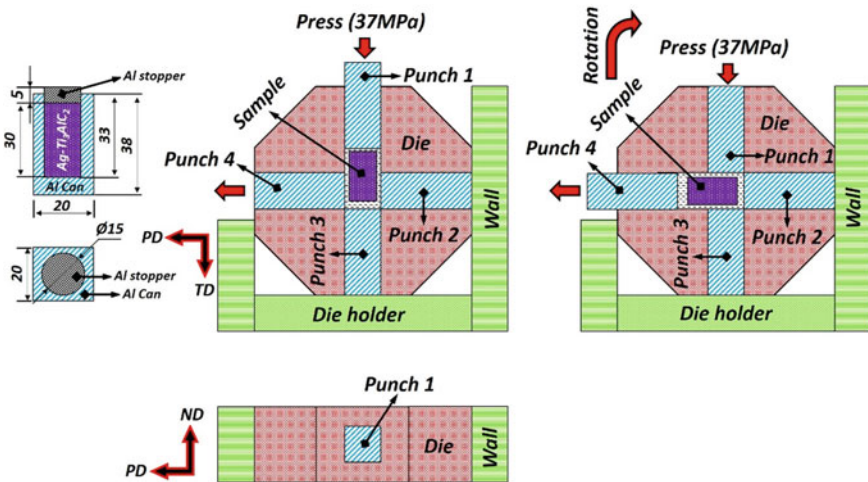


Fig. 24 Rotating ECAP process of Ag/Ti₃AlC₂ composites. Reprinted from Wang et al. [71], with permission from Elsevier. Copyright (2019)

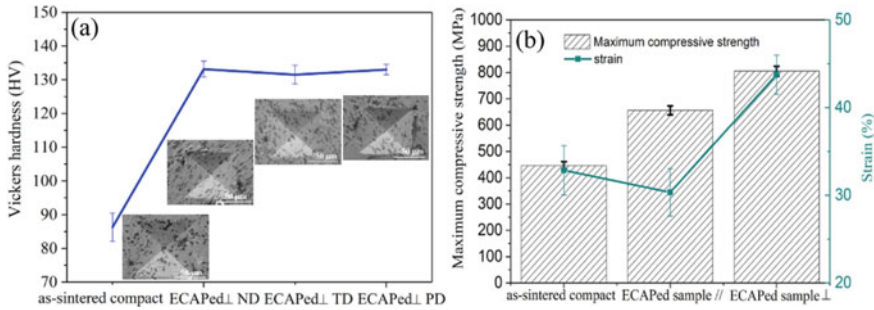


Fig. 25 **a** Hardness and **b** compressive strength values of samples. Reprinted from Wang et al. [71], with permission from Elsevier. Copyright (2019)

Grain refinement in matrix Ag and Ti_3AlC_2 particles in the internal structure of the composites obtained by this method has provided a great improvement in the hardness and compressive strength values of the composites. As seen in Fig. 25a, hardness values have increased by almost 80% in composites produced by the ECAP process. This has been attributed to the refinement of grain size and increasing the dislocation rate within the matrix by this new process for electrical contacts. In addition, it is clearly seen that the compressive strength increases in samples where the ECAP process is applied perpendicular to the array of reinforcing Ti_3C_2 particles (Fig. 25b). In addition, in the study of arc erosion surfaces, the material loss measured in composites produced by the ECAP process was found to be almost half less than that of the as-sintered composites [71].

5.3 Additive Manufacturing (AM) Process

The most effective method to be used in the fabrication of ECMs in the future is AM techniques, although it is still early for commercial manufacturers. AM is an advanced manufacturing technology that enables the production of complex-shaped parts in layers, unlike traditional manufacturing methods (Figs. 26 and 27). Besides, the graphic summarizing the operations and purposes for which AM method is used is shown in Fig. 27. Using this method, metallic materials, and different types of alloys can be produced faster, and have properties equivalent to or better than their counterparts produced by conventional methods [72]. The AM methods such as selective laser melting (SLM), and electron beam scattering that have emerged recently with the combination of laser systems and computer software have led to an important breakthrough in material production especially in the production of ECMs.

SLM method, which is among these techniques, eliminates the costly, skilled, and long-time conventional production processes that involve the fabrication of electrical contact material and contact terminal, and the combination of the contact terminal and

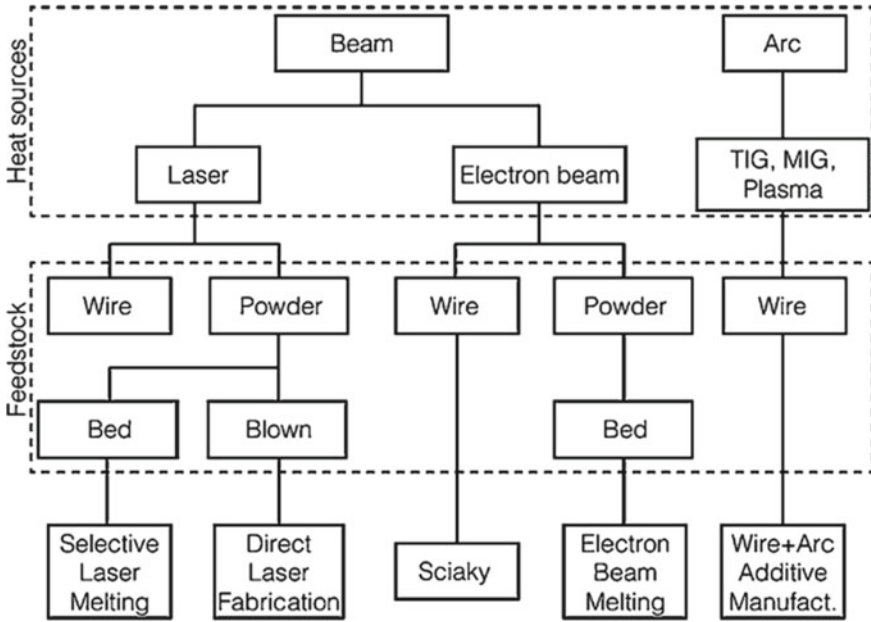


Fig. 26 The principal metal AM processes. Reprinted from Gisario et al. [73], with permission from The Society of Manufacturing Engineers. Copyright (2019)

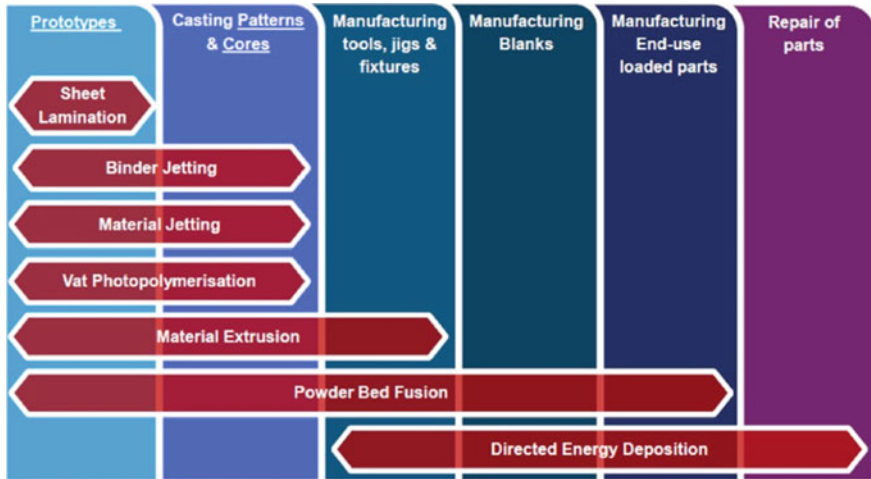


Fig. 27 AM process types and applications. Reprinted from Gisario et al. [73], with permission from The Society of Manufacturing Engineers. Copyright (2019)

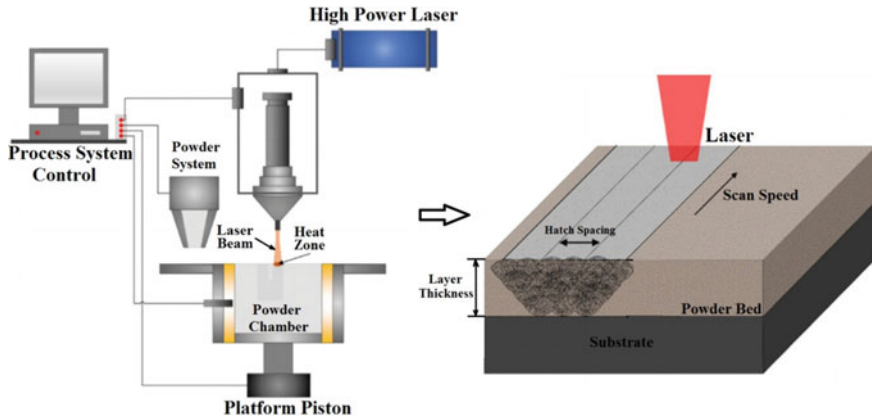


Fig. 28 Schematic illustration of SLM process. Reprinted from Fayazfar et al. [79], with permission from Elsevier. Copyright (2018)

electrical contact material and the problems (low electrical conductivity of soldering area, contact breaks from soldering area, additional machinery-equipment for hot pressing etc.) arising from this combination (Fig. 28). SLM technique is also an advanced fabrication method that has the potential to produce tens of contact terminal at the same time as the contact terminal and electrical contact material integrated and depending on the table size, and to create functional structure thanks to the layered production flexibility [74–78].

As seen in Fig. 29, when metal particles interact with the laser beam, a series of physical and chemical phenomena occur, such as the absorption of laser energy, scattering, heat transfer, phase change, and melt flow in the melt region during rapid melting and solidification. The thermodynamic and kinetic behavior of the melt material can be changed by adjusting SLM parameters such as laser power, scanning speed, layer thickness, and construction orientation [80–82].

Another advantage of SLM method in the fabrication of electrical contact materials is that two or more layered structures can be produced. In other words, functionally graded materials (FGM) can be easily produced using SLM technique. FGM are a class of advanced materials characterized by changing locally in properties according to desired objective [83, 84]. Their multifunctional properties increase rapidly their use for applications in aerospace, automotive, defense, electrical-electronic biomedical and power sectors. This advantage of SLM technique significantly complies with the performance requirements of ECMs. For the contact materials commonly used in the energy sector, the most important demand of substrate region is the electrical and thermal conductivities, while the most important demand of regions in contact with each other is the surface properties (wear resistance, hardness, and arc erosion resistance). As explained in the previous sections, the surface of the ECMs must be resistant to abrasion and at the same time, these materials must have good electrical

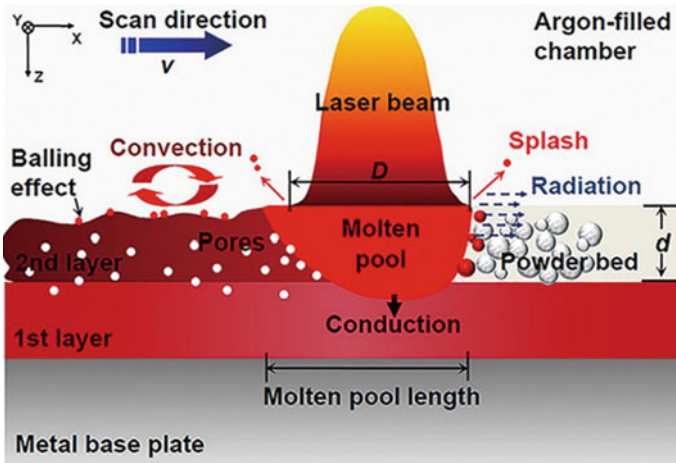


Fig. 29 Laser and metallic powder interaction in SLM method. Reprinted from Zhang et al. [80], with permission from Elsevier. Copyright (2019)

conductivity. These regional requirements of ECMs clearly show the manufacturability and applicability as the functional graded material of ECMs. Using the SLM technique, the upper surface of the electrical contact material can be produced using hard and medium conductivity layers, and the lower parts can be produced using higher conductivity layers [18, 85]. Pure Cu material in the bottom layer is considered the region with the highest electrical conductivity, while the composite layer in the upper layers provides the wear resistance [86, 87].

As it is understood, there are many criteria in the production of advanced ECMs. The most critical of these are the manufacturing methods used in the production of ECMs, the materials used, the most critical material properties, and the design of the materials produced. According to this, the critical results from the study are summarized in Table 12.

6 Conclusions

Since ECMs are the main materials that allow current flow in electrical circuits, electrical conductivity values should be as high as possible. The increase in temperature during the current transmission can cause the ECMs to melt and cause them to weld each other. Therefore, thermal conductivity values must be high as well as electrical conductivity to prevent welding problems. Oxidation problem occurs in ECMs with low electrical and thermal conductivities, the electrical resistance of the materials increases and the current passage becomes more difficult. Therefore, materials with the lowest oxidation tendency such as Au and Ag are used in the production of ECMs. However, because of the high price of these materials, Cu,

Table 12 Summary of key findings on the review of ECMs

| Fabrication methods | Critical properties | Materials selection | Materials design |
|---|---|--|---|
| <p>Compared to conventional casting, powder metallurgy, infiltration, internal oxidation, methods such as AM and ECAP, which are new methods, have become more preferred in the production of superior ECMs. Advanced featured ECMs can be produced by combining several methods such as electroless coating, powder metallurgy/AM/ECAP</p> | <p>High mechanical properties, high electrical and thermal conductivities, low contact resistance to prevent contact welding and material transfer. The lubrication of the contact interaction areas of ECMs plays a critical role for improved contact performance</p> | <p>Due to the high cost of Ag, it is preferred to improve the properties of copper-based ECMs. Ni, Pd, Li, Cr metals, and ceramic reinforcements such as Al₂O₃, B₄C, SnO₂, and ZrO₂ are added to Cu materials to improve the wear and welding resistance of Cu based ECMs</p> | <p>Development of the interface of materials used in ECMs can be provided to increase the wettability of the metal matrix for ceramic particle reinforcements in the production of metal matrix composites. In addition, FGM design has a critical role in obtaining anti-weld materials with high electrical and thermal conductivities because of its changeable different properties in each layer</p> |

which has the highest electrical and thermal conductivity values, is often preferred after these materials.

Mechanical wear prevents contact of surfaces due to the material loss over time and damaged contact surface causes the current transmission from certain areas rather than being transmitted across the entire surface. Therefore, the ECMs must have sufficient hardness. Additionally, the arc causes the heating of the ECMs in a short period of time, and the separation of the material from the surface in the form of rupture and breaking due to the regional melts, the transfer of the material from the surfaces to each other. Finally, the ECMs become unusable by the welding of the surfaces to each other.

Cu-based composite materials produced using high conductivity matrix and high hardness reinforcement materials can meet the performance requirements of ECMs with the condition of homogeneous distribution of the reinforcement material and low reinforcement ratio by powder metallurgy methods. However, it is difficult to meet these performance requirements with conventional composite materials and conventional production methods. The use of matrix or reinforcing powders coated with high oxidation and high conductivity metal powders such as Cu brings the composite properties one step closer to the target level. On the other hand, because the casting (casting-extrusion-rolling-pressing) processes require a large number of

machines and labor as well as the time and scrap losses and all are connected, which further increase production costs, the search for more qualified methods has prevailed.

The SLM method developed in recent years is an advanced production method that has an important potential to produce the electrical contact material integrated with the contact terminal and also to produce tens of contact materials depending on the table size and to create functional structure by means of layered production flexibility without conventional production processes which are very costly, skilled workforce and long time in the manufacture of electrical contact material and contact terminals and not preventing the bonding problems (low electrical conductivity of the soldering zone, contact breaks from the soldering zone, additional machine-equipment for hot pressing, etc.) between the contact terminal with the electrical contact material. Functional graded ECMs to be manufactured by powder metallurgy and SLM methods are also used as important fabrication methods in meeting the performance requirements of ECMs.

Acknowledgements The authors would like to thank the Scientific and Technological Research Council of Türkiye (TÜBİTAK) for their contribution with the project numbered 119M398.

References

1. H. Rende, E. Karaman, E. Altındal, *Mühendis ve Makina* **58**, 79 (2017)
2. E. Zengin, *A Real Application on Power Computations in Terms of Optimal Energy Consumption to Turn Different Kinds of Automobiles into Electrical Automobiles* (Mersin University, 2017)
3. *OTOMOTİV SANAYİİ 2017 YILI KÜRESEL DEĞERLENDİRME RAPORU* (Automotive Industry 2017 Global Evaluation Report) (2018)
4. Ö. Simsekoglu, *Transp. Policy* **72**, 180 (2018)
5. K.Y. Bjerkan, T.E. Nørbech, M.E. Nordtømme, *Transp. Res. Part D Transp. Environ.* **43**, 169 (2016)
6. E. Dogan, F. Seker, *Renew. Sust. Energ. Rev.* **60**, 1074 (2016)
7. P. Moriarty, D. Honnery, *Energy Policy* **93**, 3 (2016)
8. H. Mehrjerdi, *Energy Convers. Manag.* **205**, 112350 (2020)
9. C. Emeksiz, B. Demirci, *Sustain. Energy Technol. Assess.* **36**, 100562 (2019)
10. A.A. Coskun, Y.Ö. Türker, *Environ. Monit. Assess.* **184**, 1265 (2012)
11. A. Adelaja, C. McKeown, B. Calnin, Y. Hailu, *Energy Policy* **42**, 191 (2012)
12. M.S. Nazir, A.J. Mahdi, M. Bilal, H.M. Sohail, N. Ali, H.M.N. Iqbal, *Sci. Total Environ.* **683**, 436 (2019)
13. A. Aghahosseini, D. Bogdanov, L.S.N.S. Barbosa, C. Breyer, *Renew. Sustain. Energy Rev.* **105**, 187 (2019)
14. C.G. Meza, C. Zuluaga Rodríguez, C.A.D'Aquino, N.B. Amado, A. Rodrigues, I.L. Sauer, *Renew. Energy* **132**, 628 (2019)
15. W.D. Callister, D.G. Rethwisch, *Fundamental of Materials Science and Engineering: An Integrated Approach*, 3rd edn. (Wiley, 2007), pp. 247–366
16. C. Wu, D. Yi, W. Weng, S. Li, J. Zhou, *Trans. Nonferrous Met. Soc. China* **26**, 185 (2016)
17. J. Wang, S. Tie, Y. Kang, Y. Wang, *J. Alloys Compd.* **644**, 438 (2015)
18. T. Varol, *The Fabrication and Characterization of Nano Particle Reinforced-Copper Matrix Functionally Graded Electrical Contact Materials* (Karadeniz Technical University, Graduate Institute of Natural and Applied Sciences, 2016)

19. A. A. Eker, B.O. Küçükyıldırım, TMMOB MMO Mühendis ve Makina Dergisi **53**(37), 34 (2012)
20. D. Chapman, H.W. Turner, C. Turner, Copp. Dev. Assoc. **20**, 1 (2015)
21. P.G. Slade, (ed.) *Electrical Contacts*, 2nd edn., (CRC Press, 2017), pp. 231–546
22. T. Mützel, P. Braumann, R. Niederreuther, in *Electrical Contacts—2009 Proceedings of the Fifty Fifth IEEE Holm Conference on Electrical Contacts*, 200 (2009)
23. D. Chapman, H.W. Turner, C. Turner, Copp. Dev. Assoc. Publ. **223**, 40 (2015)
24. I.H. Sung, J.W. Kim, H.J. Noh, H. Jang, Tribol. Int. **95**, 256 (2016)
25. H. Nagasawa, K. Kato, Wear **216**, 179 (1998)
26. M. Li, M. Chao, E. Liang, J. Yu, J. Zhang, D. Li, Appl. Surf. Sci. **258**(4), 1599 (2011)
27. M. Gedeon, *Silver as a Coating Material* (2012). https://materion.com/-/media/files/alloy/new_sletters/technical-tidbits/issue-no-39---silver-as-a-contact-material.pdf. Accessed 30 March 2020
28. J.R. Davis (ed.), *Metals Handbook*, Desk Edition, (ASM International, 1990). pp. 56–63
29. G. Holmbom, B.E. Jacobson, J.-E. Sundgren, in *Technology Proceedings AESF SUR/FIN 95*, ed. by P.E. Ted Mooney (Elsevier, 1995), pp. 333–347
30. R. Rofagha, U. Erb, D. Ostrander, G. Palumbo, K.T. Aust, Nanostruct. Mater. **2**, 1 (1993)
31. N. Togasaki, Y. Okinaka, T. Homma, T. Osaka, Electrochim. Acta **51**, 882 (2005)
32. Z. Lin, S. Liu, J.-G. Li, J. Chen, M. Xie, X. Li, M. Zhang, Q. Zhu, D. Huo, X. Sun, Mater. Des. **108**, 640 (2016)
33. C. Weichan, L. Shuhua, Z. Xiao, W. Xianhui, Y. Xiaohong, Int. J. Refract. Met. Hard Mater. **29**, 237 (2011)
34. R.Z. Valiev, Y. Estrin, Z. Horita, T.G. Langdon, M.J. Zehetbauer, Y. Zhu, JOM **68**, 1216 (2016)
35. G. Faraji, H. S. Kim, H. T. Kashi, in *Severe Plastic Deformation* (Elsevier, 2018), pp. 275–306
36. Ö. Güler, E. Evin, J. Mater. Process. Technol. **209**, 1286 (2009)
37. V. Rajkovic, D. Bozic, M.T. Jovanovic, Mater. Des. **31**, 1962 (2010)
38. L. Zhang, J. Xiao, K. Zhou, Tribol. Trans. **55**(4), 473 (2012)
39. O. Güler, T. Varol, Ü. Alver, A. Canakci, Mater. Today Commun. **24**, 101153 (2020)
40. M.R. Akbarpour, H. Mousa Mirabad, S. Alipour, Ceram. Int. **45**, 3276 (2019)
41. C. Ayyappadas, O.S. Shanu, A. Vijayan, I.A. Mohammed, V. Vishnu, M. Shammadh, J. Phys. Conf. Ser. **1355**, 012035 (2019)
42. H.M. Mallikarjuna, C.S. Ramesh, P.G. Koppad, R. Keshavamurthy, D. Sethuram, Vacuum **145**, 320 (2017)
43. S. Bera, W. Lojkwosky, I. Manna, Metall. Mater. Trans. **A 40**, 3276 (2009)
44. Y. Chang, W. Zheng, Z. Zhou, Y. Zhai, Y. Wang, J. Electron. Mater. **45**, 5647 (2016)
45. X. Hao, X. Wang, S. Zhou, H. Zhang, M. Liu, Mater. Chem. Phys. **215**, 327 (2018)
46. P. Jiang, F. Li, Y. Wang, IEEE Trans. Components Packag. Technol. **29**, 420 (2006)
47. R. Yang, S. Liu, J. Chen, H. Cui, M. Liu, F. Zhu, Y. Yang, M. Xie, X. Sun, X. Li, Ceram. Int. **45**, 1881 (2019)
48. Q. Zhang, S. Liang, L. Zhuo, J. Alloys Compd. **708**, 796 (2017)
49. P.G. Koppad, H.R.A. Ram, C.S. Ramesh, K.T. Kashyap, R.G. Koppad, J. Alloys Compd. **580**, 527 (2013)
50. H.M. Mallikarjuna, C.S. Ramesh, P.G. Koppad, K.T. Kashyap, R. Keshavamurthy, P.G. Koppad, K.T. Kashyap, R. Keshavamurthy, Indian J. Sci. Technol. **9**, 1 (2016)
51. H.M.M. Mallikarjuna, K.T.T. Kashyap, P.G.G. Koppad, C.S.S. Ramesh, R. Keshavamurthy, Trans. Nonferr. Met. Soc. China **26**, 1755 (2016)
52. T. Varol, A. Canakci, J. Alloys Compd. **649**, 1066 (2015)
53. A. Canakci, T. Varol, H. Cuvanci, F. Erdemir, S. Ozkaya, Sci. Eng. Compos. Mater. **22**, 425 (2015)
54. P.G. Koppad, K.T. Kashyap, V. Shraithin, T.A. Shetty, R.G. Koppad, Mater. Sci. Technol. **29**, 605 (2013)
55. P.G. Koppad, V.K. Singh, C.S. Ramesh, R.G. Koppad, K.T. Kashyap, in *Carbon Materials for Advanced Technologies* (John Wiley & Sons, Inc., Hoboken, NJ, USA, 2013), pp. 331–376
56. X. Zhou, D. Yi, L. Nyborg, Z. Hu, J. Huang, Y. Cao, J. Alloys Compd. **722**, 962 (2017)

57. S. Zeon Han, K.H. Kim, J. Kang, H. Joh, S. M. Kim, J. H. Ahn, J. Lee, S. H. Lim, B. Han, *Sci. Rep.* **5**, 17364 (2015)
58. M. Madej, *Arch. Metall. Mater.* **57**, 605 (2012)
59. R. Bollina, J. Landgraf, H. Wagner, R. Wilhelm, S. Knippscheer, B. Tabernig, in *Proceedings—2006 International Symposium Microelectronics IMAPS 2006*, San Diego, 8–12 October 2006
60. R. Bollina, J. Landgraf, S. Knippscheer, T. Mrotzek, H. Wagner, in *ATW Advanced Substrates Next Generation Semiconductors* (2008), pp. 1–5. https://www.researchgate.net/publication/264933295_Thermal_Management_and_Packaging_with_Diamond_Composites
61. Q. Xiuqing, S. Qianhong, Z. Lingjie, C. Lawson, F. Xianping, Y. Hui, *Rare Met Mater. Eng.* **43**, 2614 (2014)
62. S. Liu, Q. Sun, J. Wang, H. Hou, *J. Alloys Compd.* **792**, 1248 (2019)
63. P.G. Koppad, H.R.R. Aniruddha Ram, K.T.T. Kashyap, *J. Alloys Compd.* **549**, 82 (2013)
64. O. Güler, Ü. Alver, T. Varol, *J. Alloys Compd.* **835**, 155278 (2020)
65. X. Zhang, Y. Zhang, B. Tian, J. An, Z. Zhao, A.A. Volinsky, Y. Liu, K. Song, *Compos. Part B Eng.* **160**, 110 (2019)
66. W. S. Barakat, A. Wagih, O.A. Elkady, A. Abu-Oqail, A. Fathy, A. EL-Nikhaily, *Compos. Part B Eng.* **175**, 107140 (2019)
67. M. Khaloobagheri, B. Janipour, N. Askari, *Adv. Mater. Res.* **829**, 610 (2013)
68. S.C. Vettivel, N. Selvakumar, N. Leema, A. Haiter Lenin, *Mater. Des.* **56**, 791 (2014)
69. P.K. Prajapati, D. Chaira, *Trans. Indian Inst. Met.* **72**, 673 (2019)
70. M. Balog, F. Simancik, O. Bajana, G. Requena, *Mater. Sci. Eng. A* **504**, 1 (2009)
71. D. Wang, W. Tian, A. Ma, J. Ding, C. Wang, Y. You, P. Zhang, J. Chen, Y. Zhang, Z. Sun, *J. Alloys Compd.* **784**, 431 (2019)
72. N. Li, S. Huang, G. Zhang, R. Qin, W. Liu, H. Xiong, G. Shi, J. Blackburn, *J. Mater. Sci. Technol.* **35**, 242 (2019)
73. A. Gisario, M. Kazarian, F. Martina, M. Mehrpouya, *J. Manuf. Syst.* **53**, 124 (2019)
74. G. Kaya, *Characterization of the Structural and Tribological Properties of Ti6Al4V Alloy Produced in Different Production Parameters Using Selective Laser Melting* (Erzurum Technical University, 2019)
75. S. Şenol, *The Effect of Surface Roughness on Mechanical Behavior of Commercially Pure Titanium Implants Produced by Selective Laser Melting* (İstanbul Technical University, 2018)
76. K. Turalioğlu, *Determination of Tribology Behavior of Self Lubricant Surfaces by Using Selective Laser Melting Method* (Erzurum Technical University, 2018)
77. A. Fathy, A. Wagih, A. Abu-Oqail, *Ceram. Int.* **45**, 2319 (2019)
78. Y. Zhang, B. Song, X. Zhao, Y. Shi, *Nano Mater. Sci.* **1**(3), 208 (2019)
79. H. Fayazfar, M. Salarian, A. Rogalsky, D. Sarker, P. Russo, V. Paserin, E. Toyserkani, *Mater. Des.* **144**, 98 (2018)
80. S. Zhang, H. Zhu, Z. Hu, X. Zeng, F. Zhong, *Powder Technol.* **342**, 613 (2019)
81. J. Metelkova, Y. Kinds, K. Kempen, C. de Formanoir, A. Witvrouw, B. Van Hooreweder, *Addit. Manuf.* **23**, 161 (2018)
82. P. Wang, H.C. Li, K.G. Prashanth, J. Eckert, S. Scudino, *J. Alloys Compd.* **707**, 287 (2017)
83. B. Kieback, A. Neubrand, H. Riedel, *Mater. Sci. Eng. A* **362**, 81 (2003)
84. W.M. Rubio, G.H. Paulino, E.C.N. Silva, *Mater. Des.* **41**, 255 (2012)
85. O. Güler and T. Varol, in *Advanced Surface Coating Techniques for Modern Industrial Applications*, ed. by S. Roy and G. Bose Kumar (IGI Global Publisher, 2021), pp. 150–187
86. J. Mirazimi, P. Abachi, and K. Purazrang, *Acta Metall. Sin. English Lett.* **29**, 1169 (2016)
87. M.A.F. Afzal, P. Kesarwani, K.M. Reddy, S. Kalmodia, B. Basu, K. Balani, *Mater. Sci. Eng. C* **32**, 1164 (2012)

Organosulfur Polymer Composites by Free Radical Polymerization of Sulfur with Vegetable Oils



**Amin Abbasi, Ali Shaan Manzoor Ghumman, Mohamed Mahmoud Nasef,
Wan Zaireen Nisa Yahya, Muhammad Rashid Shamsuddin,
and Muhammad Moniruzzaman**

Abstract The dependence of conventional petroleum-based polymers on the oil industry continues to increase the environmental burden and thus immense efforts are devoted to develop alternative biopolymers and polymers made from waste residues. Among green monomers used to produce biopolymers, vegetable oils occupy a special position due to their cheap price, abundance, and their versatile molecular compositions, which are full of vinylic groups acting as reaction sites, and therefore they have drawn a lot of attention in recent years. Inverse vulcanization is a new technique to copolymerize elemental sulfur, a by-product in oil and gas refineries, with a vinylic monomer(s) using free radical polymerization at the molten state of sulfur to obtain stable sulfur-based polymers having green nature and unique properties. This new class of polymers has been found very promising for various applications including environmental remediation, energy storage in Li–S batteries, fertilizers, optical devices, and healable polymeric materials besides varieties of unfolded applications. This chapter briefly reviews the progress taking place in the application of the inverse vulcanization process for the preparation of organosulfur polymeric composites made using vegetable oils as green monomers. As a matter of comparison, the properties of the reported organosulfur polymeric composites made on the bases of a variety of vegetable oils (linseed, olive, sunflower, canola, and soybean, corn oil, and rubber seed) are also discussed. Finally, the challenges and the future perspective of this type of environmentally friendly and low-cost polymeric composites are outlined.

A. Abbasi · A. S. M. Ghumman · W. Z. N. Yahya · M. R. Shamsuddin · M. Moniruzzaman
Chemical Engineering Department, Universiti Teknologi PETRONAS, 32610 Seri Iskandar,
Perak, Malaysia

M. M. Nasef (✉)

Department of Chemical and Environmental Engineering, Malaysia Japan International Institute
of Technology, Universiti Teknologi Malaysia Kuala Lumpur, Jalan Sultan Yahya Petra, 54100
Kuala Lumpur, Malaysia

e-mail: mahmoudeithar@cheme.utm.my

Keywords Organosulfur polymer composites · Polysulfide · Free radical polymerization · Inverse vulcanization · Elemental sulfur · Vegetable oils · Triglycerides · Green polymers

1 Introduction

Although the versatile properties and the cheap price of polymers have made them an inevitable part of almost every aspect of modern human life, the environmental disadvantages of petroleum-based polymers and their unsustainability have recently drawn a lot of attention. This has been followed by an ever-growing interest to develop alternative eco-friendly biopolymers [1, 2]. Petroleum-based polymers such as polypropylene, polyethylene, polystyrene, and nylon are widely used polymers that are made using petroleum-based monomers making them directly dependent on the oil industry [3, 4]. Biopolymers, on the other hand, are those polymers that are either naturally produced such as cellulose, natural rubber, wool, silk, proteins, and starch, or being produced using green bio-monomers derived from natural resources such as plants and animals [5–7]. In 2018, only around 2.1 million tons of bioplastics were produced globally. However and due to the versatile properties of biopolymers, their sustainability, and the cheaper price of initial monomers that they offer in many cases, it is expected to witness significant growth in their production in the upcoming years [2, 8, 9].

Among the bio-based monomers, vegetable oils have played an important role in the production of different classes of polymers including but not limited to polyesters, polyethers, polyurethanes, epoxies, and polyolefins [10–13]. Vegetable oils can be derived from almost every plant on this planet which makes them a cheap and readily available monomer [14]. Biopolymers using vegetable oils as monomers have been produced using different techniques such as cationic, condensation, free radical polymerization, and olefin metathesis reactions [10, 11, 15].

One of the latest applications of vegetable oils in the development of polymers and composite materials is in the production of sulfur-based polymers and organosulfur polymeric composites. The former is prepared by inverse vulcanization of elemental sulfur with either petro-based monomers such as 4-vinylbenzyl chloride (VBC) [16], 1,3-diisopropenylbenzene (DIB) [17], and 1,3,5-triisopropenylbenzene (TIB) [18] or pure bio-based vinylic monomers such as limonene [19], farnesene, and farnesol [20], whereas the latter is prepared by inverse vulcanization with vegetable oils [2, 21].

Inverse vulcanization is a polymerization technique that was first reported by Chung and coworkers [17] allowing elemental sulfur, naturally present in an eight-member ring form, to become bi-radical 8-member sulfur chains upon heating to its molten state, prompting the abundant sulfur to react with the available monomer forming sulfur-rich material [22]. If a petroleum-based or a pure bio-based monomer is used, a complete conversion of reactants takes place and thus a sulfur-based polymer is obtained [21]. On the other hand, if the monomer is a vegetable oil,

some sulfur remains unreacted and trapped in the formed polymeric structure giving an organosulfur polymeric composite [2, 23–25].

To date, there have been few review articles addressing the development of sulfur-based polymers, their preparation methods, properties, and applications [2, 21, 22, 26, 27]. However, review reports dedicated to organosulfur polymer composites have not appeared in the literature yet. Therefore, it is interesting to dedicate this chapter to review such green composite materials to promote more efforts to address their preparation reactions, processing techniques, and applications in various fields.

The scope of this chapter starts with a brief review of inverse vulcanization as a new technique of copolymerization of elemental sulfur with different monomers based on their resource origins.

Special attention is given to reactions of elemental sulfur with vegetable oils to produce organosulfur polymeric composites such as poly (S-rubber seed oil) and poly (S-corn oil), their properties, and potential applications. Finally, the challenges and the future perspective of this new class of sustainable and environmentally friendly polymeric composites are discussed.

2 Free Radical Polymerization of Sulfur at Molten State/ Inverse Vulcanization

Sulfur is an element that is naturally occurring in the soil surrounding volcanoes [28]. Currently, elemental sulfur can be found in high quantities mainly as a by-product of gas and petroleum refineries with an annual production of around 70 million tons, globally [20, 29, 30]. Although most of the elemental sulfur in refineries is being used in the production of sulfuric acid, gun powder, Portland cement, carbon disulfide, fertilizers, surfactants, detergents, and pesticides, vast amounts of sulfur are still left useless in open-air storages around the world that not only results in serious environmental challenges but also necessitates the search for brand new applications for this cheap and readily available material [22, 31].

Elemental sulfur consists of a yellow crystalline solid with an S_8 ring structure [28]. Elemental sulfur starts to melt at around 115 °C forming a yellow color liquid [32]. At some point above its melting temperature (around 159 °C), the molten elemental sulfur rings start to open and form bi-radical 8-member sulfur chains observable by a color change in the melt from yellow to orange [16, 29]. The ring-opened elemental sulfur starts to homopolymerize (form polysulfides) by keeping the heat. Nevertheless, the produced pure polysulfide is not stable and begins to depolymerize only after a very short time [17, 33].

Inverse vulcanization, first reported in 2013, is a recently developed polymerization technique that introduces a vinylic monomer(s) to sulfur at its molten state in order to produce sulfur-based polymers and organosulfur polymer composites that are stable and firm against depolymerization by time [17, 34]. When the ring-opening of the elemental sulfur begins above its floor temperature (159 °C), the sulfur melt

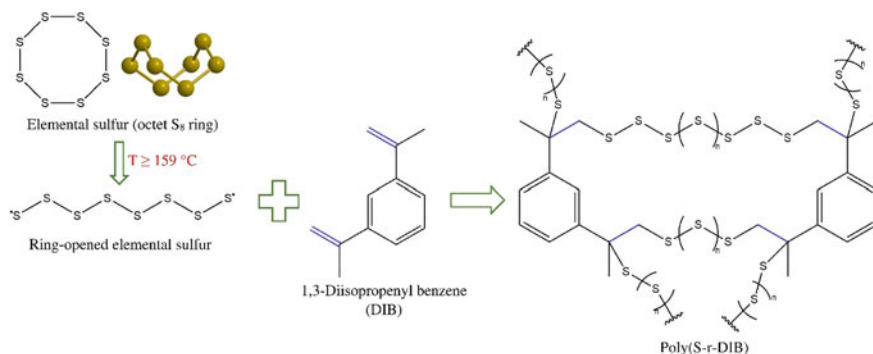


Fig. 1 Reaction of elemental sulfur at its molten state with DIB by free radical polymerization

color changes from yellow to orange [16, 29]. At this point, the comonomer will be gradually added to the melt under continuous stirring using a thermostatic oil bath while keeping the temperature constant prompting a free radical driven polymerization reaction. The vinylic bonds of the monomer open and form radicals, which react with the diradicals on the two ends of the sulfur chains forming polymeric chains [17, 35]. The reaction will be stopped after a specific amount of time, based on the monomer structure, desired properties, and the initial feed ratio. This technique does not require any type of solvents or initiators making it even more environmentally friendly and cost-effective [17, 33]. Inverse vulcanization was first reported by the utilization of petroleum-based monomers such as DIB to stabilize the ring-opened elemental sulfur chains into the polymeric structure. The resulted polymer demonstrated desirable properties such as shape-persistent stability and great electrochemical properties; however, DIB as a monomer is rather expensive and thus, the polymer was not quite economical [17, 20, 33]. Figure 1 shows the formation of a sulfur-based polymer using DIB as the comonomer.

The monomers that are already investigated in inverse vulcanization can be divided into three categories, i.e., Petroleum-based monomers, bio-based monomers, and vegetable oils [2, 22] among which only vegetable oils result in composite structures due to the presence of some unreacted elemental sulfur inside their polymeric structure. Petroleum-based and bio-based monomers can again be divided into different categories such as the number of vinylic groups or the structural properties (such as aromatic or aliphatic) [21, 22]. Based on the monomer type and in particular, the number of its vinylic groups, sulfur-based polymers can be linear to highly crosslinked polymers while demonstrating different properties from thermoplastics to thermosets with low or high stabilities against depolymerization by time [2, 29, 34, 36].

Most of the sulfur-based polymers that are already investigated were stabilized using petroleum-based monomers such as DIB [17], divinylbenzene (DVB) [37], styrene [36], TIB [18], bismaleimides (BMI) [38], 5-ethylidene-2-norbornene

(ENB) [33], VBC [16], 4-Vinylaniline [39], dicyclopentadiene [20], and 1,3-diethynylbenzene (DEB) [40], just to name a few. The main disadvantages of these monomers were first their high price and their petroleum-based nature which prevents obtaining polymers completely based on bio-based resources or waste materials. Most of the sulfur-based polymers made using petroleum-based monomers such as BMI, DVB, styrene, DEB, ENB, and DIB have been investigated as cathode materials in Li-S batteries [22, 41, 42]. It is noteworthy to mention that sulfur-based polymers can also be used in order to protect the Li-S battery anodes by forming a strong solid-electrolyte interphase layer on the Li anode [43, 44]. Some petroleum-based monomers were also used to prepare sulfur-based polymers with other applications such as lenses, insulators, and heavy metal adsorbents [18, 20, 22, 33].

Some renewable bio-based monomers have also been employed to be reacted with sulfur at its molten state. These bio-based monomers were mostly derived from plants and in some cases animals [2]. For instance, Cardanol benzoxazines [45], diallyl disulfide (DAS) [46], Eugenol allyl ether [47], squalene [34], and limonene [19, 20] which can be derived from cashew nuts, onions, and garlic, clove oil, shark liver, and citrus, respectively, are some of the bio-based monomers used in the production of sulfur-based polymers. Most of the produced polymers were used in mercury capture, palladium removal, and also as cathode materials in Li-S batteries [2, 48].

Furthermore, some vegetable oils have also been investigated in the production of organosulfur polymeric composites. However, due to the complex structure and the impurity of vinylic molecules of vegetable oils and also the composite structure of the products, there are more challenges and difficulties in the processing and characterization techniques of organosulfur polymeric composites made using vegetable oils, which requires more studies.

3 Overview of Organosulfur Polymeric Composites Using Vegetable Oils

Free radical polymerization can be extended to any vinylic, di-vinylic, multi-vinylic, or alkynyl monomers which are suitable to undergo reaction with thiyl radicals [16, 21]. Owing to environmental concerns associated with petroleum-based monomers and the high production cost of the bio-based monomers utilized in the inverse vulcanization process, Worthington and coworkers [25] introduced the utilization of vegetable oils as an alternative class of monomers for this facile method of polymerization. Later, other researchers extended this to many edible vegetable oils such as canola oil [25, 49–51], olive oil [24], corn oil [23], palm oil [52], sunflower oil [24], rice bran oil [53], soybean oil [54], and linseed oil [24]. But due to the food market demand for edible oils, Ghumman et al. [55, 56] reported the utilization of a non-edible oil (rubber seed oil) for the first time. The inverse vulcanized copolymers from non-edible oil demonstrated superior properties to edible oil-based copolymers [56]. In addition, there are some reports addressing this issue by utilizing waste cooking

Table 1 Unsaturated fatty acid composition of the vegetable oils used in the production of organosulfur polymeric composites (all numbers are in wt.%)

| | Oleic acid | Linoleic acid | Linolenic acid | Ricinoleic acid | Total unsaturated percentage | Ref. |
|-----------------|------------|---------------|----------------|-----------------|------------------------------|------|
| Castor oil | 5.5 | 7.3 | 0.5 | 84 | 97.3 | [57] |
| Canola oil | 56 | 26 | 10 | – | 92 | [58] |
| Linseed oil | 15.8 | 16.5 | 58.3 | – | 90.6 | [59] |
| Rubber seed oil | 14 | 75 | – | – | 89 | [58] |
| Olive oil | 78 | 7 | 1 | – | 86 | [58] |
| Sunflower oil | 30.7 | 55.0 | 0.1 | – | 85.8 | [60] |
| Corn oil | 31 | 52 | 1 | – | 84 | [58] |
| Soybean oil | 23 | 51 | 7 | – | 81 | [58] |
| Rice bran oil | 43.9 | 29.6 | 1.25 | – | 74.75 | [61] |
| Cottonseed oil | 16.35 | 52.89 | 0.17 | – | 69.41 | [62] |

oil in the production of sulfur-based polymers [25, 49, 51]. The unsaturated fatty acid compositions of all the vegetable oils utilized in the inverse vulcanization reaction are given in Table 1. In the case of the organosulfur polymeric composites using vegetable oils, the unreacted sulfur present in the final copolymer was the major concern for the scientists, to circumvent this issue, Ghumman et al. carried out the optimization of the inverse vulcanization reaction conditions using response surface methodology [55]. The molecular structures of the main unsaturated fatty acids of vegetable oils are shown in Fig. 2.

3.1 Preparation of the Organosulfur Polymeric Composites Using Vegetable Oils

Overall, the preparation method of all inverse vulcanized copolymers is similar with different reaction conditions. The initial steps include the melting of sulfur in a glass vial using a thermostatic oil bath under continuous stirring. The melted sulfur is then heated to a temperature above 159 °C to initiate the ring-opening of the eight-member ring sulfur and the formation of diradicals, which is indicated by the color change of melted sulfur from yellow to orange [2, 23]. At this point, the monomer (vegetable oil in this case) is added in a dropwise manner, and the mixture is allowed to undergo reaction for a required time under designed reaction conditions [21]. The reaction conditions used to produce different organosulfur polymeric composites using vegetable oils are summarized in Table 2.

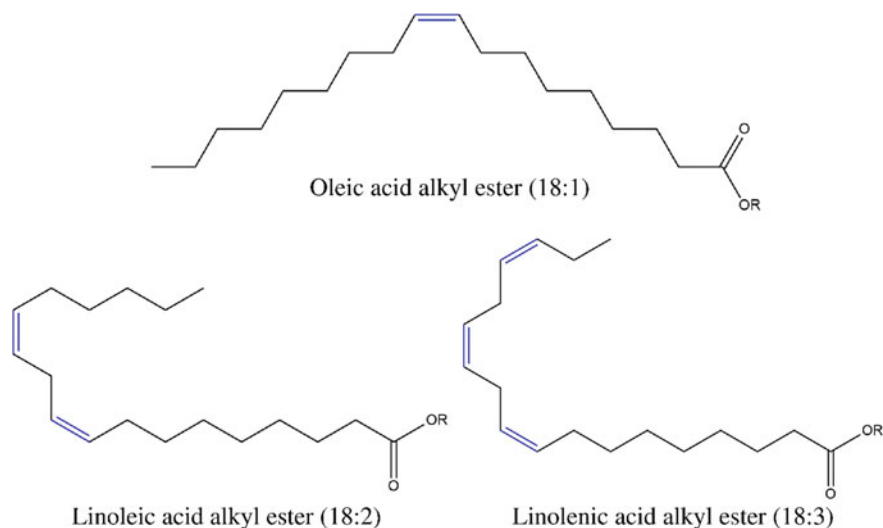


Fig. 2 Molecular structures of the main unsaturated fatty acid esters contained in the triglycerides of vegetable oils with their C:D ratio (number of carbon atoms:number of vinylic bonds)

Table 2 The reaction conditions used to produce organosulfur polymeric composites using vegetable oils

| Vegetable oil | Reaction temperature T (°C) | Reaction time t (min) | Initial sulfur feed ratio S (wt.%) | Ref. |
|-----------------------------------|-----------------------------|---------------------------------|------------------------------------|-------------|
| Corn oil | 170 | 60 | 50–80 | [23] |
| Linseed, Sunflower, and olive oil | 170 | 60 | 50–80 | [24] |
| Canola oil | 180 | 30 | 10–90 | [25, 49–51] |
| Rice bran oil | 170 | 30 | 50 | [53] |
| Soybean oil | 165 | 40 | 10–70 | [54] |
| Rubber seed oil | 164 | 73.7 | 50.57 | [55, 56] |
| Castor oil | 170 | 30 | 50 | [53] |
| Cotton seed oil | 160 | Until the reaction became solid | 20–60 | [63] |

3.2 Properties of the Organosulfur Polymeric Composites Using Vegetable Oils

The properties of the organosulfur polymeric composites highly depend on the reaction conditions and the composition of the vegetable oils used as monomers. For instance, the glass transition temperature (T_g) of the copolymer synthesized with

50 wt.% S employing rubber seed oil as the monomer is -6.41 °C, whereas the copolymer with 70 wt.% S using the same vegetable oil demonstrated a T_g of -7.85 °C [56]. This diversity in the properties of the organosulfur polymeric composites is attributed to the free radical polymerization process which results in random copolymers [17]. The properties of such polymeric composites and in particular, those using rubber seed oil and corn oil as monomers will be discussed and compared.

3.2.1 Physical Properties

The organosulfur polymeric composites using vegetable oils are usually brown colored with rubbery characteristics [21]. The mechanical strength of the polymers highly depends on the initial sulfur feed ratio with a reverse relationship [22]. An increase in the initial sulfur content increases the brittleness of the copolymers. For example, the copolymer synthesized with 50 wt.% S using rubber seed oil is dark brown and possesses rubbery properties where increasing the initial sulfur load decreases the intensity of the dark color and the rubbery behavior. The polymer with 90 wt.% S is very brittle in nature and shows light brown color [56]. This increase in brittleness of the copolymer is due to the increase in the amount of the unreacted sulfur left in the final copolymer which increases with increasing the initial sulfur content [55]. The overall mechanical strength of the organosulfur polymeric composites made using vegetable oils is way less than those made using petroleum-based monomers [21]. This difference is due to the incomplete reaction of sulfur and the presence of the unsaturated fatty acid portion of vegetable oils [2, 21, 22, 56].

Most of the vegetable oil-based organosulfur polymeric composites are reported to be insoluble in conventional organic solvents such as chloroform, toluene, hexane, heptane, acetone, dimethyl sulfoxide, dimethylformamide, ethanol, methanol, water, acetonitrile, and dichloromethane [23–25, 49, 51, 54–56, 63]. However, recently it was reported by Ghumman et al. that the copolymers produced from rubber seed oil are soluble in tetrahydrofuran (THF) [55, 56]. Also, it was initially believed that pyridine is a solvent able to dissolve sulfur-based polymers; nevertheless, it was found that pyridine actually breaks the S–S crosslinking of these polymers and thus converts them to more soluble polymeric chains [49, 64]. In general, there are several factors such as the degree of crosslinking and the initial sulfur content that directly affect the solubility of sulfur-based composites and it seems like the fatty acid composition of the vegetable oils plays the major role in the degree of crosslinking of the sulfur-based composites. In other words, polymers made using vegetable oils with more linoleic (2 C=C bonds) and linolenic (3 C=C bonds) acids demonstrate lower solubility values due to their highly crosslinked structures compared with those sulfur-based polymeric composites made by the inverse vulcanization of sulfur with those vegetable oils that include more oleic acid (1 C=C bond) [21]. The physical properties of the organosulfur polymeric composites made using vegetable oils are summarized in Table 3.

Table 3 The physical properties of the organosulfur polymeric composites made using vegetable oils

| Vegetable oil | Physical appearance | Solubility | Ref. |
|-----------------------------------|---|--|--------------|
| Corn oil | Brown color rubbery material, the color of the copolymer becomes lighter with the increase in sulfur content | Insoluble in all organic solvents | [23] |
| Linseed, sunflower, and olive oil | Brown rubbery material | Limited solubility in n-heptane | [24] |
| Canola oil | 10 wt.% S yielded a black liquid, 50–80 wt.% S yielded a dark brown color rubbery material | Partially soluble in CDCl_3^* , also, pyridine helps to break the S–S crosslinking of these polymers and thus converts them to more soluble species | [25, 49, 50] |
| Soybean oil | Brown color rubbery material | Not reported | [54] |
| Rice bran oil | Brown color rubbery material | Not reported | [53] |
| Rubber seed oil | Dark brown color rubbery material up to 80 wt.% S, but with 90 wt.% S, brittle, light brown color material obtained | Fully soluble in THF | [55, 56] |
| Castor oil | Brown color rubbery material | Not reported | [53] |
| Cottonseed oil | Dark brown rubbery material, the color became light brown with 60 wt.% S | Not reported | [63] |

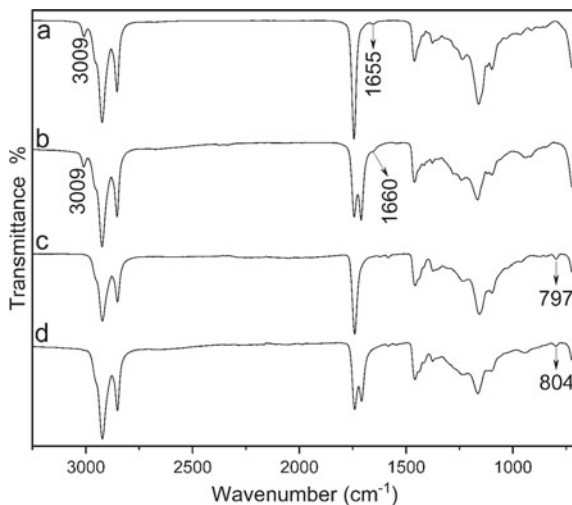
* CDCl_3 : Deuterated chloroform, or chloroform-d (C_2HCl_3)

3.2.2 Chemical Composition

Vegetable oils mainly consist of saturated and unsaturated fatty acids [2]. The reaction between sulfur and the unsaturated portion of oils is usually evident from the disappearance of the cis-alkene characteristic peaks from the Fourier transform infrared (FTIR) spectra of the copolymers. FTIR spectra of all the vegetable oils utilized for the inverse vulcanization showed the presence of C=C–H and C=C functional groups evident from the signals present at 3009 and 1660 cm^{-1} , respectively [23, 25, 54–56].

For instance, the FTIR spectra of corn oil and rubber seed oil are shown in Fig. 3 as references alongside the spectra of their resulting organosulfur polymeric composites (sulfur:oil is 50:50 in both cases). The pristine corn oil and rubber seed oil show signals at 1655 and 1660 cm^{-1} attributed to C=C stretching, respectively. The signals representing C=C–H stretching were also observed in the spectra of both vegetable oils. These signals completely vanish in the FTIR spectra of the

Fig. 3 FTIR spectra for **a** pristine corn oil, **b** pristine rubber seed oil, **c** Poly(S-corn oil) 50:50, and **d** Poly(S-rubber seed oil) 50:50



corresponding copolymers, which confirms the successful reaction of sulfur and the vinylic bonds, and as a result the formation of the polymeric structure. Moreover, new signals appeared at 797 and 804 cm⁻¹ for corn oil- and rubber seed oil-based copolymers, respectively, which are attributed to C–H rocking in the vicinity of C–S bonds which further proves the formation of copolymers [23, 24, 55, 56]. This is normal not to observe the C–S bonds in the case of the sulfur-oil polymers similar to some other sulfur-based polymers made using linseed oil and palm oil [24, 52]. The chemical composition of all the obtained organosulfur polymeric composites from the reaction of molten sulfur and vegetable oils are almost similar and such copolymers are not reported to possess any thiol groups.

3.2.3 Thermal Behavior

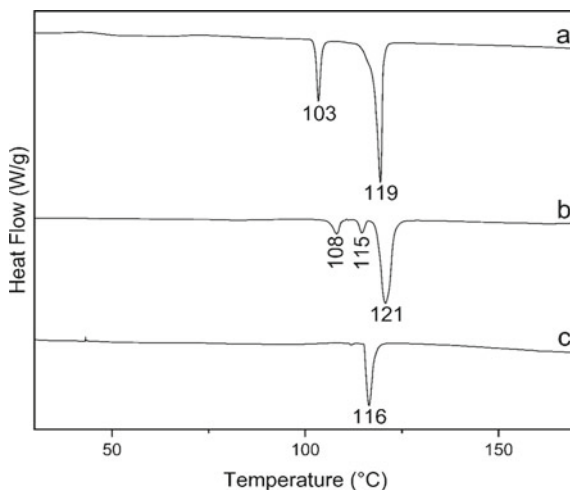
Thermal properties of the organosulfur polymeric composites are usually evaluated using differential scanning calorimetry (DSC). The DSC thermogram of elemental sulfur shows two melting peaks representing the structural transition of elemental sulfur to monoclinic from orthorhombic at 103 °C followed by the melting of the monoclinic at 119 °C [16, 23]. These endotherms evidence the crystalline structure of elemental sulfur. DSC thermograms of all the organosulfur polymeric composites obtained from the inverse vulcanization reaction of sulfur and vegetable oils showed melting peaks related to the sulfur crystals. The integrated area of those endotherms increases with increasing the initial sulfur load, and also by decreasing the reaction time [55, 56]. These observations show the influence of the reaction conditions on the thermal properties of the organosulfur polymeric composites. In the case of the polymers, the presence of the melting endotherms confirms the presence of unreacted

sulfur in the final product. This unreacted sulfur is due to the incomplete reaction of sulfur with oil.

Figure 4 shows the DSC thermograms of pure elemental sulfur and the organosulfur polymeric composites made by using corn oil and rubber seed oil (sulfur:oil is 70:30 in both cases). The thermograms of the copolymers confirm the presence of some unreacted sulfur due to the presence of melting endotherms related to sulfur crystals [23, 56]. Ghumman et al. found the amount of unreacted sulfur in the obtained copolymers made using rubber seed oil employing the calibration method and explained that the amount of sulfur left is highly dependent on the reaction conditions [55]. For instance, the organosulfur polymeric composite made using 70 wt.% initial sulfur load at a temperature of 170 °C yielded a product with 44.73% and 24.85% unreacted sulfur content for reaction times of 30 min and 60 min, respectively [55]. The amount of unreacted sulfur also depends on the ratio of the unsaturated fatty acid portion of the vegetable oil. For example, only 84% of corn oil consists of unsaturated fatty acids whereas rubber seed oil contains 89% unsaturated fatty acids which itself explains why the intensity of the melting endotherms of the corn oil-based organosulfur polymeric composite is more than the rubber seed oil-based organosulfur polymeric composite [55, 56].

Thermal stability of the organosulfur polymeric composites synthesized using vegetable oils can be evaluated using thermogravimetric analysis (TGA). All the polymeric composites obtained using vegetable oils as monomers were found to be thermally stable up to 200 °C, where the weight loss usually onsets with the decomposition of the loosely bonded sulfur and unreacted sulfur present in the copolymer [23–25, 54–56]. The pure elemental sulfur onsets to degrade at around 200 °C, and it will be completely decomposed at 360 °C, whereas the obtained organosulfur polymeric composites were found to be more stable than elemental sulfur, since they do not fully degrade even at 800 °C.

Fig. 4 DSC thermograms for **a** elemental sulfur, **b** Poly (S-corn oil) 70:30, and **c** Poly (S-rubber seed oil) 70:30



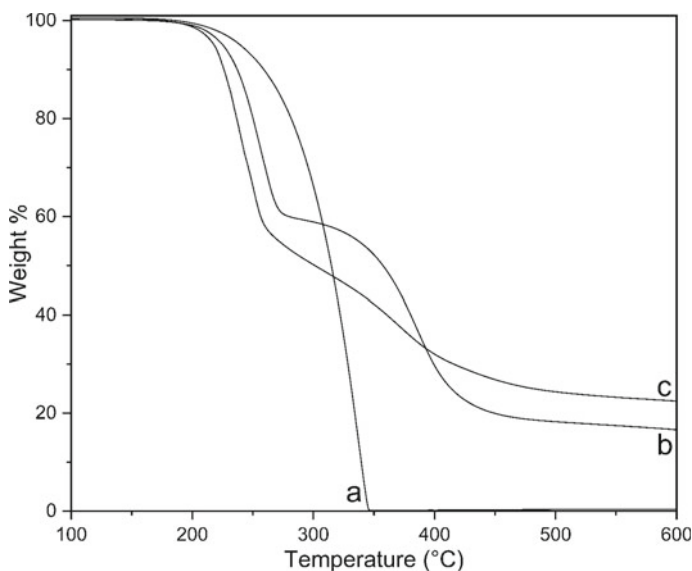


Fig. 5 TGA thermograms for **a** elemental sulfur, **b** Poly (S-corn oil) 50:50, and **c** Poly (S-rubber seed oil) 50:50

The TGA thermograms of elemental sulfur and the organosulfur polymeric composites obtained using corn oil and rubber seed oil (sulfur:oil is 50:50 in both cases) are shown in Fig. 5. It can be observed that the copolymers irrespective of the oil type start to decompose sooner compared to elemental sulfur. However, the char residue left at high temperatures in the case of the organosulfur polymeric composites indicates the formation of complex structures. At 800 °C, poly (S-rubber seed oil) shows a residue of 19.8 wt.%, whereas poly (S-corn oil) demonstrates a residue of 10.2 wt.% [23, 55, 56]. Both poly (S-rubber seed oil) and poly (S-corn oil) degrade in a three-step pattern. The first step of weight loss is due to the decomposition of the loosely bonded sulfur, and also the unreacted sulfur present in the composite structure and is almost identical for both polymers. In the second step, the polyunsaturated fatty acid part starts to decompose which is more prominent in the case of poly (S-corn oil). The third and final step of decomposition is due to the gradual decomposition of the monounsaturated acids and tightly bonded sulfur (C-S) [23, 55, 56].

3.2.4 Structural Properties

X-ray diffraction (XRD) can be used to study the structural properties of the organosulfur polymeric composites obtained by the inverse vulcanization technique. Most of the inverse vulcanized copolymers were found to be amorphous regardless of the type of monomer used. This is confirmed due to the absence of any crystalline

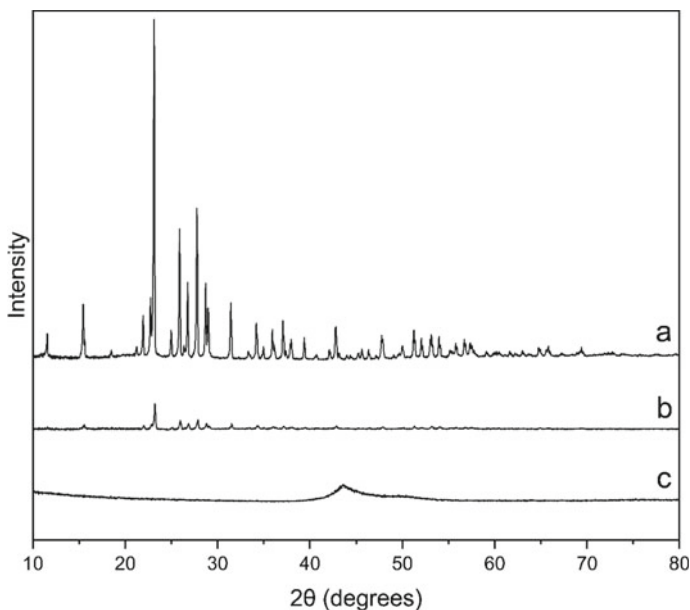


Fig. 6 Powder XRD patterns for **a** elemental sulfur, **b** Poly (S-corn oil) 50:50, and **c** Poly (S-rubber seed oil) 50:50

peaks related to copolymers. However, the diffractogram of the copolymers obtained using vegetable oils as monomers confirmed the presence of unreacted sulfur in the composite structure as peaks related to sulfur crystals appeared (at scattering angle 2θ of 23°, 26°, 27.9°, and 37°) [24, 25, 49, 54–56].

Figure 6 depicts the powder XRD diffractograms of elemental sulfur together with poly (S-corn oil) and poly (S-rubber seed oil) (sulfur:oil is 50:50 in both cases). The diffractogram of the poly (S-corn oil) shows some peaks related to the unreacted sulfur confirming the findings from DSC. It can be observed that the intensity of the peaks is higher in the case of poly (S-corn oil) compared with poly (S-rubber seed oil), which demonstrates a better sulfur conversion for poly (S-rubber seed oil) due to a higher percentage of unsaturated fatty acid portion in the rubber seed oil. The diffractograms clearly confirm the amorphous structure of the obtained organosulfur polymeric composites.

3.2.5 Morphological Properties

The morphological properties of the inverse vulcanized copolymers were evaluated using Scanning Electron Microscopy (SEM). The copolymers obtained from the inverse vulcanization of sulfur with vegetable oils have demonstrated composite-like morphology [23, 25, 56]. The SEM images revealed that the surfaces of the

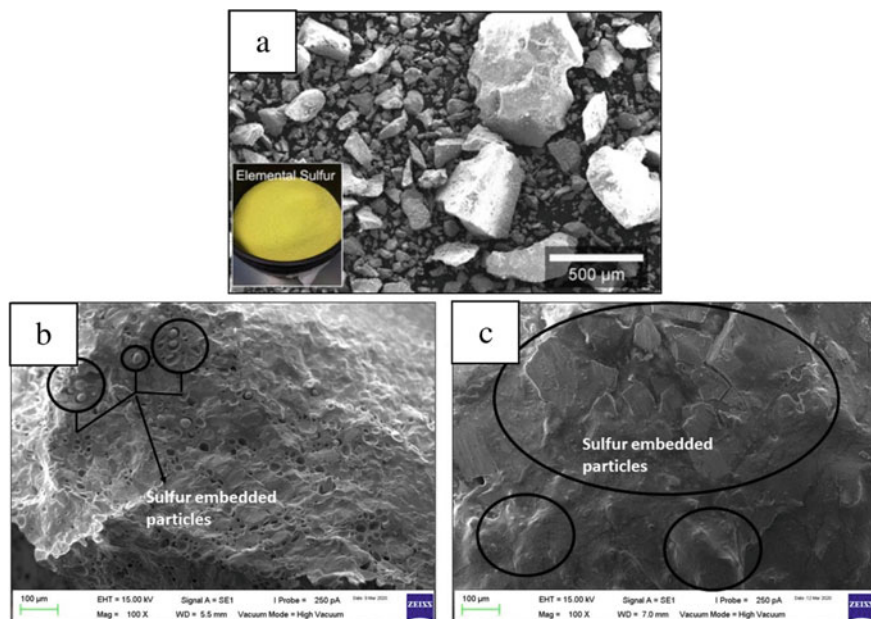


Fig. 7 SEM images of **a** elemental sulfur. Adapted from Moon et al. [65], with permission from Elsevier. Copyright (2016), **b** Poly (S-corn oil) 70:30, and **c** Poly (S-rubber seed oil) 70:30

copolymers contain a smooth surface as well as some isolated particles of unreacted sulfur [54].

Figure 7 displays the SEM images of poly (S-corn oil) and poly (S-rubber seed oil) (sulfur:oil is 70:30 in both cases) together with an SEM image of elemental sulfur as a reference. The SEM image of the poly (S-corn oil) shows that it contains a smooth surface and some isolated unreacted sulfur particles, whereas the poly (S-rubber seed oil) image depicted that it contains some embedded particles of the elemental sulfur. It can be observed that the corn oil's corresponding copolymer shows a microporous structure which is likely formed due to the release of H_2S gas caused by hydrogen abstraction [23, 55, 56]. However, poly (S-rubber seed oil) does not possess micropores, which confirms that there is no release of H_2S during the copolymerization of rubber seed oil with sulfur [55, 56].

3.3 Applications of the Organosulfur Polymeric Composites Using Vegetable Oils

The interesting properties of the organosulfur polymeric composites made using vegetable oils make them a suitable replacement for the conventional polymers in several applications to address many issues regarding the environment, energy, and

food [21]. Mercury is considered a serious source of health concern and its removal from wastewater has drawn a lot of attention [25, 48]. The organosulfur polymeric composites have been investigated as mercury-selective adsorbents due to their great affinity to mercury. Additionally, their color changes after adsorbing only a small amount of mercury which makes it possible to utilize them as mercury detecting devices. Salt-porogen was used to increase their surface area which showed a significant improvement in their mercury removal efficiency [25, 51, 53, 66]. To enhance the mercury adsorption capacity of the sulfur-based polymers, a modified sulfur-cottonseed oil polymer using nitrogen-containing modifiers showed considerable improvements [67]. A recent full review on mercury removal using sulfur-based polymers can be found elsewhere [48]. These copolymers were also found to be effective for iron removal from aqueous solutions [51]. Furthermore, Lundquist et al. [68] used an adsorbent containing sulfur-canola oil polymer and activated carbon for perfluorooctanoic acid and perfluorooctanesulfonic acid removal. The developed adsorbent acted as a support for powdered activated carbon and thus significantly decreased its risks. In another study, Lundquist and Chalker [69] reported lead adsorption using the same adsorbent structure with a great polymeric barrier that substantially decreased the lead leaching from the used adsorbent.

Organosulfur polymeric composites obtained using vegetable oils as monomers were also used as hydrophobic membranes to control the release of the nutrient from the NPK (Nitrogen, phosphate, and potassium) fertilizers [50, 54]. Composites of two different natural phosphate sources in an inverse vulcanized sulfur-soybean oil matrix also showed considerable improvements in the release of both sulfur and phosphate in soil [70]. These copolymers have also demonstrated promising performance as an active material for Li-S battery cathodes which is regarded as an attractive alternative to conventional batteries while also showing great potential as a new way for Li anode protection [24, 43, 44]. Moreover, sulfur-based polymers using vegetable oils as monomers have shown great potential to produce insulating composites, as recently, a mixture of wool and sulfur-canola oil polymer showed enhanced insulating and mechanical properties [71]. Although these composites have been investigated in several applications, it seems like more research is required to expand their scope of utilization.

4 Challenges and Future Perspective

Although several vegetable oils have already been investigated in the production of organosulfur polymeric composites, the obtained polymers and their polymerization process still face some challenges to be addressed. The stability of these polymers is one of the biggest challenges compared to the other sulfur-based polymers obtained by the reaction of pure monomers [54–56]. This can be addressed by defining a correct response to optimize the reaction conditions of the inverse vulcanization reaction to achieve the desired stability against depolymerization over time. Very few studies have reported the optimization of reaction conditions for organosulfur polymeric

composites to enhance the conversion of elemental sulfur [16, 55]. Particularly, the optimization of conditions for the reaction of sulfur and rubber seed oil including reaction temperature, time, and initial feed ratio was carried out to minimize the amount of unreacted sulfur in the obtained polymeric composites [55]. More work is needed to further establish the optimum conditions for various oils-sulfur systems and enhance the stability of organosulfur polymeric composites.

Nonetheless, the fact that some of these polymer composites are not firm enough against depolymerization over a period of time can be considered as an advantage in a number of applications such as slow-release fertilizers in which a biodegradable green product can be guaranteed while offering an improved efficiency compared to conventional fertilizer products [50, 54, 70]. Thus, additional investigations of the biodegradability of these polymers are highly needed to understand their mechanism of depolymerization and widen their applications.

Another big challenge to these organosulfur polymers is due to the presence of some unreacted elemental sulfur, and also the saturated portion of the vegetable oil that does not take part in the polymerization reaction in their structure [23, 24, 53]. This poses a real challenge to applications that require high purity such as cathode development for S-Li batteries. There have been few studies that investigated the elimination/reduction of the unreacted sulfur [16, 54] and oil present in the organosulfur polymeric structures by introducing a second crosslinker like dicyclopentadiene (DCPD) [70], or utilizing different vegetable oils with various triglyceride compositions [71]. In addition, such studies have addressed the tuning of the properties (e.g., solubility, color, glass transition temperature, molecular weight, and mechanical properties) of sulfur-rich polymer composites toward desired applications, but more research is highly sought to fully overcome these challenges [72, 73].

On the other hand, the thermodynamics and kinetics of sulfur/monomer and sulfur/oil polymerization reactions have not yet been investigated making it difficult to fully understand their mechanism of the reaction and ensure complete sulfur conversion [22]. This, however, can be a difficult task due to the complex composition of vegetable oils varying based on their species and the growing conditions [15]. More research is required to study the mechanism of the reaction of organosulfur polymeric composites made using vegetable oils.

The release of hydrogen sulfide gas during the polymerization process is another serious challenge, especially when reactions are carried out above 180 °C at high temperatures, which poses hazardous effects to human health and the environment [20, 25, 33, 74]. Moreover, H₂S released during the inverse vulcanization process directly affects the structure of the polymer and reduces the yield of the polymerization [23]. The release of H₂S gas can be also eliminated/minimized by optimizing the reaction conditions and by choosing lower reaction temperatures.

Finally, the recycling process of organosulfur polymers in relation to their applications must be taken into consideration to ensure that such a new class of polymers fully meets the requirements of green polymers. The biodegradable nature of these polymers can help their recycling process although it poses a limitation to their applications. Also, reusing sulfur-based polymers with the help of the chemical properties

of these polymers can be possible through further processing to help overcome the problem of reshaping these polymers using conventional methods such as extrusion or compression molding due to their thermosetting properties [21, 23]. For example, a new report introduced a new reactive compression molding method for sulfur-based polymers, particularly, a polymer made of sulfur-canola oil, in which the reactive interfaces of the sulfur-based polymer were brought into contact and as a consequence, a chemical reaction took place at the interfaces of the polymer by S–S metathesis making it possible to recycle this type of polymers [75].

The last issue that obscures the widening of the organosulfur applications is the lack of solubility in the conventional solvents, unlike the sulfur-based polymers made using petro-based monomers, making it difficult to process them using solution-based processing techniques such as electrospinning or solution casting and thus more investigation is required to identify new solvents or solvent combinations to address this issue [21–23].

5 Conclusion

Inverse vulcanization using vegetable oils as comonomers is a technique to obtain fully green organosulfur polymeric composites using bio-based monomers and waste residue. Organosulfur polymeric composites already made using vegetable oils employing the inverse vulcanization technique were reviewed based on their properties, reaction conditions, and applications. Due to the structural similarity of different vegetable oils, these polymers almost showed similar properties including product color, chemical composition, thermal properties, morphological properties, and structural properties. Most of these polymeric composites demonstrate brownish color which becomes lighter by increasing the sulfur load. Some of the composites show no solubility in organic solvents, while others were proved to be partially or fully soluble in a number of solvents. Depending on the molecular composition of each vegetable oil, the obtained polymer can be heavily crosslinked especially, if the unsaturated fatty acid portion of the vegetable oil consists of more linoleic and linolenic acids compared with oleic acid which has a single vinylic bond. Organosulfur polymeric composites using vegetable oils demonstrate either a two-step or a three-step weight-loss trend in which the first degradation step represents the decomposition of the loosely bonded sulfur and the unreacted sulfur present in the composite structure. These polymeric composites demonstrate a fully amorphous structure confirmed by XRD while melting peaks of different elemental sulfur crystalline structures were visible in DSC thermograms confirming the presence of unreacted elemental sulfur in most cases. Also, the SEM images of most of these polymers show a composite structure consisting of a smooth surface (polymeric structure) in which unreacted sulfur microparticles are embedded. These polymers can be directly used as they are in several applications such as heavy metal removal, slow-release fertilizers, and Li–S battery cathodes. However, more investigation is required in order to find brand new applications for this new class of environmentally friendly polymers as

well as to address the challenges among their properties and preparation such as their low stability against depolymerization in some cases, their composite structure which indicates the incomplete conversion of sulfur, lack of knowledge on their mechanism of the reaction, H₂S gas release especially at high temperatures, hard processing due to the highly crosslinked structure, and also their recycling and waste management.

References

1. M.R. Rahman, N.-A.A.B. Taib, M.K. Bin Bakri, S.N.L. Taib, in *Advances in Sustainable Polymer Composites*, ed. by Md. Rezaur Rahman. A volume in Woodhead Publishing Series in Composites Science and Engineering (Elsevier, 2020), p. 1
2. A. Abbasi, M.M. Nasef, W.Z.N. Yahya, *Sustain. Chem. Pharm.* **13**, 100158 (2019)
3. A. Rudin, P. Choi, *The Elements of Polymer Science and Engineering* (Elsevier, 2013), pp. 521–535
4. M. Nagalakshmaiah, S. Afrin, R.P. Malladi, S. Elkoun, M. Robert, M.A. Ansari, A. Svedberg, Z. Karim, in *Green Composites for Automotive Applications*, ed. by G. Koronis, A. Silva. A volume in Woodhead Publishing Series in Composites Science and Engineering (Elsevier, 2019), p. 197
5. N. Berezina, S.M. Martelli, in *Renewable Resources for Biorefineries*, ed. by C. Lin, R. Luque, Green Chemistry (Royal Society of Chemistry, 2014), p. 1
6. A. Shrivastava, *Introduction to Plastics Engineering*, 1st edn. (Elsevier, 2018), pp. 1–16
7. R. Mülhaupt, *Macromol. Chem. Phys.* **214**, 159 (2013)
8. R. Hatti-Kaul, L.J. Nilsson, B. Zhang, N. Rehnberg, S. Lundmark, *Trends Biotechnol.* **38**, 50 (2020)
9. C. Maraveas, *Polymers (Basel)* **12**, 1127 (2020)
10. K.F. Adekunle, *Open J. Polym. Chem.* **5**, 34 (2015)
11. M.R. Islam, M.D.H. Beg, S.S. Jamari, *J. Appl. Polym. Sci.* **131**(18), 40787 (2014)
12. N. Karak, *Veg. Oil-Based Polym: Properties, Processing and Applications*. (Woodhead Publishing, 2012), pp. 54–95
13. S. Miao, P. Wang, Z. Su, S. Zhang, *Acta Biomater.* **10**, 1692 (2014)
14. C. Zhang, T.F. Garrison, S.A. Madbouly, M.R. Kessler, *Prog. Polym. Sci.* **71**, 91 (2017)
15. Y. Xia, R.C. Larock, *Green Chem.* **12**, 1893 (2010)
16. A. Abbasi, M.M. Nasef, W.Z.N. Yahya, M. Moniruzzaman, A.S.M. Ghumman, *Eur. Polym. J.* **143**, 110202 (2021)
17. W.J. Chung, J.J. Griebel, E.T. Kim, H. Yoon, A.G. Simmonds, H.J. Ji, P.T. Dirlam, R.S. Glass, J.J. Wie, N.A. Nguyen, B.W. Guralnick, J. Park, Á. Somogyi, P. Theato, M.E. Mackay, Y.-E. Sung, K. Char, J. Pyun, *Nat. Chem.* **5**, 518 (2013)
18. T.S. Kleine, N.A. Nguyen, L.E. Anderson, S. Nannabat, E.A. LaVilla, S.A. Showghi, P.T. Dirlam, C.B. Arrington, M.S. Manchester, J. Schwiegerling, R.S. Glass, K. Char, R.A. Norwood, M.E. Mackay, J. Pyun, *ACS Macro Lett.* **5**, 1152 (2016)
19. M.P. Crockett, A.M. Evans, M.J.H. Worthington, I.S. Albuquerque, A.D. Slattery, C.T. Gibson, J.A. Campbell, D.A. Lewis, G.J.L. Bernardes, J.M. Chalker, *Angew. Chemie Int. Ed.* **55**, 1714 (2016)
20. D.J. Parker, H.A. Jones, S. Petcher, L. Cervini, J.M. Griffin, R. Akhtar, T. Hasell, *J. Mater. Chem. A* **5**, 11682 (2017)
21. A.S.M. Ghumman, M.M. Nasef, M.R. Shamsuddin, A. Abbasi, *Polym. Polym. Compos.* **29**(8), 1333 (2020)
22. A. Abbasi, M.M. Nasef, W.Z.N. Yahya, *Green Mater.* **8**(4), 172 (2020)
23. A. Abbasi, M.M. Nasef, W.Z.N. Yahya, M. Moniruzzaman, A.S. Ghumman, *Polym. Polym. Compos.* **29**(8), 1179 (2020)

24. A. Hoefling, Y.J. Lee, P. Theato, *Macromol. Chem. Phys.* **218**, 1600303 (2017)
25. M.J.H. Worthington, R.L. Kucera, I.S. Albuquerque, C.T. Gibson, A. Sibley, A.D. Slattery, J.A. Campbell, S.F.K. Alboaiji, K.A. Muller, J. Young, N. Adamson, J.R. Gascooke, D. Jampaiah, Y.M. Sabri, S.K. Bhargava, S.J. Ippolito, D.A. Lewis, J.S. Quinton, A.V. Ellis, A. Johs, G.J.L. Bernardes, J.M. Chalker, *Chem. - A Eur. J.* **23**, 16219 (2017)
26. Y. Zhang, R.S. Glass, K. Char, J. Pyun, *Polym. Chem.* **10**, 4078 (2019)
27. J. M. Chalker, M.J.H.H. Worthington, N.A. Lundquist, L.J. Esdaile, *Top. Curr. Chem. (Z)* **377**, 16.(2019)
28. D.A. Boyd, *Angew. Chemie Int. Ed.* **55**, 15486 (2016)
29. S. Diez, A. Hoefling, P. Theato, W. Pauer, *Polymers (Basel)* **9**, 59 (2017)
30. J.C. Bear, W.J. Peveler, P.D. McNaughter, I.P. Parkin, P. O'Brien, C.W. Dunnill, *Chem. Commun.* **51**, 10467 (2015)
31. R.W. Strickland, in *Riegel's Handbook of Industrial Chemistry*, ed. by J.A. Kent (Springer Netherlands, 1992), pp. 458–479
32. B. Meyer, *Chem. Rev.* **76**, 367 (1976)
33. J.A. Smith, X. Wu, N.G. Berry, T. Hasell, *J. Polym. Sci. Part A Polym. Chem.* **56**, 1777 (2018)
34. D.J. Parker, S.T. Chong, T. Hasell, *RSC Adv.* **8**, 27892 (2018)
35. J.J. Griebel, R.S. Glass, K. Char, J. Pyun, *Prog. Polym. Sci.* **58**, 90 (2016)
36. Y. Zhang, J.J. Griebel, P.T. Dirlam, N.A. Nguyen, R.S. Glass, M.E. Mackay, K. Char, J. Pyun, *J. Polym. Sci. Part A Polym. Chem.* **55**, 107 (2017)
37. I. Gomez, D. Mecerreyes, J.A. Blazquez, O. Leonet, H. Ben Youcef, C. Li, J.L. Gómez-Cámer, O. Bondarchuk, L. Rodriguez-Martinez, *J. Power Sources* **329**, 72 (2016)
38. M. Arslan, B. Kiskan, E.C. Cengiz, R. Demir-Cakan, Y. Yagci, *Eur. Polym. J.* **80**, 70 (2016)
39. Y. Zhang, T.S. Kleine, K.J. Carothers, D.D. Phan, R.S. Glass, M.E. Mackay, K. Char, J. Pyun, *Polym. Chem.* **9**, 2290 (2018)
40. J. Liu, B. Campbell, R. Ye, J. Bell, Z. Mutlu, C. Li, Y. Yan, M. Ozkan, C. Ozkan, *MRS Adv.* **2**, 3271 (2017)
41. R. Fang, J. Xu, D.-W. Wang, *Energy Environ. Sci.* **13**, 432 (2020)
42. X. Zhang, K. Chen, Z. Sun, G. Hu, R. Xiao, H.-M. Cheng, F. Li, *Energy Environ. Sci.* **13**, 1076 (2020)
43. G. Li, Y. Gao, X. He, Q. Huang, S. Chen, S.H. Kim, D. Wang, *Nat. Commun.* **8**(1), 850 (2017)
44. G. Li, Q. Huang, X. He, Y. Gao, D. Wang, S.H. Kim, D. Wang, *ACS Nano* **12**, 1500 (2018)
45. S. Shukla, A. Ghosh, P.K. Roy, S. Mitra, B. Lochab, *Polymer (Guildf)* **99**, 349 (2016)
46. I. Gomez, O. Leonet, J.A. Blazquez, D. Mecerreyes, *Chemsuschem* **9**, 3419 (2016)
47. A. Hoefling, D.T. Nguyen, Y.J. Lee, S.-W. Song, P. Theato, *Mater. Chem. Front.* **1**, 1818 (2017)
48. J.M. Chalker, M. Mann, M.J.H. Worthington, L.J. Esdaile, *Org. Mater.* **3**, 362 (2021)
49. M.J.H. Worthington, C.J. Shearer, L.J. Esdaile, J.A. Campbell, C.T. Gibson, S.K. Legg, Y. Yin, N.A. Lundquist, J.R. Gascooke, I.S. Albuquerque, J.G. Shapter, G.G. Andersson, D.A. Lewis, G.J.L. Bernardes, J.M. Chalker, *Adv. Sustain. Syst.* **2**(6), 1800024 (2018)
50. M. Mann, J.E. Kruger, F. Andari, J. McErlean, J.R. Gascooke, J.A. Smith, M.J.H. Worthington, C.C.C. McKinley, J.A. Campbell, D.A. Lewis, T. Hasell, M.V. Perkins, J.M. Chalker, *Org. Biomol. Chem.* **17**, 1929 (2019)
51. N.A. Lundquist, M.J.H. Worthington, N. Adamson, C.T. Gibson, M.R. Johnston, A.V. Ellis, J.M. Chalker, *RSC Adv.* **8**, 1232 (2018)
52. A. Abbasi, M.M. Nasef, W.Z.N. Yahya, M. Moniruzzaman, *E3S Web Conf.* **287**, 02014 (2021)
53. A.D. Tikoalu, N.A. Lundquist, J.M. Chalker, *Adv. Sustain. Syst.* **4**(3), 1900111 (2020)
54. S.F. Valle, A.S. Giroto, R. Klaić, G.G.F. Guimarães, C. Ribeiro, *Polym. Degrad. Stab.* **162**, 102 (2019)
55. A.S.M. Ghumman, R. Shamsuddin, M.M. Nasef, W.Z. Nisa Yahya, A. Abbasi, *Polymer (Guildf)* **219**, 123553 (2021)
56. A.S.M. Ghumman, M.R. Shamsuddin, M.M. Nasef, W.Z.N. Yahya, M. Ayoub, B. Cheah, A. Abbasi, *ChemistrySelect* **6**, 1180 (2021)
57. J. Salimon, D.A.M. Noor, A.T. Nazrizawati, M.M. Firdaus, A. Noraishah, *Sains Malays.* **39**(5), 761 (2010)

58. Typical Fatty–Acid Compositions of Some Common Fats, Portland State University. <https://web.pdx.edu/~wamserc/C336S12/fat.pdf>. Accessed 16 July 2021
59. A. Lewinska, J. Zebrowski, M. Duda, A. Gorka, M. Wnuk, *Molecules* **20**, 22872 (2015)
60. N. Vingerling, M. Oseredczuk, L. du Chaffaut, J. Ireland, M. Ledoux, Oléagineux. *Corps Gras, Lipides* **17**, 185 (2010)
61. R.B. Latha, D.R. Nasirullah, *J. Food Sci. Technol.* **51**, 335 (2014)
62. A. Yang, M. Qi, X. Wang, S. Wang, L. Sun, D. Qi, L. Zhu, Y. Duan, X. Gao, S. Ali Rajput, N. Zhang, *Food Sci. Nutr.* **7**, 1027 (2019)
63. Y. Liu, Y. Chen, Y. Zhang, Y. Chen, L. Wang, X. Zan, L. Zhang, *Polymers (Basel)* **12**, 10 (2020)
64. S.J. Tonkin, C.T. Gibson, J.A. Campbell, D.A. Lewis, A. Karton, T. Hasell, J.M. Chalker, *Chem. Sci.* **11**, 5537 (2020)
65. J. Moon, P.D. Kalb, L. Milián, P.A. Northrup, *Cem. Concr. Compos.* **67**, 20 (2016)
66. A.N. Rollinson, J. Bhuptani, J. Beyer, Y. Ismawati, T. Radu, *Int. J. Phytoremediation* **22**(13), 1431 (2020)
67. Y. Chen, A. Yasin, Y. Zhang, X. Zan, Y. Liu, L. Zhang, *Materials* **13**, 632 (2020)
68. N.A. Lundquist, M.J. Sweetman, K.R. Scroggie, M.J.H. Worthington, L.J. Esdaile, S.F.K. Alboaiji, S.E. Plush, J.D. Hayball, J.M. Chalker, A.C.S. Sustain, *Chem. Eng.* **7**, 11044 (2019)
69. N.A. Lundquist, J.M. Chalker, *Sustain. Mater. Technol.* **26**, e00222 (2020)
70. S.F. do Valle, A.S. Giroto, H.P.G. Reis, G.G.F. Guimarães, C. Ribeiro, *J. Agric. Food Chem.* **69**, 2392 (2021)
71. I.B. Najmah, N.A. Lundquist, M.K. Stanfield, F. Stojcevski, J.A. Campbell, L.J. Esdaile, C.T. Gibson, D.A. Lewis, L.C. Henderson, T. Hasell, J.M. Chalker, I. Bu Najmah, N.A. Lundquist, M.K. Stanfield, F. Stojcevski, J.A. Campbell, L.J. Esdaile, C.T. Gibson, D.A. Lewis, L.C. Henderson, T. Hasell, J.M. Chalker, *ChemSusChem* **14**(11), 2352 (2021)
72. J.A. Smith, S.J. Green, S. Petcher, D.J. Parker, B. Zhang, M.J.H. Worthington, X. Wu, C.A. Kelly, T. Baker, C.T. Gibson, J.A. Campbell, D.A. Lewis, M.J. Jenkins, H. Willcock, J.M. Chalker, T. Hasell, *Chem. – A Eur. J.* **25**(4), 10433 (2019)
73. C.V. Lopez, M.S. Karunarathna, M.K. Lauer, C.P. Maladeniya, T. Thiounn, E.D. Ackley, R.C. Smith, *J. Polym. Sci.* **58**, 2259 (2020)
74. M. Arslan, B. Kiskan, Y. Yagci, *Macromolecules* **49**, 767 (2016)
75. N.A. Lundquist, A.D. Tikoalu, M.J.H. Worthington, R. Shapter, S.J. Tonkin, F. Stojcevski, M. Mann, C.T. Gibson, J.R. Gascooke, A. Karton, L.C. Henderson, L.J. Esdaile, J.M. Chalker, *Chem. – A Eur. J.* **26**(44), 10035 (2020)

Index

A

- AA2024 alloy composite, 318
- Abrasion, 51, 99, 102, 152, 236, 252, 329, 345, 354, 356, 360, 361, 363, 427, 493, 594
- Abrasion resistance, 54, 360, 538
- Abrasive structure, 495
- Abrasive wear, 236, 242, 243, 252–254, 345, 349, 363
- Absorber, 161, 169, 175, 189, 198, 199, 225, 280, 285, 409
- Absorption, 17, 54, 134, 145, 147, 160, 161, 175, 191, 262, 278, 280, 369, 370, 372, 373, 377, 379, 380, 385, 410–412, 518, 557, 594
- Absorptivity, 5, 143
- Accelerator, 197
- Acetic, 272
- Acetic acid, 19
- Acetone, 160, 241, 243, 293, 608
- Acid blue, 475
- Acid hydrolysis, 276, 277, 281
- Acidic medium, 279
- Acidity, 465
- Acid targets, 68
- Acoustic absorption, 175
- Acrylate, 99, 122, 146, 156, 157, 170, 403
- Actin, 275
- Activated carbon, 233, 236, 246, 249, 251, 263, 463, 474–477, 481, 497, 506–509, 513, 520, 615
- Actuators, 24, 52, 124, 128, 132, 137, 145, 156, 157, 163, 176, 279
- Additive manufacturing, 121, 122, 124, 125, 139, 141, 149, 151, 158, 160, 170, 176, 537, 544, 565, 592
- Additives, 75, 124, 127, 140, 163, 192, 194, 284, 460, 541, 542, 577–579, 581, 583, 585, 588
- Adhesion, 51, 98, 133, 148, 272, 280, 283, 284, 331, 354, 401, 427, 496, 572, 574
- Adhesive wear, 236, 362
- Adsorbent, 59–66, 68–73, 75–78, 81, 82, 87, 88, 289, 395, 412, 451, 452, 463–465, 468, 470, 471, 473–476, 480, 492, 497–499, 501–503, 505, 506, 519, 521–524, 605, 615
- Adsorbent composite, 491, 501, 502, 505–519, 522–525
- Adsorption, 5, 61–66, 68, 70, 76, 78, 83, 85, 87, 274, 286, 295, 377, 382, 412, 451, 453, 462–464, 468, 471–476, 482, 483, 491–493, 497–502, 504–507, 517–524
- Adsorption capacity, 64, 65, 71, 73, 78, 81, 85, 412, 452, 456, 470, 472, 474–476, 478–482, 492, 499–501, 503–506, 516, 519, 520, 615
- Adsorption efficiency, 82
- Adsorption isotherms, 474, 499
- Adsorption mechanism, 68, 82, 88, 464, 497, 504, 523
- Advantage, 8, 24, 25, 29, 39–41, 44, 45, 60, 63, 66, 70, 72, 78, 85, 87, 121, 127, 136, 137, 141, 148, 149, 158, 160, 161, 163, 169, 171, 173, 174, 176, 177, 189, 196, 271, 274, 289, 345, 369, 393, 407, 427, 452, 454, 455, 460, 462, 464, 495, 496, 498, 539, 543, 553, 557, 559, 583, 585, 586, 594, 616

- Aeroengine, 538
 Aerogels, 39, 114, 288, 289, 407, 523
 Aeronautics, 43, 121, 134
 Aerospace, 1, 5, 8, 14, 24–26, 29, 37, 39, 42, 45, 121, 173, 236, 318, 319, 344, 346, 409, 537–540, 559, 594
 Aerospace industry, 26, 39, 173, 364
 Agglomeration, 15, 17, 40, 65, 78, 81, 99, 235, 243, 249, 251, 255, 259, 263, 404, 427, 493, 538, 588
 Aging, 299, 468, 470, 554, 555, 557, 560
 Aging temperature, 554, 555
 AGr-6 alloy composite, 317
 Agrochemicals, 492
 Agro-industrial residues, 491
 Air, 23, 24, 27, 148, 151, 164, 235, 238, 240, 241, 277, 319, 386, 427, 452, 476, 479, 480, 540, 554, 587
 Aircraft brakes, 24, 25
 Al₂O₃, 42, 52, 53, 191, 235, 237, 318, 424–427, 431, 444, 455, 460, 462, 468, 473, 478, 481, 483, 538, 579, 580, 596
 Alcohol, 122, 129, 194, 276, 281, 321, 396
 Alginate, 46, 269, 275, 280, 286, 289, 294, 298, 300, 303, 514–516
 Alkali, 279, 285, 402, 455, 456, 458, 462, 470
 Alkaline, 76, 279, 281, 454–456, 460, 462, 465, 468, 470, 471, 519
 Alkoxy group, 272
 Alkyl, 19, 272
 Alkyl group, 272
 Alloy, 7, 8, 15, 24, 25, 27, 42, 50, 156, 189, 190, 201, 318, 319, 326, 329–332, 339, 340, 397, 399, 424, 426, 427, 540, 542, 544, 557, 558, 565, 575–581, 586, 587, 592
 Alloy coatings, 347, 577
 Alloy composites, 317–320, 322, 326–333, 336, 337, 339, 340, 343–347, 350–356, 358–361, 363, 364, 426
 Alumina, 7, 11, 24, 25, 53, 100, 235, 344, 350, 360, 404, 424, 426, 454, 460, 463, 465, 468, 470, 473, 480, 513, 517, 523, 579
 Aluminium, 319, 328, 343–345, 347–353, 357–359, 361–364, 423–425, 427, 428, 431, 440, 465
 Aluminium oxide, 349–351, 359
 Aluminosilicate, 452, 453, 455–457, 462, 463, 470, 476, 480
 Aluminum foam, 191
 Aluminum powder, 8
 Amine, 62, 64, 243, 277, 371, 398, 403, 508, 513, 519, 523
 Amine groups, 21, 280, 371, 405
 Amine nitrogens, 271
 Amino acid, 275, 280
 Ammo level, 95
 Ammonium peroxydisulfate, 16
 Ammonium persulfate, 287, 288, 290
 Ammunition, 98, 104
 Amorphous, 7, 40, 272, 276–278, 293, 457, 460, 463, 470, 473, 474, 522, 523, 577, 612, 613, 617
 Analcime, 466, 478
 Analysis of variance (ANOVA), 323, 335, 336, 340, 354, 356, 358, 359, 428, 436, 437
 Aniline, 16, 19, 271, 272, 287–290
 Anionic, 279, 280, 289, 474, 497, 506, 520
 Anisotropic, 3, 4, 10, 170, 236, 398, 424
 Anisotropy, 138, 496
 Annealing, 344, 350, 386, 400, 558–560, 583
 Antibacterial, 45, 47, 48, 170, 286, 413
 Antibacterial activity, 47, 48, 170, 300
 Antibiotics, 46, 73, 85
 Antimicrobial, 39, 46–48, 50–52, 54, 171, 279, 299, 300
 Antimicrobial activity, 46, 54, 155, 279, 300
 Antioxidant, 39, 50, 279, 286, 299, 300
 Anti-welding, 579
 Application, 1, 4, 5, 7, 8, 10, 11, 13, 14, 23–29, 37–40, 42–46, 48, 49, 51–55, 59, 60, 62, 63, 65–67, 70–75, 77, 79, 82–84, 86, 87, 102, 121, 125, 127, 128, 132, 134, 137–139, 145, 148–150, 154–157, 161, 163, 164, 166–174, 176, 177, 188, 190, 202, 234, 236, 237, 240, 245, 246, 262, 269, 270, 273, 274, 276–291, 293–295, 297–300, 302, 303, 318, 319, 323, 340, 345, 348, 349, 364, 369–371, 382, 384–387, 391, 392, 397, 400, 401, 406, 407, 409–414, 424, 427, 435, 447, 451, 453, 454, 460, 463, 469, 471–473, 476, 481, 482, 492, 493, 496, 497, 499, 506, 519–521, 523–525, 539, 541, 554, 558, 565, 566, 569, 593, 594, 601–603, 605, 614–617
 Aramid, 12, 23, 24, 26, 29, 95, 97, 98, 113, 146

- Aramid/epoxy, 95, 96, 105, 109, 110
Aramid/epoxy composites, 95, 96, 105, 109, 110
Aramid fabric, 98, 99, 102, 103, 107, 109, 113, 114
Arc erosion, 570–573, 575, 578, 579, 581–583, 588, 592
Arc erosion resistance, 567, 569, 573, 579, 588, 594
Arc melting, 548
Areal density, 98, 104, 110, 115
Arhar fiber, 235, 236, 238, 245, 246
Armors, 23, 24, 93–95, 98, 111, 114, 128, 354
Aromatic components, 63, 78
Aromatic ring, 17, 97, 272, 274, 508, 519
Artificial vessel stents, 169
Aspect ratio, 11, 78, 277, 405, 406, 414, 549, 556
Athermal effect, 557, 558
Atomic, 8, 38, 40, 198, 286, 392, 393, 401, 408, 497, 543, 557
Atomic force microscopy (AFM), 291, 292, 395, 445
Atomic number, 189, 198
Atom transfer radical polymerization (ATRP), 403
Attapulgite (ATP), 62
Attenuation, 160, 189–196, 201, 202, 225, 376, 380
Attenuation properties, 189–191, 193–196
Attenuator, 189
Attraction, 173, 475, 498
Attractive force, 498
Auger recombination, 381
Automation, 173, 543
Automobile, 23–25, 27, 39, 42, 43, 234, 318, 354, 364, 497, 568
Automobile industry, 236, 318, 344, 540
Auxetic, 121, 128, 131, 134, 145, 147, 148, 175, 176
Auxetic response, 166
Auxetic structures, 134, 147, 148, 175, 176
Avrami kinetic constant, 504
- B**
Back face, 95, 101, 104, 109, 111
Back face deflection, 93, 98, 99, 104, 111
Backing clay, 104
Backscattered electron imaging, 556
BaCO₃, 191
Bacterial cellulose, 277, 285, 287–289, 302, 513, 524
Baking, 5
Ballistic applications, 93, 96, 99, 100, 102, 103
Ballistic behavior, 102–104
Ballistic impact, 100–110, 112, 113, 115
Ballistic impact mechanisms, 93, 94, 103, 104
Ballistic limit value, 99
Ballistic limit velocity, 99, 101
Ballistic performance, 98–100, 105, 110, 111, 114, 115
Ballistic resistance, 99
Ballistics, 23, 24, 93–95, 97–100, 102–104, 110, 111, 113–115, 128
Ballistic shot, 96
Ballistic test, 93, 98–101, 104, 108, 109, 111, 114
Ballistic test setup, 104
Ballistic threat, 94, 95, 101, 115
Ball mill, 161, 460, 543
Ball milling, 38, 165, 238, 404, 452, 454, 460–462, 483, 542
Bamboo, 235, 246
Bandgap, 405, 408
Barrier, 1, 50, 154, 161, 167, 276, 279, 394, 395, 410, 615
Basalt, 12
Basalt fabric, 98
Basalt fiber, 194
Base alloy matrix, 328
BaSO₄, 191
BaTiO₃, 52, 192
Battery, 1, 39, 53, 274, 288, 301, 395, 410, 615, 616
Beam, 28, 108, 126, 127, 139, 156, 163, 168, 198, 200–202, 380, 540, 544, 594
Beam splitter, 372
Bearing material application, 318, 339
Bentonite, 507, 509, 510, 517, 522
Benzophenone, 194
Benzoxazine, 605
Benzoxazine resin, 192
Bevel gear, 343
Bi₂O₃, 52, 191–195
Bi₂O₃ nanoparticles, 193, 195
Bibliometric analysis, 125, 491, 493, 505, 506
BiClO, 193
Binder, 43, 51, 125, 126, 407, 494, 585
BiNO, 188, 189, 201–203, 206, 209, 210, 225
Bioactivity, 154, 279, 413

- Biochar, 233, 236, 246, 263, 497, 506, 509, 510, 519, 520, 522
- Biocompatibility, 47, 48, 53, 82, 170, 171, 279, 281, 285, 286, 392, 413, 541
- Biocompatible, 73, 151, 154, 170, 171, 280–284, 294, 497
- Bio-composite, 29, 235, 236
- Bio-composite gear materials, 235
- Biodegradability, 141, 279, 281, 295, 616
- Biodegradable, 275–277, 281–285, 297, 386, 413, 425, 616
- Biodegradable polymers, 270, 275, 280, 282, 289
- Biofluid, 73, 85, 280
- Biological markers, 370
- Biological molecules, 59, 79
- Biomass, 263, 276, 278, 406, 472, 480, 520
- Biomass ash, 454, 469, 472, 473, 482
- Biomaterials, 170, 171, 281, 284, 294, 299, 392
- Biomedical materials, 121
- Biomedical purpose, 275
- Biomimetic, 146, 154, 170, 171
- Biomimetic materials, 154
- Biomimetic structures, 174
- Bio-monomers, 602
- Biomorphic, 137
- Bionanocomposite, 290, 297
- Bioplastics, 602
- Biopolymer, 275, 276, 282–284, 293, 398, 519, 601, 602
- Biosensor, 45, 49, 171, 286, 295, 297, 298, 303, 391, 413
- Bismaleimide resins, 5
- Bismuth nitrate, 187
- Bismuth nitrate pentahydrate, 189, 195
- Bismuth oxide, 190, 194
- Bismuth trioxide, 192, 194
- Bismuth tungstate, 512, 522
- Bisphend-A, 192
- Bisphenols, 71, 80
- Blast furnace slag (BFS), 454, 460, 468, 473
- Blending, 43, 85, 326, 394, 408
- Blood, 128, 170, 289, 414, 541
- Body armor classifications, 96
- Bonding, 17, 21, 28, 42, 75, 76, 83, 85, 126, 154, 168, 235, 243, 245, 246, 252, 256, 258–260, 318, 331, 363, 392, 394, 408, 496, 499, 541, 597
- Bonding strength, 327, 328, 498
- Bone, 27, 47, 48, 53, 146, 164, 165, 170, 171, 174, 281–283, 520, 541
- Bone tissue engineering, 169
- Borax, 194
- Boron, 12, 23, 24, 26, 189, 234, 549
- Boron carbide, 25, 195, 196
- Boron nitride, 93, 101, 124, 190, 408
- Boron nitride nanoplatelets (BNNP), 123, 155, 160, 171
- Bottom-up, 38, 158, 161, 405
- Boundary condition, 114, 134, 138, 375, 379
- Boundary representation, 122, 133
- Brittle, 7, 8, 102, 236, 249, 251, 258–261, 282, 294, 345, 496, 539, 543, 553, 608, 609
- Building, 23, 28, 70, 71, 121, 125, 153, 159, 171, 285, 392, 396, 456, 463
- Bullet, 95, 96, 98, 101, 104, 106, 107, 109, 111
- Bullet expansion, 111
- Bullet-proof vests, 102
- Byproduct, 281–283, 491, 601
- C**
- Cable, 24, 174, 240, 566
- Cadmium oxide, 190, 193, 579
- Calcium oxide, 100
- Calibration, 100, 611
- Camphor sulfonic acid, 16
- Canola oil, 425, 605–607, 609, 615, 617
- Capacity, 61, 69, 83, 88, 138, 149, 171, 277, 299, 413, 442, 452, 455–457, 464, 465, 468, 470, 471, 473–476, 478, 479, 498, 520, 524, 540, 560, 569
- Car, 25, 168, 414, 568, 569
- Carbide, 24, 318, 358, 427, 495
- Carbohydrate, 85, 275, 276, 278
- Carbon, 1–3, 8, 10–12, 23, 25–27, 29, 41, 42, 45, 62, 65, 75, 78, 81, 82, 87, 101, 102, 114, 123, 124, 128, 143, 147, 149, 151, 159, 165, 175, 234, 236, 238, 246, 270, 272, 273, 277, 282, 283, 290, 346, 392, 393, 396, 403, 406, 408, 467, 470, 473, 474, 477, 481, 482, 494, 515, 520, 523, 542, 552, 579, 581, 607
- Carbon-based additives, 579
- Carbon-based composite, 497
- Carbon black, 43, 54, 62, 143, 145, 195, 196, 270, 581
- Carbon composite, 1, 2, 8, 25, 26, 165, 396, 397, 409, 456, 473–475, 520
- Carbon dioxide, 299

- Carbon disulfide, 603
- Carbon emissions, 568
- Carbon fiber, 5, 9, 10, 23, 24, 26, 27, 42, 60, 61, 87, 101, 102, 114, 123, 131, 144, 147, 149, 168, 172, 234, 235, 393, 409
- Carbon fiber composites, 10, 101, 114
- Carbon fiber reinforced composites (CFRC), 93, 101, 102, 149, 235
- Carbon materials, 60, 63, 65, 66, 75, 85, 161, 392
- Carbon monoxide, 568
- Carbon nanotube, 2, 4, 11, 15, 41, 43–45, 51, 54, 60, 93, 99, 101, 122, 124, 131, 165, 347, 386, 392, 395, 397, 399, 403, 406, 408, 412, 425, 426, 445, 497, 506, 512, 521, 522, 538, 542, 548, 579
- Carbon nitride, 87, 512
- Carbon quantum dots (CQDs), 81, 82
- Carbon steel fibers, 495
- Carboxy groups, 371
- Carboxylic acid groups, 403, 521
- Cartilage, 53, 146, 170, 280, 283, 289
- Cashew nutshell Oil, 423, 428, 432, 436, 438, 441, 445, 447
- Casting, 42, 197, 327, 345, 346, 348, 349, 351, 354, 358, 359, 542, 543, 545, 560, 583, 585, 596
- Castor oil, 425, 606, 607, 609
- Catalysis, 39, 40, 274, 295, 398, 400, 401, 407, 482
- Catalyst, 37, 39, 40, 43, 157, 270, 274, 283, 284, 301, 395, 397, 401, 403, 404, 411, 412, 464, 525
- Catalytic activity, 400, 401, 408, 475
- Cathode, 43, 53, 301, 399, 573, 616
- Cathode materials, 605
- Cationic, 274, 279, 280, 289, 413, 452, 474, 480, 482, 497, 506, 513, 517, 519, 522, 602
- Cation removal, 473, 478, 481
- CaWO₄, 192
- CCD camera, 372
- CdTe, 191
- Cell, 39, 40, 46, 48, 49, 53, 86, 133–135, 143, 145–148, 151, 154, 160, 164, 167, 169–171, 188, 191, 275, 276, 278–284, 294, 299, 301, 303, 391, 392, 407, 410, 413, 414, 519, 541
- Cellular, 50, 121, 135, 145, 146, 151, 168, 170, 412
- Cellular architected materials (CAM), 122, 134, 137, 139–142, 177, 236
- Cellular materials, 127, 134, 148
- Cellular printed composites, 131, 141, 168, 169
- Cellulose, 145, 146, 154, 238, 269, 270, 275–279, 286–289, 291, 293–300, 302, 303, 386, 511, 515, 521, 602
- Cellulose nanocrystals (CNC), 277, 284, 290–292, 515
- Cellulose nanofiber (CNF), 75, 81, 82, 123, 147, 191, 277, 286–288, 292, 295
- Cellulose whiskers, 277
- Cellulosic fiber, 10, 288
- Cement composites, 192
- Ceramic, 2, 3, 7, 11, 14, 25–27, 39–42, 48, 52, 53, 94, 95, 124, 156, 161, 166, 176, 189, 190, 318, 403, 404, 477, 478, 480–482, 493, 495, 496, 541, 544, 585, 588
- Ceramic matrix, 1, 3, 7, 14, 25, 41, 42, 505
- Ceramic particles, 329, 344, 348, 363, 588, 589, 596
- Ceramic powder, 40, 404
- Ceramic reinforcements, 424, 538, 543, 596
- Ceramics, 361
- Chains, 62, 97, 151, 270, 273–277, 279–283, 285, 287, 291–293, 602–604, 608
- Chain-shaped, 196
- Chang-Chang failure criteria, 111
- Characteristics, 17, 19, 21, 38, 42, 47, 48, 51, 62, 72, 75, 82, 83, 85, 87, 102, 103, 132, 154, 169–171, 173, 174, 176, 189–196, 200, 201, 233, 234, 236, 243, 254, 263, 270, 272, 274, 301, 317, 318, 320, 323, 325, 327, 337, 343–345, 348, 355, 359, 364, 374, 385, 391, 394, 403, 405, 407, 408, 411, 412, 424, 426, 445, 446, 452, 453, 456, 465–467, 476, 492–494, 505, 506, 520, 521, 538, 541, 544, 548, 551, 608, 609
- Charge transfer, 496
- Charge transport, 290
- Charpy pendulum, 102
- Chemical, 2, 3, 10, 11, 14, 23, 26, 28, 38–42, 45, 48, 50, 60, 64, 65, 70, 72, 76, 78, 82, 97, 99, 100, 158, 161, 164–166, 174, 189, 201, 202, 240, 246, 270–275, 277, 279, 280, 285, 287, 288, 290–293, 295–298, 301, 354, 357, 373–375, 378–380,

- 382–385, 392–394, 396, 398, 405, 407, 408, 428, 446, 451, 454, 455, 466, 469, 474, 476, 478, 480, 491–493, 497–499, 506, 519–522, 524, 541, 543, 544, 566, 594, 609, 610, 616, 617
- Chemical adsorption, 464, 498, 522, 524
- Chemical grafting, 288
- Chemical pollutants, 451
- Chemical precipitation, 38, 476
- Chemical reduction, 395, 396, 398, 403
- Chemical reduction method, 407
- Chemical reduction of graphite derivatives, 395
- Chemical resistance, 37, 54, 99
- Chemical stability, 45, 64, 65, 70, 71, 75, 82, 272, 293, 505, 523, 524, 565
- Chemical synthesis, 38, 271–274
- Chemical vapor deposition, 38, 42, 82, 384, 385, 395, 401, 410
- Chip stack, 171
- Chitin, 46, 275, 279, 286, 297, 298, 519
- Chitosan, 19, 21, 22, 65, 76, 85, 269, 270, 279, 280, 286, 291, 293, 298, 300, 303, 405, 412, 413, 475, 477–479, 481, 497, 506–508, 514, 519, 523
- Chromatography, 68, 71
- Chromium, 50, 289, 478
- Circuit, 28, 29, 52, 128, 143, 148, 167, 174, 274, 301, 385, 414, 565, 566, 571
- Circulating fluidized bed fly ash (CFA), 454–458, 460, 467–469, 473–476, 480
- Classification, 1, 3, 5, 8, 125, 128, 133, 249, 396, 491, 493–497
- Clay, 192, 235, 397, 480, 506, 520, 522
- Clay minerals, 522
- Clay-polyethylene composites, 192
- Clinical application, 169
- Coagulation, 492
- Coagulation precipitation, 476
- Coalescence, 165
- Coal fly ash, 454, 457, 460, 467, 468, 474, 478
- Coating, 13, 41, 42, 45, 46, 51, 54, 63, 68, 83–85, 87, 98, 143, 151, 158, 173, 279, 281, 287, 288, 330, 345–350, 356, 371, 375, 391, 414, 478, 576, 577, 588
- Cobalt Octoate, 197
- Cobalt Octoate accelerator, 197
- Coconut oil, 425
- Coconut shell, 235
- Coding, 188
- Coefficient of friction, 322, 330, 332, 334, 338–340, 345, 353, 354, 423–426, 432
- Coefficient of thermal expansion, 3, 6, 12, 24, 285, 349, 406, 427
- Collagen, 270, 275, 281
- Colloidal, 14, 40, 42, 50, 377, 404, 521
- Colloidal processing, 404
- Colloids, 38, 377
- Column solid-phase extraction, 60, 63, 64, 87, 88
- Combat vehicles, 538
- Combustion-assisted casting, 543
- Combustion-assisted synthesis (CAS), 543
- Commercial software, 111
- Compacting, 585, 589
- Complex, 29, 59–61, 65, 67, 70–72, 75, 76, 81, 88, 95, 103, 127, 129, 137, 148, 149, 152, 154, 159, 162, 163, 165–167, 169, 170, 172–174, 176, 177, 196, 279, 282, 411, 413, 427, 453, 537, 543, 544, 549, 555, 560, 565, 592, 616
- Complex geometry, 121, 125, 127, 128, 130, 131, 133, 134, 136–139, 141, 143, 148, 149, 151, 154, 155, 158–161, 163, 164, 166–169, 177
- Complex structures, 127, 128, 133, 152, 160, 165, 171, 172, 174, 176, 278, 605, 612
- Composite, 1–10, 13–15, 18, 19, 23–29, 37, 38, 42, 48, 59–65, 67–71, 73–79, 81–88, 93, 98, 100, 101, 104–107, 109–111, 113–115, 121, 124, 125, 128, 130–133, 135, 137, 141, 143–155, 158, 160–174, 176, 177, 187–197, 199–204, 206, 207, 210, 211, 213, 215, 217, 218, 220, 223, 225–228, 233–238, 240, 241, 243, 245, 246, 249, 251–263, 269, 274, 278, 279, 285, 287, 288, 295, 299, 300, 302, 318, 320, 321, 323, 325–336, 339, 340, 343–364, 369–371, 374, 387, 391, 393–404, 406–411, 414, 415, 423–431, 438, 440, 447, 451, 452, 456, 473–476, 478–483, 491–497, 499, 500, 503, 505, 506, 518–524, 539, 540, 542, 543, 545, 548, 550–552, 555–557, 565, 574, 579–581, 583–585, 588–592, 595, 596, 601, 603–605, 608, 611–613, 615–618

- Composite aluminum alloy gears, 345
- Composite materials, 1–4, 7, 9, 11, 23, 24, 26–29, 39, 41, 59, 60, 88, 93, 100, 106, 111, 115, 121, 148, 171, 190, 191, 194, 196, 197, 201, 234, 235, 237, 240, 243, 246, 285, 319, 350, 387, 393–396, 399, 400, 409, 426, 451, 456, 473–476, 478–481, 483, 491–494, 497, 505, 538, 541, 542, 550, 551, 557, 579, 581, 583, 596, 602
- Composite nanomaterials, 37
- Compound, 14, 28, 65, 67, 71, 73, 76, 85, 122, 129, 191, 192, 201, 299, 370, 396, 397, 407, 468, 469, 491, 492, 494, 497, 518, 521, 523
- Compression, 103, 106, 149, 158, 173, 321, 349, 410, 542, 591
- Compression failure, 106
- Compression molding, 106, 617
- Compression-shear, 100
- Compression strength, 338, 349, 351, 499
- Compressive, 11, 112, 113, 134, 144, 160, 347, 547
- Compressive conditions, 149
- Compressive strain, 106
- Compressive strength, 113, 143, 317, 318, 321, 328, 329, 338–340, 351–353, 424, 545, 592
- Compressive stress, 106, 110, 440, 442, 558
- Compton scattering, 202
- Compton scattering technique, 193
- Computational tools, 177
- Computer-Aided Design, 122, 130, 137
- Computer-Aided Engineering, 122, 137
- Computer-Aided Manufacturing, 122, 137
- Concentration, 46–51, 99, 105, 137, 144, 148, 153, 158, 160, 161, 163, 166, 188, 193–195, 202, 203, 206, 209, 210, 225, 272, 273, 276–278, 283, 293–297, 327, 347, 369, 371, 377, 387, 392, 395, 407, 426, 440, 442, 455, 456, 459, 460, 464, 469, 471, 474, 476, 480, 482, 492, 500, 502, 503, 507–517, 574
- Concrete, 23, 28, 189, 190, 225, 496
- Condensation, 38, 275, 276, 403, 602
- Conducting fillers, 406
- Conducting polymer, 15, 269–272, 274, 276, 285–293, 295, 298–301, 303, 391, 396, 414
- Conductive, 11, 39, 154–157, 162, 165, 166, 171, 172, 174, 175, 270, 272, 274, 280–282, 286–289, 292–294, 299–302, 386, 397, 410, 570
- Conductive membrane, 286, 287
- Conductive polymer composites (CPCs), 406, 407
- Conductivity, 2, 13, 25, 29, 37, 43, 45, 51, 52, 54, 158, 270, 272–274, 287–289, 293, 294, 296, 301, 303, 391, 394–397, 401, 406–408, 410, 411, 566, 570, 571, 575–581, 583, 586, 588–590, 594–597
- Confocal Raman microscope, 372
- Conical back face deflection, 107
- Connectors, 39, 113, 566, 567
- Constructive solid geometry, 133
- Contact angle, 104, 110
- Contactors, 565–567
- Contact performance, 571, 573, 574, 576–579, 581, 596
- Contact resistance, 571, 575, 577, 596
- Contact terminal, 584, 585, 592, 594, 597
- Contamination, 77, 130, 158, 452, 492, 585
- Continuous, 3, 10, 23–25, 103, 123, 124, 130, 131, 138, 144, 146, 147, 149, 150, 154, 167, 173, 174, 234, 236, 285, 287, 288, 301, 359, 372, 384, 385, 424, 453, 493, 494, 496, 502, 538, 549, 551, 559, 566, 604, 606
- Continuous fiber-reinforced lightweight composite structures (CFRCLSs), 123, 149, 173
- Continuous liquid interface production, 163
- Continuous liquid light processing, 123, 154
- Convection, 386, 501
- Cooling rate, 543, 554
- Coordinating ligands, 64
- Copolymer, 43, 76, 122, 129, 170, 282, 283, 605–615
- Copper, 11, 19, 21, 22, 25, 51, 99, 104, 144, 235, 273, 319, 403, 468, 473, 476, 495, 558, 570, 576, 589, 596
- Copper, 83, 347, 358
- Copper matrix composites, 581, 585
- Co-precipitation method, 588
- Core-shell engineering, 381
- Core-shell structures, 376, 582
- Corn cob, 235
- Corrosion, 5, 26, 42, 172, 347, 356, 493, 567, 569
- Corrosion rate, 427
- Corrosion resistance, 3, 5, 28, 156, 345, 347, 426, 493, 537

- Corrosion resistant coating, 395
 Corrosive wear, 236
 Cost, 5, 8, 23, 39, 40, 43–45, 55, 60, 65, 66, 75, 100, 106, 136, 138, 141, 147, 149, 163, 171, 172, 189, 190, 201, 234, 236, 239, 271, 273, 282, 295, 298, 301, 303, 343, 345, 346, 371, 385, 386, 391, 397, 402, 407–409, 414, 424, 425, 447, 455, 456, 460, 462, 471, 473–476, 480, 491, 492, 496–498, 505, 520, 522, 523, 541, 543, 544, 569, 570, 575, 585, 596, 597, 601, 604, 605
 Covalent interaction, 75
 Covalent organic frameworks, 60
 COVID 19, 127, 128
 Crab shell, 235
 Cracking, 101, 357, 453
 Crack nucleation, 538
 Creep deformation, 539
 Creep rates, 539
 Creep resistance, 3, 539, 540, 559
 Critical parameters, 105, 149, 161, 163
 Crosslinking, 83, 153, 160, 161, 281, 608, 609
 Cross section, 113, 126, 187, 189, 190, 196, 200–202, 210, 226, 227, 254, 299, 300, 583
 Crushing, 104
 Crystalline, 7, 10, 15, 40, 70, 158, 270, 276, 277, 279, 282, 284, 293, 400, 452, 453, 455–457, 460, 463, 465, 468, 470, 523, 603, 610, 612, 617
 Crystallization, 170, 402, 453, 455, 457, 462, 468, 469, 471, 473, 474, 478
 Cubic boron nitride (CBN) wheel, 426
 Curing, 13, 154, 159–161, 176, 177, 197, 238, 240, 403
 Current, 11, 60, 65, 87, 176, 203, 270, 272, 302, 385, 392, 400, 407, 411, 436, 544, 557–559, 565, 566, 570–572, 574, 575, 595
 Current density, 302, 411, 557–559, 566
 Current transmission, 566, 570, 572, 595, 596
 Cutting fluid, 425, 428, 440, 442
 Cutting force, 427, 428, 433, 434, 436–438, 440, 442, 444, 447
 Cyanate ester resins, 5
 Cyclic heating, 548
 Cyclic voltammetry, 297
 Cyclic voltgram, 400, 401
 Cylinder liner, 25, 540
 Cylindrical grinding, 425, 447
 Cylindrical grinding machine, 423, 428, 430
D
 2D cellular materials, 141
 3D, 98, 101, 110, 114, 121, 122, 124, 127, 131–134, 144, 147–149, 151–153, 156, 158, 160, 161, 163, 164, 166–177, 302, 406, 439, 441, 445, 495
 3D cartesian printer, 150
 3D composites, 114
 3D printed composites, 134, 135, 150, 151, 173
 3D printing, 124, 125
 4D printing, 132, 133, 166
 4D structures, 154, 167
 Damage mechanism, 103
 Damage size, 95, 96
 Dark-field scattering optical microscope, 372
 Dark modes, 371
 Deacetylation, 279, 519
 Decantation, 492
 Decay lifetime, 376
 Decision matrix, 323, 324, 336, 338
 Decontamination, 174
 Definition, 141, 202, 203, 206, 372, 493
 Deformation, 95, 100, 101, 104, 105, 107–109, 132, 134, 151, 155, 330, 347, 357, 394, 555, 556, 581
 Deformation mechanism, 104
 Degrees of freedom, 336, 437, 497
 Delamination, 100, 101, 104–106, 108, 109, 114, 168, 335
 Dendrimers, 38, 39, 60
 Density, 3, 6, 10–12, 25, 46, 47, 95, 97, 99, 102, 103, 113, 133, 134, 144, 152, 153, 158, 165, 173, 189, 194, 198, 200, 201, 203, 226, 238, 243, 261, 286, 320, 322, 325, 326, 337, 338, 340, 344, 347–350, 370, 375, 381, 392, 413, 442, 493, 496, 505, 521, 541, 543, 557, 558, 570, 580, 588, 589
 Density functional theory, 288, 289
 Deposition, 38, 41, 42, 122, 123, 125, 127, 141, 151, 153, 154, 163, 281, 285, 290, 303, 348, 350, 400, 401, 549, 553
 Desalination, 478

- Design, 4, 5, 7, 9, 13, 44, 88, 94, 95, 98, 114, 125, 127, 129, 131–133, 135–139, 145, 146, 149, 152, 154, 158, 159, 166, 167, 171–177, 197, 199, 201, 245, 319, 321, 323, 334, 340, 343, 358, 371, 410, 415, 425, 427, 430, 435, 438, 497, 502, 544, 581, 582, 584, 595, 596
- Design-Expert 8.0, 436
- Design matrix, 436
- Desirability, 438, 439, 442, 443, 447
- Desoxyribonucleic acid (DNA)), 270, 275, 297, 413
- Deterioration, 47, 245, 496
- Device, 38, 39, 44, 45, 52, 82, 125, 130, 137, 143, 148, 153, 154, 161, 167, 171, 172, 174, 176, 274, 278, 283, 284, 289, 294–296, 301, 303, 369, 370, 372, 382, 384–387, 391, 411, 414, 540, 565, 566, 584, 585, 615
- Diamond, 8, 10, 24, 130, 164, 172, 393, 426, 431, 466, 581, 587
- Diamond indenter, 320
- Diamond wheel, 425
- Dichroic beam splitter, 372
- Dichroic mirror, 372
- Diclofenac sodium, 507–513, 515, 517–520, 522
- Dicyanate ester, 192
- Dielectric, 13, 28, 39–41, 52, 175, 289, 370–372, 379, 386, 405
- Dielectric composite, 369, 372, 377, 380, 384, 387
- Dielectric constant, 29, 52, 379
- Dielectric microcavities, 369
- Differential scanning calorimetry (DSC), 610, 611, 613, 617
- Diffraction limit, 387
- Diffractiongram, 613
- Diffusion, 65, 132, 159, 165, 447, 464, 499, 501, 503, 506, 548, 552, 554, 557, 565, 585
- Diffusivity, 503, 557
- Digital, 101, 142, 160, 163, 167
- Digital light processing (DLP), 123, 130, 154, 156, 160–162, 172, 174–176
- Digital light system, 172
- Digital logic method, 318
- Dip coating, 290, 303
- Dipole, 370, 371, 377, 379, 380, 384
- Dipole antenna, 167
- Direct hydrothermal, 454, 462
- Direct ink writing (DIW), 123, 130, 152–154, 156, 161, 162, 171, 172
- Direct laser deposition (DLD), 537, 544, 549–554, 560
- Direct reaction synthesis (DRS), 543
- Disadvantage, 3, 40, 176, 189, 271, 272, 294, 345, 452, 454, 460, 462, 565, 602, 605
- Discontinuous, 3, 4, 10, 23–25, 173, 234, 496, 537, 538, 541, 560
- Dislocation, 329, 538, 539, 553, 558, 592
- Dispersion, 8, 11, 39, 40, 76, 151, 152, 154, 159–161, 163, 165, 235, 240, 281, 288, 327, 329, 397, 399, 402, 404, 415, 426, 438, 447, 521, 542, 543, 545, 553, 554, 557, 588
- Dispersive micro-solid-phase extraction (D- μ -SPE), 60–63
- Dispersive solid-phase extraction (DSPE), 60–63, 87, 88
- Displacement current, 370, 371
- Distribution, 14, 15, 27, 60, 70, 103, 105, 132, 134, 137, 149–151, 162, 165, 170, 173, 238, 243, 253, 254, 256, 280, 301, 333, 346, 373, 375–384, 386, 394, 397, 463, 473, 493, 494, 496, 499, 506, 524, 538, 539, 541, 542, 546, 558, 566, 577, 585, 587–589, 596
- DNA sequencing, 275
- Dopant, 49, 188, 190, 194, 270, 274, 290, 386
- Doping ratio, 192, 193, 195
- D-optimal design, 427, 428, 430, 435
- Drop-casting, 290, 303
- Drug, 39, 63, 64, 76, 79, 155, 156, 158, 159, 167, 169, 298, 300, 303, 400, 412, 413, 491–493, 499, 505–519, 521–525
- Drug adsorption, 500, 503, 505, 520
- Drug contaminants, 492, 506
- Drug delivery, 39, 128, 166, 169, 171, 277, 279–281, 283, 300, 391, 412, 413, 482
- Drug dissolution, 158
- Dry grinding, 425, 426
- Ductility, 39, 42, 251, 258–261, 328, 344, 346, 348, 350, 351, 362, 424, 426, 493, 494, 499, 548, 554
- Dye, 40, 63, 288, 289, 297, 395, 409, 412, 456, 473, 474, 476, 479, 492, 497
- Dye removal, 67, 286, 452, 472, 474, 475, 479–482

- Dynamic architectures, 154
 Dynamic failure mode, 109
 Dynamic test, 98
 Dyneema, 95, 97, 99, 104, 106, 113
- E**
- Eco-friendly, 37, 39, 47, 201, 240, 396, 406, 407, 425, 602
 Economy, 27, 234, 235, 343, 524
 Ecosystem, 491, 492
 Edge effects, 405
 EDOT, 290
 Effective atomic number, 190, 192, 196, 198, 203
 Effective electron density, 190, 196, 203
 Effective mode volume, 376
 Efficiency, 24, 26, 37, 44, 61, 70, 83, 87, 98, 114, 121, 125, 133, 148, 161, 174, 193, 206, 289, 293, 301, 349, 386, 408, 413, 424, 426, 428, 446, 452, 454, 468, 473, 478, 479, 491, 492, 497, 505, 524, 538, 542, 543, 565, 569, 615, 616
 Effluent treatment systems, 492
 Eggshell, 235, 236, 249, 250
 E-glass fiber, 29, 100
 Elastic compliance, 571
 Elastic composite, 190
 Elasticity, 281, 285, 344
 Elastic modulus, 93, 113, 145, 148, 160, 234, 284, 344, 346, 359, 392, 393, 426, 539, 542
 Electrical, 2, 10–12, 23, 26, 28, 29, 37, 39, 45, 51, 52, 54, 100, 151, 155, 158, 161, 165, 174, 269–273, 279, 280, 282, 285, 287–289, 291, 293, 294, 296, 301, 303, 348, 387, 395–397, 401, 406, 407, 409–411, 414, 424, 455, 521, 565–567, 569–571, 574–581, 583, 586–590, 592, 594–597
 Electrical circuits, 161, 566, 595
 Electrical conductance, 407
 Electrical contact materials (ECMs), 565–575, 577–579, 581, 583–592, 594–597
 Electrical fuses, 566, 567
 Electrically insulating, 172, 174
 Electrical percolation threshold (Pc), 406
 Electrical sensor, 286, 291, 414
 Electrical switches, 566, 567
 Electrical wear, 572
 Electric arc furnace (EAF) slag, 468
 Electric cars, 566, 568, 569
 Electric cars and renewable energy sources, 568
 Electric dipolar resonance, 370
 Electric field, 52, 405
 Electric motors, 566
 Electric vehicles, 566, 568, 569
 Electro catalysis, 400
 Electrochemical biosensors, 395
 Electrochemical deposition, 350, 400, 401
 Electrochemical method, 38, 85, 271, 272
 Electrochemical polymerization, 272, 290
 Electrochemical supercapacitor, 286, 290
 Electrode, 13, 14, 43, 49, 168, 174, 272–274, 279, 286, 289–291, 302, 386, 395, 399, 409, 410, 548
 Electrodeposition, 42, 272, 399
 Electroless coating, 589, 596
 Electroless Ni coating, 589
 Electrolyte, 1, 272, 273, 288, 293, 302, 385, 399, 605
 Electromagnetic, 128, 147, 175, 191, 274, 289, 375, 379, 381
 Electromagnetic interference (EMI), 274
 Electromagnetic properties, 165, 172
 Electromagnetic radiation, 41, 188, 379
 Electromagnetic switches, 566
 Electromagnetic waves, 94, 456
 Electron-beam curing, 13
 Electron beam scattering, 592
 Electron density, 198
 Electronic, 25, 28, 29, 37, 39, 43–45, 52, 143, 167, 171, 188, 241, 243, 270, 274, 281, 294, 321, 407, 408, 410, 414, 424, 497, 566, 594
 Electronic cross section, 198
 Electronic device, 39, 44, 156, 171, 172, 188, 282, 284, 293, 294, 410
 Electronic properties, 161, 408
 Electronic system, 27, 566
 Electropolymerization, 272, 290, 303
 Electro-pulsing treatment (EPT), 537, 557–560
 Electro-shocking treatment (EST), 558–560
 Electrospinning, 291–293, 409, 478, 617
 Electrostatic attraction, 78, 405, 506
 Electrostatic interaction, 64, 75, 77, 82, 280, 370, 387, 398, 401, 521–524
 Elongation, 6, 10, 282, 284, 328, 346, 349, 539, 545, 547–551, 553, 555
 Emerging contaminants, 492, 497, 502, 505, 524

- Emission, 299, 369–376, 379, 381, 382, 384, 385, 387, 427, 472, 480, 568
- Emissivity, 5, 387
- Emulsion, 195, 280
- Endotherm, 610, 611
- Energy, 27, 28, 39, 41, 43, 52, 93, 101–104, 106–108, 113, 115, 125–128, 134, 138, 145, 149, 151, 175, 187–196, 199–208, 211–225, 228, 245, 262, 276, 279, 283, 294, 299, 301, 343, 370, 374, 377, 381, 385, 393, 394, 407–410, 425, 426, 428, 441, 455, 457, 458, 460, 462, 496, 498, 500, 501, 518, 519, 538, 542, 544, 548, 557, 559, 560, 565, 566, 569, 574, 594, 614
- Energy absorption, 98, 101, 103, 105, 106, 111, 113–115, 135, 519
- Energy absorption build-up factor, 192
- Energy conversion, 301
- Energy density, 301, 302, 374, 411, 548, 549, 552
- Energy-dispersive X-Ray spectroscopy (EDS), 372
- Energy storage, 24, 282, 286, 290, 295, 299, 301–303, 395, 407, 601
- Energy transfer, 369, 371, 379, 381, 387, 411
- Enthalpy, 501
- Entropy, 501
- Environment, 5, 25, 39, 45, 54, 83, 167, 188, 197, 235, 236, 249, 251, 253, 345, 412, 428, 440, 452, 458, 464, 465, 473, 497, 568, 569, 579, 614, 616
- Environmental, 29, 51, 52, 59, 62, 67, 68, 70, 71, 73, 74, 76–78, 81–83, 85, 86, 174, 189, 235, 271, 274, 293, 299, 301, 321, 411, 425, 452, 482, 483, 519, 524, 565, 568, 601–603, 605
- Environmental conditions, 99, 249, 251, 252, 438
- Environmental remediation, 451, 455, 471–473, 476, 480, 481, 601
- Enzymatic biofuel cell, 301
- Enzyme, 278–280, 282, 297, 301
- Epitaxial growth, 385, 395
- Epoxy, 2, 5, 6, 24, 26, 29, 75, 93, 95, 100, 101, 114, 156, 169, 191, 194, 235–238, 240, 243, 245–247, 251, 252, 254, 256, 258, 260, 288, 403, 495, 521, 602
- Epoxy composites, 26, 100, 114, 191, 234, 237, 240, 244–256, 258, 260, 262, 410
- Epoxy matrix composite, 101, 403
- Epoxy polyvinyl alcohol, 194
- Epoxy resin, 5, 191, 233, 235, 238, 240, 243, 246, 255, 258–260
- Equal Channel Angular Pressing, 591
- Equilibrium, 465, 474, 498–502, 504
- Erosion, 45, 100, 233, 234, 236, 237, 241, 242, 249–252, 257–263, 579, 581
- Erosion test, 241, 242, 258
- Erosion time, 241, 260, 261
- Erosion wear test, 233, 241, 249, 257, 259, 262, 263
- Erosive wear, 236, 251, 260, 356
- Erosive wear rate, 241
- Ethanol, 19, 163, 165, 273, 278, 279, 301, 399, 404, 608
- Ethylenediamine, 68, 80
- Ethylene propylene diene monomer (EPDM), 194
- European Center for Nuclear Research (CERN), 200
- Excitation rate, 380, 381
- Exciton-exciton coupling, 369
- Exfoliation, 39, 392, 396, 402, 521
- Exhaust emissions, 568
- Exothermic, 518
- Exothermic diffusion method, 542, 543, 560
- Exothermic reaction, 543, 544
- Expansion, 3, 29, 132, 333, 411, 444, 494, 502, 522, 557
- Experimental data, 100, 106, 187, 323, 430, 436, 447, 491, 499
- Exponential, 199, 202, 259, 376
- Exposure build-up factor, 192
- Exposure time, 188
- Ex-situ, 235, 240, 397, 398, 400, 401, 537, 560
- Extraction efficiency, 62, 63, 65, 66, 68, 73, 75, 76, 84, 85, 87
- Extraction performance, 61, 66, 87
- Extrinsic, 270
- Extrusion, 126, 141, 143–149, 151, 152, 176, 284, 394, 591, 596, 617
- Extrusion based 3D composites, 141, 143
- F**
- Fabric structures, 93, 98, 102–104, 107, 115
- Factor, 11, 48, 61, 62, 66, 68, 72, 73, 76, 78, 84, 85, 102, 103, 115, 167, 173,

- 235, 273, 293, 295, 299, 330, 334, 340, 343, 345, 356–358, 361, 362, 364, 427, 428, 435–438, 440, 447, 457, 471, 480, 498, 500, 501, 548, 551, 570, 608
- Failure, 4, 11, 93, 96, 97, 101, 103–107, 109–113, 115, 148, 174, 235, 236, 241, 243, 246, 364, 393
- Failure mechanism, 101
- Far-field scattering, 379
- Fast neutron, 187, 189–191
- Fast ultraviolet curing method, 192
- Fatigue wear, 236
- Fatty acid, 282, 291, 608, 612
- FDTD Solutions 8.6, 379
- Fe₂O₃, 191, 474, 477, 481, 507
- Feed rate, 242, 425, 427, 440
- Ferric chloride, 287
- Fertilizers, 482, 601, 603, 615–617
- Fiber, 3–5, 8, 10–13, 23–29, 41, 42, 46, 48, 53, 54, 82–87, 93, 94, 96–107, 109, 110, 112–115, 122, 130, 138, 139, 143, 144, 146–150, 155–157, 161, 163, 164, 166, 169, 173, 176, 233–238, 253, 254, 257–259, 262, 269, 275–278, 281, 284, 288, 291, 293, 386, 393, 409, 410, 426, 494–496, 509, 513, 515, 538, 540, 579
- Fiber-based material, 95
- Fiber coir, 235
- Fiber pull-out, 101, 106, 109
- Fibrin, 275
- Fibrous, 3, 281, 494, 496
- Field, 2, 29, 37–39, 42, 44, 45, 53, 55, 60, 65, 75, 82, 124, 130, 134, 137, 167, 168, 171, 177, 188, 190, 200, 284, 285, 289, 293, 295, 328, 346, 369–372, 375, 376, 379, 380, 385–387, 391, 394, 395, 404, 408, 413, 414, 473, 497, 525, 537, 539, 541, 544, 557, 559, 603
- Field emission scanning electron microscope, 288, 323
- Filament, 26, 122, 129, 130, 141, 146, 148, 149, 151–154, 172, 173, 239, 496
- Filler, 27, 28, 45, 163, 164, 172, 189, 233–238, 240, 243, 245, 246, 249–263, 278, 325–328, 344, 347, 350, 351, 355–358, 361–364, 391, 392, 395–397, 402–404, 406–408, 411
- Filler content, 189, 243, 245, 246, 249, 251, 252, 255–259, 318, 322, 323, 331, 334–336, 339, 340, 344, 346, 351, 361
- Film, 1, 38, 40, 41, 83, 155, 161, 270, 272–274, 277, 279, 281, 289–292, 294, 345, 350, 361, 385, 386, 399, 406, 408, 411, 415, 427, 432, 442, 446, 477–479, 503, 576, 577
- Filter, 50, 53, 171, 246, 372
- Filtration, 66, 246, 459, 492
- Finite-difference time-domain (FDTD), 379
- Finite element, 113, 114, 122, 135, 146
- Finite element theory, 111
- Fixed bed adsorption, 502
- Flake-like, 543
- Flame-ionization detection, 82
- Flexibility, 11, 29, 81, 98, 115, 148, 149, 177, 278, 280, 283, 284, 286, 292, 295, 392, 394, 406, 483, 544, 594, 597
- Flexible circuit, 143, 151
- Flexible composite, 194
- Flexible electrode, 288, 414
- Flexible electronic, 166, 171, 286, 289, 294
- Flexible substrate, 294
- Flexural strength, 7, 169, 241, 243, 246–248, 253–256, 317, 327, 328, 337, 338, 340
- Flexural-strength (F), 320
- Flexural test, 168, 241, 247, 248
- Flocculation, 492
- Fluid, 45, 98, 174, 276, 280, 425, 426, 428, 442, 446, 463, 464, 497, 498
- Fluidity, 161, 318
- Fluorescence, 47, 371, 381, 382, 405, 409
- Fluorescence spectroscopy, 370
- Fold-unfold ability, 167
- Food supplements, 492
- Forgings, 345, 351, 538, 542
- Fossil, 270, 275, 343, 568
- Fossil fuel, 299, 568, 569
- Fourier transform infrared, 17, 288, 609
- Fractals, 127, 167
- Fractional abundance, 198
- Fractional order, 502, 504
- Fracture, 27, 42, 104, 168, 174, 302, 347, 348, 426, 496, 551, 553
- Fracture strain, 148, 548, 559
- Fracture strength, 395
- Fracture toughness, 7, 25, 42, 234, 343, 347, 348, 538
- Fragility, 189, 496

- Free radical polymerization, 601–605, 608
Freeze extraction, 289
Frequency, 188, 296, 370, 379, 381, 382, 411, 431, 432
Friction, 24, 42, 98, 108, 110, 113, 236, 321, 330, 331, 336, 343–345, 348, 349, 354, 355, 359, 362, 364, 410, 442, 462, 551
Friction coefficient, 82, 331, 332, 347, 355, 360, 542, 544, 548, 583
Fruit peels, 475
Fuel, 1, 23, 25, 27, 45, 234, 278, 301, 343, 568
Fuel biocells, 301
Fuel cell, 24, 39, 43, 301–303, 410
Full width at half maximum, 377
Fully functional assemblies, 122, 128
Fully stressed structures, 138
Functional applications, 121
Functional complexity, 137
Functional group, 64, 66, 75, 84, 279, 281, 393, 398, 399, 403, 405, 409, 464, 499, 521, 523, 609
Functionally graded materials (FGM), 594, 596
Functional waves, 193
Function representation, 122, 133
Fungicides, 68, 69, 278
Fused deposition, 122, 128, 172
Fusion, 126, 140, 142, 176, 188, 452, 454, 456–458, 460, 462, 469, 471, 474, 475, 552
Fusion assisted ultrasonic hydrothermal, 454
Fusion casting method, 542, 560
Fusion-facilitated alkaline hydrothermal treatment, 456
- G**
Gallic acid, 61
Galvanostatic, 273, 400, 401
Gamma, 46, 189–196, 199, 201, 202, 210, 225
Gamma attenuation, 188, 190, 192, 201
Gamma rays, 188, 190
Gamma spectrometer, 187, 189, 199
Gas, 1, 5, 23, 24, 26, 27, 39, 41, 45, 49, 52, 78, 102, 129, 392, 394, 395, 410, 452, 455, 464, 468, 472, 473, 475, 476, 479, 480, 482, 483, 497, 501, 520, 548, 568, 601, 603, 614, 616, 618
Gas chromatography, 69
Gaseous pollutant, 476
Gas-foaming, 151
Gas sensor, 45, 49, 286, 296, 298
G-code, 141, 142, 152, 153
GEANT4 simulation, 190, 196, 201, 202, 210
GEANT4 simulation toolkit, 200
Gear, 27, 45, 151–153, 169, 236, 343, 345, 364, 540
Gear application, 343, 364
Gear material, 343, 364
Geiger-Müller detector, 195, 196
Gelatin, 123, 146, 153, 156, 280–282, 497, 512, 522
Gelatinization, 276, 293
Gelation, 197, 294
Gel-like material, 277
Gel-spinning, 99
Generative design, 122, 136, 137, 140
Gene therapy, 275, 413
Geopolymer, 473, 475, 477, 480, 481
Germanium, 359, 370
Glass, 9, 10, 12, 15, 23–27, 29, 48, 51, 100–102, 105, 146, 149, 168, 189, 190, 234, 237, 238, 253, 255, 257, 258, 272, 274, 290, 294, 295, 318, 403, 404, 454, 476, 477, 494, 497, 606
Glass/basalt, 192
Glass fiber composites, 10, 102, 254, 255, 258, 259
Glass fiber (GF), 10, 23, 26, 96, 100, 233–240, 253, 254, 256–263, 408, 426
Glass transition temperature, 5, 132, 148, 151, 282, 607, 616
Glassy polymer, 154
Global warming, 568, 569
Glucose, 170, 276, 279, 282, 283, 286, 298
Gold microcavity, 369
Gold sphere, 369–376, 378, 387
Gradient composites, 553, 554, 582, 583
Gradient structures, 122, 133
Grain boundary, 539, 548, 549, 553, 558
Granular, 290, 468, 541, 543, 548
Grapheme, 393, 401, 405, 408
Grapheme nanoplatelets (GNP), 93, 101, 123, 145, 155, 160
Graphene, 41, 45, 49, 60, 65, 75, 77, 85, 93, 123, 143–145, 151, 160, 163–165, 168, 171, 279, 302, 391–415, 426,

- 477, 481, 509, 517, 524, 538, 548, 550, 551
- Graphene aerogels (GAs), 407, 514, 524
- Graphene Bioactive Composites, 408
- Graphene colloidal suspensions, 404
- Graphene fillers, 414
- Graphene inorganic material composite, 396
- Graphene membrane, 394
- Graphene nanoplates, 101
- Graphene nanosheets, 392, 396, 403
- Graphene oxide, 62, 123, 392, 395–399, 402, 403, 405–407, 409–414, 496, 497, 506, 508, 511, 519, 521, 542
- Graphene polymer composite, 396, 397, 402, 410, 413
- Graphene quantum dots (GQDs), 82, 405
- Graphene sheet, 151, 393, 394, 401, 402, 412
- Graphite, 8, 10, 318, 319, 325–332, 334, 335, 337, 356, 358, 359, 362, 392, 396, 402, 406, 521, 542, 551, 574, 579, 581
- Graphite nano particles, 233, 254, 255, 263
- Graphite nanoplatelets, 2, 172
- Graphite oxide, 396
- Graphite sheets, 521
- Graphitic carbon nitride (g-C₃N₄), 233, 238, 239, 254–259, 263, 522
- Gravel, 496
- Gravity die casting technique, 429
- Green composite materials, 603
- Green polymer, 616
- Grinding, 277, 423–428, 430, 431, 438–441, 445–447, 460
- Grinding force, 424–427, 440–442
- Grinding rate, 423
- Grinding speed, 425, 440
- Grinding wheel, 424–426, 431, 432, 441, 442, 444, 446
- H**
- Half value layer, 190–193, 196, 198
- Hardener, 197, 238, 240, 403
- Hardening, 112, 138, 346, 403, 543, 545
- Hardening process, 197
- Hardness, 15, 48, 51, 174, 237, 246, 260, 317, 318, 320, 326–328, 331, 337, 338, 340, 343–354, 359, 362, 364, 424, 440, 496, 544, 545, 548, 551, 553–555, 565, 571, 572, 575–581, 588–590, 592, 594, 596
- Hardness test, 344, 349
- Harmful effects, 54, 187, 392, 568
- Harmful gases, 476, 568
- Harmful gas removal, 475, 479
- H-boron nitride, 408
- Healable polymeric materials, 601
- Healing, 557–559
- Heat, 10, 12–15, 25, 28, 41, 49, 102, 132, 138, 141, 152, 168, 171, 302, 336, 348, 351, 357, 359, 384, 402, 404, 407, 410, 423, 425, 429, 440, 442, 444, 493, 495, 543, 544, 551, 552, 556, 557, 570, 575, 594, 603
- Heat capacity, 493
- Heat sink, 145, 171, 172
- Heat transfer coefficient, 425
- Heat treatment, 25, 350, 351, 354, 537, 538, 548, 549, 551, 554–558, 560
- Heavy metal, 67, 76, 77, 79, 411, 452, 468, 472–476, 497, 605
- Heavy metal ions, 497
- Heavy metal removal, 395, 452, 471, 472, 475, 617
- Hematite, 191, 192, 195
- Heptane, 608, 609
- Herbicides, 67, 68, 73, 78, 79
- Heterogeneous, 4, 39, 149, 168, 549, 550, 552
- Heterogeneous system, 497
- Hexagonal, 10, 75, 84, 143, 190, 384, 385, 392, 408
- Hexavalent chromium, 289
- Hierarchical complexity, 137
- Hierarchical effects, 151
- High-current circuits, 566
- High-density polyethylene (HDPE), 12, 190, 193–196
- High-pass filter, 148
- High-performance liquid chromatography, 61, 69
- High-power ultrasonication, 406
- High purity germanium (HPGe) detector, 187
- High temperature resistance, 537, 538
- High vacuum casting apparatus, 319, 337
- Hill model, 522
- Histogram, 378, 381
- Hollow carbon nanospheres (HCSs), 78
- Hollow fiber, 478
- Homogeneous, 9, 39, 40, 163, 274, 277, 290, 362, 364, 371, 377, 382, 496, 503, 524, 588, 596

- Homogeneous solid diffusion models (HSDM), 502, 503
 Honeycomb, 27, 75, 131, 134, 135, 141, 143–145, 147, 148, 155–158, 160, 166, 167, 173
 Honeycomb structures, 27, 145, 148, 149
 Horizontal spindle, 423, 428, 430
 Hot extrusion, 328, 344–346, 351, 542
 Hot extrusion method, 584
 Hot forging, 362, 585, 588
 Hot isostatic pressing (HIP), 27, 53, 344, 350, 542
 Hot pressing, 42, 589, 591, 594, 597
 Hot press method, 406
 Hot-press process, 194
 HPGe detector, 187, 192, 195, 196, 199, 201
 Human, 50, 51, 53, 63, 70–72, 115, 164, 174, 188, 281, 299, 413, 451, 476, 492, 541, 602
 Human health, 54, 452, 568, 579, 616
 Humidity, 286, 296–298
 Hyaluronan, 280
 Hyaluronic acid (HA), 280
 Hybrid, 2, 14, 26, 28, 29, 64, 101, 113, 115, 127, 130, 149, 156, 162, 164, 165, 170, 172, 174, 233, 235, 237, 238, 240, 241, 258–261, 263, 318, 371, 377, 382, 385, 387, 396, 407, 408, 412, 424, 427, 452, 474, 479, 480, 483, 523, 524, 542, 583
 Hybrid composite, 19, 29, 101, 192, 234–240, 254–257, 259, 260, 262, 350, 353, 354, 358, 362, 407, 480, 505, 583
 Hybrid fibers, 192
 Hybridization, 66, 99, 234, 256, 258, 392, 396–398, 407–409
 Hybrid polymer composites, 233, 234, 236–238, 241, 245, 253, 263
 Hybrid printer, 161
 Hybrid processing, 161
 Hybrid reinforcement, 164, 165, 234
 Hybrid thermoplastic composite armor, 98
 Hydrated aluminum, 522
 Hydrated bacterial cellulose, 287
 Hydraulic presses, 565, 585
 Hydrazine, 396
 Hydrazine hydrate, 396, 399
 Hydrocarbon-based fuels, 568
 Hydrocarbons, 245, 453, 568
 Hydrochloric, 276, 287
 Hydrogel, 153, 154, 167, 169–171, 174, 279, 281, 288, 294, 299, 300, 483, 507
 Hydrogenation reaction, 400
 Hydrogen bond, 64, 77, 277, 278, 287–289, 520–524
 Hydrogen bonding, 17, 61, 62, 64, 71, 75, 78, 82, 277
 Hydrogen peroxide (H₂O₂), 272, 298, 400, 406, 409
 Hydrogen sulfide, 616
 Hydrolysis, 276, 281, 283, 284, 400, 401
 Hydrolysis process, 399, 404
 Hydrophilic, 51, 62, 75, 77, 85, 280, 411, 522, 523
 Hydrophilic compounds, 62, 87
 Hydrophilicity, 48, 62, 87, 293, 479
 Hydrophilic molecule, 403
 Hydrophobic, 54, 62, 64, 67, 68, 70, 78, 82, 83, 85, 278, 281, 284, 411–413, 480, 521, 523
 Hydrophobicity, 62, 75, 87
 Hydrophobic membrane, 615
 Hydrothermal, 39, 40, 64, 76, 82, 83, 400, 406, 407, 452, 454–460, 462, 468–471, 473–476, 478, 480, 483
 Hydroxyapatite, 27, 53, 122, 512
 Hydroxyl, 19, 21, 75, 278, 279, 459, 519, 521
 Hydroxyl groups, 21, 82, 278, 279, 523
 Hydroxy sodalite (HSOD), 457, 468
- I**
 Illite, 522
 Ilmenite, 195
 Imaginary index, 370
 Imine nitrogens, 271
 Impact, 10, 39, 48, 54, 94, 100–103, 106–108, 110, 114, 125, 135, 138, 146, 148, 152, 154, 158, 160, 161, 165, 177, 188, 235–237, 249, 258, 260, 262, 299, 318, 321, 325, 330, 334, 343, 347, 424, 427, 428, 440, 442, 457, 465, 473, 476, 478, 538
 Impact mechanism, 94
 Impact resistance, 284, 328
 Impact strength, 317, 318, 321, 328, 337, 338, 340, 343
 Impact test, 100, 109
 Impact velocity, 104, 105, 113, 236, 242, 251, 257–263
 Impact waves, 104

- Impregnation process, 98
 Induction skull melting (ISM), 543
 Industrial, 23–25, 28, 55, 63, 102, 121, 138,
 168, 177, 237, 278, 280, 286, 299,
 345, 349, 424, 451–454, 457, 460,
 462–464, 467, 473, 480, 482, 492,
 524, 541, 566
 Industrial chemicals, 492
 Industrial effluents, 452, 476, 492
 Industrial purpose, 453
 Industry, 14, 23, 28, 29, 39, 42, 43, 51, 53,
 101, 102, 121, 125, 167, 176, 240,
 275, 298, 409, 424, 467, 474, 476,
 479, 480, 482, 565
 Infection, 46–48, 170, 299
 Infiltration, 14, 42, 587, 596
 Infiltration process, 587
 Ingot, 543, 544, 583
 Inhomogeneity, 160
 Inhomogeneous, 585
 Injection molding, 14, 284
 Injuries, 45, 46, 169, 298
 Ink, 39, 152–154, 156, 167, 171, 172
 Inkjet, 166, 167
 Inkjet printing, 166, 167, 290, 303
 Inorganic arsenic, 68
 Inorganic chemical, 5, 470
 Inorganic oxide, 453, 468, 469
 Inorganic semiconductor, 270
 In-situ, 7, 43, 235, 287, 288, 290, 292,
 397–401, 537, 541–545, 548, 550,
 560
 In-situ polymerization, 15, 43, 273, 294,
 295, 302, 391, 402, 403
 In-situ synthesis, 299, 537, 541–543
 Insolubility, 272, 279
 Insoluble, 273, 274, 276, 277, 279, 499,
 608, 609
 Insulating material, 270, 282, 285, 294
 Insulation, 23, 28, 39, 51, 100, 285
 Intensity, 153, 161, 170, 189, 191, 198,
 201, 203, 206, 372, 373, 375–385,
 387, 496, 608, 611, 613
 Intercalation, 15, 43, 167, 402, 403
 Intercalation polymerization, 402
 Intercalative process, 15
 Interface, 37, 64, 67, 69, 114, 159, 235,
 253, 277, 336, 346, 354, 363, 393,
 407, 414, 425, 427, 441, 442, 463,
 464, 493, 494, 501–503, 538, 541,
 553, 557, 560, 583, 585, 586, 589,
 596, 617
 Interfacial adhesion, 235, 276
 Interfacial shear stress, 393
 Interference, 64, 177, 376–378
 Interlaminar shear strength analysis (ILSS),
 235, 409
 Interlaminar stress, 104
 Intermetallic compounds, 7, 538, 552
 Intermolecular force, 464, 498
 Intermolecular interactions, 99, 292
 Internal combustion engine, 568
 Internal oxidation process, 585, 587
 Inter-yarn friction, 98, 113
 Intraparticle diffusion coefficient, 503
 Intrinsic, 60, 75, 270, 369, 376
 Inverse vulcanization, 601–606, 608–610,
 612, 613, 615–617
 Iodine, 270
 Ion-dipole interaction, 506
 Ion exchange, 453, 455, 463, 464, 471, 475,
 476
 Ion exchange capacity, 465, 471, 479
 Ionic, 41, 53, 76, 85, 279, 283, 464
 Ionic assisted dispersion, 399
 Ionic conductivity, 288, 293
 Ionic liquids (ILs), 60, 76, 85, 87, 511, 514,
 515
 Ionizing radiation, 13, 187, 188, 192, 195,
 225, 464
 Iron, 15, 94, 122, 143, 147, 156, 173, 193,
 195, 235, 237, 273, 274, 288, 295,
 319, 406, 426, 468, 474, 475, 507,
 513–515, 521, 524, 615
 Iron oxide nanoparticles (ION), 123, 153
 Iron silicates, 522
 Irradiation, 46, 160, 457, 460, 470, 483
 ISO/ASTM 52900, 126
 Isomixed cellular wood composites, 141
 Isophthalic resin-based composites, 195
 Isothermal, 491, 497, 500, 501, 516
 Isotherm model, 499
 Isotropic, 94, 113, 345, 424, 496
 Isotropy, 496
 ITQ-37, 453
- J**
 Joining methods, 565, 584, 585
 Joint, 27, 47, 53, 131, 144, 541
 Joint defects, 170
 Joint errors, 565, 585
 Jute, 234, 235
- K**
 Kaolinite, 480, 522

- K-edge absorption energy, 206
 Kerosene, 245, 249
 Ketoprofen, 509–511, 513, 514, 521
 Kevlar, 27, 95, 97–99, 101, 114, 143, 147, 149, 234, 409
 Kevlar fibers, 11, 101
 Kinetic, 43, 160, 162, 370, 375, 380, 387, 491, 497, 501, 503–505, 594, 616
 Kinetic energy, 39, 95, 99, 101, 104, 106, 107, 109, 113, 114, 262, 499, 569
- L**
 La₂O₃, 193
 Lack-of-fit test, 436, 438
 Lambert-Beer equation, 198
 Lambert-Beer law, 202
 Lamina composites, 9
 Laminated composites, 95, 104–108, 111, 112, 148
 Laminate thickness, 105
 Langmuir–Blodgett (LB), 290, 303
 Langmuir model, 519–524
 Laser, 38, 50, 53, 126, 127, 158, 163, 165, 168, 169, 372, 374, 376, 377, 379, 380, 384–387, 409, 544, 548, 549, 551–553, 560, 573, 576, 592, 594, 595
 Laser based polymerization, 152
 Laser excitation, 371, 376, 384, 385
 Laser irradiation technique, 426
 Latex, 270, 282, 285
 Lattice, 75, 127, 130, 135, 144, 155, 156, 160, 344, 350, 392, 393, 555, 557
 Layer-by-layer (LBL), 141, 163, 290–292, 303, 384
 Lead, 19, 40, 51, 53, 75, 104, 111, 153, 189–191, 193, 195, 235, 243, 246, 254, 256, 259, 261, 262, 270, 272, 281, 284, 291, 303, 319, 331, 332, 343, 381, 394, 402, 403, 426, 427, 440, 442, 453, 455, 465, 471, 473, 475, 476, 478, 479, 482, 493, 538, 541, 554, 557, 615
 Lead adsorption, 615
 Lead-based materials, 190
 Lead oxide, 194
 Least-squares fitting method, 199
 Lewis acid, 81, 83
 Li anode, 605, 615
 Ligands, 49, 71, 279, 523
 Light, 28, 39, 45, 49, 53, 126, 130, 132, 144, 154, 156, 158, 160, 161, 170, 172, 173, 194, 271, 295, 345, 369, 370, 372, 373, 375–377, 379, 384–387, 394, 406, 409–411, 414, 608, 609
 Light confinement, 370, 387
 Light diffraction, 369
 Light emission, 369, 374, 384, 385, 387
 Light-emitting diodes, 44, 124, 163, 274, 370, 371, 391, 414
 Light irradiation, 398
 Lightweight, 3, 26–28, 42, 75, 99, 102, 131, 137, 138, 141, 147, 149, 171, 193, 201, 294–296, 302, 409, 410, 414
 Light weight material, 39, 225, 234
 Lightweight sandwich structure, 173
 Lignin, 270, 276–278, 286, 289, 290
 Li-ion battery, 400, 401
 Limit of detection, 61
 Linear attenuation coefficient, 189, 192, 196, 198, 201, 203
 Linear chains, 99
 Linear density, 103
 Linear driving force, 502, 503
 Linoleic, 606, 608, 617
 Linolenic, 606, 608, 617
 Linseed, 601, 605–607, 609, 610
 Liquid, 7, 10, 14, 40, 42, 48, 115, 123, 126, 153, 154, 156, 158, 166, 245, 277, 281, 293, 296, 345, 356, 358, 359, 373, 402, 405, 409, 453, 455, 464, 465, 480, 492, 497–499, 502, 503, 506, 520, 521, 549, 603, 609
 Liquid adsorption technique, 497
 Liquid-liquid extraction (LLE), 60
 Liquid-phase exfoliation, 406
 Liquid temperature, 319
 Li-S batteries, 601, 605
 Li-S battery cathodes, 615, 617
 Lithium ion battery, 40, 286, 291, 293
 Lithography, 152, 160, 290, 303
 Load, 1, 28, 42, 99, 134, 138, 150, 155, 158, 167, 169, 237, 241, 254, 256, 320, 321, 323, 327, 330, 331, 335–337, 343, 346, 348, 349, 352–356, 358, 359, 361–363, 393, 409–411, 424, 432, 442, 494, 496, 506, 540, 548, 560, 608, 610, 611, 617
 Longitudinal, 105, 106, 112, 113, 134, 549, 553
 Longitudinal loading, 104
 Low-density polyethylene (LDPE), 192
 Low-energy, 107, 188, 191, 194, 195, 202, 225, 498, 557

- Ls-Dyna, 111
 Ls-Dyna MAT162 material model, 100
 Lubricant, 8, 252, 280, 330, 356, 362, 423, 425–427, 429, 431, 432, 441, 579, 585
 Lubrication, 354, 423, 425, 427, 447, 579, 596
- M**
- Macroscopic effective removal
 cross-section, 199
 MAESTRO software, 199
 Magnesium, 42, 319, 346, 349, 424, 495
 Magnesium oxide, 100
 Magnet, 39, 53, 66, 129, 153, 154
 Magnetic, 2, 16, 52, 53, 122, 128, 129, 133, 146, 158, 173, 285, 319, 370, 371, 377, 379, 380, 384, 386, 404, 476, 477, 481, 505, 507–512, 514, 516, 519–524
 Magnetic adsorbent, 66, 67, 79, 80, 519
 Magnetic chitosan, 497
 Magnetic composite, 66–68, 70–72, 75–78, 81, 82, 400, 519
 Magnetic dipolar resonance, 370
 Magnetic field, 52, 69, 132, 153, 170, 370, 520, 524, 566
 Magnetic nanocomposite, 71, 76, 521
 Magnetic particles, 70, 82, 173
 Magnetic solid-phase extraction (MSPE), 66–68, 70–79, 81, 82, 87, 88
 Magnetic transformers, 173
 Magnetite, 195, 507, 511, 513, 524
 Maintenance cost, 568
 Marine, 26, 28, 29, 121, 275, 409, 496
 Martensite, 554
 Martensitic, 554
 Mass, 11, 96, 103, 105, 108, 109, 114, 124, 132, 187, 190, 192, 196, 198, 201, 202, 236, 270–272, 278, 281, 286, 288, 322, 359, 483, 492, 502, 517, 540, 543, 551
 Mass attenuation coefficient, 189, 190, 192, 196, 198, 201, 202
 Mass spectrometry, 69, 71
 Mass transfer, 69, 78, 497, 501–503
 MAT54 material model, 111
 Material complexity, 137
 Material degradation, 100, 245, 249
 Material jetting, 126, 166
 Material loss, 253, 262, 330, 570, 571, 588, 589, 592, 596
- Materials design, 187
 Matrix, 1–5, 8, 10, 11, 15, 23, 25, 26, 28, 29, 42, 43, 53, 59, 62–64, 66, 67, 70, 71, 73, 75, 76, 78, 80, 81, 88, 98, 101, 104, 106, 107, 112–114, 134, 145, 146, 149, 154–158, 160, 161, 164–166, 169, 234–238, 243, 245, 246, 249, 254, 256, 258, 262, 270, 280, 282, 285, 288, 293, 299, 300, 318, 320, 323–328, 331, 332, 343–354, 357, 361–364, 385, 393, 394, 402–404, 406–408, 411, 414, 423, 426, 427, 429, 431, 440, 447, 452, 473, 475, 478, 479, 482, 492, 494–496, 524, 538, 539, 541–543, 545, 548, 550, 551, 553–556, 560, 579, 581, 583, 585, 587–589, 591, 592, 596, 615
 Matrix cracking, 101, 104, 106, 108, 110
 Matrix damage, 104
 Matrix material, 3, 5, 7, 41, 105, 114, 189, 235
 MCNPX, 192
 Mean free path, 190, 196, 199, 200, 202, 210, 227
 Mechanical, 24, 25, 38, 39, 42, 48, 52, 72, 75, 132, 138, 140, 143, 149, 150, 153, 155, 156, 158, 160, 165, 170, 172–174, 193, 194, 233–235, 237, 238, 240, 241, 243, 246, 251–253, 255, 257, 258, 263, 274, 276, 277, 279, 280, 293–295, 298, 317–320, 325, 327, 331, 337, 343–345, 347–351, 359, 364, 393–395, 410, 411, 414, 424, 426, 475, 478, 493, 505, 521, 523, 543, 550, 565, 566, 585
 Mechanical alloying, 344, 350, 364, 537, 542–544, 560
 Mechanical breakdown, 394
 Mechanical loadings, 103
 Mechanical milling, 38, 588
 Mechanical mixing, 394, 408
 Mechanical properties, 5, 10, 11, 37, 39, 43, 45, 47, 48, 97, 99–102, 127, 128, 132, 135, 137, 138, 141, 144, 152, 158, 160, 171, 173, 192, 235, 237, 245, 269, 273, 276, 277, 279–281, 284, 285, 287, 289, 293, 301, 303, 318, 343, 344, 346–353, 393, 394, 397, 403, 406, 409, 411, 424, 426, 491, 493, 494, 496, 499, 506, 521, 524, 538, 539, 541, 542, 545, 547,

- 548, 553, 571, 578, 579, 585, 587,
596, 615, 616
- Mechanical resistance, 170, 284, 496, 519
- Mechanical stability, 64, 65, 78, 83, 87,
294, 405, 478, 522
- Mechanical strength, 2, 48, 81, 134, 170,
233, 235, 237, 241, 243–246, 251,
257, 263, 281, 289, 393, 396, 397,
409, 608
- Mechanical structures, 154
- Mechanical wear, 570, 571, 575, 596
- Mechanism, 8, 45, 60, 61, 108, 148,
150–152, 188, 274, 288, 292, 297,
329, 335, 336, 344, 345, 349,
353–355, 359, 360, 363, 364, 370,
385, 398, 412, 415, 453, 456, 457,
464, 501, 544, 557, 560, 616, 618
- Medical, 39, 45–47, 54, 127, 128, 154, 167,
169, 170, 177, 188, 191, 200,
281–284, 295, 298–300, 392, 492,
497
- Medical field, 169, 541
- Medical physics, 188
- Medicines, 64, 170, 174, 386, 491, 492,
505, 541
- Meloxicam, 511, 522
- Melting, 127, 261, 284, 345, 409, 456,
542–544, 548, 551, 557, 560,
570–572, 574, 587, 588, 606, 610,
611, 617
- Melting temperature, 97, 282, 567, 603
- Melt-mixing, 15
- Melt solidification process, 543
- Membrane, 43, 46, 48, 286, 287, 291, 292,
409, 414, 452, 476–482, 525
- Membrane composite, 452, 478, 479
- Membrane extension, 109
- Mercury, 481, 615
- Mercury capture, 605
- Mesh size, 379
- Mesoporous, 453, 473, 475, 481
- Metal, 1–3, 5, 7, 11, 14, 15, 27, 40, 42, 48,
50, 64, 66, 87, 93, 125, 150, 156,
158, 162, 168, 176, 236, 279, 284,
294, 301, 319, 343–345, 348, 349,
351, 353, 357, 362–364, 369–371,
387, 396–399, 402, 404, 407, 424,
455, 473, 474, 493, 495, 497, 506,
510, 516, 523, 543, 544, 557, 559,
565, 566, 570–572, 574–576, 578,
579, 583, 585–590, 593, 594, 596
- Metal-based ECMs, 566, 575
- Metal Based Electrical Contact Materials,
575
- Metal biomaterial, 541
- Metal ceramics, 538
- Metal fiber, 41, 494
- Metal ions, 59, 63, 68, 73, 77, 87, 279, 451,
478, 523
- Metallic, 7, 26, 27, 51, 68, 281, 361, 369,
370, 392, 494, 495, 570, 590, 592,
595
- Metallic composites, 495
- Metallic fibers, 11, 270, 495
- Metallic glass, 15, 351
- Metallic nanoparticles, 38, 153, 281
- Metal matrix composites, 1, 3, 7, 24, 26,
349, 356, 424, 425, 427, 505,
585–588, 596
- Metal matrix nanocomposites, 14, 42, 424,
426
- Metal organic frameworks, 60
- Metal oxide, 40, 41, 48, 49, 54, 85, 195,
397–399, 477, 481, 496
- Metal polymer composites, 172
- Metal-semiconductor composites, 369
- Metals plates, 95
- Metamaterials, 127, 128, 144, 145, 158
- Methoxy groups, 278
- Methylene blue (MB), 78, 475, 476, 479,
510
- Methyl ethyl ketone peroxide (Mekp), 197
- Methyl orange (MO), 476, 479, 553
- Methyl vinyl silicone rubber, 194, 195
- Microbial fuel cell, 301, 303
- Micro-bullets, 394
- Microcapsules, 193
- Microcavity, 369, 370, 375, 376, 379, 381,
384, 387
- Micro content fabrication, 189
- Microcracks, 425, 444, 445, 557
- Microdiamonds, 145, 151, 172
- Microfiber composites, 407
- Microhardness, 262, 344, 347, 349, 544,
548, 550
- Micro-nano, 369, 370
- Micro-nano photonics, 370
- Micro-nano plastics, 492
- Microorganism, 519
- Microparticle, 194, 195, 617
- Microporosity, 475
- Microporous, 453, 463, 473, 614
- Microwave, 13, 41, 144, 145, 156, 175,
391, 392, 400, 401, 404, 405, 452,
456, 457, 459, 460, 462, 474, 483

- Microwave-assisted synthesis, 399, 404
 Microwave-assisted thermal treatment, 406
 Microwave hydrothermal treatment, 454
 Microwave irradiation, 41, 49, 457
 Microwave irradiation hydrothermal process, 454
 Microwave radiation method, 398
 Mie resonances, 369, 379
 Mie scattering theory, 370
 Military industries, 173, 538
 Mineral, 53, 74, 197, 245, 249, 425, 453, 458, 463, 464, 468, 472, 480, 483, 495
 Mineral acid, 396
 Mineral composites, 495
 Mineral matrix, 496
 Mineral matrix composites, 495
 Minimum quantity lubrication (MQL), 423, 425–428, 430, 431, 433, 434, 436–438, 440–443, 445, 447
 Mismatch, 371
 Mixer, 165, 197, 565, 585
 Mixing, 2, 15, 40, 66, 68, 76, 165, 194, 197, 201, 241, 346, 350, 398, 404, 456, 473, 542, 585
 Mixture, 15, 19, 40, 42, 63, 68, 87, 161, 192, 197, 201, 225, 238, 240, 278, 281, 287, 290, 294, 295, 302, 319, 320, 350, 404, 411, 452, 456–458, 460, 465, 468, 478–480, 482, 606, 615
 Mixture rule, 210
 Mobility, 75, 94, 246, 278, 391, 395, 408, 452, 499, 557
 Modified Hummers' method, 396
 Modulation, 376, 387, 544
 Modulus, 6, 10, 12, 24, 42, 99, 113, 145, 149, 234, 393, 409, 410, 537, 539, 541, 559
 Moisture, 5, 10, 45, 51, 99, 102, 235, 276, 278, 279, 523
 Moisture sensitivity, 5
 Molecularly imprinted polymers (MIPs), 60, 66, 72–75, 83, 87
 Molecular structure, 99, 495, 606, 607
 Molecular weight, 47, 94, 95, 97, 99, 272, 278, 280, 284, 291, 616
 Molten-slat method, 454
 Molybdenum, 76, 495, 512, 520
 Monolithic aerogels, 407
 Monolithic material, 318
 Monomer, 16, 71, 75, 84, 158, 160–162, 270, 271, 273–276, 282–284, 287–290, 294, 295, 394, 402, 403, 512, 601–608, 611–613, 615–617
 Monte Carlo simulation code, 192
 Monte Carlo simulation (GEANT4), 187–189, 199, 200, 202, 203, 206, 225
 Montmorillonite, 43, 406, 510, 512, 522
 Morphological properties, 288, 613, 617
 Morphology, 19, 22, 75, 76, 165, 167, 168, 170, 246, 249, 251, 269, 272, 273, 276, 288–291, 323, 335, 345, 349, 354, 386, 427, 428, 444, 446, 477, 521, 524, 554, 571, 572, 583, 613
 Mullite, 7, 455, 476
 Multi-hit performance, 100
 Multi-specimen Tribo-tester, 321
 Multi-walled, 408, 521, 522, 542
 Multiwalled Carbon Nanotubes, 62, 78, 122, 154, 347, 349, 408, 509, 511, 581, 583, 588

N
 N220 block, 191
 Na₂WO₄, 191
 Na₃PO₄·12WO₃·H₂O, 193
 NaA zeolite, 468–471, 478, 481
 NaI(Tl) detector, 193, 195, 196
 Nanocapacitor, 400
 Nanocellulose, 286, 288, 295, 511
 Nanoclays, 43, 54, 146, 279
 Nanocomposite, 1, 2, 11, 14–23, 37–45, 47, 49, 50, 55, 83–85, 128, 151, 158–160, 170, 171, 175, 243, 247, 269, 279, 284–300, 302, 303, 344, 350, 391, 399, 403–405, 412, 414, 424, 426–428, 445, 475, 480, 482, 497, 505, 510, 514, 515, 583
 Nanocrystals, 38, 269, 276, 369, 377, 398
 Nano-cutting fluid, 425, 426
 Nano diamond, 538
 Nanoelectronics, 172
 Nanofiber, 38, 42, 62, 63, 123, 276, 281, 287, 291–293, 298, 385, 406, 409
 Nanofibrils, 38, 154, 277, 295
 Nanofibrous, 296, 299, 300, 478
 Nanofiller, 43, 45, 101, 235, 243, 251, 391, 406, 407, 414
 Nano-flowers, 399
 Nanofluid, 425–429, 442, 445–447
 Nano-hardness, 542, 544
 Nanohydroxyapatite, 122, 510, 511

- Nanomaterials, 38–41, 48, 50–52, 54, 66, 149, 159, 160, 165, 171, 269, 275, 285, 386, 404, 408, 427, 428, 521
- Nanopapers, 286, 292, 294, 295
- Nanoparticle, 38–40, 42, 43, 45–51, 53, 54, 63, 66, 152, 153, 156, 157, 162, 163, 165, 169, 174, 176, 191, 194, 237, 243, 256, 279–282, 284, 287, 291, 293, 297, 347, 348, 397–399, 411, 412, 423, 424, 426–428, 431, 432, 440, 442, 444, 446, 447, 478, 507
- Nanophotonics, 128, 369, 386, 387
- Nanoporous materials, 38, 39, 115
- Nanorods, 15–17, 19, 38, 54, 401
- Nanoscale, 39, 44, 45, 285, 369, 370, 385, 408, 445, 497, 585
- Nanoscale lasers, 370, 386
- Nanosheets, 65, 72, 75, 93, 101, 385–387, 392, 405, 412, 510, 520, 548
- Nano SiC, 423, 424, 427–429, 433, 434, 438, 440, 441, 444, 447
- Nanostructure, 15, 38, 81, 160, 269, 285, 291, 295, 386, 397, 398, 410, 521
- Nano TiO₂, 235, 237, 423, 428, 429, 432, 436, 438, 441, 445, 447
- Nano-titania, 62
- Nanowhisker, 279, 288
- Natural leather, 193
- Naturally radioactive nuclei, 188
- Natural polymer, 269, 270, 275, 279, 285, 286, 290–293, 295, 298–301, 303
- Natural rubber, 191, 193, 282, 285, 286, 291, 298, 602
- Natural rubber-based composites, 191
- Natural tissue, 53, 170
- Near-field interaction, 376
- Nerve canals, 169
- Neutron, 187–191, 193, 194, 196, 199–201, 210, 225, 227, 228
- Neutron shielding, 187, 189, 190, 194, 195, 200, 210, 225
- Nickel, 25, 344, 347, 348, 468, 474, 479, 514, 575, 577, 578, 589, 590
- Nickel filler, 344
- Nitrogen oxides, 568
- Nitrosamines, 62
- Noble metal, 301, 385, 398, 411
- Non-conducting polymers, 391, 396, 406
- Non-covalent interaction, 11, 398
- Non-covalent linking, 402
- Non-ionizing radiation, 188
- Non-linear, 407
- Nonmetals, 385, 396
- Non-radiative decay, 381
- Non-radiative emission, 381
- Non-symmetric, 98
- Non-toxic, 38, 281, 283, 425, 452, 497
- Non-woven, 46, 102, 110
- Norfloxacin, 507, 508, 511, 516, 521
- Normalization, 324, 338
- Normal load, 322, 330–332, 334–336, 339, 340, 352–356, 358, 361, 362, 364
- Nozzle, 25, 45, 126, 130, 135, 148–152, 154, 167, 427, 431, 571
- Nozzle diameter, 148, 151
- Nozzle parameters, 148
- Nuclear, 25, 187–189, 199, 272, 464
- Nuclear fission, 188
- Nuclear power reactors, 200
- Nuclear reaction, 188
- Nucleation, 163, 398, 399, 412, 453, 462, 549, 550, 552, 557
- Nucleotide monomer, 275
- Numerical model, 100, 111–113
- Numerical modeling, 111, 115
- Numerical simulation, 93, 100, 106, 424
- Nylon, 6, 7, 131, 145, 147, 149, 602
- O**
- Ohmic losses, 370
- Oil industry, 470, 601, 602
- Olefin metathesis reactions, 602
- Oleic acid, 606, 608, 617
- Olive oil, 605–607, 609
- Onion ring, 94
- Open mold cast technique, 195
- Operation loops, 468
- Optical, 2, 25, 38, 39, 50, 52, 53, 104, 124, 174, 274, 279, 285, 295, 296, 298, 349, 360, 369–378, 384–387, 392, 395, 402, 408, 411
- Optical devices, 39, 601
- Optical gain, 369
- Optical microscopy, 373, 546, 556
- Optical resonance, 370
- Optimization, 41, 47, 94, 99, 138, 140, 317, 383, 386, 435, 438, 447, 499, 556, 606, 615, 616
- Optoelectronic devices, 289
- Ordinary concrete, 191
- Organic, 2, 5, 26, 44, 48, 66, 70, 71, 76, 78, 85, 87, 132, 162, 235, 246, 273, 278, 290, 301, 385, 392, 404, 410, 412, 452, 460, 473, 480, 492, 494, 497, 499, 506, 511, 516, 519–521, 523, 524

- Organic acid, 40, 499, 519
Organic aromatic components, 64
Organic compounds, 59, 61, 78, 84, 86,
412, 506, 519, 523
Organic-inorganic composites, 505
Organic matrix composites, 26, 495
Organic precursor, 161
Organic solvent, 274, 277, 279, 280, 291,
608, 609, 617
Organic synthesis, 395
Organosulfur polymer composites, 603
Organosulfur polymeric composites,
601–603, 605–617
Origin 7.5 program, 199
Oscillation amplitude, 370
Outgassing, 5
Out-of-autoclave, 14
Overall preference value (ψ_j), 325
Overload currents, 566
Oxidant, 16, 78, 273, 287, 292, 294, 295,
301
Oxidation, 78, 271, 272, 274, 288, 299,
301, 357, 392, 396, 474, 476, 496,
521, 539, 551, 565, 585, 595, 596
Oxidation resistance, 539–541, 550, 565,
570, 575, 576, 589, 590
Oxide, 12, 14, 19, 21, 22, 40, 49, 50, 53, 54,
87, 122, 123, 155–157, 191, 193,
195, 196, 351, 361, 397, 399, 455,
474, 475, 495, 508, 509, 513, 521,
524, 538, 556, 570, 586
Oxidizing agent, 272–274, 287, 288, 290,
301
Oxygen, 1, 17, 43, 64, 83, 163, 166, 301,
392, 397–399, 403, 411, 452, 453,
463, 520, 521, 543, 557
Oxygen diffusion, 586
- P**
Palladium removal, 605
Palm oil, 470, 473, 475, 605, 610
Palm oil mill fly ash (POMFA), 454, 470,
471
Panel-core structure, 149
PAni/CNC, 290
Para-aramid, 95, 97, 99, 109, 111
Paracetamol, 155, 159
Paraffin, 193, 426
Parameter, 14, 51, 103, 105, 108–112, 127,
130, 132, 135, 138, 141, 150–152,
154, 158, 163, 165, 173, 189–193,
196, 201–203, 206, 210, 233, 236,
241, 242, 249, 257, 262, 320–323,
334, 335, 339, 345, 347, 354, 356,
358–360, 364, 373, 407, 424, 425,
427, 430, 435, 436, 438–440, 447,
462, 468, 469, 471, 474, 482,
498–504, 506, 518, 544, 548, 549,
552, 553, 556, 560, 583, 589, 594
Particle reinforcements, 340, 350, 496, 538,
585, 596
Particulate composites, 8, 233, 238, 243,
496
Pb₂O₃ nanoparticle, 193
PbCl₂, 192
PbCl₂-doped composite, 192
PbI₂ doped polyester composites, 192
PbO, 191, 194–196
PbWO₄ powder, 195, 196
PEDOT, 123, 155, 158, 280, 286, 290, 293,
296, 298, 300, 302, 303
PEDOT/Lignin, 290
Penetration, 15, 50, 64, 93, 94, 98, 100,
102, 104–106, 108, 113, 236, 287
Perforation ratio, 111
Performance, 10, 13, 14, 23, 25, 29, 37, 39,
43, 45, 47–49, 52, 61, 65, 68, 77, 78,
85, 100, 103, 110, 114, 125, 127,
134, 137, 138, 141, 143, 150, 158,
160, 168, 172, 187, 189, 198, 199,
234–237, 240, 249, 253, 254, 258,
260, 263, 276, 279, 293, 295, 302,
317, 318, 321, 323, 324, 331, 334,
336, 339, 340, 343, 345, 347, 349,
354, 360, 364, 385–387, 391,
393–395, 397, 400, 410, 414,
423–429, 435, 436, 438, 439, 441,
442, 447, 464, 493, 521, 537–540,
548, 549, 552, 557, 559, 560, 565,
570, 573, 577, 578, 588, 594, 596,
597, 615
Performance criteria, 336, 338, 340
Peripheral nerves, 169
Permeability, 48, 278, 279, 478, 479
Pesticides, 62, 63, 65, 67, 68, 73, 76, 79,
276, 603
Petrochemical, 538
Petroleum-based polymers, 601, 602
pH, 14, 273, 280, 281, 289, 291, 294, 296,
371, 453, 462, 466, 471, 474, 475,
492, 499, 502, 506–517, 519–524
Pharmaceutical compounds, 492
Pharmaceutical products, 491
Phase, 3, 4, 10, 15, 39, 41, 59, 64, 65, 82,
100, 101, 104, 107, 109, 133, 141,

- 151, 158, 162, 165, 193, 234, 243, 284, 285, 319, 320, 323, 361, 385, 391, 452–454, 457, 460, 462–465, 467, 468, 470, 471, 473, 476, 479, 480, 482, 492, 494, 496–499, 502, 503, 537, 541, 543–545, 548–550, 554, 555, 560, 585, 594
- Phase separation, 480
- Phase transformation, 453, 554, 555, 557
- Phenolics, 5, 7, 70, 105, 278
- Phenyl group, 278
- Photocatalytic, 51, 82, 476
- Photocatalytic degradation, 297, 401
- Photochemical reduction, 398
- Photodiode, 44, 372
- Photoelectric effect, 202
- Photoelectrocatalytic response, 297
- Photoinduced current, 400
- Photoinitiators, 158, 161, 162
- Photoluminescence, 82, 371–378, 380–382, 384, 387
- Photoluminescence decay spectra, 375, 376, 380
- Photon, 187, 188, 190–193, 195, 198, 199, 201–203, 371, 374, 376
- Photon attenuation, 187, 202
- Photonic detectors, 369
- Photonic modulators, 370
- Photo-peak, 199
- Photopolymerization, 154, 160, 163, 171
- Photopolymers, 126, 166
- Photosensitive polymer, 123, 160
- Photovoltaic cells, 44, 370
- Photovoltaics, 39, 44, 45, 274, 386, 400, 401
- Photovoltaic wire, 395
- Phthalate esters (PAEs), 67, 86
- Physical, 2, 11, 38, 42, 48, 60, 65, 85, 97, 104, 132, 133, 137, 138, 154, 158, 192, 201, 202, 240, 285, 292, 293, 296, 317, 318, 320, 325, 337, 349, 351, 370, 385, 408, 423, 424, 446, 451, 452, 454, 491–494, 496–499, 502, 506, 520, 524, 543, 557, 585, 594, 608, 609
- Physical adsorption, 76, 81, 464, 498, 524
- Physiological structure, 170
- Phy-X/PDS software, 192
- Piezoelectric, 52, 53, 165, 282, 283
- Piezo resistivity, 163–165, 410
- Pin-on-disc testing apparatus, 242
- Π -ion bond, 506
- Π - π conjugation, 391
- Π - π interactions, 394, 520–522, 524
- Π - π stacking, 400, 401, 413, 414, 520
- Piston, 24, 540
- Pitch, 10, 12
- Plane wave, 379
- Plasmon, 369
- Plasmonic, 369–371, 373–376, 384, 387, 401
- Plasmon resonanc, 161, 162, 370
- Plastic deformation, 262, 336, 353, 539, 558, 559, 591
- Plasticized polyvinyl chloride, 191
- Plasticizer, 281, 284
- Poisson, 134
- Poisson coefficient, 148
- Poisson ratio, 113, 134
- Polar functional groups, 78, 272, 403
- Polarity, 13, 62, 81, 82, 296
- Polarization, 41, 52, 167, 347, 370–375, 377–379, 386, 387
- Pollutant, 73, 78, 82, 274, 286, 295, 412, 451, 452, 464, 473, 479, 481, 482, 568
- Pollution, 235, 299, 345, 452, 492, 523
- Polyacrylonitrile (PAN), 10, 12, 413, 513, 523
- Polyamide, 122, 123, 144, 146, 168, 291, 403, 407, 495
- Polyaniline, 15–19, 21, 22, 86, 270–272, 279, 285–289, 302, 397, 403, 511, 515, 522
- Polycaprolactone (PCL), 122, 123, 143, 146, 151, 154, 156, 169, 170, 282, 284
- Polycarbonate-based composites, 193
- Polychlorinated Biphenyl, 68
- Polycyclic aromatic hydrocarbons (PAHs), 67–71, 73, 74, 78, 82, 83, 87, 291, 292
- Polydimethylsiloxane, 82, 124, 167, 191
- Polyester, 5, 26, 28, 144, 164, 188–193, 195–197, 200, 202, 204, 206, 207, 210, 211, 213, 215, 217, 218, 220, 222, 223, 225–228, 275, 282–284, 495, 602
- Polyester mesh (PM), 191
- Polyester resin-based composite, 189, 191, 195
- Polyetheretherketone, 495
- Polyethers, 6, 7, 602
- Polyethylene, 7, 47, 63, 82, 94, 95, 99, 114, 124, 147, 162, 167, 194, 196, 275, 402, 407, 413, 414, 495, 509, 602

- Polyethylene chains, 99
 Polyethylene fibers, 97, 99
 Poly(ethylene glycol), 94, 98, 156, 158
 Poly (hydroxyethyl methacrylate), 192, 193, 196
 Polyimide, 5, 124, 403
 Polyisoprene, 282, 285
 Polylactic acid, 122, 129, 283, 289
 Polymer, 1, 3, 5, 11, 14, 15, 23, 24, 28, 40, 42–45, 47, 54, 60, 62, 66, 70, 72, 73, 76, 85, 98, 99, 123, 124, 129, 132, 133, 141, 147–152, 154, 155, 158, 160–167, 176, 189–191, 194, 196, 197, 201, 233–235, 269–276, 279–284, 286–288, 291, 293, 295, 298, 300, 301, 303, 391, 393–398, 402, 403, 407, 409–415, 478, 479, 493–495, 497, 512, 601, 602, 604, 605, 608–610, 612, 614–617
 Polymer-based composite, 3, 187, 189
 Polymer chain, 15, 18, 97, 270, 272, 279, 291, 394
 Polymer composite, 2, 24, 26, 28, 29, 121, 171, 177, 189, 192, 195, 197, 201, 234–237, 245, 246, 257, 258, 263, 391, 393, 395, 396, 406, 409–411, 414, 478, 616
 Polymeric, 11, 28, 40, 41, 43, 49, 51, 121, 125, 128, 132, 148, 151, 160, 161, 235, 270, 274, 275, 278, 284, 287, 288, 290, 293, 298, 415, 464, 480, 483, 493–496, 601, 603, 604, 608, 610, 611, 615–617
 Polymerization, 13, 15, 43, 73, 126, 158, 161, 163, 197, 270, 272–275, 278, 283, 284, 287, 288, 290, 292, 299, 397, 402, 403, 480, 602–605, 615, 616
 Polymer matrix, 1, 3, 5, 7, 10, 15, 23, 43, 158, 197, 234, 236, 249, 393, 394, 402, 403, 407, 409, 410, 477, 505
 Polymer nanocomposites, 11, 15, 43, 238, 277, 286, 298, 299
 Poly methyl methacrylate, 192
 Polynucleotides, 275
 Polyolefins, 602
 Polypeptide, 275, 280, 281
 Polyphenylene sulfide, 2, 6, 7
 Polypropylene, 2, 6, 7, 98, 275, 602
 Polypropylene sulfide, 2
 Polypyrrole, 65, 76, 86, 87, 270–273, 281, 286, 287, 296, 297, 299, 402, 515
 Polysaccharides, 47, 275–279, 413
 Polystyrene, 7, 62, 99, 407, 495, 602
 Polystyrene composites, 406
 Polysulfide, 603
 Polythiophene, 76, 270, 271, 273, 274, 285
 Polyurethane (PU), 94, 98, 164, 411, 602
 Polyvinyl acetate (PVA), 94, 98, 124, 168, 169, 194, 195, 282, 284, 409, 413, 477–479, 481, 482
 Polyvinyl alcohol, 170, 195, 284, 407, 413, 478, 479, 508, 515
 Poly vinyl chloride, 195
 Population, 139, 235, 452, 491, 492
 Pore, 66, 81, 83, 152, 165, 170, 246, 291, 407, 453, 463–465, 479–481, 493, 499, 501, 505, 520–524, 587
 Pore size, 62, 70, 78, 81, 191, 246, 465, 473, 478, 481, 522
 Porosity, 48, 62, 65, 66, 83, 87, 127, 130, 152, 154, 155, 164, 165, 262, 280, 293, 329, 331, 424, 426, 446, 471, 478–480, 493, 499, 519, 523, 547, 548, 553, 560, 587, 588
 Porous, 53, 61, 64, 65, 70–72, 82, 83, 127, 130, 146, 153, 163, 164, 166, 169, 170, 246, 247, 252, 280, 289, 351, 452, 464, 473, 474, 476, 477, 480–482, 513, 520, 521, 523, 541
 Porous silica, 61
 Portability, 406
 Potential difference, 296
 Potentiodynamic, 273, 347
 Potentiometric, 297
 Potentiostatic, 273
 Powder, 14, 41, 42, 126, 143, 149, 151, 163, 165, 166, 191, 272, 273, 276, 319, 326–328, 333, 344, 346, 347, 350, 351, 364, 400, 459, 479, 541–545, 548, 549, 552, 554, 560, 581, 585, 588–591, 595, 596, 603, 613
 Powder metallurgy, 42, 344, 349, 351, 355, 359, 363, 537, 540, 542, 545, 547, 560, 565, 585, 586, 588, 589, 591, 596, 597
 Powder processing, 404
 Power, 27, 28, 39, 152, 165, 173, 301, 359, 372, 374, 376, 379, 381, 382, 384, 431, 432, 467, 548, 551, 552, 565, 566, 569, 575, 594
 Power density, 171, 301, 372, 407
 Precursor, 8, 10, 14, 15, 40–42, 66, 153, 165, 285, 398, 400, 401, 403, 455, 458–460, 468, 480, 483

- Preference selection index (PSI), 317–319, 323, 325, 336, 337, 339, 340
- Preference variation value (PVj), 325
- Pressure, 13, 14, 16, 24, 26, 39, 46, 65, 106, 130, 145, 151, 153, 154, 165, 168, 172, 236, 241, 253, 277, 298, 354, 394, 410, 427, 458, 459, 470, 473, 478, 479, 557, 559, 591
- Price, 149, 283, 565, 568, 595, 601, 602, 605
- Printability, 127, 133, 152, 165
- Pristine, 51, 75, 87, 175, 302, 327, 385, 408, 609, 610
- Processing, 14, 15, 42, 59, 60, 127, 151, 170, 173, 190, 196, 235, 269, 272, 281, 285, 344, 346, 348, 358, 377, 394, 402, 404, 414, 424, 426, 428, 464, 538, 541–544, 548, 549, 551–553, 558, 560, 585, 603, 605, 617, 618
- Process parameters, 40, 127, 428, 457, 474, 553
- Progressive damage, 100, 108
- Projectile, 99, 101, 103–110, 113, 114
- Projectile geometry, 104
- Projectile properties, 103
- Properties, 2–12, 28, 29, 37–39, 41, 43–54, 59, 60, 63, 65, 70–73, 82–85, 87, 88, 98, 102, 104, 110, 113, 114, 121, 132–134, 137, 138, 148–151, 155–157, 161, 164–167, 169, 170, 173–176, 189–195, 200–202, 225, 233–238, 240, 243, 245, 246, 252, 261, 263, 269–271, 273, 274, 276, 279–289, 291, 293–297, 299, 301, 303, 318, 338, 344–351, 354, 355, 359, 362–364, 370–373, 386, 387, 391–397, 399, 402, 405–411, 414, 424, 428, 442, 446, 452, 454, 455, 460, 463, 464, 466, 472, 475, 477, 478, 480, 492–497, 499, 519–524, 538, 539, 542, 543, 545, 549–551, 553–557, 560, 565, 569, 575, 578–581, 583, 585, 586, 588, 590, 592, 594–596, 601–605, 607–609, 614, 616–618
- Protection, 54, 94, 95, 97, 100, 115, 128, 187, 189, 190, 200, 201, 206, 363, 411, 412, 615
- Protein, 47, 71, 72, 270, 275, 279–281, 291, 392, 602
- Pseudo-first order, 502, 504
- Pseudo-reactive models, 502
- Pseudo-second order, 502, 504
- Pulverization process, 454, 459, 462
- Purcell factor, 370, 376
- Pyrethroids, 62, 64, 68
- Pyridine, 512, 608, 609
- Pyrolysis, 38, 42, 161, 166, 246, 520
- ## Q
- Quadrupole, 379, 384
- Quadrupole resonance, 379, 380
- Quality factor, 376
- Quantum confinement, 405
- Quantum dots, 38, 39, 75, 369–377, 379–385, 387, 405, 406
- Quantum dots photoluminescence, 371
- Quantum yield, 371, 380, 381, 386
- Quasi-isotropy, 496
- Quasi-static, 94, 100, 103, 109
- Quasi-static penetration test, 109
- Quenching, 15, 371, 372, 376, 555
- ## R
- Radiation protection efficiency, 189, 196, 199, 203
- Radiation shielding, 187–196, 198, 200–202, 225
- Radiation transmission factor (TF), 203, 206, 222–224
- Radiative, 376, 381
- Radiative emission, 375, 376
- Radical, 158, 163, 274, 299, 602–604
- Radioactive decay, 188
- Radioactive source, 195, 196, 201
- Radiological, 187
- Raman microscopy, 393
- Ranking criteria, 323
- Ranking optimization, 336
- Rapid melting, 548, 594
- Rapid solidification processing (RSP), 537
- Rapid solidification technology, 542, 543, 560
- Rayon, 10
- Reaction spontaneous infiltration method (RSI), 544
- Reactive hot pressing, 542, 560
- Reagent, 272
- Recovery, 61–65, 68, 69, 71, 73–75, 78–80, 82, 86, 146, 147, 149–151, 169, 468, 470, 476, 480, 482, 521
- Recyclability, 141, 524
- Recycling, 275, 616, 618
- Redox potential, 399

- Redox reaction, 400
- Reduced graphene oxide, 62, 123, 392, 395–399, 405, 406, 408–410, 412, 474, 511, 521
- Reducing agent, 38, 395, 396, 412
- Reduction–oxidation, 290
- Re-entrant auxetic, 134, 147
- Refractive index, 370, 376, 387
- Refractory alloying, 345
- Regeneration, 128, 169–171, 277, 280, 289, 298–300, 502, 520
- Rehabilitation, 28, 169
- Reinforced composite, 4, 8, 10, 100–102, 106, 149, 150, 152, 158, 168, 173, 191, 193, 195, 234, 236, 258, 344, 361, 364, 408, 438, 447, 496
- Reinforcement, 1, 3, 4, 7–10, 24, 28, 29, 42, 145, 151, 152, 154, 158, 159, 161, 163, 165, 169, 234, 235, 238, 245, 249, 258, 262, 263, 278, 285, 317–319, 326–328, 330, 334, 335, 339, 343–349, 351, 355, 356, 359–364, 393, 408, 409, 424, 426, 440, 494–496, 538, 539, 541–545, 548, 549, 553–555, 560, 581, 583, 585, 588, 596
- Remediation, 451, 452
- Renewable, 269, 270, 275, 276, 283, 301, 303, 492, 519, 605
- Renewable energy, 299, 301, 569
- Residual string formation, 148
- Residual velocity, 100, 104, 106
- Resin, 5, 7, 10, 13, 14, 23, 27, 28, 48, 51, 124, 145, 155–161, 166, 171, 172, 175, 194, 197, 234, 235, 238, 239, 275, 403, 464
- Resin film infusion (RFI), 14
- Resistance, 5, 7, 10, 26, 28, 29, 39, 41, 42, 45, 51, 52, 54, 67, 99, 102, 108, 172–174, 233–237, 249, 251, 258, 260, 262, 263, 285, 286, 328, 348, 358, 361, 363, 364, 385, 405, 410, 411, 440, 464, 496, 497, 503, 556, 557, 570, 581, 595, 596
- Resistivity, 258, 259, 288, 297
- Resolution, 133, 141, 148, 154, 158, 160, 161, 163, 174, 176, 177, 372, 373
- Resonance, 370, 371, 379–381
- Resource formation, 573, 574
- Response surface methodology (RSM), 237, 423, 427, 428, 430, 435, 436, 447, 606
- Reverse imaging modeling, 122, 133
- Reversible, 75, 273, 290, 411, 495, 498
- Rheological properties, 289, 429
- Rhodamine, 297, 412, 479
- Rhodamine-B (RB), 297, 412, 479
- Ribonucleic acid (RNA), 275
- Rice husk, 235, 406, 454, 469, 470, 473, 474
- Rice husk ash (RHA), 469, 470
- Rigidity, 99, 160, 168, 173, 278, 285, 348, 424, 494–496
- Robot, 24, 146, 156, 166, 168
- Robotic freedom, 149
- Rod, 24, 28, 97, 277, 319, 344, 349, 351, 466
- Roll milling, 394
- Roughness, 291, 349, 441
- Rubber, 194, 282, 285, 411, 601
- Rubber seed oil, 603, 605–614, 616
- Rupture, 101, 394, 502, 572, 596
- ## S
- Sacrificial structure, 148
- Saline water medium, 245
- Salt, 47, 76, 162, 273, 288, 392, 397, 453, 458–460, 462, 483, 544, 615
- Sand, 194, 241, 242, 258, 260, 262
- Sandwich structure, 9, 10, 121
- Satin weaves, 102
- Saturation capacity, 502
- Saturation point, 502
- Scaffold, 128, 143, 146, 151–155, 164–166, 169–171, 177, 280, 281, 284, 286, 289, 293, 296, 299, 300, 413
- Scanning electron microscopy (SEM), 19, 20, 22, 23, 47, 123, 151–154, 165, 166, 292, 293, 317, 323, 335–337, 340, 344, 346, 349–351, 354, 359, 360, 377, 379, 428–430, 444, 446, 467, 476, 553, 573, 574, 576, 578, 613, 614, 617
- Scattering, 295, 370–372, 377, 379, 380, 594, 613
- Scintillation detector, 189
- Scotch tape method, 395
- Screen printed, 290
- Selective laser melting (SLM), 537, 544–549, 553, 554, 560, 573, 592, 594, 595, 597
- Selective laser sintering, 124, 163
- Self, 51, 54, 156, 167, 236, 291, 292, 385, 411, 551
- Self assembly, 153, 401

- Self healing, 170, 557
- Self-propagating high-temperature synthesis, 537, 542, 543, 560
- Self-renewal contact material, 590
- Semiconductor, 40, 52, 369, 370, 385, 392, 408
- Semi-crystalline, 21, 143, 276, 279, 284
- Sensor, 39, 44, 45, 52, 53, 104, 165, 174, 274, 279, 282, 284, 286, 295–298, 303, 386, 407, 408, 410, 411, 414, 525
- Separation, 60, 63, 66–70, 72, 73, 76–78, 87, 113, 114, 151, 394, 396, 452, 473, 475, 476, 480–483, 520, 524, 565, 572, 585, 596
- Separation efficiency, 78
- Sequential F test, 436
- Serpentine, 191
- Sesame oil, 425
- S-glass fiber, 100
- Shape memory, 123, 131, 132, 143, 150, 151, 161, 174, 176
- Shape memory materials, 123, 151
- Shape-morphing, 132, 146
- Shear, 11, 94, 100, 103, 105, 107–109, 112, 113, 151, 152, 158, 165, 393
- Shear damage, 109
- Shear failure, 109
- Shear forces, 154, 357, 393
- Shear loading, 108, 110
- Shear plugging, 108
- Shear plugging mechanism, 107
- Shear strength, 10, 26, 112, 114, 409
- Shear thickening fluids (STF), 94, 98, 99, 103
- Sheet lamination, 124, 126, 168, 169
- Sheet metal cutting, 584
- Shielding, 128, 145, 175, 187–195, 199, 201–203, 274
- Shielding ability, 195, 210, 406
- Shielding absorber, 188, 225
- Shipbuilding, 537
- Shock compression, 100
- SiC multifilament, 12
- Sierpinsky tetrahedrons antennas, 148
- Signal to noise, 334
- Signal-to-noise (S/N) ratio, 322, 323, 334–336, 438
- Silica, 43, 48, 65, 100, 114, 146, 152, 235, 241, 242, 246, 262, 399, 404, 405, 454, 455, 457, 458, 460, 463, 467–471, 473, 474, 476, 480, 506, 513, 517, 522, 523
- Silica/chitosan, 497
- Silica particles, 98, 405
- Silicon, 25, 44, 51, 54, 124, 194, 318, 347, 361, 362, 370, 371, 377, 379–381, 385–387, 394
- Silicon-based composite, 192
- Silicon carbide, 7, 11, 24, 25, 41, 124, 347, 349, 351, 353, 354, 359, 363, 424, 496, 579
- Silicone, 157, 166, 191
- Silicone rubber, 190, 193
- Silicone/tungsten, 192
- Silicon microcavity, 369, 387
- Silicon nitride, 7, 350, 354
- Silicon particle, 25, 355, 369–372, 377, 379–382, 384, 387
- Silk, 153, 157, 280, 281, 409, 602
- Silver nitrate, 124, 162, 172
- Simulated mechanical properties, 141
- Simulation, 100, 103, 108, 132, 135, 137, 138, 141, 148, 188–190, 193, 194, 196, 200–202, 225, 288, 289, 386
- Single-photon emissions, 370
- Single-walled, 11, 39, 43, 124, 165, 399, 521
- Size, 2, 7, 14, 18, 19, 38, 39, 43, 48, 50, 52, 54, 63, 72, 125, 134, 135, 137, 148, 149, 151, 152, 154, 165, 169, 172, 194, 195, 233–235, 237, 238, 242–244, 252, 253, 262, 263, 280, 283, 290, 319, 321, 326, 328, 329, 333, 343, 344, 347, 350, 351, 362–364, 370, 373, 374, 376, 377, 379, 382, 387, 393, 398, 414, 415, 426, 428, 454, 458, 470, 471, 478, 480, 493, 499, 520, 522–524, 541–543, 548, 551–556, 591, 592, 594, 597
- Slag, 235, 457, 468, 469, 473, 480
- Sliding, 318, 321, 330–333, 336, 339, 343, 347, 354, 355, 358, 359, 361–363, 566, 591
- Sliding distance, 243, 322, 323, 332–336, 338–340, 343, 356–362, 364
- Sliding speed, 330, 335, 354–359
- Sliding velocity, 321–323, 329–331, 334–336, 339, 340, 343, 354–358, 361, 364
- Sliding wear, 317, 318, 321, 323, 335–337, 343, 345, 346, 348, 354, 356, 358–360, 364
- Sliding wear performance, 317–319
- Sludge, 464, 475, 515

- Small mode volume (V), 370
 Smart manufacturing, 121, 125
 Sodium borohydride, 396, 398
 Softening parameters, 100
 Soil, 73, 74, 76, 87, 190, 275, 452, 482, 520, 603, 615
 Soldering, 565, 584, 585, 594, 597
 Sol-gel, 14, 15, 38, 40, 42, 43, 98, 391, 399, 403, 407, 470, 523
 Solidification, 14, 15, 42, 166, 428, 544, 548, 557, 594
 Solid-phase extraction, 60
 Solid-phase microextraction, 59, 60, 82
 Solid solubility, 543
 Solid solution, 545, 554–557
 Solid-state reaction, 82
 Solid surface, 497
 Solidus, 319
 Solubility, 161, 273, 274, 279, 280, 291, 412, 415, 519, 608, 609, 616, 617
 Soluble, 47, 272–274, 276, 279, 281, 284, 397, 523, 608, 609, 617
 Solution casting, 617
 Solution casting method, 279
 Solution mixing, 15, 396, 409
 Solvent extraction method, 469
 Solvent-free synthesis, 452, 454, 460, 462
 Solvothermal synthesis, 82
 Sorption, 452, 456, 468
 Sorption capacity, 64, 72, 455, 457
 Soybean oil, 82, 425, 605–607, 609, 615
 Span to punch diameter ratio, 109
 Spark plasma sintering (SPS), 542, 543
 Spatial coherence, 376
 Spatial decomposition, 133
 Spatial distribution, 134, 375–377, 387
 Spatial interference pattern, 370
 Specific area, 2, 278, 392, 503, 521
 Specific energy, 425–427, 440
 Specific energy absorption, 101
 Specific penetration resistance, 102
 Specific stiffness, 3, 537
 Specific strength, 3, 24, 424, 537–539, 541, 559
 Specific surface area, 62, 63, 70, 71, 75, 78, 83, 377, 407, 408, 470, 475, 477, 478
 Specific wear, 329, 355
 Specific wear rate, 322, 329–333, 339, 340, 353, 355–358, 360, 364
 Spectra, 17, 19, 21, 69, 97, 99, 372–375, 377, 379–382, 400, 424, 522, 609, 610
 Spectrophotometer, 371
 Speed, 13, 14, 104, 109, 130, 135, 141, 148, 150, 153, 154, 161, 163, 173, 174, 176, 301, 319–321, 348, 350, 351, 354, 356, 387, 394, 427, 432, 447, 459, 460, 498, 501, 502, 506, 548, 552, 566, 594
 Spin, 290, 303
 Spiral, 155, 285
 Spongy, 133, 290
 Spray, 290, 303, 347
 Spray pyrolysis, 14, 38, 42
 Stacking sequence, 98
 Standard Triangulation Language, 122, 141
 Starch, 269, 270, 275, 276, 281, 283, 298, 300, 507, 517, 602
 Static, 98, 241, 277
 Steady state, 321, 329, 336, 339, 362
 Steel, 3, 10, 15, 25, 27, 83–85, 94, 101, 114, 234, 242, 319, 321, 346, 348–350, 354, 362, 393, 394, 426, 427, 468, 469, 480, 538, 557
 Steel chips, 318
 Steel fragment, 99
 Steel industry, 468
 Stereolithography (SLA), 123, 154–160, 171, 176
 Stiffness, 5, 8, 10, 11, 24, 27, 28, 138, 144, 151, 234, 345, 493, 499
 Storage, 52, 138, 140, 189, 225, 245, 275, 279, 476, 603
 Storage device, 52, 295, 299, 301–303
 Storage modulus, 149, 152
 Strain parameters, 100
 Strength, 3, 5, 7–12, 24, 26–29, 42, 48, 53, 97, 99, 102, 103, 134, 138, 149, 151, 156, 168, 169, 234–237, 243, 245, 246, 249, 253–256, 263, 280, 281, 328, 345, 347, 348, 354, 393, 394, 405, 409, 410, 457, 465, 473, 493, 494, 496, 538–541, 545, 548, 551, 554, 555, 557, 560, 589
 Stress, 52, 105–108, 111, 112, 135, 144, 148, 150, 151, 160, 165, 166, 169, 246, 253, 254, 335, 343, 348, 349, 393, 408, 411, 414, 440, 548, 556–558
 Stress shielding effect, 541
 Stress waves, 103–107, 109, 114
 Striking face, 101
 Structural, 4, 5, 7–9, 15, 23–29, 37, 39, 42, 51, 67, 100, 106, 128, 133, 138, 157, 166, 234, 236, 270–273, 275, 351,

- 354, 385, 386, 409, 424, 455, 496,
497, 538, 539, 543, 548, 549, 610,
617
- Structural 3D composites, 173
- Structural properties, 1, 5, 14, 235, 476,
477, 604, 612, 617
- Structural structures, 133
- Structure, 2, 7, 10, 18, 19, 21, 24, 27–29,
37–40, 45, 48, 52, 53, 61, 64–68,
70–72, 75, 78, 82–84, 87, 88, 93–95,
97–111, 113–115, 125, 127–135,
138, 140, 141, 143, 145–149, 151,
153–158, 160, 161, 163–177, 235,
240, 246, 252, 270, 275–279, 281,
285, 287–290, 295, 299, 323, 324,
333, 344, 349–351, 373, 385–387,
392, 394, 397, 402, 408, 410–413,
424, 452, 453, 455, 460, 462–465,
467–469, 471, 477, 482, 496, 497,
506, 520–524, 537, 539, 541, 542,
545, 548, 550, 555, 557, 560, 581,
583, 585–588, 591, 592, 594, 597,
603–605, 608, 610, 612–618
- Submarine pressure shells, 538
- Subtractive manufacturing, 122, 127, 136
- Sub-wavelength, 369, 371
- Sugarcane bagasse, 277, 454, 471
- Sugarcane bagasse fly ash (SCBFA), 471,
472
- Sugar mills, 471
- Sulfonamide antibiotics (SAs), 61, 142, 470
- Sulfur-based polymers, 601–606, 608, 610,
615–617
- Sulfur conversion, 613, 616
- Sulfuric acid, 124, 165, 272, 276, 603
- Sunflower, 425, 601, 605–607, 609
- Supercapacitor, 288, 296, 301–303, 400,
401, 408
- Surface area, 38, 54, 61, 70, 75, 78, 81, 83,
84, 87, 160, 167, 277, 291, 294, 397,
406, 408, 411, 413, 414, 426, 456,
475, 479, 480, 493, 499, 505,
519–524, 615
- Surface coating, 98, 356, 542
- Surface damage, 317, 364
- Surface free energy, 497
- Surface plasmons, 369, 370
- Surface properties, 5, 87, 350, 425, 571,
578, 594
- Surface roughness, 424–428, 430, 433, 434,
436–442, 445, 447
- Surface texture, 571
- Surface to volume ratio, 243
- Surfactant, 49, 76, 288, 404, 415, 492, 512,
513, 603
- Survivability onion, 94, 95
- Susceptibility, 72, 77, 496
- Suspension, 16, 160, 163, 277, 281, 290,
371, 386, 398, 399, 404, 412
- Sustainability, 345, 425, 428, 492, 519,
524, 602
- Sustainable, 269, 290, 425, 476, 480, 482,
519, 603
- Sustainable grinding, 423, 442, 447
- Switch, 411, 565, 566
- Symmetric, 98
- Symmetrical, 102, 112
- Synergetic, 98, 134
- Synergy, 127, 161
- Synthesis, 15, 38–40, 42, 43, 49, 54, 60, 67,
76, 81, 82, 93, 114, 125, 149, 151,
158, 159, 161, 165, 235, 270,
272–274, 281, 284, 287–289,
294–297, 301, 302, 350, 359,
395–397, 402, 404, 405, 408,
451–463, 467–471, 473–475, 480,
482, 483, 506, 519, 543, 544, 560
- ## T
- Ta₂O₅, 191
- Taguchi design, 323
- Taguchi method, 334, 350
- Taguchi methodology, 317
- Taguchi orthogonal array, 321
- Tangential grinding force, 427, 431, 432,
440
- Target, 49, 59–67, 69, 72, 73, 75, 76, 78,
82, 84–88, 104, 106–108, 110, 203,
249, 262, 596
- Temperature, 1, 3, 5, 7, 8, 11, 13, 19,
24–27, 29, 39, 40, 42, 43, 45, 51, 52,
71, 76, 78, 99, 132, 135, 141, 145,
148, 149, 151, 153, 154, 161, 167,
170, 172, 192, 197, 235, 238, 240,
242, 255, 258, 262, 272, 273, 281,
283, 286, 290, 296–298, 302, 319,
328, 329, 331, 344, 347–350,
354–357, 362, 375, 384, 392, 395,
406, 407, 410–412, 424, 426, 427,
432, 442, 455, 456, 458–460, 462,
464, 467–471, 474–476, 479, 480,
492, 494–496, 499, 501, 506–517,
519, 520, 522, 539, 540, 542, 544,
548, 554–560, 565, 566, 571, 580,
585, 587, 591, 595, 603, 604, 606,
607, 611, 612, 616, 618

- Temperature gradient, 170, 386
- Template-assisted chemical vapor deposition, 406
- Template synthesis, 14, 15, 42, 43
- Tensile, 105, 112–114, 144, 168, 241, 243, 246, 253–257, 409, 499, 550, 552, 560
- Tensile load, 148
- Tensile modulus, 11, 97, 141
- Tensile ply failure, 109
- Tensile strength, 2, 6, 7, 10, 12, 54, 97, 100, 113, 148, 149, 155, 234, 241, 243–248, 253–256, 281, 282, 284, 286, 293, 317, 318, 328, 338–340, 344, 346, 347, 349, 351, 353, 392, 393, 406, 424, 426, 440, 539, 548, 550, 551, 553, 555, 556
- Tensile stress, 100, 110
- Tensile test, 174, 244, 245, 247, 248, 320
- Tension, 11, 28, 103, 105, 109, 150, 167, 397, 542
- Tension-shear, 100
- Tenth value layer, 190, 196, 202
- Terminal materials, 584
- Tetrahydrofuran (THF), 273, 274, 608, 609
- Textile materials, 104
- Theoretical, 75, 187, 189, 190, 193, 196, 198, 201, 202, 204, 206, 210, 211, 213, 215, 218, 220, 225, 301, 320, 325, 362, 364, 377, 504, 543, 560, 580
- Thermal, 2, 8, 10, 25, 29, 37–39, 51, 52, 75, 82, 97, 100, 126, 127, 131, 132, 149, 155, 171, 172, 176, 193, 194, 285, 288, 331, 348, 349, 361, 386, 392, 395, 400, 403, 407, 411, 414, 423, 424, 426, 444, 475, 479, 492, 494, 520, 521, 523, 556–558, 566, 571, 581, 610
- Thermal conductivity, 2, 3, 6, 8, 12, 25, 29, 145, 149, 348, 392, 395–397, 406, 408, 414, 442, 493, 494, 544, 565, 567, 569, 570, 575, 576, 579, 583, 587, 594–596
- Thermal conductors, 395
- Thermal decomposition, 82, 480, 520
- Thermal degradation, 99
- Thermal dissipation, 172
- Thermal effect, 370, 557
- Thermal gravimetric analysis, 288
- Thermally conductive, 171, 172
- Thermal properties, 235, 411, 493, 570, 610, 617
- Thermal relays, 566
- Thermal resistance, 235, 288, 519, 583
- Thermal stability, 2, 62, 72, 73, 83, 87, 235, 246, 283, 287, 293, 410, 460, 466, 473, 478, 493, 522, 555, 556, 560, 611
- Thermal treatment, 160, 459
- Thermodynamic adsorption parameters, 501
- Thermogram, 610–612, 617
- Thermogravimetric analysis (TGA), 235, 611, 612
- Thermomechanical, 42, 132, 149
- Thermoplastic, 5–7, 23, 28, 173, 249, 258, 276, 281, 283, 284, 409, 415, 495, 604
- Thermoplastic Polyurethane, 122, 131
- Thermoplastic Resins, 7
- Thermosets, 5, 6, 13, 23, 249, 258, 494, 495, 604
- Thermosetting polyesters, 5, 23
- Thermosetting polyimide, 5
- Thermosetting Resins, 5
- Thermostatic oil bath, 604, 606
- Thickness, 51, 100, 103, 105, 110, 111, 113, 149, 156, 161, 165, 170, 173, 187, 189, 190, 194, 196, 198, 200–203, 210, 225, 227, 228, 238, 241, 289, 321, 346, 356, 432, 440, 548, 594
- Thiyl radicals, 605
- Thread density, 103
- Threat types, 93, 95
- Time-resolved fluorescence decay, 400
- Time-resolved mode, 370
- Tin, 319
- Tin oxide, 297, 579
- Tissue engineering, 53, 151, 157, 164, 169–171, 277, 282–284, 286, 293, 298–300, 303, 391, 413
- Titanium, 5, 24, 25, 50, 53, 152, 348, 495, 538, 541, 542, 545, 547, 549, 551
- Titanium alloy, 27, 538, 539, 541, 542, 544, 545, 551, 556, 559
- Titanium dioxide (TiO₂), 43, 50, 51, 54, 98, 233, 235, 237, 238, 240, 259–263, 293, 318, 398, 399, 401, 426, 432–435, 438, 442, 443, 445–447, 475–477, 480, 481, 508, 509, 520
- Titanium forgings, 538
- Titanium matrix, 539, 541, 545
- Titanium matrix composites (TMCs), 537–546, 548–557, 559, 560

- Top-down, 38, 405
Topology, 131, 133, 135, 162
Topology optimization, 122, 134, 136, 138–140
Total atomic cross section, 198
Total internal reflection, 370
Toughness, 4, 11, 39, 41, 42, 48, 99, 103, 113, 148, 174, 346, 409, 493, 499, 541, 552
Toxicity, 46, 50, 189, 190, 201, 413, 472, 492, 522
Toxic metal, 476, 480, 482
Transducer, 53, 295, 296
Transition temperature, 554
Transmission, 23, 24, 28, 39, 52, 124, 165, 173, 188, 190, 196, 200, 210, 225, 227, 228, 372, 409, 565, 566, 570
Transmission electron microscope (TEM), 15, 16, 22, 23, 69, 124, 165, 166, 290, 300, 344, 346, 349, 372, 373, 375, 377, 379, 559
Transmission factor, 189, 192, 196
Transparency, 284, 295, 406
Transparent conductor, 399, 401
Transport, 11, 174, 225, 280, 409, 501
Transportation, 189, 190, 301, 549, 568
Transverse, 112, 113, 134, 146, 148, 549, 591
Transverse impact, 104
Transverse waves, 105, 106
Treatment, 23, 45, 48, 49, 85, 98, 188, 277, 299, 345, 451–460, 462, 464, 467–471, 473–476, 480, 482, 483, 492, 502, 554, 557–559
Tribological, 233, 235–237, 318, 337, 340, 343–345, 347, 348, 352, 355, 359–361, 363, 364, 432, 435, 442
Tribological factors, 343
Tribological performance, 263, 321, 343, 432, 435
Tribological testing, 238, 241
Triglycerides, 607, 616
Tungsten, 24, 49, 123, 192–196, 372, 385, 495
Tungsten doped composite, 192, 195
Twill, 102, 103
Twill weaves, 103
- U**
Ultimate tensile strength, 318, 344, 346, 349, 350, 545, 547, 549, 550
- Ultrahigh molecular weight polyethylene (UHMWPE), 94, 95, 99, 101–103, 108, 109, 111, 115, 191
Ultrasonication, 60, 76, 161, 165, 168, 404, 467
Ultrasonic irradiation treatment, 457
Ultrasonic processor, 359
Ultrasonic vibration, 168, 426, 553
Ultrasonic vibration assisted minimum quantity lubrication (UMQL), 426
Ultrasonic waves, 158, 159
Ultrasound, 15, 160, 393, 457, 458, 470
Ultraviolet curing, 13
Ultraviolet (UV) radiation, 160, 162, 412
Ultraviolet-visible spectroscopy (UV-vis), 123, 159, 162
Underground water, 491, 492
Unidirectional laminates, 99, 111
Unit cell, 130, 135, 144, 149, 164
Unit cost method, 318
Unsaturated fatty acid, 606–609, 611, 613, 617
Unsaturated resin, 190
Unzipping, 395
UV, 50, 54, 123, 168, 171, 412, 474
UV irradiation, 51, 172
UV light, 153, 161
UV photons, 160
UV rays, 160
- V**
Vacuum, 5, 14, 41, 319, 358, 399, 428, 543, 557, 587
Vacuum infusion process, 106
Van der Waals force, 11, 277, 392, 464, 498, 520
Vascular, 130, 147
Vascular engineering, 170
Vascular scaffolds, 170
VAT polymerization, 126, 154, 176
Vector, 158, 413
Vegetable oil, 275, 425, 426, 428, 429, 432, 601–611, 613–617
Vehicle efficiency, 343
Velocity, 96, 98–108, 111, 113, 236, 355–357, 362, 386, 440, 444
Versatile method, 161
Veterinary, 492
Vickers hardness, 320
Vinyl acetate, 94, 284
Vinyl ester, 5, 23, 495
Vinyl bonds, 604, 607, 610, 617

- Vinyl groups, 601, 604
 Vinyl monomer, 601–603
 Viscoelastic, 5, 282
 Viscoelasticity, 280
 Viscosity, 13, 151, 161, 165, 293, 402, 432, 442
 Visible, 106, 123, 295, 370, 371, 379, 386, 444, 617
 Void, 64, 106, 134, 176, 317, 325, 326, 337, 338, 340, 452
 Void fraction, 320, 325, 326
 Voltage fluctuations, 566
 Voltage regulators, 566, 567
 Voltammetry, 297
 Volume fraction, 42, 43, 106, 123, 233, 237, 254, 255, 260, 261, 346, 347, 351, 355, 358, 359, 361–363, 424, 426, 493, 550, 552, 554, 555
 Voxel-based method, 134
- W**
- Waste, 158, 235, 236, 451, 452, 454–456, 458, 460, 464, 465, 467–474, 476, 478, 480–483, 507, 509, 512, 515, 519, 522, 601, 605, 617, 618
 Waste materials, 278, 454, 467, 605
 Waste removal, 452, 478
 Wastewater, 63, 79, 411, 412, 451, 464, 468, 471–476, 478, 483, 491, 615
 Wastewater treatment, 411, 451, 455, 457, 464, 471, 472, 479, 482
 Water, 5, 14, 16, 19, 23, 29, 47, 48, 51, 54, 62, 64, 67–71, 73, 74, 76, 78–84, 87, 99, 132, 147, 154, 159, 160, 245, 246, 249, 252, 273, 276–281, 283, 284, 289, 302, 320, 384, 386, 397, 399, 405, 411, 427, 451–453, 455, 456, 458, 459, 462, 464, 466, 468, 476, 478, 480, 482, 492, 499, 506, 523, 554, 555, 608
 Water solubility, 68
 Water-soluble, 523
 Wavelength, 49, 158, 160, 188, 295, 370–372, 374–377, 379, 384, 385, 387, 409
 Wave-vector, 371
 Wear losses, 236, 243, 352, 353, 355, 356, 358, 359, 362, 572
 Wear mechanisms, 317, 331, 346, 354, 427
 Wear rate, 236, 242, 249, 252, 253, 259–262, 321–323, 330, 333–336, 338–340, 347, 353–363, 424, 544, 548, 551, 575
 Wear resistance, 3, 24, 25, 48, 237, 252, 260, 318, 339, 344–347, 349, 351, 353–357, 361–363, 424, 496, 538, 541, 542, 544, 545, 550, 551, 565, 575–579, 583, 584, 590, 594, 595
 Weave, 100, 102, 103, 105, 107, 109
 Weight, 10, 11, 25, 27, 29, 45, 94, 98, 102, 114, 130, 146, 150, 167, 173, 193, 197, 234, 240, 241, 243, 246, 251, 254, 258, 278, 282, 318, 320, 326–328, 330, 331, 333, 344, 345, 355–358, 360, 394, 411, 414, 424, 428, 438, 440, 447, 540, 541, 579, 611, 612, 617
 Weight ratio, 3, 28, 187, 189, 473, 579, 583
 Welding, 127, 570–572, 574, 575, 595, 596
 Wettability, 15, 246, 254, 479, 579, 585, 587, 588, 596
 WGM radiation loss, 370
 Wheel speed, 423, 428, 432–434, 437, 438, 440, 441, 447
 Whisker-like, 543
 Whispering-gallery-mode, 369, 370
 WinXCOM, 192, 193, 201–203, 206, 207, 225
 WinXCOM software, 187, 189
 Wire drawing method, 584
 WO₃, 49, 123, 157, 191–195
 Wolfram carbide, 195, 196
 Wood, 9, 94, 143, 169, 234, 284
 Workpiece speed, 423, 428, 433, 434, 438, 440, 447
 Wound healing, 45, 280
 Woven, 98, 101–103, 110, 114
 Woven fabric, 99, 102, 103, 106, 108, 111, 113
- X**
- X-ray, 24, 191, 193–195
 X-ray curing, 13
 X-ray diffraction (XRD), 15, 16, 18, 21, 22, 293, 453, 467, 468, 470, 612, 613, 617
- Y**
- Yarn properties, 110
 Yarn pull-out force, 98, 103
 Yarns, 98, 99, 103–107, 110, 113, 114, 144
 Yield, 41, 235, 257, 258, 273, 283, 349, 427, 456, 457, 462, 470, 616
 Yield point, 145

- Yield strength, 152, 318, 344, 346, 349, 351, 424, 426, 539, 545, 547, 548, 551
- Young's modulus, 42, 100, 135, 144, 145, 160, 318, 391, 393, 395, 538, 541, 553
- Z**
- ZA-27 alloy, 317–320, 326–328, 330–332, 337, 339, 340
- Zener pinning effect, 555
- Zeolite, 451–483, 510, 512, 513
- Zeolite A, 455, 457, 458, 463, 465, 466, 468, 469, 472, 476, 480
- Zeolite-composites, 452, 473, 477–481, 483
- Zeolite-composites membrane, 476
- Zeolite-like materials, 454, 458
- Zeolite types, 455, 458, 466, 468, 470–472, 474, 482
- Zeolite X, 456, 458, 465–468, 472
- Zeolite-Y, 453, 466, 470, 472
- Zinc, 192, 319, 328, 330, 331, 333, 359, 476, 512, 523
- Zinc aluminium, 347
- Zinc-aluminum alloy, 344, 347
- Zinc aluminum (ZA-27) alloy composite, 325, 331, 335
- Zinc ions, 170
- Zinc oxide, 50, 51, 54, 124, 143, 151, 170
- Zirconia, 53, 235, 404, 459, 475, 513
- Zirconium-based (Zr) structures, 523
- ZnO, 15–20, 48, 50, 52, 53, 98, 124, 170, 279, 359, 364, 397, 400, 571, 572